9th SEATUC SYMPOSIUM

27-30 JULY 2015

SURANAREE UNIVERSITY OF TECHNOLOGY

Contents

Energy, Environment and Earth System Science

EVALUATION OF AIR QUALITY AND ITS CHANGES OVER THAILAND DURING 2002-2013 USING SATELLITE-BASED AEROSOL OPTICAL DEPTH DATA

Kasemsan Manomaiphiboon
The Joint Graduate School of Energy and Environment, King Mongkut's University of Technology Thonburi, Thailand, and
Center for Energy Technology and Environment, Ministry of Education, Thailand

ABSTRACT

The study evaluated the spatial patterns and changes in satellite-based aerosol optical depth (AOD) over Thailand during recent 11 full years (Nov., 2002 to Oct., 2013), comparing averages in the two different seasons and those in the two defined 6-year periods. The results presented and discussed include both simple average AOD and upper-tailed average AOD. AOD is a light-attenuation parameter that can be used to indicate the degree of particulate matter present in the atmosphere. Utilizing the obtained results to assess the coverage of the existing standard air quality monitoring stations in Thailand was also demonstrated, and technical suggestions for future improvement are given.

INTRODUCTION

Thailand has long made substantial and continuous efforts to have or achieve good air quality for the public (Pollution Control Department or PCD, 2013). However, industrialization, urbanization, infrastructure development, and transportation have also increased over time and then led to air pollution problems or concern of worsened air quality in many areas. Monitoring air quality conditions is essential to understand air quality in an area since it assists the identification of severity, frequency, and characteristics of air pollution.

Ground-based air quality monitoring at surface stations has become a standard practice, a network of such stations has been established in Thailand by the PCD in many provinces but does still not have a comprehensive spatial coverage. Alternatively, satellite remote sensing provides various kinds of data and information for earth sciences, including atmospheric sciences. It has some unique advantages, e.g., fast detection and large spatial coverage. In principal, a sensor on a satellite measures reflected or emitted energy from the earth, and the data is processed to derive physical or chemical quantities of interest by a specialized algorithm. In this study, aerosol optical depth (or thickness) (AOD) was considered. It is a widely used parameter that represents how much aerosols (i.e., air-borne particles or particulate matter) prevent the transmission of light by scattering or absorption (of both) of light. It is then used to determine the loading (i.e., amount) of aerosols in the atmosphere. Theoretically, it is defined as the integrated light extinction coefficient over a vertical column of unit cross section from the surface through the bulk of atmosphere. AOD generally increases over areas contaminated with air pollution, haze, smoke, or dust, but low for clean areas. It is of interest here to address how AOD across Thailand had changed in recent years by taking advantage of publicly available satellite-based AOD data. It is also hoped that the study presented here offers an alternative and simple way to evaluate air quality over an area for local air quality workers and environmental policymakers.

METHODS

The daily MODIS (Moderate Resolution Imaging Spectro-radiometer) AOD data product (Level 3) (Hubanks et al., 2008) was used here, accessible at http://ladsweb.nascom.nasa.gov. MODIS is an optical sensor on board of the NASA's earth observing satellites Terra and Aqua, each of which has a sun-synchronous (or polar) orbit around the earth. They were launched in 1999 and 2002, respectively, and are still operational today. The product has a global coverage and a horizontal grid resolution of 1 degree in latitude and longitude. AOD is derived at multiple spectral wavelengths, and AOD at 550 nm was used here. More details related to this data product and its applications can be found elsewhere, e.g., Hubanks et al. (2008), Shrestha and Barros (2010), Ruiz-Arias et al. (2013), and references therein.

A subset of the AOD-over-land data used here covers the whole of Thailand and ranging from Nov., 2002 to Oct., 2013 (i.e., 11 full years). Daily AOD derived from

both satellites were averaged grid-cell-wise. Seasonal averages and differences between two periods were computed and compared. Here, the two main seasons of Thailand (dry: Nov.-Apr. and wet: May-Oct.) and the periods of first 6 years (P1) and last 6 years (P2) were considered. In general, the wet season tends to have better air quality than the dry season because rain is well or more present, scavenging air-borne pollutants and particles from the atmosphere. In context of air quality management, large concentration of pollutant is of particular interest since it poses serious risk. It does generally not occur as frequently as small concentration. Since simple averaging over all values may balance out small and large AOD values present in a set of data, obscuring the problem. Thus, averaging over upper-tailed (i.e., very large) AOD values for each season was additionally considered. Here, the 80th percentile of daily AOD was used as the cutoff for the upper-tailed values.

RESULTS AND DISCUSSION

In Fig. 1, Bangkok and its vicinity tend to have the largest AOD, which is seen in the dry season. The grey shading in the figure (and also later figures) denotes "not computed or not averaged" due to the amount of undefined or missing values beyond a threshold (here, set to 50% of total number of days). More grey cells are seen in the wet season due mainly to more clouds present in this season, compromising the optical measurement by MODIS. AOD is mostly not large (<0.4) in the dry season but monthly variability in this season is quite large, as seen from the contrast between Mar. and Dec. in Fig. 2. For the changes in AOD from P1 to P2, both the spatial pattern and the magnitude of AOD in each of the dry and wet seasons do not change much (<0.05 in magnitude) (Figs 3 and 4). As for upper-tailed AOD, it is >0.6 for most of upper Thailand in both seasons. Note that upper Thailand comprises all regions but the southern region (Fig. 7). The wet season tends to have lower values than the dry season (Figs. 5 and 6). The largest upper-tailed AOD (>0.8) was found in Bangkok and its vicinity in the dry season. In the central and eastern regions, the positive change in upper-tailed AOD was found to be 0.025-0.1, more evident than the previous case in Fig. 3.

The above results can be utilized to address the coverage of the PCD's existing standard air quality monitoring stations (Fig. 7). First, look at the changes in AOD between the two periods (in both simple and upper-tailed averages). However, they were not found to be substantial in all cases (<0.1). Next, look at upper-tailed AOD (especially, in the dry season in Fig. 5) and also at the coverage of the station network. It is seen that the northeastern region and the lower part of the northern region have relatively large values but still not sufficiently covered by the network. This suggests that the network be extended more to these areas in the future.

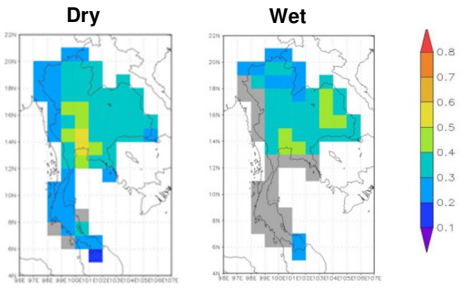

Fig. 1 AOD by season

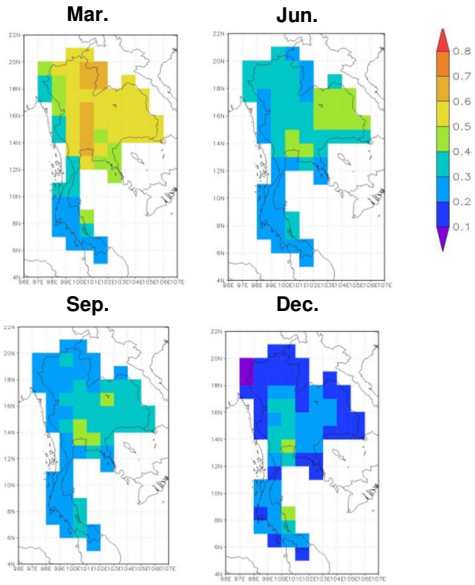

Fig. 2 AOD in Mar., Jun., Sep., and Dec.

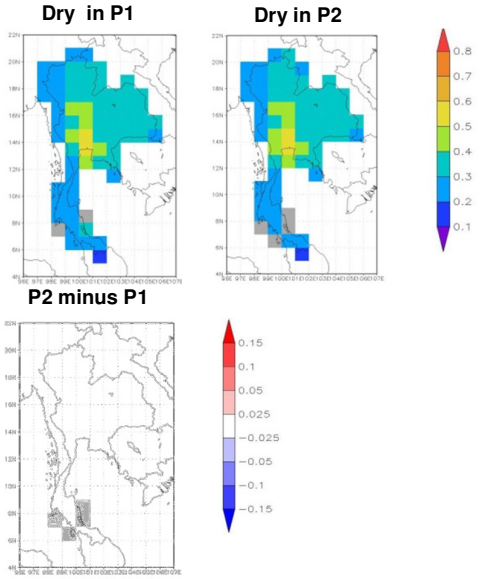

Fig. 3 Dry-season AOD in P1 and P2 and difference between the two periods

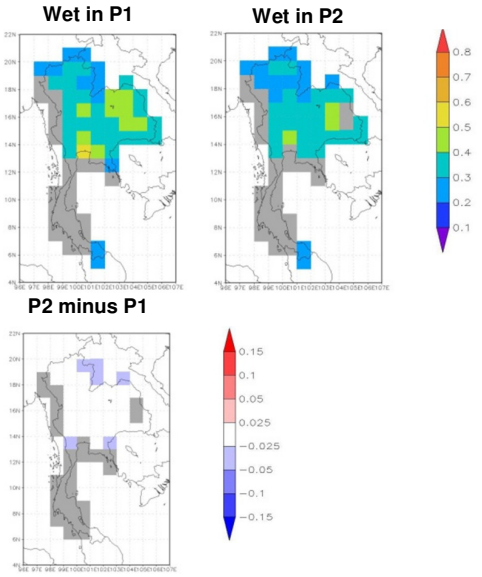

Fig. 4 Wet-season AOD in P1 and P2 and difference between the two periods

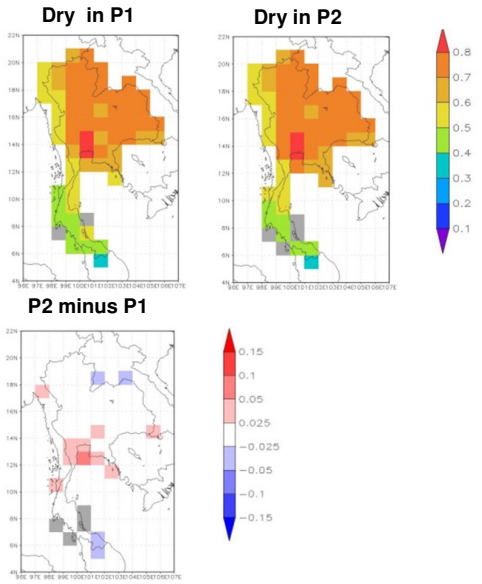

Fig. 5 Dry-season upper-tailed AOD in P1 and P2 and difference between the two periods

(Intentionally left blank)

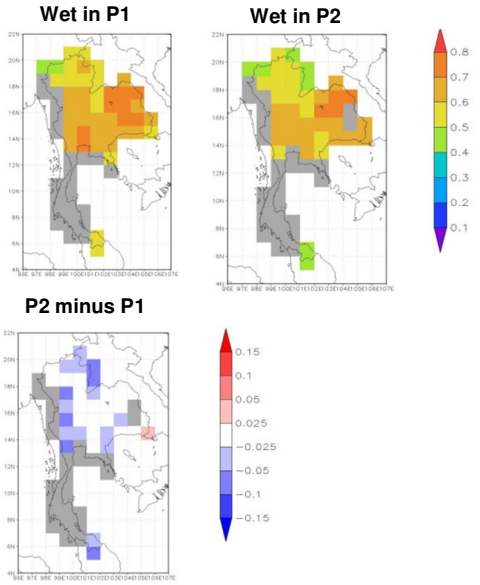

Fig. 6 Wet-season upper-tailed AOD in P1 and P2 and difference between the two periods

Fig. 7 PCD's air quality monitoring stations (solid circles) (as of 2014-2015) and the regions of Thailand.

CONCLUSIONS

The spatial patterns of 1-degree MODIS AOD were investigated over Thailand for recent 11 years by season. The degree of change in AOD between the two 6-year periods was evaluated, and both simple and upper-tailed

average AOD were considered. As seen, using the satellite-based data allowed the investigation to cover the country-wide domain. It was also shown that the results obtained can be further utilized to assess the coverage of the existing air quality monitoring stations in Thailand. Nevertheless, one should be cautioned that AOD is a column-integrated parameter and may not linearly relate to aerosol or particulate matter concentration at the surface level where humans live and most of their activities take place. This should be a next step for investigation, i.e., relating AOD and surface-level particulate matter level. In addition, due to that Terra and Aqua pass Thailand only a few times a day and do not necessarily pass over the same areas on the same day, the temporal resolution is then somewhat low, compared to an hourly resolution generally given by a standard air quality monitoring station. Another improvement to the examination will be using AOD data with a higher resolution if available.

ACKNOWLEDGEMENTS

The author thank the NASA for the publicly available MODIS AOD data and the Computational Laboratory at Bang Khun Tian Campus for assistance. This work is part of ongoing research activities supported by the Joint Graduate School of Energy and Environment (JGSEE) and the Postgraduate Education and Research and Development Office. The JGSEE and King Mongkut's University of Technology Thonburi kindly sponsor the author's symposium participation.

REFERENCES

Hubanks, P., King, M., Platnick, S., and Pincus, R., MODIS atmosphere L3 gridded product algorithm theoretical basis document. Collection 005 Version 1.1, No. ATBD-MOD-30, NASA, 2008.

PCD. State and Management of Air and Noise Pollution Problems 2010. Annual Report, Bureau of Air Quality and Noise Management, Thailand, 2011.

Ruiz-Arias, J.A., Dudhia, J., Gueymard, C.A., Pozo-Vazquez, D., Assessment of the Level-3 MODIS daily aerosol optical depth in the context of surface solar radiation and numerical weather modeling. Atmos. Chem. Phys., 13, 675–692, 2013.

Shrestha P., Barros, A. P., Joint spatial variability of aerosol, clouds and rainfall in the Himalayas from satellite data, Atmos. Chem. Phys., 10, 8305-8317, 2010.

Kasemsan Manomaiphiboon has worked for the JGSEE as faculty member since 2006.
E-mail: kasemsan_m@jgsee.kmutt.ac.th

TREND OF SURFACE OZONE OVER AN INDUSTRIALIZED COASTAL AREA IN EASTERN THAILAND AND ROLES OF METEOROLOGY

Nosha Assareh[a], Kasemsan Manomaiphiboon[a], and Thayukorn Prabamroong[a,b]

[a]The Joint Graduate School of Energy and Environment, King Mongkut's University of Technology Thonburi, and Center for Energy Technology and Environment, Ministry of Education, Thailand
[b]Environmental Technology Program, Mahasarakham University, Thailand

ABSTRACT

This study investigated the long-term (1999-2012) trend of surface ozone (O_3) in the dry season over the highly industrialized coastal area of Chon Buri (CB) province, Eastern Thailand. O_3 is an important air pollutant regulated by the Thai government, and its formation depends on both meteorological conditions and emissions of O_3 precursors. A statistical model was utilized here to formulate the relationship between O_3 and meteorological variables and also to remove (i.e., adjust) their effects on the variability in O_3. It was found that the original O_3 trend over the period considered is positive and statistically significant (at a 5% level), and so is the adjusted trend. The latter evidently indicates the O_3 problem intensified over the recent years due to emissions.

INTRODUCTION

In recent years, surface O_3 pollution has been a concern or problem in some provinces in Thailand. In the eastern region of Thailand, Chon Buri (CB) and Rayong (RY) are adjacent to the Gulf of Thailand, and their coastal areas are urbanized and highly industrialized. Air quality along the coastal areas has been known to degrade due to the continued growth of economy and industry. One of the major air quality problems found is elevated surface O_3 level (PCD 2012). O_3 is a secondary air pollutant and can be harmful to humans and plants when its concentration is high. O_3 is not directly emitted from sources but photochemically forms in the atmosphere through a series of complex reactions in the presence of its precursors, mainly nitrogen oxides (NO_x), and volatile organic compounds (VOC). A recent modeling study by Prabamroong et al. (2012) shows that O_3 in CB can be effectively managed by controlling or limiting VOC emissions from some specific industrial sources. Another study (Assareh et al., 2014) performed analysis using back-trajectory modeling and clustering and O_3 level in each of CB and RY, finding O_3 to be dependent on synoptic weather conditions.

In fact, there are several aspects of the O_3 pollution in these coastal areas, needed for investigation. In this study, we focused particularly on the coastal area of CB and attempted to examine the long-term trend of O_3. Specifically, we examined whether O_3 had increased or decreased in recent years. More importantly in context of air quality management, given both meteorology and emissions of the precursors, how the O_3 trend was affected by emissions alone?

METHODS

A set of surface observation data (both air quality and meteorology) during 1999-2012 was obtained from the Pollution Control Department (PCD). In addition, a set of meteorological data was from the Thai Meteorological Department (TMD). After some data screening and quality checking, only data from three PCD stations (P1, P2, and P3) and two TMD stations (T1 and T2) were used (Fig. 1). Since we considered the air quality over the coastal area (as opposed to a single site or location), we computed the area-based values of a particular parameter or variable (of air quality or meteorology) by simple averaging over the values pooled from all stations available, and we call them "city-wide values". Only the dry season (i.e., Nov.-Apr.) was considered because O_3 tends to elevate in this season due to its more favorable conditions (e.g., minimal rainfall, less clouds, and then strong solar radiation).

Air-mass back-trajectory modeling by the FLEXTRA model (Stohl et al., 2010) was also performed since back-trajectory information can be used to help quantify the degree of long-range transport of O_3 and its precursors. For each day, a daily trajectory was run to migrate backward in time for 3 days and driven by wind fields given by 0.5°-resolution 6-hourly CFS reanalysis data (Saha et al., 2010). The arrival time and height of each trajectory were set to 1pm and 500 m above ground level, respectively. The resulting daily back-trajectories were then clustered using R software (R development core team, 2014) into distinct groups representing distinct synoptic weather conditions of the area, as seen in in Fig.

2. Besides, the conventional meteorological parameters and back-trajectories, we derived hourly daytime mixing height using AERMET, the meteorological preprocessor of the AERMOD dispersion modeling system of the US EPA (Cimorelli et al., 1998). Daytime wind-run and recirculation factors (Allwine and Whiteman, 1994) were also calculated in order to take into account local ventilation and recirculation due to winds. For trend analysis, the average of daily daytime (10-18 LT) maximum O_3 over all days in the dry season was computed for each year, forming a time series spanning the 14-year period in question. As in Camalier et al. (2007), a generalized linear model (GLM) was utilized to formulate the relationship between daily O_3 and daily meteorological conditions, which was later used to explain the variability of O_3 in the original time series by that of meteorology. As a result, the original O_3 time series was adjusted, and its variability due mostly to emissions remains. Here, a log link function was used and a natural spline of the predictor variables (i.e., meteorological parameters) was employed to allow for non-linear response between meteorological parameters and response variable.

RESULTS AND DISCUSSION

In the GLM modeling, a number of daily meteorological variables were initially tried as potential candidates, and a final economical set was selected (Table 1). Once the GLM model was parameterized, the meteorological adjustment on the original time series was then performed to account for the variability of O_3 due to that of meteorology. The original and adjusted daily O_3 time series were then averaged for each year to get annual time series. To determine the trend and its magnitude of each of the original and adjusted times series, simple linear regression was used, and the slope of the linear fit of the model represents the trend. The statistical significance of trend (against a null hypothesis of no trend) was inspected using the non-parametric Mann-Kendall test. Fig. 3a displays the original O_3 time series, and its variability is caused by the combined effects of meteorology and emission. Its associated trend was found to be about 0.5 ppb (per year) and also significant. After the adjustment, the resulting variability is mainly due to emissions as mentioned previously, and the trend increases to about 0.8 ppb and is still significant (Fig. 3b). The latter evidently indicates that the O_3 problem had been intensified over the recent years due to emissions. Some key economic indicators reported for Chon Buri province over the same period, e.g., GPP (gross provincial product) and fuel consumption, were also examined (not shown here), which are generally used as a proxy or surrogate for emissions. It was found that their trends are also positive, which is in line with the adjusted trend of O_3 and then confirms a need to manage O_3 over CB through emission controls.

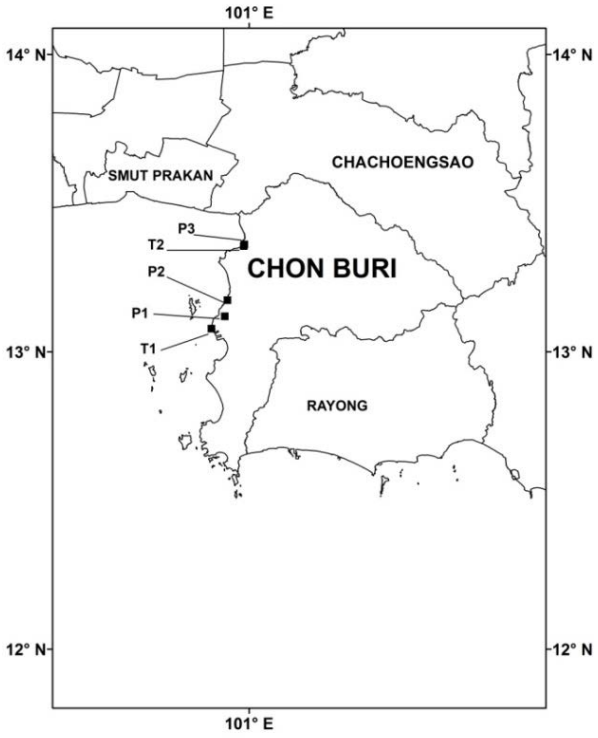

Fig.1 Chon Buri province and the monitoring stations

Table 1. Final parameters selected in the statistical model

Parameter
Daily daytime maximum temperature
Daily daytime average relative humidity
Daily daytime average cloud cover
Daily daytime average mixing height
Daily daytime average sea-level pressure
Wind run
Daily rain
Recirculation factor
Back-trajectory cluster

(Intentionally left blank)

a) Daily simulated trajectories

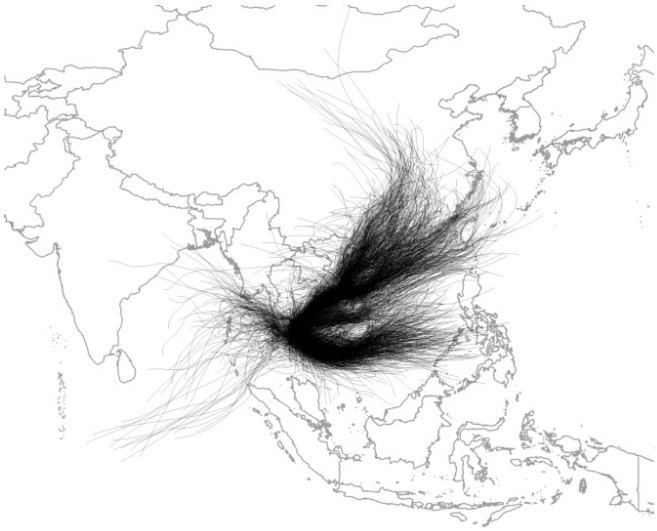

b) Back-trajectory clusters

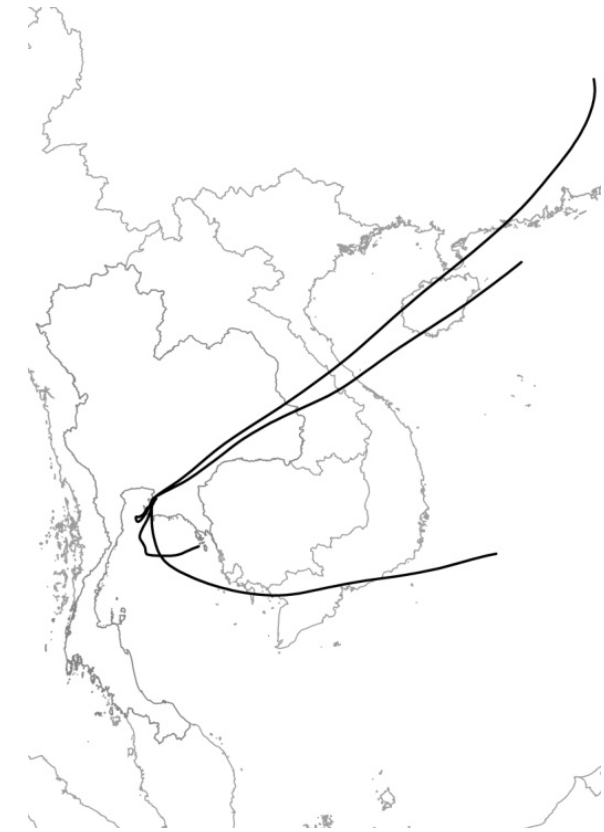

Fig. 2 Simulated back-trajectories

(Intentionally left blank)

a) Original

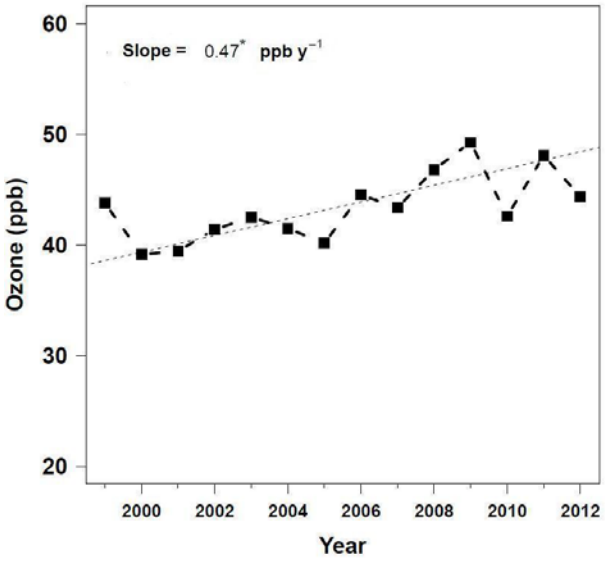

b) Adjusted

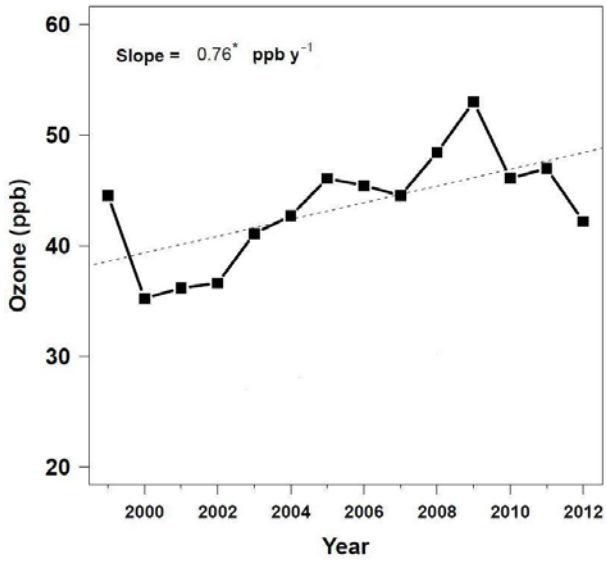

Fig. 3 Original and adjusted O_3 trends. The asterisks denote "statistically significant".

CONCLUSIONS

The long-term (1999-2012) O_3 trend over CB and the roles of meteorology were investigated. Using the statistical modeling (here, GLM) can relate O_3 to meteorology. Importantly, it was used to assess the variability in O_3, which is by nature masked by both meteorology and emissions. As shown here, O_3 is not constant but varies year to year in CB, like other places. With the adjustment made, the resulting trend is shown to be significantly positive, indicating the O_3 pollution worsening over the recent years due to emissions. Before ending, it is noted that the study presented here is part of

ongoing research, which may be subject for further enhancement.

ACKNOWLEDGEMENTS

The authors sincerely thank the Pollution Control Department and the Thai Meteorological Department for the observation data. The study is supported by the Joint Graduate School of Energy and Environment.

REFERENCES

Assareh, N., Manomaiphiboon, K., Prabamroong, T., synoptic circulation and ozone pollution over two major cities in eastern Thailand, Proceeding of the fifth international conference on sustainable energy and environment, Bangkok, Thailand, 2014.

Allwine, K.J., Whiteman, C.D., Single-station integral measures of atmospheric stagnation, recirculation and ventilation, Atmospheric Environment, vol. 28, pp. 713-721, 1994.

Camalier, L., Cox, W., Dolwick, P., The effects of meteorology on ozone in urban areas and their use in assessing ozone trends, Atmospheric Environment, vol. 41, pp. 7127-7137, 2007.

Cimorelli, A.J., Perry, S.G., Venkatram, A., Weil, J.C., Paine, R.J., Wilson, R.B., Lee, R.F., Peters, W.D., Brode, R.W. AERMOD: A dispersion model for industrial source applications. Part I: General model formulation and boundary layer characterization, Journal of Applied Meteorology, vol. 44, pp. 682-693, 2005.

PCD, Thailand state of pollution report 2011, 2012.

Prabamroong, T., Manomaiphiboon, K., Limpaseni, W., Sukhapan, J., Bonnet, S., Ozone and its potential control strategy for Chon Buri city, Thailand, Journal of the Air & Waste Management Association, vol. 62, pp. 1411-1422, 2012.

R Development Core Team. The R project for statistical computing. Version 3.1.0, 2014.

Stohl, A., Wotawa, G., Seibert, P., Kromp-Kolb, H., Interpolation errors in wind fields as a function of spatial and temporal resolution and their impact on different types of kinematic trajectories, Journal of Applied Meteorology, vol. 34, pp. 2149-2165, 1995.

Saha, S., et al. The NCEP climate forecast system. Bulletin of the American Meteorological Society, vol. 91, pp. 1015-1057, 2010.

Nosha Assareh is a doctoral candidate at the Joint Graduate School of Energy and Environment (JGSEE), King Mongkut's University of Technology Thonburi, Bangkok, Thailand. E-mail: nosha_assare@yahoo.com

Kasemsan Manomaiphiboon (PhD) is a faculty member at the JGSEE. E-mail: kasemsan_m@jgsee.kmutt.ac.th

Thayukorn Prabamroong (PhD) is a former graduate student and a former researcher at the JGSEE, and currently a faculty member at the Mahasarakham University. Email: thayukorn.envi@gmail.com

Highly Selective Transport of Palladium from Electroplating Wastewater using Emulsion Liquid Membrane Process

Norul Fatiha Binti Mohamed Noah[1], Norasikin Othman[2], Norela Binti Jusoh[1]

[1] Faculty of Chemical Engineering,Universiti Teknologi Malaysia, 81310 UTM Johor Bahru, Malaysia.

[2]Centre of Lipids Engineering & Applied Research (CLEAR), Ibnu Sina Institute for Scientific and Industrial Research, Universiti Teknologi Malaysia, 81310 UTM Johor Bahru, Johor.

Abstract. A new liquid membrane formulation containing phosphinic acid groups was developed for the selective extraction of palladium over chromium by emulsion liquid membrane (ELM) process from electroplating wastewater effluents. ELM system comprises of three phase dispersion system, with the primary emulsion consisting of organic and internal phase being dispersed into the feed or effluent phase, which is the phase to be treated. The extraction of palladium is attractive due to its special electric conductivity together with limited resources. It was found that 99% of the palladium can be extracted selectively using Cyanex 302 as a carrier with an acidified solution of thiourea as stripping agent. At these conditions, the extraction and of palladium from matrices solutions were successful and Cyanex 302 was found to be very selective towards palladium over chromium.

Keywords : Emulsion liquid membrane ; palladium ; chromium; electroplating waste.

1.0 INTRODUCTION

Nowadays, the uses of Palladium in electroplating industry have generated the toxic wastewater. Exposure to Palladium can cause acute toxicity or hypersensitivity with respiratory symptoms, urticaria and less frequently, contact dermatitis. Epidemiological studies have demonstrated that Palladium ions are one of the most frequent reacting sensitizers. This effect on the immune system represents the most important health hazard to humans (Iavico and Fontana, 2011).

Other than that, palladium are known to possess unique physical and chemical properties that are suitable for manufacturing industrial materials such as decorative items for jewellery and consumer hardware, battery parts, contact finishing for lead frames for IC packaging, edge card connectors, solderable contact and end terminations for multi-layered ceramic capacitors, etch resists for printed wire boards and semiconductor optoelectronic devices for packing. These applications all take benefit of palladium's lower cost and material properties, which, in many instances, are superior to gold. Therefore, the extraction of palladium is attractive due to the toxicity and its unique physical and chemical properties (Othman et al., 2014). There are a large number of separation processes applicable to recover palladium from industrial wastewater which is biosorbent, ion exchange, membrane separations, precipitation and adsorption (Park et al., 2010; Wolowics and Hubicki, 2011; Takahiko et al., 1996; Dakshinamoorthy et al., 2008; Hubicki and Wolowics, 2009) but these methods have some limitation. The development of a cheap and simple technology to treat the sludge while also recovering the palladium is required to help the industries solve their environmental problems.

Currently, one of the promising techniques is Emulsion Liquid Membrane (ELM). The simultaneous extraction and stripping operation is very attractive, because it can transport the solute of interest from a low concentration solution to a high concentration solution with suitable carrier in one step process (Othman et al., 2005). Many studies have reported the successful application of membrane processes in recovering metals from various industrial wastewaters and in generating high quality treated water for further reuse in the industry (Sugita, 1989; Chai et al., 1997; Benito and Ruiz, 2002; Eliceche et al., 2002; Othman et al., 2014; Noah et al., 2014). Therefore, the emulsion liquid membrane process has a good opportunity to be the key separation and purification operation in the future of electroplating waste treatment as these processes ensure low energy requirements and high product value.

2.0 EXPERIMENT

2.1 Reagents and solutions

There are four components in ELM system namely carrier, surfactant, stripping agent and diluent. All four components are manufactured for laboratory grade and were used as received. Cyanex 302 as a carrier for palladium was obtained from Sigma. Thiourea and Sulfuric acid was purchased from Merck (M) Sdn. Bhd.

Kerosene and span 80 as a diluent and surfactant respectively were purchased from Fluka Chemika. The apparatus used including Homogenizer Heidolph Silent Crusher M Emulsifier, Perkin Elmer Flame Atomic Absorption Spectrometer (AAS) for concentration measurement of palladium ion.

2.2 Palladium in simulated electroplating wastewater.

Palladium (II) nitrate was dissolved into real electroplating wastewater in the concentration range of 1 – 15 ppm. Initial pH of the feed phase was measured. pH for each sample was adjusted in the range of 3.0 – 3.5. In this preparation, two types of waste solutions were considered in the electroplating process, which were Waste 1 and Waste 2 for entry and exit effluents, respectively, as shown in Fig. 1.

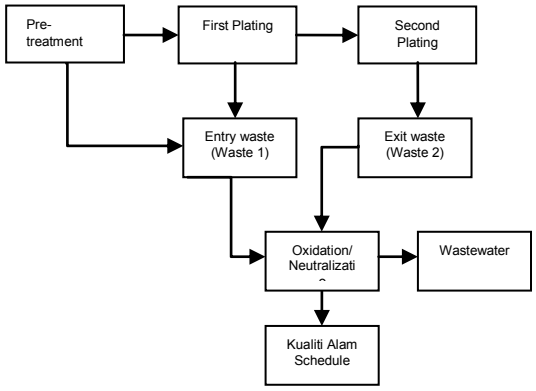

Fig. 1 Wastewater flow diagrams for electroplating process

2.3 Metal Content Analysis

All metals concentration analysis is important to characterize the simulated electroplating wastewater as well as to find out metal concentration in the liquid phase after extraction. In order to measure the metallic elements in ppm level, an Atomic Absorption Spectrophotometer (AAS), principal tool was used. A liquid phase was put in the plastic tube and placed into a flame chamber, and the flame evaporated all the liquid content. Thus, breaking all the molecules into atoms and atoms were excited into a high energy level. The concentration was measured by the absorption of light by atoms in the flame.

2.4 Experimental Procedures

The organic solution was prepared by dissolving an appropriate concentration of the carrier (Cyanex 302) and the surfactant (Span 80) in a diluent (kerosene). The internal aqueous phase was a Thiourea in H_2SO_4 solution. An equal volume of 5mL portions of organic phase and aqueous phase were stirred continuously at 12000 rpm for about 3 minutes using a motor driven emulsifier to obtain stable water in oil emulsion. The emulsion must be freshly prepared before each experiment of extraction study. The prepared emulsion then dispersed into external phase containing palladium in the agitated vessel and stirred at 200 rpm for 5 minutes. The aqueous phase was filtered in order to remove entrainment and the raffinate phases are analyzed by AAS. The volume of emulsion before and after extraction was measured for emulsion stability study. The range parameter used in the ELM extraction of palladium from simulated electroplating wastewater was listed in Table 1. The liquid membrane component for this study such as type of diluents and stripping agent and its concentration for palladium extraction are taken from previous studies (Othman et al., 2014). All experiments were performed at a room temperature (26±1 °C).

Table 1. Experimental conditions used for the preparations of ELMs (Noah et al., 2015)

Solvent	*Kerosene*
Carrier	*0.20 M Cyanex 302*
Surfactant	*2 % (w/v) Span 80*
Stripping agent (SA)	*1.0M Thiourea in 1.0 M H_2SO_4*
Extraction time (T_{ex})	*5 minutes*
Emulsifying time (T_{em})	*3 minutes*
Treat ratio (TR)	*1:3*
Homogenizer speed (S_h)	*12000 rpm*
Agitation speed (S_a)	*200 rpm*

The percentage of palladium extraction and swelling or breakage was determined by using Eq. 1 and 2:

$$\text{xtraction } (\%) = \frac{[\text{Pd}]_\text{i} - [\text{Pd}]_\text{f}}{[\text{Pd}]_\text{i}} \text{x } 100\% \qquad (1)$$

$$\text{Swelling/Breakage } (\%) = \frac{\text{V}_\text{f} - \text{V}_\text{i}}{\text{V}_\text{i}} \text{ x } 100\% \qquad (2)$$

Where,

$[Pd]_i$: Initial concentration of pd ion in aqueous before extraction

$[Pd]_f$: Final concentration of pd ion in aqueous after extraction

V_i : Initial volume of emulsion before extraction

V_f : Final volume of emulsion after extraction

3.0 RESULTS AND DISCUSSION

3.1 Metals content in simulated electroplating wastewater

Results from metal contents analysis of the electroplating waste effluents are presented in Table 2 for Waste 1 (entry) and Waste 2 (exit) waste respectively. The characterizations of the electroplating waste were carried out in order to determine the cations compositions. Results shows that only chromium exists in high concentrations in the electroplating waste 2 and the other metals exist less than 0.5 ppm.

Table 2: Metal contents in real electroplating wastes solution, Waste 1 (entry waste)

Cations	Concentration Waste 1 (ppm)	Concentration Waste 2 (ppm)
Pb	0.01	0
As	0.3	0.14
Cu	0.02	0
Fe	0.04	0.027
Ni	0.01	0
Cd	0.01	0.04
Cr	0	42.62
1 ppm Pd	1.04	1.60
10 ppm Pd	6.64	9.33
15 ppm Pd	9.35	16.03

3.2 Transport Mechanism of Palladium in ELM Process

In the ELM process, both the extraction and stripping steps occur simultaneously. The mechanism for the extraction of palladium using ELM process is based on the liquid-liquid extraction as shown in Fig. 2. In this mechanism the selected carrier, Cyanex 302 chemically reacts with the cationic palladium in kerosene to form complexes of Pd-Cyanex 302 at the membrane-external interphase (Othman et al., 2014).

After that, the Pd-Cyanex 302 complexes diffuse through the membrane phase from the membrane-external interphase to the membrane-internal interphase. Then, the Pd-Cyanex 302 complexes at the membrane-internal interphase undergo the stripping process by reacting with acidic thiourea from the internal phase. The Pd-thiourea complexes released to the internal phase and the carriers diffuse back to the membrane-external interphase to react with other Pds.

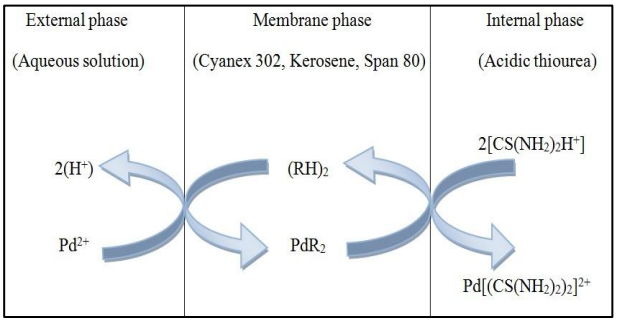

Fig. 2 Schematic transport mechanism of pd by ELM from the aqueous solution using Cyanex 302.

3.3 Extraction of Palladium from Waste 1

The extraction efficiency of palladium was examined by dissolving the metal in simulated electroplating solution (entry waste) as depicted in Table 3. The results show that at low initial palladium concentrations (1ppm), the percentage of extraction is high. This is owing to the low Pd ion concentration as compare to larger amounts of carrier. But when the initial concentration of palladium is increased, the degree of metal extraction decreased slightly, which is coherent with the necessary amount of carrier to transport a larger quantity of metal. Its decrement might be attributed to the possible swelling of emulsion due to differences in ion strength and osmotic pressure between the two phases that partly hinder against solute transfer. In addition, the saturation of internal droplets in the peripheral region of the emulsion is achieved faster for high concentrations in the external solution. Hence, diffused Pd-Cyanex 302 complexes cannot be stripped in the internal phase. As a result, extracted Pd (Pd-Cyanex 302 complexes) had accumulated in the membrane phase and no carrier had diffused back to react with Pd. The solute moves toward the emulsion globules by diffusion. At low initial solute concentrations, since driving force for the mass transfer is low, the molecules take a longer time to reach the emulsion globules. However, this is compensated by the increased distribution coefficient by increasing the initial palladium concentration. Thus, the Pd dissolves rapidly in the membrane phase, resulting in faster extraction. Conversely, although the increased palladium concentration results in faster diffusion toward the emulsion globules, the extraction rate decreases owing to a decreased distribution coefficient. Moreover, at high Pd concentrations, the internal droplets in the peripheral region are more readily saturated with the solute. Since the degree of extraction increases with the decrease in palladium concentration, thus it can be conclude that formulation for Pd ELM is more suitable for palladium removal and recovery selectively from dilute aqueous solutions.

Table 3 Percentages of palladium extraction at various initial feed solutions from simulated electroplating solutions Waste 1 (entry) (Experimental conditions: pH of external phase = 3.30; and T = ± 26 ºC)

Initial [Pd] (ppm)	Extraction (%)
1	95
10	82
15	72

3.4 Extraction of Palladium from Waste 2

In order to investigate the selectivity of Pd from others metals, various initial concentrations of palladium in simulated electroplating wastewater (exit waste) were used and the results were obtained as shown in Table 4. The results presented showed that Cyanex 302 is very selective to palladium over chromium.

Table 4 Extraction and recovery percentage of palladium and chromium at various initial feed solutions from simulated electroplating solutions Waste 2 (exit) (Experimental conditions: pH of external phase = 3.27 and T = ± 26 ºC)

Initial feed phase concentration (ppm)		% Extraction
1	Pd	97.25
	Cr	6.71
10	Pd	98.85
	Cr	0
15	Pd	75.86
	Cr	2.79

The chromate ion may exist in the liquid phase in different ionic forms ($HCr_2O_7^-$, CrO_4^{2-}, $Cr_2O_7^{2-}$, $HCrO_4^-$). $Cr_2O_7^{2-}$ anions dominate in acidic chromium (VI) water solutions. According to Lewis acid base theory, soft acid-soft base (Pd-Cyanex 302) interactions are stronger than hard acid-soft base (Cr-Cyanex 302) interactions. In addition, sulphur substitution of Cyanex 302 causes this extractant acidity to increase, making them particularly suitable for the extraction of soft Lewis acid metal ions such as Pd (II) which are in accordance with the HSAB principle (Pearson, 1963). In addition, organics sulphides are selective for Pd over all other metals except gold (Du and Preston, 2002). The extraction efficiency decreases with the increase of palladium concentration from 1 to 15 ppm. It is because internal droplets achieve its saturation conditions. When the initial Pd concentration increases, the peripheral droplets are fast to exhausted, requiring the

Pd to permeate deeper within the globule prior to being stripped.

4.0 CONCLUSION

The findings of this study can be concluded as the extraction and of palladium from simulated electroplating wastewater were successful and Cyanex 302 was found to be very selective towards palladium over chromium. Since the degree of extraction and recovery increases with the decrease in palladium concentration it may be concluded that formulation for Pd ELM is more suitable for palladium removal and recovery selectively from dilute aqueous solutions within 1 to 10 ppm and from real matrices solutions with chromium.

5.0 ACKNOWLEDGEMENT

The authors would like to acknowledge the Ministry of Higher Education (MOHE) and Universiti Teknologi Malaysia for financial support to make this research possible.

REFERENCES

Lavicoli, I. and L. Fontana. (2011). "Palladium: Exposure Uses, and Human Health Effects." *Encyclopedia of Environmental Health*. O. N. Editor in Chief: Jerome Burlington, Elsevier: 307-314.

Othman N., N. F. M. Noah, N. Harruddin, N. A. Abdullah, S. K. Bachok. 2014. Selective extraction of Palladium from Simulated Liquid Waste Solution by Emulsion Liquid Membrane process using D2EHPA as a Mobile Carrier. Jurnal Teknologi.

Park, J., S. W. Won., J. Mao., I. S. Kwak., and Y. S. Yun. 2010. Recovery of Pd(II) from hydrochloric solution using polyallylamine hydrochloride-modified *Escherichia coli* biomass. *Journal of Hazardous Materials*. 181(1-3): 794-800.

Wolowics, A. and Z. Hubicki. 2011. Comparison of strongly basic anion exchange resins applicability for the removal of palladium(II) ions from acidic solutions. *Chemical Engineering Journal*. 171(1) : 206-165.

Takahiko, K., G. Masahiro. and N. Fumiyuki. 1996. Separation of platinum and palladium by liquid surfactant membranes utilizing a novel bi-functional surfactant. *Journal of Membrane Science*. 120(1): 77-88.

Dakshinamoorthy, A., P. S. Dhami., P. W. Naik., N. L. Dudwadkar., S. K. Munshi., P. K. Dey. and V. Venugopal. 2008. Separation of palladium from high level liquid waste of PUREX origin by solvent extraction and precipitation methods using oximes. *Desalination*. 232(1-3): 26-36.

Hubicki, Z. and A. Wołowicz. 2009. Adsorption of palladium(II) from chloride solutions on Amberlyst A 29 and Amberlyst A 21 resins. *Hydrometallurgy*. 96: 159–165.

N. Othman, H. B. Mat and M. Goto. 2005. Selective Extraction of Silver From Liquid Photographic Waste. *Journal of Solvent Extraction Research and Development Japan*. 12: 27-34.

Sugita, N. (1989). Process and Apparatus for Recovery of Precious Metal Compound, US Patent 4880511.

Chai, X., Chen G., Yue P. L. and Mi Y. (1997). Pilot scale membrane separation of electroplating wastewater by reverse osmosis. *Journal of Membrane Science.* 123, 235–242.

Benito, Y. and Ruiz M. L. (2002). Reverse osmosis applied to metal finishing wastewater. *Desalination.* 142, 229–234.

Eliceche, A. M., Corvalan S. M. and Ortiz I. (2002). Continuous operation of membrane processes for the treatment of industrial effluents. *Computers & Chemical Engineering.* 26, 555–561.

N. Othman, N.F. Noah, R.N.R. Sulaiman, N.A. Abdullah, S.K. Bachok, 2014. Liquid-liquid extraction of palladium from simulated liquid waste using phosphinic acid as a carrier, Jurnal Teknologi. 68:41-45.

Noah N. F. M, N. Othman, S.K. Bachok and N. A. Abdullah. 2015. Palladium Extraction Using Emulsion Liquid Membrane Process – Stability Stud. Abdullah Advanced Materials Research. 1113:376-381.

Pearson R. G. (1963). Hard and soft acids and bases. *Journal of American Chemical Society*. 85, 3533-3543

Du Preez, A. C.; Preston, J. S. 2002. The solvent extraction properties of di-n-hexyl sulphoxide in relation to the refining of platinum-group metals. International solvent extraction conference, eds. K. C. Sole, P. M. Cole, J. S. Prestonand D. J. Robinson. 2:896-901.

Norul Fatiha Binti Mohamed Noah received B.E (2011). She just finished her M.E (2015) at Universiti Teknologi Malaysia. Her main interest is Liquid Membrane Separation of metals from wastewater.

Assoc. Prof. Dr Norasikin Othman received the M.E (1999), D.E (2006) at the Universiti Teknologi Malaysia. She is a dedicated lecturer in the Department of Chemical Engineering, Faculty of Chemical Engineering. Dr. Norasikin's main research is solute/metals extraction from liquid wastes solution using emulsion liquid membrane process and solvent extraction processes.

Norela Binti Jusoh received B.E (2012). She is a pHD student at Universiti Teknologi Malaysia. Her main interest is Liquid Membrane Separation of succinic acids from pineapple waste.

MONITORING OF SUSPENDED SEDIMENT AND NITROGEN TRANSFORMATION IN SAIGON RIVER

Truong Anh Tuan[1], Tran Hong Duc[1], Nguyen Tan Phong[1*], Julien Némery[2]
[1]Ho Chi Minh City University of Technology, Vietnam
[2]Grenoble-INP, France
[*]Email: ntphong@hcmut.edu.vn

ABSTRACT

Currently the environmental monitoring stations along the Saigon River from upstream to downstream mainly focus on analyzing the pollution parameters such as pH, BOD, COD, turbidity, SS, TN, TP, and Coliform. There is no further research into indicators of nitrogen transformation in form of $N\text{-}NH_4^+$, NO_3^-, NO_2^-, and TKN. In this study we have monitored nitrogen transformation of sampling samples from upstream to downstream at 5 locations namely Ben Cui, Ben Suc, Phu Cuong, Binh Phuoc, and Phu An. Analysis of parameters such as suspended sediment (SS), $N\text{-}NH_4^+$, NO_3^-, NO_2^-, and TKN. At each location three level of water depth was taken at 1m depth (surface water), 3m (between water layer), 5m (bottom water layer) from the parameters that assess pollution compared with the national technical standards for surface water QCVN 08: 2008/BTNMT, assess the degree of contamination of the above parameters. The result of monitoring of SS and nitrogen transformation at 5 locations show that of change in level of pollution parameters of nitrogen and the correlation between parameters, since it found the research approach to study the parameters to minimize pollution in Saigon River.

Keywords: Suspended sediment, nitrogen transformation, Saigon River.

1. INTRODUCTION

The Saigon River is a river in Southern of Vietnam. It begins at Dau Tieng Lake near the bounder country of Cambodia. The river flows south and south-southeast for about 150 kilometers. Most of the rivers in the Mekong Delta region have a water-table and canal connection. The system of rivers and canals for southern Vietnam helps with water transport for commercial activities (Nguyen, 2009). The water supplies many businesses and agricultural (farm) operations.

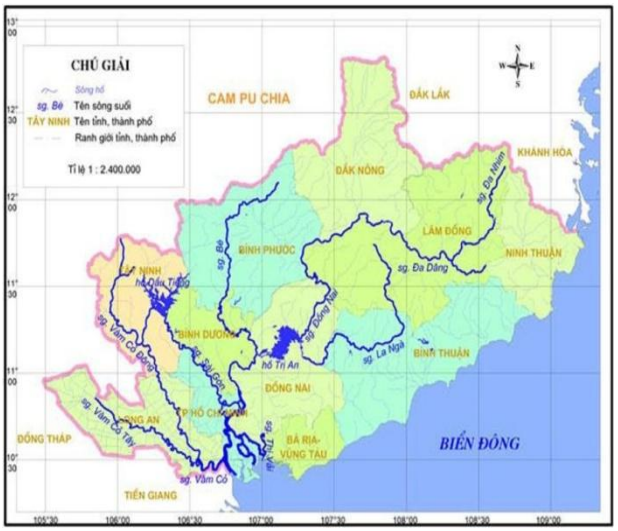

Figure 1 Saigon river valley

Saigon River is so important in providing the water for both domestic and industry activities in area of Saigon city, it is still the source for Tan Hiep water treatment plan (Bao, 2011). However, in the recent years, the Saigon water quality have been nearby decreased seriously because of the discharged sources from humans as domestic, hospital, industrial waste water, the oil leakages from aquatic traffics, landfill sites and agricultural activities. Among those problems, domestic waste water is the highest polluted source, many indicators excess the permit level, rising high each year as the organic excess double time, ammonium excesses eightfold to tenfold, and microorganism concentration always excess five to seven time the permission. Domestic waste water usually considers high suspended sediment (SS) and nitrogen concentration so when discharged to river; the SS and nitrogen concentration in river will rise high. For that reason, the monitoring of SS and nitrogen transformation

process and its effect to water quality in Saigon River will be assessed.

2. MATERIALS AND METHODS

2.1. Sampling

Sampling samples at 5 locations from upstream to downstream of the Saigon River is shown in Figure 2. At each location 3 samples taken at three different depths: 1m (surface water), 3m (between water layer), 5m (lower water layer). The analysis parameters are shown in Table 2. After the analysis is completed the pollution parameters of each position are compared with the national technical standards for surface water QCVN 08: 2008 / BTNMT show in Table 3.

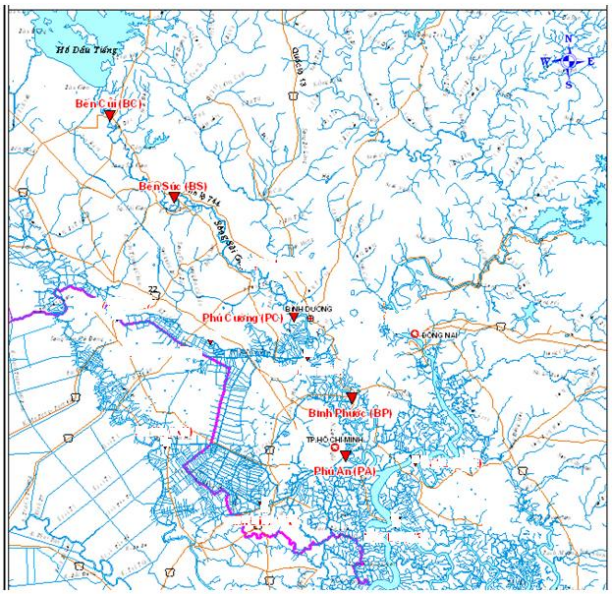

Figure 2 Sample sites in Saigon River

Table1 Sampling location monitoring

No	Location	Coordinates X:Y
1	Ben Cui	1247309.317:0066095.124
2	Ben Suc	1233622.941:0076586.136
3	Phu Cuong	1214431.400:0097624.549
4	Binh Phuoc	1201235.506:0105793.589
5	Phu An	1193533.254:0105358.637

Table 2 Analytical indicators

No	Indicators	Unit
1	pH	-
2	Temperature	^oC
3	Suspended sediment (SS)	mg l^{-1}
4	Nitrite (NO_2^-)	mg l^{-1}
5	Nitrate (NO_3^-)	mg l^{-1}
6	Amonia (NH_4^+)	mg l^{-1}
7	Total Kjeldahl Nitrogen (TKN)	mg l^{-1}

Table 3 National technical regulations surface water quality

Parameter Pollution	SS (mg l^{-1})	NH_4 (mg l^{-1})	NO_3 (mg l^{-1})	NO_2 (mg l^{-1})
QCVN 08:2008/BTNMT A1	20	0.1	2.0	0.01

2.2 Analysis

The analysis of indicators in Saigon River samples is based on the base on document of Standard Methods for Examination of Water and Wastewater 19th APPHA, 1998 show in table 4. The indicators of ammonium, TKN, nitrite, nitrate are concerned to assess the nitrogen concentration in Saigon River.

Table 4 Indicators and analytical methods

Indicator	Analytical method	Tools & equipments
pH	Direct measurement	Toledo pH probe combined with sensor
SS	Measuring the mass variance of filter paper before & after filtration	Analytical balance, vacuum filter, filtered paper and drying oven
$N\text{-}NH_4^+$	Distillation, column titration	Kjeldahl distiller, burette
TKN	Distillation, column titration	Kjeldahl distiller, burette
$N\text{-}NO_2^-$	Colorimetric	DR2800 spectrophotometer
$N\text{-}NO_3^-$	Colorimetric	DR2800 spectrophotometer

3. RESULTS AND DISCUSSIONS

Results of the analysis of indicators SS, NH_4, NO_3, NO_2, TKN of the 5 locations at Ben Cui, Ben Suc, Phu Cuong, Binh Phuoc, Phu An is shown in Figure 3, Figure 4, Figure 5, Figure 6, Figure 7 and Table 5.

Target SS in the watershed is the lowest position at the Ben Cui SS = 2-3 mg l^{-1} while SS in place of Ben Suc is the highest SS = 22-58 mg l^{-1}. SS concentration tends to increase gradually from upstream to downstream.

Particularly, in place of Ben Suc and Binh Phuoc are much higher than other positions at 3 meters depth because Ben Suc water flow rate is very high. On the other hand, Ben Suc position gets wastewater from industrial factory and household that discharged to the river without proper treatment.

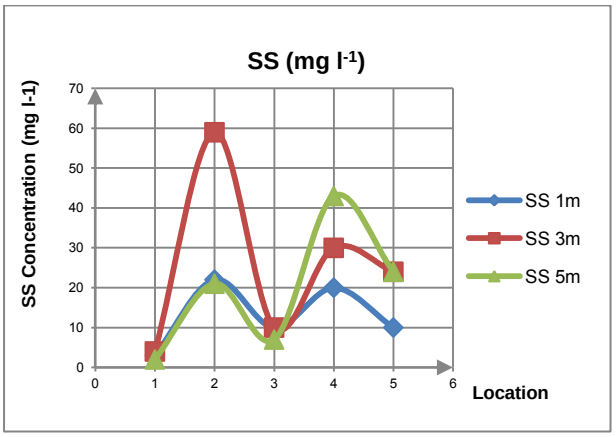

Figure 3 Graph the change of SS

Target position in the Ben Cui NH_4 is lowest NH_4 = 1.12 mg l^{-1}. NH_4 position in Phu An is highest NH_4 = 3.36 mg l^{-1}. NH_4 increased from upstream to downstream. Phu An is the main station receive so much domestic wastewater discharged from household in Ho Chi Minh City.

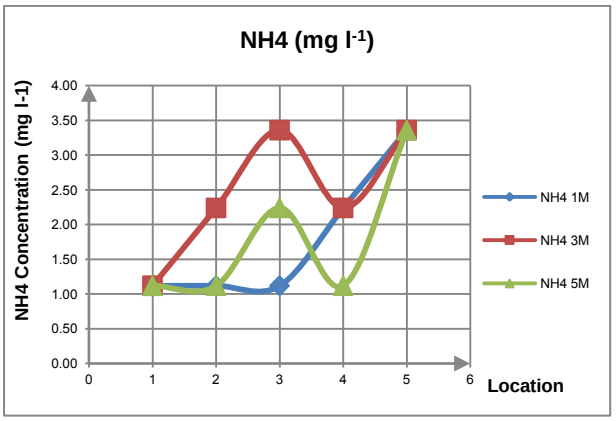

Figure 4 Graph the change of NH_4

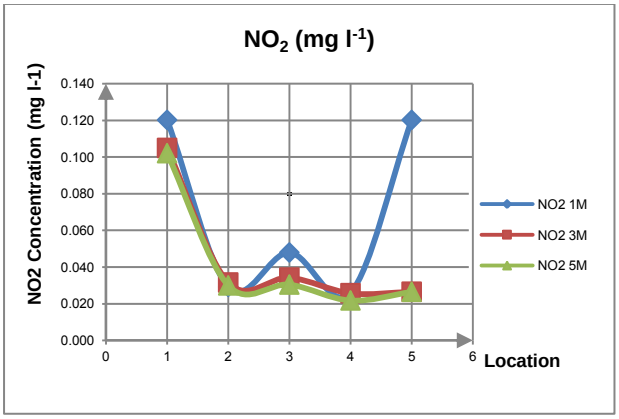

Figure 5 Graph the change of NO_2

Target NO_2 in position upstream is highest at Ben Cui NO_2=0.1-0.12 mgl^{-1}. NO_2 tend to decrease downstream. Lowest position is in Binh Phuoc NO_2 =0.02-0.03mg l^{-1}. The NO_2 is lowest at downstream because an amount of NH_4 is converted to NO_2 by ammonium oxidation bacteria (AOB).

Target position in the upstream NO_3 is high NO_3 = 0.94-1.1 mg l^{-1}. The lowest is Ben Suc NO_3 = 0.56-0.66 mg l^{-1}. From the position of Ben Suc downstream, the NO_3 tend to increase because NO_2 is converted to NO_3 by nitrite oxidation bacteria (NOB).

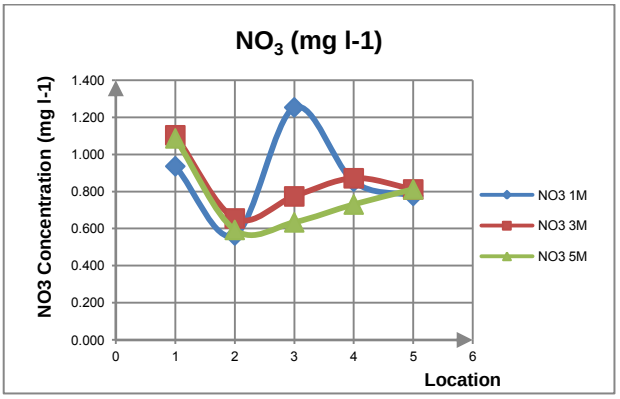

Figure 6 Graph the change of NO_3

Target position in the Ben Cui TKN is the highest, TKN = 5.6-6.72 mg l^{-1}. The lowest is Ben Suc, TKN = 3.36-4.03 mg l^{-1}. From the position of Ben Suc to downstream, TKN tends to increase. The TKN at Ben Cui is highest because Ben Cui is the upstream so the nitrogen discharge at the first form of organic and NH_4.

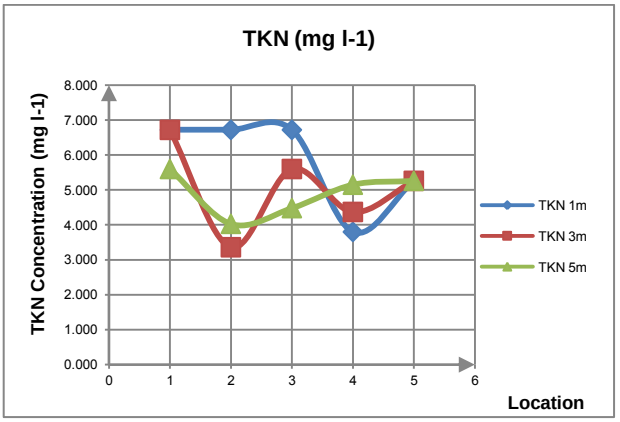

Figure 7 Graph the change of TKN

The pollution parameters at the depth of 3m and 5m changed very less and the graphs of concentration for each sampled location get the same trend.

The concentration of pollution parameters at 1m depth changes so different when comparing with the depth of 3m, 5m.

According to the previous studies on parameters of water pollution, parameters of pollution concentration usually increase from upstream to downstream due to water from Dau Tieng Lake get low pollution level, but when flowing to downstream, because of human activities in discharging wastewater (domestic and industrial wastewater) into the river so causing the rising the concentration of pollutants in river water (Ha, 2008 a) and (Ha, 2008 b). In fact, when observing in the location from upstream to downstream, some target positions at the middle source get the pollution concentrations higher than the upstream and downstream. The reason can be due to the stretch at the sampling location get wastewater sources that directly discharged without treatment into the river, causing the occur of pollution levels locally; the flow of the tide that flows from upstream to downstream or from downstream to upstream; or the river water is high or low during sampling process, the flow rate velocity.

Table 5 Results of the analysis

No	Location	Depth (m)	Parameter Pollution				
			SS mg l^1	NH_4 mg l^1	NO_2 mg l^1	NO_3 mg l^1	TKN mg l^1
1	Ben Cui	1	3	1.12	0.12	0.94	6.72
		3	4	1.12	0.11	1.10	6.72
		5	2	1.12	0.10	1.09	5.60
2	Ben Suc	1	22	1.12	0.03	0.56	6.72
		3	59	2.24	0.03	0.65	3.36
		5	21	1.12	0.03	0.59	4.03
3	Phu Cuong	1	10	1.12	0.05	1.25	6.72
		3	10	3.36	0.03	0.77	5.60
		5	7	2.24	0.03	0.63	4.48
4	Binh Phuoc	1	20	2.24	0.03	0.85	3.80
		3	30	2.24	0.03	0.87	4.37
		5	43	1.12	0.02	0.73	5.15
5	Phu An	1	10	3.36	0.02	0.78	5.26
		2	24	3.36	0.03	0.81	5.26

Compared with the national technical standards for surface water QCVN 08: 2008 / BTNMT the NH_4, NO_2 at positions are sub-standard. SS position at Ben Cui, Phu Cuong is to set standard.

At the location of Ben Suc, Binh Phuoc, Phu An is sub-standard. NO_3 at all locations are sub-standard. All the form of nitrogen transformation is varied depend on speed velocity, flow rate, water depth, organic, nitrogen, tide wave, and suspended sediment at each position.

4. CONCLUSION

SS and NO_3 concentrations in the Saigon River water from upstream to downstream is very good, lower than QCVN 08: 2008 / BTNMT. The concentration of NH_4, NO_2 is higher than the QCVN 08: 2008 / BTNMT. SS concentration in the position of Ben Suc is very high compared to other places but the parameters NH_4, NO_3, NO_2, and TKN are lower than other positions.

There may be a negative correlation between SS and NH_4, NO_3, NO_2. This may be due to suspended solids concentrations can affect the metabolism of NH_4, NO_3, NO_2. The research opens the correlation such as research on the impact of suspended sediment on nitrogen metabolism in the Saigon River.

REFERENCES

Nguyen, T.V.H., Integrated Study on Factors Affecting Water Quality of the Saigon River System in Vietnam. PhD thesis, The University of Tokyo, Japan, 2009.

Bao, T., Study of Dynamic Mode Marine and Estuarine Water Quality Zone Saigon - Dong Nai, PhD thesis, Institute of Meteorology Hydrology and Environment, 2011.

Ha, N. T. V., Takizawa, S., Hang, N. V. M., Phuong, P. T. D. Assessment and control of main pollutants for Saigon River, Vietnam. The first international conference for Environment and Natural Resources on Environmental Protection for Urban and Industrial Zones to International Integration, Ho Chi Minh City, Vietnam, 20-28, 2008a.

Ha, N.T.V., Hang, N.V.M., Phuong, P.T.D., Takizawa S., Assessment and control of main pollutants for Saigon River, Vietnam. The First international conference for Environment and Natural Resources on Environmental Protection for Urban and Industrial Zones to International Integration, ICENR 2008, HCMC, Vietnam, 125-134, 2008b.

Laboratory Assessment of Healing of Fractures in Rock Salt under Stresses and Elevated Temperatures

Prueangprach Charoenpiew, Kittitep Fuenkajorn, and Decho Phueakphum
Geomechanics Research Unit, Institute of Engineering,
Suranaree University of Technology

ABSTRACT

Healing tests have been performed to assess the healing effectiveness of rock salt fractures as affected by the applied stress, fracture types, temperatures and healing time for analyzing the structure stability in storage salt caverns. The effort involves healing tests under constant axial loading from 0.5, 1.0, 1.5 and 2.0 MPa. The temperatures are varied from 25, 70, 150 to 200°C. The ultra-sonic waves, P-wave and S-wave are monitored on healed fractures under axial loading for every 7 days throughout 56 days. The point load tests on the healed fractures have been compared with intact rock salt to determine the healing effectiveness under various test conditions. The results show that, the healing effectiveness increases with increasing healing time and axial stress, and slightly increases with temperature.

1. INTRODUCTION

The challenge on the underground facilities related with salt mining such as solution cavern for storage technology (such as compressed-air energy storage, natural gas storage, nuclear waste disposal in salt mining) is that the cracks or fractures induced by naturally occurring and the damage during excavation may cause instability of the surrounding salt and leakage of storage materials from cavern. The change of pressure and temperature during pressure release from the compressed-air cavern can induce and propagate fractures in salt around the cavern. The temperature induced by the chemical reaction from waste has an effect on mechanical stability of the storage cavity. The healing of rock salt fractures around air or gas storage caverns also affects the designed storage capacity and the mechanical stability of the caverns (Katz & Lady, 1976). However, the micro-cracks and fractures can be recovered or healed when subjected to sufficiently under confinement (hydrostatic and non-hydrostatic) and temperatures. When cracks are closed, permeability can be reduced by several orders of magnitude (Renard, 1999). The size reduction of the micro-cracks can increase the salt stiffness and strength (Miao, et al., 1995). Fuenkajorn & Phueakphum (2011) performed the laboratory to assess the healing effectiveness of rock salt fractures as affected by the stress conditions, fracture types, and time. The effort involved healing tests under uniaxial and radial pressures, gas flow permeability tests to monitor the time-dependent behavior of the salt fractures, and point loading and diameter loading tests to assess the mechanical performance of the fractures after healing. The results suggest that the primary factors governing the healing of salt fractures are the origin and purity of the fractures, and the magnitude and duration of the fracture pressurization. Inclusions or impurities significantly reduce the healing effectiveness. The hydraulic conductivity of the fractures in pure salt can be reduced permanently by more than 4 orders of magnitude under the applied stress of 20 MPa for a relatively short period. However, they performed only for short period and do not consider the influencing of temperature during the fracture healing. The objectives of this study have focused on the healing of rock salt fractures under high temperature and long-term duration on saw-cut surfaces and tension induced fractures. It can reveal how to prevent the leakage of the nuclear waste or chemicals which may affect the environment in and surrounding areas by the mechanisms of fracture healing under such conditions. This paper presents the initial results, discussions, and some conclusions.

2. SAMPLES PREPARATION

The salt specimens used were drilled from the Middle and Lower members of the Maha Sarakham Formation in the Khorat Basin, northeast of Thailand. The core specimens were from depths ranging between 250 and 400 m. The drilling was carried out by the Siam Submanee Co., Ltd. The cores are dry-cut to obtain cylindrical shaped specimens with nominal dimensions of 48 mm diameter and 72 mm length. The average density is measured as 2.20 ± 0.02 g/cm^3. Specimens with smooth fracture are simulated by using saw-cutting surfaces. To obtain the tension-induced fractures, the

cylindrical specimens are subjected to point loading or diameter loading (Brazilian tension test) (Fig. 1). The point-loaded fracture is normal to the specimen axis, and is prepared for healing under uniaxial loading tests. The aerial percentage of the inclusions is calculated with respect to the total fracture area. These inclusions included all associated and foreign minerals or materials that are not sodium chloride. The sample preparation and test procedures followed as much as practical the ASTM standard practices (i.e. ASTM D2938, ASTM D3967, ASTM D4543 and ASTM D5731).

3. HEALING UNDER UNIAXIAL TEST

3.1 Healing under Uniaxial Loading

Two types of salt fractures are simulated in the laboratory: 1) tension-induced fractures and 2) fractures formed by saw-cut surfaces. All fractures are well mated. The loading schemes are employed to assess the healing behavior of the salt fractures. The applied normal stresses are maintained constant at 0.5, 1.0, 1.5 and 2.0 MPa on the tension induced fractures under dry conditions. For salt specimens under elevated temperatures, they are wrapped with heating tape, foil and insulator throughout the test (Fig. 2). The specimen temperatures are assumed to be uniform and constant with time during the mechanical testing (i.e., isothermal condition). The temperatures on fractures healing are selected as 25 and 200°C. A dead weight compression loads frame applies constant loading onto the fractures (Fig. 3). The load is removed after 7, 28, 56 days.

3.2 Point Load Tests

The point load tests on the healed fractures are performed to assess the mechanical performance of the fractures after healing (Fig. 4).

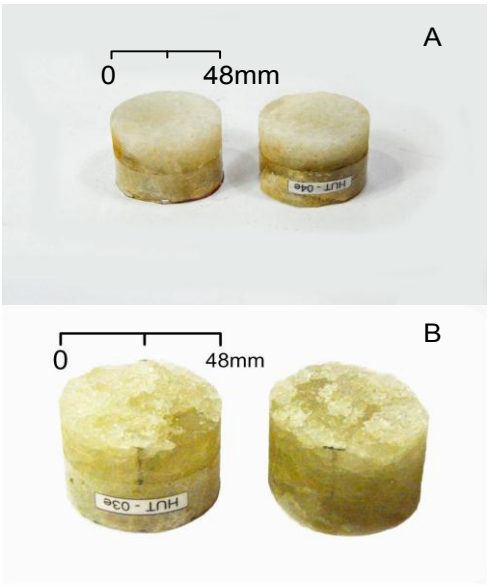

Fig. 1 Some salt specimens with normal fractures formed by saw-cut fracture (A) and tension induced fractures normal to specimen axis.

Fig. 2 Salt specimens wrapped with heating tape for elevated temperature testing.

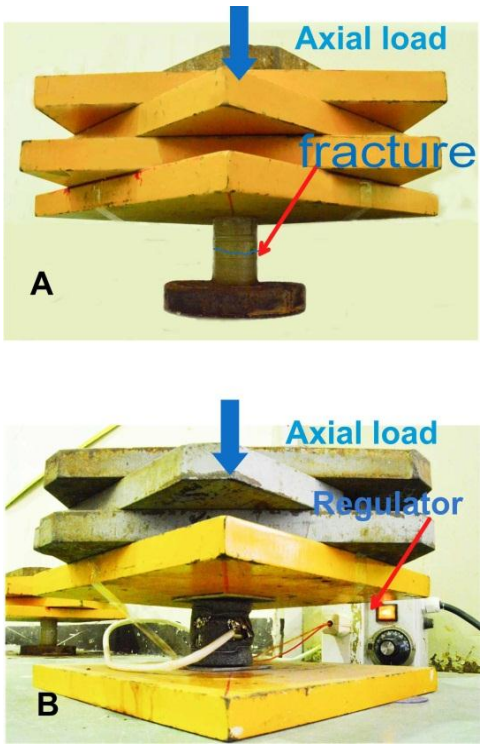

Fig. 3 Healing test under uniaxial loading (A). Healing tests under uniaxial loading and temperatures condition (B).

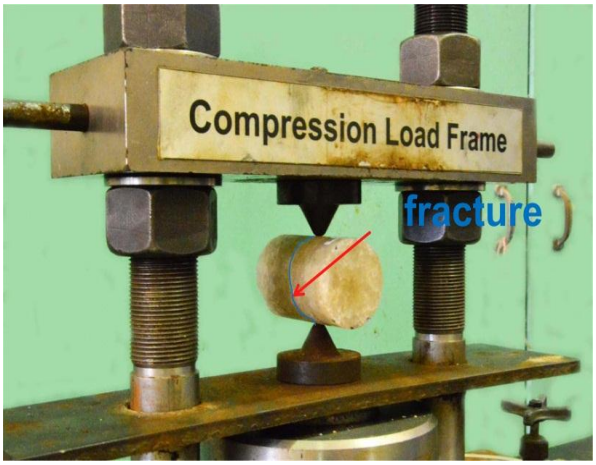

Fig. 4 Healing effectiveness is assessed by point load testing.

The point load tests on the healed fractures have been compared with intact rock salt to determine the healing effectiveness under the test conditions. The point load strength of the healed fracture (I_H) is calculated by dividing the failure load (P) by the diameter square (D^2). The healing effectiveness (H_e) of each fracture is defined by the percentage ratio of I_H to Is, (point load strength of the intact salt obtained previously from inducing a fracture in the same specimen). The results indicate that the healing effectiveness tends to decrease as the amount of inclusion increases. All the saw-cut fractures remained separable with no healing. The healing effectiveness of tension induced fractures increase with increasing healing time and axial stress (Fig. 5 and Table 1). Temperatures slightly increase the healing effectiveness (Fig. 6).

4. WAVE VELOCITY TESTS

The ultra-sonic waves, P-wave and S-wave are monitored from the salt specimens with the healed fractures under axial loading for every 7 days throughout 56 days of testing (Fig. 7). The wave velocity of the rock salt increases rapidly during the first 7 days, and after that the P-wave are slightly increases steadily with time (Fig. 8). These results indicate that some parts of the salt fractures are closed or healed, and some parts cannot be recovered or healed. These generally agree with the experimental observations by Chen, et al. (2013).

CONCLUSIONS

The laboratory tests indicate that the effectiveness of healing is sensitive to the both axial stress and healing time more than to the temperature (within the range up to 200°c). The healing effectiveness increases This agrees with the test results obtained by Fuenkajorn and Phueakphum (2011). Temperatures can induce the slight increase of the healing effectiveness. This is different from the conclusions drawn by Chen, et al. (2013), who found that the temperatures have a large effect on healing effectiveness. This may be due to that they tested micro cracks and this study is concentration on salt fractures. When the temperature is increased the P-wave velocity increases rapidly during the first 7 days of the test, and after that the P-wave slightly increases with time. This observation agrees with Chen, et al. (2013). The healing of salt fractures depends largely on the origin of the fractures. If a fracture is formed by separation or splitting of salt crystals, it can be easily healed even under relatively low stress for a short period. The splitting failure of salt crystals occurs by a separation of cleavage planes, which means that healing is likely to occur if the salt crystals on both sides of the cleavage plane return to their original position.

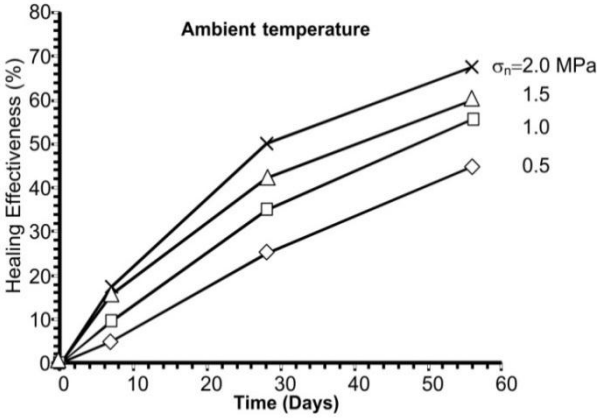

Fig. 5 Healing effectiveness (H_e) as a function of healing time (t) of tension-induced fractures.

Table 1. Point load test results for tension-induced factures after healing under constant axial stress and healing time.

Specimen no.	Inclusion (%)	Time (days)	Axial loading (MPa)	Point load strength index		Healing effectiveness $H_e = [I_s/I_H] \times 100$ (%)
				Intact salt, P (kN)	Salt with healed fracture, P (kN)	
HUT-01e	1	56	2.0	1.85	1.25	67.57
HUT-10e	5	56	0.5	2.00	0.90	45.00
HUT-12e	10	56	1.0	2.20	1.25	55.55
HUT-13e	15	56	1.5	2.50	1.50	60.00
HUT-14e	10	28	0.5	2.00	0.50	25.00
HUT-15e	10	28	1.0	2.00	0.70	35.00
HUT-16e	5	28	1.5	1.90	0.80	42.11
HUT-11e	5	28	2.0	2.00	1.00	50.00
HUT-19e	10	7	0.5	2.00	0.10	5.00
HUT-20e	10	7	1.0	2.10	0.20	9.52
HUT-21e	5	7	1.5	1.90	0.30	15.79
HUT-22e	5	7	2.0	2.00	0.35	17.50

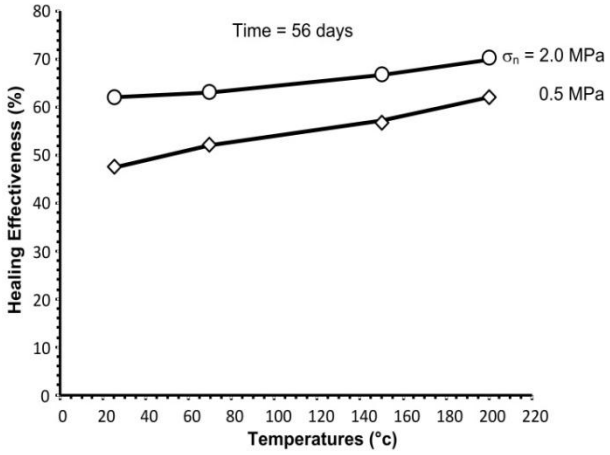

Fig. 6 Healing effectiveness (H_e) as a function of temperatures (T) of tension-induced fractures.

Fig.7 Wave velocity measurements after fracture healing under uniaxial loading.

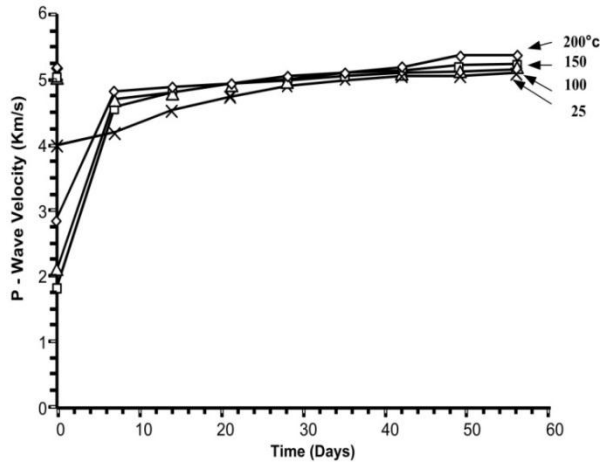

Fig. 8 P-wave velocity (H_e) as a function of time (t) of tension-induced fractures.

with increasing healing time and axial stress. For the fractures formed by separation of inter-crystalline boundaries, healing will not be easily achieved. In particular, if the fracture surface is coated with any inclusions, healing will not occur.

ACKNOWLEDGEMENTS

This study is funded by Suranaree University of Technology and by the Higher Education Promotion and National Research University of Thailand. Permission to publish this paper is gratefully acknowledged.

REFERENCES

ASTM D3967-81, Standard test method for splitting tensile strength of intact rock core specimens, In: Annual book of ASTM standards, American Society for Testing and Materials, Philadelphia, 04.08, 1981.

ASTM D4543-85, Standard practice for preparing rock core specimens and determining dimensional and shape tolerances, In: Annual book of ASTM standards, American Society for Testing and Materials, Philadelphia, 04.08, 1985.

ASTM D5731-95, Standard test method for determination of the point load strength index of rock, In: Annual book of ASTM standards, American Society for Testing and Materials, Philadelphia, 04.08123, 1995.

ASTM D2938-79, Standard test method for unconfined compressive strength of intact rock core specimens, In: Annual book of ASTM standards, American Society for Testing and Materials, Philadelphia, 04.08, 1979.

Chen, J., Ren, S., Yang, C., Jiang, D., and Li, L., Self-healing characteristics of damage rock salt under different healing conditions, Materials, Vol. 6, pp. 3438 -3450, 2013.

Fuenkajorn, K., and Phueakphum, D., Laboratory assessment of healing of fracture in rock salt, Bull. Eng. Geol. Environ., Vol. 70, pp. 665-672, 2011.

Katz, D.L., and Lady, E.R., Compressed air storage for electric power generation, Dept. of Energy, Pacific Northwest, Richland, Washington, 1976.

Miao, S., Wang, M.L., and Schreyer, H.L., Constitutive models for healing of materials with application to compaction of crushed rock salt, Journal of Engineering Mechanics (ASCE), Vol. 10, No. 121, pp. 1122–1129, 1995.

Renard, F., Pressure solution and crack healing and sealing, Institute of Geology and Department of Physics. Charles University, Prague; Summer school on: Geology related to nuclear waste disposal, July 5–11, Roztez, Czech Republic, University of Oslo, Norway, 1999.

PHYSICAL MODEL SIMULATIONS OF SUPER-CRITICAL SUBSIDENCE AS AFFECTED BY MINING SEQUENCE AND EXCAVATION RATE.

Naruemol Saoanunt, and Kittitep Fuenkajorn
Geomechanics Research Unit, Institute of Engineering,
Suranaree University of Technology.

ABSTRACT

Physical model simulations have been performed to study the surface subsidence under super-critical condition. This paper is focused on the effects of the mining sequence and excavation rate on the angle of draw, maximum ground surface subsidence and trough volume. Clean and uniform sand with nominal size of 2 mm is used to simulate individual blocks of the overburden. The results indicate that the angle of draw and maximum subsidence decrease with increasing opening depth, and increase with increasing excavation width. These effects become larger under low excavation rate. The subsidence trough profiles obtained from the high excavation rates show smoother curve than those obtained from the low excavation rates. Consecutive mining sequence from one side to another side gives the highest angle of draw and lowest maximum subsidence. The angle of draw and maximum subsidence decreases with increasing opening depth. The findings can be used to evaluate the subsidence profile for underground mining as affected by excavation sequence and rate in fractured rock mass.

1. INTRODUCTION

Surface subsidence is a consequential damage from underground mining. The movements of the ground surface may damage to surface structure (e.g. buildings, roads, railway lines, oil pipelines). Therefore, the subsidence magnitude must be acceptable range. Physical modeling is one of the most effective techniques in studying the rock strata behavior affected by longwall mining (Whittaker and Reddish, 1989). It has been used by many researchers to simulate longwall mining-induced subsidence and other related problems (Huayang et al., 2010; Liu et al., 2011). Processes such as surface movement, crack propagation, caving, substrata movements and the overburden movement after sequential multiple-seam mining can be investigated by physical modeling (Liu et al., 2011). Ghabraie et al. (2014) investigate the subsidence mechanisms from sequential extraction of overlapping coal longwall panels, and find that the zone of the two long wall panels under goes greater total subsidence compared to a single seam of equivalent thickness.

Many methods exist for predicting the value of maximum subsidence and volume of trough induced by underground mining. Thongprapha et al. (2014) study the surface subsidence above an underground opening using a trap door apparatus to determine the effects of underground opening configurations on surface subsidence under super-critical conditions. They find that the angle of draw and maximum subsidence increase with increasing opening length and tends to approach a limit when opening length-to-width ratio equals 3. For the same opening geometry, increasing the opening depth reduces the angle of draw and maximum subsidence. The volume of the subsidence trough increases with increasing opening height and width. Cui et al. (2000) predict the subsidence caused by underground mining from theory and those experienced in practice. By using non-linear geometrical field theory, the deformation factors are modified and the limitation of linear elastic theory is established to determine maximum subsidence and angle of draw. They found that the physical models are helpful for understanding the subsidence mechanisms and suitable for rectangular panels. The predicted results are usually smaller than the measured field values. Singh and Yadav (1995) predict the ground surface subsidence by using a visco-elastic modeling. The results indicate that excavation time can affect the surface subsidence and that the subsidence increases continuously during the first two years after excavation. Three types of subsidence profiles are observed in Indian coalfields under different mining conditions and different geological environments: Continuous subsidence profile observed in deep coal mines, stepped subsidence profile observed in shallow coal mines with strong (rigid) overburden and continuous subsidence profile with many small steps observed in coal mines with weak overburden.

Even though extensive studies have been carried out in and attempt to predict the surface subsidence behavior under various underground excavation methods, the

effects of mining sequence and excavation rate have rarely been addressed. This is primarily because such effects of excavation rate and mining sequence occur in the post failure region, and hence it is difficult, if at all possible, to study them with numerical model simulations. This study is therefore focused on the effects of mining sequence and excavation rate on the angle of draw, maximum subsidence and trough shape under super-critical. This paper presents the initial results.

2. MATERIALS SIMULATING OVERBURDEN

Clean and uniform sand with nominal size of 2 mm in diameter is used as the test material. Efforts are made to determine on the grain size distribution and shearing resistance. The grain size analyzing test method and calculation follow the ASTM (D422-63) standard practice. The uniformity coefficient (Cu) is 1.29 and the coefficient of curvature (Cc) is 1.07. The uniform sand is classified as poorly graded sand or SP in accordance with ASTM (D2487-06). The sand is distinguished by comparing with the Power (1953) classification system. The sphercity of sand is high and the roundness is sub-angular.

The direct shear test is performed to determine the cohesion and friction angle of the sand. The test method and calculation follow the ASTM (D5607-08) standard practice. The cohesion of material is 15.61 kPa, and friction angle is 24.7 degree. The shear strength is calculated based on the Coulomb's criterion (Jaeger et al., 2007) which is classified as cohesion less soil.

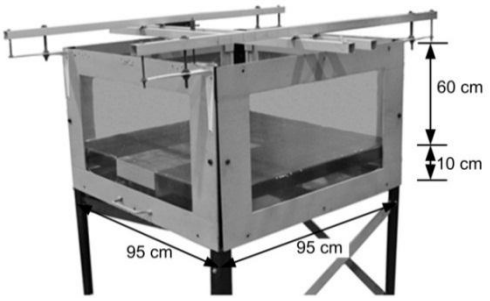

Fig.1.Trap door apparatus used for physical model testing (Thongprapa et al., 2015)

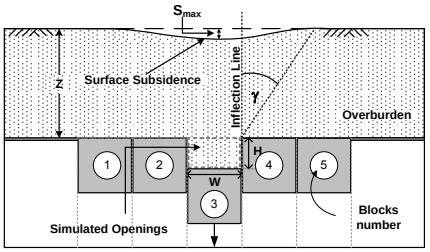

Fig.2.Variables used in physical model simulations and analysis: W= opening width, H = opening height, Z = opening depth, γ = angle of draw, S_{max} = maximum subsidence and B = half width of surface subsidence trough.

3. PHYSICAL MODEL TESTING

A trap door apparatus (Thongprapa et al., 2015) is used in the physical model simulations, as shown in Figure 1. The sample container is filled with the clean and uniform sand to a pre-defined overburden thickness. The sand is lightly packed and the top surface is flattened before the test. The underground opening is simulated by systematically pulling down the blocks underneath the sample container. Single or multiple blocks can be pulled down to simulate various opening configurations. Figure 2 shows the test parameters and variables defined in the simulations. A trap door apparatus can be simulated the opening width (W) from 50 mm to 250 mm with and increment of 50 mm. The opening length (L) can be simulating from 50 mm up to 500 mm with 50 mm increment. The opening height (H) is from 5 mm to 50 mm with 5 mm increment. In this study, overburden thickness (Z) is varied 50 mm, 100 mm, 150 mm and 200 mm for all cases.

3.1 Mining sequences

Three case of mining sequence is simulated to study the effect of excavation orders of the mine panel, as shown in Figure 3. The numbers in the blocks indicate the order of panel excavation row. Each panel excavation is made by simultaneously moving down of 6 blocks (L/W=6, when L=300 mm and W= 50 mm) in defined location. This is because the effect of the opening ends decrease eventually disappear when the opening length-to-width (L/W) ratio beyond 3 (Thongprapa et al.,2015). Figure 3(A) show excavation from one side to the other. Figure 3(B) and 3(C) start the excavation from the center of the panel.

The physical model is simulated of opening width (W) starting from 50 mm to 250 mm, the opening length (L) is 300 mm and the opening height (H) is 50 mm for all cases. The laser scanner measures the surface profile of the sand before and after the subsidence is induced. An example of a cross section of surface subsidence in mining sequence and excavation rate is shown in Figures 4.

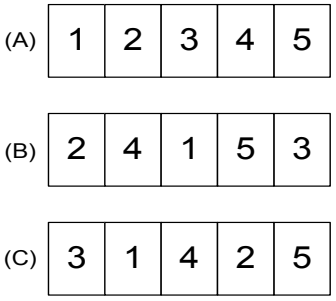

Fig.3.Mining sequences used in physical models. The numbers indicates for case (A), (B) and (C) the sequence of mining excavation.

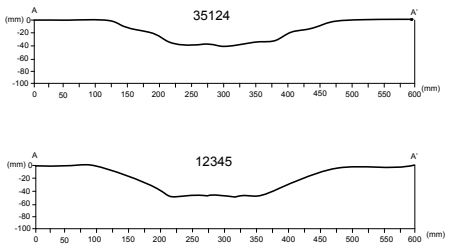

Fig.4.Subsidence profile of cross-section (A-A′) of surface subsidence in mining sequence.

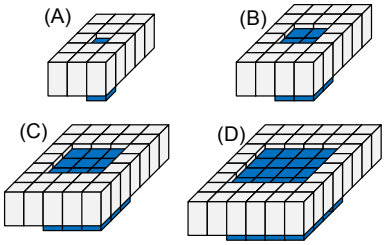

Fig.5.Effects of excavation rate assessed by using different areas of excavation.

3.2 Excavation rate

The effect of excavation rate is investigated by systematically moving down of the blocks to simulate the mining excavation with different rates. This study considers two rates: high excavation rate = 0.25×10^{-4} m^3/sec (with 50 mm increment of opening height), and low excavation rate = 0.025×10^{-4} m^3/sec (with 5 mm increment of opening height). These excavation rates are used to simulate four cases of excavation area (Fig. 4). The excavation area (width×length) are 50×50, 100×100, 150×150 and 200×200 mm^2.

4. RESULTS

The measurement results are presented in terms of the angle of draw (γ) and the maximum subsidence (S_{max}). The angle of draw is a parameter used for defining the position of the limit of subsidence at the surface. The angle of draw is the angle between a vertical line from the edge of the underground opening and a line from the edge of the opening to the point of zero surface subsidence. The point of maximum surface subsidence is located in the center of the trough. Surface subsidence profiles due to different mining sequences are shown in Figure 5. Various mine panel simulations affect the subsidence trough profile. Under mining sequence in Figure 3(A) show the trough profile smoother than the trough obtained from mining sequence in Figure 3(C), and hence the angle of draw and maximum subsidence change. Figure 6 shows the angle of draw as a function of opening depth-to-heigth (Z/H) ratio for various mining sequences. The angle of draw decreases with increasing Z/H ratio for all cases, particularly for Z/H=1 where the effect of mining sequence characteristics become larger. The maximum subsidence-to-height ratio (S_{max}/H) tends to decrease with increasing Z/H ratio (Fig. 7).

Figure 8 shows subsidence profiles under various excavation rates. Under low excavation rate the subsidence trough profile shows small steps of slope. The subsidence trough profile tends to be smoother when excavation rate is higher. Figures 9 and 10 show the angle of draw and S_{max}/H as a function of opening depth-to-height ratio for various excavation areas. The angle of draw (γ) and S_{max}/H decrease with increasing Z/H ratio. Under the same excavation area, higher excavation rates give the lower angle of draw for all excavation areas. This is because the high excavation rates tend to inter-lock above the opening more than the low excavation rate.

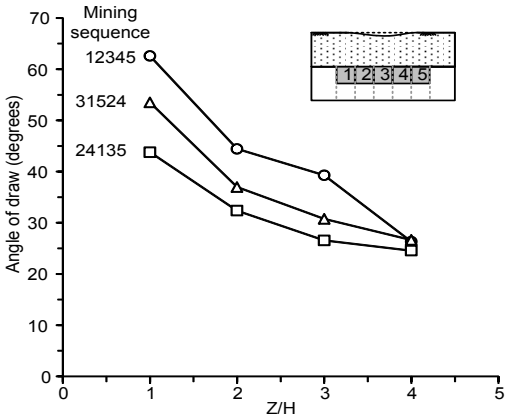

Fig.6. Angle of draw (γ) as a function of opening depth-to- height (Z/H) ratio.

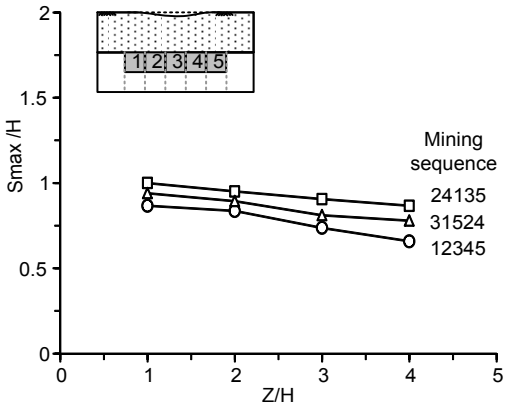

Fig.7. Maximum subsidence-to-height (S_{max}/H) ratio as a function of opening depth-to-height (Z/H) ratio.

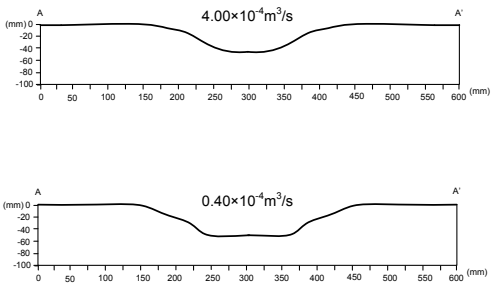

Fig.8. Subsidence profiles of cross-section (A-A′) of surface subsidence in excavation rates.

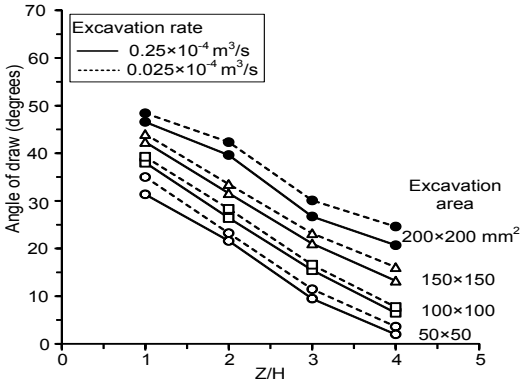

Fig. 9. Angle of draw (γ) as a function of opening depth-to-height (Z/H) ratio.

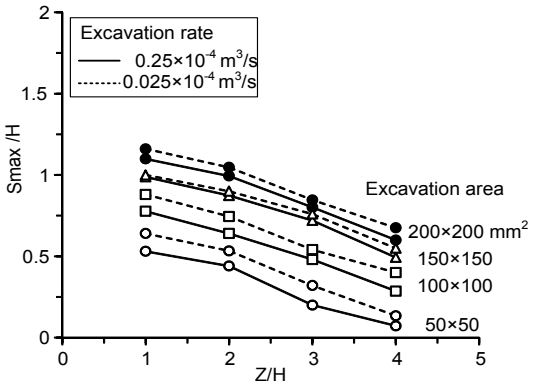

Fig.10. Maximum subsidence-to-height ratio as a function of opening depth-to- height (Z/H) ratio.

CONCLUSTIONS

The effects of mining sequence and excavation rate are determined to predict the supper-critical surface subsidence. The physical model test results indicate that the angle of draw and the maximum subsidence are controlled by the characteristics of mining sequence and excavation rate of the underground openings.

The subsidence has been found to decrease with the increase of overburden thickness. This is due to that the subsidence in the physical has created new voids in the overburden above the opening.

The excavation by the remaining longwall panel before excavation completely shows the small curves of subsidence trough. As opposed to the excavation from one side to the other, the trough is smoother.

The angle of draw and the maximum subsidence decrease with increasing Z/H ratio. For the high excavation rate (0.25×10^{-4} m^3/s) the angle of draw and maximum subsidence value is less than the low excavation rate (0.025×10^{-4} m^3/s) because the overburden tend to create new voids when the openings are slowly excavated.

ACKNOWLEDGEMENT

This study is funded by Suraneree University of Technology and by the Higher Education Promotion and National Research University of Thailand. Permission to publish this paper is gratefully acknowledged.

REFERENCES

ASTM Standard D2487-06, Standard Practice for Classification of Soils for Engineering Purposes (Unified Soil Classification System). Annual Book of ASTM Standards, American Society for Testing and Materials, West Conshohocken, PA, 2006.

ASTM Standard D422-63, Standard Test Method for Particle-Size Analysis of Soils. Annual Book of ASTM Standards, American Society for Testing and Materials, West Conshohocken, PA, 2007.

ASTM Standard D5607-08, Standard Test Method for Performing Laboratory Direct Shear Strength Tests of Rock Specimens Under Constant Normal Force. Annual Book of ASTM Standards, American Society for Testing and Materials, West Conshohocken, PA, 2008.

Ghabraie B., Ren G., Ghabraie, K., Xie Y, J. Smith, Physical modeling of subsidence from sequential extraction of partially overlapping longwall panels and study of substrata movement characteristics. International Journal of Coal Geology, 2014.

Huayang, D., Xugang, L., Jiyan, L., Yixin, L., Yameng, Z., Weinan, D., Yinfei, C., Model study of deformation induced by fully mechanized caving below a thick loess layer. International Journal of Rock Mechanics and Mining Sciences , 1027 – 1033, 2010.

Jaeger, J.C., Cook, N.G.W., Zimmerman, R.W., Fundamentals of Rock Mechanics, fourth ed. Blackwell Publishing Ltd, Malden, MA, 2007.

Liu, Y.-k., Zhou, F.-b., Liu, L., Liu, C., Hu, S.-y., An experimental and numerical investigation on the deformation of overlying coal seams above double-seam extraction for controlling coal mine methane emissions. International Journal of Coal Geology, pp.139 – 149, 2011.

Power, M.C., A new roundness scale for sedimentary particle. Journal of Sedimentary Research. pp.117-119, 1953.

Ramesh P. Singh, Ram N. Yadav, Prediction of subsidence due to coal mining in Raniganj coalfield, West Bengal, India. Engineering Geology (1995), pp. 103-111, 1995.

T. Thongprapha, K. Fuenkajorn, J.J.K. Daemen, Study of surface subsidence above an underground opening using a trap door apparatus. Tunnelling and Underground Space Technology (2015), pp. 94–103, 2015.

Whittaker, B. N., Reddish, D. J., SubsidenceOccurrence, Prediction and Control. Vol. Volume56. Elsevier, 1989.

X.Cui, X. Miao, J. Wang, S. Yang, H. Liu, Y. Song, H. Liu, X. Hu, Improved prediction of diferential subsidence caused by underground mining.International Journal of Rock Mechanics and Mining Sciences (2000), pp. 615-627,2000.

COMPOSTING OF MODEL KITCHEN WASTE USING *TEMPEH* AND *TAPAI* AS MICROBIAL INOCULANTS

Yee Van Fan, Chee Woh Leow, and Chew Tin Lee*
Faculty of Chemical Engineering, Department of Bioprocess Engineering, Universiti Teknologi Malaysia

ABSTRACT

In this study, the composting materials consisting of model kitchen waste, dried leaves and rice bran were inoculated with four formulation of microbial inoculants namely 100% *Tempeh* (Te), 100% *Tapai* (Ta), 50% *Tempeh* +50% *Tapai* (Te+Ta), Effective Microorganism^{TM} (EM) and water as control. It was found that the temperature of all four composting materials with microbial inoculants can be heat up to temperature above 50^{o}C than the control. The enzymatic activities were not able to indicate significant differences between the inoculated compost against the control. The highest activity of amylase (73-129 U/g) and cellulase (75-148 U/g) occurred at the beginning of the composting process. The maximum activities of lipase (5-10 U/g) and protease (46-72 U/g) were observed at the middle stage of the composting process. However, the results suggested that *Tempeh* and *Tapai* can be used as microbial inoculants to degrade kitchen waste as their performance was comparable with EM. The necessities of using inoculants in composting of kitchen waste need to be further verified by maturity, stability and quality test on the matured composts.

1. INTRODUCTION

Improper disposal of food waste causes a series of problems to environmental pollution and treatment cost (COM,1996; Sakai *et al.*, 2001). Composting can be a viable food waste management however less research works have focused on using fermented food as microbial inoculants to degrade small scale kitchen waste. Fermented food contains a variety of microorganisms and they have been widely used in Takakura home compositing method (Ying and Ibrahim, 2013). In this study, *Tempeh* (Te) and *Tapai (Ta*) were chosen as a source of microbial inoculants to use in composting of kitchen wastes and the performance was compare with EM and water (control). Characterization of enzymatic activities can reflect the dynamics of the composting process in terms of the decomposition of organic matter (Raut *et al.*, 2008; Ismail *et al.*, 2013a; Kazemi *et.al*, 2014). Since there are limited studies reporting on the enzymatic activities especially in compost inoculated with microbial from fermented food, four types of enzymatic activities including amylase, cellulase, protease and lipase were evaluated. Besides, temperature and moisture contents of the composts were monitored.

2. EXPERIMENT

2.1 Experiment Design

In this study, the composting process was carried out in plastic bin at a static condition covered with fabric. A total of 4kg identical composting materials were mixed with fermenting solution, EM and water as shown in Table 1. The moisture content was maintained between 40-60% and the composting materials were aerated manually once in a week. Model kitchen waste was prepared according to the composition and ratio stated by Hafid *et al*. (2010). While the dried leaves that collected from Universiti Teknologi Malaysia (UTM) compound was autoclaved before mixed with rice bran and the model kitchen waste.

2.2 Preparation of Fermenting Solution

200g of brown sugar was dissolved in 3L of distilled water and autoclaved at 121^{o}C for 15min. Next,

100g of Te and Ta was added into 3L of brown sugar solution separately. The solutions were placed in room temperature at a static condition for 2-3days until the optical density reading was 0.7 at 545nm. Commercial EM from EMRO Malaysia Sdn Bhd was activated according to the user manual for 5-7 days until the pH was below 3.5.

Table 1: Composition of composting materials

Name	Composition
Te	2:1:1 ratio of model kitchen wastes to dried leaves to rice bran with fermenting solution from 100% of *Tempeh*
Ta	2:1:1 ratio of model kitchen wastes to dried leaves to rice bran with fermenting solution from 100% of *Tapai*
Te+Ta	2:1:1 ratio of model kitchen wastes to dried leaves to rice bran with fermenting solution from 50% of *Tempeh* and 50% of *Tapai*
Water (Control)	2:1:1 ratio of model kitchen wastes to dried leaves to rice bran with distilled water
EM	2:1:1 ratio of model kitchen wastes to dried leaves to rice bran with commercial EM

2.4 Pysico-chemical Analysis

Temperature of composts was determined daily using thermometer. Moisture content was determined weekly using dry oven method at 105^{o}C for 24 hours (Kutsanedzie *et al.,* 2012) to maintain the moisture content within 40-60% during the composting process.

2.5 Enzymatic Analysis

Enzymatic activities were evaluated weekly during the composting process. Amylase, cellulose, protease and lipase activity of all the five samples was determined using aqueous compost extracts that extracted using different buffer solution. Amylase activity was evaluated using 1.1% w/v soluble starch as substrate (Mishra and Behera, 2008). The colorimetric determination of reducing sugar released from 2% w/v carboxymethyl cellulose was used to estimate the cellulase activity (Zhang *et al.*, 2009). Glucose was used as standard substrate for the both assays. Protease activity was quantified using 0.65% casein as substrate and tyrosine as standard (Cupp-Enyard, 2008). Lipase activity was analyzed using 10µL of *p*-nitrophenyl butyrate as substrate and nitrophenol as standard (Margesin *et al.*, 2002). All measurements were performed in duplicates and calculated in the unit of micrograms per minute per grams (U/g)

3. ANALYSIS

3.1 Temperature

The change of temperature during the composting process indicated the change of microbes in the composts. Composting is required to go through thermophilic phase to ensure the safety of compost from pathogens (Bernal *et al.*, 2009). Based on Sundberg *et al.* (2004), thermophilic temperatures are approximately from 45 to 70^{o}C. It was found that the temperature of all four composting materials with microbial inoculants can be heat up higher (>50^{o}C) than the control. The control set of composting materials that without microbial inoculants does not heat up to 45^{o}C for at least three days in continuously. The maximum temperature was 46 ^{o}C and appeared for only two days. This was probably due to contain lesser diverse communities of microorganisms when compare with inoculated composting materials as well as the small composting scale (Dickson *et al.*, 1991; Abdullah *et al.* 2013).

The composting materials that contain microbial inoculants produced from fermented food performed better than those inoculated with EM as their temperature rise higher and continue for a longer period. Among the all, composting material that contained 50% of Te and 50% of Ta shows the best temperature profile. In this study, the temperatures of the five composting materials were starting to or in cooling phase after the 3 weeks of composting. This suggested the maturation and stabilization of organic matter has been reached. Consequently, it makes the use of temperature for predicting could be ineffective. Therefore, the temperature profiles needs to employ with other additional parameters to further determine the maturity and stability of composts. The ambient temperatures were ranged between 24 to 31 ^{o}C during the composting process.

3.4 Enzymatic assays

Enzymes are the main mediators of degradation process and they control the degradation rates of different substrate (Ismail *et al*., 2013a) . Measurement of enzymatic activities illustrates the enzymes which participate in the bioconversion of the composting materials. In this study amylase, cellulase, lipase and protease were chosen to measure the possible available inducers in the composting materials. Amylase, cellulose, lipase and protease activity of the composts which under different treatments namely 100% Ta, 100% Ta, 50% Te+ 50% Ta, EM and water as control show a similar ending trend. The lower activity during the end phase indicates the completion of the decomposition process (Ying and Ibrahim, 2013). The activities of cellulase and protease were observed to have been decreased and stabilized on week 3 while amylase, lipase were on week 4 and 5 respectively. Table 2 shows the summary of results.

For amylase activity during the composting process, the highest activity of amylase occurred at the beginning of composting process and decreased gradually until a stabilized level. This trends was similar with the finding by Ismail *et al*. (2013a), the high activity at the

beginning could be due to the starchy materials available in the kitchen wastes which is easier to degrade.

Cellulose activity also has an analogous trend with amylase, the maximum activity happens at the beginning. However, the decline shows in cellulase activity is sharper than the happening in amylase activity. This was most probably due to the limited substrate in the composting materials. The composting materials that make up by kitchen waste, rice bran and dried leaves has more recalcitrant carbon due to the present of lignin from dried leaves. Rice bran contain 27% cellulose, 37 % hemicellulose, 5 % lignin (Baig *et al*., 2005), the available and easier degrade cellulose was mainly from rice bran and kitchen wastes . Therefore, the dramatic decrease in the cellulase activity was believed due to the fast degradation at the beginning of the process contributed by the easier degrading cellulose materials and the low remaining cellulose content after one weeks. Moreover, the type of cellulase that was determined in this study is endoglucanase.

On the other hand, lipase and protease activity shows a pattern that is normally obtained in present studies where the enzymatic activities was increasing with time as the composting proceeds until to a maximum activity at the middle stage followed by declined (Raut *et al*., 2008; Ying and Ibrahim, 2013). These indicate the capability of microorganisms in synthesizing with enzymes that essential for hydrolysis of various complexes organic compounds. Table 2 shows the maximum enzymatic activity happened during the composting process. The maximum amylase and cellulase activity occured on the initial stage of composting process (week 0). While the maximum lipase and protease activities were observed on week 4 and week 2 respectively.

Table 2: Maximum enzymatic activity during the composting process

Maximum activity (U/g)	Treatment				
	Te	Ta	Te+ Ta	Water (control)	EM
Amylase	73.23	83.03	105.48	101.2	128.82
Cellulase	137.3	75.64	84.25	147.03	114.94
Protease	46.87	58.98	57.86	63.06	71.5
Lipase	8.01	9.23	5.62	8.69	8.24

No significant different ($p>0.05$) was found among the composting materials inoculated with or without microbial inoculants. The enzymatic activities of composting materials treated with microbial inoculants developed from fermented food are almost the same as the composting materials treated with EM and also with barely water. In term of the total accumulated enzymatic activity along the whole composting process for a 8 weeks duration, EM have the highest amylase activity (510.47 U/g), 100% Te has the highest cellulase (247.63 U/g) as well as protease activity (347.13 U/g) and 100% Ta has the highest lipase activity (46.64 U/g).

4. CONCLUSION

Although rather preliminary in some aspects, our results still indicate the potential of using *Tempeh* and *Tapai* as microbial inoculants to degrade small scale kitchen waste especially the technique are user friendly and the sources of microbial inoculant are readily accessible by households. The temperature profile and odor performance was outstanding (data not shown), beside the enzymatic assays are comparable with the composting performance of EM even though no difference can be indicated when compare with the control (water). Continuous study can be carried out on the C: N ratio, germination index, humic acid content, nutrient content and pathogen analysis to further comparing the effectiveness of Te and Ta as microbial inoculants with EM and water as controls.

5. REFERENCES

Abdullah, N., Chin, N. L., Mokhtar, M. N., & Taip, F. S. (2013). Effects of bulking agents, load size or starter cultures in kitchen-waste composting. *International Journal of Recycling of Organic Waste in Agriculture, 2*(1), 1-10.

Baig, M., Zetzl, C., & Brunner, G. (2005). Conversion of extracted rice bran and isolation of pure bio-ethanol by means of supercritical fluid technology.

Bernal, M. P., Alburquerque, J. A., & Moral, R. (2009). Composting of animal manures and chemical criteria for compost maturity assessment. A review. *Bioresource Technology, 100*(22), 5444-5453.

COM. (1996). Communication from the Commission to the council and the European Parliament. Strategy paper for reducing methane emissions.

Cupp-Enyard, C. (2008). Sigma's non-specific protease activity assay-casein as a substrate. *Journal of visualized experiments: JoVE*(19).

Dickson, N., Richard, T., Kozlowski, R., & Sobel, P. L. (1991). Composting to reduce the waste stream: a guide to small scale food and yard waste composting: Northeast regional agricultural engineering service.

Dougherty, M. (1998). Composting for municipalities: planning and design considerations: Natural Resource, Agriculture, and Engineering Service, Cooperative Extension.

Gómez-Brandón, M., Lazcano, C., & Domínguez, J. (2008). The evaluation of stability and maturity during the composting of cattle manure. *Chemosphere, 70*(3), 436-444.

Hafid, H. S., Nor'Aini, A., Omar, F. N., Phang, L., Suraini, A., & Hassan, M. A. (2010). A comparative study of organic acids production from kitchen wastes and simulated kitchen waste. *Australian Journal of Basic and Applied Sciences, 4*(4), 639-645.

Ismail, K. A., El-Din, H. M. S., Mohamed, S. M., Latif, A. B. M. A., & Ali, M. A. M. (2013a). Monitoring of Physical, Chemical, Microbial and Enzymatic Parameters during Composting of Municipal Solid Wastes: A Comparative Study. Journal Pure and Applied Microbiology, 8(1), 211-224.

Kazemi, K., Zhang, B., Lye, L., & Lin, W. (2014). Performance of locally available bulking agents in Newfoundland and Labrador during bench-scale municipal solid waste composting. *Environmental Systems Research, 3*(1), 1-10.

Kutsanedzie, F., Rockson, G. N., Aklaku, E. D., & Achio, S. (2012). Comparisons of Compost Maturity Indicators for two Field Scale Composting Systems. *International Research Journal of Applied and Basic Science, 3*(4), 713-720.

Margesin, R., Feller, G., Hämmerle, M., Stegner, U., & Schinner, F. (2002). A colorimetric method for the determination of lipase activity in soil. *Biotechnology Letters, 24*(1), 27-33.

Mishra, S., & Behera, N. (2008). Amylase activity of a starch degrading bacteria isolated from soil receiving kitchen wastes. *African journal of biotechnology, 7*(18).

Raut, M., William, S. P., Bhattacharyya, J., Chakrabarti, T., & Devotta, S. (2008). Microbial dynamics and enzyme activities during rapid composting of municipal solid waste–a compost maturity analysis perspective. *Bioresource Technology, 99*(14), 6512-6519.

Sakai, S.-i., Hayakawa, K., Takatsuki, H., & Kawakami, I. (2001). Dioxin-like PCBs released from waste incineration and their deposition flux. *Environmental science & technology, 35*(18), 3601-3607.

Sundberg, C., Smårs, S., & Jönsson, H. (2004). Low pH as an inhibiting factor in the transition from mesophilic to thermophilic phase in composting. *Bioresource Technology, 95*(2), 145-150.

Ying, G. H., & Ibrahim, M. H. (2013). Local Knowledge In Waste Management: A Study Of Takakura Home Method *Journal of Environmental Science 2*, 528-533.

Zhang, Y. P., Hong, J., & Ye, X. (2009). Cellulase assays *Biofuels* (pp. 213-231): Springer.

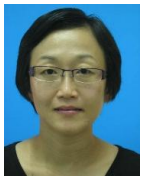

Assoc. Prof. Dr Lee Chew Tin
B. Eng, M.Eng (UTM), Ph.D University of Cambridge (UK)
Research Interest: Soil microbial & metabolite profiling, composting & organic waste management

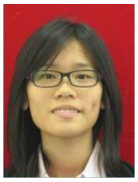

Fan Yee Van
B.Sc. (UTM), Current: Master student, Department of bioprocess engineering (UTM)

Leow Chee Woh
B.Eng., M.Eng. (UTM), Current: Phd student, Department of bioprocess engineering (UTM)

Improvement of Biogas Heating Value by Water Condensation

SOMSAK SIWADAMRONGPHONG* and WUNLOP BOONRONG
School of Manufacturing Engineering, Suranaree University of Technology
111 University Avenue Muang, Nakhon Ratchasima 30000 Thailand
*Contact: somsaksi@sut.ac.th, 044-224-236

ABSTRACT

This study was experimental based research to separate water from biogas. The separation of water was using condenser unit with chilled water of 20 ℃ and a flow rate 50 m3/hr. The condenser unit was designed and built based on biogas from anaerobic wastewater treatment at a rate of 300-2,000 m3/hr with water moisture contamination do not exceed 4% by volume. Condenser was installed in biogas pipe line prior to hot oil boiler gas burner. The separated water data was collected for 40 days operating. It was found that water moisture contaminant separated at the condenser with average 46.95 liter/hr at biogas flow rate 1,826.44 m3/hr (2.57% by volume). It was calculated the increase of biogas heating value from 3,500 kcal/m3 to 3,517 kcal/m3 or 0.486%. It would be considered that due to saving of heat from evaporation of separated water moisture. This research may yield saving of bunker oil grade C about 4.1 liter/hr.

Keywords: Biogas, Heating value, Condenser, Anaerobic wastewater treatment.

1. Introduction

Nowadays mostly Starch Industry in Thailand using aerobic wastewater treatment system from starch manufacturing process. The treatment processes yields biogas production and the gas is able to use as fuel of heat for starch drying process. The biogas is basically apply in direct heating at boiler and alternatively for generating of electricity to reduce cost of thermal energy and electrical energy. Moreover it could be considered that the biogas generating process also help to reduce global warming from emitting greenhouse gas.

One starch company, one of the biggest starch companies in Thailand, located in North-east of Thailand. The company has capacity more than 200,000 tons starch per year. The aerobic wastewater treatment system from cassava starch production can produces biogas approximately 1,500-2,000 m^3/hr which used as the fuel of burner for using in dying processing

From using biogas more than 9 years, the problem of gas explosions in burner was frequently found. It was discussed that happened from the large volumes of biogas contaminated by water. Therefore, the simply solution was applied by using fuel oil mixing with biogas as fuel in burner. The proportion of biogas and fuel oil was about 80:20. The other effect of water contamination in biogas is known as reducing of heating value of biogas. It is due to some fraction of heat has been lost for evaporation of the water into gas phase. Therefore, so it is absolutely necessary to separate water from biogas before using to reduce these problems.

This research aims to improve the heating value of biogas by reducing the volume of water that came along with biogas from 4% (by volume) [1] and increase heating value of biogas.

2. Literature review

Condenser is a heat exchanger which has tube design used to condense the water that came along with biogas by using chilled water of 20 C and flow rate 50 m^3/hr. The condenser unit was designed based on biogas at rate of 300-2,000 m^3/hr and temperature does not exceed 40 C. As the design of condenser based on law of conservation of energy, the rate of heat transfer from heated fluid equal to rate of heat transfer from chilled fluid. The Log Mean Temperature Difference (LMTD) [2] was applied to calculate as shown in eq. (1) – (4).

$$Q_{cold} = m_c C_{pc}(T_{c,out}-T_{c,in}) \quad (1)$$

$$Q_{hot} = m_h C_{ph}(T_{h,out}-T_{h,in}) \quad (2)$$

$$Q = UA\Delta Tm \quad (3)$$

Which Q_{cold} = heat load of chilled water

m_c = mass of chilled water

C_{pc} = specific heat of chilled water

$T_{c,out}$ = outlet temp. of chilled water

$T_{c,in}$ = inlet temp. of chilled water

Q_{hot} = heat load of biogas

m_h = mass of biogas

C_{ph} = specific heat of biogas

$T_{h,out}$ = outlet temperature of biogas

$T_{h,in}$ = inlet temperature of biogas

U = overall heat transfer coefficient

A = heat transfer area

ΔTm = Log Mean Temp. Difference

$$\Delta Tm = \frac{(T_{h2} - T_{c2}) - (T_{h1} - T_{c1})}{\ln[(T_{h2} - T_{c2}) / (T_{h1} - T_{c1})]} \quad (4)$$

LMTD method has been assumed that specific heat of fluid do not changing by temperature and heat transfer coefficient (U) is constant. [4] Shown in eq. (5) below.

$$\frac{1}{U} = \left[\frac{1}{h_1} + \frac{L}{\lambda} + \frac{1}{h_2}\right] \quad (5)$$

Which U = overall heat transfer coefficient

h1= heat transfer coefficient of water

h2= heat transfer coefficient of biogas

L = pipe thickness

λ= heat conduction of stainless pipe

3. Research methodology

This study was experimental based research to separate water from biogas by actual installation in the process of biogas production. The collected data of machine performance was calculated theoretically increasing heating value of biogas. The step of research methodology shown in Fig.1

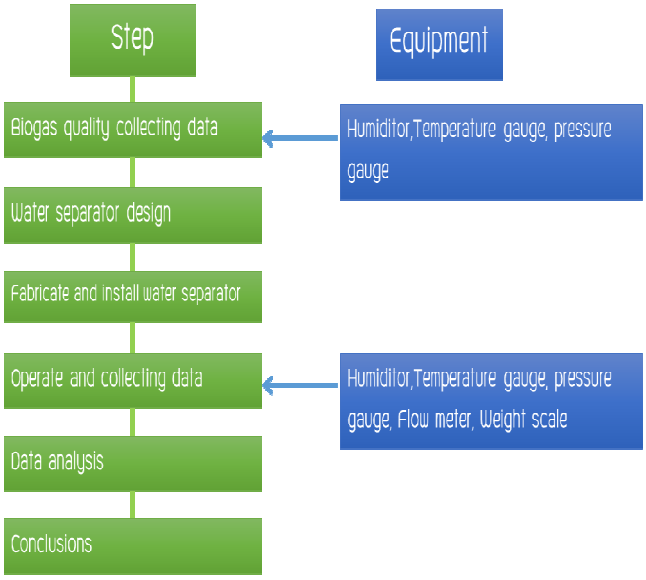

Figure 1 Step of research methodology

3.1 Water separator design

The condenser unit was designed as shell and tube using stainless steel pipe which has one-inch diameter, 600 mm long and 10s schedule thickness. Number of pipe that needed was calculated and found that 189 pipes is needed. The design of condenser has shown in Fig.2.

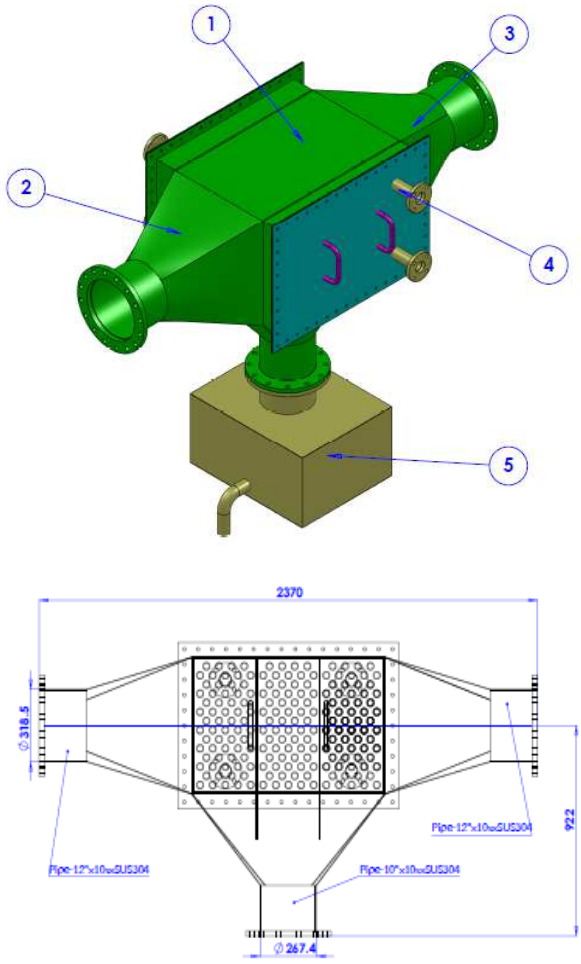

Figure 2 Water separators (condenser)

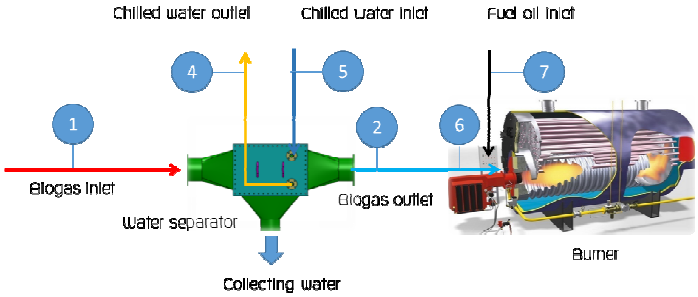

Figure 3 Setting position of instrument

3.2 Condenser fabricating and setting

Condenser was set in the system of biogas pipelines with equipment and instrument as Fig.3

The instrument in Fig. 3 composed of
No.1: Measured tools of air humidity and temperature.
No.2: Dial thermometer
No.3: Dial thermometer
No.4: Dial thermometer
No.5: Digital weighting
No.6: Measured tools of biogas flow rate and dial pressure gauge
No.7: Flow meter for fuel oil

4. Results

Data was recorded for 40 days to find water separation rate from biogas and compared with previous specification value before setting water separator. From the experiment results, it was calculated that heating value increase as assumption as follows.

4.1 Data before testing

Facts of biogas in 2013 were based data for designing water separator which it shows in table1.

Table1: Facts of biogas in 2013

Details	unit	Data (Maximum)
Biogas temperature from biogas pond	^{o}C	39.2
Biogas humidity from pond (%RH)	%	45.2
Biogas flow rate	m^3/h	2,015
Biogas pressure	mbar	340
Fuel oil flow rate	L/h	102.72

4.2 2 Data after testing

After setting water separator into the system of biogas pipelines, test of all systems as normal running condition for 40 days. Experiment results showed in table 2.

Table2: Biogas data from testing

Details	Unit	Data (Avg.)
Inlet temperature of biogas	^{o}C	36.81
Outlet temperature of biogas	^{o}C	34.80
Water residue in inlet biogas	kg	48.40
Water residue in outlet biogas	kg	1.45
Inlet temperature of chilled water	^{o}C	19.49
Outlet temperature of chilled water	^{o}C	23.35
Water separated	kg/h	46.95
Biogas flow rate	m^3/h	1,826.44
Biogas pressure	mbar	350
Specific heat of inlet biogas	kcal/m^3	3,500
Specific heat of outlet biogas	kcal/m^3	3,517
Fuel oil flow rate	L/h	99.78

5. Conclusions

From experimental results, it could be concluded as following;

5.1 Amount of water that came along with biogas equal to 48.40 kg/h, at rate of 1,826.44 m^3/hr Biogas or 2.65% (by volume). The condenser can separate water equal to 46.95 kg/h, or 1.45 kg/h or 0.08% by volume of water contaminated in biogas after the condenser.

5.2 Amount of separated water is 46.95 kg/h was calculated back to heating value of biogas and found that the heating value of the biogas was increased from 3,500 kcal/m^3 to 3,517 kcal/m^3 or 0.486%.

5.3 Amount of separated water of 46.95 kg/h was equivalent to amount of C grade fuel oil 4.1 l/h.

5.4 Payback period for this project is about 1.05 year, calculated by counting required investment including The cost of condenser and installation, cost of energy from electrical system of chiller and pump.

6. Referance

Ministry of energy. 2011. Bangkok. [On-line], Linked : http://www.able.co.th/ Upload/File/21.pdf.html.

Ministry of energy. 2011. Bangkok. [On-line], Linked : http://www2.dede.go.th/kmber/Attach/ Biogas-present.pdf.html.

Cengel, Y. A., Turner, R. H., Cimbala, J. M. (2012), Fundamentals of Thermal-fluid Sciences, 4th edition, MeGraw-Hill Book Co., New York.

Frank W. Schmidt et al. (1993). Introduction to thermal sciences. John Wiley & Sons, Inc., New York.

Pritamashutosh. 2014, April. Heat exchangers. [Online]. Available : http://pritamashutosh. wordpress.com/2014/04/09/heat-exchangers.html

Vienna university technology (Austria). 2012, May. Biogas to bio-methane technology review [Online]. Available : http://www.aile.asso.fr/wp-content/uploads/2012/06/ wp3-1-1_technologyreview_english.pdf.html

Yildiz Bayazitoglu and M. Necati Ozisik. (1988). Elements of heat transfer. MeGraw-Hill Book Co., New York.

A STUDY OF A DESICCANT AIR DEHUMIDIFIER REGENERATED BY HOT AND COLD WATER HEATER

Pichet Lertboonkankit, Surapong Chirarattananon
The Joint Graduate School of Energy and Environment, King Mongkut's University of Technology Thonburi, Bangkok, Thailand

ABSTRACT

A desiccant dehumidifier regenerated by hot and cold water heater were investigated under a hot and humid climate (Thailand) in this study. A heat exchanger coated with silica-gel were used in the experiments.The results indicate that the system can be used to handle latent load of spaces effectively. Higher flow rate of hot and cold water and hotter water temperature lead to increase the performance of the system. While colder water temperature and low air velocity helps to improve the dehumidification and COP_{th} of the system.

1.INTRODUCTION

Nowadays, there are many various dehumidification systems available, desiccant dehumidifications one of them. Previously these systems were not efficient, but some researchers (Zhao, Y., Ge, T.S., Dai, Y.J., Wang, R.Z., 2014.) developed desiccant coated heat exchanger (DCHE) to solve this problem.

In this component, solid desiccant material was coated on the surface of a fin-tube heat exchanger. Cooling water inside the tube is cooling down the passed process air of the dehumidification process.

In this study, the experiments result of a desiccant air dehumidifier regenerated by hot and cold water heater is proposed and investigated experimentally under the natural hot and humid climate conditions in Thailand. The system was installed at a laboratory building at King Mongkut's University of Technology Thonburi, Bang Khun Tien Campus, Thailand. A series of dehumidifier can continuous work in dehumidification and regeneration at the same time. A heater supplies hot water for regeneration process and a chiller supply cold water for the dehumidification process. The performance of the system is also discussed.

2. DESCRIPTION OF THE SYSTEM, EXPERIMENTAL METHODS AND PERFORMANCE INDICATORS

The dehumidification systems are illustrated in Fig. 1. The system consists of two sets of heat exchangers which are coated by mashed silica gel. Two set of the heat exchangers were designed to be switchable when moisture in the desiccant was saturated. Hot water was supplied into the heat exchanger for regeneration process and was produced by using electric heater in hot water tank.While the cold water which was produced by chiller was supplied into the rest heat exchanger in dehumidification process. Both hot and cold water were driven by individual circulating pumps while water directions were assigned by 3-way motorized valves which are controlled by weekly timer.

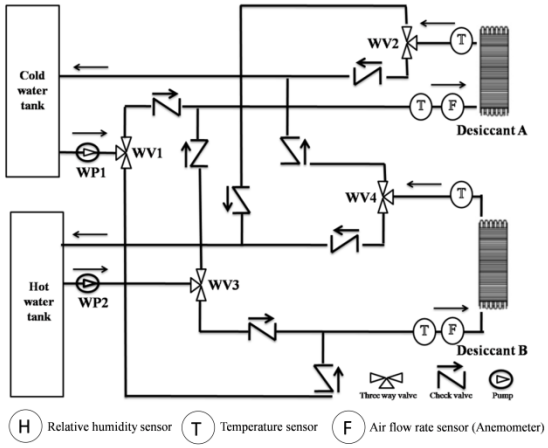

Fig. 1. Schematic diagram of the desiccant dehumidification system.

The system was constructed by using PPR pipes (For high temperature) insulated with PE foam as shown in Fig. 2. The temperatures of air and water were measured by high accuracy PT-100 while air relative humidity was measured by multi-functional digital hot wire anemometer (type:AM4224SD produced by Lutron Instruments).

(a)

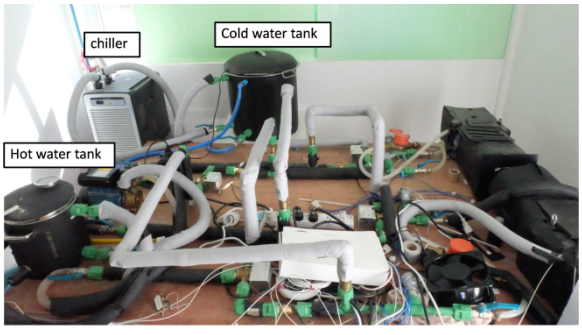

(b)

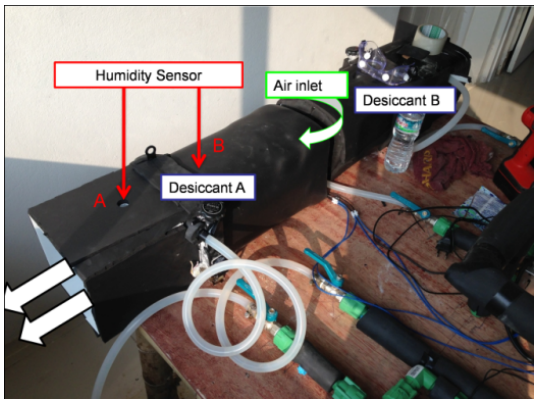

Fig. 2(a), (b) Pictorial view of the dehumidification system.

There were 4 performance indicators used for assessing the system.

1) Moisture removal rate (D)

Moisture removal rate is evaluated the performance of desiccant dehumidification which is defined by eq (1).

$$D = D_{a,in} - D_{a,out} \quad (1)$$

Where $D_{a,in}$ and $D_{a,out}$ are humidity ratio of process air inlet and outlet, respectively in (g/kg) .The value of the dehumidification and regeneration procedure are recorded as 10 sec for every experiments.

2) Coefficient of performance (COP_{th})

Thermal performance COP_{th} is used to show the overall energy efficiency. It is defined as the ratio between average enthalpy exchanged of process air in efficiency dehumidification process (Q_{cool}) and average heat exchanged of water in effective regeneration process (Q_{reg}).The electrical power input of the fans is neglected for heat energy is the primary source of energy.

$$\text{COPth} = \frac{Q_{cool}}{Q_{reg}} = \frac{m_a(h_{a,in}-h_{a,out})}{C_w m_h(T_{h,in}-T_{h,out})} \quad (2)$$

3) Dehumidification effectiveness (E_{deh})

E_{deh} represents the ratio between the humidity reduction across the heat exchanger and the inlet humidity ratio, (Mandegari MA., Pahlavanzadeh H., 2009).

$$\text{Dehumidification effectiveness} = \frac{Y_{in}-Y_{out}}{Y_{in}} \quad (3)$$

4) Regeneration effectiveness (E_{reg})

The calculation of the amount of regeneration heat that consumed for desorbed water is given in the regeneration effectiveness (E_{reg}).

$$\text{Regeneration effectiveness} = \frac{Y_{in}-Y_{out}}{Y_{in}} \quad (4)$$

The considered influencing factors and ranges of each parameter are shown in Table1.

Table 1 Operation condition of parametric study

Parameters	Variation range
Temp.of cold water ($T_{w,c}$)/°C	15,20,25,30
Temp. of hot water ($T_{w,h}$)/°C	60,70,80
Temp. of inlet air (T_a)/°C	35-38
Velocity of inlet air (m/s)	0.5,0.8,1.2
Cycle time (sec)	360,480,600,720,900
Flow rate of hot water (l/min)	10,16
Flow rate of cold water (l/min)	5,10

3.RESULTS AND DISCUSSIONS

This section describes results of the study by describing separately of each influencing factoras follows.

3.1Effect of cycle time

Fig. 3(a), (b) shows the influence of different cycle time and effectiveness on system. The effectiveness of system from each case seems to be not significantly different. However the optimum cycle time is likely to be 600 seconds for high air flow rate and water flow rate.

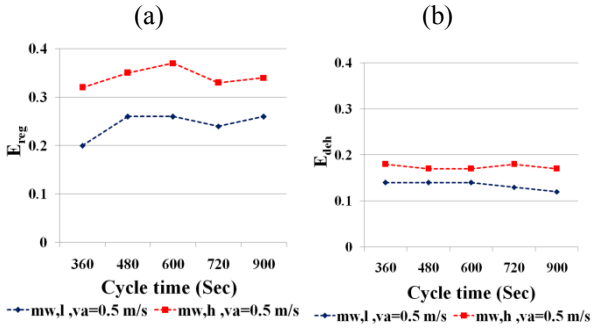

Fig. 3. Effect of cycle time on (a) dehumidification effectiveness (E_{deh}) and (b) regeneration effectiveness (E_{reg}).

3.2Effect of air velocity

Fig. 4 shows the influence of inlet air velocity v_a on the system performance; D_{ads}, D_{des}, E_{deh}, E_{reg},and COP_{th}. When v_a increase from 0.5 m/s to 1.2 m/s,D_{ads} of both conditions increase from 3 g/kg to 3.5 g/kg and 3.9 g/kg to 5 g/kg, respectively. The result is inconsistent with the study in (Zhao, Y., Ge, T.S., Dai, Y.J., Wang, R.Z., 2014) which indicates the D_{ads} should be decreased when increasing air velocity. The reason of the results is from uncontrollable inlet air temperature and humidity ratio which are one of main influencing factors (But not considered in this study) before supply

to system. However the disagreement will be investigated by calculation in the near future. Apart from that COP_{th} are also increased when increasing air velocity.

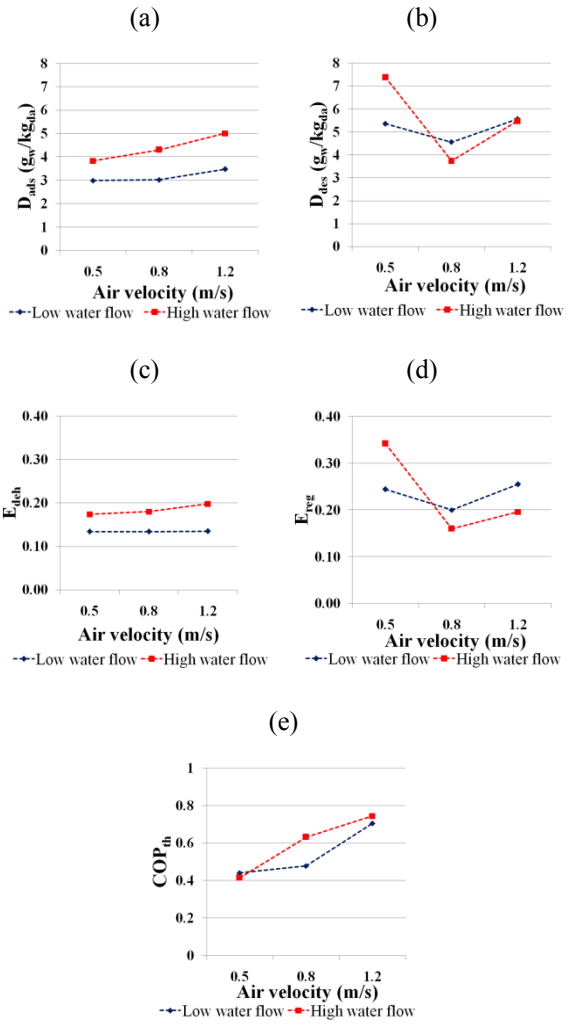

Fig. 4. Effect of air velocity on (a)D_{ads}, (b)D_{des} , (c)E_{deh} , (d)E_{reg} , and (e)COP_{th}.

3.3Effect of water flow rate

Fig. 5 shows the influence of water flow rate to performances of the system. In the experiments, the flow rate of hot and cold water are unequal due to different pump capacity. Each level of water and air flow are shown in Table 1. The results indicate that D_{ads} and E_{deh} are increased when increasing water flow rate. D_{des} and E_{reg} are also increased when increasing water flow rate in case of v_a is 0.5 m/s, for higher air flow, the results seem to be opposite. The reason this phenomenon is under investigation by computer simulation program but the results are not shown in paper. COP_{th} seems to be larger for higher water flow rate except the case of low air flow rate.

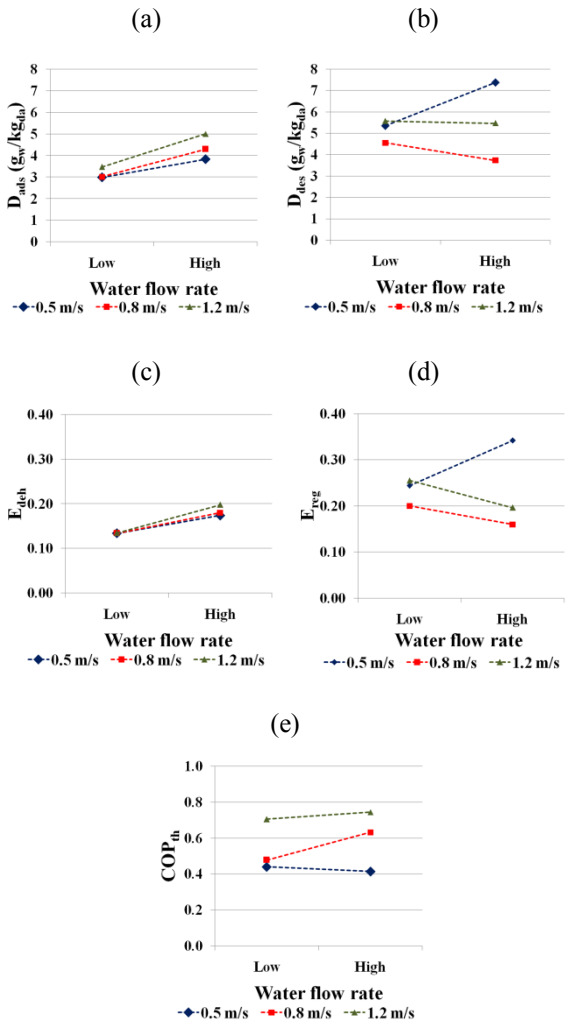

Fig. 5. Effect of Water flow rate on (a) D_{ads}, (b)D_{des}, (c)E_{deh}, (d)E_{reg}, and (e)COP_{th}.

3.4Effect of hot water temperature

As mentioned before, the hot water was used for regeneration process. Figure 6 show the influence of hot water temperature on the system performance. The water temperature($T_{w,h}$) is in the range of 60,70and 80°C. The results indicate that higher hot water temperature leads to increase D_{des} and E_{reg} but COP_{th} of the system is getting lower.

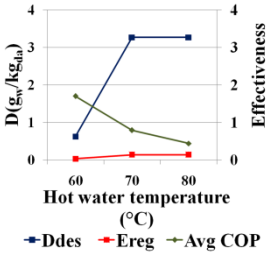

Fig.6. Effect of hot water temperature ($T_{w,h}$) with performance of system.

3.5Effect of cold water temperature

Fig. 7 show the performance of the system by varying the cold water temperature in dehumidification process. The results show that lower cooling water temperature helps to increase D_{ads}, E_{deh}, and COP_{th} of the system.

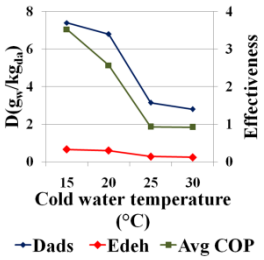

Fig. 7. Effect of cold water temperature ($T_{w,c}$) with performance of system

CONCLUSION

In this study, a desiccant-coated on heat exchanger with using silica-gel driven by heater and chiller are investigated. A system was conducted on tropical climate (Thailand). The dehumidifier supply by realistic ambient air. High temperature and humidity effect to the performance of the system. It cannot control the ambient air condition. The main finding can be summarized as;

- Cold water temperature is influence with the performance of system. D_{ads} and COP_{th} increase with lower cold water temperature. Higher water temperature can enhance D_{ads} and D_{des}, but COP_{th} decrease. The suitable temperature for hot water is about 80°C for regeneration process. While cold water at 20°C can consume more performance of dehumidification process.
- The air velocity is influence effect with the adsorption and desorption process. In this experiment, the effective air velocity is 0.5 m/s or low air velocity. Because it can enhance D_{ads} and D_{des} of dehumidification and regeneration process.

REFERENCES

Ge, T.S., Dai, Y.J., Wang, R.Z.,Performance study of silica gel coated fin-tube heat exchanger cooling system based on a developed mathematical model. Energy Convers. Manag. 52,2329e2338,2011.

Ge, T.S., Dai, Y.J., Wang, R.Z., Peng, Z.Z., Experimental comparison and analysis on silica gel and polymer coated fin-tube heat exchangers. Energy 35, 2893e2900,2010.

Jia, C.X., Dai, Y.J., Wu, J.Y., Wang, R.Z., Experimental comparison of two honeycombed desiccant wheels fabricated with silica gel and composite desiccant material. Energy Convers. Manag. 47, 2523e2534,2006.

Jia, C.X., Dai, Y.J., Wu, J.Y., Wang, R.Z., Use of compound desiccant to develop high performance desiccant cooling system. Int. J. Refrigeration 30, 345e353,2007.

Mandegari MA.,Pahlavanzadeh H., Introduction of a new definition for effectiveness of desiccant wheel.Energy ;34;797-803,2009.

Yin, Y., Zhang, X., Chen, Z., Experimental study ondehumidifier and regenerator of liquid desiccant cooling airconditioning system. Build. Environ. 42, 2505e2511, 2007.

Zhao, Y., Ge, T.S., Dai, Y.J., Wang, R.Z., Experimental investigation on a desiccant dehumidification unit using fin tube heat exchanger with silica gel coating. Appl. Therm. Eng. 63 (1), 52e58,2014.

NOMENCLATURE

C_w	:specific heat of water [J/kg·K]
COP_{th}	:thermal coefficient of performance
D	:moisture removal rate [g/kg]
h	:enthalpy [kJ/kg]
E	:effectiveness
$\dot{m}$	:mass flow rate [l/min]
MRC	:moisture removal capacity [kg/h]
MRR	:moisture removal regeneration [kg/h]
Q	:quantity of heat [kW]
T	:temperature [°C]
v	:air velocity [m/s]
Y	:humidity ratio [g/kg]

Subscripts

a	:air
ads	:adsorption
avg	:average
c	:cooling
deh	:dehumidification
des	:desorption
h	:heating
in	:inlet
out	:outlet
reg	:regeneration
w	:water

Abbreviations

DCHE:desiccant coated heat exchanger

Mr.PichetLertboonkankit received the B.E(2012), degree Civil Engineering from King Mongkut's University of Technology Thonburi, Bangkok, Thailand

Prof.Dr.Surapong Chirarattananon obtained his degrees in electrical engineering from Australia, including his Ph. D. from the University of Newcastle, M. Eng. from Monash University, and B. Eng. from the University of New South Wales

An Examination of Aerosol Optical Depth Observed during a Dry Season at a Site in Bangkok

Nishit Aman[a,b], Kasemsan Manomaiphiboon[a,b], Panwadee Suwattiga[c], Nosha Assareh[a,b], Vacharaporn Soonsin[a,b], Vithaya Saetang[c]

[a] The Joint Graduate School of Energy and Environment, King Mongkut's University of Technology Thonburi, Thailand
[b] Center for Energy Technology and Environment, Ministry of Education, Thailand
[c] Faculty of Applied Science, King Mongkut's University of Technology North Bangkok, Thailand

ABSTRACT

This study deals with aerosol optical depth (AOD) measured in the daytime (900-1630 local time) during Jan.-Mar. 2014 at a general urban site in North Bangkok using a handheld sunphotometer. The AOD characteristics examined includes diurnal variation, weekday/weekend comparison, and daily series of average AOD, with emphasis on AOD at the spectral wavelength of 500 nm. It was found that AOD (in terms of average) slightly changes from morning to early afternoon but decreases in late afternoon. This may be due to change in wind speed or local aerosol emissions or both combined. Interestingly, AOD tends to be larger over weekends than weekdays, especially in the afternoon. This may be caused by a shift or contrast of traffic loads between weekdays and weekends in the area, assuming that the influence of meteorological factors is not much different. Morning AOD apparently shows an increasing trend over time from Jan. to Mar, so does afternoon AOD, which could partly be related to southerly winds starting to blow or prevail during Feb. and Mar, potentially transport aerosols from the upwind area, which is the urban core of Bangkok to the measurement site. However, the results presented here are still deemed as preliminary.

Keywords: Aerosol optical depth, Air pollution, Diurnal variation, Sunphotometer.

INTRODUCTION

Atmospheric particulate matter or aerosols are simply tiny or small particles suspended in the atmosphere. It can be directly emitted, formed in the air by gas-to-particle conversion, or by the disintegration of liquids or solids. Their size varies from 10^{-4} μm to 100 μm. They can affect both human's health and the physical environment. In atmospheric science, its ability to scatter and absorb solar radiation is one of the important subjects intensively studied. Aerosols may cause negative surface forcing (cooling) and positive surface forcing (heating), perturbing the weather in different temporal and spatial scales. At a local-to-regional scale, they play a role in regulating or affecting atmospheric stability, winds, and photosynthesis (Friedlander, 2000).

A number of measures have been used to indicate to the degree of how much aerosols are present in the atmosphere, one of which is aerosol optical depth or thickness (AOD). By definition, AOD reflects how light is attenuated (i.e., atmospheric turbidity) by aerosols, which can be technically related to visual range or visibility (i.e., how far in terms of distance once can see) However, since AOD is a column-integrated quantity, the linkage between AOD and visual range may not be direct or straightforward. AOD is also a function of wavelength of light. Given AOD at different wavelengths, it is possible to derive certain information of optical properties and aerosol size distribution. Numerous studies on AOD measurement and characterization can be found in the literature, whose scope of investigation ranges from a local area to city/ region/continental/global scales and spans from a short period (days) to seasons or multi-years (Srivastava et al., 2008, Reddy et al., 2011, Ganesh et al., 2008, and references therein). Ground-based AOD networks, such as AERONET (Aerosol Robotic Network) and SKYNET, have been established in many parts of the world to monitor or track changes in AOD. Satellite-derived AOD data are also available and useful for monitoring over large areas.

Over a local area, AOD typically changes with time, depending on factors such as the evolution of atmospheric boundary layer (ABL), emissions, and long-range transport. At present, little AOD studies have been done in the urban background of Bangkok, the capital of Thailand (Janjai et al., 2009 and 2012), and further investigation is still needed to supplement the current knowledge of AOD and its characteristics, especially temporal variability and factors influencing it.

Air pollution has been a great concern in Bangkok, the capital and the most populated province of Thailand. A very important air pollutant in Bangkok is particulate matter (PCD, 2013). Here, a preliminary investigation of AOD data collected from a short-term AOD monitoring program at a general urban background site in Bangkok was conducted, and its results are presented.

AOD MEASUREMENT

The measurement of AOD was carried out using a handheld sunphotometer MICROTOPS-II by Solar Light (US) (Morys, et al., 2001). The site was at the rooftop of the building of the Faculty of Applied Science, King Mongkut's University of Technology North Bangkok (Figure 1). The rooftop is about 44 m high (above ground level), sufficient to avoid significant interferences from human activities at the surface near or around the site. The sunphotometer used here has five different wavelengths (440 nm, 500 nm, 675 nm, 870 nm, and 936 nm). The device was fixed on a tripod stand, to secure the alignment of its aperture to the sun. The measurement spanned Jan. 8 – Mar. 18, 2014. Data was collected for 65 days between these periods. Data was collected every half an hour, starting at 9am and ending at 4:30pm each day. A couple measurements were taken each time. Any data that were found or judged as bad or questionable were excluded. Due to presence of missing data due to cloudy sky, only 53 days data was used for analyzing the trend of daily average AOD. In addition, one-day AOD measurement (on Mar. 26, 2014) was made at Silpakorn University, Nakhon Pathom, where an AERONET (Aerosol Robotic Network, http://aeronet.gsfc.nasa.gov) station is located (Figure 1). We then compared the results from MICROTOPS-II and AERONET and found satisfactory correspondence (detailed not shown), assuring the quality of the handheld sunphotometer used.

Fig.1. Measurement site and AERONET site

RESULTS AND DISCUSSION

In the following, we only describe the results of AOD at 500 nm (or AOD_{500}) for conciseness. It is noted that AOD_{500} was here used as a surrogate for fine aerosol particles in the atmosphere. Figure 2 shows the diurnal variation of AOD_{500}. As seen, AOD_{500} (on average) does not vary much particularly in the morning but gradually decrease from early afternoon towards the evening. A possible reason is change in wind speed or local aerosol emissions or both combined. The effect of varying mixing height over daytime hours may not be strong given AOD as a column-integrated quantity.

Figure 3 shows the "weekday/weekend effect" on AOD_{500}. Most of the weekend values (in terms of average) turn out to be relatively large, which is counter-intuitive to that vehicular emissions is generally thought to be lower during weekends. At this point, we only hypothesize that there was not systematic and drastic differences in meteorology between the weekday period and the weekend period. Then, we imply a shift in aerosol loadings emitted from major sources, traffic emissions in particular, i.e., a large volume of traffics also present during the weekends.

Figures 4 and 5 show the daily sequences of morning AOD_{500} and afternoon AOD_{500}. It is readily noticed that both have a positive (i.e., increasing) trend from Jan. to Mar. It is not possible at this point to identify its cause. Based on our investigation of air-mass back-trajectories over the time period in question (details not shown), southerly winds from the Gulf of Thailand begin to prevail in Feb. and especially in Mar., may be part of the reason in that they effectively transport high aerosol loading from the urban core of Bangkok downwind to the site. Other meteorological factors were not thought to be important to cause the apparent trends since Jan.-Mar. still possess common features of the dry season, omitting the role of photochemistry to aerosol level in the atmosphere. Nevertheless, this is a somewhat conservative and crude viewpoint, and more detailed investigation is needed.

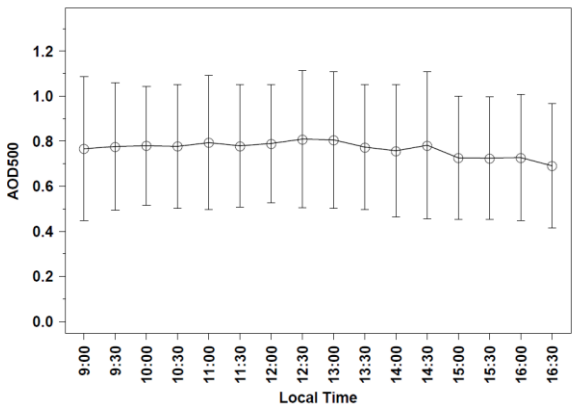

Fig. 2. Diurnal variation of AOD_{500}

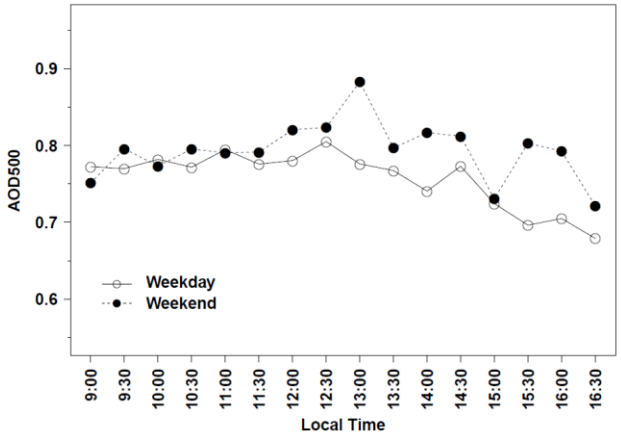

Fig. 3. Diurnal variation of AOD_{500} during weekday and weekend periods

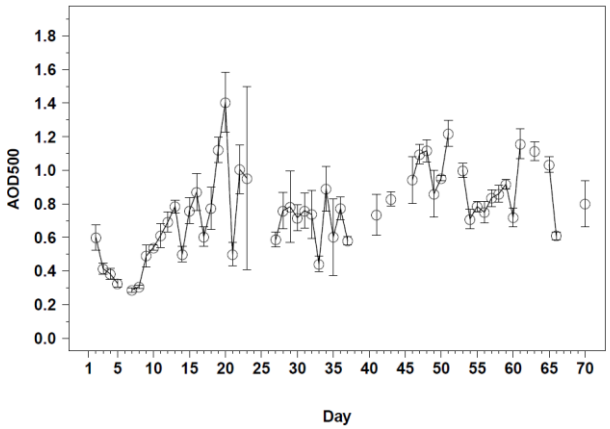

Fig. 4. Daily morning AOD_{500}

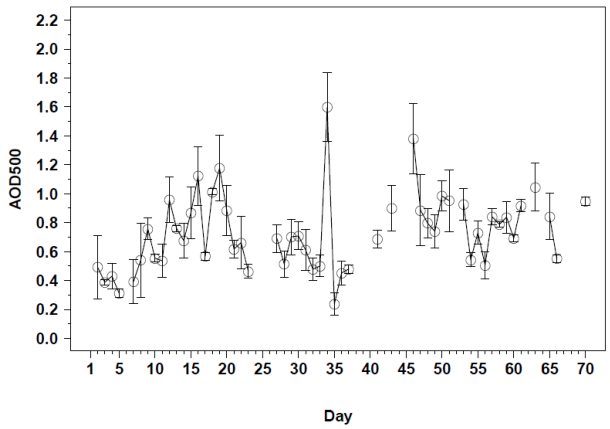

Fig. 5. Daily afternoon AOD_{500}

SUMMARY

The field measurement of AOD was conducted over 10 dry-season weeks in 2014 at a general-urban-background site in Bangkok. The results of AOD_{500} were presented; their key summary is given as follows:

- Slightly increase in AOD in the afternoon, from morning, and then slightly decrease, may be due to change in wind speed or local aerosol emissions or both combined.
- Higher AOD during weekends, compared to that during weekdays, may be due to a shift in aerosol loadings emitted from major sources, particularly traffic emissions.
- Gradual increase in AOD from Jan. to Mar. shows the potential effect of the prevailing southerly wind from the Gulf of Thailand, transporting aerosols from the urban core to the measurement site.

It should be noted that the results presented are still deemed as preliminary, requiring further and detailed investigation.

ACKNOWLEDGEMENTS

The authors thank assistants in the field measurement and the AERONET station (PI: Dr. Serm Janjai) for the data for comparison. The study is part of the ongoing research supported by the Joint Graduate School of Energy and Environment (JGSEE), King Mongkut's University of Technology North Bangkok, and the Postgraduate Education and Research Development Office.

REFERENCES

Friedlander, S.K., Smoke Dust and Haze: Fundamental of Aerosol Dynamics, Oxford University Press, New York, 2008.

Ganesh, K.E., Umesh, T.K., Narasimhamurthy, B., Site specific aerosol thickness characteristics over Mysore, Aerosol and Air Quality Research, vol. 8, pp. 295-307, 2008.

Janjai, S., Suntaropas, S., Nunez., Investigation of aerosol properties in Bangkok and suburbs, Theoretical and Applied Climatology, vol. 96, pp. 221-233, 2009.

Janjai, S., Nunez, M., Masiri, I., Wattan, R., Buntoung, S., Jantarach, T., Promsen, W., Aerosol optical properties at four sites in Thailand, Atmospheric and Climate Science, vol. 2, pp. 441-453, 2012.

Morys, M., Mims, F.M., Hagerup, S., Anderson, S.E., Baker, A., Kia, J., Walkup, T., Design, calibration and performance of MICROTOPS-II handheld ozone monitor and sun photometer, Journal of Geophysical Research, vol. 106. pp. 14573-14582, 2001.

PCD, Thailand state of pollution report 2013. Report No. 06-053, ISBN 978-616-316-205- 2, 2014.

Reddy, B.S.K., Kumar, K.R., Balakrishnaiah, G., Gopal,

K.R., Reddy, R.R., Reddy, L.S.S., Narasimhulu, K., Rao, S.V.B, Kumar, T.K., Balanarayana, C., Moorthy, K.K., Babu, S.S., Aerosol climatology over an urban site, Tirupati (India) derived from columnar and surface measurements: First time results obtained from 30-day campaign, Journal of Atmospheric and Solar-Terrestrial Physics, vol. 73, pp. 1727-1738, 2011.

Srivastava, A.K., Devara, P.C.S., Rao, Y.J., Kumar, Y.B., Rao, D.N., Aerosol optical depth, ozone and water vapor measurement over Gadanki, a tropical station in peninsular India, Aerosol and Air Quality Research, vol. 8, pp. 459-476, 2008.

AUTHORS OF THE PAPER

Nishit Aman is a PhD student at the JGSEE. Email: aman.bae@gmail.com

Kasemsan Manomaiphiboon (PhD) is a faculty member at the JGSEE. Email: kasemsan_m@jgsee.kmutt.ac.th

Panwadee Suwattiga (PhD) is a faculty member at KMUTNB.

Nosha Assareh is a PhD candidate at the JGSEE.

Vacharaporn Soonsin (PhD) is a former researcher at the JGSEE.

Vithaya Saetang is a Master graduate student at KMUTNB.

Study of Parameters for Performance Improvement on Small Biomass Brazier

Somsak Siwadamrongpong[1]*,Pongsiri Wisataso[2] and Teerasan Chaiyaphuk[2]
[1]School of Manufacturing Engineering, [2]Energy Management Engineering,
Suranaree University of Technology, 111 University Avenue Muang, Nakhon Ratchasima 30000 Thailand
*Contact: somsaksi@sut.ac.th, 044-224-236

ABSTRACT

The energy is a necessary to subsistence of human, especially in the country side of developing country. It is known that cost of energy is trending to increasing in the future. The renewable energy is an alternative which able to decrease an expenses of living. The Energy Provincial Office of Ang Thong province in Thailand has an innovation of a small biomass brazier which higher performance than the conventional one. The brazier is using updraft gasifier concept. However, the brazier was expensive compared to basic wage in Thailand. This study was aimed to investigate geometric dimension parameters of the modified brazier, the cheaper, to its performances using design of experimental criterion. 3 parameters were studied, % opening of inlet air gate, diameter at the top of hot chamber and height of cooking ware from brazier. The small brazier was built and tested using eucalyptus wood as fuel material. The brazier performance was indicated in term of temperature and time to keep temperature with constant mass of fuel material. It was expected that the results of this study may yield a cheap brazier with high performance.

Keyword: Brazier, Biomass, Design of Experiment, Gasifier

1. INTRODUCTION

A small biomass brazier is simple to operate. A fuel material is filled on top of the brazier then do kindle air inlet will come in at the duct below. The combustion and burning yields the CO, CH_4 and H_2 gases at the inner tube. The gases go through the hole around outer tube then move up to the top of reactor and yield the second burning of the gases. This section area, top of the hot chamber, is reacting as the reduction zone. Temperature in this section could be reached high temperature as 820°C. The high performance brazier, shown in Fig. 1, was developed and reported by Ministry of Energy, Thailand. However, high cost the brazier is such a barrier of country wide using of the brazier.

The brazier was developed for the target of lower cost by changing material and some details, but its performances is still no reported. The low cost brazier was showed in Fig. 2. There are three parameters that will be affected to the rate of fuel consumption and performance of a small biomass brazier. The first one is the height of grate gas stove, the second is a chamber's diameter at the top of brazier and the other one is flow rate of air inlet. The 3 parameters were brought to key parameters in factorial design.

Fig. 1 Small biomass brazier

Fig. 2 Low cost small biomass brazier

2. EXPERIMENTAL PROCEDURE

2.1 2^k Factorial Design

3 factors that affect temperature and performance of the brazier were brought in to this study. There are nine experimental cases including the low cost a small biomass brazier (use as reference) as shown in table 1. The 3 factors were shown as follow, and indicated in Fig. 4;

a) Factor A is height of cooking ware from brazier,
b) Factor B is a diameter at the top of hot chamber and
c) Factor C is % opening of inlet air gate.

Table 1 9 cases of 2^3 factorial design with reference

Type of Brazier	No.	Parameters					
		height of cooking ware from brazier (A)		diameter at the top of hot chamber (B)		% opening of inlet air gate (C)	
		3 cm	5 cm	4 inch	5 inch	50%	100 %
Reference	1	4 cm		6 inch		open 100%	
This study	2	■		■		■	
	3	■		■			■
	4	■			■	■	
	5	■			■		■
	6		■	■		■	
	7		■	■			■
	8		■		■	■	
	9		■		■		■

2.2 Structure of Brazier

Figure 3 is showing the path of air inlet and gasification zone of a low cost biomass brazier while figure 4 is showing a small biomass brazier in this study. It is obvious that the top of the hot chamber was set smaller size than reference. The air inlet gate was set to adjustable.

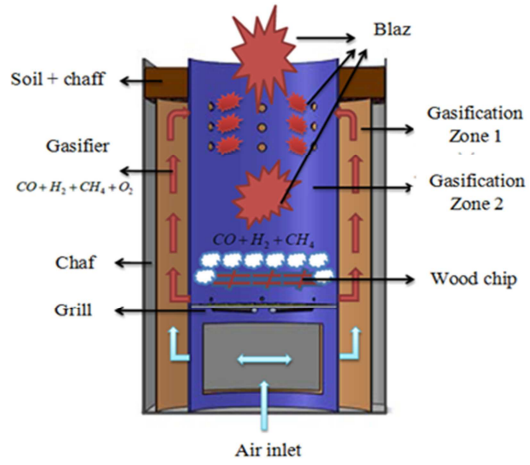

Fig. 3 Low cost small biomass brazier (reference)

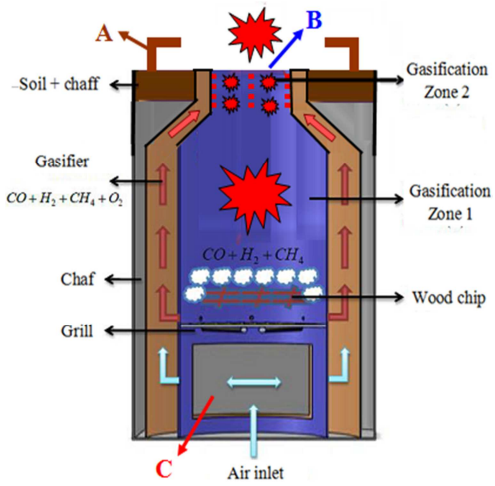

Fig. 4 Low cost small biomass brazier in this study

2.3 Measurement

- Thermocouple was using to measure the temperature at top chamber and water.
- Humidity Meter is using to measure the humidity of wood chip to ensure the value is not over upper limit.
- Kilogram Meter is using to measure the wood ship to ensure each experimental were used a weight net 1 kg.
- Stop watch is using to counter a period time every 1 minute then record both of temperature data.

2.4 Material & Tool

- A eucalyptus wood chip was used as fuel material and the length was about 10 cm. The wood was chopped to separate into four pieces.
- 1 kg of water was used as load of the brazier.
- The pot of 3 kg volume capacity without lid was used as water pot.

2.5 Experimental Procedures

The brazier was starting to fire with 5 sheets of A4 paper as starting fuel. 20% of the eucalyptus wood chip was laid on the bundle of paper in the brazier. After ignition and fire starting for about 2 minute, the rest of the eucalyptus wood chip was put into the brazier. The pot of water without lid was put over the brazier. Water temperature and Brazier temperature at the top of hot chamber were measured from 3 minute after put on the pot. The temperatures were recorded every 1 minute until 60 minute.

3. Results and Discussion

3.1 Temperature Profile

Fig. 5 and 6 indicated temperature profile of a temperature at the top chamber and water

temperature, respectively. From the Fig. 5, maximum temperature and area under the curve were tracked and brought into DOE analysis, shown in Table 2. From Fig. 6, maximum temperature or water, area under the curve, time to reach 90 C of the water and duration time to keep over 90 C were tracked and displayed in Table 3.

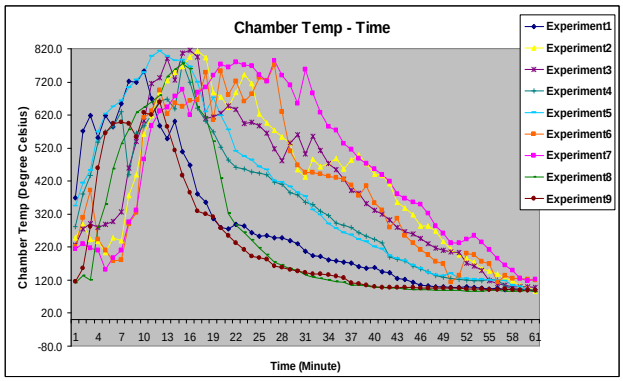

Fig. 5 Temperature profile at the top chamber

Table 2 Maximum temperature at the top of hot chamber and area under the curve from Fig 5

No.	A	B	C	Max Temp (℃) / Area under the curve
2	-1	-1	-1	814.3 / 25,702
3	1	-1	-1	814.5 / 23,838
4	-1	1	-1	778.9 / 21,338
5	1	1	-1	813.5 / 23,343
6	-1	-1	1	769.7 / 24,091
7	1	-1	1	784.3 / 27,696
8	-1	1	1	774.3 / 15,484
9	1	1	1	659.5 / 13,944

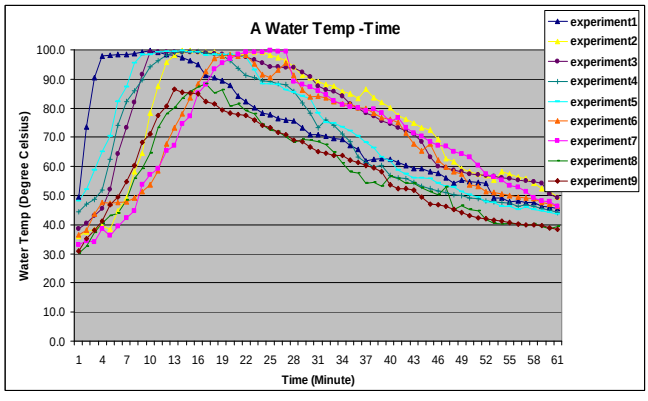

Fig. 6 Temperature profile of water

Table 3 Time to reach 90 C of the water and duration time to keep over 90 C from Fig. 6

No.	Max Temp (°C) / Area under the curve	Time to reach 90 ℃ (min) / Duration to keep over 90 °C of water (min)
2	99.8 / 4,521	11 / 18
3	99.3 / 4,576	9 / 21
4	99.5 / 4,199	9 / 15
5	99.8 / 4,349	7 / 16
6	98.2 / 4,167	17 / 15
7	99.7 / 4,208	17 / 16
8	88.4 / 3,533	(Max 87 C) / 9
9	88.5 / 3,545	(Max 86 C) / 7

3.2 DOE Analysis

MiniTab V14 was employed to analyze the data statistically. Fig. 7 showed the influence of the 3 factors to maximum temperature at the hot chamber. Fig. 8 indicated the influence of the 3 factors on the area under the curve of temperature profile, which was implied the energy amount transfer pass the top of the chamber.

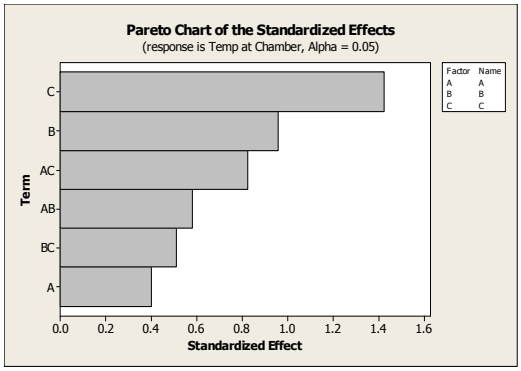

Fig. 7 Pareto of effect or influence of 3 factors to maximum temperature at the top chamber

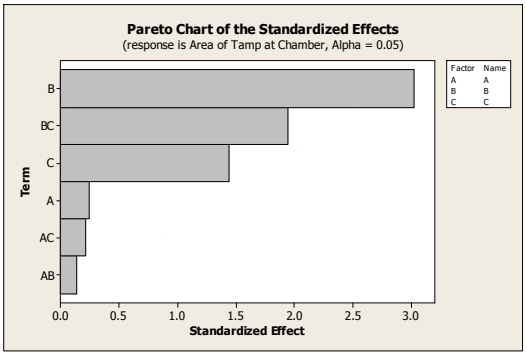

Fig. 8 Pareto of effect or influence of 3 factors to area under the curve of temperature profile at the top chamber

Fig. 7 and 8 indicated obviously that temperature and heat transferred to the top chamber were only affected by factor B and C, diameter at the top of hot chamber and %opening of inlet air gate. However, please note that all effects were not significant statistically and all influenced effects were in minus sign.

Fig. 9 showed the influence of the 3 factors to maximum temperature of water. Fig. 10 indicated the influence of the 3 factors on the area under the curve of temperature profile of water, which was implied the energy amount transfer pass to the water. It was obviously to discuss that diameter at the top of hot chamber and %opening of inlet air gate, factor B and C, had played the major role to affect water temperature and heat transferred to water. All significant effects were in minus sign. It could be concluded that small diameter of top chamber and reducing of %opening air gate would yield better performance of water temperature and heat transferred to water.

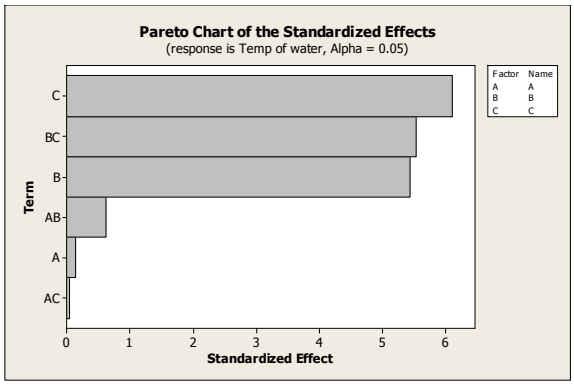

Fig. 9 Pareto of effect or influence of 3 factors to maximum temperature of water

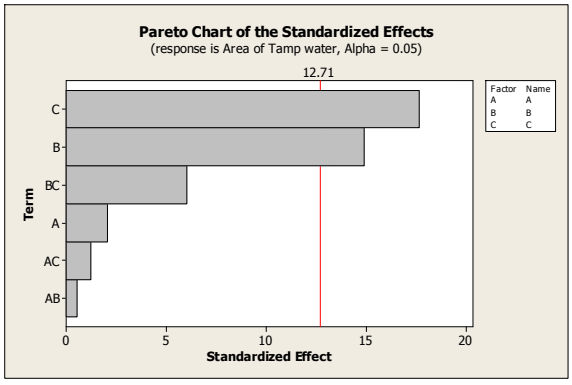

Fig. 10 Pareto of effect or influence of 3 factors to area under the curve of temperature profile of water

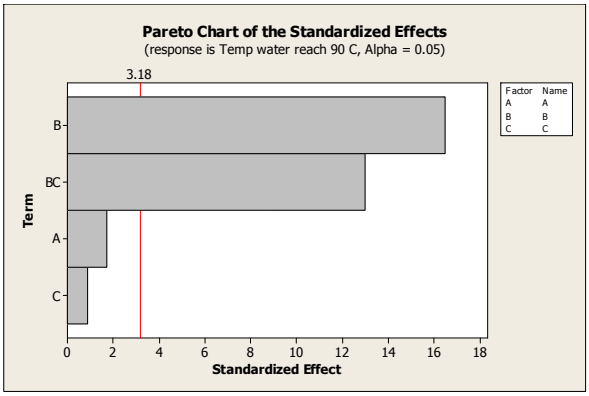

Fig. 11 Pareto of effect or influence of 3 factors to time use to rise water temperature to 90 C

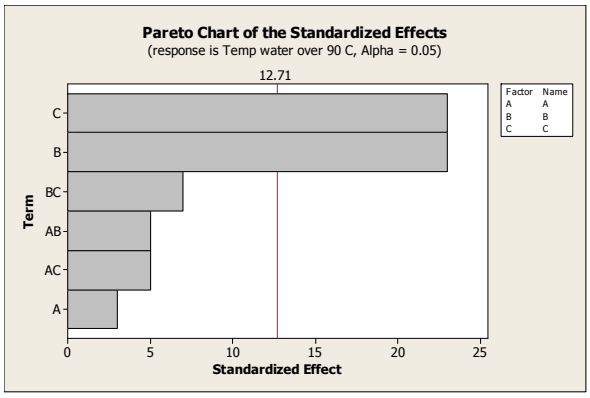

Fig. 12 Pareto of effect or influence of 3 factors to duration time kept water temperature over 90 C

Fig. 11 showed the influence of the 3 factors to time use for rising the water temperature to 90 C. Fig. 12 indicated the influence of the 3 factors on duration time kept water temperature over 90 C. It was obviously to discuss that diameter at the top of hot chamber and interaction between its effect with %opening of inlet air gate, factor B and BC, had played the major role to affect the time use for rising the water temperature to 90 C. Both effects were in minus sign. It could be concluded that small diameter of top chamber and wide open of air gate would yield shorter time to rise water temperature to reach 90. On the other hand, small diameter of top chamber and reducing of %opening of air gate would yield longer time to hold and keep water temperature over 90.

3.3 Discussion

The small biomass brazier was considered that suitable for using in suburban area. Its characteristics should be able to keep long time at high temperature.

The 3 factors described above could be discussed as follow;

Factor A- seems to be no influence at least in this study.

Factor B and C- seem to play the most important factors that affect to all responds in this study.

Interaction between B and C- seems to play an important role on some respond such as maximum temperature of water and time to rise water temperature.

4. CONCLUSION

This study was aimed to evaluate the performance of a small biomass brazier by varying 3 factors. 2^3 Factorial Design Criterion was employed to carry out through the experiment and data analysis. It could be concluded that diameter at the top of hot chamber and %opening of inlet air gate are the most influence factors to performance of the brazier. Small diameter at the top of hot chamber and reducing of %opening of inlet air gate may yield better performance of the brazier.

REFERENCES

Environmental Impact and Social Return of the Use of Biomass in Community and Household Levels
Visakha Phujinda, Develop management institute Bangkok, Thailand 2014b.

Develop of Biogas Using from Livestock Manure and Agricultural Wastes
Supot Keidmee, Phetchabun Rajabhat University,Thailand

Somsak Siwadamrongpong
He is lecturer in School of Manufacturing Engineering, Suranaree University of Technology

Pongsiri Wisataso
He is working at Seagate Technology Company in Thailand and studying M.Eng. in Energy Management Engineering at Suranaree University of Technology

Teerasan Chaiyaphuk He is working at The Energy Provincial Office of Ang Thong province in Thailand and studying M.Eng. in Energy Management Engineering at Suranaree University of Technology

SOME CALCULATION RESULTS FOR A HORIZONTAL AXIS WIND TURBINE BLADE WORKING AT LOW WIND SPEEDS

Mich T. Nguyen[1], Cuong H. Do[1], Hao C. Nguyen[2]
[1] Hanoi University of Science and Technology, Ha noi, Viet Nam
[2] Viet Duc Industrial College, Thai Nguyen, Viet Nam

ABSTRACT

The article presents some initial results in study and design for horizotal axis wind turbines, which work at a wind speed in the range of 6 to 7.5m/s in Vietnam. The turbines have 3 blades with a power of 20kW, the theight of the tower H = 18 m, and cutting machine with rotating blades, survival wind speed 25m/s. The research focuses on studying wind turbine aerodynamics and design of the blade, by using NACA airfoils, dynamical section blade element momentum analysis of angle effects, methods of speculation about the flow coefficient, and calculated pressure section for each blade element.

1. OVERVIEW OF VIETNAM WIND POWER AND ALTERNATIVES

Renewable energy in general and wind energy in particular is a source of clean energy, endless. Vietnam is located in the tropical monsoon region, with a coastline of 3,444 km and breezes from the East Sea – the favorable conditions for the development of wind energy. According to a survey by the World Bank in Vietnam, the wind speed of about 6 to 7.5 m/s occupies about 30% of the territory of our country, less than 6m/s accounted for 60% (WB, 2001). There is a few regions with a wind speed over 7.5m/s. In many countries and territories around the world, with the average wind speed of 12m/s, they have developed wind generators for many decades. Wind generators in the world are manufactured to exploit the power under the average 12m/s wind speed, so the capacity of calculation is for the wind speed of 12m/s and the rotor is designed to ensure the desired power and stable conditions for wind generators eventhough the wind speed is greater than 12m/s. The design proposal is consistent with the countries with high average wind speeds than or equal to 12m/s, and ensure the design capacity with low investment rates. If the wind turbines are imported and installed in Vietnam, where the average wind speed is around 7.5m/s, the actual generated capacity is only about 1/3 of the design capacity.

Accordingly, to have a wind turbine installed in Vietnam, generating power as high as designed, it is necessary to study and design a new generation of wind generators working at a wind speed 6m/s.

2. SELECTION OF THE CONFIGURATION AND DETERMINATION OF THE BASIC SIZE OF WIND GENERATORS

In this paper, we will design a turbine with the following parameters: power P = 20kW; cut-in wind speed 3.5m/s; working wind speed 6m/s; survival wind speed 25m/s. The turbine will be a horizontal-axis wind generator with the number of the blades N = 3, the tower height H = 18 m.

3. SOME RESULTS OF THE STUDY, CALCULATIONS, AND DESIGN OF THE WIND GENERATOR

3.1 Calculation of the rotor radius R:

The radius of the rotor is given as

$$R = \sqrt{\frac{P}{\frac{1}{2}.\rho.V_{\infty}^{3}.\pi.\eta}}$$

Where, P = 20kW, power coefficent η = 0.3 ÷ 0.5 (theoretically ηmax = 0.593; actually only 0.3 ÷ 0.5), the density of air ρ = 1.2 kg/m^3, working wind speed v_{∞} = 6m/s. Substituting these values to the above formula gives R = 9.8 ÷ 12,6m. Accordingly, we choose R = 10m.

In this study, we base on the relationship between the tip speed ratio and the number of the blades to choose a tip speed ratio λ of 4 (Tony Burtun, et al, 2001). Therefore, the angular velocity is:

$$\Omega = \frac{\lambda V_{\infty}}{R} = 2.4 rad/s = 22.9 rpm$$

3.2 Blade profile

The lift and drag forces act on the blade when the turbine works. The values of these forces depend on angles of attack α. When, the turbine output become higher as is the ratio of the drag to lift forces C_l / C_d decreases. The NACA airfoil series are often used to the

study the aerodynamic characteristics, and applied to design the blade of horizontal axis wind rotors. We choose the airfoil NACA63415 characterized as follows: C_d/C_l min = 0,01 at $\alpha^0 = 4^0$. According to the graph of the variation of Cl with respect to α, C_l is equal to 0.8 at $\alpha = 4^0$. Using this angle is to calculate distribution of the pitch angle and the chord length along the blade (Tony Burtun, et al, 2001) .

3.3 Determination of the chord length

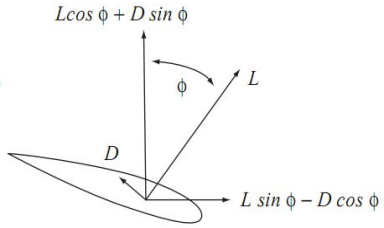

Figure 1. Velocities and forces acting on the blade section

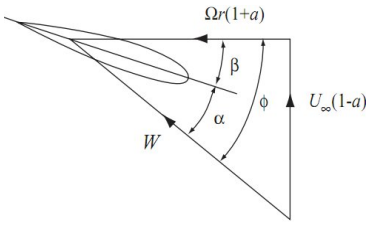

Figure 2. The velocity triangle

From the velocity triangle, the relative velocity of the flow with blade section is given as:

$$w = \sqrt{U_\infty^2(1-a)^2 + \Omega^2 r^2(1+a')^2} \qquad (1)$$

The angle of flow is determined by the expression:

$$\sin\phi = \frac{U_\infty.(1-a)}{W}$$

$$\cos\phi = \frac{\Omega r(1+a')}{W}$$

The angle of pitch is: $\beta = \phi - \alpha$

Then lift and drag on the blade section are:

$$\delta L = \frac{1}{2}\rho W^2.c.C_l.\delta r$$

$$\delta D = \frac{1}{2}\rho W^2.c.C_d.\delta r$$

We assume that the axial and angular induction factors, *a* and *a′*, are constant in the swept area of the section, and that there is no interaction between adjacent stream.

The aerodynamic force acting on the section N[th] in the direction of the rotation axis is:

$$\delta L.\cos\phi + \delta D.\sin\phi = \frac{1}{2}\rho W^2.N.c.(C_l.\cos\phi + C_d.\sin\phi)$$

The aerodynamic force acting on the section N[th] in the tangent direction is:

$$\delta L.\sin\phi - \delta D.\cos\phi = \frac{1}{2}\rho W^2.N.c.(C_l.\sin\phi - C_d.\cos\phi)$$

Momentum of the airflow passing through the swept area is given as:

$$m\Delta v = \rho U_\infty(1-a).2\pi.r\delta r.2a.U_\infty = 4\pi\rho U_\infty^2 a(1-a).r.\delta r$$

Pressure drop because of rotary traces:

$$\Delta p = \frac{1}{2}.\rho.(2.a'.\Omega.r)^2$$

Balancing forces in axial rotation:

$$\delta L.\cos\phi + \delta D.\sin\phi = m.\Delta v + \Delta p.\delta s \qquad (2)$$

Since the term $\Delta p.\delta s << m.\Delta v$, for ease of calculation, $\Delta p.s$ is assumed to be zero, equation (2) becomes:

$$\frac{1}{2}\rho W^2 Nc(C_l\cos\phi + C_d\sin\phi)\delta r = 4\pi\rho U_\infty^2 a(1-a)r\delta r$$

$$\frac{W_2}{U_\infty^2}.N.\frac{c}{R}.(C_l.\cos\phi + C_d.\sin\phi) = 8\pi.x.a.(1-a)$$

Angular momentum of the gas stream passing through the swept area of the blade element changes:

$$\rho.U_\infty.(1-a).\Omega.2a'r.2\pi r.\delta r = 4\pi\rho.U_\infty.(1-a).\Omega.a'r.r\delta r$$

Balancing the tangental forces gives:

$$\delta L.\sin\phi - \delta D.\cos\phi = 4\pi\rho.U_\infty.(1-a)\Omega.a'r.r$$

Thus:

$$\frac{\rho}{2}W^2 Nc(C_l\sin\phi - C_d\cos\phi)\delta r = 4\pi\rho U_\infty(1-a)\Omega a'r^2\delta r$$

$$\frac{W^2}{U_\infty^2}.N.\frac{c}{R}.(C_l.\sin\phi - C_d.\cos\phi) = 8\pi.\lambda.x^2a'(1-a)$$

From the expression related to the torque of the rotor, for ease of calculation, assuming $C_d \approx 0$, then:

$$\frac{W^2}{U_\infty^2}.N.\frac{c}{R}.(C_l.\sin\phi - C_d.\cos\phi) \approx \frac{W^2}{U_\infty^2}.N.\frac{c}{R}.C_l.\sin\phi \qquad (3)$$

$$= 8\pi.\lambda.x^2a'(1-a)$$

Substituting $\sin\phi = \frac{(1-a)U_\infty}{W}$ and $W = \sqrt{U_\infty^2.(1-a)^2 + \Omega^2.r^2(1+a')^2}$ to equation (3), we have: $N.\frac{c}{R}.C_l = 8\pi.\lambda.\mu^2a'.\frac{U_\infty}{W}$

Or: $$N.\frac{c}{R}.C_l = .\frac{8\pi.\lambda x^2 a'}{(1-a)^2 + \lambda^2x^2(1+a')^2} \qquad (4)$$

The right hand side of equation (4) depends on the factors *a* and *a′*, to achieve the maximum performance, a and a' must satisfy:

$$a = \frac{1}{3};\quad a' = \frac{a(1-a)}{\lambda_r^2} = \frac{2}{9.\lambda^2.x^2}$$

Therefore:

$$N.\frac{c}{R}.C_l = .\frac{16\pi}{9\lambda\sqrt{\frac{4}{9} + (\lambda x + \frac{2}{9\lambda x})^2}} \qquad (5)$$

From the lift coefficient and number of blades N = 3, we have the variation of $\frac{c}{R}$ with respect to x (the ratio of the radius x) as shown in the table 1:

Section	Ratio of the radius $x = \frac{r}{R}$	Ratio of the chord with radius $\frac{c}{R}$	Chord length *c (mm)*
I	0,1	0,16117	1611,7
II	0,2	0,15420	1542
III	0,3	0,14582	1458,2
IV	0,4	0,13794	1379,4
V	0,5	0,12975	1297,5
VI	0,6	0,12155	1215,5
VII	0,7	0,11375	1137,5
VIII	0,8	0,09794	979,4
IX	0,9	0,09020	902
X	1,0	0,08297	829,7

Table 1: Index of profil

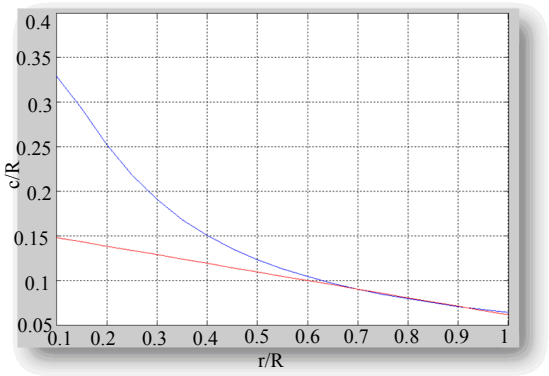

Figure 2. The graph $\frac{c}{R}$ dependent the ratio of the radius x

According to figure 3, the chord becomes larger as closer to the axis of rotation, leading to an increase fabrication material and the fabrication of this blade is very difficult to reach high accuracy. To reduce the blade material and facilitate fabrication, the chord length distribution is often linearized. To do so, we draw a line through the 70% and 90% of the radius of the high efficiency, ensuring the angle of attack to be 4^0, we have the ratio of the chord to the radius varied with *x* (Laird D, 2004), as follows:

$$\frac{c}{R} = -0{,}096.x + 0{,}158 \qquad (6)$$

3.4 Angle put blade

C_l is determined from the equation (5):

$$C_l = \frac{16\pi}{9.N.\lambda \frac{c}{R}\sqrt{\frac{4}{9} + (\lambda x + \frac{2}{9\lambda x})^2}}$$

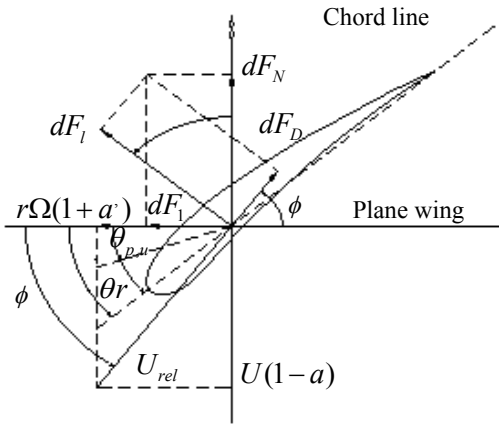

Figure 3. The relations between α, φ, ϕ the velocities and forces acting on a wind turbine blade element.

Combining this equation with the equation (6) will determine the variation of the lift coefficient along the length of the radius of the blade:

$$C_l = \frac{16\pi}{9N.\lambda(-0{,}96.x + 0{,}1580).\sqrt{\frac{4}{9} + (\lambda x + \frac{2}{9\lambda x})^2}}$$

We use the lift coefficient expression: $C_l = 7{,}162.\alpha + 0{,}3$ to calculate the angle of attack of the blade.

So the angle of pitch is: $\beta = \phi - \alpha$

The angle of flow is then determined according to the formula(Roskam & Jan/ Lan, C. T., 2000) :

$$tg\phi = \frac{(1-a)U_\infty}{(1+a')\Omega r} = \frac{2}{3\lambda x(1 + \frac{2}{9\lambda^2 x^2})} = \frac{2}{3\lambda x + \frac{2}{3\lambda x}}$$

Calculated flow angle, angle of attack, pitch angle are shown in the table :

Ratio radius $x = \frac{c}{R}$	*Angle of flow* ϕ $(^0)$	*Angle of attack* α $(^0)$	*Angle of Pitch* β $(^0)$
0,1	34,49	21,7	12,79
0,2	25,70	15,55	10,48
0,3	19,12	11,79	7,33
0,4	14,97	9,45	5,52
0,5	12,24	9,91	2,33
0,6	10,32	9,96	3,36
0,7	8,91	6,58	2,33
0,8	7,83	6,56	1,27
0,9	6,99	6,21	0,78
1,0	6,30	5,61	0,69

Table 2: Value of α, φ, ϕ at *x*

3.6 Cross section blade

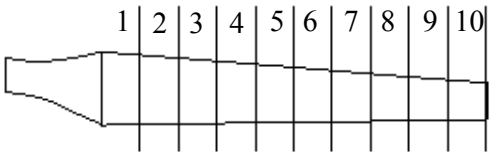

Figure 4. Cross section on blade

Parameters for NACA 63415 with C = 352mm are given in the table below:

Chord C *(mm)*	*Radius R (mm)*
0,02C	7,77
0,1C	18,13
0,2C	25,81
0,4C	27,73
0,5C	23,59
0,6C	17,92
0,7C	12,74
0,8C	9,23
0,85C	6,58
0,9C	3,71

3.7 Rendering3D of the blade:

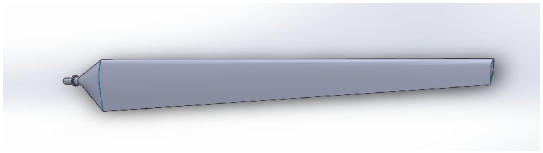

Figure 5. 3D blade

Curve of relationship between capacity coefficient and coefficient λ and Cp .

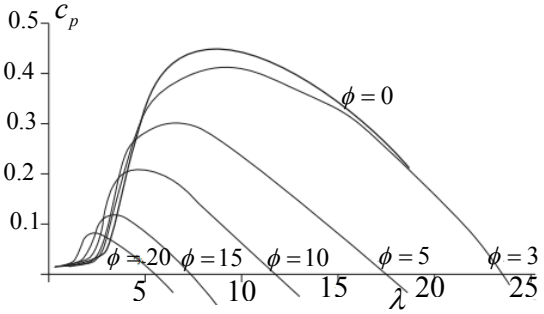

Figure 7. Relationship between capacity coefficient Cp and ratio λ

CONCLUSION

Some above studies and calculations are preliminary results on the design and calculation of the wind generator with a working low wind speed of 6 m / s. Future, characteristics of generators low wind speed is studied by using blade element theory, method speculate on stream coefficients, calculated power for each sub-component separate blade ... according to the iterative process, to obtain the optimal design.

REFERENCES

World Bank, Wind energy resource atlas of Southeast Asia, 2001

Tony Burtun, Nick Jenkins, David Sharpe, Ervin Bossanyi, "Wind Energy Handbook", John Wiley & Sons, Ltd, England, 2001.

Laird D,. "Blade design Codes", Sandia National Laboratories, 2004 Wind Turbine Blade Workshop.

Roskam, Jan/ Lan, C. T., Airplane Aerodynamics and Performance, 2000

NOMENCLATURE

α : Angle of attack
ω : Rotational speed of wind turbine
φ : Local flow angle
ϕ : Pitch angle
C_l : Lift coefficient
C_d : Drag coefficient
R: Radial extention of wind turbine blade
a: Axial induction factor
a' : Angular induction facor

Mich T. Nguyen received the B.E (1977) degree in mechanical enginneering from Hanoi University of Science and Technolog (HUST), the D.E (1984) degree in Manufacture and Calibration of Pressure Meters, from Grenoble France. He is a Professor, School of Transportation Engineering, HUST. Current interests include cavitations and turbomachines.

Cuong H. Do received the B.E. (1991) degree in mechanical engineering from HUST, the D.E. (2005) degree from HUST. He is a lecturer, School of Transportation Engineering, HUST. Current interests include hydraulic machines and automation equipment.

Hao C. Nguyen received the B.E. (2006) degree in Mechanics from Vietnam National University, Hanoi (VNU), the M.E. (2011) degree from VNU. He is a lecturer, Viet Duc Industrial College (VIDC). Current interests include hydraulic machines and automation equipment.

The Evaluation of Specific Energy Consumption Indices For Electronics Part Manufacturing

Somsak Siwadamrongpong[1]* and Thana Luntha[2]
[1]School of Manufacturing Engineering, [2]Energy Management Engineering,
Suranaree University of Technology, 111 University Avenue Muang, Nakhon Ratchasima 30000 Thailand
*Contact: somsaksi@sut.ac.th, 044-224-236

ABSTRACT
It is known that energy conservation in one of the current global trends for industries on green manufacturing concept. Specific Energy Consumption (SEC) is the key parameter to compare how much energy per unit they use for manufacturing. Industries could help in energy conservation by benchmarking their SEC to others in the same industry. The objective of this study was to evaluate energy specific consumption indices of electronics part manufacturing. The 2 years manufacturing data was collected from one company in Thailand. The SEC was separated into 4 categories, component manufacturing, part assembly, compressed dried air system and air conditioning/ventilation system. The data was analyzed by using least square multiple linear regressions. The SEC was achieved from coefficient of energy equation of each category. The SEC was test by using in energy consumption forecasting for 3 months. It was found that the forecasting is within 10% deviation, acceptable by company criteria. The SEC could be used as tool for forecasting and monitoring energy consumption of the company. It would be more advantage if this information is shared with stakeholders to adjust design/requirement for more conserved energy.

Keyword: Specific energy consumption, Multiple linear regressions, Electronics part, Energy conservation

1. INTRODUCTION

Since electricity is an important factor of the production processes of industries and the energy costs are continuously increasing. The analysis of energy data and the prediction of the directions of the energy consumption of all production processes are the important factors of all businesses that consume energy.

One electronics part manufacturing company in Nakornratchasima Province, Thailand pays attention to the important of SEC analysis. The company has shared their production information and electricity consumptions to this research. The company is approximated annually uses 25 - 20 GWh of electricity. This is considered as one of companies which highly consuming energy in the province. The consumption also tends to increase every year and the portion spent in production and related processes is the majority according to the information about the energy consumption in 2014, shown in Figure 1.

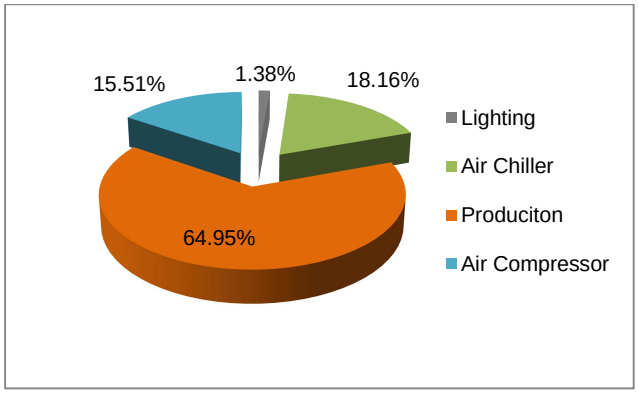

Figure 1 – The Ratio of the Energy Consumptions in 2014

The prediction of energy consumption with the energy equations and specify energy consumption indices of products is a tool that the company uses for preparing budgets and setting standards for the energy consumption of each product. The objectives of the study were establishment of energy equations and evaluation of energy specific consumption of the company.

2. EXPERIMENT

The study has four steps as follows.

2.1 Data Collection & Screening

Collected data was screened and separated into 4 categories by using similarity & assembly processes. It is expected that products in each categories would consume energy for assembly process in the same level.

2.2 Multiple Linear Regressions

Multiple linear regression techniques were employed to create the energy equations and expanded to explain the SEC value of each

product. Quality of regression will be judged by R^2 must over 85% and confidence interval 95% (P-Value<0.05).

,

2.3 Validation of Energy Equation / SEC

The equation was validated with data, production and consumption, of the first quarter in 2015.

3 Results and Discussion

3.1 Data Collection & Screening

Data was separated and grouping into 4 categories

3.1.1 ***Part Assembly***

The assembled part data was grouped into A1, A2, A3 and A4 product groups. The total energy consumption of the 4 product groups was historically collected for two years (2013 - 2014) as shown in Table 1. The irregular data (May 2013) was eliminated.

Table 1 – The Energy Consumption of Group A

Production	A1	A2	A3	A4	KW.H
Jan 13	94,181	97,738	9,204		97,809
Feb 13	89,612	83,859	7,781		68,012
Mar 13	91,026	69,356	7,668		64,517
Apr 13	80,364	125,831	9,143		70,373
Jun 13	88,835	125,902	9,975		99,978
Jul 13	96,638	125,543	7,859		93,777
Aug 13	94,473	86,849	5,463		89,286
Sep 13	56,130	67,407	6,077		54,448
Nov 13	47,853	58,322	5,467		54,187
Jan 14	51,601	45,936	5,499	5,943	50,281
Feb 14	46,535	21,407	4,574	11,007	51,099
Mar 14	47,806	19,159	4,458	14,094	50,024
Apr 14	43,053	12,784	5,722	14,185	44,678
May 14	34,312	15,540	6,245	21,517	55,957
Jun 14	24,460	13,544	6,430	15,436	49,865
Jul 14	28,199	14,068	7,494	14,706	51,392
Aug 14	26,535	18,700	6,950	11,030	54,280
Sep 14	22,256	18,730	7,088	14,881	67,515
Oct 14	28,799	27,838	6,255	60,659	68,586
Nov 14	30,363	27,339	7,261	54,633	60,305
Dec 14	23,011	25,042	7,617	38,378	55,764

3.1.2 **Component Manufacturing**

The component data was grouped into B1, B2, B3, B4, B5 and B6 product groups. The total energy consumption of the 6 product groups was historically collected as shown in Table 2.

3.1.3 **Compressed dried air system**

The consumption of energy for running compressed dried air system was collected. The amount of production was the summary of Part Assembly (A) and Component Manufacturing (B).

3.1.4 **Air conditioning system**

The consumption of energy for running air conditioning system was collected. The amount of production was the summary of Part Assembly (A) and Component Manufacturing (B).

Table 2 – The Energy Consumption of Group B

Production	B1	B2	B3	B4	B5	B6	KW.H
Jan 13	2,281,958	24,939,776	2,150,600	1,068,310	-	3,192,577	109,213.67
Feb 13	1,897,890	21,763,758	3,246,300	1,151,832	-	4,447,433	123,326.50
Mar 13	2,441,000	31,058,708	7,219,400	1,473,632	-	4,313,348	159,061.83
Apr 13	2,574,500	26,354,224	6,038,400	1,322,291	-	7,589,665	167,869.40
May 13	2,471,000	31,782,816	6,993,400	1,585,459	-	6,907,902	184,766.33
Jun 13	2,389,000	29,829,072	5,544,400	1,345,462	-	6,211,030	162,539.67
Jul 13	1,925,000	34,061,664	6,259,200	1,286,211	-	7,830,495	168,387.21
Aug 13	2,128,500	36,373,376	8,663,300	1,264,766	-	6,638,146	174,790.49
Sep 13	2,389,000	25,448,226	6,712,400	1,321,826	-	5,634,824	151,165.30
Oct 13	1,874,500	27,332,864	5,573,900	1,502,814	-	4,771,898	143,819.75
Nov 13	2,600,000	25,270,024	5,481,100	1,432,049	-	5,533,427	162,088.21
Dec 13	2,161,000	20,070,648	4,895,800	869,401	656,283	5,233,537	136,820.00
Jan 14	2,416,845	27,121,536	7,144,400	1,261,493	625,360	8,166,354	169,792.56
Feb 14	2,740,500	28,138,968	8,008,300	1,261,713	1,327,832	7,210,757	178,399.90
Mar 14	2,437,500	27,987,434	7,944,200	1,411,721	2,234,018	8,365,403	193,605.82
Apr 14	2,468,000	27,295,528	6,337,543	1,191,755	964,297	7,598,360	171,091.04
May 14	2,287,500	26,647,192	7,672,000	1,506,109	1,102,701	6,311,490	189,015.88
Jun 14	2,719,500	25,275,107	7,245,500	1,486,889	1,756,917	8,119,707	187,920.68
Jul 14	2,425,500	23,455,951	5,607,530	1,563,483	439,810	6,070,179	186,105.84
Aug 14	2,782,000	21,818,160	5,326,400	1,812,001	2,998,649	4,918,643	184,382.28
Sep 14	2,420,500	21,937,032	2,965,320	1,741,435	3,735,000	3,017,412	175,903.55
Oct 14	2,421,500	22,841,208	3,664,700	1,904,299	3,710,020	3,963,204	180,446.66
Nov 14	2,180,000	24,977,680	3,772,600	1,713,667	3,290,000	3,092,181	165,074.07
Dec 14	2,119,000	22,684,896	3,052,700	1,322,614	2,030,000	3,034,334	161,539.51

3.2 Multiple Linear Regressions

The data was analyzed and used for creating the energy equations using multiple regression analysis technique.

3.2.1 ***Part Assembly***

The data of part asembly groups was analyzed indicated below. It was found that the R^2 =98.71% and P = 0.00000 (regression). The energy equation was formulated from coefficients of the regression and diplayed below.

Regression Analysis

Term	Coef	SE Coef	T	P
A1	0.332834	0.199697	1.66670	0.134
A2	0.291960	0.054185	5.38819	0.001
A3	0.076782	0.297882	0.25776	0.803
A4	0.217088	0.149220	1.45482	0.184

R-Sq = 98.71% R-Sq(adj) = 98.07%

Analysis of Variance

Source	DF	Adj MS	F	P
Regression	4	90942426	153.254	0.000000
A1	1	164841161	2.778	0.134135
A2	1	1722817936	29.033	0.000655
A3	1	3942613	0.066	0.803099
A4	1	125594705	2.116	0.183804
Error	8	4.747E+08	4.747E+08	5934079

Energy Equation

KW.H = 0.332834 A1+0.29196 A2+ 0.0767819 A3 + 0.217088 A4

The residual analysis from the energy equation of the Part Assembly group from the data during 2013 – 2014 was plotted as shown in Figure 2.

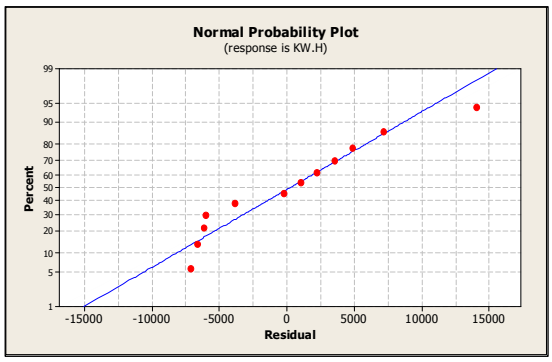

Figure 2 The Graph of the Energy Equation of the Part Assembly.

The ***Specific Energy Consumption*** (SEC) is the coffeicient of the equation with the following values.

SEC A1=0.332834
SEC A2=0.291960
SEC A3=0.076782
SEC A4=0.217088

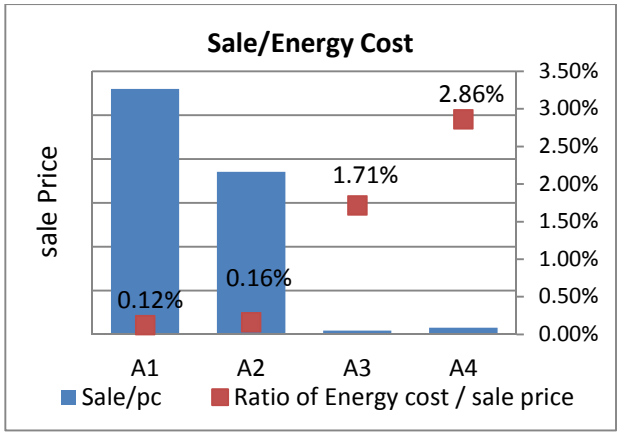

Figure 3 The Ratio of the Energy Cost and Sale Price

According to Figure 3, It was found that Product A1 had the lowest energy cost compared to Products A2, A3 and A4 with higher sale price.

3.2.2 **Component Manufacturing**

The data of component manufacturing groups was analyzed indicated below. It was found that the R^2 =99.79% and P = 0.00000 (regression). The energy equation was formulated from coefficients of the regression and diplayed below.

Regression Analysis

Term	Coef	SE Coef	T	P
B1	0.0131387	0.0066450	1.97724	0.064
B2	0.0008426	0.0005551	1.51801	0.146
B3	0.0027371	0.0018923	1.44643	0.165
B4	0.0425255	0.0112502	3.77998	0.001
B5	0.0062615	0.0021939	2.85399	0.011
B6	0.0053286	0.0018939	2.81354	0.011

R-Sq = 99.79% R-Sq(adj) = 99.72%

Analysis of Variance

Source	DF	Adj MS	F	P
Regression	6	1.1185E+11	1407.95	0.000000
B1	1	3.10581E+08	3.91	0.063536
B2	1	1.83064E+08	2.30	0.146380
B3	1	1.66207E+08	2.09	0.165247
B4	1	1.13510E+09	14.29	0.001371
B5	1	6.47085E+08	8.15	0.010541
B6	1	6.28869E+08	7.92	0.011498
Error	18	1.429E+09	1.429E+09	7.944E+07

Energy Equation

KW.H = 0.01313870 B1 + 0.00084256 B2+
0.00273708 B3 + 0.0425255 B4+
0.00626149 B5 + 0.00532862 B6

The residual analysis from the energy equation of the component manufacturing group from the data during 2013 – 2014 was plotted in Figure 4.

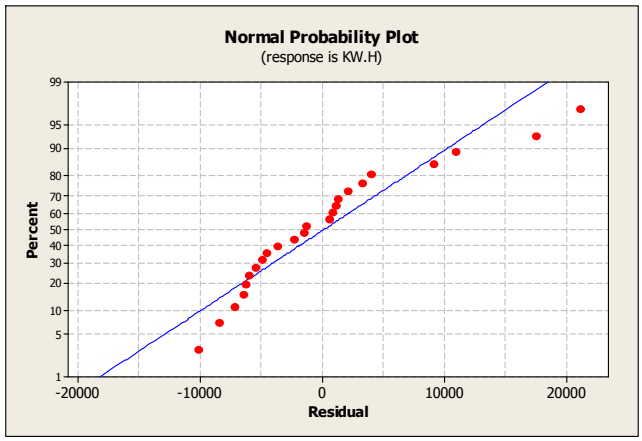

Figure 4 – The Graph of the Energy Equation of the Component Manufacturing.

The values of the ***Specific Energy Consumption*** (SEC) are as follows.

SEC B1=0.0131387
SEC B2=0.0008426
SEC B3=0.0027371
SEC B4=0.0425255
SEC B5=0.0062615
SEC B6=0.0053286

3.2.3 **Compressed dried air system**

The energy consumption of compressed dried air system was analyzed with production data, group A and B. The regression result was obtained with

R^2 = 99.38% and P = 0.0000.

The energy equation of the compressed dried air system was indicated as following.

KW.H = 0.00660596 B + 0.0347381 A

3.2.4 **Air conditioning system** (Chiller)
The energy consumption of air conditioning system was analyzed with production data, group A and B. The regression result was obtained with

R^2 = 97.79% and P = 0.00000.

The energy equation of the air conditioning system was indicated as following.

KW.H = 0.00366185 B + 0.0563867 A

3.3 Validation of Energy Equation / SEC

The energy equations, part assembly, component manufacturing, compressed dried air system and air conditioning system, were validated with production data for 3 months in the first quarter of 2015. The validation results were displayed in table 3-6 and Figure 5-8.

3.3.1 ***Part Assembly***
Tables 3 showed the prediction of the energy consumption during Jan-Mar 2015 by using the energy equation of part assembly. Figure 5 illustrated the comparison between prediction and actual energy consumption and error. It was found that the errors were within 10%, even it tended to grow in minus direction.

Table 3 The Prediction Results for the Part Assembly Group with the Energy Equations (kWh)

Product	Jan-15	Feb-15	Mar-15
A1	7,567	7,091	7,618
A2	18,612	15,133	10,350
A3	1,712	1,657	1,571
A4	14,549	13,148	19,254
kWh	**42,492**	**37,028**	**38,794**

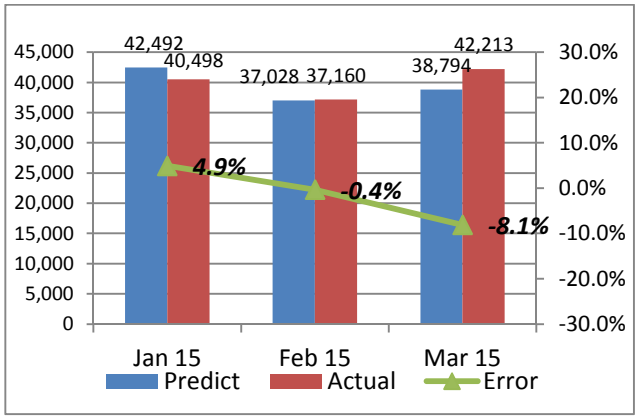

Figure 5 Comparison between Prediction and Actual Energy Consumption and Error for Part Assembly Group.

Table 4 The Prediction Results for the Component Manufacturing Group with the Energy Equations (kWh)

Product	Jan-15	Feb-15	Mar-15
B1	1,748,000	2,156,500	2,984,500
B2	23,001,680	25,688,944	27,694,784
B3	3,594,800	3,938,100	4,181,400
B4	1,204,714	1,512,064	1,637,726
B5	4,540,000	3,062,775	3,600,000
B6	2,965,119	4,063,810	4,375,616
kWh	**147,645**	**165,891**	**189,495**

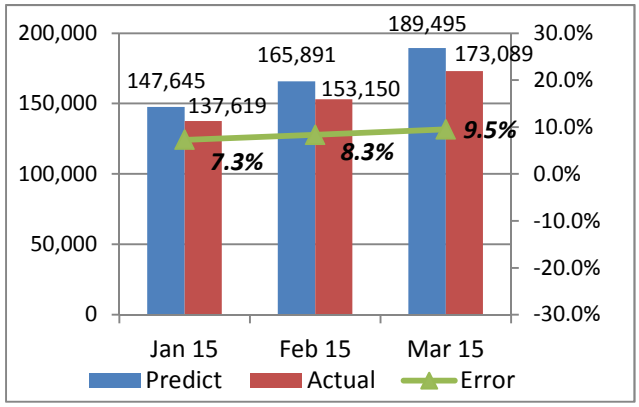

Figure 6 Comparison between Prediction and Actual Energy Consumption and Error for Component Manufacturing Group.

3.3.2 **Component Manufacturing**
Tables 4 showed the prediction of the energy consumption during Jan-Mar 2015 by using the energy equation of component manufacturing. Figure 6 illustrated the comparison between prediction and actual energy consumption and error. It was found that the errors were within 10%, and it tended to grow in plus direction.

3.3.3 **Compressed dried air system**
Tables 5 showed the prediction of the energy consumption during Jan-Mar 2015 by using the energy equation of compressed dried air system. Figure 7 illustrated the comparison between prediction and actual energy consumption and error. It was found that the errors were within 10%.

3.3.4 **Air conditioning system** (Chiller)
Tables 6 showed the prediction of the energy consumption during Jan-Mar 2015 by using the energy equation of air conditioning system. Figure 8 illustrated the comparison between prediction and actual energy consumption and error. It was found that the errors were more than 10%, and it will be discussed later.

Table 5 The Prediction Results for the Compressed Dried Air System with the Energy Equations (kWh)

Product	Jan-15	Feb-15	Mar-15
A	252,706	300,057	295,775
B	8,322	8,246	7,050
kWh	**261,028**	**308,304**	**302,825**

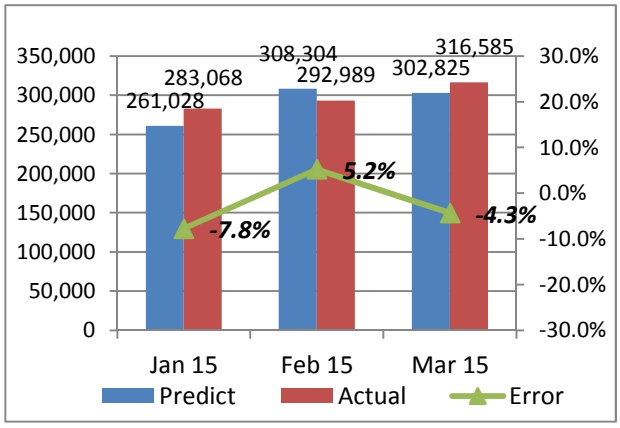

Figure 7 Comparison between Prediction and Actual Energy Consumption and Error for Compressed Dried Air System

Table 6 The Prediction Results for the Air Conditioning System (Chiller) with the Energy Equations (kWh)

Product	Jan-15	Feb-15	Mar-15
A	13,508	13,386	11,444
B	140,082	166,329	163,956
kWh	**153,589**	**179,715**	**175,399**

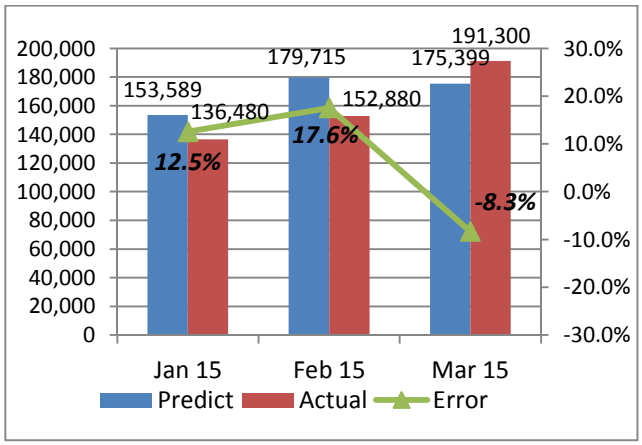

Figure 8 Comparison between Prediction and Actual Energy Consumption and Error for Air Conditioning System (Chiller)

From Figure 8, the accuracy of energy equation that over 10% error in Jan and Feb of 2015, then rapidly drop to minus error of 8.3%. It could be considered that may be affected by seasoning or weather. Jan and Feb are in cold season in Nakornratchasima while Mar is the beginning of summer season, pleased noted that no spring season in Thailand. On this case, if the 3 months prediction data were accumulated to compare with that of actual data, it was found that 5.51% error was obtained. Therefore, it could be concluded that the 4 energy equations were acceptable for using as energy consumption prediction and use as base line to compare with other related companies.

4. CONCLUSION

The 2 years manufacturing data was screened and analyzed. 4 categories of data was employed to separated data set by considering amount of energy used I each category, part assembly, component manufacturing, compressed dried air system and air conditioning system. 4 energy equations were obtained by using multiple linear regressions technique. The energy equations were validated with production data for 3 months in the first quarter of 2015. It was found that the prediction error was less than 10%. It could be concluded that the SEC could be used as tool for forecasting and monitoring energy consumption of the company.

REFERENCE

http://pirun.ku.ac.th/~faasatp/734421/data/chapter10.pdf

https://sites.google.com/site/mystatistics01/home

http://www2.dede.go.th/kmberc/datacenter/factory/plastic/chapter3.pdf

Somsak Siwadamrongpong
He is lecturer in School of Manufacturing Engineering, Suranaree University of Technology

Thana Lunta
He received the B.Eng. (1999), and studying M.Eng. in Energy Management Engineering at Suranaree University of Technology, Thailand

Information and Communication Technology

THE METHODOLOGY TO FIND APPROPRIATE K FOR K-NEAREST NEIGHBOR CLASSIFICATION WITH MEDICAL DATASETS

Pongsakorn Teerarassamee, Kittisak Kerdprasop, Nittaya Kerdprasop
School of Computer Engineering, Suranaree University of Technology, Thailand

ABSTRACT

This research studies the problem of distance-based data classification using k-nearest neighbor algorithm for classifying medical datasets. The classification of data needs to define value k of the most k nearest data points and then classifying new data point to be the same class as the majority value among the k data. If the choice of value k is not suitable, then the accuracy of the classification is lower than it should be. On the contrary, if, user is defines a lot of value of k, it will result in a very slow process. This paper presents the guideline regarding how to select an appropriate value k to the medical field, by considering the nature of the classes and instances. A different distance metric also results in different level of accuracy. In this study, we perform k-nearest neighbor classification using 8 different distance measurement. The suitable distance metric and appropriate k value and reported as a guideline to the user.

1. INTRODUCTION

The k-nearest neighbor algorithm (kNN) is a method of classification. It is categorized as supervised learning. That means the data already know the answer of Data Classification is the process of learning from data is the answer. Techniques such as the widely used, whether it is medical (Hu & Shao, 2012) or the Hydrology and Meteorology (Lee & Ouarda, 2011). The configuration value k is the scope or in the data analysis. By setting value k are the results on the use of resources to analyze data. The time it takes to process if the value of k, high processing will take longer. This research was presented on how to find the appropriate value k is applied to medical data. Such as data on asthma patients at different levels. Data for heart patients and breast cancer, etc. There is also speculation about the distance. (Medjahed, Saadi, & Benyettou, 2013). Different again In addition to the appropriate value k to reduce the processing time and also added the validity as well. In this study, Selected to 8 different distances because of the nature of distance often give an not equal, so that is why this study, those selected distance.

The people who want to use the k-Nearest Neighbor classification methods from this research can be used to configure value k of k-Nearest Neighbor immediately.

2. ANALYSIS

In this studied, purpose is to determine value k appropriate, taking into consideration the type of distance because the distance is often different to the validity different. And characteristics that affect the configuration information as well. We using 8 different distances for compare performance.

- Euclidean Distance

$$\mathrm{d}(\mathrm{p},\mathrm{q}) = \sqrt{\sum_{\mathrm{i}=1}^{\mathrm{n}}(\mathrm{q_i} - \mathrm{p_i})^2} \qquad (1)$$

Let $\mathrm{d}(\mathrm{p},\mathrm{q})$ is distance of Euclidean. $\mathrm{p_i}$ and q_i is points in dimension.

Euclidean Distance (Deza & Deza, 2009). is popular distance because easy to understand. By measuring the distance of the two points.

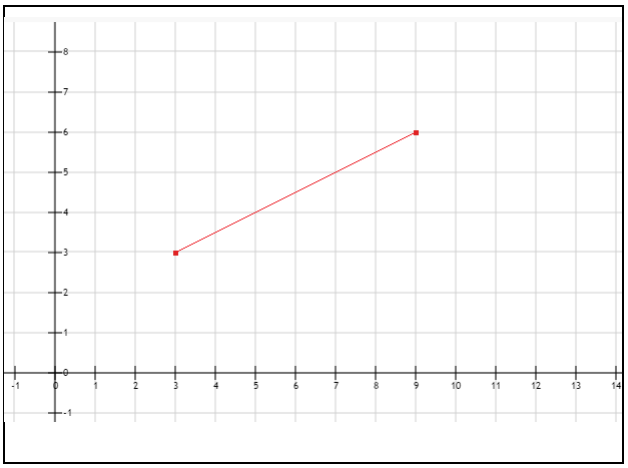

Fig. 4 Euclidean Distance.

- Cityblock (or Manhattan) Distance

$$d(p,q) = \sum_{i=1}^{n} |p_i - q_i| \quad (2)$$

Let $d(p,q)$ is distance of Cityblock. (Krause, 1987) p_i and q_i is points in dimension.

Cityblock Distance is driving route distance.

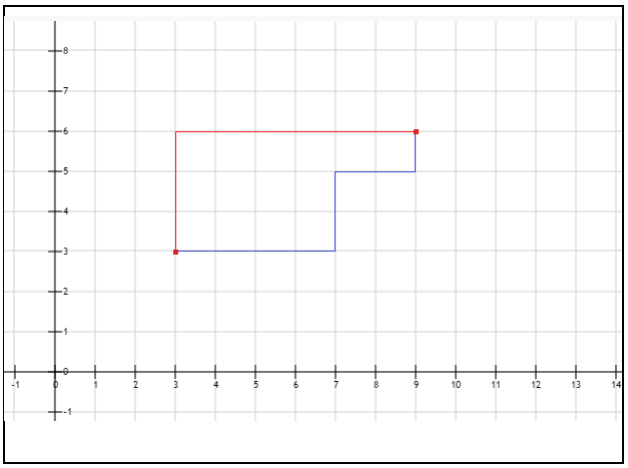

Fig. 5 Cityblock (or Manhattan) Distance (red or blue line).

- Chebyshev Distance

$$d(p,q) = \max_i(|p_i - q_i|) \quad (3)$$

Let $d(p,q)$ is distance of Chebyshev. (Cantrell, 2000) p_i and q_i is points in dimension.

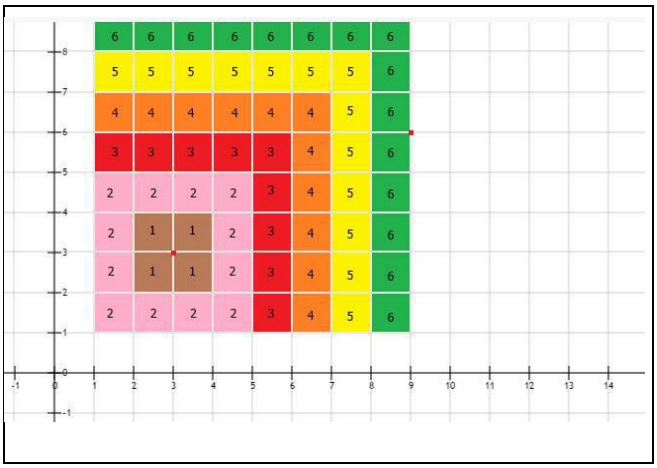

Fig. 6 Chebyshev Distance.

- Correlation Distance

$$d(p,q) = 1 - \frac{cov(p,q)}{std(p) * std(q)} \quad (4)$$

$$cov(p,q) = \sum_{j=1}^{k}(p_j - \bar{p}) * (q_j - \bar{q}) \quad (5)$$

$$std(p) = \sqrt{\frac{1}{k}\sum_{j=1}^{k}(p_j - \bar{p})^2} \quad (6)$$

$$\bar{p} = \frac{1}{k}\sum_{j=1}^{k} p_j \quad (7)$$

Let $d(p,q)$ is distance of Correlation. (Pearson, 1895) p_j and q_j is points in dimension. $cov(p,q)$ is covariance. and std(p) is standard deviation.

- Cosine Distance

$$d(p,q) = 1 - \frac{\sum_{i=1}^{n} p_i * q_i}{\sqrt{\sum_{i=1}^{n}(p_i)^2} * \sqrt{\sum_{i=1}^{n}(q_i)^2}} \quad (8)$$

Let $d(p,q)$ is distance of Cosine. (Singhal, 2001) p_i and q_i is points in dimension.

- Hamming Distance

$$d(p,q) = \sum_{k=0}^{n-1}[y_{p,k} \neq y_{q,k}] \quad (9)$$

Let $d(p,q)$ is distance of Hamming. (Hamming, 1950) $y_{p,k}$ and $y_{q,k}$ is items or points in dimension.

- Jaccard Distance

$$d(p,q) = 1 - \frac{J_{in}}{J_p + J_q + J_{in}} \quad (10)$$

Let $d(p,q)$ is distance of Jaccard. (Jaccard, 1901) J_{in} is number of intersection between item p and item q. J_p is number of item p and J_q is number of item q.

3. EXPERIMENT

In experiments, we used 2 data sets from the UCI Machine Learning Repository and 1 data set from the Maharat Nakhon Ratchasima Hospital on 8 Nov 2014 (Table 1).

We compare the 8 distances to find the appropriate k value and the best distance for k-Nearest Neighbor. The classification performances of all cases were measured by ten-fold cross validation.

Table 1 Basic information of data sets.

Name	Instances	Attributes	Classes
Breast Cancer Wisconsin	683	10	2
Heart Disease	270	13	2
Asthma	698	13	3

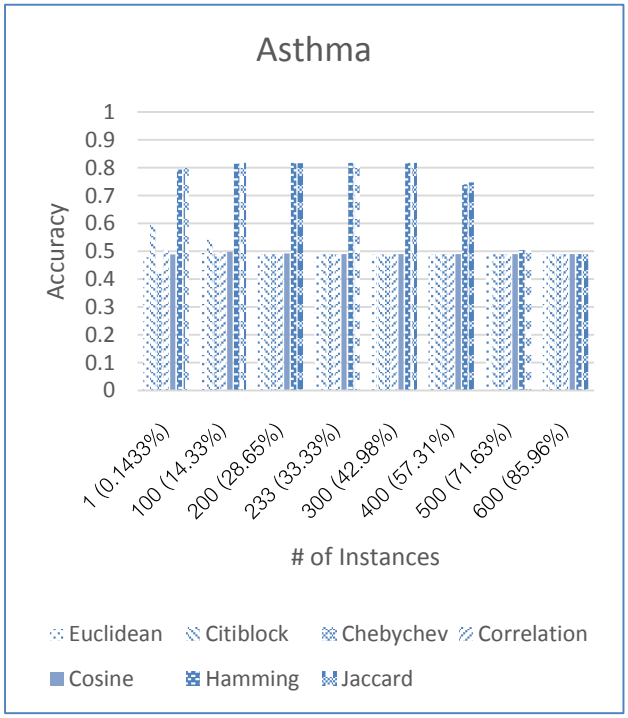

Fig. 1 Classification asthma with 7 different distances.

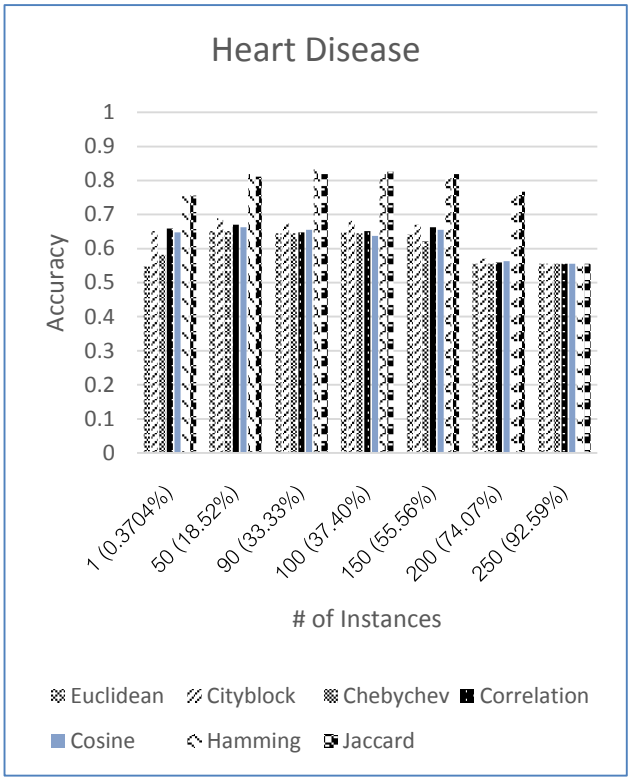

Fig. 2 Classification heart disease with 7 different distances.

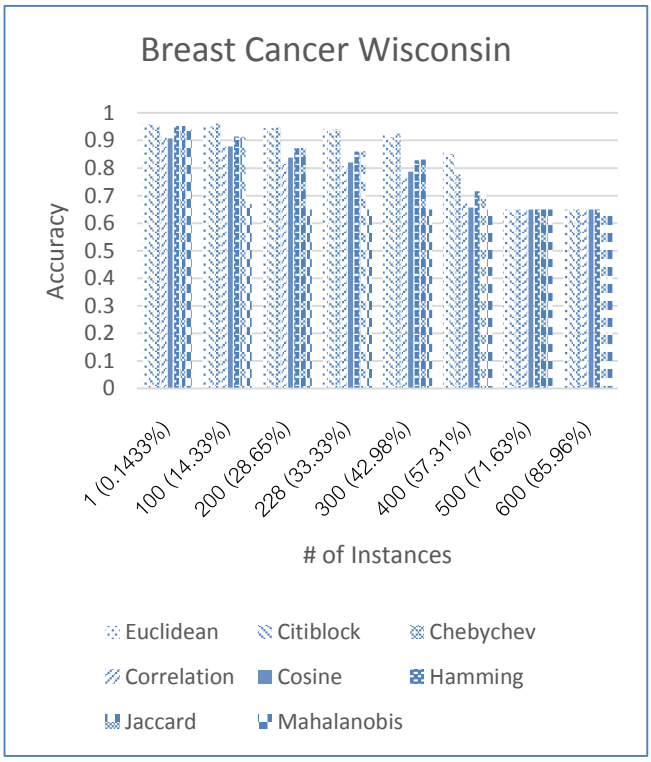

Fig. 3 Classification breast cancer wisconsin with 8 different distances.

The results showed in Fig.1 – 3 is a relationship between accuracy and number of instances. From asthma, It can be seen that Hamming Distance and Jaccard Distance have accuracy high value and is similar to heart disease. In breast cancer wisconsin

when k = 1 will give the accuracy in all the instances.

In asthma datasets and heart disease datasets can't use Mahalanobis Distance because the calculation requires covariance symmetry but all above datasets have covariance asymmetric.

4. CONCLUSION

In this study, Using 8 distances with k-Nearest Neighbor and each will have a different distance away from the results obtained are found to classes and the number of instances affect the configuration k with the following characteristics.

If there are 3 classes and a number of instances value of k that will be in the range of 30% of instances with odometer Hamming Distance and Jaccard Distance.

If there are 2 classes of data and the number of instances value of k that will be in the range of 20% of instances with all above distance but except the Hamming Distance and Jaccard Distance.

If the data is Instances least 2 classes and the appropriate k can be used as k=1 immediately.

REFERENCES

Medjahed, S.A., Saadi, T.A., and Benyettou., 2013. A Breast Cancer Diagnosis by Using k-Nearest Neighbor with Different Distances and Classification Rules. International Journal of Computer Applications. 62(1): 1-5.

Hu, S-b. and Shao, P., 2012. Improved Nearest Neighbor Interpolators Based on Confidence Region in Medical Image Registration. Biomedical Signal Processing and Control. 7: 525-536.

Lee, T. and Ouarda, T. B.M.J., 2011. Identification of Model Order and Number of Neighbors for k-Nearest Neighbor Resampling. Journal of Hydrology. 404: 136-145.

Deza, E., Deza, M. M., 2009. Encyclopedia of Distances. Springer. : 94.

Krause, E. F., 1987. Taxicab Geometry. Dover.

Cantrell, C. D., 2000. Modern Mathematical Methods for Physicists and Engineers. Cambridge University Press.

Pearson, K., 1895. Note on Regression and Inheritance in The Case of Two Parents. Proceedings of the Royal Society. 58, (pp 240–242).

Singhal, A., 2001. Modern Information Retrieval A Brief Overview. Bulletin of the IEEE Computer Society Technical Committee on Data Engineering. 24 (4): 35–43.

Hamming, R. W., 1950, Error Detecting and Error Correcting Codes. Bell System Technical Journal. 29(2): 147–160

Jaccard, P., 1901, Étude comparative de la distribution florale dans une portion des Alpes et des Jura. Bulletin de la Société Vaudoise des Sciences Naturelles. 37: 547–579.

Pongsakorn Teerarassamee

He is currently a master student with the School of Computer Engineering, Suranaree University of Technology, Thailand. His current research of interest includes Classification

Kittisak Kerdprasop

He is an associate professor and chair of the School of Computer Engineering, Suranaree University of Technology, Thailand. His current research of interest includes Data mining, Artificial Intelligence, Functional and Logic Programming Languages, Computational Statistics.

Nittaya Kerdprasop

She is an associate professor at the School of Computer Engineering, Suranaree University of Technology, Thailand. She is a member of ACM and IEEE Computer Society. Her research of interest includes Knowledge Discovery in Databases, Artificial Intelligence, Logic Programming, and Biomedical Informatics

IMPROVING MEDICAL DIAGNOSTIC MODEL WITH FILTRATION AND DISCRETIZATION TECHNIQUES

Pongsakorn Durongdumrongchai, Nuntawut Kaoungku, Kittisak Kerdprasop, Nittaya Kerdprasop
School of Computer Engineering, Suranaree University of Technology, Thailand

ABSTRACT

To apply data mining classification technique to the medical data, it is important to have a classification model that can perform effective analysis with high accuracy. There are significant amount of researches trying to find ways to improve classification model accuracy. One of the methods successfully applied is the filter technique. It is the process of preparing data before modeling. This paper presents the filter technique together with the discretization method for the important of medical diagnostic model. The proposed data filtration and discretization techniques has been tested with the six classification algorithm: support vector machine, naïve Bayes, multilayer perceptron, k-nearest neighbor, decision stump, and decision trees. The six medical data and one generated data were used for accuracy evaluation. Five medical data showed the improvement on classification accuracy

Keywords: Filters, Discretization, Classifications, Accuracy, Medical data

1. INTRODUCTION

Data mining model for classification of medical data has proved to be a success in the prediction of new data with the relatively high accuracy. Guyon & Elisseeff (2003) stated that data filtration by feature selection can help the discovery of relationships hidden in data

Feature selection is in the preprocessing of machine learning as a way to reduce the dimension by reducing the redundant and irrelevant information. This will increase the accuracy. Feature selection generally fall into two categories: filter models and wrapper model. Filter model will select some features without involving algorithm to learn any model. Wrapper model is based on the one that is preset on the selected feature. The choice of filter models studied by Guz (2011) often provide higher accuracy.

Discretization is one of the preprocessing of the machine learning. How is the nature of the data are numeric will provide a range of features that will help increase the accuracy of prediction. Many works have been action in the field of dimensionality reduction for medical diagnosis.

The following section presents the summary of those works, highlighting the strengths and weaknesses of each method. It may be observed that the Sequential Forward Feature Selection (SFFS) is impractical for feature subset selection from a large number of samples of high-dimensional features (Hall, 1998). Therefore, Hab & Yu (2010) propose the Filter-Dominating Hybrid Sequential Forward Feature Selection (FDHSFFS) algorithm for high dimensional feature subset selection. This method had been proved to be fast but wanted greatly computational complexity. A new approach called Multi Filtration Feature Selection (MFFS) had been proposed by Sasikala et al., (2014). The method used a holistic and universal method that achieved the best classification accuracy with fewest features possible.

This paper makes an attempt to design such a feature selection sequence and discretization. It is called ‘‘Multi Filtration with Feature Selection Discretization (MFFDS)’’.This paper is organized as follows: Section 3 describes the proposed method. Experimental results and discussions are presented in Section 4.

2. METHODOLOGY

Figure 1 shows the flow of our methodology. The feature selection technique has been applied to the data. Then the discretization technique is used. The accuracy is tested with the six classification algorithms

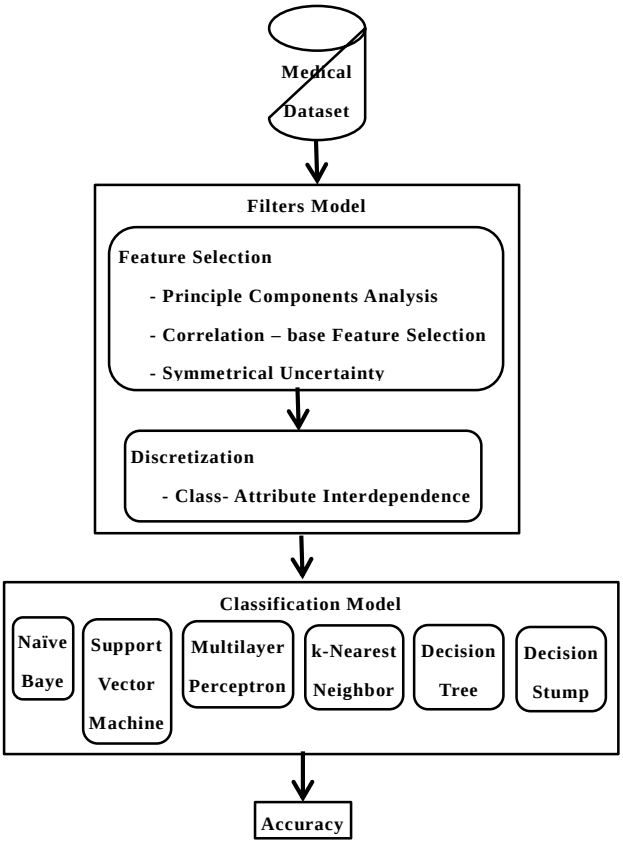

Fig. 1 System flow of the proposed MFFDS model

2.1 Principle Component Analysis (PCA)

A represented of unsupervised dimensionality reduction method is Principal Component Analysis (PCA) Moutselos et al., (1986) which aims to identifying a lower-dimensional space maximizing the variance among data Sasikala et al., (2014). PCA is a very effective approach of extracting features Vinh et al., (2011). The computation for PCA is as follows:

$$AA^{T}P = LP \tag{1}$$

Let AA^{T} is matrix L is covariance matrix and P is eigenvector.

2.2 Correlation – base Feature Selection (CFS)

The correlation between each feature and the class and between two features can be measured and best-first search. This is realized in the Correlation-based Feature Selection (CFS) method Xie, & Wang (2011). The computation for CFS is as follows:

$$\text{Merit}_{s} = \frac{k\overline{\omega_{cf}}}{\sqrt{k+k(k-1)\overline{\omega_{ff}}}} \tag{2}$$

$$\omega_{ij} = \frac{\sum(i-\bar{\imath})(j-\bar{\jmath})}{\sqrt{[\sum(i-\bar{\imath})^{2}][\sum(j-\bar{\jmath})^{2}]}} \tag{3}$$

Let s is feature subset k is feature $\overline{\omega_{cf}}$ is the average value of feature-class and $\overline{\omega_{ff}}$ is average value of feature-feature.

Let i and j is correlation between entities.

2.3 Class-Attribute Interdependence maximization (CAIM)

The goal of the CAIM algorithm is to maximize the class-attribute interdependence and to generate a (possibly) minimal number of discrete intervals Yazdani et al., (2012). The computation for CAIM is as follows:

$$\text{CAIM}(C, D|F) = \frac{\sum_{r=1}^{n} \frac{max_{r}^{2}}{M_{+r}}}{n} \tag{4}$$

Let C is class variable and D is discretization variable for attribute F.

Let n is number of intervals r = 1, 2. . . n, max_{r} is maximum value among and M_{+r} is total number of continuous values.

3. EXPERIMENT

3.1 Experimental Apparatus

The tests are carried out in a system with Intel i7-4500U, CPU 1.80GHz, 8 GB RAM, 1TB hard drive on a Windows 8 Enterprise operating system.

The proposed algorithm is implemented using Weka (2013). The input to the system is given in the Attribute-Relation File Format (ARFF). Ten-fold cross validation is performed for all classifiers (Zahedi & Sorkhi 2013). Data sets used in the expertiment are listed in Table1.

Data set names, number of rows, number of features, and the number of classes.

Name	Instance	Attribute	Class
Breast Cancer Wisconsin	569	32	2
E.coli	336	8	8
Indian Liver Patient Dataset	583	11	2
Liver	345	7	2
SPECT Heart Dataset	80	45	2
Parkinson	195	23	2
Generate Dataset	570	3	2

3.2 Result

Figure 2–7 show the experimental results of the proposed method (MFFDS) compared to the MFFS methods and the classification without any data preprocessing technique. The X-axis represents accuracy and the Y-axis represents medical data.

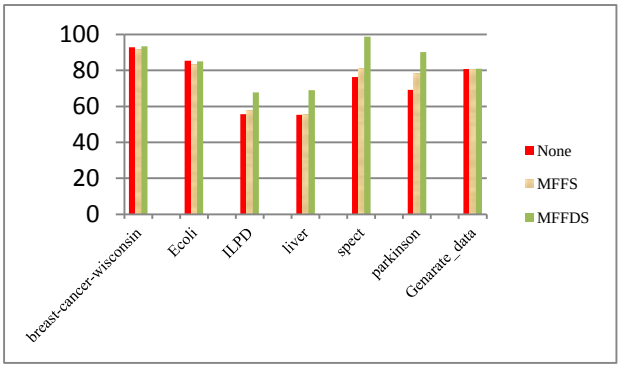

Fig. 2 Classification accuracy obtained for existing and the proposed MFFDS by naïve Bayes.

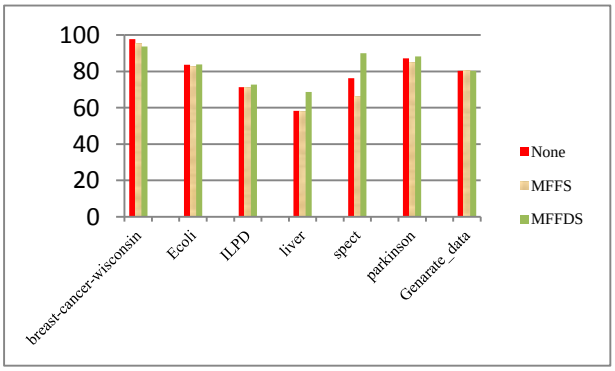

Fig. 3 Classification accuracy obtained for existing and the proposed MFFDS by support vector machine.

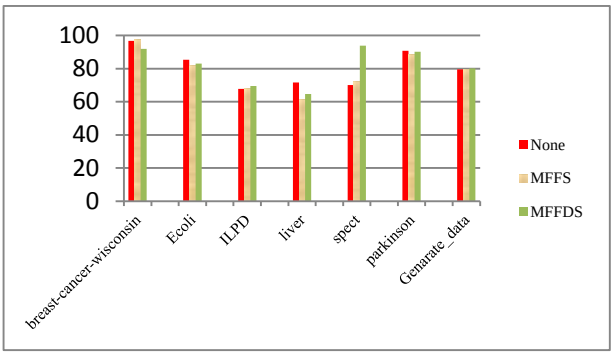

Fig. 4 Classification accuracy obtained for existing and the proposed MFFDS by multilayer perceptron.

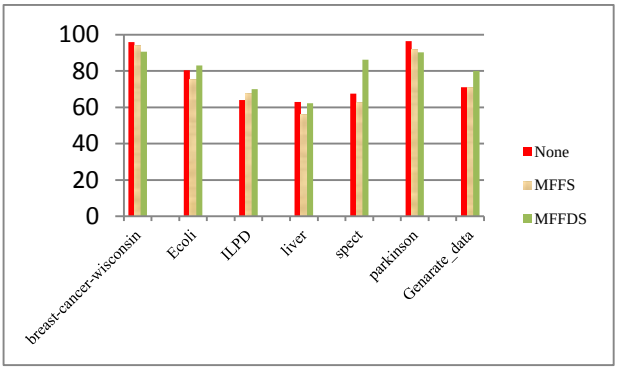

Fig. 5 Classification accuracy obtained for existing and the proposed MFFDS by k-nearest neighbor.

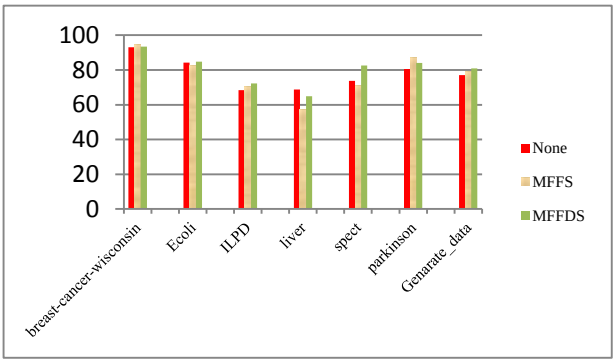

Fig. 6 Classification accuracy obtained for existing and the proposed MFFDS by decision tree.

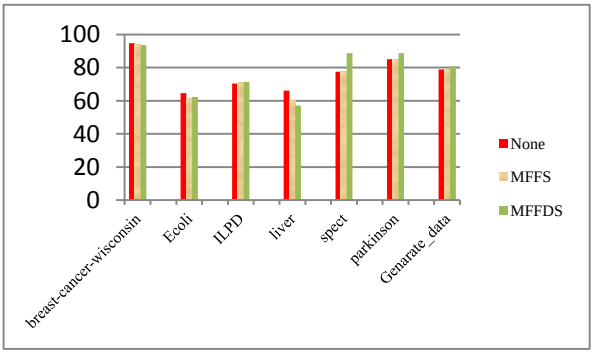

Fig. 7 Classification accuracy obtained for existing and the proposed MFFDS by decision stump.

CONCLUSION

MFFDS model performance testing with naïve Bayes, support vector machine, multilayer perceptron, k-nearest neighbor, decision tree and decision stump by using Breast Cancer Wisconsin, E.coli, Indian Liver, Patient Dataset, Liver, SPECT Heart Dataset, Parkinson and Generate data. The implication of the research is MFFDS Model for best results, performance testing is five data.

REFERENCE

Guyon, A.I., Elisseeff, A., 2003. An introduction to variable and feature selection. J. Mach. Learn Res. 3, 1157–1182.

Guz, H.U., 2011. A hybrid system based on information gain and principal component analysis for the classification of transcranial Doppler signals. Comput. Methods Programs Biomed. 107, 598–609.

Hall, M.A., 1998. Correlation based feature selection for machine learning (PhD Dissertation), Dept. of Comp. Science, Univ. of Waikato, Hamilton, New Zealand.

Han, Y., Yu, L., 2010. A variance reduction framework for stable feature selection. In: Webb, G.I., Liu, B., Zhang, C., Gunopulos, D., Wu, X. (Eds.), Data Mining. IEEE Computer Society, Sydney, Australia, pp. 206– 215.

Jolliffe, I.T., 1986. Principal Component Analysis. Springer-Verlag, New York, NY.

Moutselos, K., Maglogiannis, I., Chatziioannou, A., 2014. Integration of high-volume molecular and imaging data for composite biomarker discovery in the study of melanoma. Biomed. Res. Int. http://dx.doi.org/10.1155/2014/145243.

Sasikala, S. Appavu alias Balamurugan, Geetha ,S., 2014. Multi Filtration Feature Selection (MFFS) to improve discriminatory ability in clinical data set. Applied Computing and Informatics, In Press, Corrected Proof, Available online 5 April 2014

Vinh, L.T., Lee, S., Park, Y., Auriol, B.J., 2011. A novel feature selection method based on normalized mutual information. Int. J. Appl. Intell 37, 100–120

Xie, J., Wang, C., 2011. Using support vector machines with a novel hybrid feature selection method for diagnosis of erythemato-squamous diseases. Expert Syst. Appl. 38 (5), 5809–5815.

Yazdani, S., Shanbehzadeh, J., Shalmani, Mohammad Taghi Manzuri, 2012. RPCA: a novel pre-processing method for PCA. Adv. Artif. Intell. 1, 1–7.

Zahedi, M., Sorkhi, A.G., 2013. Improving text classification performance using PCA and recall-precision. Arab J Sci Eng (2013) 38:2095–2102.

Pongsakorn Durongdumrongchai

He is currently a master student with the School of Computer Engineering, Suranaree University of Technology, Thailand. His current research of interest includes association and Classification.

Nuntawut Kaoungku

He is currently a doctoral student with the School of Computer Engineering, Suranaree University of Technology, Thailand. His current research includes semantic web and association.

Kittisak Kerdprasop

He is an associate professor and chair of the School of Computer Engineering, Suranaree University of Technology, Thailand. His current research of interest includes Data mining, Artificial Intelligence, Functional and Logic Programming Languages and Computational Statistics.

Nittaya Kerdprasop

She is an associate professor at the School of Computer Engineering, Suranaree University of Technology, Thailand. She is a member of ACM and IEEE Computer Society. Her research of interest includes Knowledge Discovery in Databases, Artificial Intelligence and Logic Programming.

HUMAN IDENTIFICATION WITH DATA FUSION TECHNIQUE USING FINGERPRINT AND FACE IMAGE

Sak Phoemhansa, Nittaya Kerdprasop, Kittisak Kerdprasop
School of Computer Engineering, Suranaree University of Technology, Thailand

ABSTRACT

Currently technology is fast growing and widely used. The security system is consequently very importance. Biometric can be used in security system. Biometric is captured human characteristic such as fingerprint, face, which is physical characteristics of human that can be used for verification or identification. However, there is a problem in using biometric for security system in that it has low performance for identification. In this paper, we propose to use data fusion technique based on multimodal biometric technique for improving performance of human identification with k-nearest neighbor algorithm. In experiment, we compare the performance of identification between single biometric trait and fusion of multi-biometric traits.

1. INTRODUCTION

At present data is very importance because the fast growing of technology to produce tremendous amount of data exceeded human ability to analyze without proper tools. Data mining is proper tools to manage and analyze large database. It can applied in many field such as education, medical.

Biometric is biotechnology to metrics human characteristic. Biometric are categorized as physiological characteristics such as fingerprint, face and behavioral characteristics such as voice, gait of an individual. Biometric are most applied in security field to use verification or identification by compare biometric trait from an individual against pattern in database. The security system can protect important data by verification or identification form biometric trait data (Ephin, et al., 2013).

Multimodal biometric refers to the use of biometric more than one source to fusion for improving the performance of processing verification or identification. Because using single biometric may not enough in human identification system. It has cause limitations of biometric and vulnerable to spoofing (Sorin, et al., 2011).

In this paper, we propose the use of data fusion technique based on multimodal biometric with fusion two biometric traits to improve performance of human identification with k-Nearest Neighbor. In experiment we compare accuracy of human identification by using fingerprint data, face data and the dataset fused with data fusion technique.

2. RELATED WORKS

Multimodal biometric are popular technique to use for solving various problems and improve performance of biometric. Ross & Jain (2004) study an overview of multimodal biometric that it can overcome limitations of using biometric. Multimodal biometric with various levels of fusion: sensor level, feature level, matching score level and decision level. Using multimodal biometric can improve performance of identification system and reliable. Mishra (2010) study different aspects of multimodal biometric and compare feasibility and advantage over biometric. Using multimodal biometric can improve performance of identification system and reliable. Liau & Isa (2011) propose face-iris multimodal biometric based on fusion at matching score level using support vector machine and propose feature selection technique to choose optimal features of data for improve performance of identification with face data and iris data. Dhriti & Kaur (2012) propose face-fingerprint multimodal biometric based on fusion at feature level and propose feature extraction techniques with Gabor filter and PCA before identification using k-Nearest Neighbor.

3. MULTIMODAL BIOMETRIC AND CLASSIFICATION

3.1 Multimodal Biometric

Multimodal Biometric refers to fusion biometric two or more biometric modalities for applied to security system such as verification, identification, authentication and authorization because using more biometric traits can increase accuracy of system and vulnerable to spoofing.

Multimodal biometric can solve problem limitations of biometric (Mishra, 2010).

1) Noisy data: It is occur in collect data process such as a fingerprint image with a scar. Noisy data can also result from defective or improperly maintained sensors

2) Intra class variation: Biometric data used in process identification not be identical data used generating template for an individual. It is often caused by a user.

3) Inter class similarities: The multiple individual characteristic very similarities (or refer to the overlap of feature) because a large number of users.

4) Non universality: Some persons cannot provide the required standalone biometric or the poor quality of individual biometric traits.

5) Spoofing: Using single biometric is vulnerable to spoofing or forged e.g. fingerprint are also used to spoof attack.

3.1.1 Levels of fusion

The levels of fusion follows (Mishra, 2010):

1) Sensor level fusion: In sensor fusion the sensor are captured biometric traits of a user from scanner devices in form of raw data.

2) Feature level fusion: At feature level is extract data process to extracted raw biometric data to a feature set representation of an individual trait.

3) Matching score level: The extracted features are processing to compare against the corresponding template stored in database to generate matching score.

4) Decision level fusion: In decision level is final classification to uses matching score determine that accepted or rejected in identification.

3.1.2 Phases of multimodal biometric

Multimodal biometric operates in two phases follows (Sanjekar & Patil, 2013):

1) Enrollment phase: The biometric system is captured and stored individual biometric trait of a user into database. The biometric data stored in database is template for authentication phase.

2) Authentication phase: The template of biometric trait used in authentication phase for identify or verify a person. The system comparing input data by a user with corresponding template in database while verification if both biometric traits similarity are accepted.

3.2 k-Nearest Neighbor Classification Algorithm

k-Nearest Neighbor (k-NN) is simply and the most popular technique based on supervised learning. The method assign class of new data from nearest majority class in k sample of training data (Aci, et al., 2010).

3.2.1 The steps of k-nearest neighbor

1) Choose k sample for number of nearest neighbor

2) Compute the distance of all points with new point.

3) Sort order of all distance values and consider along k samples.

4) Assign class of new data.

3.2.2 Distance computation

The distance computation can compute different multiple method. Generally use Euclidean distance is normal compute between two points in linear line from equation (1) (Shyu, et al., 2003).

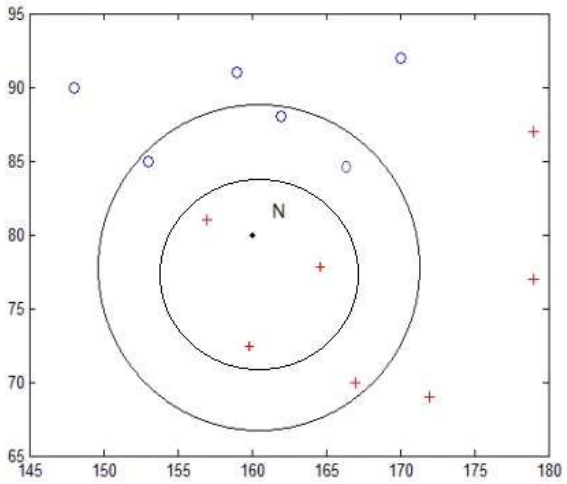

Fig. 1 The sample of k-NN classification.

$$d(X,Y) = \sqrt{\sum_{i=1}^{n}(X_i - Y_i)^2} \quad (1)$$

Where $d(X,Y)$ is distance between X and Y. X denote $X = (x_1, x_2, x_3, \dots, x_i)$. Y denote $Y = (y_1, y_2, y_3, \dots, y_i)$. n is number of all points.

Fig. 1 show a simply example of k-NN. It has two classes (blue circle and red plus). When we need classify class of new data appear (N point). The k-NN compute distance to find nearest neighbor point. In Fig. 1 if define k nearest neighbor is 3 (small circle) and k nearest neighbor is 7 (large circle). At small circle N point classified is red plus class and at large circle N point classified is red plus class because the most classes of points are red plus.

4. EXPERIMENTION AND RESULTS

4.1 Dataset

Our experiment used face and fingerprint datasets from website: Face (URL: http://www.cl.cam.ac.uk/research/dtg/www/) and Fingerprint (URL: http://fvs.sourceforge.net/download.html) in Table 1.

Table 1 The Detail of datasets.

Datasets	#Instances	#Features	#Classes
Face	400	10304	40
Fingerprint	168	6400	21

4.2 A Comparative Study

In this paper we can split our works as two phases follows:

1) First phases: We have two datasets consist fingerprint dataset and face dataset. Both datasets are image data. Therefore, we should transform both datasets to grayscale and transform to numeric data. Numeric data represent levels of color each pixels of image (0 represent black color and 255 represent white color). When obtained datasets are transformed numeric data then identify with k-

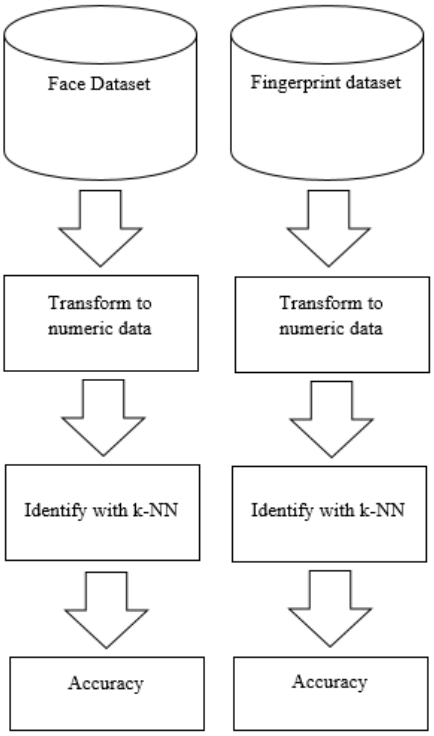

Fig. 2 The first framework of our technique.

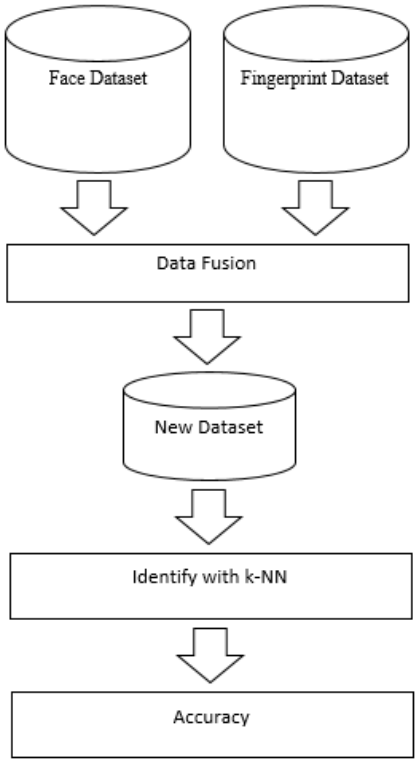

Fig. 3 The second framework of our technique.

NN algorithm. We will obtained accuracy values from identification of both datasets in Fig. 2.

2) Second phases: Both datasets transformed in first phases will fused with data fusion technique before to identify with k-NN algorithm. We will obtained accuracy values of identification from second phases in Fig. 3.

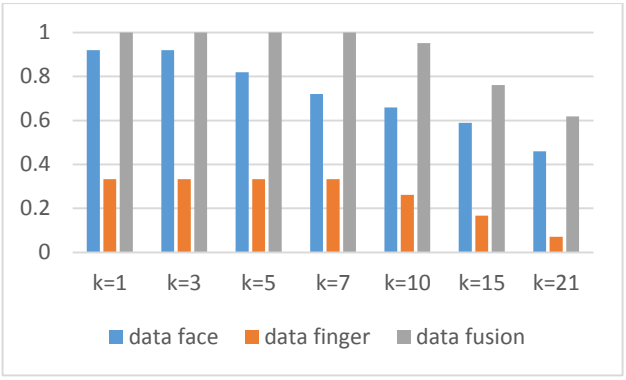

Fig. 4 Chart shows the performance in experiment.

When we obtained accuracy values from both work in first and second phases. We compare the performance of human identification and results in next section.

4.3 Experimental Results

Table 2 The results in our experiment.

k	Accuracy		
	Face	Fingerprint	Fused dataset
k = 1	0.92	0.333	**1**
k = 3	0.92	0.333	**1**
k = 5	0.82	0.333	**1**
k = 7	0.72	0.333	**1**
k = 10	0.66	0.262	**0.952**
k = 15	0.59	0.167	**0.762**
k = 21	0.46	0.071	**0.619**

The experimental implemented with Python. We performed with k-NN algorithm to human identification and used different k parameter in each datasets then compare the performance of each identification. We used single biometric trait and fusion data to human identification. For single biometric trait in our experiment is face and fingerprint.

The performance of human identification in experiments are summarized in Table 2 follows.

1) The human identification with face dataset: The accuracy obtained for identification with face dataset are between 0.92 and 0.46. The accuracy are decrease when increase k parameter.

2) The human identification with fingerprint dataset: The accuracy obtained from identification with fingerprint dataset are between 0.333 and 0.071. The accuracy are also decrease when increase k parameter. If compare accuracy of face and fingerprint indicate that fingerprint is low performance in Fig. 4.

3) The human identification with fused dataset: The accuracy obtained from identification with fused dataset are between 1 and 0.619. When we have fusion data shows that the accuracy obtained more than single biometric dataset in Fig. 4.

5. CONCLUSIONS

In this paper propose using fusion data technique based on multimodal biometric to human identification with k-Nearest Neighbor algorithm. Using single biometric trait may not enough for human identification because the limitations and various problem of biometric. These problem affect performance of identification. We fuse our both biometric dataset for improve the performance of human identification. In experimental results the performance of identification with single biometric compared against the performance of identification with dataset fused with data fusion data technique. The accuracy of fused dataset better than the accuracy of face and fingerprint dataset. Form experimental results show that fusion data can improve performance of human identification and using multiple biometric better than single biometric.

REFERENCES

Arun Ross, Anil K. Jain, Multimodal Biometrics: An overview, Appeared in proc. Of 12th European Signal Processing Conference **(**EUSIPCO**)**, pp. 1221-1224, 2004.

Ashish Mishra, Multimodal Biometrics it is: Need for future systems, International Journal of Computer Applications, vol. 3, no.4, 2010.

Ephin M, Shreya Mohan Vasanthi N. A., Survey on Multimodal Biometric using Palm print and Fingerprint, International Journal of Computer Applications, pp. 36-41, 2013.

Dhriti, Manvjeet Kaur, k-Nearest neighbor classification approach for face and fingerprint at feature level fusion**,** International Journal of Computer Applications, vol. 60, no. 14, pp. 13-17, 2012.

Heng Fui Liau, Dino Isa, Feature Selection for Support Vector Machine-based face-iris Multimodal Biometric System, Expert Systems with Applications**.** Vol. 38, pp. 11105-11111, 2011.

Mehmet Aci, Cigdam Inan, and Mutlu Avci, A hybrid classification method of k-nearest neighbor bayesian method and genetic algorithm, Expert Systems with Applications, vol. 37, no. 7, pp.5061-5067, 2010.

Sanjekar, P. S., Patil, J. B., An overview of multimodal biometrics, Signal & Image Processing: An International Journal (SIPIJ**)**, vol. 4, no. 1, pp. 57-64, 2013.

Shyu Mei-Ling, Chen Shu-Ching, Kanoksri Sarinnapakorn, Chang LiWu, A novel anomaly detection scheme based on principal component classifier, IEEE Foundations and New Directions of Data Mining Workshop, pp. 171-179, 2003.

Sorin Soviany, Cristina Soviany, Mariana Jurian, A Multimodal Approach for Biometric Authentication with Multiple Classifiers, World Academy of Science, Engineering and Technology, vol. 5, pp. 1427-1432, 2011.

Sak Phoemhansa is currently a master student with the School of Computer Engineering, Suranaree University of Technology, Thailand. He received his bachelor degree in Computer Engineering from Suranaree University of Technology in 2011. His current research includes classification.

Nittaya Kerdprasop is an associate professor at the School of Computer Engineering, Suranaree University of Technology, Thailand. She received her bachelor degree in Radiation Techniques from Mahidol University, Thailand, in 1985, master degree in Computer Science from the Prince of Songkla University, Thailand, in 1991 and doctoral degree in Computer Science from Nova Southeastern University, U.S.A, in 1999. She is a member of ACM and IEEE Computer Society. Her research of interest includes Knowledge Discovery in Databases, Artificial Intelligence, Logic Programming, and Intelligent Databases.

Kittisak Kerdprasop is an associate professor and chair of the School of Computer Engineering, Suranaree University of Technology, Thailand. He received his bachelor degree in Mathematics from Srinakarinwirot University, Thailand, in 1986, master degree in Computer Science from the Prince of Songkla University, Thailand, in 1991 and doctoral degree in Computer Science from Nova Southeastern University, U.S.A., in 1999. His current research includes Data mining, Artificial Intelligence, Functional and Logic Programming Languages, Computational Statistics.

A TECHNIQUE TO IMPROVE DATA MINING MODEL INDUCED FROM HIGHLY OVERLAPPING DATA

Rattaphong Sutamma*, Phaichayon Kongchai, Keerachart Suksut
Sak Phoemhansa, Nittaya Kerdprasop and Kittisak Kerdprasop
School of Computer Engineering, Suranaree University of Technology, Thailand

ABSTRACT

Currently, data mining technique for classification is a popular technique used in many researches. The result of classification is a model that can be used to predict some unknown value of the future data. However, mining optimal model from data with different kinds of distributions and a wide range of numeric values is difficult because most mining algorithms tend to group numeric data into too many intervals. This leads to a large classification model. Therefore, this research presents a technique to group numeric values with fuzzy c-means clustering and then analyze with the Silhouette to consider characteristic of data distribution to obtain optimal clustering. To evaluate the performance of the proposed method, we compare both accuracy and shape of the classification models. The results show that our proposed method is comparable in terms of accuracy and can generate a more compact model than traditional methods.

1. INTRODUCTION

The technical data classification is a technique widely used in data mining. Data mining is the purpose of each type is different. In the data mining However, due to the vast amount of information itself. Making models of classification is difficult to explain, since the data is distributed to each other. If, when having to deal with the distribution of the data before the analysis. Or classified data before Will make the model derived measures to tighten or its interpretation can be improved. And does not affect the accuracy of the information.

The information contained in the present. Diverse and the distribution of data in various formats. In order to limit the scope of the research. We need to synthesize the data itself to regulate distribution of data. Includes an overlay of the data.

Research on the division of the continuous numerical data are many. We can summarized the researches that related works as follows:

- Chmielewski and Grzymala-Busse (1996) proposed a typical multivariate discretization technique is cluster-based discretization.

- Attila Gyenesei (2001) proposed a new algorithm using Fuzzy set to divide the data are continuing to reduce the number if these relationships and reduce the number of association rules is useless.

- Haiyang Hua and Huaici Zhao (2009) proposed algorithm MVD-CG (multivariate discretization based on density-based clustering and genetic algorithm) to share the information that is the continuous variable for if these relationships by using the technique. Clustering and genetic techniques the algorithm is based on the MVD algorithm.

In this research, we have the information, feature information with the distribution of a group that includes the Fuzzy C-means: FCM to help in grouping the data features. And to obtain the appropriate group. This research has led Silhouette to help in the selection of the most appropriate. Analysis methods compare the accuracy of classification. And the shape of the classification model.

2. EXPERIMENTATION

In this section, we evaluated our discretizing technique base on fuzzy c-means to help in grouping the data numeric values to obtain the appropriate group. This research has led Silhouette to help in the selection of the most appropriate number of groups. Analysis method is applied to compare the accuracy of classification, as well as the shape of the classification model.

Table 1 the accuracy of the classification algorithms over a dataset with well-separated group boundary.

Classifier	Original	FCM discretization *
J48	99.8%	100%
RandomForest	100%	100%
AdaBoostM1	100%	100%
MultilayerPerceptron	100%	100%
NaiveBayes	100%	100%

Table 2 the accuracy of the classification algorithm over a dataset that the distribution in each group begins to overlap.

Classifier	Original	FCM discretization *
J48	99.6%	99.1%
RandomForest	99.6%	99.3%
AdaBoostM1	99.5%	99.5%
MultilayerPerceptron	99.3%	99.5%
NaiveBayes	99.5%	99.3%

Table 3 the accuracy of the classification algorithm over a dataset with moderately overlap data.

Classifier	Original	FCM discretization *
J48	98.8%	99.5%
RandomForest	99.0%	99.5%
AdaBoostM1	99.0%	99.0%
MultilayerPerceptron	99.1%	99.5%
NaiveBayes	98.8%	99.1%

Table 4 the accuracy of the classification algorithm over a dataset with highly overlap distribution.

Classifier	Original	FCM discretization *
J48	97.0%	96.3%
RandomForest	97.5%	96.3%
AdaBoostM1	97.1%	94.6%
MultilayerPerceptron	97.6%	96.3%
NaiveBayes	97.3%	92.8%

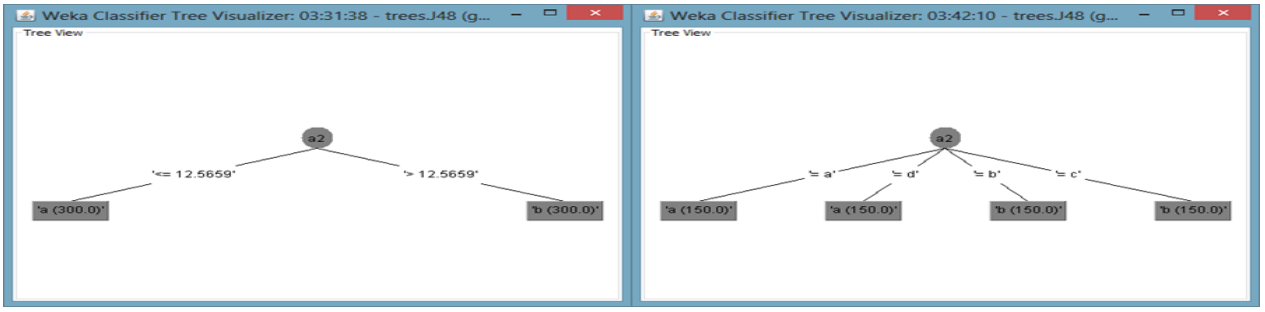

(a) model built from original data (b) model built from FCM discretization method

Fig. 1. The model with the well-separated distribution of each data groups.

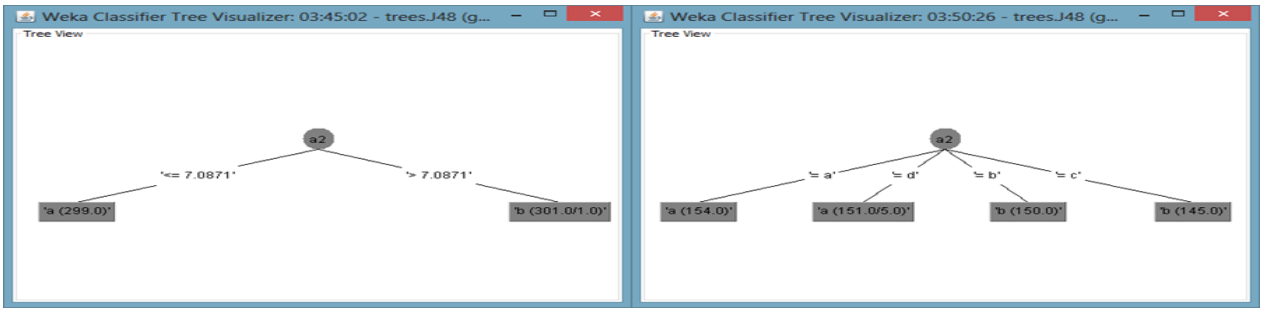

(a) model built from original data (b) model built from FCM discretization method

Fig. 2. The model with slightly overlap data in different groups.

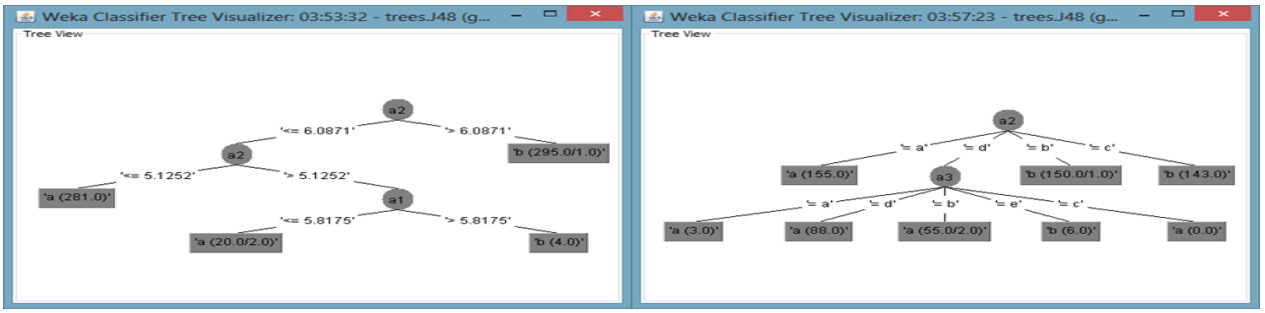

(a) model built from original data (b) model built from FCM discretization method

Fig. 3. The model with moderately overlap data in different groups.

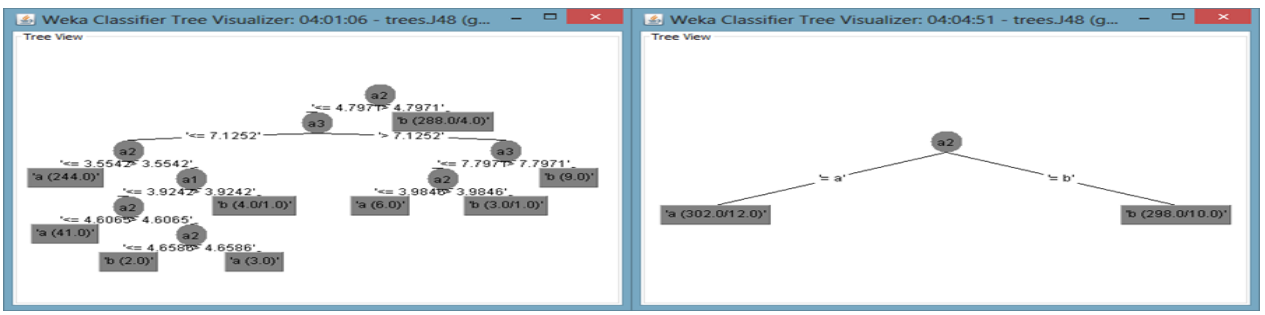

(a) model built from original data (b) model built from FCM discretization method

Fig. 4. The model with highly overlap data in different groups.

The results in Table 1-4 were summarized and discussed as follows:

- Table 1 shows the accuracy of the classification algorithms over a dataset with well-separated group boundary. When the classification is very clear that the data has to be able to make the classification more efficient.

- Table 2 shows the accuracy of the classification algorithm over a dataset that the distribution in each group begins to overlap. When the data from the overlap of data classification is similar to the original efficiency.

- Table 3 shows the accuracy of the classification algorithm over a dataset that the distribution in each group has moderately overlapped. When data are moderately overlapping of data classification, it is clearly better performance from the experimental results.

- Table 4 shows the accuracy of the classification algorithm over a dataset with highly overlap distribution. When data are overlapping of data it can not be clearly separated data classification is the classification performance is slightly reduced.

From Fig.1-4 shows the shape of the classification model from J48 were summarized and discussed as follows:

- Fig. 1. Show the model with the well-separated distribution of each data groups. When classified information that no overlap of the classification model is no different size to the FCM discretization.

- Fig. 2. Show the model with slightly overlap data in different groups (a) model built from original data (b) model built from FCM discretization method. When classified information from begins to overlap of the classification model is no different size to the FCM discretization.

- Fig. 3. Show the model with moderately overlap data in different groups (a) model built from original data (b) model built from FCM discretization method. When classified information from the moderately overlap of the classification model will be slightly larger than the FCM discretization.

- Fig. 4. Show the model with highly overlap data in different groups (a) model built from original data (b) model built from FCM discretization method. When classified information from a large overlap of the classification model will be larger than the FCM discretization clearly.

When using FCM discretization method with the overlap of different data models have to make smaller.

3. METHODOLOGY

In this section, we described our algorithm name FCM discretization composed four steps (Fig 3).

1) Data Characteristics: The data used for data mining in this research by analyzing the data to support the distribution of data and information, which are distributed to each group, there is no overlap of information, including the overlay much of the data.

2) Preprocess: Fuzzy C-means to help in grouping the data features. And Silhouette to help in the selection of the most appropriate. Fuzzy C-means (L. Hsiang-Chuan, 2008) and (T. Luis, 2009) an algorithm that allows the data in each group with overlapping or duplicated. This is a grouping which has been widely used in various fields such as medicine, science and engineering. By virtue of the membership of the group information. The acquisition is part of the measurement of the distance between the center of the group and those with Membership fees are estimated accuracy of segmentation. And to calculate the center of the groups. To the members of the group even more accurate. Silhouette (Peter J. Rousseeuw, 1987) is how to interpret and verify the information. Is technically a compact graphical representation. Can be used as a way to select the most appropriate group for the group by trying to adjust the value of each group. Within an acceptable range and choose the one that makes the best Silhouette.

3) Process: Using 5 classifier J48, RandomForest, AdaBoostM1, MultilayerPerceptron and NaiveBayes.

- J48 algorithm

J48 is an open source Java implementation of the C4.5 (Quinlan, 1993) algorithm in the weka data mining tool.

- RandomForest algorithm

Random forests (Breiman, 2001) are an ensemble learning method for classification and regression.

- AdaBoostM1 algorithm

AdaBoost (Freund Y., 1997), short for "Adaptive Boosting", is a machine learning meta-algorithm formulated by Yoav Freund and Robert Schapire.

- Multilayer Perceptron algorithm

A multilayer perceptron (MLP) (Rosenblatt, 1961) is a feedforward artificial neural network model that maps sets of input data onto a set of appropriate outputs.

- Naïve Bayes algorithm

Naïve Bayes (NB) (Caruana, 2006) based on applying Bayes' theorem with strong independence assumptions.

4) Evaluate: Using 10- fold cross validation. Analysis methods compare the accuracy of classification and shape of the classification model.

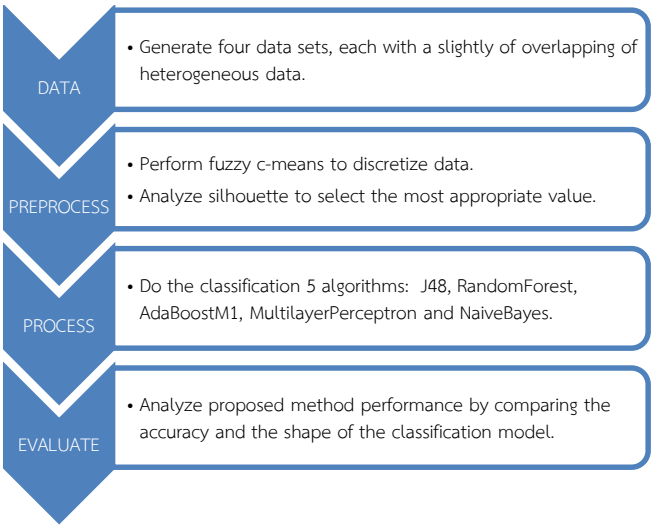

Fig. 3. The framework of process to evaluate the proposed method.

4. CONCLUSIONS

Data mining normally deals with the data that the distribution of the data is in the aggregated form. It's important to make the system capable of classifying data with good performance in any kind of distribution. We propose the technique to be used to develop the most efficient system.

The inhibition of correctly classifying information in the data is due to the unclear separation of data among groups. We propose to handle this situation by applying the fuzzy c-means clustering to help discretizing each attribute and to obtain the appropriate group. This research has also used silhouette to help in the selection of the most appropriate number of intervals in forming a set of data

subgroups. Based on a comparative analysis of the accuracy in the classification of the data our method is superimposed on a more timely information. Thus the accuracy is reduced, but not much less than 1%, and the shape of the classification model is much simplified if there is a lot of overlap in the original dataset. Models built from our proposed technique are significantly smaller than the regular model.

REFERENCES

Chmielewski, M. R. and Grzymala-Busse, J. W, Global discretization of continuous attributes as preprocessing for machine learning. International Journal of Approximate Reasoning, 15, pp.319–331, 1996.

Attila G., A fuzzy approach for mining quantitative association rules, Proceedings of the Acta Cybernetica, pp.305-320, 2001.

Haiyang H. and Huaici Z., A discretization algorithm of continuous attributes based on supervised clustering, Proceedings of the Chinese Conference on Pattern Recognition, pp.1-5, 2009.

L. Hsiang-Chuan, W. Der-Bang, Y. Jeng-Ming, and L. Shin-Wu, Fuzzy c-mean algorithm based on complete mahalanobis distances and separable criterion, Fifth International Conference on Fuzzy System and Knowledge Discovery, 2008. FSKD '08, Vol.1, pp. 87-91, 2008.

T. Luis, B. Chitta, and K. Seungchan, Fuzzy c-means clustering with prior biological knowledge, Journal of Biomedical Informatics, Vol.42, No.1, pp.74-81, 2009.

Peter J. Rousseeuw, Silhouettes: a graphical aid to the interpretation and validation of cluster analysis, Computational and Applied Mathematics 20, pp.53–65, 1987.

Jiawei H. and Micheline K., Data mining concepts and techniques, Morgan Kaufmann Publishers, 2001.

Quinlan, J.R., C4.5 programs for machine learning, Morgan Kaufmann, Los Altos, California, 1993.

Breiman, L., Random forests, Machine Learning 45 (1), pp.5–32, 2001.

Freund Y., Schapire, R.E., A decision theoretic generalization of on-line learning and an application to boosting, Journal of Computer and System Sciences 55(1), pp.119-139, 1997.

Rosenblatt, Frank. x., Principles of neurodynamics: perceptrons and the Theory of brain mechanisms, Spartan Books, Washington DC, 1961.

Caruana, R., Niculescu-Mizil, A., An empirical comparison of supervised learning algorithms, Proceedings of the 23rd international conference on Machine learning, 2006.

Rattaphong Sutamma

He is currently a master student with the School of Computer Engineering, Suranaree University of Technology, Thailand. His current research of interest includes Fuzzy set, Database and Classification mining.

Kittisak Kerdprasop

He is an associate professor and chair of the School of Computer Engineering, Suranaree University of Technology, Thailand. His current research of interest includes Data mining, Artificial Intelligence, Functional and Logic Programming Languages, Computational Statistics.

Nittaya Kerdprasop

She is an associate professor at the School of Computer Engineering, Suranaree University of Technology, Thailand. She is a member of ACM and IEEE Computer Society. Her research of interest includes Knowledge Discovery in Databases, Artificial Intelligence, Logic Programming, and Biomedical Informatics

DP-MATCHING BASED DIAGNOSIS OF CARDIAC ARRYTHMIA USING ECG DATA

Mohamad Sabri and Eiji Kamioka

Graduate School of Engineering and Science, Shibaura Institute of Technology

ABSTRACT

The advancement of computational intelligence has a huge impact on improving and finding solutions towards many complicated issues particularly in the medical field. A huge advancement in data analysis and data interpretation create alternative ways to dealing with complicated matters. In this paper, a mechanism to diagnose cardiac disorder by utilizing the computational intelligence capabilities is introduced with specific major focus on certain region of feature extraction in ECG data. Two types of symptoms will become the main concern in this research, namely Normal Sinus Rhythm and Atrial Fibrillation Rhythms. The database from Physionet.org will be used. In this paper, time domain and frequency domain methods of ECG signal segment will become the main interest area to diagnose the cardiac disorder through ECG data by using DP matching based on 60 seconds duration data. At the end of this paper, result from three segment will be introduced based on the proposed algorithm with two criteria applied to distinguish both symptom.

1. INTRODUCTION

One of the best biomedical data that represents the heart condition and its activities is an ECG (electrocardiogram) signal. Most diseases which are interconnected with the heart condition are usually serious such as heart attack and stroke and these kind of diseases often need special treatments or unexpected death may occur. Therefore, a special equipment is required to collect and analyze useful information from the ECG data. In addition to that, the process of interpreting the data after analyzing it will be done by expert and this can be a drawback in a situation where the expert are lacking in number and experience. Thus, an appropriate method is needed to assist in analyzing the ECG signal, as well as adding the capability to predict the data without relying heavily on the expert and sophisticated equipment.

The main objective of this study is to propose an efficient method to distinguish the atrial fibrillation symptom from Normal Sinus rhythm based on ECG data. By utilizing the capabilities of DP-Matching technique, the numerical value of comparing the two patterns will be utilized to distinguish both symptoms. Which segment and pattern to be considered as a reference for diagnosing ECG data and the mechanism to measure the similarity of the pattern will be highlighted in order to discriminate the two symptoms in rows.

In this paper, the pattern for Normal Sinus has been proposed since they can be the reference for a normal heart condition where it is able to differentiate two categories of symptoms in a row as either Normal Sinus or Atrial Fibrillation. By using the DP-Matching algorithm, this technique will be used as a mechanism to validate the similarities between the two patterns for a certain duration of time.

The remainder of this paper is organized as follows; Section 2 discusses some related works towards this research area. Section 3 introduces the abnormal pattern of Atrial Fibrillation and Normal Sinus Rhythm. Section 4 describes the detail working custom DP-Matching Algorithm. In section 5, the analysis of the experimental result will be discussed. In section 6, conclusions will be made with discussions on possible future research.

2. RELATED WORK

Fawziya [1] has proposed a method to diagnose cardiac arrhythmia by using Ant colony System where ECG, blood oxygen and blood pressure data become the measuring point to diagnose. She was proposing to fully computerize ECG diagnosis with less reliance on the expert in the future.

Likewise, Suzuki et al. [2] proposed a mechanism to diagnose the heart disease through certain characteristic points (CPs), where Q and S point in an ECG became the focus point. In the proposed method, 3 main components are well defined where preprocessor, a DP matching and detection algorithm are used to diagnose the heart disease. The detection algorithm was used to find the CPs from selected template pattern.

Kumar, et al. [3] have reviewed several available techniques in detecting Atrial Fibrillation from

Non-Episodic ECG Data. In this paper, they have listed several mechanisms to detect the symptoms by going through several procedures which are extracting feature and classifying extracted features. A set of feature extraction segment has been well defined in order to diagnose the Atrial Fibrillation. Segment P wave, QRS wave and R to R interval have become an important segment to diagnose the abnormalities of a heart condition.

3. TIME DOMAIN FEATURES FROM ECG

In a normal medical diagnostic proceeding, cardiologist relies on ECG rhythm visually in order to diagnose the heart condition where any kind of arrhythmia in the heart can be detected. Commonly, doctors portray their patients' heart conditions linguistically in a fashion which are difficult to understand. With the use of automated DP-matching detection algorithm, the feature extraction from several raw ECG signals will be translated where certain criteria and standard will be applied in order to diagnose the symptoms. As the end of the procedure, the numerical value will be represented as a result.

3.1 OVERVIEW OF CARDIAC DISORDER

3.1.1 Normal Sinus Rhythm.

In a normal functioning conduction system, normal sinus rhythm represents the normal condition of the heart. The electrical current follows the normal conduction pathway without interference from other bodily system or disease processes [4].

3.1.2 Atrial Fibrillation Rhythm.

Atrial fibrillation (A fib.) occurs when electrical impulses come from areas of reentry pathways of multiple ectopic foci. Each electrical impulse results in depolarization of only a small group of atrial cells rather than the whole atria. This results in the atria not contracting as a whole, causing it to quiver. Multiple atrial activities are recorded as chaotic waves, often with the appearance of fine scribbles [4].

3.2 FEATURE EXTRACTION

3.2.1 P, Q, R, S, T WAVE MORPHOLOGY.

In a healthy heart condition cycle as Normal Sinus rhythm, certain characteristics or Segments from the heart cycle may consistently appear for a certain duration. When comparisons between both Normal Sinus Rhythm and Atrial Fibrillation symptom have been made, a huge difference can be seen in many ways. The sample of the segments are shown in figure 1. One of the main reasons for selecting this segment to measure the abnormalities of a heart condition is due to the consistency of P, Q, R, S, T peak for Normal Sinus Rhythm since Normal Sinus Symptom will be the main reference pattern to compare with. Therefore, by referring to this segment consistently and comparing them with other user patterns, DP matching will be able to trigger any abnormalities based on the differences of the two patterns.

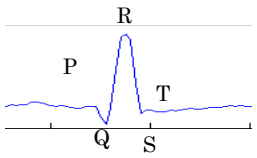

Figure 1 : Sample segment of P,Q,R,S,T

3.2.2 R TO R INTERVAL

In ECG data, one of the most visible peaks of signal to detect in a heart cycle is R peak particularly Normal Sinus rhythm. The center of each beat rhythm cycle known as R peak where the example of segment can be seen in figure 2 for Normal Sinus. R to R intervals for Normal Sinus Rhythm are very regular with only small variation between beats. Contrastively, the R to R interval during Atrial Fibrillation has greater than P, Q, R, S, T interval variations [5].

Figure 2: Sample segment of R to R interval

3.2.3 T TO P INTERVAL

There is one segment which have many uncertain signals which can describe many situation and it is T to P peak interval. For any abnormalities of a heart rhythm from this region can lead to cardiac arrhythmia especially Atrial Fibrillation. A significant difference can be seen for Atrial Fibrillation compared to Normal Sinus Rhythm where many fluctuation waves may appear in this region in various ways. It is a norm where less fluctuation appear for Normal Sinus Rhythm and most of the time, it would be a linear line for it.

Figure 3: Sample segment of T to P interval

4. PROPOSED METHOD

In this study, MIT-BIH Normal Sinus has been selected as a main reference from Physionet.org where several hundreds of patterns are available as a main resource of ECG signal. Two types of symptoms are introduced as the main symptoms to be covered for this research. They are Normal Sinus Rhythm and Atrial Fibrillation Rhythm. These cases are evaluated through algorithm designed and run by Dynamic Programming method to identify the similarity of characteristic point of ECG.

4.1 OVERVIEW OF DP MATCHING

Dynamic programming (DP) matching is a method for extracting similar sub pattern from two sequential patterns in time series of data. DP matching has high

capability to extract all similar sub patterns simultaneously while compensating nonlinear fluctuation. The result of simultaneous experiment will be represented in a numerical value [5].

The DP matching algorithm idea is summarized in the following description and figure:

4.2 THE PROPOSED ALGORITHM WITH 2 MAIN CRITERIA TO DISTINGUISH TWO SYMPTOM

The proposed algorithm by applying two criteria is composed of the following stages:

· Data configuration: create several hundreds of pattern based on P, Q, R, S, T wave, R to R interval and T to P interval in each beat for Atrial Fibrillation and Normal Sinus Rhythm for pattern matching.
· Feature Extraction and comparison pattern: Extract feature from ECG signals and compare the similarity by using Euclidean metric in DP matching after segmentation. All the numerical value of comparison in DP matching will be stored and measured through average value of each group to see the trend of the data.
· Disease Classification: Disease classification will be done after the average value of each pattern being analyzed using DP matching where two criteria will be used to distinguish both categories. The main criteria to classify the normal and abnormalities of heart condition is the average value of each reference data range above 20 is considered as a sign of abnormalities. The second criteria is that the number of average range value above 20 which are tested with 10 reference data should be at least 7 over 10 reference data. This will be the best indicator in classifying the category of diseases; be it atrial fibrillation or Normal Sinus Rhythm.

5. EVALUATION

PhysioNet [6] is a resource where it provide a lot of data related to biomedical research and development. Physionet is a free open source resource where it consists of a large collection of recorded physiologic signal and related to open-source software.

In this experiments, two types of database from Physionet.org have been selected to validate the performance of the proposed algorithm which is MIT-BIH Normal Sinus and MIT-BIH Atrial Fibrillation. 19 patient's data are used for this experiments where 10 data are taken from MIT-BIH Normal Sinus Database and 9 data are taken from MIT-BIH Atrial Fibrillation Database. Each data duration is 60 seconds per analysis.

As the experiments have been done for all 3 segment, All data are distributed inconsistently for all DP Score and Average DP Score in segment P,Q,R,S,T, R to R interval and T to P for both symptoms. This trend, therefore, made it difficult to divide both symptoms without applying some criteria towards it. One of the biggest challenges in dealing with ECG Signal data is the variability of the individuals among patients' hearts activities. In every comparison of pattern and shapes using DP-Matching technique using the reference data, the value of comparison might not get as small in value as 0 because every pattern are totally different in some ways therefore making it almost impossible to have the same shape which is the reason why the 2 criteria range of value is introduced in the first place.

As seen in the result of average DP score above 20 shown in figure 4, figure 5 and figure 6, the overall of 100% detection of Atrial Fibrillation for 9 patients data is at 55% of accuracy for both segments. The percentage demonstrated that the proposed methods are able to discriminate the symptoms by several condition. As the standard criteria were set in the proposed method where the minimum detection should be at least at 80% for each data tested, 9 data in segment P, Q, R, S, T have shown the detection of atrial fibrillation at 88% while segment R to R interval and T to P segments are at 66%. These three segments have demonstrated that this proposed method can detect atrial fibrillation over 50% from the experiment. In these experiments, two parameters are taken into consideration for discriminating two symptoms which are Average DP Distance.As shown in figure 4,5 and 6 are the result of accuracy over 9 Atrial Fibrillation patient data for segment P,Q,R,S,T , R to R and T to P where it have been tested with 10 Normal Sinus reference data.

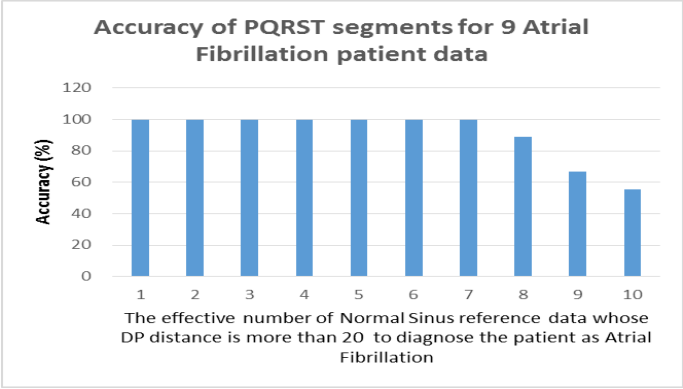

Figure 4: Result of P, Q, R, S, T segment

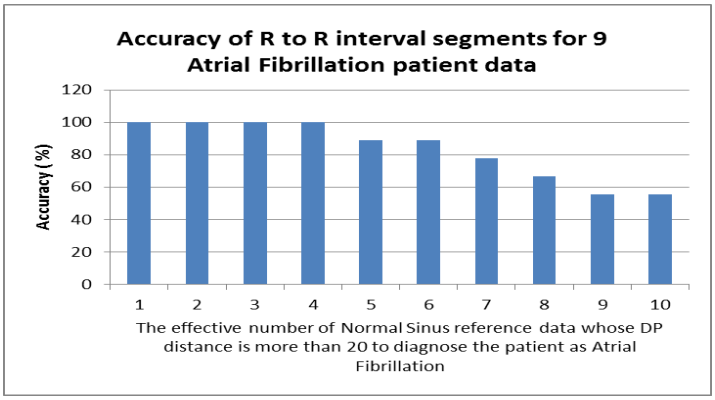

Figure 5: Result of R to R interval segment

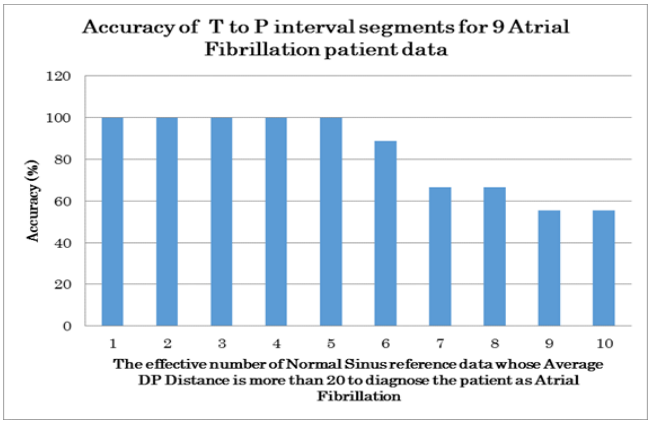

Figure 6: Result of T to P segment

There are some issues with some reference pattern which cannot be discriminated due to limitation of DP-Matching technique itself. Therefore, by setting some criteria where DP-Matching will work only as a tool to match the signal, the value of each matching pattern will be utilized by some criteria to discriminate the symptoms in some ways such as using the average DP score to compare to each DP score itself. The average value of DP score is significant because it is considered as the best approach to obtain cleaner data in order to discriminate existing noises in the data.. This is one of the factors as to why using the average DP score value is considered as one of the alternatives to interpret the data itself.

6. CONCLUSION

In this research, a Dynamic Programming matching technique has been proposed. From the result obtained by the experiments, it is proven that the proposed method by using DP-Matching has produced a high degree of detection rate in discriminating atrial fibrillation from normal sinus rhythm where it produces over 50% rate of accuracy over 9 patients data with Atrial Fibrillation symptoms. From the experiment result, it can be concluded that, the most reliable parameter to refer to determine the disorder is from average DP Distance for segment PQRST due to value of average DP Distance clearly distinguish both symptoms compared to the Standard deviation where the threshold is set range below 20 and above 20.

As a conclusion, segment P, Q, R, S, T and T to P are the best references to be utilized in detecting Atrial Fibrillation from Normal Sinus by using DP Matching tools. Both segments are the best segments as they are involved with X axis comparison where DP Matching is good at it. R to R interval segments were often dealing with Y axis pattern where it is difficult for DP matching to distinguish both symptoms based on some characteristics.

On the other hand, P, Q, R, S, T segments and T to P Segments are good İndicators to describe Atrial Fibrillation. This has not been done before. In addition to this, it is a good segment to detect fluctuation of Atrial Fibrillation while P, Q, R, S, T segment is well known as a good segment to identify Atrial Fibrillation as referred to the characteristic of Atrial Fibrillation.

In the future, increasing the rate of accuracy for detection of atrial fibrillation from normal sinus rhythm by using another technique will be studied. This is one of the justifications and proofs that to realize such a tool for diagnosing cardiac disorder is possible by using raw ECG data

REFERENCES

[1] M.R. Fawziya, "Diagnosis of Heart Disease based on Ant Colony Algorithm," International Journal of Computer Science and Information Security, May 2013.

[2] Y.Suzuki, Yukihisa Kurimoto, Sajjad Mohsin, Junji Maeda, "A Method for Extracting a QRS Wave in an ECG Based on DP Matching," T.IEE Japan, November 7, 2001.

[3] Sujit Kumar, Wenmiao Lu, Sitiani Dwi Teddy, Desok Kim, and Mengling Feng, “Detection of Atrial Fibrillation from Non-Episodic ECG Data: A Review of Method,” 33rd Annual International Conference of the IEEE EMBS, September 3, 2011.

[4] Lippincott Williams and Wilkins, “ECG Interpretation made Incredibly Easy! 5th edition,” Wolters Kluwer health, pp.1-99, 2011.

[5] U. Seiichi, Akihiro Mori, Ryo Kurazume, Rin-ichiro Taniguschi, and Tsutomu Hasegawa, "Logical DP Matching for Detecting Similar Subsequence," 8th Asian Conference on Computer Vision, pp.628-637, November 18-22, 2007.

[6] http://physionet.org/

Mohamad Sabri Bin Sinal @ Zainal obtained his Diploma in Information Technology (2008) from Island College of Technology, Penang, and Bachelor of Information Technology majoring in Software Engineering (2012) from Universiti Utara Malaysia. Currently, He is pursuing his Master of Computer Science in Graduate School of Electrical Engineering and Computer Science, Shibaura Institute of Technology. His research interests include health monitoring system, ECG, Heart Disease, context-aware computing and Ubiquitous Computing.

Eiji Kamioka is a Professor at Shibaura institute of Technology. He received his B.S., M.S. and D.S degrees in Physic from Aoyama Gakuin University. Before joining SIT, he was working for SHARP Communications Laboratory, Institute of Space and Astronautical Science (ISAS) as a JSPS Research Fellow and National Institute of Informatics (NII) as an Assistant Professor. His current research interests encompass mobile multimedia Communications and ubiquitous computing.

Automatic Illustration Creation from Novel Scenes for Supporting Reader's Comprehension

Hikaru Igarashi Eiji Kamioka
Graduate School of Engineering and Science, Shibaura Institute of Technology
3-7-5 Toyosu, Koto-ku, Tokyo, 135-8548 Japan

ABSTRACT
When reading a novel, sometimes there are sentences in a scene which cannot be understood well due to the difficult or complicated expressions. In such a situation, illustrations are helpful to comprehend the scene. However, the technologies that automatically create illustrations and insert them into the appropriate places in the novel have not as yet been established. In this paper, based on the hypothesis that illustrations can be placed into important parts in the novel, a method to estimate the important sentences using TF-IDF will be proposed. Furthermore, how to determine the most appropriate illustration to the scene considering the location information in the vicinity of the important sentences will be discussed.

1. Introduction

Figure 1 An illustration example which would help the readers' comprehension

Spread of electronic books enables us to easily obtain novels as electronic texts. In the novels, there often exist important parts to understand the scenes. In juvenile and popular novels, some illustrations are inserted in such important parts to support the readers' comprehensions. In general, however, novels consist of only texts, hence, the readers have to understand the scenes without any additional supports. It is noted that the important parts in a novel could be extracted by performing a morphological analysis from our previous work [5]. Therefore, if appropriate illustrations can automatically be created and inserted into those parts, the readers' comprehensions to the scenes would improve, then the reading the novel would be more enjoyable.

This study aims at automatically extracting the significant parts in novels, creating illustrations suitable for the scenes, and supporting the readers' comprehensions to the contents. Figure 1 shows an example illustration which would be automatically created to the sentence of *"I and she played soccer in the schoolyard at dusk."*

In this paper, two methodologies for analyzing text-based novels to achieve the goal mentioned above will be proposed. The first one is how to determine the place where illustrations should be inserted. The second one is how to extract the location information which is the most important for generating the illustrations. In addition, the result of verification experiment, which investigated which illustration generated from the sentences including location information was the most suitable for the considered scene, will be discussed.

2. Related work

There are many NLP (Natural Language Processing) based studies which associate sentences with stationary pictures or video images. Nishihara et al. [1] tried to express a blog content by images extracting the words which show the episodes in the blog. The blog content was separated by episode, and then the important words were extracted focusing on case-marking particles. The methodology which extracts important words may work effectively to this study as well. In the case of blog, however, it is much easier to identify the location in the blog compared to novels, hence, it is skeptical if only this method is enough for this study. Sunayama et al. [2] proposed a method to extract important sentences from a text-based novel. This approach determined the importance of sentences by ranking the strength of association between a word and the theme using TF-IDF and their original method. This method could be applied to this work for determining the places which illustrations should be inserted. However, the targets of their work are newspaper and theses. Therefore, the effectiveness of their approach to novels are unknown. Kijima et al. [3] estimated the important personages in the novel using TF-IDF and the occurrence rate of nouns. Furthermore, their study tried to reconstruct novel scenes by images by clarifying the relation among personages. Their approach is of some help for this study in terms of the use of TF-IDF and the method of protagonist identification. However, some improvements are required for estimating a scene and generating a single picture that shows the scene.

3. Estimation of Illustration Insertion Position Focusing on Protagonists

In this study, TF-IDF (Term Frequency – Inverse Document Frequency) is applied to determine the position where illustrations should be inserted. In general, TF-IDF is used to quantify how each word is important in the considered sentence.

Equation (1) shows how to calculate the TF-IDF value, $W_{i,j}$.

$$W_{i,j} = tf_{i,j} \times \log(\frac{N}{df_i}) \quad (1)$$

Here, $tf_{i,j}$ is defined as the following fraction.

$$tf: \frac{The\ number\ of\ the\ word\ appearances\ in\ a\ target\ sentence.}{Word\ count\ of\ the\ sentence}$$

Where,
N: The total number of documents in the book
df: The number of documents where the word appears
i: Noun
j: Sentence where the noun i appears.

In this study, after extracting nouns from the novel by morphological analysis using a software tool, MeCab [4], the average value of TF-IDF for each sentence is calculated, and then each sentence is quantified by the value which shows how important it is. From our previous work [5], it is concluded that important pages in novels can be extracted by focusing on protagonists. Therefore, the same approach is performed for this study. In the novel [6] that was targeted in this study, four important personages were detected by the analysis mentioned above, hence, the positions, which illustrations should be inserted, were estimated for each personage.

4. Extraction of Location Information

Ideally, the illustrations adapted to the sentences should be automatically obtained from Web pages. Actually, it has already been tried many times with many techniques in our previous study, however, the results have not as yet been satisfactory. Therefore, in this study, all the words in the novel which show the location information were manually extracted and the corresponding illustrations were manually obtained from Web pages. These images were stored in the hard disk of a personal computer. This seems to be strange because the final goal is to create illustrations automatically. However, this study does not focus on finding suitable images on the Internet but extracting the location information from the texts using NLP. Therefore, in this paper, the above manual operation can be accepted.

From our previous work [5], the following fact has been obtained, that is to say, the location information suitable for the important sentence can be detected within the range from 2 page before and 1 page after the sentence. Within this range, About 6.5 words which showed location information were detected, hence, it can be assumed that the most suitable location information for the considered important sentence will be detected among them. In this study, to extract location information from the sentence, particle which is one of the parts of speech in Japanese is paid attention to. Especially, case-marking particles, 'ni' and 'de' are used since these particles are usually placed just after the location words. It is noted that the case-marking particles, 'ni' and 'de' are placed not only just after location words but also just after the other words. In this study, hence, 132 location words already extracted manually were investigated to verify the hypothesis. These location words correspond to the images stored in the hard disk of the personal computer as stated at the beginning of this section. In addition to the above condition, by giving the restriction that a verb is placed just after 'ni' or 'de', the location where the personage is can be identified.
Table 1 shows the sentences which include location information extracted by the method as mentioned above.

As you can see from the result in Table 1, although no sentence was extracted to Yukawa, three sentences including location information were extracted to Yasuko, Ishigami and Kusanagi, respectively.

In the following sections, the validity of illustrations created based on Table 1 will be verified.

Table 1 Extracted sentences that include location information for each personage

Personage "Yukawa"	No estimated sentence.
Personage "Kusanagi"	Kusanagi answered the phone call over reclining his passenger seat fully.
	"Come to the Edogawa Police Station immediately."
	"You've got the instruction to go to the Edogawa Police Station."
Personage "Ishigami"	"Because I wanted the police to grasp the fact that the victim went to the scene from Shinozaki Station by bicycle. What is more, it couldn't be done by a normal bicycle."
	"It seems that the police estimated as if the criminal had wanted a newer bicycle for stealing anyway, but this is not such a simple reason. What the criminal stuck to was when the bicycle was parked at Shinozaki Station."
	Yasuko and her companions have been in a Chinese restaurant at Ginza.
Personage "Yasuko"	Her cell phone started ringing when she was crossing at the cross walk toward Shinagawa station.
	The feeling continued until she went back her apartment.
	They are two photos of Kudou and one photo of Yasuko walking into a hotel.

5. Verification Experiment

In this section, the validity of created illustrations is verified. The important parts in the novel were extracted using TF-IDF and they were ranked by the average value of TF-IDF. Using the sentences determined as the most and the second most important parts, the created illustrations were verified through an experiment. The subjects read each sentence and investigated the illustrations created based on Table 1, then chose the most appropriate illustration. 10 subjects were prepared for the experiment. As example sentences used in the experiment, the sentences determined as the second most important for each personage are shown in Table 2.

Table 2 Example sentences determined as the second most important for each personage

Personage "Yukawa"	Ishigami guessed that they saw what had been in the room.
	When Ishigami came back to his apartment while thinking about such a thing, a man had stood in front of his room.

	Moreover, almost all the students were sitting at the back so that they can leave as soon as the roll call is finished or so that they can do a selfish another work.
	Ishigami was not interested in the lecture so much, but he sat on the second seat from the left in the front row from sheer habit.
Personage ”Kusanagi”	No estimated sentence.
Personage “Isigami”	Yukawa said like that when they began to walk along the Sumida River after passing under the Shin-Ohashi Bridge.
	“Aren’t you going back to the university for research anymore?”
	What can be done in the university can be done by myself. Moreover, there would be no university which hires me at this age.
Personage “Yasuko”	No estimated sentence.

Table 3 shows the experimental result. In the Table 3, Text1 and Text2 mean the most important and the second most important sentences, respectively, determined by the proposed method. Each numerical value indicates the number of subjects who determined that the illustration was the most suitable for the considered sentence.

These results are 100% correct from the authors’ subjective evaluations.

Table 3 Result of the verification experiment

Yukawa	Room	Apartment	Seats in lecture room
Text2	0	5	5
Kusanagi	Passenger seat in the car	Police Station	-
Text1	7	3	-
Ishigami	Scene	Shinozaki Station	Chinese restaurant
Text1	2	2	6
Ishigami	Sumida River	University	-
Text2	9	1	-
Yasuko	Shinagawa station	Apartment	Hotel
Text1	3	7	0

6. Experimental result depending on the habit of reading books

One of the requirements in this study is to insert illustrations into the important parts in the novel. However, the important parts may be different depending on the reader’s reading skill. More concretely, the imagination to a scene by a reader who has the habit of reading books must be different from the one to the scene by another reader who does not have. Therefore, the important parts and the imagined illustrations in the novel could be different for these two readers. Based on this assumption, the verification of the difference in the experimental result was conducted. Table 4 presents the habit of reading books for 10 subjects. Each numerical value in Table 4 indicates the number of subjects depending on the number of books read per week.

Table 5 presents the experimental result by 5 subjects who rarely read books.

Table 4 Habit of reading books for the subjects

Rarely read books	Read a book a week	Read more than two books a week
5	3	2

Table 5 Result of the verification experiment depending on the habit of reading books

Yukawa	Room	Apartment	Seats in lecture room
Text2	0	2	3
Kusanagi	Passenger seat in the car	Police Station	-
Text1	2	3	-
Ishigami	Scene	Shinozaki Station	Chinese restaurant
Text1	1	1	3
Ishigami	Sumida River	University	-
Text2	5	0	-
Yasuko	Shinagawa station	Apartment	Hotel
Text1	1	4	0

The correctness of the results is 80% from the authors’ subjective evaluations. Here, there is an interesting tendency which is different from the result obtained by all the subjects. In the case of Text1 for the personage of Kusanagi, the subjects who rarely read books tend to select the illustration of Police Station. In this scene, actually, just after a police officer, Kusanagi, sat on the passenger seat of the car, he received a phone call from his boss and he was commanded to go back to the police station. The real location in this scene is the passenger seat of the car. The Police Station is the location information just used in the telephone conversation. The subjects who rarely read books imagined the scene at the Police Station through the conversation, that is to say, they made a mistake in grasping the scene which was difficult to understand.

It is concluded that the illustration selection must be done referring to the result obtained by the subjects who have the habit of reading books. Furthermore, the illustrations should be created based on the extracted important sentences including many personages’ names.

7. Conclusions

In this paper, a notable method, which automatically estimate the important parts in the novel and automatically select the most suitable illustrations for the scenes, have been proposed. It was based on the assumption that the places where illustrations should be inserted must be the important parts. Also it was based on the fact obtained from our previous work that the important parts can be extracted by focusing on the personages in the novel. Regarding the extraction of location information for creating illustrations, the use of case-marking particles, especially 'de' and 'ni', followed by verbs was proposed. The effectiveness of the proposed method was verified through the experiment, that is to say, the adequate sentences including location information were extracted.

As for the determination of the most appropriate illustration for a scene, an experiment based on subjective evaluations were discussed. From the experimental result, it is concluded that the selected illustrations by majority vote showed the validity of the proposed approach. In addition, the experiment brought an interesting discovery that the comprehension of the novel content depends on the habit of reading books. Readers who rarely read books tend to make a mistake in understanding the scenes. This fact shows the importance of illustrations for novels so that the readers can comprehend the complicated situations.

As a future work, scene changes must be investigated. Sometimes a scene in a novel suddenly changes without any specific grammatical changes. This is a quite challenging issue. However, if the scene changes can be detected correctly, the accuracy of extracting the important sentences would be improved. Moreover, the proposed approach should be applied to many types of novels to verify the effectiveness since the strain of novel must depend on the novel category and the author.

References

[1] Yoko Nishihara, Keita Sato, Wataru Sunayama, "Personal Experience Acquisition Support from Blogs using Event-Depicting Images," Journal of Japan Society for Fuzzy Theory and Intelligent Informatics, Vol.20, No.5, pp.757-767, 2008.

[2] Wataru Sunayama, Masahiko Yachida, "A System for Making Summary by Extracting Key Sentences Using feature keywords -A Panoramic View System-," IEICE Transactions on Information ans Systems D-I, Vol.J84-D-I, No.2, pp.146-154, 2001.

[3] Sayako Kijima, Kyoko Hikino, Masahito Hirakawa, "Generation of Pictures from a Narrative Text," Japanese Society for Artificial Intelligence, SIG-SLUD-A603-10 (03/02), pp.51-56.

[4] "MeCab: Yet Another Part-of-Speech and Morphological Analyzer,"

[5] http://mecab.googlecode.com/svn/trunk/mecab/doc/index.html

[6] Hikaru Igarashi, Eiji kamioka, "Creation of Illustrations based on Novel Scenes" IEICE Technical Report, MoNA, Vol.114, No.31, pp.25-30, 2014.

[7] Keigo Higashino, "A medical X on a suspect ," Bungeishunju Ltd., 2008.

Hikaru Igarashi is currently a master course student at Graduate School of Engineering and Science, Shibaura Institute of Technology. He received his bachelor degree from Department of Communications Engineering, Shibaura Institute of Technology.

Eiji Kamioka is a Professor at Shibaura institute of Technology. He received his B.S., M.S. and D.S degrees in Physics from Aoyama Gakuin University, Japan. Before joining SIT, he was working for SHARP Communications Laboratory, Institute of Space and Astronautical Science (ISAS) as a JSPS Research Fellow and National Institute of Informatics (NII) as an Assistant Professor. His current research interests encompass mobile multimedia communications and ubiquitous computing.

ELECTRONIC PATIENT REFERRAL SYSTEM WITH DATA EXCHANGE AND FINGERPRINT PATIENT IDENTIFICATION

Tipporn Laohakangvalvit[1], Michiko Ohkura[2], Tiranee Achalakul[3], Somchanok Tivatansakul[1]

Graduate School of Engineering, Shibaura Institute of Technology, Japan[1]
College of Engineering, Shibaura Institute of Technology, Japan[2]
Department of Computer Engineering, King Mongkut's University of Technology Thonburi, Thailand[3]

ABSTRACT

Currently many healthcare systems process electronic patient referrals in Thailand. However, these systems suffer from two main obstacles. First, they can only process referrals from hospitals that use same system. Consequently, medical staffs use such traditional methods as faxes to transfer patient data. The second obstacle is the identification of patients when they cannot provide personal information by themselves. These obstacles hamper medical diagnoses. To cope with these obstacles, this paper proposes an electronic patient referral system with data exchange and fingerprint patient identification. From the initial phase of research, we designed a healthcare platform that provides such services as data exchange that allow system to search for patient data using citizen IDs. In addition, this paper proposes an extended service, fingerprint patient identification, which responds to citizen IDs from existing fingerprint database. By combining these two services, we support medical staffs to operate referral process faster and more conveniently.

1. INTRODUCTION

Recently, focus on the inequity of access to healthcare services between citizens in rural and urban areas has increased in many countries around the world including Thailand. Healthcare systems have been developed in isolation because of the lack of unified data standards and technology. To address such problems, Thailand's government sector started in 2008 a ten-year roadmap called Smarter Health and Smarter Living to stimulate the development of efficient healthcare services, including coordination among various healthcare providers, for better health and citizen well-being (Kawtrakul, et al., 2011). The roadmap introduced a blueprint to develop healthcare systems for various healthcare processes such as patient referrals, consultations, and emergency management.

Patient referrals in Thailand have changed from a paper-based to an electronic-based system. Currently, many hospital information systems electronically process patient referrals. However, this applies to referrals only among hospitals that use systems with unified standards and infrastructure. From a 2007 survey, over 32 different hospital information systems were deployed in 750 healthcare institutes in Thailand (Information and Communication Technology Center, 2011). Although the top-five systems are used in approximately 56 percent of all the hospitals in the country, none has the capability to share or exchange data. This is the main obstacle for a patient referral process to obtain referred patient information. According to the blueprint, systems must be developed to support open standards, data conversion, and data transfer regardless of different infrastructures.

One critical healthcare situation is emergency cases when patients need to be referred from one hospital to another that can handle a particular medical problem. Even though other hospitals obviously have competent doctors who can diagnose and give medical treatment, patient information must be reported to doctors in advance. Insufficient information may cause inadequate diagnoses or even medical errors that lead to disabilities or even patient deaths.

Apart from the above obstacle, patient identification is another main obstacle for diagnosis, especially in emergency cases. In such cases, patients are often unconscious and unable to provide personal information. Therefore, another identification method must be integrated to allow the system to identify patients regardless of their condition. The utilization of biometrics was proposed by healthcare applications to protect and help manage medical records and to identify patients (International Biometric Group, 2006).

To cope with those obstacles, this paper proposes an improved design of an electronic patient referral system. A data exchange and a fingerprint patient identification are integrated. The data exchange is one service provided by the cloud-based healthcare platform proposed in the initial phase of this research (Laohakangvalvit & Achalakul, 2014). We also proposed an extended feature of this platform, which is the fingerprint identification service used

in patient referral systems in addition to the former method that uses citizen IDs. The improved design integrates these two services to provide a system that supports medical staffs to use fingerprints as input to identify patients and query for patient data from other hospitals.

The rest of our paper is organized as follows. A literature survey is presented in Section II. The cloud-based platform for healthcare services is presented in Section III. The proposed design of our electronic patient referral system is described in Section IV, including its overall system design and framework design. The last section concludes our paper and describes future works.

2. LITERATURE REVIEWS

2.1 Proposed patient referral systems

Darcy, et al. (2010) proposed an electronic patient referral system called ZEPRS for women with complications during pregnancy. Their system, which must be used through a closed network, was the successful first perinatal referral system in Sub-Saharan Africa and became the first step toward developing a complete electronic medical record system. Huang, et al. (2010) proposed an electronic emergency referral document system that allows patient data to be transferred to other hospitals in a complete and timely fashion to doctors. Their prototype developed its own referral documents for across-enterprise document sharing.

2.2 Patient identification and access control in healthcare systems

Shin, et al. (2008) and Díaz-Palacios, et al. (2013) proposed the designs of healthcare system using fingerprint as biometric access control for electronic patient records to eliminate the use of such token-based access as password, electronic signature, etc. Both researches used fingerprint recognition to search for patient information from central databases.

The surveys from Luis-Garc, et al. (2003) and International Biometric Group (2006) about biometric identification systems concluded that fingerprint technology provides many benefits among various biometric devices, such as the identification of irises, voices, faces, and hand geometry. Based on the characterization criteria (i.e., accuracy, simple use, simple implementation, and cost), fingerprints were rated as highly accurate, easy to implement, somewhat easy to use, and medium-priced. In healthcare applications, fingerprint technology can be applied to protect and manage confidential medical records, identify patients, and protect the security of medical facilities and equipment.

From literature reviews, the limitations and suggestions to identify patients in the patient referral systems can be summarized as follows:

- *Limited environment of patient referral systems:* Since the currently proposed patient referral systems mainly focus on data exchange under closed networks or specific technology, they have difficulty in practical situations since most hospitals prefer to develop their own distinctive systems.
- *Lack of an efficient method for patient identification:* Patient referral needs an efficient method to enhance speed and convenience to quickly identify patients. Fingerprint technology has greater potential for integration into systems than non-biometric methods.

Therefore, this research proposes an electronic patient referral system that integrates the data exchange service on cloud technology and the fingerprint identification service to provide a more efficient system for Thailand.

3. CLOUD-BASED PLATFORM FOR HEALTHCARE SERVICES WITH DATA EXCHANGE

Cloud-based platform for healthcare services are the initial phase of this research. Various healthcare services allow registered healthcare institutes to integrate services into their healthcare applications. The data exchange service was primarily focused in this research as previously proposed in Laohakangvalvit & Achalakul (2014). A data exchange framework (Fig. 1) was designed to allow various healthcare applications to exchange data. The data model integrated many well-known standards, such as Health Level 7 (HL7) and 50 standard files. The data exchange mechanism enabled a system to use the citizen IDs of patients as a master patient index (MPI) to submit requests for patient data through its platform. Then the platform became responsible to query for patient data from other hospitals.

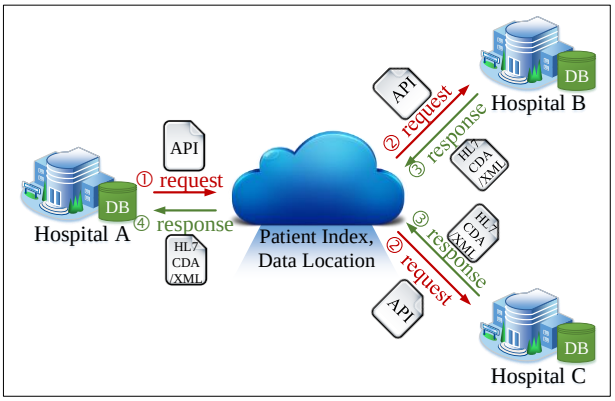

Fig. 1. Data exchange model

4. DESIGN OF ELECTRONIC PATIENT REFERRAL SYSTEM

4.1 Overall system design

A platform for healthcare services needs to have applications to utilize its provided services. An electronic patient referral system (Fig. 2) is the first proposed application that utilizes the data exchange service to obtain patient data from other hospitals. To request patient data, citizen IDs as patient identities must be used as input. In addition, we propose a new method to identify patients using fingerprints. In addition, citizen fingerprints have already been recorded in a local database which belongs to a government sector called the Department of Provincial Administration of Thailand. If our method is connected to the platform, it can be used as a reference for individuals in fingerprint patient identification service.

To realize patient identification using fingerprints, the following parts were added or modified as presented in Table 1.

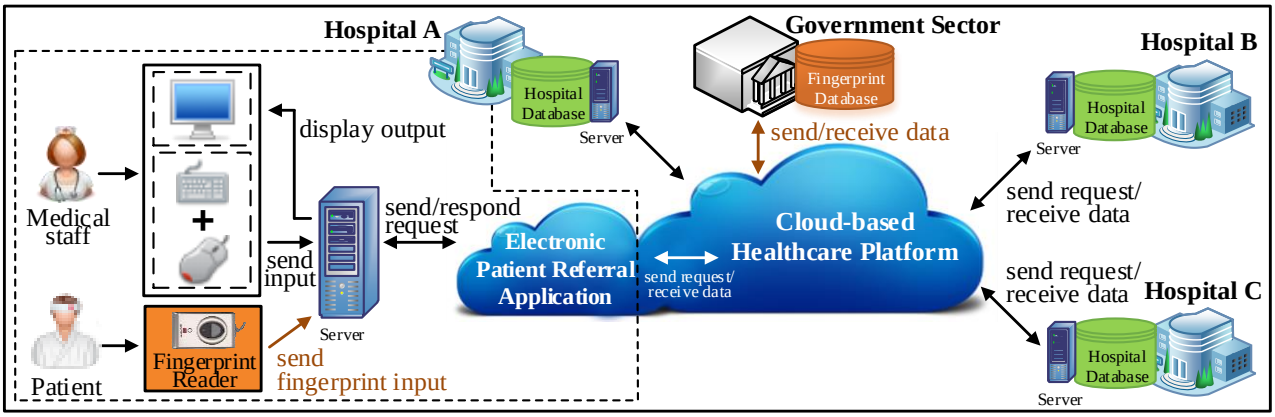

Fig. 2 Proposed design of electronic patient referral system

Table 1. Added/modified parts for patient identification

Related part	Added/modified part	Action
Input device	Fingerprint reader	Add
Electronic patient referral system	Fingerprint acquisition module	Add
	Input data package module	Modify
Cloud-based healthcare platform	Fingerprint identification service	Add
	Fingerprint database	Add
	Fingerprint matching module	Add

With this improved design, users can enter either their citizen IDs or fingerprints as identity data and provide them to the system to request patient data.

4.2 Framework design

The framework design of the electronic patient referral system with data exchange and fingerprint identification is shown in Fig. 3. It consists of four main groups. The detailed design of each part is described as follows:

4.2.1 Electronic patient referral system

- *I/O Devices:* There are four I/O devices which are fingerprint reader, keyboard, mouse, and PC display.
- *System Module:*
  - *Fingerprint acquisition module:* It is used to scan and store fingerprint data.
  - *Data query module:* It is used to submit request for patient data to platform.
  - *Local data query module:* It responds query requests using hospital database.
- *Server:* The server runs back-end system and locally store hospital database which can respond the requests for patient data query from the platform.

4.2.2 Cloud-based healthcare platform

- *Services:* Fingerprint identification service and data exchange service are two of all services on the platform used by the electronic patient referral system.

  For the *fingerprint identification service*, it receives fingerprint data from the electronic patient referral system and forwards them to the server located at the government sector. The returned result as citizen IDs are forwarded to the data exchange service to process patient data requests.

  For the *data exchange service*, it uses citizen IDs to query for hospitals that store patient data and sends requests to those hospitals. Once the requests are answered, the data are merged and returned to the hospital where the request is submitted.

4.2.3 Government sector's system

- *System Module:* Only one module, a fingerprint matching module, is responsible for matching the fingerprint input data with the existing fingerprint data of citizens and returns citizen IDs (if they exist).
- *Server:* The server stores citizen's fingerprint database. This resource currently exists and belongs to the government sector, Department of Provincial Administration of Thailand.

4.2.4 Other hospital systems

A local data query module automatically responds to the requests from the platform without a front-end system that is managed by users. The other hospital's system can also be extended to more than only one hospital when patient records are stored in the local databases of many hospitals.

5. DISCUSSION, CONCLUSION AND FUTURE WORKS

We improved the design of our proposed electronic patient referral system by adding a fingerprint patient identification service. This system has two advantages: (1) it supports faster and more convenient requests for patient data from other hospitals using only patient fingerprints, and (2) the referred patients receive better health care.

In conclusion, we proposed an improved design of an electronic patient referral system. Our proposed design includes fingerprint identification services to identify referred patients who cannot supply their own identity data by using fingerprint scanner to obtain fingerprints from patients. Our fingerprint identification service works with the data exchange service to search for patient data through the cloud-based healthcare platform.

Future work will implement and evaluate this system. Challenges include the reduction of time and improving the efficiency to identify individuals from a large database and to search and gather data from multiple sources.

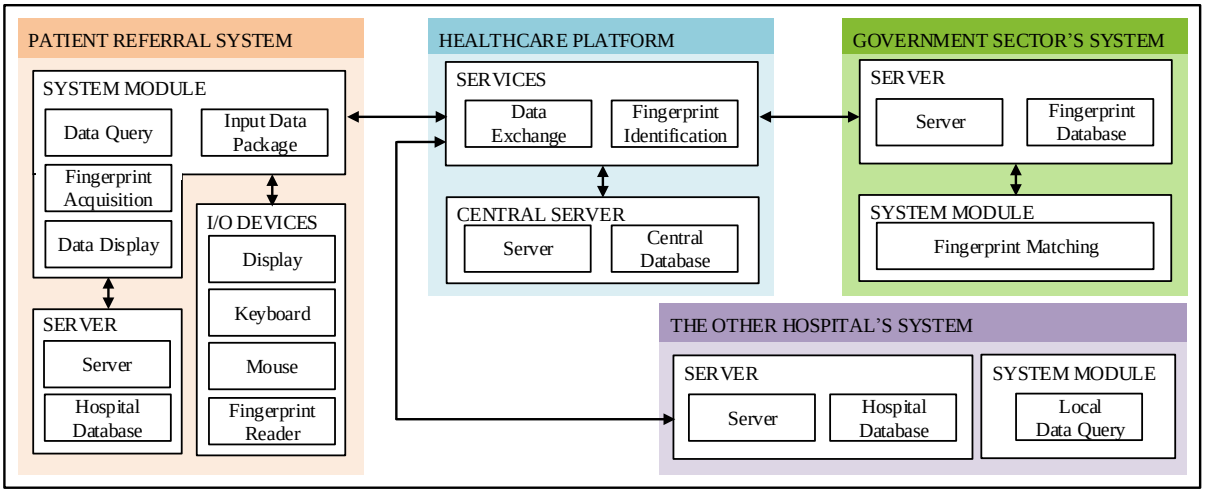

Fig. 3 Framework design

REFERENCES

A. Kawtrakul, K. Sripanidkulchai, N. Sahavechaphan, C. Tanprasert, K. Nithikethkul, C. Leangsuksun, K. Kruthkul, B. Sapsomboon, P. Tantatsanawong, Towards Development of a National Blueprint for Better and Smarter Healthcare Services in Thailand, SRII Global Conference, pp.371-377, 2011.

Information and Communication Technology Center, "ICT Strategic Plan for Ministry of Public Health in 2013-2021", Ministry of Public Health, p.76, 2011.

International Biometric Group, "Biometrics in healthcare", Biometric Technology Today, pp.9-11, 2006.

T. Laohakangvalvit, T. Achalakul, "Cloud-based data exchange framework for healthcare services", 11th International Joint Conference on Computer Science and Software Engineering, pp.242-247, 2014.

N. Darcy, C. Kelly, E. Reynolds, G. Cressman, P. Killam, "An Electronic Patient Referral Application: A Case Study from Zambia", RTI Press Publication, No.RR-0011-1003, 2010.

X. Huang; D. Liou, "Implementation of an electronic emergency referral document system", 2nd International Conference on Education Technology and Computer, vol.2, pp.V2-93 - V2-96, 2010.

Y.N. Shin, Y. Lee, E. Shin, J. Choi, "Designing Fingerprint-Recognition-Based Access Control for Electronic Medical Records Systems", 22nd International Conference on Advanced Information Networking and Applications–Workshops, pp.106-110, 2008.

J. R. Díaz-Palacios, V. J. Romo-Aledo, A. H. Chinaei, "Biometric access control for e-health records in pre-hospital care", Proceedings of the Joint EDBT/ICDT Workshops, pp.169-173, 2013.

R. Luis-Garc, C. Alberola-Lopez, O. Aghzout, J. Ruiz-Alzola, "Biometric identification systems" Signal Processing, pp.2539-2557, 2003.

Tipporn Laohakangvalvit received her B.E. (2012) degree in computer engineering from King Mongkut's University of Technology Thonburi (KMUTT), Thailand. She is currently Master's degree student at Shibaura Institute of Technology, Japan. Her research interests include healthcare system and software usability.

Michiko Ohkura received her B.S. (1976) and M.S. (1978) degrees in Mathematical Engineering and Ph. D. (1995) in Advances Interdisciplinary Studies from the University of Tokyo, Japan. She worked for some companies and is currently a professor of the SIT, Japan. Her current research interests include usability of interactive systems and emotion information processing.

Tiranee Achalakul received her B.S. degree in computer engineering from King Mongkut's Institute of Technology Ladkrabang, Thailand, in 1994 and completed Ph.D. in computer engineering from Syracuse University, New York, in 2000. She is currently an associate dean in education development for the faculty of engineering at King Mongkut's University of Technology Thonburi. Her research interests include parallel and distributed computing, software engineering, Cloud and GPU technology, and data mining applications.

Somchanok Tivatansakul received B.E. (2009) and M.E. (2012) degrees in computer engineering from KMUTT and received second M.E. (2012) degree in electrical engineering and computer science from Shibaura Institute of Technology, Japan. She is currently a Ph.D. candidate at Shibaura Institute of Technology. Her research interests include e-healthcare, emotion recognition and interactive systems.

AFFECTIVE EVALUATION FOR MATERIAL PERCEPTION OF BEAD-COATED RESIN SURFACES USING VISUAL AND TACTILE SENSATIONS –FOCUSING ON KAWAII–

***Michiko Ohkura, *Kazune Inoue, *Ryota Horie, **Masato Takahashi, **Hiroko Sakurai**
****Takashi Kojima, **Kiyotaka Yarimizu, and **Akira Nakahara**
***Department of Information Science and Engineering, Shibaura Institute of Technology**
****DIC Corporation**

ABSTRACT
We performed affective evaluation experiments on both visual and tactile material perception of bead-coated resin surfaces in which the materials, the diameters, and the hardness of beads were expanded systematically. First, we performed an experiment on the similarity of the bead-coated resin surfaces to reduce number of material samples. Second, another experiment was performed on the similarity of the evaluation items to reduce their number. Finally, we performed an affective evaluation experiment on selected samples with students and middle-aged participants to clarify the differences among the different physical attributes of resin surfaces and focused on *kawaii*.

1. INTRODUCTION

The rapid progress of computers and the internet has greatly increased the popularity of such interactive systems as computer games, simulators, and interactive arts for entertainment and/or art. The Kansei/affective value, which has become critical in Japanese manufacturing, is determined ranked as the fourth highest characteristic of industrial products after function, reliability, and cost by the Japanese Ministry of Economy, Trade and Industry (METI)(Araki, 2007). According to METI, it is important not only to offer new functions and competitive prices but also to create new values to strengthen Japan's industrial competitiveness.

Several years ago, we began new research to apply our previous research results to the systematic creation of the kansei values of artificial products, especially such digital contents as Japanese games, cartoons, and animations (JEITA, 2000). One of the main reasons for the success of digital content is the existence of kawaii characters with their highly subtle techniques (Belson & Bremner, 2004). Since such Japanese kawaii characters as Hello Kitty and Pokemon have become popular all over the world, we selected kawaii as a crucial kansei value for artificial products.

Kawaii is an adjective in the Japanese language. Recent works (Belson & Bremner, 2004) (Yomota, 2006) (Koga, 2009) (Makabe, 2009) (Sakurai, 2009) have recognized its following common attributes:
- An emotional value of Japanese origin.
- Such positive connotations as lovable and charming

Because kawaii's meaning is not exactly the same as cute or lovable and its use has become international, we directly use it both as an adjective and a noun.

Even though such Japanese kawaii characters as Hello Kitty have become popular worldwide, few studies have focused on kawaii as an affective (kansei) value. Therefore, we systematically began to analyze kawaii interfaces themselves: the kawaii feelings evoked by shapes, colors, and materials. Our objective is to describe a method for constructing a kawaii interface from research results. Kawaii is positioned as an important affective (kansei) value for future interactive systems and industrial products of Japanese industries.

We previously performed experiments with abstract objects in a virtual environment and obtained useful results for such kawaii attributes as shapes, colors, visual textures and tactile materials (Ohkura & Aoto, 2007) (Ohkura, Goto, & Aoto, 2009) (Ohkura & Aoto, 2010) (Ohkura, Komatsu & Aoto, 2013) (Ohkura, Osawa & Komatsu, 2013). However, these textures and materials were not chosen under the systematic distribution of physical parameter values (Ohkura, Osawa & Komatsu, 2013). We used bead-coated resins for affective evaluations in which each bead was made from one of three resin materials of a particular size and hardness in systematic expansions.

This article introduces our affective evaluation results of the surfaces of these bead-coated resins by focusing on kawaii.

2. BEAD-COATED RESIN SAMPLES

Bead-coated resin samples were wrapped on the sides of cans with the following characteristics:
- Resin material: PE, VI, and FP
- Bead diameter: #1 (6 um) to #7 (93 um) (Table 1)

- Bead hardness: soft (S), medium (M), hard (H), and super-hard (SH)

Three samples with different resin materials without bead-coats were also prepared.

3. PRELIMINARY EXPERIMENTS

3.1 Experiment for Sample Similarity

To reduce the number of samples for an affective evaluation experiment, an experiment was performed using 30 samples: ten samples from Table 1 for each of three resin materials. The pairs of samples shown were presented to the participants who rated the similarity.

Six participants in their 20's served as volunteers. Figs 1 and 2 show experimental scenes in visual and tactile presentations, respectively. The samples for the affective evaluation were determined as follows:

- PE: N, #2, #3, #4, #5, #6, #7, M(=#4), H, SH
- VI: N, #2, #3, #4, #5, #6, #7, M(=#4)
- FP: N, #2, #3, #4, #5, #6, #7, M(=#4), H, SH

where N means the non-bead-coated sample.

3.2 Experiment for Evaluation Factor Similarity

The candidates for the factors of the affective evaluation were collected from a survey of previous research. To choose one from some similar factors, we experimentally evaluated the similarities among factors using 12 samples: N, #1, #4, and #7 of each of the three resin materials. Participants were presented pairs of samples and asked to compare each one with a standard sample, which was one of the non-bead-coated samples. A 7 Likert scale was employed for the adjective pairs, and a 5 Likert scale was employed for the adjectives. "Impossible to evaluate" was included as an option for all the adjective pairs and adjectives. Each sample pair was presented either visually or tactilely.

Six participants in their 20's served as volunteers. After excluding the adjective pairs and the adjectives with many "Impossible to evaluate" answers, we classified them by clustering analysis. Table 2 shows the final results, the list of the adjective pairs, and the adjectives used for the affective evaluation experiment described below.

4. AFFECTIVE EVALUATION EXPERIMENT OF BEAD-COATED RESINS

4.1 Experimental Method

Based on the results of the above experiments mentioned in Section 3, we performed another experiment on the affective evaluation of the bead-coated resins of 28 samples using the adjective pairs and adjectives from Table 2. The samples were presented in three ways: visually, tactilely, or both. The orders of these three ways were counter-balanced between visually and tactilely, and both was always the last. The standard sample of each pair was one of the three samples without beads of the three resin materials. The evaluation procedure was the same as the experiment in the previous section.

4.2 Experimental Results and Discussion

Experiments were performed with 24 participants, six males in their 20's, six females in their 20's, six males in their 40's/50's, and six females in their 40's/50's.

Table 1 Combination of particle diameter and bead hardness.

	#1	#2	#3	#4	#5	#6	#7
S				+			
M	+	+	+	+	+	+	+
H				+			
SH				+			

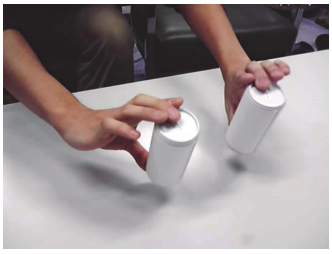

Fig. 1 Visual presentation.

Fig. 2 Tactile presentation.

Table 2 Adjective pairs and adjectives.

Adjective pair	Adjective
Chic - Ordinary	Smooth
Simple - Gaudy	Damp
Masculine - Feminine	Granular
Comfortable - Uncomfortable	Sticky
Interesting - Boring	Dry
Hot - Cold	Slippery
Easy to hold - Hard to hold	Wild
Artificial - Natural	Mild
Adult - Childish	Exciting
Favorite - Hateful	Staid
	Cool
	Kawaii

We separately performed several analyses for the 20's groups and the 40's/50's groups. A three-way analysis of variance (ANOVA) was performed for the evaluation results of each adjective pair/adjective. Table 3 shows the ANOVA results of each adjective with bead hardness, the resin material of the beads, and gender as factors for the 20's. Table 4 shows the ANOVA results for each adjective with bead diameter, the resin material of the beads, and gender as factors for the 20's.

As for kawaii, bead hardness had a significant main effect in the tactile presentation ($p<.005$). Softer beads have higher kawaii scores. Table 4 shows the following:

- Bead diameter has a significant main effect for kawaii for all presentation ways (p<.001). The smaller bead has the higher kawaii score.
- Gender has a significant main effect for kawaii for the visual and both presentation ways (p<.001). The female scores are higher than those of the males.

The intersection results were omitted from this paper to avoid the argument of the interpretation.

The ANOVA results for the 40's/50's are omitted in this paper. As for kawaii, bead hardness has a significant main effect in visual presentation (p<.001). Softer beads have higher kawaii scores. The resin material of the beads also has a significant main effect in visual presentation (p<.001). Table 4 shows the following:

- Bead diameter has a significant main effect for kawaii for all the presentation ways (p<.001). Smaller beads have higher kawaii scores.
- Gender has a significant main effect for kawaii for the visual and both presentation ways (p<.001). The scores by females were higher than those of the males.

These results are almost the same as the results for the 20's. The intersection results were also omitted from this paper.

Table 5 shows the results of the difference test between the groups of 20's and 40's/50's. *Sticky*, *dry*, and *staid* show significant differences by ages for all presentation ways. *Slippery* and *mild* have no significant differences.

We estimated the coefficients based on the multiple regression model shown equation (1):

$$y = a + b\log x_1 + cx_2 + dx_3 + ex_4 + fx_5 + gx_6 \quad (1)$$

$y : Mean\_of\_evaluation\_score$
$x_1 : Radius\_of\_bead$
$x_2 : Dummy\_var\_of\_bead\_material\_VI$
$x_3 : Dummy\_var\_of\_bead\_material\_FP$
$x_4 : Dummy\_var\_of\_bead\_hardness\_H$
$x_5 : Dummy\_var\_of\_bead\_hardness\_SH$
$x_6 : Dummy\_var\_of\_sex(M:0, F:1)$

The following are the estimated values for kawaii for the 20's and the 40's/50's:

$$a = 4.45, \quad b = -1.46, \quad c = 0.31, \quad d = 0.13$$
$$e = -0.21, \quad f = 0.33, \quad g = 0.30$$

$$a = 5.05, \quad b = -1.83, \quad c = 0.28, \quad d = 0.23$$
$$e = 0.06, \quad f = 0.21, \quad g = -0.06$$

From these results, we obtained the following:

- The kawaii effects for resin material and bead hardness have the same order.
- The kawaii effects for gender only have the same order as the above factors in the 20's.
- The kawaii effect of the log of the bead diameter is larger than the above factors.

CONCLUSION

The authors continue to systematically research kawaii as an affective value. Experiments were performed for the affective evaluation for both visual and tactile material perception of bead-coated resin surfaces in which the resin materials, diameters, and hardness of beads were expanded systematically.

Employing 20's and middle-aged participants, we experimented on the affective evaluation of the samples of bead-coated resin surfaces to clarify the differences among different physical attributes of resin surfaces. The relation between the physical attributes of beads and the affective evaluation results were clarified from ANOVA and multiple regression analysis results.

Further work will continue our analysis and investigation product application.

ACKNOWLEDGEMENTS

We thank all the participants.

REFERENCES

Araki, J., Kansei and value creation initiative, Journal of Japan Society of Kansei Engineering, vol. 7, no. 3, pp. 417-419, 2007.

Belson, K., and Bremner, B., Hello Kitty: The Remarkable Story of Sanrio and the Billion Dollar Feline Phenomenon; John Wiley & Sons, New Jersey, 2004.

Japan Electronics and Information Technology Industries Association (JEITA), Statistics of Exports/ Imports of Software in 2000, available: http://it.jeita.or.jp/statistics/software/2000/index.html. (in Japanese).

Koga, R., Kawaii no Teikoku, Seidosha, Tokyo, 2009. (in Japanese)

Makabe, T., Kawaii Paradigm Design Kenkyu, Heibonsha, Tokyo, 2009. (in Japanese)

Ohkura, M., and Aoto, T., Systematic Study for "Kawaii" Products, Proc. 1st Intern. Conf. on Kansei Engineering and Emotion Research, Sapporo, 2007.

Ohkura, M., and Aoto, T., Systematic Study of Kawaii Products: Relation between Kawaii Feelings and Attributes of Industrial Products, Proc. ASME 2010 Intern. Design Engineering Technical Conf. & Computer and Information in Engineering Conf. (IDETC/CIE 2010), DETC2010- 28182, Montreal, 2010.

Ohkura, M., Goto, S., and Aoto, T., Systematic Study for 'Kawaii' Products: Study on Kawaii Colors Using Virtual Objects, Proc. 13th Intern. Conf. on Human-Computer Interaction, San Diego, pp. 633- 637, 2009.

Ohkura, M, Komatsu, T., and Aoto, T., Rules of Kawaii, Proc. First Intern. Symposium on Affective Engineering 2013 (ISAE2013), 3B-3, Kitakyushu, 2013.

Ohkura, M., Osawa, S., and Komatsu, T., Kawaii feeling in material perception Proc. the 5th Intern. Congress of International Association of Societies of Design Research (IASDR2013), 07C-2, Tokyo, 2013.

Sakurai, T., Sekai Kawaii Kakumei, Ascii Media Works, Tokyo, 2009. (in Japanese)

Yomota, I., Kawaii Ron, Chikuma Shobo, Tokyo, 2006. (in Japanese)

Michiko Ohkura received her B.S. (1976) and M.S. (1978) degrees in Mathematical Engineering and Ph. D. (1995) in Advances Interdisciplinary Studies from the University of Tokyo, Japan.

She worked for some companies and is currently a professor of the Shibaura Institute of Technology, Japan. Her current research interests include usability of interactive systems and emotion information processing.

Table 3 ANOVA for bead-hardness, resin material, and gender of 20's

	Visual			Tactile			Both		
Adjective	Hardness	Material	Gender	Hardness	Material	Gender	Hardness	Material	Gender
Smooth									
Damp									
Granular	**			*		**	***		
Sticky				*					
Dry	*				*				
Slippery	***	*		*			***	*	
Wild			*						*
Mild								*	
Exciting				*		*			*
Staid								*	
Cool									
Kawaii				*					

***: p<.0001, **: p<0.01, *: p<0.05

Table 4 ANOVA for bead-diameter, resin material, and gender of 20's

	Visual			Tactile			Both		
Adjective	Diameter	Material	Gender	Diameter	Material	Gender	Diameter	Material	Gender
Smooth	***	***		***			***		
Damp	***		**	**			***		
Granular	***	***		***			***		
Sticky									
Dry	***	**		***		**	***		**
Slippery	***			***			***		***
Wild	***	***		***			***	*	
Mild	***	***		***		***	***	**	
Exciting	***	***		***			***	***	**
Staid	***	***	**	***			***	*	**
Cool									
Kawaii	***		***	***			***		**

***: p<.0001, **: p<0.01, *: p<0.05

Table 5 Results of difference test between generations

Adjective	Visual	Tactile	Both
Smooth			*
Damp			*
Granular		**	**
Sticky		***	***
Dry	**	***	*
Slippery			
Wild		*	
Mild			
Exciting			*
Staid	***	*	**
Cool		*	***
Kawaii	**	*	

***: p<.001, **: p<0.01, *: p<0.05

ENVIRONMENTAL FRIENDLY OPPORTUNISTIC BEAMFORMING BASED ON HOURLY USERS' DISTRIBUTION

Nur Ellina Binti Ishak and Eiji Kamioka
Graduate School of Engineering and Science, Shibaura Institute of Technology

ABSTRACT

Many recent studies on beamforming inside cellular network focus on increasing the data transmission rate by directing the beam only into a static area. However, as time goes by, smart phone users are not stationary in one place; they keep moving according to their daily activities. Therefore, an energy efficient opportunistic beamforming, which follows the hourly user distribution, is proposed in order to provide a more realistic beamforming. In the proposed beamforming, the radio signal is transmitted only to the high usage area. Its signal's direction can be changed dynamically according to users' distribution pattern. If there is no high users' distribution area, the base station will keep its omni-directional transmission. Finally, the call dropping rate of the proposed method will be discussed in order to verify our works.

1. INTRODUCTION

Information and Communication Technologies (ICTs) play a major key role in providing us with the latest information from all over the world and connecting us with other peoples. ICTs devices such as mobile phone and laptop computer have become a part of human's life and it makes our life easier. According to Cisco White Paper, the number of mobile phone has outnumbered the world's population in 2014 [1]. As the number of the ICTs users has increased, the mobile data traffic has also increased. This has also been proved by Japan Ministry of Internal Affairs and Communications. In 2014, Japan's total mobile cellular data traffic increased almost 50% compared to the data traffic in 2013 and it has a tendency to rapidly increase in the near future [2]. Many cellular base stations have been built to cover the need of every user. However, the rapid growth of the base station's number escalates the total energy usage and the operational costs. According to Vodafone, the base stations are the most energy usage part because it has consumed about 60% of the total typical cellular network power [3]. It also takes up a lot of spaces to build and deploy; this can lead to the deforestation. Deforestation, which is the clearing of the forest to substitute it with other uses, has become the prime reason of increase in greenhouse emission. It is crucial for us to create more environmental friendly base station so that the side effect from the rapid growth of base station can be reduced.

Energy efficiency in the base station is a growing concern for cellular operators to not only maintain profitability, but also to reduce the overall environment effects. Recently, many researchers have strived to reduce the power consumption of the base station and this has been addressed as the green base station project. The green base station project involves the improvement of the base station hardware design, power saving protocol, network self-organizing technique and use of renewable energy resources [4]. The conventional methods for the green network self-organizing technique are sleeping base station and coordinated multipoint (CoMP) [5][6][7]. In the existing sleeping base station method, one or all parts of the base station will be turned off and when it is turned on, the transmission occurs in omni-directional manner. On the other hand, the existing coordinated multipoint method involves the base station to cooperate with another base station to focus both of their signals on one designated area. However, its transmission is static and cannot dynamically move. When the users are moving from one place to another, there will be vacant areas inside the cell. A lot of energy is wasted as the conventional base station keeps transmitting the signal to the vacant area where there is no user who will utilize the signal.

An environmental friendly opportunistic beamforming is proposed to overcome the limitations of the conventional base station transmission. Here, the beamforming transmission will be occurred only on the highly user distributed area. As the first step to develop an energy efficient opportunistic beamforming, the proposed scheme is based on the hourly users' distribution.

This paper is structured as follows: Section 2 will explain the basic concepts used inside the proposed scheme which are opportunistic beamforming and

maximum signal-to-interference ratio. The proposed hotspot determination process, the proposed opportunistic beamforming transmission scheme and users daily distribution pattern will be explained in section 3. Next, in Section 4, the total power consumption of the base station and the call dropping rate under the proposed transmission method will be analyzed. Finally, the conclusions will be drawn in the last section.

2. BEAMFORMING

Beamforming is a signal processing technique that can direct the signal transmission in a narrow angle. It is created by a directional base station and consists of main lobe, back lobe and side lobe.

2.1 Opportunistic Beamforming

Opportunistic beamforming is a beamforming that will only occur whenever there is an opportunity that the user exists in an area. The opportunistic beamforming can be realized through smart antenna system inside the directional base station. This system consists of the directive antenna and the digital signal processing. In the digital signal processing, adaptation process to satisfy the specified optimization goal is performed through changing the direction-of arrival estimation algorithm and adaptive antenna algorithm. The framework for smart antenna system is shown in Figure 1.

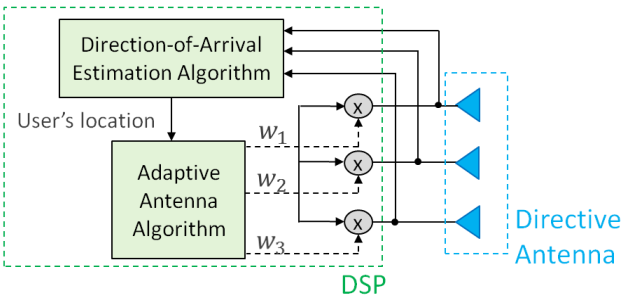

Figure 1: Framework of the Smart Antenna System

When the directive antenna received the user's signal from the mobile phone, the signal's data will move to the direction-of-arrival estimation algorithm. Here, the received array's angle and magnitude will be estimated. After the user location is determined, the adaptive antenna algorithm will process the information and provide the most optimum weight for each of the directive antenna. The antenna's beam direction can be changed by appropriately controlling the multiple arrays' weight magnitude gain and phase. Next, the directive antenna will transmit the beamforming to the desired user. Some examples of the weight algorithm for the beamforming are Maximum Signal-to-Interference Ratio (Max SIR), Minimum Mean-Square Error (MMSE), Least Mean Squares (LMS) and Sample Matrix Inversion (SMI) [8].

2.2 Maximum Signal-to-Interference Ratio

Maximum signal-to-interference ratio beamforming weight's algorithm can be used to enhance the received desired signal and to minimize the interfering signals. It is the basic form for a fixed weight beamforming algorithm. The algorithm is done by satisfying the condition to the unknown weight vector.

For example, when there are three element arrays with one desired received vector, $\boldsymbol{y}_s$ and two interference received vectors, y_i, the array steering vector, $\bar{a}_{N-1}$ is given by the following equation (1).

$$\bar{a} = [e^{-jkd\sin\theta} \quad 1 \quad e^{-jkd\sin\theta}]^T \tag{1}$$

where constant k is equal to $2\pi/\lambda$, d is the spacing between the arrays and θ represents the angle of the signal received. The weight of each antenna, w_N can be estimated through the received vector equation (2). The received vector is equal to the multiplication of weight, w_N and steering vector $\bar{a}_{N-1}$

$$y = \bar{w}^H \cdot \bar{a} = w_1 e^{-jkd\sin\theta} + w_2 + w_3 e^{jkd\sin\theta} \tag{2}$$

Thus, the condition that needs to be satisfied is represented in equation (3).

$$\begin{aligned} y_s &= \bar{w}^H \cdot \bar{a}_0 = w_1 e^{-jkd\sin\theta_0} + w_2 + w_3 e^{jkd\sin\theta_0} = 1 \\ y_1 &= \bar{w}^H \cdot \bar{a}_1 = w_1 e^{-jkd\sin\theta_1} + w_2 + w_3 e^{jkd\sin\theta_1} = 0 \\ y_2 &= \bar{w}^H \cdot \bar{a}_2 = w_1 e^{-jkd\sin\theta_2} + w_2 + w_3 e^{jkd\sin\theta_2} = 0 \end{aligned} \tag{3}$$

The desired vectors, $\boldsymbol{y}_s$ must be equal to 1 and other interference vectors, y_i must be 0, where it can reject the undesired interference signal. This algorithm is used inside the proposed opportunistic transmission scheme in order to provide the real characteristics of the beamforming.

3. PROPOSED METHOD

In this study, one base station and K users are randomly distributed inside the macro-cell according to the hourly human mobility pattern. The base station has 2 directional antennas with N transmission arrays and each user device has M_k received antennas. The macro-cell is divided into two areas which are the upper part and the lower part as shown in Figure 2. The residential area is marked with red color and the commercial area is marked with blue and green color. The uplink and downlink transmissions are also considered.

3.1 Hotspot Determination

In the uplink transmission, the base station will collect each user's coordinate in $x+iy$ complex number form. Then, it is converted into polar form with the moving radius, d and the deflection angle, θ. Next, the user with received signal strength (RSS) more than -80 [dBm] will

be assumed as an active user and the hotspot determining process will be performed.

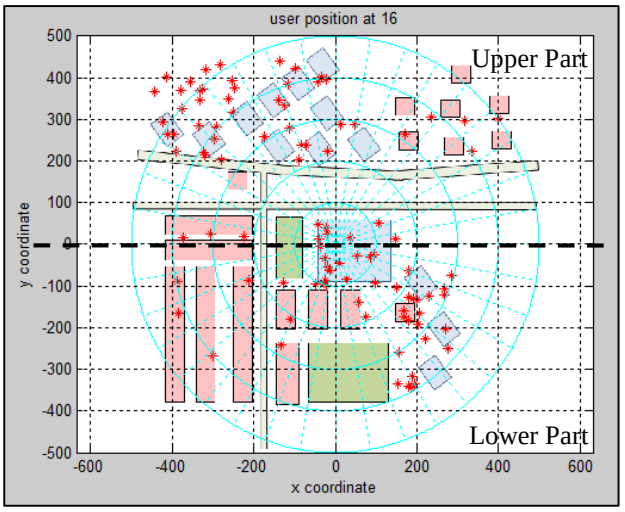

Figure 2: System Model of the Proposed Opportunistic Beamforming

The active users will be divided into 36 small areas with the deflection of 10 degree. Then, the small area is grouped into a larger area with deflection from 20 degree to 180 degree. Each of the larger grouped area will compare its number of users with the adjacent group. The scanning process will finish when it finds that the number of users reaches more than 1/3 of the total active user inside half of the cell, and then the area is considered as a high-density user area. Here, the high-density user area is called hotspot. Both of the upper part and lower part have the same process of determining the hotspot area.

3.2 Transmission Scheme

After the hotspot determination process completed, the most suitable energy efficient transmission scheme will be chosen. In the proposed opportunistic beamforming scheme, the base station can change its transmission mode according to the surrounding user's geographic distribution. Two transmission modes are considered which are the beamforming transmission and omni-directional transmission.

In the first transmission mode, the beamforming will only occur when there is a hotspot area that exists inside the cell. Here, two directional antennas are used to provide the beamforming mode for the upper part and the lower part. If there is no hotspot detected or the users are equally distributed inside the cell, the base station's transmission will become the second transmission mode which is omni-directional transmission. In the omni-directional transmission, each of the two directional antennas' main lobe will have a 180 degree beam width. Thus, omni-directional 360 degree transmission can be achieved by combining the beam width of the both directional antenna's main lobes.

3.3 User Distribution Pattern

The transmission scheme is based on the user distribution pattern. Human daily traffic pattern is used to design the user hourly distribution. According to the report by KKDI Corporation, the peak hour for mobile data traffic in the residential areas is in the night-time. Meanwhile, the peak hour in the business districts is in the daytime (KDDI, 2014). From the mobile data traffic trends, the user distribution pattern is designed, where between 7pm until 8am; all of the users are distributed only inside the residential area. When it is daytime from 9am until 6pm; only 20% of the users will stay at the residential area and another 80% of the users will be distributed at the business districts. The example for the upper part is shown in the Figure 3. From Figure 3(a), at 10am, most of the users are distributed inside the business district, and then the base station focuses its main lobe on the left side of the upper part in the macro cell. Meanwhile, in Figure 3(b), at 10pm, all of the users are distributed at the residential area; hence, the right side of the upper part is focused by the main lobe of the beamforming.

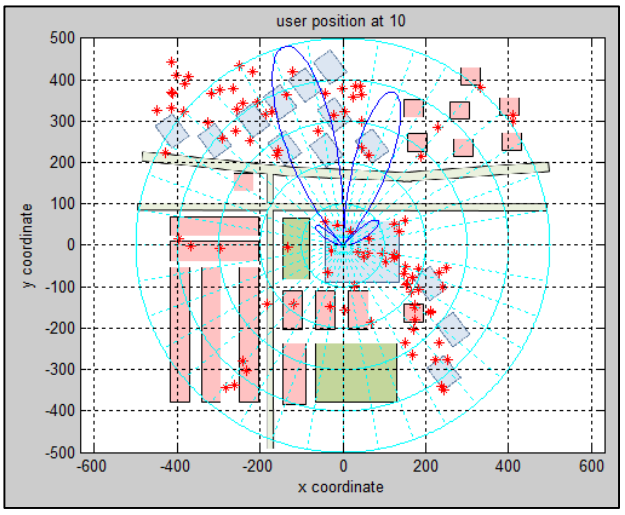

(a) User Distribution at 10am

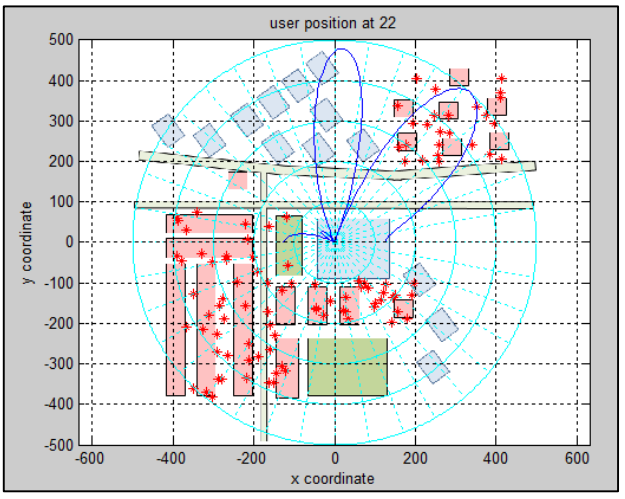

(b) User Distribution at 10pm

Figure 3: The User Hourly Distribution and Upper Part Beamforming

4. RESULT AND DISCUSSION

In this section, the simulation result is provided to demonstrate the performance achieved by the proposed environmental friendly opportunistic beamforming based on hourly users' distribution. The preliminary result is based on the total call dropping rate for each hour and it is given in Figure 4. In our proposed study, the call dropping rate is defined as the percentage of upper part's user uncovered by the beamforming.

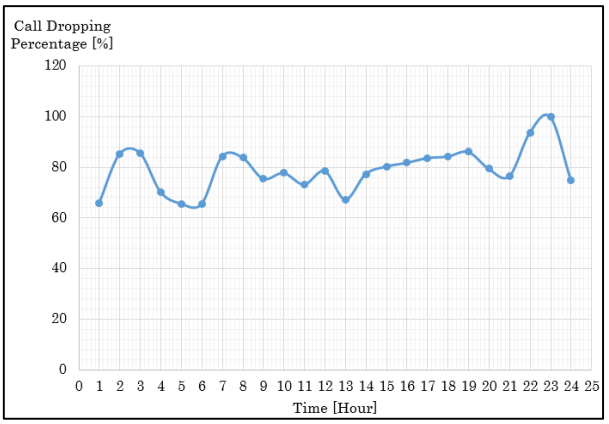

Figure 4: Call Dropping Rate for each Hour

From Figure 4, the call dropping rate for each hour is above 60%. This indicates that the proposed beamforming still cannot cover most of the user inside the upper part of the macro-cell. It is due to the beamforming's shape which cannot cover the whole hotspot area. Here, the shape depends on the base station's array weight and the number of array inside each antenna.

CONCLUSION

Conclusively, the environmental friendly opportunistic beamforming based on hourly users' distribution has been introduced. According to the results obtained, the call dropping rate for each hour is above 60%. This prove that many future studies and detailed works are still necessary in order to improve the proposed beamforming method.

In future, the weight algorithm for the proposed method will be further developed. Next, the lower part of the macro-cell will be studied and the overall call dropping rate will be analyzed. This is to justify that the proposed method is effective to provide environmental friendly base station in the long run.

REFERENCES

[1] Cisco Visual Networking Index: Global Mobile Data Traffic Forecast Update, 2014-2019, Cisco White Paper, pp. 1-42, February 2015.

[2] Japan Ministry of Internal Affairs and Communications, 2014. Internet: Japan Ministry of Internal Affairs and Communications, 2014. Internet: http://www.soumu.go.jp/johotsusintokei/field/tsuushin06.html

[3] Tomas Edler, Green Base Stations – How to minimize CO2 Emission on Operator Networks, Ericsson, Bath Base Station Conference, 2008.

[4] Chethana R. Murthy, C Kavitha, A Survey of Green Base Stations in Cellular Networks, Proceedings of International Journal of Computer Networks and Wireless Communications (IJCNWC), Vol. 2, No. 2, pp. 232-236, April 2012.

[5] Z. Niu, Y.Wu, J. Gong, Z.Yang, Cell Zooming for Cost-Efficient Green Cellular Networks, IEEE Communications Magazine, pp.74-79, November 2010.

[6] Sourjya Bhaumik, Girija Narlikar, Subhendu Chattopadhyay, Satish Kanugovi, Breathe to stay cool: adjusting cell sizes to reduce energy consumption, Proceedings of ACM SIGCOMM workshop on Green networking, pp.41-46, 2010.

[7] T. Han, N. Ansari, On Greening Cellular Networks via Multicell Cooperation, IEEE Wireless Communications, Vol.20, Issues 1, pp.82-89, February 2013.

[8] Frank Gross, Smart Antennas for Wireless Communication with MATLAB, Chapter 8: Smart Antennas, McGraw-Hill, 2005.

BIBLIOGRAPHY

Nur Ellina Binti Ishak obtained her Diploma Degree in Electrical Engineering (2012) from Industrial University of Selangor (UNISEL), Malaysia and B. Eng. in Electrical Engineering (2014) from Tokyo University of Science (TUS), Japan. Currently she is pursuing her M. Eng. at Shibaura Institute of Technology (SIT), Japan. Her research interest includes wireless mobile communication, green technology and antenna theory.

Eiji Kamioka is a Professor at Shibaura Institute of Technology. He received his B.S., M.S. and D.S degrees in Physics from Aoyama Gakuin University, Japan. Before joining SIT, he was working for SHARP Communications Laboratory, Institute of Space and Astronautical Science (ISAS) as a JSPS Research Fellow and National Institute of Informatics (NII) as an Assistant Professor. His current research interests encompass mobile multimedia communications and ubiquitous computing.

Toward A Simple Handover in Wireless Network Based on Software Defined Networking

Toan Nguyen-Duc and Eiji Kamioka
Graduate School of Engineering and Science, Shibaura Institute of Technology

ABSTRACT.

Wireless network interfaces including Wi-Fi, Bluetooth and NFC have been integrating into laptops, mobile phones, tablets, and other portable devices. Each interface has its own standards and protocols since it was designed for a different purpose. Hence, the devices commonly use one interface at any given time. As a result, when the active interface has lost its connection, the ongoing applications may meet some delays or possibility being interrupted. In this paper, a new handover system based on Software Defined Networking is proposed to handle this issue. The system provides a virtual interface to manage all physical wireless network interfaces and make them become transparent to the application layer. It also has ability to collect network information such as RSSI in order to make a right decision on triggering the handover process. The feasibility of the system has been verified on a real testbed. The primary results show that the system has ability to maintain an ICMP flow when a vertical handover between Bluetooth and Wi-Fi occurred.

1. INTRODUCTION

Wi-Fi and Bluetooth have become two widely used wireless communication technologies in our daily lives. These technologies can operate at the same 2.4 GHz UL frequency band and have capacity to provide multimedia content to mobility users. However, Bluetooth is initially designed for short-range wireless communication which allows transmissions through walls and other objects. It also provides a precision locating and tracking by using distance measurements between radios. In contrast, Wi-Fi is more generally intended for replacing high speed cabling in local area network. Wi-Fi allows higher speed network connections over greater distance compare to Bluetooth. Although the two technologies are conceived for the similar kind of applications, almost all of applications are not designed to operate over multiple network interfaces simultaneously. That means to keep an ongoing session, it requires the possibility to transfer the connection between different networks, or vertical handover. Vertical handovers may cause delays or connection loss. In this paper, utilizing software defined networking as one possible solution for a new handover scheme in heterogeneous wireless networks, the network behavior at the packet level is exhaustively studied.

Software defined networking (SDN) was designed to separate the control of network devices, i.e., OpenFlow switches, from themselves [3]. It works based on the packet lookup and forwarding mechanism. In that mechanism, whenever a new packet reaches an OpenFlow-based network device, its header is taken out and is compared to flow rules which are stored in a database called a flow table. If no matching is found, the device then asks a computer software, or a network controller, about what action (i.e., forward to an output port) should be applied to the packet. By doing this, the network administrator has more flexibility in controlling the network devices. However, since SDN was initially designed for wired network, applying SDN to a wireless environment raises other challenges. For example, if the wireless nodes connect directly to the others, i.e., in an ad-hoc manner, it is hard to make a communication between the nodes and the controller as the controller only talks with the OpenFlow switches via OpenFlow protocol. Besides, even if there is a way to connect the controller to the wireless nodes, the connection between them can be dropped at any time due to their mobility. Therefore, to effectively apply SDN technology to a wireless environment, one potential solution is to let SDN control the access points to which the wireless nodes connect. However, the centralized model of current SDN architecture probably brings single point of failure or bottle neck to the control path between the controller and the devices. Thus, it is desirable that the connection from the switch to the controller does not go down in almost any situations.

There are several related works which are to bring SDN to the wireless environment. For example, Bruno [4] used SDN to enable cooperation between wireless nodes and provide capability of sharing services. Ali-Ahmad [5] solved the traffic demand issues in wireless networks densification with SDN. All the mentioned works above, however, pay attention to applying SDN to the core network, base stations or network gateways rather than solving mobility issues. There are also some authors who are interested in handover in wireless networks. For instance, Carlos [6] executed a L2 handover procedure, which is based on Media Independent Handover (MIH) procedures, between several OpenFlow-enabled access points. This work requires an OpenFlow-based environment and focus on horizontal handover. Izard [7] combined SDN and a virtual private network (VPN) to handover IPv4 traffic between Wi-Fi and WiMAX connections. The author pays attention on the intermediate layer above the virtual point-to-point connection of VPN rather than whole the communication stack.

Different from other studies, in this study, SDN is applied to every mobile node and the intermediate layer below the routing (IP) layer is utilized to manage the state information for all physical network connections. This will help to improve both the

efficiency and resilience of wireless networking through the use of multiple wireless network interfaces. All network interfaces are now managed by a software OpenFlow switch, i.e., Open vSwitch (OVS) [8]. The switch runs as a kernel module and does not require any modification in the application and physical layers, making it transparent to the end users. The control of the switch is performed by a local SDN controller. Although the local controller only manages the switch on the same node, its function is enriched, hence, it has capability to gather network state and make decision based on the collected information. The performance of the proposal system was conducted in a primary testbed where two wireless nodes communicate together via an access point. The results show that ICMP transit traffic from the sender node, to which a SDN controller and an OpenFlow switch has been integrated, was smoothly switched from current interface to another interface in a failure scenario.

The rest of the paper is organized as follows. In Section 2, the background of this work including basics of Wi-Fi technology, Bluetooth technology and SDN OpenFlow switch will be described. In Section 3, the proposed handover system and the architecture as well as the handover procedures will be explained. Finally, the paper will be concluded in Section 4.

2 THEORETICAL BACKGROUND

2.1 Wi-Fi technology

The IEEE introduced 802.11 as a standard for wireless local area networks (WLANs) in 1997. Until now, the 802.11 family, or Wi-Fi, has been developed, aiming to replace high speed cabling at an average range (i.e., 100 meters). The basic block of the 802.11 WLAN is a cell, or the basic service set (BSS). A BSS typically consists of several wireless station with an access point (AP). This operation mode requires existing infrastructures (i.e., APs), hence, it is called as the infrastructure mode. The stations can also communicate directly among themselves in ad-hoc mode, however, in this paper, only the infrastructure mode is focused on. If a station wants to send messages via the AP, it must be associated with the AP. To get the association, the station firstly scans all channels either in passive mode or active mode. In passive mode, the station waits for the beacon frame periodically sent from the AP. The beacon frame contains the service set identifier (SSID) and the media access control (MAC) address of the AP. From that frame, the station decides with which AP to be associated. Whereas, in active mode, the station broadcasts a probe frame to advertise itself. Normally, it will receives several responses from the nearby APs. The station then selects an AP among the responded APs to be associated with. Note that choosing an AP algorithm in both modes is not defined by the 802.11 standard. After the station selects one AP, it needs to send an association request frame to the selected AP and wait for its response. When the request/response handshake is finished, the station is associated to the AP. Now the station is required to authenticate itself to the AP. After the authentication process, the station sends DHCP discovery message to the AP to obtain the IP address. Once the address is obtained, the station can start sending and receiving data frames to and from the AP.

2.2 Bluetooth technology

The Bluetooth specification was introduced in 1999 and was standardized by the IEEE. However, since IEEE does not maintain this standard, the Bluetooth was managed by Bluetooth Special Interest Group (SIG). The Bluetooth is designed for exchanging data over a short range radio link among fixed or mobile devices. In a Bluetooth network, data is transmitted via low-power radio waves between 2.402 GHz and 2.480 GHz. The weak signals (i.e., 1mW) help to avoid interfering with other systems, however, it limits the Bluetooth communication range to about 10 meters. The Bluetooth device uses 79 frequencies randomly changed from one to another on a regular basis called spread spectrum frequency hopping. The frequency is also changed 1600 times every second on the transmitters to prevent two transmitters to be on the same frequency at the same time.

All of the Bluetooth networks are ad-hoc networks in which the devices communicate directly to the others and organize the communication by themselves. This means a Bluetooth network can grow, shrink and fragment without asking permission from a central authority. Normally, all Bluetooth devices are in standby mode. In this mode, unconnected device periodically listens for messages every 1.28 seconds. On the other hand, a device acts as master and keeps sending out inquiry messages over 32 of the 79 channels to scan for other devices within its range. If a standby device receives the inquiry message, it will send its address and timing information to the master and wait for the master to page it. When the master identifies all the devices in its range, it starts to form a Piconet of up to eight devices. The master sends a paging message to inform the slave of the destination address. When the slave hears the message, it enters paging scan state and replies a confirmation packet. After that, the master sends synchronization information to its slaves. The slaves send a response message and then enter the connection state. At this moment, all slaves have been synchronized with the master clock and can communicate with the others via the master.

2.3 SDN OpenFlow switch

In SDN networks, the network devices, i.e., OpenFlow switches, are controlled by one or more SDN controller. The controller interacts with the switch by using a secure protocol named OpenFlow [3]. The initial function of the protocol is to install, modify or remove entries on a flow table embedded in the switch. Each entry contains a flow description and a list of actions which decides how to handle that flow. The action that applies to the packet may be drop the packet or forward it to one or more OpenFlow switch ports. In some scenarios, i.e., in a load balancing system, the packet header information such as MAC addresses, IP addresses, and TCP/UDP ports need to be modified. Therefore, from the Openflow specification version 1.3, the function

of OpenFlow protocol is enhanced to be able to modify the packet header information. The header of the packet is extracted when the packet reaches the switch. The detail of the header then is compared to the flow description of the flow table entries. If a matching is not found, the switch will invokes a message to the controller asking for the action that should be applied to the packet. If the controller answers to ask the switch to install an entry on the flow table, all packets that meet the description in the entry will be treated with the same set of actions, hence, forming a flow of packets.

3. PROPOSAL HANDOVER SYSTEM

3.1 System architecture

Figure 1 illustrates the system topology which includes three mobility nodes and an AP. Three nodes form a Piconet with a master node and two clients. Two clients are talking with the other via a Bluetooth connection and have ability to connect to the AP via their Wi-Fi interfaces. The system operates with an assumption that two clients can always connect to the AP when they lose their Bluetooth connection and vice versa. Each node, which can be either a tablet, mobile phone or a laptop, has an embedded SDN controller and an Open vSwitch (OVS). In this work, we used three laptops equipped with Core 2 Duo @2.26 GHz and 2GB RAM. The OVS creates a bridge which will act as a virtual interface that controls physical wireless interfaces and makes them become transparent to end-users. On the other side, the operation of the switch is under control of the SDN controller. As mentioned in section 2.3, the basic function of the controller is to install, remove or modify the entries of flow table on the OVS. However, since the controller is a local one, it can only manage the OVS which is on the same node. Thus, we have developed an extended part (Fig. 2) for the controller so that it can gather network information such as received signal strength indicator (RSSI) to support its management decisions.

Figure 2 describes the control logic of the system. The network state is collected to the network manager component (NW) which is proposed as an extension to the traditional SDN controller. From the collected network information, i.e., RSSI value, the NW can understand whether the node is going out of the coverage of the Bluetooth or Wi-Fi connection. When the connection is going to be lost, the ongoing traffic can be alive if it is switched to a new connection on the other interface. However, it will meet some delays due to the establishment of a new connection. In addition, the new interface, which has its own MAC address, is assigned a new IP address, thus, makes the upper layer applications confuse and sometimes interrupts them. Our extended SDN controller handles these issues by modifying the network stack behavior without patching the Linux kernel or changing in the application and physical layers. Basically, it works based on MAC and IP address rewriting logic and provides appropriate responses to selective ARP requests.

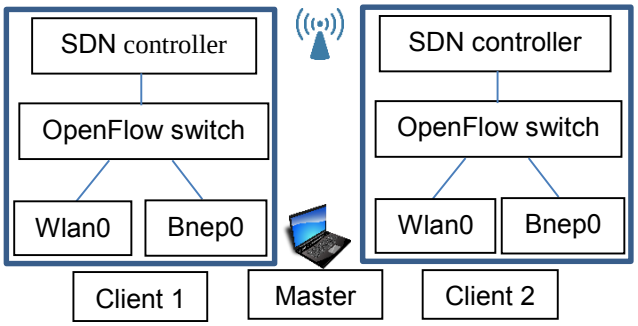

Fig. 1: System topology

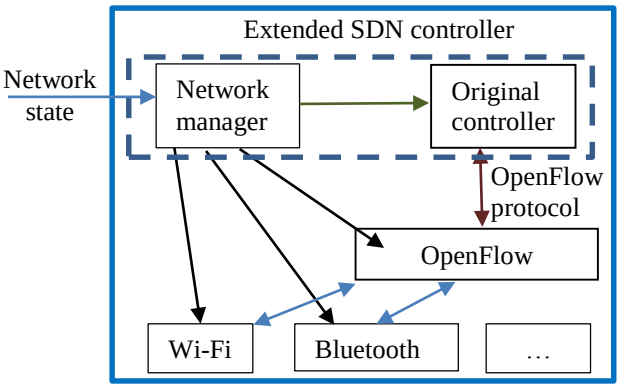

Fig. 2: Control logic of the system

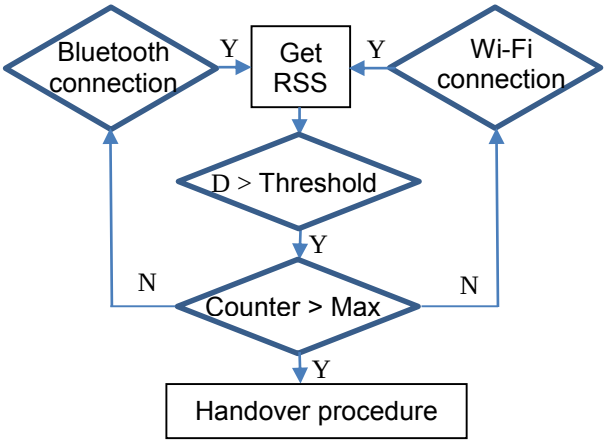

Fig. 3: Handover detection

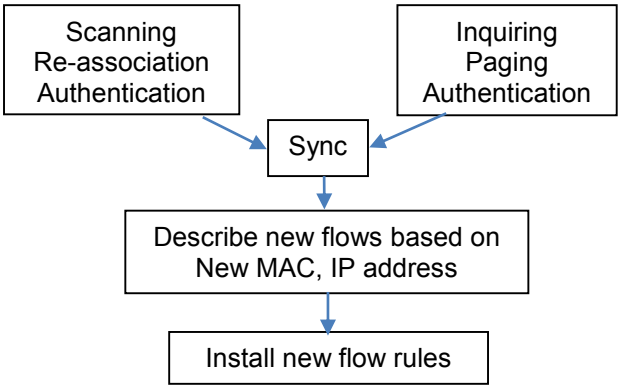

Fig. 4: Handover procedure

3.2 Handover procedure

In the system, the handover process starts if the NW detects that the current connection is going to be lost. The simple detection procedure is described in Fig. 3, in which the distance D is estimated based on the collected RSSI value and is stored to predict the next location of the node. If the node is going to be

out of the current connection's coverage, the handover procedure is invoked.

Figure 4 describes the handover procedure. When it is called, the NW performs an initial process to establish a connection on the other wireless network cards. For example, the process is the Wi-Fi association or the Bluetooth paring. In this process, a software called Blueman is utilized for setting up Bluetooth connections so that the whole configuration process can be executed by a script. The configuration steps for the Wi-Fi connections is also automated. The automation procedure was executed in a mix of shell commands and python scripts. As a result, the initial process is controlled by the extended controller. Note that, the network management service must be disabled to pass the control of physical interfaces to the OVS. After the association process is completed, the node sends out a message to tell this information to the other one and wait for his reply. When both sides confirm that the association process has been completed, the extended controller defines new routes for the connection between two hosts. When the routes are installed, in wired network, the OVS allows packets to go out on the new interface and head to the expected destination without any requirement of assigning an IP address for the interface. However, in the wireless network, when the hosts connect to the others via an AP, the AP generally only allows packets with the source MAC address of NIC that completed the initial handshake. Therefore, the extended controller must assign a new IP address for the new interface. Consequently, the destination sends out an ARP request asking for MAC address of the new IP address. We have handled this issue by replying appropriate ARP REPLY messages to selective ARP REQUEST messages. After that, the packets continue to travel between two nodes, or the handover procedure is completed.

3.3 Evaluation

To test the feasibility of our system, the number of sending and receiving packets were observed when a vertical handover between Wi-Fi and Bluetooth occurred. The testing scenario was as follow, the sender randomly made a vertical handover decision during sending 2000 ICMP packets to the receiver at the rate of 10ms via Bluetooth connection. Note that the handover detection procedure was not focused on this work, hence, the handover decision was made randomly. In addition, the two clients are assumed they already knew the other's network information including the AP's SSID, the AP's key, the IP address and the MAC address of all virtual and physical interfaces. Observing the number of transit packets, we found that the continuity of the ICMP flow was insured when the ICMP flow was switched to the Wi-Fi connection. Moreover, the amount of loss packet mainly depends on the association time. For example, if the association time was less than 1 second, the packet loss rate was zero. In contrast, the longer the association time was, the more packets were lost.

4. CONCLUSION

In this paper, a new vertical handover system between wireless network interfaces of mobile devices based on Software-Defined Networking is proposed. The system has improved the wireless network in term of resilience. For example, the network traffic can be switched from one network interface to the other in case of a connection loss. In addition, an extended SDN controller, which is embedded in every mobility nodes, is introduced to bring a minimal risk of losing the connection between the controller and the OpenFlow switch. It also open a possibility to collect network state and make decision based on collected information.

In the future work, the detail analysis of the handover procedure in a variety of testbeds and protocols will be concentrated on.

REFERENCES

[1] Bluetooth Specification, www.bluetooth.com/developer/specification

[2] IEEE 802.11 standard, www.ieee.org/getieee802/802.11

[3] McKeown et al: "Openflow: enabling innovation in campus networks". SIGCOMM Comput. Commun. Rev. 38(2) 2008.

[4] Bruno A. A. Nunes et al: "Capacity Scaling in Ad Hoc Networks With Heterogeneous Mobile Nodes: The Subcritical Regime". In IEEE Communications Magazine 2014.

[5] H. Ali-Ahmad et al: "CROWD: An SDN Approach for DenseNets". In Proc. EWSDN, 2013.

[6] Carlos Guimarπes et al: "Empowering Software Defined Wireless Networks Through Media Independent Handover Management". In Proc. 2013 Globecom, Atlanta, USA, Dec 2013.

[7] Izard et al: "An openflow testbed for the evaluation of vertical handover decision algorithms in heterogeneous wireless networks". TridentCom14, Guangzhou 2014

[8] Open vSwitch. http://openvswitch.org/.

Eiji Kamioka is a Professor at Shibaura Institute of Technology. He received his B.S., M.S. and D.S degrees in Physics from Aoyama Gakuin University, Japan. Before joining SIT, he was working for SHARP Communications Laboratory, Institute of Space and Astronautical Science (ISAS) as a JSPS Research Fellow and National Institute of Informatics (NII) as an Assistant Professor. His current research interests encompass mobile multimedia communications and ubiquitous computing.

Toan Nguyen-Duc is currently pursuing his PhD in Shibaura Institute of Technology, Japan. He received the B.S. (2004) and M.S. (2006) degrees in electronic and telecommunication engineering from Hanoi University of Science and Technology. Before studying at SIT, he is a researcher at Hanoi University of Science and Technology. His current interests

include mobile computing, wireless networks and wireless network communication protocols.

GRAPH SEGMENTATION BASED METHOD IN THERMAL CAMERA OBJECT DETECTION

Hung V. Nguyen[2], Linh H. Tran[1], Tri M. Cao[2]

[1]Hanoi University of Science and Technology, [2]Institute of Science and Technology

hungitd@yahoo.com, linh.tranhoai@hust.edu.vn, gsttbttm@yahoo.com

ABSTRACT

The paper presents the application of graph-based segmentation algorithm in image object detection. The input images are taken from thermal camera for night surveillance application. The graph-based algorithm was selected due to its low complexity, which allows us to process each image with the complexity of $O(n \log n)$ where n is the number of pixels, and due to the fact that thermal images contains smaller number of regions of colors. With the detected regions, some additional measures are used to filter out the artifacts to correctly detect the object in the images. The numerical results have proved the high quality of the proposed solutions.

1. INTRODUCTION

Automatic object detection plays a very important role in surveillance systems. Among the proposed methods, computer vision based methods are quite popular due to many advantages such as non invasive method of data acquisition, long distance surveillance available,… However, detecting objects based on computer vision is also a hard problem because the images or videots quality strongly depend on environment conditions (such as lights, weather parameters,…) and object detection algorithms are still under development.

Different methods of object detection in image and video have been being developing. Most of them base on a set of samples and their features vectors to train a (nonlinear) model and the used features have a strong influence on the final performance of the model.

For object detection in image and video we can use various methods of features extraction based on pixels, lines/edges, contours,… These methods differ from each other in algorithm complexity, speed and accuracy. In this paper we will use the graph segmentation method (Ratan 1999) for object detection from images taken from thermal camera. The graph segmentation method was selected because: 1. It's fast (its complexity is almost linear in the number of image pixels), 2. The thermal image usually has lower number of segments than normal images. On the other hand, for thermal images, the edge based methods are unstable since the images are blur and the edges have high variation.

2. OBJECT DETECTION AND TRACKING USING GRAPH-BASED SEGMENTATION METHOD

Object detection plays an important role in image processing. The object can be detected due the difference in color, in patterns,… in comparison with the background and with other objects in the image. There are different methods for this purpose. We can group them into:

- the pixel-based methods: like in (Moravec 1979, Harris and Stephens 1988, Lowe 2004, Mikolajczyk and Schmid 2002,…),
- the thinning skeleton methods: as proposed in (Comaniciu and Meer 1999, Shi and Malik 2000, Caselles et al. 1995,…),
- the texture-based methods : like in (Stauffer and Grimson 2000, Oliver et al. 2000, Toyama et al. 1999, Monnet et al. 2003,…),…

The main problem of most of the algorithms are their computational complexity, which make them available rather on PC than on portable devices. The situation is even worsen for video processing. In this paper, the graph-based segmentation method is used due to its low complexity of $O(n \log n)$ where n is number of pixel.

2.1. The graph-based segmentation method

A given input image I can be seen as a matrix of pixels. Each pixel has its color components represented by a value, for example a pixel in RGB mode has 3 components and may needs 3 bytes to store the values of

the RGB components. A pixel in CMYK mode has 4 components but a gray pixel has only 1 component. Let's denote $I(i,j,k)$ - the k-th color component of the pixel at row i-th and j-th column. From an input image I, we construct a graph $G=\{V,E\}$ where V – set of vertices, E – set of edges. Each pixel (i,j) of the input image is a vertex of the graph. Each pixel is connected to a number of the so called neighbor pixels. In this paper we use the standard 8-connected neighborhood, i.e. the pixel $.(i,j)$ is connected to pixels $.(i\pm1,j\pm1)$. (excluding the self connection). The edge connecting v_α and v_β vertices is associated with a weight proportional to the difference between pixels' colors, i.e.

$$w(v_\alpha,v_\beta)=\sqrt{\sum_k\left[I(\alpha_i,\alpha_j,k)-I(\beta_i,\beta_j,k)\right]^2} \quad (1)$$

The segmentation algorithm will divide the image into the so called regions R_i of pixels ($\bigcup_i R_i=V$). We define some measures used in the proposed graph based algorithm.

- The internal difference of a region $Int(R)$: to be the largest weight in the minimum spanning tree (MST) of the region

$$Int(R)=\max_{e\in MST(R,E)} w(e) \quad (2)$$

- The minimum internal difference between two regions $MInt(R_i,R_j)$:

$$MInt(R_i,R_j)=\min\left(Int(R_i)+\tau(R_i),Int(R_j)+\tau(R_j)\right) \quad (3)$$

where $\tau-$ threshold function to control the dissimilarity between two regions and $\tau(R_i)=\frac{k}{|R_i|}$ with k is a preselected constant.

- The difference between two regions $Diff(R_i,R_j)$:

$$Diff(R_i,R_j)=\min_{v_\alpha\in R_i,v_\beta\in R_j} w(v_\alpha,v_\beta) \quad (4)$$

With those measures, the graph-based segmentation algorithm is described as follow:

Input: A graph (undirected) $G=\{V,E\}$ defined for the given input image. Lets $|V|=n-$ number or vertices, $|E|=m-$ number of edges.

Output: Regions $R_1,R_2,\ldots$ of the input image.

Step 1: Sort the egdes with the ascending order of the edges' weights.

$$E\to\left\{e_{i_1},e_{i_2},\ldots,e_{i_m}: w(e_{i_1})\le w(e_{i_2})\le\ldots\le w(e_{i_m})\right\}$$

Step 2: Start with an initiatial set of n regions containing only single vertex $R_i^{(0)}=\{v_i\},i=1,2,\ldots,n.$

Step 3: For each edge e_{i_j} with the weight from the smallest weighted edge to the biggest ($j=1,\ldots,m$), update the regions $\left\{R_i^{(j-1)}\right\}\to\left\{R_i^{(j)}\right\}$ as follow: Let the edge e_{i_j} connect two vertices v_α and v_β. If the two vertices already belong to the same region then no update is needed ($\forall i: R_i^{(j)}=R_i^{(j-1)}$) and the algorithm continues Step 3. Otherwise, let $v_\alpha\in R_p^{(j-1)},v_\beta\in R_q^{(j-1)}$. If the weight of e_{i_j} is smaller or equal the minimum internal distance between the two regions $R_p^{(j-1)}$ and $R_q^{(j-1)}$ (it means the two regions are quite similar)

$$w(e_{i_j})< MInt\left(R_p^{(j-1)},R_q^{(j-1)}\right) \quad (5)$$

then we combine the two regions into one new single region:

$$R_p^{(j)}=R_p^{(j-1)}\cup R_q^{(j-1)};R_q^{(j)}=\varnothing. \quad (6)$$

The empty regions are removed later for simplification.

After m iterations of Step 3, the remaining regions form the results of the algorithm. On Figures 1, 2 and 3 some example results of the proposed algorithms are presented.

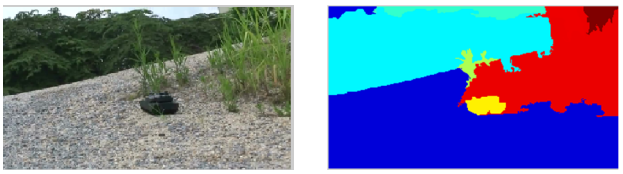

(a) *(b)*

Figure 1: A picture containing a model of a tank in the field (a) and its segments (b)

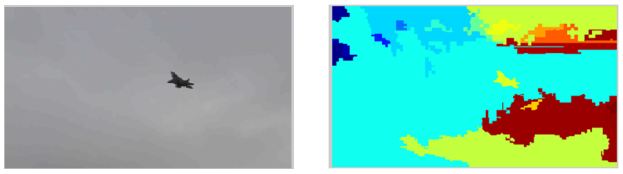

(a) *(b)*

Figure 2: A picture containing a flying plane (a) and its segments (b)

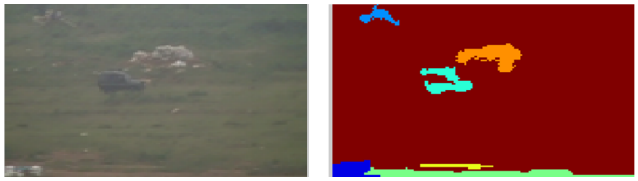

(a) (b)

Figure 3: A picture containing a van in the field (a) and its segments (b)

3. OBJECT DETECTION AND TRACKING IN THERMAL IMAGES AND VIDEOS

Thermal cameras are very popular in surveillance systems, especially in night vision systems. These cameras make pictures from heat, not visible light. All objects arounds us emit thermal energy. The hotter the object is the more thermal energy it emits. Good cameras can detect small differences in heat and display them as shades of grey in black and white images or videos. The sources of heat can be warm-blooded animals (like people), working engines,... Other things like the land, trees, backgounds emit the heats that they absorbed earlier from the environment or from the sun,… For the images from thermal camera not only the proposed above segmentation algorithm is fast with complexity equal $O(n\log n)$ but we have also found that it works very good because:

- The pixels are monochrome (gray scaled)
- The number of regions is small because only heat sources are clearly visible (high intensity) on the images.

An example of a thermal image and its regions found by the above algorithm is shown on Fig. 4.

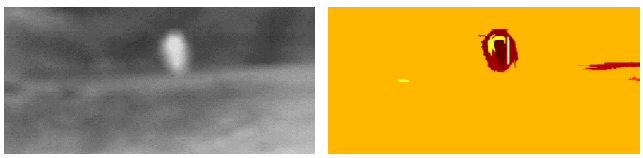

(a) (b)

Figure 4: A thermal picture of a person walking at distance of 40m (a) and its 4 detected segments (b)

After segmentations, each regions are futher processed to reject the unwanted regions. For each region, we calculate: 1. the maximum distances in x- and y-axis, 2. the area (the number of pixels belonging to the region). The regions with too big sizes in x- and y-axis are likely the backrounds. Only the regions with the area within a predefined range and the propotion between the sizes in x- and y-axis are selected as the ROI (*Regions Of Interest*).

4. NUMERICAL RESULTS

In this paper we have tested the object detection method using the graph based segmentation algorithms with the images taken from the FLIR Tau 2 and the 100mm len. The camera and the len are shown on Fig. 5.

Figure 5: The FLIR Tau 2 thermal camera and its 100mm len used in the experiments

We tested 2 scenarios: 1. a video containing 390 frames of a walking person from the distance of 40m and 2. A video containing 1028 frames of a van from the distance of 600m. The examples of images for the 2 scenario are presented on Fig. 6. As it can be seen the camera is quite good during night vision. The person is clearly visible on the image 6a. Because of the long distance (600m), the van is less visible on the image despite that its engine generates much more heat than the human body.

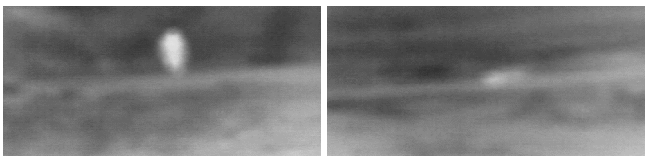

(a) (b)

Figure 6: The thermal image of a walking person at 40m (a) and a van at 600m (b)

The example results of segmentation algorithm are shown on Fig. 7.

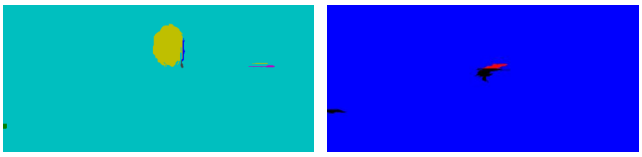

(a) (b)

Figure 7: The segmented images of a walking person at 40m (a) and a van at 600m (b)

We can see from the results, the segmentation algorithm worked great. It filtered out most of the artifacts. By using additional measures as the area of the region, the x- and y-axis ratio, the object was detected successfully in all of the frames of the recorded videos.

5. CONCLUSIONS

The paper has presented the graph-based algorithm for image segmentation and its application in object detection. The algorithm was successfully used for

images from thermal camera to detect heating object during night surveillance. The proposed algorithm has low complexity which makes it available for online video processing application. In the future we will test it with streams of images (frames) from video and for object trajectory detection and estimation.

REFENRENCES

Ali A., Aggarwal J., *Segmentation and recognition of continuous human activity*, IEEE Workshop on Detection and Recognition of Events in Video, pp. 28–35, 2001.

Athanesious J., Suresh P., "*Systematic Survey on Object Tracking Methods in Video*", International Journal of Advan Computer Engineering & Technology (IJARCET), pp. 242-247, 2012.

Beaulieu J., Goldberg M., *Hierarchy in picture image segmentation: A step wise optimization approach*, IEEE Transactions on Pattern Analysis and Machine Intelligence, vol. 11, pp. 150–163, 1989.

Belongie S., Malik J., Puzicha J., *Shape matching and object recognition using shape context*, IEEE Trans. on Pattern Analysis and Machine Intelligence, vol. 24, pp. 509-522, 2002.

Bertalmio M., Sapiro G., Randall G., *Morphing active contours*, IEEE Trans. on Pattern Analysis and Machine Intelligence, vol. 22(7), pp. 733–737, 2000.

Caselles V., Kimmel R., Sapiro G., "*Geodesic active contours*," in Proc. Int. Conf. Computer Vision '95, Boston, MA, pp. 694–699, 1995.

Comaniciu D., Meer P., *Mean shift analysis and application*, Proceedings of IEEE Conf. on Computer Vision and Pattern Recognition, pp. 1197–1203, 1999.

Felzenszwalb P. F., Huttenlocher D. P., *Efficient Graph-Based Image Segmentation*, International Journal of Computer Vision, vol. 59(2), pp. 167 – 181, 2004.

Harris C., Stephens M., *A combined coner and edge detector*, Proceeding of 4th Alvey Vision Conference, pp. 147-151, 1988.

Jae-Yeong Lee; Wonpil Yu, "*Visual tracking by partition-based histogram backprojection and maximum support criteria*, 2011 IEEE International Conference on Biomimetics (ROBIO), pp. 2860-2865, 2011.

Lowe D., *Distinctive image features from scale-invariant keypoints*, International Journal of computer Vision, 60(2), pp. 91-110, 2004.

Mikolajczyk K., Schmid C., *A performance evaluation of local descriptors*, IEEE Conference on Computer Vision and Pattern Recognition (CVPR), pp. 1615-1630, 2003.

Monnet A., Mittal A., Paragios N., Ramesh V., *Background modeling and subtraction of dynamics scenes*, IEEE Int. Conf. on Computer Vision, pp. 1305 – 1312, 2003.

Moravec H. P., *Visual Mapping by a Robot Rover*, Int. Joint Conf. on Artificial Intelligence, pp. 598-600, 1979.

Oliver N. Rosario B., Pentland A., *A Bayesian computer vision system for modeling human interactions*, IEEE Trans. on Pattern Analysis and Mach. Intell., vol. 22(8), pp. 831 – 843, 2000.

Ratan A.L., Maron O., Grimson W.E.L., Lozano-Perez T., *A framework for learning query concepts in image classification*, . IEEE Conference on Computer Vision and Pattern Recognition, pp. 423–431, 1999.

R. S. Rakibe, B. D. Patil, "*Background Subtraction Algorithm Based Human Motion Detection*", Int. Journal Research Publications, vol 3(5), pp. 1-4, 2013.

Sen-Ching S. Cheung, Chandrika Kamath, "*Robust techniques for background subtraction in urban traffic video*", Journal on Applied Signal Processing, vol. 1, pp. 2330-2340, 2005.

Shi J., Malik J., *Normalized cuts and image segmentation*, IEEE Transactions Pattern Analysis Mach. Intell., vol. 22(8), pp. 888-905, 2000.

Srinivasan K., Porkumaran K., Sainarayanan G., "*Improved Background Subtraction Techniques For Security In Video Applications",* 3rd Int. Conf. on Anti-counterfeiting, Security and Identification in Communication (ASID), pp. 114-117, 2009.

Stauffer C., Grimson W., *Learning patterns of activity using real time tracking*, IEEE Transactions on Pattern Analysis and Mach. Intell., vol. 22(8), pp. 747-767, 2000.

Toyma K., Krumm J., Meyers B., *Wallflower: Principles and practices of background maintenance*, IEEE International Conference on Computer Vision, pp. 255-261, 1999.

Integration of Equal Gain Combining and MAJORITY Rule for MIMO Cognitive Radio Systems

Rattasat Laikanok, Peerapong Uthansakul, and Monthippa Uthansakul
School of Telecommunication Engineering, Suranaree University of Technology

ABSTRACT

It is obvious that for cognitive ratio technology the success of using it depends on how accurate of spectrum sensing is. For MIMO systems, there are multiple antennas which can be more utilized for spectrum sensing than only one antenna like conventional systems. However, in literatures, the use of multiple antennas for sensing approach is based on two-state decision; available or occupied spectrums. In this paper, multi-state decision so called soft decision has been proposed to improve the performance of spectrum sensing for MIMO systems. Also this paper proposes the integration of Equal Gain Combining and MAJORITY Rule for sensing the spectrum. The results show that the proposed technique provides the best performance in comparing with other techniques.

1. INTRODUCTION

At present, the frequency resources allocated to primary users in the use of certain frequencies are not occupied all the time and they have a limited area where the communication signals in the frequency band are strong only, which is referred as a spectrum hole [1] as shown in Fig. 1. This causes researchers to find higher efficient technique to utilize resources. A Cognitive Radio (CR) technology has emerged to support the issue mentioned above and many associated techniques have introduced to improve its performance in various aspects. The popularity of CR technology gains the demand of its validation on the compliance with IEEE 802.22 standard as detailed in [2]. Following this standard, the information on the frequency allocation of the TV channels as shown in Tables 1 and 2 will be adopted for simulation in this paper.

The main objective of spectrum sensing is to increase the opportunities for secondary users (SUs) to access the spectrum without interfering to the primary networks. For Multiple Input Multiple Output (MIMO) systems, ther are more than one antenna operating at the same time. Hence, it is possible to utilize the use of multiple anenna for spectrum sensing. The higher accurate sensing results are expected from MIMO systems.

In literatures, the authors have surveyed many spectrum sensing techniques for CR technology that can apply to MIMO systems. One technique among those in literatures is the cooperative sensing concept [3]. In [4], the work described the various techniques of the cooperative sensing and presented the performance comparison of various methods, the advantages-disadvantages of each method. However, the cooperation of many antennas refers to the wasteful use of resources. This is because those methods make a decision based on two-state results either available or occupied spectrum. Hence, the cooperative mechanism can be predicted from two levels fo dicision which the performance can not be improved much for multiple antennas.

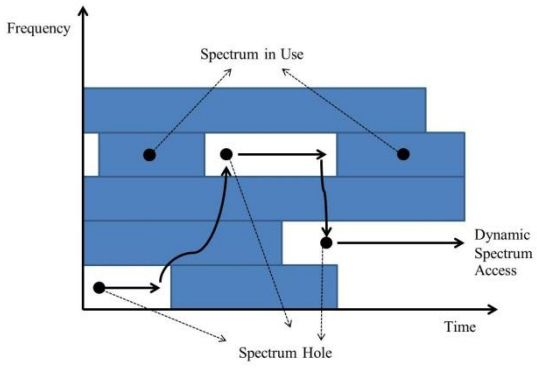

Fig. 1 Spectrum hole concept.

In this paper, the multi-state decision so called soft decision is proposed to the principle of cooperative sensing for array antennas in order to support MIMO

systems. Moreover, this paper also presents that the integration of two cooperative sensing techniques, Equal Gain Combining (EGC) and MAJORITY Rule (MJ), provides the best performance among other techniques in literatures.

TABLE 1 FREQUENCY OF TV CHANNELS IN WESTERN EUROPE AND MANY OTHER COUNTRIES IN AFRICA, ASIA, AND THE PACIFIC (BW=7 MHZ)

CH	f_c(MHz)	CH	f_c(MHz)	CH	f_c(MHz)
2	50.5	6	184.5	10	212.5
3	57.5	7	191.5	11	219.5
4	64.5	8	198.5	12	226.5
5	177.5	9	205.5		

TABLE 2 FREQUENCY OF TV CHANNELS IN WESTERN EUROPE AND MANY OTHER COUNTRIES IN AFRICA, ASIA, AND THE PACIFIC (BW=8 MHZ)

CH	f_c (MHz)	CH	f_c (MHz)	CH	f_c (MHz)	CH	f_c (MHz)	CH	f_c (MHz)
21	474	31	554	41	634	51	714	61	794
22	482	32	562	42	642	52	722	62	802
23	490	33	570	43	650	53	730	63	810
24	498	34	578	44	658	54	738	64	818
25	506	35	586	45	666	55	746	65	826
26	514	36	594	46	674	56	754	66	834
27	522	37	602	47	682	57	762	67	842
28	530	38	610	48	690	58	770	68	850
29	538	39	618	49	698	59	778	69	858
30	546	40	626	50	706	60	786		

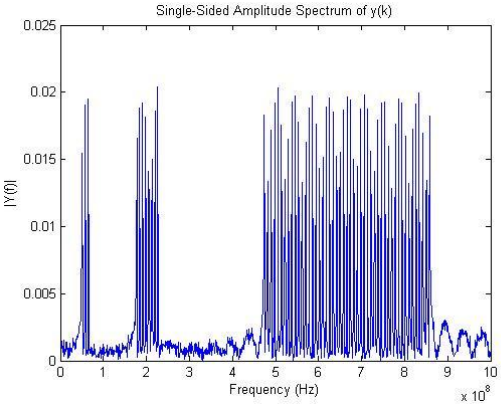

Fig. 2 Received spectrum when all channels are occupied.

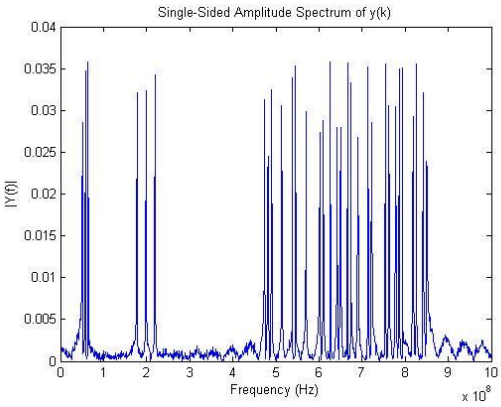

Fig. 3 Received spectrum when some channels are available.

The remainder of this paper is organized as follows. The basis of the energy detector method is given in Section 2. Then, the overview of EGC and cooperative decision rules including MJ are presented in Section 3. In Section 4, the proposed techniques including the integration of various methods and the soft decision are given in details. The simulation results and discussion are presented in Section 5 and then followed by the conclusion in Section 6.

2. ENERGY DETECTION METHOD

The principle of spectrum sensing can be understood easily [5-6] because only the interested spectrum is in just two hypotheses, including H_0 (availabe) and H_1 (occupied). The state is availabe when the primary user (PU) signal is not detected. The received signal is just ambient noise in the radio frequency (RF) environment. For the another, the state is occupied when the received signal would be consisted of the PU signal and the ambient noise, that can be explained by

$$\begin{aligned} H_0&: y(k) = w(k) \\ H_1&: y(k) = s(k) + w(k)\,, \end{aligned} \tag{1}$$

when $y(k)$ represents the received signal, $w(k)$ represents the ambient noise, and $s(k)$ represents the PU signal, for $k = 1, \ldots, n$, and n is the number of received samples. In fact, there are many spectrum sensing techniques in literatures such as energy detection, cyclostationary and etc. Among those, the energy detection method is very popular due to its ease for implementation. This paper develops the sensing technique based on the energy detector (ED) because it costs the less for multiple antennas in practice. Also this approach has the advantage that it is easy to distinguish the status of the spectrum energy in a way that is quite straightforward. Hence, it can be implemented as multi-state rather than availabe or occupied.

The simulations are based on the channel from IEEE 802.22 standard. The received spectrum when all channels in Tables 1 and 2 are occupied is presented in Fig. 2. The authors random some channels to be available in order to investigate the performance of sensing techniques. The example of received spectrum when some frequencies are available is illustrated in Fig. 3.

The performance evaluation of spectrum sensing techniques can be significantly viewed from two probabilities: probability of detection P_D and probability of false alarm P_{FA}.

P_D is the probability of detecting a signal on the considered frequency when it truly appears, or can be described in another form which is the probability of remaining apart from the probability of missed detection P_{MD}. This can be written as

$$P_D = 1 - P_{MD}, \tag{2}$$

when P_{MD} is the probability of detecting a signal when the occupied channel is detected as the channel is available. It occurs when the enegy of the received signal is lower than the detection threshold τ. The P_{FA} is the probability of detecting a signal when the available channel is detected as the channel is occupied. it is usually caused by a misunderstanding that interference is too high in the available channel. The P_{MD} and P_{FA} can be defined as

$$P_{MD} = Prob\{Decide\ H_0|H_1\}, \quad (3)$$

$$P_{FA} = Prob\{Decide\ H_1|H_0\}. \quad (4)$$

It can be seen that the P_{FA} is associated with P_D in such a way that P_{FA} is one of the forms of P_D when the total number of signal that is detected. Then, there is a certain amount of noise that is misunderstood.

The probabilities P_{FA} and P_{MD} in the forms of a simple analysis with the signals are modeled as a zero-mean stationary white Gaussian process, independent of the observation white Gaussian noise, which can be calculated as

$$P_{FA} = \Gamma_u(n\tau, n), \quad (5)$$

$$P_{MD} = \Gamma_u(\frac{n\tau}{1+SNR}, n), \quad (6)$$

where $\Gamma_u(.,.)$ is the upper incomplete gamma function [7].

In practice, we can separate the various frequencies of each channel from the received signal in (1) as follows:

$$y(k) = \sum_{ch=1}^{CH} u_{ch}(k), \quad (7)$$

where CH is the number of considered channels.

Then, take the signal being considered in each channel into the one-bit decision equation as:

$$U_{ch} = \begin{cases} 0, avg(|u_{ch}(k)|^2) < \tau \\ 1, avg(|u_{ch}(k)|^2) > \tau \end{cases}. \quad (8)$$

To demonstrate the concept of energy detection, the preliminary simulation has been performed. When the available channels are random for 2,000 times, the comparison between closed form solution appeared in (5) and simulated results can be shown in Fig. 4. In this figure, the evaluation of the probabilities P_D and P_{FA} is presented and this figure is well known as the Receiver Operating Characteristic (ROC) curve. The ROC shows the sensitivity in the terms of P_D and the specificity in the terms of P_{FA}. Therefore, the ROC curve that approaches 1 for P_D and 0 for P_{FA} is the ideal case. This figure also shows that the results of the simulation results of the spectrum sensing with energy detector is close to the theoretical analysis, when we refer the channels from Tables 1 and 2.

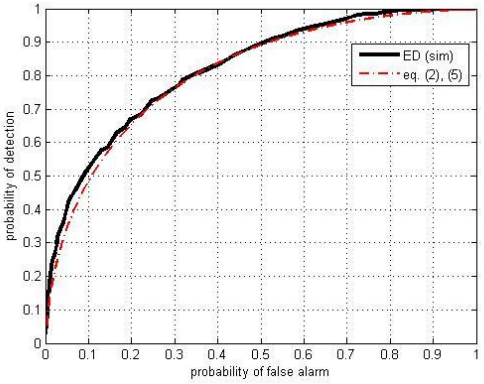

Fig. 4 ROC curves of the normal ED where $SNR = -30$ dB, and $n = 2000$.

3. EGC AND COOPERATIVE DECISION RULE

The difference of normal CR and MIMO CR users is the number of antennas on receiver. Hence, for MIMO CR, the method to utilize the use of multiple antennas is very important. In literatures, there are many techniques that can utilize many antennas for spectrum sensing so called cooperative techniques. Among those, two popular techniques are EGC and cooperative decision rule. This section presents the foundation of developed technique to support the cognitive radio technology in MIMO systems.

3.1 Equal Gain Combining

Equal Gain Combinng (EGC) method fuses all the received signals from each antenna to obtain the following combining result [4]:

$$y_{EGC}(k) = (\frac{1}{M})\sum_{m=1}^{M} y_m(k), \quad (9)$$

where M is the number of antenna elements.

The use of EGC is to take the EGC received signal $y_{EGC}(k)$ in (9) into (7) and (8) instead of $y(k)$.

3.2 Cooperative Decision Rule

The cooperative deicsion rule refers to three different formats including OR rule, AND rule and MAJORITY (MJ) rule. After the signal is received, each signal of each antenna element will be sent to separated detector by (7), and next to (8). Finally, we have the data points $\boldsymbol{U_{ch}}$ of all channels of each antenna, total points of the corresponding channel to perform the final decision according to the following logic rule [4], as follows:

$$U_{total}(k) = \sum_{m=1}^{M} U_m(k) \begin{cases} < \kappa, & H_0 \\ > \kappa, & H_1 \end{cases}, \quad (10)$$

where κ is the decistion factor which the OR rule corresponds to the case of $\kappa = 1$, the AND rule corresponds to the case of $\kappa = M$, and the MAJORITY rule corresponds to the case of $\kappa = M/2$.

4. PROPOSED TECHNIQUES

4.1 MAJORITY++ Rule

From both methods in Section 3, the authors combine them to imrpove the performance of spectrum sensing even better. The authors have named this proposed method as MAJORITY++ (MJ++). The proposed MAJORITY++ rule technique is created by adding the assistant signal:

$$y_{M+1}(k) = (\frac{1}{M})\sum_{m=1}^{M} w_m * y_m(k), \qquad (11)$$

that was taken from the EGC method, and w_m is weighting coefficients. The reason of adding w is is that the received signal of each antenna element has a phase shift from the principle of array antenna [8].

Then we take the signal from (11) and normally received signals to get into the process of normal decision by (7) and (8) respectively. After that, the MJ rule is taken according to (10). The decision factor of this method is given by

$$\kappa_{MJ++} = (\frac{M+1}{2}). \qquad (12)$$

The result in (12) is used for the final decision in (10).

4.2 MAJORITY++ Rule with Soft Decision

Based on a one-bit decision shown in (8), the deficiency is that there are only two-state results. Only either available or occupied channels are the final output. In some cases, the available channel can be the final decision even the signal is slightly below the threshold. This is because the two-state system strictly keep comparing with the threshold level no matter how much the difference between signal and threshold is. In this light, the authors propose the new idea to increase the opportunity for those weak signals being slightly lower than the threshold to give them a greater voice in decision making. By dividing the threshold into mutiple levels L , so called as multi-state threshold, and giving the proper decistion points to them, then we can have the leveled decision, so called as soft decision as shown in (13).

$$U_{L,ch} = \begin{cases} 0, avg(|u_{ch}(k)|^2) < l\tau \\ \downarrow \qquad\qquad \downarrow \\ 1, avg(|u_{ch}(k)|^2) \geq L\tau \end{cases}, \qquad (13)$$

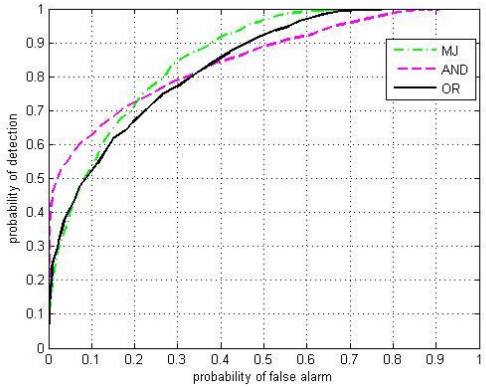

Fig. 5 Comparison of ROC curves for OR rule, AND rule and MJ rule, where M = 4, $SNR = -30$ dB, and $n = 2000$.

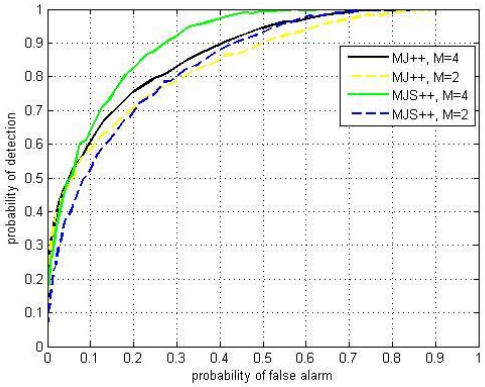

Fig. 6 Comparison of ROC curves for MJ++ and MJS++, where = 2 and 4, $SNR = -30$ dB, and $n = 2000$.

where l is a constant increase in the number of levels up to L. The value of $U_{L,ch}$ is between 0 and 1 as same as U_{ch} in (8). The authors have named this proposed method as MJS++ for a short reference.

5. SIMULATION RESULTS AND DISCUSSION

Based on information in Tables 1 and 2, the simulated signals with the random of available channels is generated. Then, the probability of detection P_D and probability of false alarm P_{FA} are calculated by various spectrum sensing techniques. Fig. 5 shows the ROC comparison of the cooperative decision rules. The results in Fig. 5 reveal that MJ rule is the most effective method among those three cooperative decision rules. Thus, this paper select the MJ rule for the integration of EGC with soft decision as presented in the next results.

Fig. 6 shows the ROC comparison of MAJORITY++ rule (MJ++) and MAJORITY++ rule with solf decision (MJS++), where $SNR = 30$ dB, the number of samples $n = 2000$, the transmitted power of primaly user $P_t = 1$ dBW, and the presence of the signal in each channel has occurred randomly. For the MIMO systems, M is the number of antennas which is limited to 2 and 4 antennas as related to the practical issue.

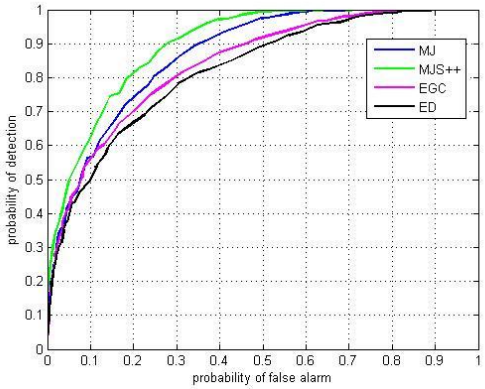

Fig. 7 Comparison of ROC curves for normal ED ($M = 1$), EGC ($M = 4$), MJ rule ($M = 4$) and MJS++ ($M = 4$), where $SNR = -30$ dB and $n = 2000$.

As seen Fig. 6, MJS++ rule offers a better performance than MJ++ rule for both cases of the number of antennas. The results reveal the benefit of soft decision for spectrum sensing. Also in this figure, the more number of antennas, the better performance can be obtained. The results imply the advantage of using the proposed technique for the MIMO CR users.

In Fig. 7, the results show the comparison of the proposed techniques and the existing techniques in literatures, where $SNR = 30$ dB, $n = 2000$, $P_t = 1$ dBW, $M = 4$. For a energy detection technique, the antenna is set to 1 because there is no cooperative help on traditional systems. As expected, the proposed techniques outperform the others. At the 90% probability of detection, the MJS++ technique can reduce the chance of false alarm from 50% of ED technique to 26%. This 24% improvement can indicate the success of proposed technique for practical use.

6. CONCLUSION

This paper has presented the new concept for sensing the spectrum for MIMO CR users. The proposed concept is to divide the decision threshold into multi-state decision so called as soft decision. Also, the soft decision has been applied to the integration of EGC and MAJORITY rule. The performance of proposed techniques has been examined in terms of ROC curve. The results show that the proposed techniques outperform the other existing techniques. Also the better performance can be obtained using the soft decision.

REFERENCES

I. F. Akyildiz, W. –Y. Lee and M. C. Vuran, "Next generation/dynamic spectrum access/cognitive radio wireless network: A survey," Science Direct, pp. 2127-2130, 2006.

802.22-2011 - IEEE Standard for Information technology-- Local and Metropolitan area networks-- Specific requirements-- Part 22: Cognitive Wireless RAN Medium Access Control (MAC) and Physical Layer (PHY) specifications: Policies and procedures for operation in the TV Bands.

T. Yucek and H. Arslan, "A survey of spectrum sensing algorithms for cognitive radio applications," IEEE Commun. Serv. Tutor., vol. 11, no. 1, pp. 116-130, 2009.

C. Hunifang, X. Lei and N. Xiong, "Reputation-based hierarchically cooperative spectrum sensing scheme in cognitive radio networks," Selected papers from IEEE/CIC ICCC2013, pp. 12-25, Jan. 2014.

K. Tourki, K. A. Qaraqe, H-C. Yang and M-S. Alouini, "Exact performance analysis of MIMO cognitive radio systems using transmit antenna selection," IEEE J. Select. Areas Commun., vol. 32, no. 3, Mar. 2014.

F. A. Khan, K. Tourki, M-S. Alouini and K. A. Qaraqe, "Performance analysis of a power limited spectrum sharing system with TAS/MRC," IEEE Tran. Signal Processing, vol. 62, no. 4, Feb. 2014.

A. M. Wyglinski, M. Nekovee and T. Hou, Cognitive Radio Communications and Networks, ELSEVIER Inc. 2010.

J. Foutz, A. Spanias and M. K. Banavar, "Narrowband direction of arrival estimation for antenna arrays," A publication in the Morgan & Claypool publishers series.

A REVIEW OF KINECT APPLICATIONS FOR ELDERLY POPULATIONS

Katlin Kreamer-Tonin[1,2] and Jonathan H. Chan[1]
[1] Data and Knowledge Laboratory, School of Information Technology, King Mongkut's University of Technology Thonburi, Bangkok, Thailand
[2] Division of Engineering Science, University of Toronto, Toronto, Canada

ABSTRACT

The aging population of the world results in a high demand for technology to care for elderly subjects. Some challenges faced by this growing population segment are falls in the home, rehabilitation from injury, and maintaining a healthy and independent lifestyle. This paper will explore how the Microsoft Kinect has been applied to problems facing the elderly populations, and would suggest future directions and development needed to address them. Future directions recommended include dealing with false alarms and occlusion in fall situations, customizing Kinect algorithms for elderly patient rehabilitation, recognizing human postures and gaits, and extracting more insightful information from meal tracking Kinect technology.

1. INTRODUCTION

The world has become an ageing society since the year 2000, meaning people who are 65 years old or over account for 7% or more of the total population (Chan, 2015). Population ageing is due to higher life expectancy and lower birth rates on a worldwide basis. Active ageing is the process of optimizing opportunities for health, participation and security in order to enhance quality of life as people age (WHO, 2002). This increase in population age shows a significant need for resources to be developed to care for the elderly. Good health is necessary if elderly populations are to remain independent and to play a part in family and community life.

Significant challenges that arise frequently in elderly populations are accidental falls in the home setting, rehabilitation from sustained injury, and how to maintain a healthy and independent lifestyle. These challenges have been tackled by many practitioners with a variety of techniques, but still remain largely as unsolved problems.

The Microsoft Xbox Kinect was originally a video game controller, but open software development kits have allowed it to be opened up to many more applications. This paper will provide an overview of how the Kinect has been used for problems facing the elderly populations and suggests future directions and development.

Not discussed in this paper, but of significant interest, are applications involving guiding a blind person through a building, translating from sign language to text and speech with real time gesture-based controls, or surgeons interacting with static medical imagery onscreen via the Kinect. These challenges could also involve elderly patients, but are still at the idea phase and have not yet been prototyped.

2. BACKGROUND

2.1 Falls

Falls are the second leading cause of accidental or unintentional injury deaths worldwide, and 37.3 million falls that are severe enough to require medical attention occur each year (WHO, 2011). Falls can result in serious injuries such as hip fractures and head traumas, which reduce mobility and independence and lead to an increased risk of early death (WHO, 2012). Older adults living alone are at significant risk of delayed assistance following a fall, as they may be unable to get up or call for medical attention (Stone and Skubic, 2015).

Current solutions for fall detection involve wearable devices or signaling mechanisms, or cameras mounted in the home. These solutions have failed because wearable technology could be forgotten to put on by the elderly subjects, and there are privacy concerns that come with the use of cameras for monitoring purpose, as well as challenges in low lighting conditions for cameras (Stone and Skubic, 2015).

2.2 Rehabilitation

After suffering from injury or disease, many seniors require rehabilitation. Some causes could be stroke, Parkinson's disease, or after surgery. Rehabilitation therapy often takes place over many visits to a hospital to see a physical or occupational therapist. If it was possible to provide in-home rehabilitation and reduce these hospital visits, it would dramatically reduce healthcare costs (Kitsunezaki et al, 2013). Patients would also be able to perform rehabilitation exercises more frequently, not just when they had an appointment.

As a result, there is high demand for computer-aided tools which support in-home rehabilitation in order to care for patients without using up hospital resources.

2.3 Healthy Lifestyle

Maintaining a healthy and independent lifestyle is part active aging, and deemed significantly important by the World Health Organization (WHO, 2002). Using the Kinect to create "exergames" (exercise games) specifically for elderly patients could allow them to help prevent things such as falls, by training postural control in the home environment (Ejupi et al., 2014).

The Kinect could also be used for things such as meal monitoring. Keeping track of nutritional health in elderly patients would reduce risks chronic diseases and general morbidity, including cardiovascular conditions (Cunha et al, 2014).

3. CURRENT PROJECTS

3.1 Falls

Several groups have attempted to use the Kinect to monitor and detect falls in elderly patients in a home environment.

Skeletal tracking with Kinect SDK was the original method of tracking falls. However, a reason for not using this technique is the limited range of the skeletal tracking, approximately 1.5 to 4 m from the Kinect (Webster and Celik, 2014). This range is insufficient to capture falls through a home environment. Webster and Celik (2014) present an overview of many early stage trials, both with and without skeletal tracking. They showed that systems that worked in situations with a lack of light, where video camera systems would fail. However, they did not tackle the challenge of significantly occluded falls.

One method for dealing with occlusion is by using multiple Kinect cameras from different angles, to give a more complete image. This has been done by Kaenchan et al. (2013), where each camera's coordinate system is transformed to a reference coordinate system. The composed skeleton is formed by averaging all the transformed joints. This study was aimed at looking at abnormal balance in walking and therefore fall prevention, but could be applied to fall detection as well. Pasadu et al. (2012) also show an effective joint tracking project, where the recognized gesture patterns of the study are stand, sit down, and lie down.

Stone and Skubic (2015) present a two-stage fall detection system. The first stage of the detection system characterizes a person's vertical state in individual depth image frames, and then tracks relation to ground events over time. The second stage uses decision trees to compute a confidence that a fall occurred. Their study was unique in that it occurred over 9 years, in 13 homes of elderly patients. The dataset includes 454 falls, 445 falls performed by trained stunt actors and nine naturally occurring resident falls. Overall this study was largely successful, but there was at least one missed fall and several challenges due to occlusion and sunlight interference.

Similarly, Booranrom et al. (2014) have designed a "Smart Bedroom" to monitor falls from a bed in a realistic setting. The locations of the skeleton joints relative to the bed are used to determine the probability of a fall. Kinect was used as part of a system to allow remote control of appliances via gesturing as well.

3.2 Rehabilitation

Kinect's ability to accurately capture upper extremity movements is consistently reported as sufficient for clinical use with regards to the elbow and wrist joint tracking; however, mixed results have been reported with more complex joints such as the shoulder.

Kitsunezaki et al. (2013) have shown that a system for Kinect rehabilitation programs is a viable project, but did not do any testing with elderly patients. Their project involved a "get up and go" test. The patient is observed and timed while he rises from an arm chair, walks 3 meters, turns, walks back, and sits down again. This can be used to predict the patient's ability to go outside alone safely. The test was mostly effective, but trials need to be done with an elderly population.

Sin and Lee (2013) created a virtual reality rehabilitation program specifically for hemiplegic stroke survivors. The patients studied showed significantly improved function of their upper extremities after using the program. However, the effects of the virtual reality training may have been a result of the greater total rehabilitation time in the training group compared with the control group. This is one of the benefits of Kinect – home-based systems could lead to more time doing rehabilitation exercises.

3.3 Healthy Lifestyle

Ejupi et al. (2014) did a study that evaluates elderly patients' stepping speed to evaluate fall risk using exergame technology. They found that the Kinect could accurately predict patients prone to falling in an elderly community. This system could be used in assessment or to train patients via games with the Kinect. The benefits of this kind of test are that they are portable, low cost and unobtrusive to patients.

Cunha et al. (2014) present a way to monitor elderly patients' eating habits by using skeleton tracking to see food and drink patterns. They were able to recognize upper body movements that indicated meal intake.

However, the only data that they currently collect for the patient is that whether or not they are eating, in terms of time and duration. No data was analyzed about how much or what the patient is eating.

In addition to trying to gather nutritional information, Visutarrom et al. (2014) propose that patients could have their posture tracked while watching television. Since television is a significant pastime for the elderly, this data could help physicians to understand and monitor behavior and health.

4. FUTURE DIRECTIONS

4.1 Falls

Significant challenges are still present in fall detection in the homes of elderly patients. Occlusion is still a significant problem, especially in situations involving sitting falls where the chair often blocks the patient. Lying down falls are also missed in some algorithms because of the smaller peak velocity of the center of mass.

Although falls can be detected in low light conditions, challenges arise in conditions with lots of sunlight interfering with the depth signal (Stone and Skubic, 2015). Although the Kinect is designed for use indoors, situations do occur where sunlight can come through a window. It is important to be aware of these challenges when setting up the system in a home.

False alarms of a fall are also still present in all tested systems. They could be triggered by visiting children dropping to the floor while playing, certain pets jumping down from furniture, visitors (such as family and maintenance staff) sitting or lying down on the floor quickly, or dropping large object onto the floor (Stone and Skubic, 2015). It would be possible to eliminate these false alarms if we could determine a way to only track elderly people, not all moving objects. However, no such algorithms currently exist.

The most interesting yet difficult problem that could be tackled is a fall prevention system. Rather than just detecting falls, being able to analyze gait and deliver an early warning about an increased risk of falling would be very beneficial to elderly patients.

4.2 Rehabilitation

Currently, movements must be relatively large to be tracked with the Kinect. In many cases (especially for cognitive injuries), small movements are very significant in rehabilitation programs. These small postural movements cannot currently be detected in systems mentioned above.

Another challenge being faced in Kinect rehabilitation applications is that non-participant objects such as wheelchairs or walkers create occlusion. Algorithms could be adjusted for scenarios involving these objects. Proportional biases such as the pelvis, sternum or shoulders should also be adjusted for specific patients or scenarios.

4.3 Healthy Lifestyle

Exergames as a method for improving quality of life and diagnostic purposes have a lot of potential for the elderly demographic. However, more work must be done to customize these applications for older populations.

In meal monitoring technology with the Kinect, it would be helpful to monitor not only the number of meals eaten, but also the type of meal and how much was consumed. This could then help provide nutritional suggestions or alert medical professionals if there was something abnormal about the patient's habits.

Posture detection while watching television is an interesting concept, but the data collected from current techniques must still be interpreted to find its significance. Detection must be real time and address the problem of occlusion. Furthermore, this information must be presented effectively to medical practitioners in order to justify the use of Kinect in this application.

5. CONCLUSIONS

The Kinect has many potential applications in caring for elderly patients. Although significant progress has been shown, much work must be done in customizing algorithms for these applications to deal with occlusion, tracking smaller movements, and extracting more information about the patient.

REFERENCES

Booranrom, Y., Watanapa, B., and Mongkolnam, P., Smart Bedroom for Elderly using Kinect, Proc. International Computer Science and Engineering Conference (ICSEC), pp. 427-432, 2014.

Chan, J. H., Digital information and communication in the ageing society, Frontiers in Artificial Intelligence and Applications, vol. 275, pp. 3-11, 2015.

Cunha, A., Padua, L., Costa, L., and Cunha, P., Evaluation of MS Kinect for Elderly Meal Intake Monitoring, Proc. International Conference on Health and Social Care Information Systems and Technologies, Procedia Technology, vol. 16, pp. 1383-1390, 2014.

Ejupi, A., Brodie, M., Gschwind, Y. J., Schoene, D., Lord, S., and Delbaere, K., Choice stepping reaction time test using exergame technology for fall risk assessment in older people, Proc. Annual International Conference for IEEE Engineering in Medicine and Biology Society, pp. 6957-6960, 2014.

Kaenchan, S., Mongkolnam, P., Watanapa, B., and Sathienpong, S., Automatic multiple Kinect cameras setting for simple walking posture analysis, Prof. International Computer Science and Engineering Conference (ICSEC), pp. 250-254, 2013.

Kitsunezaki, N., Adachi, E., Matsuda, T., and Mizusawa, J., KINECT Applications for The Physical Rehabilitation, Proc. IEEE International Symposium on Medical Measurements and Applications, pp. 294-299, 2013.

Patsadu, O., Nukoolkit, C., and Watanapa, B., Human gesture recognition using Kinect camera, Proc. Ninth International Joint Conference on Computer Science and Software Engineering (JCSSE), pp. 28-32, 2012.

Sin, H. and Lee, G., Additional virtual reality training using Xbox Kinect in stroke survivors with hemiplegia, American Journal of Physical and Medical Rehabilitation, vol. 92, no. 10, pp. 871-880, 2013.

Stone, E. E. and Skubic, M, Fall Detection in Homes of Older Adults Using the Microsoft Kinect, IEEE Journal of Biomedical and Health Informatics, vol. 19, issue 1, pp. 290-301, January 2015.

Visutarrom, T., Mongkolnam, P., and Chan, J. H., Multiple-stage classification of human poses while watching television, Proc. International Symposium on Computational and Business Intelligence (ISCBI-II), 2014.

Webster, D. and Celik, O., Systematic review of Kinect applications in elderly care and stroke rehabilitation, Journal of NeuroEngineering and Rehabilitation, vol. 11, pp. 108, 2014. [http://www.jneuroengrehab.com/content/11/1/108]

World Health Organization (WHO), Active Ageing: A Policy Framework, April 2002. [Retrieved May 15, 2015, from http://whqlibdoc.who.int/hq/2002/WHO_NMH_NPH_02.8.pdf?ua=1]

World Health Organization (WHO), Media Center: Falls, October 2012. [Retrieved May 15, 2015, from http://www.who.int/mediacentre/factsheets/fs344/en/]

World Health Organization (WHO), What are the public health implications of global ageing? September 2011. [Retrieved May 15, 2015, from http://www.who.int/features/qa/42/en/]

Katlin Kreamer-Tonin is an undergraduate student at the University of Toronto, and doing a summer internship at King Mongkut's University of Technology Thonburi. She studies biomedical engineering, and is interested in system level design and prototyping medical technologies.

Jonathan H. Chan received his B.A.Sc. (1984) in Engineering Science, M.A.Sc. (1986) and Ph.D. (1995) in Chemical Engineering from the University of Toronto. He is an Associate Professor at the School of Information Technology, King Mongkut's University of Technology Thonburi. His current interests include mathematical modeling and simulation, bioinformatics, signal processing and analysis, knowledge engineering and social computing, and parallel and grid computing.

MAMMOGRAPHY IMAGES CATEGORIZATION WITH K-MEANS CLUTERING

Kedkarn Chaiyakhan*, Nittaya Kerdprasop, and Kittisak Kerdprasop
School of Computer Engineering, Suranaree University of Technology, Thailand

ABSTRACT

Mammography is an extraordinary type of low-powered x-ray process that provides detailed images of the internal structure of the breast. Many researches show that the dense masses in the breast density are one of the strongest indicators of developing breast cancer. In this paper, we proposed an approach to automatically appraise the density of breast using gamma correction to increase the intensity dense pixels which has light intensity vice versa decrease the intensity sparse pixels which has dark intensity. In clustering process we use k-means clustering to cluster image into 3 categories: benign, malignant and normal. The result shows that our approach be able to cluster three type of mammography after gamma correction process in the correct class which has rather high accuracy.

1. INTRODUCTION

Breast cancer is a type of cancer origination from breast tissue, and it accounts for 23% of all cancers in women. The most effective way to detect breast cancer is through the breast mammogram screening. However, the major limitation for mammography diagnosis is sensitivity. Mammography is the most common imaging technique to detect breast cancer. Many methodologies have been proposed to solve the problem providing assistance on the advanced cancer detection and diagnosis tools.

During the last year, different algorithms have been proposed for breast density segmentation. For instance, Oliver. et al.(2010), proposed a statistical approach for breast density segmentation They provide connected density clusters taking the spatial information of the breast into account. Quantitative and qualitative results show that their approach is able to correctly detect dense breasts, segmentation the tissue type accordingly. Brzakovic. et al. (2009), was presented a methodology that based on modeling a set of patched of either fatty or dense parenchyma using statistical analysis. They analyzed two different strategies to perform this modeling process such as principal component analysis and linear-discriminant-based model. Once the tissue models have been learned, each pixel of a new mammogram is classified as being fatty or dense tissue, taking its corresponding neighborhood into account. Ferrari, et al. (2004) and Aylward, et al. (1998), used mixtures of Gaussian for modeling and segmentation the breast into four and five regions, respectively. However, these related approaches do not take spatial information into account providing segmentations with too many disconnected regions. Moreover, an initial pre-processing step is needed to remove noisy pixels. Aiming to include this spatial information into account, Saha, et al. (2001), included a fuzzy affinity function in their proposed work, while Zwiggelarar (2004), employed textural features to take the spatial distribution of the pixel and its neighborhood into account. Shi, et al. (2010), presented fuzzy support vector machine to automatically detect and classify mass using ultrasound images. They also provided the feature extraction and feature selection using image preprocessing and membership value, respectively.

In this paper, we proposed the clustering method using k-means clustering, we also used image preprocessing technique algorithm namely gamma correction. After preprocessing process, we input the data into k-means clustering which set k=3, since we know that each image belong to one of three classes from the well-known DDSM database which annotated from the experts. In the experimental result shows that our purposed work has capability to categorized the images correctly, with pretty high accuracy that illustrated by the confusion matrix, the cluster plot and the silhouette plot.

2. METERIALS AND METHODS

2.1 Gamma Correction

Gamma correction is the name of nonlinear operation used to code and decode luminance on image systems. Each pixel in an image has brightness level, called luminance. This value is between 0 to 1, where 0 means absolute darkness (black), and 1 is brightest (white). Different camera devices do not correctly capture luminance and do not display luminance precisely. So, we need to correct them using gamma correction function. Gamma correction function is used to correct image's luminance. It controls the whole brightness of an image. Images which are not corrected can look either light region darker or dark region lighter. Suppose a computer

monitor has 2.2 powers function as intensity to voltage response curve. This just means that if we send a message to the monitor that a certain pixel should have intensity equal to x, it will actually display a pixel which has intensity equal to $x^{2.2}$. Because the range of voltages sent to monitor are between 0 and 1, it means that the intensity value displayed will be less than what we wanted it to be. Hence, the gamma corrected formula is written as

$$Corrected = 255 * (\frac{Image}{255})^{(\frac{1}{\gamma})} \quad (1)$$

where γ is the encoding or decoding value. If value γ < 1 is called and encoding gamma or gamma compression, conversely if γ > 1 is called a decoding gamma or gamma expansion. The effect of gamma correction on an image if γ > 1 shadow in image will be darker, whereas, if γ < 1 dark region will be lighter.

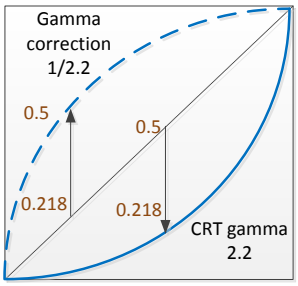

Fig. 1 Gamma correction model.

2.2 K-means Clustering

K-means clustering is one of the easiest unsupervised learning algorithms that solve the clustering problem. The procedure follows a simple and uncomplicated way to cluster a given data set through a certain number of clusters (suppose k clusters). The main concept is to determine k centers, one of each cluster. These centers should be locating them in the brilliant way because of different location causes different result. Therefore, the optimal choice is to locate them as much as possible far away from each other. The next step is to take each point belonging to a given data set and associate it to the nearest center. Clustering data are represented as $D = \{x_1, \dots, x_N\}$. Since the data is p-dimensional, then represent it as $X_n = \{x_{n,1}, \dots, x_{n,p}\}$. The distance function is $d(X_n, X_m)$ between two data points. The k groups has distinguish the data into $\{z_1, \dots, z_N\}$ where $x \in \{1, \dots, K\}$.

3. PROPOSED WORK

In our proposed medical image clustering system, we get benefit from the gamma correction and k-means clustering algorithm. As shown in Fig. 2, the proposed medical image clustering system consists of 6 stages: image acquisition, image resize, gamma correction, image to vector, vector to CSV and clustering images. In the first process we acquired images from DDSM database. Because of each image has very larch size about 3000x5000 pixels which effect long computation time. Thus, in the second process, we resized image to 300x500 pixels.

The main idea of doing the 3 classes (malignant, benign and normal) of image to the different properties is image preprocessing using gamma correction. Because the images from DDSM are gray scale image which 3 classes look rather similar intensity and low contrast. Therefore, we used gamma correction to increase bright pixel and decrease dark pixel. So we will get the different properties of 3 classes image because malignant case has the lighter intensity and dense pixel more than benign case. Likewise, benign image has the lighter intensity and dense pixel more than normal case. In the fourth and fifth process we converted every pre-pressing images to vector and save data in to CSV file, this process make less computation time because no need to read every images in the clustering process. In the last process, we input the CSV file into the clustering process using k-means that set k = 3.

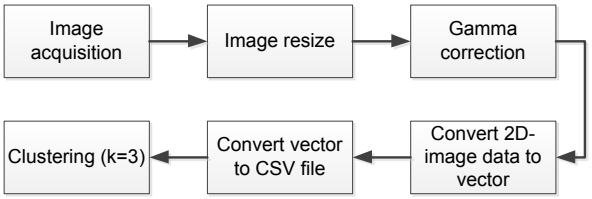

Fig. 2 The framework of the proposed work.

3.1 Image Preprocessing using Gamma Correction

In the image pre-processing process, we adjusted the brightness and darkness of image using gamma correction algorithm. In Fig. 3 shows the result of gamma correction with malignant case, benign case and normal case. In Fig. 3a illustrates the malignant tumor before gamma correction, it seem not clear between the tumor area and fatty area.

In Fig. 3(a), this image is malignant case, after we used gamma correction and get the result in Fig. 3(d), we will see that the tumor area has lighter intensity and density more than original image, that we can input the image after pre-processing in to clustering process using k-means. In Fig. 3(b), and Fig. 3(c) we use the gamma correction process same as Fig 3(a). In Fig 3(b) and Fig. 3(c) are benign tumor and normal tumor respectively. Consequently, we will see the result in Fig 3(e) that it is the benign tumor and after gamma correction process, the area of benign tumor is lighter more than original. If we compare between Fig. 3(d) and Fig. 3(e), they are rather different because Fig. 3(d) is the malignant tumor and it has light intensity pixel and dense intensity pixel more

than Fig. 3(e) that it is benign tumor. Accordingly, in Fig. 3(c), we also apply gamma correction in the image, it is normal case and it has no tumor in this image. Thus the result in Fig. 3(f) has poor light intensity pixel and low dense pixel.

3.2 K-means Clustering on Mammogram Images

After image preprocessing using gamma correction process. We obtained images that corrected brightness and darkness which illustrate in Fig. 3. Subsequently, we input images in clustering process using k-means which set k=3, because after image preprocessing step, the intensity and density of pixels in each image (malignant, benign and normal) rather different. Therefore, k-means can cluster images in the correct class accurately.

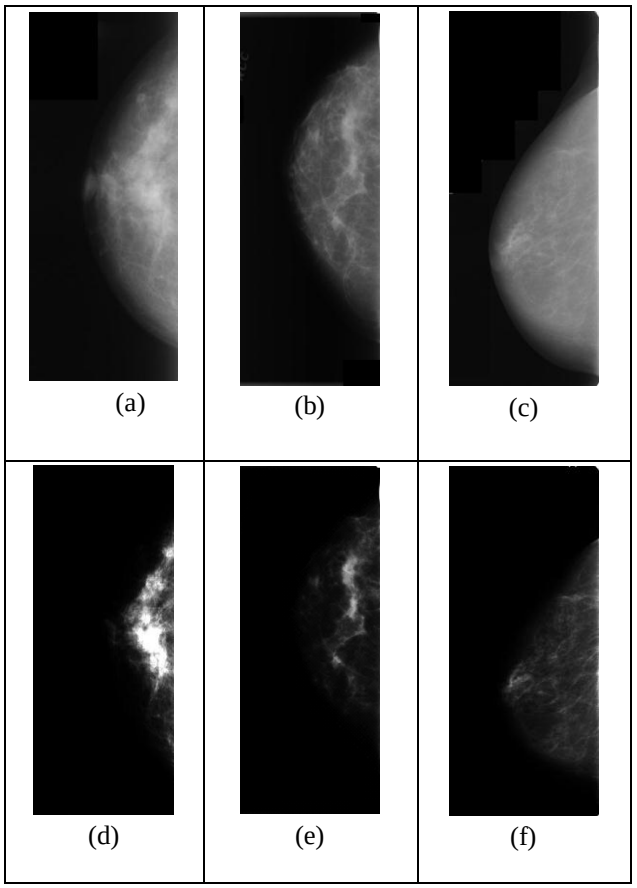

Fig. 3 (a) Original malignant, (b) original benign, (c) original normal, (d) corrected malignant, (e) corrected benign, (f) corrected normal.

4. EXPERIMENTAL RESULTS

In this research we used data set from DDSM (Digital Database for Screening Mammography). We selected 60 images from DDSM that include 3 cases such as malignant, benign and normal (each 20 images). This work was implemented using R language. We run our experiments on a core i5/2.4 GHZ computer with 4 GB RAM. Table 1 shows the result of clustering that pretty good clustering. The clustering process using k-means can clustered the images in a correct class such as benign case can clustered in class 1 which has 18 out of 20, malignant case can clustered in class 2 which has 19 out of 20 and normal case can clustered in class 3 which has 18 out of 20. Consequently, the accuracy rate of our proposed work is 91.67%.

In Fig. 4 demonstrates the two components of 3 clusters plot which are malignant case, benign case and normal case. The two-dimensional clustering plot of the three clusters and lines show the distance between clusters.

The result of clustering seems rather good, because it identifies three clusters, corresponding to three classes. Moreover, in Fig. 5 show their silhouettes plot. From the silhouette plot, the averages S_i are 0.22, 0.85 and 0.74, respectively. According to the silhouette, the first cluster is not well clustered, but the second and third clusters are well clustered. As a result, the average silhouette width is 0.62.

Table 1 Confusion matrix of 3 clusters.

	Benign	**Malignant**	**Normal**
1	**18**	0	1
2	2	**19**	1
3	0	1	**18**

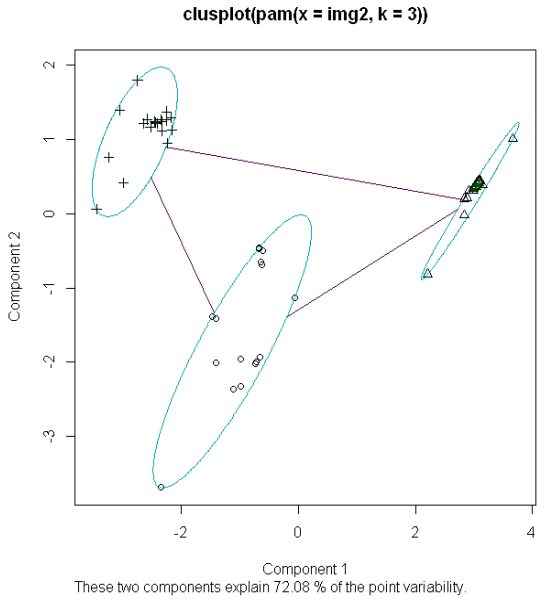

Fig. 4 Two components of clustering plot.

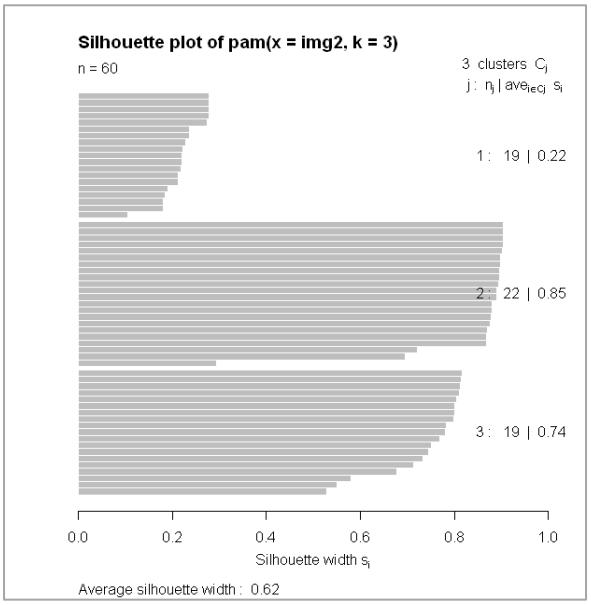

Fig. 5 The silhouette plot when k=3.

5. CONCLUSION

The k-means clustering with gamma correction method that we proposed in this paper can cluster the mammography images from the well-known DDSM database correctly. It clustered images into malignant case, benign case and normal case which has the accuracy 91.67%. Since gamma correction be able to improve the clearness of brightness intensity and it can decrease the poor dark intensity which mean that the area of malignant and benign tumor will appear explicitly and in the normal case which has no tumor area, it appear only fatty which dark intensity pixels. When we input the image after gamma correction process into k-means clustering with k=3, then the k-means be able to cluster the images into correct class, because of an intensity brightness level in images was different.

In our future work we will extract the region of interest (ROI) of tumor using other image preprocessing techniques and we will also use other classification techniques such as support vector machine or artificial neural network to improve the performance of classify and increase the accuracy rate.

REFERENCES

Oliver, A., Llado, X., Perez, E., Pont, J., Denton, E., Freixener, J., and Marti, J., Journal of digital imaging, vol. 23, no. 5, pp. 527-537, 2010.

Brzakovic, D., Vujovic, N., Neskovic, M., Brzakovic, P., and Fogarty, K., IEEE transaction in medical image, vol. 9, no. 3, pp. 233-241, 1990.

Ferrari, R., Rangayyan, R., Borges, R., and Frere, A., Medical biology engineering computation, vol. 42, pp. 378-387, 2004.

Aylward, S., Hemminger, B., and Pisano, E., International workshop in digital mammography, pp. 305-312, 1998.

Saha, P., Udupa, J., Conant, E., Chakraborty, P., and Sullivan, D., IEEE transaction in medical image, vol.20, no. 8, pp. 792-803, 2001.

Zwiggelaar, R., and Denton, E., International workshop in digital mammography, pp. 751-757, 2004.

Shi, X., Cheng, H., Liming, H., Wen, J., and Jiawei, T., Digital signal processing, vol. 20, pp. 824-836, 2010.

Kedkarn Chaiyakhan is currently a Ph.D. student in the School of Computer Engineering, Suranaree University of Technology, Thailand. She received her bachelor degree in Computer Engineering from Rajamangala University of Technology Thanyaburi in 1998 , master degree in Computer Engineering from King Mongkut's University of Technology Thonbuti in 2007. Her current research includes image classification and image clustering.

Nittaya Kertprasop is and associate professor at the School of Computer Engineering, Suranaree University of Technology, Thailand. She received her bachelor degree in Radiation Techniques from Mahidol University, Thailand, in 1985, master degree in Computer Science from the Prince of Songkla University, Thailand, in 1991 and doctoral degree in Computer Science from Nova Southeastern University, U.S.A, in 1999. She is a member of ACM and IEEE Computer Society. Her research of interest includes Knowledge Discovery in Databases, Artificial Intelligence, Logic Programming, and Intelligent Databases.

Kittisak Kerdprasop is an associate professor and chair of the School of Computer Engineering, Suranaree University of Technology, Thailand. He received his bachelor degree in Mathematics from Srinakarinwirot University, Thailand, in 1986, master degree in Computer Science from the Prince of Songkla University, Thailand, in 1991 and doctoral degree in Computer Science from Nova Southeastern University, U.S.A., in 1999. His current research includes Data mining, Artificial Intelligence, Functional and Logic Programming Languages, Computational Statistics.

A COMPARATIVE STUDY OF TIME SERIES CLASSIFICATION BY USING DECISION TREE AND SUPPORT VECTOR MACHINE

Keerachart Suksut*, Nittaya Kerdprasop, Kittisak Kerdprasop
School of Computer Engineering, Suranaree University of Technology, Thailand

ABSTRACT

Time series analysis can be used to forecast future events. There are many techniques for classifying time series data such as CTREE, Random Forest, and SVM. In this research, we perform a comparative study in terms of accuracy and time usage for classification with CTREE, Random Forests, and SVM. From the result we found that SVM has higher accuracy than Random Forests and CTREE respectively. CTREE can classify faster than SVM and Random Forests, respectively. We also applied Discrete Wavelet Transform (DWT) to extract features and classify with CTREE, Random Forests, and SVM. We found that with DWT Random Forests can classify better than SVM and CTREE. In terms of time usage, we found that CTREE can classify faster than Random Forests, and SVM respectively.

1. INTRODUCTION

At present, business is often highly competitive since there are many new companies. By different companies competing for their efforts as one or as a leader of the company, and is known as a successful business or organization will need to plan for the future. In general, it will use statistical knowledge to apply to their business or organization.

In planning to forecast future events can have a many techniques. Popular techniques, using time series analysis Such as the daily closing value of the Dow Jones industrial average or used to predict air travel in the next two years.

Time series analysis can be applied to many field. Wong, et al. (2014), propose blind biosignal classification model for automatically identify the type (ECG, EEG, EMG or others) of a blind biosignal, and thus can classify a disease or symptom without knowing the type of the source biosignal. Roumani, et al. (2015), propose model for predict the number of vulnerabilities using time series models and to find whether vulnerabilities have trends, levels, and seasonality components.

In this research, we show comparative time series classification with different technique (CTREE, Random Forests, and Support Vector Machine) in term of accuracy and time usage.

2. BACKGROUND

2.1 Time Series

Time series data are data that has relation with time such as the daily closing value of the Dow Jones industrial average. Time series data may be in the manner which the annual data,quarterly or monthly. This all depends on the proper implementation of the benefits.

Time series are used in many fields such as statistics, signal processing, pattern recognition, mathematical finance, weather forecasting and earthquake prediction (Hamilton & Douglas, 1994).

Elements of time series consists of four parts(trend, season, cyclical, irregular component) (Brockwell, et al., 2009).

- Trend is data changes are smooth straight line or curve in the increase or decrease. The value trend of the data movement in a relatively long period.
- Season is data changes are an increase or decrease in the same manner of the period, one that certainly. Also called seasonal changes.The unit of time may be for hourly, daily, weekly, monthly, quarterly, annual data no seasonal variation.Seasonal changes that define the duration of a single iteration in past quite certainly.
- Cyclical are similarities to the seasonal changes. The different is that changes in cycles, each cycle takes longer.
- Irregular component is the change of time series of events that we can not predict such as earthquake, flood or fire.

2.2 Classification Method

2.2.1 Decision Tree Classification

Decision tree are more techniques to classify such as Iterative Dichotomiser 3 (id3), successor of ID3 (C4.5), Classification And Regression Tree (CART), Conditional Inference Trees (CTREE), Random Forest etc. In this research we used CTREE and Random Froests to classify time series data.

CTREE (Hothorn, et al., 2006) is a non-parametric class of regression trees embed tree-structured regression models into a well defined theory of conditional inference procedures. Ctree recursive partitioning for continuous, censored, ordered, nominal and multivariate response variables in a conditional inference framework.

Random forests (Svetnik, et al., 2003) improve predictive accuracy by generate a large number of bootstrap trees (based on random sample of variable), classify a case by use each tree in this new forest, and decide a final predict outcome by combining the results across all of the trees (an average in regression, a majority vote in classification).

2.2.2 Support Vector Machine Classification

SVM (Support Vector Machine) algorithm (Cortes & Vapnik, 1995) is algorithm for classify that has been widely applied to many fields. The concept of SVM are to provide input on practice as a vector in space N dimension, then create hyperplane to separate groups of input vector into various class example for separate data into two class show in figure 1.

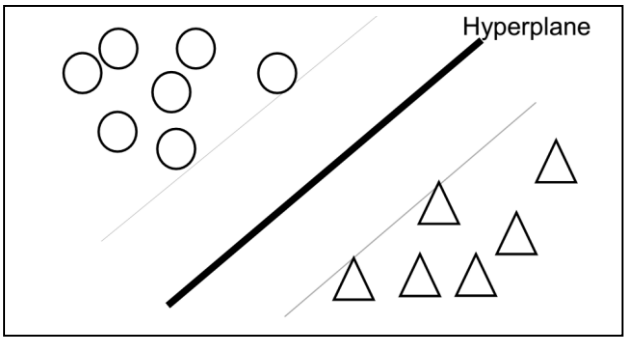

Figure 1. Hyperplane for separate data two dimension.

2.3 Extracted Features

2.3.1 Discrete Wavelet Transform

Wavelet transform (Burrus, et al., 1998) is a mathematical process to describe the structure of the signal system that contain multiple individual signals combined into one signal by signal, the signal is only a small wave called "wavelet". It is a wave that is changing continuously.

The format of the wavelet transform. In general, it can be divided into two types of wavelet (continuous wavelet transform and discrete wavelet transform).

- Continuous wavelet transform formats are similar to the signal analysis for every value of the frequency.

- Discrete wavelet transform (DTW) is the wavelet transform with analysis features by developing patterns to scale and position in a range of not continuous.

In this research we use Discrete Wavelet Transform to extract features from time series and create classification model.

3. METHODOLOGY

Researchers have designed the process of the comparative time series classification with different techniques as show in figure 2.

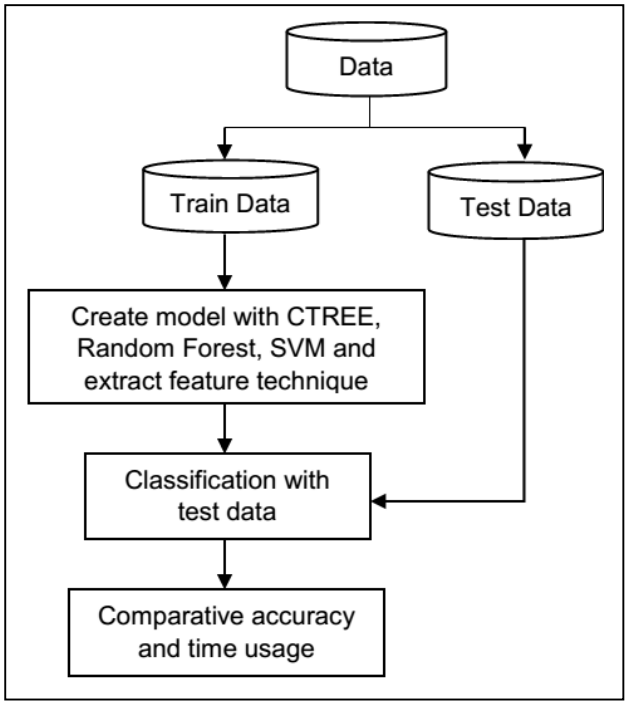

Figure 2. A research framework.

In create model process, we split task into two part, the first part we create model with train data by using CTREE, Random Forests and SVM. Second part we create model with applied Discrete Wavelet Transform to extract features from train data and create model by using CTREE, Random Forest and SVM.

In classification process, we used test data for the evaluation of the accuracy and time usage.

4. EXPERIMENTION AND RESULTS

4.1 Dataset

Our experiment used synthetic control chart time series, japanese vowels and spoken arabic digits from UCI machine learning repository.

- synthetic control chart time series dataset has 600 instances with 60 attributes and the target class has 6 class show in figure 3.

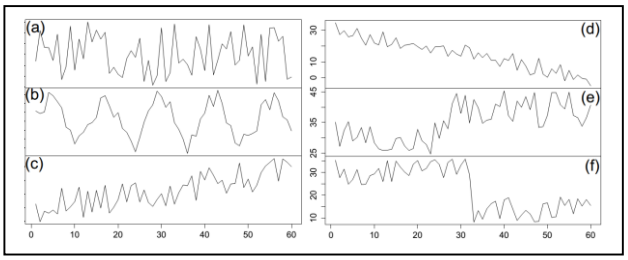

figure 3. class of synthetic control chart time series dataset (a) Normal, (b) Cyclic, (c) Increasing trend, (d) Decreasing trend (e) Upward shift and (f) Downward shift.

- japanese vowels dataset has 9,684 instances with 12 attributes and the target class has 10 class but in this research we used 3,005 instances with 12 attributes classify with 3 class (speaker 1, speaker 2, speaker 3) The target class show in figure 4.

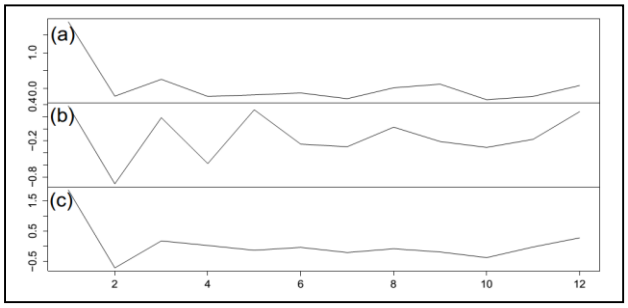

figure 4. class of japanese vowels dataset (a) Speaker 1, (b) Speaker 2, (c) Speaker 3.

- spoken arabic digits dataset has 359,118 instances with 13 attributes and the target class has 10 class but in this research we used 5,288 instances with 13 attributes classify with 2 class (male speaker, female speaker) because this dataset have large data and out of memory. The target class show in figure 5.

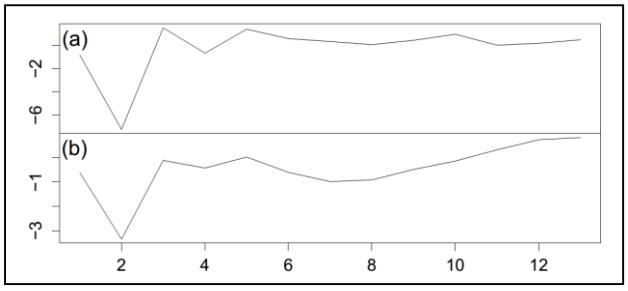

figure 5. class of spoken arabic digits dataset (a) Male speaker, (b) Female speaker.

4.2 Classification Result

In this section, we used 3 classification technique (CTREE, Random Forest, Support Vector Machine). The result show accuracy between classify with original data and used dynamic time warping before classify of each classification technique.

4.2.1 Classification result

Table 1. Comparative accuracy and time usage of synthetic control chart time series dataset.

	CTREE		RF		SVM	
	Acc.	Time	Acc.	Time	Acc.	Time
Ori	80.00	**0.41**	97.79	0.73	**98.3**	0.88
DTW	87.78	**3.2**	**96.11**	3.35	70.0	3.83

*ori = original data, DTW = dynamic time warping, Acc = accuracy, RF = random forest, SVM = support vector machine

From table 1. show the comparative accuracy and time usage for synthetic control chart time series dataset. It can be seen that when we create model with train data and classifying with different classification technique, in term of accuracy we found that SVM (98.30%) can classify better than Random Forest (97.79%) and CTREE (80.00%) respectively. In terms of time usage we found that CTREE (0.41s) can classify faster than Random Forest (0.73s) and SVM (0.88s) respectively. And when we create model with applied DTW to extract features from train data and classifying with different classification technique, in terms of accuracy we found that with DTW Random Forest (96.11%) can classify more than CTREE (87.78%) and SVM (70.00%) respectively. In terms of time usage we found that CTREE (3.20s) can classify faster than Random Forest (3.35s) and SVM (3.83s) respectively.

4.2.2 Classification japanese vowels

Table 2. Comparative accuracy and time usage of japanese vowels dataset.

	CTREE		RF		SVM	
	Acc.	Time	Acc.	Time	Acc.	Time
Ori	92.49	**0.28**	96.50	1.07	**97.58**	0.36
DTW	86.82	**7.8**	92.43	9.22	**95.41**	8.08

*ori = original data, DTW = dynamic time warping, Acc = accuracy, RF = random forest, SVM = support vector machine

From table 2. show the comparative accuracy and time usage for japanese vowels dataset. It can be seen that when we create model with train data and classifying with different classification technique, in terms of accuracy we found that SVM (97.58%) can classify better than Random Forest (96.50%) and CTREE (92.49%) respectively. In terms of time usage we found that CTREE (0.28s) can classify faster than SVM (0.36s) and Random Forest (1.07s) respectively. And when we create model with applied DTW to extract features from train data and classifying with different classification technique, in terms of accuracy we found that SVM (95.41%) has higher accuracy than Random Forest (92.43%) and CTREE (86.82%) respectively. In terms of time usage we found that CTREE (7.80s) can classify faster than SVM (8.08s) and Random Forest (9.22s) respectively.

4.2.3 Classification spoken arabic digits

Table 3. Comparative accuracy and time usage of spoken arabic digits dataset.

	CTREE		RF		SVM	
	Acc.	Time	Acc.	Time	Acc.	Time
Ori	68.96	**0.6**	74.63	3.15	**77.55**	2.23
DTW	69.29	**14.26**	**80.79**	17.05	79.69	17.86

*ori = original data, DTW = dynamic time warping, Acc = accuracy, RF = random forest, SVM = support vector machine

From table 3. show the comparative accuracy and time usage for spoken arabic digits dataset. It can be seen that when we create model with train data and classifying with different classification technique, in terms of accuracy we found that SVM (77.55%) has higher accuracy than Random Forest (74.63%) and CTREE (68.96%) respectively. In terms of time usage we found that CTREE (0.60s) can classify faster than SVM (2.23s) and Random Forest (3.15s) respectively. Then we create model with applied DWT to extract features from train data and classifying with different classification technique, in terms of accuracy we found that Random Forest (80.79%) can classify better than SVM (79.65%) and CTREE (69.29%) respectively. In terms of time usage we found that CTREE (14.26s) can classify faster than Random Forest (17.05s) and SVM (17.86s) respectively.

5. CONCLUSIONS

In this research, we show comparative in terms of accuracy and time usage for time series classification with CTREE, Random Forest, and SVM. In terms of accuracy we found that SVM can classification better than Random Forest and CTREE respectively. In term of times usage we found that CTREE can classify faster than SVM and Random Forest respectively.

We use Discrete Wavelet Transform (DWT) to extract features and create model we found that when we used extract features technique can increase accuracy for some dataset and some classification technique but as a result, it take more time. In terms of accuracy we found that with DTW Random Forest has higher accuracy than SVM and CTREE respectively. In term of times usage we found that CTREE can classify faster than Random Forest and SVM respectively.

REFERENCES

Brockwell, Peter, J. and Richard, A. D., Time series: theory and methods, Springer Science & Business Media, 2009.

Burrus, C.S., Gopinath, R.A. and Guo, H., Introduction to Wavelets and Wavelet Transforms: A Primer, Prentice-Hall, Inc., 1998.

Cortes, C. and Vapnik, V., Support-vector networks, Machine learning, vol. 20, no. 3, pp. 273-297, 1995.

Hamilton and Douglas, J., Time series analysis, Princeton: Princeton university press, Vol. 2, 1994.

Hothorn, T., Hornik, K. and Zeileis, A., Unbiased recursive partitioning: A conditional inference framework, Journal of Computational and Graphical statistics, vol. 15, no. 3, pp. 651-674, 2006.

Roumani, Y., Nwankpa, J. K., Roumani, Y. F., Time series modeling of vulnerabilities, Computers & Security, vol. 51, pp. 32-40, 2015.

Svetnik, V., Liaw, A., Tong, C., Culberson, J. C., Sheridan, R. P. and Feuston, B. P., Random forest: a classification and regression tool for compound classification and QSAR modeling, Journal of chemical information and computer sciences, vol. 43, no. 6, pp. 1947-1958, 2003.

Wong, D. F., Chao, L. S., Zeng, X., Vai, M. I. and Lam, H. L., Time series for blind biosignal classification model, Computers in biology and medicine, vol. 54, pp. 32-36, 2014.

Keerachart Suksut is currently a PHD. student with the School of Computer Engineering, Suranaree University of Technology, Thailand. He received his bachelor degree and master degree in Computer Engineering from Suranaree University of Technology in 2011 and 2013 respectively. In his current research includes classification time series.

Nittaya Kerdprasop is an associate professor at the School of Computer Engineering, Suranaree University of Technology, Thailand. She received her bachelor degree in Radiation Techniques from Mahidol University, Thailand, in 1985, master degree in Computer Science from the Prince of Songkla University, Thailand, in 1991 and doctoral degree in Computer Science from Nova Southeastern University, U.S.A, in 1999. She is a member of ACM and IEEE Computer Society. Her research of interest includes Knowledge Discovery in Databases, Artificial Intelligence, Logic Programming, and Intelligent Databases.

Kittisak Kerdprasop is an associate professor and chair of the School of Computer Engineering, Suranaree University of Technology, Thailand. He received his bachelor degree in Mathematics from Srinakarinwirot University, Thailand, in 1986, master degree in Computer Science from the Prince of Songkla University, Thailand, in 1991 and doctoral degree in Computer Science from Nova Southeastern University, U.S.A., in 1999. His current research includes Data mining, Artificial Intelligence, Functional and Logic Programming Languages, Computational Statistics.

Data Mining in Highly Imbalanced Big Data

Kittipong Chomboon, Kittisak Kerdprasop, Nittaya Kerdprasop
School of Computer Engineering, Suranaree University of Technology, Thailand

ABSTRACT

This research studies about the problems of data mining via using big data, because the big data is the large data set it have high dimensions. The big data using a lot of memory in learning process on data mining task. This research aim to using big data base on classification task with two feature selection techniques chi-squared and information gain. This research we using KDD'98 dataset it is imbalanced dataset, 95% of positive class and 5% of negative class. We compare the result of classification by regression trees and Naïve Bayes, the result shown regression trees with both feature selection have the same accuracy 94.3%, Naïve Bayes with both feature selection have accuracy around 74% but it can identify minority class better than regression trees.

1. INTRODUCTION

Present computer technology change from the past it has progressed at a speed and it has tremendous effect to the storage data. With enormously increasing data, data mining has been proposed to automatic analysis of large data. Data mining (Cabena, et-al., 1998) is focus on discovery of interesting patterns from large data. Discovered patterns can be in various forms such as tree model for classification, a set of rules for association. The large data who has high dimension and tremendous instances we can call "Big Data".

The popular algorithms for classification task is Naïve Bayes (Rish, 2001) and trees (Prasad, et-al., 2006), there are powerful techniques to discover a model for future event prediction. But for a big data in the learning process of algorithm it used very much memory and time to create model some time it out of memory to use, this problem we used feature selection to decrease dimensions of big data for able to create model. In this research we use two feature selection chi-squared (Rao, 1984) and information gain (Kent, 1983).

In this research, we compare true positive, true negative, time of creating model, time of predict test data, f-measure on both class and accuracy (Hastie, et-al., 2005) using chi-squared and information gain feature selection with Naïve Bayes and regression tree algorithms .

2. ANALYSIS

In this section we will describe shortly about the algorithms and techniques are using in this research.

2.1 ALGORITHMS

- Naïve Bayes
  Naïve Bayes classifier are the algorithm base on probabilistic to classify new data. It can often outperform more sophisticated classification methods.

- Regression Trees
- Regression trees are create predictive tree model with maps observations about an item to the target class.

2.2 FEATURE SELECTION

- Information Gain
  Information gain used finds weights of discrete attributes basing on their correlation with continuous class attribute. If it have high weights it mean high importance to use that attribute for a good results.

- Chi-Squared
  Chi-squared or x^2 is the algorithm finds weights of discrete attributes basing on chi-squared test. If have a high chi-squared value it mean that attribute can be used for a good results.

2.3 FRAMEWORK

This section we present the framework of our research show as Fig. 1.

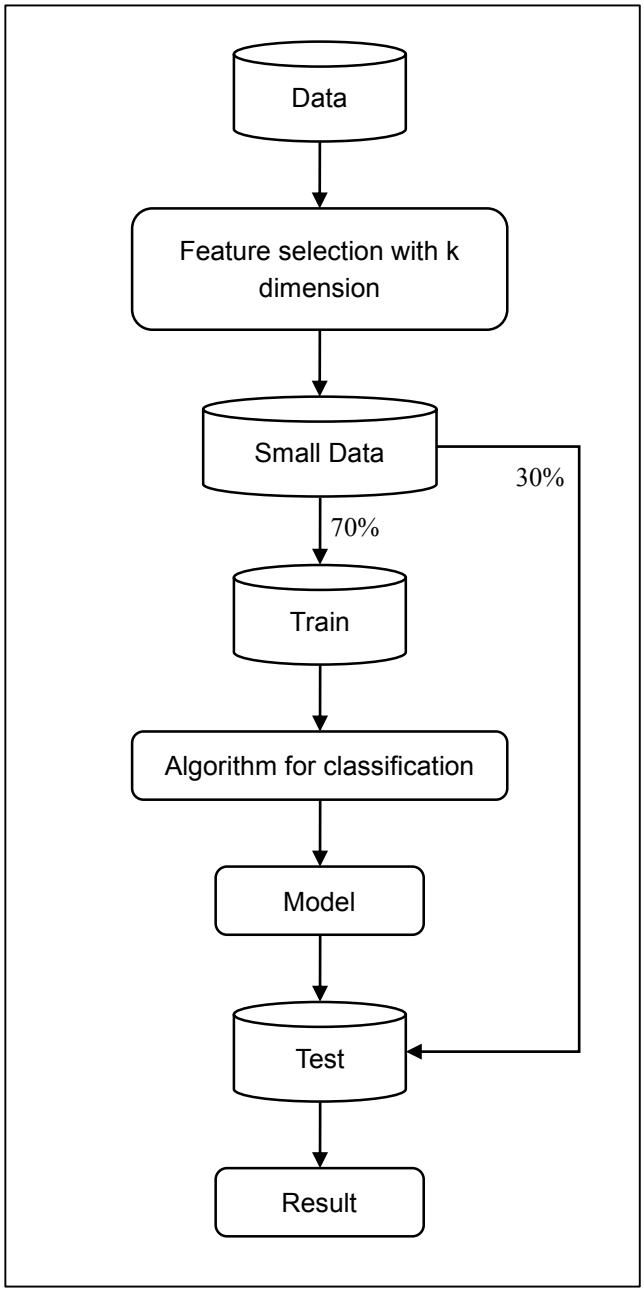

Fig. 1. The framework of this research

Then we will describe these framework step by step. Step one: we use KDD93' dataset to decrease dimension by using two feature selection chi-square and information gain for select k dimension, in this research we set k = 2, 5, 10, 20, 30, 40, 50 for each round.

Step two: now we have small dataset then we split small dataset 70% to train data and 30% to test data, train data are the data for using to create model and test data is the data for using to validating model.

Step three: we use train data to create model using Naïve Bayes and regression tree for each round. Now we already have model for validate.

Step four: we validating model with test data, then we have the result for analysis in next section.

3. EXPERIMENT

This section we will show the environment setup and result from our framework.

The data for using with our framework is KDD'98 dataset, it have 95412 instances 64 dimension 90569 (95%) instances for positive class and 4843 (5%) instances for negative class.

The result we show comparative about Naïve Bayes and regression tree algorithms between both feature selection techniques show as Table 1 – 6 and Fig. 2 – 7.

Table 1 Time used for create model

k	Algorithms			
	Regression Tree		Naïve Bayes	
	IG	CS	IG	CS
2	6.654	6.693	0.144	0.290
5	6.940	6.928	0.136	0.135
10	8.013	7.842	0.201	0.195
20	9.551	9.423	0.310	0.291
30	10.852	10.796	0.449	0.392
40	12.312	11.967	0.567	0.460
50	13.466	13.534	0.627	0.621

Table 2 Time use for predict

k	Algorithms			
	Regression Tree		Naïve Bayes	
	IG	CS	IG	CS
2	0.085	0.096	6.276	5.137
5	0.056	0.054	8.054	8.410
10	0.093	0.081	12.247	12.326
20	0.143	0.144	20.568	20.454
30	0.136	0.121	26.504	26.740
40	0.160	0.167	33.489	33.098
50	0.215	0.200	39.842	39.143

Table 3 TP rate

k	Algorithms			
	Regression Tree		Naïve Bayes	
	IG	CS	IG	CS
2	99.35%	99.35%	79.96%	79.96%
5	99.35%	99.35%	79.86%	79.86%
10	99.35%	99.35%	77.25%	77.25%
20	99.35%	99.35%	75.96%	77.30%
30	99.35%	99.35%	76.47%	76.51%
40	99.35%	99.35%	76.50%	75.85%
50	99.35%	99.35%	75.87%	75.83%

Table 4 TN rate

k	Algorithms			
	Regression Tree		Naïve Bayes	
	IG	CS	IG	CS
2	0.75%	0.75%	19.18%	19.18%
5	0.75%	0.75%	21.16%	21.16%
10	0.75%	0.75%	28.63%	28.63%
20	0.75%	0.75%	32.80%	30.82%
30	0.75%	0.75%	32.74%	32.53%
40	0.75%	0.75%	32.60%	34.18%
50	0.75%	0.75%	34.38%	34.24%

Table 5 F-measure on positive class

k	Algorithms			
	Regression Tree		Naïve Bayes	
	IG	CS	IG	CS
2	97.07%	97.07%	86.77%	86.77%
5	97.07%	97.07%	86.75%	86.75%
10	97.07%	97.07%	85.31%	85.31%
20	97.07%	97.07%	84.60%	85.40%
30	97.07%	97.07%	84.92%	84.94%
40	97.07%	97.07%	84.94%	84.56%
50	97.07%	97.07%	84.58%	84.55%

Table 6 F-measure on negative class

k	Algorithms			
	Regression Tree		Naïve Bayes	
	IG	CS	IG	CS
2	1.34%	1.34%	7.81%	7.81%
5	1.34%	1.34%	8.55%	8.55%
10	1.34%	1.34%	10.40%	10.40%
20	1.34%	1.34%	11.34%	11.17%
30	1.34%	1.34%	11.50%	11.45%
40	1.34%	1.34%	11.47%	11.74%
50	1.34%	1.34%	11.82%	11.76%

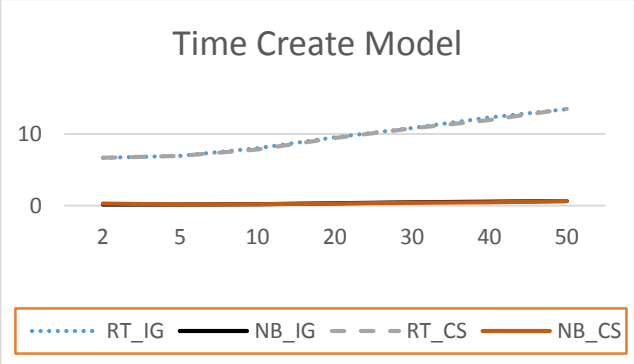

Fig. 2. Time used create model

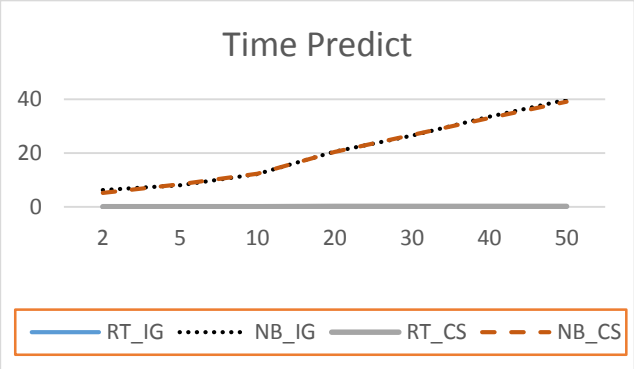

Fig. 3. Time used predict

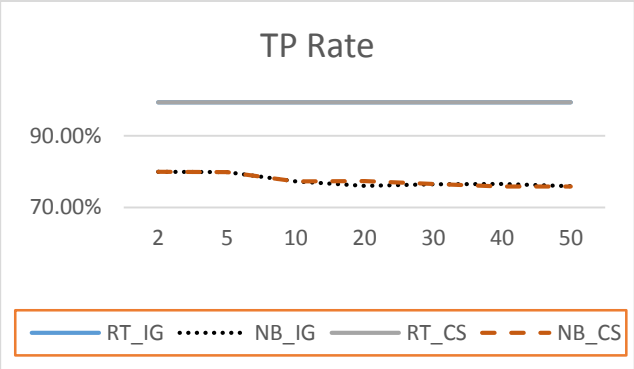

Fig. 4. Overview TP rate

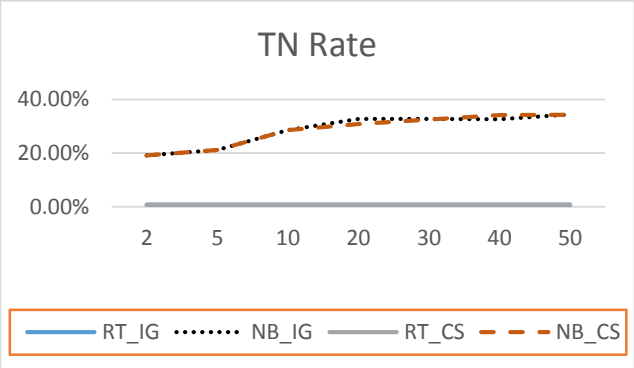

Fig. 5. Overview TN rate

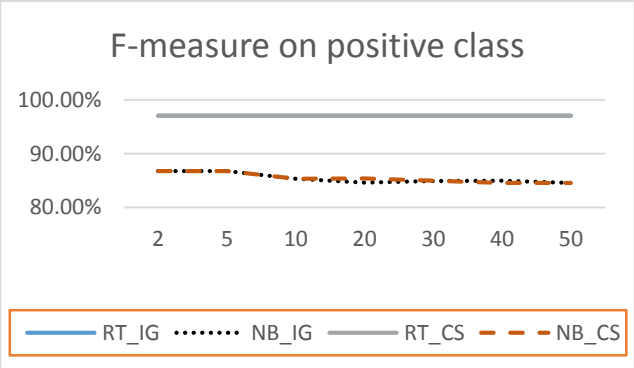

Fig. 6. Overview F-measure on positive class

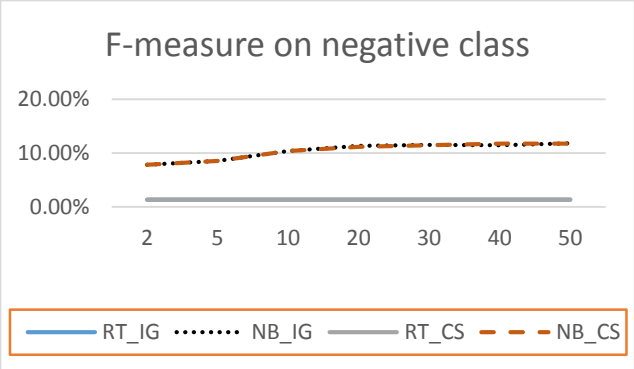

Fig. 7. Overview F-measure on negative class

4. CONCLUSION

In this research we proposed techniques to classify big data with two feature selection and two algorithm with imbalanced big data. We use KDD'98 dataset it contain 2 class, 90569 (95%) instances for positive class and 4843 (5%) instances for negative class. The result present both feature selection does not have deferent result, but the algorithm for classify really affect for TN rate. Shown as Fig. 4 and 7, Naïve Bayes algorithm can identify negative class better than regression tree algorithm, but Naïve Bayes used time to predict more than regression tree.

REFERENCES

Cabena, P., Hadjinian, P., Stadler, R., Verhees, J., and Zanasi, A., Discovering data mining: from concept to implementation. Prentice-Hall, Inc, 1998.

Hastie, T., Tibshirani, R., Friedman, J., and Franklin, J., The elements of statistical learning: data mining, inference and prediction. The Mathematical Intelligencer, 27(2), 83-85, 2005.

Kent, J. T., Information gain and a general measure of correlation, Biometrika 70, no. 1: 163-173, 1983.

Prasad, A. M., Iverson, L. R., and Liaw, A., Newer classification and regression tree techniques: bagging and random forests for ecological prediction. Ecosystems 9, no. 2: 181-199, 2006.

Rao, J. N., and Scott, A. J., On chi-squared tests for multiway contingency tables with cell proportions estimated from survey data. The Annals of Statistics, 46-60, 1984.

Rish, I., An empirical study of the naive Bayes classifier, In IJCAI 2001 workshop on empirical methods in artificial intelligence, IBM New York, vol. 3, no. 22, pp. 41-46, 2001.

Kittipong Chomboon

He is currently a PhD candidate student with the School of Computer Engineering, Suranaree University of Technology, Thailand. His current research of interest includes Classification

Kittisak Kerdprasop

He is an associate professor and chair of the School of Computer Engineering, Suranaree University of Technology, Thailand. His current research of interest includes Data mining, Artificial Intelligence, Functional and Logic Programming Languages, Computational Statistics.

Nittaya Kerdprasop

She is an associate professor at the School of Computer Engineering, Suranaree University of Technology, Thailand. She is a member of ACM and IEEE Computer Society. Her research of interest includes Knowledge Discovery in Databases, Artificial Intelligence, Logic Programming, and Biomedical Informatics

AN EMPIRICAL STUDY TO REDUCE MODEL COMPLEXITY WITH THE MULTIVARIATE OUTLIER DECTECTION

Ratiporn Chanklan*, Kittisak Kerdprasop, Nittaya Kerdprasop
School of Computer Engineering, Suranaree University of Technology, Thailand

ABSTRACT

This research studies the outliers using multivariate outlier detection. Outlier is a very different data value from other data. If use data with outlier to create model for classification, the model will has complex to make classification process delay and poor performance. We use outlier detection in multivariate data by the statistics value and a box and whisker plot (sometimes called a boxplot). We use whisker length in boxplot with four values: 1xIQR, 1.5xIQR, 2xIQR and 2.5xIQR. Outliers may be plot as individual points in outside area of whisker. We apply data that remove outlier and outlier data to create model by decision tree algorithm. Then we compare size of tree and accuracy.

1. INTRODUCTION

Different data value which has more and less when compare other data is call outlier. Outlier is causes of classification are inaccurate. Outlier detection have many studies such as Hawkins, et al. (2002), use replicator neural networks (RNNs) to provide a measure of the outlier of data records. Outlier detection can be applied during the data cleansing process of data mining to identify problems with the data itself, and to fraud detection where groups of outliers are often of particular interest. Filzmoser, et al. (2005), propose method for multivariate outlier detection able to distinguish between extreme values of a normal distribution and values originating from a different distribution (outliers). To display multivariate outliers spatially on a map, the multivariate outlier plot. Vijayarani, et al. (2011), outlier detection is a very important research problem in data mining. Clustering algorithms are used for detecting the outliers efficiently. They used algorithms PAM, CLARA, CLARANS and ECLARANS. The outlier detection accuracy is very good in the propose ECLARANS clustering algorithm.

In this research we show the comparative which data that remove outlier and outlier data classification with decision tree algorithm in term size of tree and accuracy.

2. ANALYSIS

2.1 Multivariate Outlier Detection

Multivariate outlier detection is apply from univariate outlier detection apply it to multivariate data. It use box and whisker plot or called a boxplot to find outlier, find outlier for each component, which gives a list of outliers, union all list of outliers in data (Yanchang, 2012). The summary of boxplot show the important characteristics of a distribution of scores. It is a graph that presents information from a five of statistics value on a boxplot: the minimum score, the maximum score, the median score, the 1st (Q1) and 3rd (Q3) quartiles (Salkind, 2007). The central box shows the distance between the first and third quartiles with the median, the ends of the box are the upper and lower quartiles, so the box is spans the interquartile range. The line extended from the box is call whisker, a length equal to 1.5xIQR. The points in the outside area of whiskers marked with a diamond are outlier.

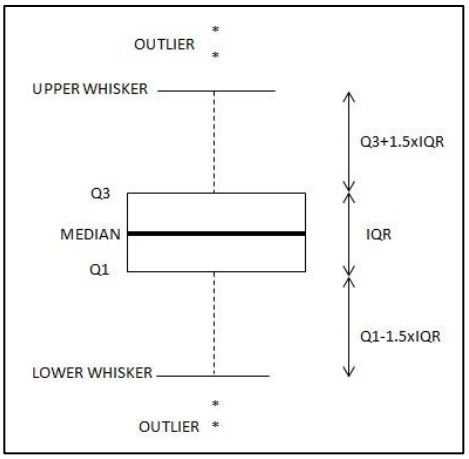

Fig. 1 Univariate outlier detection with boxplot.

2.2 Decision Tree Algorithm

Decision trees represented rules, which can be understand easy and used in knowledge system such as database. Decision trees can handle both categorical and numerical data. It is use data creation to predict the model in form of a tree. The decision tree is similar to inverted tree, the top node in a decision tree called root node. For each node is feature or attribute, each branch will display the results value of the test and leaf (Leaf node) is schedule classes. The order attributes are chosen by Information Gain value, high Information Gain value is root node and next node has Information Gain value descending order (Quinlan, 1986). One problem when create decision tree models is the model has a deep branch and node that causes model to complex (Yao et al, 2009)

3. METHODOLOGY

We used breast cancer data sets from the UCI Machine Learning Repository. Breast cancer data set has 699 instances with 10 attributes and the target class has 2 classes: benign and malignant. It has missing attribute values 16 instances. In this paper we use multivariate outlier detection techniques to find outlier data and decision tree algorithm to create model for compare size of tree and accuracy. The process of implementation in this paper is shown in Figure 2.

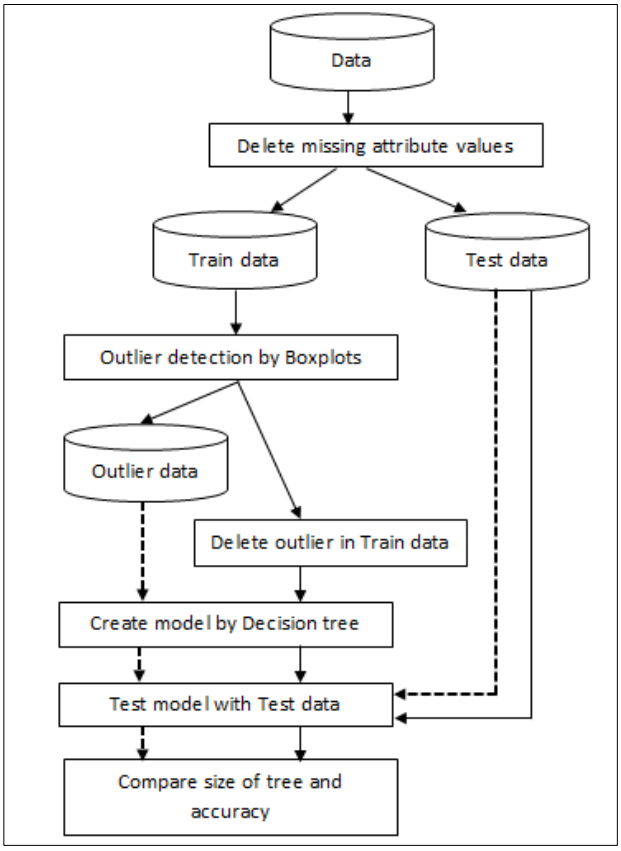

Fig. 2 The process of implementation.

This paper use R language by RStudio program. The first step we delete 16 instances that missing attribute values from data to remaining original data 683 instances, split train data 478 instances and test data 205 instances. We use train data to find outlier data by boxplot function, use length whiskers in boxplot four values: 1xIQR, 1.5xIQR, 2xIQR and 2.5xIQR. Then, input deleted outlier in train data and outlier data to create model by decision tree algorithm. We test model by input test data to model and compare size of tree for each model and accuracy.

4. EXPERIMENT AND RESULTS

This research measure the performance of the model by compare accuracy and size of tree from decision tree. The experimental results create tree from train data, remove outlier in train data and outlier data as follows figure 3 and 4.

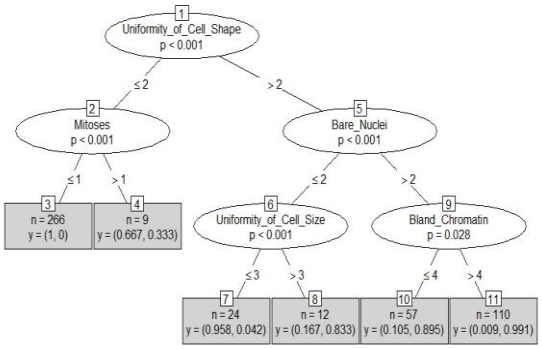

(a) Train data (# of out = 0, accuracy = 94.63%)

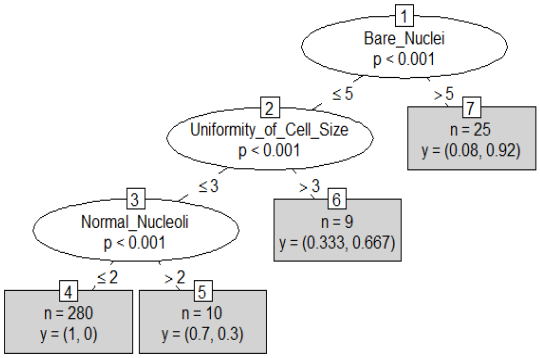

(b) 1xIQR (# of out = 154, accuracy = 94.63%)

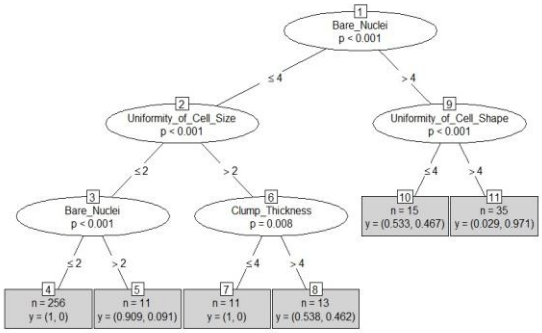

(c) 1.5xIQR (# of out = 137, accuracy = 81.95%)

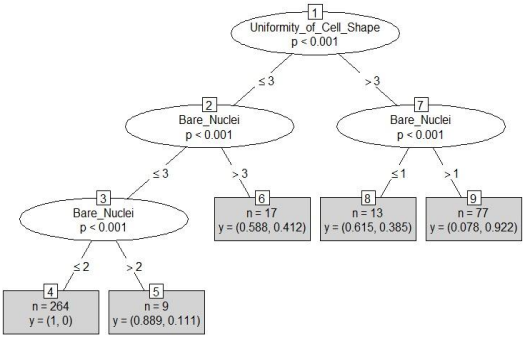

(d) 2xIQR (# of out = 98, accuracy = 88.78%)

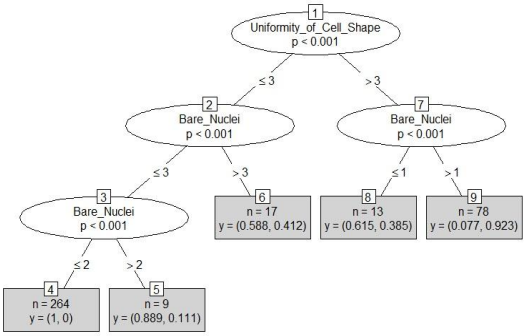

(e) 2.5xIQR (# of out = 97, accuracy = 88.78%)

Fig. 3 Trees from train data and data remove outlier.

Figure 3 shows trees from train data and data removed outlier use length whiskers 1xIQR, 1.5xIQR, 2xIQR and 2.5xIQR. A tree in train data has 5 nodes and accuracy 94.63% from 478 instances, 1xIQR is a small tree has 3 nodes, outlier 154 instances and accuracy 94.63% from 324 instances, 1.5xIQR has 5 nodes, outlier 137 instances and accuracy 81.95% from 341 instances, 2xIQR is a small tree has 4 nodes, outlier 98 instances and accuracy 88.78% from 380 instances, 2.5xIQR has 4 nodes, outlier 97 instances and accuracy 88.78% from 381 instances. After delete outlier in data, a size of tree mostly reduce size is change with reduced accuracy.

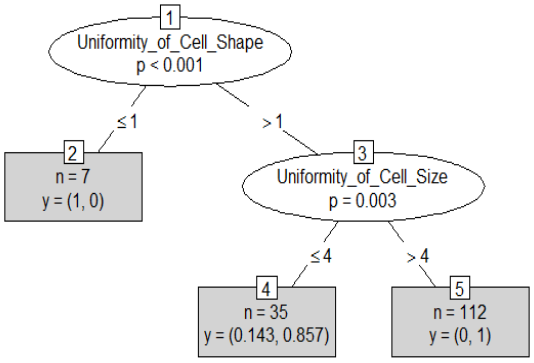

(a) 1xIQR (# of out = 154, accuracy = 83.41%)

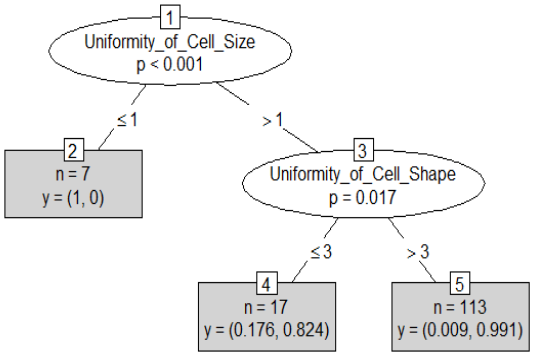

(b) 1.5xIQR (# of out = 137, accuracy = 84.87%)

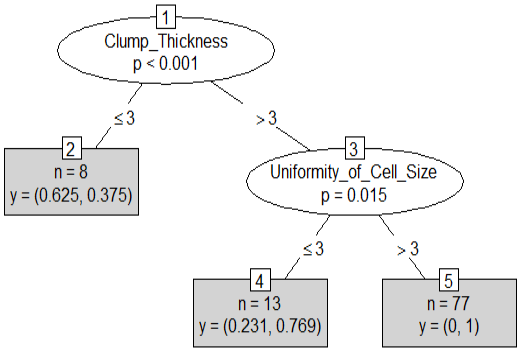

(c) 2xIQR (# of out = 98, accuracy = 71.22%)

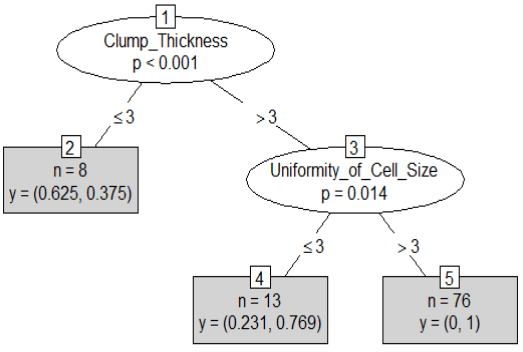

(d) 2.5xIQR (# of out = 97, accuracy = 71.22%)

Fig. 4 Trees from outlier data.

Figure 4 shows trees from outlier data. We also use outlier data to find by use length whiskers 1xIQR, 1.5xIQR, 2xIQR and 2.5xIQR. We create tree and test performance tree by test data same as test data in figure 3. Size of tree in 1xIQR has 2 nodes and accuracy 83.41%, 1.5xIQR has 2 nodes and accuracy 84.87%, 2xIQR has 2 nodes and accuracy 71.22%, 2.5xIQR has 2 nodes and accuracy 71.22%. It is surprise that outlier data is different value from main data but when use create to tree, it have small size and accuracy is not less than 70%.

5. CONCLUSION

In this research we show the comparative size of tree and accuracy. We find outlier for each column in multivariate data by boxplot, then union outlier all columns in data. Moreover we create model by decision tree. The results show when delete outlier in data before create tree, tree is mostly compact but change accuracy reduce. When delete outlier in train data by 1xIQR, tree is compact and accuracy value same as train data. Furthermore we use outlier data to create model, tree very compact and accuracy values reduce 10%. In our future work we will use tree create from outlier data and will try to improve performance in classification.

REFERENCES

Vijayarani, S., and S. Nithya., An Efficient Clustering Algorithm for Outlier Detection. International Journal of Computer Applications , Vol.32, No.7, 0975-8887, 2011.

Hawkins, S., He, H., Williams, G., Baxter, R., Outlier detection using replicator neural networks. In Data warehousing and knowledge discovery . Springer Berlin Heidelberg, pp.170-180, 2002.

Filzmoser, Peter, Robert G. Garrett, and Clemens Reimann., Multivariate outlier detection in exploration geochemistry. Computers & Geosciences, Vol.31, No.5, pp. 579-587, 2005.

Zhao, Yanchang., R and data mining: Examples and case studies. Academic Press, pp.64-73, 2012.

Neil J. Salkind ., Encyclopedia of Measurement and Statistics, pp.111-112, 2007.

J. R. Quinlan., ductio of Decisio Trees. Machine Learning , vol.1, No.1, pp. 81-106, 1986.

Yu, Y., Z. Fu, X. Zhao, and W. Cheng Yu., Combining classifier based on decision tree. Information Engineering ICIE'09., Vol. 2, pp. 37-40, 2009.

Ratiporn Chanklan is currently a master student with the School of Computer Engineering, Suranaree University of Technology, Thailand. She received his bachelor degree in Computer Engineering from Suranaree University of Technology in 2013. Her current research of interest includes Classification

Kittisak Kerdprasop is an associate professor and chair of the School of Computer Engineering, Suranaree University of Technology, Thailand. He received his bachelor degree in Mathematics from Srinakarinwirot University, Thailand, in 1986, master degree in Computer Science from the Prince of Songkla University, Thailand, in 1991 and doctoral degree in Computer Science from Nova Southeastern University, U.S.A., in 1999. His current research includes Data mining, Artificial Intelligence, Functional and Logic Programming Languages, Computational Statistics.

Nittaya Kerdprasop is an associate professor at the School of Computer Engineering, Suranaree University of Technology, Thailand. She received her bachelor degree in Radiation Techniques from Mahidol University, Thailand, in 1985, master degree in Computer Science from the Prince of Songkla University, Thailand, in 1991 and doctoral degree in Computer Science from Nova Southeastern University, U.S.A, in 1999. She is a member of ACM and IEEE Computer Society. Her research of interest includes Knowledge Discovery in Databases, Artificial Intelligence, Logic Programming, and Intelligent Databases.

ON IMPROVING K-MEANS CLUSTERING EFFICIENCY WITH IMPORTANCE AND CORRELATION ANALYSES

Tippaya Thinsungnoen*, Kittisak Kerdprasop, Nittaya Kerdprasop
Data engineering research unit, School of computer engineering
Suranaree university of technology, Thailand

ABSTRACT

The k-means clustering has been a popular technique widely used and used with data distribution both gaussianity and non-gaussianity, which if data distribution is non-gaussianity making the efficiency of data clustering will be low. This research aims at study of improve the efficiency for k-means clustering with feature selection. The experimental comparing feature selection techniques between random forests and correlation, using real data various 4 data sets from UCI machine learning repository. Evaluate the effectiveness of the clustering used by the purity value and f-measure value. The results showed that both feature selection technique provide higher efficiency for k-means clustering in all data sets.

Keyword: k-Means clustering, Random forest, Correlation, Purity, F-measure.

1. INTRODUCTION

A data clustering is process of knowledge discovery in databases. There are various algorithms for data clustering, but one popular algorithm is k-means algorithm is due to a simple operation and a fast processing (Theodoridis et al., 2010). The principle of k-means algorithm is separate data into k cluster and then calculating the means to represent each cluster, which the means represented centroid for measuring the similarity and dissimilarity of the same cluster (Shahbaba and Beheshti, 2014).

Despite such advantages as previous mention, however, k-means clustering has also a limitation, it works well with data that is hyper-spherical cluster shapes and performs poorly when the true underlying clusters are arbitrarily shaped (Ryali et al., 2015). In addition, the data used for clustering may contain features that are not suitable for processing such as has the number of attributes more, each attribute irrelevant, the scale of the data is very different (high or low) and so on. The limitations mentioned above, we must find solution to improve the efficiency of clustering method.

Lee et al. research on the automatic detection of pulmonary edema can help show abnormalities in the lung by CT image using by random forest technique, and presented structure for the hybrid-random forest base on according to the classification of pulmonary nodule from the clustering. The experiments conducted by using scans of the lung patients, including 32 patients and 5,721 images, which are marked by projecting an expert radiologist. The result shows sensitivity best is 98.33%, and the specificity best is 97.11%.

Saha et al. has proposed clustering algorithm named Incremental learning based multiobjective fuzzy clustering for categorical data. The research offered the adjustment multiobjective base on the principles of fuzzy clustering algorithms then integrated with random forest. The experiment finding from a comparison with other method to synthesize 6 data sets and real 4 data sets, the results shows that better than other methods.

Ai-li et al. have proposed clustering and correlation Analysis of the Industry Networks so considered the structure of the network and the correlation weight to determine the correlation analysis. The study has found that it can optimize the industrial structure.

Tosi et al have proposed clustering traffic information based on the correlation analysis for select a variable that is outstanding for the group. The study evaluated the experiment with multiple data sets. The synthetic data and real data The results showed that the accuracy and durability than conventional clustering methods are available.

Yu et al. have presented the concept of clustering that can be grouped to data from multiple different sources and different structure of the data. By strategies called selection features important information for the group. This new concept in the evaluation to selection features by combining the use of the correlation included in their selection techniques. The experimental data and information from the UCI cancer gene operating results showed that the method presented better results with all data sets and more effective strategy than all other options are compared.

Therefore, this paper, has studied performance improvements for k-means clustering technique chosen by comparative feature selection such as random forest and correlation. By selecting a specific importance value of feature assign to k-means clustering. In experiments using real 4 data sets from the UCI, using purify measure and f-measure for evaluating the performance of the clustering.

2. METHODOLOGY

2.1 k-Means clustering method

The k-means clustering technique has been the most widely used because it is easy to understand the process is not complicated. The Means was the center of the cluster. The k-Means algorithm can be described by the following steps.

Algorithm: k-means clustering (Kwedlo, W., 2011)

(a) Choose initial centroids $\{m_1,\ldots,m_k\}$ of the clusters $\{C_1,\ldots,C_k\}$.

(b) Calculate new cluster membership. A feature vector x_j is assigned to the cluster C_i if and only if

$$= \arg\min_{k=1,\ldots,k} ||x_j - m_k||^2 \quad (1)$$

(c) Recalculate centroids for the cluster according.

$$m_i = \frac{1}{|C_i|} \sum_{x_j \in C_i} x_j. \quad (2)$$

(d) If none of the cluster centroids have changed, finish the algorithm. Otherwise go to Step (b).

2.2 Feature selection with random forest technique

Random forest is a combination of tree predictors such that each tree depends on the values of a random vector sampled independently and the same distribution of trees. An application randomly features selection for each node. Internal estimation to determine the strength of the error and relationships and is used to show an increasing number of features used in isolation. The estimation also used to measure the importance of feature (Breiman, L., 2001).

The random forest technique is the classification accuracy than other methods due to (i) reduce the average of variance of feature (ii) reduce of correlation between specific feature and other feature (Lee, SLA, 2010). The selected appropriate feature led to classify successfully. An exploration for importance of feature can be observed from the plot of the means of accuracy show in fig. 1. The figure shows that relationship between means of accuracy and feature for example, if the appropriate feature greater than and equal to 2 we have to be select including V2, V3, V7, V8, V9, V10, V12 and V13.

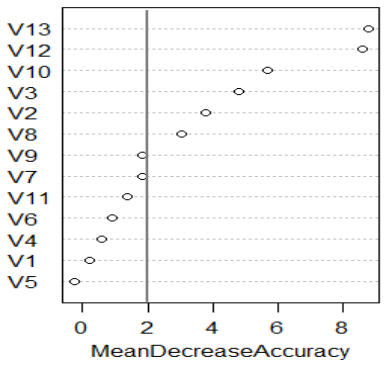

Fig. 1 Measure of variable importance for random forest.

2.3 Feature selection with correlation technique

Correlation coefficient or another word that Pearson's product moment is shows the linear relationship. It has ranged from -1.0 to +1.0 (Correlation coefficient. 2015).

An exploration for correlation coefficient can be observed from the plot of importance value show in fig. 2. if an appropriate is importance >= 0.3 we have to be select including V3, V8, V9, V10, V12 and V13.

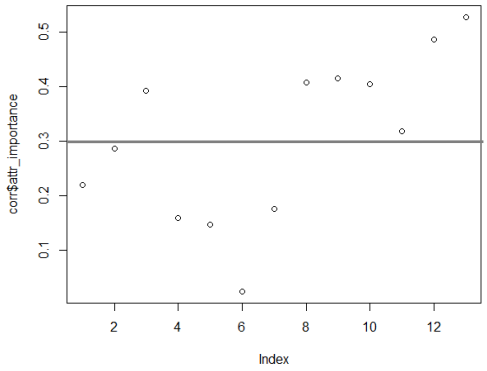

Fig. 2 Measure of variable importance for correlation analysis.

3. EXPERIMENTAL AND RESULT

3.1 Experiments on real data sets

This research was, experiment on real 4 data sets that are characteristic of different data, different number of features and different scale of value inside each feature. The experimental setting data are training data and testing data such as 70:30 percent respectively. Details of the trial are shown in Table 1.

Table 1 Statistics of real data sets.

Data set	Instance	Attribute	Class
Thyroid-disease	7,200	21	3
Heart disease	270	13	2
Pima Indians diabetes	768	8	2
Breast cancer Wisconsin	699	10	2

The experiment we used k-means clustering techniques to clustering with 4 data sets of comparative data in three formats. i.e, original data and data from using feature selection techniques such random forest and correlation analysis. The result shows that the clustering method with data sets was through feature selection can be separate very clear. As shown, the plot results grouped in Table 2.

3.2 Evaluate the clustering efficiency

In evaluating the performance of the clustering has various measures (Mohammed et al., 2014). This paper, we has two measures for clustering evaluate that are purity value and f-measure value, principle as follows.

a. The purity value is the measurement that member are clustering situation, the Purity for cluster C_i defined below.

$$purity_i = \frac{1}{n_i} \max_{j=1}^{k} \{n_{ij}\} \quad (3)$$

Therefore, the purity of clustering C is defined as the weighted sum of the cluster-wise purity values.

$$purity = \sum_{i=1}^{r} \frac{n_i}{n} purity_i = \frac{1}{n} \sum_{i=1}^{r} \max_{j=1}^{k} \{n_{ij}\} \quad (4)$$

b. The f-measure consisting of the two necessary values as precision value and recall value. The precision value of the members in the cluster C_i defined as follows.

$$prec_i = \frac{1}{n_i} \max_{j=1}^{k} \{n_{ij}\} = \frac{n_{ij_i}}{n_i} \quad (5)$$

The recall value of the cluster C_i defined as follows.

$$recall_i = \frac{n_{ij_i}}{|T_{j_i}|} = \frac{n_{ij_i}}{m_{j_i}} \quad (6)$$

where $m_{ji} = |T_{ji}|$. It measures the fraction of point in partition T_{ji} shared in common with cluster C_i.
Therefore, the f-measure for cluster C_i is given as.

$$F_i = \frac{2}{\frac{1}{prec_i} + \frac{1}{recall_i}} = \frac{2 \cdot prec_i \cdot recall_i}{prec_i + recall_i} = \frac{2\, n_{ij_i}}{n_i + m_{j_i}} \quad (7)$$

The f-measure for the clustering C is the mean of cluster-wise f-measure values.

$$F = \frac{1}{r} \sum_{i=1}^{r} F_i \quad (8)$$

Table 2 Visualization of k-means clustering in comparison with original data and feature selection (random forest, correlation).

Data set	k-means clustering		
	Original data	Random forest	Correlation
Thyroid disease	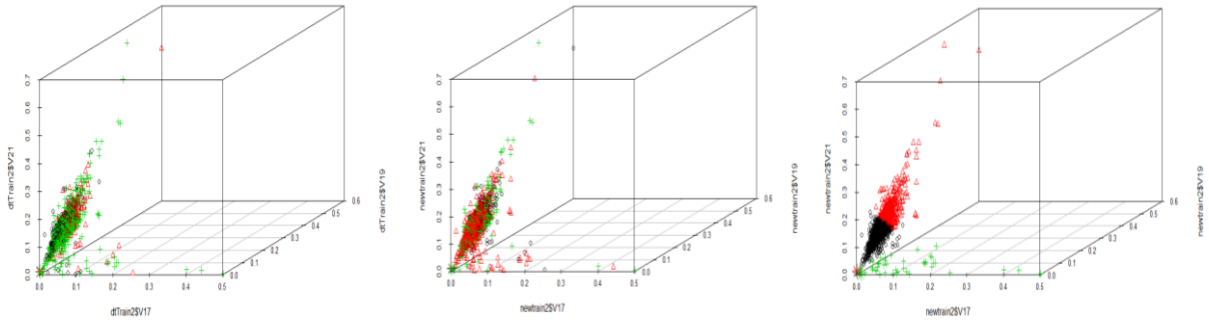		
Heart disease	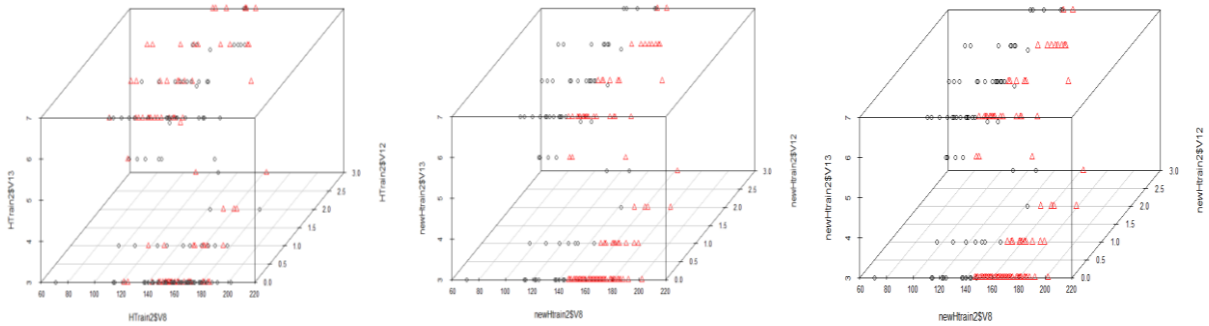		
Pima Indians diabetes	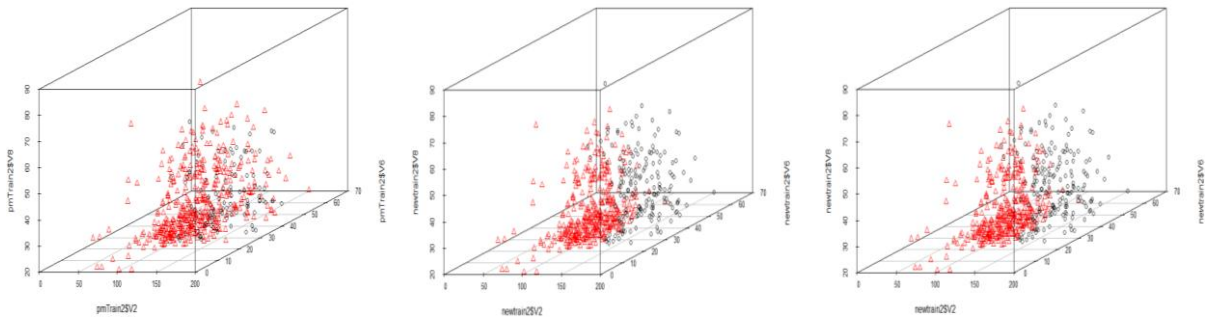		
Breast cancer Wisconsin	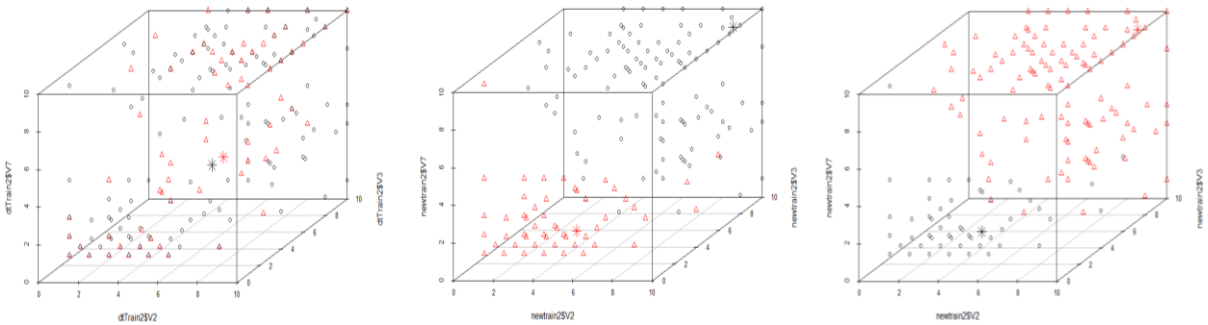		

The experiment we evaluate the performance of the data clustering by compare results showed that the clustering via the feature selection present the purify value and f-measure value are better than original data. As shown in Table 3.

Table 3 Performance evaluation of k-means clustering in comparison with original data and feature selection (random forest, correlation)

Data set	k-Means clustering		
Evaluate	Original data	Random forest :% increment	Correlation :% increment
Thyroid-disease			
#feature	21	7	4
Purity	0.929	0.929 : 0.0%	0.929 : 0.0%
F-measure	**0.464**	**0.474 : 2.3%**	0.449 : -3.2%
Heart disease			
#feature	13	8	9
Purity	0.581	**0.716 : 23.3%**	**0.716 : 23.3%**
F-measure	0.579	**0.712 : 22.9%**	**0.712 : 22.9%**
Pima Indians diabetes			
#feature	8	5	4
Purity	0.628	**0.756 : 20.41%**	**0.756 : 20.41%**
F-measure	0.562	**0.740 : 31.66%**	**0.740 : 31.66%**
Breast cancer Wisconsin			
#feature	10	8	8
Purity	0.659	**0.967 : 46.8%**	**0.967 : 46.8%**
F-measure	0.539	**0.963 : 78.7%**	**0.963 : 78.7%**

CONCLUSIONS

The data clustering with not suitable data such as distribution is non-gaussianity, each feature are irrelevant, or the scale of each value inside feature is very different etc, led to low efficiency clustering. This study, we propose to improve the efficiency of the data clustering via a principle of feature selection technique as random forest and correlation analysis. The experiments with real data results show that the performance of k-means clustering given improving purity value and f-measure for all data sets. In addition, also found that if you want to use clustering method with imbalance data then the result of data clustering will performance increase only slightly.

REFERENCES

Ai-li, F., Qi-sheng, G., Si-ying, Z. (2009). Clustering and correlation analysis of the industry networks. System engineering–theory & practice. Vol.29(6), Online english edition of the Chinese language journal.

Breiman, L. (2001). Random forests. Machine learning. Vol.45(1), pp.5–32.

Correlation coefficient. (2015). Wikipedia the free encyclopedia, Retrieved May 8, 2015, from http://en.wikipedia.org/wiki/Correlation_coefficient.

Kwedlo, W. (2011). A clustering method combining differential evolution with the k-means algorithm. Pattern recognition letters. Vol.32, pp.1613–1621.

Lee, S.L.A., Kouzani, A.Z., Hu, E.J. (2010). Random forest based lung nodule classification aided by clustering. Computerized medical imaging and graphics. Vol.34, pp.535–542l.

Mohammed J. Zaki, Wagner Meira Jr. (2014). Data Mining and Analysis: Fundamental Concepts and Algorithms. Cambridge university press, USA.

Ryali, S., Chen, T., Padmanabhan, A., Cai, W. and Menon, V. (2015). Development and validation of consensus clustering-based framework for brain segmentation using resting fMRI. Journal of neuroscience methods. Vol.240, pp.128–140.

Shahbaba, M., Beheshti, S. (2014). MACE-means clustering. Singnal processing. Vol.105, pp.216-225.

Saha, I., Maulik, U. (2014). Incremental learning based multiobjective fuzzy clustering for categorical data. Information sciences. Vol.267, pp.35–57.

Theodoridis, S., Pikrakis, A., Koutroumbas, K., Cavouras, D. (2010). An introduction to pattern reccognition: A MATLAB approach. academic press, USA.

Tosi, S., Casolari, S., Colajanni, M. (2013). Data clustering based on correlation analysis applied to highly variable domains. Computer networks. Vol.57, pp.3025–3038.

Yu, Z., Li, L., Gao, Y., You, J., Liu, J., Wong, H., Han, G. (2014). Hybrid clustering solution selection strategy. Pattern recognition. Vol.47, pp.3362–3375.

Tippaya Thinsungnoen received the B.E. (1999) degrees in computer science from Nakhon Ratchasima Rajabhat Institute, M.E. (2007) degrees in computer engineering from Suranaree University of Technology. She is a Lecturer, Informatics program, Faculty of science and technology, Nakhon Ratchasima Rajabhat University. Her research of interest includes Knowledge Discovery in Databases, k-means clustering.

Nittaya Kerdprasop is an associate professor at the School of Computer Engineering, Suranaree University of Technology, Thailand.

She received her bachelor degree in Radiation Techniques from Mahidol University, Thailand, in 1985, master degree in Computer Science from the Prince of Songkla University, Thailand, in 1991 and doctoral degree in Computer Science from Nova Southeastern University, U.S.A, in 1999. She is a member of ACM and IEEE Computer Society. Her research of interest includes Knowledge Discovery in Databases, Artificial Intelligence, Logic Programming, and Intelligent Databases.

Kittisak Kerdprasop is an associate professor and chair of the School of Computer Engineering, Suranaree University of Technology, Thailand.

He received his bachelor degree in Mathematics from Srinakarinwirot University, Thailand, in 1986, master degree in Computer Science from the Prince of Songkla University, Thailand,in 1991 and doctoral degree in Computer Science from Nova Southeastern University, U.S.A., in 1999. His current research includes Data mining, Artificial Intelligence, Functional and Logic Programming Languages, Computational Statistics.

THE STUDY OF THE BEST PROBABILITY DISTRIBUTION TO PREDICT A GOLD PRICE WITH LINEAR REGRESSION

Teetawat Kaewwijit, Nuntawut Kaoungku, Kittisak Kerdprasop, Nittaya Kerdprasop
School of Computer Engineering, Suranaree University of Technology, Thailand

ABSTRACT

This paper presents a best probability distribution for predict a gold price by linear regression. The dataset is a gold price, refer by oil price for compare and parameter to predict a gold price by used AIC to find the best model. The probability distribution used 3 models gaussian, gamma, inverse gaussian and link function used 2 models Identity, log total 6 models. We will implement these imputation techniques with R language. From experiment a best probability distribution is gamma and a link function is log by AIC is 55287.

Keyword: linear regression, gold price, probability distribution, R language

1. INTRODUCTION

From the present state of society in the era of globalization, the environment is changing rapidly. The perception is extremely important. The technology, trade, communication and information system have no borders. The competition is rising in all events. Including economic investment factors were also associated with an investment in a variety of formats for the exchange of goods and products directly, such as financial market shares or bonds, Investment in the oil market and gold market.

Gold is another important investment. There are currently investing in the gold market as a universal and global network. Gold is a metal that has a luster and beauty that has been popular in jewelry making. Gold have four basic features that make them stand out as the gold market demand, including beauty and durability is a rare mineral. And can be reused by recycling purified by annealing. It also has to be utilized such as gold.

1. Jewelry Industry From past to present, gold is a metal used in jewelry making has been the most popular.

2. Economic and fiscal stability since gold is a rare metal with a high demand for gold as a medium of exchange and is a metal that is used as an international reserve. As a result, gold is used as a tool for market speculation.

3. Gold in the Electronics Industry The gold was used as components in the electronics and communications telecommunication connections such as semiconductor materials and transistors.

4. Benefits of Transport and Communications. Gold has the ability to reflect radiation, such as infrared radiation. It has been used on the space shuttle and space suits.

5. Medical and dental benefits. Has been used in radiation and reflected radiation to be used in auscultation.

The demand for gold has made a number of high gold prices and price volatility. The composition and related factors are including the price of gold.

1. The price of crude oil on the world market. (Chang, et al., 2013), (Zhang, et al., 2010)

2. The US dollar is the main currency in the foreign currency exchange.

3. The need to buy (demand) and needs to sell (supply) at different times and circumstances.

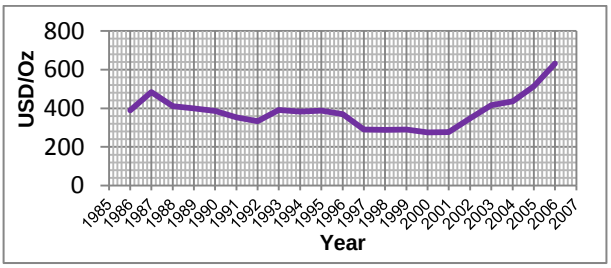

Fig. 1 shows the relationship between gold prices each year.

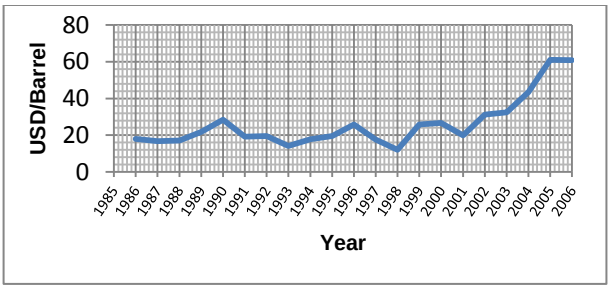

Fig. 2 shows the relationship between oil prices each year.

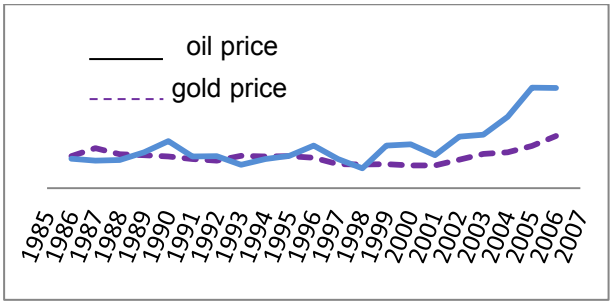

Fig. 3 shows the relationship between gold prices and the price trend of crude oil each year.

Figure 1 shows that the price of gold (World Gold Council, 2015) is increasing each year, which is significantly higher during the years 2001-2006.

Figure 2 shows that crude oil prices (Crude Oil Prices: West Texas Intermediate (WTI) - Cushing, Oklahoma (DCOILWTICO), 2015) is increasing each year, which is significantly higher during the years 2001-2006, as well as gold.

Figure 3 is a comparison chart between gold prices and the trend of crude oil prices. The price of crude oil and gold prices have different scales. It used for comparative only. The graph showed a trend in the same direction.

From the context of trade and investment in the gold market. The analysis Research and find out how to become a tool to predict gold prices as predicting gold prices by way of artificial neural networks (Parisi, et al., 2008) and to predict the price of gold by using an inflation factor (Ismail, et al., 2015), the researcher is interested to study. To find the best probability for predict the price of gold, based on correlation with the price of crude oil using a linear regression data as an alternative to predict the price of gold.

2. METHOLOGY

This research aims to determine the best approach is probably best used for predict the price of gold, based on correlation with the price of crude oil using linear regression. And test the models using the AIC is a measure that models do best, which is how the research stage.

1. Studied Akaike's Information Criterion (AIC) (Akaike, 1981). AIC is the criteria for selecting the most appropriate model for comparing multiple criteria. It has been thought up by Mr. Akaike and Called Akaike's Information Criterion (AIC). The best model have minimum of AIC. This works best on large data samples. However, when the data is small compared to the number of parameters estimate. The models will be selected over a number of independent variables (Over-fit) by the AIC has the following equation.

$$AIC = 2k - 2\ln(L) \qquad (1)$$

AIC = Akaike's Information Criterion

L = maximized value of the likelihood function

k = the number of estimated parameters in the model

2. Studied Generalized Linear Model (GLM) General linear model equation model was first proposed by Nelder and Wedderburn in 1972 (Nelder, et al., 1972). The model consists of three parts. Random component, Systematic component and Link function by has the following equation.

$$y_i = \beta_0 + \beta_1 X_1 + \cdots + \beta_i X_i \qquad (2)$$

Random component are variables associated with the probability distribution of the dependent variable (response variable) or type of exponential family.

Systematic component is assigned the function of independent variables used to predict which variables are two types. 1. β = correlation 2. X = the values of the independent variables.

Link function is an indication of the relationship between the variable component and system components. The variable in the equation is y_i

3. R language. R Language is a computer language used in statistics and display data in graphical form. R. language can be widely because of the function blocks (libraries packages) and many are free, so it is widely used in education. And business, in which the research is an important statement as follows (Kerdprasop, 2012).

-price<-read.csv(file="goldpriceoil.csv") command is used to import data from "goldpriceoil.csv" stored in a variable name "price".

-myformular<-price$gold ~ price$oil + price$month + price$year command is used to stored function to variable name "myformular".

-gaussian.iden<-glm(myformular, family=gaussian(identity)) commands used in the linear regression equation used is "myformular" with a probability value is gaussian and link function is identity. Model stored in the variable name "gaussian.iden".

-pred.gauiden<-predict(gaussian.iden, type="response") command is used to predict "gaussian.iden" model and stored predict variable in " pred.gauiden".

- summary(gaussian.iden) command is used to showing the value of the variable in this example is to show models "gaussian.iden".

- plot(price$num, price$dollar) command is used to create graph. The first variable is plotted on the x axis and the second variable is the axis y.

4. The concept of research. The main idea of this research is design the algorithms to find the best probability. The conceptual framework of the research shown in figure 4 and for the process used to find the best probability is divided into 3 steps.

Step 1: get gold and crude oil prices dataset to create a linear model. The probability is that the gaussian and link function is indentity.

Step 2: use regression analysis to find the AIC and change the probability and link function.

Then use regression analysis to find the AIC with every model. (The probability has 3 types gaussian, gamma and inverse gaussian. The link function uses 2 types is identity and log. Total has 6 models).

Step 3: observe the AIC from each model and compared to find the best model.

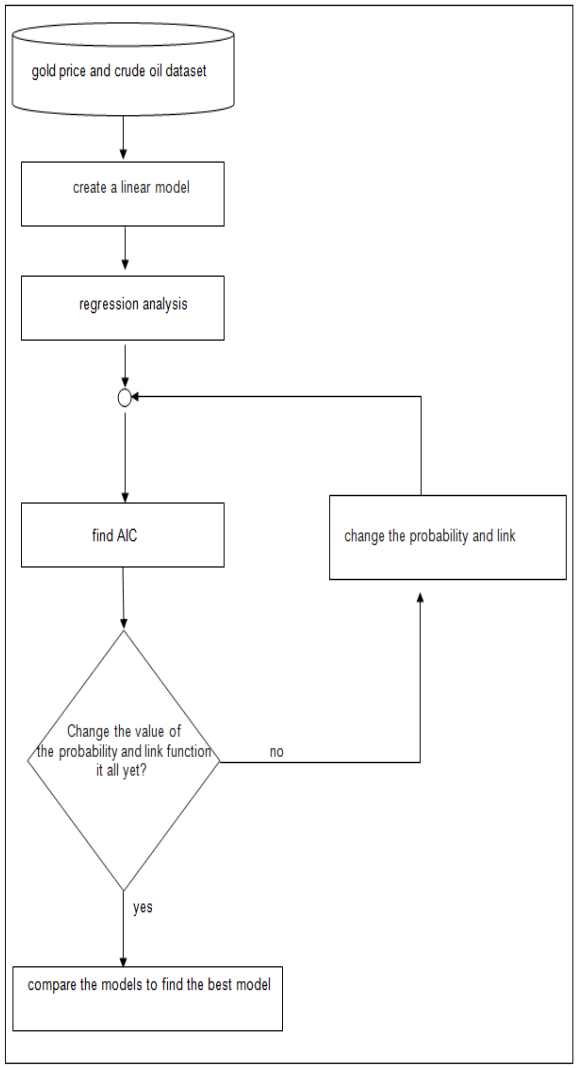

Figure 4 framework of research in the algorithm form.

Table 1 displays the results of the AIC from 6 models.

Probability Distribution	Link Function	
	Identity	Log
Gaussian	55826	55639
Gamma	55420	55287*
Inverse gaussian	55415	55313

3. EXPERIMENTAL RESULT

This research was test to compare the AIC of each model. The probability has 3 types, gaussian gamma and Inverse gaussian. The link function uses 2 types identity and locked. A total of 6 models with models that minimum of AIC is a best model, which means that the probability and the link function of the model is the best value to predicting the gold price.

From table 1 model was used probability gaussian and link function identity the AIC was 55826. Model was used probability gaussian and link function log the AIC was 55639. Model was used probability gamma and link function identity the AIC was 55420. Model was used probability gamma and link function log the AIC was 55287. Model was used probability inverse gaussian and link function identity the AIC was 55415. Model was used probability inverse gaussian and link function log the AIC was 55313. From 6 models with the minimum AIC is the model that the probability of gamma and the link function is log, the AIC is equal to 55287, it is the best model.

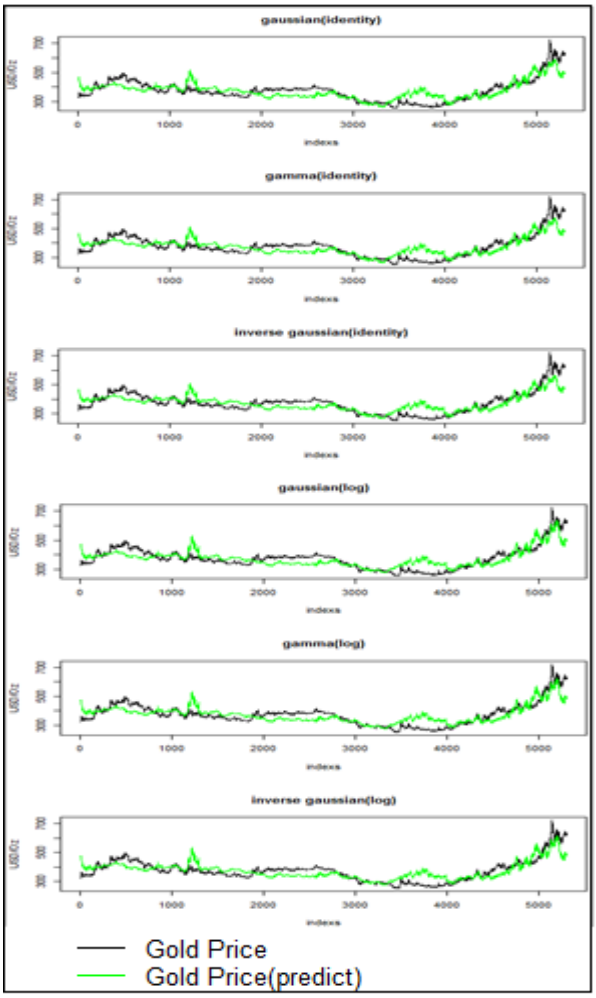

Figure 5 shows a comparison chart between the gold price and gold price prediction.

Figure 5 shows that the prediction is likely to be in line with the gold price. The graph to predict the individual values are very similar.

CONCLUSION

Linear regression was used to predict from the linear equation to determine the relationship of the variables involved in functions that have been established. This can be used to predict the price of gold.

The results showed that the models used to value the probability of gamma and use the link function is locked, the AIC has minimal value in the six models, so this model is a best model for prediction the gold prices by using linear regression.

REFERENCES

Akaike, H., Likelihood of a model and information criteria, Journal of econometrics, vol. 16(1), pp. 3-14, 1981.

Chang, H. F., Huang, L. C., Chin, M. C., Interactive relationships between crude oil prices, gold prices, and the NT–US dollar exchange rate—A Taiwan study, Energy Policy, vol. 63, pp. 441-448, 2013.

Crude Oil Prices: West Texas Intermediate (WTI) -Cushing, Oklahoma (DCOILWTICO), https://research.stlouisfed.org/fred2/series/DCOILWTICO/downloaddata, 2015.

Ismail, Z., Yahya, A., Shabri, A., Forecasting gold prices using multiple linear regression method, American Journal of Applied Sciences, vol. 6(8), pp. 1509, 2009.

Nelder, J. A., Baker, R. J., Generalized linear models, Encyclopedia of Statistical Sciences, 1972.

Parisi, A., Parisi, F., Díaz, D., Forecasting gold price changes: Rolling and recursive neural network models, Journal of Multinational financial management, vol. 18(5), pp. 477-487, 2008.

World Gold Council, http://www.gold.org/research/download-the-gold-price-since-1978, 2015.

Zhang, Y. J., Wei, Y. M., The crude oil market and the gold market: Evidence for counteraction, causality and price discovery, Resources Policy, vol. 35(3), pp. 168-177, 2010.

Kerdprasop, K., Data Mining Methodology and Development, Retrieved October 20, 2012, from https://sites.google.com/site/kittisakthailand55/home/datamining2-55

Teetawat Kaewwijit
He is currently a master student with the School of Computer Engineering, Suranaree University of Technology, Thailand. His current research of interest includes Classification.

Nuntawut Kaoungku
He is currently a doctoral student with the School of Computer Engineering, Suranaree University of Technology, Thailand. His current research includes semantic web and association.

Kittisak Kerdprasop
He is an associate professor and chair of the School of Computer Engineering, Suranaree University of Technology, Thailand. His current research of interest includes Data mining, Artificial Intelligence, Functional and Logic Programming Languages, Computational Statistics.

Nittaya Kerdprasop
She is an associate professor at the School of Computer Engineering, Suranaree University of Technology, Thailand. She is a member of ACM and IEEE Computer Society. Her research of interest includes Knowledge Discovery in Databases, Artificial Intelligence, Logic Programming, and Biomedical Informatics

Architecture, Urban Planning and Design

Integration of Logistic Regression and Markov Chain Analysis in Modelling and Predicting Future Urban Growth in Kaduna, Nigeria

Yakubu Aliyu Bununu[1], Ahmad Nazri Muhammad Ludin[2] and Nafisa Hosni[3]

[1] Researcher, Department of Urban and Regional Planning, Faculty of Built Environment, Universiti Teknologi Malaysia, Johor, Malaysia. Email: abyakubu2@live.utm.my

[2] Professor, Centre for Innovative Planning and Development, Faculty of Built Environment, Universiti Teknologi Malaysia, Johor, Malaysia. Email: b-anazri@utm.my

[3] Senior Lecturer, Department of Urban and Regional Planning, Faculty of Built Environment, Universiti Teknologi Malaysia, Johor, Malaysia. Email: nafisa@utm.my

Abstract

Land use changes in developing countries generally occur in the form of new building construction in the peripheral areas of cities mostly for residential purposes. This fast pace of urban development has thrust to the fore a number of research initiatives that make use of new applications for modeling such phenomenon. In this study, urban expansion is examined in Kaduna, Nigeria, using a hybrid model that combines Cellular Automata (CA) techniques and Markov chain analysis with logistic regression. Land use change between 1990 and 2001 was analyzed and the results showed huge conversion of green areas and open lands to built-up areas. Environmental variables dealing with urban expansion were evaluated to determine their influence on urban expansion and operationalized to develop transition potential sub-models. A transition potential map is then derived from the transition potential sub-model which was employed to simulate future urban growth. The model was subsequently evaluated and validated using ROC statistics and the results were found to be acceptable.

Keywords: Land use change, logistic regression, Markov chain, cellular automata, Kaduna

1. Introduction

The most prevalent form of urban growth and urban land use in developing countries is the proliferation of informal residential development in the peripheral areas of cities commonly referred to as urban sprawl (Arsanjani et al., 2011). Urban sprawl is a highly complex and complicated process that results from the interactions between biophysical and individual factors in space and time at different scales (Barredo et al., 2004). The assessment, forecast and evaluation of future land use involves a complicated set of tasks in land use modelling that require expensive modelling software, gathering extensive urban data and the requisite modelling and statistical skills, most of which are hard to come by in developing countries. This is why very few urban growth models have been developed for African cities (Barredo and Demicheli, 2003; Barredo et al., 2004; Vermeiren 2012) and there is little or no use of these models in African urban planning systems. Added to the factors listed above are the issues raised by Lee (1973) in a seminal critique of land use models as planning tools, some of which remain relevant today and are seen as the main inhibitors to their wide scale application especially in developing countries (Vermeiren, 2012).

To demonstrate how these practical and technical constraints to the use of land use models can be overcome, this paper utilizes freely available archived satellite imagery from the Global Land Cover Facility (GLCF) to develop an urban growth model for Kaduna in northwest Nigeria. The first step in the implementation of the model was the acquisition of freely available medium resolution satellite imagery from the GLCF. The satellite images are the commonly utilized 30m resolution Landsat TM and Landsat ETM+ scenes covering the study area for 1990, 2001 and 2009. These images were used to map urban land cover change and urban expansion from the base year of 1990 to the year 2009. Secondly, pattern analysis of the mapped data

revealed a likely correlation between land cover change and urban expansion with physical and environmental factors such as accessibility and topography. These factors were then taken as explanatory variables and were subsequently empirically derived from existing data of the study area like roads and elevation. The explanatory variables were then used to develop a transition potential model using logistic regression. Change prediction was subsequently carried out up to the year 2009 for model validation and calibration, and subsequently until 2019. This provided insights into the future pattern and location of urban growth in Kaduna that can be used by planners and policy makers in ensuring a sustainable and well managed future for the city.

2. Study Approach, Data and Methods

2.1 The study area

The study are is Kaduna in northwest Nigeria. In the hierarchy of Nigerian cities, Kaduna is considered a relatively young city. It was established by the British colonial administration headed by Lord Frederick Lugard in 1912 (Haruna, 2012). By 1919, 7 years after its establishment as the capital of the Northern Nigerian region, the estimated population was only 3,000. By 1930, it had risen to 10,000 people – an increase of 330%. Between 1952 and 1963, Kaduna recorded an annual average growth rate of 12.5%. 10.1% higher than the 2.4% average growth rate estimated for developing countries. From 1963 to 1985, Kaduna is estimated to have grown at an average of 7% per annum. Two types of urban growth are discernible in Kaduna – growth by fusion and outward expansion of the city's built mass. The former was basically the annexation of adjoining villages while the latter was the outward expansion of the city in directions where there were no previous settlements (Agboola, 1986). Between 1917 and 1930, the total extent of the city was 12.5km^2. In 1982, it had grown to approximately 100km^2 and by 1985 it was estimated at 140km^2 (Agunbiade et al., 2012). By 2010, Kaduna's physical extent had grown to 420km^2.

2.2 Land cover maps and other input data

Landsat TM imagery of Kaduna for 1990 and Landsat ETM+ imagery of Kaduna for 2001 and 2009 were used in the extraction of land use maps of the study area. Three land cover categories namely built up, water bodies and open savannah were identified by means of visual interpretation of the true colour composites of the Landsat imagery, multi-temporal high resolution imagery available from Google Earth and ground-truthing through field visits and observations. Built-up areas include all paved and unpaved areas such as residential, commercial, industrial buildings, roads, parking lots, urban parks and open spaces. The resulting land cover maps of the study area are illustrated in Figures 2.1, 2.2 and 2.3.

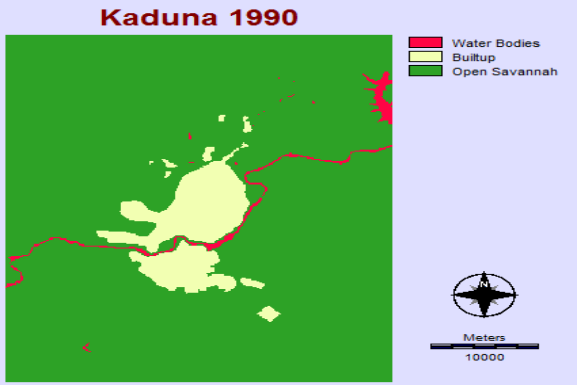

Fig. 2.1: Extracted land cover map of 1990

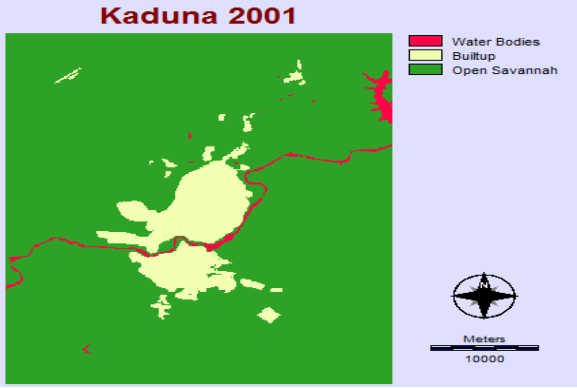

Fig. 2.2: Extracted land cover map of 2001

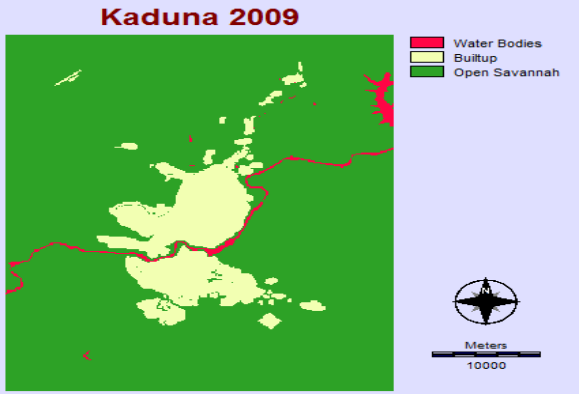

Fig. 2.3: Extracted land cover map of 2009

Poelmans and Van Rompaey (2010) and Dubovyk et al. (2011) have identified common factors that influence land use change and summarized them into two categories, a) environmental and b) socio-economic factors. The selected land use change drivers in this study belong to the first class and are topography, slope, proximity to roads and proximity to existing built-up areas.

2.3 Methods

2.3.1 Change analysis

Land use change analysis was conducted for the study area by cross tabulation of the earlier derived land cover map of 1990 as the input earlier land cover image and the 2001 land cover map as the input later land cover image.

2.3.2 Transition potential modeling with logistic regression

Transition potential modeling was used to group land use transitions into a set of sub-models and then utilized to explore the potential power of the chosen explanatory variables. In the current study, the change analysis showed that there is only one set of transition, from open savannah category to built-up category. The explanatory variables were evaluated to determine their contribution using Cramer's V static. In order to predict change, the transition was empirically modelled using logistic regression. Logistic regression performs binomial logistic regression, in which the input dependent variable must be binary in nature, that is, it can have only two possible values (0 and 1). Such regression analysis is usually employed in estimating a model that describes the relationship between one or more continuous independent variable(s) to the binary dependent variable (McCullagh and Nelder 1989; Anselin, 1988). The basic assumption is that the probability that the dependent variable takes the value of 1 (positive response) follows the logistic curve, and its value can be estimated with the following formula:

$$P(y = 1|X) = \frac{exp(\sum BX)}{1+\exp(\sum BX)} \quad \ldots\ldots\ldots\ldots\ldots\ldots\ldots\ldots\ldots\ldots (1)$$

Where:

P is the probability of the dependent variable being 1;

X is the independent variables,

$X = (x_0, x_1, x_2 \ldots. x_k)$, $x_0 = 1$

B is the estimated parameters,

$B = (b_0, b_1, b_2 \ldots\ldots b_k)$

To linearize the above model and remove the 0/1 boundaries for the original dependent variable (that is the probability), the following transformation is applied:

$$p' = 1n\left(\frac{p}{(1-p)}\right) \ldots\ldots\ldots\ldots\ldots\ldots\ldots\ldots\ldots\ldots\ldots (2)$$

The transformation is known as the logit transformation. After the transformation, P can assume any value between plus and minus infinity (Hill and Lewicki, 2007). The logit transformation of binary data ensures that the dependent variable will be continuous and the new dependent variable (logit transformation of the probability) is boundless. It also ensures that the probability surface or transition potential map will be continuous within the range 0 to 1. Performing the logit transformation on both sides of the above regression model results in a standard linear regression model:

$$1n\left(\frac{p}{(1-p)}\right) = b0 + b1x1 + b2x2 + \cdots bkxk + \epsilon \ldots\ldots (3)$$

2.3.3 Cellular Automata-Markov model

This model integrates Cellular Automata and Markov chain modules to produce a single module. The module acquires the quantity of change by way of the Markov chain analysis and allocates the change to suitable pixels by means of Cellular Automata. The Markov chain model is a model of a stochastic process that describes likelihood of one state changing to another (Arsanjani, et al., 2013 pp. 267). One key descriptive tool associated with the Markov chain model is the transition probability matrix (Mousivand et al., 2007).

2.3.4 Change prediction and model validation

The transition potential modeled previously was used to create several types of predictions through a dynamic land cover change process. After specifying an end date, the quantity of change in the transition from open savannah to built-up is modeled using the Cellular Automata-Markov model. The land use change is predicted using two basic models of change: a hard prediction model and a soft prediction model (Eastman, 2015). The hard prediction model is based on a competitive land allocation model similar to a multi-objective decision process. The soft

prediction yields a map of vulnerability to change for the selected set of transitions.

For model validation, the ROC statistics is employed. The ROC module employs the Relative Operating Characteristic (also known as the Area Under the Receiver Operating Characteristic Curve – or AUC), an excellent method to assess the validity of a model that predicts the location of the occurrence of a class by comparing a suitability image depicting the likelihood of that class occurring (i.e., the input image) and a Boolean image showing where that class actually exists (i.e., the reference image). For example, the ROC could be used to compare an image of modeled probability for deforestation against an image of actual deforestation (Eastman, 2015).

3. Results

3.1 Analysis of land use change

Figs 3.1 and 3.2 highlight the land use changes that have taken place in the study area within the 11 year period for which change analysis was carried out: the built-up category gained 10.65% while the open savannah category lost 1%. As such, the built-up category grew to 14,127.02ha in 2001 from 12,767.25ha in 1990, an increase of 1,359.77ha. The water bodies' category recorded neither increase nor decrease, which is consistent with expectations. Most of the expansion of the city within the period under consideration occurred in the northern and southern axis as defined by the Abuja-Kaduna-Kano federal highway, and in the western sector buoyed by the presence of the western bye pass and the influence of the industrial developments to the south. Very little or no expansion of the city is seen in the eastern sector during the period under consideration because of the natural barrier created between that part and the rest of the city by River Kaduna.

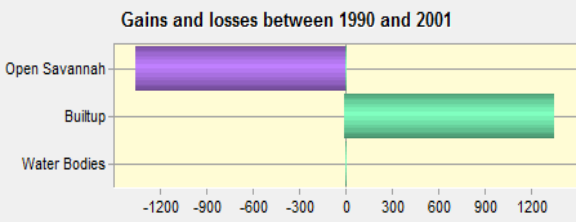

Fig. 3.1: gains and losses by by land cover category in hectares

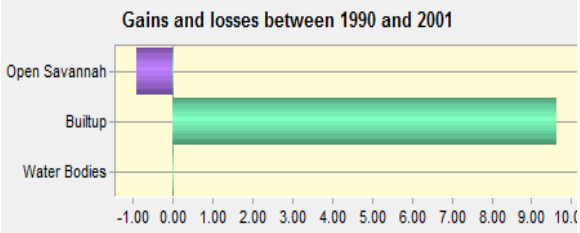

Fig. 3.2: % of gains and losses between 1990 and 2001

3.2 Model validation and land use change prediction

Based on the results of the land use change analysis for the period between 1990 and 2001, the evaluation of the 6 explanatory variables in the transition potential sub-model and the transition potential map (Figure 3.3) that was subsequently created, the model was calibrated and employed to predict and simulate urban growth over an 8-year period from 2001 until the year 2009. The choice of 2009 as the end date of the first stage of land use change prediction is based on the availability of the actual land cover map for that year which can be used in evaluating and validating the model. The simulated map for 2009 is shown in Figure 3.4.

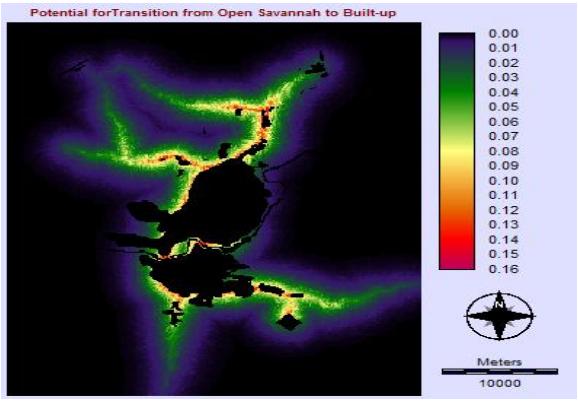

Fig. 3.3: Potential for transition from open savannah to Built-up

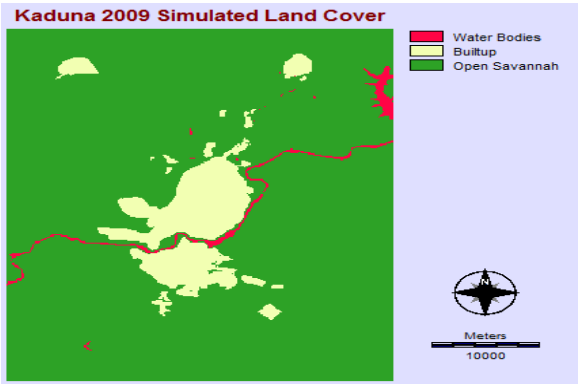

Fig. 3.4 2009 simulated land cover map of Kaduna

Between 2001 and 2009, the built-up category increased by 981.1757ha (approximately 6.95%), growing to 15,108.1936ha. The open savannah category reduced by the same measure with which the built-up increased (981.175ha) and the water bodies category remained unchnged.

In validating the model, the ROC statistic was obtained at 0.69, a reasonably strong value that is good enough to make the results of the simulation acceptable. Further visual analysis and comparison of the simulated and actual land use maps of 2009 reveal that the customized model is generally a reliable estimator in terms of change quantification, allocation and continous space modelling.

Having obtained satisfactory results from the model validation process, the model was then calibrated with the 2009 data and urban growth for Kaduna was further simulated to 2019 so as to further investigate its future pattern and extent over the next decade and the result is shown in on the map in Figure 3.5. From the simulated map of 2019, it can be deduced that the built-up category will further increase by 8.06% (i.e from 15,108.1936ha to 16,325.5285ha) invariably reducing the size of the open savannah category. It is also evident from the simulated land cover map that urban expansion in Kaduna will maintain its sprawled pattern that is made up of a mixture of radial development along the edges of already built-up areas and leap-frog developments stimulated by the pattern of infrastructure development and the growth of existing nearby villages serving as satellite towns to the city.

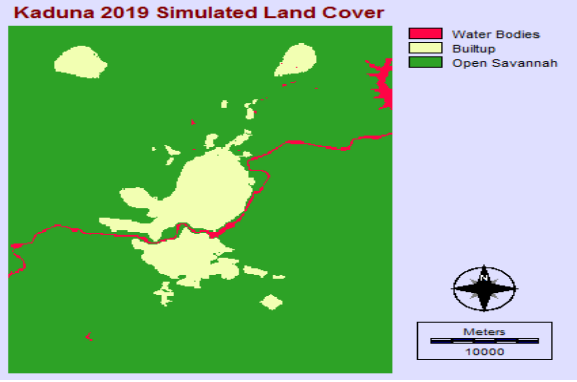

Fig. 3.5: 2019 simulated land cover map of Kaduna

4.0 Dscussion and Conclusion

In the last three decades, kaduna has experienced a high rate of population growth and invariably, accelerated urban expansion. The city's population grew from 664,162 to 1,561,000 people between 1985 and 2010 (UNDESA, 2009; Kaduna State Government, 1985), almost a 200% increase! This increase has been as a result of migration by people from the surrounding rural areas and other parts of the country in search of better living and economic opportunities. This makes Kaduna an appropriate case study for dynamic land use change modelling. The customized land use change model employed in this study integrates the strengths of Markov Chain analysis, Cellular Automata and the logistic regression model. This allowed for the use of urban growth explanatory variables like topography, proximity to city center, proximity to already built up sites and proximity to roads in the model thereby improving the accuracy of prediction.

This study considered the amount and percentage of change in the case study and using that simulated the quantity and location of change by preparing land use maps of 1990, 2001 and 2009. Investigation into land use changes between 1990 and 2009 revealed that the built-up area of Kaduna expanded tremendously, leading to the inevitable conclusion that the city has sprawled. Change prediction was achieved using modelled transition potentials that are based on the selected explanatory variables. A major strength of this being the ability to define variables as either static or dynamic as explained in section 2.3.2. Subsequently, the model was implemented to predict the change for 2009 based on land use maps of 1990 and 2001 and the change analysis conducted. The simulated maps were compared with the actual maps to evaluate the preliminary results of 2009 and validate the ability of the model to make reasonably accurate predictions of the future and thereafter employed in making land use change predictions for an additional ten years from 2009 to 2019. The results showed that the models results are valid and can be reliable in performing land use change predictions into the future.

References

Anselin, L., Spatial Econometrics. Methods and Models. Kluwer Academic Publishers, Dordrecht, 1998.

Agboola, T., City Profile: Kaduna. Cities Volume 3, 283-352, 1986.

Agunbiade, M.E., Rajabifard A., and Bennet R., The dynamics of city growth and the impact on urban land policies in developing countries. International Journal of Urban Sustainable Development, 4:2, 146-165, 2012.

Arsanjani, J. J., et al., Integration of logistic regression, Markov chain and cellular automata models to simulate urban expansion. International Journal of Applied Earth Observation and Geoinformation 21: 265-275, 2013.

Arsanjani, J. J., et al., Tracking dynamic land-use change using spatially explicit Markov Chain based on cellular automata: the case of Tehran. International Journal of Image and Data Fusion 2(4): 329-345, 2011.

Barredo, J. I. and L. Demicheli, Urban sustainability in developing countries' megacities: modelling and predicting future urban growth in Lagos. Cities 20(5): 297-310, 2003.

Barredo, J. I., et al., Modelling future urban scenarios in developing countries: an application case study in Lagos, Nigeria. Environment and Planning B 31(1): 65-84, 2004.

Dubovyk, O., et al., Spatio-temporal modelling of informal settlement development in Sancaktepe district, Istanbul, Turkey. ISPRS Journal of Photogrammetry and Remote Sensing 66(2): 235-246, 2011.

Eastman, J.R., IDRISI 16: The TerrSet edition. Clark University, Worcester, MA, 2015.

Haruna, M., A Brief History of Kaduna: the City of Crocodiles. People and Politics, 2012.

Hill, T., Lewicki, P., STATISTICS Methods and Applications. StatSoft, Washington, D.C, Available at: http://www.statsoft.com/textbook/neuralnetworks/ linear, 2007.

Kaduna State Government, 1963 Census Population and Projections from 1978-1985 by Districts and Local Government Council Areas. M. o. E. D. Statistics Division. Kaduna, Statistics Division, Ministry of Economic Development, 1985.

Lee, D.B., Jr., Requiem for large-scale models. Journal of the American Institute of Planners, 39(3), 163-178, 1973.

McCullagh, P., Nelder, J., Generalized Linear Models. CRC Press, Boca Raton, 1989.

Mousivand, A.J., Alimohammadi Sarab, A., Shayan, S., A new approach of predicting land use and land cover changes by satellite imagery and Markov chain model (Case study: Tehran). MSc Thesis. Tarbiat Modares University, Tehran, Iran, 2007.

Poelmans, L. and A. Van Rompaey, "Complexity and performance of urban expansion models." Computers, Environment and Urban Systems 34(1): 17-27, 2010.

UNDESA, World Urbanization Prospects: The 2009 Revision, Department of Economic and Social Affairs, United Nations Organization, 2009.

Vermeiren, K., et al., Urban growth of Kampala, Uganda: Pattern analysis and scenario development. Landscape and urban planning 106(2): 199-206, 2012.

USER'S MOTIVATION IN CULTURALLY INFLUENCED SETTLEMENTS: A THEORETICAL FRAMEWORK FOR SAMA-BAJAU COASTAL DWELLINGS

Iziq Eafifi, Abdullah Sani
Department of Architecture, Universiti Teknologi Malaysia

ABSTRACT

User needs is an important aspect in considering whether a house could be considered a home. Preferences, congruency, and satisfactions are often considered as dynamic mechanism that revolves around the people's behavior towards their environment. Several theoretical models have been proposed to understand end user's preferences in their built environment by focusing on certain aspects such as culture and basic user needs. This paper discusses a theoretical framework proposed to fit Sama-Bajau coastal settlement in Sabah that is actually rich with cultural value but has gone unnoticed due to the external constraints imposed upon their daily lives. The model also proposed to evaluate attributes within Sama-Bajau built environment to user's reasoning and preferences by understanding their congruity to the living environment thus contributing to the future well-being of Sama-Bajau coastal dwellers in Sabah

1. INTRODUCTION

1.1 PERSONALIZATION AND SAMA-BAJAU BUILT ENVIRONMENT

Kopec (2006) & Fernandez (2007) describe personalization as a substantiated symbolism of personal identity, and delineating territories. When urbanization increased, so does the notion of 'individualism' diluting the concept of communal living of the community even in present days. What was once called egalitarian society based on the kinship relation (Miller, 2011), now they have become more and more individualistic due to the materialistic affection promotes by the rapid waves of globalization.

Communal personalization as opposed to the individual personalization however fairly exist in Sama-Bajau coastal settlement in terms of kinship distribution within a certain area they deemed theirs. Collective personalization or group personalization (Lawrence 1987, Rapoport 1981, Brown & Werner 1985, Giuliani et al. 1988, Bentley et al. 1985) also presents in certain settlements which also known as group personalization. Group personalization also can also closely be associated with territorial personalization. As personalization goes between individualism and group, there is territorial personalization. Greenbaum & Greenbaum (1981) suggests that at the group level, territorial personalization may function as an ecological mechanism indicative of group membership and domain. It shows the cultural traits that bleed kinship and social values. Though when we look at individual level of dwellings, there seems to be less to appraise compared to the shared value they demonstrate, the value of this community need to be look upon a larger networks in which their space organization prevails- a sign of values Sama-Bajau express indirectly within their settlement placement.

2. THE FRAMEWORK

This paper aims to develop a model reflecting the coastal dwellings of Sama-Bajau based on means end chain proposed by Gutman (1982) that has been further elaborated in housing preference research such as Jusan & Sulaiman (2005); Sirgy et al (2005); and Poor & Jusan

(2010). User's exclusive motivational level is not of critical part as they are further apart from urbanized society. While on the mass housing within the urbanized area, cultural direction might be diluted due to the globalization causing the change in decision making towards housing preference, Referring the Maslow's hierarchy of needs (Maslow, 1970), the Sama-Bajau seems to be had little over gratification on any hierarchy of needs presented. Though it may seems that economic factors govern the life of Sama-Bajau, it does not change the fact that external constraints such as political (Saat, 2004; 2008) and inter-ethnic prejudice (Sendera, 2008) also had major influence on the life of this community. Functioning living environment always seems to be the goal with the existence of typical design that has been used sporadically all over the settlement before personalization come into place. Therefore theoretical model presented below can represent the personalization within coastal settlement of Sama-Bajau in Sabah.

2.1 ATTRIBUTES

The attributes in the proposed framework are more likely to resemble of those in Jusan & Sulaiman (2005) as they are deem to be universal; as in concrete and abstract nuances. The built environment of Sama-Bajau borrows heavily from their ancestral realm that has been passed through generations. Compounded by the ongoing globalization and continuous acculturation, coastal dwellings of Sama-Bajau have produced more than typical representation of their rudimentary space composition with little to no variation of building materials. Many have gone modern by adopting additional spaces to match the growing need of social organization and the introduction of contemporary spaces in the dwellings; subsequently turning it from a mere abode to a home- desirable living structure that conforms to the user needs. These attributes, in all representation are the result of certain underlying needs that are the social and personal evaluation upon reaching certain goals, or values.

2.2 FILTER AND EVALUATION

Filter and evalution is the most important part in the theoretical framework whereby the essence of PEC relies heavily on. In this framework, filter is divided into two signifying external filter that is the culture and lifestyle; and personal filter indicating individual preferences. The 'culture' or lifestyle is the terminal of certain values individual or community trying to achieve, personal could also share the same values and might be intertwined with each other. However, the presence of a new culture and lifestyle (globalization) coincided with the existing social fabric of Sama-Bajau has made the goal ambiguous. Many of the east-coast Sama-Bajau happens to be more conservative of their own culture as in the case of Sama-Bajau sub-group Pala'u. However, the rest of them like those of littoral Sama that majority of them reside in the coastal areas of Sabah are more diluted by the global and urban mainstream.

They tend to be more individualistic as oppose to the community-oriented worldviews of the Pala'u. It comes to the point where ancestral traditions and have become obsolete and irrelevant in their daily lives, let alone within their built environment. This fact effectively divided Sama-Bajau into having two conflicting culture into their lives, with acceptance of a new culture indicating their social mobility. It has become apparent due to the constant acculturation and political governance dictating their lives instigate individualism among coastal Sama-Bajau. Their dwellings have become more personalized with their build environment attributes conforming to the personal needs. This is where Maslow's theory is applied to segregate those with underlying personal motivation far greater than those tradition needs. However, as far as individualism separate itself from traditional culture that requires them to be more communal, it is highly possible that new culture (individualistic values) and traditional culture (traditional values) would coincide with each other thus advocating assimilation.

2.3 CONSEQUENCES

Person environment congruence is the key turning point of the framework. It dictates on whether the attributes match well with ideology and values that Sama-Bajau partook. Self-congruity could channel positive evaluation towards certain attributes that could be influential in housing personalization. Self-congruity could mean that the attributes are desirable to the values that they vying for. Congruity would go so far before any individual within household feel the need to change due to underlying reasons; a situation of self-incongruity. Self-incongruity or self-dissonance mark the point that the attributes fail to conform to the values that certain household would want to achieve. Given that the coastal houses are commonly associated

with incomplete spatial configuration that can be adapted to the modern lifestyle, strengthen the fact that many would feel incongruity towards current attributes in their dwellings. However, in certain cases due to the external constraints (see constraints section), some household would resort to functional; the forced satisfactory onto their living condition. As long as the dwellings space, materials, structure are enough for them to live in, they would be satisfied.

2.4 PREFERENCES

In respond with congruity and incongruity, there would be a repercussion on how the occupant of a certain household would modify their house to their likings. Like the framework by Jusan & Sulaiman (2005), this part is where personalization occurs. Personalization would be in the action of modification and beautification of attributes within household. Coastal dwellings have seen almost every house is made to be modified due to certain constraints at the time the household is being constructed. Other than that, household usually tend to move away. Many of the coastal dwellings are deem to be temporary before they decide the house to be permanent therefore they personalized it or they move away to different area but still within the Kampong compound.

2.5 CONSTRAINTS

The key addition to the framework is the constraints that apply to the personalized coastal house of Sama-Bajau. While there is nothing stopping them from Sama-Bajau to personalize their house should they have the capacity to do so, they still face uncertainties especially those that occupy native land. The land is liable to Land Ordinance Cap.68 (Section 78) which stated that it could be revoke anytime by the Yang Dipertua Negeri (YDPN) Sabah and many of this land is gazette in the east coast and north coast of Sabah. The land status could jeopardize the intensity of personalization of their house due to fact that it would not be permanent. However, recent study found that while they are aware of this uncertainty, it would not stop them from beautifying and adding spaces to their house as they believe the area they are living in is too far from development and urban area; and they believe that their legacy would certainly move out from the area. The dwelling would be enough to sustain his generation until the next. Another fundamental constraint which has been the focal reason of the existence of coastal dwellings would be the economic factor. The reasoning coastal dwellers gave for their existence in littoral area would be based of economic deficiency. Another apparent constraint also be in the form of racial prejudice against these people. However, this prejudice would only apply to those of Pala'u due to many of their negative adage to other ethnics.

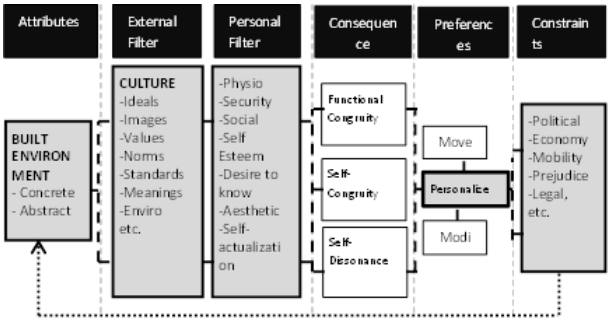

Figure 9: Theoretical Model of Personalization for Cultural Oriented Community and Individuals

3. CONCLUSION

This paper suggests that in within home making among Sama-Bajau coastal dwellers, there exist underlying human motivations and cultural adherence that the community trying to preserved. Contrary to the popular beliefs that Sama-Bajau settlement is a manifestation of their impoverishments is not true. The Sama-Bajau houses are always capable of expansion due to flexible nature of its construction and materials. Space expansion is particularly common whether it is individual or communal. Space usage also could reflect the lifestyle of the people which leads to revelation of the activity systems. Studying personalization among Sama-Bajau settlement is important in knowing their intrinsic values and household preferences. Though it might not be the absolute solution to prepare the Sama-Bajau for resettlement, it could at least contribute to one part of many that can contribute to the betterment and compassion to the forgotten community. On the other note, establishing systematic linkages that consider many important aspects of the coastal community in Sabah would definitely contribute to the research pool of housing personalization in general. Apart from that, it might as well prepare the future designer in the design process wherein the end user's preference could be addressed which is

fundamental to achieve quality housing design.

References

Brown, B. & Werner, C. 1985. Social cohesiveness, territoriality, and holiday decorations. The influence of cul-de-sac. *Environment and Behavior,* 17**,** 539-565.

Fernandez, K. 2007. Personalising The Home. *ANZMAC.* New Zealand.

Gutman, J. 1982. A Means-End Chain Model based on Consumer Categorization Processes. *Journal of Marketing, 46*, 60-72.

Greenbaum, P.E. & Greenbaum, S.D. 1981. Territorial Personalization: Group Identity and Social Interaction in a Slavic-American Neighborhood. *Environment and Behavior,* 13**,** 574-589.

Giuliani, M., Bonnes, M., Amoni, F. & Bernard, Y. 1988. Home and the theory of place. IN CANTER,

Poor A.S.J. Jusan, M.M. 2010. Exploring housing attributes selection based on Maslow's hierarchy of needs. Procedia-Social and Behavioral Sciences. 42 .2012. 311 – 319. AcE-Bs 2010 Kuching

Jusan, M. Sulaiman, A.B. 2005. *Personalization as a sustainable approach to mass housing: The fundamental theory*. Conference on sustainable building South East Asia. Kuala Lampur.

Kopec, D. 2006. *Environmental psychology for design*, New York, Fairchild Publications Inc.

Lawrence, R. J. 1987. What Makes a House a Home? *Environment and Behavior,* 19**,** 154-168. 340 *Erdayu Os'hara Omar et al. / Procedia - Social and Behavioral Sciences 49 (2012) 328 – 340* Lustig, M.W & Koester, J. 2003. Intercultural Competence: Interpersonal Communication across Cultures. Boston: Allyn And Bacon.

Maslow, A. 1970. *Motivation and personality*. New York: Harper and Row.

Miller, M.T. 2011. Social Organization of West Coast Bajau. SIL Electronic Working Papers 2011-009, September 2011

Saat, Gusni. 2004. Peribumi Teluk Sepanggar. Publisher Universiti Kebangsaan Malaysia. 2004

Saat, Gusni. 2008. Implikasi Politik Melayuisme Sama-Bajau di Malaysia. Sari 26 (2008) 63-70

Sendera. H, Mohd Yakin. Nornis, Saidatul, Hj. Mahali. 2008. *Duang: the semiotic interpretation and perception of the Bajau-Sama community in Sabah*. Jurnal Komunikasi, 24 . pp.63-71.

Sirgy, M. Joseph, Stephan Grzeskowiak, and Chenting Su. 2005. "Explaining Housing Preference and Choice: The Role of Self-congruity and Functional Congruity," Journal of Housing and Built Environment, 20, 329-347

Iziq Eafifi received the Diploma (2009) and Bachelor's Degree (2012) in Architecture from Universiti Teknologi Malaysia. He is currently pursuing PhD in Architecture.

Abdullah Sani holds his Phd in Landscape Architecture (2001) from Universiti Teknologi Malaysia.
He is an associate professor in Department of Architecture, Universiti Teknologi Malaysia.

FRAMEWORK FOR EVALUATING MOBILITY ENVIRONMENT WITH DERIVED INDEX OF TRAVELER PERCEPTION

Shittu AbdulMajeed .O and Muhammad Zaly Shah
Department of Urban and Regional Planning,
Faculty of Built Environment,
University Teknologi Malaysia

ABSTRACT

To pursue in depth quantitative assessment of mobility, a reliable mobility trend data base is needed, which most cities of developing nations lack. This challenge is heightened by the seeming lack of wherewithal and political will to build required databases upon which urban mobility analysis can rest. As a result, it becomes improbable to apply advanced, high end, data hungry models of urban mobility evaluation in such situations. Additionally, the difficulty experienced in leveraging outputs of complex mobility appraisal techniques for policy rationalization is also a drawback in these kinds of setting, usually due to inadequate skill and manpower. Therefore, urban mobility issues are approached in a subjective, uncoordinated and piecemeal fashion. Consequently, how urban movement goes on in cities with these attributes can hardly be described, on the one hand, on the other, the mobility support qualities such cities offer also remain unknown. To ameliorate this problem, it is conjectured that, a systematic evaluation of travel perception influencing factors may provide hints about the degree to which urban areas hinder or enhance mobility, by indexing mobility complexities in a spatial entity, from perceived effects of individual's travel perception. More so, the progressive urbanization cities of developing nations are experiencing, in the face of inadequate or total lack of holistic planning, underscores the need to explore other possible alternatives of appraising mobility environments. The method involved a meta – analysis of techniques of evaluating urban mobility with quantitative models, as a way of deriving lessons and criteria for framework development. The framework suggested is expected to enable local authorities develop a cost effective and parsimonious way of identifying urban mobility challenges, so as to provide a strategic pathway for a city's mobility environment to be objectively appraised, in order to satisfactorily target interventions at improving both the mobility environment and the quality of life of city inhabitants.

Key Words: mobility environments, mobility perception influencers, travel perception, mobility complexities, model complexity.

1.0 INTRODUCTION

The close connection between mobility, individual's independence, well being and quality of life has been elicited by (Spinney *et al*, 2009). The fact that mobility provides increased opportunities for individuals to undertake fundamental tasks beyond the home environment, such as work, recreation and shopping, as a necessity in satisfying inherent psychological needs necessary for well being, as stated by (Vella – Brodrick *et al*., 2013), accords mobility a life support attribute. This stance had earlier been reiterated by Patla and Shamway – Cook (2003) that adequate mobility is needed to realistically meet necessary Instrumental Activity of Daily Living (IADL), thus putting mobility or ability to move amongst the fundamental requirements of human existence. In agreement, Cresswell (2010) asserts that mobility is a central fact of modern and post modern life, stating that the defining characteristic of mobility, that is movement - puts the phenomenon on centre stage of human existence.

The important role mobility plays in meeting the demands for human survival in urban areas cannot be over emphasized. Because improved levels and inclusive mobility facilitates accessibility to employment, education, health and other urban services necessary for enhanced welfare (Adeniji, 2001; Haider and Badami, 2004; Olufemi and Oluseyi, 2007). Zhu (1998) also tied accessibility levels to city vibrancy. Against this backdrop, it becomes necessary to understand and apply findings around mobility as an observable reality, in urban planning and development. The fact that mobility has been recognized as a "leading issue" is evidence of its importance as a research agenda (Cresswell, 2010). The central task thus, is to encourage mobility assessment techniques and policies that will cater for the mobility needs of urban residents in a targeted, economically efficient and socially inclusive manner, towards improved urban productivity, livability and sustainability.

However, as important as understanding mobility is, the question of inadequate or lack of secondary and trend data to effectively run mobility analysis conventionally for some cities of developing nations has been recognized as a major drawback in the effort at understanding urban mobility in such settings. The seeming unwillingness and lack of political will to gather the needed data to adequately run mobility analysis is also a bane. This makes applicability of conventional data hungry mobility models in mobility evaluation for planning purposes in such situations unfeasible. Also, the computational complexity of high end models of mobility analysis brings about some loathing on the part of policy makers of cities fitting this description.

In technical terms, a common trait among contemporary mobility models, whether employed in the evaluation of mobility patterns based on studying trajectories, dynamic proximity networks or flow on networks is that, they cannot adequately capture constraints of human mobility, a critical determinant of mobility capabilities of individuals (Isaacman *et al*, 2012; Azevedo *et al*, 2009; Calabrese *et al*, 2010; Hong , 2010; Wang, 2011). For these reasons mobility evaluation in data deficient cities remain largely unexplored, where some data are available, they are most often than not, dirty. The dire shortage of expertise to handle advance modeling techniques for policy development and planning at the local levels is also a source of worry.

Despite all of these debilitating factors, mobility planning still proceeds, without concrete bases in cities such as described, because authorities of data deficient cities continue to make investment that target urban mobility improvements, even though disjointed and intermittent. This creates a need to fashion out alternative ways of assessing mobility needs and requirements of such cities. Hence, a parsimonious traveler percept based index option of assessing urban mobility environments, as a sub set of mobility analysis is suggested. Based upon indicators that can help gauge mobility ease from the context of what is deducible from the interaction between the moving subject (humans) and the containment within which mobility takes place (the environment). Tapping into the culminating stated perception of travel or movement by the traveler, from which engendered inhibitors and enhancers of mobility can be deciphered, may be a useful aid in urban mobility planning in data deficient settings as obtainable in some cities of the developing world. This paper puts forward an alternative framework for appraising mobility environments, where the application of contemporary mobility modeling techniques may not be appropriate.

2.0 METHODICAL AND PROCEDURAL CONSIDERATIONS

Mobility as an occurrence has been connected to accessibilty and social equity (Colleoni, 2013). Its evaluation is thought to provide useful clues in dealing with socio – economic, transportation, and human physical activity problems, thereby pointing to prevalent and associated factors underlying related occurrences (Florindo, *et al.* 2009). Bearing this in

mind, four important considerations are examined towards grounding the framework; these are approaches to evaluating mobility, the phenomenon "perception", the prospect of deriving a perception based index, and the likelihood of deriving a useful tool for appraising a city's mobility environment, out of them.

2.1 Methods of Evaluating Mobility

One of the main purpose of studying human or urban mobility is to investigate the population flow between different places (Hunter *et al*, 2011; Holme *et al*, 2003), at the microscopic and macroscopic level. Three major approaches have been employed over the years; the pragmatic, the mathematical and the interactive.

2.1.1 The Pragmatic Approach

The pragmatic approach attempts to develop an inclusive description of mobility behaviour via a mixture of qualitative and quantitative studies which are in turn presented in a non – quantitative form supported by simple tabulations and correlations. Specific aspects are then modeled by means of regular econometric techniques. For example, the non – quantitative description may be used to specify the circumstances under which movement take place. An example of this type of approach is Musselwhite and Hadad's (2010) classification of mobility need, see Fig. 1, the study classified mobility need into three groups, namely;

- Utilitarian or primary needs for mobility;
- Affective or secondary needs for mobility; and
- Aesthetics or tertiary needs for mobility

Figure 1: Three levels of Mobility Needs

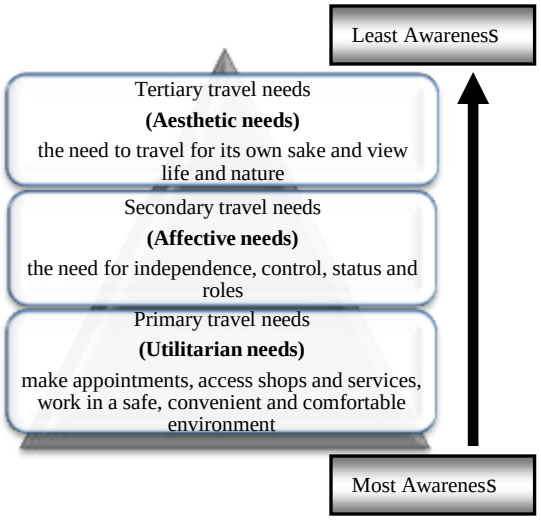

Source: Musselwhite and Hadad, 2010

At the *utilitarian* level, mobility needs are seen as derived demand for travel and as requirements in accessibility. Here, travel is tied to serving a function of accessing other human necessities, which means mobility is viewed as a means to an end. Similarly, *affective* need based mobility connotes movement carried out to affirm independence, control, and status in other to perform defined roles or participate in the society. The third type describes *aesthetic* needs for mobility. This explains travel done for its own sake, as a way of viewing life and enjoying nature, or for such purposes as recreation. The underscoring theme of this approach is its description of mobility as a necessity for human survival and independence.

2.1.2 The Mathematical Approach

The mathematical approach starts from the same descriptive base, but seeks to translate it into rigorous analytical models. These kinds of models are categorized according to their design and targets. The first class of models account for the properties characterizing the regular reappearance of users at a set of preferred locations, the SLAW group of models exemplifies this approach (Lee *et al*, 2009). The second group focuses on reproducing realistic temporal patterns of human mobility, explicitly including repetitive daily activities in human schedules (Zheng, 2010). The third class, are those aiming at incorporating sociality into models, thus considering human relations as the main driver of individual movements. For example, the SPoT model developed by Karamshuk *et al*, (2013), which sorts to link together all the three dimensions of human mobility using a flexible and controllable framework, which can be instantiated to the desired mobility scenario and which is naturally suited for mathematical analysis. Asgari *et al.* (2013) further classified mathematical models of mobility evaluation along three baselines (Fig. 2), namely dynamic proximity networks, trajectory based and flow on networks studies.

Mobility researchers have traditionally relied on expensive data collection methods, such as surveys and direct observations, to get a glimpse into the way people are moving. This requires that, a realistic model confront the individual (or household) with own travel environment and invite him to respond to changes, representing the policy or planning issues under review, in a distinct way. The fact that this is difficult to achieve, spurned the third approach to mobility evaluation.

Fig 2: Three main baselines of mathematical mobility studies

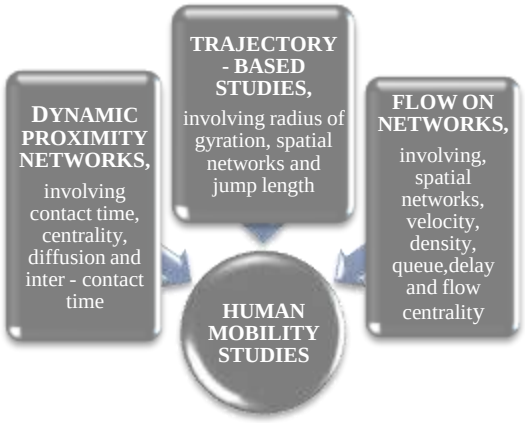

Source: Asgari *et al*, 2013

2.1.3 The Interactive Approach

The interactive approach questions the very basis of current econometric techniques. Stating that, if one cannot capture the essentials of an individual's decision making process in a finite set of mathematical equations, then why not use the individual (or household group) as a surrogate for this part of the model. These kinds of models are not all that common, although, all the priority evaluator and various interactive graphic techniques include the individual in their operational model. None of the techniques has yet offered a wholly satisfactory way of modeling mobility behaviour (Hong, 2010; Clauset *et al*, 2007). They deal in abstractions too far removed from the framework within which most individuals arrive at decisions. Therefore, the interactive approach considers it more useful to study social behaviours or group activity rather than individual trajectories, contact time and flow on networks (Clauset *et al*, 2007).

From the foregoing, it can be gleaned that a traveler centered approach to mobility evaluation is practicable, without necessarily carrying the complexities and huge data requirements of contemporary mobility models along, meaning, that a parsimonious technique that can suite the skill level and economic capabilities of underprivileged cities can be crafted.

2.2 Perception as a Phenomenon

The second important consideration as mentioned earlier, is the phenomenon "perception". The notion that perception affords the perceiver the opportunity to gather, process, and organize information about the environment in order to make sense out of it (Kovalik and King, 1998), is the main hinge of the procedure. Perception is important because it results from sensory experience of the world around us, shaped by environmental stimuli and actions in response to these stimuli. Through the perceptual process we gain information about properties and elements of the environment that are critical to our survival (Cherry, 2010). More so, Diener *et al.*, (1985) described perception as an important issue in research on subjective matters. In another submission, reiterating the significance of personal insights, Doi *et al*., (2008) related that conventional ease of access measures fail to include people's values or behavioural criteria and ability, which reduce the value for planners to evaluate practical issues, thus, leading to a conclusion that, objective conditions are not necessarily the best predictors of subjective satisfaction. This is so because researcher chosen factors cannot totally represent people's own judgment, owing to differences in individual capabilities in aspects regarding things like mobility. Consequently, urban mobility planners cannot rely only on the result of objective measurement as a way of understanding space for planning. Therefore, perception based assessments can help contribute valuable information towards improving mobility conditions by summing across individuals' perception within specific domains (Shafer *et al.*, 2000). The edge here is the capability of perception based constructs to directly show an individual's predisposition towards certain factors and installations around the city, given effect on personal mobility, thereby providing an opportunity to sum across samples.

2.3 Applicability of Perception Based Constructs in Urban Analysis

Many perception based urban studies have been carried out to determine a number of issues. To get insight into the determinants of cycling to school, Aarts, *et al.* (2013) used school pupils parent's perception of cycling routes in socio – ecological models (individual, social and physical environmental factors) to identify correlates at multiple levels. Cole *et al.* (2010) also used perception of traffic to demonstrate that demographic and environmental factors, such as traffic and busy roads can determine whether an individual's perception of an environment within which mobility takes place is negative or positive. Likewise, a study on a walking intervention programme, towards creating safe walking routes to school in a rural area of California, USA, succeeded in increasing walking rates to school, by using perception based criteria to identify needed interventions (Alton, *et al.* 2007). Another study showed how transit is perceived to be for the elderly,

the poor and the socially or physically disadvantaged, especially where car ownership levels are very high. Therefore, "perception" as a phenomenon lends itself well to urban analysis, a sub set of which is mobility evaluation. Also, the fact that each individual perceiver contributes in a unique manner to rating the mobility environment as either an enhancer or inhibitor of mobility is an important element of strength the tool imbibes. The process itself embeds democratic traits, and fosters user participation, consequently reducing the index of top – bottom influence common in developing nations.

2.4 Prospect of Deriving a Perception Based Index Construct

There are some major considerations in using indicators or index constructs in the measurement of phenomenon. Mingshun (2006) mentioned policy relevance, scientific soundness and measurability among some of the major attributes that should be considered. Off these three concepts, measurability is the most pertinent in this effort. In terms of measurability, indicators or index derivations should be based on data that are:

i. Readily available at reasonable cost versus benefit ratio;
ii. Easily understood and applicable by potential users;
iii. Acceptable to stakeholders;
iv. Adequately documented , of good quality; and
v. Updated at regular intervals.

To resolve the issue of measurability, two known methods of aggregating indicators into indices are applicable. These are the weighting and the non – weighting index aggregation techniques. Weighting indicators have been commonly used in the aggregation of environmental indicators, the preeminent example of weighting aggregated environmental indicators is provided in the works of Adriaanse (1993) and Hammond *et al.,* (1995). However, it is the introduction of normalization technique which scales all numeric variables between the range [0, 1] as explained by (Saitta, 2007), without units and disregarding physical dimensions, thereby eliminating bias and worries stemming from differing dimensional attributes of factors influencing perception, that enables direct comparison of values across board. This underscores the possibility for reliable measurement and indexing. It is therefore, evident that an indicator or index based construct to appraise a city's mobility environment qualities is attainable, because both objective and subjective indicators, including individual's self – report about conditions, subjective perception and other relevant social – economic indicators, such as employment rate have been used to gain insight into user sensitivity matters, mainly because a rational methodology to execute such a procedure can be attained. The normal process of an indicator programme is the same as building an information pyramid (Mingshun, 2006).

3.0 Framework for Percept Based Index Technique of Appraising Mobility Environment

An index provides an empirical and numerical basis for evaluating performance, calculating the impact of activities, categorizing, or connecting past and present activities to attain future goals (Giorgos and Gillian, 2005). An index jointly summarizes a system or indicates its status. To arrive at a descriptive index of the mobility support qualities of a city's environment, a thirteen (13) step procedure is proposed. The progressions are as listed below;

i. Harvest a list of potential mobility influencing factors from related literature, so as to create a compendium for further assessment.
ii. Enable expert contextual relevance assessment of harvested mobility influencing factors, in order to identify factors that are truly representative of situation in the environment under examination.
iii. Extract contextually relevant mobility influencing factors as per expert/practitioners recommendations;
iv. Categorize contextually relevant mobility influencing factors into thematic areas based on attribute similarities. For instance, factors with attributes describing road network characteristics are listed under such a thematic area. Characterization is required to justify group by group comparison of results, since factors work in unison to shape the perception of individual, as attested to by Sokolowska (2014);
v. Conduct a city wide mobility influencing factors' perception survey, based on template derived from thematic characterization;
vi. Rank factors based on general perception survey feedback using weighted mean;
vii. Assign accentuated factor Rank Order of Importance Points (ROIP), to define magnitudes of rank positions;
viii. Derive (ROIP) factor Index Equivalents (IE), by normalizing the sum of accentuated factor

Rank Order of Importance Points (ROIP) sequentially;

ix. Develop index interpretation table with mathematically attainable IE maximum and minimum accruable values;

x. Assignment of factor Index Equivalents (IE) according to perception defined rank positions for each city sub unit,

xi. Derive Average Category Index Equivalent (ACI) for thematic areas, as previously grouped;

xii. Compute city sub unit percept based estimate of mobility enhancement/hindrance level, by adding ACI values for all thematic categories;

xiii. Lastly, estimate City Mobility Environment support quality Index by finding the average value for all city sub units. Then compare resultant value to the index interpretation table, as described in ix above.

Fig 3: Schema of Urban Mobility Environment Appraisal Framework

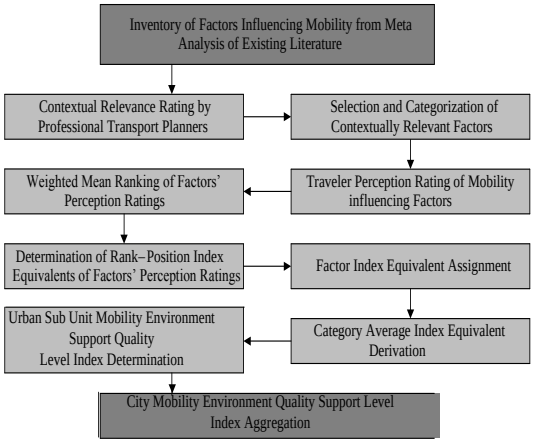

Two types of surveys are needed to acquire the minimal required data and information. The first one target urban mobility and transportation practitioners, while the second type is directed at general respondents. The experts are expected to help with factor contextualization and reduction exercise. The general survey on the other hand, is to elicit traveler percepts of contextually relevant mobility influencing factors, and to seek information regarding socio – economic characteristics and mobility needs of respondents'. Sampling should consider the official spatial sub-units of the city, administrative or planning districts or wards as the case may be. This is important for appropriate spatial delineation, questionnaire allotment, and task planning. The ultimate aim of the approach is to help identify constraints of mobility, so as to ease movement and foster adequate accessibility to component areas of a spatial entity, in a manner that will accommodate motorized and non – motorized travelers. This will expectedly be achieved by enabling proper issue targeting by decision makers.

4.0 Applicability of Perception Based Mobility Environment Appraisals

The percept based concept is conceived to provide an alternative avenue for urban mobility assessments, where standard, complex and contemporary instruments may not be appropriate. It is targeted at reducing the negative implications of data inadequacy, indeterminate mobility levels and seemingly baseless and piecemeal interventions that characterize mobility appraisals in cities such as earlier described. The tool will be useful in such scenarios because it uses minimal, cost effective and easily gathered data to appraise urban mobility environment support levels in cities without standard data bases for urban mobility assessments. City managers can employ the index tool in identifying where, when and what kind of interventions are needed to improve mobility, as such cities evolve. Index interpretations can also provide urban managers with an understanding of the kind of environment preferred by citizens within the planning district, by helping to establish a local benchmarking system. More so, the tool can help classify and rate environmental challenges to mobility as perceived by cross sections of the population. Intervention prioritization and budgeting matters is expected to become even more straightforward and objective. Ultimately, the tool will enable comparative analysis of mobility environment qualities within and between spatial units of interest, such as neighbourhoods, districts and cities. The framework can be used to identify lagging districts of cities or compare one city to another. The overall requirements of attaining stated mobility targets for different situations can easily be identified, pursued and monitored. The relative simplicity of the tool makes leveraging outputs or results for policy rationalization simple. The tool is likely to be more acceptable to policy makers who seem to loath highly technical approaches that usually require specialized knowledge to interpret. It is necessary to try options such as this in gauging urban mobility environment support qualities, not only for its simplicity, but also because it captures aspects of human mobility complexities, alongside being useful where data problems are evident. Parsimonious techniques such as this are therefore essential, if quality of life issues, urban mobility problems and their secondary, tertiary and quaternary offshoots are not to persist, in already disadvantaged settings.

References

Adeniji, K. 2000. Transport challenges in Nigeria in the Next Two Decades. Monograph Ibadan: Nigerian Institute of Social and Economic Research (NISER), Transport Studies Unit.

Adriaanse, A. 1993. Policy Performance Indicators. SDU Publishers, the Hague.

Asgari, F., Gauthier, V., and Becker, M., 2013. A Survey on Human Mobility and its Applications. Available from: complex.luxbulb.org/bibliography?f (author) = 121, Retrieved: 17th November, 2013.

Alton, D., Adab, P., and Barret, T. 2007. "Relationship between walking levels and perceptions of the local neighbourhood environment" Archives of Diseases in Childhood. 92(1): 29-33.

Aarts, M. J., Mathijssen, J.P., van Oers, J.M., and Schuit, A. 2013. Associations between environmental characteristics and active commuting to school among children: a cross -sectional study. International Journal of Behavioural Medicine, 20:538–555.

Azevedo, T.S., Bezerra, R.l., Campos, C.A., and de Moraes, L.F., 2009. An Analysis of Human Mobility using Real Traces. Wireless Comunications and Networking Conference, WCNC 2009. IEEE. (2009), 1-6. Federal University of Rio de Janeiro.

Calabrese, F., Di Lorenzo, G. and Ratti, C., 2010. Human Mobility Prediction based on Individual and Collective Geographical Preferences. Intelligent Transportation Systems (ITSC), 13th International IEEE Conference. 312 – 317.

Cherry, K. 2010. The Everything Psychology Book: An Introductory Guide to The Science of Human Behavior. 2nd Edition, Adams Media

Clauset, A., Eagle, N., 2007. Persistance and Periodicity in a dynamic proximity network. Proceeding of DIMACS Workshop on Computational Methods for dynamic interaction Network.

Cole, R., Burke, M., Leslie, E., Donald, M., and Owen, N. 2010. Perceptions of representatives of public, private and community sector institutions of barriers and enablers of physical active transport. Transport Policy, 17, 496 – 504.

Colleoni, M., 2013. Mobility, Accessibilty and Social Equity: A Comparative and Interdisciplinary Empirical Study in the Metropolitan Areas of Milan, Bologna and Turin. In Henckel, D et al eds. Space – Time Design of the Public City, Urban and Landscape Perspectives. Springer Science

Cresswell, T. 2010. Towards a politics of mobility. Environment and Planning D: Society and Space 28: 17‑31.

Diener, E., Emmons, R., Larsen, R.,and Griffin, S. 1985. The satisfaction with life scale. Journal of Personality Assessment, 49(1), 71 – 75.

Doi, K., Kii, M., and Nakanishi, H. 2008. An Integrated evaluation method of accessibility, quality of life and social interaction. Environment and Planning: Planning and Design, 35, 1098 -1116.

Florindo, A., Guimaraes, V., Cesarm C., Barros, m., Alves, M., and Goldbaum, M. 2009. Epidemiology of leisure, transportation, occupational, and household physical activity: Prevalence and associated factors. Journal of Physical Activity and Health, 6, 625 - 632.

Giorgos, M, Gillian, A and Kate, B., 2005. Modeling Rurality using Spatial Indicators. Available at: http://iisd.ca/measure/default.htm. Retrieved: 27th November, 2014

Haider, M and Badami, M (2004): Public Transit for the Urban Poor in Pakistan: Balancing Efficiency and Equity. *Regional Focus*; New Delhi, India.

Hammond, A., Adriaanse, A., Rodenburg, E., Bryant, D.,Woodward, R., 1995. Environmental Indicators: A Systematic Approach to Measuring and Reporting on Environmental Policy Performance in the Context of Sustainable Development. World Resources Institute, Washington, DC, 50 pp

Holme, P., et al. 2003. Congestion and centrality in traffic flow on complex network. Advances in complex systems, 163 – 176.

Hong, S., 2010. Human Movement Patterns, Mobility Models and Their Impacts on Wireless Applications. A dissertation submitted to the Graduate Faculty of North Carolina State University in partial fulfillment of the requirements for the Degree of Doctor of Philosophy Computer Science Raleigh, North Carolina.

Hunter, T., Moldovan, T., Zaharia, M., Merzgui, S., Ma, J., Franklin, J.M., Abbeel, P., and Bayen, A.M.

2011. Scaling the mobile millennium system in the cloud. Proceedings of the 2nd ACM Symposium on Cloud Computing – SOCC '11, 1 - 8.

Isaacman, S,. Becker, R., Caceres, R., Martonosi, M., Rowland, J,. Varshavsky, A,. and Willinger, W,. 2012. Human Mobility at Metropolitan Scales. Mobisys'12

Karamshuk, D., Boldrini, c., Conti, M. and Passarella. 2011. Human mobility models for opportunistic networks, Communication Magazine, IEEE 49 (12) 157 – 165.

Kovalik, C. and King, M.E. 1998. Visual Literacy, Available:http://www.educ.kent.edu/community/VLO; Retrieved 27th November, 2014

Lee, K., Hong, S., Kim, S., Rhee, I., and Chong, S. 2009. A new mobility model for human walks, in IEEE/ACM Transactions on 17 (5) 1564 – 1577.

Mingshun, Z., 2002. Measuring urban Sustainability in China. Thesis Submitted in Partial fulfillment of the Award of PhD to the Institute for Housing and Urban Development Studies (IHS) and Erasmus University, Rotterdam, the Netherlands.

Musselwhite, C., Haddad, H. 2010. Mobility, accessibility and quality of later life. *Quality in Ageing and Older Adults*, 11(1), 25-37.

Olufemi, O.B. and Oluseyi, M.S. (2007): The Urban Poor and Mobility Stress in Nigeria; *Environmental Research Journal* 1(1 – 4): 1 – 8, Medwell Online.

Patla, A.E., and Shumway – Cook, A., 1999. Dimensions of Mobility: Defining the Complexity and Difficulty Associated with Community Mobility. Journal of Aging and Physical Activity. 7. Pp. 7 – 19, Human Kinetics Publishers, Inc.

Shafer, C., Lee, B., and Turner, S. 2000. A tatle of three greenway trails: User perceptions related to quality of life. Landscape and Urban planning, 49, 163 – 178.

Sokolowska, K. 2014. Determinants and Perceptions of Social Mobility in Poland, 1992 – 2008, Contemporary Economics, Vol. 8, No. 1, pp. 89 – 109.

Spinney, J., Scott, D., and Newbold, B. 2009. Transport mobility benefits and quality of life: A time use perspective of elderly Canadians. Transport Policy, (16), 1 -11.

Vella – Brodrick, D.A., and Stanley, J. 2013. The Significance of Transport Mobility in Predicting Well Being, Transport Policy, Vol. 29, Pg. 236 - 242

Wang, S., 2011. Analysis of Human Mobility Modeling Methods. Seminar presented at the Florida Institute of Technology and Computer Science. USA.

Zheng, Q., Hong, X., Liu, J. and Cordes, D. 2010. Agenda driven mobility modeling, International Journal of Ad Hoc and Ubiquitous Computing 5 (1).

Zhu, Y. 1998. 'Formal' and 'informal urbanization' in China: Trends in Fujian Province, Third World Planning Review 20(3):267-284.

Shittu AbdulMajeed is a PhD candidate of the transport research group, department of urban and regional planning, University Teknologi Malaysia (UTM). Shittu's research interest areas include urban transportation, mobility and urban design.

Shittu AbdulMajeed has published articles in Open Journal of Social Sciences, IOSR Journals, Construction Focus, Maiduguri Journal of Arts & Social Sciences, and Journal of the Centre for Settlements, Housing & Urban Development.

He is a lecturer with the department of Urban & Regional Planning, Ahmadu Bello University, Zaria – Nigeria.

Muhammad Zaly Shah obtained his B.Sc. in industrial engineering from Bradley University, Peoria, Illinois, USA in 1992 and M.Sc. and Ph.D. in transportation planning from Universiti Teknologi Malaysia (UTM), Skudai Johor, Malaysia in 1998 and 2002, respectively.

He is an Associate Professor in the field of Transportation Planning at the Faculty of Built Environment, Universiti Teknologi Malaysia. He has published extensively and his articles have appeared in Safety Science, Transport Review, Land Use Policy and Traffic Injury Prevention. His current research interests include pedestrian modelling and traffic safety.

Dr. Muhammad Zaly Shah is a chartered member of the Chartered Institute of Logistics and Transport (CILT). Dr. Muhammad Zaly Shah is the recipient of Outstanding Teaching Award of UTM in 2007 and Outstanding Service Award in 2015.

URBAN CONFIGURATION EFFECT ON URBAN MICROCLIMATE AND THERMAL COMFORT

Lin Yola[1] and Ho Chin Siong[2]
[1]Department of Built Environment, Universiti Teknologi Malaysia and UCSI University, Malaysia
[2]Department of Built Environment, Universiti Teknologi Malaysia, Malaysia

ABSTRACT
Study on urban microclimate and thermal comfort had been addressed to stress the use of the both aspects as well as their impact on human and built environment. The debate emphasizes that both variables result two significant influences that could relate each other. This study investigates the gap by conducting the study from the urban configuration perspective. The hypothetical urban configuration model simulation was used to examine the impact of different urban configuration scenario to see the gap of the two variables. The finding indicates significant impact of the urban configuration on two variables, where the gaps vary according to the choice of the urban configuration and direction. This emphasizes that urban planners and designers have to analyze the urban configuration scenario before come to the design and planning decision on early stage of urban development plan.

Key words: Urban Configuration, Urban Micro Climates, Urban Thermal Comfort.

1. INTRODUCTION

Urban development has been causing stress on social and environmental issues. Rapid population in urban area requires multiple demands on development, which one major part of it is buildings and living environment. Increasing number of residential and commercial buildings however causes the spatial problem 'fighting for space'. The urban development goes vertical as alternative dealing with space issue (Lin and Ho, 2013). Green area becomes the 'sacrificed' space to accommodate more built up are for city dwellers' activities, where most of open space is covered by concrete and road. Both building and pavement surface contribute more heat in city area. Extreme increase of heat has been a global concern since it is a direct cause of climate change which not only will affect the future of the earth but it starts to influence the human activity especially in the urban area nowadays. Unfortunately, as result of the extreme heat in urban area, the high demands of air conditioning which consume more energy also release more Co_2 and pollution concentration to the environment. This phenomenon continuously causes higher temperature increase and poor thermal comfort for both indoor and outdoor urban environment. More studies and scholar strategies from scientists have been attempted to mitigate bigger damages or to minimize the development impact. This paper is illustrating how the simulation study could be one of the methods to quantitatively investigate that the heat increase is possibly avoided through urban design and planning strategies.

2. URBAN MICROCLIMATE AND THERMAL COMFORT IN URBAN SCENARIO

Technically, urban heat is directly related to urban microclimate and urban thermal comfort. From the scientific and human perspective, both aspects are an urge to the current and future scenario. Urban microclimate is usually measured by air temperature (Ta), surface temperature, and solar radiation (Mehdi et al. 2014). Air temperature significantly contributes the major measure of Urban Heat Island (UHI). Urban Heat Island phenomena is again mainly caused by rapid urban development, it recorded that high city development has 9℃ -10° C warmer that surrounding rural open (Garstang et al. 1975 and Oke, 1982). The increase of air temperature in urban area directly influences on city dwellers' thermal measures towards the environment, especially outdoor. Due to this matter, urban thermal comfort which is measured by Meant Radiant Temperature (Tmrt), Physiological Equivalent Temperature (PET) etc. always been an issue for human activities in outdoor environment in most of tropical country like Malaysia (Ghazizadeh, 2010 and Monam, 2011). The heat that is influenced by direct and diffuse solar radiation, building and paving materials, high concentration of pollution etc. has been highlighted contributed not only by high density urban development but also by the urban design and planning strategies. For instance, urban building blocks are always crowdedly constructed in the city center without proper planning. Urban designers and planners have been highlighting that the measure of urban microclimate could actually be modified by strategizing urban design (Katzschner, 2011). The spaces between the buildings could be planned as a cooler area which is shaded by the surrounding urban building blocks. Scientists, urban designers and urban planners stress in many studies that urban microclimate could be adjusted by knowing the better scenario of controlling solar radiation, wind flow and direction, as well as humidity. However, there are many debates on the indicators that affect it and to which extend it could be technically applied through the urban design and planning strategies, which one of it is urban configuration (S. Glawischnig et al., 2015). Therefore, this paper attempts to pin point that the degree of urban configuration could create the cool outdoor area in order to reduce the urban microclimate as well as improving the outdoor thermal comfort and how both variable create the gaps each other.

3. METODOLOGY

In order to investigate the said gap, this study performed a simulation study on urban configuration. Five hypothetical urban block configuration models were designed according to open space direction to solar angle (Refer to Fig.1). The urban site is a 10 grids area with the ratio of basic model (Model A) built up to open space ratio is 32:68. Model A as the basic was designed with enclosed open space. Model B was design with 4 grids lesser with open space is heading to one side of urban block was exposed to solar. Model C and D were designed with two sides open to solar, Model C was designed bigger opening exposed to solar while Model D was designed as canyon and the open space is in between blocks. Model E is the only model designed as single block exposed and directed to solar radiation. The receptor was planned as the constant variable and location, which is located in the middle of the open space.

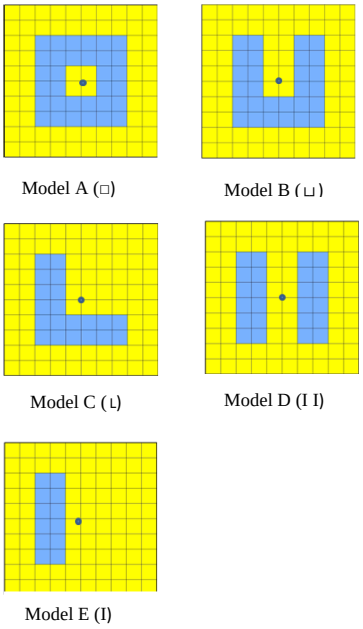

Fig. 1: Five hypothetical urban block configurations

Envi-met 3D microclimate analysis was chosen as the most suitable tool to perform the study (Lin and Ho, 2014). It has the feature of investigating both air temperature and thermal comfort. In order to fairly examine the influence of the urban block direction to the both variables, the simulation was grouped into four cardinal directions, East, West, South and North. The model location was adjusted in Kuala Lumpur City Center (coordinate 3°9' N 101°43' E). To avoid the influences from the external factor to the simulation, it was assumed that the site was situated with stand-alone scenario without any surrounding buildings, human made or natural features.

The data was taken for 24 hours in order to get day and night data. This is due to this study aims to investigate the night data beside the day data to extract the Urban Heat Island data through the air temperature. The data was taken 0 meter from the land surface. As the simulation was situated in Kuala Lumpur, the property data was set as follow: temperature was at 293° K, all temperature layer of soil data were at 300°K, wind direction at 10m level was 1.6 m/s, relative humidity was at 83%, wind direction was at 225, heat transmission walls was 1.94 W/m2K and heat transmission roofs was at 6W/m2K, while the albedo was at 0.3 and albedo roof was at 0.5.

4. RESULT DISCUSSION

In order to determine the gap between the two variables, the data is presented and analyzed according to air temperature as well as meant radiant temperature.

4.1 AIR TEMPERATURE

The air temperature data is justified according to urban configuration and urban block direction. Model A resulted constant air temperature which is 27.35°C. Model B resulted East direction has the highest air temperature (27.20° C), followed by West (27.14° C), South (27.08° C) and North (27.04° C). Model C shows that East direction resulted the highest air temperature (27.49° C), followed by North (27.38° C), South (27.04° C) and West (226.71° C). Model D indicated the highest air temperature resulted by North direction (27.70° C) followed by East and West (27.29° C) and South direction (26.97° C). Model E indicates South direction resulted the highest air temperature (27.80°C) followed by East direction (27.40° C), West direction (27.32° C) and North direction (27.24° C). The data shows that the highest air temperature is resulted by Model E when facing South and Model D while facing North, followed by Model C facing East and Model E facing East (Fig.2). The lowest air temperature is resulted by Model C facing West and Model D facing South.

As summary, the average of air temperature if the four cardinal urban block direction shows that Model E indicates the highest air temperature (27.04° C) followed by Model A (27.35° C), Model D (27.31° C), Model C (27.16° C) and Model B (27.12° C) (Fig.3). Model E that result the highest air temperature due to it was designed just with one side block and that means it lacks of the shading from direct solar radiation. Contrary, Model A that is enclosed for four sides resulted the second highest air temperature (27.35° C). This is due to the heat is trapped without any opening for wind access to the open space area. Model B resulted the lowest air temperature scenario as the three sides shade the open space from the direct solar direction as well as the availability of wind access from the open side of the site.

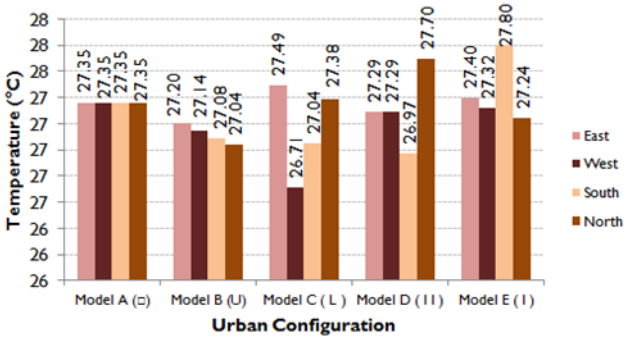

Fig. 2: Air temperature according to hypothetical urban configurations

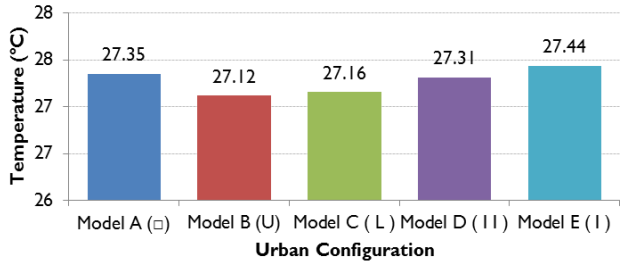

Fig. 3: Summary of air temperature according to hypothetical urban configurations

When the urban direction was kept constant, the data is presented and detailed as Fig.4. This data will be useful when urban designers and urban planners are given the fixed or suggested urban block direction in remodeling the site. However, when the data were analysed according to the average of all urban configurations, East direction resulted the highest air temperature (27.35° C) followed by North direction (27.34° C), South (27.25° C) and West (27.16° C) (Fig.5). The East direction indicated this data due to the temperature raise from morning to noon, while the West direction resulted the lowest because the air temperature reduced when it reached evening.

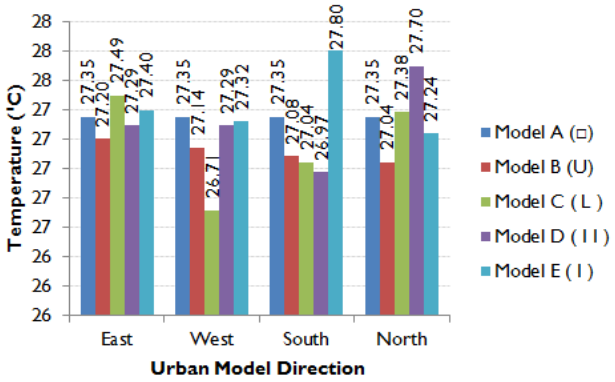

Fig. 4: Air temperature according to urban direction

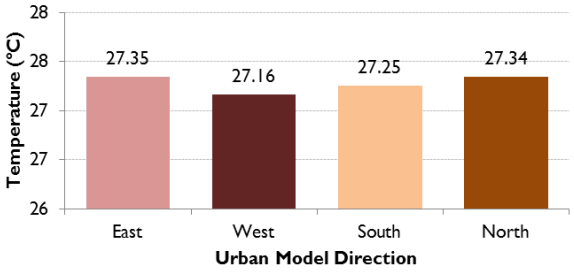

Fig. 5: Summary of air temperature according to urban direction

4.2 MEANT RADIANT TEMPERATURE

Meant radiant temperature (Tmrt) data shows more variety gap of temperature among urban configuration models and directions. Model A resulted East direction with highest Tmrt (33.36℃), followed by South direction (30.94℃) and both West and North direction (28.51℃). Model B indicated West direction with the highest Tmrt (37.70℃), followed by South direction (36.77℃), East direction (35.84℃) and North direction (28.06℃). East direction was recorded has highest Tmrt for Model C (37.60℃), followed by North direction (34.53℃), South direction (31.70℃) and West direction (25.80℃). Model D indicated East direction resulted highest Tmrt (48.87℃), followed by South direction (43.82℃), West direction (38.78℃) and North direction (27.10℃). Lastly, Model E resulted East direction with the highest Tmrt (43.52℃), followed by South direction (38.64℃), West direction (33.75℃) and North direction (24.71℃).

In overall, Model D facing East resulted the highest Tmrt followed by Model E facing East, while the lowest Tmrt was recorded by E facing North followed by Model C facing West (Fig.6). As summary, the average data of all urban models shows that Model D results the highest Tmrt while Model A has the lowest Tmrt (Fig.7). This indicates that urban configuration choice influences the level of the occupants' Tmrt. Model D which was designed in urban canyon scenario has the highest Tmrt that is influenced by the two sides are exposed to solar radiation. While Model A indicates the lowest Tmrt due to all four cardinal direction are protected by the urban block from the direct solar radiation.

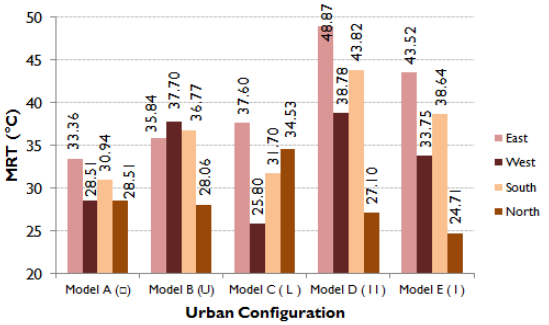

Fig. 6: Tmrt according to hypothetical urban configurations

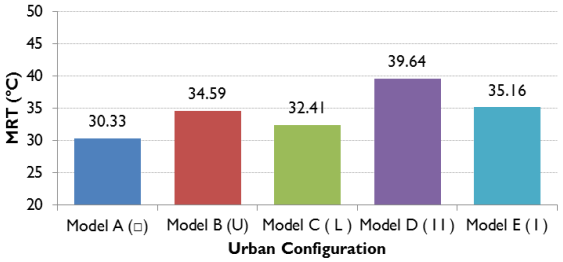

Fig. 7: Summary of Tmrt according to hypothetical urban configurations

The same details of Tmrt level according to the urban model direction for all urban configurations also presented as Fig.8. However, when the data were grouped according to the urban model direction, East direction has the highest Tmrt followed by South direction, West direction and North direction (Fig.9). Again, this indicates that East direction is exposed to rise of solar radiation between morning and noon time resulted the highest Tmrt which will not be comfortable for city dwellers to conduct their outdoor activities.

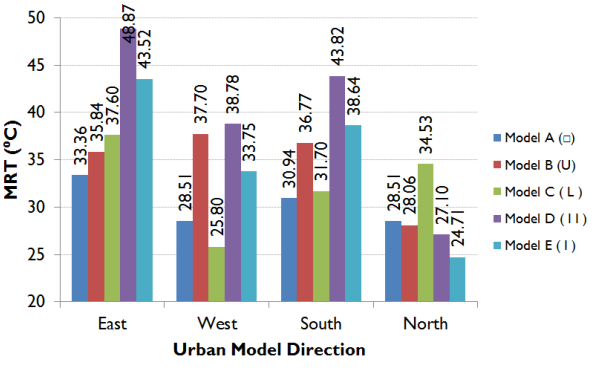

Fig. 8: Tmrt according to urban block direction

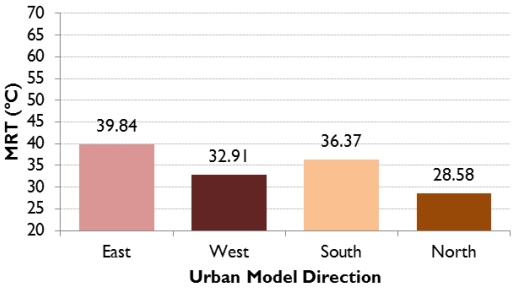

Fig. 9: Summary of Tmrt according to urban direction

4.3 SUMMARY

The comparison of final measures of air temperature and Tmrt presents the gap between the two variables. In order to do this, the average air temperature and the average of Tmrt are used for comparison. Table 1 shows the comparison of both variables from the choice of urban configuration while Table 2 indicates the comparison of two variables from the urban direction scenario. The results highlight that the air temperature difference is slightly minor where the Tmrt varies with the big gap. Model A with the enclosed open space indicates a slight gap between the air temperature and the Tmrt (2.98˚C), while Model D with urban canyon scenario shows the biggest gap (12.33˚C). This result indicates that the trend of both air temperature and Tmrt do not significantly influence each other. From the urban direction investigation, East direction results the highest gap between air temperature and Tmrt (12.49˚C) while North direction has the minimum gap (1.24˚C). Again, this shows that both variables of air temperature and Tmrt don't significantly affect each other.

Table 1: Comparison of Air Temperature and MRT according to Urban Model Configuration

Urban Configuration	Air Temperature (˚C)	Tmrt (˚C)	Gap (˚C)
Model A (□)	27.35	30.33	2.98
Model B (U)	27.12	34.59	7.47
Model C (L)	27.16	32.41	5.25
Model D (I I)	27.31	39.64	12.33
Model E (I)	27.44	35.16	7.72

Table 2: Comparison of Air Temperature and Tmrt according to Urban Model Direction

Urban Direction	Air Temperature (˚C)	Tmrt (˚C)	Gap (˚C)
East	27.35	39.84	12.49
West	27.16	32.91	5.75
South	27.25	36.37	9.12
North	27.34	28.58	1.24

5. CONCLUSSION

The data present the quantitative proof of urban configuration could be one of the features of urban design and planning that could be adjusted and planned to achieve the maximum attempt to reduce both outdoor air temperature and meant radiant temperature. The study justifies that the choice of urban configuration which utilize urban block to shade the open space between the high density urban development in order to mitigate the Urban Heat Island which indirectly affects the level of city dwellers' outdoor thermal comfort. When air temperature changes due to how extend the open spaces between buildings exposed to direct solar direction, the meant radiant temperature also changes due to how the open space is exposed to direct and indirect solar radiation and wind access. Even though the trend of both variables are not significantly identic each other, but the gap between the readings of the air temperature could affect the Urban Heat Island enough in a general scenario. For the meant radiant temperature, the data clearly present the significant impact of urban configuration on the thermal comfort. When applicable, the choice of urban block direction also could reduce both air temperature and meant radiant temperature. This finding contributes to urban and planning strategies in order to compromise with climate issues caused by built environment scenario. Furthermore, some further detail studies on the urban configuration are needed to apply this finding comprehensively on urban design and planning.

REFERENCES

Garstang, M., Tyson, P.D., Emmitt, G.D. 1975. The structure of Heat Islands. Rev. Geophys. Space Phys., 13. 139-165.

Ghazizadeh S. Neda, Monam Alireza, Mahmoodi Amir Saeid, 2010. The impact of the Architectural Design on the Thermal Comfort of the Outdoor Spaces in Residential Complexes. Honar-ha-ye-Ziba, 42 (2010) 59-70.

Katzschner Lutz, 2011. Urban Climate Strategies Againts Future Heat Conditions. Architecture and Climate. Manual of Bioclimatic Design for Architects and City Planners. USA. Princeton University Press.

Lin Yola and Ho Chin Siong (2013). Understanding Vertical City Concept. 4th International Graduate Conference on Engineering, Science, and Humanities. Universiti Teknologi Malaysia.

Lin Yola and Ho Chin Siong (2014). Modelling and Simulation Approach of Assessing Urban Form (A Review). International Journal of Emerging Trends in Commerce, Humanities and Social Science (CEHSS).

Mehdi Shahrestani, Runming Yao, Zhiwen Luo, Erdal Turkbeyler, Hywel Davies. 2014. A Field Study of Urban Microclimates in London. Renewable Energy Journal 71(2015) 3-9.

Monam Alireza. Comfortability in Urban Open Spaces; Evaluation of outdoor Thermal Comfort in Urban Parks. (PhD), Iran University of Science and Technology, Tehran.

Oke, T.R., 1982. The Energetic Basis of the Urban Heat Island. Q. J. R. Met. Soc. 108. 1-24.

S. Glawischnig, K. Hammerberg, M. Vuckovic, K. Kiesel & A. Mahdavi, 2015. A Case of Geometry-Based Automated Calculation of Microclimatic Attributes. eWork and eBusiness in Architecture, Engineering and Construction – Martens, Mahdavi & Scherer (Eds). Taylor & Francis Group, London, ISBN 978-1-138-02710-7.

STUDY of WIND CATCHER and SOLAR CHIMNEY PERFORMANCE to INCREASE VENTILATION in BUILDINGS

Alireza Gharakhani[a], Eka Sediadi[b] ,Hadi bagheri sabzevar[c] and Mohd Yunus Embok mosik[d]

[a]alireza_gharakhany@yahoo.com, [b] ekasediadi@utm.my, [c] hbagheris@yahoo.com, [d]fagatfriend@gmail.com

ABSTRACT

This study aims to review the effectiveness of solar chimney and wind catcher in the tropical climate. It concentrates on residential buildings without air conditioner. It helps to improve the design of green high rise residential buildings in Malaysia. This research focuses on increasing air velocity (air flow rate) by natural ventilation. The aim of this research is to investigate the potential of wind catcher and solar chimney to help provide thermal comfort conditions in high rise residential buildings. This research tried to improve usage of science to help build low carbon economies and to develop potential of renewable energies. To improve the effectiveness of natural ventilation, solar chimneys are always integrated with other technologies. According to researchers' opinion, solar chimney performance can be enhanced through a combination of natural cooling systems. The mechanism suggested is a combination of solar chimney and wind catcher that can raise air velocity in buildings.

INTRODUCTION

Changing climate and increase of air temperature are the major challenges in terms of the steadiness of civil society, the protection of access to natural resources, and the ecological integrity of the human environment. This has also caused serious natural disasters and unexpected in some countries such as floods in Malaysia (Siong Ho, 2007). A decrease of non-renewable fossil fuel consumption especially in the building sector is a one of the important things to be done. Some countries have a very good potential in renewable energies (Azhari, 2008). One of the methods to reduce the energy consumption is natural ventilation. Natural ventilation is considered as a technology providing acceptable indoor air quality. It also maintains the healthiness and comfort which makes it more favorable than mechanical ventilation (H. Montazeri et al, 2010). Passive cooling is known as one of the big challenges in some countries with tropical region. In view of this, there is a need to improve on natural ventilation (Hamdan, 2006). In this research, how to increase natural ventilation (through increase air velocity) was studied in tropical climate with the use of solar chimney and wind catcher in residential buildings.

Natural Ventilation

One of the most important challenges in tropical regions is Passive Cooling. The physiological cooling in residential buildings could be possible through increasing the wind speed. Recent data from the Meteorological Service Departments and wind profile in some countries of tropical climate such as Malaysia show that average outdoor air movement reduces nearer the lower levels especially at the ground level of buildings. Based on this observation, natural ventilation needs to be improved (Hamdan, 2006). Also in Malaysia, the average indoor air velocities in activity level (1.1m) is less than the minimum required air velocity (0.6 m/s– 1m/s) for thermal comfort condition (temperatures 26ºC – 33ºC and humidity 80% and 90%). Using a solar chimney to stack induced ventilation could modify ventilation. Nugroho et al., (2007) believe that installing a solar chimney in hot and humid tropical climates to reduce indoor temperature and increase indoor air velocity as well as natural ventilation can improve the performance. In addition, the wind catcher system captures wind from the external air stream and directs it into the building to cool the inside space with physiological cooling. The experimental studies show the potential of the wind catcher to improve the natural ventilation inside buildings (Montazeri et al., 2008).

Solar chimney

Natural ventilation is the air flow generated by temperature differences, pressure differences or both them. The basic mechanism of natural ventilation is the air movement between inside and outside spaces. Oftentimes the wind and pressure difference between inside and outside the buildings are known as the dominant driving mechanism in natural ventilation; however, the temperature differences between indoor and outdoor plays its important role (Linden, 1999). To raise the temperature of the ventilation path which is separated from occupied spaces, one can use a system known as solar chimney where the

solar radiation heat provides buoyancy to remove the heat of interior spaces (Montazeri et al., 2010).

Previous studies (Chok Chai et al., 2007; and Khedar et al., 2000) confirm that this technique is effective in hot and humid climate with high solar radiation. Solar chimney is a thermo syphoning air channel in which thermal buoyancy leads to air flow as the main driving mechanism. This mechanism enjoys solar radiation to improve the ventilation. Due to the heat of solar radiation and density of the air inside the chimney, the temperature drops which in turn results in the air rising and expelling out of the chimney. This system can be used as an independent element in buildings; however, to obtain effective natural ventilation, solar chimneys are always integrated with other technologies. Zhai (2011) believes that the solar chimney could be an effective and economical method for low carbon buildings. To improve the stack ventilation, a combination of solar chimney with solar induced ventilation could be a good alternative. Solar chimney also provides passive heating or cooling that can reduce overall heating and cooling load. However, according to Khanal and Lei (2011), the design parameters still prove unclear and meeting the ventilation requirements involves a guideline. Moreover, despite continuous research on the solar chimney, this system should be investigated deeper to consider passive ventilation strategy in different aspects.

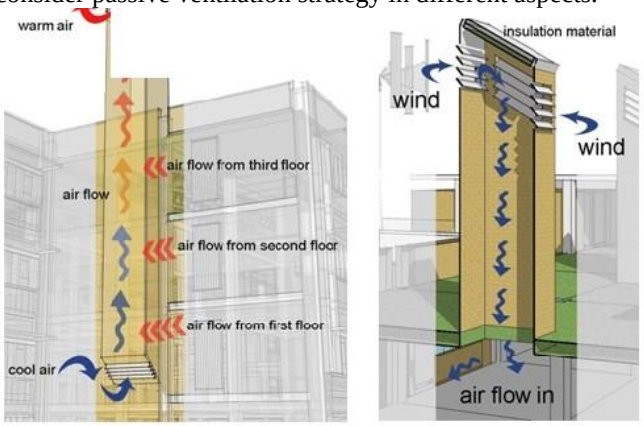

Fig. 1 Passive cooling system: a) solar chimney; b) wind tower, (Yiwei Liu, Wei Feng, 2011)

To investigate the possibility of using solar chimney as stack induced ventilation strategy in a terraced house in Malaysia, Hamdan et al., (2006) did a research on the development of tropical solar architecture and the use of solar chimney as a stack induced ventilation strategy. Their suggested mechanism was a solar chimney that could induce the flow of natural ventilation regardless of the outside wind. This research highlights the effectiveness of passive natural ventilation in thermal comfort performance in terraced houses.

Wind catcher

Natural ventilation has become an increasingly attractive method for reducing energy consumption and cost. This technology also helps to provide acceptable indoor environmental quality and maintain a healthy, comfortable, and productive indoor climate compared to mechanical ventilation approach. The wind catchers keep natural ventilation inside buildings due to wind as well as buoyancy effects (Nouanegue, 2008). The wind catcher system catches the wind from the external air stream and generates it into the indoor spaces.

Fig. 2. Samples of wind catchers in hot and humid climates of Iran such as Bandar Abbas and Qeshm Island.

The researches done by Mahmudi, M and Mofidi, S (2008) about wind-catcher background in pre-Islamic Iran provide valid evidence extracted from literary texts, historical background of wind-catcher around the world certainly goes back to BC however, it is not known who was the first to invent it. At present, the oldest document is papyrus map from 1500 BC in Egypt (wind-catcher was called required in Egypt) and it goes back to 4000 BC in Iran based on existing works. Archaeologists have found a part of a building in North of Shahrood (Masuda - Iran) that includes a possible wind catcher. They are still unsure about the function of this part of building (It can be just a fire place chimney). The oldest Arabic texts that relate to the 5th century AH used a Persian word that is Badhanj and also the oldest present wind-catchers are in the courtiers South of Iran in UAE which are related to Bastek areas of Iran whose inhabitants had emigrated from Iran to Bastek of UAE and started to build buildings with significant wind-catchers. Therefore, it can be concluded that Iranians had used wind-catchers before Arabs in Persian Gulf area which inspired them to apply the technique later. The present wind-catchers in the south of Persian Gulf countries had been made like the wind-catchers in hot and humid climates of Iran such as Bandar Abbas, Bandar-Lengeh, Kong and Qeshm Island. Traditional architecture in the neighboring countries of Iran is also seen such as Pakistan, (interlude), Afghanistan, Iraq, and also the Mediterranean regions such as Syria, Lebanon, Palestine, Turkey, and Mesopotamia Island. In other areas, the simplest one has

been seen among Muchika Indians of Peru (Mahmudi, M. Mofidi, S., 2008).

Categories and Various Generations of Wind-catchers

Wind-catchers of hot and dry climate or hot and humid climate in Iran have been always used in the summer-staying part of houses, that is, the southern part of the courtyard. Due to climatic conditions and favorable wind direction, wind-catchers have been made short in some areas like Birjand and height in some areas such as Yazd. Wind-catchers of cities like Birjand have no scaffold in their wall due to the area low altitudes. In cities such as Yazd, because of wall height of wind-catchers, there are scaffolds. Materials used in wind-catchers are canvas materials such as clay and brick. Roof of wind-catchers have been designed and built in either flat and steep or curved. All wind-catchers studied in the areas of Birjand and Yazd have brick eaves (a row of protrusive bricks in the upper part of the roof) in order to protect and provide more durability for wind-catcher opening. To comply with symmetry principle, more than 95% of wind-catcher openings areas studied in Birjand, Iran have been designed in odd numbers (from 3 to 9 openings) (Hashemi Zarj Abad, H., Masudi, Z., 2012).

Wind-catchers can be divided into and examined from three perspectives: performance, climate and angle of windward to wind direction. Based on their functions, wind-catchers are divided into two categories: purely functional and functional - symbolic (Meamariyan, 2008). Also wind-catchers typology can be divided into and examined from two perspectives: General Form of the Wind-catcher plan and form of the inside blades.

General Form of the Wind-catcher Plan are generally seen with circular, hexagonal, octagonal, square and rectangle plans. Wind-catchers with rectangular plan are the most common type of wind-catcher in Yazd.

Form of inside blades divide the wind-catcher channel into several smaller channels. These blades can be classified into two groups: main blades and blade sub-divided. The main blade height is from 1.5-2.2 meter from the ground floor to the ceiling of wind-catcher and divides the wind-catcher channel into the smaller channels.

Operating System of Wind-Catchers in Hot and Humid climate

The main function of wind-catchers of buildings is to aid ventilation and suck fresh air to interior spaces which is also used as cooling foods by placing the food in the path of wind-catcher channels. Wind-catchers will help to ventilation and cool down the air inside the rooms via convection, air movement and evaporation (evaporation cooling) (Vafamehr, M., Pour Johari, A., 2008). Some other methods have been used to strengthen the cooling performance of wind-catcher and using the evaporative cooling. For example, there is a wind-catcher in Bam city which is about 50 meters away of the building and is connected to it by an underground canal. There is a little garden above this canal. After watering the garden, its moisture will penetrate into the wall of the connected canal and the breeze makes the wind blowing from the wind-catcher to the building even cooler. In some cases, mat, clay and or thorn bushes were also put on the wind-catcher openings and sprayed water on it and thereby, humidity and inside air cooling were increased (Ghobadiyan, 2006. Pirnia, 1986) but hot and humid climate, the wind-catcher makes cool the air only through convection and air movement and evaporative cooling process is not used in which there was not full control of air flow and the amount of moisture and cooling (Vafamehr, M., Pour Johari, A., 2008). The best sample of wind-catchers can be seen in hot and humid areas in the south of Iran in Qeshm Island (Laft), Bandar-e- Lengeh and Bandar-e Kang. The massive, four-sided wind-catchers are still the main symbol of these cities. Wind-catcher mechanism in this region is similar to the central region of Iran; just as it was mentioned before; Cooling function of these wind-catchers is only done through air movement. Another thing is that air breeze and local winds generally in this region are less severe than those in central areas of Iran and therefore, wind-catcher should be larger to carry a greater flow of air into the room. In some cases, the cross-sectional area of the wind-catcher is more than 8 square meter and covers the whole of the room roof (Ghobadiyan, 2006).

CONCLUSION

This study tried to improve usage of science and innovation to help build low carbon economies that researcher seeks to develop potential of renewable energies and improve the research base in this crucial area. This research suggested further studies to obtain the suitable using of solar chimney and wind catcher that their potential in the form of simulation could be shown in residential buildings. It seems to continue this study will add value to the body of knowledge of green building and green energy use which can help to enhance the functioning of natural ventilation systems and passive design that help to increase thermal comfort in hot and humid climates.

Acknowledgment

This research is supported by Research University Grant Scheme Tier 1(GUP-PY/2014/02177) Universiti Teknologi Malaysia. The authors gratefully acknowledge the financial support provided by Universiti Teknologi Malaysia and the cooperation and research support from the Department of Architecture, Faculty of Built Environment, also Center for Information Communication and Technology (CICT) of UTM. As well as the support and assistance by Abdolreza dashtizade head of Heritage culture office (Qeshm Free zone, QFE).

REFERENCES

Azhari, A. W., Sopian, K., Zaharim, A., & Ghoul, M. A new approach for predicting solar radiation in tropical environment using satellite images-case study of Malaysia. WSEAS Trans. Environ. Dev, 4, 373-378, 2008.

Chungloo, S., & chok chai, B. Application of passive cooling systems in the hot and humid climate: The case study of solar chimney and wetted roof in Thailand. Building and Environment, 42(9), 3341-3351, 2007.

Ghobadiyan, V. Ecological study of traditional buildings, the Institute of Tehran University Publishing and Printing, 2006

Hamdan, M. Nugroho, A. Possibility to Use Solar Chimney to Improve Stack Ventilation in Tropical Climate. Alam Bina, 8(1), 1-22, 2006.

Khanal, R., & Lei, C. Solar chimney—A passive strategy for natural ventilation. Energy and Buildings, 43(8), 1811-1819, 2011.

Khedari, J., Mansirisub, W., Chaima, S., Pratinthong, N., & Hirunlabh, J. Field measurements of performance of roof solar collector. Energy and Buildings, 31(3), 171-178, 2000.

Hashemi Zarj Abad, H. Masudi, Z. Wind-catcher, A Masterpiece of architectural Traditional engineering in the desert; architectural typology analysis of the desert wind-catcher in South Khorasan - Cultural Studies - Social Khorasan, 5 (24), 166 - 198, 2012.

Lin, W., Gao, W., & Liu, T. A parametric study on the thermal performance of cross-corrugated solar air collectors. Applied Thermal Engineering, 26(10), 1043-1053, 2006.

Linden, P. F. The fluid mechanics of natural ventilation. Annual review of fluid mechanics, 31(1), 201-238, 1999.

Mahmudi , M . Mofidi , Seyed Majid . Iranian identity wind-catcher and finding its background in Iranian architecture, Journal of City identity, 2 (2), 25-33, 2008

Montazeri, H., Montazeri, F., Azizian, R., & Mostafavi, S. Two-sided wind catcher performance evaluation using experimental, numerical and analytical modeling. Renewable Energy, 35(7), 1424-1435, 2010.

Nouanegue, H., Alandji, L., & Bilgen, E. Numerical study of solar-wind tower systems for ventilation of dwellings. Renewable Energy, 33(3), 434-443, 2008.

Nugroho, A. M. Solar chimney geometry for stack ventilation in Malaysia terrace house. Universiti Teknologi Malaysia, Fakulti Alam Bina, 2007.

Pirnia, M. K, a collection of lectures on archeology section, Tehran, 1986

Vafamehr, M . Pour Johari, A –Wind-catcher; achievements of traditional Iranian architecture –Civil International Journal - 64 , 2008.

Siong , & Fong, W. K. Planning for Low Carbon Cities-The case of Iskandar Development Region, Malaysia, 2007.

Zhai, X., Song, Z., & Wang, R. A review for the applications of solar chimneys in buildings. Renewable and Sustainable Energy Reviews, 15(8), 3757-3767, 2011.

Alireza Gharakhani received the B.Arch. (1998), M.E. (2001).

He is currently a PhD student in Department of Architecture, Faculty of Built Environment Architecture from Universiti Teknologi Malaysia, Johor Bahru, Johor, Malaysia. His Current interests include Green Building and Sustainability Architecture.

Eka Sediadi received the B.Arch. (1985) and PhD (1996).

He is an Associate Professor, Department of Architecture, Faculty of Built Environment Architecture from Universiti Teknologi Malaysia, Johor Bahru, Johor, Malaysia. His Current interests include Solar Energy in Building and Green Architecture.

.

Hadi Bagheri Sabzevar received received the B.Arch. (1998), M.E. (2001).

He is currently a PhD student in Department of Architecture, Faculty of Built Environment Architecture from Universiti Teknologi Malaysia, Johor Bahru, Johor, Malaysia. His Current interests include Green Building and Sustainability Architecture.

.

Mohd Yunus Embok mosik is currently a M.E student in Department of Architecture, Faculty of Built Environment Architecture from Universiti Teknologi Malaysia, Johor Bahru, Johor, Malaysia. His Current interests include Solar Energy in Building and Green Building.

Bioscience, Biological and Engineering Science

ROLE OF HAND IN POSTURE BALANCE CONTROL

Aizreena Azaman, and Shin-ichiroh Yamamoto
Department of Bioscience and Engineering, Shibaura Institute of Technology

Abstract: The aims of this study is to investigate the influence of fingertip touch to center of pressure (COP) displacement so that contribution of hand role in balance process can be determine. External translational platform perturbation at anterior-posterior direction was applied to the subject at five different frequency. Subjects were asked to maintain their position when fingertip touch and vision input were manipulated. Touch force, wrist motion and the COP displacement were measured and compared. The results have shown that a small amount of touch allowed subject to increase based of support (COP) and significantly improved stability. Horizontal fingertip touch force shows a significant change with vision input. However, wrist movement and fingertip did not show any significant correlation. Thus, touch significantly improve stability, however, uncorrelated motion between wrist and fingertip still leave an empty space for further investigation and discussion.

1. INTRODUCTION

At late 1990s, there were several research done in order to determine the effect of touch towards improvement of balance ability. Individual with specific disease such as vestibular loss patient (Lackner, Rabin, & DiZio, 2001), diabetes patient (Dickstein, Shupert, & Horak, 2001), peripheral neuropathy patient (Dickstein & Laufer, 2004) and also elderly people (Tremblay, Mireault, Dessureault, Manning, & Sveistrup, 2004) took more benefits of touch information when compared with healthy individuals and they was reported applied more touch force than healthy person. They were reported able to reduce their postural sway when asked to maintain stance position during particular feet position (Baldan, Alouche, Araujo, & Freitas, 2014). Previous study also have reported that, with amount of less than 1N able to reduce postural sway by providing neurological support. Those finding have raise a question on the effect of touch especially when individual facing a massive external disturbance. Does touch will still able to maintain posture balance and provide sufficient support to individual?

These study aims to investigate the influence of fingertip touch to the COP displacement so that contribution of hand role in balance process can be determine. Thus, a clear understanding on the effect of haptic information from touch especially improvement of balance condition during perturbed stance can be achieved.

2. EXPERIMENT

In this study, 11 healthy young subjects (aged 24.24± 2.19 years old) participated. Each subject was fully briefed regarding any possible risk and provided informed written consent prior to participation. Subjects were exposed to external platform perturbation (anterior-posterior direction) at five different frequencies (0 (quiet standing (QS)), 0.2, 0.4,0, 6, and 0.8 Hz) by a movable platform (MB-150, COSMATE, JAPAN) with a

translational displacement of 70mm. Furthermore, subject's vision (eyes-closed (**EC**) and eyes-opened (**EO**)) was manipulated. For additional somatosensory input, subjects were asked to maintain their standing position with their right fingertip touching (**T**) on a 3-axis pressure sensor with a built in amplifier (MFS20-010, LINIAX, Japan) at a waist level.

Kinematic data was collected using motion analysis with 7 high precision infrared cameras (HWK-200RT camera, Motion Analysis, USA) at a sampling frequency of 200 Hz using 17 reflective markers. Meanwhile, a force plate (9286A, KISTLER, JAPAN) and a pressure sensor recorded at a sampling frequency of 1 kHz. Each trial was recorded for 40s with knee joints locked using splint to prevent bias movement from knees. The experimental set-up is shown in Fig. 1. The coordinates of each marker were then analysed to determine the position of each joint. Pressure data from the pressure sensor was low pass filtered at a 60Hz cut-off. Paired t-test and Pearson's correlation coefficient (r) were used to determine significant levels of force at different directions. Furthermore, multi-way ANOVA was used to determine a significance level of $p<0.05$. All measurements were made using MATLAB software.

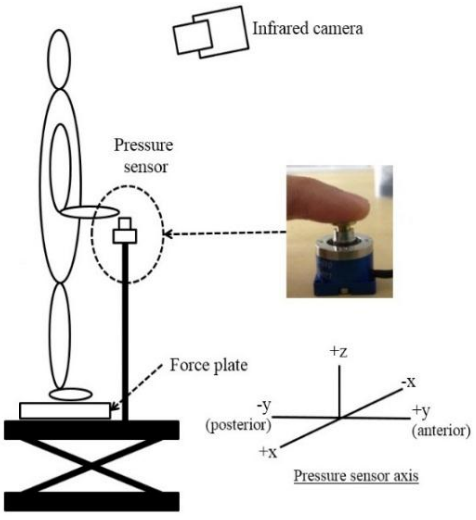

Fig. 1 Experiment Set up

3. RESULTS

The results in Fig. 2 (Top) illustrates the displacement of COP at both anterior and posterior direction under the perturbed stance. The average COP was observed increased with frequency with significant different found at all sensory conditions ($p <0.05$). By comparing between sensory condition, with existence of touch, COP displacement was increased and significant different was found at all perturbation frequency ($p <0.05$).

Based on results in Fig. 3, fingertip force (z-direction) significantly increases with frequency [$F (4, 79) = 5.9$, $p <0.05$]. The force increases up 2 N from 0.2 Hz to 0.8 Hz. When comparing the different vision conditions, force is higher with closed eyes compared to open eyes at all frequencies but insignificant difference ($p>0.05$). Furthermore, horizontal force at y and x directions was found to be insignificantly different between frequencies with $F (4, 79) =0.18$, $p=0.94$ and $F (4, 79) =2.11$, $p=0.097$, respectively. And also, insignificantly with vision condition except at 0.8 Hz. For force at the y-direction, difference force direction pattern was observed between EO and EC. This preference is unique and may indicated the change of hand motion due to loss of sensory input.

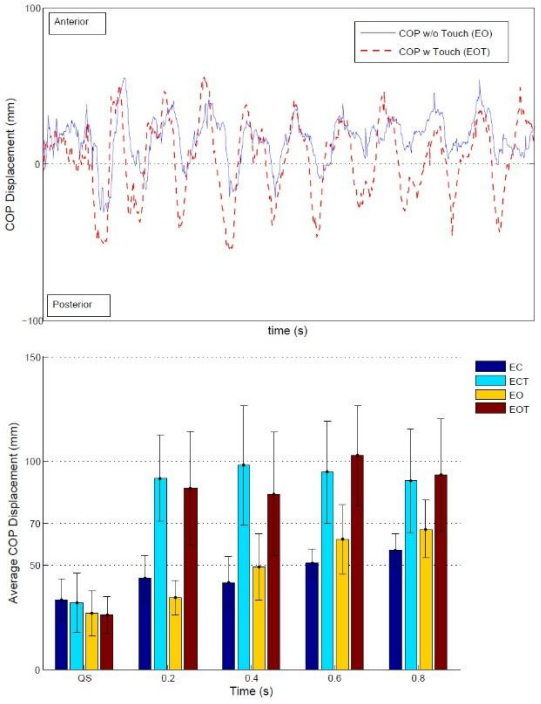

Fig. 2 (Top) Illustration of COP displacement during perturbed stance. (Bottom) The average COP displacement.

These have encourage for further investigation on wrist flexion and extension movement (z-direction) which may

contributed to this even to be happen according to previous research (Su, Chou, Yang, Lin, & An, 2005) .

Fig. 4 below shows that, wrist at superior and inferior direction increased with the increase of frequency with significant different found only at inferior direction ($p<0.05$). Based on the statistical analysis of superior direction, there is no significant different found ($F(1, 47) = 0.05$; $p = 0.8271$). A similar results also recorded on inferior direction ($F(1, 47) = 0.27$; $p = 0.6078$). These insignificant results have indicated that the wrist movement might not correlated with vestibular dysfunction or more specifically vision input.

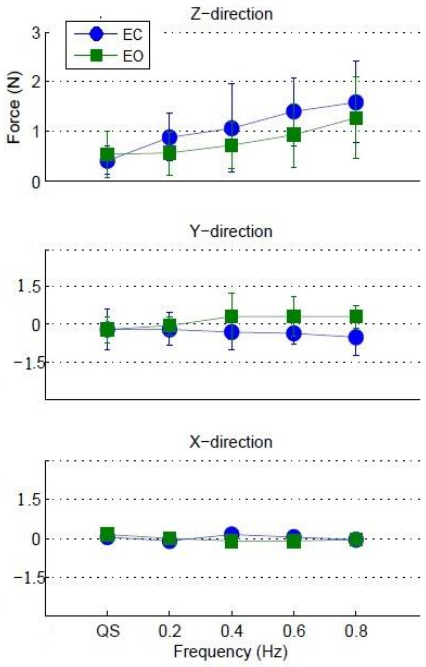

Fig. 3 Average vertical force (z-direction) and horizontal force (y-direction and x-direction) produced by fingertip during EO and EC (M±SE).

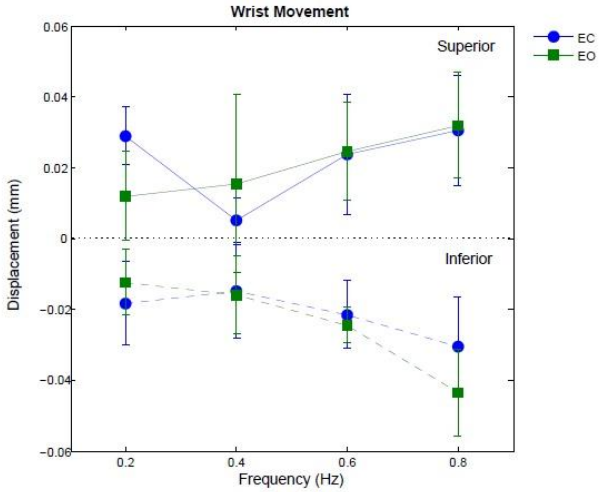

Fig. 4 Wrist movement displacement at both superior-inferior direction during EC and EO

4. DISCUSSION

It is widely recognised that the existence of additional haptic information from touch allows the hand to move and provide spatial contact information; while also allowing a considerable range of body sway; which in this study, is exceed almost 40% from the platform displacement range. This followed the concept of human balance described by Pollock (2000), where a better sensory inputs, individual able to provide a bigger based of support to always make sure the COM lays within the COP range. Previous research by (Gatev, Thomas, Kepple, & Hallett, 1999) reported that, absence of vison have increase the body sway included COP. Furthermore, additional sensory information like fingertip touch, was observed reduced postural sway when comparison make especially between balance and unbalance individual. When compared with absence of vision, many research reported that COP displacement during EC higher than EO. This only can be seen at QS and 0.2 Hz of recent study.

Vertical pressure generated at the fingertips was shown to be higher during no vision (EC). This indicates that, without vision subjects depended on fingertip receptors to sense and provide information about the body's orientation. In perturbed standing, a pressure of more than 50g (~0.5N) was required to provide significant postural stabilization. This supported by previous research where vertical force of 40 ± 7 g produced during when subject standing heel-to-toe (Lackner, et al., 2001) . Furthermore, one interesting finding is about horizontal force at anterior – posterior's direction. Different directions of force were recorded between EC and EO conditions; where a significant difference was observed at 0.8 Hz. This indicates the possible existence of different fingertip position preferences; with respect to loss of vision input. According to F.-C. Su et al, (2005), motion of wrist reported influenced the fingertip motion. They have determine negative slope from regression analysis that demonstrated the so called ''reciprocal'' nature of joint motion (Su, Chou, Yang, Lin, & An, 2005). For example, during wrist extension, passive finger joint flexion was induced and, alternatively, during wrist flexion full finger joint extension was induced.

However, based on the investigation of wrist position, there were no significant different found between different vision inputs. As mentioned in the results section, effect of different vision input influenced fingertip movement but not the wrist. Pressure dependent receptor at fingertip connected directly to ulnar nerve which plays an important role in response to afferent-efferent information transfer in dorsal spinal tract that control the upper part of the body (Proske & Gandevia, 2012).

The wrist flexion and extension degree much influenced by the intensity of perturbation frequency. However, due to limited amount of information due to wrist motion, a detail analysis on the wrist flexion-extension movement cannot be done. The evaluation of wrist motion were depended only on the marker coordinated at ulna bone. For further study on this matter, more market position is suggested in order to gather more information about the wrist movement especially at dorsal surface of hand.

CONCLUSION

In conclusion, this study able to demonstrated the COP response with existence of additional somatosensory and different vision input to posture stability during perturbed stance. A small amount of touch allow sufficient neurological support for posture control, which then increase the COP magnitude. A larger base of support increases stability. However, insignificant between hand motion and stability still leave an empty space for further investigation and discussion.

REFERENCE

Pollock, A.S, Durward, B. R., Rowe, P.J.,Paul, J. P, "What is balance?," *Clinical Rehabilitation*, vol. 2000, p. 6, 2000.

Baldan, A. M. S., Alouche, S. R., Araujo, I. M. G., & Freitas, S. M. S. F. (2014). Effect of light touch on postural sway in individuals with balance problems: A systematic review. *Gait & Posture, 40*(1), 1-10.

Dickstein, R., & Laufer, Y. (2004). Light touch and center of mass stability during treadmill locomotion. *Gait & Posture, 20*(1), 41-47. doi:

Dickstein, R., Shupert, C. L., & Horak, F. B. (2001). Fingertip touch improves postural stability in patients with peripheral neuropathy. *Gait & Posture, 14*(3), 238-247.

Gatev, P., Thomas, S., Kepple, T., & Hallett, M. (1999). Feedforward ankle strategy of balance during quiet stance in adults. *The Journal of Physiology, 514*(Pt 3), 915-928.

Lackner, J. R., Rabin, E., & DiZio, P. (2001). Stabilization of posture by precision touch of the index finger with rigid and flexible filaments. *Exp Brain Res, 139*(4), 454-464.

Proske, U., & Gandevia, S. C. (2012). *The Proprioceptive Senses: Their Roles in Signaling Body Shape, Body Position and Movement, and Muscle Force* (Vol. 92).

Su, F. C., Chou, Y. L., Yang, C. S., Lin, G. T., & An, K. N. (2005). Movement of finger joints induced by synergistic wrist motion. *Clinical Biomechanics, 20*(5), 491-497.

Tremblay, F., Mireault, A. C., Dessureault, L., Manning, H., & Sveistrup, H. (2004). Postural stabilization from fingertip contact: I. Variations in sway attenuation, perceived stability and contact forces with aging. *Exp Brain Res, 157*(3), 275-285.

Aizreena Azaman received her B. Eng from Universiti Teknologi Malaysia and M.Eng in biomedical engineering from University of Malaya. Recently, she is PhD candidate at Shibaura Institute of Technology.

Shin-ichiroh Yamamoto is Professor at Department of Biomedical and Engineering, Shibaura Institute of Technology. His research interest including neuro-rehabilitation engineering and neural mechanism for human motor control.

CHEMICAL COMPOSITION CHANGES IN CASHEW APPLE FERMENTED WITH *Lactobacillus casei*

Ratchadaporn Kaprasob, Orapin Kerdchoechuen, and Natta Laohakunjit
School of Bioresources and Technology,
King Mongkut's University of Technology Thonburi, Bangkok, THAILAND

ABSTRACT : Fresh cashew apple pulp was fermented with *Lactobacillus casei* for 0, 12, 24, and 48 h to produce probiotic cashew apple, which were monitored for their functional properties. Changes in chemical composition (pH, total titratable acidity, total sugar, reducing sugar, ascorbic acid, total phenolic, condensed tannin and hydrolysable tannin contents) and antioxidant activities (DPPH$^{\bullet}$ and ABTS$^{\bullet+}$) of cashew apple during fermentation were investigated. The profile of total titratable acidity measured throughout fermentation period in fermented cashew apple was in agreement with the pH trend. The pH, total sugar, reducing sugar, and hydrolysable tannin contents were decreased after 48 h of fermentation. However, the highest vitamin C, total phenolic content and antioxidant activity were obtained in fermented cashew apple after 12 h of fermentation. The DPPH$^{\bullet}$ and ABTS^{+} radical scavenging activities of fermented cashew apple were greater than 70% and 90%, respectively, indicating fermented cashew apple has a good potential for free radical scavenging.

1. INTRODUCTION

Anacardium occidentale L. is a tropical tree, which its pseudo-fruit (known as the cashew apple) are the part of the tree connecting to the cashew nut (the real fruit and a well-known product worldwide). Cashew apples are an excellent source of nutritions including ascorbic acid, vitamins, minerals, organic acid, phenolics (anacardic acids), carbohydrate, reducing sugars (fructose and glucose), and some amino acids (Gyedu-Akoto, 2011). The cashew apple is very popular and highly consumed as ready-to-drink and concentrated juice (Zepka, et al., 2009) due to their appropriate taste, flavor, availability, high sugar and water content (moisture content), and overall chemical composition.

Nowadays, technological advances have made possible to alter some structural characteristics of fruit and vegetables matrices by modifying food components in a controlled way (Betoret, et al., 2003). This could make them ideal substrates for the culture of probiotics, since they already contain beneficial nutrients such as minerals, vitamins, dietary fibers, and antioxidants (Yoon, et al., 2004), while lacking the dairy allergens that might prevent consumption by certain segments of the population. There is a genuine interest in the development of fruit juice based functional beverages with probiotics because they have taste profiles that are appealing to all age groups and because they are perceived as healthy and refreshing foods (Yoon, et al., 2004). Lactobacilli are extensively used in industrial food production and nowadays as functional ingredients (Havenaar, et al., 1992). Food cultures that have beneficial effects on human health have been termed "probiotic" and can be defined as "Live microorganisms, which when administered in adequate amounts, beneficially affect the host". The growth of lactobacilli is affected by fermentation conditions as pH, temperature, media formulation and others. According to Ranadheera, et al. (2010) the food vehicle can also influence parameters of probiotic growth, survival and functionality. Comparing dairy and non-dairy probiotic products, Zhou, et al. (2009) reported viable cell counts of 8.59±0.04 Log CFU/mL after fermentation, when *L. casei* was inoculated in mare milk, while Sheehan, et al. (2007) reported viable cell counts of 8.20±0.01 Log CFU/mL of *L. casei* in pineapple juice. Fruits and vegetables have been suggested as ideal media for probiotic growth because they inherently contain essential nutrients, they are good-looking and have good taste. Therefore, the objective of this study was to investigate the chemical composition (pH, total titratable acidity, total sugar, reducing sugar, ascorbic acid, total phenolic, condensed tannin and hydrolysable tannin contents) changes in cashew apple as a raw material for production of probiotic cashew apple juice during fermentation *by Lactobacillus casei*.

2. EXPERIMENT

2.1 Materials and Chemicals

Cashew apple was kindly provided by Heritage Grower Corporation Ltd. in South of Thailand. The cashew apple was washed with water and then cut into small pieces. The edible pieces were homogenized using a Waring blender for 5 min and kept at -20°C during the period of the study. Testing chemicals, including 1, 1-diphenyl-2-picrylhydrazyl (DPPH) and 2, 2'-azino-bis (3-ethylbenzthiazoline-6-sulphonic acid) (ABTS) were purchased from Sigma-Aldrich (USA).

2.2 *Lactobacillus casei* Cultures Preparation

Lactobacillus casei TISTR 390 were obtained from Thailand Institute of Scientific and Technological Research (TISTR), Thailand. Cell cultivation was carried out statically in an incubator until the cell density spectrophotometrically determined reached 1.000 at 600 nm that corresponded to 15×10^{8} CFU/mL, using the McFarland scale (Chapin & Lauderdale, 2003).

2.3 Fermentation of Probiotic Cashew Apple

Fermentation experiments were conducted in sealed Erlenmeyer flask, each containing 20g of pasteurized cashew

apple without supplementary nutrients or water and inoculated with *L. casei* (2.0 mL of inoculum). The fermentation process was performed at 37°C for 48 h. Samples for chemical analyses were taken at 0, 12, 24, and 48 h.

2.3.1 Viable Cell Counts Determination: Viable cell counts were obtained by serial dilution with 0.7% NaCl solution until 10^{-6} dilution. Aliquots of 0.1 mL of dilution were plated, in triplicate in plates containing MRS Agar (spread plate method). The plates were incubated for 72 h at 37°C. Plates containing 20-350 colonies were measured and recorded as colony forming units (CFU) per mL of solution.

2.3.2 pH, Total Titratable Acidity, and Sugar Determination: The pH of probiotic cashew apple was measured using a pH meter. Total titratable acidity, expressed as lactic acid, was determined by titration with 0.1M NaOH using the method of AOAC (2000). Reducing sugar content was analyzed as glucose equivalents by Nelson-somogyi method of Somogyi (1952). Total sugar content was was analyzed as glucose equivalents by the phenol sulfuric acid method of Dubois, et al. (1956).

2.3.3 Vitamin C Content: Ascorbic acid analysis of sample extraction was done with 2,6-dichloroindolphenol according to the Official titrimetric method (AOAC, 2000). Vitamin C content was expressed as mg ascorbic acid equivalents (AAE)/ 100g dry weight (DW).

2.3.4 Tannin Content: Condensed tannins or proantrocyanidins were measured using the modified Vanillin Assay described by Sun, et al. (1998). Three milliliters of 4% methanol vanillin solution and 1.5 mL of concentrated HCl were added to 100 µL of sample. The mixture was kept for 15 min, and the absorbance was measured at 500 nm against methanol as a blank. Results were expressed as mg (+)-catechin equivalent /100g dry weight (DW). Hydrolysable tannins were determined according to the method of Saad, et al. (2012). A 2.5 mL of KIO_3 aqueous solution (2.5% w/v) was added to the test tube and heated for 7 min at 30°C, and then 0.5 mL of sample was added. After additional 2 min of tempering at 30°C, the absorbance was measured at 550 nm, using distilled water as a blank. Results were expressed as mg tannic acid equivalent (TAE)/ 100 g dry weight (DW).

2.3.5 Total Phenolic Content: Total phenolic content was measured using the Folin–Ciocalteu colorimetric method (Huang, et al., 2005). Sample (20 µL) was added to the test tube and mixed with 80 µL of distilled water and 2 mL of 2% (w/v) Na_2CO_3 solution. After incubation for 3 min, 100 µL of Folin-Ciocalteu reagent was added. After standing for 30 min at room temperature, absorbance was measured at 750 nm, using distilled water as a blank. Results were expressed as mg gallic acid equivalents (GAE)/ 100g dry weight (DW).

2.3.6 Methods to Estimate Antioxidant Capacity

Two methods were used to evaluate the antioxidant capacities of fermented cashew apple using DPPH• and ABTS•+ assays.

1) DPPH (2,2-diphenyl-1-picrylhydrazyl) Radical Scavenging Efficiency: The scavenging effect was measured according to the modify method of Bersuder, et al. (1998). A 10 µL aliquot of the sample extract was added to the test tube and mixed with 30 µL of distilled water. Two milliliter of 0.1 mM DPPH dissolved in 95% ethanol was added to the sample. The mixture was shaken and left for 30 min in the dark at room temperature, and was read the absorbance at 517 nm. The percent DPPH scavenging effect (%) was calculated by the following equation:

$$\text{DPPH scavenging effect (\%)} = \frac{A_{Blank} - (A_{Sample} - A_{Control})}{A_{Blank}} \times 100$$

where A_{Blank} = absorbance at 517 nm of 40 µL distilled water + 2 mL of 0.1 mM ethanolic DPPH• solution, A_{Sample} = absorbance at 517 nm of 40 µL aqueous sample + 2 mL of 0.1 mM ethanolic DPPH• solution, and $A_{Control}$ = absorbance at 517 nm of 40 µL aqueous sample + 2 mL of ethanol.

2) ABTS (2,2'-azino-bis 3-ethylbenzthiazoline-6-sulfonic) Radical Scavenging Activity: The scavenging activity was measured according to Shan, et al. (2005). ABTS•+ radical cation was generated by reacting 7 mM ABTS and 2.45 mM potassium persulfate in the dark for 24 h at 20°C. Before analysis, the ABTS•+ solution was diluted to obtain an absorbance of 0.700 ± 0.020 at 734 nm with ethanol. An aliquot of the sample (10µL) was added to the test tube and mixed with 70 µL of distilled water. After adding 4 mL of the diluted ABTS•+ solutions, which was prepared daily to the sample, the absorbances was measured at 734 nm after exactly 6 min of initial mixing, using distilled water as blank. The antioxidant activity of the sample was calculated by the same equation as DPPH•.

2.3.7 Statistical Analysis: All experiments were carried out in triplicate, and each sample was analyzed in duplicate. The results are expressed as mean ± S.D. (standard deviation). The SAS program (SAS Institute, 2004, USA) was used to analyze the experimental data. Significant differences ($p<0.05$) between means were determinated by Duncan's multiple range test (DMRT).

3. ANALYSIS

Changes in pH, total titratable acidity, reducing sugar and total sugar of the probiotic cashew apple are shown in Table 1. The pH of the fermented cashew apple was decreased throughout the fermentation period from 3.86 to 3.77 after the 48 h fermentation. The profile of total titratable acidity measured throughout fermentation period in fermented cashew apple was in agreement with the pH trend. The total titratable acidity expressed as percent lactic acid of fermented cashew apple, which decreased from 0.55% to 0.49% after the 48 h fermentation at 37°C. The patterns of pH and acidity exhibited are in agreement with the findings of Ibanoglu, et al. (1995), who have reported that lactic acid bacteria have been responsible for the production of lactic acid during fermentation.

The changes in the population of the enumerated microbial groups of cashew apple are shown in Fig. 1. The initial cell counts of *L. casei* were 7.49 Log CFU/mL. The population of *L. casei* were sharply decreased within the first 24 h fermentation, and then still remained at 6 Log CFU/mL at 48 h fermentation. Yoon, et al. (2006) reported that *L. casei* was unable to survive at the low pH and high acidity conditions in fermented cabbage juice.

The sugar content of cashew apple has usually been assessed in terms of total sugar or reducing sugar. The total

sugar levels of fermented cashew apple were slightly decreased significantly from an initial value of 2.98 to 2.68 g/ 100 g DW ($p \leq 0.05$) (Table 1). This finding agrees with the changes in reducing sugar content of the fermented cashew apple that decreased from an initial value of 3.18 to 3.00 g/ 100 g DW after the 48 h fermentation. Results indicated that *L.casei* utilized fruit sugar and produced lactic acid without any additional nutrient (Sreenath, et al., 2001).

The ascorbic acid content of *L. casei* cashew apple was rapidly increased at fermentation time of 0 to 12 h from an initial value of 2118.78 to 2923.13 mg AAE/ 100 g DW and then decreased until 48 h fermentation, as shown in Fig. 2 (a). The *L. casei* cashew apple was the highest ascorbic acid content at 12 h fermentation. Rakin, et al. (2007) reported that the fermented beetroot juice with lactic acid bacteria was higher vitamin C content than those of non-fermented beetroot juice. However, the total phenolic result of *L. casei* cashew apple was decreased after 48 h of fermentation ($p \leq 0.05$) (Fig. 2 (b)). The *L. casei* cashew apple had the highest total phenolic content at 12 h fermentation (97.71 mg GAE/ 100 g DW).

Table 1 Changes in pH, total titratable acidity, reducing sugar and total sugar during fermentation of cashew apple by *Lactobacillus casei*.

Fermentation time (h)	pH	total titratable acidity (% lactic acid) [x]	reducing sugar [y] (g/100g DW)	total sugar [y] (g/100g DW)
0	3.86±0.00^{b}	0.55±0.02^{a}	2.98±0.07^{a}	3.18±0.10^{a}
12	3.88±0.01^{a}	0.54±0.04^{ab}	2.87±0.14^{ab}	3.09±0.08^{ab}
24	3.86±0.01^{b}	0.51±0.02^{ab}	2.78±0.12^{bc}	3.10±0.11^{ab}
48	3.77±0.00^{c}	0.49±0.05^{b}	2.68±0.04^{c}	3.00±0.03^{b}
F-test	*	ns	*	ns
LSD	0.01	0.06	0.16	0.13
C.V.(%)	0.19	6.88	3.64	2.75

The results are expressed as means ± standard deviation (SD) with three replications. Values with different superscript letters in a column are significantly different at $p<0.05$.
[x] Expressed as lactic acid (%)
[y] Measured as glucose equivalent and expressed as g/100g dry weight (DW)

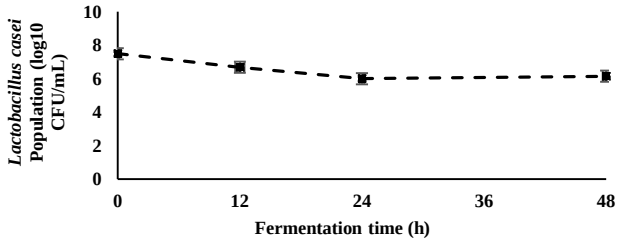

Fig. 1 Changes in population of *Lactobacillus casei* cashew apple for 0, 12, 24 and 48h fermentation at 37°C.

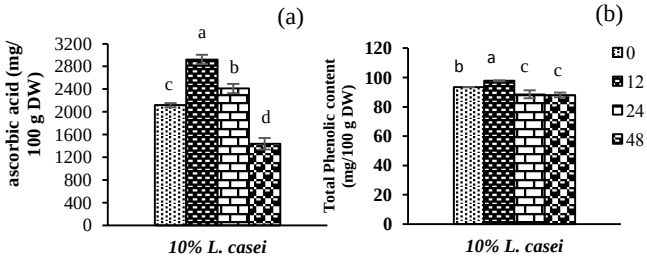

Fig. 2 Changes in (a) ascorbic acid and (b) total phenolic content of fermented cashew apple for 0, 12, 24 and 48h fermentation at 37°C. [a,b,c,…]different letters indicate significant difference at $p<0.05$.

Biologically active compounds with antioxidant properties included condensed tannins or proanthocyanidins, which were the oligomers and polymers of flavan-3-ols (Havsteen, 2002). The hydrolysable tannin of fermented cashew apple was sharply decreased at fermentation time of 0 to 12 h from an initial value of 19.35 to 15.19 mg TAE/ 100 g DW and then still remained until 48 h fermentation, as shown in Fig. 3. The condensed tannin content of all fermentation time of *L. casei* cashew apple was not different ($p>0.05$) (Fig. 3).

The highest DPPH• and ABTS•+ free radical scavenging activity was 71.85% and 91.73%, respectively, at 12 h fermentation, indicating cashew apple has a good potential for free radical scavenging, as shown in Fig. 4. Increases in antioxidant activities during the beginning of fermentation (12 h) might be associated with the production of phenolic compounds and ascorbic acid having antioxidant capacity. A decrease in antioxidant activity throughout fermentation (48 h) could be due to oxidation or degradation of compounds with antioxidant (Johnson, et al., 2011).

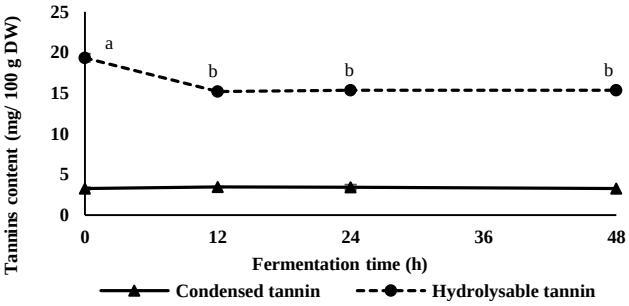

Fig. 3 Changes in condensed and hydrolysable tannins content of fermented cashew apple for 0, 12, 24 and 48h fermentation at 37°C. [a,b,c,…]different letters indicate significant difference at $p<0.05$.

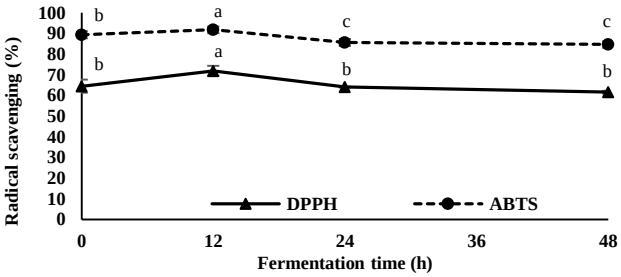

Fig. 4 DPPH and ABTS radical scavenging changes of fermented cashew apple for 0, 12, 24 and 48h fermentation at 37°C. [a,b,c,…]different letters indicate significant difference at $p<0.05$.

CONCLUSION

Cashew apple fermented with 10% *Lactobacillus casei* at 12 h fermentation was the optimum condition, which the highest ascorbic acid and total phenolic content. Moreover, fermented cashew apple exhibited the highest antioxidant activity with the two methods of DPPH• and ABTS•+ used. The results obtained that fermentation process induced an important loss in sugar, phenolic compounds, ascorbic acid, and hydrolysable tannin contents. The *L. casei* probiotic cashew apple might serve as a probiotic functional beverage for developing healthy food and/or drinks.

REFERENCES

AOAC, Association of Official Analytical Chemists, 14, Washington D.C, 2000.

Bersuder, P., Hole, M. and Smith, G., Antioxidants from a heated histidine-glucose model system. I: Investigation of the antioxidant role of histidine and isolation of antioxidants by High-Performance Liquid Chromatography, J. Am. Oil Chem. Soc., vol. 75, no. 2, pp. 181-187, 1998.

Betoret, N., Puente, L., Dıaz, M., Pagán, M., Garcıa, M., Gras, M., Martínez-Monzó, J. and Fito, P., Development of probiotic-enriched dried fruits by vacuum impregnation, J. Food Eng., vol. 56, no. 2, pp. 273-277, 2003.

Chapin, K.C. and Lauderdale, T., Reagents, stains, and media: bacteriology, In manual of clinical microbiology. Murray, P.R., Baron, E.J., Jorgensen, J.H., Pfaller, M.A. and Yolken, R.H., ASM Press, Washington, D.C., pp 358, 2003.

Dubois, M., Gilles, K.A., Hamilton, J.K., Rebers, P.A. and Smith, F., Colorimetric method for determination of sugars and related substances, Anal. Chem., vol. 28, no. 3, pp. 350-356, 1956.

Gyedu-Akoto, E., Utilization of some cashew by-products, Nutr. Food Sci., vol. 41, no. 6, pp. 393-400, 2011.

Havenaar, R., Ten Brink, B. and Huis, J.H., Selection of strains for probiotic use, in probiotics, Springer, pp 209-224, 1992.

Havsteen, B.H., The Biochemistry and Medical significance of the flavonoids, Pharmacol. Ther., vol. 96, no. 2-3, pp. 67-202, 2002.

Huang, D., Ou, B. and Prior, R.L., The chemistry behind antioxidant capacity assays, J. Agric. Food. Chem., vol. 53, pp. 1841-1856, 2005.

Ibanoglu, S., Ainsworth, P., Wilson, G. and Hayes, G.D., The effect of fermentation conditions on the nutrients and acceptability of tarhana, Food Chem., vol. 53, no. 2, pp. 143-147, 1995.

Johnson, M.H., Lucius, A., Meyer, T. and Gonzalez De Mejia, E., Cultivar evaluation and effect of fermentation on antioxidant capacity and in vitro inhibition of α-Amylase and α-Glucosidase by highbush blueberry (*Vaccinium corombosum*), J. Agric. Food. Chem., vol. 59, no. 16, pp. 8923-8930, 2011.

Rakin, M., Vukasinovic, M., Siler-Marinkovic, S. and Maksimovic, M., Contribution of lactic acid fermentation to improved nutritive quality vegetable juices enriched with Brewer's yeast Autolysate, Food Chem., vol. 100, no. 2, pp. 599-602, 2007.

Ranadheera, R.D.C.S., Baines, S.K. and Adams, M.C., Importance of food in probiotic efficacy, Food Res. Int., vol. 43, no. 1, pp. 1-7, 2010.

Saad, H., Charrier-El Bouhtoury, F., Pizzi, A., Rode, K., Charrier, B. and Ayed, N., Characterization of Pomegranate peels tannin extractives, Ind. Crop Prod., vol. 40, no. 1, pp. 239-246, 2012.

Shan, B., Cai, Y.Z., Sun, M. and Corke, H., Antioxidant capacity of 26 spice extracts and charactrization of their phenolic constituents, J. Agric. Food. Chem., vol. 53, pp. 7749-7759, 2005.

Sheehan, V.M., Ross, P. and Fitzgerald, G.F., Assessing the acid tolerance and the technological robustness of probiotic cultures for fortification in fruit juices, Innov. Food Sci. Emerg. Technol., vol. 8, no. 2, pp. 279-284, 2007.

Somogyi, M., Determination of reducing sugars by Nelson-Somogyi method, J. Biol. Chem., vol. 200, pp. 245-245, 1952.

Sreenath, H.K., Moldes, A.B., Koegel, R.G. and Straub, R.J., Lactic acid production by simultaneous saccharification and fermentation of alfalfa fiber, J. Biosci. Bioeng., vol. 92, no. 6, pp. 518-523, 2001.

Sun, B., Ricardo-da-Silva, J.M. and Spranger, I., Critical factors of vanillin assay for catechins and proanthocyanidins, J. Agric. Food. Chem., vol. 46, no. 10, pp. 4267-4274, 1998.

Yoon, K.Y., Woodams, E.E. and Hang, Y.D., Probiotication of tomato juice by lactic acid bacteria, J microbiol, vol. 42, no. 4, pp. 315-8, 2004.

Yoon, K.Y., Woodams, E.E. and Hang, Y.D., Production of probiotic cabbage juice by lactic acid bacteria, Bioresour. Technol., vol. 97, no. 12, pp. 1427-1430, 2006.

Zepka, L.Q., Borsarelli, C.D., Da Silva, M.A.A.P. and Mercadante, A.Z., Thermal degradation kinetics of carotenoids in a cashew apple juice model and its impact on the system color, J. Agric. Food. Chem., vol. 57, no. 17, pp. 7841-7845, 2009.

Zhou, Q., Wang, J., Guo, Z., Yan, L., Zhang, Q., Chen, W., LIU, X.M. and ZHANG, H.P., Fermentation characteristics and transit tolerance of lactobacillus casei zhang in reconstituted mare milk during storage, Int. J. Dairy Technol., vol. 62, no. 2, pp. 249-254, 2009.

Ratchadaporn Kaprasob received the B.Sc. (2007) degree in Food Science from Burapha University, and M.Sc. (2010) degree in Biochemical Technology from King Mongkut's University of Technology Thonburi. She is a PhD candidate from School of Bioresources and Technology, King Mongkut's University of Technology Thonburi.

Orapin Kerdchoechuen (Assoc. Prof.) received the B.Sc. (1976) and M.Sc. (1990) from Kasetsart University, and PhD. (1996) in Plant Physiology in Horticulture from Mississippi State University. She is an academic staff, Department of Biochemical Technology, King Mongkut's University of Technology Thonburi.

Nutta Laohakunjit (Assoc. Prof.) received the B.Sc. (1988) and M.Sc. (1996) from Chulalongkorn University, and PhD. (2003) degree in Postharvest and Food Process Engineering from Asian Institute of Technology. She is an academic staff, Department of Biochemical Technology, King Mongkut's University of Technology Thonburi.

BIOLOGICAL ACTIVITIES AND FUNCTIONAL PROPERTIES OF SUNFLOWER PROTEIN HYDROLYZED BY BRPMELAIN

Pastraporn Thongimpong, Natta Laohakunjit, and Orapin Kerdchoechuen
School of Bioresources and Technology, King Mongut's University of Technology Thonburi

ABSTRACT: Enzymatic protein hydrolysis was able to generate protein hydrolysates which had biological activity and functional property. The purpose of this study was to characterize the antioxidant and functional properties of sunflower protein hydrolysates by endoproteases; bromelain. Degree of hydrolysis (DH) increased with increasing enzyme concentrations and hydrolysis times. DH affected antioxidant and functional properties of sunflower protein hydrolysates. The sunflower protein hydrolysates having higher DH showed stronger DPPH$^{\bullet}$ (1, 1-diphenyl-2-picrylhydrazyl) and ABTS$^{+\bullet}$ (2, 2'-azino-bis (3-ethylbenzthiazoline-6-sulphonic acid)) radical scavenging activity. In the other hand, the foaming and emulsifying capacity was high at low DH.

1. INTRODUCTION

Sunflower seeds are used in the food industry as a source of edible oil. One of byproducts of the oil extraction process is sunflower meal which has a high protein content (40 - 50%), making sunflower meal an attractive protein source (Gonzalez-Perez et al., 2007). Sunflower meal consists of essential amino acids (Salunkhe et. al., 1992). Although sunflower protein contains low level of lysine, it is relatively rich of sulphur-containing amino acids of methionine and cysteine (Canibe et al., 1999), glutamic and aspartic acid (Villanueva et. al., 1999) compared to other oil seeds. Sunflower meal has already been used for high added-value protein hydrolysates (Villanueva et al., 1999). During the industrial extraction of sunflower oils, sunflower proteins suffer a denaturation process that reduces their solubility. That cause to reduce the biological activities and functional properties of protein in sunflower meal (Yust et al., 2003).

Enzymatic hydrolysis has been used to recover and added value of protein by-products such biological wastes to protein hydrolysates, which have improved biological and functional properties (Arogundade et al., 2012; Véstag et al., 2011; Jamdar et al., 2010; Wiriyaphan et al., 2012).

The bioactivity of protein hydrolysates could be affected by different parameters, such as source of protein and type of protease used. Different proteases lead to different DH, molecular weight distribution, amino acid composition and sequence, which greatly influence the antioxidant activities of the hydrolysates (Venuste et al., 2013).

The possibility of the functional properties improvement of proteins in sunflower meal through their limited proteolysis was to justify and investigate in this research work. The purpose of this study was to characterize biological (antioxidant) and functional (emulsifying and foaming) properties of sunflower meal protein hydrolysates by bromelain.

2. EXPERIMENT

2.1 Preparation of sunflower protein hydrolysates (SPHs)

Defatted sunflower meals 10 g were steriled with autoclave and added distilled water to 250 mL and then incubated in water bath at 50°C. Bromelain solutions were prepared and varied at the different concentration of enzyme at 0-20% (gram of enzyme per gram of sunflower). Enzymes were activated in water bath at 50°C for 5 min and then mixed enzyme solution with sunflower meal solution and incubated at 50°C for 1, 3, 6, 12 and 18h. Hydrolysis was stopped by heating at 95 °C for 15 min. Hydrolysates were clarified by ultrafiltration through Whatman No.1 to remove insoluble substrate.

2.2 Degree of hydrolysis measurement

The degree of hydrolysis (DH) was measured according to Flavia and Maria (1998) by determined the soluble nitrogen of treated sample in trichloroacetic acid (TCA). Hydrolyzed sunflower meal 2.5 mL was mixed with 2.5 mL of 20% TCA and then filtered through Whatman No.1. The soluble nitrogen in supernatant and total nitrogen were determined by the Kjeldahl method (AOAC, 2000). The percent DH was calculated as follows:

$$\text{DH (\%)} = \frac{\text{soluble nitrogen in TCA solution (mg)} \times 100}{\text{total nitrogen (mg)}}$$

2.3 Antioxidant capacity

2.3.1 DPPH radical scavenging activity assay

The scavenging effect of SPHs on l,l-diphenyl-2-picrylhydrazyl radicals or DPPH free radical was measured according to the method of Pan et al. (2011). Sunflower protein hydrolysates (20 µL) were diluted with 980 µL distilled water and added 3 ml of 0.1 mM DPPH dissolved in 95% ethanol. The mixture was shaken and left for 30 min in dark at room temperature. The absorbance of the resulting solution was measured at 517 nm. A lower absorbance represents a higher DPPH

scavenging activity. Radical scavenging activity was calculated using the following formula.

$$\text{DPPH scavenging activity (\%)} = \frac{(A_{cont} + A_{blank} - A_{test}) \times 100}{A_{cont}}$$

where A_{cont} is the absorbance of the control reaction (containing all reagents except sample), A_{blank} is the absorbance of color of sample (using ethanol instead of DPPH) and A_{test} represent the absorbance of sample.

2.3.2 $ABTS^{\bullet+}$ radical scavenging activity assay

Total antioxidant activity was measured by reacting with 7.0 mM $ABTS^{\bullet+}$ (2, 2-azinobis (3-ethylbenzo-thiazoline-6-sulfonic acid)) radical scavenging (ABTS) method (Cai et al., 2004) with minor modifications. In brief, 7.0 μM ABTS and 2.45 μM potassium persulphate were mixed for the production of ABTS cation ($ABTS^{\bullet+}$) and kept in the dark (16 h, 22±1 ◦C). The solution was diluted with ethanol until an absorbance was 0.70 (±0.05), obtained at 734 nm. Sunflower protein hydrolysates (20 μL) was diluted with 980 μL distilled water and added 4 mL $ABTS^{\bullet+}$ for 6 min in a dark condition. Then, the absorbance was taken at 734 nm by the spectrophotometer.

2.4 Functional properties

2.4.1 Emulsifying properties

Emulsifying capacity (EC) was evaluated according to the method of Chandi and Sogi (2007) and Cao et al. (2009). Sunflower protein hydrolysates solutions at 50% v/v concentration (10 mL) were taken in a centrifuge tube (size 50 mL). Refined peanut oil (2.5 mL) was added and the solutions were homogenized at 10,000 rpm for 1 min, and then centrifuged at 1,200 g for 5 min. The emulsifying capacity was calculated as volume of emulsion to volume of solution multiplied by hundred.

2.4.2 Foaming properties

Foaming capacity (FC) was determined according to the method of Chandi and Sogi (2007) and Cao et al. (2009). Sunflower protein hydrolysates dispersions (50%, 10 mL) were prepared and taken in a 100 mL cylinder. The dispersions were then whipped in a mechanical homogenizer (Ultra-turrax T25 basic, Germany) at 10,000 rpm for 1 min. The volumes before and after whipping were recorded and the foam capacity was calculated. Overrun percentage was calculated as volume of foam to volume of solution multiplied by hundred.

2.5 Statistical analysis

All treatments were carried out in triplicate. The results are expressed as mean ± S.D. (standard deviation). The SAS statistical computer package was used to analyze the experimental data (SAS User's Guide version6, 4thedn., SAS Institute, Cary, NC, USA, 1990). Significant differences ($p \leq 0.05$) between means were determined by Duncan's Multiple Range Test.

3. ANALYSIS

The chemical compositions of defatted sunflower meals are shown in Table 1. Defatted sunflower meal was an excellent protein source for protein hydrolysate production because it contained protein content greater than 30% (dry weight) (Sonklin et al., 2011).

The progress of hydrolysis was monitored in terms of degree of hydrolysis (DH), which is presented in Fig. 1. DH has been defined as the percent ratio of the number of peptide bonds cleaved to the total number of peptide bonds in the substrate studied (Adler-Nissen, 1982). It is the proportion of cleaved peptide bonds in a protein hydrolysate (Rutherfurd, 2010). Enzyme concentration and time of hydrolysis had significantly effect on DH. DH rapidly increased during the initial time of hydrolysis (1-6 h) because the enzyme was in excess and saturated with the substrate. Based on the results, the DH for most of the enzymes reached the plateau after 6 h hydrolysis, confirming that hydrolysis was completed. However, increasing of bromelain concentration gave the effect on DH increased slightly with increase in bromelain concentration to 20%.

The DPPH radical scavenging activity of SPHs obtained by various bromelain concentrations is shown in Fig. 2a. In this study, the DPPH radical scavenging acticity was increased after hydrolyzed by bromelain. However, the DH was stable that effect on DPPH radical scavenging ability after hydrolysis time for 6 h.

The $ABTS^{\bullet+}$ radical scavenging activity of SPHs prepared by bromelain is shown in Fig. 2b. The higher DH value of SPHs occurs, the stronger free radical scavenging activities is. The reason was that hydrolysates with high DH after the proteases digestion are expected to expose more hydrophobic amino acid residue side chain groups and become more accessible to free radical (Venuste et al., 2013).

Hydrolysis process could improve foaming and emulsifying property of sunflower protein (Fig 3 and Fig.4). Foaming and emulsifying capacity of SPHs were decreased with increasing in enzyme concentration and hydrolysis time because of the effect of DH. A good foaming and emulsifying capacity might attribute to an increase in the surface activity is due to partial hydrolysis that produced greater number of polypeptide chain and therefore allowed more air to be incorporated (Kuehler and Stine, 1974). Moreover, the low level of degree of hydrolysis of protein molecules by protease had contributed to the high emulsifying capacity because of the increase of larger peptide units at the oil-water interface that provided a larger surface area (Diniz and Martin, 1997).

Table 1 Chemical composition of defatted sunflower meal (DSM)

Compositions	Content (g/100g DSM dry basic)
Protein	59.98
Carbohydrate	25.29
Lipid	0.40
Fiber	5.58
Ash	8.75

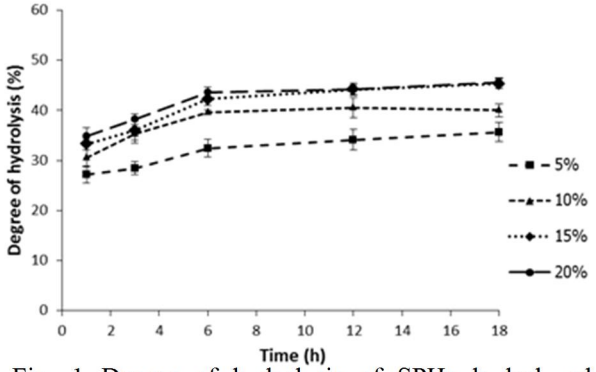

Fig. 1 Degree of hydrolysis of SPHs hydrolyzed by bromelain at various concentrations of enzyme and hydrolysis time

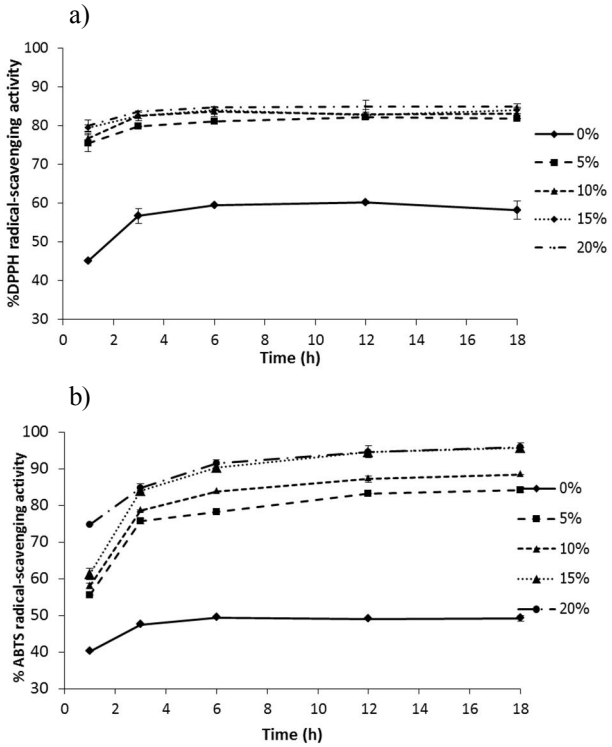

Fig. 2 Antioxidant activities of SPHs hydrolyzed at various concentrations of bromelain and hydrolysis time by a) DPPH$^{\bullet}$ and b) ABTS$^{\bullet+}$ radical scavenging assay

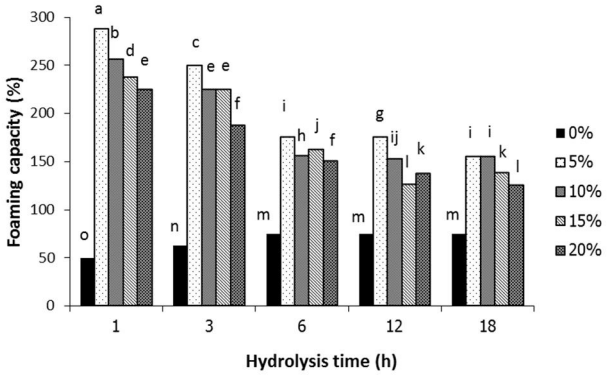

$^{a,b,\cdots}$Different letters indicate significant difference at $p < 0.05$

Fig. 3 Foaming capacity of SPHs hydrolyzed by bromelain at various concentrations of enzyme and hydrolysis time

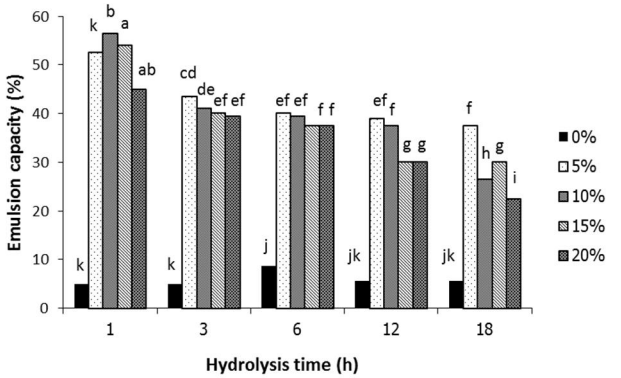

$^{a,b,\cdots}$Different letters indicate significant difference at $p < 0.05$

Fig. 4 Emulsion capacity of SPHs hydrolyzed by bromelain at various concentrations of enzyme and hydrolysis time

CONCLUSION

Hydrolysis by proteolytic enzymes, bromelain, produced high antioxidative peptide against DPPH$^{\bullet}$ and ABTS$^{\bullet+}$ redical scavenging effect. Although the sunflower protein hydrolysis at 15% bromelain for 6 h resulted in high DH and high antioxidant activities, the foaming and emulsifying capacities was highest at 5% bromelain for 1 h. According to our results, sunflower meal is a promising protein source for production of antioxidative peptides which might be utilized to develop functional or supplementary food.

REFERENCES

Adler-Nissen, J., Limited enzymic degradation of proteins: A new approach in the industrial application of hydrolases, J. Chem. Technol. Biotechnol, vol. 32, pp. 138–156, 1982.

Arogundade, L.A., Mu, T.H. and Anon, M.C., Heat-induced gelation properties of isoelectric and ultrafiltered sweet potato protein isolate and their gel microstructure, Food Res. Int., vol. 49, pp. 216–225, 2012.

Cai, Y., Luob, Q., Sunc, M. and Corke, H., Antioxidant activity and phenolic compounds of 112 traditional Chinese medicinal plants associated with anticancer, Life Sci., vol. 74, pp. 2157-2184, 2004.

Canibe, N., Martin, M., Robredo, L. and Knudsen, K., Chemical composition, digestibility and protein quality of 12 sunflower (*Helianthus annuus* L) cultivars, J. Sci. Food Agric., vol. 79: pp. 1775-1782, 1999.

Cao, X., Wen, H., Li, C. and Gu, Z., Differences in functional properties and biochemical characteristics of congenetic rice proteins, J. Cereal Sci., vol. 50, pp. 184–189, 2009.

Chandi, G.K. and Sogi, D.S., Functional properties of rice bran protein concentrates, J. Food Eng., vol. 79, pp. 592–597, 2007.

Diniz, A.M. and Martin, A.M., Optimization of nitrogen recovery in the enzymatic hydrolysis of dogfish (*Squalus acanthias*) protein: Composition of the hydrolysates, Int. J. Food Sci. Nutr., vol. 48, pp. 191–200, 1997.

Flavia, M.N. and Maria, A., Production and characterization of enzymatic hydrolysate from soy protein isolate, Food Sci. Technol. Int., vol 31, pp. 624–631, 1998.

González-Pérez, S. and Vereijken, J.M., Sunflower proteins: overview of their physicochemical, structural and functional properties, J. Sci. Food Agric., vol. 87, pp. 2172-2191, 2008.

Jamdar, S.N., Rajalakshmi, V., Pednekar, M.D., Juan, F., Yardi, V. and Sharma, A., Influence of degree of hydrolysis on functional properties, antioxidant activity and ACE inhibitor activity of peanut protein hydrolysate, Food Chem., vol. 121, pp. 178–184, 2010.

Kuehler, C.A. and Stine, C.M., Effect of enzymatic hydrolysis on some functional properties of whey protein, J. Food Sci., vol. 39, pp. 379-382, 1974.

Pan, M., Jiang, T.S., Pan, J.L., Antioxidant activities of rapeseed protein hydrolysates, Food and Bioprocess Tech., vol. 4, pp. 1144-1152, 2011.

Rutherfurd, S.M., Methodology for determining degree of hydrolysis of proteins in hydrolysates: A review, J. AOAC Int, vol. 93, pp. 1515–1522, 2010.

Salunkhe, D.K., Chavan, J.K., Adsuleand, R.N. and Kadam, S.S., World oilseed chemistry technology and utilization", New York: Van Nostrand Reinhold Co., pp. 97-128, 1992.

Sonklin,, C., Laohakunjit, N and Kerdchoechuen, O., Physicochemical and flavor characteristics of flavoring agent frommungbean protein hydrolyzed by bromelain, J. Agric. Food Chem., vol. 59, pp. 8475–8483, 2011.

Vasštag, Z., Popović, L., Popović, S., Krimer, V. and Peričin, D., Production of enzymatic hydrolysates with antioxidant and angiotensin-I converting enzyme inhibitory activity from pumpkin oil cake protein isolate, Food Chem., vol. 124, pp. 1316–1321, 2011.

Venuste, M., Zhang, X., Shoemaker, C.F., Karangwa, E., Abbas, S. and Kamdema, P.E., Influence of enzymatic hydrolysis and enzyme type on the nutritional and antioxidant properties of pumpkin meal hydrolysates, Food Funct., vol. 4, pp. 811, 2013.

Villanueva, A., Vioque, J., Sánchez, V.R., Clement, A., Pedroche, J., Bautista, J. and Millán, F., Peptide characteristics of sunflower protein hydrolysates, J. Am. Oil Chem. Soc., vol. 76, pp. 1455-1460, 1999.

Wiriyaphan, C., Chitsomboon, B. and Yongsawadigul, J., Antioxidant activity of protein hydrolysates derived from threadfin bream surimi byproducts, Food Chem., vol. 132, pp. 104–111, 2012.

Yust, M.M., Pedroche, J., Megías, C., Girón-Calle, J., Alaiz, M., Millán, F. and Vioque, J., Improvement of protein extraction from sunflower meal by hydrolysis with alcalase, Grasas y Aceites, vol. 54, pp. 419-423, 2003.

Pastraporn Thongimpong received the B.Sc in Biotechnology, (first-class honors) from King Mongkut's University of Technology North Bangkok. She is a PhD candidate from School of Bioresource, King Mongkut's University of Technology Thonburi.

Nutta Laohakunjit (Assoc. Prof.) received the B.Sc. (1988), M.Sc. (1996), and D.Sc. (2003) degrees in Postharvest and food process engineering from Asian Institute of Technology. She is a Professor, School of Bioresource and Technology, King Mongkut's University of Technology, Thonburi.

Orapin Kerdchoechuen (Assoc. Prof.) received the B.Sc. (1976), M.Sc. (1990), and D.Sc. (1996) degrees in Horticulturefrom Mississippi State University. She is a Professor, Department of biochemical technology, King Mongkut's University of Technology, Thonburi.

Process Development and Characterization Studies of Fed-Batch Fermentation for the Plasmid DNA Production Using Design of Experiments

Sarawuth Noppiboon[1], Panit Kitsubun[2, 3*], Lalintip Hocharoen[3], Jindarat Pimsamarn[1], Saengchai Akeprathumchai[4], Yaowaluck Maprang Roshorm[4]

[1]Department of Chemical Engineering, King Mongkut's University of Technology Thonburi, Thung Khru, Bangkok 10140, Thailand.

[2]Biopharmaceutical Research and Development Laboratory, National Center for Genetic Engineering and Biotechnology, Klong Luang, Pathumthani 12120, Thailand.

[3]National Biopharmaceutical Facility (NBF), King Mongkut's University of Technology Thonburi, Bang Khun Thian, Bangkok 10150, Thailand.

[4]School of Bioresources and Technology, King Mongkut's University of Technology Thonburi, Bang Khun Thian, Bangkok 10150, Thailand.

ABSTARACT

A systematic approach to characterize the fed-batch fermentation process of the plasmid DNA production by *E.coli* DH5α was developed using design of experiments. This study aims to determine parameters which are temperature, pH, dissolved oxygen, cultivation time and feed rate, that have significant effects on supercoiled DNA content, and define the operational ranges of these parameters. The experimental designs were created using the definitive-screening designs (DSDs) at three levels. The DSDs require 16 runs including 3 additional center points. The predictive model was built to simulate the operational range for capability analysis. In conclusion, cultivation time and pH were identified as critical process parameters.

1. INTRODUCTION

Implementing a robust fermentation process is a challenge during the early stage of process development due to lack of information from process characterization studies. One efficient tool to achieve a proper process characterization is design of experiment (DOE) by using Definitive-screening designs (DSDs) (Jones and Nachtsheim, 2011; Erler et al., 2013). The main advantage of DSDs is an increased amount of information gained from fewer of runs when compared to conventional experimental designs. The goals of the DOE in the process characterization studies are identifying which process parameters have significant effects on the quality attributes, and thus, define the operational ranges of manufacturing process that delivers products of pre-determined specification. Moreover, manufacturers are required to establish the edges of failure to support the process validation in commercial scale production (PDA, 2013), which can be achieved by DOE studies

By using definitive-screening designs, the influences of temperature, pH, dissolved oxygen, cultivation time and feed rate on the supercoiled content were characterized in this study.

2. MATERIALS AND METHODS

2.1 Host Strain and Plasmid

Cultivation experiments were carried out with *E. coli* strain DH5α. The plasmid used was pTH.PRRSV_*GP5*.

2.2 Culture Medium

Luria Bertani (LB) and minimal media containing KH_2PO_4, Na_2HPO_4, NH_4Cl_2, $MgSO_4$, yeast extract, glycerol and glycerol as a feeding solution.

2.3 Cultivation Methods

2.3.1 Seed Culture 1 %(v/v) of working seed bank was inoculated with LB medium in 50-mL Falcon tube and grown overnight at 37 °C, 200 rpm.

2.3.2 Fermentation The cultivations were carried out in 2 L bioreactors equipped with the BIOSTAT B Plus. The cultures were started with the batch phase. When the initial glycerol was totally consumed, the fed-batch phase started. The conditions were varied as followed in Table 1.

2.3.3 pDNA Quality Analysis Plasmid DNA samples was applied to a 0.7% agarose gel stained with ethidium bromide to analyze supercoiled content. The minimum specification of supercoiled (%SC) content of the plasmid DNA must be >80% supercoiled form DNA (U.S.FDA, 2007).

3. RESULTS, ANALYSIS and DISSCUSSIONS

The DSDs data in Table 1 is used to develop a predictive quadratic model that can capture the curvature data. The predictive model was built using Forward Selection and All Subsets regression techniques as described by Erler et al., (2013).

Predictive model:

$$\%SC = 77.69 - 1.06(\%DO) + 0.62(Feed\ Rate) - 1.60(Cultivation\ Time) - 2.04(pH)^2 + 1.44(pH)(Cultivation\ time) + 0.86(Temperature)(Cultivation\ time)$$

Impact of Process Parameters on %SC content

In Figure 1, %SC content increased with increasing feed rate, and decreased with increasing %DO, cultivation time, and temperature. Additionally, pH decreased with increasing at mid-high value.

Process Parameter Optimization

To define the optimal point for process parameter, the Prediction Profiler was used to maximize the %SC content and minimize the variations of process parameters. The results from robust optimization were shown in Figure 1

The results of the DSD indicated that the cultivation time and pH have a significant effect on the %SC content (Figure 1, yellow shaded), these parameters were defined as a critical process parameter (CPP).

Process Risks: Edge of Failure Analysis

Edge of failure is defined as the point in the operational ranges where individual lots or batches will fail specification (Little, 2014). To illustrate the multivariate interactions, 3D projections of all parameter combinations within the process parameter ranges are shown in Figure2. In Figure 2, we easily found that the failure batches (red dot) were contributed by the integrations of studied ranges.

4. CONCLUSION

DOE was proven as a powerful tool in characterization of significant fed-batch fermentation process parameters. Cultivation time and pH were identified as critical process parameter. The predictive model was a useful tool for optimizing the process. The utilization of knowledge gained in this study can be used to improve the process performance during the process development.

Table 1 Definitive-screening design (DSDs) for plasmid DNA production.

Run	*pH*	*Temperature*	*%DO*	*Feed Rate*	*Cultivation Time*	*%SC Content*
1	1	1	1	-1	0	73.27
2	-1	-1	-1	1	0	77.40
3	-1	1	0	1	-1	78.10
4	1	-1	0	-1	1	75.26
5	1	1	-1	0	-1	76.15
6	-1	0	1	-1	-1	76.88
7	1	-1	1	1	-1	77.02
8	-1	-1	1	0	1	70.18
9	-1	1	-1	-1	1	73.85
10	0	1	1	1	1	76.53
11	1	0	-1	1	1	76.73
12	0	-1	-1	-1	-1	80.35
13	0	0	0	0	0	79.45
14	0	0	0	0	0	76.90
15	0	0	0	0	0	76.50
16	0	0	0	0	0	78.13

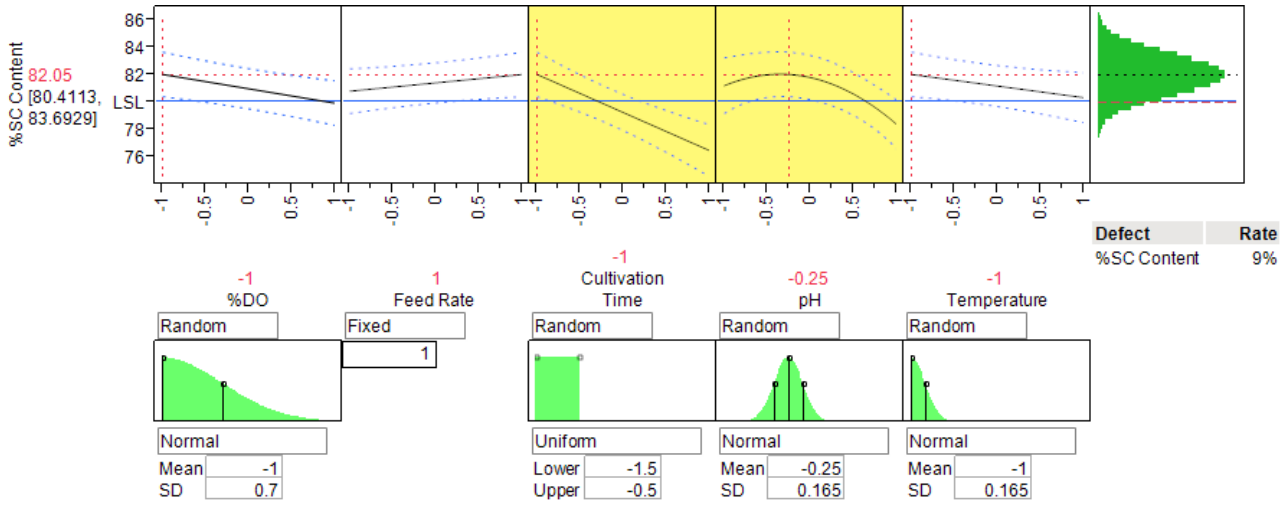

Figure 1 Prediction profiler for sensitivity analysis of process parameters on %SC Content.

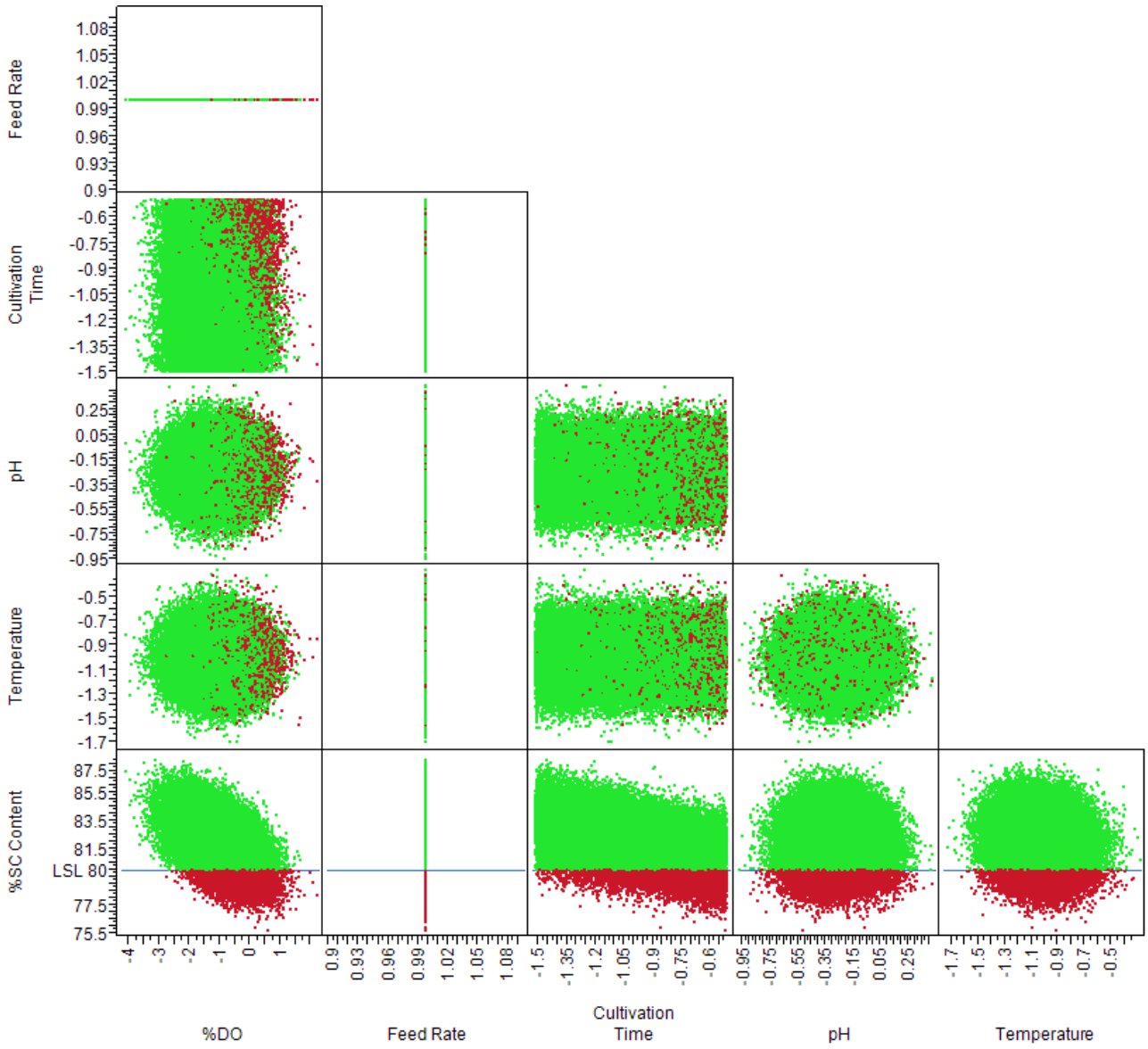

Figure 2 Edge of failure visualization helps to assess and define process risks. (Red indicates failure).

ACKNOWLEDGEMENTS

We are grateful for a financial support by National Science Technology and Innovation Policy Office. We thank Dr. Yaowaluck Maprang Roshorm for plasmid pTH .We thank School of Bioresources and Technology as well as National Biopharmaceutical Facility, King Mongkut's University of Technology Thonburi for their contributions.

REFERENCES

Erler, A., de Mas, N., Ramsey, P. and Henderson, G., 2013, "Efficient Biological Process Characterization by Definitive-Screening Designs: The Formaldehyde Treatment of a Therapeutic Protein as a Case Study", **Biotechnol Lett**, Vol. 35, No. 3, pp. 323-9.

Jones, B. and Nachtsheim, C.J., 2011, "A Class of Three-Level Designs for Definitive Screening in the Presence of Second-Order Effects", **Journal of Quality Technology**, Vol. 43, No. 1.

Little, T.A., 2014, "Evaluating Design Margin, Edge of Failure, and Process Capability", **BioPharm International**, Vol. 27, No. 9.

PDA, 2013, **PDA Technical Report No. 60 – Process Validation: A Lifecycle Approach**, Pages.

U.S.FDA, 2007, **Guidance for Industry: Considerations for Plasmid DNA Vaccines for Infectious Disease Indications**, [online], Available: http://www.fda.gov/BiologicsBloodVaccines/GuidanceComplianceRegulatoryInformation/Guidances/Vaccines/default.htm [Aug,7th 2014].

OS Number: OS04

Antifungal activity of Clove and Cinnamon oils against the opportunistic yeast *Candida albicans*

Nitnipa Soontorngun and Sirilak Baramee

Biochemical Technology Division, School of Bioresources and Technology, King Mongkut's University of Technology Thonburi

ABSTRACT

Treatment of fungal infections is hampered due to drug resistance. Research on the biological activities of natural products such as Thai herbs has increased recently. In this study, clove, cinnamon and coriander oils were selected to test for antifungal activity against yeast *Candida albicans* that is known to be the key opportunistic fungal pathogen in human. The antifungal activities of clove, coriander, cinnamon oils were examined via spot test and broth microdilution assays. The results showed that increasing herbal oil concentrations of clove and cinnamonoils results in reduction of fungal growth on both tests. Thus, essential oils of Thai herbs, clove and cinnamon, extracted via n-Hexane, show antifungal activities that could be applied for development of topical antifungal agents.

INTRODUCTION

Natural products are important sources for topical treatment of bacterial and fungal infections. Herbal products are often characterized by the volatile organic compounds or the secondary products present in different parts of plant, including leaves, bark, and fruit for example (Hili et al., 1997). Often, herbal products are also used as aroma materials in spa and cosmetics such as soaps, perfumes and toiletries. Uses of essential oils to control microbial growth served as the basis for many applications, including food preservation, pharmaceuticals and alternative medicines, and therapies (Yousef and Tawil, 1980; Lis-Balchin and Deans, 1997). Clove and cinnamon are among the local herbs found in many tropical countries, including Thailand. Studies on the antimicrobial and antifungal activities of essential oils extracted from steam distillation and the tests against some microbes have been shown in various studies (Nejad Ebrahimi et al.; Hili et al., 1997; Prabuseenivasan et al., 2006; Pinto et al., 2009). This includes their antifungal activities against opportunistic pathogen such as *C. albicans*, which is considered as a commensal organism of warm-blooded animals, including humans but harmful when host's immunity is compromised. Multidrug resistance (MDR) is caused by several mechanisms. Overexpression of cell surface drug efflux pumps, which expels the drug to minimize the drug toxicity is one important mechanism observed in yeasts which makes antifungal drug development an urgently issue. This study aimed to characterize the antifungal activities of

essential oils obtained from coriander seed, clove bud and cinnamon bark, extracted by n-Hexane, against the yeast *C. albican* strains.

EXPERIMENT

Essential oils

Three essential oils extracted from Thai herbs including clove bud, cinnamon bark and coriander seed were tested. One hundred grams of each dry herb were mashed and transferred to Erlenmeyer flasks containing hundred milliliters of n-Hexane. Herb oils were extracted by shaking and kept at room temperature for 18 h. After that, herb residues were dispersed, using a Buchner funnel fitted with filter paper, a suction flask, and a vacuum pump. The filtrate was composed of herbal oils that were dissolved in n-Hexane and evaporated using an evaporator (BUCHI Rotavapor R-200) to separate herb oils at 800 mbar and 55 ^{o}C.

Media and strains

The liquid yeast peptone dextrose (YPD) and yeast peptone dextrose agar (YPDA) media were used for the yeast culture. 10g of yeast extract, 20 g of Bacto-peptone, and 20 g of dextrose were made up in 1 liter of distilled water (YPD) (Adams et al., 1997). The microorganisms used in this study were *C. albicans* SGY243 (*ade2*/*ade2*Δ*ura3::ADE2*/Δ*ura3::ADE2*) and the Δ*cwt1* strains that lacked *CWT1* gene.

Spot dilution method

The yeast strains *C. albicans* SGY243 and the Δcwt1 strains were grown in liquid yeast peptone dextrose (YPD) overnight. Cells were then spun, re-suspended in distilled water, and diluted to the optical density (OD_{600}) of 0.1. After, they were serially diluted and spotted on appropriated plates. The agar YPD plates were prepared by spreading 100 µl of herbal oils at the final concentrations of 0 to 250 mg/ml of herbal oils as shown in the figures. Cells were incubated at 30 ºC for 2-3 days to observed growth on plates.

Minimal Inhibitory Concentration (MIC) assay

The wild-type SGY243and zinc cluster deletion *Δcwt1* strains were grown as described above till mid-log phase (OD_{600}= 0.7).The bioactive compound (oils or drug) used in this assay were prepared at different concentrations. A hundred microliters of each compound was added to 96-well microtiter plates and then mixed with equal amount of the yeast strain. The plates were incubated at 30°C for 24 hours and the absorbance (600 nm) of each strain at each concentration were measured using a spectrophotometer. Each assay were held in triplicates and performed for at least two independent experiments.

RESULTS and DISCUSSION

Antifungal activity of clove and cinnamon oils via spot assays

The herbal oils have been tested for antifungal activities against the *C. albicans* yeast strains. Growths of the *C. albicans* was determined via spot assays on plates containing clove bud oil and cinnamon bark oil in the range of final concentrations of 0-250 mg/ml. The yeast strains were grown in liquid yeast peptone dextrose (YPD) overnight. Cells were spun at 3,000 rpm and the liquid media was removed and re-suspended in distilled water and then diluted to the optical density (OD_{600}) of 0.1. After, it was serially diluted and spotted on appropriated plates. The agar YPD plate was

prepared to contain 100 µl of herbal oils at various concentrations. It was found that increasing concentrations of clove bud and cinnamon oils reduced cell growth of *C. albicans* was observed as indicated by the spot of cells on plates. For clove oil, the minimum fungicidal concentration was identified to be approximately 200 and 250 mg/ml for clove oil and 50 and 100 mg/ml for cinnamon oil for the SGY243 and *Δcwt1* strains, respectively (Fig. 1). Thus, cinnamon oil had stronger antifungal activity than clove oil. This may due to different composition or bioactive components within the clove and cinnamon oils.

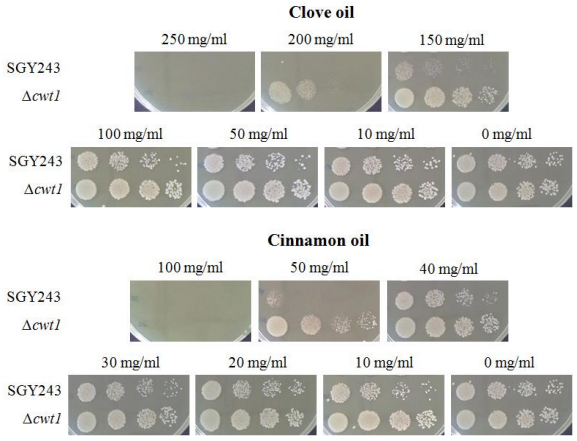

Fig. 1 Growth *C. albican*s wild-type SGY243 and *Δcwt1* strains on plates, containing clove bud or cinnamon bark oils, at concentrations between a range of 0-250 mg/ml for clove oil and 0-100 mg/ml for cinnamon oil via the drop diffusion method (See Materials and methods for details).

Minimal fungicidal concentration of Thai herb oils

Clove oil, cinnamon oil were (diluted with DMSO) used to identify the minimum inhibitory concentration of each essential oil via broth micro dilution assay after 24 h. of incubation.

As expected, it was found that increasing herbal oil concentration results in decreased cell growth. The MIC_{50} value of clove and cinnamon oils were found to be 0.28 and 0.21 mg/ml for the wild-type SGY243 and 0.60 and 0.29 mg/ml for the *Δcwt1* deletion strain, respectively (Fig. 2). It suggests that the deletion of the *CWT1* gene resulted in increased sensitivity to both clove and cinnamon oils suggesting for antifungal property of unique bioactive compounds present in clove and cinnamon oils.

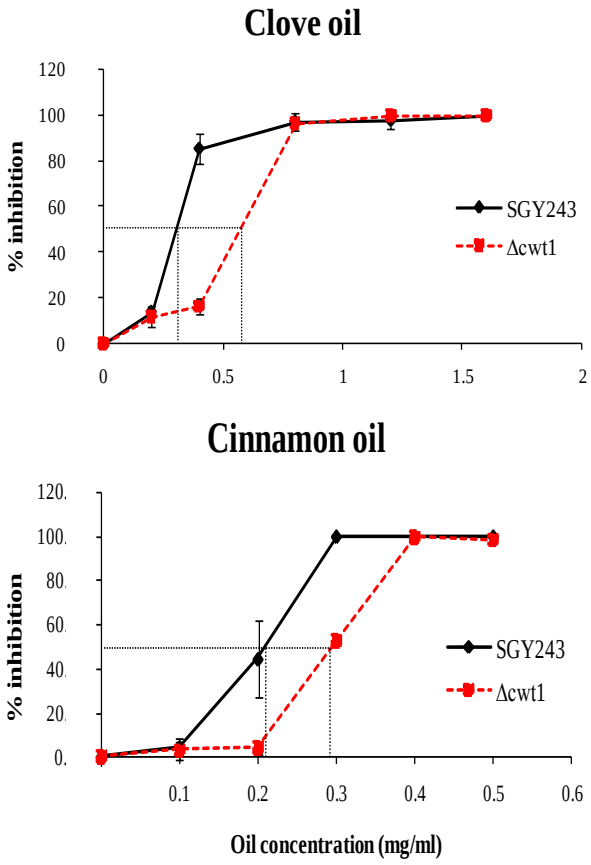

Fig 2. The antifungal activity of herbal extracts and bioactive compounds against *C.albicans* wild-type (SGY243 background) and the *Δcwt1* deletion strains. The lines indicate the antifungal activity of extracts against wild- type (solid black) and the *Δcwt1* (dash red) strains, respectively.

CONCLUSION

In summary, the clove bud and cinnamon bark oils displayed some antifungal activity against the pathogenic yeast *C. albicans.* Cinnamon oil showed better antifungal activity against *C. albicans* as compared to clove oil. This may be due to different bioactive compounds present in the oils. The transcription regulator Cwt1 appears to play an important role in mediating sensitivity to herbal oils, isolated from clove and cinnamon which contain eugenol and cinnamondehyde as main bioactive compounds. Further investigation onto the role of Cwt1 and its mechanism of actions will be worthy for future investigation to gain insight into multidrug resistance. Importantly, this study also proposes the potential use of Thai herbal oils as new alternative biosources for topical treatment of fungal infections.

ACKNOWLAGEMENTS

We like to express our special thanks to Dr. Bernard Turcotte (McGill University, Canada) for a gift of strains. This work is supported by the National Research Council of Thailand (NRCT) and a travel grant from King Mongkut's University of Technology Thonburi**.** We also acknowledge KMUTT for facility and travel fund to attend SEATUC2015 conference.

REFERENCES

Hili, P., Evans, C.S. and Veness, R.G. 1997. Antimicrobial Action of Essential Oils: The Effect of Dimethylsulphoxide on the Activity of Cinnamon Oil. Letters in applied microbiology 24: 269-75.

Lis-Balchin, M. and Deans, S.G. 1997. Bioactivity of Selected Plant Essential Oils against Listeria Monocytogenes. Journal of Applied Microbiology 82: 759-62.

Nejad Ebrahimi, S., Hadian, J. and Ranjbar, H. Essential Oil Compositions of Different Accessions of *Coriandrum Sativum L.* From Iran. Natural Product Research 24: 1287-94.

Pinto, E., Vale-Silva, L., Cavaleiro, C. and Salgueiro, L. 2009. Antifungal Activity of the Clove Essential Oil from Syzygium Aromaticum on *Candida*, Aspergillus and Dermatophyte Species. Journal of Medical Microbiology 58: 1454-62.

Prabuseenivasan, S., Jayakumar, M. and Ignacimuthu, S., 2006, In Vitro Antibacterial Activity of Some Plant Essential Oils. BMC Complementary and Alternative Medicine 6: 39-46.

Yousef, R.T. and Tawil, G.G. 1980. Antimicrobial Activity of Volatile Oils. Pharmazie 35: 698-701.

Nitnipa Soontorngun received B.Sc. degree in Biochemistry and Molecular Biology from University of British Columbia, Canada and Ph.D degree in Biochemistry from McGill University, Canada. Her current interests include Gene and Enzyme Technology, Yeast Genetics and Antifungal drug development.

Sirilak Baramee received the B.Sc. degrees in Biotechnology from Silpakron University and M.Sc. degrees in Biochemical technology from King Mongkut's University of Technology Thonburi. Her current interests include resistance to bioactive compound isolated from Thai herbs in the yeast *S. cerevisiae*.

OS Number: **OS04**

Examination of the in *vitro* interaction between Amphotericin B and *Xylaria sp.* extract against *Saccharomyces cerevisiae* by Micro-dilution checkerboard method

Attaporn Poonsawad and Nitnipa Soontorngun
Division of Biochemical Technology, School of Bioresources and Technology
King Mongkut's University of Technology Thonburi

ABSTRACT

Combinatorial antifungal therapy is used to improve treatment of fungal infections and to reduce the ability of fungal tolerance to different antifungal drugs. As a result of various drug resistant mechanisms developed by fungi, new combination of drugs is required to improve treatments. Present study aimed to investigate the effectiveness of *Xylaria sp*. crude extract when combined with current antifungal drug Amphotericin B (AmB) against the model yeast *Saccharomyces cerevisiae* by using micro-dilution checkerboard assay based on LA-base model. Percentages of growth were calculated as Fractional inhibition concentration index (FICI) and corresponding to Synergy, Additive, Indifference, or Antagonism effect representing. Results indicated that *Xylaria sp*. crude extract increased antifungal activity when used in combination with AmB with relative density of cell measurement of approximately 80% and 90% decreased at 24 and 48 h, respectively. The lowest FICI (0.625) show the *additive* effect to Amphotericin B at the concentration 1 mg/ml of *Xylaria sp.* crude extract and 0.5 μg/ml of Amphotericin B

1. INTRODUCTION

Immunodeficiency in patients who require prolonged treatments leads to high clinical significant mortality rates as a result of fungal drugs-resistant infectious and lack off effective drugs and treatments. Especially traditional antifungal drug has single target with various side effects to human health (X. Chen, 2014). A combinatorial antifungal therapy is a process that can be used to improve in medical treatment for difficult-microbial infection caused by drug resistant pathogens. Various important evidences show the ability in microorganism to develop tolerance in current drug treatment by formation of biofilm at surfaces (Paraje M.G., 2011). Interaction between drugs is an *in vitro* method to investigate the antifungal properties of each drug for increasing the potential or rate killing of the fungal both susceptible and resistant pathogens (Johnson, 2004). Drug combination has been classified into three types by using micro-dilution checkerboard method; synergy, additive and antagonism. Synergy is a positive effect when two drugs are combined that demonstrate greater inhibition properties than single drug used, In contrast, negative effect of drug combination show less potential than one drug tested is known as antagonism. No interaction or indifferent of effect drugs is identified as additive or no interaction (Manuel Cuenca-Estrella, 2004). *Saccharomyces cerevisiae* is also known as baker yeast which can be classified in fungal kingdom. It is often used as a model organism for study of drug resistance due to its ability to develop drug resistance, ease of genetic manipulation and available molecular biology tools for in depth investigation (Feldmann and Horst, 2010)

Xylaria species are classified in fugal kingdom that can be found in tropical rain forests and grow in dead-wood as a natural decomposer in ecology (Osono, 2011). Chinese traditional medicine uses *Xylaria nigripes* (Wu Ling Shen) for immune and circulatory disorder treatment (Ko, 2011). Secondary metabolites in *Xylaria* species are interesting and found to contain important bioactive substances related to various bioactive properties such as antimicrobial, antioxidant and anticancer (Whalley, 1996). Chemical compounds in *Xylaria* species are Xylarine and Xylaramide that be reported by Schneider G. in 1996.

Amphotericin B (AmB) is an antimicrobial drug which classified in polyene antifungal class. Usually, it is used for fungal infections treatment but only effective for some infections. Amphotericin B is believed to target at the ergosterol, a component of fungal cell membrane biosynthesis and leads to leak of ions at cell membrane and contribute the cell membrane leakage. This drug shows high toxicity and has some side effects such as fever, anaphylaxis (allergic symptom), headache, nausea, vomiting, stomachache, blood pressure drop and may induce kidney problems (The American society of Health-system Pharmacists).

In this study, we investigate the qualitative and quantitative effectiveness of synergy's drugs interaction between *Xylaria sp.* crude extract and Amphotericin B against *Saccharomyces cerevisiae* by using micro-dilution checkerboard method which minimum concentrations and percentage of growth are evaluated in the presence of drugs.

2. EXPERIMENT

2.1 Yeast strains and culture conditions

The *Saccharomyces cerevisiae* BY4742 wild type strains were used as the test microorganism. The yeast strain was cultured on yeast peptone dextrose (YPD) media (1% yeast extract, 2% peptone and 2% glucose) and grown overnight (14-18 h) at 30 °C with shaking, The final inoculum before used must between $0.5 \times 10^5 - 2.5 \times 10^5$ CFU/mL

2.2 Preparation of *Xylaria* extracts

The obtained crude extract was kept at -20 ˚C. Before used, extract was dissolved with methanol. Prepared the initial concentration at 8 mg/ml and concentration rang of crude extract was series diluted at 0.0625 to 2 mg/ml.

2.3 Preparation of drug

Amphotericin B (AMB) solution was freshly prepared in DMSO and initial concentration at 16 µg/ml. Rang of AMB concentration used was between 0.25 to 4 µg/ml.

2.4 Checkerboard micro-dilution method studies

Checkerboard micro-dilution method assay was derived from The European Committee Antimicrobial Susceptibility Testing (EUCAST) protocol for determination of broth micro-dilution minimum inhibitory concentrations of antifungal agents for yeast. This method was performed for AMB interacted with *Xylaria sp*. crude extract by using 96-well flat bottom plate (Fig.1) 100 µl of cells and 50 µl of drug and crude extract were used with a range of final concentrations of 0.0625 to 2 mg/ml of *Xylaria sp*. extract (rows A to F), rows A started at concentration 2 mg/ml, and 0.25 to 4 µg/ml of AMB (columns 1 to 12), column 1 started at concentration 4 µg/ml. At rows G and column 12 is free drug as a control. Cells were incubated in the 96-plate at 30°C with shaking and then measure absorbance at 600nm after 24 and 48 h to obtain the percent growth of cells. Fractional inhibition concentration index (FICI) was based on LA-base model to determine the combination antifungal drug activity which be calculated after incubated for 48 h.

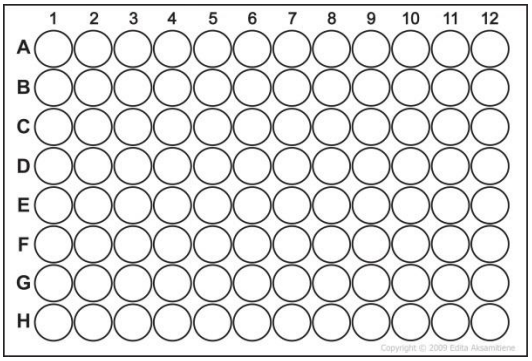

Fig.1 96-well flat bottom plate of Checkerboard micro-dilution method

LA-base model (FICI) was calculated as sum of minimum inhibition concentration of each drug when used in combination divided by minimum inhibition concentration of drug when used alone. FICI was determined to interaction. FICI of $\leq$ 0.5 represents synergistic effect, additive effect (0.5-1), indifferent effect (1-4) and antagonism effect (>4) (R.E. Lewis, 2002). To calculate formulation by; in which MIC is minimum inhibition concentration

$$\sum FICI = \left\{\frac{MIC \text{ of A at } Combination}{MIC \text{ of A } Alone}\right\} + \left\{\frac{MIC \text{ of B at } Combination}{MIC \text{ of } BAlone}\right\}$$

3. RESULTS

In previous study, Schneider G. in 1996 reported *Xylaria* species extract has potent antifungal activity. This result is interesting and motivates us to continue investigation of possible antifungal activity of *Xylaria* extracts to increase the property of their antifungal activity. Therefore, the non-pathogenic yeast *S. cerevisiae* is used as a model to investigate the antifungal activity and mechanism of drug resistance. In vitro study, we proposed that *Xylaria sp.* extract may increase the potential antifungal activity when combined or interacted with AmB drug at the appropriate concentration by using micro-dilution Checkerboard method to investigate the synergistic between them.

After 24 h of incubation, the results demonstrated the antifungal activity of *Xylaria sp.* extract when combined with AmB at increasing concentrations reduce almost 80 percentages of cell growth when compared with

controls (no drug wells) (Table 1 and Fig. 2). The interaction with AmB at each concentration rang(0.25 - 4μg/ml) were shown (Table 1). At 48 h of incubation, the results showed the decrease in the percentages of cell growth continuously to approximately 90 percentages. (Fig.3)

Fractional inhibition concentration index (FICI) based on LA-base model calculated by using the results obtained from table 1. showed the percentage of growth in each well after 48 h incubated. Minimum inhibition concentrations presented the 85% growth inhibition (MIC_{85}) were calculated; the highest FIC value equaled to 1.06 (combined 4 μg/ml of AmB and 0.125 mg/ml of *Xylaria sp.* extract) represented indifferent effect of antifungal drug while the lowest FIC value was 0.62 (combined 0.5 μg/ml of AMB and 1 mg/ml of *Xylaria sp.*) represented additive effect antifungal drug. Susceptibilities testing yeast *Saccharomyces cerevisiae* against with Amphotericin B alone and in combined were shown ≥ 4 μg/ml of Amphotericin B and 2 mg/ml of *Xylaria sp*. crude extract (Table 1).

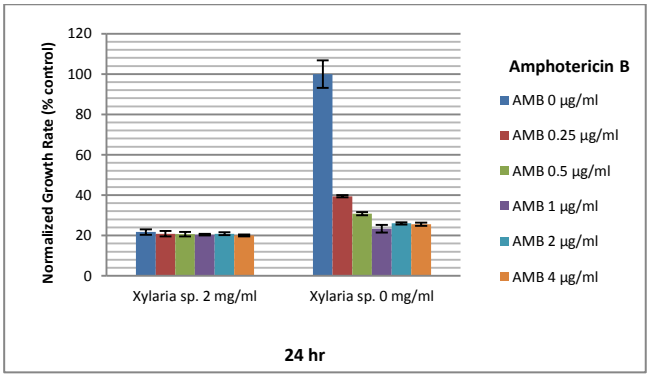

Fig.2 Relative growth rate of *S. cerevisiae* treated with various concentrations of AmB alone and in combination with *Xylaria sp.* Extract. Cells were incubated with various concentrations drug and extract for 24 h and monitored the cell density at OD_{600} using micro-plate reader. Control (no drug in well) presented in highest bar 100% growth rate of cells.

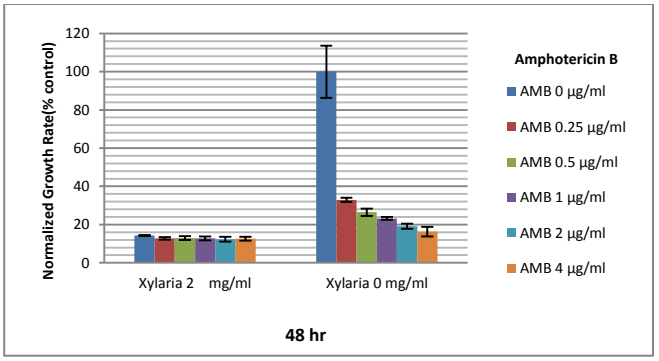

Fig.3 Relative growth rate of *S. cerevisiae* treated with various concentrations of AmB alone and in combination with *Xylaria sp.* extract. Cells were incubated with various concentrations drug and extract for 48 h and monitored the cell density at OD_{600} using micro-plate reader. Control (no drug in well) presented in highest bar 100% growth rate of cells.

Table1. Assessments of in *vitro* interaction between AmB and *Xylaria sp*. crude extract against yeast *S. cerevisiae* BY4742 wild-type strain using LA-base model. Micro-dilution Checkerboard method showed the percentage of growth for each combination, control showed 100 percentage of growth rate (yellow area), combinations with >15% growth (gray area). ∑FIC indices were calculated (light blue area), combinations with ∑FIC indices were between 0.5 –1 (underlined percentage), and combination with the lowest ∑FIC (0.62) which corresponding to the FICI (showed in the dark blue area).

	AMB 4 μg/ml	AMB 2 μg/ml	AMB 1 μg/ml	AMB 0.5 μg/ml	AMB 0.25 μg/ml	AMB 0 μg/ml
Xylaria 2 mg/ml	12.6	12.3	12.8	12.9	12.8	14.3
Xylaria 1 mg/ml	13.7	13.4	12.9	14.5	15.2	16.5
Xylaria 0.5 mg/ml	13.8	15.1	15.7	15.5	17.1	18.2
Xylaria 0.25 mg/ml	14.5	16.2	16.6	16.9	16.9	19.4
Xylaria 0.125 mg/ml	14.2	16.2	17.5	17.7	17.5	18.5
Xylaria 0.0625 mg/ml	15.5	17.1	17.2	16.9	17.7	19.1
Xylaria 0 mg/ml	16.3	19.1	23.2	26.5	32.9	100

3. CONCLUSION

It is summarized that in *vitro* drugs interaction between AmB and crude extract of *Xylaria sp.* shows increasing the potential of antifungal when acted alone and combined or interacted with drug (AmB) at the various concentrations. Fractional inhibition concentration index (FICI) showed the *additive* effect to antifungal drug. This study provided information the antifungal activity of *Xylaria sp.* crude extract in combination and positive effect or iso-effective to antifungal drug (AmB).

4. ACKNOWLEDGMENTS

This study was supported by the National Research Council of Thailand (NRCT). We acknowledge Dr. Laran Jensen (Mahidol University, Thailand) for the generous gifts of strains. We are grateful to Carbohydrate Technology and Enzyme Technology Laboratories (King Mongkut's University of Technology Thonburi, KMUTT) for equipment. We also acknowledge KMUTT for facility and travel fund to attend SEATUC2015 conference.

5. REFERENCES

Lewis R.E., Comparison of Etest, chequerboard dilution and time kill studies for the detection of synergy or antagonism between antifungal agents tested against *Candida* species, Journal of Antimicrobial Chemotherapy, vol. 49, pp. 345-351, 2002.

Jonhson M.D., Combination Antifungal Therapy, Antimicrobial agents and Chemotherapy, vol. 48, No. 3, pp. 693-715, 2004.

Arendrup M. C., Method for the determination of broth dilution minimum Inhibitory concentrations of antifungal agents for yeasts, EUCAST definitive document EDef 7.2 revision

Manuel Cuenca-Estrella., Combinations of antifungal agents in therapy-what value are they?, Journal of Antimicrobial Chemotherapy., vol. 54, pp. 854-869, 2004.

Feldmann, Horst., Yeast Molecular and Cell bio, Wiley-Blackwell, 2010.

Pajare M.G., Antimicrobial resistance in biofilm, science against microbial pathogen, Formatex., 2011

Osono, T., To-Anun, C., Hagiwara, Y. and Hirose, D., Decomposition of wood, petiole and leaf litter by *Xylaria* species from north Thailand, fungal ecology., Vol. 4, No. 3, pp. 210-218, 2011.

Whalley, A. J. S., The *xylariaceous* way of life, Mycological research., Vol. 100, No. 8, pp. 897-922,1996.

Ko, H.-J., Song, A., Lai, M.-N and Ng, L.-T., Immunomodulatory propertry of *Xylaria* nigripes in peritoneal macrophage cells of Balb/c mice, Journal of Ethnopharmacology., Vol. 138, No.3, pp. 762-768, 2011.

Schneider, G., Anke, H. and Sterner, O., Xylaramide, a new antifungal compound, and other secondary metabolites from *Xylaria langipes*, Zeischrift fur Naturforschung. C, Journal of biosciences., Vol. 51, No. 11-12, p. 802, 1996.

Rafael L., Amphotericin B ; side effect and toxicity, Revista Iberoamericana de Micologı´a, vol. 26, No. 4, pp. 223-227, 2009.

Chen X., ASDCD ; Antifungal Synergistic Drug Combination Database, Plos ONE, 2014.

Attaporn Poonsawad received the B.ATM. (Applied Thai Traditional Medicine) degree from MAE FAH LUANG University, Chiangrai, Thailand. Present, Master degree student (Biochemical technology) at King Mongkut's University of Technology Thonburi, Bangkok, Thailand.

His study is focused on Yeast Genetics: antibacterial and antifungal compounds obtained from *Xylaria* species and their mechanism of action.

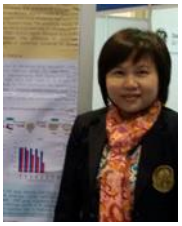

Nitnipa Soontorngun received the B.Sc. (Biochemistry and Molecular biology) from University of British Columbia, Vancouver, Canada and Ph.D. (Biochemistry) from McGill University, Montreal, Canada.

She is an Assistant Professor, Division of Biochemical Technology, School of Bioresources and Technology, King Mongkut's University of Technology Thonburi, Bangkok, Thailand.

Her research interests include Gene and Enzyme Technology, Yeast Genetics and Molecular Biology, and Antimicrobial drug development.

OS Number: **OS04**

PLEIOTROPIC DRUG RESISTANCE REGULATOR IS INVOLVED IN TOLERANCE ANTIFUNGAL ACTIVITY OF *XYLARIA OBOVATA*

Pichayada Somboon and Nitnipa Soontorngun
Division of Biochemical Technology, School of Bioresources and Technology
King Mongkut's University of Technology Thonburi

ABSTRACT

In a previous study, crude extract of *Xylaria obovata* was reported as an antifungal compound against *Saccharomyces cerevisiae.* Present study aims to investigate mechanism of *S. cerevisiae* which is responsible for resistance to antifungal activity of crude extract of *X. obovata.* Antifungal activity of the extract was tested by minimum inhibition concentration (MIC) and minimum fungicidal concentration (MFC) assays against the *Δstb5* strain. Stb5 regulator is involved in regulatory of genes in multidrug resistance mechanism and oxidative stress. Compared with wild-type, Δ*stb5* presented higher sensitivity to crude extract with MIC_{50} of 0.04 mg/ml and MFC of 0.12 mg/ml. Results indicated that Stb5 is a regulator that confers resistance to antifungal activity to crude extract of *X. obovata.* This probably occurs because target genes of Stb5 play a role in yeast cell defense mechanism against *X. obovata* extract.

1. INTRODUCTION

During the past years, the healthcare problem has been the lack of effective chemical drugs in the treatment of fungal pathogenic infections which leads to antifungal drug resistance. Widespread and prolonged use of antifungal drugs results in developing tolerance to the drugs and also increases resistance to other drugs. In humans, drug resistance causes harmful therapeutic management in immunocompromised patients who have experienced transplantation surgery, cancer chemotherapy and HIV infection (Cowen and Steinbach, 2008). The ability to develop resistance of fungi to a variety of drugs and unrelated compounds was called a pleiotropic drug resistance (PDR). Drug resistance can be driven by mechanisms that are specific for each antifungal drug. For instance, fungi resist to azole drug by the mutation in *ERG11,* which encodes 14α-demethylase and is a target of azole drug. However, increasing the *ERG11* expression and alteration of ergosterol synthesis pathway also cause resistance to azole. Polyene tolerance is caused by decreasing membrane ergosterol content (Morschhäuser, 2010). Although the activating mutation in genes related to cell membrane composition is important for drug tolerance, the most important mechanism is transporting drugs out of the cell to reduce intracellular concentration of a drug because this can function with all unrelated drugs with different mode of action. In fungi, PDR is displayed by two classes of efflux pumps that are ATP-binding cassette (ABC) transporters and major facilitator superfamily (MFS) transporters. Their differentiations are from using energy source; ABC transporters use an ATP molecule as a power source while proton gradient is provided as energy for pumping the drug across the membrane by MFS transporters (Prasad and Rawal, 2014). *Saccharomyces cerevisiae* is an excellent model organism for PDR study because of its similarity with most important fungal pathogens, *Candida albicans* and other yeasts of the *Candida* genus. The advantages of using *Saccharomyces cerevisiae* as a model organism are that complete genomic study, cost-effectiveness, rapid growth and many of the mechanisms underlying toxicity and resistance to chemicals and other kinds of environmental stress are conserved. Moreover, collections of yeast deletion strains and overexpression libraries have been used to investigate drug targets (Paul and Moye-Rowley, 2014).

In *S. cerevisiae*, Pdr5 is a major transporter in the PDR mechanism since many compounds are considered to be substrates, such as azole drug, cycloheximide and xenobiotics. On the other hand, Pdr5 is important because of high similarity to homologue transporter in *Candida albicans,* Cdr1. However, the PDR system is controlled by many transcription factors. Major transcription regulators of PDR mechanism are Pdr1 and Pdr3 which directly activate the promoters of various PDR transporters including *PDR5, SNQ2* and *YOR1* (Fardeau, et al., 2007, Kolaczkowska, et al., 2008, Mamnun, et al., 2002). Pdr1 and Pdr3 are members of zinc cluster regulators; they are transcription regulators consisting of a zinc finger in their

structure and contain a DNA binding domain (DBD), which has conserved motif Cys-X_2-Cys-X_6-Cys-$X_{5–16}$-Cys-X_2-Cys-$X_{6–8}$-Cys. Zinc cluster regulators bind to PDRE promoter of PDR genes at everted repeat CCGCGG. Pdr1p is the main regulator of *PDR5* and can form homodimer and heterodimer with Pdr3. Besides, Pdr3 and Pdr1 also form heterodimer with Stb5, which is a regulator involved in regulating multidrug resistance and oxidative stress response (Akache, et al., 2004). Stb5 forms a heterodimer with Pdr1 in activating expression of PDR genes including *PDR5* and *SNQ2* (Akache, et al., 2004). Therefore, lack of *STB5* gene makes cells sensitive to drugs and various kinds of environmental stress such as cycloheximide, 5-fluorouracil, hydrogen peroxide and caffeine (Akache and Turcotte, 2002). Moreover, Stb5 also regulates genes belonging to oxidative stress response, such as Zwf1 (cytoplasmic glucose-6-phosphate dehydrogenase) which is a key enzyme in NADPH production (Hector, et al., 2009).

So far, bioactive compounds isolated from microorganism have been shown an increased interest looking for new and better effective antifungal compounds to defend increasing amount of fungi that develop the PDR mechanism. Wood-decay fungi such as Xylariaceae family is a well-known family in tropical forests in most countries in the world (Whalley, 1996). Naturally, this fungus works as a decomposer and some species are endophytes. Various studies report that *Xylaria* is a perfect source of bioactive compounds such as multiplolides A and B (Boonphong, et al., 2001), 7-amino-4-methylcoumarin (Liu, et al., 2008). Some of them have been used in folk medicine (Ko, et al., 2009). However, the study of Xylaria spp. bioactive compounds in Thailand has not been extensive, so the knowledge is scarce.

In previous study, we investigated antifungal activity of *Xylaria obovata* against *S. cerevisiae* (Somboon and Soontorgun, 2013). Therefore, in present study, we investigate the influence of the deletion of PDR regulator genes for elucidating exportation PDR mechanism involved in antifungal activity of *X. obovata* against *S. cerevisiae* BY4742 and deletion strains.

2. EXPERIMENT

2.1 Yeast strains and culture conditions

Saccharomyces cerevisiae BY4742 and deletion strains were used as a model for the study of the mechanism; those were: Δ*stb5* [(*MAT*∝ *his3*Δ*31 leu2*Δ*0 lys2*Δ*0 ura3*Δ0) Δ*stb5::kanMX4*]. The yeast strain was cultured on yeast peptone dextrose (YPD) media (1% yeast extract, 2% peptone and 2% glucose).

2.2 Preparation of *Xylaria* extracts

Xylaria colonies were grown in malt extract agar (MEA) (Fig.1) before extraction with ethyl acetate and dried with rotary evaporation.

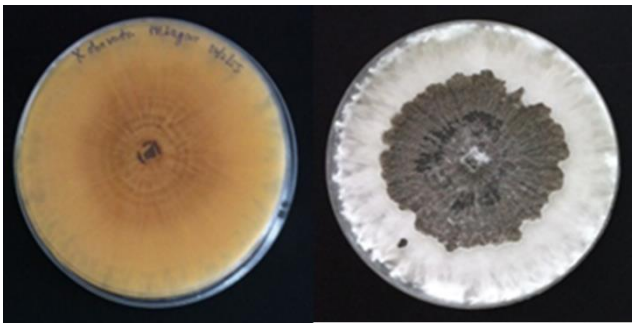

Fig.1 *Xylaria obovata* grown on MEB agar media.

2.3 Susceptibility testing: minimum inhibition concentration (MIC) and minimum fungicidal concentration (MFC) assay

To determine antifungal activity of the extract, the minimal inhibition concentration (MIC) assay was performed using a 96-well plate. Concentrations of the extract ranged between 0.00-1.00 mg/ml. The starting inoculum was diluted to 0.001 at OD_{600}. Plate was incubated for 24 h at 30 °C and 150 rpm. After incubation time, OD_{600} of the plate was monitored using a microplate reader. The haft MIC (MIC_{50}) was calculated from these results. Next, a culture in each well was spread on YPD agar plate and incubated at the same temperature for 48 h. Colonies developed on the plate were counted and calculated MFC. MFC was defined as minimum concentration of the extract that inhibits growth of yeast. Studies were performed in triplicate.

3. RESULTS

In previous study, we reported that *Xylaria obovata* crude extract had antifungal activity against wild-type strain of *S. cerevisiae* (Somboon and Soontorgun, 2013). This result makes us continue investigating possible mechanisms that function as cell defense program. We suggested PDR as a resistance mechanism because of diverse substrate types that can be recognized (Cowen and Steinbach, 2008).

According to the result shown in Fig. 2, the lack of *STB5* led to defective growth of *S. cerevisiae.* This was noted by MIC50 values of wild-type and Δ*stb5* strains that were 0.11 mg/ml and 0.04 mg/ml, respectively. After 24 h treatment with the *X. obovata* extract, the culture was taken to perform MFC assay (Fig. 3a and b). The colony number of wild-type cells was clearly decreasing when the concentration of *X. obovata* extract accounted for 0.25 mg/ml. Wild- type strain showed larger resistance to the extract than Δ*stb5*

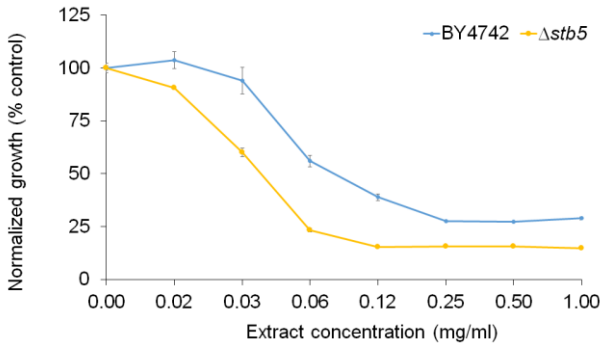

Fig.2 Relative growth rate of *S. cerevisiae* and deletion of PDR genes treated with various concentrations of *X. obovata.* Cells were incubated with various concentrations of the extract for 24 h and the cell density at OD_{600} was monitored using a microplate reader. Wild-type cell was presented as blue line, Δ*pdr1* as orange line, Δ*pdr3* as grey line and Δ*stb5* as yellow line. Standard deviation was calculated from three experiments.

because wild-type cells need higher concentration of the extract to show its lethal effects (Fig.3a and c). As expected, the Δ*stb5* strain was more sensitive to *X. obovata* exposure than wild-type and MFC of 0.12 mg/ml. (Fig.3b and c).

A possible explanation of these results could be their functions; Stb5 is a transcription regulator involved in both PDR mechanism and oxidative stress and target *PDR5, SNQ2* and genes in pentose phosphate pathway and NADPH production (Larochelle, et al., 2006, Matsufuji, et al., 2010). Lack of Stb5 transcription regulators results in a cell not being able to resist toxic compounds produced from *X. obovata.* This might be a defect in both PDR and oxidative stress resistance mechanisms.

3. CONCLUSIONI

It can be concluded from the results that crude extract of *X. obovata* has harmful effects on a cell resulting in the cell being able to develop PDR mechanism to protect the cell from antifungal activity of this extract. Moreover, the results show that Stb5 might be a part of cell's response to *X. obovata* effect by regulating target genes in PDR mechanism such as *PDR5* encoding mainly membrane transporter in *S cerevisiae.* In addition to target genes in PDR, Stb5 also regulates genes in oxidative stress response in the production of NADPH, which is a necessary metabolite for oxidative stress resistance (Larochelle, et al., 2006). This study provided information to better understand cell's response to the extract and showed putative new substrates of these PDR genes.

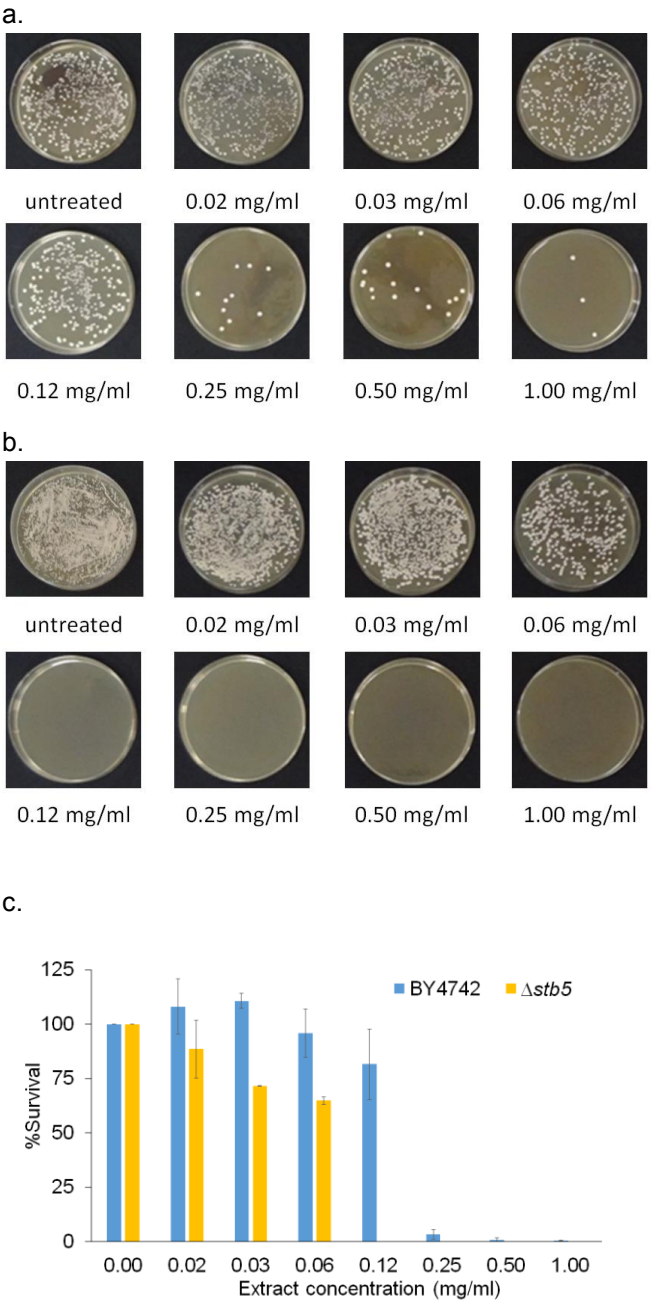

Fig.3 Illustrated MFC values of BY4742 and the Δ*stb5* strains during exposure to *X. obovata* extract at various concentrations. (a) Wild-type BY4742 and (b) the Δ*stb5* strain formed colonies on YPD plate after surviving cells were counted and calculated. (c) Wild-type and the Δ*stb5* cell were calculated for the percentage of survival and compared with untreated cells, shown as blue bar and yellow bar, respectively. Standard deviation was calculated from three experiments.

4. ACKNOWLEDGMENTS

This study was supported by the National Research council of Thailand (NRCT). We acknowledge Dr. Laran Jensen (Mahidol University) for the generous gifts of strains. We are grateful to Carbohydrate Technology and Enzyme Technology Laboratories (King Mongkut's University of Technology Thonburi, KMUTT) for the equipment

5. REFFERENCES

Akache, B., MacPherson, S., Sylvain, M. A. and Turcotte, B., Complex interplay among regulators of drug resistance genes in *Saccharomyces cerevisiae*, *The Journal of biological chemistry*, vol. 279, no. 27, pp. 27855-27860, 2004 of conference.

Akache, B. and Turcotte, B., New regulators of drug sensitivity in the family of yeast zinc cluster proteins, *The Journal of biological chemistry*, vol. 277, no. 24, pp. 21254-21260, 2002 of conference.

Boonphong, S., Kittakoop, P., Isaka, M., Pittayakhajonwut, D., Tanticharoen, M. and Thebtaranonth, Y., Multiplolides A and B, New Antifungal 10-Membered Lactones from *Xylaria multiplex*, *Journal of Natural Products*, vol. 64, no. 7, pp. 965-967, 2001 of conference.

Cowen, L. E. and Steinbach, W. J., Stress, drugs, and evolution: the role of cellular signaling in fungal drug resistance, *Eukaryotic cell*, vol. 7, no. 5, pp. 747-764, 2008 of conference.

Fardeau, V., Lelandais, G., Oldfield, A., Salin, H., Lemoine, S., Garcia, M., Tanty, V., Le Crom, S., Jacq, C. and Devaux, F., The central role of PDR1 in the foundation of yeast drug resistance, *The Journal of biological chemistry*, vol. 282, no. 7, pp. 5063-5074, 2007 of conference.

Hector, R. E., Bowman, M. J., Skory, C. D. and Cotta, M. A., The *Saccharomyces cerevisiae YMR315W* gene encodes an NADP(H)-specific oxidoreductase regulated by the transcription factor Stb5p in response to NADPH limitation, *New Biotechnology*, vol. 26, no. 3–4, pp. 171-180, 2009 of conference.

Ko, H. J., Song, A., Lai, M. N. and Ng, L. T., Antioxidant and antiradical activities of Wu Ling Shen in a cell free system, *The American journal of Chinese medicine*, vol. 37, no. 4, pp. 815-828, 2009 of conference.

Kolaczkowska, A., Kolaczkowski, M., Goffeau, A. and Moye-Rowley, W. S., Compensatory activation of the multidrug transporters Pdr5p, Snq2p, and Yor1p by Pdr1p in *Saccharomyces cerevisiae*, *FEBS Lett*, vol. 582, no. 6, pp. 977-983, 2008 of conference.

Larochelle, M., Drouin, S., Robert, F. and Turcotte, B., Oxidative stress-activated zinc cluster protein Stb5 has dual activator/repressor functions required for pentose phosphate pathway regulation and NADPH production, *Molecular and cellular biology*, vol. 26, no. 17, pp. 6690-6701, 2006 of conference.

Liu, X., Dong, M., Chen, X., Jiang, M., Lv, X. and Zhou, J., Antimicrobial activity of an endophytic *Xylaria* sp.YX-28 and identification of its antimicrobial compound 7-amino-4-methylcoumarin, *Appl Microbiol Biotechnol*, vol. 78, no. 2, pp. 241-247, 2008 of conference.

Mamnun, Y. M., Pandjaitan, R., Mahe, Y., Delahodde, A. and Kuchler, K., The yeast zinc finger regulators Pdr1p and Pdr3p control pleiotropic drug resistance (PDR) as homo- and heterodimers *in vivo*, *Molecular microbiology*, vol. 46, no. 5, pp. 1429-1440, 2002 of conference.

Matsufuji, Y., Nakagawa, T., Fujimura, S., Tani, A. and Nakagawa, J., Transcription factor Stb5p is essential for acetaldehyde tolerance in *Saccharomyces cerevisiae*, *Journal of basic microbiology*, vol. 50, no. 5, pp. 494-498, 2010 of conference.

Morschhäuser, J., Regulation of multidrug resistance in pathogenic fungi, *Fungal Genetics and Biology*, vol. 47, no. 2, pp. 94-106, 2010 of conference.

Paul, S. and Moye-Rowley, W. S., Multidrug resistance in fungi: regulation of transporter-encoding gene expression, *Frontiers in physiology*, vol. 5, p. 143, 2014 of conference.

Prasad, R. and Rawal, M. K., Efflux pump proteins in antifungal resistance, *Frontiers in Pharmacology*, vol. 5, p. 202, 2014 of conference.

Somboon, P. and Soontorgun, N., Identification of wood-decay fungi *Xylaria obovata* extract with antifungal activity, *Burapha University International Conference 2013*, Burapha University, Thailand.

Whalley, A., The xylariaceous way of life, *Mycological Research*, vol. 100, no. 8, pp. 897-922, 1996 of conference.

Pichayada Somboon received the B.Sc. (biotechnology) from Silpakorn University, Nakoonpathom, Thailand. The M.Sc. (Biochemical technology) from King Mongkut's University of Technology Thonburi, Bangkok, Thailand.

Her study is focused on yeast genetics: antifungal compounds obtained from *Xylaria* species and their mechanism of action.

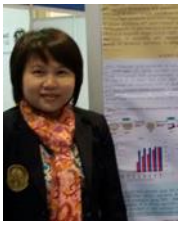

Nitnipa Soontorngun received the B.Sc. (Biochemistry and Molecular biology) from University of British Columbia, Vancouver, Canada and Ph.D. (Biochemistry) from McGill University, Montreal, Canada.

She is a lecturer at the Division of Biochemical Technology, School of Bioresources and Technology, King Mongkut's University of Technology Thonburi, Bangkok, Thailand.

Her research interests include Gene and Enzyme Technology, Yeast Genetics and Molecular Biology, and Antifungal drug development.

Development of Active Upper Limb Orthosis To Support Activities of Daily Living

Fumiya Shiki[1], Haruki Ishii[1], Akihiko Hanafusa[1]

Kengo Ohnishi[2], Jiro Mizusawa[3]

[1]Department of Systems Engineering and Science, Shibaura Institute of Technology

[2]Department of Engineering and Science, Tokyo Denki University

[3]Department of Training, General incorporated foundation Keiseikai

ABSTRACT The total percentage of the people who suffered from arm disability is about 25 % of the overall figure from those identified as orthopedically-impaired. Patients who suffer Erb's paralysis, a type of arm disability, have paralysis on their shoulder and elbow, although they can move their wrist. Therefore, the disability defects Activities of Daily Living (ADL). In order to improve ADL of these patients, we have been developing active upper limb orthosis. The movement of the orthosis is controlled by an electromyogram (EMG) measured by the movement of the patient's wrist. In this paper, the configuration of the orthosis system, the discrimination result of the wrist movement by the EMG measuring system, experimental results of the joint's movement and wire tension measurement and the manufactured orthosis that can be fixed to the trunk are described.

1. INTRODUCTION

Brachial plexus palsy is one type of functional disability that demands for an upper limb orthosis. The paralysis occurs when the patient's upper limb is caught and rolled up by a traffic accident or sports. Sometimes the degree of the disability exceeds the amputation level for upper limb (Alexander et al., 2005). Under the above condition, Erb's paralysis, caused by injury to the upper part of the brachial plexus. Although the symptoms vary, most commonly they will suffer paralysis on their shoulder and elbow, with preserved wrist function. Thus, activity of daily living (ADL) may be severely restricted in patients with the disorder and supports required in daily life (Murata, 1977; Langer et al., 2012).

Previous study mainly focused on myoelectric prostheses that used electromyogram (EMG) of the upper part of the arm to distinguish motor activities, for an example, pneumatic muscles (Kim et al., 2011) as an actuator and a mechanic supporting arm mounted on a wheelchair (Yamada, 2011). However, study on the upper limb orthoses that used EMG as a control signal are under developed.

2. SYSTEM CONFIGURATION

As shown in Fig.1, the configuration system started when the EMG evoked by the wrist movement is measured and the motion is determined by the EMG measurement system. Parallel to the upper limb function, shoulder and elbow are moved. There are three degrees of freedom in the orthosis, consists of: 1) flexion 2) extension of the elbow and the shoulder, and 3) internal, external rotation of the upper arm. The relation of the wrist and orthosis movements are assigned as follows (Fig.2): radial flexion to elbow and shoulder flexion, ulnar flexion to elbow and shoulder extension, flexion to internal rotation and extension to external rotation.

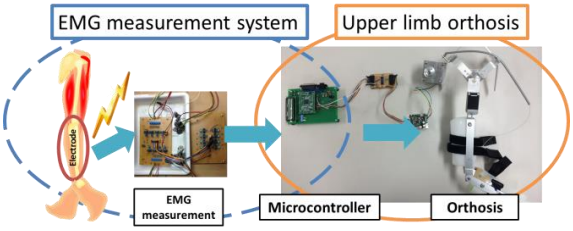

Fig.1: The system configuration

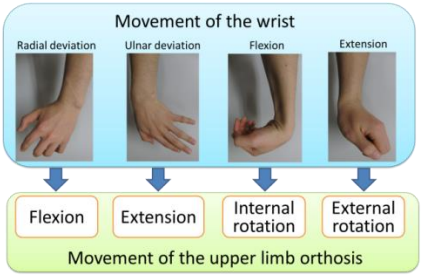

Fig.2: The relationship of the movement between the upper limb orthosis and wrist

2.1 EMG measurement system

Fig.3 shows the configuration of the circuit used for EMG measurement. The noise was removed from the high pass filter part, then the signal is magnified 20,000 times by the amplifier part, and finally the signal is rectified and averaged by the last low pass filter part.

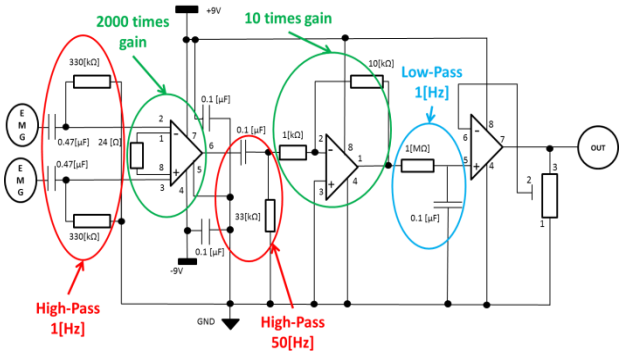

Fig.3: Circuit for EMG measurement

2.2 Upper limb orthosis

Fig.4 shows the structure of the developed orthosis. The orthosis consisted of an external skeletal structure. The elbow and shoulder joints are maintained in a flexed position, where another axis are added to the frame between elbow and shoulder to rotate the upper arm. Two motor systems are used to realize movement of flexion and internal rotation. In this, flexion movement is performed by pulling the wire hanged on the pulley that is connected to the motor. Stoppers are set both on the shoulder and the elbow joint to limit the bending angle to 90 [deg] and 60 [deg] respectively. Hence, two joint movements, elbow joint is bend until 90 [deg] and the shoulder joint is bent up to 60 [deg] is controlled by single motor system (Fig.5). Internal and external rotation are realized by the motor connected to the shaft holder mounted between the elbow and shoulder joint as shown in Fig.6.

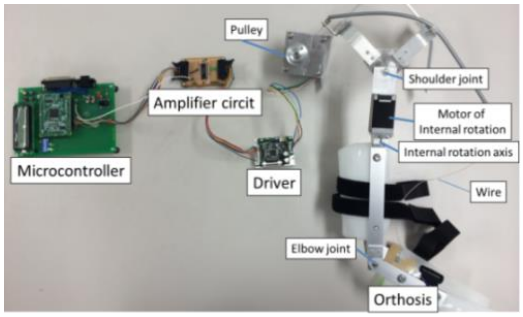

Fig.4: System configuration of the orthosis

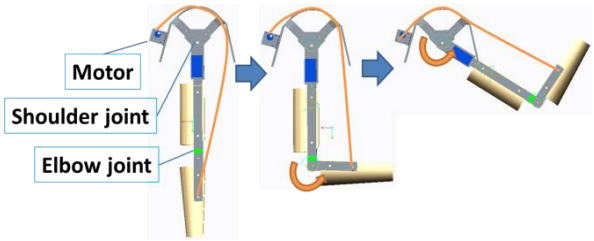

Fig.5: Movement of flexion

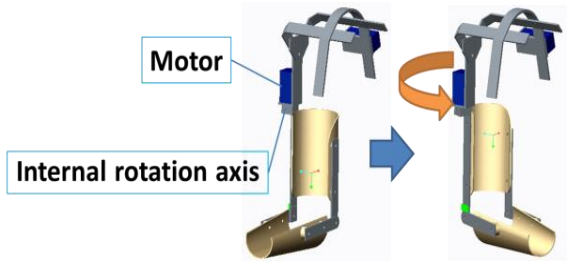

Fig.6: Movement of internal rotation

3. EMG MEASURMENT EXPERIMENT

3.1 Purpose

Four wrist movements to control the orthosis has been shown to be very accurate in discriminating four classes of motion, namely extension, flexion, ulnar flexion and radial flexion. The purpose of the experiment is to evaluate which method is appropriate to discriminate the motion.

3.2 Methods

Disposable electrodes (Vitorodo F-150S by Nihon Kohden Corp.) are used for 8ch measurement. At first, EMG of the six movements of extension, flexion, ulnar, radial flexion, finger flexion and extension were measured for 5 [s] in every 10 [s] interval, including free relax state for 5 [s]. This set is performed three times by changing the back of the hand towards up, down and right. These measured data are used as a reference data for discriminating. Next, data for calculating the discriminant rate is measured by the same movement, except for when the back of the hand towards right for which supination and pronation movement are added to the original six movements as shown in Fig.7. During the experiment, the shoulder joint is relaxed and elbow joint was bent in 90 [deg].

Consequently, the discriminant ratio is evaluated by two different inputs; the direct voltage and relative value divide by the total voltage of 8 channels. For discrimination, machine-learning techniques based on Euclid distance (EUC), Mahalanobis distance (MH) and support vector machine (SVM) was used and the results are compared.

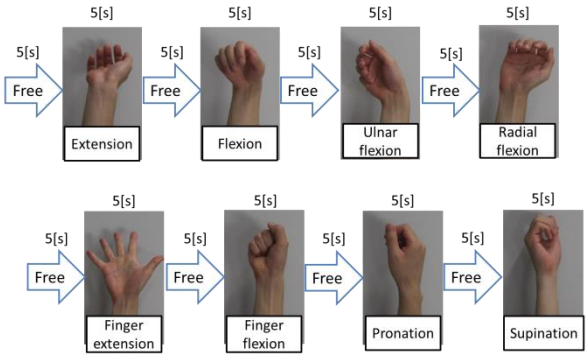

Fig.7: The order of wrist and hand movements

3.3 Results

Table 1 and Fig.7 show the averaged results of extension, flexion, ulnar and radial flexion by ten subjects when the direct voltage (a) is used and relative value (b) is used. The highest discriminant rate is obtained by the SVM method using voltage as input signal. For EUC method, discriminant rate that uses the relative value tends to higher, on the other hand, for MH and SVM methods tends to lower.

Table 1: Average discriminant rate [%]

Voltage value	euc	mh	svm	average
Extension	83.7	97.1	98.3	93.0
Flexion	82.3	90.2	88.1	87.0
Ulnar flexion	94.1	88.1	99.2	93.8
Radial flexion	78.7	77.5	78.9	78.4
average	84.8	88.2	91.1	88.1

Rate of value	euc	mh	svm	average
Extension	89.4	91.8	96.7	92.6
Flexion	84.7	82.6	87.0	84.8
Ulnar flexion	97.6	80.0	95.7	91.1
Radial flexion	80.4	67.8	74.4	74.2
average	88.0	80.6	88.5	85.7

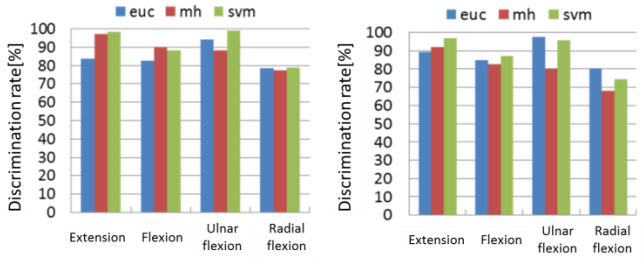

(a) Voltage (b) Relative value

Fig.8: The discriminant rate [%]

4. TENSION AND JOINT ANGLE MESUREMENT EXPERIMENT

4.1 Purpose

The most convenient orthosis must provide a small, lightweight, which is easy and suitable to carry. The tension of the wire during the movement of elbow and shoulder joints is measured for this purposed. Furthermore, it is necessary to estimate the least torque to move the orthosis to estimate whether the motor can be downsized.

4.2 Methods

The tension of the wire was measured by the load cell (TCLS-20L, by Toyosokki Corp.) that was fixed to the wire tip. The movement of the orthosis with upper limb was measured by the three-dimensional motion analysis system MAC3D (Motion Analysis Corp.). Markers were set to shoulder joint, upper arm rotation axis, elbow joint and the tip of the orthosis and two ends of the wire fixed point. The measured movements were flexion of elbow and shoulder joints, then return movement of extension. The subject comprised of physically healthy male and five trials for 30 [s] measurement time are performed. The shoulder and elbow joint angles and the trajectory of the orthosis are calculated using the three-dimensional coordinates of markers acquired at a sampling frequency of 200 [Hz].

4.3 Results

Fig.9 shows the result of the elbow flexion, shoulder flexion and wire tension after averaging five trials. First, the elbow joint is bent up to 90 [deg] in 7 [s], then the elbow joint is fixed and the shoulder joint is bent about 30 [deg] up to 9 [s]. Fig.10 (a) and (b) shows the trajectory of the elbow and shoulder movement. The orthosis was then extended until 22 [s]. During the extension, as shown in Fig.10 (c) elbow and shoulder joints were extended simultaneously. The wire tension becomes 120 [N] when the elbow is bent 90 [deg] and the tension becomes maximum value of 160 [N] when the shoulder bent to the maximum. During extension, wire tension gradually decreases. To generate maximum tension of 160 [N], the required motor torque is 2.5 [Nm]. As current motor torque has capability of 4 [Nm], it can be downsized. In addition, it is possible to further reduce the size if weight, compensate mechanism can be developed and maximum tension is reduced.

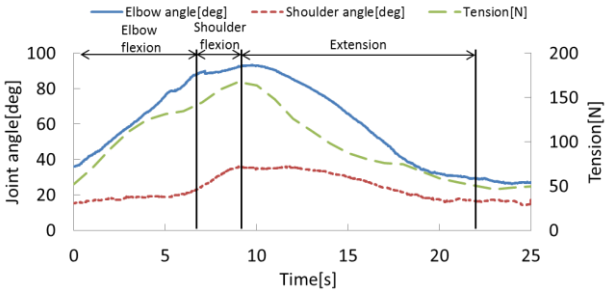

Fig.9: Result of the elbow, shoulder joint angle and the tension of wire

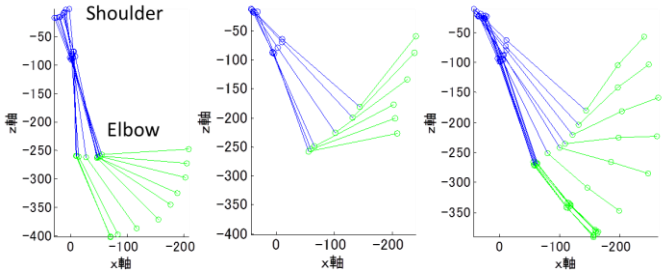

Fig.10: Movement of the orthosis

(a) Flexion of elbow (b) Flexion of shoulder (c) Extension

5. PRODUCTION OF THE ORTHOSIS THAT CAN BE MOUNTED TO THE TRUNK

The orthosis used in the experiments was prototyped structure to verify whether it can apply to the upper limb. To date, current orthosis does not function to fix to the subject's body trunk. Moreover, the orthosis that can be mounted to the trunk has been manufactured by the prosthetist as shown in Fig.11. As shown, casting of the human trunk was done using the water curable resin to fit the orthosis to the trunk. On the other hand, adjustment

function is included in the orthosis in order to perform the experiments by many subjects who have various body sizes. However, stable fixation to the trunk is realized by the developed orthosis. When the upper arm is rotated inward, the abduction of the shoulder also occurs. Therefore the new axis that enables abduction is added to the shoulder joint. The twin axis type joint is used for elbow joint of the orthosis to match the axis to that of human elbow. In addition, limit of bent angle can be adjusted manually with the dial of the joint. Further evaluation is necessary for the manufactured orthosis.

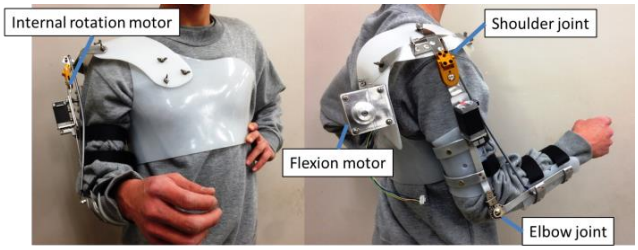

Fig.11: The orthosis manufactured by prosthesist.

6. Conclusion

As a conclusion, EMG measurement and motion discrimination system have been developed. The result of the EMG measurement experiment using the developed system, the highest discriminant rate is obtained by the SVM method using voltage as input signal. The method that improves discriminant rate still need to be investigated. Prototype orthosis that supports ADL for the patients who suffers brachial plexus palsy have been developed. According to the result of the orthosis drive test, the movement of elbow and shoulder joints differs when they are flexed and extended. Additionally, based on the result of measurement of wire tension, the motor size can be further reduced. It is desirable to develop weight compensation mechanism to minimize the peak value of the tension, thus smaller motor size can be used. Moreover, the orthosis that can be fixed to the human trunk has been manufactured by the prosthetist. However, additional experiments to evaluate the manufactured orthosis is necessary by the larger population of healthy subjects followed by an additional cohort of Erb's paralysis patients to evaluate the overall performance of the orthosis.

REFERENCES

(1) Ministry of Health, Labor and Welfare, Social Welfare and War Victims' Relief Bureau, Department of Health and Welfare for Persons with Disabilities", Survey on persons with physical disability", 2008

(2) Masahiro Yoshikawa et. al., "Real-time Hand Motion Classification Using EMG Signals with Support Vector Machines in Japanese", The Institute of Electronics, Information and Communication Engineers (D), Vol.J92, No.1, pp.93-103, 2009

(3) Shin Alexander Y et al., "Adult traumatic brachial plexus injuries", The journal of the American academy of orthopaedic surgeons, Vol.12, No.6, pp.382-396, 2005

(4) Jakub S. Langer et al.," The Importance of Shoulder External Rotation in Activities of Daily Living: Improving Outcomes in Traumatic Brachial Plexus Palsy", The Journal of hand surgery, Vol.37, No.7, pp.1430-1436, 2012

(5) Hideo Murata, "About the joint range of motion of the elbow joint and activities of daily living in Japanese", Rehabilitation Medicine, Vol.14, No.3, pp.251-260, 1977

(6) Kyung Kim et al., "Assistance of the elbow flexion motion on the active elbow orthosis using muscular stiffness force feedback", Journal of Mechanical Science and Technology, Vol.25, No.12, pp.3195-3203, 2011

(7) Yasuyuki Yamada, "Development of Upper Limb Orthosis with Shoulder Joint Tracking System in Japanese", Transactions of the Japan Society of Mechanical Engineers, Series C, Vol.77, No.775, pp.366～375, 2011

Fumiya Shiki received his BE from the Department of Bio-science and Engineering from the Shibaura Institute of Technology (SIT). He has been studying for his ME since April 2014 at the Systems Engineering and Science division of SIT.

Akihiko Hanafusa received his PhD from the University of Tokyo in 2002. He became a Lecturer and Associated Professor at Polytechnic University. He has been working as a full-time professor at the Shibaura Institute of Technology since 2009. His interests lie in the fields of human welfare and engineering.

Haruki Ishii is a student in the Department of Bio-science and Engineering, Shibaura Institute of Technology.

Kengo Ohnishi is a full-time professor at the Department of Science Mechanical Engineering, Tokyo Denki University.

Jiro Mizusawa is an associate manager at the Department of Training, General incorporated foundation Keiseikai.

OS Number: **OS04**

The anti-oxidant activities of Thai red and black rice extracts

Rinsai Palajai[1], Malyn Chulasiri[2] and Nitnipa Soontorngun[1]
[1]Division of Biochemical Technology, School of Bioresources and Technology
King Mongkut's University of Technology Thonburi
[2]S&J International Enterprises Public Company Limited.

ABSTRACT

Rice is one of the most important economic crops of Thailand and currently gains much research interests for product development of cosmetics and food supplements. In this study, the antioxidant property of red and black rice bran extracts was evaluated using DPPH Free Radical Scavenging assay of two strains of rice extracts of red and black Thai rice variety, namely Kum Doi saket Rice and Red Rose Rice. Antioxidant activities of these rice extracts were expressed as percentages of DPPH radical inhibition. Our results showed that the DPPH radical inhibition percentages were found to be 31.26 % for Red Rose Rice and 18.74 % for Kum Doi saket Rice. The percentage inhibition of rice extracts indicated that these rice strains contribute to unequal antioxidant activity while further examination will be required to explain the observed effects. Nevertheless, it is clear that these rice extracts has promising components for future development of cosmetic and food supplement products.

INTRODUCTION

Rice (*Oryza Satival*) is one of the most important staple cereal foods for about half of the world's population and contains a wide range of bioactive compounds such as phenolic acids and flavonoids (mainly anthocyanins) (Tian, Nakamura & Kayahara, 2004; Zhou et al., 2004). Most of phytochemicals in the whole grain rice is present in the bran fraction, consisting of bran layers (pericarp, seed coat, nucellus, and aleurone) and the germ. Phytochemicals in whole grain rice are present in lipophilic, hydrophilic, and insoluble forms. Tocopherols, tocotrienols, and c-oryzanol, are major lipophilic fractions of whole grain rice and their health-beneficial potential have been proposed (Cicero& Gaddi, 2001).

Rice bran obtained after removal of hulls contains anthocyanins and proanthocyanins, leading to red or black colours (Min,McClung, & Chen, 2011). In black rice, the anthocyanins are mainly in free form which accounts for 99.5–99.9% of total anthocyanin (Zhang, Zhang, & Liu, 2010). Black rice has been considered to be highly nutritional due to the presence of high level of anthocyanins, in addition to phenolic acids (Escribano-Bailón, Santos-Buelga & Rivas-Gonzalo, 2004; Goffman & Bergman, 2004).The main anthocyanins in black rice are cyanidin-3-glucoside (C3G) and peonidin-3-glucoside (P3G) with the content of the former being significantly higher than the latter (Lee, 2010; Ryu, Park, & Ho, 1998). While the flavonoids include flavonols, flavan-3-ols, flavones andflavanones (Lin&Tang, 2007). Many phenolic compounds in rice, such as diferulic acid, ferulic acid,p-coumaric acid, vanillic acid, caffeic acid, syringic acid and sinapinic acid. Ferulic acid is known for its antioxidant activities, which accounts for almost 50–65% of total bound phenolic acids, which result in inhibition of inflammation and tumor initiation and also acts as a food preservative (Adom&Liu2002; Adom, Sorrells, Liu, 2003).

Because of its high antioxidant capacity and more lengthy residence time in the body than vitamin C, ferulic acid has a wide range of therapeutic effects against many chronic conditions such as inflammation, cancer, apoptosis, diabetes, cardiovascular and neurodegenerative dis-eases (Srinivasan, Sudheer, & Menon, 2007). Epidemiological and medical studies revealed that high consumption of whole grain could reduce the risks of coronary heart disease and stroke with at least 20% and perhaps 40% (Flight& Clifton, 2006).

Nevertheless, less is known about antioxidant property of Thai rice strains despite being the main product and important bioresources of our country. Thus, this study aims to investigate the anti-oxidant activity of Thai red and black rice extracts for future application in cosmetics and food supplements.

2. EXPERIMENT

2.1 Rice strain used in this study

A)

B)

Fig.1 A) Kum Doisaket Rice and B) Red Rose Rice

2.1 DPPH Free Radical Scavenging

The free-radical scavenging capacity of each extract was evaluated according to the procedure of Liyana-Pathirana and Shahidi (2007) with some modifications. Briefly, 500 ul of extract was added to the freshly prepared 0.1 mM DPPH solution (3.5 ml), and the mixture was kept at room temperature in a dark room for 30 min. The absorbance was read at 517 nm relative to the control (as 100%) (Fig.1) and the percentage of scavenging effect was calculated as [1 - (A517 of sample / A517 of control)] x 100. The experiments were performed at least two times.

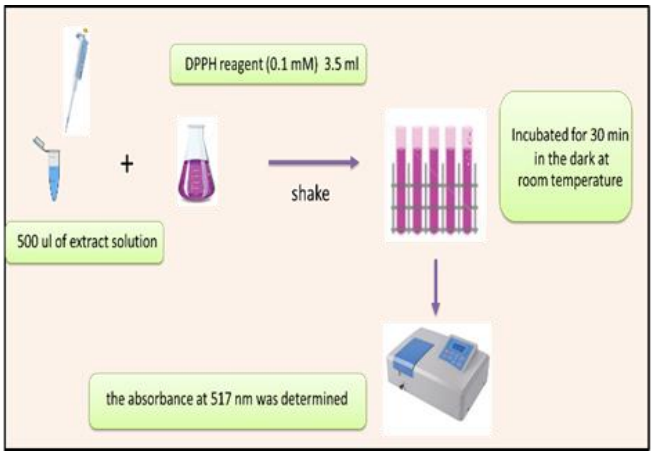

Fig.2 Methodology of DPPH Free Radical Scavenging with two rice strains

3. RESULTS AND DISCUSSION

3.1 DPPH Free Radical Scavenging

The free-radical scavenging activities of the extracts of rice were evaluated using the DPPH method. The ability to scavenge DPPH radical by rice was in the order of Red Rose Rice and then Kum Doisaket Rice as shown in Fig. 3. The DPPH radical scavenging varied from 31.26 ± 1.01 % of Red Rose Rice and 18.74 ± 1.86 % of Kum Doisaket Rice (Fig.3). A freshly prepared DPPH solution exhibited a deep purple color with an absorption maximum at 517 nm. This purple color generally fades when antioxidant molecules quench DPPH free radicals (i.e. by providing hydrogen atoms or by electron donation, conceivably via a free-radical attack on the DPPH molecule). Despite the deeper color was found after prolonged incubation, the results of DPPH free radical scavenging remain similar with slight increase in % inhibition (data not shown).

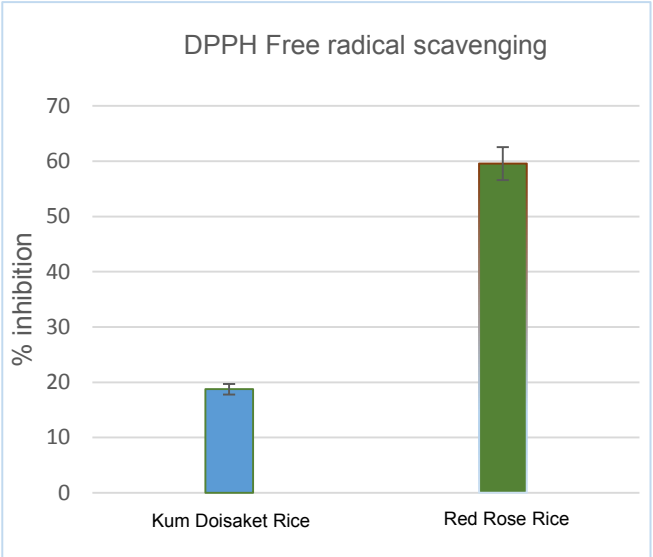

Fig.3. % inhibition of Red Rose Rice and Kum Doisaket Rice.

Previous study, Sunan Butsat and Sirithon Siriamornpun in 2010 reported the results depended on the strains origin and the anti-oxidant components (c-oryzanol, a-tocopherol and phenolic acids). Further examination using high performance liquid chromatography (HPLC) would help to obtain the data on bioactive ingredients found in these two rice variety which may be useful for future product development. The insight into the mechanism of bioactive compounds is also warrant further investigation.

4. CONCLUSION

The results of the antioxidants in the rice extracts show that the Red Rose rice (% DPPH free radical scavenging of 31.26 ± 1.01) and Kum Doisaket rice ((% DPPH free radical scavenging of 18.74 ± 1.86). It is clear that the rice extracts, Red Rose Rice has higher % inhibition than Kum Doisaket rice. This study provides the importance of rice extracts with promising antioxidant property as natural and abundant sources for useful applications in the cosmetic industry and food supplement.

5. ACKNOWLEDGMENTS

This study is financially supported by Thailand Research fund (TRF) and Office of Higher Education Commission (OHEC) of Thailand. Palajai R is the recipient of RRI scholarship under Research and Researcher for Industry (RRI) and S&J International Enterprises Public Company Limited. Soontorngun N is the recipient of TRF new scholar. We are also grateful to King Mongkut's University of Technology Thonburi (KMUTT) for facility and travel fund to attend SEATUC 2015.

6. REFFERENCES

Adom, K.K., Liu, R.H. (2002). Antioxidant activity of grains. J. Agric. Food Chem, 50, 6182-6187.

Adom, K.K., Sorrells, M.E., Liu, R.H., 2003. Phytochemical profiles and antioxidant activity of wheat varieties. J. Agric. Food Chem, 51, 7825e7834.

Butsat, S.& Siriamornpun, S. (2010). Antioxidant capacities and phenolic compounds of the husk, bran and endosperm of Thai rice. Food Chem, 119, 606-613.

Cicero, A. F. G., & Gaddi, A. (2001). Rice bran oil andc-oryzanol in the treatment of hyperlipoproteinemias and other conditions. Phytotherapy Research, 15, 277–289.

Escribano-Bailón, M. T., Santos-Buelga, C., & Rivas-Gonzalo, J. C. (2004). Anthocyanins in cereals. Journal of Chromatography A, 1054, 129–141.

Flight, I., & Clifton, P. (2006). Cereal grains and legumes in the prevention of coronary heart disease and stroke: A review of the literature.European Journal of Clinical Nutrition, 60, 1145–1159.

Goffman, F. D., & Bergman, C. J. (2004). Rice kernel phenolic content and its relationship with antiradical efficiency. Journal of the Science of Food and Agriculture, 84, 1235–1240.

Lee, J. H. (2010). Identification and quantification of anthocyanins from the grains of black rice (Oryza sativaL.) varieties.Food Science and Biotechnology, 19, 391–397.

Li, W. D., & Beta, T. (2011). Evaluation of antioxidant capacity and aroma quality of anthograin liqueur.Food Chemistry, 127, 968–975.

Lin, J.Y., Tang, C.Y., 2007. Determination of total phenolic andflavonoid contents in selected fruits and vegetables, as well as their stimulatory effects on mouse splenocyte proliferation. Food Chem. 101, 140e147.

Min, B., McClung, A. M., & Chen, M. H. (2011). Phytochemicals and antioxidant capacities in rice brans of different color.Journal of Food Science, 76, 117–126.

Ryu, S. N., Park, S. Z., & Ho, C. T. (1998). High performance liquid chromatographic determination of anthocyanin pigments in some varieties of black rice.Journal of Food and Drug Analysis, 6, 729–736.

Srinivasan, M., Sudheer, A. R., & Menon, V. P. (2007). Ferulic acid: therapeutic potential through its antioxidant property.Journal of Clinical Biochemistry and Nutrition, 40, 92–100.

Tian, S., Nakamura, K., Kayahara, H., 2004. Analysis of phenolic compounds in white rice, brown rice and germinated brown rice. J. Agric. Food Chem. 52, 4808-4813.

Zhang, M. W., Zhang, R. F., Zhang, F. X., & Liu, R. H. (2010). Phenolic profiles and antioxidant activity of black rice bran of different commercially available varieties. Journal of Agricultural and Food Chemistry, 58, 7580–7587.

Zhou, Z.K., Robards, K., Helliwell, S., Blanchard, C., 2004. The distribution of phenolic acids in rice. Food Chem, 87, 401-406.

Rinsai Palajai recieved the B.Sc. (biotechnology) from Silpakorn University, Nakoonpathom, Thailand. She is a M.Sc. (Biochemical technology) student from King Mongkut's University of Technology Thonburi, Bangkok, Thailand.

Her study is focused on Yeast Genetics: antioxidant compounds obtained from rice variety and mechanism of action.

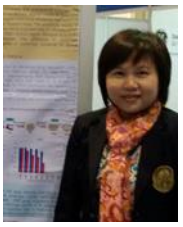

Nitnipa Soontorngun received the B.Sc. (Biochemistry and Molecular biology) from University of British Columbia, Vancouver, Canada and Ph.D. (Biochemistry) from McGill University, Montreal, Canada.

She is an Assistant professor, Division of Biochemical Technology, School of Bioresources and Technology, King Mongkut's University of Technology Thonburi, Bangkok, Thailand.

Her research interests include Gene and Enzyme Technology, Yeast Genetics and Molecular Biology, and Natural product development.

MACRO- AND MICRO- CIRCULATORY ADAPTATION IN RESPONSE TO CHRONIC HYPOXIA

Saki Hamashima and Masahiro Shibata
Department of Bioscience and Engineering, Shibaura Institute of Technology

ABSTRACT

To examine how cardiovascular adaptation to chronic hypoxia might evolve, the responses to blood pressure (Pt) and hematocrit (Ht) during long-term systemic exposure to hypoxia were observed in awake rats. Furthermore, the total peripheral vascular resistance (TPR) was estimated using direct measurements of systemic blood pressure (Ps) and blood flow (Qs) in carotid artery based on Darcy's law (TPR=Ps/Qs), and evaluated the remodeling procedure in the microcirculation in hypoxia. BP and Ht under normoxic conditions were kept almost constant, while hypoxic exposure immediately increased Hct from 45% to 58% and, thereafter, it remained stable. The TPR values showed no significant differences between hypoxic and normoxic conditions. These results suggest that effects of high viscosity caused by increasing Ht on peripheral vascular resistance can be compensated by inducing microvascular remodeling with the arteriolar dilation and capillary angiogenesis.

1. INTRODUCTION

INTRODUCTION

Whether the long-term exposure of hypoxia results in significant harmful effects to the cardiovascular system or induces protective properties that mediate vascular remodeling remains unclear (1). In studies of the pathophysiological effects, hypoxic exposure has been used to develop an animal model for pulmonary hypertension (2), while hypoxic training is believed to be capable of potentiating greater performance improvements (3). In addition, the morbidity rates of hypertension and coronary heart disease are reportedly lower in populations residing at high altitudes (4). The purpose of the present study was to examine how cardiovascular adaptation to chronic hypoxia might develop. For this purpose, the blood pressure (Pt) and hematocrit (Ht) responses during long-term systemic exposure to hypoxia were observed in awake rats.

Furthermore, the total peripheral vascular resistance(TPR) was estimated using direct measurements of systemic blood pressure (Ps) and blood flow (Qs) in carotid artery based on Darcy's law (TPR= Ps/Qs) to evaluate the remodeling procedure in the microcirculation.

2. MATERIAL AND METHODS

2.1 Experimental Protocols

All animal procedures were approved by the Shibaura Institute of Technology Animal Care and Use Committee. A total of twenty-nine male Wister rats weighing 130-220 g (5-8 weeks old) were used in this study. Fourteen rats were used to measure the Pt and Ht responses to chronic exposure of hypoxia for two weeks. After Pt and Ht measurements during chronic exposure of hypoxia, these rats were provided to determine the TPR value. The TPR values under normoxic conditions were obtained by the remaining fifteen rats. The chronic exposure to hypoxia of rats was carried out by housing the animals in a hypoxic chamber (ProOx110) for two weeks, in which this chamber was kept at an oxygen concentration of 10% by injecting nitrogen. The oxygen concentration of 10% is equivalent to oxygen concentration at an altitude of 5,500 m. The breeding room including the animal chamber and, the Pt and Ht measuring area were maintained a temperature of 20 degrees.

2.2 Blood pressure (Pt) and hematocrit (Ht) measurements

Pt and Ht were measured every three days during two weeks exposure to hypoxia. Pt was measured non-invasively using the tail-cuff oscillometric method (Softron, Japan) and the obtained Pt value was represented as the mean blood pressure. Ht, is known as packed cell volume (PCV), is the volume percentage (%) of red blood cells in blood. The Ht value was obtained with the conventional method by blood sampling from a tail vein. We took blood samples by

grass capillary tubes. Then, red blood cell, plasma, etc, are separated by centrifugal separator (KUBOTA3220, Japan).Only during a measuring period the rats were anesthetized by inhalation of ether and kept on the heated mat to prevent the reduction of body temperature.

2.3Determination of total peripheral resistance (TPR)

The changes in total peripheral vascular resistance (TPR) under hypoxic and normoxic conditions were determined to measure the Ps and Qs in carotid artery under anesthesia with urethane. First, Qs meas

urement was performed using a transit time blood flowmeter for small arteies (Transonic Systems, USA). The flow probe was attached to a carotid artery and obtained the flow signal continuously with mean value. On the other hand, to measure the Ps, the catheter was cannulated to carotid artery and connected to the pressure transducer (Ohmeda, USA). In this measurement, Ps value was also represented by the mean blood pressure. On the other hand, based on these measured Ps and Qs values, Darcy's law was applied to determine a total peripheral vascular resistance as TPR = Ps/Qs. All animals in which the Ps or Qs value fell to < 60mmHg or < 3 mL/min during experiment were excluded.

2.4 Data analysis

All data are reported as means ± SD. Data within each group were analyzed by analysis of variance for repeated measurements (ANOVA). Differences between groups were determined using a t-test with the Bonferroni correction. Differences with a p-value of < 0.05 were considered statistically significant.

3 RESULTS

3.1 Changes in blood pressure and hematocrit to hypoxia

Figure 1 shows the changes in mean Pt and Ht under hypoxic conditions in awake rats. Mean Pt and Ht under normoxic conditions before exposure of hypoxia remained almost constant (Pt: 78 ± 8.0 mmHg, Ht: 45 ± 3.5 %), while hypoxic exposure immediately increased Ht to 58% and, thereafter, it remained stable. The mean Pt during hypoxic exposure showed no significant changes: from 81 ± 8.6 mmHg at the beginning to 84 ± 8.4 mmHg at the end.

3.2 Comparison of peripheral vascular resistance (TPR)

To compare the peripheral vascular resistance under normoxic and hypoxic conditions, the blood flow (Qs) and mean blood pressure (Ps) in carotid artery were measured directly in anesthetized rats. The measured Qs and Ps values with carotid artery during two weeks hypoxic exposure are shown in Fig. 2.

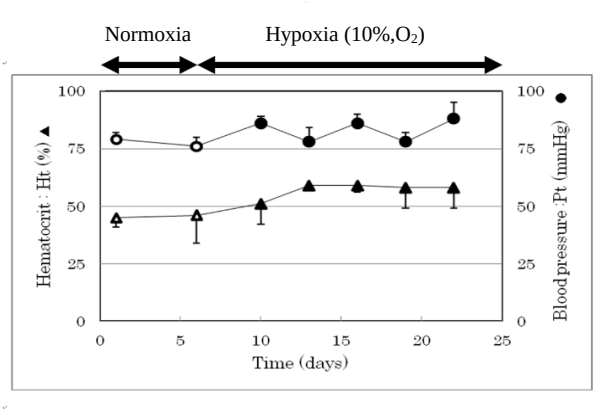

Fig.1 Changes in mean blood pressure (Pt) measured by the tail-cuff method and Hct under normoxic and hypoxic conditions. All measurements were carried out under anesthesia by inhalation of ether.

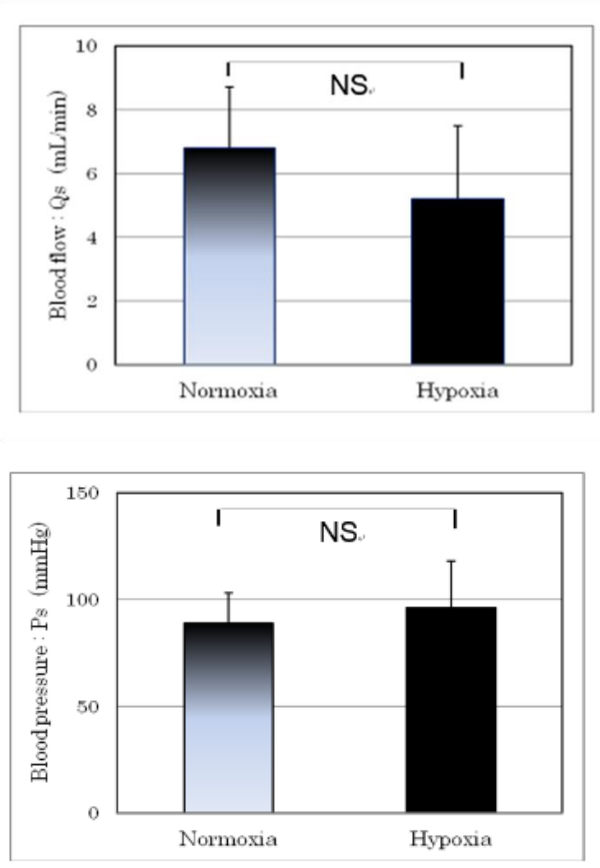

Fig. 2 The direct measured blood flow (Qs) and mean blood pressure (Ps) in carotid artery under normoxic conditions and after two weeks hypoxic exposure. There were no significant differences between normoxic and hypoxic values.

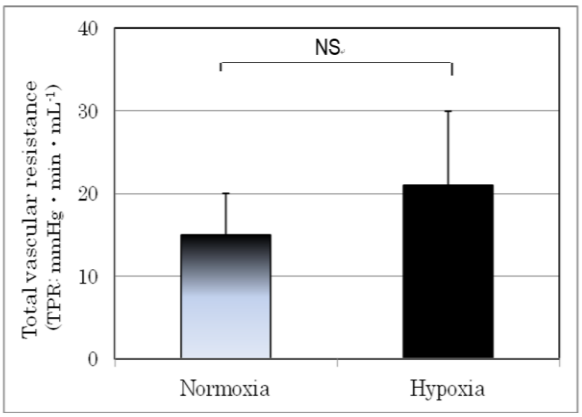

Fig. 3 The total peripheral resistance (TPR) values under normoxic conditions and after two weeks hypoxic exposure obtained by Qs and Ps. There are no significant differences between the values under hypoxic and normoxic conditions.

Although the blood flow after two weeks hypoxic exposure has a tendency to decrease, there were no significant differences compared with those of normoxic conditions (hypoxia: Qs and Ps: 5.2 ± 2.3 mL/min and 96 ± 22 mmHg, normoxia: 6.8 ± 1.9 mL/min and 89 ± 14 mmHg,). The total peripheral resistance (TPR) values obtained by Qs and Ps are shown in Fig. 3. Again, there are no significant differences between TPR values under hypoxic and normoxic conditions (21 ± 10 and 15 ± 5 mmHg・min・mL^{-1}).

4. DISCUSSION

In the present study, we aimed to clarify how cardiovascular adaptation to chronic hypoxia would evolve. For this purpose, the responses to blood pressure and hematocrit during two weeks systemic exposure to hypoxia were observed in awake rats. The total peripheral vascular resistances under hypoxic and normoxic conditions were compared to evaluate the remodeling procedure in the microcirculation. The Ht values under hypoxic exposure immediately increased to 58% and, thereafter, remained stable. These changes in Ht are well-known responses to hypoxia or hypobaric conditions (5, 6). On the other hand, the blood pressure was kept almost constant during two weeks exposure to hypoxia in this study. This constancy of blood pressure implies successful adaptation to chronic hypoxia through protective mechanisms that mediate vascular remodeling. There are many reports that the hypoxia induced microvascular angiogenesis (7, 8) and vasodilation (9), in which one of the major factors is the high vascular wall shear stress induced by increased blood viscosity. Increased shear stress increases the endothelial nitric oxide production. The successful process of cardiovascular adaptation to chronic hypoxia considered from the present study is shown in Fig. 4.

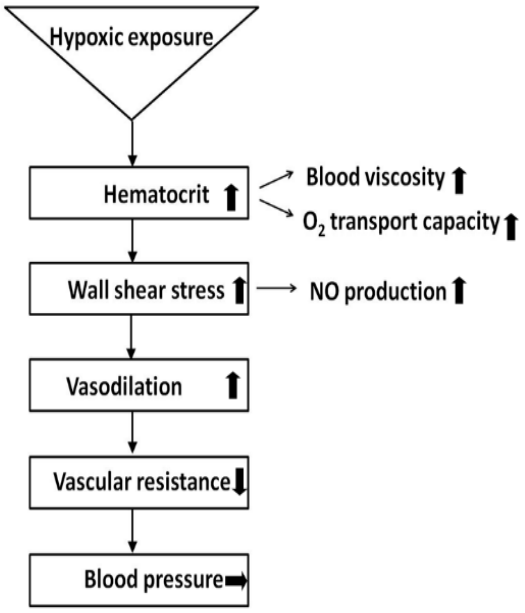

Fig. 4 The successful process of cardiovascular adaptation to chronic hypoxia

5. CONCLUSION

These results suggest that the effects of high viscosity caused by increasing Hct on peripheral vascular resistance can be compensated by inducing microvascular remodeling with arteriolar dilation and capillary angiogenesis.

REFERENCES

1. Essop Faadiel M. (2007) Cardiac metabolic adaptation in response to chronic hypoxia. J Physiol 584: 715-726
2. Ostadal B, Ostadalova I, Dhalla NS. (1999) Development of cardiac sensitivity to O_2 deficiency: comparative and ontogenetic aspect. Physiol Rev 79: 635-659
3. Lara B, Salinero JJ, Del Coso J. (2014) Altitude is positively correlated to race time during the marathon. High Alt Med Biol
4. Mortimer EA Jr, Monson RR, MacMahon B. (1977) Reduction in mortality from coronary heart disease in men residing at high altitude. N Engl J Med 296: 581-585
5. Núñez-Espinosa C, Douziech A, Ríos-Kristjánsson JG, Rizo D, Torrella JR, Pagès T, Viscor G. (2014) Effect of intermittent hypoxia and exercise on blood

rheology and oxygen transport in trained rats. Respir Physiol Neurobiol 192: 112-117
6. Takuwa H, Masanoto K, Yamazaki K, Kawaguchi H, Ikoma Y, Tajima Y, Obata T, Tomita Y, Suzuki N, Kanno I, Ito H. (2013) Long-term adaptation of cerebral hemodynamics response to somatosensory stimulation during chronic hypoxia in awake mice. J Cerebral Blood Flow & Metabolism 33: 774-779
7. Harik SI, Hritz MA, LaManna JC. (1995) Hypoxia-induced brain angiogenesis in the adult rat. J Physiol 485: 525-530
8. Boero JA, Ascher J, Arregui A, Rovainen C, Woolsey T. (1999) Increased brain capillaries in chronic hypoxia. J Appl Physiol 86: 1211-1219
9. Shibata M, Ichioka S, Ando J, Togawa T, Kamiya A. (2005) Non-linear regulation of capillary\\ perfusion in relation to ambient pO_2 changes in skeletal muscle. Eur. J Appl Physiol 94: 352-355

Hamashima Saki received the BS in Bio-science and Engineering from Shibaura Institute of Technology. Since 2014, she has been in a master course student in Graduate School of Engineering and Science, Shibaura Institute of Technology.

Masahiro Shibata received the BS in Applied Physics and his PhD in Biomedical Engineering from Hokkaido University, Japan. Since 2008 he has been with the Department of Bio-Science and Engineering, Shibaura Institute of Technology, where he is a Professor of System Physiology. His research interests include hemo- and oxygen dynamics in microcirculation.

Development of shear flow generator, and its application for understanding the shear stress related hemolysis -Flow scale as the possible additional trigger to hemolysis-

Sunao Ueda[1], Kentaro Nagagshima[2],Taku Oguri[2],Toshihiro Mita[2] , Nobuo Watanabe[1,2]
[1] Graduate School of Engineering and Science, Shibaura Institute of Technology
[2] College of Systems Engineering and Science, Shibaura Institute of Technology

ABSTRACT
In addition to the conventional knowledge that shear stress and its exposure time should give a great impact on hemolysis. In last decade, it became to be obvious that surface roughness would be the new additional factor for high shear induced blood trauma[2)]. Concerning this phenomenon, we predicted that the flow scale should act as the additional factor. The purpose of this study is to develop the constant shear generator as the method to provide the controlled shear flow field to the blood cells, and its preliminary application for the examination of our hypothesis. We prototyped shear flow chamber. This chamber had three flow scales of 1.00, 1.25, and 1.5mm, and their surface roughness degrees were distributed into the several levels. Using this shear chamber, we examined how the flow scale and the surface roughness gave the effect on hemolysis. Results of our experiment showed positive correlation as we supposed.

1. Introduction

For the usage of totally implantable blood pump within the patient's body, the blood pump size should be enough minimized. Especially for small body heart failure patients such as ladies and infants, greatly tiny rotary blood pump should be applied, however, the minimization should result in generation of the very high shear field within the blood pump, which should lead to the blood damage known as hemolysis, and also destruction of coagulation-related proteins.

For the development of the more excellent blood pump, it is very important to understand the hemolysis in detailed.

Conventional researches have been done using shear flow chamber, which having the smooth surface. And their research results were summarized and it was revealed that the hemolysis level increased as the function of input constant shear stress and its exposure time using following equation[1)].

$$\Delta Hb/Hb(\%)=3.62\times10^{-5}\times t^{0.785}\times\tau^{2.416} \quad ①$$

[t:time(s),τ:shear stress(Pa)]

Half a decade ago, an additional article was reported, and it said that the surface roughness of blood contacting surface also relate to blood damage[2)]. If it is truth, we supposed that the flow scale should also relate to the hemolysis phenomenon.

Therefore, our study purpose is firstly to develop the experimental setup which can provide well defined constant shear stress to the blood under the several combination of surface roughness and flow scale, and secondly to examine the feasibility of our prediction performing the preliminary blood tests.

2. Materials and Methods

2.1 Design of Constant shear flow chamber

The structure of the designed shear flow chamber is normal cone-cup rotating viscometer (cylindrical type). Outer aclyric cup rotates, while the inner cone remains stationary. The rotation of outer cup generates the Couette flow resulting in the uniform shear stress exposure to the blood cells. The assumed shear stress generation can be calculated using the following equation ②.

$$\text{Side sher stress } \tau_1 = \mu \times \frac{\omega \times R}{h1} \ldots ②$$

Where, the R is the radius of rotor cup's inner surface [m], and L is flow clearance between the inner and outer wall surfaces [m], ω is angular velocity [m/s], and μ is the viscosity of the operating fluid[Pa s].

The shear stress within the bottom clearance region can be provided as the function of radial position h2[m] and the radious of the inner cylinder r[m], and the angular velocity ω[rad/s] using the following equation.

$$\text{Bottom shear stress } \tau_2 = \mu \times \frac{\omega \times r}{h2} \ldots ③$$

The *tan θ* can be approximately described by θ when θ is slightly small, therefore the following equations can be expressed.

$$\tau_2 = \mu \times \frac{\omega \times r}{\mathrm{rtan}\,\theta} = \mu \times \frac{\omega \times r}{r\theta} \fallingdotseq \mu \times \frac{\omega}{\theta} \ldots ④$$

$$\mu \times \frac{\omega \times R}{bh1} = \mu \times \frac{\omega}{\theta}, \theta = \frac{h1}{R}.$$

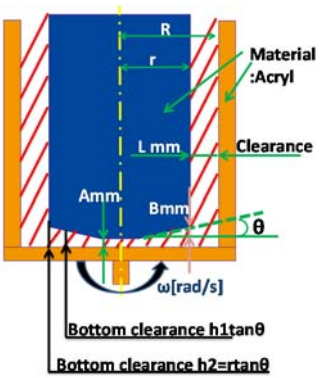

Fig.1 Schematic drawing of the desin of constant shear flow chamber

$$\text{So } \tau_2 \fallingdotseq \mu \times \frac{\omega}{\theta} = \mu \times \frac{\omega \times R}{h1} = \tau_1.$$

$$[\mu: \text{viscosity(Pa・s)},$$

$$\omega: \text{angular velocity} \left(\frac{\text{rad}}{\text{s}}\right), \theta: \text{bottom angle(rad)}]$$

In order to provide the same stress level between the side and bottom clearances, values of the above twe equations should coincide, that resulted 'h2=rtanθ'. Cone tip was cut to prevent the friction related heat generation at the bottom center position. The black color region in Fig.2 represents the lower shear stress region than the supposed shear stress level, where we call Dead space. The volume of this region was set to be 3.2% of the whole sample blood volume, which effect would be negligible.

Fig.2 Dead space within the chamber, where the shear level would be lower than the supposed constant shear stress

Conventional research[3] suggested at least 1500[dynes/cm^2], which can be also expressed as 150[Pa], would be nessesary for the hemolysis. So we used high speed motor (Oriental motor Co. Ltd., BMU230A-1), which available up to 4000rpm. The blood chamber was designed to be the Acrylic material, and the rest parts were to be the alminium.

2.3 Manufacturing the shear test device with three levels of flow scale and its Evaluation

The cup and cone was designed refering the gap clearances shown in the clinical pump mera monopivot centrifugal blood pump, the australian artificial heart 'BiVACOR',and the gap withn the blood shear chamber reported by Maruyama et al[2].

Table.1 Gap within the blood flow devices

	Side Clearance[mm]	Max shear rate[1/s]
Mera monopivot centrifugal blood pomp	2	7065
BiVACOR	2	2500
2)Enviromental for experiment	0.85	3750
Our shear flow chamber	0.2	31400

Table.1 shows the gap clearance of above mentioned blood pumps, approximate 2[mm].Therefore our shear chamber adopted clearance of 1.00,1.25,1.50[mm] by setting the diameter of the cone to be φ28,27,26[mm].

Fig.3 The prototyped Shear stress generator

The prototyped shear device was shown in Fig.3, and we verified the device was operated with no problem. Therefore we decided to perform the hemolysis tests, which is described in detailed below.

2.4 Ajustment of Inner cone surface roughness

We validate whether the ratio of the surface roughness to the flow scale (ε/L) related to hemolysis or not. For this purpose, the inner cone shaft surface roughness was modified into three levels, without any smoothing after manufacturing with turning machine, then it was polished through the sponge abrasives, and then it was additionaly hand-polished through the wrapping sheet. Before and after these polishing procedure, we measured the surface roughness using the commercial furface roughness device, MITSUTOYO, SJ410. After each smoothing procedure, the next hemolysis test was further performed.

Table.2 Clearance=1mm

Clearance=1[mm]			
Number of revolution	Angular Velocity	Shear rate	Shear stress
N[rpm]	ω[rad/s]	du/dy[1/s]	τ [Pa]
1500	157	2355	8.5
2000	209	3140	11.3
2500	262	3925	14.1
3000	314	4710	17

Table.3 Clearance=1.25mm

Clearance=1.25[mm]			
Number of revolution	Angular Velocity	Shear rate	Shear stress
N[rpm]	ω[rad/s]	du/dy[1/s]	τ [Pa]
1500	157	1884	
1875	196	2355	8.5
2000	209	2512	9.1
2500	262	3140	11.3
3000	314	3770	13.6

Table.4 Clearance=1.5mm

Clearance=1.5[mm]			
Number of revolution	Angular Velocity	Shear rate	Shear stress
N[rpm]	ω[rad/s]	du/dy[1/s]	τ [Pa]
1500	157	1570	5.7
2000	209	2093	7.5
2250	236	2355	8.5
2500	262	2617	9.4
3000	314	3140	11.3

2.5 Hemolysis test procedure

The uniform shear stress of 8.5[Pa] was exposed to the porcine blood using three kinds of flow scales, 1.00,1.25 and 1.50[mm] respectively and several kinds of surface roughnesses. The blood was exposed to the shear stress for 30,60, and 90[min]. And then, the sample blood was centrifuged by

KUBOTA:3220 with the condition of 3000[rpm] for 10[min]. Then, the plasma free hemoglobin level was assessed by the spectrophotometer (Uvmini-1240,shimadzu) using the previously correlated data between light absorbance versus hemoglobin density level. Hemoglobin levels using experiment measure by hemocytometer [Celltacα,MEK-6450, Nihon-Kohden], we divide it by free hemoglobin lebels and calculated a hemolysis rate. Concerning to the three flow scales of our shear device, the combinations under the three clearances among the motor speed, the angular velocity, the shear rate, and the shear stress are shown in Table.2, 3, and 4 respectively.In order to load the constant shear stress of 8.5[Pa] using three kinds of flow scales, 1.00, 1.25, and 1.50[mm], the motor speed of 1500, 1875, and 2250[RPM] were adopted for the hemolysis test.

3.Results of surface roughness measurement and Hemolysis test

Table.5 shows the radial clearance of flow field inside the shear chamber, the measured surface roughness of inner shaft without polishing and the ratio of surface roughness to the clearance(ε/L), and Fig.4 shows hemolysis result of shear experiment. Under the every clearance data, as the time elapsed, the hemolysis degree increased parabolically. And also as the clearance decreased, the hemolysis level increased, showing agreement with our hypothesis. The larger the surface roughness and the smaller the flow scale, the hemolysis level increased parabolically.

Table.5 Surface roughness

Clearance[mm]	Surface roughness[μm]	ε/L[μm/mm]
1	0.92	0.92
1.25	0.47	0.38
1.5	0.42	0.28

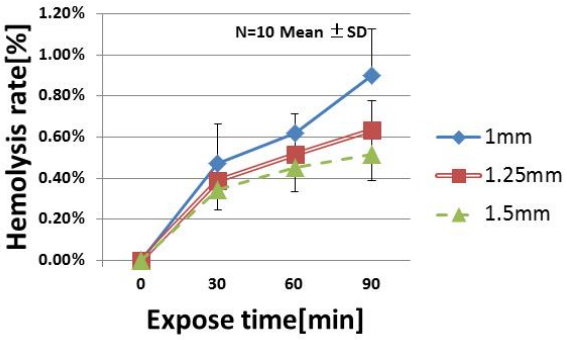

Fig.4 Result of Hemolysis test with the coarse surface shaft right after the manufacturing without polishing

Table.6 shows the surface roughness after polishing by sponge abrasive, and Fig.5 corresponding hemolysis result. Each plot showed the tendency to increase hemolysis level with time.

Compare to surface roughness, 1.25[mm] cone showed the higher hemolysis level than that of 1.00[mm] cone. This was out of our expectation.

Table.6 Surface roughness after sponge abrasive polishing

Clearance[mm]	Surface roughness[μm]	ε/L[μm/mm]
1	0.37	0.37
1.25	0.25	0.20
1.5	0.35	0.23

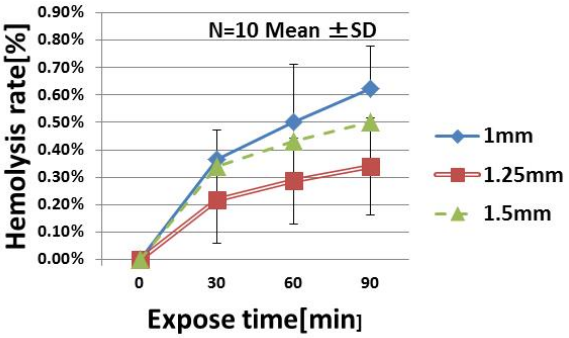

Fig.5 Result of Hemolysis test with polished surface by the sponge

Table.7 is measured surface roughness of inner shaft after the wrapping sheet polishing. And Fig.6 shows the hemolysis test result with the shaft.The hemolysis rate didn't correlate the surface roughness to clearance ratio.

Table.7 Surface roughness after wrapping sheet polishing

Clearance[mm]	Surface roughness[μm]	ε/L[μm/mm]
1	0.22	0.22
1.25	0.2	0.16
1.5	0.14	0.09

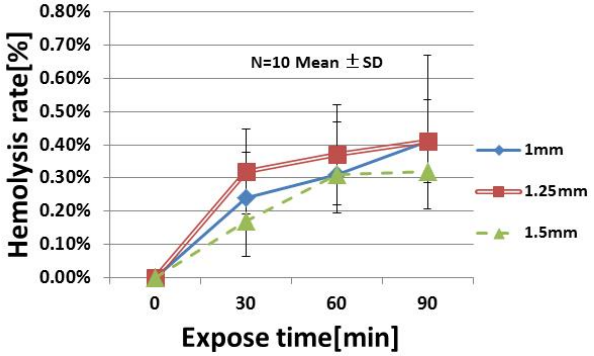

Fig.6 Results of hemolysis test after wrapping sheet polishing

When we performed the experiment with 1[mm] clearance condition, the hemolysis rate was 0.24%, 0.31%,and 0.41% at the exposure time of 30[min], 60[min] and 90[min], respectively. Under the clearance of 1.25mm and 1.50mm, the hemolysis level slightly increased with the exposure time.

We expected that the less surface roughness, the less hemolysis rate, however, the surface roughness wasn't reflected on a hemolysis rate in these experiments.

4. Discussion

Compared with the theoretical hemolysis level expressed by the equation①, the plasma free hemoglobin level in our study were much smaller (see the data shown in Table8 below), and similer level reported by Maruyama et al. Therefore we considered that our data were validated.

Table.8: Theoretically assessed hemolysis rate(8.5[Pa])

	0	30[min]	60[min]	90[min]
Theoretical value(%)	0	2.29%	3.94%	5.42%
Max hemolysis shown in our study(%)	0.00%	0.47%	0.62%	0.90%

Table.9 hemolysis data shown by Maruyama et al (shear rate 13.5[Pa], time 30[min]) compared to the theoretical data using the hemolysis equation [1].

	Theoretical value(%)	Measured valued[ε=0.8(μm)]
hemolysis rate(%)	7%	1%

Maruyama et al concluded that threshold value of surface roughness that greatly increase the hemolysis existed between 0.6[μm] and 0.8 [μm], and the hemolysis rate didn't show significant difference under the surface roughness less than 0.6[μm]. In the other side, the hemolysis occurred under less roughness conditions in our experiments. Fig.7 shows hemolysis rate acquired at two conditions with surface roughness of 0.35 and 0.37[μm] and clearance of 1.50 and 1.00[mm], respectively. As shown in this figure, in spite of the same surface roughness, shear stress and expose time, Hemolysis rate differed.

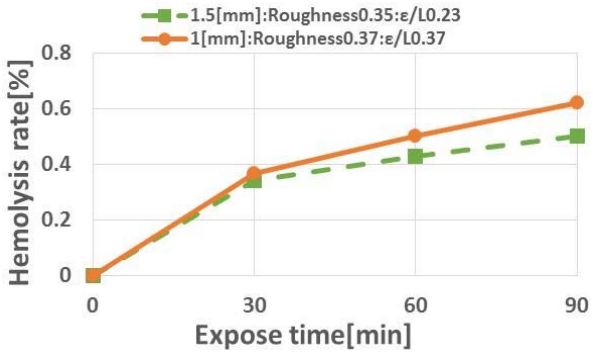

Fig.7 Comparison of hemolysis rate under the flow scale conditions of 1.00 and 1.50 [mm] under the similar levels of 0.35&0.37

Fig.8 shows the hemolysis result under the condition with 1.5mm clearance and 0.42 [μm]face roughness, and 1.00[mm] clearance and 0.37 [μm] surface roughness, respectively.
In this figure, the hemolysis level enlarged with the roughness to flow scale ratio, which coincided with our hypothesis.

5. Conclusion

We developed the uniform shear flow chamber, which can provide three different flow scales, 1.00, 1.25, and 1.50[mm], respectively. Hemolysis test were performed with the variation of inner shaft's surface roughness under the constant shear stress of 8.5[Pa]. Then, our results showed that the flow scale affected on the hemolysis, and its ratio to the surface roughness would be important for hemolysis amount.

Acknowledgement

Special thanks to Dr. Miki and Prof. Morita at Saitama University for their kind support on the surface roughness measurements.

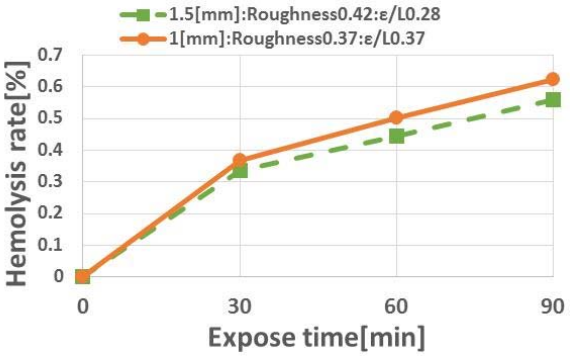

Fig.8 Hemolysis rate:ε/L 0.28&0.37

REFERENCES

1) R. Paul,et al.,(2003), Artif Organs 27, 517-529
2) O. Maruyama, et al. (2006), *Ibaraki district conference 2006*, 47-48
3) L.B.LEverett, et al. (1972), *Biophys J*, 12, 257

Sunao Ueda, BS
He received the bachelor degree in bioscience and engineering from Shibaura Institute of Technology at 2014. He is currently the Master student, and has been involved in this research project for three years.

Kentaro Nagashima, BS
He received the bachelor degree in bioscience and engineering from Shibaura Institute of Technology at 2015. He is also the main contributor for this project. His current interest is the clinical engineering.

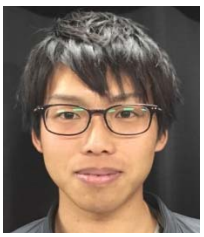

Taku Oguri
He has just started to support this project. He is currently the bachelor candidate at Shibaura Institute of Technology.

Toshihiro Mita, BS
He received BS from Shibaura Institute of Technology at 2013. He supported this project with first stage designing (2012-2013). Currently he is belonging to the Max CO. Ltd.

Nobuo Watanabe, Ph.D.
Bachelor of Engineering at 2000, and Master of Engineering at 2002 from Shibaura Institute of Technology, and Ph.D. at 2006 from Tokyo Medical and Dental University. He is the organizer of this research project.

Equipment development for visualization of red blood cell's deformation and rheological behavior process in high-shear flow

Takahiro Shimada, Ryohei Hara, Nobuo Watanabe
Biofluid Science Laboratory, Dept. of Bio-Science and Engineering,
College of Systems Engineering and Science,
Shibaura Institute of Technology, Saitama, Japan

ABSTRACT

It is known that a red blood cell is destroyed by shear stress produced by a blood pump.[(1)-(3)] The method to visualize how red blood cell would be destroyed is proposed in this study. We developed the shear chamber which adopted the counter rotating mechanism, which allow us to monitor a single red blood cell within the middle position at the gap clearance. The preliminary study resulted the short time observation time to monitor red cell with eight seconds. This reason was considered that the blurring in the operation of the device. And then, the further modification of the experimental setup was performed. After that, we further evaluated the feasibility of the setup with the measurement of the axis stability using the dial gauge. As the result, better stability was shown. The additional visualization study showed the possibility to monitor the red cells for longer time over 30 seconds.

1. Introduction

It is known that hemolysis occurs because of the shear that a blood pump produces. In addition, about shear stress and the hemolytic relations, it is reported that hemolysis rate ΔHb/Hb [%] is expressed in expression (1) in t[sec] at same shear stress τ[Pa] and the time that are made to pass.[(4)]

ΔHb/Hb[%]=

$$3.62 \times 10^{-5} \times t^{0.785}[s] \times \tau^{2.416}[Pa] \ldots (1)$$

This expression was derived by the optical technique that used plasma hemoglobin density and correlation with the absorbance to increase at the time of hemolysis.[(5)] Actually, there is not the example visualized up to the hemolysis that individual red blood cells were caused by shear. Therefore we thought that we might understand a process of the blood corpuscle destruction if the direct observation of the blood corpuscle in the shear flow ground was enabled. If this is enabled, we think that the possibility that information expressed in a conventional expression is overturned is possible enough in some cases. For example, we may be safe for a red blood cell if the time when even high shear is exposed is an instant. Therefore It was aimed for the visualization of the red blood cell damage process in the high shear flow for the last time in this laboratory and at first was intended that it allowed to be stable and to monitor the transformation flow of the red blood cell.

2. Method

2.1 Design concept

Rotatory direction was reverse each other, and the red blood cell shear load device to develop took in the truth bad fortune motion (cf. Fig1) of the parallelism flat board that turned at the same speed to be able to always photograph red blood cells in a monitor judging from an object lens by a laborer of the mechanical structure from beginning to end. We used a cup and the corn shape that we showed in Fig.2 for real mechanism. A cup and the gap center between the corn deny each other's flows, and the thing in there does not move in an appearance. In other words observation is possible theoretically continuously even if the red blood cell which exists there by observing a central location of the flow ground was given shear stress.

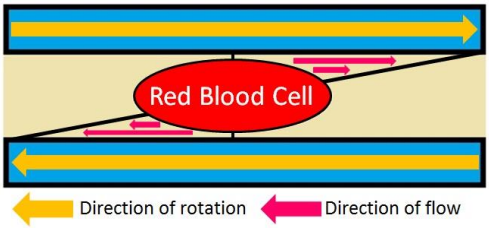

Fig.1 Mechanism plan to observe a single red blood cell under high shear

Shear stress τ [Pa] is demanded by structure of the cup corn by the following expression. But it is r: It is radius of gyration position, degree of leaning θ [rad] of the angular velocity ω [rad/s], conical section. When a cup and angle of rotation speed of the corn assume it +ω/2[rad/s],-ω/2[rad/s] each, can express shear stress τ [Pa] occurring in a gap in the following expressions (2).

$$\tau = \mu r\omega / r\tan\theta \cong \mu\omega/\theta \ldots (2)$$

Thus, it becomes the same shear in all radius positions. We show a conception diagram in Fig.2. Rotatory direction of the corn is reverse to a cup, but may really express it easily like Fig.2 as you already spoke it to make an estimate of the shear speed because we can consider corn to turn in ω[rad/s] for a standstill cup if I relatively watch it. In addition, We aim at avoiding corn and the interference between the cup, and preventing

thermogenesis by cutting a corn cone leader 0.01[mm] like a figure.

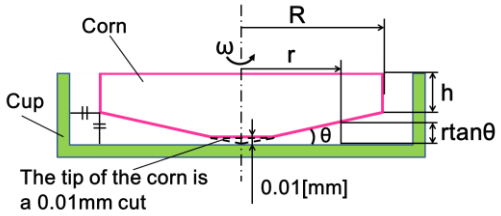

Fig.2 Schematic diagram of shear chamber

2.2 Design and production

We show Fig.3, the device which we produced in Fig.4 in the shear flow generator cross section which we designed. We produced the device which did the output of the motor for movement of equal speed and the backlashing using a gear. It can take in the source of light from a microscope by producing a corn part with acrylic. For a trial product evaluation, we really performed a blood experiment.

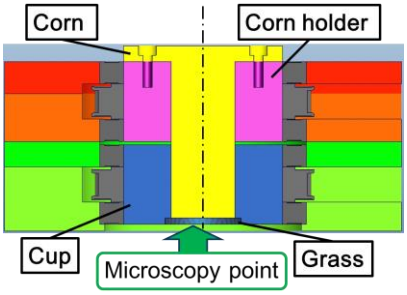

Fig.3 Cross-sectional view of the shear generator

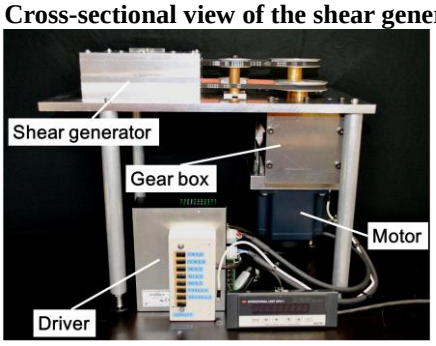

Fig.4 Assembled experimental setup

3. Device evaluation experiment

We mounted the device which we produced behind a microscope (IX71 made in OLYMPUS) and, for (Fig.5), the solution including the red blood cell, performed an experiment to photograph a red blood cell in the state that we operated a device, and produced shear. The blood uses the thing which it diluted for 200 times using PBS solution with the pig blood which 10% of sodium citrate was added in as an anticoagulant. In addition, we added dextran (product made in Acros Organics) 30% as a thickener. We poured this blood between cup corn parts and produced shear speed by reversing a cup corn part and observed blood given shear stress. The microscopic object lens used 40 times. We succeeded in taking a single red blood cell under shear stress as showed it in Fig.6. However, the state that a flow was distracted with was observed afterwards briefly with 8[s] at the time when we could observe a blood corpuscle. It was thought whether it was a cause that influence by axis blurring or the centrifugal force was strongly given for this cause. Therefore we performed an axis blurring inspection experiment more.

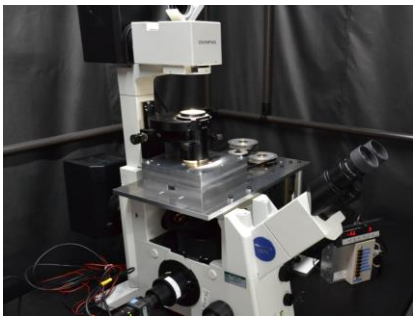

Fig.5 Setup mounted on the microscope

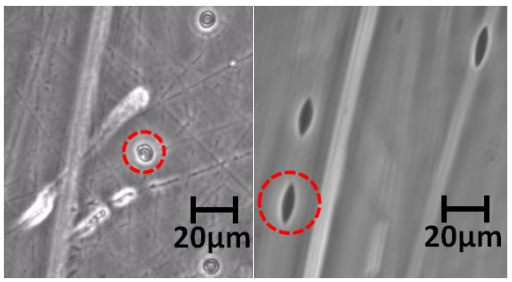

Fig.6 Red blood cell during shear load experiment (The left: In no load, The right: Shear stress 24Pa)

4. Axis blurring inspection experiment

We attached a dial gauge to a milling machine to show it in Fig.7 and measured the part which became a guide of the corn. In other words we measured axis blurring by measuring it in a dial gauge for a form of pipe part of the corn holder part which remained which removed the corn of the device cross section of Fig.3. We found out the part which a dial gauge could not wave and established a value of X, Y of the part when it was a middle arbor. The location of measurement assumed a corn insertion mouth a point zero and assumed height 0[mm] and performed depth 20[mm], a position of 30[mm]. Because the measurement of a near position was necessary for this by a shear outbreak position, we measured the value of this position. The result of a measurement was the clearance that bearing had every measurement, and a measurement error appeared every time. Therefore the precision that this experimental device had understood that it was X ± 0.01[mm], Y ± 0.015[mm] at standstill.

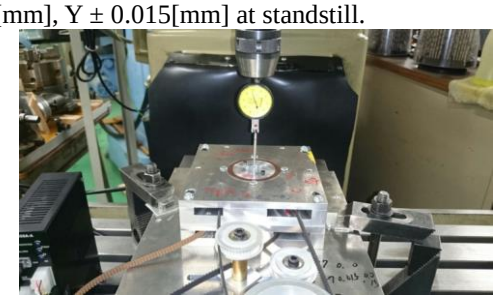

Fig.7 Experimental view to check the axis of the corn holder

Table.1 Middle arbor measurement result

Depth Z[mm]	Average X[mm]	Y[mm]
0mm	0	0
20mm	0.018	0.018
30mm	0.015	0.032

5. Visualization experiment using microscope for axis blurring evaluations

It was revealed that a picture showed blurring periodically by a microscope in the animation which we photographed. Therefore we measured it with a dial gauge how long you moved slightly. Furthermore, we planned reduction of the blurring by winding 0.01[mm] Thickness tape around bearing in itself to a thing of clearance 0.04[mm] of the bearing which we running fit the gap to reduce blurring and had.

As a result, 0.01[mm] was able to reduce blurring at the time of the experimental device movement from 0.03[mm] by winding 0.01[mm] Thickness tape around bearing. Therefore when this was because it thought that it was stable, and it might observe a red blood cell in a flow, we evaluated it and tested it. For 24 [Pa] shear stress, it appeared to realize and steady observation longer-time than the last time called 30[s] was with possibility flow more stable than (Fig.8). However, it was stable and included what we could not observe when we put up a thing and the number of revolutions that a picture flow might happen like Fig.8 and could not observe clearly. It is thought whether this is a problem of the precision of crying bearing under the influence of clearance. Therefore we performed the re-choice of the bearing and the re-design of the device with it.

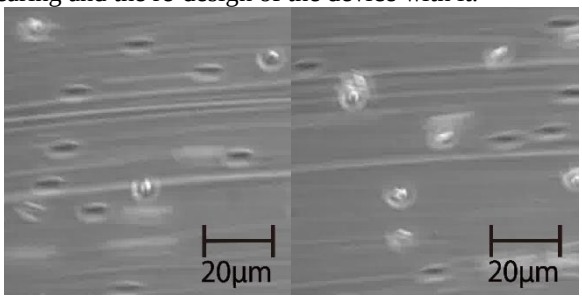

Fig.8 Red blood cell during a shear load experiment after device improvement
(left: Start 10[s], right: Start 30[s])

6. Re-design of the device

Bearing using is a ball bearing of class 0 now. However, when it is this bearing, the touch to the radial direction is up to 20[μm], and it is thought that we may influence an animation. Therefore thought that few animations of the touch might be provided by giving a class of the bearing;, thus, of the bearing re-; chose it. The improvement of the device with the re-choice reached, too. It is expected that we can minimize outbreak of the blurring by the clearance by using stationary fit, and building it in order to minimize the influence of the (Fig.9) clearance. However, it is unknown whether you can reduce quantity of how much blurring by improving it. we analyzed the blood corpuscle behavior to have of the device as of that purpose and considered it how long you could suppress the blood corpuscle behavior.

Table.2 The re-choice of the bearing

	Before	After
Type	Ball bearing	Angular bearing
Precision	Class 0	Class 4
Thickness	7[mm]	10[mm]
Radial	20[μm]	4[μm]
Axial	–	4[μm]

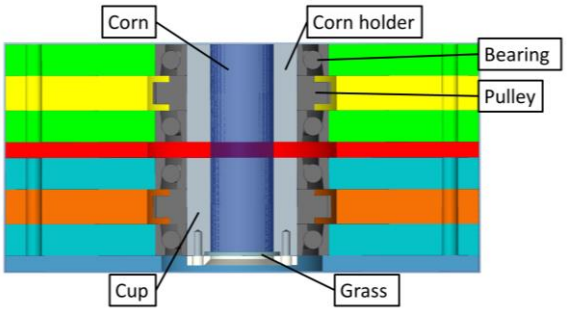

Fig.9 The idea of further improvement

7. Blood corpuscle behavior inspection

We thought that we might elucidate laboratory finding expectation after the device improvement and a cause of the blood corpuscle behavior by inspecting the blood corpuscle behavior of the current device and performed blood corpuscle behavior inspection. The inspection inspected rotatory direction and the behavior of the radial direction. In addition, we tested it under conditions of in 5rpm,10rpm,15rpm to inspect whether behavior by the rotary speed changed.

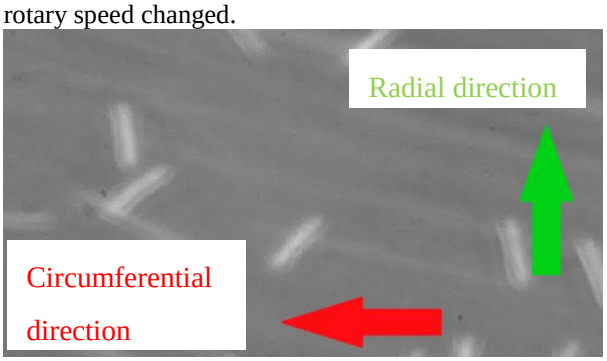

Fig.10 Observed blood cell behavior

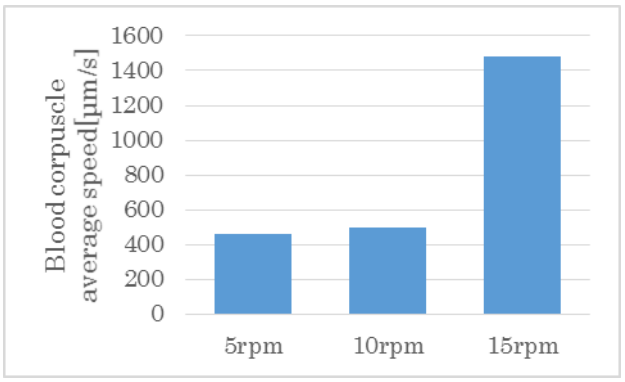

Fig.11 Blood cell behavior displacement along to the Circumferential direction

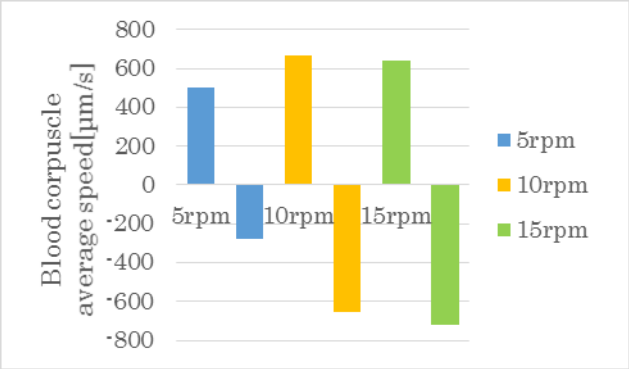

Fig.12 Blood cell behavior displacement along to the radial direction

Because corn and the material of the cup are acrylic and glass each, as for the blood corpuscle behavior of the rotatory direction, surface rough degrees are different. It is thought that it became the blood corpuscle behavior showing in Fig.11. Therefore it is thought that there may be the need to prepare a surface fault degree of the mechanism that an upper turn board and a lower turn board have speed-setting on each or both material to reduce behavior of the rotatory direction. In addition, as for the blood corpuscle behavior of the radial direction, the radial direction was able to grasp the behavior that went up and down. Because blood corpuscle speed changed as number of revolutions rises, it is thought that this behavior is influence of the centrifugal force. It is thought that this value may appear after device improvement.

8. Result

We planned reduction by catching Schickness tape in the clearance of the bearing by the axis blurring to have of the shear flow generator. As a result, it was possible for only blood corpuscle observation of 8[s] so far, but it came to be possible to 30[s]. However, it was stable and included what we could not observe when we raised the number of revolutions that a picture flow happened. It is thought whether this is a problem of the precision of crying bearing under the influence of clearance. Therefore we performed the re-choice of the bearing and the re-design of the device with it. We inspected the blood corpuscle behavior in the current device to judge device performance after the improvement with the re-design of the device, and a result such as Fig.11,Fig.12 was provided. It is thought that difference between corn and material of the cup and influence of the centrifugal force are related to this. We produce the trial product of the device which we designed and will intend to work, and to inspect it in future.

9. Conclusion

As a result of producing the experimental device which photographed a red blood cell under shear using the structure of the reverse exercise parallelism flat board, and having inspected the movement, the instability behavior of the flow by the axis gap became clear. By the laborer who reduced the gap between the assembling elements, we was able to reduce the axis gap quantity. As a result, it was possible for only blood corpuscle observation of 8[s] so far, but it came to be possible to 30[s]. However, it was stable and included what we could not observe when we raised the number of revolutions that a picture flow happened. It is thought whether this is a problem of the precision of crying bearing under the influence of clearance. Therefore we performed the re-choice of the bearing and the re-design of the device with it.

References

[1] Carl A. Johnson Jr, Stijn Vandenberghe1, Amanda R. Daly, Joshua R. Woolley, Shaun T. Snyder, Josiah E. Verkaik, Sang-Ho Ye, Harvey S. Borovetz, James F.Antaki, Peter D. Wearden, Marina V. Kameneva, William R. Wagner," Biocompatibility Assessment of the First Generation PediaFlow Pediatric Ventricular Assist Device" Artificial Organs 35(1),2011,p9-21.

[2] Setsuo T, Hideo H, Kennichi T, Katsuhiro O, Makoto N, Junichio A, Tadahiko S, Masaharu Y," Feasibility of a Miniature Centrifugal Rotary Blood Pump for Low-Flow Circulation in Children and Infants" ASAIO Journal 51(5), 2005, p557-562

[3] Chris H.H. Chan, Ina Laura Pieper, Rebecca Hambly, Gemma Radley, Alyssa Jones, Yasmin Friedmann, Karl M. Hawkins, Stephen Westaby, Graham Foster, and Catherine A. Thornton, "The CentriMag Centrifugal Blood Pump as a Benchmark for In Vitro Testing of Hemocompatibility in Implantable Ventricular Assist Devices" Artificial Organs 39(2),2014,p1-9

[4] Giersiepen M, Wurzinger LJ, Opitz R, Reul H, "Estimation of shear stress-related blood damage in heart valve prostheses-in vitro comparison of 25 aortic valves." Artificial Organs 13(5), 1990, p302

[5] Reinhard Paul, Jörn Apel, Sebastian Klaus, Frank Schügner, Peter Schwindke,and Helmut Reul,"Shear Stress Related Blood Damage in Laminar Couette Flow" Artificial Organs 27(6), 2003, p517-519

Takahiro Shimada; He is the Master course student in S.I.T. He has been working on this project from 2014. He is interested in the medical device development.

Ryohei Hara; He concerned this project between 2012 and 2014 as the master course student under the guidance of Prof. Watanabe. He received MS from SIT at 2014.

Nobuo Watanabe; Assistant Prof. in S.I.T. He received B.E.(2000), M.E.(2002), in S.I.T, and Ph.D.(2006) at Tokyo Medical and Dental University. He organized this project.

RELATIONSHIP BETWEEN EXERCISE INTENSITY AND CAPILLARY BLOOD FLOW IN RAT SKELETAL MUSCLE

Tomoyuki Otake and Masahiro Shibata
Department of Bioscience and Engineering, Shibaura Institute of Technology

ABSTRACT

The objective of this study was to determine the optimal exercise efficiency for physical training based on the direct observation of capillary blood flow in rat skeletal muscle. The capillary blood flow of cremaster muscle in anesthetized rat was observed by intravital microscopy. The exercise was performed topically by the electrical stimulus directly to the muscle surface, in which the electrical stimulus performed to muscle contraction and relaxation continuously. The optimal exercise intensity was evaluated as the increments of arteriolar diameter and capillary blood flow before and during muscle stimulus. The arteriolar diameter and capillary blood flow increased during the muscle stimulus with high frequency (10Hz) compared with that of low frequency (0.2Hz). It was two times increased at 10Hz than 0.2Hz stimulus. From these results, it was considered that high frequency muscle movements would be efficient for the physical training and has a possibility to apply for rehabilitation.

1. INTRODUCTION

Exercise is performed by contraction and relaxation of the muscle. Quantification of momentum is often used oxygen consumption rate which depends on the momentum because quantification of momentum is difficult. In previous studies, there are many reports of the oxygen consumption rate during exercise at systemic levels were measured using a Spirometer. The momentum of the report for a single muscle under in vivo is less because it is difficult to measure the oxygen consumption rate in a single muscle during exercise. On the other hand, oxygen supply to the muscles is performed by the microcirculation. In the skeletal muscle at rest (oxygen consumption rate; low) is limited to less than 20% of heart mass inflow blood flow by the arterioles contract. At the time of exercise (oxygen consumption rate; high) arterioles will have to supply about 80% of the cardiac output by extending to the skeletal muscle tissue. Capillary blood flow of skeletal muscle considered to be dependent on the oxygen consumption rate of muscle.

In the present study, we have examined the relationship between the movement exercise efficiency based on exercise intensity and oxygen consumption rate of the muscle by performing the measurement of skeletal muscle capillary blood flow.

2. METHODS

Animal preparation

Adult male Wistar rats weighing between 150 and 180 g were anesthetized with urethane intramuscularly (1 g/kg body wt). The left cremaster was prepared for intravital microscopy. Briefly, the cremaster was isolated, cut longitudinally, separated from the testis and epididymis, and gently spread over a semicircular lucite platform. The edges of the tissue were secured with insect pins to maintain tension but not stretch the muscle. The cremaster muscle, having a thickness of 200–400 μm, was spread out in a special bath chamber with an optical port for transillumination, and the surface of the cremaster muscle was suffused with a 37°C Krebs solution with 5% CO2 in 95% N2, adjusted to pH 7.3–7.4. The Arteriolar diameter measurements were performed at several locations in the rat cremaster muscle (Figure 1). Arterioles and venules were classified according to their branching order in the microscopic field. The central cremasteric artery was designated as first order (A1, 80–120 μm in diameter). Branches of first-order arterioles were designated as second order (A2, 50–80 μm in diameter).

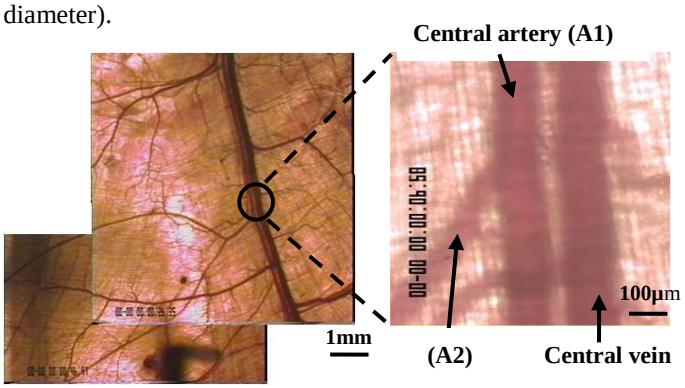

Figure 1 Intra microscopic images of the microcirculation in rat cremaster muscle. A1 and A2 indicate the main and branch arteriole in diameter measurements (a: 53x b: 480x) .

Phosphorescence quenching laser microscope.

Figure 2 shows a schematic diagram of the system used in this study. The bath chamber containing the cremaster muscle was placed on a three-way movable stage equipped with a 20-W halogen lamp for transillumination. A general observation of the microcirculation was performed using a modified OLYMPUS microscope with a ×10 long working distance dry objective.

The microcirculation was filmed using a charge-coupled device (CCD) camera connected to a videotimer and video recorder, and the image was displayed on a 20-in. high-resolution television monitor at a final magnification of approximately ×550.

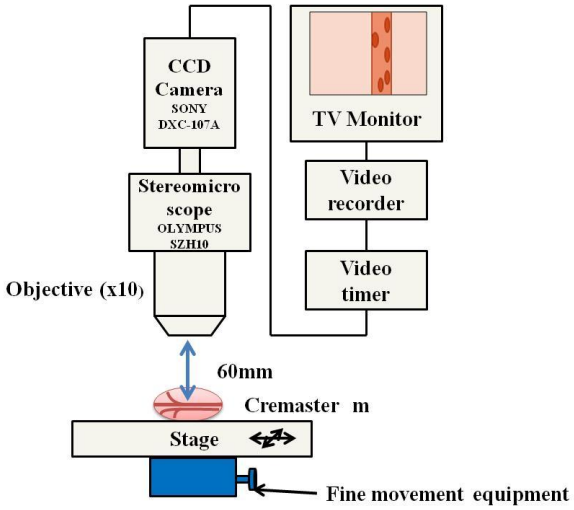

Figure 2 A general observation of the microcirculation was performed using a modified OLYMPUS microscope with a charge-coupled device camera.

Electrical stimulation

Electrical stimulations were stimulated directly using a flat tip of the needle (φ0.5mm) that was placed in close proximity. The distance between the electrodes is 0.5mm. Electrical stimulation condition Duration 3ms, the voltage 6V ~ 10V, frequency 0.2Hz, 0.5Hz, 1.0Hz, 2.0Hz, 5.0Hz, 10Hz was loaded with movement of various intensities by using a six square wave. Low frequency stimulation of the muscle contraction interval is longer and high frequency stimulation of the muscle contraction interval is short. Electrical stimulation frequency is 0.2Hz to cause 12 times muscle contraction in 1 minute, total stimulation time of 1 minute is 36ms. We think this total stimulation time was exercise load. Table 1 shows the number of stimulus to the muscle of the other electrical stimulation.

Table 1 The stimulus condition used in this study

frequency	number of stimulation	total stimulation time(ms)
0.2Hz	12	36
0.5Hz	30	90
1.0Hz	60	180
2.0Hz	120	360
5.0Hz	300	900
10Hz	600	1800

Experiments

Experiments to measure the arteriolar diameter on which to keep the blood arteriolar contracted state by topical application of Phenylephrine (10^{-11}mol / l) in order to reduce variation in individual difference at A1, A2 arterioles diameter. After was performed 1 minute electrical stimulation 0.2Hz, will continue to continuously recorded the arteriolar diameter to return to control values. Measurement of arteriolar diameter was subjected to measurement using what was recorded video imaged based. Arteriolar diameter to measure the inner diameter excluding the arteriolar wall.

3. RESULT& DISCUSSION

Table 2 shows the changes in arteriolar diameter before and after topical application of Phenylephrine. Average arteriolar diameter of the A1 in the control is 100 ± 10μm, after topical application of Phenylephrine decreased about 5% arteriolar diameter. Average arteriolar diameter of the A2 in the control is 60 ± 10μm, after topical application of Phenylephrine decreased about 5% arteriolar diameter.

Table 2 The changes in arteriolar diameter before and after topical application of Phenylephrine

	control	Phenylephrine
A1(μm)	100±10	95±5
A2(μm)	60±10	55±5

note:1) Values are mean ± SD

The A1 arteriolar diameter after topical application of Phenylephrine to 100%. Figure 3 shows the A1 relative average rate of change in arteriolar diameter of the electrical stimulation of 0.2Hz, 1.0Hz, 10Hz from addition 60 seconds. Began to arteriolar diameter is extended with electrical stimulation onset, it was maximum extension at about 150 seconds. Then arteriolar diameter gradually decreased. After that arteriolar diameter is gradually beginning to decrease, about 240 seconds at 0.2Hz, about 360 seconds at 1.0Hz, decreased to the same value as the control at 10Hz in about 450 seconds. Figure 4 shows the relative average rate of change of the A2 arterioles diameter. Began to arteriolar diameter is extended with electrical stimulation onset, it was maximum extension at about 120 seconds. After that arteriolar diameter is gradually beginning to decrease, about 270 seconds at 0.2Hz, about 300 seconds at 1.0Hz, decreased to the same value as the control at 10Hz in about 450 seconds. Figure 5 shows the maximum extension during the relative average rate of change of the A1 and A2. A1 is 12 ± 2% at 0.2Hz, 17 ± 2% at 1.0Hz, 22 ± 2% at 10Hz of vasodilation has been confirmed. A2 is 15±4% at 0.2Hz, 18±6% at 1.0Hz, 27±9% at 10Hz of vasodilation has been confirmed. A1 and A2 expansion coefficient of both arteriolar diameter tended to continue to increase as the frequency increases. Comparing the lowest frequency of the 0.2Hz and the highest frequency

10Hz, became vasodilation rate of 10Hz showed about twice the value of 0.2Hz. From the above we thought that muscle contraction time is longer becomes efficient exercise.

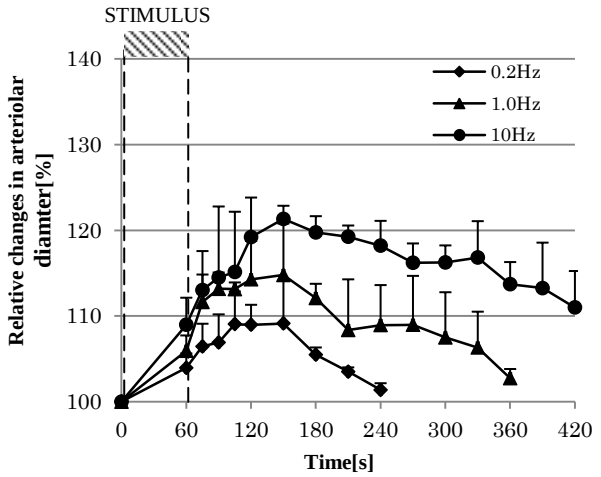

Figure 3 The changes in A1 arteriolar diameter before and after muscle stimulus

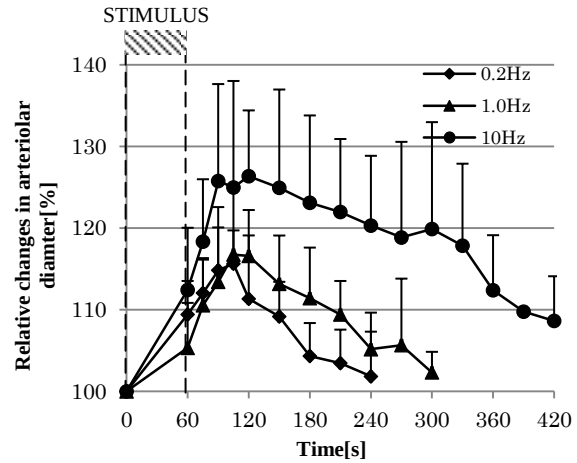

Figure 4 The changes in A2 arteriolar diameter before and after muscle stimulus

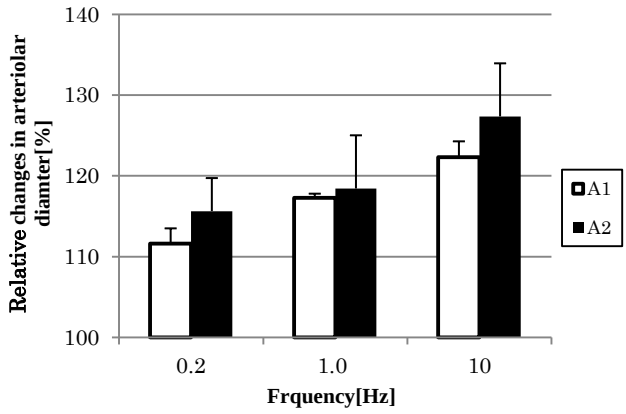

Figure 5 The maximum increment of A1, A2 arteriolar diameter after muscle stimulus

REFERENCES

1) Shibata M, Ichioka S, Togawa T, Kamiya A. Arterioles' contribution to oxygen supply to the skeletal muscles at rest. European Journal of Applied Physiology 97: 327-331, 2006

.

2)Shibata M, Ichioka S, Ando J, Kamiya A. Microvascular and interstitial Po 2measurements in rat skeletal muscle by phosphorescence quenching. Journal of Applied Physiology 91: 321-327, 2001

3) Whyte JJ, Harold Laughlin M. The effects of acute and chronic exercise on the vasculature. Act Physiol 199: 441-450, 2010

4)Ashok K., Coral L. Skeletal muscle contraction-induced vasodilator complement production is dependent on stimulus and contraction frequency. American Journal of Physiology - Heart and Circulatory Physiology 297: 433-442,2009

Tomoyuki Otake has been with department of Bio- Science and Engineering, Shibaura Institute of Technology Since 2013. His research interests include bioengineering and cardiovascular phiology.

Masahiro Shibata received the BS in Applied physics and his PhD in Biomedical Engineering from Hokkaido University, Japan. Since 2008 he has been with department of Bio- Science and Engineering, Shibaura Institute of Technology, where he is a Professor of System physiology. His research interests include hemo- and oxygen dynamics in micro circulation.

OS Number: OS04

OPTIMIZATION OF A LATERAL FLOW IMMUNOASSAY TEST STRIP FOR THE SENSITIVE DETECTION OF ROTAVIRUS IN FECAL SAMPLES

Do Thi Thu Ha[1], Luong Trinh Thuy Linh[1], Nguyen Thi Ngoc Anh[1], Ngo Thu Huong[2], Nguyen Dang Hien[2], Truong Quoc Phong[1*]

[1] Hanoi University of Science and Technology, Vietnam

[2] Center for Research and Production of Vaccines and Biologicals

ABSTRACT

.

Rotavirus infection is the most common cause of severe diarrhea in infants and young children. It may cause serious dehydration and require hospitalization. Simple tools for detection of rotavirus in diarrheal patients are required. He we reported the results of optimization of conditions for generating a lateral flow test trip. The conjugate of antibody and gold nanoparticles should be performed at pH $\geq$ 8.5, at room temperature. The conjugate pad was prepared by the submergence of conjugate pad material J2 in the conjugate solution (20mM Sodium borate, 2% BSA, 3% sucrose, 0.6 M NaCl, 0.2% Tween-20) and dried at 42^{o}C for 30-45 min. Immobilizing antibodies should be prepared in 1X PBS, pH7.4, 2% sucrose and spread on the membrane Vivid170. The cellulose membrane could be processed at 42^{o}C for 30 min to immobilize antibodies. The sample pad solution of 1X PBS, 0.1 M NaCl, 0.5% Tween 20 was used to release virus from fecal samples and detector reagents from the conjugate pad during test. The generated test trip was high reproducibility and no cross-reactivity.

Keywords: diarrhea, feces, lateral flow immunoassay, optimization, rotavirus

1. INTRODUCTION

Rotavirus is the cause of up to 50% of the hospitalized cases of diarrheal illness in infants and young children. Rotavirus infection can cause gastroenteritis and diarrhea leading to dehydration and disturbance of the body's normal electrolyte balance (Yolken and Murphy, 1982). In tropical climates rotavirus infection can occur year round. The age groups most susceptible to the disease are that of infants and children and geriatric patients. Rapid detection of rotavirus infection could help in effective treatment of diarrheal patients. Diagnosis of rotavirus could be based on the identification of rotavirus particles in the feces. These particles may be observed by electron microscopy (EM), detected by immunological methods (ELISA or immunochromatographic method). The presence of rotavirus in feces could be also detected by genetic material-based methods (RT-PCR, sequencing, RNA electrophoresis) (WHO, 2009; Wilde et al., 1991; Zhan et al., 2013). Detection of rotavirus infection in patients requires a quick, simple method and could be performed on site. Therefore among of these methods, immunochromatographic lateral flow assay (LFA) is estimated as the best suitability for rotavirus detection from patients (Weitzel et al., 2007; Zhang et al., 2009). Rotaviruses are antigenically complex with multiple serotypes (Doan et al., 2003; Maneekarn and Ushijima, 2000; Nishio et al., 2000; Szucs et al., 1995). Detection of rotavirus based on monoclonal may face to the false negative result. Using polyclonal antibody for development of immunochromatographic test could over this limitation. In this study, we present optimization of conditions for generating a lateral flow test strip using polyclonal antibodies applied for the sensitive detection of rotavirus in feces.

2. MATERIALS AND METHODS

2.1 Materials

Standard rotavirus sample was from ProSpecT^{TM} Rotavirus Microplate Assay (Oxoid Ltd, UK). Sera samples from rotavirus infected rabbits and guinea pigs were from POLYVAC – Ministry of Heath. Materials for making lateral flow strip were purchased from Shanghai

JY-Biotech™. Protein A – Sepharose 4B conjugate was purchased from Invitrogen (USA). Chemicals for IgGs purification, polyacrylamide gel electrophoresis and buffers for immunochromatographic lateral flow assay were purchased from Sigma, Merck, Fermentas,…

2.2 Methods

2.2.1 Conjugation of IgG and colloidal gold nanoparticles

Procedure for conjugating IgG with the colloidal gold nanoparticles (AuNP) was performed according to (Zhang et al., 2009). Briefly, the colloidal gold suspension (OD_{529} = 7.0) is adjusted the pH to 9.0 with 0.2 M K_2CO_3. Appropriate amount of antibody is added to the colloidal solution, mixed rapidly and then incubated at room temperature for 1-2h. One ten volume of 10% BSA in 20 mM sodium borate is added and mixed rapidly, then incubated for further 15 min at room temperature. Unbound IgG is removed by centrifugation. The pellet is washed twice with 20 mM sodium borate containing 1% BSA. Finally, the pellet (IgG-AuNP conjugate) is suspended in 20 mM sodium borate containing 2% BSA, 3% sucrose, 0.6 M NaCl, 0.2 % Tween 20 to make the conjugate solution.

2.2.2 Preparation of conjugate pad

The conjugate pad is generated by embedding the empty pad in the IgG-AuNP conjugate solution and then drying at the different temperatures until complete dryness. The conjugate pad should be stored at 4°C for further investigations.

2.2.3 Preparation of blotting membrane

The nitrocellulose membrane was cut into pieces with appropriate sizes and assembled on the CAMAG Linomat 5 automatic sampler platform. The antibody solutions at experimental concentrations were dispensed onto the membrane at 1.0 µl/ cm. The blotted membrane then is dried at the different temperatures in an air drying oven. The membrane could be stored at 4°C for several months.

3. RESULTS AND DISCUSSIONS

3.1 Establishment of a lateral flow immunoassay strip

On the basis of the preliminary study (Do Thi Thu Ha et al., 2015) , a standard condition of 0.1 µg guinea pig IgG immobilized on the membrane, 0.25 µg rabbit IgG conjugated to AuNP was set up for generating a lateral flow immunoassay (LFIA) strip. In general, a protein maximally absorbs on the gold nanoparticle (GNP) surface at the isoelectric point (pI) of the molecule or 0.5 pH units higher (Zhang et al., 2009). For optimal binding of the antibody while retaining a high degree of specific activity, the pH value of the gold solution must be adjusted to slightly higher than the pI of the coating antibody prior to conjugation. The pH of colloidal gold nanoparticle solution was adjusted higher than 9.0 before conjugating with IgGs. The result showed the appearance of a significant intensity band on the strip after loading the standard rotavirus sample (Fig. 1). This condition was starting point for further optimization.

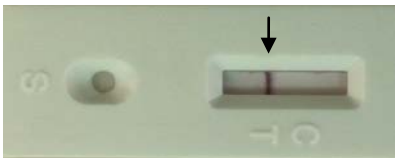

Fig. 1 The lateral flow immunoassay strip. Arrow indicates the appearance of expected signal band.

3.2 Optimization of conditions for generating the conjugate pad

3.2.1 Optimal conditions for preparation of IgG-AuNP conjugates

** pH:*

In order to investigate the effect of pH on the efficiency of conjugation, the pH values of the gold solution were adjusted to 7.5 and 8.5 before conjugation with polyclonal antibodies. The result indicated that there was a slight difference in signal intensity between two pH conditions (Fig. 2). The pH 8.5 gave better signal than pH 7.5, therefore the higher pH 8.5 could be applied for next experiments.

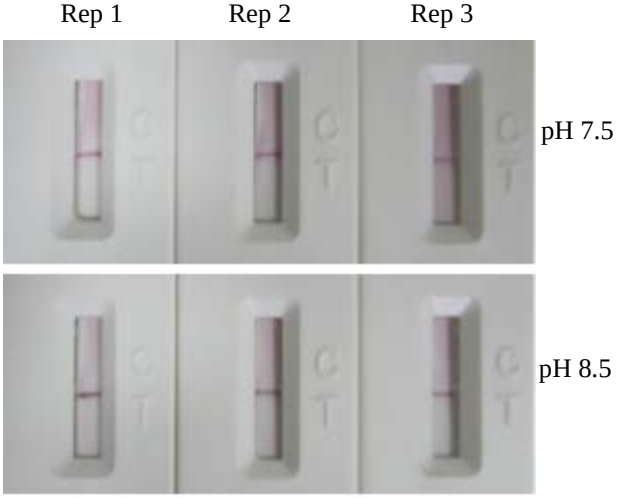

Fig. 2 Conjugation of IgG and AuNP at different pHs (7.5 and 8.5). Experiments were replicated three times (Rep).

** Temperature*

The temperature could affect on the activity of antibody and adsorptive efficiency of antibody on the surface of gold nanoparticles. The conjugation reaction was carried out at three different temperatures (4, 25 and 37°C) and the result indicated that the same signal intensity was observed in all experimental temperature conditions (Fig 3). For more convenience, the room temperature was chosen for conjugation of antibody and gold nanoparticles.

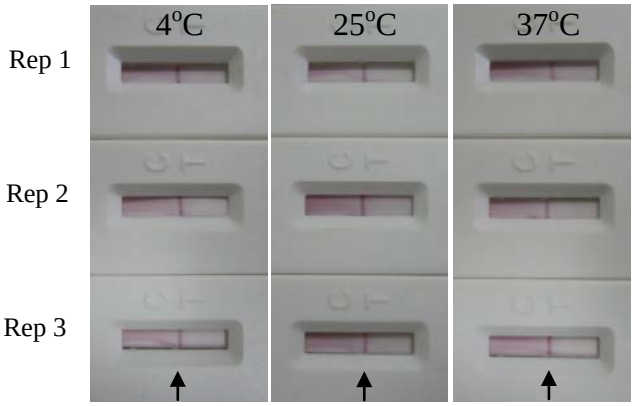

Fig. 3 Conjugation of IgG and AuNP at the different temperatures (4, 25 and 37°C). Experiments were replicated three times.

3.2.2 Optimal conditions for the preparation of conjugate pad

When sample flows into the conjugate pad, the detector reagent (conjugate) solubilizes, lifts off the pad material and moves with the sample front into the membrane. Therefore, one of the most important roles of conjugate pad is uniform transfer of the detector reagent and test sample onto the membrane. The expected conjugate pad material should be: low non-specific binding, consistent flow characteristics, consistent bed volume, low extractables and good web handing characteristics. To generate a good conjugate pad, some conditions have been investigated and optimized.

** Conjugate pad materials*

In the present study, 5 different conjugate pad materials were tested and the results indicated that signal intensities of five samples were similar at final observation (Fig. 4). However, the observation during flowing showed that the absorption and release of detector reagent of J2 material was better than others; therefore the time of analysis was shorter (3-5 min).

Fig. 4 The use of different conjugate pad materials for test strip.

** Conjugate pad buffer*

The conjugate pad buffer (CB) could be used to solubilize the conjugate (detector reagent), then blotted onto the conjugate pad and dried. Therefore, chemical components of conjugate pad buffer could affect on the stability of detector reagent, release of detector reagent from conjugate pad, interaction between antibody and antigen at the test line,… In the present study, 8 different formulations of conjugate pad buffer (**CB1**: 20mM Sodium borate, 2% BSA, 3% sucrose, 0.6 M NaCl, 0.2% Tween-20; **CB2**: 20mM Sodium borate, 3% sucrose, 0.6 M NaCl, 0.2% Tween-20; **CB3**: PBS 1X, pH 7.4, 2% BSA, 3% sucrose, 0.4 M Nacl, 0.2% Tween-20; **CB4**: 1X PBS pH 7.4, 3% sucrose, 0.4 M NaCl, 0.2% Tween-20; **CB5**: 20mM Sodium borate; 2% BSA; 3% sucrose, 0.2% Tween-20; **CB6**: 20mM Sodium borate, 3% sucrose, 0.2% Tween-20; **CB7**: 1X PBS, pH 7.4, 2% BSA, 3% sucrose, 0.2% Tween-20; **CB8**: 1X PBS, pH 7.4; 3% sucrose, 0.2% Tween-20) were tested and indicated that the highest signal was observed with the formulation of CB1 (Fig. 5).

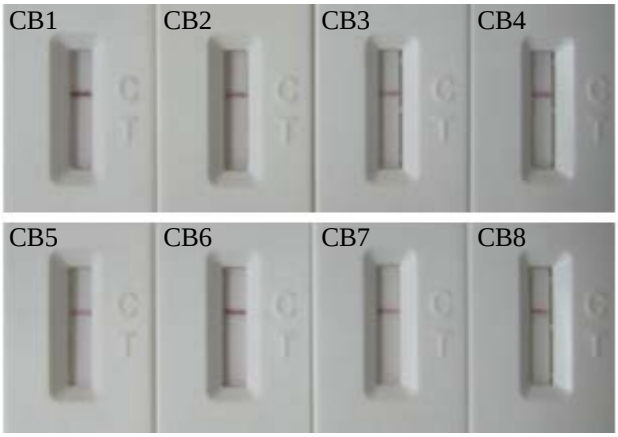

Fig. 5 Different formulations of conjugate pad buffer

** The temperature for drying the conjugate pad*

In procedure, the conjugate pad needs to be dried. However the stability of antibody is dependent on the temperature condition. The lower temperature is better for antibody stability but takes longer time. Therefore the conjugate pad was dried at three different temperatures (4°C, 25°C, 42°C).

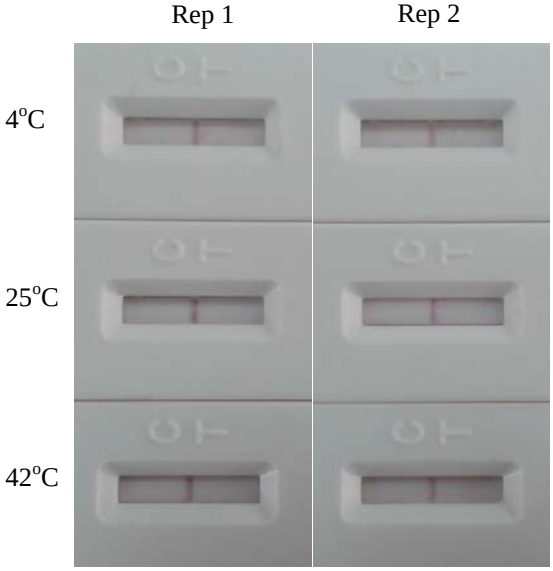

Fig. 6 The drying of the conjugate pad at different temperatures. The experiments were replicated twice.

In the lower temperature (4°C, 25°C), the drying time will take longer up to 18-24 hours. The conjugate pad is completely dried at 42°C for 30-45 min. The drying of the conjugate pad resulted in the same signal intensity at the different temperatures (Fig. 6). For more convenience, the conjugate pad should be dried at 42°C for shorter time (30-45 min).

3.3 Optimization of conditions for immobilizing antibody on the membrane

The immobilization of antibody onto the membrane could affect the stability of antibody, interaction between immobilized antibody and antigen, the flow of detector reagents,… The effect of antibody immobilization is depended on the membrane types, antibody solution and drying condition.

**** Membrane types***

The membrane is probably the most important material used in a lateral flow test strip. Physical and chemical attributes of the membrane affect its capillary flow properties. The capillary properties in turn affect reagent deposition, sensitivity, specificity and test line consistency. In this study, antibodies were immobilized on four different types of the membrane from the different sources and applied for lateral flow strip. The result indicated that the membranes of HF135 and HF180 from Millipore showed stronger signal band than others; however the membrane of Vivid170 from Pall showed the sharpest band. In negative control, no signal band was detected in all of these membranes and this implicated that the membranes were nonspecific binding (Fig. 7).

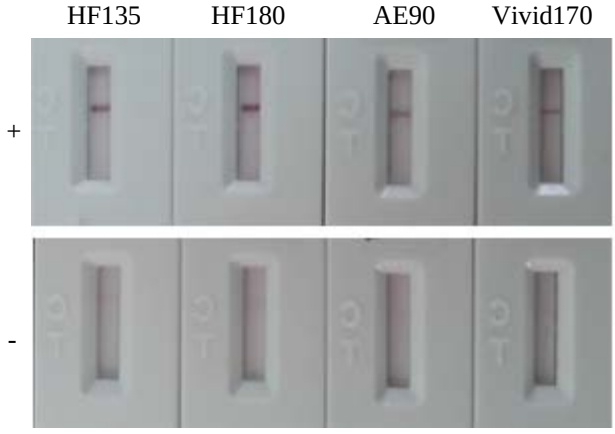

Fig. 7 Different types of the membrane for lateral flow strip. The membranes were different in physical and chemical properties. The membranes were tested with both positive and negative control.

**** Antibody immobilizing buffer***

The immobilizing buffer affects capillary flow and specially the stability of immobilized antibody during storage. In the present study, four different buffers (**IB1**: 1X PBS, pH 7.4; **IB2**: 1X PBS, pH7.4, 2% sucrose; **IB3**: 1X PBS pH 7.4, 2% sucrose, 1% BSA; **IB4**: 1X PBS stabilizer) were used to immobilize antibody on the membrane and antibody activity was checked after each month storage. The result showed that antibody activity was still remained after 6 months storage when it was immobilized in IB1 and IB2 buffers (Fig. 8). Antibody activity immobilized in IB2 buffer was stronger than IB1. Obtained results indicated that the presence of sucrose could help protect antibody from degradation during storage.

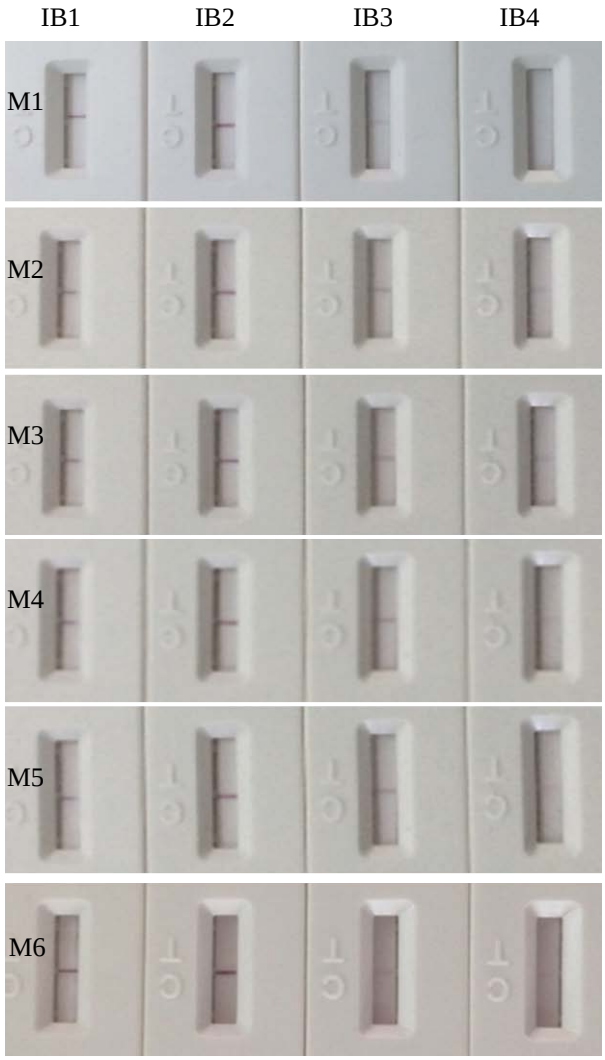

Fig. 8 Immobilization of antibody on the membrane in different buffers (IB1-IB4). The stability of antibody was estimated for 6 months.

**** The temperature for immobilizing antibody on the membrane***

After spreading antibody, the membrane needs to be dried to immobilize the antibody. The drying of membrane was carried out at 4, 25 overnight and 42°C for 30 min and indicated that the increase of temperature reduced activity of antibody (Fig. 9). However, the drying of membrane at 42°C for 30 min still remained activity of antibody. The drying of the membrane at lower temperature will take longer time.

Fig. 9 The drying of the membrane at different temperature for immobilizing antibody.

3.4 Optimization of conditions for generating the sample pad

The sample pad can be used to promote the even and controlled distribution of the sample onto the conjugate pad. It may also control the rate at which liquid enters the conjugate pad, preventing flooding of the device.

**** Sample pad types***

Six different types of sample pad was tested in this study and showed that signal band was similar at final observation (Fig 10). However, observation during test indicated that the sample pad material B2 was better in liquid absorption and release.

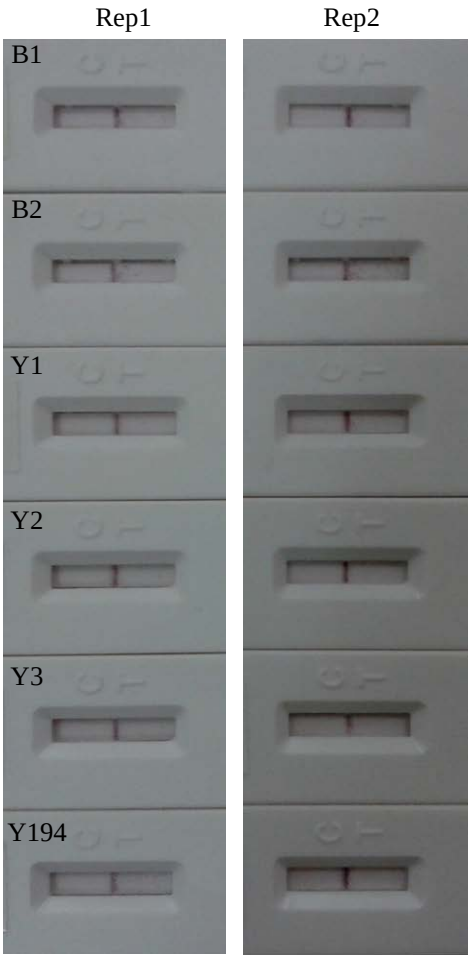

Fig. 10 Different types of sample pad

*** Sample pad solution**

In lateral flow test strip, the sample pad solution is used to prepare fecal samples and applied onto the test strip. This solution is required to release virus from sample, solubilize the detector reagents in the conjugate pad, prevent the conjugate and analyte from binding non-specifically to any of the downstream materials and provide normal condition for interaction between antibody and antigens. Due to important role in the test trip, five different formulation of sample pad solution (**SPS1**: 1X PBS, 0.1 M NaCl, 0.05% Tween 20; **SPS2**: 1X PBS, 0.1 M NaCl, 0.2% Tween 20; **SPS3**: 1X PBS, 0.1 M NaCl, 0.5% Tween 20; **SPS4**: 1X PBS, 0.1 M NaCl, 0.5% Tween 20, 1% BSA; **SPS5**: 1X PBS, 0.5% NaCl) were tested and showed that the same signal intensities were observed in all tested formulations of sample pad solution. The increase of detergent concentration Tween20 up to 0.5% in sample pad solution did not affect interaction between antibody and antigen. Higher concentration of detergent could minimize non-specific binding of components in the test trip (Fig. 11).

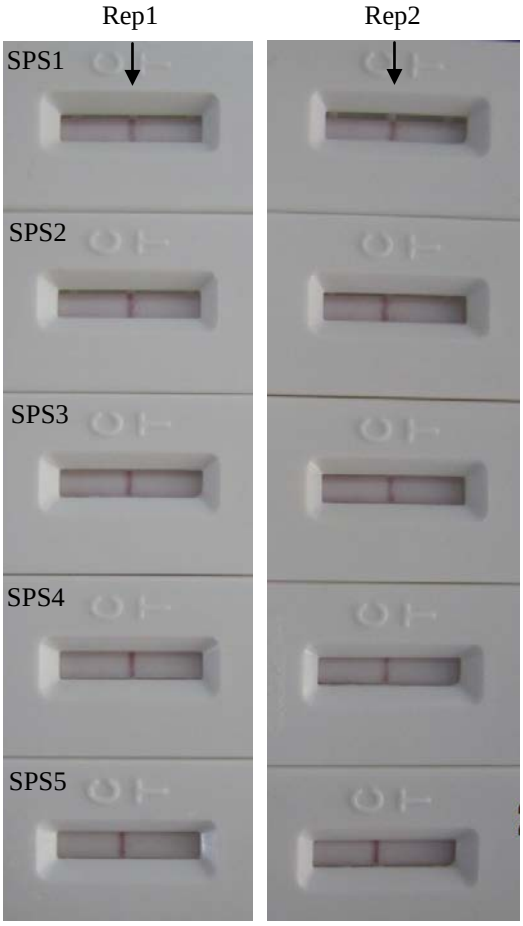

Fig. 11 Different sample pad solutions for lateral flow strip. The experiments were replicated twice.

3.5. Properties of generated lateral flow test trip

For generating the complete test strip, the second line (control line) containing antibody against rabbit IgG was probed on the membrane. Some properties of generated lateral flow test trip were determined. Reproducibility of the test trip was determined by 10 times testing with

positive and negative samples. The result showed that no change in intensity of signal band was detected upon repeated testing of the sample (Fig.12).

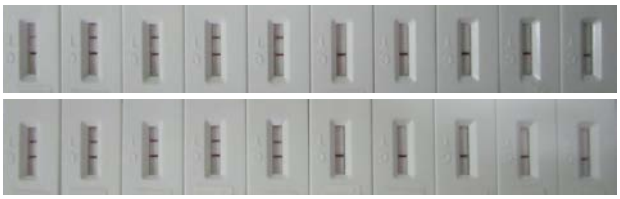

Fig. 12 Reproducibility of the test strip

The generated strip was also tested with several intestinal pathogens to check the cross-reactivity. The absence of signal in the test line indicated that the anti-rotavirus antibodies employed in this kit were found not to recognize the following common intestinal pathogens: *Salmonella enteritidis, Proteus mirabilis, Clostridium sporogenes, Candida albicans, Vibrio haemolyticus, Escherichia coli, Shigella flexneri, Polio virus I, II, III* (Fig.13)

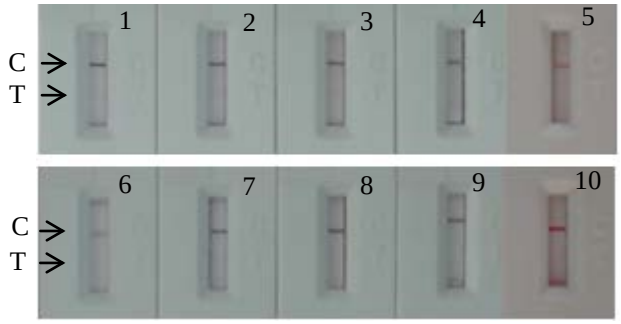

Fig. 13 Cross-reactivity of the test trip with intestinal pathogens: (1) *Salmonella enteritidis,* (2) *Proteus mirabilis,* (3) *Clostridium sporogenes,* (4) *Candida albicans,* (5) *Poliovirus I,* (6) *poliovirus II,* (7) *Shigella flexneri,* (8) *Escherichia coli,* (9) *Vibrio haemolyticus,* (10) *Polio virus III*. C, control line; T, test line.

CONCLUSION

Lateral flow immunoassay test is considered as the most powerful tool for rapid detection of rotavirus in the fecal samples at the hospitals and medical centers. Determination of optional conditions for generating a lateral flow test trip supported the production of effective test strips for rapid detection of rotavirus in fecal samples of diarrheal children patients.

REFERENCES

Do Thi Thu Ha, Ngo Thu Huong, Nguyen Dang Hien, Le Thi Luan, Luong Trinh Thuy Linh, Truong Quoc Phong, 2015, Development of a lateral flow immunoassay strip for rapid detection of rota. Vietnam Journal of Biology 37, 12-17.

Doan, L.T., Okitsu, S., Nishio, O., Pham, D.T., Nguyen, D.H., Ushijima, H., 2003, Epidemiological features of rotavirus infection among hospitalized children with gastroenteristis in Ho Chi Minh City, Vietnam. J Med Virol 69, 588-594.

Maneekarn, N., Ushijima, H., 2000, Epidemiology of rotavirus infection in Thailand. Pediatr Int 42, 415-421.

Nishio, O., Matsui, K., Lan, D.T., Ushijima, H., Isomura, S., 2000, Rotavirus infection among infants with diarrhea in Vietnam. Pediatr Int 42, 422-424.

Szucs, G., Matson, D.O., Uj, M., Kukan, E., Mihaly, I., Jelenik, Z., Estes, M.K., 1995, Group A rotavirus G type prevalence in two regions of Hungary. Arch Virol 140, 1693-1703.

Weitzel, T., Reither, K., Mockenhaupt, F.P., Stark, K., Ignatius, R., Saad, E., Seidu-Korkor, A., Bienzle, U., Schreier, E., 2007, Field Evaluation of a Rota- and Adenovirus Immunochromatographic Assay Using Stool Samples from Children with Acute Diarrhea in Ghana. Journal of Clinical Microbiology 45, 2695-2697.

WHO, 2009, Manual of rotavirus detection and characterization methods, . The WHO Document Production Services WHO/IVB/08.17.

Wilde, J., Yolken, R., Willoughby, R., Eiden, J., 1991, Improved detection of rotavirus shedding by polymerase chain reaction. Lancet 337, 323-326.

Yolken, R., Murphy, M., 1982, Sudden infant death syndrome associated with rotavirus infection. J Med Virol 10, 291-296.

Zhan, F., Zhou, X., Xing, D., 2013, Rapid and sensitive electrochemiluminescence detection of rotavirus by magnetic primer based reverse transcription-polymerase chain reaction. Anal Chim Acta 761, 71-77.

Zhang, G., Guo, J., Wang, X., 2009, Immunochromatographic Lateral Flow Strip Tests, In: Rasooly, A., Herold, K.E. (Eds.) Methods in Molecular Biology: Biosensors and Biodetection. Humana Press.

Acknowledgement: The research was supported by project “Research on the generation of LFA strip for rotavirus detection in the diarrheal children patients” with No.B2014-01-66.

Truong Quoc Phong received the B.S. (2001), M.S. (2004), degrees in Biochemistry from University of Science, Hanoi National University. He received the Doctor degree (2008) in Molecular Biology from Greifswald University, Germnay. He is a Head of Laboratory for Proteomics, Hanoi University of Science and Technology. His current interests include: Production of recombinant proteins/enzymes, Establishment of new methods for rapid test and detection of target organisms, Application of proteomics in biomarker screening and early diagnosis of dangerous human disease

OS Number: OS04

MOLECULAR CLONING AND EXPRESSION OF NATTOKINASE IN *BACILLUS MEGATERIUM*

Truong Quoc Phong*, Trinh Thi Hong Nhung, Nguyen Lan Huong
Hanoi University of Science and Technology, Vietnam

ABSTRACT

Nattokinase (NK) is a potent fibrinolytic protease which has effective thrombolysis activity, therefore the products containing NK has been used in the prevention of stroke and myocardial infarction. The NK purification from wild strains requires a number of complex processes leading to activity reduction. Therefore, it is very important to produce NK by recombinant DNA technology. In this study, NK gene from *B. subtilis* M1 strain was cloned and expressed successfully in *B. megaterium* strain. Fibrinolytic activity of recombinant NK was 23±2 fibrinolytic units/ml culture after 9 hours induction with 0.5% xylose. This is considered as the first report on NK expression in *B. megaterium*.

Keywords: Bacillus megaterium, Bacillus subtilis, Nattokinase, Recombinant,

1. INTRODUCTION

Heart disease and stroke are the leading causes of death in top 10 deadly diseases (WHO, 2014). One important caution of the two diseases is the formation of blood clots in vessels. Nattokinase (NK) has been known as an enzyme derived from *Bacillus* which has high thrombolysis activity (Sumi et al., 1987). Fibrinolytic activity of NK is 4 times higher than plasmin in human tissue (Urano et al., 2001) and the enzyme degrades blood clots by three different ways (Fujita et al., 1995). NK effect could be enhanced and pro-longed in the plasma when NK was taken orally (Sumi et al., 1990; Suzuki et al., 2003). NK has high potential to become a thrombosis drug. However, the NK purification from wild strains requires a number of complex processes leading to the reduction of enzyme activity. Therefore, it is very important to produce NK by recombinant DNA technology. *B. megaterium* is a generally recognized as safe (GRAS) organism. Utilization of *Bacillus* host allows for foreign protein expression in the extracellular environment with precise folding without inclusion body or inactive problems like *E. coli* expression system (Rygus and Hillen, 1991). This is a prerequisite requirement for active enzyme synthesis. Some enzymes, antigens, antibodies, toxins and other special proteins have been successfully synthesized in this expression system (Jordan et al., 2007; Radha and Gunasekaran, 2008; Stammen et al., 2010). *Bacillus megaterium* is considered as a suitable host for the high-level production of recombinant proteins. Therefore, the aim of this study is to construct a recombinant *B. megaterium* host to express extracellular nattokinase.

2. MATERIALS AND METHODS

2.1 Materials

The strains and plasmids were used in this study are listed in Table1. *B. subtilis* M1was isolated from the natto, and stocked at Hanoi University of Science and Food Technology (HUST).

Table 1 Bacterial strains and plasmids.

Plasmid/strain	Property	Source
pJet1.2/blunt	3kb, *eco477R*, Ap^R	*Thermo Scientific*
pSpLipA	6,6kb, Ap^R, Tc^R, *Pxyl*, *Lipase* signal peptide, *E. coli & B. megaterium* Ori	*Mobitec*
*B. subtilis*M1	Nattokinase producing bacterium, wild strain	*Isolated by SBFT*
E. coli BL21(DE3)	Removing*lon*, *ompT* protease	*SBFT collection*
B. megaterium VTCC-B-1091	Wild strain	*Vietnam type culture collection*

2.2 Methods

2.2.1 DNA extraction

Total DNA from *B. subtilis* M1 strain and plasmid DNA from *E. coli* were isolated by the methods as described in (Sambrook and Russell, 2001). *B. megaterium* plasmid DNA was isolated by the same method with additive step of lysozyme.

2.2.2 Amplification and cloning of *nat* gene

To amplify *nat* gene, total DNA extract from *B. subtilis* was used as the template for PCR using specific primers (5' TAAGAGCTCCTGCCGGAAAAAGCAGT3' and 5' TTAGGATCCATTGTGCCGCCGCTTGTA3'). Amplification reactions were carried out with the following program: 95°C for 5 min; 30 cycles of denaturation at 95°C for 45 sec, primer annealing at 60° for 45 sec, and extension at 72°C for 30 sec; final extension at 72°C for 10 min. PCR product was blunted and then was cloned into the pJet1.2 blunt vector according to the manufacturer's instruction to generate a recombinant vector pJet1.2::*nat*.

Construction of expression vector pSpLipA::nat

The *nat* gene was eluted from recombinant vector pJet1.2::*nat* after treatment with *Sac*I and *Bam*HI (New England Biolabs, USA). Eluted *nat* gene was ligated into *Sac*I/*Bam*HI pretreated pSpLipA vector and transformed into *E. coli* cells for screening of positive clones by ampicillin selective medium and restriction enzymes.

2.2.3 Construction of recombinant *B. megaterium*

In order to transform recombinant plasmid (pSpLipA-hp::*nat*) into *B. megaterium* protoplast, polyethylene glycol (PEG) 6000 40% (m/v) was added to the mixture of plasmids and protoplasts. After 2 minutes reaction with PEG, cells were stabled in SMMP for 1 hour before culturing on LB agar plate containing tetracyclin 10 µg/ml. Following the stabilization and plating, cells were incubated at 30ºC for overnight.

The recombinant *B. megaterium* strain was checked by colony PCR and the plasmids from positive clones were extracted and checked by plasmid PCR.

2.2.4. Expression of recombinant nattokinase in *B. megaterium*

For expression experiments, liquid LB pre-culture containing tetracyclin was inoculated with single recombinant *B. megaterium* colony and incubated at 30°C for overnight. Negative control was the *B. megaterium* carrying empty plasmid (pSPLipA-hp). Next, 50 ml of growth medium were supplemented with tetracyclin and inoculated in the ratio of 1:100 with the pre-culture until the OD_{600} was 0.8, then added 0.5% (w/v) xylose for induction. Samples were taken at different time points after induction of recombinant gene expression for analysis.

Assay of fibrinolytic activity

After induction, the culture was centrifuged to collect the supernatant. For qualitative analysis, the fibrin agar plate was prepared by dissolving 0.4 % fibrin and 2 % agar in Tris-HCl buffer pH7.4, and generating the holes with 0.5 mm in diameter. The supernatant samples (50 µl) were dropped into the holes on the agar plate and incubated at 37ºC for 20h. The fibrinolytic activity was estimated by the clear zone on the agar plate. For quantitative analysis, the fibrinolytic activity of recombinant enzyme was determined according to the Anson's method (Anson, 1938). Briefly, 200µl of enzyme (diluted 20 times) was incubated with 0.4% fibrin solution for 1 hour at 37°C. The reaction was quenched by adding 1.5M trichloroacetic acid (TCA). The supernatant was collected by centrifugation and measured at 275nm in wave length. Amount of released amino acid was calculated based on the tyrosine standard curve. One fibrinolytic unit (FU) is defined as the quantity of required enzyme to hydrolyze fibrin into free amino acid equivalent to 1.0 µM of tyrosine per minute at pH 7.5 at 37°C.

Western blotting

About 120 µl of the supernatant culture was precipitated and concentrated by using 70% ethanol, then was separated by sodium dodecyl sulfate-polyacrylamide gel electrophoresis (SDS-PAGE) method (Laemmli, 1970). The protein pattern was transferred onto the polyvinylidene difluoride (PVDF) membrane (Bio-Rad Laboratories). The membrane was incubated with His-Tag antibodies overnight and goat anti-rabbit antibody for 2 hours, respectively. Finally, the membrane was developed in the nitro blue tetrazolium chloride and 5-bromo-4-chloro-3-indolyl-phosphate (NBT/BCIP) solution.

3. RESULTS

3.1 Amplification of truncated nattokinase gene from *B. subtilis*

Total DNA extract from *B. subtilis* M1 strain was used as template for PCR to amplify a truncated nattokinase gene (without signal peptide). As designed, the desired size of target gene should be 1077 bp in length. The appearance of a strong band of approximately 1,1 kb on the agarose gel electrophoresis pattern indicated that the target gene *nat* was successfully amplified using specific primers. This product will be used for further experiments.

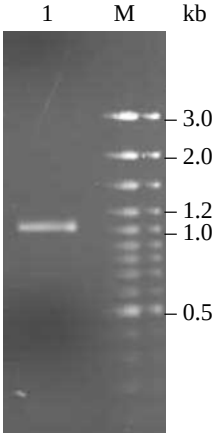

Fig. 1 Agarose gel electrophoresis pattern of PCR product of nattokinase gene. Lane 1, PCR product of *nat* gene; lane M, DNA ladder (Thermo scientific, USA)

3.2 Cloning of *nat* gene in pJET1.2 blunt vector

The *nat* gene was ligated into pJET1.2 blunt vector and transformed into the competent *E. coli* cells as described by (Sambrook and Russell, 2001; Thermo Fisher Scientific Inc., 2014). Positive clone selected from ampicillin selective medium was further confirmed by sequencing and showed in the Fig. 2. The result indicated that an open reading frame for a mature nattokinase was cloned and determined. The nucleotide blast showed that the nucleotide sequence of cloned gene has 99% sequence homology with serkinase-nattokinase gene of *Bacillus subtilis* var. natto (data not shown). These results indicated that the *nat* gene from *Bacillus subtilis* was successfully cloned in pJET1.2 blunt vector.

```
gccggaaaaagcagtacagaaaagaaatacattgtcggatttaagcagacaatgagtgcc
 A  G  K  S  S  T  E  K  K  Y  I  V  G  F  K  Q  T  M  S  A
atgagttccgccaagaaaaaggatgttatttctgaaaaaggcggaaaggttcaaaagcaa
 M  S  S  A  K  K  K  D  V  I  S  E  K  G  G  K  V  Q  K  Q
tttaagtatgttaacgcggccgcagcaacattggatgaaaaagctgtaaaagaattgaaa
 F  K  Y  V  N  A  A  A  A  T  L  D  E  K  A  V  K  E  L  K
aaagatccgagcgttgcatatgtggaagaagatcatattgcacatgaatatgcgcaatct
 K  D  P  S  V  A  Y  V  E  E  D  H  I  A  H  E  Y  A  Q  S
gttccttatggcatttctcaaattaaagcgccggctcttcactctcaaggctacacaggc
 V  P  Y  G  I  S  Q  I  K  A  P  A  L  H  S  Q  G  Y  T  G
tctaacgtaaaagtagctgttatcgacagcggaattgactcttctcatcctgacttaaac
 S  N  V  K  V  A  V  I  D  S  G  I  D  S  S  H  P  D  L  N
gtcagaggcggagcaagcttcgttccttctgaaacaaacccataccaggccggcagttct
 V  R  G  G  A  S  F  V  P  S  E  T  N  P  Y  Q  A  G  S  S
cacggtacgcatgtcgccggtacgattgccgctcttaataactcaatcggtgttctgggc
 H  G  T  H  V  A  G  T  I  A  A  L  N  N  S  I  G  V  L  G
gtagcgccaagcgcatcattatatgcagtaaaagtgcttgattcaacaggaagcggccaa
 V  A  P  S  A  S  L  Y  A  V  K  V  L  D  S  T  G  S  G  Q
tatagctggattattaacggcattgagtgggccatttccaacaatatggatgttatcaac
 Y  S  W  I  I  N  G  I  E  W  A  I  S  N  N  M  D  V  I  N
atgagccttggcggacctactggctctacagcgctgaaaacagtagttgataaagcggtt
 M  S  L  G  G  P  T  G  S  T  A  L  K  T  V  V  D  K  A  V
tccagcggtatcgtcgttgctgccgcagccggaaacgaaggttcatccggaagcacaagc
 S  S  G  I  V  V  A  A  A  A  G  N  E  G  S  S  G  S  T  S
acagtcggttaccctgcaaaatatccttctactattgcagtaggtgcggtaaacagcagc
 T  V  G  Y  P  A  K  Y  P  S  T  I  A  V  G  A  V  N  S  S
aaccaaagagcttcattctccagcgtaggttctgagcttgatgtaatggctcctggcgtg
 N  Q  R  A  S  F  S  S  V  G  S  E  L  D  V  M  A  P  G  V
tccatccaaagcacacttcctggaggcacttacggcgcttataacggaacgtccatggcg
 S  I  Q  S  T  L  P  G  G  T  Y  G  A  Y  N  G  T  S  M  A
actcctcacgttgccggagcagcagcgctaattctttctaagcacccgacttggacaaac
 T  P  H  V  A  G  A  A  A  L  I  L  S  K  H  P  T  W  T  N
gcgcaagtccgtgatcgtttagaaagcactgcaacatatcttggaaactctttctactat
 A  Q  V  R  D  R  L  E  S  T  A  T  Y  L  G  N  S  F  Y  Y
ggaaaagggttaatcaacgtacaagcagcagcacaa
 G  K  G  L  I  N  V  Q  A  A  A  Q
```

Fig. 2 Nucleotide sequence and deduced amino acid sequence of *nat* gene.

3.3 Construction of expression vector for *Bacillus megaterium*

The expression vector pSpLipA-hp is an effective system for production of heterologous proteins in *B. megaterium* host (MoBiTec, 2011). This vector contains LipA signal peptide therefore recombinant protein will be exported to extracellular medium. In the present study, *nat* gene was inserted into pSpLipA-hp vector to generating a recombinant vector and transformed into *E. coli*. Positive clone was screened by ampicillin selective medium and restriction enzyme digestion of plasmid. The appearance of DNA band of approximately 1,1 kb on the agarose gel electrophoresis pattern after *Sac*I/*Bam*HI digestion of transformant plasmid (Fig. 3) indicated that the *nat* gene was cloned into expression vector.

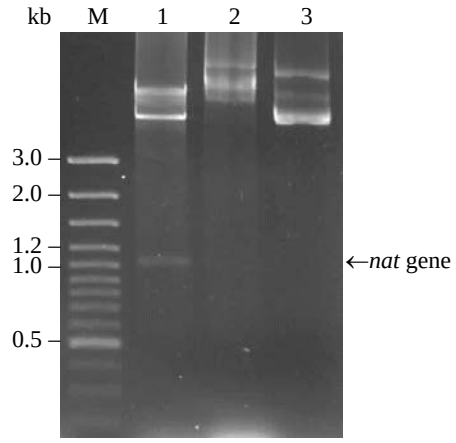

Fig. 3 Checking the recombinant plasmid from positive clone by *Sac*I/*Bam*HI digestion. Lane 1, product of plasmid digestion; lane 2, undigested plasmid; lane 3, empty plasmid (pSpLipA-hp); M, DNA ladder.

3.4 Construction of recombinant *B. megaterium* strain

To generate the host for expression of extracellular natokinase, the recombinant construct (pSpLipA-hp::*nat*) was transformed into *B. megaterium* protoplasts and screened by tetracycline selective medium. Plasmids from two positive clones were used as the template for PCR. The result showed that the PCR products with desired size of *nat* gene were observed in both selected clones. This result indicated that two selected recombinant clones of *B. megaterium* containing *nat* gene were successfully constructed and further investigated for fibrinolytic activity.

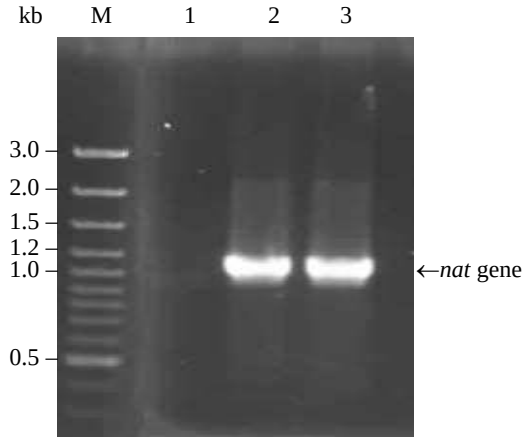

Fig. 4 Checking positive clones of *Bacillus megaterium* by PCR using specific primers. Lane 1, product of negative control (containing empty plasmid); lane 2, 3, PCR products from two selected clones; M, DNA ladder.

3.5 Expression of recombinant nattokinase in *B. megaterium*

To confirm expression of recombinant nattokinase in *B. megaterium*, recombinant *B. megaterium* clone was grown in the appropriate medium and the extracellular proteins were collected after xylose induction. The protein pattern on SDS-PAGE showed the appearance of protein band of approximately 30 kDa. This protein band could be recombinant nattokinase.

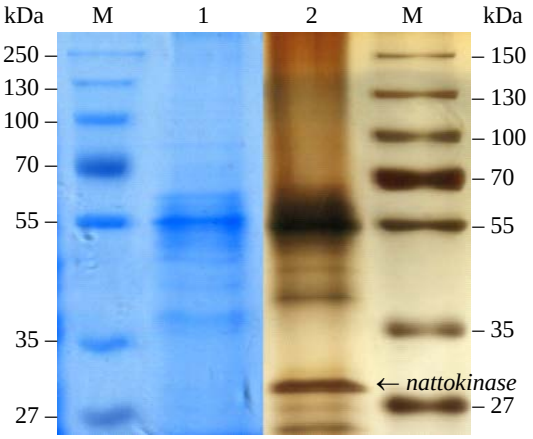

Fig. 5 Polyacrylamide gel electrophoresis protein pattern of extracellular extracts from control (lane 1) and recombinant clone (lane 2) of *B. megaterium*.

A western blot experiment was performed using anti-His tag antibody and demonstrated that protein band of approximately 30 kDa was recombinant nattokinase (Fig. 6).

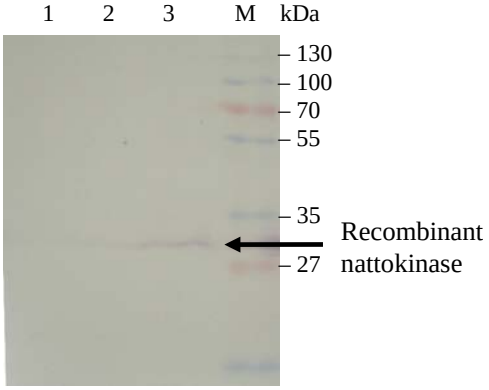

Fig. 6 Western blot pattern of extracellular extract from *B. megaterium*. Lane 1, extracellular extract from control; lane 2, 3, extracellular extract from recombinant clone without and with xylose induction; M, protein marker.

Fibrinolytic activity

For qualitative analysis, the fibrinolytic assay of recombinant nattokinase was carried out by clear zone method in the presence of fibrin as substrate. The extracellular extract of control and recombinant clone after induction with 0.5% xylose was used to determine fibrinolytic activity of nattokinase. The result showed that clear zones were only present in case of the extracts from recombinant clone (Fig. 7). The fibrinolytic activity was higher in 30^{o}C culture compared to 20^{o}C. By quantitative analysis, the fibrinolytic activity was reached 23±2 fibrinolytic units per milliliter culture.

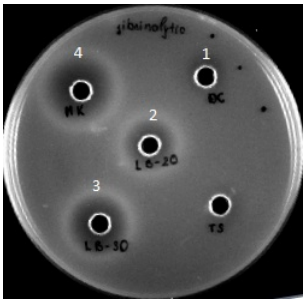

Figure 7. Fibrinolytic activity of nattokinase in *B. megaterium*. 1, the extracellular extract from negative strain; 2, 3 the extracellular extract from recombinant clone cultured at 20 and 30^{o}C respectively; 4, commercial nattokinase.

4. CONCLUSION

Gene coding for nattokinase from *Bacillus subtilis* was cloned and sequenced. The recombinant expression vector harboring *nat* gene was constructed and transformed into *Bacillus megaterium* strain to produce the recombinant extracellular nattokinase. The recombinant *B. megaterium* strain could be used for further investigation in high-level production of nattokinase.

REFERENCES

Anson, M.L., 1938, The Estimation of Pepsin, Trypsin, Papain, and Cathepsin with Hemoglobin. J Gen Physiol 22, 79-89.

Fujita, M., Hong, K., Ito, Y., Fujii, R., Kariya, K., Nishimuro, S., 1995, Thrombolytic effect of nattokinase on a chemically induced thrombosis model in rat. Biol Pharm Bull 18, 1387-1391.

Jordan, E., Hust, M., Roth, A., Biedendieck, R., Schirrmann, T., Jahn, D., Dubel, S., 2007, Production of recombinant antibody fragments in Bacillus megaterium. Microb Cell Fact 6, 2.

Laemmli, U.K., 1970, Cleavage of structural proteins during the assembly of the head of bacteriophage T4. Nature 227, 680-685.

MoBiTec, 2011, hp-vector expression systems for Bacillus megaterium.

Radha, S., Gunasekaran, P., 2008, Sustained expression of keratinase gene under PxylA and PamyL promoters in the recombinant Bacillus megaterium MS941. Bioresour Technol 99, 5528-5537.

Rygus, T., Hillen, W., 1991, Inducible high-level expression of heterologous genes in Bacillus megaterium using the regulatory elements of the xylose-utilization operon. Appl Microbiol Biotechnol 35, 594-599.

Sambrook, J., Russell, D.W., 2001, Molecular Cloning: A Laboratory Manual, Vol 1, 3 Edition. Cold Spring Harbor Laboratory Press, New York, 2100 p.

Stammen, S., Muller, B.K., Korneli, C., Biedendieck, R.,

Gamer, M., Franco-Lara, E., Jahn, D., 2010, High-yield intra- and extracellular protein production using Bacillus megaterium. Appl Environ Microbiol 76, 4037-4046.
Sumi, H., Hamada, H., Nakanishi, K., Hiratani, H., 1990, Enhancement of the fibrinolytic activity in plasma by oral administration of nattokinase. Acta Haematol 84, 139-143.
Sumi, H., Hamada, H., Tsushima, H., Mihara, H., Muraki, H., 1987, A novel fibrinolytic enzyme (nattokinase) in the vegetable cheese Natto; a typical and popular soybean food in the Japanese diet. Experientia 43, 1110-1111.
Suzuki, Y., Kondo, K., Matsumoto, Y., Zhao, B.Q., Otsuguro, K., Maeda, T., Tsukamoto, Y., Urano, T., Umemura, K., 2003, Dietary supplementation of fermented soybean, natto, suppresses intimal thickening and modulates the lysis of mural thrombi after endothelial injury in rat femoral artery. Life Sci 73, 1289-1298.
Thermo Fisher Scientific Inc. 2014. CloneJET PCR Cloning Kit.
Urano, T., Ihara, H., Umemura, K., Suzuki, Y., Oike, M., Akita, S., Tsukamoto, Y., Suzuki, I., Takada, A., 2001, The profibrinolytic enzyme subtilisin NAT purified from Bacillus subtilis Cleaves and inactivates plasminogen activator inhibitor type 1. J Biol Chem 276, 24690-24696.

Truong Quoc Phong received the B.S. (2001), M.S. (2004), degrees in Biochemistry from University of Science, Hanoi National University. He received the Doctor degree (2008) in Molecular Biology from Greifswald University, Germnay.

He is a Head of Laboratory for Proteomics, Hanoi University of Science and Technology. His current interests include: Production of recombinant proteins/enzymes, Establishment of new methods for rapid test and detection of target organisms, Application of proteomics in biomarker screening and early diagnosis of dangerous human disease

OS Number: OS04

OPTIMIZATION OF CULTURE CONDITIONS FOR HIGH-LEVEL EXPRESSION OF HUMAN ROTAVIRUS VP6 PROTEIN IN *ESCHERICHIA COLI*

Do Thi Thu Ha, Truong Quoc Phong*

Hanoi University of Science and Technology, Vietnam

ABSTRACT

VP6 protein is the most immunogenic and is highly conserved within group A of rotavirus. This antigen protein was used as biomarker for diagnosis of rotavirus infection and potential candidate for the development of novel vaccine against human rotavirus. In the present study, we reported that human rotavirus VP6 protein was successfully expressed in *E. coli* BL21 (DE3). Some appropriate conditions for high-level expression of this protein were determined including the IPTG concentration (0.05 mM), temperature (37 ^{o}C), induction time (4 h). Optimal conditions could be applied to produce large amount of VP6 protein for further applications.

Keywords: Escherichia coli, optimization, recombinant, rotavirus, VP6 protein

1. INTRODUCTION

Rotavirus is the main cause of severe, dehydrating diarrhea in children worldwide. This virus is the cause of up to 50% of the hospitalized cases of diarrheal illness in infants and young children. Rapid detection of rotavirus infection could help in effective treatment of diarrheal patients. VP6 protein is encoded by RNA fragment 6 of rotavirus genome and located in the intermediate capsid layer of rotavirus (Estes and Cohen, 1989). This protein is highly conserved within group A rotavirus strains (Tang et al., 1997). The intermediate capsid layer is composed of 780 molecules of VP6 and therefore the VP6 protein provides the greatest molecular mass of any protein in the rotavirus particle. Possibly due to its high prominence, the majority of antibody generated in an infected individual is directed against this protein and therefore it could be considered as the most immunogenic protein in rotavirus (Ward and McNeal, 2010).

Due to importance of VP6 protein in immunity, several researches have been performed to generate the host cells harboring VP6 protein for development of vaccine. A codon-optimized rotavirus VP6 gene was constructed in the expression vector for production of target protein in *E. coli* BL21 (DE3) and Rosetta (DE3). Immunization experiment indicated that intranasal administration of recombinant VP6 protein induced protection in mice (Choi et al., 2004). In 2010, Lee et al constructed recombinant *Bacillus subtilis* vaccine strains to express group A bovine and murine rotavirus VP6. Recombinant VP6 protein was investigated in their ability to induce immune responses and protection in mice (Lee et al., 2010). The gene of the rotavirus structural protein VP6 was successfully cloned in *Saccharomyces cerevisiae* strain (Rodriguez-Limas et al., 2011). Co-expression of three rotavirus proteins of VP6, VP2 and VP7 were carried out in the yeast host to generate the rotavirus-like particle. Furthermore, a *Lactococcus lactis* surface display system was also constructed to express the rotavirus VP6 protein in the form of an immunogenic cell-wall anchored fusion protein (Esteban et al., 2013). This recombinant system was demonstrated to induce rotavirus-specific serum antibodies in mice without adjuvant.

In the present study, a native gene of human rotavirus VP6 was constructed in the expression vector pET32 and successfully expressed in *E. coli* BL21 (DE3). Some appropriate conditions for the high-level expression of VP6 protein were also determined.

2. MATERIALS AND METHODS

2.1 Materials

The recombinant pET32::VP6 construct used in this study was from Proteomics Lab., Center for Research and Development in Biotechnology, School of Biotechnology and Food Technology, Hanoi University of Science and Technology. *Escherichia coli* BL21 (DE3) strain was transferred from Genetic Engineering Laboratory, Institute of Biotechnology, VAST. Chemicals for protein

expression and analysis were purchased from Sigma-Aldrich (USA), Thermo scientific (USA), Merck (Germany).

2.2 Methods

2.2.1 Expression of recombinant VP6 protein in *E. coli*

The recombinant construct pET32::VP6 was transformed into the expression strain *E. coli* BL21 (DE3) by the heat-shock method described in (Sambrook and Russell, 2001). Expression of recombinant VP6 protein was performed in *E. coli* cells under the induction of isopropyl-1-1-thio-β-D-galactoside (IPTG).

2.2.2 Optimization of expression conditions of VP6 protein in *E. coli*

The expression level of recombinant VP6 protein in *E. coli* was tested at the different concentrations of IPTG inducer (0, 0.1, 0.3, 0.5, 0.7, 0.9, 1.3 and 1.5 mM), temperatures (20, 25, 30 and 37^{o}C) and times. (0, 1, 2, 3, 4, 5 and 18 h).

2.2.3 Protein extraction from the bacterial cells

The bacterial cells were harvested by centrifugation at 10 000 x g for 2 min and washed with deionized water. For lysate and inclusion body preparation, the cell pellet was dissolved in 10 mM Tris, 1 mM EDTA pH 8.0, 100 µg/ml lysozyme, 100 100 µg/ml proteinase K and incubated at 37^{o}C for 1 h followed by sonification. The suspension was centrifuged at 12 000 x g for 30 min. The supernatant was collected to new tube as the lysate. The remaining pellet was dissolved in 135 mM Tris pH 6.8 and 8 M urea as the inclusion body and heated at 95^{o}C for 10 min. For preparation of the whole cell lysate, the cells was dispended in 8 M urea and heated at 95^{o}C for 10 min. The suspension was clarified by centrifugation at 12 000 x g for 15 min. The supernatant was transferred into new tube and stored at -20^{o}C for further analysis.

2.2.4 Protein electrophoresis and stain

The protein extracts were processed with 1X loading dye buffer (50 mM Tris pH 6.8, 2% SDS, 1 mM DTT, 10% glycerol and a trace of bromophenol blue) at 95^{o}C for 5 min before loading on the 12.5% polyacrylamide gel. Electrophoresis was performed at 100 V until the dye front reaches the bottom of the gel.

After electrophoresis, the gel was submerged in the fixing solution (50% ethanol, 10% acetic acid) and heated to 90^{o}C. After fixation, the gel was stained in 5% ethanol, 8% acetic acid and 0.001% Coomassie Brilliant Blue) at 90^{o}C until the development of clear band.

2.2.5 Quantitation of target protein band

After scanning, analysis of the gel images was performed with the Quantity One 4.6.9 (Bio-rad, USA). The volume of target band was calculated based on the areas and pixel intensities of bands. The volume of target band was normalized to total volume of the corresponding lane and used to compare between samples.

3. RESULTS AND DISCUSSIONS

3.1 Bacterial expression of human rotavirus VP6 protein

The constructed recombinant (pET32::VP6) and empty plasmids (pET32) were transformed into *E. coli* BL21 (DE3). According to design, target protein is a fusion protein of VP6 antigen (42 kDa) and protein tags (20 kDa). As shown in Fig. 1, there was the appearance of a strong protein band of approximately 62 kDa after induction with ITPG inducer for recombinant clone (lane 1); whereas there was no corresponding band in sample without induction (lane 2) and with empty plasmid (lane 3). This observation indicated that target protein was successfully expressed in *E. coli* BL21 (DE3).

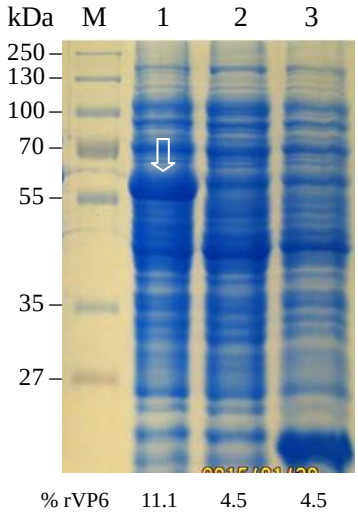

Fig. 1 The SDS-PAGE protein pattern of the control (pET32a) and recombinant (pET32::vp6) *E. coli* extract. Lane M, standard protein ladder (Thermo scientific, USA). Lane 1, 2: the protein extracts from *E. coli* BL21 (DE3) containing recombinant vector pET32*::vp6* with and without IPTG induction, respectively. Lane 3, the protein extracts after induction from *E. coli* BL21 (DE3) containing empty vector pET32. Expected protein band (approximately 62 kDa) was indicated by arrow.

3.2. Optimization of culture conditions for expression of recombinant VP6 protein

3.2.1. The concentration of IPTG inducer

In *E. coli* BL21 (DE3) strain, the gene coding for T7 RNA polymerase is inserted into the genome under the control of *lac* promoter and operator. The gene coding for the lac repressor protein (LacI) is located in both the host chromosome and plasmid. In the absence of inducer, the lac repressor binds to the operator sequence on DNA and prevents transcription of target gene. Whenever the LacI falls of the lac operator sequence of DNA in both the host chromosome and plasmid, the transcription and translation of T7 RNA polymerase and target protein will be occurred. When inducer binds to LacI it changes the conformation in the protein structure and leads to

incapable of binding to the operator DNA sequence. Both lactose and IPTG are inducers for triggering expression of target gene in *E. coli*. Unlike lactose, IPTG is not a substrate and will not broken down or used by the cell. Thus the concentration of IPTG added remains constant. The final concentration of IPTG used in several previous works was varied from 0.1 to 1 mM (Liu and Yang, 2012; Tolia and Joshua-Tor, 2006) and need to be optimized in particular expression system. In order to determine appropriate concentration for induction, a range of 0 – 1.5 mM IPTG was investigated in the present study. The result indicated that the expression level of target protein was different at the different concentrations of IPTG inducer (Fig. 2). The expression level of VP6 protein was increased when the IPTG concentration was changed from 0.01 – 0.05 mM and unchanged in IPTG range of 0.05 – 1.5 mM. Therefore, the appropriate concentration of IPTG used for further experiments was 0.05 mM.

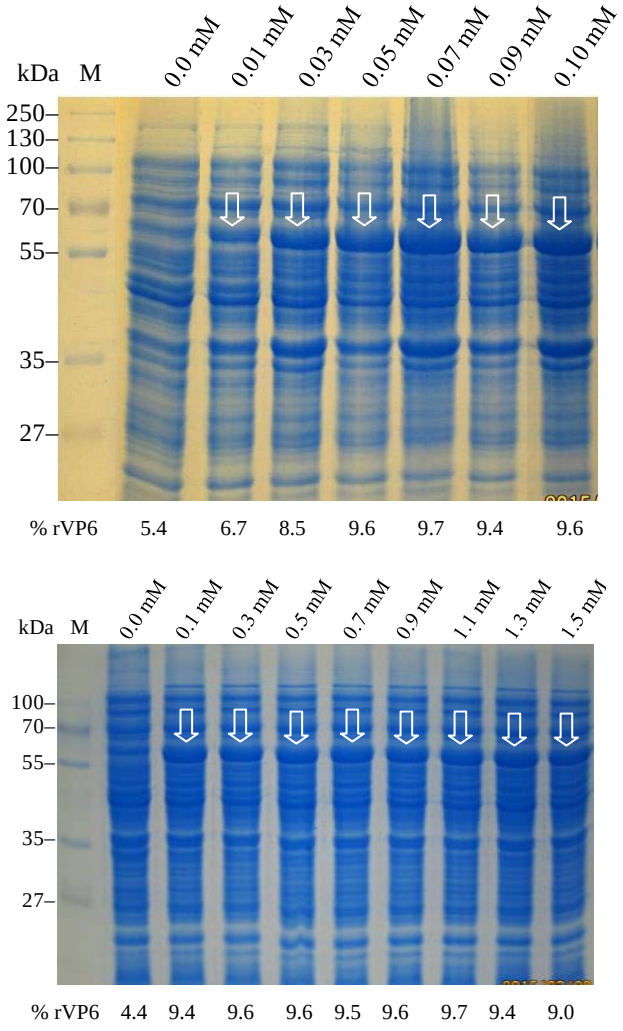

Fig. 2 The SDS-PAGE protein pattern of the extracts at the different IPTG inducer concentrations (0.01, 0.03, 0.05, 0.07, 0.09, 0.1, 0.3, 0.5, 0.7, 0.9, 1.3, 1.5 mM). Lane M, standard protein ladder (Thermo scientific, USA). Expected protein bands (approximately 62 kDa) were indicated by arrow.

3.2.2. Optimization of culture temperature

The temperature is one of the critical factors for bacterial expression of recombinant protein. This factor not only affects on the bacterial growth but also changes the status of recombinant protein. The quick growth of bacteria can induce the formation of inclusion body of target protein. In the present study, expression of recombinant protein was carried out at the different temperatures (20, 25, 30 and 37 ^{o}C). The result showed that the expression levels of VP6 protein were no significant differences between the different culture temperatures (Fig. 3). Observation of the protein pattern (Fig. 3) indicated that recombinant VP6 protein was expressed in an inclusion body form at all investigated culture temperatures. The temperature of 37 ^{o}C was chosen for further experiments.

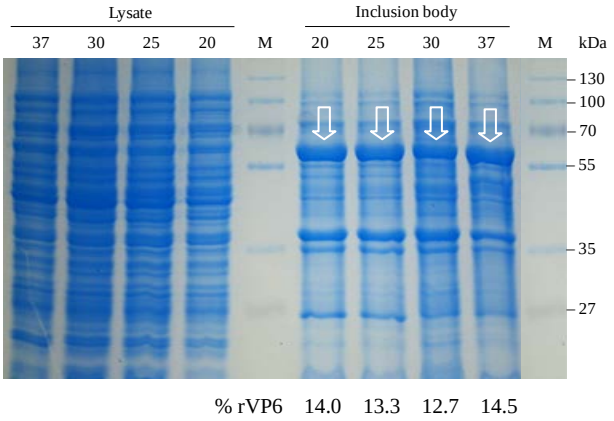

Fig. 3 The SDS-PAGE protein pattern of the extracts at the different culture temperatures (20, 25, 30 and 37^{o}C). Lane M, standard protein ladder (Thermo scientific, USA). Protein extracts were from the cell lysate and inclusion body.

3.2.3. Optimization of induction time

The recombinant *E. coli* BL21 (DE3) strain harboring rotavirus VP6 gene was cultured in LB liquid medium and induced by IPTG for 1, 2, 3, 4, 5 and 18 h.

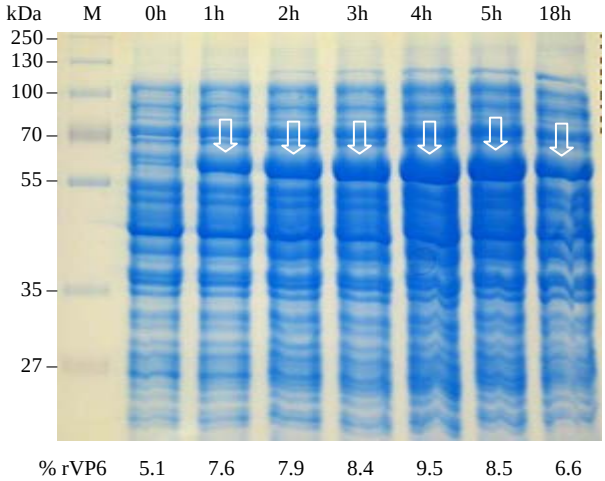

Fig. 4 The SDS-PAGE protein pattern of the extract at the different times of induction (0, 1, 2, 3, 4, 5 and 18 hours). Lane M, standard protein ladder (Thermo scientific, USA). Expected protein bands (approximately 62 kDa) were indicated by arrow.

The result indicated that the expression level of recombinant VP6 protein was increased when increasing the induction time from 0 – 4 h and decreased for longer induction. The decrease of recombinant VP6 protein may be due to the protein degradation in the presence of protease at the late phase of growth.

CONCLUSION

A native VP6 protein was successfully expressed in *E. coli* BL21 (DE3) with optional conditions. The recombinant VP6 protein may be applied in serological assays and vaccine development against rotavirus infection.

REFERENCES

Choi, A.H., Basu, M., McNeal, M.M., Bean, J.A., Clements, J.D., Ward, R.L., 2004, Intranasal administration of an Escherichia coli-expressed codon-optimized rotavirus VP6 protein induces protection in mice. Protein Expr Purif 38, 205-216.

Esteban, L.E., Temprana, C.F., Arguelles, M.H., Glikmann, G., Castello, A.A., 2013, Antigenicity and immunogenicity of rotavirus VP6 protein expressed on the surface of Lactococcus lactis. Biomed Res Int 2013, 298598.

Estes, M.K., Cohen, J., 1989, Rotavirus gene structure and function. Microbiol Rev 53, 410-449.

Lee, S., Belitsky, B.R., Brinker, J.P., Kerstein, K.O., Brown, D.W., Clements, J.D., Keusch, G.T., Tzipori, S., Sonenshein, A.L., Herrmann, J.E., 2010, Development of a Bacillus subtilis-based rotavirus vaccine. Clin Vaccine Immunol 17, 1647-1655.

Liu, Z.Q., Yang, P.C., 2012, Construction of pET-32 alpha (+) Vector for Protein Expression and Purification. N Am J Med Sci 4, 651-655.

Rodriguez-Limas, W.A., Tyo, K.E., Nielsen, J., Ramirez, O.T., Palomares, L.A., 2011, Molecular and process design for rotavirus-like particle production in Saccharomyces cerevisiae. Microb Cell Fact 10, 33.

Sambrook, J., Russell, D.W., 2001, Molecular Cloning: A Laboratory Manual, Vol 1, 3 Edition. Cold Spring Harbor Laboratory Press, New York, 2100 p.

Tang, B., Gilbert, J.M., Matsui, S.M., Greenberg, H.B., 1997, Comparison of the rotavirus gene 6 from different species by sequence analysis and localization of subgroup-specific epitopes using site-directed mutagenesis. Virology 237, 89-96.

Tolia, N.H., Joshua-Tor, L., 2006, Strategies for protein coexpression in Escherichia coli. Nat Methods 3, 55-64.

Ward, R.L., McNeal, M.M., 2010, VP6: A candidate rotavirus vaccine. J Infect Dis 202 Suppl, S101-107.

Acknowledgement:

This works was partially supported by project “Research on the generation of LFA strip for rotavirus detection in the diarrheal children patients” with No.B2014-01-66.

Truong Quoc Phong received the B.S. (2001), M.S. (2004), degrees in Biochemistry from University of Science, Hanoi National University. He received the Doctor degree (2008) in Molecular Biology from Greifswald University, Germnay. He is a Head of Laboratory for Proteomics, Hanoi University of Science and Technology. His current interests include: Production of recombinant proteins/enzymes, Establishment of new methods for rapid test and detection of target organisms, Application of proteomics in biomarker screening and early diagnosis of dangerous human disease.

Robotics and Mechanical Engineering

MODEL-BASED SYSTEM ENGINEERING OF UPPER LIMB SPASTICITY PART-TASK TRAINER

Noor Ayuni Che Zakaria[1,2], Takashi Komeda[1], Cheng Yee Low[2], Kaoru Inoue[3], Fazah Akhtar Hanapiah[4]
[1]Graduate School of Engineering, Shibaura Institute of Technology, Japan
[2]Faculty of Mechanical Engineering, Universiti Teknologi MARA, Malaysia
[3]Division of Occupational Therapists, Tokyo Metropolitan University, Japan
[4]Faculty of Medicine, Universiti Teknologi MARA, Malaysia

Abstract: Physiotherapists and occupational therapists mastering spasticity assessment techniques Modified Ashworth Scale (MAS) and Tardieu Scale based on self-experiences starting from a young novice therapists during their clinical practice in year three undergraduate therapists school. Thus, we have developed an upper limb spasticity part-task trainer to increase the frequency of the novice therapist training as an education tool and licensed therapists as well in order to improve raters' variability in spasticity assessment by repetitively simulate spasticity symptoms through upper limb spasticity part-task trainer. This paper present a model-based system engineering using specification techniques CONSENS^{TM} as a framework to guides the development team in optimizing the different process and the diverse specialization of the members.

1. INTRODUCTION

Following the aviation industry, simulation has been applied in therapy education since 50 years before (Barrows, 1968). Simulated Learning Program (SLP) consists of role playing, e-learning programs, low fidelity mannequins, part-task trainers, student/educators as Standardized Patient, medium fidelity mannequins, Standardized Patient actors, high fidelity mannequins, virtual reality and others in their pre-clinical education program. The areas of which the simulation is used in pre-clinical education programs consists of cardio respiratory, musculoskeletal, neurology, electrotherapy, orthopedics (in patient), pediatrics, and etc. Almost 80% of the SLP is applied during year 3 of therapist bachelor degree (Physiotherapy, 2010). However simulator or part-task trainer of upper limb spasticity has not yet been developed and applied in the SLP. With a goal to develop a new education tool, a team consists of engineers, physician, experience therapists and business unit is needed to make the project a success. Different specialization field need to be balances as each member might have different perspectives in evaluating final value of the development process. Thus, a specification techniques has been implied in this innovation process to guide the team.

2. SPECIFICATION TECHNIQUE CONSENS^{TM}

During designing an advance medical simulator systems for education purposes, a cross-domain system model is importance which combines different aspects of engineering technology, medical knowledge and education comprehension. Therefore we have acquired an

effective and continuous cooperation and communication between development team members during the whole development process. This model-based system engineering provide first analysis on the system level helping in verifying and validating the final output of the system at the designing stage. To establish this requirements, a specification technique called "CONceptual design Specification technique for the ENgineering of complex Systems" abbreviated as CONSENS™ (Gausemeier, Cheng Yee, Steffen, & Deyter, 2008; Jürgen Gausemeier, 2014) was used.

Following the previous example of the implementation of this specification technique in medical device by (Noor Ayuni Che Zakaria, 2012) as a reference, we have started our own model-based system engineering as summarize in Fig. 1. The technique is used to described principle solution to develop an upper limb spasticity part-task trainer for the education purpose. The aspects of functions, active structure, behavior-states, behavior-activities and shapes are exemplified in the next sections.

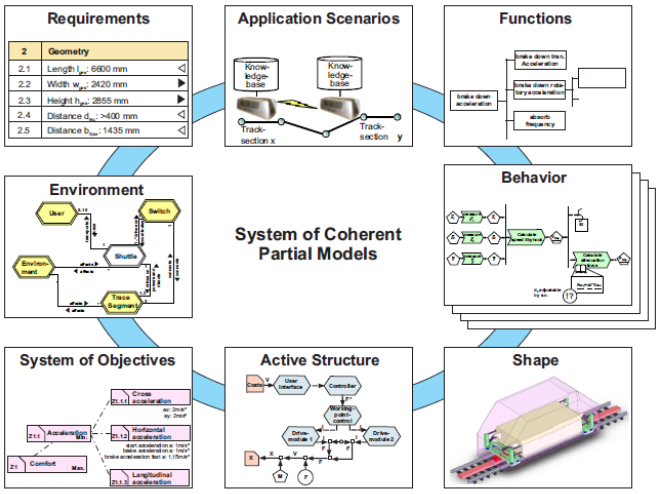

Fig.1 System of coherent partial models based on CONSENS™ technique illustrating details of system behavior, active structure, and other partial models (Gausemeier, et al., 2008; Jürgen Gausemeier, 2014).

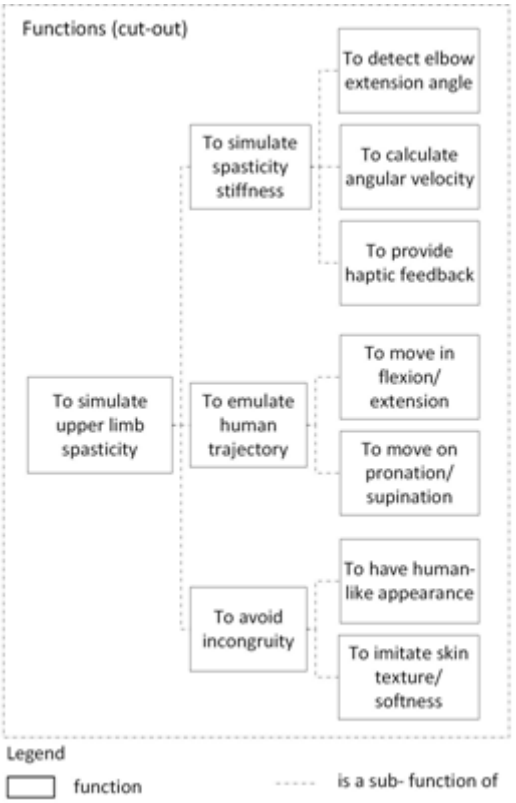

Fig. 2 Functions of upper limb spasticity part-task trainer built based on the specification technique CONSENS™

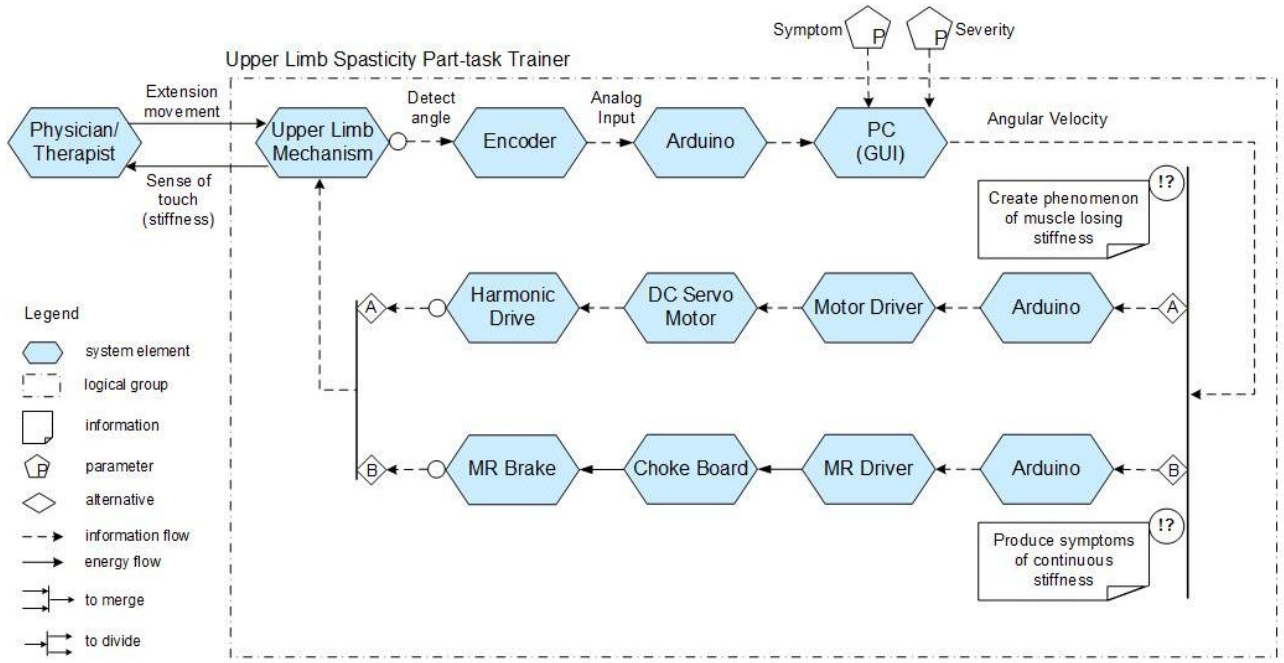

Fig. 3 Active structure of upper limb spasticity part-task trainer

Functions. This section describes functions of upper limb spasticity part-task trainer. The main function of the part-task trainer is to simulate upper limb spasticity. In supporting the main function, it is decomposed into three sub-functions; simulating spasticity stiffness, to emulate human arm trajectory and to avoid incongruity as shown in Fig. 2. To simulate spasticity stiffness, the part-task trainer must be able to detect forearm extension angle, calculate the angular velocity as the spasticity is a velocity-dependent symptom and provide spasticity stiffness based on the calculated angular velocity and angle. For reference, a set of clinical database has been collected (Che Zakaria et al., 2014) to execute a specific spasticity characteristics similar to patient's movement. Additionally, the part-task trainer need to be able to emulate human arm trajectory in flexion/extension and pronation/supination as well as to avoid incongruity, the part-task trainer shall have human-like arm part-task trainer and able to imitate human skin softness as published in (Noor Ayuni binti Che Zakaria, 2014).

Active structure. Active structure is portrayed as system configuration encompasses system elements and their relations. Fig. 3 illustrates the active structure for upper limb spasticity part-task trainer. Prior to physician or therapist manipulating upper limb part-task trainer forearm, encoder will detect the forearm angle input and through Arduino board; an open-source computer platform based on simple micro controller board theory, angular velocity is calculated thus interpreting the haptic feedback output for actuator A or B. Parameter A will activate actuator A and vice versa.

Behavior states. Referring Fig. 4. From the active structure built, we are able to manipulate the states of upper limb part-task trainer based on the clinical data collected. When the part-task trainer detected event E1:Angular velocity $> \omega_c$, the state is changed to fast extension state. Similarly with the event E2 where the angular velocity detected is less than ω_c, the part-task trainer is translated into slow extension state and transferred into constant rigidity movement. ω_c is representing angular velocity when the muscle catch occurred based on the clinical data collected as per sample of one subject shown in Fig. 5. The input inserted during fast extension state and slow extension state are based on the torque T_c and muscle catch angle θ_c from the sample shown.

Shapes. Pursuing the functions listed for the upper limb spasticity part-task trainer, the prototype is built with one Degree Of Freedom (DOF) of elbow joint. Besides flexion and extension, the forearm is able to emulate pronation and supination movement using a spherical bearing placed in the elbow shaft. Fig. 6 shows the developed upper limb spasticity

part-task trainer. Two actuators are selected to simulate spasticity stiffness, Actuator A: DC servo motor (SANYO Corp. L404-011NE) and Actuator B: Magneto Rheological (MR) brake (LORD Corp. RD-2087-01) has been applied in the prototype.

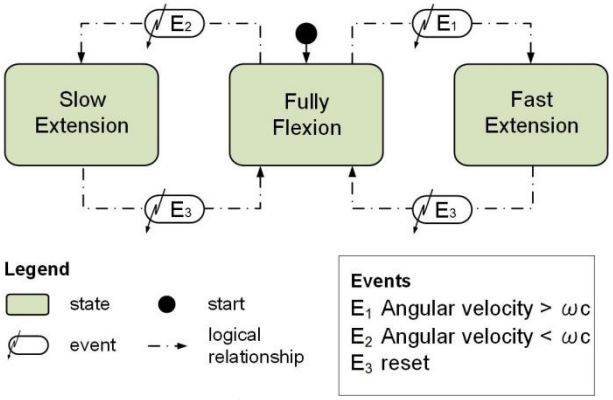

Fig. 4 Behavior states for upper limb spasticity part-task trainer

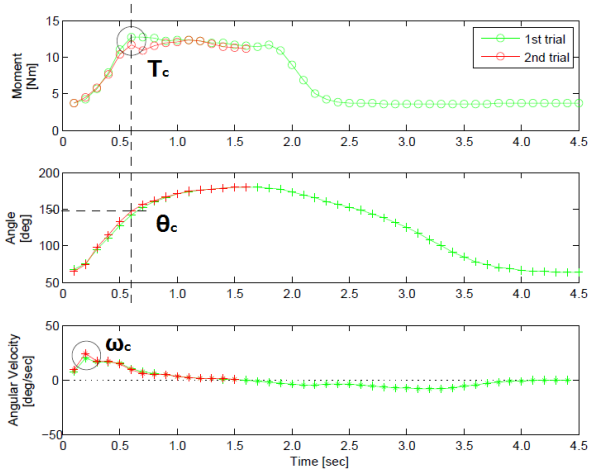

Fig. 5 Sample of clinical data collection showing characteristics of spasticity symptom for Modified Ashworth Scale level 1+.

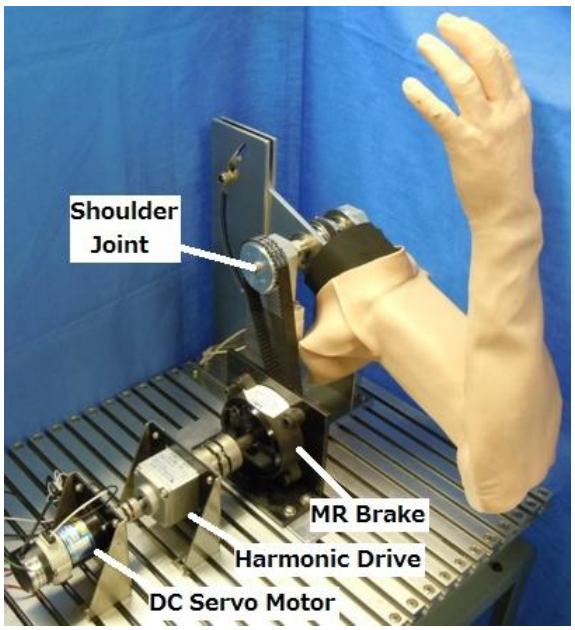

Fig. 6 Upper limb spasticity part-task trainer prototype

3. CONCLUSION

Established from the model-based system engineering rooted from the specification technique CONSENS™, a prototype of upper limb spasticity part-task trainer focusing on therapists education tool has been developed. The reviewed model-based system engineering helps guiding the development team to focus on the same objective without discarding the value of the project. Continuing the completion of the prototype, the controller environment is currently under computation with referring to the behavior-states of the upper limb spasticity part-task trainer. Further evaluation of the hardware and software is needed in assessing the successful of the suggested model-based system engineering.

REFERENCE

Barrows, H. S. (1968). Simulated Patients in Medical Teaching. *Canad. Med. Ass. J., 98*, 674-676.

Che Zakaria, N. A., Low, C. Y., Hanapiah, F. A., Komeda, T., Inoue, K., Shazidi, M. S., & Hamsan, H. M. (2014). Evaluation of Upper Limb Spasticity towards the Development of a High Fidelity Part-task Trainer. *Procedia Technology, 15*(0), 818-827. doi: http://dx.doi.org/10.1016/j.protcy.2014.09.055

Gausemeier, J., Cheng Yee, L., Steffen, D., & Deyter, S. (2008, 7-10 April 2008). *Specifying the Principle Solution in Mechatronic Development Enterprises.* Paper presented at the Systems Conference, 2008 2nd Annual IEEE.

Jürgen Gausemeier, F. J. R., Wilhelm Schäfer. (2014). *Design Methodology for Intelligent Technical Systems: Develop Intelligent Technical Systems of the Future*: Springer Science & Business Media.

Noor Ayuni binti Che Zakaria, T. K., Cheng Yee Low and Kaoru Inoue. (2014). Emulating Upper Limb Disorder for Therapy Education. *Int J Adv Robot Syst, 11*(183). doi: 10.5772/58893

Noor Ayuni Che Zakaria, T. K., Cheng Yee Low, Mohri Makoto, Masayuki Kobayashi, Ahmad Yusri Ismail, Roman Dumitrescu. (2012). Development of foolproof catheter guide system based on mechatronic design. *Production Engineering, 7*(1), 81-90. doi: 10.1007/s11740-012-0430-6

Physiotherapy, C. (2010). Report for Physiotherapy: Health Workforce Australia National Simulated Learning Project.

NOOR AYUNI CZ is currently a Doctoral Candidate in Department of Functional Control System, Shibaura Inst. of Technology. Her research interests is in Rehabilitation Engineering and Human Robot Interaction.

Takashi KOMEDA is the Vice President for Shibaura Inst. of Technology. His research interest is in Medical Engineering consists of patient rehabilitation, mobile robots, neural networks and surgery robotics.

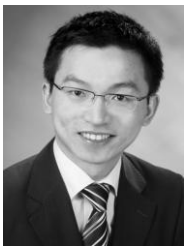

Cheng Yee LOW is a senior lecturer in Faculty of Mechanical Engineering, Universiti Teknologi MARA, Malaysia. His research interest is in mechatronic system, design methodology and rehabilitation engineering.

Kaoru INOUE is a licensed therapists and currently is an Associate Professor in Tokyo Metropolitan University. Her fields of specialties are Occupational Therapy Education, Well-Being Science, Assistive Technology, and adaptation robots for seniors with Dementia.

Fazah Akhtar HANAPIAH is a rehabilitation physician in Universiti Teknologi MARA, Malaysia. Her research interests is in brain injury rehabilitation, cognitive rehabilitation and rehabi-litation medicine.

NUMERICAL SIMULATIONS OF SOLIDIFICATION OF SIMPLE AND COMPOUND DROPS

Truong V. Vu, Anh V. Truong, and Duong K. Tran

School of Transportation Engineering, Hanoi University of Science and Technology, Hanoi, Vietnam

ABSTRACT

We present a front-tracking method for simulating solidification with volume change of simple and compound liquid drops. The interface between two phases is represented by connected points that move on a stationary grid. The solid–liquid interface is propagated with a normal velocity that is calculated from the normal temperature gradient across the front and the latent heat. The liquid–gas front is advected by the velocity interpolated from nearest bulk fluid flow velocities. The evolution of the solid–air front is simply the temporal imprint of the triple point. The Navier–Stokes equations are solved for the whole domain with the zero velocities in the solid phase. The solidified drop shape is strongly affected by the volume change and triple point conditions.

INTRODUCTION

Simple and compound drops appear in various industrial fields such as membrane, chemical, and biochemical technologies as well as metallurgy. In metallurgy, compound drops can be formed by dropping techniques (Vu et al., 2010) in which the drops solidify during falling. This type of solidification is called "containerless solidification", which has been played an important role in producing very pure material since the solid phase comes directly from the melt, which is confined by its own surface tension. Many methods of growing crystals from melts such as Czochralski crystal growth and float-zone processing are based on containerless solidification. The form of the solidified product is determined by the evolution of the solidification interface, i.e. the interface separating the solid and liquid phase, and the tri-junction conditions (Ajaev & Davis, 2004). Density difference between the solid and liquid in conjunction with the tri-junction effect can produce a curious shape with an inflection point near a cusp of a solidified drop (Ajaev & Davis, 2004; Satunkin, 2003). Thus, developing a robust numerical scheme for solidification with volume change and with local contact-line conditions is our main subject.

Several numerical methods have been used for studies of solidification problems such as the front-tracking for dendritic solidification, phase-field method, level-set methods as well as volume of fluid method. However, there are relatively few methods for solidification including volume change and the tri-junction effect. Accordingly, the present work deals with solidification with volume change and the presence of the tri-junction. We base on the front-tracking/finite difference method for dendritic solidification (Al-Rawahi & Tryggvason, 2002) and impose physically motivated and simple tri-junction conditions to simulate drop solidification.

MATHEMATICAL FORMULATION AND NUMERICAL METHOD

Fig. 1 shows an investigated problem where an axisymmetric compound drop is locally cooled at a point *P* on the outer surface. At this point, we impose a total heat flux q_0 as follows (Ajaev & Davis, 2004),

$$\partial T/\partial n = -q_0 e^{-\xi^2/a^2} \Big/ \left(k_s a\sqrt{\pi}\right) \tag{1}$$

where ξ is the distance to *P* along the arc-length of the solid-air interface, *a* the width of the heat flux distribution. And thus, the solidification front propagates, with the normal velocity V_n, from the bottom to the top of the drop

$$V_n = -\dot{q}_f \Big/ \left(\rho_s L_h\right) \tag{2}$$

where

$$\dot{q}_f = k_s \left.\frac{\partial T}{\partial n}\right|_s - k_l \left.\frac{\partial T}{\partial n}\right|_l \tag{3}$$

To track this front as well as other interfaces, we here use the front-tracking method (Tryggvason et al., 2001) in which the interfaces are represented by connected

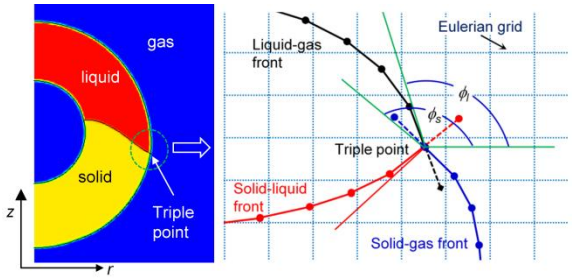

Fig. 1 Containerless solidification of a compound drop: (a) physical representation and (b) computational representation in terms of the front-tracking method.

elements that move on the Eulerian grid. The three phases and their properties such as density ρ, viscosity μ, thermal conductivity k, and specific heat capacity C_p are specified using indicator functions that are determined from known positions of the interface points: the points of the solid–melt and solid–gas fronts are used to construct the indicator I_s (I_s = 0 in solid and I_s = 1 in liquid and gas) while the indicator I_l (I_l = 0 in liquid and solid and I_l = 1 in gas) is built from the points on the solid–gas and melt–gas interfaces. Accordingly, the values of the material property fields at every location are then given by

$$\varphi = \varphi_g I_l + (1-I_l)\left[\varphi_l I_s + (1-I_s)\varphi_s\right] \tag{4}$$

where φ stands for ρ, μ, C_p, or k.

In terms of one-fluid formulation, the governing equations include

$$\frac{\partial(\rho\mathbf{u})}{\partial t} + \nabla\cdot\rho\mathbf{u}\mathbf{u} = -\nabla p + \nabla\cdot\left[\mu\left(\nabla\mathbf{u} + \nabla\mathbf{u}^T\right)\right] + \rho\mathbf{g} + \int_f \sigma\kappa\delta(\mathbf{x}-\mathbf{x}_f)\mathbf{n}_f\, dS \tag{5}$$

$$\frac{\partial}{\partial t}\left(\rho C_p T\right) + \nabla\cdot\left(\rho C_p T\mathbf{u}\right) = \nabla\cdot(k\nabla T) + \int_f \dot{q}_f\delta(\mathbf{x}-\mathbf{x}_f)dS + \int_f q_0\delta(\mathbf{x}-\mathbf{x}_f)dS \tag{6}$$

$$\nabla\cdot\mathbf{u} = \frac{1}{L_h}\left(\frac{1}{\rho_s} - \frac{1}{\rho_l}\right)\int_f \delta(\mathbf{x}-\mathbf{x}_f)\dot{q}_f\, dS \tag{7}$$

Here, $\mathbf{u}$ is the velocity vector, p is the pressure, and $\mathbf{g}$ is the gravitational acceleration. At the interfaces, denoted by f, σ is the interfacial tension acting on the gas–liquid front. κ is twice the mean curvature, and $\mathbf{n}_f$ is the normal vector to the interface. The Dirac delta function $\delta(\mathbf{x}-\mathbf{x}_f)$ is zero everywhere except at the interface $\mathbf{x}_f$. T and the superscript T denote respectively the temperature and the transpose. S indicates the drop and solidification surfaces.. Equation (7) accounts for volume change at the solidification front due to density difference between solid and liquid. The numerical method for the current study is similar to the one used by Esmaeeli and Tryggvason (2004). Detailed description of the method can be found in Esmaeeli and Tryggvason (2004). Here we just describe how we incorporate conditions at the tri-junctions (or triple points in 2D view). We have three types of interfaces. Each is updated as follows. The solidification front propagates with the normal velocity V_n, while the liquid-gas fronts are advected by the velocity interpolated from the fixed grid velocities. At the triple point, where the solidification and liquid-gas fronts meet, we correct the position of this point by applying a constant growth angle (Virozub et al., 2008). We do this by introducing extended lines at the end of each interface lines. We then estimate the tangent vector of each interface at the triple point by fitting a third-order polynomial through the triple point, the other point on the extended line and two adjacent points on the nearest elements. Thereby, the growth angle is defined as $\phi_{gr} = \phi_s - \phi_l$, where ϕ_s and ϕ_l are the angles between the tangent to the solid-air interface and the horizontal and between the tangent to the liquid-air interface and the horizontal. We adjust the position of the triple point to satisfy the prescribed growth angles.

Initially, the drop has spherical interfaces with a small nucleus of solid phase of radius r_0 near the point P. We use initial and boundary conditions near the point P similar to that described in Ajaev & Davis (2004). We fix the values of a and r_0: $r_0 = 0.2R_2$, $a = r_0/10$.

NONDIMENSIONAL PARAMETERS

We choose the outer radius of the compound drop, R_2, as scaling length, and $\tau_c = \rho_l C_{pl} R_2^2/k_l$ as the characteristic time scale. The temperature and the time t are nondimensionalized as $\Theta = (T-T_m)/(q_0R_2/k_l)$, $\tau = t/\tau_c$. With the above choices, it is possible to show that the dynamics of the problem is governed by the following dimensionless parameters: Prandtl number $Pr = C_{pl}\mu_l/k_l$; Stefan number $Pr = C_{pl}q_0R_2/(k_lL_h)$; Weber number $We = k_l^2/(\rho_l\sigma R_2 C_{pl}^2)$; Bond number $Bo = \rho_l g R_2^2/\sigma$; density ratios $\rho_{sl} = \rho_s/\rho_l$ and $\rho_{gl} = \rho_g/\rho_l$; viscosity ratios $\mu_{sl} = \mu_s/\mu_l$ and $\mu_{gl} = \mu_g/\mu_l$; thermal conductivity ratios $k_{sl} = k_s/k_l$ and $k_{gl} = k_g/k_l$; heat capacity ratios $C_{psl} = C_{ps}/C_{pl}$ and $C_{pgl} = C_{pg}/C_{pl}$; and radius ratio $R_{12} = R_1/R_2$.

METHOD VALIDATION

We first compare our computational results with analytical solutions for a 2D Stefan problem (Carslaw & Jaeger, 1986) in which a line heat source Q causes a circular solid seed at the center to evolve in the direction of increasing the radius of the seed. Simulations are performed for this 2D problem set at St = 0.1, 1, and 10. The initial front location and temperature used for simulations are found from the exact solutions at the moment $t = t_0$ when a small, circular solid seed with a radius $r = S(t_0) = 0.1$ has formed. Q is set at 10. Fig. 2 shows that the computational results agree well with the exact solutions at different Stefan numbers.

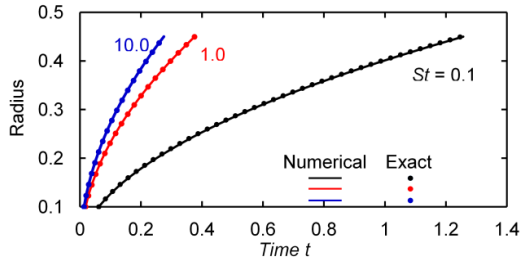

Fig. 2 Comparisons with exact solutions in Carslaw & Jaeger (1986).

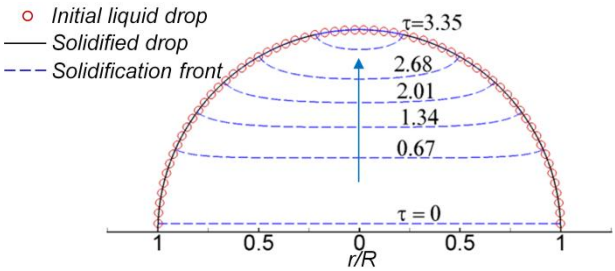

Fig. 3 Method verification with Pr = 0.02, St = 0.1, Bo = 0, We = 1, k_{sl} = 1, k_{gl} = 0.01, $C_{psl} = C_{pgl}$ = 1, μ_{sl} =5, μ_{gl} = 0.1, ρ_{sl} = 1, ρ_{gl} = 0.1 and $\phi_{gr} = 0^0$.

To verify the method, we investigate an axisymmetric drop, at melting temperature T_m, solidifying on a cold plate kept at a temperature $T_c < T_m$. The densities of solid and liquid are equal, i.e. no volume change (Fig. 3). We set the growth angle ϕ_{gr} to 0, and thus the shape of the solidified drop must be the same as that of the initial liquid drop (Ajaev & Davis, 2004). Fig. 3 confirms this.

RESULTS AND DISCUSSIONS

We first consider a typical case of containerless solidification, i.e. a drop solidifying on a cold plate, as exemplified in Fig. 3. Fig. 4 shows solidification of a Si drop on a cold plate with Pr = 0.013, $St = C_{pl}(T_m - T_c)/L_h = 0.116$, $Bo = 0.08$, $We = 0.034$, k_{sl} = 0.5, k_{gl} = 0.01, $C_{psl} = C_{pgl}$ = 1, μ_{sl} = 5, μ_{gl} = 0.05, ρ_{sl} = 0.92, ρ_{gl} = 0.05, and $\phi_{gr} = 10^0$. Here R is the wetting radius of the drop on the plate. The drop initially has a spherical cap. The solid–liquid front is almost flat except near the tri-junction during initial stages of solidification. Because of different densities of the solid and the liquid, the shape of the solidified drop is profoundly different from the liquid one. A set in Fig. 4 indicates that the growth rate is rather high during the initial stages of solidification because of a large temperature gradient. When the solidification front goes further, the solidification rate gradually decreases (Ajaev & Davis, 2004). However, when the drop has nearly solidified, the growth rate again increases since the interface area shrinks to zero (Schultz et al., 2001).

Next, we turn to the cases of compound drops. Fig. 5 shows the solidification process of a compound in which Pr = 0.013, St = 0.00193, Bo = 0, We = 0.094, k_{sl} = 0.5, k_{gl} = 0.01, $C_{psl} = C_{pgl}$ = 1, μ_{sl} = 5, μ_{gl} = 0.05, ρ_{sl} = 0.92, ρ_{gl} = 0.05, $\phi_{gr} = 10^0$ and R_{12} = 0, indicating a case of simple drop (Ajaev & Davis, 2004). The solidification front changes from concave-up to concave-down. A set in Fig. 5 shows the temporal dependence of the average normal velocity of the solidification front, which has a similar history to that in the case of the drop solidifying on a cold plate (Fig. 4). In addition, the solidified drop is about to form a cone near the top.

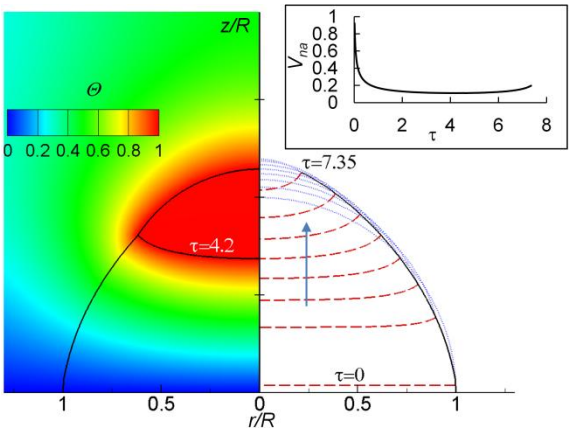

Fig. 4 A Si drop solidifying on a cold plate: left for the temperature field and right for evolution of the solidification front (dash line) plotted every $\Delta\tau = 1.05$. A set shows the time dependence of the average of normal velocities of all points on the solidification front, normalized by $k_l/(\rho_l C_{pl} R)$.

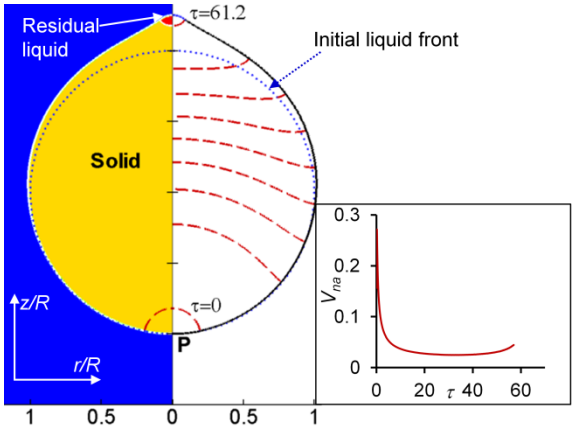

Fig. 5 A spherical Si drop solidifying under zero gravity. The solidification front (dash line) is plotted every $\Delta\tau = 7.65$. A set shows the time dependence of the average of normal velocities of all points on the solidification front, normalized by $k_l/(\rho_l C_{pl} R_2)$.

Fig. 6 shows the solidification process of a compound drop with Pr = 7.25, St = 88.4, Bo = 0, We = 0.0008, k_{sl} = 3.83, k_{gl} = 0.01, C_{psl} = 0.5, C_{pgl} = 0.24, μ_{sl} = 5, μ_{gl} = 0.05, ρ_{sl} = 0.9, ρ_{gl} = 0.05, $\phi_{gr} = 10^0$ and R_{12} = 0.5. Due to volume change and triple effect, the solidified drop has a shape that is different from that of the initial liquid drop. Fig. 6 also indicates that the inner solidified interface that is

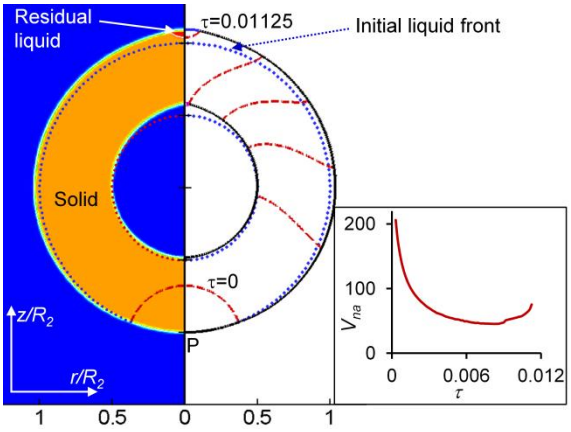

Fig. 6 A spherical compound drop solidifying under zero gravity. The solidification front (dash line) is plotted every $\Delta\tau = 0.00225$. A set shows the time dependence of the average of normal velocities of all points on the solidification front, normalized by $k_l/(\rho_l C_{pl} R_2)$.

similar to the outer solidified interface has moved upward after solidification. This is because of flow induced by volume change at solidification front during the initial stages of solidification. Similarly to the case in Fig. 5, initially, the solidification front propagates fast and slowly in the middle. Its growth rate again increases when the liquid part shrinks to zero. Fig. 6 also confirms that volume change and tri-junction conditions play an important role in the solidified drop shape.

CONCLUSIONS

We have presented simulations of drop solidification with volume change and with triple point effect by the front-tracking method. The solid–liquid and liquid–gas interfaces are updated in different ways while the evolution of the solid–gas interface is determined by the triple point conditions. At this point we applied a constant growth angle. The computational results show that the volume change and tri-junction strongly affect the final shape of the solidified drop that has a cone near the top.

ACKNOWLEDGEMENT

This research is funded by Vietnam National Foundation for Science and Technology Development (NAFOSTED) under grant number 107.03-2014.21

REFERENCES

Ajaev, V.S., and Davis, S.H., The effect of tri-junction conditions in droplet solidification, J. Cryst. Growth, vol. 264, pp. 452–462, 2004.

Al-Rawahi, N., and Tryggvason, G., Numerical simulation of dendritic solidification with convection: two-dimensional geometry, J. Comput. Phys., vol. 180, pp. 471–496, 2002.

Carslaw, H.S., and Jaeger, J.C., Conduction of Heat in Solids, 2nd ed. Oxford University Press, USA, 1986.

Esmaeeli, A., and Tryggvason, G., A front tracking method for computations of boiling in complex geometries, Int. J. Multiph. Flow, vol. 30, pp. 1037–1050, 2004a.

Satunkin, G.A., Determination of growth angles, wetting angles, interfacial tensions and capillary constant values of melts, J. Cryst. Growth, vol. 255, pp. 170–189, 2003.

Schultz, W.W., Worster, M.G., and Anderson, D.M., Solidifying sessile water droplets, in: Interactive Dynamics of Convection and Solidification. Kluwer Academic Publishers, pp. 209–226, 2001.

Tryggvason, G., Bunner, B., Esmaeeli, A., Juric, D., Al-Rawahi, N., Tauber, W., Han, J., Nas, S., and Jan, Y.-J., A front-tracking method for the computations of multiphase flow, J. Comput. Phys., vol. 169, pp. 708–759, 2001.

Virozub, A., Rasin, I.G., and Brandon, S., Revisiting the constant growth angle: Estimation and verification via rigorous thermal modeling, J. Cryst. Growth, vol. 310, pp. 5416–5422, 2008.

Vu, T.V., Takakura, H., Wells, J.C., and Minemoto, T., Production of hollow spheres of eutectic tin-lead solder through a coaxial nozzle, J. Solid Mech. Mater. Eng., vol. 4, pp. 1530–1538, 2010.

Truong V. Vu received the B.E. (2007) degree in mechanical engineering from Hanoi University of Science and Technology (HUST), the M.E (2010) and D.E (2013) degrees in integrated science and engineering from Ritsumeikan University. He is a lecturer, School of Transportation Engineering, HUST. Current interests include multiphase and free surface flows, and numerical methods.

Anh V. Truong received the B.E (1995) degree in mechanical engineering from HUST, the D.E (2004) degree in mechanical engineering from Tohoku University. He is an Asso. Professor, School of Transportation Engineering, HUST. Current interests include cavitations and turbomachines.

Duong K. Tran received the B.E. (2002) degree in mechanical engineering from HUST, the M.E. (2005) degree in mechanical engineering from Bandung Institute of Technology, the D.E (2008) degree from Toyohashi University of Technology. He is a lecturer, School of Transportation Engineering, HUST. Current interests include hydraulic machines and automation equipment.

Proposal of Safety Mechanism for Biped Robot Using a Porous Material

Yoshimichi Kato, Hiroshi Hasegawa
Graduate school of Engineering and Science, Shibaura Institute of Technology

ABSTRACT

Robots are expected to join in not only a great success in industrial field but a public and a home place. However, in order to accept robots socially, when our life space are shared with them, it is essential that a safety is fully obtainable. In this paper, for the development of safety biped robot, we proposed loofahs of the porous material were applied as structural elements for biped robot. In fact, when colliding, it is possible to ease an impact because the loofah is flexible. Through this idea, after 1st prototyping of biped robot using a loofah, we confirmed the walking behavior under a standing situation. However, it was not possible to walk by an implementation of this checked walking behavior. Therefore, in this paper, we improved walking behavior of the prototyping robot via multi-body dynamics simulation, and also discussed these results.

1. INTRODUCTION

Recently, decrease of the working population is regarded as a problem of Japan, because of declining birthrate and a growing proportion of elderly people. As for one solution of this problem, development of service robot which executes person's work is expected as a countermeasure of this problem. This has to realize that people and robot are working in same space efficiently. Under such a situation as this, we can assume increasing in number of accident between human and robot. For solving this problem, many researchers have developed a safety mechanism using sensor systems. However, we can assume that accidents will happen by malfunction of sensors. Therefore, in this paper, we proposed new mechanical design of biped robot what alleviates damage, when a robot came in contact with a person.

2. CONCEPTUAL DESIGN OF BIPED ROBOT

First, we made QFD matrix of a biped robot which coexist with a person (Table 1). As a result, it is assumed that it was necessary to use a material with the lightness and the flexibility for a safe robot. Next, for realizing its objective, saving weight by reducing the number of actuators was drawn as an idea. Moreover, other idea introduced porous material as a material with the flexibility and lightness. Although it is thought that these two ideas are attractive, a biped robot's walking will be difficulty by shortage of stiffness and movable flexibility. Therefore, we tried to develop 1st prototyping of lower leg's robot using porous material structure for verification of walking functionality in this paper.

Tab. 1 Requirements and solution on QFD matrix

		Requirements \ Solutions	Image recognition	Range sensor	Learning function	Avoid obstacle	Use a carbon frame	Use a flexible material	Loading AI	Reduce an actuator	Use a High-performance actuator	Motion near a person	Made a light	Use a High-performance battery	Use a actuatir just for that purpose	Reduce sensor	Use a porous material	Use a inner frame
The robot which can coexist with a person	Hard	Safety	○	◎	○	◎		○				◎	◎			◎	◎	○
		Don't give physical damage	○	○		◎		◎				◎	◎			◎	◎	◎
		The stiffness by which work is possible					○	○			○						×	○
		Flexible joint								×	◎		×		◎			
		Simple structure					×	×		◎								×
		Cheap	×	×	×		×		×	○	×	○		×		○		
		Little energy consumption								○	×	○	○	◎	◎	○		
		Easy to control	○	○					○	◎	○	◎			◎	◎	×	
		Lightness					◎			◎			◎		○		◎	
	Function	Carry things is possible									◎	◎	○		○		×	
		Moving in spite of place is possible										◎	○			◎		
		Exchanged with voice.			◎				◎							◎		
		Clearly image recognition	◎			○			◎							◎		
		Approachability					×	○	○			◎						○
		Learning ability	○		◎				◎									
	Environment	low noise								◎	◎	○	○		○		◎	
		Used material is easy for the environmen					×							◎			◎	
		Don't give psychological fear				○		○				○		○				○

3. POROUS MATERIAL

A porous material for mechanisms of the robot was applied. This porous material is a material with pores into the interior like a sponge, and can change a weight saving and stiffness by changing the size of a pore[1]. For a human safety, we chose a loofah from a porous material. If colliding with person, it is possible to reduce damage through easing an impact by flexible structures of a loofah. In addition, a prototyping is easy because the loofah is cheap and sustainable. As for alternative natural inspired

materials, for example, pumice, activated carbon, bee hive, and bone are existed. These cannot easy buy. For this reason, it is assumed that loofah is most suitable. We can say that this is a sustainable design product inspired by nature.

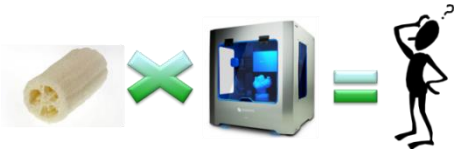

Fig. 1 Prototyping using loofah and 3D printer

4. BIPED ROBOT

Figure 2 shows prototype biped robot using loofah in lower leg. And, standing and walking behaviors of its robot were validated. As the result, standing behavior was able to be performed well. However, walking behavior could not be carried out. These reasons are as follows. A whole Center-Of-Gravity (COG) position is low, since the upper half of the body did not exist. Therefore, the robot structure did not fit for a dynamic walk. Additionally, the sole of the foot area is smaller compared with leg length.

Fig. 2 Prototype biped robot using loofah

5. IMPROVEMENT OF BIPED ROBOT

To realize walking behavior of the biped robot, we improved 1st prototype robot design based on dimensional ratio of human body. The improvement points become two points. The 1st point is to change the area of a foot part. The ideal ratio of leg length to foot area of human becomes 1 to 25 [2]. Therefore, 2.5 times of the current foot area are appropriate to foot area because the leg length and the foot area of robot were 732[mm] and 7,303[mm^2], respectively. Next, a balance weight was carried in the part of the upper half of the body so that the height of COG position is set to 878.4 [mm] because the ideal COG position becomes 1.2 times the height of the length of a leg.

6. SIMULATION

Multi-body dynamics simulation to validate 1st prototype robot's above-improvement was performed. As the result, COG movement to the horizontal direction, which was not carried out before this improvement, was completed. However, after the walk of several steps, its robot simulation model fell down. But, this simulation result showed the big improvement.

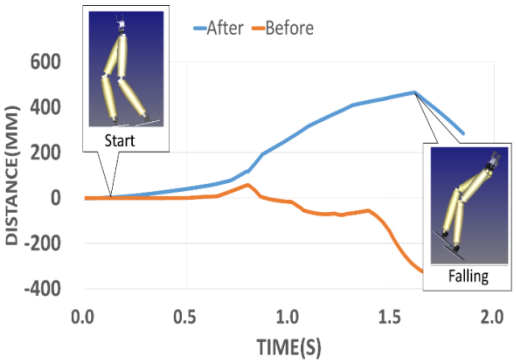

Fig. 3 Multi-body dynamics simulation results

7. CONCLUSION

This study is to design of the biped robot which reduce damage of both human and robots when a robot collided with a person. We designed a robot using loofah is natural porous material with stiffness. In our research, we have improved robot stability by using multi-body dynamics simulation. It was possible to increase walking distance by improving foot area and COG position. However, that stable walking can be performed with limitation in walking distance. From now on, it is necessary to do further improvement of stable walking.

REFERENCES

[1] Kobashi, M., The current state of the porous metal and view, Light Metals, vol.55, no.7, pp.327-332, The Japan Institute of Light Metals, 2005

[2] Obara, J., Uchida, K., Ueno, Y., Hatta, K., A human body is measured, pp.32-42, Japan publishing services Corporation, 1986(in Japanese)

[3] Sugitani, K., Shibukawa, M., Suzuki, T., Kasamatsu, K., On the Relation between the Arm・Swing and the Stability of Walking at Bipedal Locomotion, Human Engineering, vol.37, no.Special issue, pp.442-443, Japan Ergonomics Society, 2010

Yoshimichi Kato received his B.E. (2015) from Shibaura Institute of Technology, Japan. His research interests Creativity of Design for a biped robot. He is master student of Graduate School of Engineering and Science, Shibaura Institute of Technology

Hiroshi Hasegawa received his B.E. (1992) and M.E. (1994) from Shibaura Institute of Technology, Japan. He received Dr. Eng. (1998) in Mechanical Engineering from Tokyo Institute of Technology, Japan. He has been working at Shibaura Institute of Technology, and currently is a Professor.

Safety movement of electrical upper extremity prosthesis

-Development of face position estimation system using low resolution infrared array sensor-

Takuya Yomogi[1], Takashi Komeda[2], Yukio Saito[2]
[1]Graduate School of Engineering and Science, Shibaura Institute of Technology
[2]College of Systems Engineering and Science, Shibaura Institute of Technology

ABSTRACT

Electrical shoulder disarticulation and Electrical above elbow prosthesis is applied to patients with high upper limb amputation. This type of upper extremity prosthesis has a risk of contacting with patients face, because it has a high degree of freedom (DOF) mechanism and larger working area. To ensure safeness, the system should monitor the position of patients face and prevention from contacting with hand need to take place. As methods of estimating the position of the patients face, there are Stereo vision and Time of Flight (TOF). However, we unable install these systems in Electrical upper extremity prosthesis, because it is unsuitable for complex movement of upper extremity prosthesis. As such, measuring image from a single camera can estimate distance towards face by counting extracted pixel. However, there are some limitations on its applicability, critically, it unable to estimate the distance at closest position. To overcome the limitation, here, we report the distance estimation method using low resolution infrared array sensor that can obtain the image parallel to temperature distribution with cost effective and high efficiency.

1. INTRODUCTION

Development of upper extremity prosthesis is crucial to support activities of daily living of the individuals who had lost their motor function of the upper limb, for an example by road traffic accidents, work injury and other diseases [1]. Specifically, an electrical shoulder disarticulation and electrical above elbow prosthesis is applied to the patients with high upper limb amputation to provide better quality of life. This kind of upper extremity prosthesis is developed in the research phase, however, it is not yet for practical applications. Problematic in controlling the prosthesis is the major limitation of the current device in order to ensure safeness.

On the other hand, Kuiken, et al [2] proposed new control method for the shoulder disarticulation amputee. In this study, they used four channels of separated breast muscle in which nerves are innervated. There is a technical advancement in control method, however, still lacking in term of safety measurement to prevent an upper extremity prosthesis from contacting the patient's face. This group ensured safeness by limiting the working range of the device. Thus, this safety measurement will be failed by body movement as the shoulder disarticulation prosthesis is mounted on upper body.

Previous studies have been observed for robot vision to estimate the position of human, namely, stereo vision [3] and TOF [4]. This is the appropriate way to estimate the position of human accurately. However, we cannot install these systems in electrical upper extremity prosthesis, because it is unsuitable for complex movement of upper extremity prosthesis and rather expensive. Measuring image from single camera can approximate the distance towards the face by extracting objective part and relating measured distance to the number of pixels counted as the objective part. Nevertheless, in this method, if the hand extremely comes close to face, the face image will occupy the entire measured images and it is impossible to estimate the distance to the face.

In the current study, we develop the system that monitors the position relation between patient's face and the upper extremity prosthesis in real time, thus identifies the risk of contacting to the patient's face. On the other hand, the infrared array sensor can estimate the distance of variation of temperature associated with movement. Moreover, in the future, the robot may coexist in human living, therefore, this study is important to certify protection and permit effective human-robot interaction.

2. CONFIGURATION OF THE SYSTEM

2.1 Infrared array sensor

We install the infrared array sensor "Grid-Eye", developed by Panasonic CO., LTD, into the system, in order to estimate the distance between the hand and patient's face from variation of temperature. The infrared array sensor can detect the infrared rays which are emitted by an object and output to the distribution of temperature by image information (8×8 pixel). Thus we can estimate distance to the face by the variation of temperature as thermal source. We choose the output of 64 pixel because easier to process than high resolution of the CCD sensor. As such, we can

easily mount the sensor on the hand of upper extremity prosthesis, because the sensor is smaller and cheaper than any other sensors.

Table 1 Specification of infrared array sensor

Type of sensor	Grid-EYE (AMG8831)
Number of pixel	8×8 (64 pixel)
Range of temperture	0～80 [℃]
Angle of view	60 [deg]
Frame rate	10 [fps]
Output resolution	0.25 [℃]
Detection distance	Max. 5 [m]

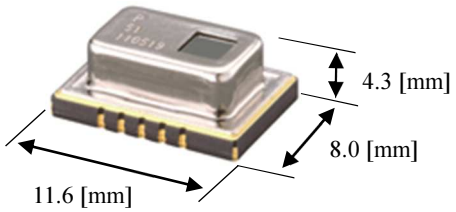

Fig. 1 Overview of infrared array sensor

2.2 Position of use's face estimation system

Figure 1 showed the diagrammatic illustration of the development system. In this system, the infrared array sensor detects temperature and figure of human faces from thermal image of 64 pixel resolution. To ensure safety, we develop the system that monitors the distance between patient's face and the prosthesis in real time for preventing the patient's face from contacting with the device. For the method of position of patient's face estimation, we proposed the new method that relates measured distance to information of sensor in different position, for example D1, D2, D3 (Figure 2). Moreover, we set the minimum distance to the face to evade contacts between patient's face and the device.

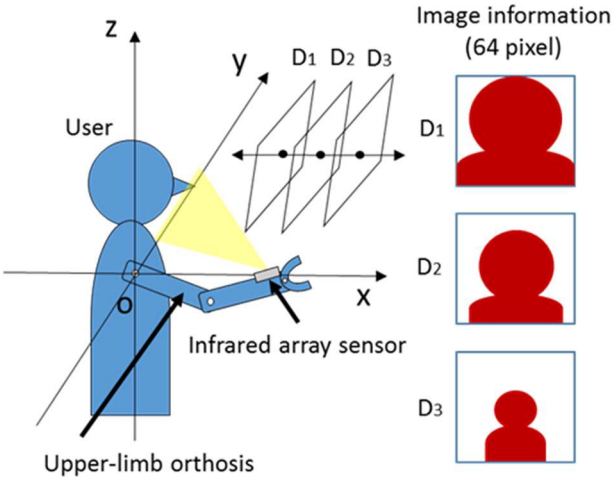

Fig. 2 Diagrammatic illustration of development system

3. Experimental system of measuring image

3.1 System configuration

We conducted the experiment for measuring image in order to estimate the distance corresponding to a pattern of image date. In this experiment, we will obtain a measured image of each coordinate of the hand, using the upper extremity orthosis simulating the use of upper extremity prosthesis. We calculate the coordinates of the hand from a measured joint angle by the potentiometer mounted on each join, by using forward kinematics. Finally, we measure the image of the infrared array sensor in this position coordinate. Figure 3 shows the configuration of experimental systems for measuring image.

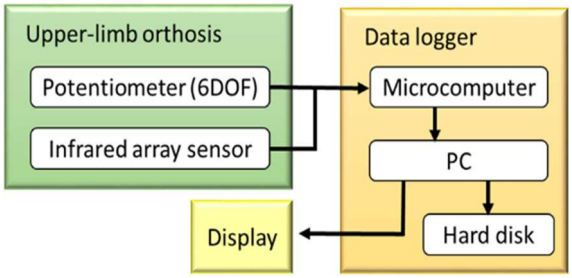

Fig. 3 Experimental system of measuring image

3.2 Configuration of upper extremity orthosis

The orthosis of each joint and rotating part on which we mount 6 numbers of potentiometer can detect the angle of each joint. On the part of extension and flexion of the wrist and the elbow, we adopt the rink mechanism and it detects the angle of them. On the rotating part of the above elbow and the below elbow, we adopt the rotational mechanism using rack and pinion gear mounted on potentiometer and it detects the angle of pronation and supination. On the shoulder part, we adopt the L-shaped rink mechanism and it detects the angle in response to the movement of backward and forward, and lateral. Moreover, we calculate the coordinate of the hand from the angle of joint of 6 DOF, using forward kinematic. Figure 4 shows upper extremity orthosis for experiment that we design.

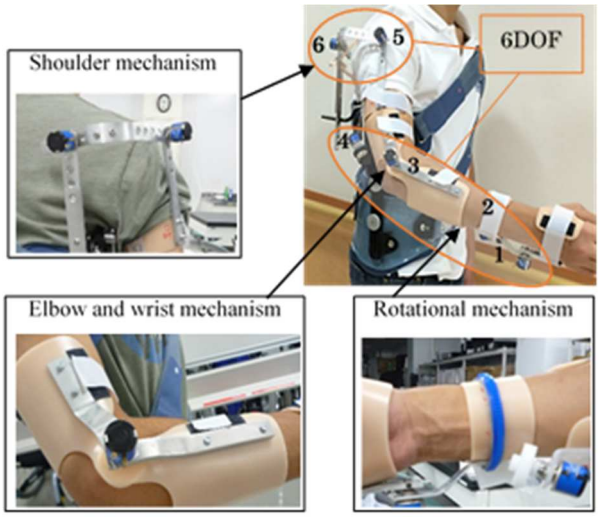

Fig. 4 Upper extremity orthosis for experiment

4. Calibration for estimating distance to face

To approximate the distance to the human face, we operated the experiment to relate measured distance and information of temperature and figure of objective part. We measured frontal view of the human face by the infrared array sensor. The measuring point is at intervals of 10 [mm] ranging from 0 to 300 [mm].

In the maximum distance about 300 [mm] of measured points, the temperature of the objective part is 30 [℃]. Hence, we set 30 [℃] for threshold to extract the objective part from the image. Figure 5 showed the measured image by an infrared array sensor. We measured temperature of the extracted objective (the part of a human face), and calculated distance to the face relating the temperature of extracting part of the distance.

As shown in Figure 6, the mean temperature of extracting pixel was increasing with approaching to the face. In the case that is difficult to recognize the figure of human face, we can estimate the distance. As the result, we adopt approximate curve to calibration date to estimate the distance.

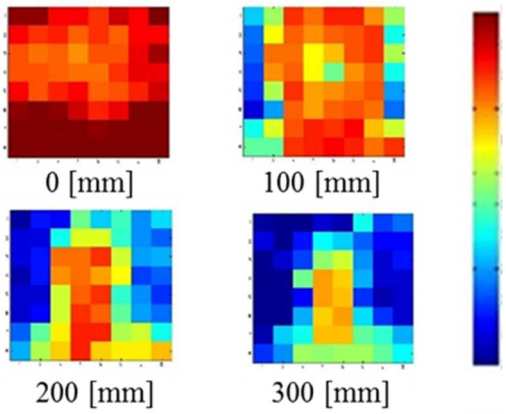

Fig. 5 Measured image by an infrared array sensor

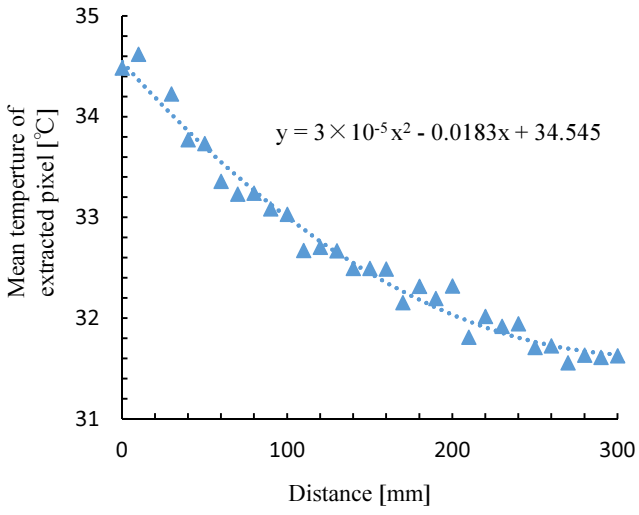

Fig. 6 Calibration date for distance estimation

5. Accuracy evaluation

We conducted the experiment to assess accuracy of the proposed distance estimation method. We measured human face in frontal view using the infrared array sensor and evaluate the distance from the result of calibration. We set five measuring points by the infrared array sensor for evaluation, which is located at 100, 150, 200, 250, 300 [mm] away from the human face, and make comparison of accuracy from absolute error at each point.

Figure7: The result of accurate evaluation of absolute error at each point. Absolute error at measuring points of 100 [mm] and 150 [mm] is lower than 5 [mm]. Therefore, we confirm that this method has high accuracy of closely position. Besides, absolute error was increased above 200 [mm]. We hypothesized that deterioration in accuracy of the distance estimation is caused by noise.

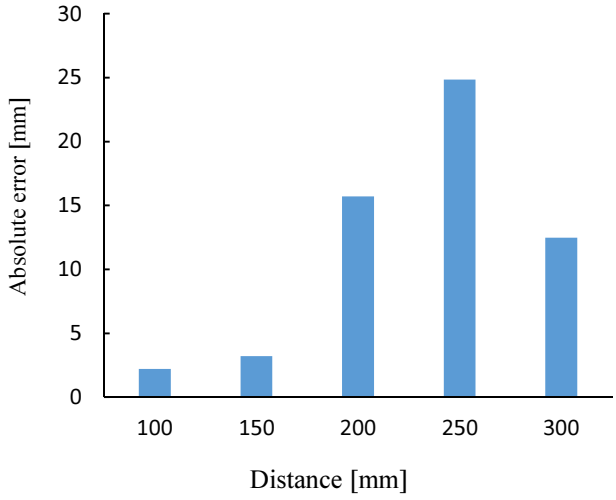

Fig.7 Result of accuracy evaluation

6. Conclusion

We proposed the new method to estimate the distance between the human face and evaluate an accuracy of the measurement, taking into advantages for safeness towards human face. The result of accuracy evaluation showed that the distance estimation method provides optimal accuracy at close range, however it provides low accuracy at distant range. To estimate the distance precisely at distant range, we have to filter out the noise of the image. In the future work, we will conduct experimental of measuring image using the upper extremity orthosis simulating the use of upper extremity prosthesis to estimate the distance in response to a different pattern.

REFERENCES

[1] K. Akazwa, R. Okuno, I. Kikuya. (1999) Present state and future of assistive technology. Present state and future of the research and development of externally powered prosthetic hands and apparatus. BME: biomedical engineering, 13.2, 34-41.

[2] KUIKEN, Todd A., et al. , (2009) Targeted muscle reinnervation for real-time myoelectric control of multifunction artificial arms. Jama, 301.6: 619-628.
[3] Hager, G. D., Chang, W. C., & Morse, A. S. (1995) Robot hand-eye coordination based on stereo vision. Control Systems, *IEEE*, *15*(1), 30-39.
[4] Fuchs S, May S. (2008) Calibration and Registration for Precise Surface Reconstruction with Time‐Of‐FlightCameras. Int. J. Intell. Sys. Tech. Appl. 5(3). pp. 274‐284 (DOI: 10.1504/IJISTA.2008.02129).

Takuya Yomogi received the bachelor degree in bioscience and engineering from Shibaura Institute of Technology in 2014. He is a student of master course at Shibaura Institute of Technology. His interest is mechatronics.

Takashi KOMEDA received the Ph.D. degree from the University of Tokyo in 1987. He became a Lecturer and an Associated Professor at Shibaura Institute of Technology in 1987 and 1990. He has been a full Professor since 1997. His interest is Mechatronics for medical and rehabilitation applications.

DESIGN AND FABRICATION OF ARTIFICIAL SKIN FOR COSMETIC ASSESSMENT

Kantawan Sarasuk[1], Takahiro Kono[2], Kae Nakamura[3], and Jun Yamada[4]

[1-3]Graduate School of Engineering and Science, Shibaura Institute of Technology

[4]College of Engineering, Shibaura Institute of Technology

ABSTRACT

In cosmetics industry, cosmetic companies usually assess the appearance of cosmetics with a visual test on made-up skin, general face skin. However, the skin has different optical characteristics for every individual that the skin appearance can change, and therefore an unreliable assessment results occur. To conduct the visual assessments, it is important to standardize the optical properties of the skin that are used for visual tests. In this study, an artificial skin that has the same optical characteristics as the actual human skin was fabricated. The artificial skin was composed of resin including TiO_2 particles and dyes that scatter and absorb light respectively. The radiative properties of the artificial skin were estimated by an inverse method. The result was concluded that the radiative properties in the artificial skin can be controlled by adjusting the particle and dye concentrations.

1. INTRODUCTION

Foundation makeup causes the skin to appear smooth and uniform by covering blemishes and scars and is important in controlling the perceived skin texture. Besides producing a uniform appearance, foundation also adds shine to the skin causing it to appear young and healthy. Since there is currently no parameter to quantitatively assess the performance of foundation makeup, the development of such a criterion is required.

Until now, foundation performance has been assessed by visual tests on made-up skin. This method yields ambiguous test results because the human skin differs according to the individual and to age. However, before determining an accurate testing method, it is important to standardize the optical properties of the skin that are used for visual tests.

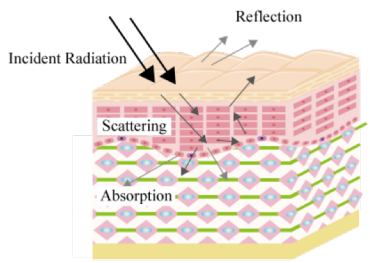

Fig. 1 Light propagation in human skin

Cosmetic companies have attempted to evaluate foundation makeup by applying it on artificial skin fabricated from silicone or urethane resin. However, artificial skin research so far has not adequately replicated the actual human skin because the optical characteristics of these synthetic materials are far from those of the actual skin.

Light propagation in human skin is schematically shown in Fig. 1. When irradiated light incident on the top of skin, 93 - 96% of energy is penetrated into the skin. This means that the appearance of the skin is greatly affected by the behavior of penetrating light that is not absorbed leaves the skin after being scattered numerous times. Therefore, if the light propagation inside the artificial skin behaves like human skin, this artificial skin can be used for evaluating the performance of foundation. The radiation transfer of scattering media as skin may be expressed by the equation [Wilson, B. C., 1986].

$$\frac{1}{\beta_\nu(s)}\frac{dI_\nu(s,\Omega)}{ds}+I_\nu(s,\hat{\Omega})=\frac{\omega}{4\pi}\int_{\Omega'=4\pi}p(\hat{\Omega}'\cdot\hat{\Omega})I_\nu(s,\hat{\Omega})d\Omega'$$

where Ω is a unit vector representing the radiation direction and s is the distance in that direction. This equation includes three radiative properties, namely, the extinction coefficient (β), albedo (ω) and scattering phase function (p). The function p is the angular intensity distribution of light scattered by a particle at all angles and is also called the probability density function, β is the rate at which a light beam is attenuated as a result of scattering and absorption events inside the medium and represents the visual quality of the material, and ω is the ratio of scattering to total extinction (including both absorption and scattering) and represents the brightness and color tone of the material. In order to evaluate the radiation transfer from this equation, it is necessary to determine the values of these properties.

The aim of this work was to fabricate artificial skin with the same optical properties as those of the actual human skin.

2. METHODOLOGY

2.1 Materials

Silicone resin KE-1603A/B (Shin-Etsu Chemical Co., Ltd.), which is translucent, was selected for the artificial skin fabrication. This type of silicone resin is composed of two liquid resins: A and B. The standard ratio between the amounts of the curing agents of A and B is 1:1. The viscosities of A and B are 85 Pa·s and 50 Pa·s, respectively. These materials remain fluid and workable for 90 min at 23°C, and the standard curing time is 24 h at 23°C.

Since the cellular structures and tissues inside the skin cause light scattering and absorption, white particles and dyes, which were assumed to control scattering and absorption, respectively, were added to the silicone resin. The particles studied here were 4-μm diameter Al_2O_3 particles from CB-P05 (Showa Denko K.K.) and 15-nm diameter TiO_2 particles from FINEX50W-LP2 (Sakai Chemical Co., Ltd.). Polylon Dyes of twelve colors were obtained from Tanakanao-Senryoten Co., Ltd.

2.2 Experiments

In the preliminary experiment, scattering and absorption were studied separately. After these properties were determined and applied to the silicone resin, also called the artificial skin, the radiative properties β and ω were estimated by our previous study [Yamada J., 2005], called an inverse method. The details of the preliminary experiments are as follows.

Scattering coefficient: The sample was prepared by mixing the particles into the silicone resin and radiative properties β and ω were then evaluated by an inverse method. To compare the trends in the spectral properties of particles and the human skin, the radiative properties of the samples with Al_2O_3 and TiO_2 particles were measured. The concentration of particles was varied to determine the concentration that would yield the scattering coefficient closest to that of the actual skin. Moreover, as p is a required input of the inverse method, it was measured in our previous study [Naito K., 2010]. We adopted the Henyey-Greenstein (HG) function with the asymmetry factor, g of 0.9, as shown below.

$$p_{HG}(g) = \frac{\left(1-g^2\right)}{\left(1+g^2-2g\cos\theta\right)^{3/2}}$$

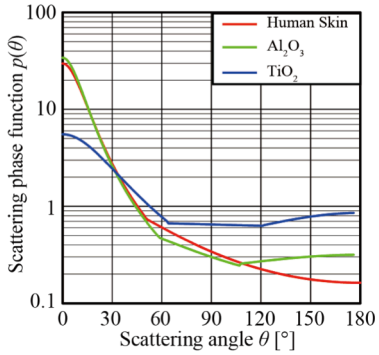

Fig. 2 Scattering phase function

This phase function is often used in numerical simulations of radiation transfer in human skin. The results are shown in Fig. 2.

Absorption coefficient: The absorption coefficients of liquid resin A and B were measured with a spectrophotometer (U-5100, Yamato, Japan). The results demonstrate that the absorption coefficient of liquid resin A tends to follow theory more closely than does that of liquid resin B. We believe this behavior results from a chemical reaction between the dye and liquid resin. Therefore, liquid resin A was selected as the medium. The sample was prepared by mixing dyes into liquid resin A, and then the absorption coefficient was measured with the spectrophotometer. Before measuring, liquid resin A and the dye were thoroughly mixed with a mixer (40-L, Primix, Japan). To understand the effects of dye concentration, the absorption coefficients of all dye colors were measured at concentrations of 0.02 wt.%, 0.04 wt.%, 0.06 wt.%, 0.08 wt.% and 0.10 wt.%. After that, the relationship between the absorption coefficient and concentration was assessed to determine which concentration yielded the best fit to the actual skin data, as simulated by MATLAB with the non-negative least squares (NNLS) method.

After determining the optimum particle and dye concentrations, both the particles and dyes were mixed into the silicone resin. Finally, the radiative properties of the artificial skin were estimated by an inverse method.

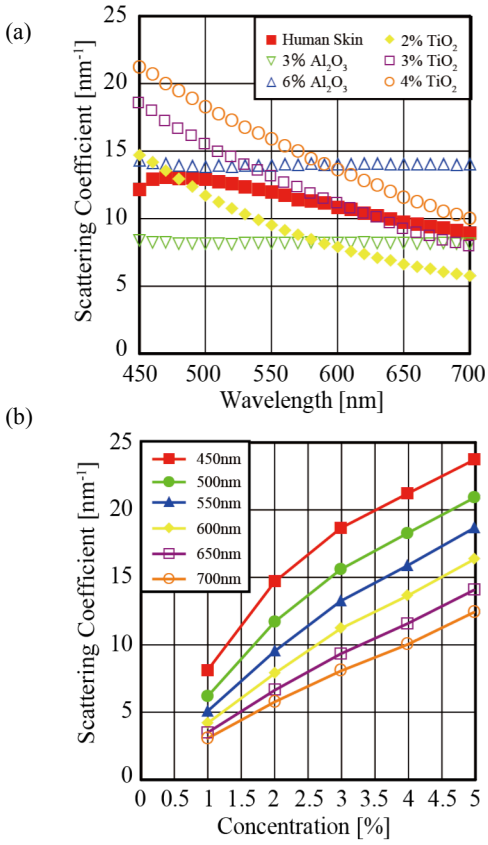

Fig. 3 Scattering coefficients of mixed TiO_2 particles

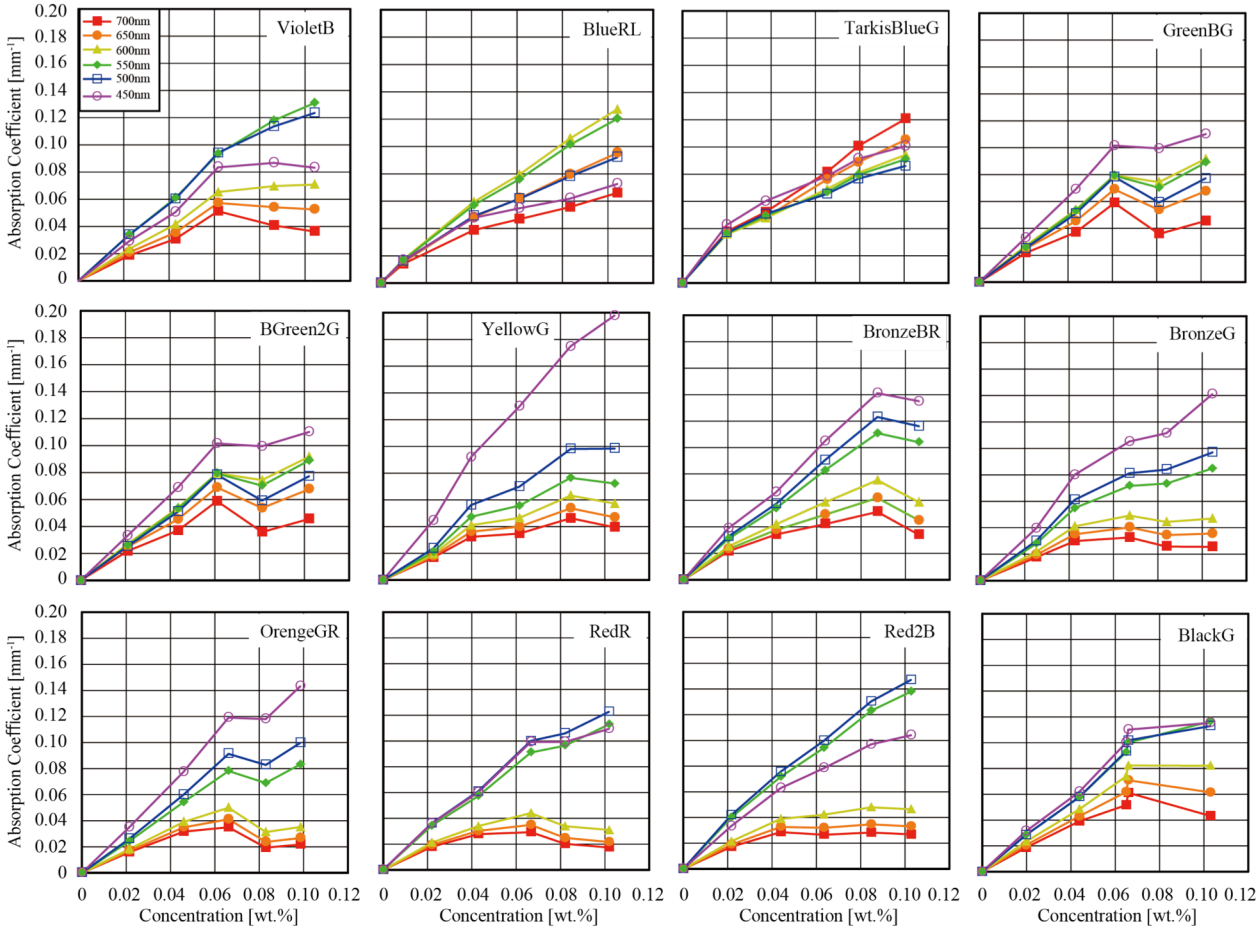

Fig. 4 Absorption coefficients of dyes

3. RESULTS AND DISCUSSION

3.1 Preliminary experiment: scattering coefficient of particles

The scattering coefficients of the materials containing different percentages of Al_2O_3 and TiO_2 particles are shown in Fig. 3(a). The scattering coefficients of 4-μm diameter Al_2O_3 particles follow a straight linear trend, which is different from that of the human skin. In contrast, the trend in the scattering coefficients of 15-nm diameter TiO_2 particles is too steep compared to that of the human skin. Since the trend of the TiO_2 particles is more similar than that of the Al_2O_3 particles to that of the human skin, TiO_2 particles were selected for the artificial skin fabrication. The various concentrations of the mixed TiO_2 particles in the silicone resin are shown in Fig. 3(a). In the intermediate wavelength range of about 500 nm – 600 nm, the scattering coefficient of the human skin is between those of the materials with 2 wt.% and 3 wt.% concentrations of TiO_2 particles. The results at 550 nm were further examined to determine the exact concentration in Fig. 3(b), and it was found that a 2.6 wt.% particle concentration yielded the scattering coefficient closest to that of the human skin.

3.2 Preliminary experiment: absorption coefficient of dyes

The absorption coefficients corresponding to various concentrations of all 12 dyes indicate that they tend to increase with the increasing of concentration. At low concentrations between 0 wt.% and 0.04 wt.%, the absorption coefficient and concentration display a linear relationship, whereas this relationship is not linear at higher concentration as shown in Fig. 4. After the results for each dye were fitted to the corresponding skin data curve simulated by MATLAB with the NNLS method, it was determined that the best fit curve was produced by mixing YellowG and Red2B dyes at concentrations of 0.0525 wt.% and 0.0235 wt.%, respectively. The absorption coefficients of the mixed dye and human skin are shown in Fig. 5. This figure demonstrates that the absorption coefficient of the mixed dye is similar to that of the human skin.

3.3 Artificial skin

The spectral properties of the artificial skin and human skin are shown in Fig. 6. The scattering coefficient trend for the artificial skin is as expected. In

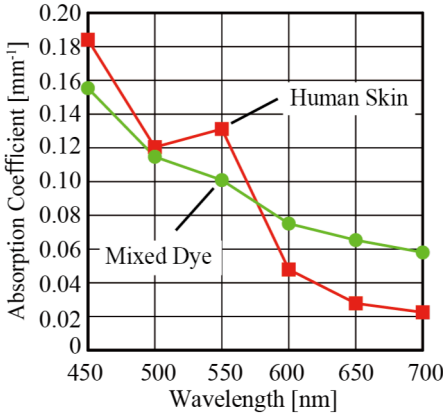

Fig. 5 Comparison of absorption coefficients of human skin and mixed dyes

245

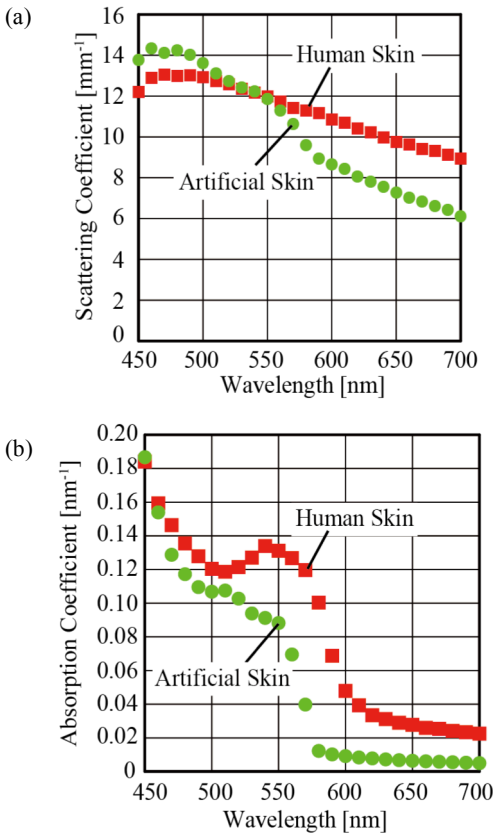

Fig. 6 Radiative properties of the artificial skin and human skin

Fig. 6(a), the coefficient for the artificial skin at a wavelength of 550 nm, which is considered to be the wavelength at which the concentration of TiO_2 particles was determined in the preliminary experiment, is almost identical to the expected coefficient for the human skin. Fig. 6(b) shows the absorption coefficients of the artificial and human skin. The artificial skin line is the result of increasing, by about six times, the dye concentration obtained from the preliminary experiment. In other words, the artificial skin whose properties are shown in Fig. 6(b) had a dye concentration greater than that determined by the preliminary experiment. The absorption coefficient of the artificial skin was not as expected, probably owing to the required use of the scattering phase function in the inverse method, which consequently affected the value of ω. If there was even slight variation in the scattering phase function, the estimated absorption coefficient was affected significantly.

4. CONCLUSION

In this study, artificial skin was fabricated in order to assess the performance of cosmetics. It was concluded that the radiative properties in the artificial skin can be controlled by adjusting the particle and dye concentrations. However, the spectral trend of the absorption coefficient of the artificial skin was not as expected, perhaps because of variations in ω, which is significantly affected by even minor errors in the scattering phase function required in the inverse method. In future work, we will address this issue by studying a variety of particle sizes.

REFERENCES

Naito K., Yamada J., Ogawa K., Takata S., Measurement of scattering phase function of human skin, Japan J. Society of Thermophysics Properties, vol. 24, pp. 101-108, 2010.

Tearney, G. J., Brezinski, M. E., Southern, J. F., Bouma B. E., Hee, M. R., Fujimoto, J. G.; "Determination of the refractive index of highly scattering human tissue by optical coherence tomography", Optics Letters, Vol.20, No.21, pp.2258-2260 1995.

Wilson, B. C., Patterson, M. S.; "The physics of photodynamic therapy", Physics in Medicine and Biology, Vol.31, No.4, pp.327-360, 1986.

Yamada J., Kawamura A., Miura Y., Takaba S., Ogawa K., Study on radiation transfer in human skin for cosmetics, J. Quantitative Spectroscopy & Radiative Transfer, vol. 93, pp.219-230, 2005.

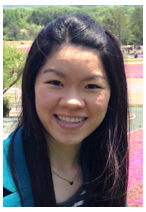

Kantawan Sarasuk received B.E. (2008) in chemical engineering from King Mongkut's University of Technology Thonburi (KMUTT), Thailand, M.E. (2013) in mechanical engineering from Shibaura Institute of Technology and is currently enrolled as a doctoral student at Shibaura Institute of Technology.
Her current interest is radiation transfer in human skin.

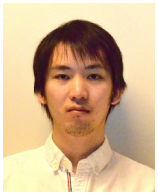

Takahiro Kono received B.E. (2012) and M.E. (2014) in mechanical engineering from Shibaura Institute of Technology and is currently enrolled as a doctoral student at Shibaura Institute of Technology.
His current interest is radiation transfer in human skin.

Kae Nakamura received B.E. (2007) and M.E. (2009) in mechanical engineering from Shibaura Institute of Technology and is currently enrolled as a doctoral student at Shibaura Institute of Technology.
Her current interest is radiation scattering by cosmetic particles.

Jun Yamada received B.E. (1982) and M.E. (1984) and D.E (1994) in Tokyo Institute of Technology. He is a professor of Mechanical Engineering Department, Shibaura Institute of Technology, Japan.
His current interests include radiation transfer in human skin, scattering by cosmetic particles.

A development of Cryogenic Auto - Cascade Refrigeration System

Warangkana Kaewchai[1] and Atikorn Wongsatanawarid[1]
[1]Department of Mechanical Engineering, King Mongkut's University of Technology Thonburi

ABSTRACT

In the present, cryogenic system plays important role in business of industry, medicine, science and also in engineering research. It is well-known that cryogenic system is also crucial to develop various technologies. In Thailand, the cryogenic system is still not widespread in commercial business whereas demand of cryogenic system use is continue increasing and imported technology which is highly cost. In order to replace the imported technology, this study realizes the benefit that will bring new knowledge about cooling system and continue developing.

This research aims to study and design the cryogenic auto-cascade refrigeration system that is operating with refrigerant mixtures and using a single compressor. Refrigerants mixtures compose of Propane (R-290), and Nitrogen (R-728). In the separating process, the condensed refrigerants (liquid) will be removed from the vapor stream so that Propane and Ethane will be used as cooling refrigerants. To design the cryogenic auto-cascade refrigeration system, one compressor will be needed and 2 or more refrigerants will be used to run in the same circuit but no interaction. This study will design for the an auto-cascade refrigeration system that reach a temperature below -40ºC. The problem of the previous heat exchanging effect is overcome by higher heat effectiveness of heat exchanger. The study of optimum refrigerants mixing ratios are carried out to get the lowest evaporating temperature.

1. INTRODUCTION

Recently, cooling system with the temperature below 100 K is important for the preservation of cell reproduction that must be kept at temperature of -196.15 ºC. Using liquid nitrogen and storage of blood cells should be stored at -80°C, as well as examples of microorganisms [2]. In advance materials called superconductor which is zero electrical resistance are also controlled at a very low temperature. High Temperature Superconductor has critical temperature below 90 K [5].

An auto-cascade refrigeration system is commonly used in medical sciences, biological engineering, advance materials engineering and so on. A temperature addresses below 100 K is known as cryogenic temperature which will need unconventional refrigeration system. A modified cascade refrigeration system was commonly used for cryogenic system so-called auto-cascade system consists of single compressor with high pressure ratio [6]. The designated system is advantage for industrial use for widely range of design cooling temperature at the evaporator with only one compressor led the system to easily build and inexpensive.

The auto-cascade system was developed to use mixed refrigerants that are not interact with each other in chemical reaction called zeotropic refrigerants. The refrigerants were studied to proper mix and match to be condensed in the circuit and expanded to use as a cooling fluids [4]. Phase Separator will be also used to divide the refrigerants between liquid and vapor phase [3]. Auto - cascade refrigeration also help to reduce the complexity of general cryogenics cooling system and non-CFCs refrigerants will be used that have less effect to the atmosphere of the Earth. It is said that leaking of CFCs into the environment will destroy ozone in the atmosphere. Therefore, the cooling system will be developed by using a refrigerant that does not contain chloride, fluoride, carbon (non-CFCs) instead of CFCs.

Auto cascade refrigeration system is similar to the cascade refrigeration system in basically operation however the cascade refrigeration needs to use 2 or more compressors for various refrigerants in the different circuits [1]. Another procedure of refrigerant is using mixed refrigerant like zeotropic which is combined two or more refrigerants and it can be separated during the cycle [4]. The separation caused by different thermodynamics property in state of liquid and gas. This research aims to combine two types of refrigerants which are Propane, Ethane and Nitrogen in proper ratios. The expected temperature at evaporator inlet is at least -40ºC.

2. THEORITICAL DESIGN

2.1 Auto-cascade refrigeration system

The auto-cascade refrigeration system is operating with refrigerant mixtures and using a single compressor. There is phase separator which removes liquid refrigerants from the vapor.

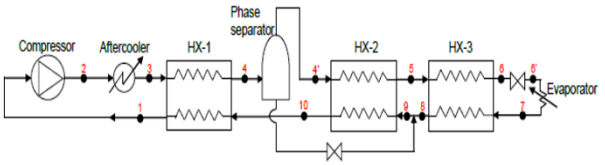

Fig.1 Auto-cascade refrigeration system

In the first stage at the compressor inlet, the mixed refrigerants consisted of propane, ethane, methane and nitrogen are all in vapor, which will be compressed to the high pressure side. The propane has the highest

boiling point, followed by ethane, methane and nitrogen at the same pressure. When the pressure is high enough to atmospheric temperature, propane and ethane refrigerant will be condensed to a liquid. All mixed refrigerants are firstly cooled in after-cooler with the cooling iced-water. Thereafter all refrigerants enter to 1st heat exchanger, which is cooled by low pressure refrigerants on the way back to the compressor, propane and ethane are condensed out at the phase separator. For methane and nitrogen refrigerant, it is still in the gas phase and then flows into phase separator. Only methane and nitrogen flow into the 2nd heat exchanger. Then it is continued flowing through the downstream at each heat exchanger that it will be cooled down by refrigerants at the low pressure side. After the 3rd heat exchanger the methane will be cooled down to the liquid phase mixed with nitrogen gas and led to the expansion valve. Since the liquid methane throttling to the lower pressure, it is ready to absorb heat from the evaporator and vaporize again. The refrigerants flow back to the other side of heat exchanger receiving heat along the flow and back to the compressor.

2.2 Thermodynamic state calculation

- Compressor discharge pressure is 21 bara and suction pressure 4 bara.
- Designed evaporator Temperature is -60ºC
- The refrigerants mixing ratio as shown in table 1;

Table 1 Ratio by mass of mixed refrigerant

Mixed Refrigerant	Ratio by mass (%)
Propane	25
Nitrogen	75

3. EXPERIMENTAL SETUP

3.1 Experimental Apparatus

The designed auto-cascade system composed of only one reciprocating compressor (Bitzer II) with welded plate heat exchanger to use as a condenser at cascading pressure. The evaporator is a simple helical coil of a copper tube such as use in a cold head. The expansion valves use of diaphragm pressure reduction for a simple throttling process. The system schematic diagram is shown in Fig.2.

3.2 Data acquisition

3.2.1. Temperature

Temperature data will be recorded by measuring the temperature of the inlet and outlet of 3 heat exchanger and evaporator which its target temperature is the lowest temperature at the evaporator with time interval of 1 second.

3.2.2. Pressure

Pressure data will be collected using pressure gauge. Importantly, pressure measurement is to prevent damage from the over-limit pressure within the system of the compressor, and also to recalculate the actual operating conditions in comparison of the design data.

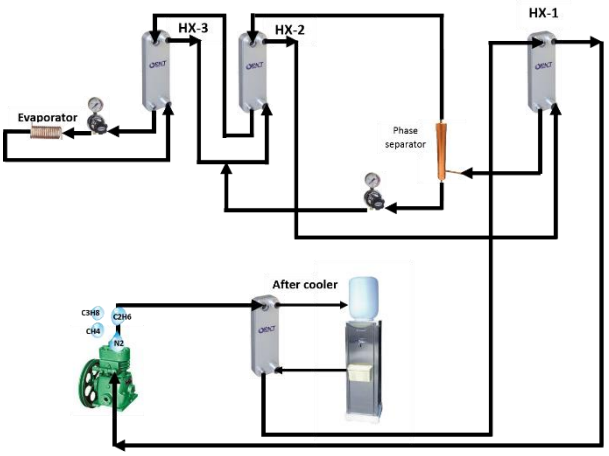

Fig.**2** Schematic diagram of auto-cascade refrigeration system

4. Results and discussion

The system is studied to obtain the optimum conditions within the range of workable pressure. Then the experiment was carried out at difference Low Pressure (L.P.)-High Pressure (H.P.) conditions. The obtained lowest temperature at the difference of operation condition is shown in table 2

Table 2 The lowest evaporator temperature at various conditions

Low Pressure side (bara)	High Pressure side (bara)	Evaporator temp. (ºC)
2	8	-44.3
3	11	-37.6
4	15	-33.9

The evaporator as shown in the table is measured at the surface of the copper tube which is a bit higher than the actual temperature of the refrigerants inside of the tube. The actual temperature of refrigerant is rather difficult to measure which the system is operated in the high pressure. The leakage of refrigerants is unacceptable that will affect the mass flow rate of the system and cooling capacity. The temperature trend when started of the operation is shown in Fig.3. We could achieve the lowest temperature within about 10 minutes.

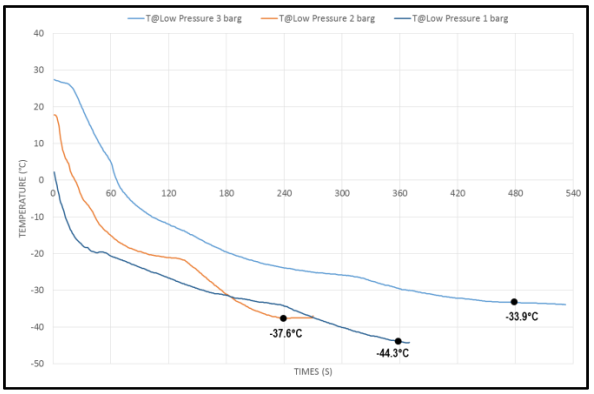

Fig.**3** The evaporator temperature descending of the operation at difference pressure

CONCLUSION

The study of auto-cascade refrigeration system using mixed R-728 : R-290 at 75:25 percentage by mass is possible for the minimum evaporating temperature of -44ºC at 1 barg. The system is simply used single reciprocating compressor with plate heat exchanger for high performance stage cooling. The designed auto-cascade system could reduce the complexity of refrigerants mixing which is cheaper and easily found in the commercial market in comparison to conventional cascading refrigeration system R-22/R-23 at the same operating temperature.

REFERENCES

[1] Kai Du, Shaoqian Zhang, Weirong Xu, Xiaofeng Niu, 2009, "A study on the cycle characteristics of an auto-cascade refrigeration system", Experimental Thermal and Fluid Science, Vol.33, pp.240-245.

[2] Maoqiong Gong, Jianfeng Wu, Quiwei Cheng, Zhaohu Sun, Jiayong Liu, Qinguo Hu, 2012, "Development of a -186°C cryogenic preservation chamber based on a dual mixed-gases Joule-Thomson refrigeration cycle",

[3] M.Q. Gong, J.F. Wu, E.G. Luo, 2004, "Performances of the mixed-gases Joule–Thomson refrigeration cycles for cooling fixed-temperature heat loads", Cryogenics, Vol.44, pp. 847-857.

[4] H. Gurudath Nayak, G. Venkatarathnam, 2009, "Performance of an auto refrigerant cascade refrigerator operating in gas refrigerant supply (GRS) mode with nitrogen–hydrocarbon and argon–hydrocarbon refrigerants", Cryogenics, Vol.49, pp.350-359.

[5] Jisung Lee, Gyuwan Hwang, Sangkwon Jeong, Byung Jun Park, Young Hee Han,2011 , "Design of high efficiency mixed refrigerant Joule–Thomson refrigerator for cooling HTS cable", Cryogenics, Vol.51, pp.408-414.

[6] Qin Wang, Rui Liu, JiangPu Wang, FuSheng Chen, XiaoHong Han, GuangMing Chen,2012 , "An investigation of the mixing position in the recuperators on the performance of an auto-cascade refrigerator operating with a rectifying column", Cryogenics, Vol.52, pp.581-589.

Miss.Warangkana Kaewchai received B.E.(2012) in mechanical engineering. She is now a second year master student in department of mechanical engineering, KMUTT

Mr.Atikorn Wongsatanawarid received B.E.(2000) from KMUTT, M.E. (2006) from Chulalongkorn University in mechanical engineering, and Dr.Eng. (2010) from Shibaura Institute of Technology, Japan. Recently, he is a lecturer in department of mechanical engineering, KMUTT

DEVELOPMENT OF MASTER SLAVE SYSTEM FOR CATHETER GUIDE -DEVELOPMENT OF MASTER WITH FORCE SENSOR-

Mio Watanabe[1], Makoto Mohri[2], Takashi Komeda[1,3]
[1]Graduate School of Engineering and Science, Shibaura Institute of Technology
[2]Mohri hospital
[3]College of Systems Engineering and Science, Shibaura Institute of Technology

ABSTRACT

The development of the master-slave system for catheter guide is crucial nowadays in order to minimize a risk of X-ray exposure to the surgeons during the interventional radiology operation. For the purpose of the operation using this system, detecting the reaction force obtained from the catheter is needed to perform the operation with high safety and operability. In this paper, we developed the force sensor for the Master; consist of two-degree-of-freedom, easy to operate, and it can perform catheterization with an operability with a sense of reality. In this system, the linear force display will use the collet chuck, while rotational force display will used motor control. Here, we did an evaluation experiment of force sensor, and the results present the performance of the force sensor of the master-slave.

1. INTRODUCTION

In recent years, minimally invasive surgeries have been established as a new surgical procedure. As an example, Interventional Radiology (IVR) is one of minimally invasive surgeries utilized a catheter and needle while observing X-Ray transparent images, vessel angiogram, ultrasonic images and CT images [1]. When a physician performs IVR, Digital Subtraction Angiography (DSA) will be employed that can gain X-Ray only to the specific vessel. However, DSA has the risk of the exposure to the X-Ray's radiation for medical service workers because it radiates in a continuous way. In present situations, the physician wear a hazmat leady suit to decrease the exposure during an operation. Nevertheless, this is not practicable as limit the movement and face and arms are still exposed to the X-Ray's radiation. In the view of keeping a distance from X-Ray, the master-slave system urgently needed for the physician to operate the catheter remotely without risk of exposure [2].

The objective of this study is to develop a master-slave system with a force sensor that can perform a catheterization with realistic sensation, in order to solve the problem of the exposure to the X-Ray's radiation for physicians.

2. EXISTING SYSTEM

The existing master-slave system can control force and position information at the same time (Fig.1) [3]. In this system, the operator uses master to drive the position commands of catheter to PC. Then, the command is directed to the motor driver of slave from the D/A Board as position signal, then the slave will operate catheter. After that force detector mechanism will detects force from the catheter, then send to PC. Finally, the force signal sends to master from the D/A Board as force display signal, thus the operator can know the force from the catheter.

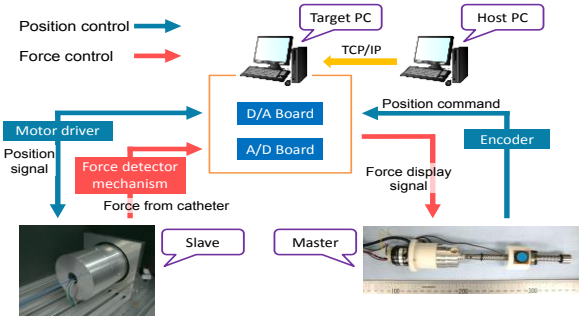

Fig1 Existing Master Slave system [3]

Table1. The proposed specifications [3]

	Linear	Rotational
Force/torque display to the doctor	2.0 [N]	2.0 [mNm]
Force display speed	150 [msec]	

3. CONCEPTUAL DESIGN

The physician operates master, so it has to reproduce real operating catheter. Existing master was not practicable as complicate by division into linear and rotational operation part. The new developed system has taken advantage of the concept of new force sensor for the master- system:

(1) It has two degrees of freedom

(2) It is easy to operate by integration of linear and rotational operation part

(3) It can perform catheterization with operability with a sense of reality using the force display from slave to master.

(4) Miniaturization and lightweight by using the small motor and resin gear.

When a physician performs IVR, the force of about 2 [N] will be displayed from the catheter [3]. In addition, user can control the force display speed at maximum as 150 [msec] [3]. Therefore, we proposed the new force sensor for master as shown in Table1.

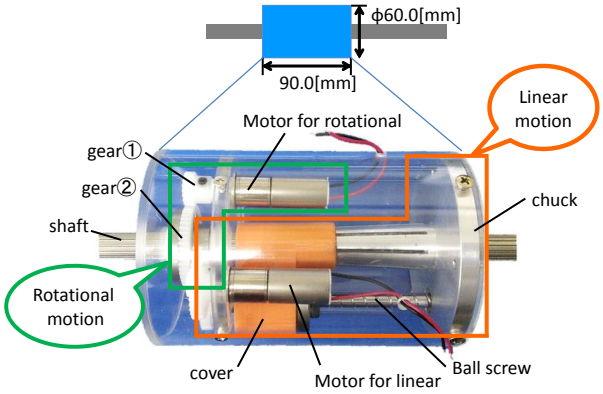

Fig. 2 New force sensor for master

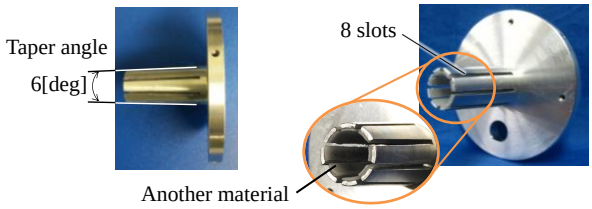

Fig. 3 Chuck for linear motion

4. DEVELOPEMENT OF FORCE SENSOR

From the concept, we developed new force sensor for master (Fig.2). The greatest diameter is 60 mm, length is 90 mm and weight is 300 [g]. The newly developed force sensor consists of two parts: linear motion and rotational motion.

Linear motion is made up of cover, motor, ball screw and chuck. Linear motion uses the collet chuck. The cover moves by the ball screw when the catheter gets into touch with blood vessel wall. The chuck has 8 slots and taper of the chuck is 6 [deg] (Fig.3). Therefore, it can close chuck by uniform pressure and it produced moving area that grasps the shaft.

Rotational motion is made up of two gears and motors. The gears control of the motor when the catheter gets into touch with blood vessel wall. We used resin gears and the spline-processed shaft that makes the gear2 possible to move specific on linear motion.

4.1 FORCE FEEDBACK OF LINEAR MOTION

Using this system, physicians can operate linear motion with open chuck. Firstly, the motion sends to slave as position command. However, if force detector mechanism detects the catheter gets into touch with blood vessel wall, the chuck will close and grasps the shaft by movement of the cover. To overcome the problem, this system will get rid of the blood vessel wall, to ensure the system performance optimization.

4.2 FORCE FEEDBACK OF ROTATIONAL MOTION

The physician can operate non-energizing type of rotational motion. The motion sends to slave as position command. However, if force detector mechanism detects that the catheter gets into touch with blood vessel wall,

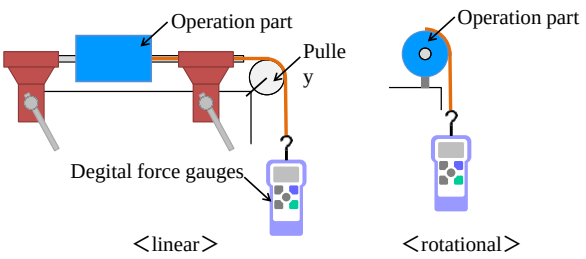

Fig. 4 Experimental methodology

the motor will controlled with energizing. We override this problem by avoiding the blood vessel wall, thus it can function as a non-energizing system.

5. EVALUATION EXPERIMENT

5.1 METHOD

We determined the linear and rotational force display in order to evaluate the force sensor. Thereby, we can determine the operating part at the level we have successfully avoided the blood vessel wall. To measure this, we place digital force gauges the end of the operation part (Fig.4). After that, we determine the value of the digital force gauges during when operational movements. In linear force display, we compared the default position of cover with the limit position of cover that can move by motor. While in a rotational force display, we compared energizing with non-energizing systems. The experiment was replicated 20 times each.

5.2 RESULT

In linear force display, the limit position of cover was 9.8[mm] from the default position. And the experimental result of linear and rotational is 2.3 [N] and 21.1 [mNm] respectively. Therefor linear and rotational force display fulfilled the proposed specifications of the new force sensor. The experimental results also showed the applicability of the force sensor of master-slave system

6. REDESIGN OF FORCE SENSOR FOR LINEAR MOTION

Linear force display fulfilled the proposed specifications of the force sensor. However, we were redesigning the cover and chuck to improve the performance in term of the maximum force of linear motion. Thereby, it may decrease the risk of penetration of the catheter into the vessel wall when it gets into contact by amplifying the force display.

Consequently, we improve the maximum force of linear motion by applying two type taper angle inside the cover. One of the taper angle is 6 [deg], the other is 12 [deg] (Fig. 5). Those angles were determined by pre and post-closing the chuck's taper angle.

Beside, we tried to improve the maximum force of linear motion by modifying the material inside chuck from fluorine to Chloroprene rubber. Chloroprene rubber is used for the wet suit of Scuba diving and it has high friction and elastic force. Moreover, we tried to improve the maximum force of linear by changing width between slot and slot from 1.0 [mm] to 1.5 [mm] (Fig.6).

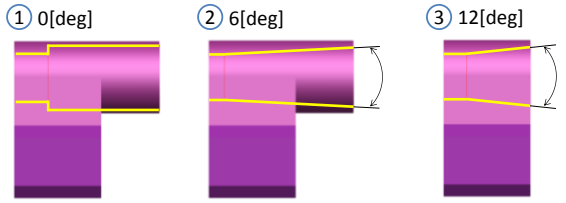

Fig.5 Redesign of cover
(Taper angle inside cover is 0 [deg], 6 [deg] and 12 [deg])

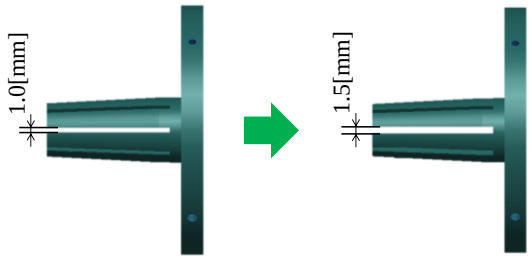

Fig.6 Redesign of chuck

Table 2 Combination of cover and chuck

	<cover>	<chuck>	
	Taper angle [deg]	Material	Width [mm]
(a)	0	fluorine	1.0
(b)	0	chloroprene rubber	1.0
(c)	0	chloroprene rubber	1.5
(d)	6	chloroprene rubber	1.5
(e)	12	chloroprene rubber	1.5

We determined the linear force display in order to compare various force sensors. Thereby, we can know which combination of cover and chuck generate the optimum performance of the master's force sensor.

6.1 EXPERIMENTS FOR COMPARING

To compare of various covers and chucks (Table 2) we place digital force gauges at the end of the operation part (Fig. 4). After that, we measure the value of the digital force gauges when operation moves. In linear force display, we compared the default position of cover with the limit position of cover that can move by motor. This trial was repeated 5 times.

Firstly, we compare between (a) and (b), it can evaluate the best possible material inside the chuck. The experimental results of (a) is 2.3 [N] and (b) is 3.8 [N] (Fig. 7). Therefore (a) and (b) force display fulfilled the proposed specifications of force sensor, and Chloroprene rubber able to improve the maximum force of linear than fluorine.

Secondly, we compare between (b) and (c). The information about the optimal width between slot and a slot for chuck will be obtained. The experimental result of (c) is 5.5 [N] (Fig. 7). Therefor (b) and (c) force display fulfilled the proposed specifications of force sensor, and width between slot is 1.5 [mm] able to advance the maximum force of linear compared to the width between slot of 1.0 [mm].

Lastly, we compare between (d) and (e), it can evaluate the best performance of the taper angle inside the cover. The experimental result of (d) is 4.6 [N] and (e) is 7.6 [N] (Fig. 7). Therefore (d) and (e) force display fulfilled the proposed specifications of the force sensor.

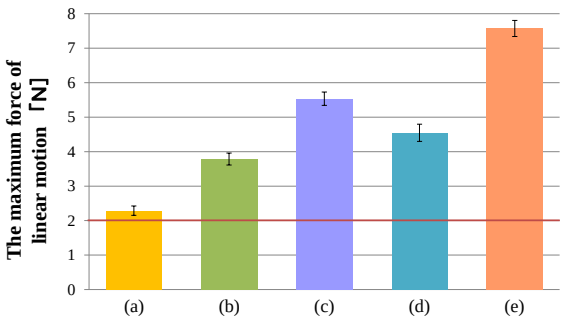

Fig.7 The experimental result

Thus, taper angle inside cover of 12 [deg] able to expand the maximum force of linear compared to 6 [deg].

From the results, total performance was shown by type (e) for the force sensor of the master-slave system.

CONCLUSION

We have developed force sensor for the master-slave system. The linear force display utilized the collet chuck, and rotational force display utilized motor control system. The experimental results showed the performance the force sensor of the system. Generally, the master's force sensor was used in this system.

Moreover, we were redesigning the cover and chuck to improve the maximum performance force of linear motion. Thus, it may decrease the risk of the penetration of the catheter into the vessel wall when it was in contact by amplifying the force display. This problem was overcome by modifying the taper angle inside cover, changing the material inside chuck and altering width between slots. The experimental results showed (e) is the optimal performance of the force sensor of the master.

However, the force sensor still has several limitations. The greatest diameter is 60mm, length is 90mm and weight is 300 [g], so it is not miniaturization and lightweight to provide wide application in medical utilization. Therefore, future studies needed to reselect parts and change form of chuck in order to provide the upgraded force display.

Subsequently, it is recommended to perform an experiments when chuck is closed and grasps the shaft by movement of middle position of cover. If it is possible, the force sensor of linear motion can change force display, so it can reproduce real operating catheter for the physician.

Moreover, newly developed master-slave systems still lacking of the position sensor and the demand for future works.

REFERENCES

[1] The Japanese Society Interventional Radiology, brochure for IVR
<Http:
//www.jsivr.jp/kouhoukara/kouhoukara.html>
[2] H.Nakamura, A.Togashi, K.Morozumi, IVR no Rinsyo to Hibaku Bougo, Iryo Kagakusya,(2004) pp.11-18, p.24
[3] Masaru Ide, Development of Master Slave system, Shibaura Institute of Technology (2002)

Mio WATANABE received the bachelor's degree (2014) in engineering from the Department of Bioscience and Engineering, SIT. She is a Master's student of SIT. Her interest is the development of a Master Slave system for catheter guide.

Takashi KOMEDA received the Ph.D. degree from the University of Tokyo in 1987. He became a Lecturer and an Associated Professor at Shibaura Institute of Technology in 1987 and 1990. He has been a full Professor since 1997. His interest is Mechatronics for medical and rehabilitation applications.

AN APPLICATION OF IMAGE PROCESSING TO CONTROL THE STRAIGHT MOTION OF FISH ROBOT

LE Khanh Dien, TRAN Anh Tuan, LE Thanh Son
Department of Mechanical Engineering, Ho Chi Minh City University of Technology

ABSTRACT

Image processing has an important role in the control of robot. Fish robot has been studied in the world in recent years in three different shapes: Anguilliform, Carangiform and Ostraciiform. To control the straight motion of fish robot, a lot of methods could be used.
In this paper, we applied the IMAGE PROCESSING to control the motion of fish robot. This is one of methods of controlling fish robot that has good performance and high reliability. The method of building the multipurpose tool, the interface, is based on the OpenCv and Visual Express C++ 2010. Via this interface, users can communicate with camera or setup an algorithm to control the motion of fish robot.The research will be applied for manufacture a new appliance for scanning objects in deep sea by image processing technology.

INTRODUCTION

Through thousands years of evolution, biological fish with multiform locomotion modes has made them to easily adapt to different kinds of harsh environments to survive. The movements of living being are attracted by many researchers in around the world and the application of fish robot becomes more popular in investigation activities such as exploration of hazardous environment, spy, entertainment…Nowadays, fish robot is a popular research in the world. Researches of the species fish in the nature help us to saving a power and increase time for work of fish robot in water. The following reviews show some researches in this field:

- Essex Robotic Fish [8] has the ability to curve its body to a great angle in a much reduced time (approximately 90°/0.20sec). The researchers continue to work on the improvement of the algorithms of training that enhances the ability of the robot to generate adaptive behaviors in changing and unpredictable environments.
- PPF-04, Koichi Hirata, NMRI, Japan [7] was developed in many projects of robotic fish (series PF and series PPF) with a view to apply, in the future, the capacities of fish to our boats and submarines. The PPF-04 is a small size remote controlled robotic fish that could be tested it in a small tank (like a bath-tub) for seeking the relation between the speed and the amplitude of the oscillations of its causal fin.

These recent researches are displayed in the figure 1:

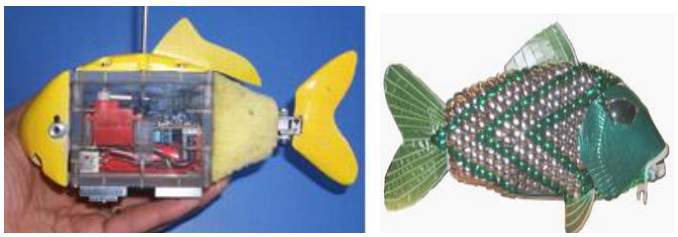

Fig.1 A- PPF-04 – NMRI [7] B- G8 fish – University of Essex [8] C- Principles of the swimming fish robot [7]

The applications of image processing to control fish robot in the recent years could be cited:

Junzhi Yu, Yimin Fang, Wei Zhao, and Long Wang, Peking University, China used CCD camera and image processing to control fish robot.

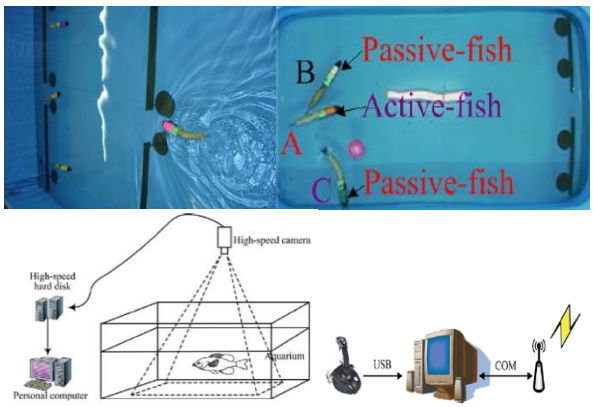

Fig.2 A: Control fish robot using image processing [1]
B: Control fish robot using image processing [2]

In 2008, Qin Yan, Zhen Han, Shi-Wu Zhang, Jie Yang, Science and Technology University, China had use CCD camera to control fish robot .The scheme of color identification is displayed in the following figure.

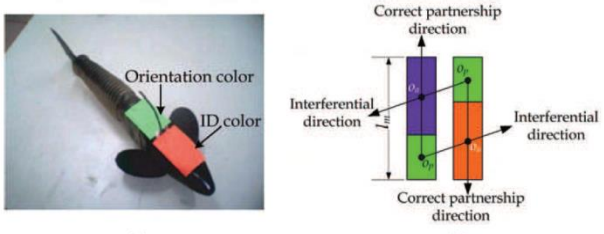

Fig.3 Scheme of color identification. (a) A robotic prototype attached a color mark; (b) Schematic of the color mark [3]

2. MECHANICAL STRUCTURE

As mentioned, Fish robot has been studied in three shapes: Anguilliform, Carangiform, and Ostraciiform. In this paper, we studied about Carangiform Fish Robot because we can use: RF control, Wi-Fi or RS-232 and CCD Camera to control its motion. The camera (figure 5A) is affixed in a positive seat so that it can obviously observe workspace of fish robot.

In figure 5B, designed by SolidWorks, our fish robot has two circles (blue and red) on its back, two RC servos in the fishtail, and two RC servos in the controlled fin and one RC servo for controlling its motions in 3D.

Fig.4 A- CCD Camera in this our research B- Model of fish robot in our research

After receiving a picture from the camera, the OpenCv is used to detect colors (blue and red circle), so we can compute and define a location of fish robot in the workspace. Image processing is performed in laptop or PC with C++ language version 2010 has integrated OpenCv version 2.4.3. Result of image processing from laptop will sent to the robot by RF to control the straight motion of fish robot. A sample time which laptop processing each frame is setup in code C++, about 10ms.

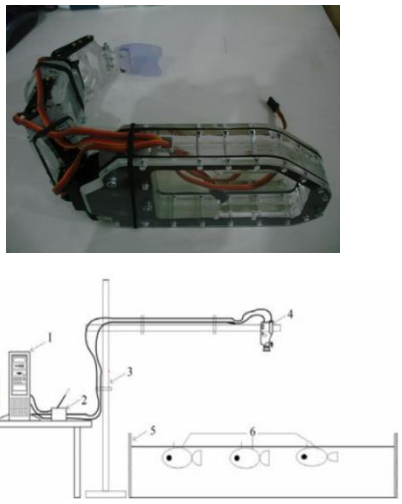

Fig.5 A- Fish robot in my project
B- Configuration of experimental robotic fish platform.

(Note: 1.strategy computer, 2. wireless communication module, 3. Supporting bracket, 4.CCD camera, 5.swim pool, 6.robotic fish.) [1]

An interface is designed to user to control the robot and to its location. For enhancing the accuracy, in the beginning, we must calibrate the camera. Calibration of the camera helps us convert from the image coordinates to the real coordinates that assist us to know the location of fish robot in the workspace and continuous control to the end of the process.

3. DYNAMICS ANALYSIS

3.1 Approach

In Microsoft Visual C++ Express 2010, the application has been supported the Image Processing Opencv 2.4.3. In the other hand, the control of the straight motion of fish robot consists of the stop point via the coordinates of red circle and blue circle on the back of the fish robot.

3.2 Dynamics

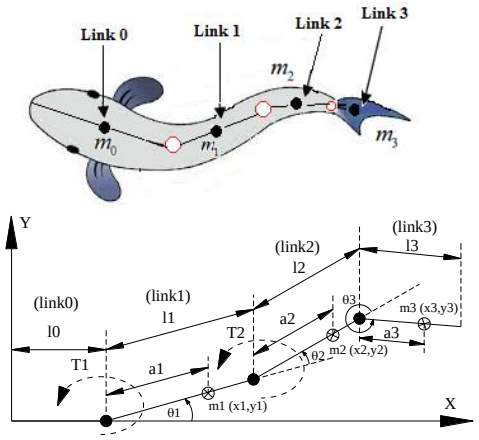

Fig.7 A: Carangiform fish robot included 4 links B: Fish robot analytical model

3.3 Method

- **Calibration camera**

First of all, we have to calibrate the camera to find all its external and internal parameters. Real coordinates of fish robot can be computed via the coordinates of the image and above parameters through the formula:

x^{im}, y^{im}: coordinates of point in the image (pixel).
X^w, Y^w, Z^w: coordinates of point in the workspace of robot.
The matrix of internal parameters , external parameters and matrix M:

(1)

$$M_{in} = \begin{pmatrix} f_x & 0 & c_x \\ 0 & f_y & c_y \\ 0 & 0 & 1 \end{pmatrix} \qquad M_{ex} = \begin{bmatrix} r_{11} & r_{12} & r_{13} & t_1 \\ r_{21} & r_{22} & r_{23} & t_2 \\ r_{31} & r_{32} & r_{33} & t_3 \end{bmatrix}$$

$$M = \begin{bmatrix} m_{11} & m_{12} & m_{13} & m_{14} \\ m_{21} & m_{22} & m_{23} & m_{24} \\ m_{31} & m_{32} & m_{33} & m_{34} \end{bmatrix} = M_{in} * M_{ex} \qquad (2)$$

Hence:

$$\begin{bmatrix} x^{im} \\ y^{im} \\ 1 \end{bmatrix} = \begin{bmatrix} m_{11} & m_{12} & m_{13} & m_{14} \\ m_{21} & m_{22} & m_{23} & m_{24} \\ m_{31} & m_{32} & m_{33} & m_{34} \end{bmatrix} * \begin{bmatrix} X^w \\ Y^w \\ Z^w \\ 1 \end{bmatrix} \Rightarrow$$

$$x^{im} = \frac{m_{11}X^w + m_{12}Y^w + m_{13}Z^w + m_{14}}{m_{31}X^w + m_{32}Y^w + m_{33}Z^w + m_{34}}$$

$$y^{im} = \frac{m_{21}X^w + m_{22}Y^w + m_{23}Z^w + m_{24}}{m_{31}X^w + m_{32}Y^w + m_{33}Z^w + m_{34}}$$

(3)

Because of the computing in the plane, $Z^w = 0$. thus:

$$\begin{cases} (m_{11} - x^{im}m_{31})X^w + (m_{12} - x^{im}m_{32})Y^w \\ \quad = x^{im}m_{34} - m_{14} \\ (m_{21} - y^{im}m_{31})X^w + (m_{22} - y^{im}m_{32})Y^w \\ \quad = y^{im}m_{34} - m_{24} \end{cases}$$

(4)

So, we can find the real coordinates (X^w, Y^w) of fish robot in workspace and control its motion.

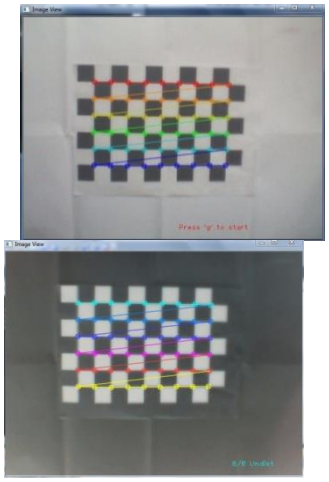

Fig.8 Calibration of the camera

Solution:

The control motion of fish robot could be performed when we know coordinates of one red CIRCLE, one green CRICLE and stop point (Green CRICLE). The coordinate of start point is really no need.

- X_1, Y_1: coordinates of the first CIRCLE
- X_2, Y_2: coordinates of the second CIRCLE
- X_3, Y_3: Stop point

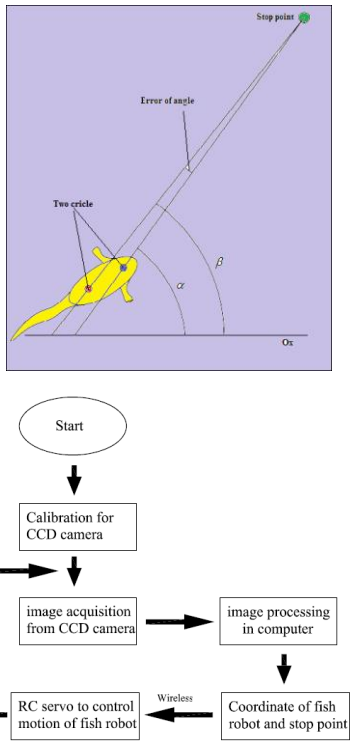

Fig.9 A: Illustration of the motion of robot fish B: Experiment instrument set-up

The equation of first straight line: (d1): $y = k_1.x + b_1$

herein $k_1 = \frac{y_1 - y_3}{x_1 - x_3} \Rightarrow Angle1 = \beta = \arctan(k_1)$

The equation of second straight line: (d2): $y = k_2.x + b_2$

herein $k_2 = \frac{y_2 - y_3}{x_2 - x_3} \Rightarrow Angle2 = \alpha = \arctan(k_2)$

Error of angle: Error = $|\alpha - \beta|$

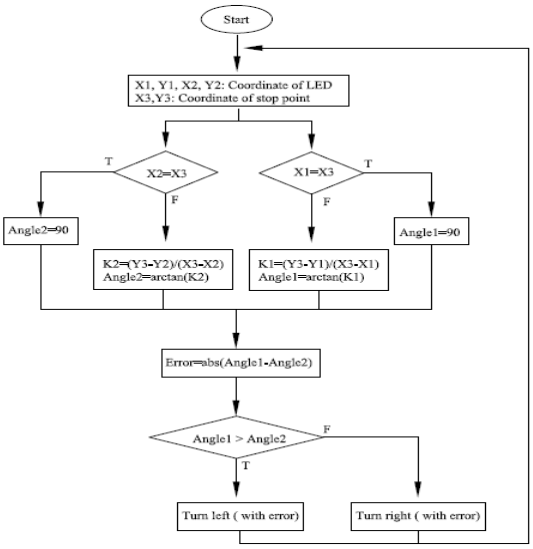

Fig.10 Algorithm flowchart of control motion of robot fish

4. SIMULATION AND RESULT

Simulation is carried out based on Visual C++ 2010 and OpenCv version 2.4.3. An interface is designed for input parameters of calibration camera, control panel with start button and stop button. Another interface is designed to help user can follow motion and coordinates of fish robot.

After press button: Start Calibration Camera. We have to enter an internal and external parameter in textbox. To control fish robot, user press button: start control fish robot and Stop control fish robot.

OX.imgY.img: Coordinate of image

OX.realY.real: Real coordinate

Fig.11 A: Coordinate system

B: Detect two red Circle on the water with real distance is 100 (mm)

Result: Table of Measure and Error

N	Measure value	Error
1	100.233	0.233
2	99.921	-0.079
3	99.256	-0.744
4	101.349	1.349
5	102.992	2.992
6	100.691	0.691
7	98.376	-1.624
8	101.549	1.549
9	101.487	1.487
10	102.348	2.348
Average	100.8202	0.8202

Fig.19 A: Tracking color and error of angle

B: Interface to control fish robot

4.1 Input

- Parameter received from calibration camera: fx, fy, Cx, Cy, rotation vector, translation vector.

- Picture from camera.

4.2 Processing

- Detecting a three point include: Stop point, first CRICLE, second CRICLE. Using detecting color.

- Using Gauss filter to filter a picture from camera.

- Computing a real coordinates of three point which detected color and angle between two line to control motion of fish robot.

4.3 Output

- Location of fish robot after each 10ms (sample time).

- Coordinates of three points: Stop point and two CRICLE after each is 10ms.

- Error of angle.

5. CONCLUSION

- A method of control motion of the fish robot using Image Processing.

- A good easy to use interface and the fish robot works perfectly with a small error.

- User can communicate and control fish robot easier, higher fidelity.

REFERENCES

[1] Junzhi Yu, Yimin Fang, Wei Zhao, and Long Wang, *Control and Coordination of Biomimetic Robotic Fish, Center for Systems and Control, Department of Mechanics and Engineering Science, Peking University, Beijing 100871, P. R. China.*

[2]Qin Yan, Zhen Han, Shi-Wu Zhang, Jie Yang, *Parametric Research of Experiments on a CarangiformRoboticFish, Department of Precision Machinery and Precision Instrumentation, University of Science and Technology of China, Hefei* 230026, *P. R. China.*

[3]AnkurAgrawal, *Elementary Introduction to Image Processing Based robots, 2009.*

[4] Gary Bradski and Adrian Kaehler, *Learning OpenCv, 2008.*

[5] Robert Laganière, *OpenCv 2 Computer Vision Application Programming Cookbook, 2011.*

[7]http://www.nmri.go.jp/eng/khirata/fish/general/principle/index_e.html

[8]http://www.nmri.go.jp/eng/khirata/fish/general/turn/index_e.html

[9]http://iopscience.iop.org/17483190/7/3/036019/article

Le Khanh Diensenior lecture, Department of Mechanical Engineering, Ho Chi Minh City University of Technology, B.E (1982), M.E (1996) in Mechanical Engineering, being doctoral candidate atHo Chi Minh City University of Technology. Email: lkdien@hcmut.edu.vn
.

TRAN Anh Tuan, Mechanical Engineer graduate student of Ho Chi Minh City University of Technology, B.E (2014), Master student.

LE Thanh Son received the The Degree of Master (2014). Hehas collaborated at National key Laboratory of Digital Control and System Engineering, University of Technology, VNU-HCM.

TOLERANCE CHARTING WITH A SPREADSHEET

Chalalai Wongwian and Yongyooth Sermsuti-anuwat
School of Industrial Engineering, Suranaree University of Technology

ABSTRACT

Tolerance Chart is a graphical representation of the dimensions that occur during the production of a machined part. This tool is used for checking if a sequence of machining operations can produce a workpiece to the blueprint dimensions prior to the actual production. Manual tolerance charting has been reported since the early 1950s. Despite the tolerance chart is a most effective tool for process planning, the charting of tolerances is a time consuming and error prone activity. Therefore, the computerized tolerance charting has been used to replacing manual charting. As a result, a substantial number of computer programs for tolerance charting are now available; but, none of them is developed under a spreadsheet application. This paper reports the research work on tolerance charting using Microsoft Excel; particularly, the routine for constructing the Rooted-Tree Graph for tolerance stack calculations in the tolerance chart.

1. INTRODUCTION

A tolerance chart is a graphical representation of a machining sequence for producing metal parts. The chart shows the basic-size and the tolerance of each machining cut and the amount of stock to be removed at each step in the sequence. It is an important tool for process planning to ensure that a tentative sequence of machining operations is appropriate for producing a product of the required dimensions

As early as 1950, the tolerance chart was mainly used for controlling dimensions of machined parts. Despite its usefulness, charting of tolerances using this technique not only requires a great deal of machining expertise but also is a time-consuming and an error-prone process. In order to alleviate the shortcomings of tolerance charting, Gadzala (1959) proposed "the method of traces"; then, Johnson, et al. (1963) and Wade (1967) attempted to systemize the charting procedures. It was not until 1984 that the computer was introduced to chart the tolerances. The work of Ahaluwalia and Karolin (1984) on the development a computer program to assist in generating tolerance charts has opened up a new area of tolerance charting by using a computer.

On the charting algorithm side, Xiaoqing and Davies (1988) developed a complex algorithm for tolerance chart calculations; then, Whybrew et al. (1990) proposed a method of using a rooted-tree graph for calculating tolerance stacks. With the latter technique, Ngoi (1992), applied the optimization technique for tolerance allocation in the tolerance chart and proposed a method of balancing the allocated tolerances.

At present, although there are many computer programs for tolerance charting developed in various programming languages and under various operating systems, but none has been found to be developed under a spreadsheet application, even though it is equipped with all the facilities that tolerance charting requires.

This paper describes an ongoing research on the development of a computerized tolerance charting program using the Microsoft Excel and basing on the rooted tree-graph for tolerance calculations.

2. ROOTED-TREE GRAPH APPROACH TO TOLERANCE CHARTING

Fig. 1, taken from an example of Wade (1967), is the blueprint of a simple machined part superimposed with capital letters for surface identifications. A tentative sequence of machining for this workpiece is shown in Table 1. To identify a surface resulting from a machining operation a numerical subscript is added to the capital letter; whenever a machined surface is re-machined, the numerical subscript for the newly cut surface will be increased by 1. This system of surface identification is the essence of the construction of the rooted-tree graph. The tolerance chart in Fig 3 is prepared from Table 1 with the order of machining cuts are indicated by numbers. This chart is slightly different from those of Wade in that no intermediate balance dimension is shown between the working dimensions. Since the tolerance is concerned with only length dimensions, other dimensions of diameters are all omitted from the chart.

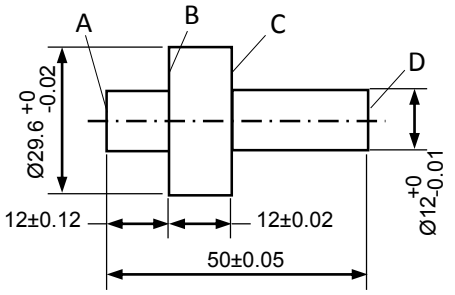

Fig.1. Workpiece dimensions (in millimeters)

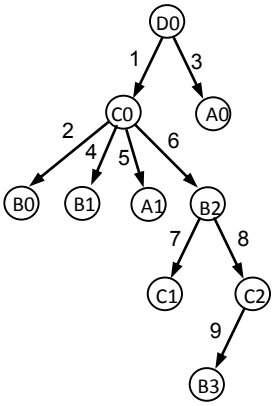

Fig.2. Rooted-tree graph.

Table 1. Tentative machining sequence for the workpiece in Fig. 1.

OP.No.	M/C USED	Cut NO.	Reference face	Machined face
10	W&S turret lathe	1	D0	C0
10	W&S turret lathe	2	C0	B0
10	W&S turret lathe	3	D0	A0
20	Harding chucker	4	C0	B1
20	Harding chucker	5	C0	A1
30	Norton cylinder grinder	6	C0	B2
40	Norton cylinder grinder	7	B2	C1
50	Rough grind 29.6 mm. dia.		-	-
60	Harden		-	-
70	Lap centers		-	-
80	Norton cylinder grinder	8	B2	C2
90	Norton cylinder grinder	9	C2	B3
100	Finish grind 29.6 mm. dia.		-	-

D0
- C0
  - B0
  - B1
  - A1
  - B2
    - C1
    - C2
      - B3
- A0

Fig.3. Rooted-tree graph with

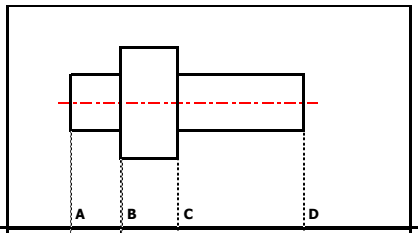

OP.NO.	Face Cut.	M/C USED	WORKING DIM.		STOCK REMOVAL	
			BASIC	±TOL/2	BASIC	±TOL/2
10	D0	W&S turret				
10	C0	W&S turret	25.880	0.050	solid cut	
10	B0	W&S turret	12.585	0.050	solid cut	
10	A0	W&S turret	50.350	0.050	solid cut	
20	B1	H. chucker	12.285	0.050	0.300	0.100
20	A1	H. chucker	24.120	0.050	0.300	0.150
30	B2	N. grinder	12.180	0.005	0.105	0.055
40	C1	N. grinder	12.120	0.005	0.060	0.010
80	C2	N. grinder	12.060	0.005	0.060	0.010
90	B3	N. grinder	12.000	0.005	0.060	0.010

BLUE PRINT		RESULTANTS	
BASIC	±TOL/2	BASIC	±TOL/2
12.00	0.120	12.00	0.065
12.00	0.020	12.00	0.005
50.00	0.050	50.00	0.100

Fig.3. Tolerance chart for the workpiece in Fig.1.

Fig.2 shows the rooted - tree graph corresponding to the machining sequence in Table 1. To draw the graph, start with the node of the first reference face, D0, at the top. Then, extend an arrow to the machined face of the first cut using D0 as the reference face; the arrow of cut 1 with the end node of C0 is now obtain. Next, the arrows of cuts 2 and 3 are drawn to the nodes B0 and A0 respectively. After this, the arrow of cut 4 is then drawn to face B, which has been previously machined to be face B0; therefore, the arrow points to face B1. Repeat drawing arrows for the rest of all cuts, the diagram of rooted–tree will be obtained.

To calculate a tolerance stack resulting from the machining operations, for example between faces A and B, look in the diagram for the last nodes representing the two faces, viz. A1 and B3; the tolerance stack is equal to the sum of the tolerances of all cuts in the path from A1 to B3.

Similarly, the tolerance of the stock removal of cut 4, is equal to the sum of the tolerances of cuts 2 and 4 in the path from nodes B0 to B1 or vice versa.

Table 2. Reversed paths from each node to the root.

No	Reference face	Machined face	Reversed Path
10	Root	D0	D0
10	D0	C0	C0 D0
10	C0	B0	B0 C0 D0
10	D0	A0	A0 D0
20	C0	B1	B1 C0 D0
20	C0	A1	A1 C0 D0
30	C0	B2	B2 C0 D0
40	B2	C1	C1 B2 C0 D0
80	B2	C2	C2 B2 C0 D0
90	C2	B3	B3 C2 B2 C0 D0

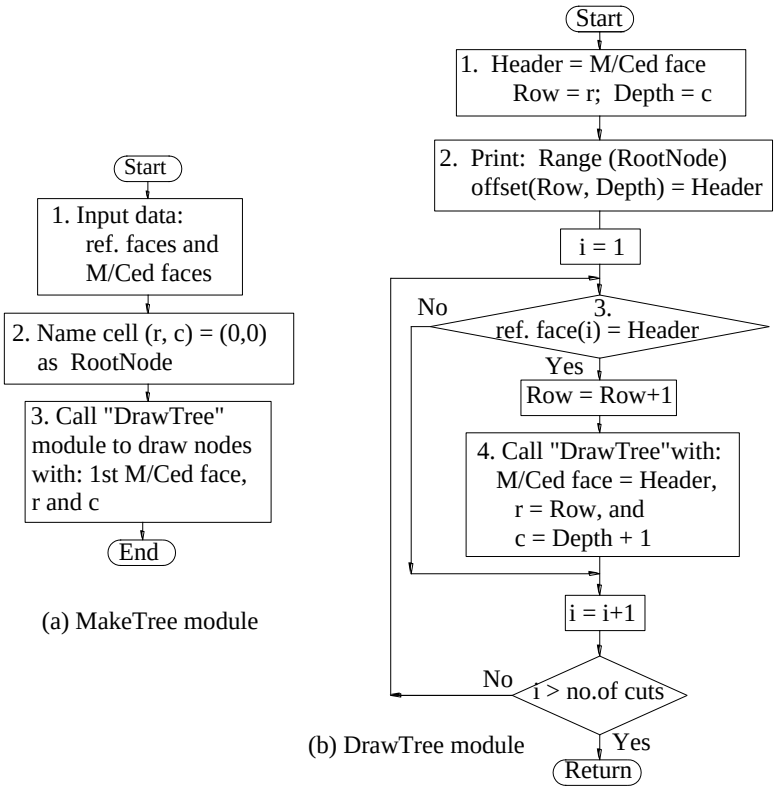

Fig.5. Flowchart

3. ROOTED-TREE GRAPH WITH EXCEL

The rooted-tree graph generated by Excel is shown in Fig. 3. Although the diagram is different from that shown in Fig. 4, it still serves the same purposes. In this diagram, each node symbolized by a capital letter and a number as before. The root node is on the farthest left side of the diagram; each node in each column is the child node of its corresponding parent node in the left hand column and at the same time is also the parent node of its child node in the right hand column. No arrow link has shown in the diagram, but it can be understandable that the nodes in two columns side-by-side are the end nodes of a link.

Fig. 5 shows the flowchart of the algorithm for generating this type of tree graph. The main program module (MakeTree Module), with the flowchart in Fig. 5a, is responsible for setting the cell name, as RootNode, for writing a tree node, and set the first node to the cell position of row 0 and column 0 of the worksheet. With these data and the name of the first cut face the module calls the sub-module, DrawTree in Fig.5b, to write all the nodes of the tree.

In this subprogram, the variable Header, which temporally holding the name of the surface previously machined or cut, is used for testing if a particular cut has its reference surface being the machined face it holds. If the result is true, then shift the RootNode cell to the next row and the next column, and call DrawTree to print the node name; otherwise, the next machining cut in the sequence will be tested. This process continues repeatedly until the nodes of all machined surfaces have been printed, that is the diagram has been completed.

With some modifications by cooperating with other program modules, the MakeTree module can be used for generating the path from each end node of the tree to the root node (or the reversed paths) as shown in Table 2, which will facilitate the calculations of both the tolerance stacks and the basic sizes in the tolerance chart.

4. TOLERANCE CHARTING AND EXCEL

One of the dominant applications of the tolerance chart is in the area of process planning for checking the practical feasibility of a machining sequence. Any tolerance stack problem if exists can be spotted by the chart and modifications can be made iteratively to the sequence until the chart arrives at a satisfactory result.

A spreadsheet like the Excel has an excellent property in automatically updating the results when some relationships or variables in the solution sequence have been modified or changed. The tolerance charting program developed under Excel application can therefore make use of this potential to its most advantage.

5. CONCLUSION

This paper reports some results of the research on computerized tolerance charting using Excel which has been being conducted in the School of Industrial Engineering at Suranaree University of Technology, Thailand. It demonstrates the computer routine for constructing the rooted-tree graph which is a powerful tool for calculating tolerance stacks. It is expected that the research work, when completed, would be beneficial to all the metal machining industries.

REFERENCES

Ahaluwalia, R. S., and Karolin, A. V., CATC A computer-aided tolerance control system, Journal of Manufacturing Systems, vol. 3, no. 2, pp. 153-160, 1984.

Gadzala, J. L., Dimensional Control in Precision Manufacturing: As Applied in Production Machining to Effect Higher Production and Lower Unit Costs, McGraw-Hill, 1959.

Johnson, A. M., Wilson, F. W., & Harvey, P. D., Manufacturing Planning and Estimating Handbook, 1963.

Ngoi, B. K. A., Applying linear programming to tolerance chart balancing, The International Journal of Advanced Manufacturing Technology, vol. 7, no. 4, pp. 187-192, doi: 10.1007/BF02601622, (1992).

Sermsuti-anuwat, Y., Whybrew, K., McCallion, H., CAPPFD – A tolerance-based feature sequencing CAPP system, Journal of Systems Engineering, vol. 5 no. 1, pp. 2-15, 1995.

Sermsuti-anuwat, Y., Tool Engineering Basics: jig, fixture & gauge design, Nonthaburi, 21st Century Publishers, 2013 (in Thai).

Wade, O. R., Tolerance Control in Design and Manufacturing,Industrial Press, 1967.

Whybrew, K., Britton, G. A., Robinson, D. F., and Sermsuti-anuwat, Y., A graphtheoretic approach to tolerance charting, International Journal of Advanced Manufacturing Technology, vol. 5, pp. 175-183, 1990.

Xiaoqing, T., and Davies, B.J., Computer aided dimensional planning, International Journal of Production Research vol. 26, no. 2, pp. 283-297, 1988.

Chalalai Wongwian is a post-graduate student in the School of Industrial Engineering, Suranaree University of technology, Thailand. The title of her masters thesis is “Tolerance charting with a spreadsheet”

Yongyooth Sermsuti-Anuwat received, Ph. D. (Mechanical engineering) from the University of Canterbury, New Zealand.

He is an Assistant Professor in the School of Industrial Engineering, Suranaree University of Technology, Thailand. His research interests are in the areas of tolerance technology, process planning and fixture design.

AN APPROACH TO ESTABLISHING THE RELATIONSHIP BETWEEN BUSH POSITION AND COMPONENT PARTS OF A DRILL JIG

Phornpan Thongpang and Yongyooth Sermsuti-anuwat
School of Industrial Engineering, Suranaree University of Technology, Nakhon Ratchasima, Thailand.

ABSTRACT

This paper describes a practical approach basing on the loop diagram and the rooted-tree graph to establishing the tolerance relationship between drill bush position and all dimensions of jig components. The concepts of the two techniques are explained through a 3-part assembly. A simple plate jig with a pin locator and a locating slot is used for illustrating the approach.

1. INTRODUCTION

More than 3 decades since an early attempt to automate the design of workholding device for metal machining operations (Cutkosky et al., 1982), the success is still to be realized. Despite the fact that, at present, a great deal of advance has been achieved in computer technology, both hard- and soft-ware, the computerized fixturing systems developed so far still lack an essential ability to generate functional dimensions on the component parts of the workholding device. This could be because most of these systems neglect to address the fundamental aspect of the device: its function is to repeatedly impart the required dimensions to the workpieces. As a consequence, the existing systems stress only on the production of the pictorial representations or assembly drawings of the jig or fixture in question (Nee et al. (1985), Pham et al. (1990) and Vukelic et al. (2011)), which leaves all the details of determining a bush position or the sizes and position of a set-block to be worked out by tool designers or tool makers at a later stage. Therefore, only partially automatic fixture design can be achieved at this stage.

Sermsuti-anuwat (2009) proposed a tolerance analysis approach to fixture design basing on the loop diagram, a technique normally used in the analysis of part dimensions to be assembled together (Gladman, 1972). The procedure can be used for identifying the functional dimensions on the component parts affecting the functional requirement of a workholding device. Then, Orawan & Sermsuti-anuwat (2009) used the rooted tree-graph (Whybrew, et al., 1990) to re-allocate the tolerances to a new set of dimensions on a machined part when there was a change in the datum for dimensioning. These two techniques, the loop diagram and the rooted tree graph, can be combined and form a systematic procedure for establishing the tolerance relationship between a functional requirement of a workholding device and the dimensions of its components.

This paper is a result of a preliminary study made prior to the development of a computer program for assisting in the determination of a bush position in a drill jig. It describes the basic concepts of the loop diagram and the rooted tree graph and their applications in determining the position of a drill bush, which can be used as a basis for computerized generating dimensions for component parts of a jig or a fixture.

2. CONCEPTS OF LOOP DIAGRAM AND ROOTED TREE GRAPH

Fig. 1 shows the half view of a simple assembly, taken from Lissaman & Martin (1982), consisting of 3 components, numbered 1 to 3. The functional requirement of this assembly is width of a gap between parts 2 and 3 which is represented by $Y \pm y$.

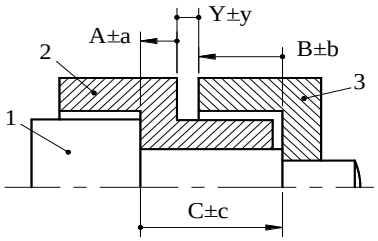

Fig. 1. The loop diagram of an assembly.

By using the method outlined in Sermsuti-anuwat (2009), the functional dimensions controlling the gap width can be identified as A±a, B±b and C±c as shown in Fig. 1.

From this diagram, the following 2 equations can be written, one for basic sizes and the other for tolerances:

$$C - A - B = Y, \text{ for basic sizes;}$$
$$\pm (a + b + c) \leq \pm y, \text{ for tolerances.}$$

The tolerances of the dimensions on a particular part can be related by a rooted-tree graph. Assuming part numbered 2 with dimensions and tolerances as shown in Fig. 2a, following the steps suggested by Orawan & Sermsuti-anuwat (2009), a tree graph relating all the

length dimensions can be constructed as in Fig. 2b, where a node corresponds to each face dimensioned on the part.

As an example of using this graph, let the Functional dimension A±a be replaced by dimension F±f, between faces 3 and 4, in Fig 2c, from which the tree graph is drawn in Fig. 2d. In order to maintain the original functional dimension (A±a) when the datum for dimensioning changes, the following equation for tolerances must be satisfied:

$$\pm (d + e + f) \leq \pm a$$

The tolerances on the left hand side of the inequality can be readily identified from the path in the tree whose nodes are the 2 faces of the omitted dimension A±a in Fig. 2d.

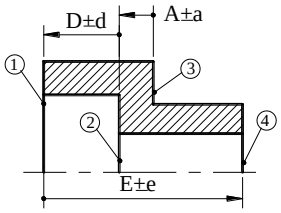

(a) Part 2 with dimensions.

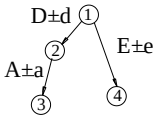

(b) The tree for dimensions in (a).

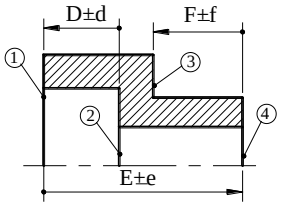

(c) Part 2 with a modified dimension.

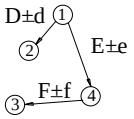

(d) The tree for dimensions in (c).

Fig. 2. An application of rooted-tree graph.

3. AN EXAMPLE

Consider the plan view of a drill jig in Fig.3a, which locates a narrow strip of workpiece by means of a slot. It is required to drill a hole at a distance of Z±z from an end of the workpiece (Fig. 3b). This is in fact the functional requirement of the jig assembly; however, it is not actually integrated with the assembly because a jig must be completely made before it can be used. Therefore, in the context of an assembly, a jig can be viewed as an incomplete assembly, and it will become a complete assembly when the hole is drilled.

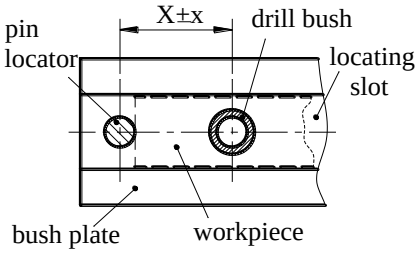

(a) Plan view of a plate jig.

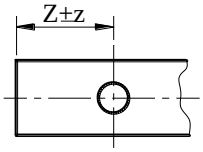

(b) Workpiece

Fig. 3. A plate jig and the workpiece.

To determine the bush position, first, the loop diagram must be constructed as shown in Fig.4. Then, 2 equations, for basic sizes and for tolerances, are formulated as follows:

$$A + Z = X, \text{ for basic sizes, and}$$

$$\pm(a + x) \leq \pm z, \text{ for tolerances.}$$

A±a is half the pin size which can be assigned corresponding to the interference fit to the mating hole in the bush plate. Hence, X±x can be calculated from these equations.

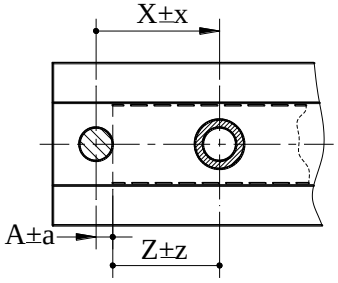

Fig. 4. The loop diagram.

In machining the bush plate, the dimensioning datum could be as shown in Fig. 5a, which requires re-allocation of tolerances, and can be accomplished using the rooted-graph as shown in Fig.5b. Then, the tolerances can be assigned to relevant dimensions according to the following inequality:

$$\pm (m + n) \leq \pm x$$

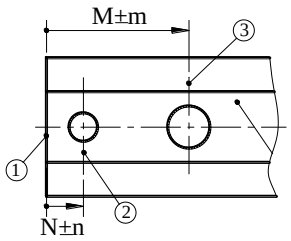

(a) New dimensions

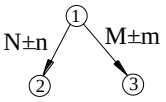

(b) Rooted-tree graph

Fig. 5. New dimensions and tree.

This simple example demonstrates a procedure of tolerance analysis which can be applied to obtain practically meaningful results despite limited of working experience.

4. CONCLUSION

The rooted-tree graph is an essential technique for allocating tolerance to dimensions a part component, while the loop diagram is for the dimensions on different assembled parts. At present, in the School of Industrial Engineering at Suranaree University of Technology, Thailand, the research on automated fixture design has been conducted with a substantial progress in developing an algorithm to combine the two techniques by basing on the procedures outlined above. It is expected that the success of this ongoing research would bring another vital step closer to the fully automated fixture design.

References

Cutkosky, M.R., Eurokawa, E., and Wright, P.K., Programmable comformable clamps, AUTOFACT Conference Proceedings, SME, Dearbon, Michigan, pp. 11.51-11.58, 1982.

Gladman, C. A., Manual for geometric analysis of engineering designs, Sydney: Australian, trade publications, 1972.

Lissaman, A. J., & Martin, S. J., Principles of engineering production, 2nd ed., ELBS and Hodder and Stoughton, 1982.

Nee, A.Y.C., Bhattacharyya, N., and Poo, A.N., A knowledge-based CAD of jigs and fixtures, Tech. Paper No. TE 85-902, SME, USA, 1985.

Orawan, N., & Yongyooth, S., An optimization technique for tolerance allocation when datum for dimensioning changes, IE Network Conference 2009. (in Thai)

Pham, D.T., Natgh, M.J., and Lazaro, A.S., AUTOFIX-an expert CAD system for jigs and fixtures, Int. J. Mach. Tool. Des. Res., vol. 30, no. 3, pp. 403-411., 1990.

Sermsuti-anuwat, Y., Milling fixture design: a tolerance analysis approach. International Journal of Mechanical Engineering Education, vol. 37, no. 2, pp. 111-117, 2009.

Vukelic, D., Tadic, B., Luzanin, O., Budak, I., Krizan, P., and Hodolic, J., A rule-based system for fixture design, Scientific Research and Essays, vol. 6, no. 27, pp. 5787-5802, 2011

Whybrew, K., Britton, G. A., Robinson, D. F., & Sermsuti-anuwat, Y., A graph-theoretic approach to tolerance charting, The International Journal of Advanced Manufacturing Technology, vol. 5, no. 2, pp. 175-183, 1990.

Phornpan Thongpang is a post-graduate student in the School of Industrial Engineering, Suranaree University of technology, Thailand. The title of her masters thesis is " Computer-aided determination of bush position in drill jig "

Yongyooth Sermsuti-Anuwat received Ph. D. (Mechanical engineering) from The University of Canterbury, New Zealand.

He is an Assistant Professor in the School of Industrial Engineering, Suranaree University of Technology, Thailand.

His research interests are in the area of tolerance technology, process planning and fixture design.

DESIGNING TO ARRANGE THE ULTRASONIC PIEZO FOR LEAF-VEGETABLE WASHING MACHINE

Le Thanh Son, Le Khanh Dien, Pham Van Duy

ABSTRACT

The matter about using fresh and safe vegetable is a high-essential demand of the people living in Vietnam and around the world. In Vietnam, the standards and regulations of the manufacture and trading vegetable and fruits are very strict. Before the situation of current vegetable - food, the research about ultrasonic washing technology (used to remove impurities in vegetable, help to improve the quality of fresh vegetable) is a new research content, should be concerned done. Research about the effects of ultrasonic on the vegetable before, during and after the process of washing is a necessary issue in order to build a safe vegetable washing process. To build this process, we should have empirical statistical samples and evaluation, so we need to design and manufacture a small model washer used ultrasonic technology for vegetable. This paper presents the theoretical design- calculation, the calculations will be used as parameters for the making process a laboratory scale washing machine. It will service research objects about ultrasonic-factors that affect the vegetable in order to build safety leafy-vegetable washing process.

1. INTRODUCTION

In vegetable processing and production technology, washing stage is an important process and determines the food safety. The solution for this matter is technology-research to ensure cleanliness of vegetable and remove chemical residues on the surface of vegetable that normal drenching and washing methods can not achieve. This research presents contents that relate to ultrasonic washing technology for industrial use detergent, using theory and model to serve for calculating designing the arrangement of *piezo* in a testing washing tank non-chemicals. It will be made in the future to serve the purposes of testing the effects of ultrasonic factors on leafy vegetable.

2. PRINCIPLES OF ULTRASONIC WASHING

To dissolve the dirt, cleaning solvents are required to impact on dirt and dissolve it completely, the reaction occurs only at the contact surface between the dirt with detergent**.**

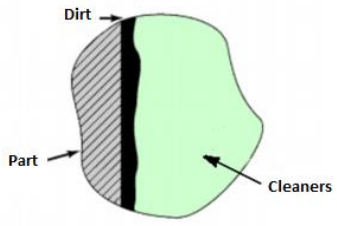

Figure 1. *Exposure between cleaners and dirt.*

In the process of dissolving dirt in cleaning solvents, a saturated layer of detergents (containing impurities) appears at the contact surface between dirt and detergent. Once this happens, the cleaning process will stop due to saturated detergent with impurities and insoluble dirt anymore and it hampers new detergent solution into contact with dirt at the same time. (Fig. 2)

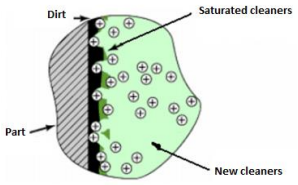

Figure 2. *Appearance of saturated detergent*

A phenomenon of creation and breakage of vacuum ball due to supersonic waves will make the breakage of the linking of saturated detergent with dirt, creating contact surface between the new detergents and dirt, this activities are ongoing until classes of impuritiesare are dissolved completely.

3. CALCULATION AND DESIGN

3.1. Diagram of the vegetable-washing by ultrasonic model

Vegetable-washer by ultrasonic including parts:

- Sinks
- Alternator of the mechanical ultrasonic vibrations.
- Power ultrasonic vibrations signal generator.
- Filter parts, water filtration.
- Water pumps and hydraulic valves.

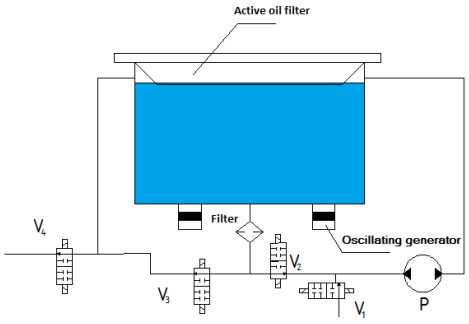

Figure 3. *Structure diagram of ultrasonic dishwasher*

3.2. Calculating the capacity of tank that containers solvent

For frequencies from 25 to 104 kHz, we use the chart in figure 4, to determine the necessary washing power. This is the chart used for the washing in industry, so it should be consulted in the design and we can use this chart to empirical testing on four types of washed vegetable:

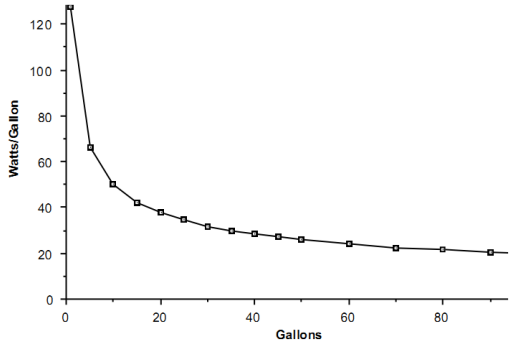

Figure 4. *Graph of power levels required for each Gallon*

The volume of the solvent tank:

$$V_b = \frac{400 \times 300 \times 300}{10^6} = 36 lits \approx 9.51 Gallons$$

Based on the chart (Figure 4), for the solvent tank that has volume 9.51 Gallons, we need to provide the average power: 50 W / Gal, so total power supply capacity should be:

$$P_{tc} = 9.51 \times 50 = 475.5 W$$

The thickness of the wash tank can be selected according to the criteria of the current ultrasonic cleaners manufacturer, is 3mm.

3.3. Designing calculating to select the geometric parameters for the piezo

When we transmit high frequency ultrasonic, its wavelength is small, so it has high directional property, the piezo will creat oscillations. They have energy that is distributed at parallel positions with the line perpendicular to the surface of the oscillation source. For each ultrasonic source, the shape of broadcasting direction will undergo two regions: near region (Fresnel zone) and remote region (Fraunhofer region) (Figure 5). Near region has broadcasting direction that is perpendicular to the surface of to the surface of the oscillation source. In this region, the centralized waves have high energy, beam width is approximately the diameter of oscillation source. Region length is calculated according to the formula:

$$l_{vg} = \frac{a_4^{'2}}{\lambda} \qquad (1)$$

With $a_4^{'}$ is the radius of the amplified metal cap. λ is the ultrasonic wavelength.

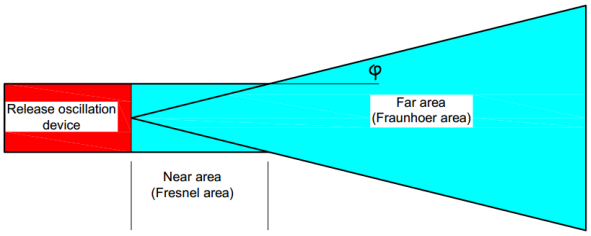

Figure 5. *Shape and direction of released ultrasonic waves*

Diffuser angle:

$$\varphi = \arcsin\left(\frac{1.22\lambda}{2a_4^{'}}\right) \qquad (2)$$

From formula (1) we find that with a fixed wavelength, the diffuser angle φ will inversely with $a_4^{'}$, so the smaller $a_4^{'}$ is the larger the diffuser angle is, this time ultrasonic energy transmitted will be spread out weaken and reduce the cleaned possibility of ultrasonic. So we can determine $2a_4^{'} \le l_4 + 31$, select the largest radius to have the smallest diffuser angle $a_4^{'} = \frac{l_4 + 31}{2}$.

Now resonant oscillation conditions are:

$$\tan\left(\frac{\omega l_4}{V_4}\right).\tan\left(\frac{\omega l_2}{V_2}\right) = q \qquad (3)$$

With the ratio of the impedance acoustic of the cone metal cap and piezoelectric element:

$$q = \frac{\rho_2 V_2 S_2}{\rho_4 V_4 S_4^{'}}$$

V_2, V_4 is the sound velocity in the piezoelectric element and the metal lid.

S_2, S_4 is the cross-sectional area of the piezoelectric element and the metal lid.

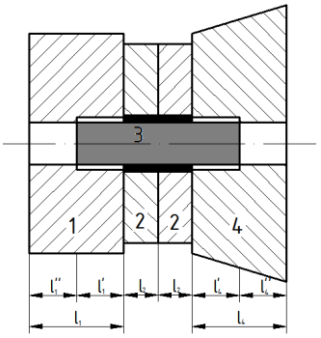

Figure 6. *Piezo model have a cone lid*

Replace the value in equation (3) we get:

$$\tan(0.5105) * \tan(39.28 l_4) = \frac{8664}{14.07 * (l_4 + 31)}$$

Settlement equation we find $l_4 = 31\ (mm)$,

$l_4^{'} = l_4 / 2 = 31/2 = 15.5\ (mm)$.

Vậy $a_4^{'} = \frac{31+31}{2} = 31\ (mm)$

Table 1. *Transmitted speed of sound in some materials at room temperature*

Materials	**Velocity (m/s)**	**Materials**	**Velocity (m/s)**
Aluminum	6374	Ceramics PZT	3200
Ceramics Barium Titanate	4000	zinc	4650
Brass	4372	Purified Water	1482
Magnesium	5823	Duralumin	6398

After calculating the size we have the completed piezo with full details and size (Figure 7).

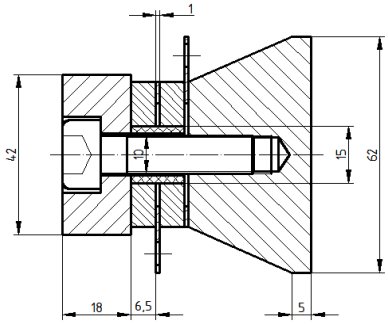

Figure 7. *The completed piezo*

3.4. Calculating and choosing the capacity of piezo

To calculate the capacity of piezo we put it on the equivalent circuit diagram (Figure 8)

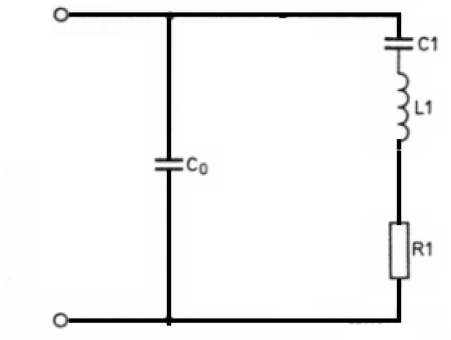

Figure 8. *Equivalent circuit diagram of the piezoelectric resonator element*

From the circuit the capacity can calculated by the formula**:**

$$P = \frac{U^2}{Z}\left(1-\tan\left(\delta\right)\right) = \omega C U^2\left(1-\tan\left(\delta\right)\right) \quad (4)$$

Velocity of sound in water: 1482 m/s (Table 1). Wavelength of sound design: 741.10-6 m. Replace number in equation (4) we have piezo capacity: P=43.3 (W).

According to designed calculations, we choose the number of piezo to use: 10 sets, corresponding to the size of the tank calibration is: 350x300x300mm is consistent with the design capacity of the wash tank. After having the full size we can easily calculate the distance of the piezo on the bottom of the tank wash (Figure 9).

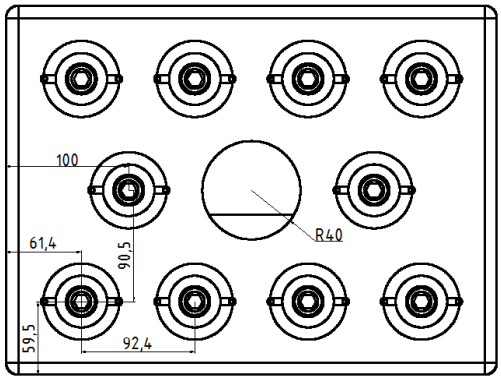

Figure 9. *Piezo's layout*

4. CONCLUSION

This paper presents the results of design calculations of washing machine which is applied of ultrasonic technology , tended to apply in industrial and in future researched team will produce a demo model for research on experimental vegetable samples to determine the essence of ultrasonic cleaning technology when applied to leafy vegetable.

Currently the team is doing research topics to wash vegetable in ultrasonic technology so in the future we will make a vegetable washing machine model using ultrasonic to applying for industrial scale, the team is expected designed productivity is 200kg / hour and volume is 1 m^3 after a successful experimental through the aforementioned demo model.

REFERENCES

E. Mori, K. Itoh, A. Imamura, "Analysis of a short column vibrator by apparent elasticity method and its application," Ultrasonics International 1977 Conference Proceedings, pp. 262-265, 1997.

Nguyen Thi Bay, fluid lectures.

Dragan D.Mancic, Milan Dj.Radmanovic, "Design of Ultrasonic Transducers By Mean of apparent Elastic Method", Facta Universitatis, Woking and Living Environmental Protection, Vol.2, pp.293 - 300, 2004.

L.Shuyu, "Design of piezoelectric Sandwich Ultrasonic Transducers with Large Cross-Section", Applied Acoustic, Vol.44, pp.249 - 257, 1995.

Wu, J., Luan, T., Lan, C., Hung Lo, T.W. and Chan, G.Y.S. (2007). Removal of residual pesticides on vegetable using ozonated water. Food Control, 18(5): p. 466-472.

Ikeura, H., Kobayashi, F. and Tamaki, M. (2011). Removal of residual pesticides in vegetable using ozone

microbubbles. Journal of Hazardous Materials, 186(1): p. 956-959.

Le Thanh Son received the The Degree of Master (2014). He has collaborated at National key Laboratory of Digital Control and System Engineering, University of Technology, VNU-HCM since 2011.

Pham Van Duy received The Degree of Master (2014). He has collaborated at National key Laboratory of Digital Control and System Engineering, University of Technology, VNU-HCM.

APPLYING PRODUCT DESIGNING METHOD AT MODULARITY FOR THE RAPID PROTOTYPING MACHINE BY LASER SINTERING

Le Thanh Son, Le Khanh Dien, Nguyen Thanh Nam

ABSTRACT

Today, the demand about 3D-scanning system, 3D-physical-modeling system for testing design to develop products of businesses is increasing so much. Research about rapid prototyping system by laser sintering technology is an optimal solution. It is selected in 10 technology-applications. This paper presents the modularity-design- theory for rapid prototyping machine using laser sintering. The basis of this study will be prerequisite for developing and mastering 3D printing technology and rapid prototyping in Vietnam about device-field. Research results of this paper focuses on building the module-theory for rapid prototyping machine and presents empirical results from making a model of rapid prototyping machine with power of the sintering laser 25W. We will research the modularity design to apply to expand the size of the rapid prototyping machine with diverse sintering-laser, higher sintering-power.

1. INTRODUCTION

Rapid prototyping machine by laser sintering is a new technology and has not been popular in Vietnam. Rapid prototyping is the process that saves production, time and optimizes the cost for testing production. Since then, the research, design for systems of rapid prototyping by laser sintering, can be used for industrial production, serves for product development are concerned very much. Laser sintering technology that is especially applied for powder metal material is a strength-side of rapid prototyping system by high power laser sintering. The growth of the rapid prototyping method is shown by the graph in figure 1.

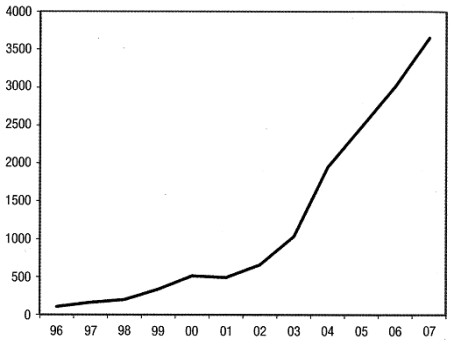

Figure 1. *Growing-graph about number of rapid prototyping systems in the world*

Currently, according to statistics-results, applications of rapid prototyping systems in automotive design (31.7%), industrial design, prototyping testing model (17%) and in the future, there are research-applications for manufacturing aviation equipment.

2. DESIGN PROCESS AT MODULARITY

The study “Design at modularity” that was applied in rapid prototype system by laser sintering is a attracting content for implementation research and it is shown in this paper. Here is the process to serve the research design for a rapid prototyping machine at modularity-design method.

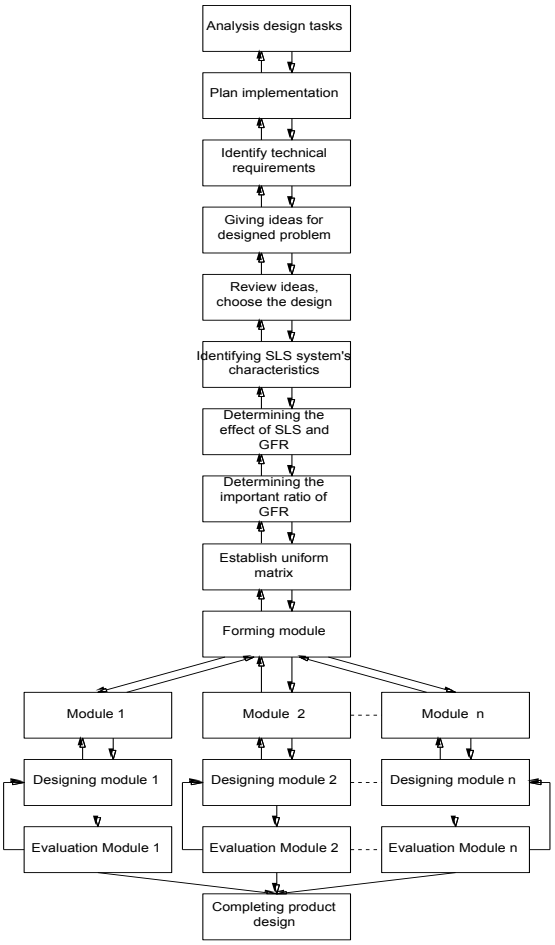

Figure 2. *Process of modularity design that is applied for rapid prototyping machines by laser sintering*

2.1 Determining the coeffient of importance GFR of rapid prototyping system

Many common functional requirements may exist for a product and a number of functional requirements are more important than others. Therefore, the coefficient of importance will be assigned to the different functional requirements. Important factor value in the range from 0.1 to 1.

Here, four general functional requirements of rapid prototyping system are equal importance so we choose the coefficient of importance 1.

2.2 Setting the uniform matrix of the prototyping system

The diagonal of the uniform matrix is empty. The other factors are determined as follows:

$$S_{i,j} = (a_1\, a_2 \ldots a_j)_{1xj} \times \begin{bmatrix} b_{11} & b_{12} & \ldots & b_{1i} \\ b_{21} & b_{22} & \ldots & b_{2i} \\ \ldots & \ldots & \ldots & \ldots \\ b_{j1} & b_{j2} & \ldots & b_{ji} \end{bmatrix}_{jxi} \times \begin{bmatrix} c_1 \\ c_2 \\ \ldots \\ c_i \end{bmatrix}_{ix1}$$

In this:

$$(a_1\, a_2 \ldots a_j)_{1xj}$$

is the vector of system characteristics rapid prototyping by laser sintering (j is the number of system characteristics).

$$\begin{bmatrix} b_{11} & b_{12} & \ldots & b_{1i} \\ b_{21} & b_{22} & \ldots & b_{2i} \\ \ldots & \ldots & \ldots & \ldots \\ b_{j1} & b_{j2} & \ldots & b_{ji} \end{bmatrix}_{jxi}$$

is the relation matrix between SLS and GFR (i is the number of common functional requirements).

$$\begin{bmatrix} c_1 \\ c_2 \\ \ldots \\ c_i \end{bmatrix}_{ix1}$$

is "the coefficient of importance" of the general functional requirements GFR.

2.3 Making modules of the rapid prototyping machine system

Components is compatible with high-level (shown with the largest value) will be grouped together in modularity design. This can be done by group-recognition algorithm CIA, creating function-modularity matrix of rapid prototyping machine as follows **[6]**:

$$(S)_{1x2}\ [1\ \ 0\ \ 0\ \ 1] \begin{bmatrix} 1 & 0 & 0 & 0 \\ 0 & 0 & 0 & 0 \\ 0 & 0 & 0 & 0 \\ 1 & 0 & 0 & 0 \end{bmatrix} \begin{bmatrix} 1 \\ 1 \\ 1 \\ 1 \end{bmatrix} = 2$$

$$(S)_{11x10}\ [0\ \ 1\ \ 0\ \ 0] \begin{bmatrix} 1 & 0 & 0 & 0 \\ 0 & 0 & 0 & 0 \\ 0 & 0 & 0 & 1 \\ 0 & 0 & 0 & 1 \end{bmatrix} \begin{bmatrix} 1 \\ 1 \\ 1 \\ 1 \end{bmatrix} =$$

$$0$$

On the basis of calculating the matrix, it will be created sets of the value that were recorded in Table 1.

Table 1. *Functionality-module matrix of rapid prototyping system*

	1	2	3	4	6	7	9	10	5	8	11
1		2	2	1	1	0	1	0	0	0	0
2	2		2	1	1	0	1	0	0	0	0
3	2	2		1	1	0	1	0	0	0	0
4	1	1	1		1	0	1	0	0	0	0
5	0	0	0	0	0	0	0	0		0	0
6	1	1	1	1		1	1	1	0	0	0
7	0	0	0	0	1		1	0	0	0	0
8	0	0	0	0	0	0	0	0	0		0
9	1	1	1	1	1	1		1	0	0	0
10	0	0	0	0	1	0	1		0	0	0
11	0	0	0	0	0	0	0	0	0	0	

Table 2. *Structure-module matrix of rapid prototyping system*

	1	2	3	4	6	7	9	10	5	8	11
1		3	3	2	1	1	1	1	1	1	1
2	3		3	2	1	1	1	1	1	1	1
3	3	3		2	1	1	1	1	1	1	1
4	2	2	2		2	1	1	1	1	1	1
5	1	1	1	1	1	1	1	1		1	1
6	1	1	1	2		2	2	2	1	1	1
7	1	1	1	1	2		1	1	1	1	1
8	1	1	1	1	1	1	1	1	1		1
9	1	1	1	1	2	1		1	1	1	1
10	1	1	1	1	2	1	1		1	1	1
11	1	1	1	1	1	1	1	1	1	1	

3. RESULTS OF RESEARCH

The results of modularity analysis that are drawn from the modularity design is proposed for components of the machine as follows:

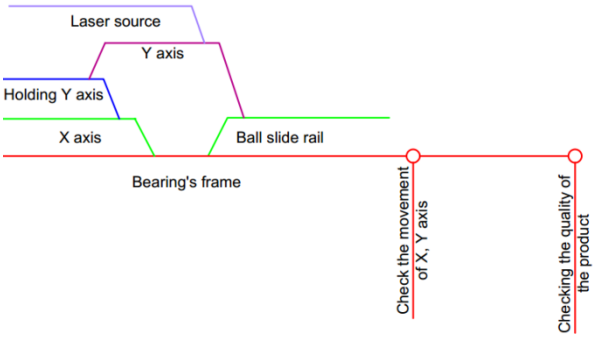

Figure 3. *Modularity model of laser sintering component*

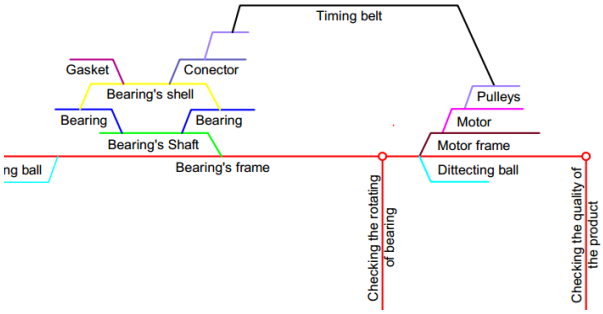

Figure 4. *Modularity model of roller component*

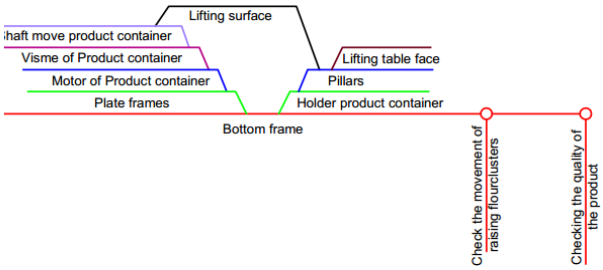

Figure 5. *Modularity model of powder-feeding component*

Based on the research and design of the modularity system described above, it will create a system of rapid prototyping laser sintering 60W, in figure 6. The process of analyzing creates a product that is a complete rapid prototyping machine by laser sintering, ensures specifications and modularized into

functional components. This research has made a model that is used for studying and evaluating the reliability of the design approach. Then, we will have the basis to conduct the calibration and development methodology.

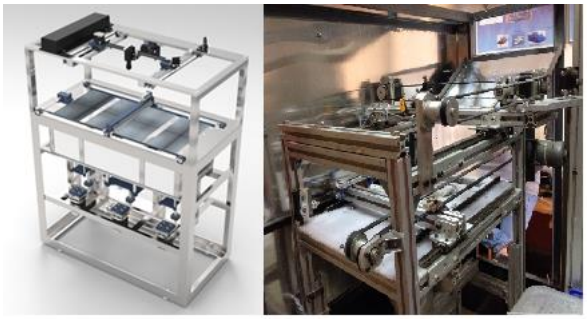

Figure 6. *Testing model of the rapid prototyping machine by laser sintering*

Processing parameters: fine-tune thickness of a sintered layer: 0.2 mm, according to the laser power source: 0,75% (60W laser source), sintering velocity: 250 mm / s, sintering temperature: ~ 160oC, runtime: 2 hours 30 minutes. (Figure 6)

Figure 6. *A model that has cylindrical helix inside it*

4. CONCLUSION

The research results of the rapid prototyping machine design at modularity analysis method have the following conclusions:

- Applying the modularity design method in the machine design is a new content and has not been applied much in the development of the rapid prototyping machines by laser sintering.

The research results have done the modularization of the machine's functional parts, By them, we have also created a model of rapid prototyping machines by laser sintering that is ensured design parameters with laser power 60W.

The research will be applied to the development of rapid prototyping machines by laser sintering with the power 25W, 30W, 60W, 120W.

REFERENCES

W.A.Y YUSOFF & A.J THOMAS, The effect of employing an effective laser sintering scanning strategy and energy density value on eliminating "orange peel" on a selective laser sintered part, International Islamic University Malaysia, Faculty of Manufacturing and Materials Engineering, P O Box 10, 50728 Kuala Lumpur, Malaysia.

M.S.Wahab,K.W.Dalgarno, R.F.Cochrane, S.Hassan Member, IAENG , Development of Polymer Nanocomposites for Rapid Prototyping Process, 2008.

Radovan HUDÁK, Martin ŠARIK,Róbert DADEJ, Jozef ŽIVČÁK,Daniela HARACHOV, Material and thermal analysis of laser sinterted products, Faculty of Mechanical Engineering, Department of Biomedical Engineering and Measurement, Technical University of Košice, Letná 9, 042 00 Košice, Slovakia.

Contuzzi, N.; Campanelli, S.L & Ludovico, A.D " 3D finite element analusis in the selective lazer melting process '', Department of Management and Mechanical Engineering, Viale Japigia,182,70126 Bari, Italia, 2011.

Carliss Y. Baldwin Kim B, Clark, " Modularity in the Design of Complex Engineering Systems'', 2004.

Carliss . Baldwin, Kim B. Clark, trích từ Design Rules, Volume 1: "The Option Value of Modularity in Design", The Power of Modularity, Harvard Business School, 16/5/2002.

LE Thanh Son received the The Degree of Master (2014). He has collaborated at National key Laboratory of Digital Control and System Engineering, University of Technology, VNU-HCM.

LE Khanh Dien senior lecture, Department of Mechanical Engineering, Ho Chi Minh City University of Technology, B.E (1982), M.E (1996) in Mechanical Engineering, being doctoral candidate at Ho Chi Minh City University of Technology.
Email: lkdien@hcmut.edu.vn

NGUYEN Thanh Nam Ph.D. (1991).
He has collaborated at University of Technology, VNU-HCM and has been the director of National key Laboratory of Digital Control and System Engineering, University of Technology, VNU-HCM.

THREE-DIMENSION SIMULATION OF COANDA SYNTHETIC JET DEFLECTION APPARATUS

Hoang Thi Kim Dung[1], Mai Van Phung[2], Do The Vuong[3], Nguyen Phu Khanh[4] and Tran Minh Ngoc[5]

[1,2,3,4]School of Transportation Engineering, Hanoi University of Science and Technology, Vietnam
No. 1 Dai Co Viet Road, Hanoi, Vietnam.
[5]CFD group, International Institute of Science and Computational Engineering
Email: khanh.nguyenphu@hust.edu.vn

ABSTRACT

Coandă effect is a classic phenomenon in fluid mechanics. One of the applications of this effect is an innovative nozzle which is designed to enhance the controllability of the system. This innovative nozzle is formerly named H.O.M.E.R., acronym of "High-speed Orienting Momentum with Enhanced Reversibility". This nozzle requires two primitive fluid streams, which produce a variable orientation synthetic without any moving mechanical part. Developing from the existing two – dimension simulations, in this paper, a three-dimension computational calculation was realized to examine the Coandă effect using ANSYS software and to find out the relationship between mass flow rate and the deflection angle.

Keywords: Coandă effect, Innovative nozzle, Control, CFD modeling

1. INTRODUCTION

Coandă effect was first discovered by the Romanian inventor Henri Marie Coandă (1886 – 1972) and named after him. As a classic phenomenon in fluid mechanics, Coandă effect describes the tendency of a fluid jet to be attracted to a nearby surface, as the result of a transverse pressure distribution which pushes the jet towards the wall, deflecting its path.

In the history of Coandă effect development, there are many of application such as: Dyson fan, Helicopter no tail rotor, Nozzle two channels, Flying saucer, An-74... Nozzle two channels is a new direction development in nozzle of turbojet, which help the fighter can take off and land with the shorter runway. Mostly it was simulated in two-dimension. So far, there has been little discussion about effect of wall to controllability of the deflection angle in three-dimension model.

In this paper, a three-dimension simulation of H.O.M.E.R model (Fig. 1, acronym of High-speed Orienting Momentum with Enhance Reversibility) was carried out. The model was designed to mix two primitive jets and to permit a controllable and selective angular deviation of the synthetic jet. This angular deviation is realized without any moving mechanical part.

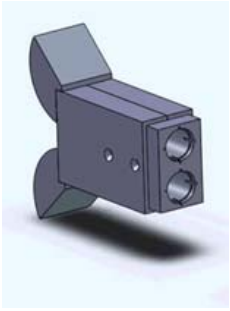

Fig. 1 H.O.M.E.R nozzle

The Nozzle is presented in Fig. 2 capable of mixing of two primitive jets 1, 2. It is designed to permit a controllable and selective angular deviation of the synthetic jet, which is produced by mixing the two primitive jets. This angular deviation is realized without any moving mechanical part.

With the aim of controlled deviation of the synthetic jet in a dynamic way, the two primitive 1 and 2 feed the nozzle and generated the synthetic outflow jet which can be governed by varying momentum of one jet 1 or 2. In this case, outflow will be deflected to curved surface of this jet. In the Fig. 1, the momentum of source 1 is greater than source 2.

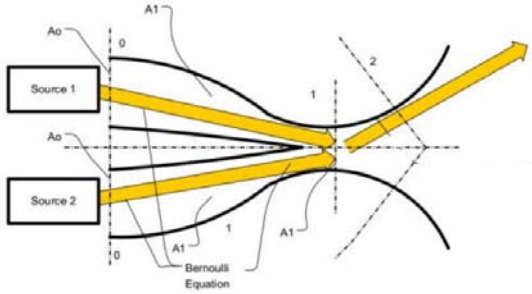

Fig. 2 Nozzle with two streams

So, What is the reason of this deflection? We discussed about the combination of three effects in Coandă effect. Explain for the phenomenon can be understood by considering the radial equilibrium of the fluid element depicted. This can be express as follow:

$$\frac{\partial p}{\partial r} = \frac{(\partial v^2)}{r} \qquad (1)$$

where: p is pressure within the jet boundary layer from the Nozzle exit slot; r is radial distance from center of curvature of surface; v is local flow speed.

It is easy to see that the pressure field thereby created forces the flow issuing from the nozzle to adhere to the surface. This field set up by requirement of radial equilibrium and will tend to force the jet towards the surface. In addition, there are two type of drag: viscous drag and entrainment of the fluid between the jet and the surface tend to deflect it to towards the surface. From the Bernoulli formula, pressure surface can be shown as follows:

$$p_S = p_\infty - \frac{\rho v^2 b}{R_c} \quad (2)$$

where: p_∞ is ambient pressure outside the Coandă flow; b is width of slot; R_c is radial of surface.

So, the value of $\rho v^2 b/R_c$ will be important. If it is larger, the more the wall pressures fall below p_∞. The wall pressure rises with distance around the surface, thereby creating an adverse pressure gradient and eventual separation.

2. MODEL DESCRIPTION

2.1 Nozzle model

In this study, based on model H.O.M.E.R, the model is described as Fig. 3.

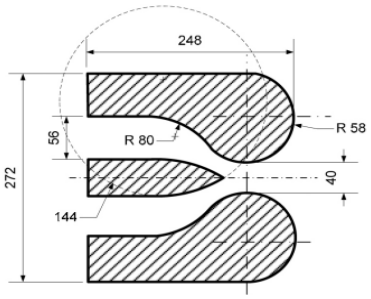

Fig. 3 Dimension of nozzle two channels

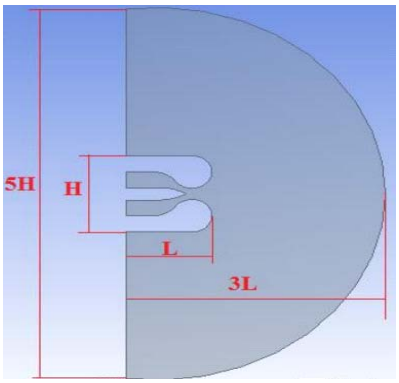

Fig. 4 Dimension of computational domain

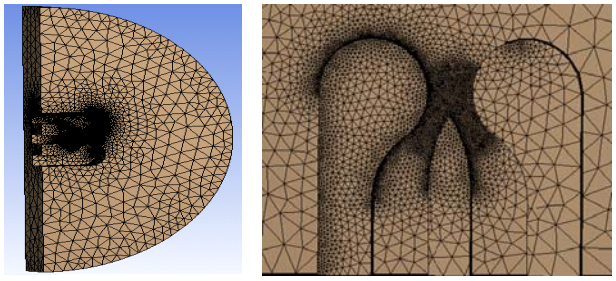

Fig. 5 Meshing

2.2 Numerical model

The Spalart-Allmaras (S-A) model is used to solve this problem. The S-A model is a one-equation model that solves a modeled transport equation for the kinematic eddy (turbulent) viscosity. The S-A model was designed specifically for aerospace applications involving wall-bounded flows and has been shown to give good results for boundary layers subjected to adverse pressure gradients.

The S-A model has been extended within ANSYS Fluent with a y^+ - insensitive wall treatment (Enhanced Wall Treatment - EWT). The EWT automatically blends all solution variables from their viscous sublayer formulation to the corresponding logarithmic layer values depending on y^+.

2.3 Boundary conditions

The required boundary conditions are described as follows:

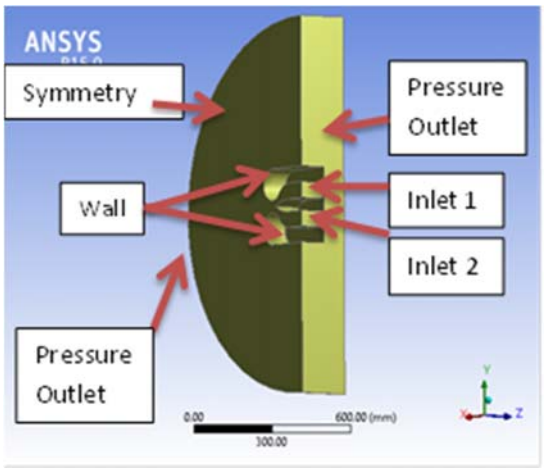

Fig. 6 Boundary conditions

- Inlet 1 boundary condition:

$$u = v = 0,\ w = w_1$$

- Inlet 2 boundary condition:

$$u = v = 0,\ w = w_2 \quad \dot{m}_1 + \dot{m}_2 = \text{const}$$

- Outlet boundary condition:

$$\frac{\partial u}{\partial z} = \frac{\partial v}{\partial z} = \frac{\partial w}{\partial z}$$

- On the wall:

$$u = v = w = 0$$

In this research, the influence of the difference between $\dot{m}_1$ and $\dot{m}_2$ to the jet is considered. The dimensionless ratio of mass flow rates $\dot{m}^*$ is defined as:

$$\dot{m}^* = \frac{\dot{m}_1 - \dot{m}_2}{\dot{m}_1 + \dot{m}_2} = \frac{w_1 - w_2}{w_1 + w_2} \quad (3)$$

3. RESULTS

3.1 Coandă effect simulation

In this three dimension simulation, the Coandă effect can be displayed clearly. In this case of $w_1 = 120 m/s$, $w_2 = 15$ m/s, $\dot{m}^* = 0.75$, the jet coming from the nozzle has a tendency to go up. The strong flow increasing its velocity dramatically comes along the round surface and drags the week one to its direction in Fig. 6. Due to the

increasing in the velocity of the first strong flow, an area of low pressure appears close to the upper wall surface of the nozzle.

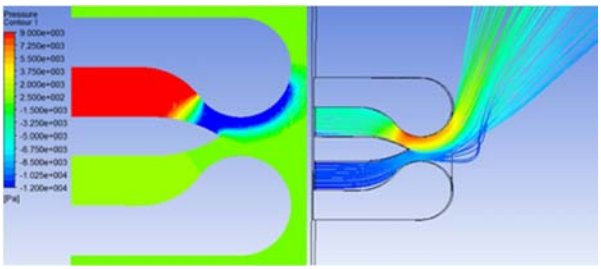

Fig. 7 Coandă effect in $\dot{m}^* = 0.75$

Fig. 8 shows that the results in 3D simulations agree well with the ones in 2D simulation in research of Michele Trancossi and Antonio Dumas, (2011) with the maximum error of 12.5%.

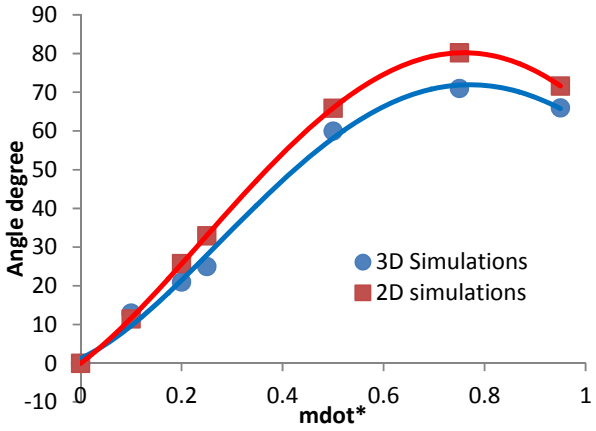

Fig. 8 Comparison between 2D and 3D simulations

A range of $\dot{m}^*$ was examined to study about its effect to the nozzle. The details are in Table 1. When $\dot{m}^*$ increases from 0.1 to 0.75, the deflection angle raise to the peak of 71 degree. After that, the deflection angle decreases in the period $\dot{m}^*$>0.75. In case of m*=0.5, streamline show that out floe attach surrounding fluid and increase velocity of it (Fig. 9). When increase m* to 0.95, this value must guarantee that Reynold number is greater than 5000.

Table 1 Influence of deflection angle on the dimensionless ratio of mass flow

Case	$\dot{m}^*$	Deflection angle
1	0.10	0
2	0.20	14
3	0.25	21
4	0.50	25
5	0.60	60
6	0.75	71
7	0.95	66

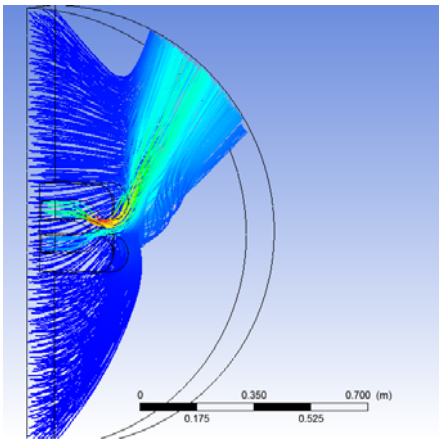

Fig. 9 Streamline in $\dot{m}^*$=0.5

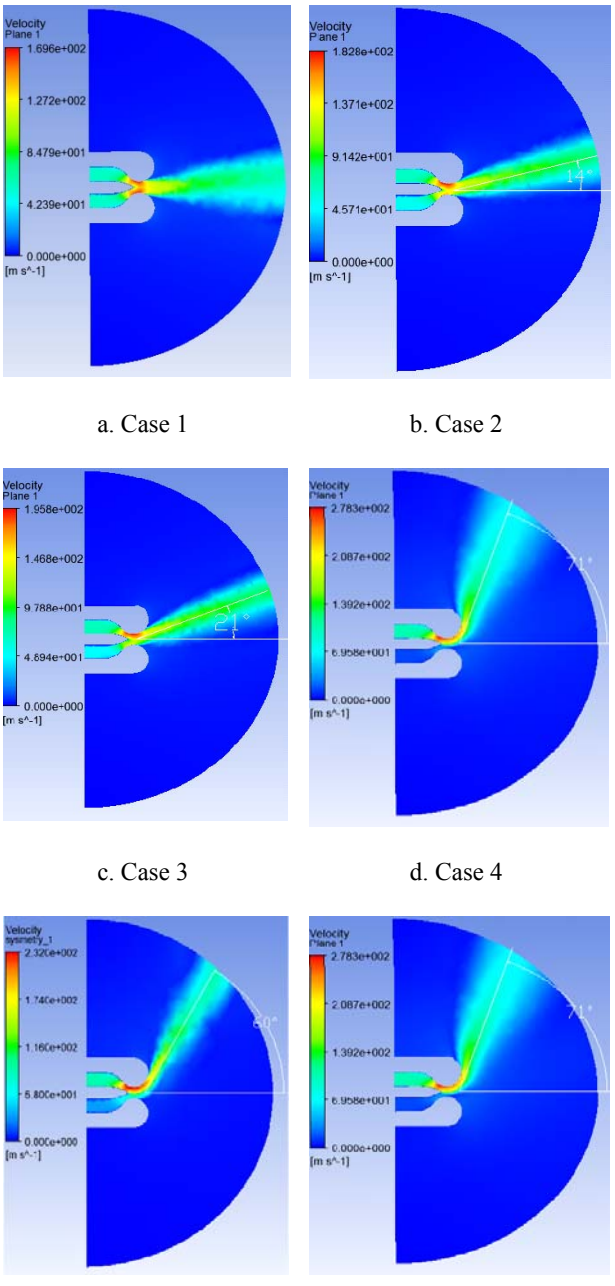

a. Case 1 b. Case 2

c. Case 3 d. Case 4

e. Case 5 f. Case 6

Fig. 10 Velocity distributions

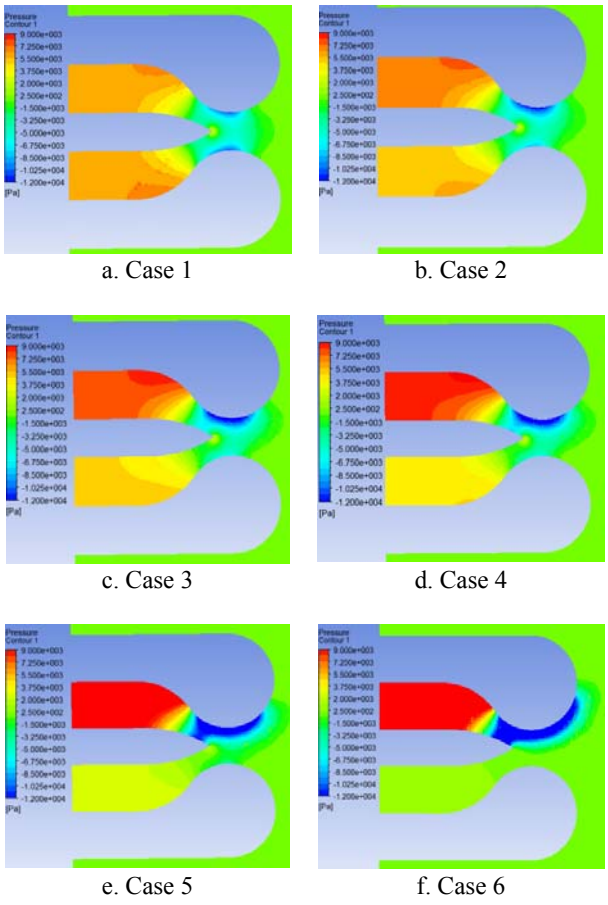

a. Case 1 b. Case 2

c. Case 3 d. Case 4

e. Case 5 f. Case 6

Fig. 11 Pressure distributions

Fig. 10 and Fig. 11 show more details about the distribution of velocity and pressure respectively when the dimension less ratio of mass flow is modified.

CONCLUSION

This study examined the Coandă effect in the nozzle. The obtained results are summarized as follows:

When there is a difference of mass flow rate between the inlets, the synthetic jet will be deflected to the side of the stronger one.

The deflection angle can be control by changing the difference between the inlets. In this case of study, the angle can be ±70o.

ACKNOWLEDGEMENTS

The authors of this paper wish to express their appreciation for the financial supports from Ministry of Science and Technology (Vietnam) through the bilateral Project 10/2014/HĐ-NĐT and from AUNSEED/Net JICA (Japan) through the CRI Project 06/CRI 2014-2016. Furthermore the supports of CFD group - International Institute for Computational Science and Engineering staffs are acknowledged.

REFERENCES

Trancossi, M., and Dumas, A., Coandă Synthetic Jet Deflection Apparatus and Control, SAE International, 2011.

Houghton, E., L., and Carpenter, P., W., Aerodynamics for Engineering Students, fifth edition, Butterworth-Heinemann, 2003.

Nguyen Phu Khanh received the B.E. (2000) in Aeronautic from Hanoi University of Science and Technology - Vietnam, M.E. (2001) in Aeronautic from National University of Mechanical and Aeronautics Engineering (ENSMA) University – France and D.E. (2006) degrees in Aeronautic from ENSMA University – France.

He is an Associate Professor, Department of Aeronautic and Space Engineering, Hanoi university of Science and Technology – Vietnam. His current interests include: Fluid Mechanics; Energy and Combustion; Nuclear Engineering; Simulation Technology

Hoang Thi Kim Dung received the B.E. (2004) in Mechanical and Aeronautical Engineering from Hanoi University of Science and Technology - Vietnam, M.E. (2005) in Aeronautical Engineering, Fluid, Acoustic and Energy from National University of Mechanical and Aeronautics Engineering (ENSMA) University – France and D.E. (2009) degrees in Aeronautical Engineering, thermal-Aerodynamics from ENSMA University – France.

She is a Doctor Lecturer, Department of Aeronautic and Space Engineering, Hanoi university of Science and Technology – Vietnam. Her current interests include: Fluid Mechanics; Energy and Combustion; Nuclear Engineering; Simulation Technology.

MODELING OF PULVERIZED COAL COMBUSTION IN THE BOILER OF POWER PLANT

Nguyen Phu Khanh[1], Hoang Tien Dat[2], Tran Viet Vu[3], Tran Minh Ngoc[4] and Hoang Thi Kim Dung[5]

[1, 2,3,5]School of Transportation Engineering, Hanoi University of Science and Technology, Vietnam
[4]CFD group, International Institute of Science and Computational Engineering
No. 1 Dai Co Viet Road, Hanoi, Vietnam.
Email: khanh.nguyenphu@hust.edu.vn

ABSTRACT

The combustion of pulverized coal particles is a heterogeneous combustion process, including 3 stages: Devolatilization, combustion of volatiles and char combustion. Rate of reactions is controlled by the diffusion rate of oxygen to particle surface and the surface reaction rate. ANSYS CFX 14.5 is a powerful simulation tool that is used in this study. The results received from CFX including temperature, velocity and NOx distributions would be analyzed in order to carry out characteristics of the combustion process. Three cases of study with three different coal analysis data would be considered to evaluate changes in the distributions.

Keywords: coal combustion, heterogeneous combustion, NO formation, CFD modeling

1. INTRODUCTION

In Vietnam, thermoelectric power accounts for approximately 17% of total electrical power. In the future, coal power plants is expected to generate 48% of electric energy to the year 2020 and 51.6% to the year 2030. Coal extracted from domestic mine is sufficient for this need, yet not qualified enough; and the country needs to import good coal in order to operate power plants. As consequence, making use of Vietnamese coal while assuring the performance of thermal plants becomes an urgent issue. One prospective solution is the mixing of Vietnamese coal with high-quality imported coal. However, the question of performance and efficiency of this solution still remains. Besides, the environmental aspect of the combustion needs to be counted. Nitrogen oxides are products of great environmental consequence but have not been thoroughly studied, comparing to carbon oxides. For those reasons, this work aims at evaluating combustion performance and emission of nitrogen oxides.

2. COMBUSTION PROCESS AND FORMATION OF NITROGEN OXIDE

The combustion process involves 3 stages in sequence: Coal devolatilization, volatile combustion and char combustion. The formation of NO involves different mechanism, two of which are studied in this work.

2.1 Coal devolatilization

In this first stage, coal particles are heated, moisture evaporates and is to be released from the particle as the temperature of the particle begins increasing. As the temperature is high enough, gaseous fuel components are released. The process can be described by the equation below:

$$\text{Raw Coal} \xrightarrow{t^o} \text{Char} + \text{Volatiles} \qquad (1)$$

To account for this process, the single rate devolatilization model (Badzioch & Hawksley, 1970) is used. The model assumes that the rate of devolatilization is first-order dependent on the amount of volatiles remaining in the particle:

$$\frac{dC_O}{dt} = -k_V C_O \quad \frac{dV}{dt} = Yk_V C_O \quad \frac{dC_{ch}}{dt} = (1-Y)k_V C_O \qquad (2)$$

where CO is the mass fraction of raw (i.e. unreacted) coal; C_{ch} is the mass fraction of residual char; V is the mass fraction of volatiles matter released in the gas phase; Y is a factor to correct for the enhancement of yield due to rapid heating; the rate constant k_V is expressed in Arrhenius form as:

$$k_V = A_V e^{-(E_V/RT_P)} \qquad (3)$$

where T_P is the temperature of coal particles (assumed uniform); R is the gas constant; and A_V and E_V are constants based on coal properties.

2.2 Coal volatile combustion

Volatile matter released from coal particles consists mainly of gaseous hydrocarbons, that burn rapidly and generate high temperature zone to initiate char combustion. Assume that the products of combustion are carbon dioxide and water vapor exclusively, the reaction occurs as follow:

$$C_xH_y + \left(x + \frac{y}{4}\right)O_2 \xrightarrow{t^o} xCO_2 + \frac{y}{2}H_2O \qquad (4)$$

The chemical reaction rate is fast relatively to the rate of diffusion of oxygen; thus, the rate of the process is controlled by the mixing rate of the fuel gas and air. In this study, the eddy dissipation model is used to calculate this process. The rate of combustion is proportional to a mixing

time defined by the turbulent kinetic energy - k, and dissipation - ε:

$$\text{rate} \propto \frac{\varepsilon}{k} \quad (5)$$

2.3 Char combustion

Once the devolatilization has completed, a char particle remains and is consumed through surface oxidation reactions at high enough temperature. The major combustible component of char is carbon. At a simple level, the process occurs is considered as follow:

$$C + O_2 \xrightarrow{t^o} CO_2 \quad (6)$$

The char reaction is determined by both the rate of diffusion to the surface and the rate of chemical reaction at the surface. The char oxidation model presented by M.A. Field, 1970, is used. The surface reaction is assumed to be first-order in the oxygen mole fraction. The rate of diffusion of oxygen per unit area of particle surface is given by: $k_d(X_g - X_S)$, where X_g is the mole fraction of oxygen in the furnace gases far from the particle boundary layer and X_S is the mole fraction of oxygen at the particle surface. The char oxidation rate per unit area of particle surface is given by $k_c X_S$. k_d and k_c are factors whose values depend on coal particle properties and gas flow conditions. The overall char reaction rate of a particle is given by:

$$\frac{dm_c}{dt} = \left(k_d^{-1} + k_c^{-1}\right)^{-1} X_g 4\pi R_p^2 \frac{P}{P_A} \quad (7)$$

where P and P_A are the local and atmospheric pressure, respectively; R_p is the particle radius.

2.4. Formation of Nitrogen Oxide

This work studies the formation of NO through Thermal mechanism and Prompt mechanism. The former mechanism, called Extended Zeldovich mechanism, is related to the reactions of free radical O and N species at high temperature. The later mechanism, on the other hand, is related to reactions of Nitrogen with radicals such as C, CH, and CH_2 fragments derived from coal's burning.

3. MODEL DESCRIPTION

A three-dimensional hex-dominant mesh containing around 140,000 elements was constructed using ANSYS MESHING. The mesh was refined in the twelve burners region at four corners of boiler model. Three types of coal with proximate and ultimate analyses are contained in Table 1.

Table 2 contains additional coal properties used by ANSYS CFX and the burner input conditions.

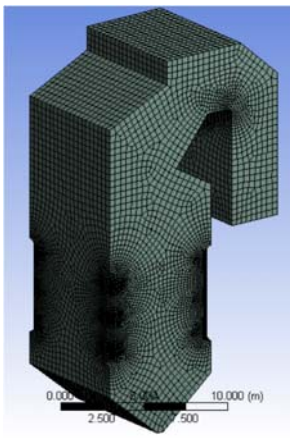

Fig. 1 3D hex-dominant mesh of the boiler model

Table 1 Proximate and ultimate analysis of three types of coal

P. Analysis (As-received)	**Fixed Carbon** (%)		**Volatiles** (%)	**Ash** (%)	**Moiture** (%)
Type A (Vietnam Coal)	60.92		7.37	25.33	6.38
Type B (Imported Coal)	31.7		38.45	9.23	20.62
Type C (Mixed 9A/1B in mass)	58.0		10.48	23.72	7.8
U. Analysis (DAF)	**C**	**H**	**O**	**N**	**S**
Type A	90.06	3.4	4.11	1.52	0.91
Type B	74.29	5.12	18.65	1.49	0.45
Type C	88.49	3.57	5.56	1.52	0.86

Table 2 Additional coal properties used in CFX

	Particle Diameter (μm)	**Lower Heating Value** (kJ/kg)
Type A	100	21844
Type B		18125
Type C		21472

Table 3 Burner inlet conditions.

Total coal mass flow rate (kg/s)	3.5
Injection type	Surface, Uniform
Injection velocity (m/s)	17
Temperature (coal & air) (°C)	250

4. RESULTS AND DISCUSSION

4.1 Temperature distribution

The distribution of temperature inside the combustion zone was considered. Fifteen cross-sections were created in order to analyze this distribution. Figures below are results of the case Coal type A, this is a kind of coal that is consumed currently in power plants in Vietnam.

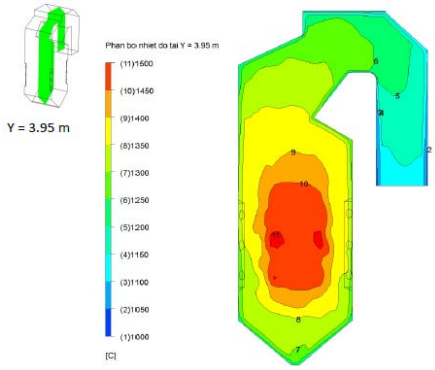

Fig. 2 Distribution of temperature at the middle vertical cross-section

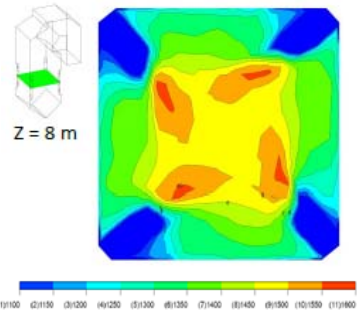

Fig. 3 Distribution of temperature at the cross-section Z = 8 m, which crosses a burner position

The highest temperature reached is 1615ºC. The high temperature zone is the center of the boiler.

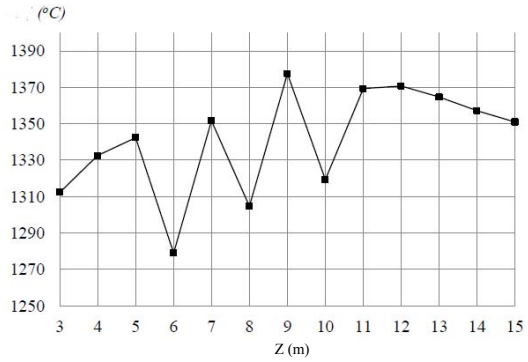

Fig. 4 Average temperature at cross-sections from the bottom up.

From the bottom to higher areas (the bottom is at Z = 0 m), the average temperature at cross-section increases and gets the highest value at Z = 9 m. The cross-sections Z = 6, 8 and 10 m cross burner positions, which have cold flow of coal and air, thus, they have lower average temperature. Results are quite suitable to experimental data measured in real boiler, the experimental value for highest temperature is around 1500ºC in the experiment with same initial conditions.

The figure 5 shows the distribution of the two rest cases. The case "Type B" has the average temperature to be low relative to cases "Type A" and "Type C". The reason is the lower content of fixed carbon, the main combustible component, present in coal B. Nevertheless, the combustion of coal B generates the highest temperature of 1726ºC, which is greater than this value of coal A, due to the higher content of volatile matter in coal B. It is clear that the trend of temperature distribution is not affected by the change in coal components.

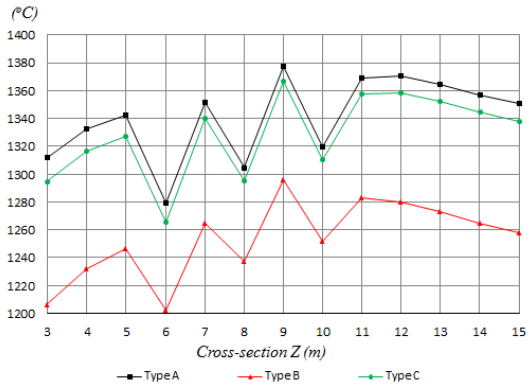

Fig. 5 The distribution of average temperature of three cases study

4.2 Emission of nitrogen oxide

The concentration of NO gas inside the boiler is studied.

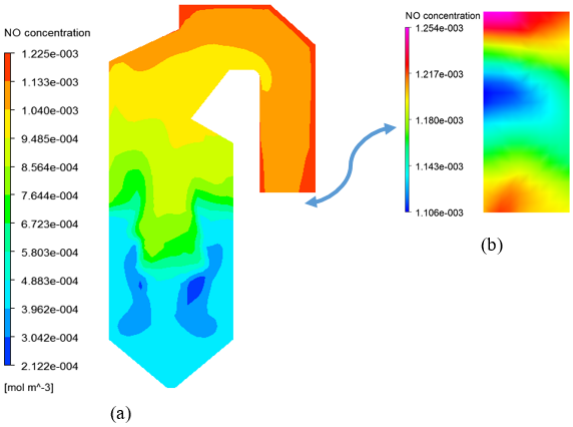

Fig. 6 NO contribution on the middle cross section (a) and the outlet section (b)

The result shows that NO molecular concentration in this case ranges approximately from $2.1*10^{-4}$ to $1.2*10^{-3}$ mol/m^3. This concentration increases gradually along the height of the boiler. The region with highest NO concentration locates around the outlet of the boiler. Maximum value is up to $1.2*10^{-3}$ mol/m^3, attains on monitor surface locating at outlet section, where NO concentration is distributed rather evenly with little fluctuation.

In the regions where concentration is low, which are lower zones of the boiler, NO concentrates mostly at the area around the boiler's center. This area is presumably the location where the combustion commences. Quite the contrary, at higher zone of the boiler with higher NO concentration, NO has the tendency to stick at the area close to wall. This can be explained by the fact that, with less turbulence, this near wall area is favorable to the formation and intensification of NO gas.

A comparison of NO distribution and temperature at the middle vertical cross-section shows that NO is not concentrate at the region with highest temperature. This complies with the NO formation theory according to which NO is not formed immediately at the flame zone but after.

CONCLUSION

This paper presented the use of numeric simulation in studying coal combustion. This approach promises potential applications, particularly in thermal power industry. The outcome of this study gives an overview of heat distribution, which prompts better supervision of boiler, for example with suitable probes disposition; as well as motivates better boiler design. It is also observed that different proportions of two kinds of coal (Vietnam coal and imported coal) result in different thermal effects.

Further studies about more coal mixture should be able to provide an optimal proportion that can be used in the future. Besides, NO formation is proved to be considerable; different solutions to prevent this emission should be carried out.

ACKNOWLEDGEMENTS

The authors of this paper wish to express their appreciation for the financial supports from Ministry of

Science and Technology (Vietnam) through the bilateral Project 10/2014/HĐ-NĐT and from AUNSEED/Net JICA (Japan) through the CRI Project 06/CRI 2014-2016. Furthermore the supports of Advantech, Jsc and Ninh Binh Thermal Power Joint-stock Company are acknowledged.

REFERENCES

Irvin, G., and Richard, A., Y., Combustion, 4th edition, Academic Press, 2008.

Eugene, S., D., Selected Values of Heats of Combustion and Heats of Formation of Organic Compounds Containing the Elements C, H, N, O, P, and S*, Journal of Physical and Chemical Reference Data, Vol. 1, No. 2, 1972.

Fawzy E., and Saad el-din Habik Fundamentals and technology of combustion, p54-73, Elsevier Science, 2002.

Warnatz, J., Mass, U. and Dibble, R. W., "Combustion", Springer, Verlag, 1996, pp.219-221.

Melte, P., C., and Pratt, D., T., Measurement of Atomic Oxygen and Nitrogen Oxides in Jet Stirred Combustion, In 15th Symposium (Int'l) on Combustion. The Combustion Institute. 1061–1070. 1974.

Kandamby, N., Lazopoulos, G., F., Lockwood, C., Perera, A., and Vigevano, L., Mathematical Modeling of NOx Emission Reduction by the Use of Reburn Technology in Utility Boilers, In ASME Int. Joint Power Generation Conference and Exhibition, Houston, Texas. 1996.

The Engineering Toolbox, Overall Heat Transfer Coefficient: http://www.engineeringtoolbox.com/overall-heat-transfer-coefficientd_434.html, last access 10/1/2015.

ANSYS Inc. (2014), ANSYS CFX User's Guide, Theory Guide and Software Tool, Release 15.0, Website: http://www.ansys.com/

Nguyen Phu Khanh received the B.E. (2000) in Aeronautic from Hanoi University of Science and Technology - Vietnam, M.E. (2001) in Aeronautic from National University of Mechanical and Aeronautics Engineering (ENSMA) University – France and D.E. (2006) degrees in Aeronautic from ENSMA University – France.

He is an Associate Professor, Department of Aeronautic and Space Engineering, Hanoi university of Science and Technology – Vietnam. His current interests include: Fluid Mechanics; Energy and Combustion; Nuclear Engineering; Simulation Technology

Hoang Thi Kim Dung received the B.E. (2004) in Mechanical and Aeronautical Engineering from Hanoi University of Science and Technology - Vietnam, M.E. (2005) in Aeronautical Engineering, Fluid, Acoustic and Energy from National University of Mechanical and Aeronautics Engineering (ENSMA) University – France and D.E. (2009) degrees in Aeronautical Engineering, thermal-Aerodynamics from ENSMA University – France.

She is a Doctor Lecturer, Department of Aeronautic and Space Engineering, Hanoi university of Science and Technology – Vietnam. Her current interests include: Fluid Mechanics; Energy and Combustion; Nuclear Engineering; Simulation Technology.

ACCURACY IMPROVEMENT FOR MARG SENSOR USING IN CONTROL OF QUADROTOR

Minh Phung Tran, Viet–Hong Tran
Department of Mechatronic Engineering, Hochiminh city University of Technology

ABSTRACT

In this paper, we propose an algorithm to estimate orientation angles (roll, pitch, and yaw) by using two Kalman filters to estimate nine elements of the Direction Cosine Matrix (DCM). The third row of DCM is estimated based on angular velocity and acceleration. The second row of DCM is estimated from roll and pitch which calculated from the third row of DCM, and magnetic values on three axes. The last three elements of the DCM are computed from the DCM orthogonalization property. Application of typical Kalman Filter in DCM method helps avoiding the first order approximation error. The performance of proposed algorithm is verified by doing experiments with the sensors attached to a quadrotor. A flight controller use an inertial measurement unit (IMU) to collect data and feed to our filter. The estimation results are compared with the data measured by a high accuracy sensor to show that the maximum error is less than 2º.

1. INTRODUCTION

An IMU is an electronic device that measures and reports a craft's velocity, orientation, and gravitational forces, using a combination of accelerometers, gyroscopes and magnetometers. It is used to estimate orientation of a rigid body relative to an Earth fixed reference frame. To describe the orientation of a rigid body, we use Euler angles roll, pitch, and yaw. IMUs are typically used to maneuver aircraft, including unmanned aerial vehicles (UAVs), among many others. A major disadvantage of using IMUs for navigation is that they typically suffer from accumulated error, including Abbe error. Because the guidance system is continually adding detected changes to its previously-calculated positions, any errors in measurement, however small, are accumulated from point to point. This leads to 'drift', or an ever-increasing difference between where the system thinks it is located, and the actual location. So that, the filters is used to estimate the true value of orientation.

Orientation determination with inertial sensors includes a propagating procedure with gyro sensor data and an updating procedure with accelerometer data. There are generally three principal methods to propagate the orientation information from the differential form such as Euler, Direction Cosine Matrix and Quaternion approaches.It has been known that the Euler approach of propagating procedure is conceptually easy to understand but it is the most computationally expensive and the state may reach to singularity (Suh, et al., 2006), (Nguyen, et al., 2006), and (Gebre-Egziabher, et al. 2004). Also, they introduced the quaternion-based Kalman filter (Marins, et al., 2001), and (Yun, and Bachmann, 2006). These papers present the real-time implementation and testing results of the quaternion-based Kalman filter. Experimental results validate the Kalman filter design, and show the feasibility of the Magnetic, Angular Rate, and Gravity (MARG) sensors for real-time human body motion tracking. The DCM method of propagation transfering matrix has been known to show the performance in-between compared with Euler and Quaternion approaches (Choukroun, 2003) and (Nebot, and Durrant-Whyte, 1999). DCM method has been widely used in attitude estimation but when extending to orientation, the number of DCM's parameters is much more than those of Euler and Quaternion parameters, In addition, the conventional State Matrix Kalman filter was used (Choukroun, 2003) to keep the natural dynamics of DCM matrix which causes the big computing burden.

In this paper, we introduce an algorithm to estimate three Euler angles from IMU and a

magnetic compass by using the DCM method and Kalman filter. This method helps avoiding the first order approximation error, and reduce the computation effort.

2. KALMAN FILTER DESIGN BASED ON DCM

2.1. DCM

Matrix ${}^E_B R$ is rotation matrix DCM from sensor body coordinate system {B} to earth coordinate system {E} (Nguyen, H.Q.P, et al., 2009).

$${}^E_B R = R_Z^{\psi}.R_Y^{\theta}.R_X^{\phi} \quad (1)$$

The corresponding Euler angles: roll(ϕ), pitch(θ), yaw(ψ) can be calculated as:

$$\phi = \text{atan2}\left({}^E_B R_{32}, {}^E_B R_{33}\right) \quad (2)$$

$$\theta = -\arcsin({}^E_B R_{31}) \quad (3)$$

$$\psi = \text{atan2}({}^E_B R_{21}, {}^E_B R_{11}) \quad (4)$$

Therefore, if we estimate elements of the DCM instead of Euler angles directly, the singularity problem in Euler based method is avoided.

2.2. Heading calculation

(Caruso, M.J., 2000) proposed a method to determine the heading using geomagnetic measurements.

$$\psi = \frac{-{}^B m_y \cos\phi + {}^B m_z \sin\phi}{{}^B m_x \cos\theta + {}^B m_y \sin\phi\sin\theta + {}^B m_z \sin\theta\cos\phi} \quad (5)$$

where ${}^B m_x$, ${}^B m_y$, ${}^B m_z$ are the components of geomagnetism in the coordinate system {B}, which are measured from magnetometers.

2.3. Proposed filter design

From Eq. (2) to Eq. (4), in order to calculate the Euler angles, we need to know five out of nine elements of ${}^E_B R$. However, the necessity to calculate whole the matrix increases the complexity and calculation time. Typically, in order to reduce the complexity, only the third row of ${}^E_B R$ is needed to calculate θ and ϕ according to Eq. (2) and Eq. (3), while ψ is calculated from Eq. (5). This method is fast, but the accuracy is low due to the drift and unstability of geomagnetic measurement.

Because the three unit vectors (each row of ${}^E_B R$) are orthogonal, so the third vector (one row) will be the cross product of the others (other two rows). Therefore, we will use a structure of two Kalman filters to estimate six elements in two rows of ${}^E_B R$, then we can construct the whole ${}^E_B R$ easily. The structure of proposed algorithm is shown in Figure 1.

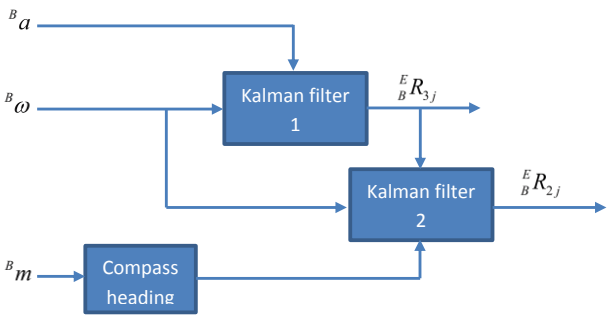

Fig. 1 Structure of proposed algorithm

The state equations of the two discrete Kalman filters are as following,

$$x_{k+1} = \Phi_k(\Delta T, \omega) x_k + w_k \quad (6)$$

$$z_{k+1} = H_{k+1} x_{k+1} + v_{k+1} \quad (7)$$

where the Φ_k is the first order approximation of the process model, and ΔT is sampling time.

$$\Phi_k = \begin{bmatrix} 1 & {}^B\omega_z.\Delta T & -{}^B\omega_y.\Delta T \\ -{}^B\omega_z.\Delta T & 1 & {}^B\omega_x.\Delta T \\ {}^B\omega_y.\Delta T & -{}^B\omega_x.\Delta T & 1 \end{bmatrix} \quad (8)$$

The Kalman filter 1 takes into account acceleration and angular velocity in {B} coordinate to estimate ${}^E_B R_{3j}$: ${}^1x_k = \begin{bmatrix} {}^E_B R_{31} & {}^E_B R_{32} & {}^E_B R_{33} \end{bmatrix}^T$,

${}^1z_k = \begin{bmatrix} {}^B a_x & {}^B a_y & {}^B a_z \end{bmatrix}^T$, ${}^1H_k = gI_3$.

The noise covariances of process model and measurement model follow:

$${}^1Q_k = E\left\{ {}^1w_k \, {}^1w_k^T \right\} = \alpha_1 I_3 \quad (9)$$

$${}^1R_k = E\left\{ {}^1v_k \, {}^1v_k^T \right\} = r_a I_3 \quad (10)$$

where α_1 and r_a are chosen depending on the noise level to maintain the smooth output response.

The Kalman filter 2 produces ${}^E_B R_{2j}$ by using geomagnetic measurement as measurement model.

${}^2x_k = \begin{bmatrix} {}^E_B R_{21} & {}^E_B R_{22} & {}^E_B R_{23} \end{bmatrix}^T$,

${}^2z_k = \begin{bmatrix} \sin\psi\cos\theta \\ \sin\phi\sin\theta\sin\psi + \cos\phi\cos\psi \\ \cos\phi\sin\theta\sin\psi - \sin\phi\cos\psi \end{bmatrix}$, ${}^2H_k = I_3$,

${}^2Q_k = E\left\{ {}^2w_k \, {}^2w_k^T \right\} = \alpha_2 I_3$, ${}^2R_k = E\left\{ {}^2v_k \, {}^2v_k^T \right\} = r_m I_3$.

The role of α_2 and r_m is similar α_1 and r_a.

Then, the state vector is normalized by

$${}^E_B R_{ij}(k) = \frac{{}^i x_k(j)}{\sqrt{\sum_{i=1}^3 {}^i x_k^2(j)}}, i = 2,3, j = 1,2,3 \quad (11)$$

$${}^E_B R_1(k) = {}^E_B R_2(k) \times {}^E_B R_3(k) \quad (12)$$

3. EXPERIMENTAL RESULTS

3.1 Experiment setup

Fig. 2 Mounting the sensors

The sensors in experiment are mounted on the base of a quadrotor, next to each other as shown in Figure 2.

For the real measurement data, we used a flight controller for multicopter integrated IMU which includes 6–DOF sensor MPU6050 and 3-Axis digital compass sensor HCM5883L. The parameters of those sensors are shown in Table 1 and Table 2.

Table 1. MPU6050 parameters

Parameter	Quantity	Unit
GYROSCOPES		
Sensitivity	131	LSB/(°/s)
Range	±250	°/s
Output rate	100	Hz
Output noise	0.05	°/s –rms
ACCELEROMETERS		
Sensitivity	16,384	LSB/g
Range	±2	g
Output rate	100	Hz
Output noise	400	μg/√Hz

Table 2. HCM5883L parameters

Parameters	Quantity	Unit
MAGNETOMETERS		
Sensitivity	230	LSb/gauss
Digital Resolution	0.73	milli-gauss
Output Rate	75	Hz

For the reference values, we used a very high accuracy sensor: inclination sensor model INY360D-F99-2I2E2-V17 whose the parameters is in Table 3.

Table 3: INY360D-F99-2I2E2-V17 parameters

Parameter	Quantity	Unit
Measurement range	0 ... 360	°(degrees)
Absolute accuracy	≤± 0.5	°(degrees)
Resolution	≤0.1	°(degrees)

3.2 Results

The measured data (raw) collected from IMU, the estimation values and the referenced values provided by inclination sensor were compared in Figure 3 to Figure 5.

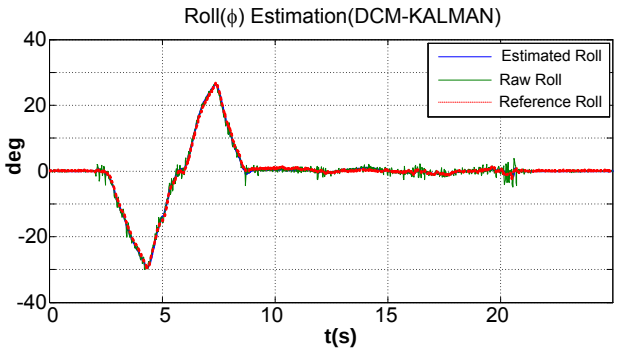

Fig. 3 Roll angles

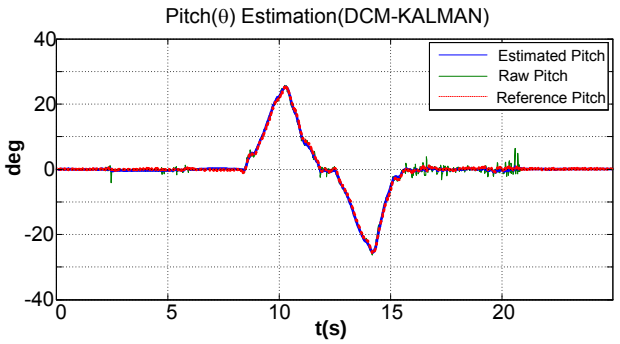

Fig. 4 Pitch angles

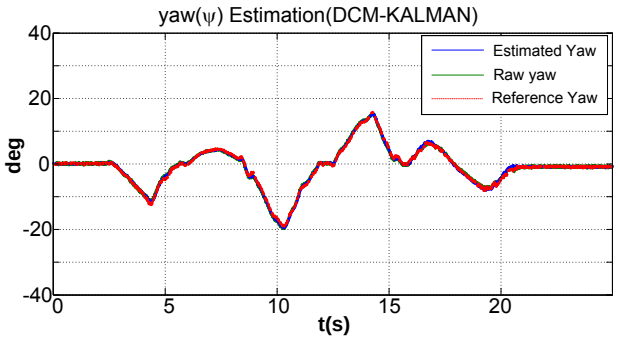

Fig. 5 Yaw angles

There are noises in the raw data, so the plot of raw data (green line) is rugged. However, the plot of estimation values is smooth and very close to the reference values.

To verify the accuracy of the algorithm, we calculate root mean square error e_{RMS} and maximum error e_{max}:

$$e_{RMS} = \sqrt{\frac{1}{N}\sum_{k=1}^{N} e^2(kT)} \quad (13)$$

$$e_{Max} = max\left|e(kT)\right| \quad (14)$$

where

$$e(kT) = \left|\text{Estimation}(kT) - \text{Reference}(kT)\right| \quad (15)$$

The results are shown in Figure 6.

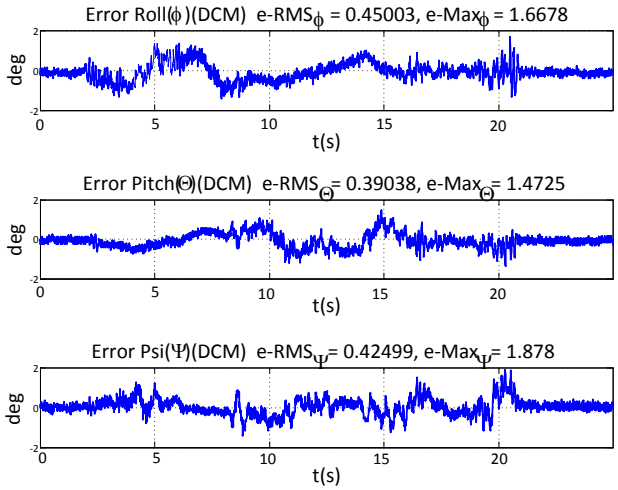

Fig. 6 Error of roll, pitch, and yaw angles compared with referenced angles

The experimental results illustrate that the maximum error of all three angles is less than 2^o, no drift and stabilization. The results show the possibility to apply this algorithm to the real system.

4. CONCLUSIONS

In this paper, we have presented and implemented the algorithm for orientation estimation with two Kalman filters based on DCM method. Just update three DCM's states out of nine states is efficient to save the computational effort. And testing results have shown many advantages of our proposed algorithm in solving original problems of orientation estimation. Instead of extended Kalman Filter in Euler-based and Quaternion-based method, the Kalman Filter that developed in DCM-based method can help avoiding error of first order approximation. That why DCM method leads others about accuracy.

REFERENCES

Caruso, M.J., Applications of magnetic sensors for low cost compass systems, IEEE Position Location and Navigation Symposium, pp. 177-184, 2000.

Choukroun, D., Novel methods for attitude determination using vector observations, PhD thesis, 2003.

Gebre-Egziabher, D., et al., Design of multi-sensor attitude determination systems, IEEE Trans. Aerosp. Electron. Syst., vol. 40, no. 2, pp. 627-649, 2004.

Marins, J.L., et al., An extended Kalman filter for quaternion-based orientation estimation using MARG sensors, Proc. IEEE/RSJ Int. Conf. on Intell. Robots and Syst., vol. 4, pp. 2003 - 2011, 2001.

Nebot, E., and Durrant-Whyte, H., Initial calibration and alignment of low-cost inertial navigation units for land vehicle applications, J. Robotic Syst., vol. 16, no. 2, pp. 81-92, 1999.

Nguyen, H.Q.P, et al., A GPS/INS integration system for land vehicle application, Proc. SICE-ICASE Int. Joint Conf., pp. 482-487, 2006.

Nguyen, H.Q.P, et al., A DCM based orientation estimation algorithm with an inertial measurement unit and a magnetic compass, *J. Universal Comput. Sci.*, vol. 15, no. 4, pp. 859-876, 2009.

Suh, Y.S., et al., Attitude estimation adaptively compensating external acceleration, JSME Int. J., Series C: Mech. Syst. Mach. Elements and Manufacturing, vol. 49, no.1, pp. 172-179, 2006.

Yun, X., and Bachmann, E.R., Design, implementation, and experimental results of a quaternion-based Kalman filter for human body motion tracking, IEEE Trans. Robotics, vol. 22, no.6, pp. 1216-1227, 2006.

Minh Phung Tran received the B.E. in 2011. He is currently a Master student in Mechatronic engineering at Hochiminh city University of Technology. He is interested in quadrotor and automation.

Viet-Hong Tran received the B.E. (2002), M.E. (2006), and PhD degree in 2011. He is a lecturer at Department of Mechatronic Engineering, Faculty of Mechanical Engineering, Hochiminh city University of Technology. His current interests include multirobot system, process control and distributed/decentralized control.

Stereo Vision-Aided Inertial Navigation System

Tung A.Dang, Duy H.Nguyen, Hao V.Nguyen
Department of Electrical & Electronics Engineering, Ho Chi Minh City University of Technology

ABSTRACT

An inertial navigation system (INS) is a navigation system that uses motion sensors and rotation sensors to continuously calculate the position, orientation of a moving object without the need for external references. Originally, INS is used in military and aerospace. In applying this technology to the field of mobile robotics, research community uses low-cost MEMS sensors instead. This enlarges the positioning error, so that it is necessary to integrate with other sensors to increase accuracy. Visual odometry (VO) technology uses stereo camera or a pair of images at the same time to estimate motion. Performance of VO is comparable to wheel odometers and GPS under certain conditions; therefore it is an accepted choice for integration with inertial navigation system especially in GPS denied environments. In this paper, the authors propose and verify a fusion method for stereo vision-aided inertial navigation system. We uses extended Kalman filter to estimate the motion of object including position and orientation. Experiment results have shown that the proposed algorithm reduces accumulation error of the INS system and achieves high performance.

1. INTRODUCTION

INS, which is IMU (Inertial Measurement Unit) based navigation system, is originally used in military applications such as spacecraft industry, and missiles due to its expensive cost. There was significantly decreasing in cost of inertial sensors using MEMS technology, followed by civil applications in the field of mobile robots. Basically, acceleration of a moving rigid object is calculated from different between returned value of the accelerometer sensor and the projection of the earth's gravity vector onto object's coordinate. Then travelled distance will be computed using double integral of acceleration. Main advantage of this navigation method is independent with object's mechanical structure.

Error from this method can be divided into two reasons. Systematic error is from sensor's quality, bias and misalignment between frames. This can be improved by careful calibration, and choose higher precision sensors [1]. Another source of error comes from estimation algorithm, or when system is moved in low speed condition. Common practice filter usually used in localization system is Kalman filter [2,3,4,5]. In addition, magnetometer can be aided to system to increase the performance [2,3]. However, double integral leads to large error over time [6]. Therefore, it is necessary to integrate with other sensors such as wheel encoders, GPS, and camera to reduce the error.

Visual odometry technology uses image processing techniques to apply to localization system. Vision sensor becomes more popular due to low cost and capability enhancement. Vision based localization system has many advantages in comparison with others: can be used both indoor and outdoor, enhance more functions to robot such as SLAM (Simultaneous Localization And Mapping), obstacle avoidance, traffic sign detection [7,8]… However, it is disturbed by environment conditions such as low or too bright light, lack of features and high speed moving [7, 8]. Moreover, it provides a low update rate because of high computation load.

Stereo vision is an active research field in visual odometry use two cameras to create a 3D image. Localization system based on stereo vision achieves high precision under 2% [15, 16]. Geiger et al. [16] describe a novel real-time algorithm to estimate the motion from two sequence couple of images. In this paper, we use stereo camera and the filter proposed by Geiger et al. [16] to provide inputs for our fusion algorithm. We propose an effective extended Kalman filter to fuse two kinds of above sensors to implement a high frequency localization system. It is a 6 DOFs system included three Euler rotation angles and position in Cartesian coordinate. This method will overcome disadvantage of each sensor and work as complementary filter. There are two main methods to integrate this system: loosely-couple and tightly-couple. In the tightly-couple system, IMU outputs are integrated directly to image processing algorithm. A common choice is support to detect feature points [9, 10], boost the calculation [11, 12] used for real-time applications. In the other hand, loosely-couple system contains two different filter for each sensor (IMU, camera), and then they are fused at a center filter. INS plays a role as process model and Vision's outputs are input for measurement model [13, 14]. This structure has an advantage that separate two sensors so that we can develop and test each filter for each sensor. Therefore, in this paper we implement and verify a loosely-couple method based on extended Kalman filter to integrate Vision system and INS.

2. STEREO VISION AIDED INS

First step in integration system is calibration to compensate misalignment and calculate transformation matrix between frames. We use a well-known method proposed by Bouguet [17] and Lobo et al [18]. To represent 3D moving of system we need to know transformation matrix 4x4 included a rotation matrix 3x3 and a translation vector 3x1:

$$H_k^{\ 0} = \{R_k^{\ 0}, t_k^0\}$$

Where $H_k^{\ 0}, R_k^{\ 0}, t_k^0$ are matrix or vector transform the coordinate at time kT to first state.

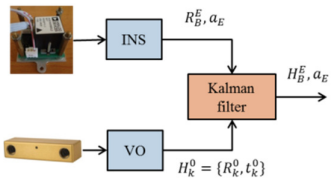

Fig 1. Loosely-couple Vision/INS system

We use quaternion to demonstrate the rotation to avoid singular case, and reduce number of variables. State variables of integrated system are presented as below:

$$\begin{cases} x = \left[q, {}^E s, {}^E v, {}^E a\right] \\ y = \left[q_y, {}^E a_y, s_y\right] \end{cases}$$

Where:

- $q = \left[q_1, q_2, q_3, q_4\right]$: four elements of a quaternion.
- ${}^E s = \left[s_x, s_y, s_z\right]$: position in Cartesian coordinate.
- ${}^E v = \left[v_x, v_y, v_z\right]$: velocity of system.
- ${}^E a_e = \left[a_{ex}, a_{ey}, a_{ez}\right]$: acceleration of system.

Process model:

$$\begin{cases} \dot{q} = \frac{1}{2} q \otimes \omega^B = \left[\frac{1}{2} R_\omega\right] q \\ {}^E\dot{s} = {}^E v \\ {}^E\dot{v} = {}^E a_e \\ {}^E\dot{a}_e = c_a {}^E a_e \end{cases} \quad (1)$$

Where: R_ω is skew-symmetric matrix

$$R_\omega = \begin{bmatrix} 0 & \omega_z & -\omega_y & \omega_x \\ -\omega_z & 0 & \omega_x & \omega_y \\ \omega_y & \omega_x & 0 & \omega_z \\ -\omega_x & -\omega_y & -\omega_z & 0 \end{bmatrix}$$

From equations (1) we rearrange to state space model as follow:

$$\dot{x} = \begin{bmatrix} \left[\frac{1}{2} R_\omega, 0_{4x9}\right] \\ \left[0_{3x7}, I_{3x3}, 0_{3x3}\right] \\ \left[0_{3x10}, I_{3x3}\right] \\ \left[0_{3x10}, c_a I_{3x3}\right] \end{bmatrix} x = \phi x \quad (2)$$

Measurment model:

$$\begin{cases} q_y = q = \left[I_{4x4}, 0_{4x9}\right] x \\ {}^E a_y = {}^E a_e = \left[0_{3x10}, I_{3x3}\right] x \\ s_y = {}^E s = \left[0_{3x4}, I_{3x3}, 0_{3x6}\right] x \end{cases} \quad (3)$$

Similarly, we derive a state space model:

$$y = \begin{bmatrix} \left[I_{4x4}, 0_{4x9}\right] \\ \left[0_{3x10}, I_{3x3}\right] \\ 0_{3x4}, I_{3x3}, 0_{3x6} \end{bmatrix} x = Hx \quad (4)$$

Quaternion and acceleration are updated from INS outputs.

Acceleration: ${}^E a_{e,k} = (R'_{EB,k-1} a_{acc,k} - g_0)$

- a_{acc}: accelerometer outputs
- $g_0 = \left[0; 0; 9.81\right]$: gravity vector
- Rotation matrix computed from quaternion

$$R_{EB} = \begin{pmatrix} 2q_1^2 + 2q_4^2 - 1 & 2(q_1 q_2 + q_3 q_4) & 2(q_1 q_3 - q_2 q_4) \\ 2(q_1 q_2 - q_3 q_4) & 2q_2^2 + 2q_4^2 - 1 & 2(q_2 q_3 + q_1 q_4) \\ 2(q_1 q_3 + q_2 q_4) & 2(q_2 q_3 - q_1 q_4) & 2q_3^2 + 2q_4^2 - 1 \end{pmatrix} \quad (5)$$

Moreover, quaternion can be calculated from three Euler angles roll, pitch, yaw ϕ, θ, ψ as below equation:

$$\begin{cases} q_1 = c\left(\frac{\psi}{2}\right) c\left(\frac{\theta}{2}\right) s\left(\frac{\phi}{2}\right) - s\left(\frac{\psi}{2}\right) s\left(\frac{\theta}{2}\right) c\left(\frac{\phi}{2}\right) \\ q_2 = c\left(\frac{\psi}{2}\right) s\left(\frac{\theta}{2}\right) c\left(\frac{\phi}{2}\right) + s\left(\frac{\psi}{2}\right) c\left(\frac{\theta}{2}\right) s\left(\frac{\phi}{2}\right) \\ q_3 = s\left(\frac{\psi}{2}\right) c\left(\frac{\theta}{2}\right) c\left(\frac{\phi}{2}\right) - c\left(\frac{\psi}{2}\right) s\left(\frac{\theta}{2}\right) s\left(\frac{\phi}{2}\right) \\ q_4 = c\left(\frac{\psi}{2}\right) c\left(\frac{\theta}{2}\right) c\left(\frac{\phi}{2}\right) + s\left(\frac{\psi}{2}\right) s\left(\frac{\theta}{2}\right) s\left(\frac{\phi}{2}\right) \end{cases} \quad (6)$$

Three Euler angles are calculated from accelerometer sensor a_x, a_y, a_z and magnetometer sensor m_x, m_y, m_z:

$$\phi = a\tan 2(a_y, a_z)$$

$$\theta = a\sin\left(\frac{-a_x}{\sqrt{(a_x^2 + a_y^2 + a_z^2)}}\right)$$

$$X = m_x \cos(\theta) + m_y \sin(\theta)\sin(\phi) + m_z \sin(\theta)\cos(\phi)$$

$$Y = m_y \cos(\phi) - m_z \sin(\phi)$$

$$\psi = a\tan 2(-Y, X)$$

From above continuous model, we discretize model using first-order approximation.

$$\begin{cases} x_k = (I + \phi T) x_{k-1} = \phi_k x_{k-1} \\ y_k = H x_k = H_k x_k \end{cases}$$

Covariance matrix of process noise: we assume that noises in 3 axes are independent with each other to simplify problem and use trial-and-error method to choose this matrix.

$$Q_k = \begin{bmatrix} \left[\frac{1}{4} T^2 R_{\omega,k-1} R'_{\omega,k-1} \sigma_q, 0_{4x9}\right] \\ \left[0_{3\times4}, \sigma_s I_{3\times3}, 0_{3\times6}\right] \\ \left[0_{3\times7}, \sigma_v I_{3\times3}, 0_{3\times3}\right] \\ \left[0_{3\times10}, \sigma_{ea} I_{3\times3}\right] \end{bmatrix} \quad (7)$$

Covariance matrix of measurement noise: to simplify problem, we assume that this matrix contains only diagonal elements

$$R_k = \begin{bmatrix} [\sigma_{qy} I_{4\times4}, 0_{4\times6}] \\ [0_{3\times4}, \sigma_{ay} I_{3\times3}, 0_{3\times3}] \\ [0_{3\times7}, \sigma_{sy} I_{3\times3}] \end{bmatrix} \quad (8)$$

Although covariance matrixes are chosen by trial-and error method, they will be verified by convergence of the filter.

Extended Kalman filter

Process model can be described as an equation:

$$\dot{x} = f(x) + w(t) \quad (9)$$

We linearize this equation to discrete equation. Let ΔT is a sample time. We use Jacobian matrix to approximate this differential equation to first-order discrete linear equation.

$$x_{k+1} = x_k + \left.\frac{df}{dx}\right|_{x_k} x_k \Delta T + w_k \quad (10)$$

Simplify equation (21) using notation Φ_k to present process model:

$$x_{k+1} = \Phi_k x_k + w_k \quad (11)$$

Where:

$$\Phi_k = I + \left.\frac{df}{dx}\right|_{x_k} \Delta T \quad (12)$$

Both equations (3), (4) are linear, measurement model will be:

$$z_k = H_k x_k + v_k \quad (13)$$

State space model:

$$\begin{cases} x_{k+1} = \Phi_k x_k + w_k \\ z_{k+1} = H_{k+1} x_{k+1} + v_{k+1} \end{cases} \quad (14)$$

At this stage, we apply extended Kalman filter follow steps described in [19].

3. EXPERIMENT

We use a steel bar and set an angle above the ground. This tilted angle creates more challenge data. A cart is pulled to slide along the bar and we collect experiment data in real-time.

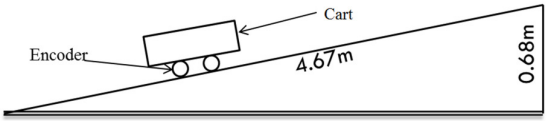

Fig 2. Experiment system

Electronic devices that we use to carry out our experiment:

- Stereo camera Point Grey Bumblebee2: data from this camera is saved on computer at around 30Hz over IEEE-1394 bus. Then computer send the order number of each frame to microcontroller board to synchronize this image with other data.
- IMU Analog Devices ADIS16407: data is collected on microcontroller board over SPI at 100Hz.
- Encoder: 2500 pulses per revolution, built in a cart to play as ground truth data, is collected by microcontroller board at 100Hz.

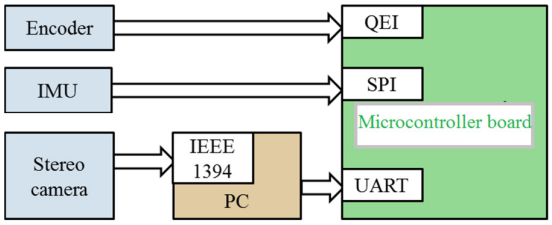

Fig 3. Data acquisition system

Cart is pulled up and down manually in 5 times (travel distance is around 50m) to get the experiment data. Then this data is simulated on MATLAB using proposed algorithm. We use 2 datasets to test the performance of our proposed filter. First dataset present a slow motion condition to check the stable and convergence of the filter, second dataset introduce higher motion.

We choose covariance matrix of process noise and some parameters based on the smooth of output as below:

$c_a = 0.9$

$\sigma_q = diag([1e\text{-}6;1e\text{-}6;1e\text{-}6;1e\text{-}6])$

$\sigma_s = diag([1e\text{-}8;1e\text{-}8;1e\text{-}8])$

$\sigma_v = diag([1e\text{-}6;1e\text{-}6;1e\text{-}6])$

$\sigma_{ea} = diag([1e\text{-}4;1e\text{-}4;1e\text{-}4])$

Covariance matrix of measurement noise is chosen by the relative precision of sensors:

$\sigma_{qy} = diag([1e\text{-}6;1e\text{-}6;1e\text{-}6;1e\text{-}6])$

$\sigma_{ay} = diag([1e\text{-}4;1e\text{-}4;1e\text{-}4])$

$\sigma_{sy} = diag([1e\text{-}6;1e\text{-}6;1e\text{-}6])$

Results from 2 datasets prove the effective of this method compared with single Vision system.

4. CONCLUSION

This work described experiment to develop stereo vision aided inertial navigation system. The authors proposed a complementary filter to integrate stereo camera and INS to improve the precision of each single localization system. We implemented a loosely-couple filter using 13 state variables to represent the 6 DoFs system. This system provides many novel features: high update rate at 100Hz, less drift error over time 2%. In the future, we will embed this algorithm to an industrial PC to run in real-time, and test it in mobile robot systems.

ACKNOWLEDGEMENT

This research is funded by National Science & Technology Foundation of Vietnam (No. KC.03.15/11-15) and Ho Chi Minh City University of Technology under grant number T-ĐĐT-2015-13.

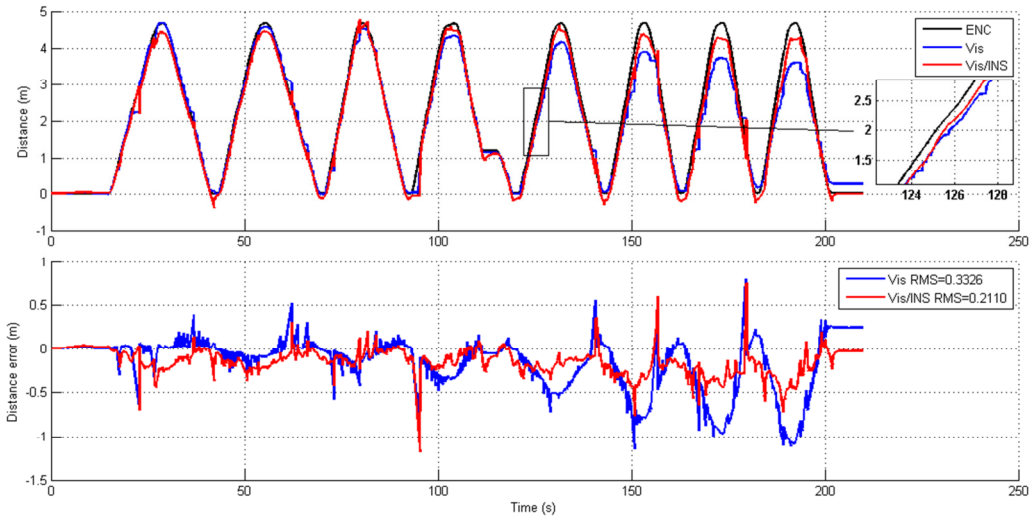

Fig 4. Result from first dataset. Black line is ground truth data calculated from built-in encoder. Blue line is distance estimated from vision system. Red line is result from our proposed algorithm integrated Vision/INS. Bottom figure is error from 2 methods with RMS value.

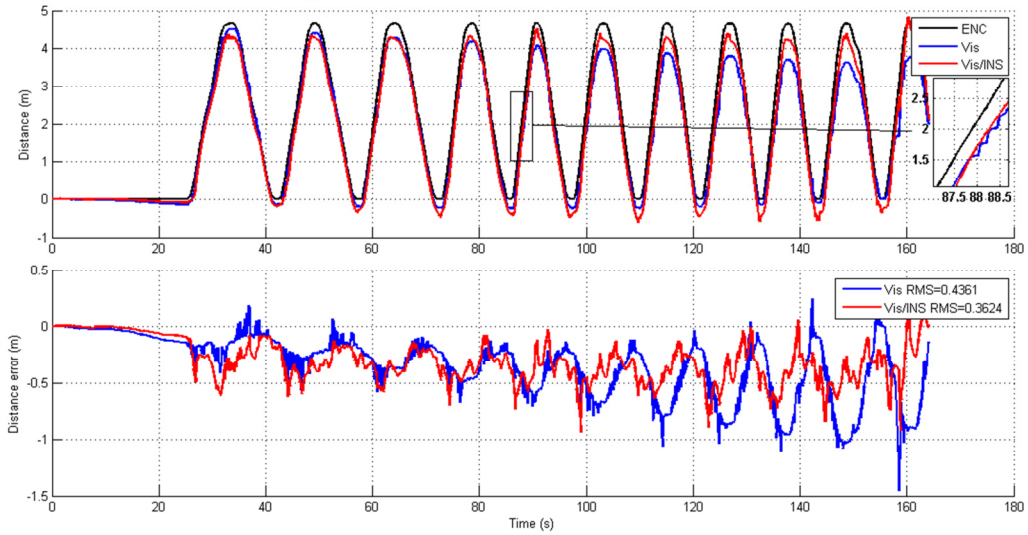

Fig 5. Result from second dataset.

REFERENCES

[1] Benjamin Peter, "Development of an Automatic IMU Calibration System" *Master Thesis,* ETHZ, 2011.

[2] Bachmann, E.R. *et al*, "Orientation Tracking for Humans and Robots Using Inertial Sensors", *In 1999 International Symposium on Computational Intelligence in Robotics & Automation,* 1999, pp.187-194.

[3] Marins, J.L., Yun, X., Bachmann, E.R., McGhee, R.B., Zyda, M.J., "An Extended Kalman Filter for Quaternion-Based Orientation Estimation Using MARG Sensors", *In Proceedings of the 2001 IEEE/RSJ International Conference on Intelligent Robots and Systems*, 2001, vol.4, pp. 2003-2011.

[4] Yun, X., Bachmann, E.R., "Design, Implementation, and Experimental Results of a Quaternion-Based Kalman Filter for Human Body Motion Tracking", *In IEEE Transactions on Robotics*, 2006, vol. 22, pp. 1216-1227.

[5] Daniel Roetenberg, *Inertial and Magnetic Sensing of Human Motion,* PhD Thesis, 2006, University of Twente.

[6] Woodman, Oliver J. "An introduction to inertial navigation" *Technical Report,* 2007.

[7] D. Scaramuzza, F. Fraundorfer, "Visual Odometry: Part I - The First 30 Years and Fundamentals", *IEEE Robotics and Automation Magazine,* vol.18(4), 2011, pp. 80–92.

[8] F. Fraundorfer, D. Scaramuzza, "Visual Odometry: Part II - Matching, Robustness and Applications", *IEEE Robotics and Automation Magazine,* vol.19(2), 2012, pp. 78–90.
[9] M. Veth and J. Raquet, "Fusion of low-cost imaging and inertial sensors for navigation*," Air Force Institute of Technology*, Tech. Rep., 2007.
[10] J. Jurado, K. Fisher, and M. Veth, "Inertial and imaging sensor fusion for image-aided navigation with affine distortion prediction," in *Position Location and Navigation Symposium (PLANS)*, 2012, pp. 518 –526.
[11] J.-O. Nilsson, D. Zachariah, M. Jansson, and P. Handel, "Realtime implementation of visual-aided inertial navigation using epipolar constraints," *in Position Location and Navigation Symposium (PLANS)*, 2012, pp. 711 –718.
[12] D. D. Diel, P. DeBitetto, and S. Teller, "Epipolar constraints for vision-aided inertial navigation," in *IEEE Workshop on Motion and Video Computing,* 2005, pp. 221–228.
[13] J.-P. Tardif, M. D. George, M. Laverne, A. Kelly, and A. Stentz, "*A new approach to vision-aided inertial navigation*." in IROS. IEEE, 2010, pp. 4161–4168.
[14] S. Roumeliotis, A. Johnson, and J. Montgomery, "Augmenting inertial navigation with image-based motion estimation" in *Robotics and Automation ICRA*, vol. 4, 2002, pp. 4326 – 4333.
[15] M. Maimone, Y. Cheng, and L. Matthies, "Two years of visual odometry on the mars exploration rovers: Field reports,"*J. Field Robot.* , vol. 24, no. 3, pp. 169–186, 2007.
[16] A. Geiger, J. Ziegler, and C. Stiller. "Stereoscan: Dense 3d reconstruction in real-time." *Intelligent Vehicles Symposium* (IV), 2011 IEEE.
[17] J. Bouguet, "Visual methods for three-dimensional modeling," Ph.D. dissertation, California Institute of Technology, Pasadena, California, 1999.
[18] Lobo, Jorge, and Jorge Dias. "Relative pose calibration between visual and inertial sensors." *The International Journal of Robotics Research* 26.6 (2007): 561-575.
[19] Greg Welch and Gary Bishop (2006). An Introduction to the Kalman Filter.

Tung A.Dang is Master student at Department of Electrical & Electronics Engineering, Ho Chi Minh City University of Technology, Vietnam. His research interests are in the areas of data estimation, control and localization system.

Duy H.Nguyen is Master student at Department of Electrical & Electronics Engineering, Ho Chi Minh City University of Technology, Vietnam. His research interests are in the areas of control and sensor fusion.

Vinh-Hao Nguyen received B.S. and M.S. degrees in electrical engineering from HoChiMinh City University of Technology, Vietnam, in 2001 and 2003, respectively, and Ph.D. degree in electrical engineering from University of Ulsan, Korea, in 2009. His research interests are in the areas of optimal state estimation, intelligent control and networked control systems.

THE ANALYTICAL HIERARCHY PROCESS BASED STUDY FOR SUSTAINED QUALITY PRACTICES

Mehran Doulat Abadi and Sha'ri Mohd Yusof
Department of Manufacturing and Industrial Engineering,
Universiti Teknologi Malaysia (UTM), Johor Bahru Campus
dmehra2@live.utm.my

ABSTRACT The purpose of this paper is to empirically evaluate and validate factors for successful sustainability of quality practices by using the Analytical Hierarchy Process (AHP) as a multiple-criteria decision making (MCDM) approach. Twenty-seven international quality experts and practitioners from various industry and sector locating in Malaysia, Thailand, Singapore, Japan, and USA were invited. Expert Choice software was performed as a decision support system tool to compute the normalized and unique priority weights of factors. The study has gone through four phases, including: (1) determining key driver factors and sub-factors; (2) structuring the problem and building the AHP model; (3) collecting data from expert; and (4) determining the normalized priority weights of individual factors and sub-factors. The result of data analysis determined the relative importance of individual factors and sub-factors, and in turn identified the key driving factors on which industry should put their efforts for successful sustainability of quality practices.

INTRODUCTION

Over the last decade, the concepts of quality including quality engineering and total quality management (TQM) have been widely adopted by various organizations. Hellsten and Klefsjo (2000) believe that the differences in terminology, makes the concept of quality management to be unclear and create confusion. Hassan et al. (2000) argue that quality management relates to soft aspects of quality, whereas quality related to the hard aspects of quality. However, both terms can overcome the same quality problem but they usually have different treatment in terms of depth and breadth. More organizations have adopted the use of quality approach as a means obtaining higher product quality and improving the level of TQM (Noviyarsi, 2005). Quality practices and implementation alongside critical factors, is another important component of TQM, which emphasizes their importance for the improvement of TQM levels and results.

This study aims to empirically evaluate and validate factors for successful sustainability of quality practices by using the Analytical Hierarchy Process (AHP) as a multiple-criteria decision making (MCDM) approach. The study attempts to gather data from quality experts and practitioners from various industry and sector locating in Malaysia, Thailand, Singapore, Japan, and USA. Expert Choice software was performed as a decision support system tool to compute the normalized and unique priority weights of factors.

As the first step, a set of critical factors and sub-factors were identified through an extensive review of literature and then validated by getting opinions from the panel of experts using the survey questionnaire. After identifying critical factors and sub-factors, a survey was then conducted separately to determine the level of practice factors within industry practices. Next, all valid replies questionnaire were recorded and analyzed.

This paper consists of six sections. Section two summarizes the relevant literature, which leads to the identification of factors for successful sustainability of quality practices. The AHP methodology and results and findings are described in section three and four respectively. Section five and six provide a brief discussion and final conclusions relevant for the successful sustainability of quality engineering practices.

DETERMINATION OF THE DRIVING FACTORS

A review of the literature indicates that previous studies on critical factors have adapted different ways in determining their success factors. In this respect, because of the unavailability of the critical factors, different approaches has been established and applied by a number of researchers for critical factors derivation particularly in Rockart (1979) study. Emory and Cooper (cited by Saunders *et al.,* 2000) suggest three methods for identifying the critical factors include: 1) search of the literature; 2) talking to a group member of individual (who are experts in the subject under investigation); and 3)

conducting interviews in form of focus group. On the other hand, however, Rockart and Bullen (1981) define the in-depth face-to-face interview as the main source in identifying the critical factors.

Previous research such as Ahire *et al.* (1995), Saraph *et al.* (1989), Porter and Parker (1995), Badri *et al*. (1995), Zairi (2002), determined a set of factors for quality management practices only based on the reviewing the relevant literature. However, Yusof and Aspinwall (2000) used both literature review and survey questionnaire in the form of a postal questionnaire to derive their success factors for TQM implementation. Black and Porter (1996) also identified their factors from the Malcolm Baldridge National Quality Award (MBNQA) criteria. Tamirni and Gershon (1995) employed the Deming's 14 principles for management as critical factors in developing their instrument for measuring quality management practices in organization.

ANALYTICAL HIERARCHY PROCESS METHOD (AHP)

The Analytic Hierarchy Process (AHP) is one of the most popular MCDM tools for formulating and analyzing decision making problems. It was originally introduced and developed by Thomas L. Saaty in 1977 and 1984 on the basis of a strong mathematical and logical groundwork. In essence, AHP is a simple, practical, powerful and comprehensive decision support tool which can be used to solve complex decision problems.

The AHP is a theory of measurement through pairwise comparisons and relies on the judgments of experts to derive priority scales (Saaty, 2008). The AHP theory is based on the concept of having *n* alternatives and their relative pairwise comparison is an approximation to the ratio of *wi/wj* which is the weight of alternative *i* to alternative *j*. It is most effective when coupled with a sensitivity analysis and supported by a feedback measure of consistency analysis.

The application of AHP to a decision problem involves three main steps including; 1) hierarchy construction, 2) priority analysis, and 3) consistency verification according to Saaty (2008). In this respect, decision makers can make judgements on the elements of the hierarchy in pairs with respect to their parent element to derive priorities then synthesise the priorities into an overall result. A hierarchical structure of AHP is formulated for the necessary composition and selection of the examination problem.

In general, the AHP approach uses a multi-level hierarchical decision model involving objectives, criteria, sub-criteria, and alternatives. In a simple AHP situation, the overall goal or objective of the decision is represented at the top level of the hierarchy followed by the criteria and sub-criteria contributing to the decision which are represented at the intermediate levels. The next higher level would consist of the criteria for judging the alternatives, and the alternatives are at the bottom. Figure 1 shows the overall structure of the AHP method which typically use in conducting decision-making problems research.

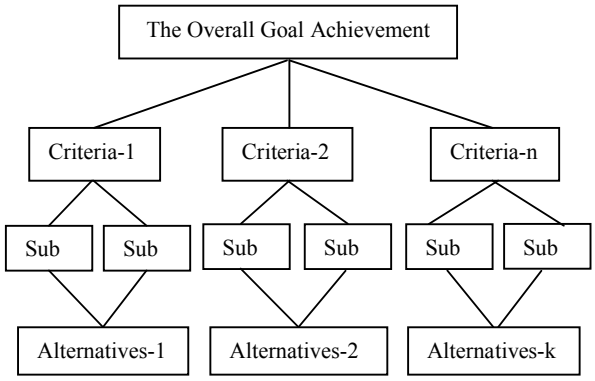

Figure 1 Overall AHP structure of a decision problem

RANKING FACTORS AND SUB FACTORS

After determining the pair-wise comparisons at all the level of AHP hierarchy model, the local and global relative weights subsequently were established. Table 1 shows the final relative importance weights for the five individual factors and 29 sub-factors. For this case, the local weight of each main criteria is derived from judgment with respect to a single factor, whereas the global weight (total weights) of each sub- criteria is obtained by multiplying the local weight of each sub-factor by the weight of its associated major factor. Based on the values obtained, it is clear which individual factor or sub-factor is regarded as more important relative to others.

DISCUSSIONS

This study provides a hierarchical model to obtain a ranking of the driving factors for successful sustainability of quality practices. Using the Analytical Hierarchy Process (AHP) as a multiple-criteria decision making (MCDM) approach. Based on the findings, five driving factors and 29 sub-factors have been evaluated and validated through 27 experts and practitioners from various industry and sector within three rounds of the AHP method. Therefore, the proposed factors represent actual situation for for successful sustainability of quality practices within the industry.

CONCLUSION

This paper has presented the results of a study on driving factors for successful sustainability of quality practices. Five driving factors and 29 sub factors have been

derived from this study. Ranking of the five factors and 29 sub factors has provided a better understanding of the industry in Asian organizations on the direction and targets for sustaining their practices for the long term. Future research could employ the normalized weight derived from the AHP methodology to develop assessment tool for industry. The developed assessment method can be used as a tool to evaluate how well an organization sustain its practices compared to other companies. It can also be used as a management model to determine the strengths of the company in term of quality implementation and improvement. Finally, it is hoped that the results of this study will be useful to continuously improve the application of quality management within the industry.

Table 1 Priority local and global weights of the criteria and sub-criteria

Main criteria	Local weight	Sub-criteria	Local weight [a]	Global weight [b]
Leadership and management Commitment (LMC)	0.423	L1. Active participation and involvement	0.4058	0.1713
		L2. Continuous support and strong commitment	0.2817	0.1191
		L3. Effective communication among individuals	0.1283	0.0542
		L4. Team spirit and motivation approaches	0.0843	0.0356
		L5. Clear vision and mission	0.0696	0.2944
		L6. Personal commitment and involvement	0.0300	0.0126
Strategic quality planning (SQP)	0.089	S1. Strategic planning system	0.2363	0.0210
		S2. Clear strategic planning process	0.2487	0.0221
		S3. Continuous improvement through strategies	0.3042	0.2707
		S4. Reviewing quality plans and policies	0.0728	0.0064
		S5. Developing the plans and policies	0.0825	0.0073
		S6. Strategic planning activity at all levels	0.0553	0.0049
Recognition and reward (RER)	0.217	R1. Recognition and reward system	0.3432	0.0744
		R2. Recognition as part of the motivation	0.1716	0.0372
		R3. Recognition and involvement	0.3302	0.0716
		R4. Recognition via senior executive	0.0974	0.0211
		R5. Continuous reward of employees	0.0574	0.0124
Communication and relationship (COR)	0.166	C1. Top down/bottom up communication	0.5749	0.0954
		C2. Communication to improve quality	0.2096	0.0347
		C3. Employee suggestion and feedback	0.0840	0.0139
		C4. Employee relations and respects	0.0589	0.0097
		C5. Communication related methods	0.0431	0.0071
		C6. Management accessibility	0.0292	0.0048
Work culture and climate (WCC)	0.104	W1. Commitment to treating employees	0.2034	0.0211
		W2. Employee awareness on excellence	0.1077	0.0112
		W3. Continuously reinforce the culture of Ex.	0.1530	0.0159
		W4. Well-being of all employees	0.1047	0.0108
		W5. Continuous quality improvement	0.1163	0.0120
		W6. Commitment to culture of excellence	0.3146	0.0327
Total weight			Σ=1.000	Σ=1.000

a. Local weight: is derived from judgment with respect to a single criteria
b. Global weight: is derived from multiplication by the priority of the criteria

REFERENCES

Amar, K. and Zain, M.Z. (2002), "Barriers to implementing TQM in Indonesia manufacturing organizations", The TQM Magazine, Vol. 14 No. 6, pp. 367-372.

Bunney, H.S. and Dale, B.G. (1997), "The implementation of quality management tools and techniques: a study", The TQM Magazine, Vol. 9 No. 3, pp. 183-189.

Chin, K.S., Chiu, S., & Tummala, V.M.R. (1999). An evaluation of success factors using AHP to implement ISO 14001 based EMS. *International Journal of Quality & Reliability Management, 16* (4), 341–361.

Clegg, B., Rees, C. and Titchen, M. (2010), "A study into the effectiveness of quality management training: a focus on tools and critical success factors", The TQM Journal, Vol. 22 No. 2, pp. 188-208.
Conference on Quality, Productivity and Performance Measurement (ICQPPM'09), Putrajaya, November 16-18.

Curry, A. and Kadasah, N. (2002), "Focusing an key elements of TQM-evaluation for sustainability", The TQM Magazine, Vol. 14 No. 4, pp. 207-216.

Eng, Q.E. and Yusof, S.M. (2003), "A survey of TQM practices in the Malaysian electrical and electronics industry", Total Quality Management, Vol. 14 No. 1, pp. 63-77.

Hassan, A., Baksh, M.S.N. and Shaharoun, A.M. (2000), "Issues in quality engineering research", International

Journal of Quality and Reliability Management, Vol. 17 No. 8, pp. 858-875.

Hellsten, U. and Klefsjo, B. (2000), "TQM as a management system consisting of values, techniques and tools", The TQM Magazine, Vol. 12 No. 4, pp. 238-244.

Hwang, J.H. (2004), "Developing a performance criteria model for school foodservice: an application of AHP", dissertation, Doctor of Philosophy, Iowa State University, Ames, IA.

ISO 9001:2000 certified companies: the Greek case", International Journal of Productivity and Performance Management, Vol. 58 No. 6, pp. 564-580.

Japanese and non-Japanese based electrical and electronics companies in Malaysia: a survey", Jurnal Teknologi, Vol. 47, pp. 75-89, e-ISSN: 2180-3722.

Kwok, K.Y. and Tummala, V.M.R. (1998), "A quality control and improvement system based on the total control methodology (TCM)", International Journal of Quality and Reliability Management, Vol. 15 No. 1, pp. 13-48.

Lau, H.C. and Idris, M.A. (2001), "The soft foundation of the critical success factors on TQM implementation in Malaysia", The TQM Magazine, Vol. 13 No. 1, pp. 51-60.

McQuater, R.E., Scull, C.H., Dale, B.G. and Hillman, P.G. (1995), "Using quality tools and techniques successfully", The TQM Magazine, Vol. 7 No. 6, pp. 37-42.

Noviyarsi (2005), "Development of a proposed quality engineering implementation framework for Malaysian automotive suppliers", thesis master degree, Universiti Teknologi Malaysia, Johor Bahru.

Putri, N.T. and Yusof, S.M. (2009), "Relationship between total quality management and quality engineering – a review and agenda for future research", Proceeding of International.

Rianto, Y., Laksani, C.S., Triyono, B. and Kardoyo, H. (2006), "Technological learning in Indonesia's autoparts SMEs", IEEE International Conference on Management of Innovation and Technology, June 21-23, Singapore, pp. 315-319.

Saaty, T.L. (1980), The Analytic Hierarchy Process, McGraw – Hill, New York, NY. Saaty, T.L. (1988), Multi Criteria Decision Making: The Analytic Hierarchy Process, RWS Publications, Pittsburgh, PA.

Saaty, T.L. and Vargas, L. (1982), Decision Making for Leaders, Lifetime Learning Publications, Pittsburgh, PA.

Shamsuddin, A., and Hassan, M. (2003), "Survey and case investigations on application of quality management tools and techniques in small-medium industries", International Journal of Quality and Reliability Management, Vol. 20 No. 7, pp. 795-825.

Spring, M., McQuater, R., Swift, K., Dale, B. and Booker, J. (1998), "The use of quality tools and techniques in product introduction: an assessment methodology", The TQM Magazine, Vol. 10 No. 1, pp. 45-50.

Thiagarajan, T., Zairi, M. and Dale, B.G. (2001), "A proposed model of TQM implementation based on an empirical study of Malaysian industry", International Journal of Quality and Reliability Management, Vol. 18 No. 3, pp. 289-306.

Wasil, E., & Golden, B. (2003). Celebrating 25 years of AHP-based decision making. *Computers and Operations Research*, *30*(10), 1419 – 1420.

ABOUT AUTHORS:

Mr. Mehran Doulat Abadi

Mehran Doulatabadi is a Doctoral Research candidate in Universiti Teknologi Malaysia (UTM), Johor Bahru Campus. He has special interest in examination issues relating to quality through the Analytical Hierarchy Process (AHP) as a multiple-criteria decision making (MCDM) approach.

Prof Ir. Dr. Sha'ri Mohd Yusof

Sha'ri Mohd Yusof is Professor of Quality Engineering and Management in Department of Manufacturing and Industrial Engineering, UTM. His primary research interests are total quality management, quality engineering and lean manufacturing.

DESIGN AND PROTOTYPING METHODS FOR E-WHEEL A NEW GENERATION OF PEDAL ELECTRIC CYCLES (PEDELECS)

Phuoc NGUYEN, LE Khanh Dien
Department of Mechanical Engineering, Ho Chi Minh City University of Technology

ABSTRACT

This paper offers an introduction to the new generation of pedal electric cycles (pedelecs) and their potential for society in the design and technology. E-Wheel, a multi-award-winning patented design, stands for *Integrated Electric Wheel*, based on **all-in-one** idea. E-Wheel is not just a redesigning of common pedelecs, however, E-Wheel will be playing on ever more significant role in our everyday mobility with very positive *"support effect"* for urban transportation. Detail CAD data and Finite Element Analysis (FEA) model are presented and there are shown that the E-Wheel will be take advantage of conventional electric bicycles or common pedelecs.

INTRODUCTION

Today, millions of people all around the world suffer from air pollution, traffic congestion, unsafe traffic conditions, noise,… while our entire planet is under thread as the result of climate change. So cycling becomes essential part of the solution to these major problems. Around 130 million bikes are produced per year, considerably more than cars, of which around 60 million were produced worldwide in 2011 (Annick Roetynck, 2011) [1]. But the pedelec has even more potential than the bike and car combined. There are hundred reasons to choose pedelec: little parking space, clean, green and definitely faster than car in crowded town, etc.

Because the motor helps you push, riding a pedelec feels as if you always have the wind behind you, even when you are going uphill or in adverse weather conditions. As a result, you never really sweat nor do you get out of breath. Riding a pedelec has a positive influence on your physical condition. You can also choose to ride your pedelec without the help of the electric motor, just as a conventional bicycle.

A pedelec is a bike with an electric motor, which supplies power assist only when you pedal. A sensor (rotation/torque sensor and Hall Effect sensors) measures whether you are pedaling, and passes this information to a controller. This sensor ensures that the motor only provides assistance when the rider is pedaling. Power is delivered by a battery pack, which can be re-charged via a suitable charger from electric network. Batteries are often mounted to the rack or onto the frame, and sometimes they are built into the frame.

Figure 1: General pedelecs structure (Credited by OXYGEN Bicycles, United Kingdom)

INDUSTRIAL DESIGN ASPECTS

For many, at first glance the pedelec is simply a bicycle with some additional electrics. For the cycle industry, the design opportunities are first limited by the reference to the fundamental "bicycle" concept, and second by the technical options available for production. But for me, the pedelec is much more than that, at least, in the point of Designer. It is not the only form of transport; it is an expression of the status and lifestyle of their owner. The task of a Designer for a product which already exists is to make them better – more functional, more beautiful and more practical. So, why it is built like a conventional bike – but with a motor? Why we do not shift to a new level?

Copenhagen Wheel [2] is the first success design of retro-fitting pedelec, since their initial announcement in 2009. The drive is not the main focus, rather the gathering of sensor data on air quality and networking to data centers and other users.

The author have designed the first pedelec concept for over a year and a half, it is called E-Wheel (abbreviation of Integrated Electric Wheel) – An integrated electric wheel bases on **all-in-one** idea. With the new cutting edge of design pedal electric cycle (pedelec) – E-Wheel will give the rider new experiments when they pedal. The designs of E-Wheel are integrated all of the electrical components very elegantly and be fitted as a kit to almost any conceivable bike.

Figure 2: E-Wheel complete assembly (commercial rendering image)

E-Wheel are suited for a wide variety of people who are not able or not willing to ride a conventional bicycle or who simply need faster transportation and most efficient means of transport in town.

E-Wheel has won two precious prizes like **ASEAN preneurs Autodesk Design Challenge** (October, 2013) [3] and worldwide **Lexus Design Award** (January, 2014) [4]. And the E-Wheel received so many praises from all over the world.

At this point, some familiar designs have announced, for example: FlyKly Smart Wheel [5] and Electron Wheel [6]. The author pretty sure that many talented industrial designers will push it as far as possible. At least, the E-Wheel still have unique features and they are used in a unique way in the context of overall design.

TECHNICAL ASPECTS

E-Wheel is not only eco-friendly but also very lightweight. It is integrated **all-in-one**: include 250W (rated power) electric motor, 36V – 8.9Ah – 320Wh lithium-ion battery, electrics drive. E-Wheel can run up to 60km on one full charged[1]and the maximum speed is 25 km/h. E-Wheel has the wireless technology for remote control and battery charge. You can control E-wheel by your mobile phone (or control console).

The E-Wheel was modeled in the Autodesk Inventor®Professional Student version CAD software with all dimensions driven by equations. That means the author could play with the model geometry, with the benefit of making small or big changes to analyze the impact in the performance.

Initially, E-Wheel are designed and optimized for 26 inches rim, with the top speed of bike is 25 kilometers per hour (6.94 meters per second), and archived by the designed power 250 Watts.

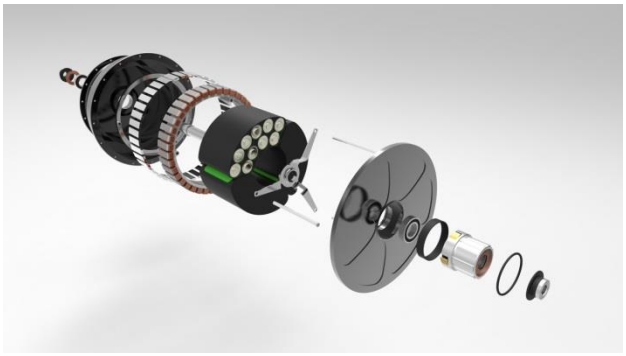

Figure 3: E-Wheel with the special BLDC Motor structure (rendering image)

Ideal angular velocity is constant:

$$speed\ at\ motor\ outer = \frac{\pi\omega_{outer} \times D_{outer}}{60}$$

$$= \frac{\pi \times (250\ rpm) \times (167.1\ mm) \times 10^{-3}}{60} = 2.19\ m/s$$

$$Total\ force\ produced = \frac{designed\ power}{speed\ at\ motor\ outer}$$

$$= \frac{250\ W}{2.19\ m/s} = 114.29\ N$$

The author apply a combination of two methods to estimate the motor constant in static DC analysis using the Lorentz force and Faraday's Law on a wire (Shane W. Colton, 2010) [7]. There are the simplest method, requiring only high-school physics, and work well for this case.

Firstly, apply Lorentz force formula:

$$\vec{F} = I\vec{L} \times \vec{B}$$

In this above formula:

$$B = B_{peak} = B_r \frac{t}{t+g} = 1.07\ T$$

The current passing through the wire would be equal 7.47 Amps.

$$F = (current\ though\ the\ wire) \times (active\ turn) \times (active\ length) \times (magnetic\ feild)$$

$$\Longrightarrow active\ turn, N = \frac{114.29\ N}{(7.31\ A) \times 2(25 \times 10^{-3}\ m) \times (1.07T)} = 293$$

So, the number of windings per tooth is 13 turn.

Secondly, using the Faraday's Law:

$$Back\ EMF, E\ (or\ V) = \frac{d\phi}{dt} = B\frac{d}{dt}(A_{north} - A_{south}) = \Delta BLv$$

$$Induced\ voltage, V = (2 \times 1.07\ T) \times (25 \times 10^{-3}\ m) \times (293\ turn) \times (2.19\ m/s) = 34.2\ V$$

Thus, the motor constant is:

$$K_t = \frac{V}{\omega_{no-load}} = 1.626\ \left(\frac{V}{rad/s}, \frac{Nm}{A}\right)$$

[1] *Maximum range based on one battery full charge, using 150% assistance mode, according to use in ideal conditions. Distance will vary depending on road conditions, riding surface, cyclist's weight and required assistance.*

Table 1: Parameters used in the calculation of motor constant

Parameters	Descriptions	Values
N	*Active turns*	*293*
B_r	*Magnet remain flux density*	*1.3 T*
t	*Magnet thickness*	*3 mm*
g	*Air gap dimension*	*0.65 mm*
B_{peak}	$B_r \frac{t}{t+g}$	*1.07 T*
B	*Field used for Lorentz force law*	*1.07 T*
L	*Active length*	*25 mm*
R	$Effective\ radius = \frac{outer\ diameter}{2}$	*83.55 mm*
K_t	$2NBLR$ *(for wye)*	*1.626 Nm/A*

The simulations of Brushless Direct-Current (BLDC) motor inside E-Wheel were performed with 2D free software called Finite Element Method Magnetics (FEMM) [8] and 3D advanced in JMAG Designer® v13.1 [9] – to predict motor performance using magneto static analysis. Viewing the flux distribution and reveals that the rotor (outer) and the stator (inner) are integrated to the magnetic circuit, carrying flux between magnets (*Figure 4 and 5*).

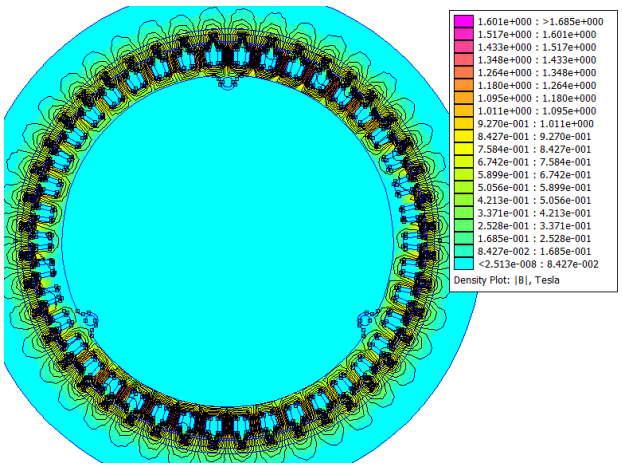

Figure 4: The flux distribution in the slotted rotor (outer) and the stator (inner) of BLDC Motor model in FEMM, driven with 7.47A

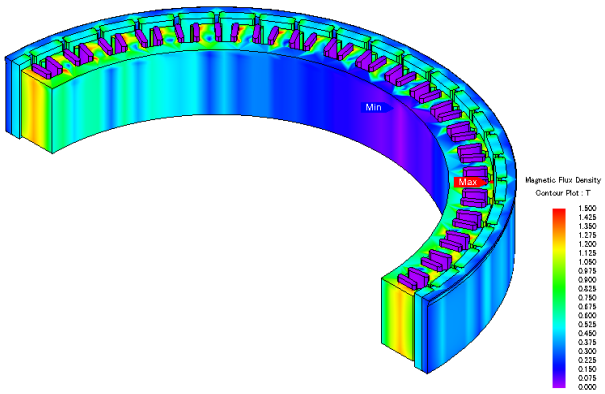

Figure 5: Three-phase 3D Finite Element simulation of the BLDC motor partial model – Magnetic flux density

The windings don't really convert power with 100% efficiency. They have some resistance that generates heat. (Similarly, the steel will also not conduct the magnetic field perfectly). To get a rough estimate of the loss in the copper, we can use the rating for 20AWG magnet wire resistance, which is about 33.31 $m\Omega/m$, over the length of two phases of windings, which is approximate 15 meters. And the heat generated is:

$$P_{dissipated} = I^2R = (7.31A)^2(0.5\Omega) = 27\ W$$

Compare this to a 25W light bulb. It's a lot of heat, including other losses, such as in the steel and friction in the bearings, the motor could still be over 80% efficient when running at 7.31A!

Table 2: Calculation of the resistance of the BLDC Motor with designed parameters

Parameters	Unit	Values
Turns per Phase (Series/Parallel)	*s/1p*	*140*
Wire Gauge	***AWG***	***20***
Wire Diameter	*mm*	*0.812*
Total Parallel Cross-Section Area	mm^2	*0.812*
Resistance per Unit Length	*mOhm/m*	*33.31*
Wire Type		*round*
Winding Termination		*wye*
Average Length per Turn	*mm*	*53.2*
Total Length per Phase	*mm*	*7448*
Estimated Resistance (wye)	*mOhm*	*248.09*
Ampacity by $10Arms/mm^2$*(wye)*	*Arms*	*7.31*
Operating Voltage	*V*	*11.40*
Total Power IN by $2VI$	*W*	*250*
Heat Generated by $2phase \times I^2 \times R$	*W*	*27*
Total Power OUT	*W*	***223***
Percent Power Loss to $2phase \times I^2 \times R$	*%*	***10.61***

Thermal is the most important in re-arrange the batteries and choose the best material for battery packs and also optimize the outer motor. Heat generated by the motor will be absorbed by the good contact parts, especially is the aluminum hub shell (outside) and the battery packs (inside) before being transferred out to the environment. In any case, a **temperature rise of 100**℃ is allowed, by far than normal operating conditions.

Li-ion battery is not the most ideally, but up to 95% of the material they contain can be recycled in existing facilities and the storage capability is higher (Thomas Lewis) [10]. On the other hand, the continuous development in battery technology are coming out of laboratory has made Li-ion higher energy density, more safety and more long life. The most common all round cell type is the **18650** design, which is mounted in very special and useful battery packs. Lithium-ion battery cell

is very sensitive. Overcharging, short circuit, physical damage raises the risk of overheating and igniting. Any electric devices (include E-Wheel) required more robust and safer batteries. That why E-Wheel has self-locking battery packs while Li-ion battery manufacturers (like Panasonic) have employed *Heat Resistance Layer* (HRL) on the surface of the electrodes which avoid overheating if short circuit occurs [11].
The battery packs have made by polyacetal: Acetal Homopolymer/Delrin or Acetal Copolymer. They have high mechanical strength, stiffness and better wear resistance (especially thermal-oxidative degradation).

Table 3: Physical properties of comparison polymer materials [12]

Properties	**Acetal Homopolymer/ Delrin**	**Acetal Copolymer**
Density (g/cm^3)	1.43	1.41
Temperature of deflection under load – method A: 1.8MPa (℃)	115	105
Max. allowable service temperature in air – continuously: 5000/20000h (℃)	105/90	115/100

Beside the most outstanding design features, the using material is very important in E-Wheel. Materials utilization was totally a selection process that involved choosing from a given, rather limited set of materials the one best suited for an application by virtue of its characteristics.

CONCLUSIONS

The E-Wheel presented in this paper is a new kind of pedal electric cycle (pedelec) was designed to fix into any conventional bikes. With the increasing demand on eco-friendly mobility transportation, E-Wheel is offer an improved quality of pedaling to everybody, especially since E-Wheel has had some initial successes with design awards and feedbacks from netizen. And the author hopes E-Wheel will be put on the road and received comment from communities in the near future.

ACKNOWLEDGMENT

The licenses of JMAG Designer v13.1 (include JMAG Express v6.1) were supported by **JSOL Corporation**, Japan and distributed by **New System Vietnam**.
E-Wheel was pressed and published by **designboom.com**(Digital architecture and design magazine) and **Toyota Motor Corporation**.

REFERENCES

[1] Annick Roetynck, *"PRESTO Cycling Policy Guide Electric Bicycles"*, ETRA Secretary General, Intelligent Energy Europe, Belgium, February 2010.
[2] Copenhagen Wheel, https://superpedestrian.com/
[3] ASEANpreneurs Autodesk Design Challenge, http://aseanpreneurs.org/autodesk_ap_design/
[4] Lexus Design Award 2014, http://www.lexus-int.com/design/lda.html
[5] FlyKly Smart Wheel,http://www.flykly.com/
[6] Electron Wheel,http://www.electronwheel.com/
[7] Shane W. Colton, *"Design and Prototyping Methods for Brushless Motors and Motor Control"*, graduate thesis of Degree of Master of Science in Mechanical Engineering, Massachusetts Institute of Technology, June, 2010.
[8] Finite Element Method Magnetics (FEMM), http://www.femm.info/wiki/HomePage
[9] JMAG International, https://www.jmag-international.com/index.html
[10] Thomas Lewis, *"Go Pedelec Handbook"*, Go Pedelec Project Coordinator & Country Manager Austria *energieautark consulting gmbh*, Hauptstraße 27/3 A-1140 Wien, Austria www.energieautark.at · www.gopedelec.eu
[11] *"Panasonic Lithium Ion Batteries Technical Handbook"*, Panasonic Corporation, June 2007.
[12] Polyacetal Catalog, Quadrant Engineering Plastic Product, Quadrant Group.

Phuoc Nguyen, currently, a final year student in Mechanical Design Engineering, Ho Chi Minh City University of Technology. He is very interested in the MOTION of things that INSPIRE him INNOVATIVE ideas. The results of his B.E graduate thesis are summarized in this paper.

LE Khanh Dien senior lecture, Department of Mechanical Engineering, Ho Chi Minh City University of Technology, B.E (1982), M.E (1996) in Mechanical Engineering, being doctoral candidate at Ho Chi Minh City University of Technology.
.Email:
lkdien@hcmut.edu.vn

Materials Science and Engineering

LOW TEMPERATURE PLASMA NITRIDING PROCESS IN THE STAINLESS STEELS

Tatsuhiko Aizawa, Takahisa Katoh
Department of Materials Science Engineering, Shibaura Institute of Technology

(12pt. Helvetica)

ABSTRACT

The plasma nitriding had been utilized as a typical surface treatment in commercial. Besides the conventional ion-, radical-, and atom-nitriding processes, various kinds of plasma nitriding systems were developed to search for their new applications. In the present paper, the essential difference between the high and low temperature nitriding processes was considered with interest on the inner nitriding behavior. Both martensitic and ferritic stainless steels were employed as test-pieces for low temperature plasma nitriding. In high temperature, the nitriding behavior was mainly governed by nitrogen diffusion process with the precipitation reaction to form CrN at the nitriding front end. In lower temperature, no precipitation reaction occurred, and, the inner nitriding behavior was governed by nitrogen diffusion process with occupation of vacancy sites in the crystalline cells of stainless steels. In the latter, the effect of nitriding temperature on this process was also discussed with comments on the solid solution process.

1. INTRODUCTION

In the market of surface treatment with use of the nitrogen, the plasma nitriding advances as the most reliable and environmentally benign processing. At present, the ion-, the radical- and the atom-nitriding systems are available in commercial in practice as discussed and surveyed in (Aizawa, 2013). Their common feature is: 1) High temperature nitriding above 773 K or 500 ^{o}C for tool and stainless steels, 2) Long duration time for nitriding, and, 3) Nitrogen diffusion governing process with precipitation reaction at the nitriding front end. Hence, the hardening accompanied with this high temperature is described by the precipitation strengthening mechanism. In fact, as stated in (Aizawa, 2013; Granito, 2002, 2003), the CrN-precipitate size and volume fraction play a role in hardening behavior. On the other hand, there are few reports in the literature on the low temperature plasma nitriding behavior when the nitriding temperature is much less than 773 K. Reference (Anzai, 2009) summarizes this low temperature plasma nitriding process for austenitic stainless steels in the function of holding temperature and processing time.

Figure 1 depicts the effect of holding temperature and duration time on the inner nitriding process. Irrespective of the grades of austenitic stainless steels, no precipitation reactions take place even after long processing time when the holding temperature is below 693 K or 420 ^{o}C. From precise XRD analyses, the nitrogen solid solution has influence on this low temperature nitriding process (Bell, 2000); no further studies have been never reported. In recent, the authors (Santjojo, 2014, Aizawa, 2014, Katoh, 2015, Aiawa, 2015) reported on the similar low temperature plasma nitriding behavior in the martensitic stainless steels. No precipitation reaction took place but the nitridied, martensitic stainless steels had higher hardness than 1200 Hv.

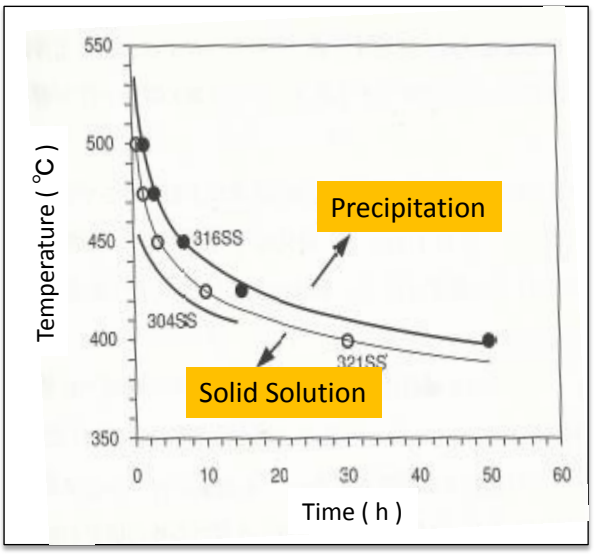

Fig. 1 Diagram of the holding temperature and the duration time in the plasma nitriding (Anzai, 2011, Katoh, 2015).

In the present study, the essential difference between the high temperature and low temperature nitriding processes is experimentally investigated for the martensitic stainless steels, which are widely utilized as a mold material. In particular, the effect of the holding temperature on the inner nitriding behavior is discussed; the duration time is fixed to be 7.2 and 14.4 ks, (or two and four hours), respectively. The plasma nitriding system is explained with comments on the quantitative plasma diagnosis. AISI-SUS420 martensitic stainless steel specimens are utilized for plasma nitriding at 693 K (or 420 ^{o}C), 673 K (or 400 ^{o}C) and 653 K (or 380 ^{o}C), respectively. XRD, SEM and EDX are employed to make quantitative analysis of nitrided layer and to describe the inner nitriding behavior.

2. EXPERIMENTALS

Our developing high density plasma nitriding system as well as specimens are stated with comments on the plasma diagnosis instrumentation.

2.1 Plasma Nitriding System

As illustrated in Fig. 2, being different from the DC- or RF-plasma generators, where the plasmas are ignited and generated in the frequency of 13. 56 MHz or its multiples, the present high density nitriding system has no mechanical matching box with slow response time of 1 s to 10 s to adjust the applied power. Since both the input and output powers are automatically matched by frequency adjustment around 2 MHz, the matching response time is only limited to 1 ms at most. This prompt power control provides to make full use of mesoscopic plasma pressure range over 50 Pa. Different from the conventional processes, the vacuum chamber is electrically neutral so that RF-power and DC-bias should be controlled independently from each other. A dipole electrode is utilized to generate RF-plasma; DC bias is directly applied to the specimens. Heating unit is located under this DC-biased cathode plate.

In the following nitriding experiments, the specimens are located on the cathode table before evacuation down to the base pressure of 0.1 Pa. Then, nitrogen gas is first introduced as a carrier gas for heating. After heating to the specified holding temperature, the nitrogen pre-sputtering is started at the constant pressure. After pre-sputtering, the hydrogen gas is added to nitrogen gas with the specified partial pressure ratio.

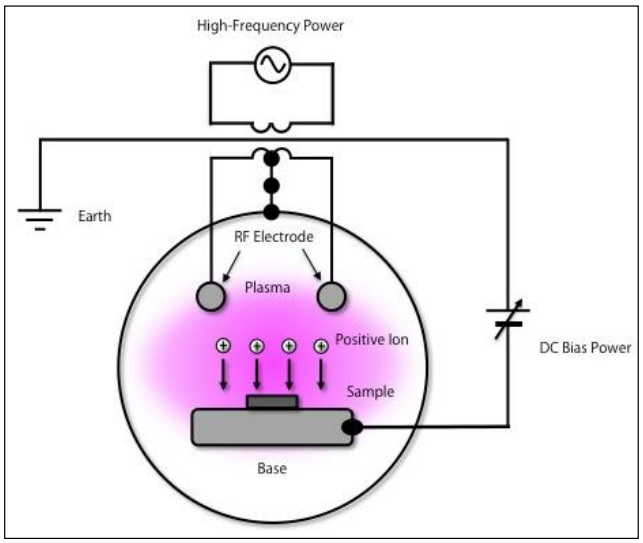

Fig. 2 High density plasma nitriding system.

In particular, the partial pressure ratio of nitrogen to hydrogen is constant by 5 to 1 as a standard condition by controlling the gas flow rate to be 100 ml/min for N_2 gas and 20 ml/min for H_2 gas, respectively. The holding temperature is varied by 693 K (or 420 °C), 673 K (or 400 °C) and 653 K (or 380 °C), respectively. The duration time is fixed to be 14.4 ks or four hours.

2.2 Specimens

AISI-SUS420 specimens were prepared for description of plasma nitriding behavior and for micro-texturing with use of masking. A square sample with 25 x 25 x 5 mm3 was commonly used to measure the hardness depth profile in the nitrided specimen.

2.3 Measurement

Optical microscope, SEM (Scanning Electron Microscope) and EDX (Energy Dispersive X-ray spectroscopy) are utilized to describe the microstructure and element distribution in the cross-section of plasma nitrided specimens. XRD is used to analyze the phase change by the low temperature plasma nitriding.

3. RESULTS

3.1 Low Temperature Nitriding

XRD analysis was first performed to describe the XRD-peak shifts by low temperature plasma nitriding at 673 K. As shown in Fig. 3, the XRD profile of martensitic stainless steels before nitriding is characterized by the α-Fe peak at 2θ = 44.7°. This high intensity peak corresponds to the (110) plain of α-Fe. After plasma nitriding for 7.2 ks or 2 Hrs, the measured XRD profile has mainly two high broad peaks at 2θ = 41.2° and 2θ = 44°. No diffraction peaks are detected at 2θ = 44.5° and 2θ = 48°; no CrN or Fe_4N were synthesized and present as a precipitate in the matrix stainless steel. After diffraction analysis of stainless steels, the first detected peak corresponds to the (111) plain of γ-Fe, and, the second, to the (110) plain of α-Fe, respectively.

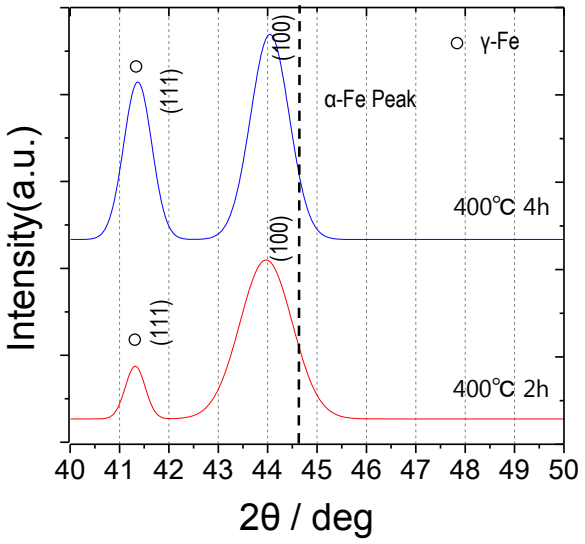

Fig. 3 Significant peak shifts in the XRD diagram by the low temperature nitriding.

The peak shift of the (110) plain before and after plasma nitriding reveals that the original α-Fe crystalline lattice or super-lattice should expand itself by occupation of nitrogen solute atom into a vacancy site as an interstitial atom. Owing to the first principle calculation on the interstitial behavior of nitrogen into α-Fe in (Domain, 2004), the above site occupation of vacancies by nitrogen interstitials advances with straining into the super-lattice. This strain results in the elongation of α-Fe super-lattice in its c-axis direction.

Although few experimental studies were reported on the α-Fe lattice expansion by nitrogen interstitial process, a significant peak shifts was experimentally detected for various martensitic Fe-Cr alloys in common after nitrogen ion implantation in (Manova,2006) at lower temperature than 693 K. Most of measured XRD diagrams indicated that the α-Fe peak shifted from 44.7° to 44°; the average strain induced in the c-axis direction by interstitial site occupation in α-Fe lattice was reported to be 3 to 5 %.

These results correspond to the peak shift of (100) plain of α-Fe in Fig. 3.

In the above theoretical and experimental studies on the lattice expansion as well as straining of α-Fe by nitrogen interstitial site occupation, no direct statements were reported on the phase transformation from α-Fe to γ-Fe. Owing to the discussion in (Domain, 2004), the gradual increase of N/(N+Fe) atomic ratio in the super-cell of α-Fe might result in the selective site occupation of vacancies in the α-Fe supercell. First and second nitrogen interstitial nitrogen solutes are allowed to be present by their occupation of one octahedral vacancy and one tetrahedral vacancy in the α-Fe supercell. This asymmetric occupation process induces the shear strain into the lattices as well as normal strain in the c-axis. If this occupation could advance further in the α-Fe supercell by more increase of N/(N+Fe) ratio, more strains could be stored in the current α-Fe supercell with sufficient amount to induce the transformation by minimization of strains in it.

In the following, SEM and EDX were utilized to describe the nitrogen concentration in the depth of nitrided layer. Figure 4 depicts the SEM and nitrogen mapping in the cross-section of nitrided martensitic stainless steel specimen.

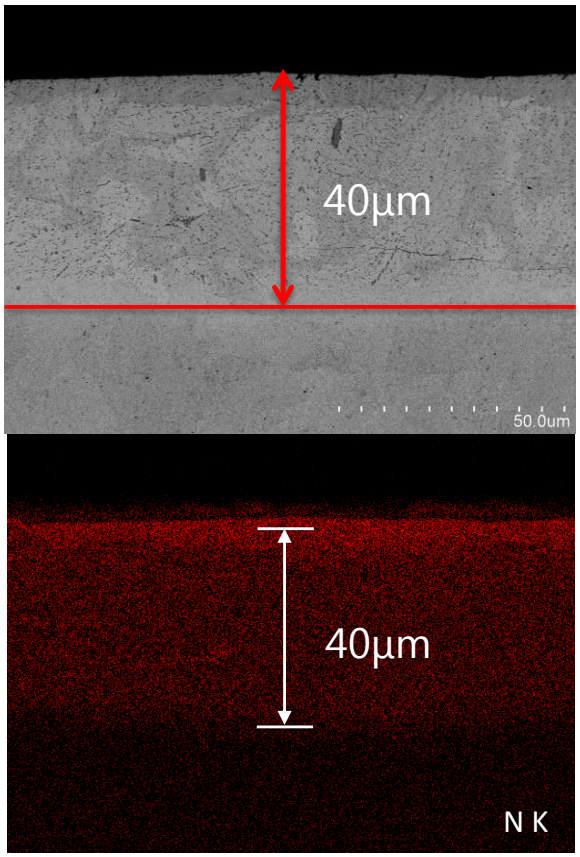

Fig. 4 SEM image and nitrogen mapping on the cross-section of nitrided layer.

Only after nitriding for 14.4 ks, the nitrided thickness reaches to 40 μm. At the vicinity of surface, the nitrogen solute content becomes 9 mass% in average. The nitrogen content decreases from this high concentration to 4 mass % in the middle range of thickness and goes to nearly zero near the nitriding front end. On the other hand, no change is detected in the chromium concentration along the depth of nitrided layer. This also proves that no CrN should be synthesized as the precipitate in the nitrided layer from the surface of specimen.

The above nitrogen mapping information reveals that N/(N+Fe) ratio is 27 to 28 at%, corresponding to 9 mass %, at the vicinity of surface and that N/(N+Fe) ratio is 15 to 17 at %, corresponding to 4 mass%, in the middle of the nitrided layer except for the vicinity of nitriding front end. Assuming that the occupation process of nitrogen interstitials into octahedral and tetrahedral vacancies or V_{oct} and V_{tra} advances from the surface, two pairs of V_{oct} and V_{tra} are occupied by nitrogen solutes at the vicinity of surface, and, one pair of V_{oct} and V_{tra}, in the middle of the nitrided layer. In the former, since the α-Fe supercell is much distorted by occupation of nitrogen into two pair of vacancies, the original α-Fe transforms to more relaxed crystalline structure or γ-Fe. On the other hand, the nitrogen solute content decreases with further nitrogen atom diffusion into the depth in the middle range of the nitrided layer; only one pair of vacancies is occupied by nitrogen. Under this occupation process, the α-Fe supercell is less strained and never accompanied with the above phase transformation.

3.2 Effect of Temperature

In Fig. 1, the inner nitriding process is governed by the solid solution process, where the nitrogen interstitials occupy the tetrahedral vacancies of austenitic stainless steel crystals or g-Fe supercell when the processing temperature is less than 693 K or 420 ºC. As pointed out also in (Manova, 2006), the solid solution with straining governs the inner nitriding of martensitic stainless steels when the processing temperature is less than 673 K or 400 ºC.

These studies suggest that the solid solution with the occupation mechanism of nitrogen interstitials into the vacancy pair has thermal sensitivity. In the following, the same AISI-SUS420 specimens were nitrided at 653K (or 380 ºC), 673 K (or 400 ºC) and 693 K (or 420 oC) for 7.2 a dn 14.4. ks; the measured XRD diagrams were compared among them.

In case of the plasma nitriding for 14.4 ks, those XRD diagrams at 653 K and 693 K are similar to that at 673 K. That is, the nitrogen solid solution from the surface to the depth is driven by high nitrogen solute concentration at the vicinity of surface. The nitriding front end advances with selective occupation of vacancy pair by the nitrogen solutes. No significant peak shifts are seen when nitriding at 653 K for 7.2 ks; the similar XRD diagram is detected when nitriding at 673 K for 7.2 ks.

The above difference in XRD diagrams of nitrided specimens for 7.2 ks between 653 K and 673 K reveals that high concentration at the vicinity of specimen is needed to drive the diffusion of nitrogen solutes into further depth of specimen. Hence, much lower temperature plasma nitriding by solid solution mechanism might be put into practice by surface activation other than thermal one.

In the higher temperature plasma nitriding with precipitation reactions, the inner nitriding behavior is simply governed by the nitrogen diffusion as well as the precipitation reaction at the nitriding front end. Hence, the nitrided layer thickness (E) is uniquely determines by the Wagner's law: $E^2 = K_p \times t$, where t is the nitriding time, and, K_p, the constant, dependent on the nitrogen diffusion constant and nitrogen solute content.

In the lower temperature plasma nitriding than 500 K, the Wagner's law is not held on to describe the growth of

nitrided layer. Figure 5 shows the relationship between E^2 and the nitriding time, t, for the nitrided specimen at 693 K. No linearity is held on in the relationship; this proves that the Wagner's is not true to the inner nitriding at the lower temperature.

As before discussed, the nitrogen solute diffusion process accompanies with occupation of vacancy pair in the α-Fe supercells. A new theoretical model is needed to explain the effect of vacancy site occupation process on the nitrogen diffusion into the depth of stainless steels.

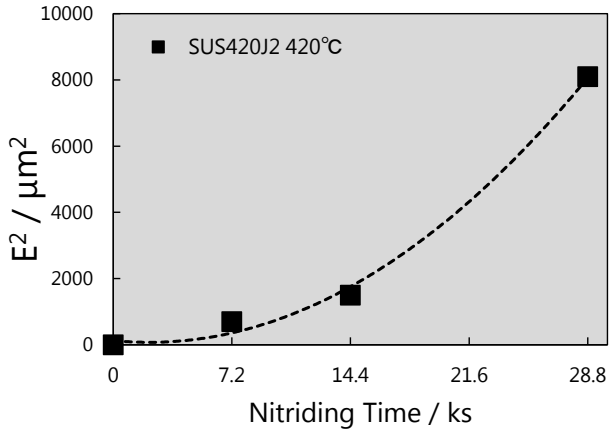

Fig. 5. Relationship between E^2 and the nitriding time, t, for the nitrided AISI-SUS420 specimen at 693 K.

4. CONCLUSION

Low temperature, high density plasma nitriding is performed for the martensitic stainless steels to reveal that inner nitriding process should be essentially different from the high temperature nitriding one. In addition to no precipitation reaction between the diffusing nitrogen solute and the constituent element chromium to CrN, the lower temperature nitriding accompanies with significantly high concentration of nitrogen solute. The average nitrogen solute content in the nitrided layer at 693 K reaches to 4 to 5 mass%, ten times higher than the analyzed solid solubility at high temperature. This high nitrogen solute concentration induces the α-Fe supercell expansion in the c-axis direction. One pair of octahedral and tetrahedral vacancy sites is occupied by nitrogen solutes. High nitrogen concentration state remains from the nitrided martensitic stainless steel surface to the vicinity of nitrding front end. In particular, much higher nitrogen solute content than 9 mass% is present at the vicinity of surface; two vacancy pairs are occupied by nitrogen solutes to drive the inner nitriding process into depth of materials. This solid solution process with vacancy site occupation mechanism significantly affects the inner nitriding behavior.

The above nitrogen solid solution process has a little sensitivity to thermal activation; much lower plasma nitraiding is feasible in practice with aid of surface activation processing.

ACKNOWLEDGEMENTS

The authors would like to express their gratitude to Mr. T. Shiratori and Mr. H. Yoshino (Komatsu Precision, Co., Ltd.) and Dr. K. Wasa (Tech-Dia, Co. Ltd.) for their help in EDX analyses. This study is financially supported in part by MEXT with the contract of #44001.

REFERENCES

Aizawa, T., Sugita, Y. (2013), High density RF-DC plasma nitriding of steels for die and mold technologies. Res. Rep. SIT 57-1, 1-10.

Aizawa, T., Yamaguchi, T. (2014), High-density plasma nitriding assisted micro-texturing onto martensitic stainless steel mold-die. Proc. IWMF2014, 31-37.

Aizawa, T., Yamaguchi, T. (2015), Plasma nitriding assisted micro-texturing into martensitic stainless steel molds for injection molding, Proc. 10th ICOMM (in press).

Anzai, M., (Ed.), (2009), Surface treatment for high qualification of dies and molds, Nikkan-Kougyo Shinbun.

Bell, T., Sun, Y. (2000) Stainless Steel. 275-278.

Domain, c., et al. (2004), Ab initio study of foreign interstitial atom (C, N) interactions with intrinsic point defects in a-Fe. Physical Review B69, 114112.

Granito, N, Kuwahara, H., Aizawa, T. (2002), Normal and anormal microstructure of plasma nitrided Fe-Cr alloys. J. Materials Science. 37, 835-844.

Granito, N. (2003), PhD Thesis, University of Tokyo.

Katoh, T., Aizawa, T., Yamaguchi, T. (2015), Plasma assisted nitriding for micro-texturing onto martensitic stainless steels. Manufacturing Review. 2-2, 1-7.

Manova, D., et al. (2006), Variable lattice expansion in martensitic stainless steel after nitrogen ion implantation," Nucl. Inst. Meth. Phys. Res. B 242, 285-288.

Santojoyo, D., Aizawa, T., Muraishi, S., Morita, H., Micro-texturing of stainless steels via high density plasma nitriding. Proc. 9th ICOMM, 2014; 90, 1-8.

Tatsuhiko Aizawa received the B.E. (1975), M.E. (1977), and D.E. (1980) degrees in the Nuclear Engineering from the University.of Tokyo. He is a Professor, Department of Engineering and Design, Shibaura Institute of Technology.

His Current interests include micro-manufacturing, innovations in manufacturing and materials processing, and, materials science and engineering.

Takahisa Katoh received the B.E. (2013) and M.E. (2015) degrees in Engineering and Design, and, Materials Science and Engineering, respectively, Shibaura Institute of Technology. His current interests include the surface treatment and micro-texturing.

SIMULTANEOUS OXYGEN PLASMA ASHING of CVD DIAMOND COATED WC (Co) TOOLS

Ersyzario Edo Yunata, Kazuhisa Yamauchi, Tatsuhiko Aizawa
Department of Material Science Engineering, Shibaura Institute of Technology
Yoshio Sugita
YS-Electric Industry, Co. Ltd.

ABSTRACT

CVD-diamond coated WC (Co) tools have been widely utilized for dry machining of carbon fiber reinforced plastic components and parts in the airplanes and automobiles. During these dry machining processes, most of CVD diamond films are worn out with chipping and damages; huge amount of tools must be recycled by complete ashing of used diamond coatings before recoating. In the present paper, non-traditional CVD-diamond ashing method is proposed to remove the used diamond films simultaneously in relative short duration without significant damage to tool geometric configuration of tools. Two CVD-coated tools are employed as test-pieces to demonstrate that both diamond films should be ashed away at the same time. Oxygen plasma processing parameters are optimized to minimize the tooth damage in practice.

1. INTRODUCTION

CVD-diamond coated WC (Co) cutting, drilling and end-milling tools have been widely utilized for dry machining of the carbon fiber reinforced plastic or thermos-plastic components and parts in the airplanes and automobiles (Asahi-Paper, 2008). Most of CVD-coatings suffer from chipping and damages on their tooth sections during severe dry machining conditions. Since the tool substrate is made from WC (Co), the substrate materials have to be recycled and reused after ashing the whole used diamond films and recoating. In addition, the tooth design in geometry must be preserved in order to stabilize the dry machining conditions even after recycling; the loss of tooth geometry and size has to be minimized during ashing the used diamond coating.

The authors have succeeded in perfect ashing the used DLC coating by using the high density oxygen plasma ashing process (Aizawa, 2014-1, Aizawa, 2014-2, Aizawa, 2015). Different from the conventional plasma ashing technology, the ashing rate of DLC coatings was much higher even when the whole DLC films as well as the metallic interlayers were completely removed. In addition, the dry machine ability with used of recoated DLC-coated tools remains to be equivalent to the virgin DLC-coated ones. This success in recycling of WC (Co) substrate stimulates to apply this ashing technology to harder coatings for machining tools.

In the present paper, a new ashing systems use to remove the whole used CVD-diamond coatings is proposed on the basis of the ashing technology in the above. The key of advanced ashing methods lies in the densification of oxygen ions and electrons in the ignited plasmas. As discussed in Refs. (Yunata, 2013; Yunata, 2014; Aizawa, 2014-3; Yunata, 2015), the hollow cathode device is developed to dense the oxygen atoms and ions as well as electrons. In order to make full use of these activated species in the plasmas, the CVD-diamond coated tools are rotated in the hollow.

At first, the details of high density oxygen plasma ashing system for removal of diamond coating are stated with comments on the hollow cathode device. In particular, a newly developed plasma ashing system is introduced to explain how to precisely remove two or more used CVD-diamond coated tools at the same time. Next, short-shank CVD-diamond coated end-milling tools are employed to prove that the diamond coating should be completely removed with minimum loss of substrate materials. Finally, newly developed ashing system is utilized to demonstrate that diamond coatings should be removed simultaneously for two CVD-diamond coated tools.

2. EXPERIMENT

2.1 Oxygen Plasma Ashing

In ashing or etching the carbon based coatings, the oxygen plasma configuration is well controlled to accelerate the ashing and etching process. Under the lower electron and oxygen ion densities, the dense nano-structured carbon-base coatings are difficult to be removed as pointed out in (Aizawa, 2015). The hollow cathode device is invented to intensity the oxygen ion and electron densities up to the order of 10^{17} – 10^{18} m^{-3}. Figure 1 illustrates the developed oxygen plasma ashing system with use of the hollow cathode system.

In this system, the RF-plasma generated by the dipole electrodes is confined in the DC-biased hollow, resulting in the above high density plasma state. Since the CVD-diamond coated end-milling tools have complex tooth structure, it is too difficult to remove the whole diamond films, especially on the back surface of teeth, when the tools are fixed at the jig. The present hollow cathode device allows rotating the diamond-coated tool inside the hollow with the DC bias also applied to both the tool and the hollow. Under this constant rotation, the whole surface of tools is radiated by the oxygen radical.

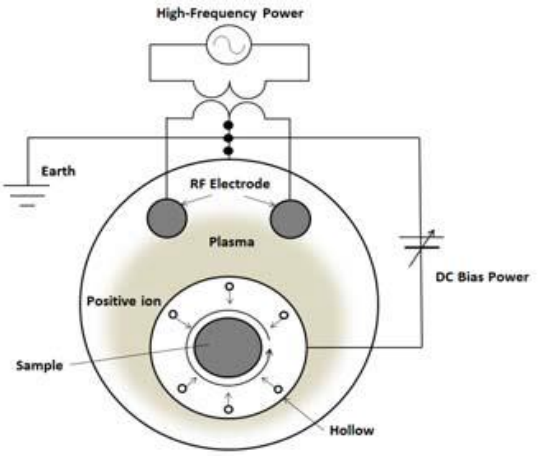

Fig. 1 High oxygen ion density of ashing system to remove the CVD-diamond coatings from the WC (Co) substrate

2.2 New Ashing Systems

A single CVD-diamond coated end-milling tool is treated by ashing. In order to make ashing of two or more tools at the same time, a double-columned or a multi-columned hollow cathode device is necessary in practice.

Fig. 2 New develop of oxygen plasma ashing system for simultaneous removal of diamond coatings for two tools

In the present study, the double-columned hollow cathode device is developed and set-up to simultaneously rotate two CVD-diamond coated tools with respect to the vertical axis. A newly developed oxygen plasma ashing system is depicted in Fig. 2. This system consists of the controlling tower, the vacuum chamber with the hollow cathode device, the carrier gas supply and the evacuation section, as seen from the right to the left in Fig. 2.

In the following experiments, the simultaneous ignition of plasma is experimentally proved together with the simultaneous removal of CVD diamond films.

2.3 Specimens

The CVD-diamond coated WC (Co) short, end-milling tools were employed as a specimen for ashing. Figure 2 depicts a typical specimen to be used in the following ashing experiments. The right-hand shaft of tool was fixed to the fixture for rotating control in Fig. 1. In the preliminary tests, the location of this tool in the hollow as well as the geometric configuration among the tool, the hollow and the DC-bias plate was experimentally optimized.

Fig. 3 CVD-diamond coated end-milling tools with the film thickness of 15 μm

2.4 Observation and Measurement

Optical microscope and SEM (Scanning Electron Microscope) were utilized for observation on the tool surface. Surface profilometer was also used to measure the change of WC (Co) tooth diameter before and after ashing.

3. RESULTS

3.1 Densification by Hollow-Cathode Device

The Langmuir probe was employed to detect the ion and electron densities in the inside of hollow. Figure 4 depicts the variation of measured ion density (Ni) and electron density (Ne) with increasing the pressure. In cases of without the hollow cathode, Ne increases and Ni decreases significantly with increasing the pressure. For an example, Ne = 1.35 x 10^{15} $m^{-3}$and Ni = 9.60 x 10^{16} m^{-3} at p = 65 Pa, while Ne = 3.30 x 10^{16} m^{-3} and Ni = 3.00 x 1016 m-3 at p = 105 Pa. This pressure dependency is common to the high density plasmas, irrespective of the cathode configuration.

On the other hand, using the hollow cathode in Fig. 3, both Ni and Ne become higher than those without the hollow cathode. For an example, Ne = 1.07 x 10^{16} $m^{-3}$and Ni = 6.99 x 10^{17} m^{-3} at p = 65 Pa, and, Ne = 7.51 x 10^{16} m^{-3} and Ni = 1.41 x 10^{17} m^{-3} at p = 105 Pa.

The hollow cathode effect on the increase of electron and ion densities is caused by confinement of plasmas in the hollow cathode. Electrons in the plasmas have more reaction cross-section with the oxygen molecules to generate more population of oxygen ions. This result is densification both in the electron and oxygen ion state.

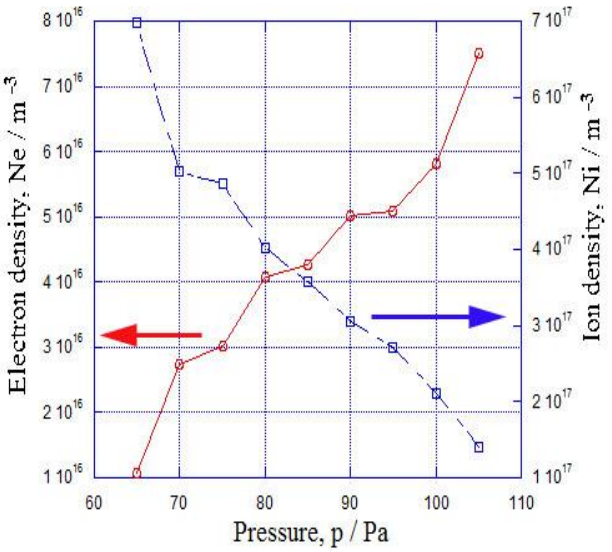

Fig. 4 The variation of the ion and electron densities in the hollow with increasing the pressure

3.2 Plasma ashing Process of Single Tool

In general, the processing parameters mainly determine the plasma state. By using the hollow device, the geometric configuration among the tool, the hollow and the DC-biased plate have influence on the confined plasma state in the hollow, besides for the processing parameters. In (Yamauchi, 2015), the quantitative plasma diagnosis was utilized to make on-line monitoring of the activated species population with the processing time. That paper found that the RF-voltage has more importance on the oxygen plasma state, which is confined in the hollow.

In this experiment, this RF-voltage was reduced from 250 V to 100 V with keeping the DC-bias by -500 V. As shown in Fig. 5 a), the whole tool surface just after ashing is covered by thin grey-colored film, which is easy to be broken away by ultrasonic cleansing. Any oxide layers were never left on the polished surface; as shown in Fig. 5b), small tints were seen just after light cleansing. Figure 5 c) depicts the microscopic image of top tooth edge. The original small holes were dotted on the tooth surface; they were made by chemical treatment before diamond coating as a nucleation site of diamond films. That is, the initial WC (Co) tooth surfaces are recovered by the present plasma ashing condition.

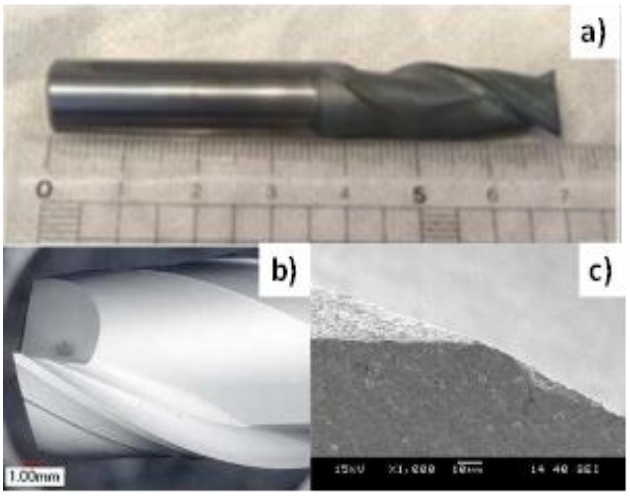

Fig. 5 The ashed specimen by the present method with the condition #3 in Table 1. a) Outlook of ashed CVD-diamond coated tool, b) A top tooth of ashed tool after cleansing, and c) SEM image of tooth edge

The outer diameter (D_m) of top tooth was measured and compared to the calculated one (D_c) by subtracting the coating thickness from the outer diameter of coated top tooth before ashing. If D_m is much less than D_c, the tooth edge and surface is significantly removed to lower the tool substrate life in recycling. Hence, $D = Dc - D_m$ plays an important parameter to evaluate the microscopic damage of tool tooth. In this experiment, D = 1 μm. Considering that the most severe goal in reduction of tool diameter is prescribed by D = 5 mm during a single ashing operation, the present ashing condition in Fig. 5 is sufficiently satisfactory to prove that this high density ashing process should work in practice.

3.3 Simultaneous Ashing Process

The present ashing method with use of the hollow cathode device is never limited to ashing treatment of single diamond-coated tools. In order that the diamond films coated on the tool should be removed from the tool substrate materials by the oxygen plasma ashing. For each diamond coated tool is independently immerged in the oxygen plasma state. In fact, the ashing process of single diamond-coated tool advances in the inside of the oxygen plasma sheath, which covers the whole tooth surface of tool.

In this experimental set-up, the geometric design of single hollow device is expanded to a double-columned hollow cathode one, where each tool in the either hollow cathode device is immerged into the oxygen plasma state. Both tools in the double-columned hollows are controlled to rotate with the DC-bias applied both to the hollows and tools.

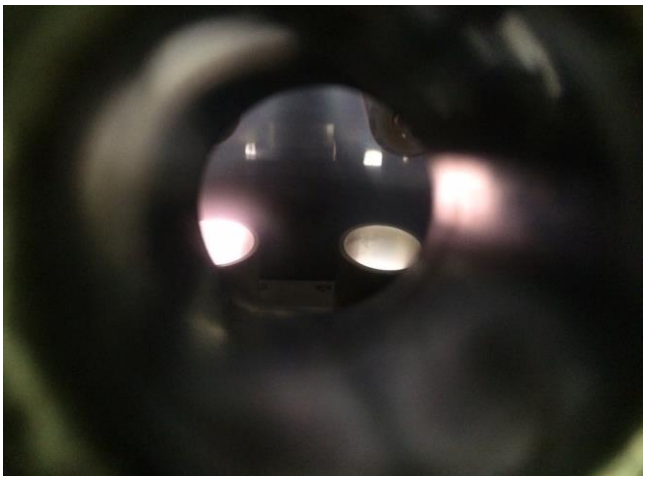

Fig.6. On-line observation on the plasma states which are independently confined in each hollow of the double-columned ashing system

Figure 6 depicts the snap-shot of double-columned hollows during the ashing process.The ion and electron densities become lower outside of the hollows; while the oxygen plasmas are confined in each hollow to have much higher electron and ion densities. During the ashing process by using this double-columned hollow cathode device, two diamond-coated tools are immerged into the above oxygen plasma sheath and rotated in the hollows.

All through the preliminary experiments, reduction of tooth diameter by ashing is kept to be minimum by optimization the RF-voltage. Even in the development of this system, on-line monitoring by quantitative plasma diagnosis is effective to search for optimum RF-voltage condition.

Figure 7 shows the optical microscopic image of ashed tool for 7.2 ks or 2 Hrs. Although the residual diamond dusts are slight left as a dot, the whole CVD-diamond film is removed away from the tooth surface. Little residuals are also seen even on the back surface of teeth; this demonstrates that the rotating tool surface should be homogeneously subjected to the oxygen plasma flux in the confined plasma sheath in the hollows.

Figure 7 b) shows the top view of ashed teeth. Little or nearly zero-loss of teeth is detected in this ashing experiment. This suggests that the multi-columned hollow cathode device might be a solution for simultaneous ashing to remove the used CVD-diamond films in the mass of tens of tools at the same time.

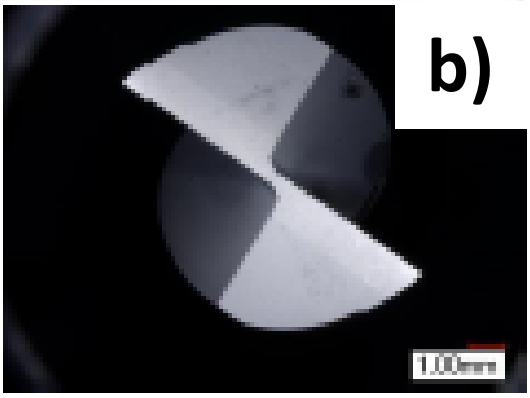

Fig. 7 Tooth surface of ashed CVD-diamond coated tool by using the double-columned hollow cathode device.

4. CONCLUSION

High density oxygen plasma ashing with use of the hollow cathode device works efficiently to remove the used CVD-diamond coatings from the WC (Co) end-milling tools. The processing parameters as well as the geometric configuration of plasma state in the hollow must be optimized to make complete ashing of diamond films with minimum loss of tool materials. In particular, the double-columned hollow cathode device is developed to make simultaneous removal of diamond-coatings from two tools at the same time on the basis of the hollow-cathode device design. Complete ashing of two diamond-coated tools by the present system proves that a mass of used CVD-diamond coated end-milling tools in the order of tens should be simultaneously ashed away by the present method.

ACKNOWLEDGEMENT

The authors would like to express their gratitude to Mr. Kaneda, (OSG, Co. Ltd.) for sample preparation and experiments. This study is financially supported in part by the MEXT with the contract of #440011.

REFERENCES

Aizawa, T., Masaki, E., Sugita, Y. (2014-1), Complete ashing of used DLC coating for reuse of the end-milling tools. Manufacturing Letters. 2, 1-3.

Aizawa, T., Masaki, E., Morimoto, E., Sugita, Y. (2014-2), Recycling of DLC-coated tools for dry machining of aluminum alloys via oxygen plasma ashing. Mechanical Engineering Research. 4 (1), 1-11.

Aizawa, T., Sugita, Y. (2014-3), High density oxygen plasma ashing for recycling and reuse of DLC-coated tools and dies. Research Report SIT (in press).

Aizawa, T., Yunata, E.E., Morita, H, (2015), High density oxygen plasma micro-texturing intoCVD-diamond coated dies for micro-embossing, Proc. 10th ICOMM (in press).

Yamauchi, K., Yunata, E.E., Aizawa, T. (2015), High density oxygen plasma ashing of used CVD diamond coating for recycling of WC (Co) tools, Proc. 15th IMFF (2015, Toyama) (in press).

Yunata, E.E., Suenaga, R., Aizawa, T., Santoyoyo, D. 2013), Quantitative argon plasma characterization by Langmuir probe, Proc. 7th SEATUC, 6-19, 1-4.

Yunata, E.E., Aizawa, T., Santojojo, D. (2014), Characterization of hollow cathode plasma for etching and ashing processes, Proc. 8th SEATUC, 6-21, 1-4.

Yunata, E.E., Aizawa, E. (2015), Micro-texturing into DLC/diamond coated molds and dies via high density oxygen plasma etching, Manufacturing Review, (in press).

E. E. Yunata received the S.Si (2009), M.Si (2012) in Physic Instrumentation from Brawijaya University, Indonesia.

Tatsuhiko Aizawa received B.E. (1975), M.E. (1977), and D.E. (1980) degrees in Nuclear Engineering from University of Tokyo. He is a professor, Department of Design and Engineering, SIT. His current interests include nano and micro-manufacturing, plasma processing, high dense nanotechnology, and surface design engineering

Kazuhisa Yamauchi received the B.E (2015), in material and science from Shibaura Institute of Technology Japan

OS Number 06

DYNAMIC OF NITROGEN AND HYDROGEN SPECIES IN A HIGH RATE PLASMA NITRIDING OF MARTENSITIC STAINLESS STEEL

D.J. Santjojo[1)], Istiroyah[1)], T. Aizawa[2)]

1 Physics Department, University of Brawijaya, Indonesia

2 Engineering and Design Department, Shibaura Institute of Technology, Japan

ABSTRACT A high rate nitriding of martensitic stainless steel was achieved by utilizing a mixture of nitrogen and hydrogen RF-DC plasma. The nitrogen and hydrogen species plays important roles in kinetics and dynamics of plasma during transportation and surface reaction in the plasma nitriding process. A combination analysis of optical emission spectroscopy and Langmuir probe measurement reveals the role of hydrogen in nitrogen ionization and excitation into N_2^+ and N_2^*. Furthermore, a low hydrogen concentration in the plasma provided NH radicals which produced atomic nitrogen on the surface of the stainless steel. The high concentration of ionized, excited and atomic nitrogen on the surface initiate the high rate diffusion into the bulk of material.

INTRODUCTION

Martensitic stainless steel has been widely utilized in many applications and machinery parts. Its wellknown characteristics are high shock resistance, high plasticity and high corrosion resistance. However, some limitations due its low hardness and poor wear resistance have been recognized in some industrial applications (Alphonsa,2002 and Pinedo,2004). One of the many methods of dealing with the drawbacks is by nitrogen atoms incorporation to form nitrided surface layer in the material. There have been many works related to the nitriding of the martensitic stainless steel(Yun-Tao et.al,2008). Our previous work revealed that low temperature plasma nitriding increases the hardness and restore the corrosion resitance due to the formation of chromium nitride (Santjojo, 2013). The nitrogen atoms are distributed as solid solution interacting with iron lattice instead of forming the chromium nitride. The interactions create a new phase which is well known as S-phase or γN. The formation of expanded martensite phase in the martensitic steel is driven by a fast and uniform diffusion of nitrogen into the iron matrix. Occupation of nitrogen in octahedral sites of the original martensitic steel results in martensitic expanded phase responsible to the solid-solubility hardening. Large concentration of nitrogen leads to further expansion and transformation to ε-$Fe_{2-3}N$ or γ-Fe_4N phases.

The diffusion of nitrogen depends on the plasma and the temperature of samples during the plasma nitriding. Furthermore, inclusion of hydrogen into the nitrogen plasma increase the density active species for the nitriding process. The dynamic of the nitrogen and hydrogen should also be important in the process.
This current work explores the dynamic of the gases from a combination of optical emission spectroscopy and langmuir probe measurements.

EXPERIMENT

Specimens for this study were produced by utilizing a high density RF-DC plasma nitriding system. The martensitic steel used was AISI 420 which was cut and shiny polished into 5 mm thick silinders with a diameter of 10 mm. The high density plasma reactor has a pair of dipole anode producing floating plasma in a high vacuum chamber. An unconventional 2 MHz plasma RF generator with an automatic electronic impedance matching was utilized to power up the plasma. The RF-DC plasma system is shown in figure1.

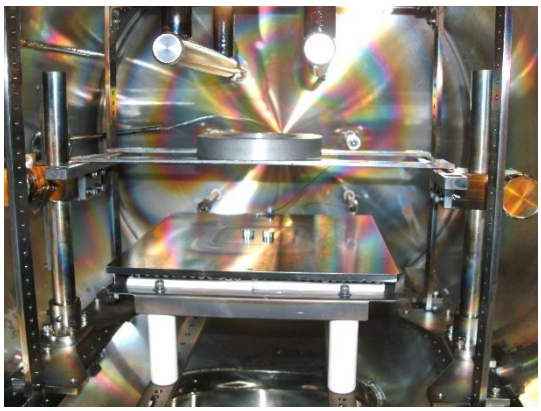

Fig.1 Interior of RF-DC Plasma nitriding system

Samples were loaded on a rectangular cathode equipped with a resistive heater. The cathode was connected to a high voltage DC power source. The DC power provide a bias voltage to direct ions to surface of substrate. Before the nitriding process, the loaded samples were bombarded to activate the metal surface with DC powered nitrogen plasma. The nitriding processes were carried out at a pressure of 70 Pa with RF power and DC bias set to 250 V and 400 V respectively. The temperature of samples was kept below 400° C to avoid the formation of CrN precipitates. All of the samples underwent to the nitriding process for two hours (7200 sec.). Dynamic of plasma during the nitrogen process depends on gas composition. Flow rate of nitrogen and hydrogen gas was varied to investigate the role of each gas in the dynamic of plasma. Plasma conditions and states during the nitriding process were monitored by means of optical emission spectroscopy (OES) and a Langmuir probe measurement. The OES measurements which were carried out with Hamamatsu multichannel analyzer spectroscope are utilized to determine the species of plasma. While the Langmuir measurements were meant to determine electron density and ion density of the plasma. The rate of nitriding process was predicted from depth composition measurement. Composition of elements of the nitride subsurface layer of the specimens was obtained from auger electron spectroscopy (AES) measurements. Composition of the elements to the depth was acquired by serial measurements of subsequent surface etching. Each of the measurements was taken after 10 minutes argon ion etching with the rate of 10 nm/min.

A high density RF-DC Plasma was utilized to produce specimens of martensitic stainless steel. The plasma system has a pair of dipole anode producing floating plasma in a high vacuum chamber.

DISCUSSION

A high rate nitriding of AISI 420 martensitic stainless steel was achieved by mixing nitrogen and hydrogen gas in the process. AES measurement which is shown in figure 2 provides evidence of the high rate nitriding by the mixture of nitrogen and hyrogen plasma which is 1.5 µm/hour compared to 0.75 µm/hour in nitrogen plasma.

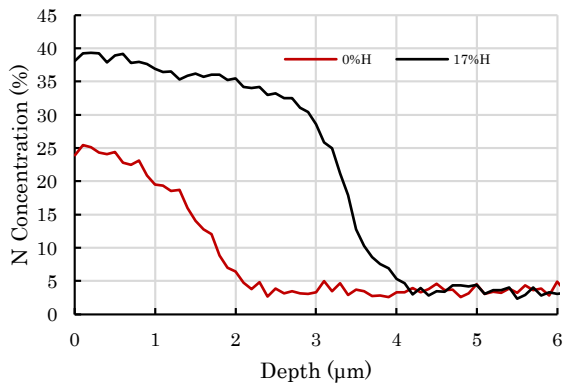

Fig.2 Depth profile of N concentration by AES measurement

Figure 2 shows a kind of plateau profiles of nitrogen concentration. The concentration of nitrogen on the surface of specimen treated with nitrogen plasma only is 25%, while the one treated with a mixture of N+H plasma is 40%. Both of the treatments produce a similar characteristic of the elemental profile. As discussed in the previous paper (Santjojo, 2014), the large concentration of nitrogen suggests that the interaction lead to transformation of the martensitic lattice into ε-$Fe_{2-3}N$ or γ-Fe_4N. It was concluded that the high concentration of nitrogen in the specimens might be results of a fast and uniform diffusion considering our short period of nitriding treatment (7200 sec.). The high rate diffusion was eventually affected by plasma conditions and samples temperature. In this study, the plasma condition was varied by mixing the nitrogen gas with hydrogen gas. The observable emmision of the plasma is shown in figure 3.

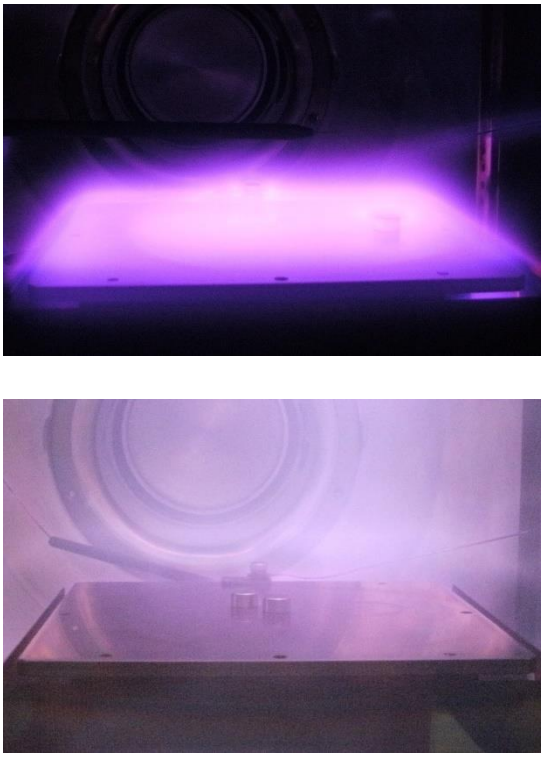

Fig.3 (a) A nitrogen plasma ; (b) A mixture of nitrogen and hydrogen plasma

A violet and darker plasma as in figure 3a indicates transitions of nitrogen species. The inclusion of hydrogen dramatically change the color of the plasma into bright whities emmision. Accurate observation was carried out by means of the OES measurements. The result of OES measurements shown in figure 4. The dramatic change in the color is related to the composition and state of the plasma indicated by changes in the peak intensities. Figure 4 shows three spectrum of plasma which are (i) nitrogen plasma, (ii) a mixture of nitrogen-hydrogen plasma with 17% hydrogen and (iii) a mixture of nitrogen-hydrogen plasma with 83% hydrogen.

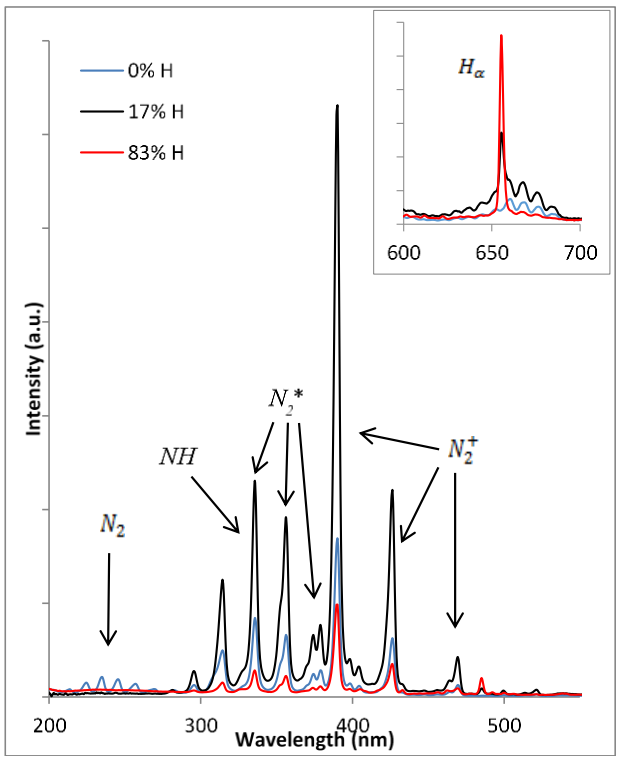

Fig. 4 Optical emission spectra of specimen nitrided with nitrogen plasma only and specimen nitride with nitrogen + hydrogen plasma

As can be seen from figure 4, the inclusion of hydrogen can be observed from the existence of hydrogen peak (Hα) at 656 nm. Pure nitrogen plasma was composed by molecular nitrogen (N_2), excited nitrogen molecule (N_2*), nitrogen radical (N_2^+) and nitrogen-hydrogen system complexes (NH). The appearance of a small amount of the NH is due to the nature of hydrogen inclusion in the vacuum system which can not be avoided. High percentage of hydrogen in the plasma mixture resulted in the decrease of all nitrogen species including the NH complexes. On the other hand, low percentage of hydrogen increased the N_2*, N_2^+ and the NH complexes. The molecular nitrogen peaks at short wavelength (< 300 nm) are disappeared.

According to Kim (2003), the active species for steel nitriding are the metastable state nitrogen such as $N_2(A^3\sum_u^+, \vartheta)$ or vibrationally excited states such as$N_2(X^1\sum_g^+, \vartheta)$. The active species cannot be observed directly from the OES spectra. However, indirect observation is possible by investigating transitions of the second positive $N_2(C^3\prod_u \rightarrow B^3\prod_g)$at 337, 358 and 370 nm which is related to the N_2* and the first negative $N_2^+(B^2\sum_u^+ \rightarrow X^2\sum_g^+)$ at 391 and 427 nm which related to the N_2^+. The second positive and the first negative bands of nitrogen play important role in the generation of atomic nitrogen by reaction with the metastable state nitrogen or vibrationally excited state nitrogen. Other important state of the plasma in the nitriding mechanism is the NH species which is found at 336 nm (Nagamatsu,2013).

During the Langmuir measurement, the exact floating voltage (V_f) could not be observed due to the voltage limit of the instrument. The I-V characteristic of the Langmuir measurement shows changes of electrical resistance related to the hydrogen inclusion in the plasma as shown in figure 5.

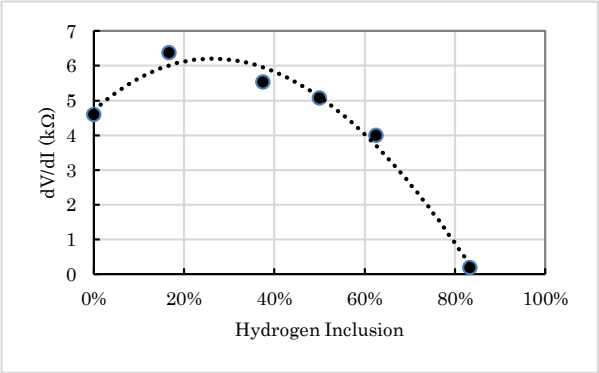

Fig.5 Plasma resistance in the ion saturation region as a function of hydrogen inclusion in the plasma

The electrical resistance was calculated from the ion saturation region of the I-V character. In this region, the higher plasma resistance indicates that the plasma contains high positively charge density. A high voltage needs to be supplied to repel the positively charge and to increase electronic current. The positively charge can be ions or other state of plasma species such as the metastable molecules and other molecule complexes. At this stage, it is impossible to specify the exact composition of resistive plasma. In any cases, it can be observed that hydrogen inclusion plays important role in the creation of the positive ions and other species which refers to the positively charge. The higher plasma resistance indicates a higher density of the species. It can be deduced from figure 5 that 30% hydrogen inclusion might produce the largest positively charge species.

As discussed earlier, the positively charge species are N_2*, N_2^+ and NH complexes. By combining the data from the OES and Langmuir measurements, a number of plasma dynamics can be predicted. Hydrogen which has lower dissociation, excitation and ionization energy than nitrogen in the plasma undergoes into reactions

$H_2 \rightarrow 2H^+ + 2e$ (dissociation)

$H_2 \rightarrow H_2^+ + e$ (ionization)

$H_2 \rightarrow 2H^*$ (excitation)

Further reactions with nitrogen are as follows

$e + N_2(X) \rightarrow N_2^+(B) + e + e$

$N_2^+(B) \rightarrow N_2^+(X) + h\upsilon$ (391 and 427 nm)

and

$$e + N_2(X) \rightarrow N_2^*(C) + e$$

$$N_2^*(C) \rightarrow N_2^*(B) + h\upsilon \text{ (337, 358 and 370 nm)}$$

NH complexes are produced by reactions

$$\left.\begin{matrix} N_2^+ + H_2 \\ H_2^+ + N_2 \end{matrix}\right\} \rightarrow N_2H^+ + H$$

$$N_2H^+ + e \rightarrow NH + N$$

$$N_2^*(B) + N_2(X) \rightarrow N_2(A) + N_2(X)$$

$$N_2(A) + N_2(A) \rightarrow N_2(X) + 2N$$

There are two main products which play important role in diffusion of nitrogen into the stainless steel, (1) the atomic nitrogen and NH. The atomic nitrogen diffuses into the steel via bombardment. On the other hand, the NH radicals reaching the surface of the steel decompose into nitrogen atoms and hydrogen gas. The NH plasma may quench of excited nitrogen atoms by collisions with atoms and molecules in it. The plasma containing the high concentration of N_2^*, N_2^+ and NH complexes produces a large amount of atomic nitrogen. This condition results in a high rate and uniform nitrogen diffusion into the stainless steel.

CONCLUSIONS

Our study concludes that the high rate nitriding is governed and controled by dynamic of nitrogen and hydrogen species in the plasma. The dynamic of the mixed gas plasma depends on the inclusion of hydrogen in the nitrogen plasma. OES and Langmuir probe measurement suggest that low concentration of hydrogen plasma (17%) contains a large density of positively charge species which are N_2^*, N_2^+ and NH complexes. Intermediate species exist in the plasma reaction and emit observable radiation. The species react on the surface producing high concentration of high energy atomic nitrogen which diffuse into the metal uniformly.

ACKNOWLEDGEMENT

Author would like to thanks CAMA (Center for Advanced Material Analysis) in Tokyo Institute of Technology, Japan for the Auger Electron Spectroscopy measurements. Author also thanks the Directorate of Higher Degree Education of Indonesia for SAME grant 2013.

REFERENCES

Alphonsa, A. Chaini, P.M Roale, B. Ganguli, P.I John, A study of martensitic stainless steel AISI 420 modified using plasma nitriding, Surf. Coat. Technol., 150, 2002.

Pinedo C. E., Waldemar A. Monteiro, On the kinetics of plasma nitriding a martensitic stainless steel type AISI 420, Surf. Coat. Technol, 179, 2004.

Yun-tao Xi, Liu Dao-xin, han Dong, Improvement of errosion-corrosion resistance of AISI 420 stainles steel by low temperature plasma nitriding, Appl. Surf. Sci., 258, 2008.

Santjojo D.J., et.al, Formation of Expanded Martensite In Plasma Nitrided AISI420 Stainless Steel, Proceeding SEATUC 8th Symposium, Malaysia, 2013.

Nagamatsu H., et.al, Steel nitriding by atmospheric pressure plasma jet using N2/H2 mixture gas, Surface & Coatings Technology, 225,2013.

D.J. Djoko H.Santjojo, received Ir. (1989) in Electrical Engineering from University of Brawijaya, MPhil. (1997) in Chemistry from Murdoch University-WA, and PhD. (2006) in Physics from Murdoch University-WA. He is a lecturer, Department of Physics, Univ. Of Brawijaya Malang. His interests include thin film technology, nano materials and complex systems.

Istiroyah received the SSi (1998)degree in Physic from Brawijaya University, M.T. (2002) degree in Material Science and Engineering from Bandung Institute of Technology. She is a Lecturer, Department of Physics, Univ. of Brawijaya, Malang Indonesia. Currently, she is a Doctor candidate (2010-), Department of Mechanical Engineering, Univ. of Brawijaya, Indonesia.

Tatsuhiko Aizawa, received B.E. (1975), M.E. (1977), and D.E. (1980) degrees in Nuclear Engineering from University of Tokyo. He is a professor, Department of Design and Engineering, Shibaura Institute of Technology (SIT). His current interests include nano and micro manufacturing, plasma processing, high dense nanotechnology, and surface design.

A study on calcination temperature of NdEuGd-Ba-Cu-O powders for fine particles size

Sunsanee Pinmangkorn[1], Atikorn Wongsatanawarid[1], Somchai Wongwises[1], Masato Murakami[2]
[1]Department of Mechanical Engineering, King Mongkut's University of Technology Thonburi, Thailand
[2]Superconducting Materials Laboratory, Shibaura Institute of Technology, Japan

ABSTRACT

Large single crystal of bulk superconductor is consisted of $(Nd_{0.33}Eu_{0.33}Gd_{0.33})Ba_2Cu_3O_x$ as a matrix in superconducting phase and $(Nd_{0.33}Eu_{0.33}Gd_{0.33})_2BaCuO_y$ as a pinning center in normal conducting phase. The sizes of initial powders are needed for the synthesizing process as fine as possible. The commercial powders existing in the market are 3-5 μm. However, the ternary NEG-Ba-Cu-O is not commercialized yet in the market. In this study the initial powders of (NEG) bulk superconductors were prepared from high purity commercial powders of Nd_2O_3, Eu_2O_3, Gd_2O_3, BaO_2 and CuO in calcination process. The calcination temperatures were studied between 820°C and 880°C resulting from compacted size, powders with particle size and chemical phase using visual measurement, scanning electron microscope and X-ray diffraction respectively.

The homemade powders which are comparable to typical commercial powders resulted in great properties. The particle sizes of homemade powders were agreed in good quality of finest size less than 5 μm for each powder observed by SEM. The chemical phase spectrum measured by XRD demonstrated the optimum calcination temperature at 820°C. We found out that the optimum temperature of both NEG-123 and NEG-211 was adjusted to the same calcination process which will lead to beneficial cost reduction for mass production.

1. INTRODUCTION

The bulk superconductors is a material that is very useful in practical applications such as train Maglev, Flywheel Energy Storage system, Fault Current Limiter, Superconducting Motors-Generators, Drug Delivery System, as well as Nuclear Magnetic Resonance Imaging. An engineering bulk superconductors should be fabricated in a large single domain that exhibits high critical current (J_c). A single rare earth element of bulk superconductors are widely researched such as Y, Nd, Gd, Dy, etc. However, the single rare earth superconductors are quite low in critical current density and magnetic flux trapping properties which is difficult to use in practical engineering. The development of ternary bulk superconductor was found by M. Muralidahr, et al [1-2] which exhibited higher magnetic properties than most single rare earth bulk superconductor [3]. The ternary compound is composed of $(Nd_{0.33}Eu_{0.33}Gd_{0.33})Ba_2Cu_3O_x$ called as NEG-123 and $(Nd_{0.33}Eu_{0.33}Gd_{0.33})_2BaCuO_y$ called as NEG-211. Currently, there is studying the synthesizing process of bulk NEG superconductor in a diameter more than 30 mm undergoing to fabricate so far [4]. So we need to study preparation of good quality initial powders. Successful bulk superconductor properties are strongly linked to the purity and particle sizes of initial powders NEG-123 and NEG-211. In the present paper, we have studied optimum temperature of calcination process to produce homemade initial powders

2. EXPERIMENT

High purity of commercial powders were used as starting powders which were Nd_2O_3, Eu_2O_3, Gd_2O_3, BaO_2 and CuO. The powders were weighed and well mixed to have the initial powder compositions of NEG-123 and NEG-211. In order to produce homemade powders NEG-123 and NEG-211, the well mixed initial powders were pressed in a compact of 35 mm in diameter and 25 g weight each. The initial compositions were pressed by uniaxial pressing under pressure about 100 MPa. Then, the compact precursors were placed in an electrical furnace following by the calcination process in air.

The calcination processes were carried out with the maximum temperature at 820,840,860 and 880˚C in closed alumina box during the process. The samples

were heated to maximum temperature with heating rate about 100˚C/h. They were held for 24 hours and cooled in furnace. The temperature profile is schematically in Fig. 1.

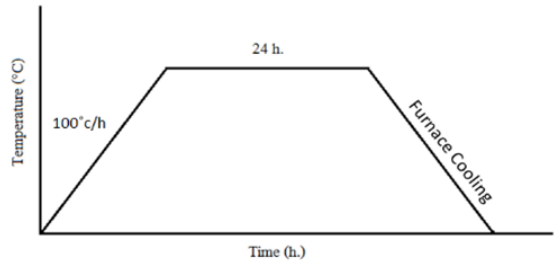

Fig.1 The temperature profile of calcination process

After each cycle, the samples were characterized by visual inspection, and measured the outer dimension and weight to calculate the density later. Then the samples were pulverized by using mortar and pestle about 2 hours. It was normally that the calcination process was repeated with the same temperature profile in the second cycle for chemical homogeneity.

Finally, the compact from the last cycle was pulverized again to characterize the particle size by scanning electron microscope. Some powders were measured the chemical phase to check the quality of the homemade powders with X-ray diffraction spectroscopy.

3. RESULTS AND DISCUSSION

As for visual inspection, the first cycles calcined compact for all studied temperature were observed which the NEG-123 and NEG-211 color changing to black and dark green respectively. However, we found that the color shade was not yet homogeneous reflected that the chemical composition was not completely decomposed. After repeated the second cycles, the compact NEG-123, which calcined at 820˚C, was the most uniform color and completely dark black. The higher temperature results were shiny grey and non-uniform color which reflected to chemical phase change and partly sintered. In contrast, the NEG-211 were similar colored in dark green for all of calcined temperatures.

(a)

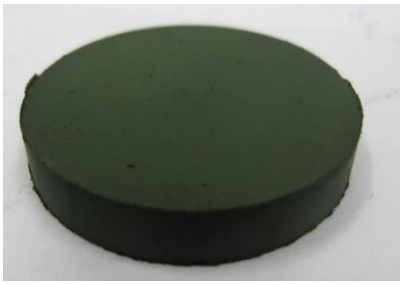

(b)

Fig. 2 The calcined compact at 820 ˚C (a) NEG-123 and (b) NEG-211

The calcined compacts were pulverized for two hours then were characterized by scanning electron microscope to measure the particles size. The average particles size were plotted in Fig. 3 showing that the targeted particles size of NEG-123 and NEG-211 less than 10 and 5 μm were achieved.

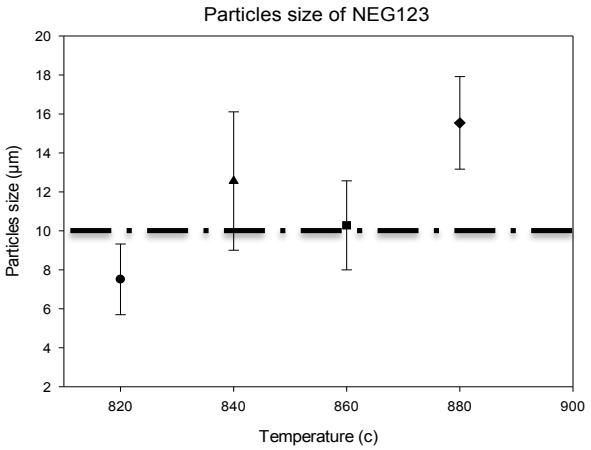

(a)

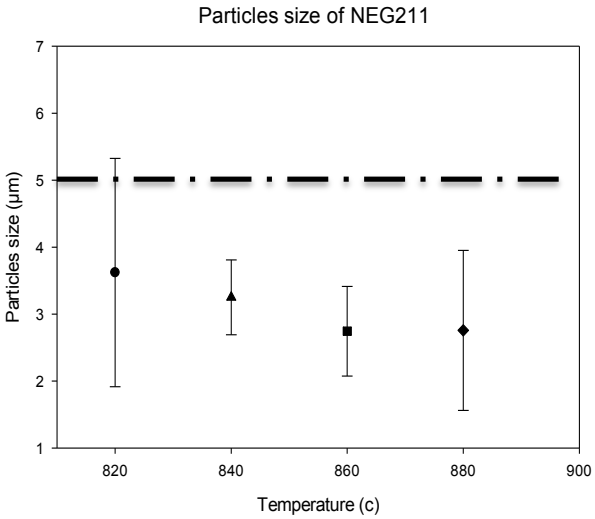

(b)

Fig. 3 The plot of average particles size achieved in each calcined temperature.

Fig. 4 shows the scanning electron microscope of the powders at 820˚C which was the finest particles size in this study.

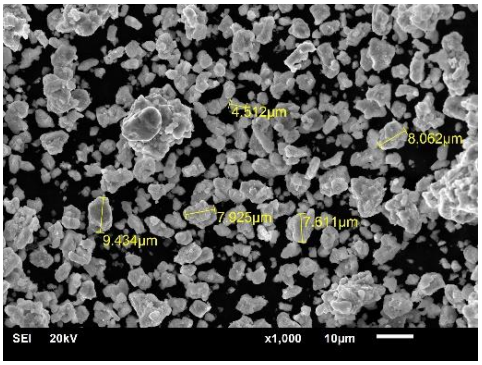

(a)

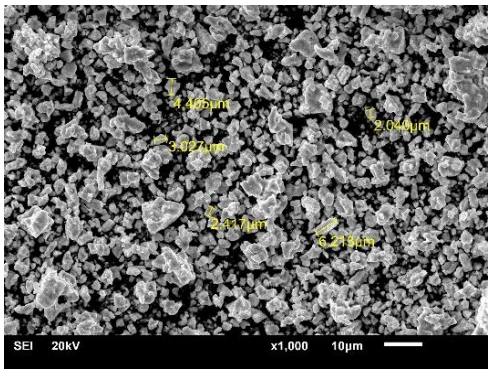

(b)

Fig. 4 The electron micrograph of particles size at 820 ˚C of (a) NEG-123 and (b) NEG-211

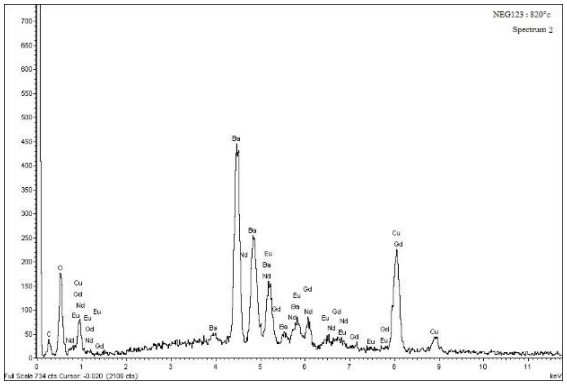

(a)

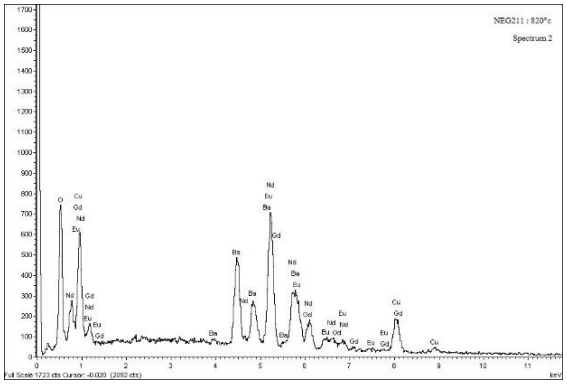

(b)

Fig. 5 The XRD spectrum of powders at 820˚C (a) NEG-123 and (b) NEG-211

The powders were separately characterized by using X-ray diffraction technique for chemical phase evaluation. The spectrum of 2θ-angle were plotted to show the chemical phase change of NEG-123 and NEG-211. The NEG-123 which demonstrate the highest peak clearly at about 33° was superconducting phase. The NEG-211 was normal conducting phase which refers the distribution of spectrum in the different from NEG-123. The XRD spectrums were shown in Fig. 5. The spectrum pattern of both NEG-123 and NEG-211 were comparable to the work of M. Muralidhar et al [4].

Conclusions

The homemade powders of NEG-123 and NEG-211 were produced of difference calcination temperature at 820, 840, 860 and 880˚C. The chemical compositions were characterized first by visual inspection following by electron microscope and X-ray diffraction technique. The optimum conditions obtained with calcined temperature at 820˚C which described to the particle size less than 10 mm for NEG0123 and 5 mm for NEG-211. The XRD patterns at the optimum temperature were in good agreement with related literature of ternary bulk superconductor

References

[1] Muralidhar, M., Nariki, S., Jirsa, M., Murakami M., Single-domain NEG-123 bulk superconductors for high magnetic field applications, Physics C, 372-376, pp. 1134-1136, 2002

[2] M. Muralidhar, M.R. Koblischka, M. Murakami Refinement of secondary phase particles for high critical current densities in Nd,Eu,Gd –Ba–Cu–O superconductors, Physics C, 1999, 313, pp.232-2

[3] Diko, P., Muralidhar, M., Koblischka, M.R., Murakami, M. Homogeneous distribution of 211 secondary-phase particles in single-grain melt-grown (Nd,Eu,Gd)Ba2Cu3O7 bulk, Physics C, 339, pp. 143-147, 2000

[4] Kikuchi, T., Wongsatanawarid, A., Homma, Y., Suzuki, K., Koshizuka, N., Murakami, M., Processing conditions for (Nd, Eu, Gd)-Ba-Cu-O ternary bulk superconductors, Physics Procedia, 2012, 27, pp. 132-135.

Miss.Sunsanee Pinmangkorn received B.E.(2012) in mechanical engineering. She is now a second year master student in department of mechanical engineering, KMUTT

Mr.Atikorn Wongsatanawarid received B.E.(2000) from KMUTT, M.E. (2006) from Chulalongkorn University in mechanical engineering, and D.Eng. (2010) from Shibaura Institute of Technology, Japan. Recently, he is a lecturer in department of mechanical engineering, KMUTT

MECHANICAL AND HYDRAULIC PROPERTIES OF SLUDGE-CRUSHED SALT MIXTURE AS APPLIED FOR BACKFILL MATERIAL IN SALT AND POTASH MINES

Adison Bumrungsuk, and Kittitep Fuenkajorn
Geomechanics Research Unit, Institute of Engineering,
Suranaree University of Technology.

ABSTRACT

Series of consolidation tests have been performed to determine the effects of sludge-to-crushed salt ratios on the mechanical and hydraulic performance for backfill material in salt and potash mines. The ratios of sludge-to-crushed salt vary from 0:100, 25:75, 50:50, 75:25 to 100:0 by weight. The constant axial stresses applied to the specimens are 2.5 MPa for 2, 7, and 15 days. The flow testing is performed to determine intrinsic permeability of sludge-crushed salt during the consolidation test. The uniaxial compressive strength is determined after the samples have been consolidated. The results indicated that the density, uniaxial compressive strength and elastic modulus increase with consolidation time. They also decrease with the sludge content.

1. INTRODUCTION

A problem of the salt and potash mining is surface subsidence due to the deformation of pillar and roof of underground mine. This problem may damage surface structure, farmland, reservoir and groundwater. One of the solutions is to return the waste crushed salt to the mine out openings underground to reduce the roof and pillar deformation. Crushed salt has been widely recognized as the most suitable backfill material (Heemann, et al. 1999; Case & Kelsall, 1987). The primary advantages of crushed salt are the availability, low cost and obvious compatibility with host rock (Stormont & Finley, 1996). Somtong, et al. (2013) have found that the volumetric strain and density of crushed salt increase with consolidation time and applied stresses. The porosity and permeability decrease with increasing density (Case & Kelsall, 1987; Stührenberg, 2007; Loken & Statham, 1997; Hansen & Mellegard, 2002; Salzer, et al. 2007). Brodsky, et al. (1995) conducted hydrostatic and triaxial compression tests with brine content of 2.5% to 3% by weight. The results indicate that the permeability decreases approximately 2.1 orders of magnitude as fractional density increases from 0.9 to 1. The unconfined compressive strength and Young's modulus of crushed rock salt also increase with respect to densification time (Miao, et al. 1995) and decreases with porosity (Kelsall, et al. 1984). However, using only crushed salt may lead to highly time-dependent deformation of the openings to be backfilled.

A common solution practiced internationally in the mining industry is to use bentonite-crushed salt as a backfill material to reduce permeability and deformation in salt mine opening. However, bentonite is expensive and exhibits low strength. Wetchasat (2013) suggest that sludge can be used as a substitute material for bentonite to be mixed with cement and water to grout in rock fractures. The sludge has been collected from the water treatment process (clarifying water system and filtering water system). Utilization of the sludge for other purposes is being considered in order to reduce the volumes of the sludge and the cost of disposal. Therefore, the objective of this study is determine the mechanical and hydraulic performance of sludge-crushed salt mixtures for use as backfill material in salt and potash mines. The task involves performing consolidation tests on variuos ratios of the sludge-to-crushed salt. This paper presents the initial results.

2. SLUDGE-CRUSHED SALT MIXTURE PREPARATION

Sludge used here is obtained from the Metropolitan Waterworks Authority in Bangkok. It is dried under sunlight. The moisture is removed again in a hot-air oven at 100°C for at least 24 hours or until its weight remains constant. The dried sludge is sieved through a mesh no. 40 to obtain grain sizes ranging from 0.001 to 0.475 mm. Crushed salt used in this study have been obtained from the Middle member of the Maha Sarakham Formation in the Korat basin, northeastern Thailand. The grains size of crushed salt ranges from 0.075 to 2.35 mm (Figure 1). The ratios of sludge-crushed salt mixtures vary from 0:100, 25:75, 50:50, 75:25 to 100:0 by weight. The 5% by

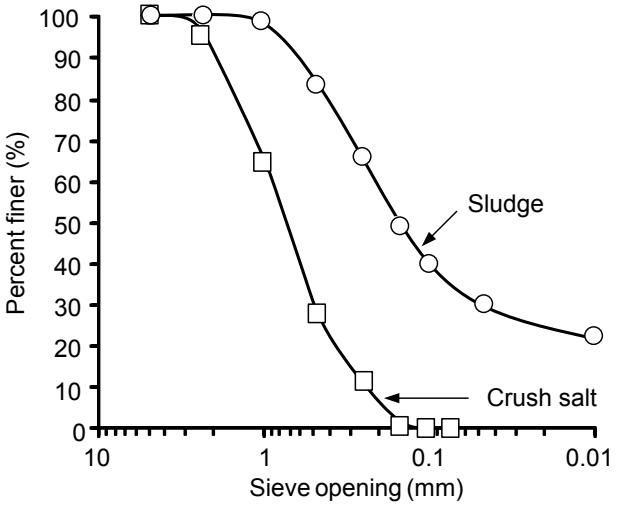

Fig. 1 Grain size distribution of sludge and crushed salt specimen.

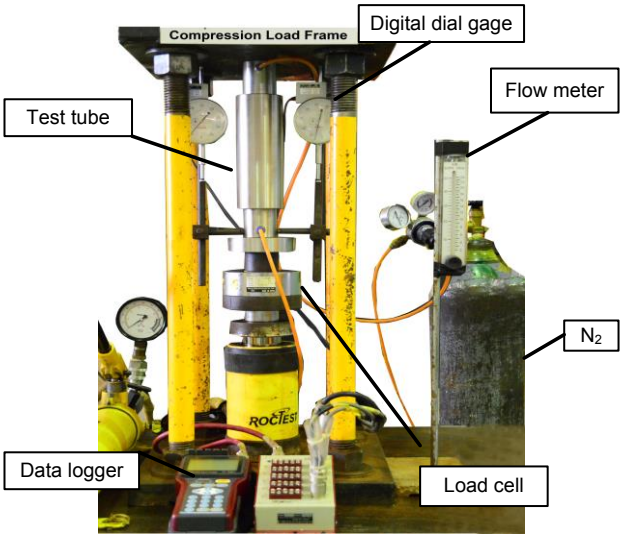

Fig. 2 Test arrangement for consolidation test.

weight of saturated brine is added to the sludge-crushed salt mixtures.

3. CONSOLIDATION TEST

The consolidation tests are performed by applying constant axial stresses on loading steel piston to the mixture installed in the 54 mm diameter steel cylinder (Figure 2). The constant axial stress of 2.5 MPa is applied for 2, 7 and 15 days. The axial displacement is continuously measured as a function of time by dial gage to calculate the change of axial strain and density. Results indicate that the consolidation magnitude and density increase with time (Figure 3).

4. FLOW TEST

The gas flow testing is performed to determined intrinsic permeability (k) of the mixture during consolidation. The flow rates under constant head are continuously monitored every 6 hours. The nitrogen gas is injected under 20 psi into the steel tube. The outflow rates are monitored using high precision flow-meter. The permeability coefficient can be calculated based on the ASTM (D2434-68): $\Delta h = (\Delta P/\gamma_f)$ where Δh is head difference (m), ΔP is difference pressure at the initial point and end point (kPa), and γ_f is unit weight of gas (kN/m^3). The hydraulic conductivity is obtained from:

$$Q = KA\,(\Delta h/L) \qquad (1)$$

where K is hydraulic conductivity (m/s), Q is flow rate (m^3/s), A is a cross-section area of flow (m^2), $\Delta h/L$ is hydraulic gradient. The hydraulic conductivity is used to calculate the intrinsic permeability (k) by Indraratna & Ranjith (2001):

$$k = (K\mu/\gamma f) \qquad (2)$$

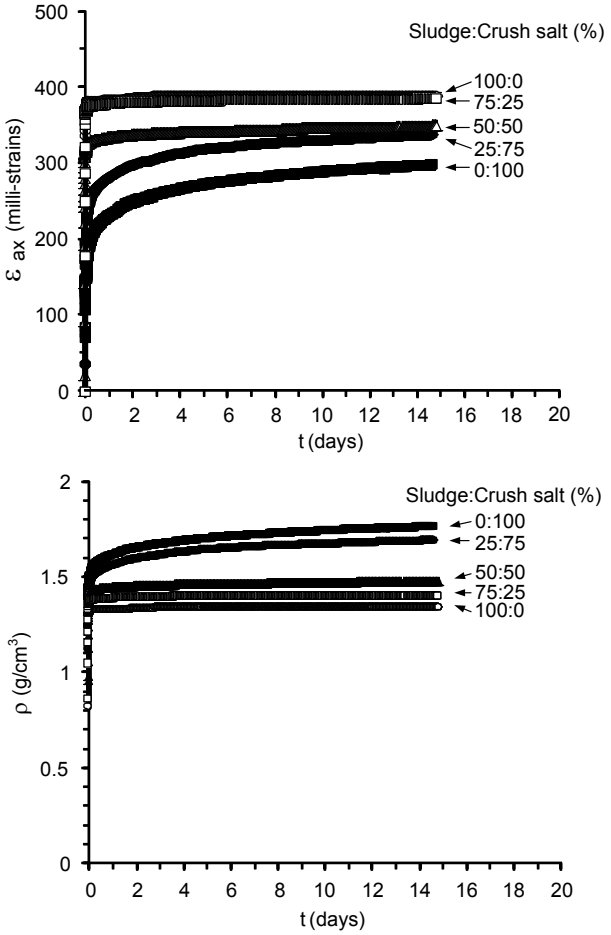

Fig. 3 Axial strain (ε_{ax}) and Density (ρ) as a function of time (t).

where k is intrinsic permeability (m^2), and μ is dynamic viscosity of N_2 (Pa·s). The results indicate that when the consolidation time and sludge content increase the intrinsic permeability decreases. The outflow of sludge-crushed salt mixture at 50:50, 75:25 and 100:0 can not

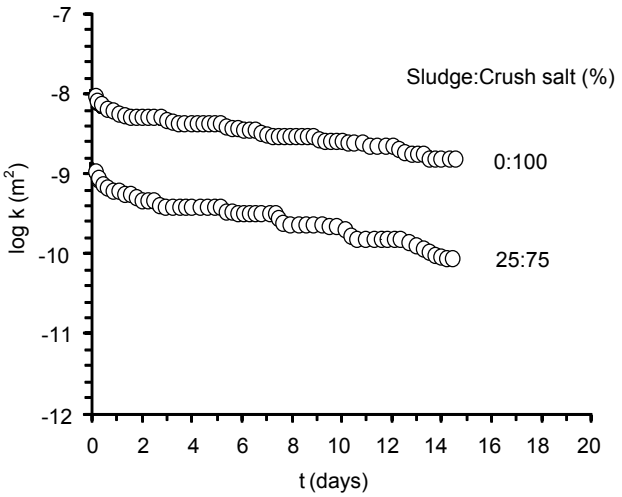

Fig. 4 Permeability (k) plotted as a function of time (t).

detected. The lower limit of the measurement system is 10^{-12} m^2 (Figure 4).

5. UNIAXIAL COMPRESSION TEST

The uniaxial compressive strength test procedure follows the ASTM (D2938) standard practice and the ISRM suggested method. The compressive strength is determined by axially loading the consolidated sludge-crushed salt mixture cylinder (after removing from the steel tube) with a nominal diameter of 54 mm and L/D ranging 2 to 3. Neoprene sheet are used to minimize the friction at the interfaces between the loading platen and the sample surface. The sludge-crushed salt mixture samples are loaded at the constant rate of 0.5-1 MPa/second until failure. The axial and lateral displacement is monitored by dial gages. The uniaxial compressive strength and elastic modulus decrease with increasing sludge content and increase with consolidation time. The Poisson's ratios decrease with increasing sludge content and consolidation time. The changes with time of these elastic parameters suggest that the sludge-crushed salt mixtures can be solidified under stress and time (Figure 5).

DISCUSSION AND CONCLUSIONS

The objective of this study is to determine the mechanical and hydraulic performance of consolidated sludge-crushed salt samples mixed with saturated brine. The results indicate that the suitable brine content for the sludge-crushed salt mixture is 5% by weight. The volumetric strain and density increase with consolidation time. These findings agree well with those from other researchers (Stührenberg, 2007; Loken & Statham, 1997; Hansen & Mellegard, 2002; Salzer, 2007). The volumetric strain increases and density decrease with increasing sludge content. The intrinsic permeability decreases as the consolidation time and sludge content increase. The uniaxial compressive strength and elastic

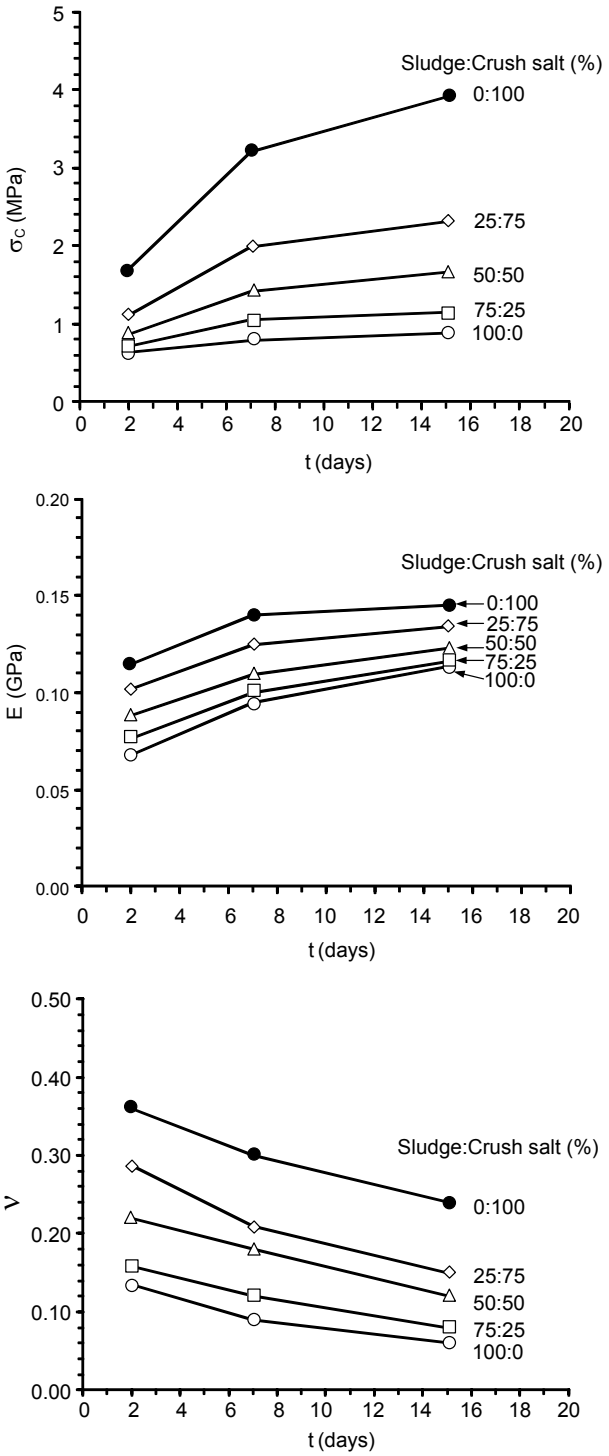

Fig. 5 Uniaxial compressive strength (σ_c), Elastic modulus (E) and Poisson's ratio (ν) as a consolidation time (t).

modulus decrease with increasing sludge content and increase with consolidation time, while the Poisson's ratios decrease with sludge content and consolidation time. The consolidated sludge-crushed salt weight ratio of 50:50 may be suitable for use as a sealing material because it shows lower permeability than using pure crushed salt. Its volumetric strain is relatively small because the sludge is classified as elastic silt with over

90% of its particles is smaller than 0.047 mm. The main mineral composition is silica. The proposed results can be used to predict the mechanical and hydraulic properties of sludge-crushed salt after installation as backfill material in the mine openings. The ongoing tests are carried out to determine the strength and elastic parameters of the mixtures under longer period of consolidation. Sets of mathematical equations will also be derived to link the volumetric strain and mean stress with the compressive strengths, elastic parameters and consolidation time. Such relation will be useful for the determination of the installation parameters for the sludge-crushed salt mixtures in the mine openings. They can also be used to predict the mechanical and hydraulic properties and the solidification of the sludge-crushed salt backfill as a function of time. Such time–dependent properties can, in principle, be incorporated into a numerical model, and hence the mechanical stability of the mine openings (after backfilling) and the subsidence of the ground surface and the overlying formations can be accurately assessed.

ACKNOWLEDGEMENT

This study is funded by Suranaree University of Technology and by the Higher Education Promotion and National Research University of Thailand. Permission to publish this paper is gratefully acknowledged.

REFERENCES

Brodsky, S., Zeuch, H., and Holcomb, J., Consolidation and permeability of crushed WIPP salt in hydrostatic and triaxial compression, Proc. of the 35th US Symposium on Rock Mechanics, pp. 497-502, 1995.

Case, J.B., and Kelsall, P., Laboratory investigation of crushed salt consolidation, Int J Rock Mech Min Sci Geomech Abstr, vol. 5, no. 5, pp. 216-223, 1987.

Fuenkajorn, K., and Daemen, J.J.K. (Eds.), Sealing of Boreholes and Underground Excavations in Rock, Chapman and Hall, London, 1996.

Hansen, F.D., and Mellegard, K.D., Mechanical and permeability properties of dynamically compacted crushed salt, Basic and Applied salt Mechanics, pp. 253-256, 2002.

Heemann, U., Heusermann, S., Sarfeld, W., and Faust, B., Numerical modeling of the compaction behavior of crushed rock salt, In Proceedings of the 7th International Symposiums, Graz, Austria, pp. 627-632, 1999.

Kelsall, P.C., Case, J.B., Nelson, J.W., and Franzone, J.G., Assessment of crushed salt consolidation and fracture healing in a nuclear waste repository in salt. D'Appolonia Waste Mangement Services, 1984.

Loken, M., and Statham, W., Calculation of density and permeability of compacted crushed salt within an engineered shaft sealing system, J. Comput. Civ. Eng.-ASCE, pp. 485–492, 1997.

Miao, S., Ming, L., and Schreyer, L., Constitutive model for healing of materials with application to compaction of crushed rock salt, J. Eng. Mech.-ASCE, vol. 121, pp. 1122–1129, 1995.

Salzer, K., Popp, T., and Böhnel, H., Mechanical and permeability properties of highly pre-compacted granular salt bricks, Proc. of the 6th Conference on the Mechanical Behavior of Salt, Germany, pp. 239-248, 2007.

Stührenberg, D., Long-term laboratory investigation on backfill, Proc. of the 6th Conference on the Mechanical Behavior of Salt, Germany, pp. 223-229, 2007.

Stormont, J.C., and Finley, R.E., Sealing boreholes in rock salt, Sealing of Boreholes and Underground Excavations in Rock, K. Fuenkajorn and J.J.K. Deamen (eds), London: Chapman & Hall, pp.184-224, 1996.

Stührenberg, D., Long-term laboratory investigation on backfill, Proc. of the 6th Conference on the Mechanical Behavior of Salt, Germany, pp. 223-229, 2007.

Somtong, S., Tepnarong, P., and Fuenkajorn, K., Strength and Permeability of Consolidated Crushed Salt, In Proceeding of the EIT-JSCE International Symposium on International Human Resource Development for Disaster-Resilient Countries, September 12-13, Impact Queen's Park Hotel, Bangkok, Thailand, 2013.

Wetchasat, K., and Fuenkajorn, K., Laboratory Assessment of Mechanical and Hydraulic Performance of Sludge-Mixed Cement Grout in Rock Fractures, In Proceedings of the Fourth Thailand Symposium on Rock Mechanics, January 24-25, 2013, Wang Nam Keaw, Nakhon Ratchasima, Thailand, pp. 259-268, 2013.

SHEAR STRENGTH OF COMPACTED SLUDGE-CRUSHED SALT MIXTURES

Pongpoj Sattra, and Kittitep Fuenkajorn
Geomechanics Research Unit, Institute of Engineering,
Suranaree University of Technology.

ABSTRACT

Direct shear tests have been performed to assess the mechanical performance of compacted sludge-crushed salt seals for the openings (boreholes, shafts and tunnels) in salt and potash mines. Crushed salt is sorted to obtain diameters of 0.075-2.35 mm. They are mixed with the sludge, collected from the water treatment plant. The percentage weight ratios of the sludge to crushed salt specimens are from 10:90 to 100:0. The results indicate that the optimum brine contents are from 4% to 34% with the corresponding maximum dry densities from 12.5 to 17.5 kN/m^3. The peak shear strengths of the sludge:crushed salt mixture with 10:90 ratio show the cohesion and friction angle of 0.167 MPa and 46 degrees. When the sludge content is increased to 100:0 the cohesion and friction angle decrease to 0.068 MPa and 32 degrees. The result clearly show that the shear strength increase with increasing crushed salt weight ratio. The findings can be useful to define the initial installation parameters of the mixture in the opening of salt and potash mines.

1. INTRODUCTION

Openings in salt and potash mines require adequate sealing to prevent inflow of water or unsaturated brine during operation and upon decommissioning. Such inflows could cause salt dissolution, with resultant collapses and deformations of the overburden that may be difficult to predict. Overburden deformations could further affect aquifers as well as the ground surface. The reliable sealing material is the key to reduce such environmental impacts. The sealing materials may include mixtures of cement, bentonite, granular materials, depending upon the site-specific requirements. The seal system performance (seal, host rock and their interface) should also be evaluated in terms of the mechanical stability, containment integrity and chemical compatibility, while considering the economic constraints and the local resources (Fuenkajorn, 2007).

A common solution practiced internationally in the mining industry is to use bentonite-crushed salt as a sealing material. The bentonite is, however, expensive and can be highly consolidated even under low loading. Alternative materials such as sludge is of interest for use to mix with the waste crushed salt. Sludge is also the waste material from the water treatment plant. The objective of this study is to determine the mechanical performance of the compacted sludge-crushed salt mixtures. The efforts primarily include series of compaction test and direct shear test on the mixtures with various proportions of sludge, crushed salt and saturated brine. This paper describes the initial test result.

2. TEST MATERIALS

Crushed salt, sludge and saturated brine are the primary components used in this study. Crushed salt is prepared from the Middle and Lower Members of the Maha Sarakham Formation, northeastern Thailand. The salts are crushed by hammer mill (2HP-4 POLES, Spec jis c-4004) and sorted by sieve No. 8 to obtain particle size ranging from 0.075 to 2.35 mm in diameter. Sludge is collected from the Metropolitan Waterworks Authority (MWA). It has particle sizes ranging from 0.075 to 0.475 mm. Sludge is subjected to the Atterberg's limits and specific gravity measurements. The equipment and test procedure follow the ASTM standards (D422, D854) practice. The results are summarized in Table 1. Saturated brine is prepared from pure salt (NaCl) 2.7 kg with distilled water in plastic tank and stirred by a plastic

Table 1. Atterberg's limits and specific gravity of the sludge

Test Condition	Sludge
Liquid limit	55
Plastic limit	22
Plasticity index	23
Specific gravity	2.56

stick continuously for 20 minutes. The proportion of salt to water is over than 39% by weight. Specific gravity of the saturated brine can be calculated by

$$SG_B = \frac{\rho_{Brine}}{\rho_{H_2O}} \quad (1)$$

where SG_B is specific gravity of saturated brine, ρ_{Brine} is density of saturated brine (measured with a hydrometer (kg/m^3)) and ρ_{H2O} is density of water (kg/m^3) equal 1,000 kg/m^3. The SG of the saturated brine in this study is 1.211 at 21° C.

3. COMPACTION MOLDS AND THREE RINGS DIRECT SHEAR DEVICE

Unlike the standard compaction mold the three-ring mold used in this study consists of top, middle and bottle rings (Figure 1). The inner diameter is 10.16 cm, outer diameter is 11.2 cm and the combined height is 20 cm. The three rings are secured on the base plate using steel bolts and two steel clamps. The top and bottom rims of the rings have no locking edge. The steel clamps are used to prevent the rings from displacing during compaction. These clamps are removed when the mold is placed into a direct shear load frame, and hence they can be laterally displaced (sheared) when the lateral force is applied during shear test. This means that the mold will become shear box in the shear frame. Note that the two rings of the standard mold cannot be laterally displaced due to the locking edges at the rims of the rings (Figure 1). The three-ring mold is designed to be used with a new shear test frame for the direct shear test. There are two incipient shear planes of the compacted soil sample in the three-ring mold, one between the top and middle rings and the other between the middle and bottom rings. The main components for the shear test frame are the lateral load system for pushing the middle ring, and the vertical load system for applying a constant normal load on the compacted soil sample (Figure 2). The applied loads are obtained from two 20-ton hydraulic load cells connected to hydraulic hand pumps. Pressure gages are used to measure the loads. The shear and normal displacements are monitored by high precision dial gages

4. COMPACTION TESTS

Sludge to crushed salt ratios (S:C) range from10:90, 20:80, 30:70, 40:60, 50:50, 60:40, 70:30, 80:20, 90:10 to 100:0. The compaction test perform for each mixing ratio with the saturated brine of 0, 5, 10, 15, 20, 25, 30, 35 and40% by weight is used to determine the optimum brine contents. The mold with 10.31 cm diameter and 15.19 cm height are used as compacted mold. The compacted sludge-crushed salt is dynamic compaction with a release of weight steel hammer 10 pounds in mold of 27 times per layer in six layers. Energy of compaction can be calculated by equation (2) (Proctor, 1933).

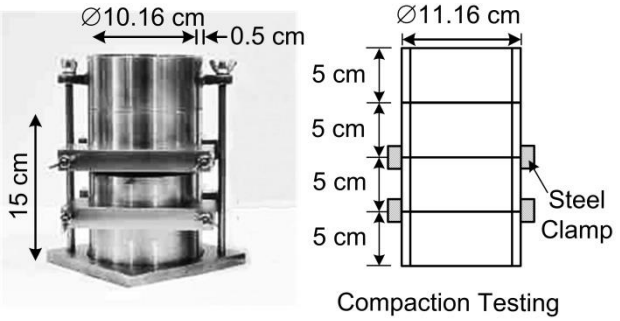

Fig. 1 Three-ring mold.

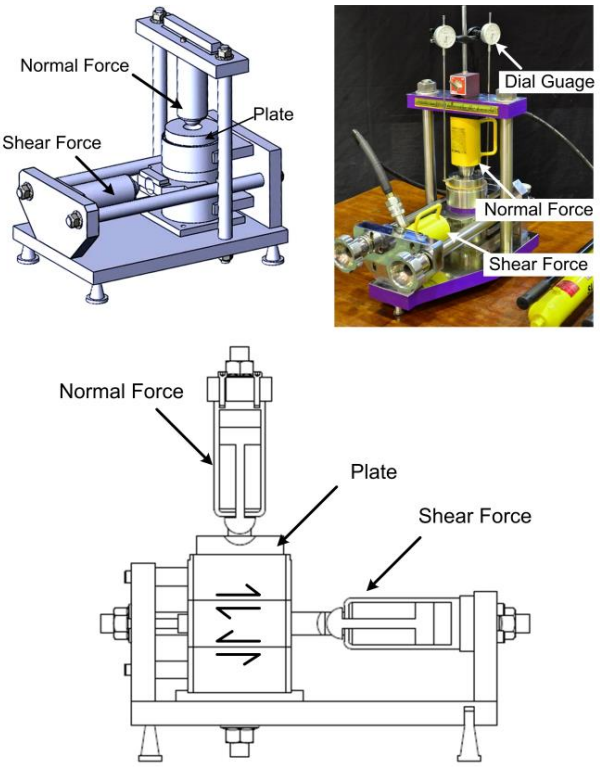

Fig. 2 Direct shear test frame developed for use with the three-ring mold.

$$n = \frac{J \times V}{W \times L \times t} \quad (2)$$

where J is compaction energy per unit volume, W is weight of hammer, L is height of drop of hammer, t is number of layers, n is number of blows per layer and V is volume of mold. The brine content can be calculated by (Fuenkajorn, 1988):

$$W_B = \frac{[100 + S_B] \times [W_1 - W_2(\frac{W_i}{100})(W_2 - W_{can})] \times 100}{100 \times (W_2 - W_{can}) - SB(W_1 - W_2)} \quad (3)$$

where W_B is brine content (%), W_i is initial water content (%), W_{can} is weight container (g), W_1 is weight wet mixture and container (g), W_2 is weight dry mixture and

container (g) and S_B is solubility of salt in dissolved water (weight crushed salt /weight water)×100%.

The dry densities and brine contents are plotted to determine the maximum dry density and optimum brine content. The optimum brine contents range from 4 to 34 percent, and the maximum dry density are from 12.5 to 17.5 kN/m^3 (Figures. 3 and 4). These ratios are used for the preparation of the saturated brine and sludge-crushed salt mixtures for the shear tests in this study.

5. DIRECT SHEAR TESTS

The direct shear tests are performed to determine the maximum shear stress of sludge-crushed salts mixtures with the optimum brine content after compacted in the three ring mold. The normal force is applied by the vertical hydraulic load cell are 0.1, 0.2 and 0.4 MPa. Shear force is applied by a horizontal hydraulic load cell. The peak shear strength is used to calculate the cohesion and friction angle. The shear stresses as a function of shear displacement from the three-ring direct shear test are shown in Figure. 5. The shear stresses increase with shearing displacement, particularly under high normal stresses. The higher percentages of crushed salt are show in higher shear strength, as shown in Figure 6.

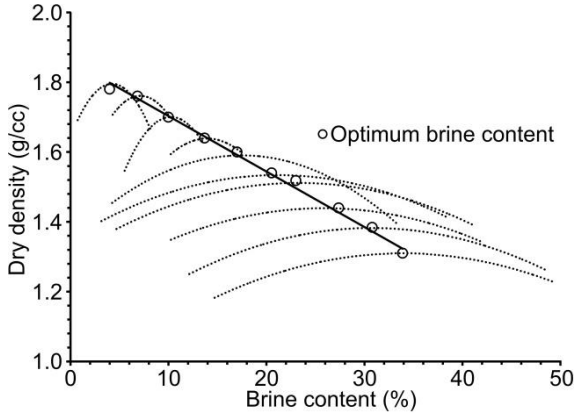

Fig. 3 Relationship between brine content and maximum dry density of mixtures.

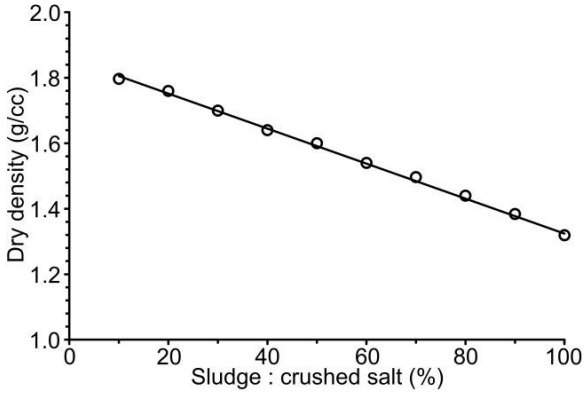

Fig. 4 Relationship between sludge contents and maximum dry density of mixtures.

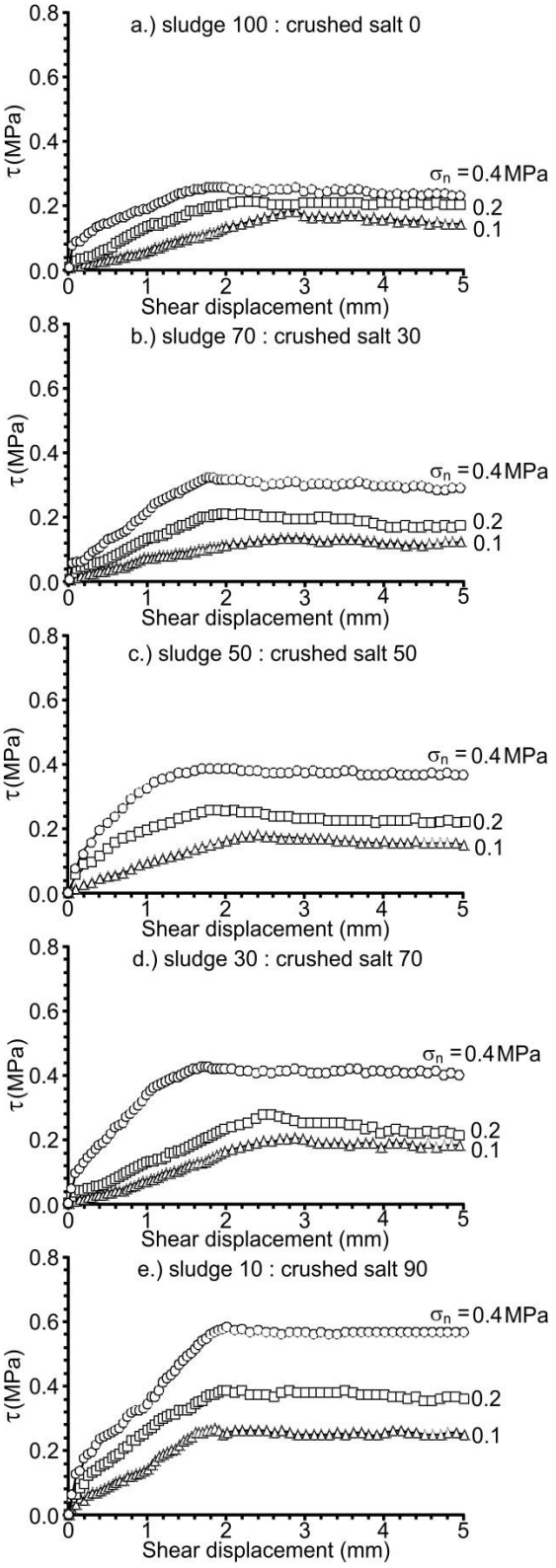

Fig. 5 Some shear stresses as function of shear displacement (a) S:C=100:0, (b) S:C=70:30 , (c) S:C=50:50 , (d) S:C=30:70 and (e) S:C=10:90.

The figure shows the peak shear stresses of the mixtures as a function of normal stresses. Table 2 summarizes the friction angles and cohesion when increase with the crushed salt content.

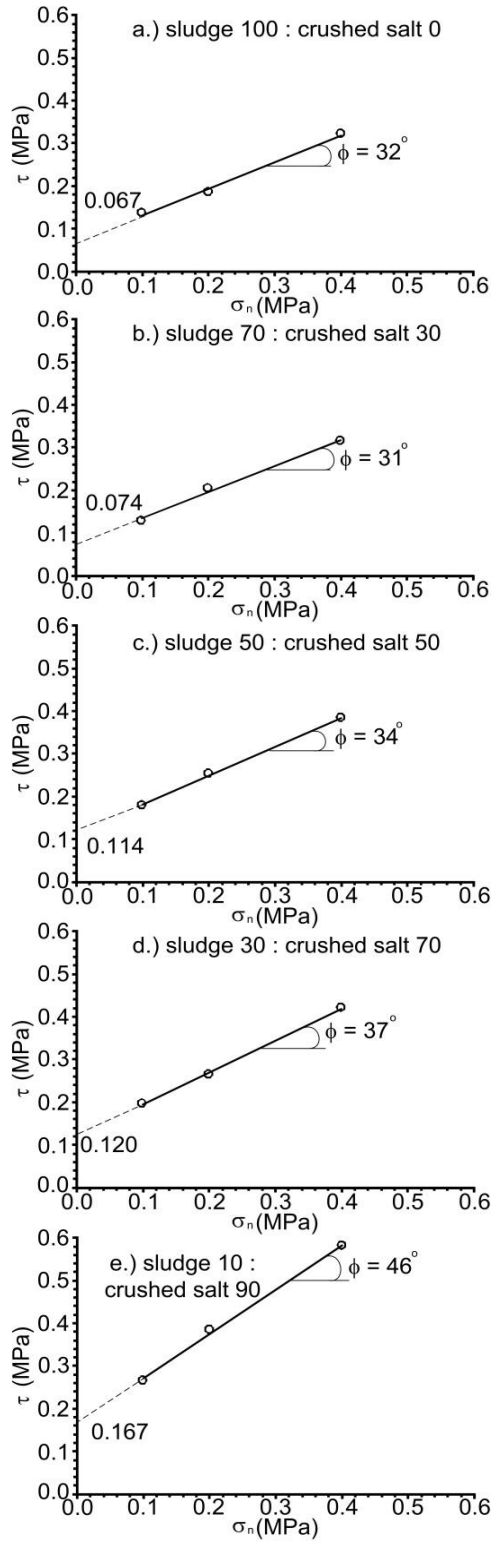

Fig. 6 Some shear strength as function of normal stress (a) S:C=100:0, (b) S:C=70:30 , (c) S:C=50:50 , (d) S:C=30:70 and (e) S:C=10:90.

6. DISCUSSIONS AND CONCLUSIONS

Results from the compaction tests on the 10 percentage of sludge specimens mixed with saturated brine provide the optimum brine content of 4% with the corresponding maximum dry density about 17.5 kN/m^3.

Table 2. Cohesion and friction angles of compacted mixtures.

Sludge : crushed salt (%)	ϕ_p (degrees)	Sludge : crushed salt (%)
100:0	32	0.068
90:10	31	0.071
80:20	32	0.065
70:30	31	0.074
60:40	32	0.065
50:50	34	0.114
40:60	35	0.114
30:70	37	0.120
20:80	39	0.117
10:90	46	0.167

The pure sludge mixed with saturated brine provides the optimum brine content of 34% and maximum dry density about 12.5 kN/m^3. The direct shear test results show the shear strengths varying from 0.12 to 0.58 MPa under normal stresses of 0.1, 0.2 and 0.4 MPa. The results from compaction test and direct shear test indicate that the compacted mixtures with higher crushed salt content give grater dry density and shear strength than those with the lower crushed salt content.

ACKNOWLEDGEMENT

This study is funded by Suranaree University of Technology and by the Higher Education Promotion and National Research University of Thailand. Permission to publish this paper is gratefully acknowledged.

REFERENCES

ASTM Standard D1557–09., Standard Test Method for Laboratory Compaction Characteristics of Soil Using Modified Effort. Annual Book of ASTM Standards, American Society for Testing and Materials, West Conshohocken, PA, 2009.

Fuenkajorn, K., Borehole closure in salt. Department of Mining and Geological Engineering University of Arizona, 1988.

Fuenkajorn, K., Design process for sealing of boreholes in rock mass. Rock mechanics proceedings of the first Thailand symposium: pp. 245-252, 2007.

Sonsakul, P. and Fuenkajorn, K., Development of Three-Ring Compaction and Direct Shear Test Mold for Soils with Oversized Particles. Research and Development Journal of The Engineering Institute of Thailand, 24(2): 1-7, 2013.

Sonsakul, P., Walsri, C. and Fuenkajorn, K., Shear strength and permeability of compacted bentonite-crushed salt seals. In Proceedings of the Fourth Thailand Symposium on Rock Mechanics, pp. 99-109, 2013.

Wetchasat, K. and Fuenkajorn, K., Laboratory Assessment of Mechanical and Hydraulic Performance of Sludge-Mixed Cement Grout in Rock Fractures. In Proceedings of the Fourth Thailand Symposium on Rock Mechanics, pp. 143-152, 2013.

COMPACTED BENTONITE – CRUSHED SALT MIXTURES AS SEALENTS IN ROCK SALT AND POTASH OPENINGS.

Usachon Niewphueng, and Kittitep Fuenkajorn
Geomechanics Research Unit, Institute of Engineering,
Suranaree University of Technology.

ABSTRACT

Direct shear tests have been performed to investigate mechanical properties of compacted bentonite-crushed salt mixtures with saturated brine as sealing material in opening in salt and potash mines. The grain size of the crushed salt is ranging from 0.075 to 2.35 mm. The mixing ratios of commercial grade bentonite to crushed salt are from 10:90 to 100:0 by weight. The compaction tests results indicate that the optimum brine content are from 2.2% to 20% with the corresponding maximum dry densities from 15.9 to 19.0 kN/m^3. The mixtures with higher crushed salt content also increase the shear strength. The friction angles of the mixtures increases with increasing crushed salt content, which range from 23 to 43 degrees. The cohesion of all ratios ranges from 0.20 to 0.28 MPa. The compacted bentonite-crushed salt weight ratio of 30:70 is recommended for use as a sealing material.

1. INTRODUCTION

Rock salt and potash openings require sealing to satisfy to minimize groundwater circulation around the opening. The sealing materials should have suitable performance with the host rock (Fuenkajorn & Damen, 1996). Bentonite is used extensively for sealing. It is an excellent sealant material because of its low permeability, desirable swelling self-healing characteristics and longevity in nature (Ouyang & Damen, 1990). A mixture of bentonite and ballast material is also considered as sealant for borehole because it decreases shrinkage potential increases the bearing capacity of the sealant and minimize creep or settlement (Dixon et al., 1985). This study selects the crushed salt mixed with bentonite to eliminate the salt waste after mining completed. The use of bentonite and crushed salt mixtures may be extended future for abandoned underground mine openings and should be demonstrated to be practical and acceptable.

Compacted bentonite-based materials have been proposed as possible sealing and sealing materials in geological repositories for the high-level radioactive waste disposal in several countries (Wang, 2014). Johannesson, et al. (1999) recommend the compacted bentonite-crushed salt weight ratio of 30:70 used as backfilling in the tunnels. Their results show that the hydraulic conductivity of the mixtures decreases with increasing bentonite content. The hydraulic conductivity of the suitable mixtures is equal to 1×10^{-9} m/s.

Most of the previous researchers have been concentrated on hydraulic conductivity of the mixtures. However, the mechanical properties of bentonite-crushed salt remain important to prevent separation from sealing**.** The objective of this study is to determine the mechanical performance of the compacted bentonite-crushed salt mixtures with saturated brine. The efforts include compaction and direct shear test on the mixtures with various properties of bentonite, crushed salt and saturated brine. The paper describes the initial test results

2. TEST MATERIALS

Materials used in this study are bentonite, crushed salt and saturated brine. Crushed salt is prepared from the Lower Members of the Maha Sarakham Formation, northeastern Thailand. The salts are crushed by hammer mill until has grain sizes ranging from 0.075 to 4.75 mm. The particle size distribution of crushed salt is shown in Figure 1. The size range is equivalent to those expected to obtain as waste product from the salt mines. Bentonite has a specific gravity of 2.50, plastic limit (PL) is 108 %, liquid limit (LL) is 48.9 % and plastic index (PI) is 59.0 %. Saturated brine is prepared from pure salt (NaCl) with distilled water in plastic tank and stirred by a plastic stick continuously. The proportion of salt to water is over 39% by weigh. Specific gravity of the saturated brine can be calculated by :

$$SG_B = \frac{\rho_{Brine}}{\rho_{H20}} \quad (1)$$

where SG_B is specific gravity of saturated brine, ρ_{Brine} is density of saturated brine (measured with a hydrometer (kg/m^3)) and ρ_{H2O} is density of water (kg/m^3) equal 1,000 kg/m^3. The SG of the saturated brine in this study is 1.211 at 21°C.

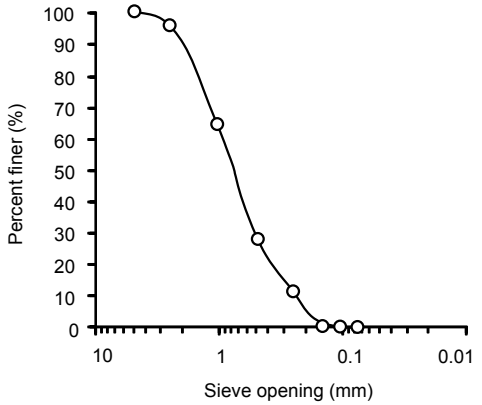

Fig. 1. Grain size distribution of crushed salt.

3. COMPACTION MOLDS AND THREE-RING DIRECT SHEAR DEVICE

The three ring mold (Sonsakul, 2013) is used in this study (Figure 2). The three rings are secured on the base plate using steel bolts and two steel clamps. The top and bottom rims of the rings have no locking edge. The inner diameter is 10.16 cm, outer diameter is 11.2 cm and the combined height is 20 cm. The steel clamps are used to prevent the rings from displacing during compaction. These clamps are removed when the mold is placed into a direct shear load frame, and hence they can be laterally displaced (sheared) when the lateral force is applied during shear test. This means that the mold will become shear box in the shear frame (Figure 3). Note that the two rings of the standard mold cannot be laterally displaced due to the locking edges at the rims of the rings.

The three-ring mold is designed to be used with a new shear test frame for the direct shear test. There are two incipient shear planes of the compacted soil sample in the three-ring mold, one between the top and middle rings and the other between the middle and bottom rings. The main components for the shear test frame are the lateral load system for pushing the middle ring, and the vertical load system for applying a constant normal load on the compacted soil sample. The applied loads are obtained from two 20-ton hydraulic load cells connected to hydraulic hand pumps. Pressure gages are used to measure the loads. The shear and normal displacements are monitored by high precision dial gages (Figure 3).

4. COMPACTIONS TEST

Bentonite and crushed salt are mixed with the saturated brine with percentages of saturated brine of 5, 10, 15, 20, and 25%.

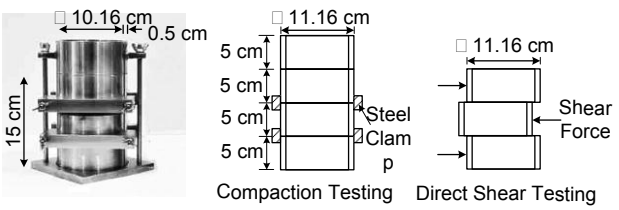

Fig. 2. Three-ring compaction and direct shear mold.

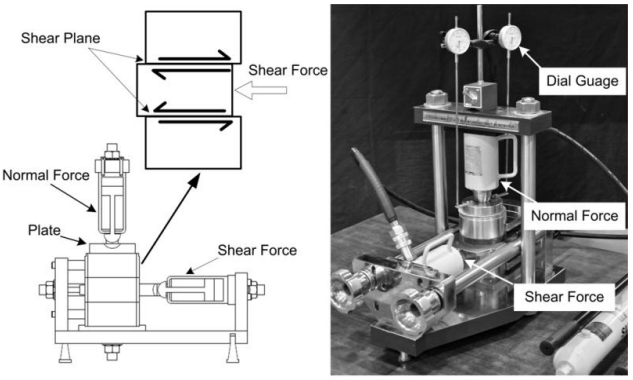

Fig. 3. Direct shear tests frame for three-ring mold.

The mixing ratios of the bentonite-to-crushed salt vary from 100:0 to 10:90 by weight. The mixtures are placed in the three-ring mold for compaction tests. The diameter and height of the three-ring mold are 10.16 cm and 15.19 cm. The compacted bentonite and crushed salt dynamic compaction with a release of weight steel hammer 10 pounds in mold of 27 times per layer in six layers. Energy of compaction can be calculated by equation (1) (Proctor, 1933).

$$n = \frac{(J \times V)}{(W \times L \times t)} \tag{2}$$

where J is compaction energy per unit volume, W is weight of hammer, L is height of drop of hammer, t is number of layers, n is number of blows per layer and V is volume of mold. Specimen weights of three-ring molds are 6100 g. The brine content can be calculated by (Fuenkajorn, 1988):

$$W_B = \frac{\{[100+S_B]\times[W_1 - W_2(W_i/100)\cdot(W_2 - W_{can})]\times 100\}}{[100\cdot(W_2 - W_{can}) - S_B\cdot(W_1 - W_2)]} \tag{3}$$

where W_B is brine content (%), W_i is initial water content (%), W_{can} is weight container (g), W_1 is weight wet mixture and container (g), W_2 is weight dry mixture and container (g) and S_B is solubility of salt in dissolved water (weight crushed salt / weight water)×100%. The dry density and brine contents are plotted to determine the maximum dry density and optimum brine content. The mixtures provide the optimum brine contents range from 2.2 to 20 percents with the corresponding maximum dry densities are from 15.9 to 19.0 kN/m^3 as shown in Table 1. All ratios of optimum brine content are used for the preparation of the saturated brine and bentonite – crushed salt mixtures.

5. DIRECT SHEAR TEST

The direct shear tests are performed to determine maximum shear stress of compacted bentonite - crushed salt mixtures with the optimum brine content. The normal force is applied by the vertical hydraulic load cell. Normal stresses used are 0.1, 0.2 and 0.4 MPa. Shear force is applied by a horizontal hydraulic load cell. The

Table 1. Maximum dry density and optimum brine content of compaction test.

Mixtures B:S (%)	Maximum dry density (g/cc)	Optimum brine content (%)
10:90	1.88	2.2
20:80	1.86	4.2
30:70	1.85	5.5
40:60	1.80	8.1
50:50	1.74	10.5
60:40	1.68	11.5
70:30	1.66	14.0
80:20	1.62	16.0
90:10	1.61	18.0
100:0	1.59	20.0

Table 2. Cohesion and friction angles of direct shear test.

Mixtures B:S (%)	Friction angle (degrees)	Cohesion (MPa)
10:90	43	0.28
20:80	42	0.26
30:70	38	0.26
40:60	35	0.25
50:50	33	0.24
60:40	30	0.23
70:30	27	0.22
80:20	26	0.21
90:10	24	0.20
100:0	23	0.20

shear stresses as a function of shear displacement from the three-ring direct shear test are shown in Figure 4. The shear stresses increase with shearing displacement, particularly under high normal stresses. Higher shear strength are obtained from the mixtures with higher percentages of crushed salt. Figure 5 shows some peak shear stresses of the mixtures as a function of normal stresses to determine to cohesion and friction angle. The friction angle increases with crushed salt content while cohesion ranges from 0.20 to 0.28 MPa (Table 2).

DISCUSSION AND CONCLUSIONS

The weight ratios of the bentonite-crushed salt (B:S) mixtures used in this study are varied from 10:90 to 100:0%. Normal stresses used are 0.1, 0.2 and 0.4 MPa. The results indicate that the compacted mixtures with higher crushed salt content show greater shear strength than those with the lower crushed salt content.

When the normal stress is increased, the shear strength increases. The friction angles of compacted mixtures increases with increasing crushed salt content from 23 to 43 degrees. Cohesions are from 0.20 to 0.28 MPa, and tend to be independent of the salt content. These results confirm that the crushed salt can increase the mechanical performance of sealing material. From previous studies, the compacted bentonite-crushed salt

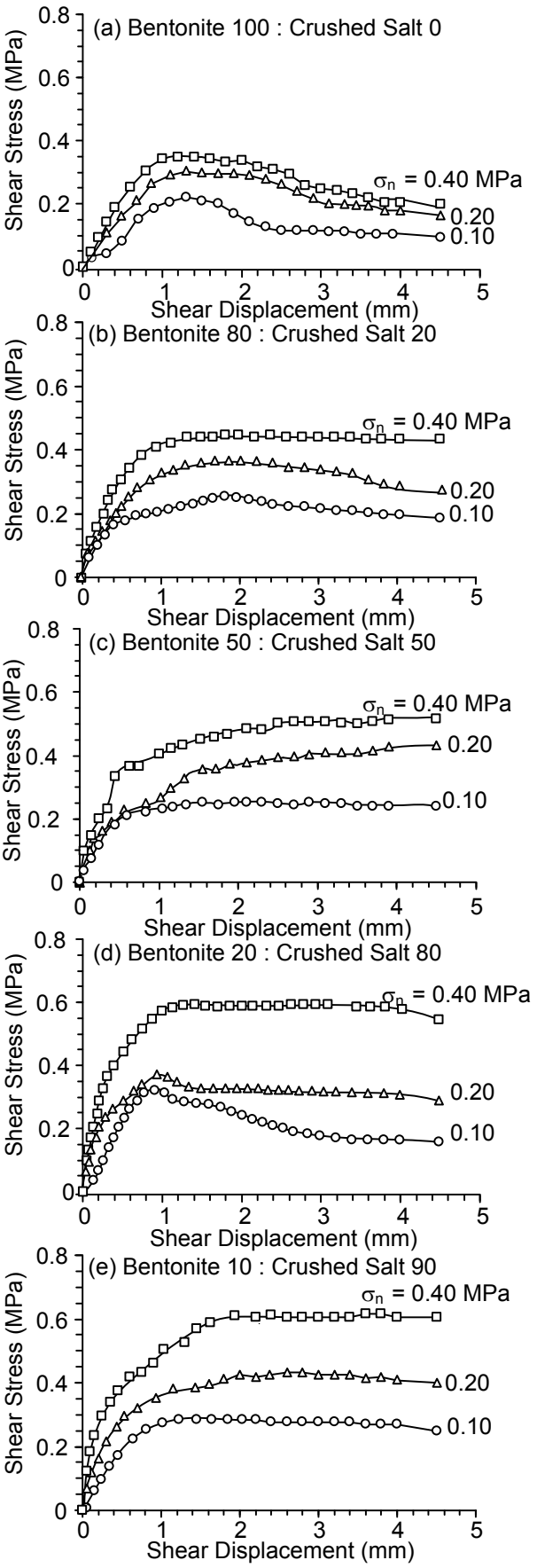

Fig.4. Shear stress as function of displacement for (a) B:S=100:0, (b) B:S=50:50, (c) B:S=50:50, (d) B:S=20:80, and (e) B:S=10:90.

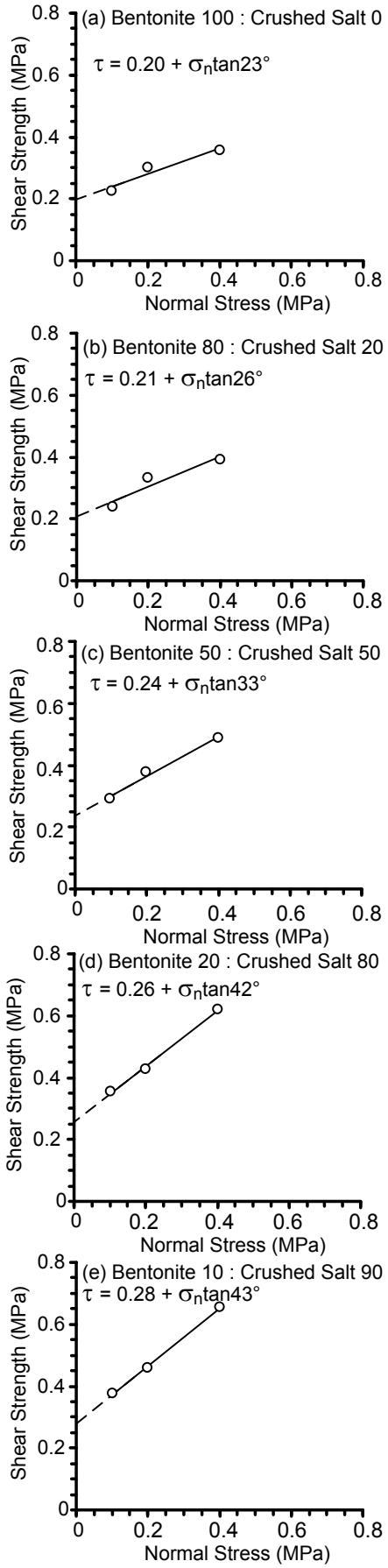

Fig. 5. Shear stress as a function of normal stress for (a) B:S=100:0, (b) B:S=50:50, (c) B:S=50:50, (d) B:S=20:80, and (e) B:S=10:90.

weight ratio of 30:70 has acceptably low hydraulic properties for use as sealing material (Johannesson, et al., 1999). The mechanical properties of the recommended ratio in this study show the shear strength, cohesion and friction angle are comparable to the compacted pure crushed salt. Therefore, the bentonite-crushed salt weight ratio of 30:70 shows good potential to be used as sealing material in salt and potash openings.

The results obtained here can be used as an initial installation parameters of the bentonite-crushed salt backfill in some locations of the mine openings. These locations may require good hydraulic performance, such as boreholes, bulkheads or shafts. The soft and plastic behavior of the compacted bentonite-crushed salt backfill would allow small deformations of the host surrounding salt while maintaining acceptable hydraulic integrity.

ACKNOWLEDGEMENT

This study is funded by Suraneree University of Technology and by the Higher Education Promotion and National Research University of Thailand. Permission to publish this paper is gratefully acknowledged.

REFERENCES

ASTM Standard D1557–09. Standard Test Method for Laboratory Compaction Characteristics of Soil Using Modified Effort. Annual Book of ASTM Standards, American Society for Testing and Materials, West Conshohocken, PA, 2009.

Dixon D.A, Gray M.N. and Thomas A.W., A study of the compaction properties of potential clay-sand buffer mixtures for use in nuclear fuel waste disposal. Eng. Geol. 21, pp. 247-255, 1985.

Fuenkajorn, K., Borehole closure in salt. Department of Mining and Geological Engineering University of Arizona, 1988.

Fuenkajorn, K. and Daemen, J.J.K., Sealing of Boreholes and Underground Excavations in Rock. Chapman and Hall, London, 1996.

Johannesson, L-E., Borgesson, L., and Sanden, T., Backfill materials based on crushed rock (Part 2). Geotechnical properties determined in laboratory. SKB Progress Report IPR-99-33, 1999.

Sonsakul, P and Fuenkajorn, K., Development of Three-Ring Compaction and Direct Shear Test Mold for Soils with Oversized Particles. Research & Development Journal of the Engineering Institute of Thailand, 24(2), pp. 1-7, 2013.

Ouyang, S. and Daemen, J.J.K. Sealing Performance of Bentonite and Bentonite/Crushed Rock Borehole Plugs. Department of Mining & Geological Engineering University of Arizona, 1992.

Wang, Q. Cui, Y., Tang, A., Delage, P., Gatmiri, B and Ye, W. Long-term effect of water chemistry on the swelling pressure of a bentonite-based material. Applied Clay Science. 87: pp. 157-162, 2014.

INFLUENCE OF FLY-ASH BASED GEOPOLYMER ON SHEAR STRENGTH OF COMPACTED SOILS

Soe Thiha and Decho Phueakphum
Geomechanics Research Unit, Institute of Engineering,
Suranaree University of Technology

ABSTRACT

The objective of this study is to experimentally assess the efficiency of geopolymer for soil strengthening. Geopolymer is a utilizing of fly-ash mixed with sodium hydroxide (NaOH) and sodium silicate (Na_2SiO_3). The ratio of alkaline activator (NaOH and Na_2SiO_3) is 1:1. Three soil types are used and individually mixed with FA based geopolymer of 10% of dry soil by weight. Alkaline activator is fixed at 10% of optimum moisture content (OMC) of soil. Two conditions were prepared; soil with fly-ash based geopolymer and with water. They were compacted at OMC state; then performed the direct shear test to determine non-curing strength (0 day) and curing strength (7 days). Soils with fly-ash based geopolymer tend to higher state of peak shear strength for curing sample about two times of soils with water. This suggests that fly-ash based geopolymer is enhancing the shear strength of soils by increasing cohesion and friction angle.

1. INTRODUCTION

The shear strength is a challenging aspect of soil engineering works as soil slope stability in dam construction and retaining structure in foundation. To be stable the soil slope, shear strength is essential to resist overburden pressure of soil strata. Cohesion and friction are main parameters for shear strength of soil (Hausmann, 1990).

The compaction of soils is an important parameter for building roads, foundations and all ground structures to improve mechanically. The amount of water will not be changed through soil compaction process and inter granular soil empty space reduced through removing the air, large pores will be changed to small one and water moved into soil. The purpose of compaction is to improve shear strength and bearing capacity of soil. Moreover, compaction caused for reduction of shrinkage potential, subsidence and permeability. Thus, shearing parameters of compressed soil are important such as foundation bearing capacity, soil lateral pressure and slopes stability. Moisture and compaction rates of shear strength parameters (cohesion and angle of internal friction) are obtained through some tests on soil specimens (Kalhor, 2012).

Many researchers have extensively being studied on various materials to improve soil strength by chemical modification. Geopolymer is one of popular chemicals to increase the strength of soil in ground improvement techniques as a green material with many advantages, such as low cost, high strength, durability of weathering and friendly environment. The production of ordinary Portland cement (OPC) is an energy-intensive process and emits a very large amount of greenhouse gas, carbon dioxide into the atmosphere and the production of one ton of OPC releases about one ton of CO_2 (Khedari, et al., 2005). In soil engineering works, it is simplified that the geopolymer becomes an alternative and sustainable material to OPC.

In this study, the soil strengths are mechanically and chemically enhanced through the compaction and geopolymer. The shear stresses of compacted soils are experimentally developed by using geopolymer based on non-curing and curing condition. This reveals changes of cohesion and friction angle that indicate how the shear strength can be improved by using geopolymer at the same moisture content rather than by using water only.

2. TEST MATERIALS

2.1 Raw Material

Three soil types are collected from Ban Nong Bong, Muang district and Dan Keen, Chok Chai district, Nakhon Ratchasima and Bang Khen water treatment sludge, Metropolitan Waterworks Authority of Thailand (MWA). Based on the Unified Soil Classification System (ASTM D2487), they can be classified as silty sand (SM), high

plasticity silt (MH) and high plasticity clay (CH) for soil, which are collecting from Ban Nong Bong, Dan Keen and Bang Khen, respectively. Index properties of soils used in this study are summarized in Table 1 and test procedure are followed ASTM standards as much as practical (ASTM D422, ASTM D854, ASTM D4318) .

Table 1. Index properties of three types of soils

Locations	SG	LL (%)	PL (%)	Soil Types
Ban Nong Bong, Muang district, Nakhon Ratchasima	2.68	2.71	0.6	Silty sand (SM)
Dan Keen, Chok Chai district, Nakhon Ratchasima	2.67	68.0	29.2	High plasticity clay (CH)
Bang Khen water treatment plant, Bangkok	2.56	55.0	23.0	High plasticity silt (MH)

2.2 Fly-ash Based Geopolymer

Fly-ash based geopolymer is a combination of fly-ash and liquid alkaline activator. In this study, fly-ash (FA) used is obtained from Mae Moh power plant in Northern Thailand.

Liquid alkaline activator (AL) is formulated by blending different proportions of commercial sodium silicate (Na_2SiO_3) solution and sodium hydroxide (NaOH). Sodium silicate is composed of 15.5 wt% Na_2O, 32.75 wt% SiO_2 and 51.75 wt% H_2O and sodium hydroxide (NaOH) is 12.5 molars in solution. Both of chemicals are ready at liquid state. The ratio of Na_2SiO_3/NaOH is one.

3. COMPACTION TEST

Soils samples are prepared in two conditions, such as soil with water and soil with fly-ash based geopolymer (Gp). For soil with water, the soil is normally mixed with water as procedures of conventional compaction test. For soil with geopolymer, the soil is blended with a mixture of liquid alkaline activator (Na_2SiO_3 and NaOH), fly ash and soil. In this study fly ash to soil ratio is fixed at 0.1 and AL to water ration is 0.1 as well. The Na_2SiO_3/NaOH ratio is 1.0. After blending soil with fly ash and liquid alkaline activator, then they are used as testing materials. The schematic mix design process is as shown in Figure 1.

The compaction test is performed to carry out optimum moisture contents (OMCs) and maximum dry densities (MDDs) of three types of soils. The mixtures are compacted in three-ring mold. The three-ring mold is consists of three-rings as lower, upper and middle ring. The diameter and height of the mold are 10.16 cm and 15.19 cm (Fig. 2). The soil samples are dynamically compacted with a release of steel hammers (10 lb) in 27 blows per each layer of six layers with same energy of ASTM modified protector test (ASTM D 1557). The three-ring test results are as shown in Table 2. The three rings results are similar to ASTM standard mold (Sonsakul, et al., 2013).

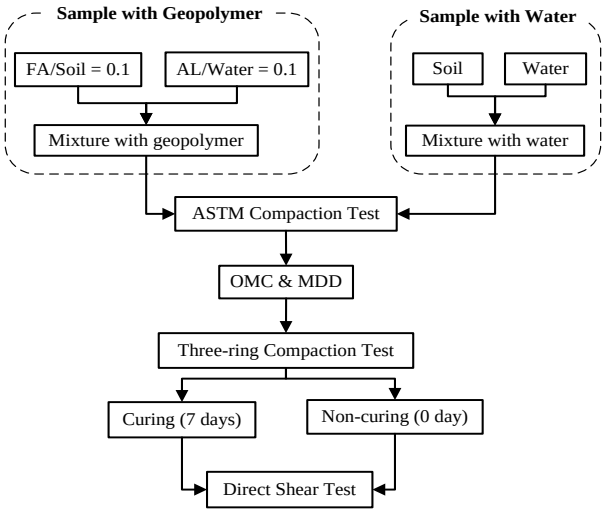

Fig. 1 Schematic mix-design process for soil specimens

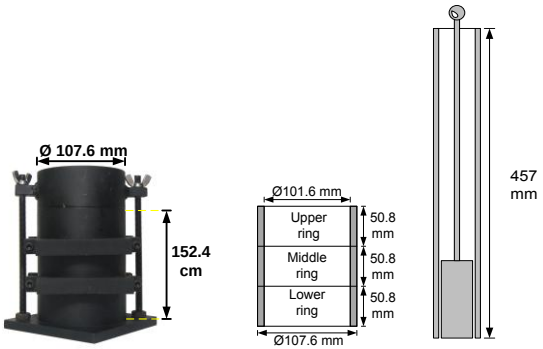

Fig. 2 Three-ring mold

Table 2. Compaction test results for three-types of soils

Soil Type	OMC (%)		MDD (kg/m^3)	
	Water	Gp	Water	Gp
SM	7.8	9.5	1940	1925
MH	26	32	1360	1250
CH	19	21	1634	1571

4. DIRECT SHEAR TEST

The three-ring shear testing device is used to measure the shear strength of compacted soils for actual field conditions. This testing device is developed and proposed by Sonsakul (2013). It serves as both compaction mold and shear box

without sample disturbance of ASTM standard mold. The three-ring mold can allow the maximum grain size of up to 10 mm. Soils with larger grain sizes demonstrate the higher shear strength than smaller grain sizes.

The soil samples after compacting in three-ring mold are performed the direct shear test based on curing period. Horizontal normal stress and lateral shear force are applied from 20-tons hydraulic hand pump to all compacted soil samples in shear device. Normal stresses are 0.4, 0.6, 0.8 and 1.0 MPa, and shear displacement rate is about 0.02 mm/s to be significant and distinct shear behaviors.

Shear strengths of soils are measured for non-curing (at 0 day) and curing (at 7 days) of compacted sample under ambient temperature. After the soil mixtures are compacted in three-ring mold, the compacted sample for non-curing (0 day) condition is directly installed in three-ring shear testing device as shown in Figure 3. For curing strength, the compacted sample is kept in air-tight plastic bag under ambient temperature to outcome shear strength development of soil on curing time for 7 days. When reached at seventh day, the sample is taken out of plastic bag to perform three-ring direct shear test.

The shear test data are plotted on a graph with relationship of shear stress and shear displacement. Under different four normal loads, the peak shear stress and residual shear stress are attained. The peak shear stresses are related with shear strength and normal stress. According to the soil behaviors, peak and residual shear strength vary with the curing period. Silty sand and high plasticity silt are same in behaviors. All of peak and residual strengths are display as the curing period increases the shear strength of compacted samples with geopolymer, expect of clay sample in cured residual shear strength (Figure 4). In addition, the shear strengths of each soil samples are arranged in Table 3. The test results show that the manners of peak and residual shear strength are depended on soil type.

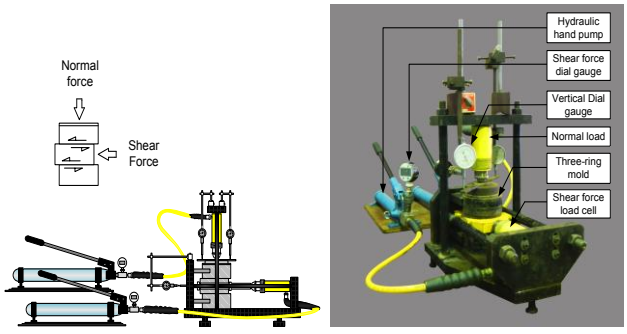

Fig. 3 Three-ring direct shear device and cross-sectional diagram

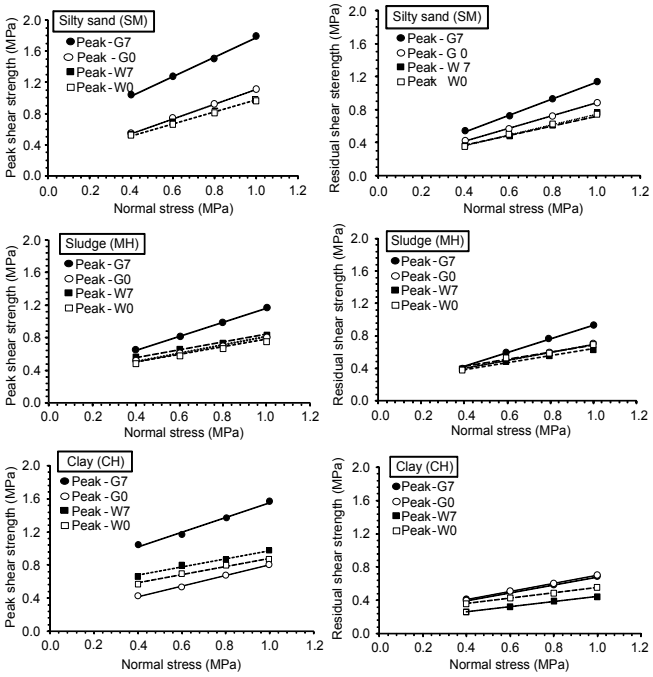

Fig. 4 Peak and residual shear strength for curing (7 day) and non-curing (0 days)

Table 3. Shear strength parameters of three types of soil on a function of curing and non-cuing time

Soil Type	Curing Time (days)	Tested Samples with	Peak		Residual	
			c_p (MPa)	ϕ_p (°)	c_r (MPa)	ϕ_r (°)
SM	0	Water	0.20	37.8	0.11	32.5
		GP	0.22	43.3	0.12	37.3
	7	Water	0.23	36.7	0.11	32.4
		GP	0.59	51.4	0.13	45.1
CH	0	Water	0.38	26.5	0.23	18.0
		GP	0.17	32.4	0.21	26.2
	7	Water	0.48	26.2	0.14	17.4
		GP	0.66	41.8	0.24	25.2
MH	0	Water	0.32	25.0	0.25	23.8
		GP	0.30	27.2	0.19	26.8
	7	Water	0.37	25.4	0.21	23.3
		GP	0.29	41.3	0.08	40.5

5. DISCUSSIONS AND CONCLUSIONS

Theory of soil mechanics generally indicates that moisture contents of a soil sample beyond OMC decrease the dry density of that soil under the same compaction energy. Both of silty sand (SM) and high plasticity silt (MH) agree with this concept, except of high plasticity clay (CH). OMC of silty sand and high plasticity silt

which mixed with fly-ash based geopolymer is slightly higher than those of sample mixed with tap water. When high plasticity clay is mixed with fly-ash based geopolymer, the dry densities are decreased but OMC is also decreased against the theory of soil mechanics concept.

For all soil types, the internal friction angle of peak and residual strength are merely different between curing periods when those samples are mixed with water. But when those samples are mixed with FA based geopolymer, the friction angles are started to increase since non-curing state. After curing for 7 days, the friction angle is almost double increased. All of cohesions in residual strength state are similarly increased with respect to internal friction angles of those soils. The cohesions of peak strength are not stable and flocculated.

The strain softening imply on three soils samples that silty sand and high plasticity silt sample behave as ductile behavior until curing of soil sample mixed with FA based geopolymer. After curing for 7 days, the strain softening with FA based geopolymer are found as brittle behavior. In high plasticity clay, the strain softening is occurred as already brittle condition before cured strain softening for 7 days and it proves higher brittle behavior after curing for 7 days.

This paper is concluded as the clay soil is normally low internal friction angle but the compacted condition with geopolymer makes a higher internal friction angle. Moreover, the compaction increases the shear strength of soil mechanically and the soils mixed with geopolymer transform to more brittle behavior in strain softening. Soils mixed with fly-ash based geopolymer tend to give a higher state of the peak shear strength through the curing time. Fly-ash based geopolymer enhances the shear strength of soils by increasing of cohesion and friction angle.

6. ACKNOWLEDGEMENT

The work was supported by Suranaree University of Technology, the Higher Education Promotion and National Research University of Thailand and Thai International Cooperation Agency (TICA). Permission to publish this paper is gratefully acknowledged.

7. REFERENCES

Hausmann, M.R., Engineering Principles of Ground Modification. McGraw-Hill, New York, 632 pp, 1990.

Khedari, J., Warsanasathapron, P. and Hirunlabh, J., Development of giber-based soil-cement block with low thermal conductivity. Cement & Concrete Composites, 7(1): 111-116, 2005.

ASTM D 422, Standard test method for particle-size analysis of soils, The American Society for Testing and Materials, Philadelphia, 2007.

ASTM D 854, Standard test methods for specific gravity of soil solids by water pycnometer. The American Society for Testing and Materials, West Conshohocken, United States, 2010.

ASTM D 4318, Standard Test Methods for Liquid Limit, Plastic Limit, and Plasticity index of Soils. The American Society for Testing and Materials, West Conshohocken, United States, 2010.

ASTM D 2487, Standard Practice for classification of soils for engineering purposes (Unified Soil Classification System), The American Society for Testing and Materials, Philadelphia, 2011.

ASTM D 1557, Standard test method for laboratory compaction characteristics of soil using modified effort, The American Society for Testing and Materials, Philadelphia, 2012.

Kalhor, A., The shear strength analyses of soil with various compactions under vertical load in direct shear test. Intl. Res. J. Appl. Basic. Sci., 3 (S): 2815-2821, 2012.

Sonsakul, P., Walsri, C. and Fuenkajorn, K., Performance assessment of three-ring compaction and direct shear mold. Proceeding of th fourth Thailand Symposium on Rock Mechanics, January 24-25, 2013, Im Poo Hill Resort, Thailand. Publish by Geomechanics Research Unit, Suranaree University of Technology, Nakhon Ratchasima, pp. 133-141, 2013.

EVALUATION OF OSTEOBLASTIC - CELL LINE MC3T3-E1 RESPONSE TO CARBONATE APATITES OBTAINED BY DIFFERENT HYDROTHERMAL TREATMENT TEMPERATURES

Nguyen Xuan Thanh Tram[1,2], Kanji Tsuru[1], and Kunio Ishikawa [1]
[1]Department of Biomaterials, Faculty of Dental Science, Kyushu University, Japan
[2]Department of Silicate Materials, Faculty of Materials Technology, Ho Chi Minh city University of Technology, Vietnam

ABSTRACT

This study investigated the osteoblastic – cell line MC3T3-E1 response to carbonate apatites obtained by hydrothermal treatment of calcite precursor in phosphate solution at 100°C and 200°C. Initial cell attachment after 7 hours of incubation was counted using hemocytomer and the rate of cell proliferation was estimated using Presto Blue Assay. The results showed that carbonate apatites hydrothermal treated at 100°C enhanced the cell attachment and proliferation when compared with carbonate apatites obtained at 200°C. As a conclusion, carbonate apatite materials obtained at low hydrothermal treatment temperature have high carbonate content and low crystallinity that is favorable for the biological responses of bone cells.

INTRODUCTION

Autograft are the gold standard for bone repair and substitution. However, the use of autografts has some serious drawbacks, such as donor site morbidity, limited donor bone supply, anatomical and structural problems. One of the main challenges of the biomaterials scientific community is developing an advanced synthetic material overcoming the disadvantages of autograft. Therefore, the fabrication and properties of carbonated apatite materials have received considerable attention due to their important role for clinical applications. Carbonated apatites (CO_3Ap) have composition similar to that of natural bone exhibiting good osteoconductive and osteogenic properties [1-2]. Previous studies [3-5] reported that the properties of CO_3Ap influenced by the treatment conditions, for example temperature and pH under which the fabrication process is carried out. This study was used to evaluate osteoblastic - cell line MC3T3-E1 response of carbonate apatites obtained via hydrothermal treatment of calcite precursor in phosphate solution at 100°C and 200°C based on dissolution-precipitation reaction. As a consequence of various hydrothermal treatment temperatures, the physicochemical and structural characteristics of two carbonate apatites are different and hence, resulting in distinctive cell response behaviors.

MATERIALS AND METHOD

Carbonate apatite blocks preparation

Calcium hydroxide $Ca(OH)_2$ powder (Wako Pure Chemical Industries Ltd., Osaka, Japan) was pressed unaxiallly with an oil press machine (Riken Power, Riken Seiki, Tokyo, Japan) at 40 MPa pressure to obtain a block-type specimens. The $Ca(OH)_2$ blocks were placed in a ceramic electric tubular furnace (ARF-30MC, Asahi Rika Seisakusho Co., Ltd., Chiba, Japan) and heated from room temperature to 700°C at a rate of 5°C/min and kept at 700°C for 12h in a controlled atmospheres of CO_2 (100ml/min) to carbonate the $Ca(OH)_2$ blocks. Obtained calcite blocks was placed in a closed vessel containing 1 M (mol/l) disodium hydrogen phosphate (Na_2HPO_4 Wako Pure Chemical Industries Ltd., Osaka, Japan) solution and heated at 100°C and 200°C in a drying oven (ON-300S, ETTAS, As One Corp., Osaka, Japan) for 14 days and 1 day, respectively. Subsequently, specimens were taken out from Na_2HPO_4 solution, rinsed with distilled water and dried in oven at 60°C for 12 hours. The obtained CO_3Ap materials were characterized by X-ray diffraction (XRD), Fourier transform infrared spectroscopy (FTIR) and CHN analysis.

Cell culture

Osteoblastic - cell line MC3T3-E1(Riken Bioresource Centre, Tsukuba, Japan) were cultured in alpha minimum essential medium (α-MEM, GIBCO/Invitrogen, Grand

Island, NY, USA) supplemented with 10% fetal bovine serum and 1% antibiotics in an humidified atmosphere containing 5% CO_2 at 37°C. Specimens were placed in a 48 well plate and pre-incubated with the culture medium for 24 hours. After pre-incubation, the culture medium was removed and the cells were seeded onto surface of block specimens. For initial cell attachment, cells were cultured at a density of 1.5×10^4 cells/well for 7 h. After washing by phosphate buffering solution (PBS) and trypsinization, attached cells were counted on a hematocytometer (Burker-Turk counting chamber, ERMA Inc., Tokyo, Japan). For cell proliferation test, cells were seeded at a density of 0.5×10^4 cells/well and analyzed after 4, 8 and 12 days using Presto Blue Assay (Biosource International, Camarillo, CA). At each time point, the medium was replace by 0.5 ml culture medium with 10% Prestoblue reagent and the cells were further incubated for 1h. After incubation, 100 μl of the solution from each well was transferred to the 96-well-plate in triplicate and read at 560/590 nm for fluorescence.

RESULTS AND DISCUSSION

XRD analysis of specimens after hydrothermal treatment at 100°C and 200°C indicated that all main peaks correspond to apatite phase. Duration for complete phase transformation from calcite precursor to apatite phase was up to 14 days and peak broadening observed when hydrothermal treatment was conducted at lower temperature. The broadening peaks and the overlapping of peak (211) and peak (112) are mainly due to the low crystallinity of apatite phase obtained at low temperature [2]. Table 1 summary the carbonate content of carbonate apatites measured by CHN analysis. As shown in table 1, increasing temperature can cause the reduction in carbonate content.

Table 1 Percentage of carbonate content of CO_3Ap obtained at 100°C and 200°C.

	Weight percentage of carbonate content (wt %)
HT100°C	10.25± 0.65
HT200°C	4.13± 1.50

All the FTIR spectra show the bands of apatite at about 1090–1050 cm^{-1} (ν_3 PO_4^{3-}), 960 cm^{-1} (ν_1 PO_4^{3-}) and 601-560 cm^{-1} (ν_4 PO_4^{3-}) together with those at 1460–1410 cm^{-1} (ν_3 CO_3^{2-}) and 873 cm^{-1} (ν_2 CO_3^{2-}), characteristic of B-type CO_3Ap. The absence of the band at 712 cm^{-1} indicates that the $CaCO_3$ precursor had reacted completely. The spectrum of CO_3Ap obtained at 200°C display the typical band of high crystallinity apatite at 630 cm^{-1} (νOH^{-1}) but that band is absent in the spectrum of CO_3Ap obtained at 100°C. In addition, when hydrothermal treatment at 100°C, it can be found the PO_4^{3-} band becomes broadening and decreases in intensity. The observed broadening of PO_4^{3-} band and the absence of OH^{-1} implied that low crystallinity CO_3Ap could be obtained at 100°C [8-10]. Moreover, FTIR result is in agreement with CHN analysis, the spectrum of CO_3Ap with higher carbonate content show the stronger intensity of CO_3Ap bands. Thus, from XRD, CHN and FTIR results, it can be assumed that CO_3Ap had the low crystallinity and high carbonate content when hydrothermally treated at low temperature. As soaking in phosphate solution at 100°C, it took 14 days for complete phase transformation from calcite to carbonate apatite whereas it took only 1 day to convert from calcite to carbonate apatite as soaking in phosphate solution at 200°C. Different heat treatment temperatures lead to the difference in carbonate content of CO_3Ap materials and probably affect the biological performance of them.

The percentages of cell attachment to the test materials showed in table 2. Initial cell attachment was significantly better in CO_3Ap hydrothermal treated at 100°C than CO_3Ap prepared at 200°C. Cell attachment on biomaterial is the first step in cell-material interactions. Depending on the degree of cell attachment, the capacity to proliferate and differentiate may be determined.

Table 2 MC3T3-E1 cell attachment results after 7h of incubation

	Attached cell (%)
HT100°C	45.55± 16.15
HT200°C	17.77± 6.57

Figure 1 shows the cell proliferation results after 4, 8 and 12 days of incubation. The results show that proliferation rate increases as the incubation time increases. There was a significant difference in proliferation rate between the two-carbonate apatites. Cells have greater viability on CO_3Ap obtained at 100°C than the one obtained at 200°C implying that CO_3Ap prepared at low temperature has favorable biological properties.

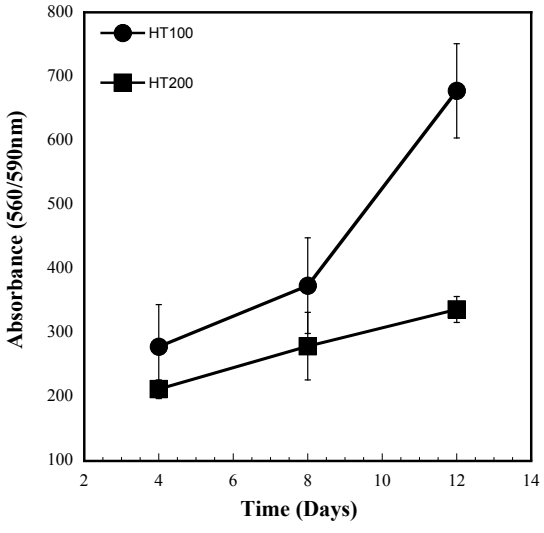

Figure 1. MC3T3-E1 cell proliferation results after 4, 8 and 8 days of incubation.

The superior osteogenic properties of carbonated apatites formed at low temperature can be explained by the microstructure and composition. It is demonstrated that surface chemistry and topography of lower crystallinity is

favorable for cell activities [6-7]. A decrease in crystallinity resulted in an increased calcium release. Therefore, low crystallinity materials show greater surface change than crystalline materials and display a dynamic zone in which dissolution and precipitation occurs. Consequently, a new layer of carbonate precipitated and that carbonate apatite stimulated the growth and adhesion of cells. This is supported by the fact that osteoblasts were observed to specifically adhere to particle boundaries which contain greater surface reactivity to influence initial protein interactions that control subsequent cell adhesion. The hydrophilic and hydrophobic characteristics of a material are also of great importance for cell adhesion. Apatites with high carbonate contents allow for an optimal adsorption of proteins improving cell adhesion. Cell adhesion is generally better on hydrophilic surfaces. A surface to which cells can more readily attach would promote cell adhesion and proliferation and lead to effective integration of implants.

Conclusion

The results demonstrate that CO_3Ap materials prepared by hydrothermal treatment of calcite precursor in phosphate solution at 100°C and 200°C supported osteoblastic – cell line MC3T3-E1 growth and attachment. Differences in cell response to the two-carbonate apatites could be attributed to the differences in crystallinity and carbonate content. CO_3Ap prepared at lower temperatures and containing high carbonate contents have been shown to have lower crystallinity and exhibit higher initial attachment and proliferation. In summary, it can be concluded that CO_3Ap materials fabrication by hydrothermal treatment at 100°C have great potential for use in bone substitutes as they exhibit good *in vitro* performance with no cytotoxicity.

Acknowledgement

The authors thank to ASEAN University Network/Southeast Asia Engineering education Development Network (AUN/SEED-Net) through the Japan International Cooperation Agency (JICA) for financial supports.

Reference

1. Landi E., Celotti G., Logroscino G., Tampieri A. Carbonated hydroxyapatite as bone substitute. J. Eur. Ceram. Soc. 2003; 23 (15): 2931-2937.
2. Vallet-Regi M. and Gonzalez-Calbet J. M. Calcium phosphates as substitution of bone tissues. Prog Solid State Ch. 2004; 32 (1-2): 1-31.
3. LeGeros R.Z. Apatite crystallites: Effect of carbonate on morphology. Science. 1967; 155: 1409-1411
4. Baig A.A., Fox J.L., Hsu J., Wang Z., Otsuka M., Higuchi W.I., LeGeros R.Z. Effect of carbonate content and crystallinity on the metastable equilibrium solubility behavior of carbonated apatites. J. Colloid Interface Sci.1996; 179 (2): 608-617.
5. Baig A.A., Fox J.L., Young R.A., Wang Z., Hsu J., Higuchi W.I., Chhettry A., Otsuka M. Relationships among carbonated apatite solubility, crystallite size, and microstrain parameters. Calcified Tissue Int. 1999; 64 (5): 437-449.
6. Porter A., Patel N., Brooks R., Best S., Rushton N., Bonfield W. Effect of carbonate substitution on the ultrastructural characteristics of hydroxyapatite implants. J. Mater. Sci.-Mater. Med. 2005; 16 (10): 899-907.
7. Suzuki T., Hukkanen M., Ohashi R., Yokogawa Y., Nishizawa K., Nagata F., Buttery L., Polak J. Growth and adhesion of osteoblast-like cells derived from neonatal rat calvaria on calcium phosphate ceramics. J. Biosci. Bioeng. 2000; 89 (1): 18-26.
8. Jokanovic V., Izvonar D., Dramicanin M.D., Jokanovic B., Zivojinovic V., Markovic D., Dacic B., Hydrothermal synthesis and nanostructure of carbonated calcium hydroxyapatite, J. Mater. Sci.-Mater. Med. 2006; 17 (6): 539-546.
9. Wang Y., Moo Y.X., Chen C., Gunawan P., Xu R. Fast precipitation of uniform CaCO3 nanospheres and their transformation to hollow hydroxyapatite nanospheres, J. Colloid Interface Sci. 2010; 352 (2): 393-400.
10. Slosarczyk A., Paszkiewicz Z., Paluszkiewicz C. FTIR and XRD evaluation of carbonated hydroxyapatite powders synthesized by wet methods. J Mol Struct. 2005; 744: 657-661.

Nguyen Xuan Thanh Tram received the Bachelor of Engineering (2008) in Silicate Materials Technology from Vietnam National University – Ho Chi Minh University of Technology, Master of Materials Engineering (2010) in Biomaterials – Bioceramics from University of Science Malaysia and Doctor of Philosophy (2014) in Dental Science from Kyushu University, Faculty of Dental Science, Department of Biomaterials.
She is a lecturer of Department of Silicate Materials, Faculty of Materials Technology, Ho Chi Minh City University of Technology, Vietnam. Current interests include Bioceramics - Bone substitute materials, Dental materials and Advanced materials.
Email: nxttram@hcmut.edu.vn

APPLICATION OF COBALT CATALYSTS IN THE OXIDATION OF 1-OCTENE BY HYDROGEN PEROXIDE IN STATIC AND STIRRING CONDITION

Mohamad Haqzim Ayob, Sheela Chandren, Mustaffa Shamsuddin and Hadi Nur
Department of Chemistry, Faculty of Science, Universiti Teknologi Malaysia
Centre for Sustainable Nanomaterials, Ibnu Sina Institute for Fundamental Scientific and Industrial Research, Universiti Teknologi Malaysia

ABSTRACT

Cobalt(II) salicylaldimine complex with different types of supporting material were prepared as catalyst for the oxidation of 1-octene. In order to obtain the optimum condition, the effect of stirring and static condition during experiment was conducted. The best result was obtained when the reaction was carried out in stirring condition. Results from the oxidation of 1-octene gave 1-2 epoxyoctane as the major product. As comparison with all of the catalyst prepared, the cobalt oxide supported on silica-covered magnetite showed the highest conversion of 1-octene.

1. INTRODUCTION

For industrial applications, cobalt has been widely used as diamond polisher, drying agent, pigments and catalysts (De Boeck, et al., 2003). The application of cobalt as catalyst may vary depends on its oxidation state; Co^{2+} or Co^{3+} (Wang, 2006). From previous studies, many researchers have reported the usage of cobalt as catalyst in oxidation of alkenes (Jinka et at., 2007 and Buranaprasertsuk, et al., 2007).

Oxidation of alkenes produces epoxides as the products. These epoxides are important in industrial reactions because they are widely used as precursors in synthesizing a variety of chemicals. Apart from that, epoxides also have a wide application in pharmaceutical industry as drug intermediates, in the preparation of epoxy resins, polymers and paint (Jinka, et al., 2007). In commercial manufacturing, epoxides are produce from chlorohydrin and Halcon process (Jinka, et al., 2007). The problem is both processes cause pollution to our environment. In order to produce epoxide with no harmful effect to the environment, single oxygen donor reagent can be used. One of the best oxygen donor reagents is hydrogen peroxide (H_2O_2). This material is low in cost and environmental-friendly (Jinka, et al., 2007)

In the present study, the oxidation of 1-octene by H_2O_2 using cobalt complex with different types of supporting material as catalyst is reported.

2. EXPERIMENTAL

2.1 MATERIALS

Iron(II) sulfate heptahydrate ($FeSO_4.7H_2O$, QRëC), Iron(III) chloride hexahydrate ($FeCl_3.6H_2O$, QRëC), tetraethyl orthosilicate (TEOS, 98%, Acros organic), cobalt(II) chloride hexahydrate ($CoCl_2.6H_2O$, DAE JUNG), salicylaldehyde (99%, ACROS organics), 3-aminopropyl-trimethoxysilane (3-APTMS, 97%, ALDRICH), 1-octene (97%, MERCK), hydrogen peroxide (H_2O_2, 30%, MERCK), ethanol (approx. 95%, QRëC), *n*-hexane (MERCK) and molecular sieve were used.

2.2 Synthesis of magnetite (Fe_3O_4)

Co-precipitation method was used for synthesis of magnetite (Majewski et al., 2007 and Teja et al., 2009). The detailed procedure has been reported in a previous paper (Ayob, et al., 2014).

2.3 Synthesis of silica covered magnetite (SiO_2@ Fe_3O_4)

The method used for synthesis of silica covered magnetite was Stöber method (Ibrahim et al., 2010). The detailed procedure has been reported in a previous publication (Ayob, et al., 2014).

2.4 Synthesis of cobalt(II) salicylaldimine complex/SiO_2@Fe_3O_4

This cobalt complex was prepared according to procedure reported by Ayob et al., (2014). 3–APTMS was functionalized on SiO_2@Fe_3O_4 and added dropwise into the cobalt(II) salicylaldehyde containing molecular sieve, while being sonicated in an ultrasonic bath for 30 min. The mixture solution was then left for aging process for few days at room temperature. The product was collected by removing the molecular sieve and washed with ethanol, followed by hexane. The product was dried at 50 – 60 °C for 1 h.

2.5 Synthesis of cobalt(II) salicylaldimine complex/SiO_2

Cobalt salicylaldehyde was prepared by mixing salicylaldehyde (0.006 mol) with cobalt(II) chloride hexahydrite (0.003 mol). In a round bottom flask containing molecular sieve and cobalt salicylaldehyde, 3–APTMS was added dropwise into it. This reaction was carried out in an ultrasonic bath and sonicated for 30 min and the molecular sieve was removed. The product was collected and washed using ethanol followed by hexane. The product was dried at 50 – 60 °C for 1 h in the oven.

2.6 Synthesis of cobalt(II) salicylaldimine complex/TEOS

Cobalt salicylaldehyde was prepared by mixing salicylaldehyde (0.006 mol) with cobalt(II) chloride hexahydrite (0.003 mol). In a round bottom flask containing molecular sieve with cobalt salicylaldehyde, 3-APTMS was added dropwise into it. This reaction was carried out in an ultrasonic bath and sonicated for 30 min. Molecular sieve was taken out. Then, tetraethyl orthosilicate was added into mixed solution. The mixed solution was stirred for 1–2 days. The product was collected and washed using ethanol followed by hexane. The product was dried at temperature of 50 – 60 °C for 1 h in the oven.

2.7 Synthesis of cobalt oxide/SiO_2@Fe_3O_4

Cobalt oxide/SiO_2@Fe_3O_4 was obtained by calcining cobalt(II) saliclyaldimine complex/SiO_2@Fe_3O_4 at 550 °C for 10 h.

2.8 Characterization of the catalysts

Nicolet iS10 Thermo Scientific Fourier Transform Infrared Spectroscopy (FTIR) (Omnic) was used to detect the functional groups in the cobalt catalysts. The samples were prepared by KBr pellet technique. The weight ratio between the sample and KBr used was 1:100. The samples were scanned in the wavelength range of 4000 – 400 cm^{-1} with 32 numbers of scans. The decomposition of the catalyst was analyzed by using thermogravimetric analysis (TGA/SDTA 851 Mettler Toledo). The weight of sample used was ~5 mg with the temperature of 25 – 700 °C. The diffuse reflectance ultra violet visible spectra (DRUV-vis) of the catalysts were obtained in the range of 200 – 800 nm by using a Perkin Elmer Lambda 35.

2.9 Catalytic testing

50 mg of catalyst was weighed and placed in a small sample bottle, followed by the addition of 1–octene and H_2O_2. The experiment was carried out in both stirring and static conditions. For the static condition, the reaction mixture was left at room temperature for 24 h. Meanwhile, for stirring condition, the reaction mixture was stirred at room temperature for 24 h. The identification of the products was done by using a gas chromatography (GC) (Shimadzu GC-2014) equipped with a flame ionization detector (FID) and non-polar capillary column (BPX5). About 0.1µl of the diluted samples (0.1 ml of sample in 0.9 ml of ACN) were injected into GC using a 1 µl syringe. The GC calibration was done with standard solution prepared individually and ACN as the solvent.

3. RESULTS AND DISCUSSION

3.1 Functional groups

Figure 1 shows the FTIR spectra for complex/SiO_2, complex/TEOS, and complex/SiO_2@Fe_3O_4. From all of the spectra, it is clear that the vibration bands at 1000 – 1200 cm^{-1} belong to the Si–O–Si group. As shown in Fig 1 (a), (b) and (c), the spectra of these catalysts are almost similar. At 2800 – 2900 cm^{-1}, C–H alkane (stretching) can be observed. The peaks around 1600 and 1450 cm^{-1} are contributed by the N–H bending vibration and –CH_2 (bend) of alkane, respectively (Kooti and Afshari, 2012).

In addition, the sharp band at 1650 cm^{-1} is assigned to the –C–N stretching vibration of the imine group of the ligand. This band was shifted to higher region due to the coordination of imine moiety through nitrogen atom to cobalt metal (Kooti and Afshari, 2012).

Figure 1 (d) shows the FTIR spectrum of cobalt oxide/SiO_2@Fe_3O_4. After calcination, all of the hydrocarbons have been decomposed. Therefore, no peak for hydrocarbon compounds can be observed at this spectrum. A few peaks can be observed corresponding to the Si–O–Si bond, Co–O and Fe–O at wavenumber 1000–1200, 600 – 650 and 500 – 550 cm^{-1}, respectively (Mekhemer, et al., 1999, Tang et al., 2008 and Tsoncheva et al., 2012).

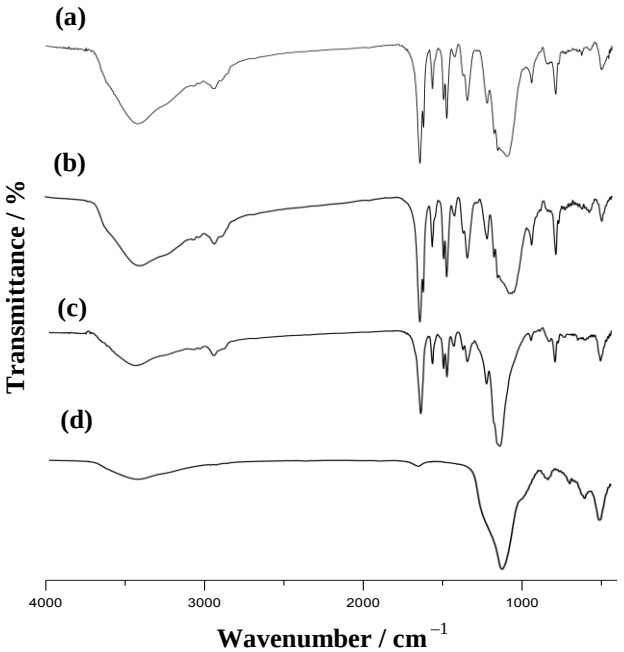

Figure 1 FTIR spectra of (a) cobalt complex/SiO_2, (b) cobalt complex/TEOS, (c) cobalt complex/SiO_2@Fe_3O_4 and (d) cobalt oxide/SiO_2@Fe_3O_4

3.2 Decomposition of organic compounds

TGA was used to measure the changes in weight according to the changes in temperature. The measured weight loss gives information on the changes in sample composition and thermal stability. For complex/SiO_2@Fe_3O_4 and SiO_2@Fe_3O_4, the TGA curves obtained are shown in Figure 2. From the figure, SiO_2@Fe_3O_4 was stable as the temperature increased. Meanwhile, the mass of complex/ SiO_2@Fe_3O_4 decreased significantly as the temperature increased. This is due to the ligands (organic part) that were attached to the cobalt, which started to decomposed when the temperature went above 100 °C. This TGA analysis proofed that the complex was successfully attached to the silica@magnetite

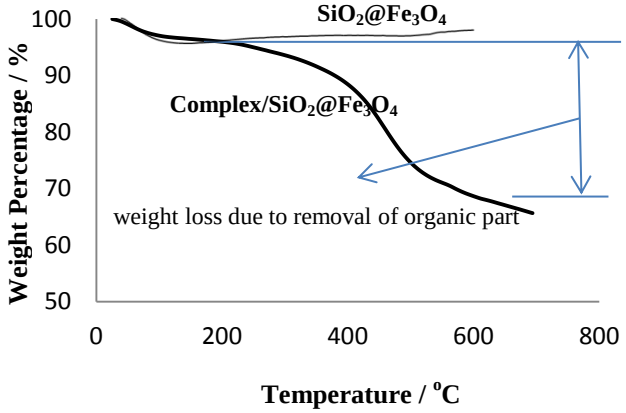

Figure 2 Thermogravimetry graph of complex/SiO_2@Fe_3O_4 and SiO_2@Fe_3O_4

3.3 Coordination of the catalysts

Figure 3 shows the DRUV-vis spectra of the (a) cobalt complex/TEOS, (b) cobalt complex/SiO_2 and (c) cobalt complex/SiO_2@Fe_3O_4. The peak for salicylaldimine ligand at 200 – 250 nm shows the $\pi - \pi^*$ transition of aromatic ring and imine (C=N) group for spectra (a), (b) and (c). Ligand-metal charge transfer (LMCT) band of the compound can be observed at around 400 – 410 nm.

In spectrum (d), the three absorption band at ~410, 430 and 500 nm can be observed and are attributed to the Co^{2+} in the compound. In addition, an absorption band around 650 – 700 nm is observed and it may be attributed to d–d transitions in low spin of octahedral coordinated Co^{3+}. Therefore, it can be concluded the cobalt oxide consist of Co^{2+} and Co^{3+} ions mixture (Rudolf et al., 2014)

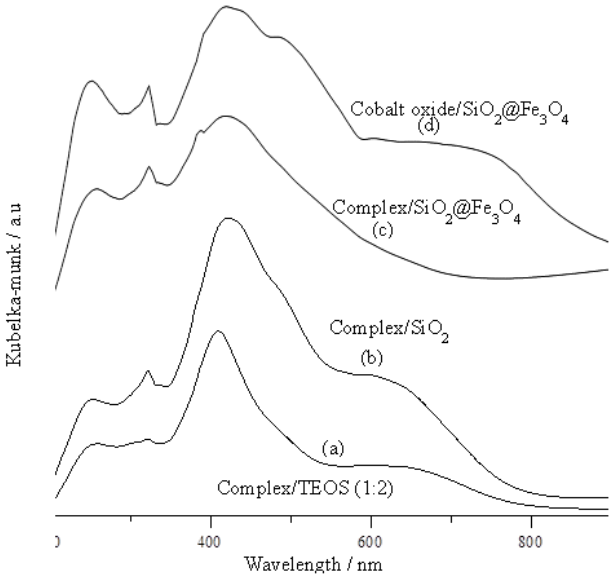

Figure 3 DRUV-vis spectra of (a) cobalt complex/TEOS, (b) cobalt complex/SiO_2, (c) cobalt complex/SiO_2@Fe_3O_4 and (d) cobalt oxide/SiO_2@Fe_3O_4

3.4 Catalytic testing

Figure 4 show catalytic activity results of the cobalt catalysts in the oxidation of 1-octene by H_2O_2 under stirring and static conditions. From the bar chart, cobalt oxide/SiO_2@Fe_3O_4 (d) shows the highest conversion of 1–octene in the stirring condition. From the results, it can be conclude d that static condition is not ideal for the oxidation reaction to occur. This is due to the lack of interaction between the catalyst, reactants and molecular oxygen.

Under stirring condition, much better results can be seen. This is most probably due to the well-mixed and homogeneous reaction mixture. This in turn increased the interaction between the catalyst and reactants, resulting in better catalytic activity.

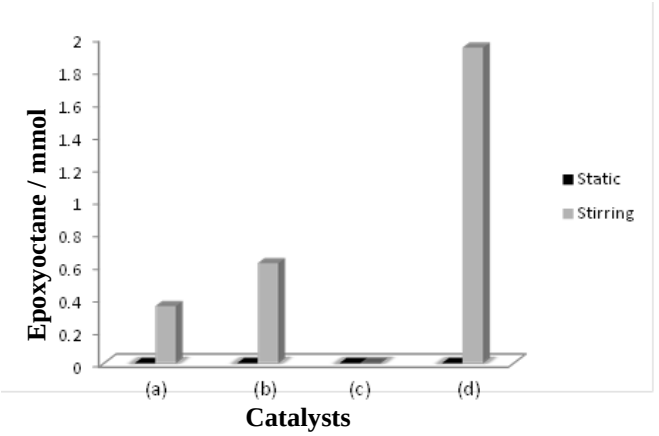

Figure 4 catalytic activity of (a) cobalt complex/ SiO_2, (b) cobalt complex/TEOS, (c) cobalt complex/SiO_2@Fe_3O_4 and (d) cobalt oxide/SiO_2@Fe_3O_4

4. Conclusion

Cobalt complex/ SiO_2, cobalt complex/TEOS, cobalt complex/SiO_2@Fe_3O_4 and cobalt oxide/SiO_2@Fe_3O_4 have been successfully synthesized and characterized. By carrying out reactions in both static and stirring conditions, it was proven that stirring condition gave better results in the oxidation of 1–octene to produce epoxyoctane as the product. In addition, cobalt oxide/SiO_2@Fe_3O_4 shows very high catalytic activity for this reaction under stirring condition.

5. References

De Boeck M., Kirsch-Volders, M. & Lison, D. (2003) Cobalt and Antimony: Genotoxicity and Carcinogenicity, Mutation Research/Fundamental and Molecular Mechanisms of Mutagenesis, 533(1–2), 135-152.

Wang S. (2006) Cobalt—Its Recovery, Recycling, and Application. JOM Journal of the Minerals, Metals and Materials Society, 58(10), 47-50.

Jinka K. M., Sebastian, J. & Jasra, R. V. (2007). Epoxidation of Cycloalkenes with Cobalt(II)-Exchanged Zeolite X Catalysts Using Molecular Oxygen, Journal of Molecular Catalysis A: Chemical, 274(1-2), 33-41.

Buranaprasertsuk P., Tangsakol, Y. & Chavasiri, W. (2007). Epoxidation of Alkenes Catalyzed by Cobalt(II) Calix[4]Pyrrole, Catalysis Communications, 8(3), 310-314.

Ayob M. H., Effendi, J., Chandren, S., Nur, H. (2014). Synthesis and Characterization of Cobalt(II) Salicylaldimine Complex Supported on Silica Covered Magnetite, Jurnal Teknologi, 69:5, 21–23.

Kooti M. and Afshari M. (2012). Molybdenum Schiff Base Complex Covantly Anchored to Silica–Coated Cobalt Ferrite Nanoparticles as a Novel Heterogeneous Catalyst for the Oxidation of Alkenes. Catal Lett, 142, 319-325.

Mekhemer G. A. H., Abd-Allah H. M. M. and Mansour S. A. A. (1999). Surface Characterization of Silica-Supported Cobalt Oxide Catalysts, Colloids and Surfaces A: Physicochemical and Engineering Aspect, 160, 251-259.

Tang C. W., Wang C. B. and Chien S. H. (2008). Characterization of Cobalt Oxides Studied by FT-IR, Raman, TPR and TG-MS. Thermochimica Acta, 473, 68-73.

Tsoncheva T., Gallo A., Scotti N., Dimitrov M., Delaigle R., Gaigneaux E. M., Kovacheva D., Santo V. D. and Ravasio N. (2012). Optimization of the Preparation Procedure of Cobalt Modified Silicas as Catalysts in Methanol Decomposition. Applied Catalysis A: General, 417-418, 209-219.

.

Rudolf C., Dragoi B., Ungureanu A., Chirieac A., Royer S., Nastroc A. and Dumitriua E. (2014). NiAl and CoAl materials derived from takovite-like LDHs and related structures as efficient chemoselective hydrogenation catalysts. Catal. Sci. Technol., 179.

Ibrahim I.A.M., Zikry A.A.F., Sharaf M.A. (2010). Preparation of Spherical Silica Nanoparticles: Stober Silica. Journal of American Science, 6(11).

Majewski P. and Thierry B. (2007). Functionalized Magnetite Nanoparticles-Synthesis, Properties and Bio-applications. Solid State and Material Sciences, 32:203, 215.

Teja A. S. and Koh P. Y. (2009). Synthesis, Properties and Applications of Magnetic Iron Oxide Nanoparticles. Progress in Crystal Growth and Characterization of Materials, 55, 22-45.

Mohamad Haqzim Ayob received his Bachelor's degree (2012) in Chemistry from Universiti Teknologi Malaysia. He is currently a PhD student at the Department of Chemistry, Faculty Science, Universiti Teknologi Malaysia. His current interest is catalysis.

Sheela Chandren received her Bachelor's degree in Industrial Chemistry (2006) and Master's degree in Chemistry (2009) from Universiti Teknologi Malaysia. She then obtained her PhD. in Materials Science and Engineering (2012) from Hokkaido University, Japan. At present, she is a Postdoctoral Fellow in Ibnu Sina Institute for Fundamental Science Studies, Universiti Teknologi Malaysia. Her current research interests include photocatalysis, catalysis, selective organic synthesis, materials science and nanotechnology.

Mustaffa Shamsuddin received his Bachelor's degree (1983), MSc. (1986) from University of East Anglia and his PhD. (1994) from University of Leeds, England. He is a Professor at the Department of Chemistry, Faculty Science, Universiti Teknologi Malaysia. His current interest includes synthetic and structural inorganic chemistry

Hadi Nur received his B.Sc (1992) and M.Eng. (1995) in Chemistry and Mechanical Eng. from Institut Teknologi Bandung, Indonesia. He then received his PhD (1998) from Universiti Teknologi Malaysia. He is a Professor at the Department of Chemistry, Faculty Science, Universiti Teknologi Malaysia. His current interest includes zeolite chemistry and catalysis, photocatalysis, semiconductor nanoparticle polymer composite, bifunctional oxidative and acidic catalysts and phase-boundary catalysis.

OS Number 06012

RECYCLING OF MELAMINE FORMALDEHYDE WASTE IN LIGHTWEIGHT CONCRETE AS AGGREGATE REPLACEMENT

Chalermchai Chaitongrat*[,1], and Somsak Siwadamrongpong[2]
[1)] School of Mechanical Engineering, [2)] School of Manufacturing Engineering
Suranaree University of Technology, Thailand

ABSTRACT

This paper presented the study results of the utilization of melamine formaldehyde (MF) waste in the production of lightweight concrete. This MF waste was used for partially replacing river sand. Investigation was carried out on two different forms of MF waste for mortar samples, one made with MF waste granules and, second made with MF waste powder, in which river sand was partially replaced by MF wastes in percentages of 0%, 15%, 25% and 35% by volume, constant water-to-cement ratio of 0.50 and unit weight of 1,000 kg/m^3. From the studies, it was found that the lightweight concrete contained MF waste was slightly variance density, the compressive strength and water absorption were increased and the thermal conductivity was not significantly different. The results gathered would form a part of useful information for recycling MF waste in lightweight concrete mixes.

Keyword: Recycling, Melamine formaldehyde waste, Fine aggregate, Lightweight concrete, Replacement.

1. INTRODUCTION

Plastic, one of the most significant innovations of 20th century, is ubiquitous material. A substantial growth in the consumption of plastic is observed all over the world in recent years, which also increases the production of plastic-related waste. The plastic is now a serious environmental threat to modern civilization. Plastic is composed of several toxic chemicals, and therefore plastic pollutes soil, air and water.

Plastics can be divided into two types. The first type is thermoplastic, which can be melted for recycling in the plastic industry. The second type is thermosetting plastic. This plastic cannot be melted by heating because the molecular chains are bounded firmly with meshed crosslinks. At present, these plastic wastes are disposed by either burning or burying. However, these processes are costly. If the thermosetting plastic wastes can be reused, the pollution that is caused by the burning process as well as the cost of these waste management process can be reduced.

Land-filling of plastic is also dangerous due to its slow degradation rate (more than a hundred years) and bulky nature. The waste mass may hinder the ground water flow and can also block the movement of roots. Plastic wastes also contains various toxic elements especially cadmium and lead, which can mix with rain water and pollute soil and water.

Recycling plastics is a possible alternative. As aggregate is application into construction materials has been conducted, particularly for the concrete wall in buildings (Rebeiz, 1996; Soroushian, 1999; Choi et al., 2005; Batayneh et al., 2007). In Thailand, lightweight concrete is extensively used for the construction of interior and exterior walls of building for the case where the walls are not designed for lateral loads. This is due to the special characteristics of lightweight concrete. Lightweight concrete can be produced by introducing: (i) gassing agents such as aluminum powder or foaming agents, (ii) lightweight mineral aggregate such as perlite, pumice, expanded shale, slate, and clay, or (iii) plastic granules as aggregate, e.g., expanded polystyrene foam (EPS), polyurethane or other polymer materials. Recycling of plastic waste to produce new materials, such as cement composites, appears as one of the best solution for disposing of plastic waste, due to its economic and ecological advantages and recycling MF wastes to river sand for concrete production can be one of the environmentally friendly methods.

Therefore in this study, melamine formaldehyde wastes have been recycled for use as fine aggregate for partially replacing river sand in lightweight concrete. This study has investigated the properties of concrete using MF waste, conducting tests which analyze density and mechanical properties to achieve this purpose; a study of these MF wastes for application into construction materials has been conducted, particularly for the concrete wall in buildings.

2. EXPERIMENT

2.1 Materials

2.1.1 Cement

The cement used in this study is Portland cement type I as per ASTM C150-12. Its density is 412 kg/m^3. The chemical composition of cement is given in Table 1.

Table 1 Chemical composition of cement

Components	Mass%
Calcium oxide (CaO)	66.33
Silica (SiO_2)	18.60
Ferric oxide (Fe_2O_3)	4.03
Alumina (Al_2O_3)	3.77
Sulphuric anhydride (SO_3)	2.67
Magnesium oxide (MgO)	2.13
Sodium oxide (Na_2O)	1.39
Potassium oxide (K_2O)	0.46
Loss on ignition	-

2.1.2 Sand

River sand was used as the fine aggregate in the concrete mixes with 1.97 fineness modules (FM) 2.52 specific gravity and 0.33% water absorption are given in Table 2. Its particle size distribution, obtained fine aggregate according to ASTM C33-13, is provided on Fig. 1.

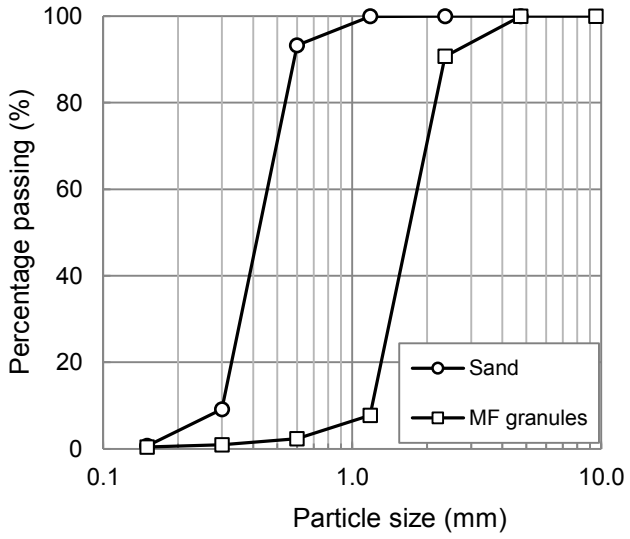

Fig. 1 Gradation of sand and MF granules.

2.1.3 MF wastes

Melamine formaldehyde wastes come from the flash on melamine products in activities industry. They were provided by a manufacturer of Srithai super ware public company limited, in two different forms of MF wastes: a form containing “scrap” waste was produced by shaving flash of melamine products and a form containing “powder” waste was produced by flatting edge of melamine products (Fig. 2a and 3). And both two forms are studied here. Only the first form (“scrap” waste) was granulated by grinding machine to small granules (Fig 2b). The MF waste granules was separated under sieve no. 8 with 3.98 fineness modules (see Fig. 1) 1.50 specific gravity and 5.51% water absorption (see Table 2). On the other hand the MF waste powder was separated under sieve no. 140 to removal of grime particles. Its mean and standard deviation of particle size are 34 and 29 micrometer (see Fig. 4), respectively. These MF wastes were used to replace a fraction of river sand in the concrete mixtures (by volume).

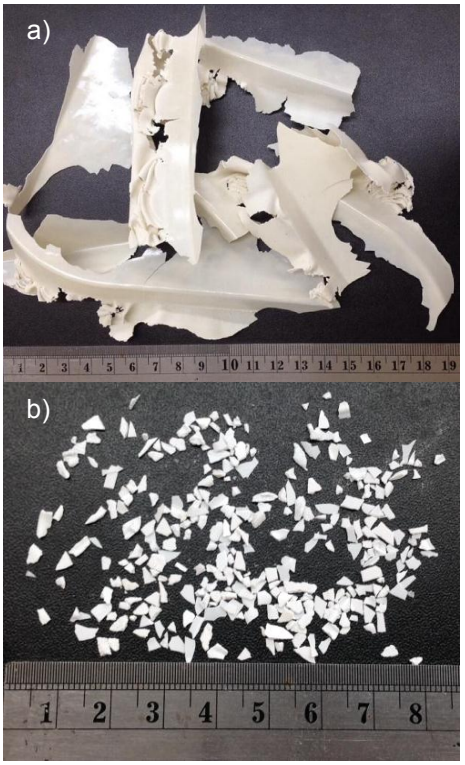

Fig. 2 Recycled MF waste (a: before ; b: after crushing).

Fig. 3 MF wastes powder.

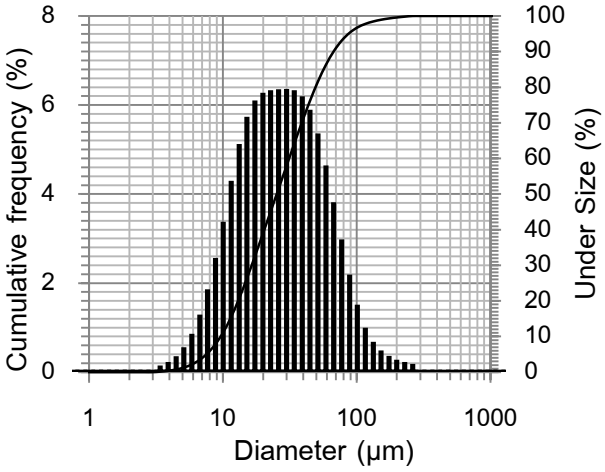

Fig. 4 Particle size of MF waste powders.

Table 2 Physical and mechanical properties of lightweight aggregate (LWA) and MF wastes

Aggregate	Shape	FM/particle size*	Specific gravity	Water absorption
Sand	Round and smooth	1.97	2.52	0.33
MF waste granules	Flaky and rough	3.98	1.50	5.51
MF waste powders	powder	*34 micron	1.50	-

Table 3 Methods of testing properties

Properties	Detail of test	Specification
Wet density	The wet density of concrete was determined by measuring the mass and volume of fresh concrete	ASTM C138-14
Compressive strength	The 50 x 50 x 50 mm cubic specimens were used to determine the compressive strength of concrete at the concrete ages of 3, 7, 14, 28 and 60 days. A "ELE" compression machine with a loading capacity of 200 kN was used for the experiment	ASTM C109-13
Water absorption	The The 50 x 50 x 50 mm cubic specimens were used to determine the water absorption (W_a) by measuring $W_a = ((M_{sat.air} - M_d) / M_d)$ of concrete at the concrete ages of 28 and 60 days.	ASTM D6489-12
Thermal conductivity	The 65 x Θ69 mm cylinder specimens were used to determine the thermal conductivity of concrete at the concrete ages of 28 and 60 days.	ASTM E1225-13

2.1.3 Foaming agent

The foaming agent was diluted with water in ratio of 1:40 by weight, and then aerating to a density of 50 kg/m^3. Water and liquid chemical creates many small air bubbles in the cement paste. The sizes of air bubbles are in the range of 0.1-1.0 mm. these small air bubbles, which are entrained in the mass of concrete, cause an expansion of concrete mass. Thus the foaming agent was used to density controlled of concrete mixes. This type of lightweight concrete is then called cellular lightweight concrete (CLC).

2.2 Sample preparation

The concrete mixtures were prepared in the laboratory. The design characteristic compressive strength by Chandra and Berntsson (2003) at day 28 and 60 of control specimen (i.e., MF0) without MF wastes. The concrete mixtures were prepared with a cement content of 412 kg/m^3 and water-to-cement ration of 0.50. The proportion of river sand was designed at 412 kg/m^3. The MF wastes were used to replace 0%, 15%, 25% and 35% by volume of sand in the four mixes. The mix proportions of the concrete are shown in Table 4 and 5.

The wet density of the concrete mixtures was determined before casting the concrete in molds. For each concrete mixture, 20 numbers of 50 x 50 x 50 mm cube specimens were cast for the determination of the compressive strength, 2 numbers of 65 mm high x 69 mm diameter cylindrical specimens were cast for the determination of the thermal conductivity and two numbers of 50 x 50 x 50 mm cube specimens were prepared for measuring the water absorption. After 24 h. casting, all the specimens were then de-molded and immediately covered with plastic sheets before being air-cured in the laboratory at room temperature and dry curing until the ages of testing.

Table 4 Mix proportions of concrete mixtures

Mix code	MF0	MF15	MF25	MF35
Replacement (%)	0	15	25	35
Cement (kg/m^3)	412	412	412	412
Sand (kg/m^3)	412	350	309	267
MF (kg/m^3)	0	62	103	144
Water (kg/m^3)	206	206	206	206

Table 5 Code of concrete mixtures

Code	MF waste form
Mix I	MF waste granules
Mix II	MF waste powders

Table 6 Specification of non-load-bearing lightweight concrete (ASTM C129)

Type	Compressive strength (MPa)		Density (kg/m^3)
	Average of three units	Individual unit	
II	4.1	3.5	1680

2.3 Test methods

The test method and the associated specifications for determining the properties are reported in Table 3. Each of the tested values reported in Section 3 is the averaged results.

3. RESULTS and DISCUSSION

3.1 Density

The dry densities of the different concrete mixtures are reported in Fig. 5. The results show that the density of the control concrete (MF0) was changeless from wet density control (1000 kg/m^3). On the other hand values of dry density slightly variance from wet density for mixtures containing of MF wastes aggregate when compared with river sand. Due to the water absorption of MF wastes higher than sand result to the difficulty control dry density.

3.2 Compressive strength

The results of compressive strength of the concrete are presented in Table 7. It can be seen that at all test ages, the compressive strength were increased with the increase in MF wastes content and it was also found that the compressive strength of concrete contain MF waste powder showed the highest at 25% MF wastes content. The ratios of 28 and 60 days compressive strength values of the concrete mixes prepared with MF waste replacement to that of the control (MF0) are shown in Fig. 6.

This strength increasing can be explained by the following reasons:

(1) A combination of the two aggregate (sand and MF waste) has resulted in a better gradation which contributed to increased compressive strength.

(2) Angular particles with rough surface texture provide more surfaces and thus result in increased bond strength between the MF wastes and cement paste.

(3) The bond is characterized by the presence of a thin layer which bridges the aggregate with paste. This layer is formed as a result of a chemical reaction between the cement paste and aggregate.

3.3 Comparison between the test results and standards

Based on the above results, the optimum proportions of MF wastes powder is 25%. The results of compressive strength and dry density, which are 4.24 MPa and 1089 kg/m^3 respectively, are comparable to the specifications for non-load-bearing lightweight concrete according to ASTM C129-11 Type II standard, as shown in Table 6. It was found that the compressive strength and water absorption of MF wastes lightweight concrete is close to the class 2 of for non-load-bearing lightweight concrete (ASTM C129-11).

3.4 Water absorption

Water absorption values of different mixtures are given in Fig. 7. The experimental results reveal that the water absorption was increased with increase in MF wastes content. However, for higher content, water absorption seems to increase with MF waste content.

3.5 Thermal conductivity

The results of thermal conductivity of the concrete are presented in Fig.8. The experimental results reveal that at all replacing (in volume) of sand by MF wastes do not exert a significant influence on thermal conductivity of the concrete in comparison with the control concrete (MF0).

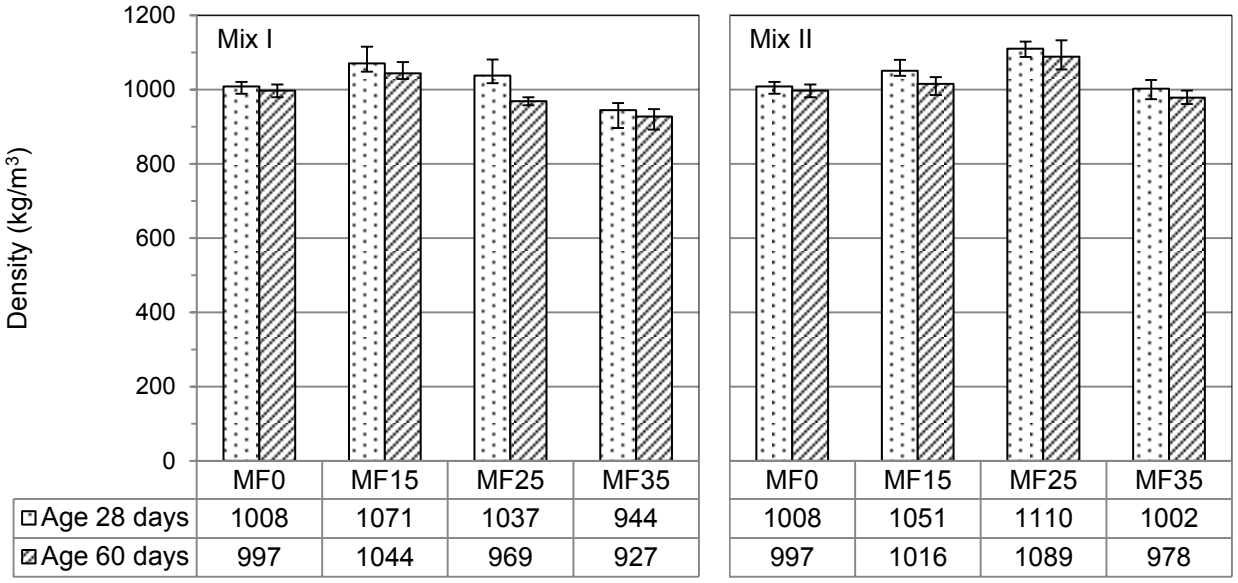

Fig. 5 Density of concrete mixtures.

Table 7 Compressive strength of concrete mixtures

Code	Mix code	Sand content (kg/m^3)	MF content (kg/m^3)	Compressive strength (MPa)				
				3 days	7 days	14 days	28 days	60 days
Mix I	MF0	412	0	0.95	1.15	1.21	1.21	1.49
	MF15	350	62	1.03	1.44	1.48	2.17	2.29
	MF25	309	103	1.11	1.79	2.00	2.09	2.41
	MF35	267	144	0.84	1.30	1.32	1.74	1.89
Mix II	MF0	412	0	0.95	1.15	1.21	1.21	1.49
	MF15	350	62	1.33	1.62	2.05	2.16	2.18
	MF25	309	103	2.35	2.69	2.71	3.71	4.24
	MF35	267	144	1.25	1.59	1.92	2.20	2.40

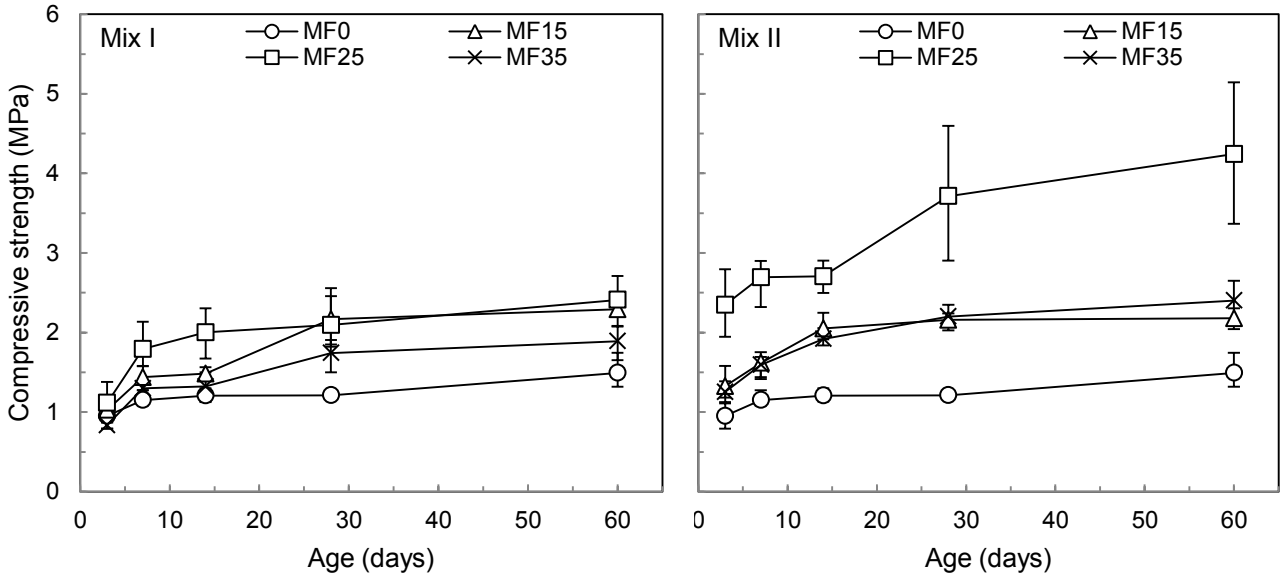

Fig. 6 Compressive strength of concrete mixtures.

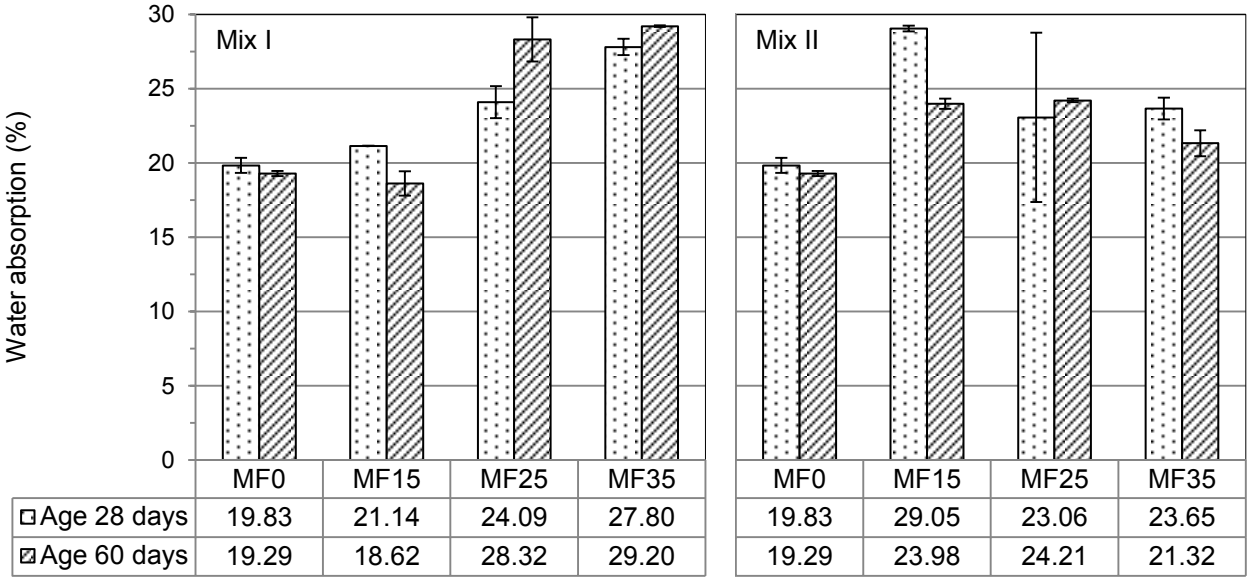

	MF0	MF15	MF25	MF35
Age 28 days	19.83	21.14	24.09	27.80
Age 60 days	19.29	18.62	28.32	29.20

	MF0	MF15	MF25	MF35
Age 28 days	19.83	29.05	23.06	23.65
Age 60 days	19.29	23.98	24.21	21.32

Fig. 7 Water absorption of concrete mixtures.

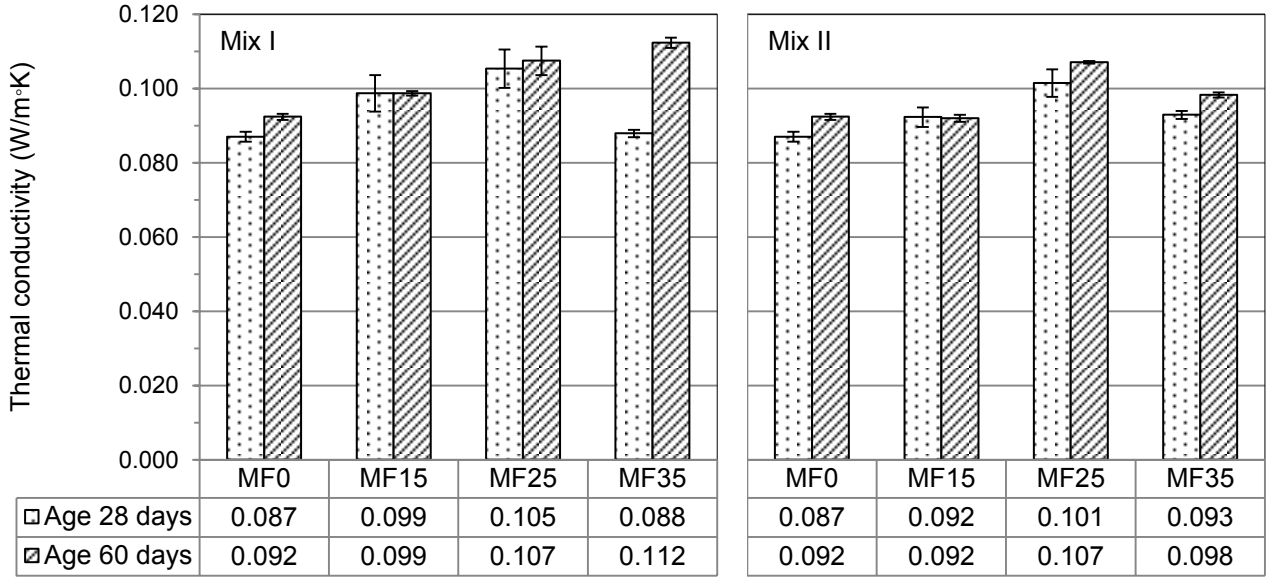

	MF0	MF15	MF25	MF35
Age 28 days	0.087	0.099	0.105	0.088
Age 60 days	0.092	0.099	0.107	0.112

	MF0	MF15	MF25	MF35
Age 28 days	0.087	0.092	0.101	0.093
Age 60 days	0.092	0.092	0.107	0.098

Fig. 8 Thermal conductivity of concrete mixtures.

4. CONCLUSION

This paper presented the results of a systematic study on the effect of incorporating MF wastes on the properties of lightweight concrete. The following conclusion can be drawn:

With an increase of replacement ration of river sand by MF wastes:

1. The dry density was slightly variance.
2. The compressive strength was increased.
3. The water absorption was increased.
4. The thermal conductivity was significantly not different.

The results of the study would form a part of useful information for recycling scrapped MF wastes in lightweight concrete mixes. The results show that the MF waste powder derived from flatting edge of melamine products has potential to be used as aggregates to replace sand for making non-load-bearing lightweight aggregate concrete. The optimal replacement percentage should be within 25% by volume.

REFERENCES

Batayneh, M., Iqbal, M., Ibrahim, A., 2007. Use of selected waste materials in concrete mixes. Waste Management 27 (12), 1870-1876.

Chandra,S., Berntsson, L., 2003. Lightweight aggregate concrete. Noyes Publication, Norwich, N.J.

Choi, Y.W., Moon, D.J., Chung, J.S., Cho, S.K., 2005. Effects of waste PET bottles aggregate on the properties of concrete. Cement and Concrete Research 35, 776-781.

Marzouk,O.Y., Dheilly, R.M., Queneudec, M., 2007. Valorization of post-consumer waste plastic in cementitious concrete composites. Waste Management 27, 310-318.

Phaiboon P., Mallika P., 2007. Reuse of thermosetting plastic waste for lightweight concrete. Waste Management 28, 1581-1588.

Rebeiz, K.S., 1996. Precast use of polymer concrete using unsaturated polyester resin based on recycled PET waste. Construction and Building Materials 10 (3), 215-220.

Soroushian, C., 1999. Experimental investigation of the optimized use of plastic flakes in normal-weight concrete. Magazine of Concrete Research (February), 27-33.

PERFORMANCE STUDY OF REDUCED GRAPHENE OXIDE SPEEK FOR DIRECT METHANOL APPLICATION

Farah Syuhada Abdul Halim, Sheela Chandren, Madzlan Aziz and Hadi Nur
Department of Chemistry, Faculty of Science, Universiti Teknologi Malaysia
Centre for Sustainable Nanomaterials, Ibnu Sina Institute for Scientific & Industrial Research, Universiti Teknologi Malaysia

ABSTRACT

The purpose of this research is to study the direct methanol fuel cell (DMFC) performance testing of modified membrane electrode assembly (MEA) of reduced graphene oxide sulfonated poly(ether ether ketone) (SPEEK/rGO). The reduction of oxide method was employed to synthesize reduced graphene oxide (rGO) and solution blending technique was applied to form SPEEK/rGO membrane. The structure of rGO and SPEEK were confirmed by Fourier transform infrared (FTIR) spectroscopy. The electrical properties of rGO measured show high conductivity at 1.36 x 10^4 S/m. The DMFC performance of the blended rGO with SPEEK was substantially enhanced by 8 – 15% of open circuit voltage (OCV) and power density compared to those of commercial nafion 112 membrane. Therefore, the fabrication of SPEEK/rGO membrane is proven to improve the DMFC performance.

Keyword: SPEEK/rGO membrane, MEA, DMFC, power density

1. INTRODUCTION

The usage of fuel cell has been growing rapidly in transportation, telecommunication, portable power and micro power (Jung, et al., 2007). This kind of system can boost energy multiplicity, environmental friendly through their higher fuel-to electricity conversion, and offer a transition to renewable energy sources (Seger, et al., 2009). Direct methanol fuel cell (DMFC) has a very simple design system and is capable of using unreformed methanol as the fuel (Perez, et al., 2009). DMFC system works at low temperature between 30 – 120 °C and has the tendency to produce high power density and high energy efficiency (Li, et al., 2010). The efficiency of the DMFC system can be affected by the concentration of methanol consumption. Normally, utilization of 1 to 2 (intermediate concentration) molar aqueous methanol solutions is used to prevent methanol crossover problem (Xin, et al., 2011).

In fuel cell system, utilization of materials with good chemical resistance and high conductivity is preferable. (Cao, et al., 2011). The existence of perfluorinated ionomers, like nafion membranes, in DMFC caused the complexity of high methanol permeability throughout electrolyte membranes, at which the fuel wastage has resulted in the loss of cathode performance and tendency for catalyst poisoning to occur, due to the absence of appropriate proton conducting membranes (Lin, et al., 2013). Some prevention are applied by decreasing electrocatalyst nanoparticles' size, reducing the electrocatalyst's loading at electrodes, improving the performance of carbonaceous catalyst support and development of MEA (Herman, et al., 2005). Focusing on the MEA's development, DMFC performance can be improved by introducing new non-fluorinated polymer, sulfonation process to polymers and integration of inorganic filler materials into polymer (Jung, et al., 2007, Ma, et al., 2003).

Therefore, the introduction of newly synthesized rGO into SPEEK membrane as an alternative in substituting perfluorinated membrane for DMFC has been carried out in this work. Previous works had investigated rGO-based materials' performance as polymer composites due to its excellent electrical, mechanical, and thermal properties (Lin, et al., 2013). rGO has better particle distribution than graphene oxide (GO) that can lead to low absorption of methanol in membrane and literature stated that carbonaceous material is important in maximizing the performance of fuel cell (Seger, et al., 2009).

2. EXPERIMENT

2.1 MATERIALS

Pure graphite powder (Thermo-Pure), concentrated sulphuric acid (H_2SO_4 98%, Qrec), potassium permanganate ($KMnO_4$, Qrec), hydrogen peroxide (H_2O_2 5%, Qrec), hydrochloric acid (HCl 35%, Qrec), sodium hydroxide pellets (NaOH, Merck), sodium borohydrite ($NaBH_4$, Qrec), poly(ether ether ketone) (PEEK, Vitrex Inc.), Nafion 122 (DuPont de Nemours Co.), methanol (CH_3OH 99.9%, Merck), N-methyl pyrolidine (NMP, Qrec), platinum on carbon paper nafion treated (Pt 40%, Fuel Cell Earth.ltc) and platinum ruthenium on carbon paper nafion treated (PtRu 40%, Fuel Cell Earth.ltc) were used as received.

2.2 PREPARATION OF SULFONATED POLY (ETHER ETHER KETONE) (SPEEK) POLYMER

Dried poly(ether ether ketone) (PEEK) powder was dissolved in concentrated H_2SO_4 at room temperature. After 1 h, the solution was stirred and heated at 55 – 60 °C for 3 h. Colour changes can be observed from colourless to light orange colour and finally to dark reddish brown. The sulfonated polymer solution was poured into ice water under continuous stirring and left for one night to remove any residual acid. The product was filtered and washed repeatedly with distilled water until a neutral pH value was achieved. Then, the polymer was dried at 60 °C for 24 h.

2.3 PREPARATION OF SPEEK/rGO MEMBRANE

GO was prepared based on modified Hummer's method (Wu, et al., 2010). GO powder was dispersed into water and sonicated for 30 min. $NaBH_4$ solution was then added drop-wise and stirred at room temperature for 24 h. The rGO powder was obtained after the mixture was filtered, rinsed with ethanol and distilled water and at 70 °C for 24 h. For SPEEK/rGO solution, 10 wt% of SPEEK solution was prepared by dissolving SPEEK into N-methyl pyrolidine (NMP) solution in constant stirring. In another flask, small amount of rGO was added and stirred for 24 h to produce a homogenous solution. After the solutions were totally homogeneous, the rGO solution was added to the SPEEK solution and vigorously stirred for 24 h to produce a homogeneous mixture. The mixture was casted on glass plate by pneumatic casting machine and dried at 60 °C for 24 h. Afterwards, the membrane was treated with 1 M of H_2SO_4 for 24 h to convert into H^+ form, rinsed several times with distilled water to eliminate remaining acid and dried at ambient temperature.

2.4 PREPARATION OF MEMBRANE ELECTRODE ASSEMBLY (MEA)

The membranes were cut into 4.0 cm x 4.0 cm and the electrodes were cut into 2.0 cm x 2.0 cm sizes. The electrodes used were 40 % Pt on carbon paper nafion treated and 40 % PtRu on carbon paper nafion treated at the cathode and anode. The process involves SPEEK/rGO membrane sandwiched between the anode and cathode. The MEAs are prepared with hot press technique by hot pressing the anode and cathode to the membrane at 80 °C for 2 min. The same electrodes were utilized for DMFC performance testing of SPEEK, SPEEK/rGO, and nafion 112 membranes.

2.5 SAMPLE CHARACTERIZATION

FTIR spectra from Perkin Elmer Spectrum One FTIR were used to observe the availability of functional groups in the samples. Electrical properties of rGO was measured through Four Point Probe, model Four Probe Dfp-02. Performance evaluation was analyzed with Single cell DMFC recorded by PRO200F, PRO-POWER inc fuel cell analyzer.

3. RESULTS AND DISCUSSION

3.1 FUNCTIONAL GROUP ANALYSIS

The FTIR spectra of GO and rGO are shown in Figure 1. GO spectrum (Fig. 1 (a)) shows various type of oxygen bonds assigned to the C=O stretching, O–H stretching, and C–O stretching, which is in good agreement with previous works (Cao, et al., 2011 and Li, et al., 2008).By comparing all of the spectra, the rGO's spectrum (Fig. 1 (b)) shows some differences. The O–H groups with broad peaks can be seen at 3445.39 cm^{-1}, 3400.18cm^{-1}, 1583.00 cm^{-1} and 1563.00 cm^{-1}. The presence of the two sp^3 C-H peaks at 2923.78 cm^{-1} and 2851.64 cm^{-1} (Fig. 1 (a)) indicates that the product is in an acidic phase. The peaks at 1717.45, 1220.88 and 1050.79 cm^{-1} are assigned to the C=O and C–O stretching, respectively, which originated from the carbonyl groups in the product. The peak at 1717.43 cm^{-1} in GO vanished in Fig. 1 (b), which shows the successful deduction of carbonyl group during the reduction process. Thus, the structures of GO and rGO have been validated by FTIR study.

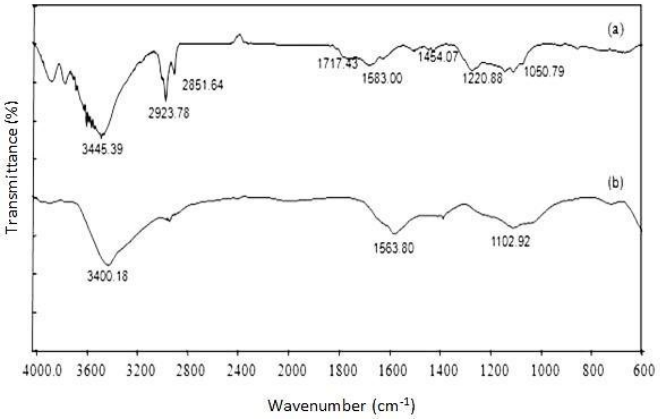

Figure 1: FTIR spectra of (a) GO and (b) rGO

The confirmation of sulfonation process was also analyzed by the FTIR and the spectra are shown in Figure 2. From the spectrum of SPEEK polymer, the aromatic O=S=O symmetric and asymmetric stretching vibrations were detected at 1081.93 and 1024.82 cm^{-1}, respectively. The peak at 1471.54 cm^{-1} was identified as the C–C aromatic ring, which is caused by the attachment of sulfonic acid group at 1,2,4-substitution aromatic ring. Moreover, the presence of a broad peak at 3412 cm^{-1} proves the existence of O–H vibration from the sulfonic acid group.

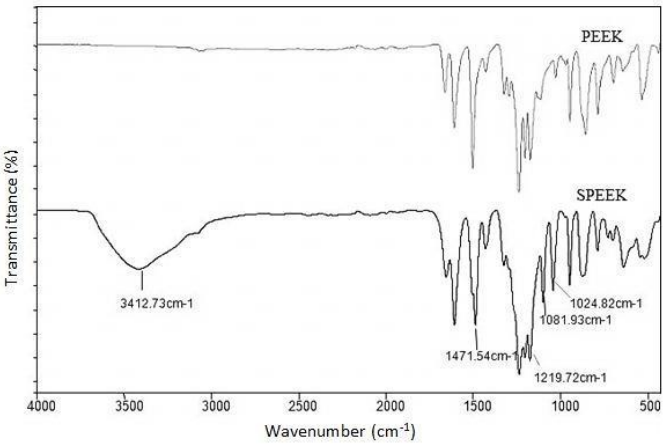

Figure 2: FTIR spectra of PEEK and SPEEK

3.2 ELECTRICAL PROPERTIES STUDIES

Electrical conductivity of GO and rGO were measured using four point probe at room temperature and tabulated in Table 1. The table shows the conductivities of GO and rGO are 3.58 x 10^1 S/m and 1.36 x 10^4 S/m, respectively. Owing to no interference of restoring carbon sp^2 network, rGO displayed higher conductivity, which was about three orders of magnitude better than GO. According to literature, the minimum conductivity value desired as catalyst's support material is in the range of 1.25 x 10^2 – 1.25 x 10^3 S/m, and for that reason the synthesized rGO can be a suitable candidate for catalyst support in fuel cell (Striebel, et al., 2001).

Table 1: Electrical conductivity data of GO and rGO

Material	Conductivity (S/m)
GO	3.5800 x 10^1
rGO	1.3560 x 10^4

3.3 EFFECT OF SPEEK/rGO AT 1 M AND 2 M METHANOL CONCENTRATION.

The results of DMFC performance using SPEEK/rGO in Figure 3 and Figure 4 indicated that the current density and power density increased as the methanol concentration increased. The polarization curve of SPEEK/rGO polymer membrane exhibited the highest OCV performance, as compared to those of SPEEK and commercial nafion 112 membranes. The addition of filler into the original SPEEK successfully achieved the highest OCV for both concentrations. The high OCV value is closely associated with low methanol permeation. The OCV readings of SPEEK/rGO improved by 11 – 15 % than nafion 112 for high methanol concentration compared to the lower concentration.

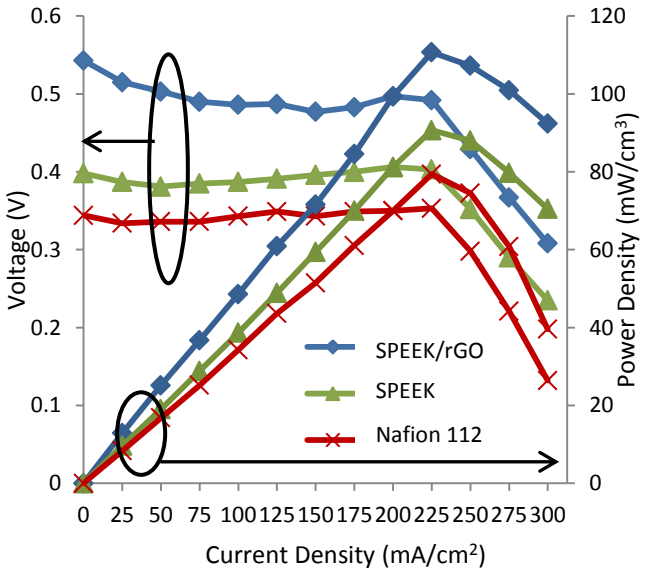

Figure. 3 :DMFC performance for SPEEK/rGO, SPEEK and Nafion112 membrane at 1 M methanol

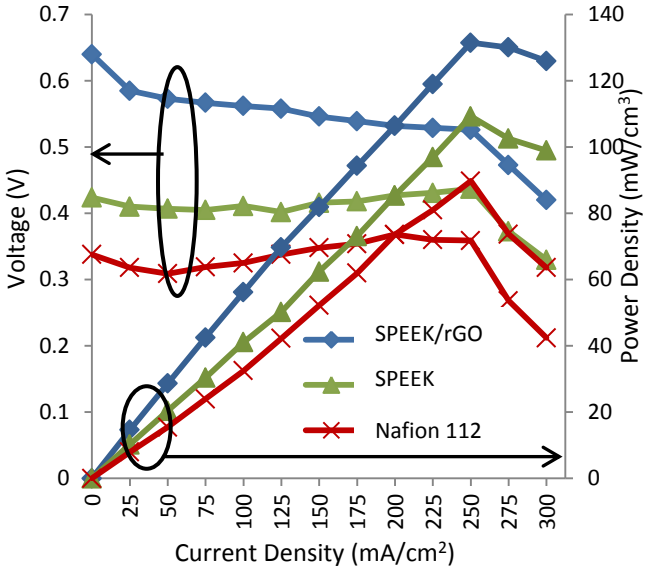

Figure. 4: DMFC performance for SPEEK/rGO, SPEEK and Nafion112 membrane at 2 M methanol

In a typical DMFC system, the DMFCs deal with the problems of methanol crossover and low power density that are caused by poor kinetics of the anode reactions. From Figure 3, the maximum power densities of SPEEK/rGO, SPEEK and nafion 112 measured are 110.7, 90.7, and 79.4 $mWcm^{-2}$, respectively. Figure 4 shows that the highest power densities achieved are 131.5, 109.3, and 89.8 $mWcm^{-2}$, in the sequence of SPEEK/rGO, SPEEK and nafion 112 membranes. To some extent, the addition of rGO as additive in SPEEK polymer gives positive result through power density.

3.4 POWER DENSITY OF SPEEK/rGO MEA

For further performance evaluations of all the membranes through MEA, power density measurements were also carried out. Figure 5 shows the influence of rGO as inorganic filler to the SPEEK polymer on the performance of DMFC in 1 M and 2 M of methanol, respectively. Since DMFC's performance is largely limited by charge transfer kinetics, low methanol crossover and high power density, catalyst's membrane should enhance cell performance. It was found that the power density increased with the increase of methanol concentration. All of the membranes experienced similar behavior with the increased in methanol concentration. The synthesized SPEEK/rGO membrane has 8% improvement through MEA compared to the commercial membrane.

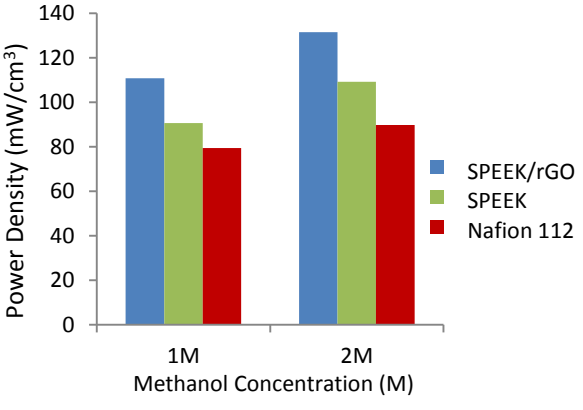

Figure 5 : Power density of membranes at different methanol concentration.

4. CONCLUSION

By increasing methanol concentrations, SPEEK/rGO membrane showed the highest OCV value at 0.64 V, maximum current density of 250 $mAcm^{-2}$, and maximum power density at 131.5 $mWcm^{-3}$. Addition of reduced graphene oxide as inorganic filler to the pristine SPEEK polymer signifies the maximum power density of nafion 112 membrane. Hence, fabrication of MEA with blended SPEEK/rGO has extensively improved the performance of DMFC performance by 8 – 15%.

REFERENCES

Cao, Y. C., Xu, C., Wu, Xu., Wang, X., Xing, L., Scott, K . A Poly(Ethylene Oxide)/Graphene Oxide Electrolyte Membrane for Low Temperature Polymer Fuel Cells. J. of Pow. Sources. Vol. 196, pp. 8377-8382, 2011.

Hermann, A., Chaudhuri, T., Spagnol, P. Bipolar plates for PEM fuel cells: A review. Int. J. Hydrogen Energy. Vol. 30, pp. 1297- 1302, 2005.

Jung, H. Y., Park, J. K. Blend Membranes based on Sulfonated Poly (Ether Ether Ketone) and Poly(Vinylidene Fluoride) for High Performance Direct Methanol Fuel Cell. Electrochemica Acta. Vol. 52, pp. 7464-7468, 2007 .

Lee, S. H., Kakati, N., Jee, S. H., Maiti, J., Yoom, Y. S. Hydrothermal Synthesis of PtRu Nanoparticles Supported on Graphene Sheets for Methanol Oxidation in Direct Methanol Fuel Cell. Mat. Letters. Vol. 65, pp. 3281-3284, 2011.

Li, D., and Kaner. R. B. Graphene-Based Materials". Materials Science. vol. 320, pp. 1170-1171, 2008.

Li, W., Manthiram, A., Guiver, M. D., Liu, B. High Performance Direct Methanol Fuel Cells based on Acid-base Blend membranes Containing Benzotriazole. Electrochem Communication, Vol. 12, pp. 10-607, 2010.

Lin, C. W., Lu, Y. S. Highly Ordered Graphene Oxide Paper Laminated with a Nafion Membrane for Direct methanol Fuel Cells. J. of Pow. Sources. Vol. 237, pp. 187-194, 2013.

Ma, Z. Q., Cheng, P., and Zhao, T. S. A Palladium-Alloy Deposited Nafion Membrande for Direct Methanol Fuel Cells. J. of Memb. Science. Vol. 215, pp. 327-336, 2003.

Perez, G., Pastor, E., Zinola, C. F. A Novel Pt/Cr/Ru/C Cathode catalyst for Direct Methanol Fuel Cell (DMFC) with Simultaneous Methanol Tolerance and Oxygen Promotion. Int. J. of Hydrogen Energy. Vol. 34, pp. 9523-9530, 2009.

Seger, B. and Kamat, P. B. Electrocatalytically Active Graphene-Platinum Nanocomposites. Role of 2-D Carbon Support in PEM Fuel Cells, Phy. Chem Lett., Vol. 113, pp. 7990-7995, 2009.

Striebel, K. A., Shim, J., Wang, C. W., Sastry, A. M. Anode Performance and Matrix Conductivity in Lithium Battery Electrolytes. Power Sources. Vol. 93, pp.123 – 133, 2001.

Vijay, R. Engineering a Membrane Electrode Assembly. The Electrochem. Soc. Interface. Pp. 40-43, 2006.

Wu, J., Bai, S., Shen, X., Jiang, L. Preparation and characterization of Graphene/CdS Nanocomposites. Applied Surface Science. Vol. 257, pp. 747-751, 2010.

Xin, Y., J. G. L., Zhou, Y., Lie, W., Gao,J., Xie, Y., Yin,Y., Zou, X. Preparation And Characterization Of Pt Supported On Graphene With Enhanced Electrocatalytic Activity In Fuel Cell. J. Of Pow. Sources, Vol. 196, pp. 1012-1018, 2011.

Farah Syuhada Abdul Halim received her BSc (2011) in Industrial Chemistry and MSc (2014) in Science Chemistry from University Teknologi Malaysia. She is a PhD student at the Department of Chemistry, Faculty of Science, Universiti Teknologi Malaysia. Her current research interest includes battery, fuel cell and catalyst.

Sheela Chandren received her BSc. in Industrial Chemistry (2006) and MSc. in Chemistry (2009) from Universiti Teknologi Malaysia. She then obtained her PhD. in Materials Science and Engineering (2012) from Hokkaido University, Japan. At present, she is a Postdoctoral Fellow in Ibnu Sina Institute for Fundamental Science Studies, Universiti Teknologi Malaysia. Her current research interests include photocatalysis, catalysis, selective organic synthesis, materials science and nanotechnology.

Madzlan Aziz received his BSc (1983) in Applied Chemistry from Newcastle-U-Tyne Polytechnic, U.K., MSc (1987) in Solid State Chemistry, University of Manchester, U.K. and PhD (1996) in Solid State Battery, De Montfort University, Leicester, U.K. He is a Professor at the Department of Chemistry, Faculty of Science, Universiti Teknologi Malaysia. His current interest includes physical chemistry, corrosion, nanoparticle polymer composite, semiconductor, battery, and fuel cell.

Hadi Nur received the BSc (1992) in Chemistry, M.Eng. (1995) in Mechanical Engineering. from Institut Teknologi Bandung, Indonesia and PhD (1998) in Science Chemistry from Universiti at the Teknologi Malaysia. He is a Professor, Department of Chemistry, Faculty of Science, Universiti Teknologi Malaysia. His current interest includes zeolite chemistry and catalysis, photocatalysis, semiconductor, nanoparticle polymer composite, bifunctional oxidative and acidic catalysts and phase-boundary catalysis.

OS Number 06

EFFECT OF PARTICLE SIZE AND CONTENT OF WASTE MELAMINE FORMALDEHYDE ON MECHANICAL PROPERTIES OF HIGH DENSITY POLYETHYLENE COMPOSITES

Somsak Siwadamrongpong*, Janjira Aphirakmethawong
School of Manufacturing Engineering.
Institute of Engineering. Suranaree University of Technology.
111 University Avernue, Muang District, Nakhonratchasima 30000, Thailand.
* E-mail: somsaksi@sut.ac.th. Tel: 0-4422-4236, Fax: 0-4422-4566

Abstract

Waste melamine formaldehyde powder (PWMF) was generated by grinding process of Melamine products and there are cannot be reformed or reused. PWMF was used as filler of HDPE matrix by 2 factors, particle size and content of PWMF. HDPE/PWMF composites were prepared using internal mixer and test specimens were formed by injection machine. Mechanical properties including tensile strength, tensile modulus, impact strength and hardness of composites were investigated. Influence of 2 factors on mechanical properties of composite was examined by using the analysis of variance (ANOVA) with the level of significant 0.05. The result was indicated that hardness is increase and impact strength is decrease with increasing PSMF content. It was also found that decreasing of particle size leads to increase of tensile strength and hardness, but impact strength is decrease. However, Young's modulus and hardness of HDPE/PWMF were higher than reference all whereas impact strength was lower.

Keyword: Melamine formaldehyde resin, factorial design, particle size, particle reinforced, HDPE composites.

1. INTRODUCTION

Nowadays, Polymers have used widely and more desire to use especially plastic because light low-cost and suitable for various application. So, could increasing concern regarding the environment and plastic waste disposal problem. The alternative methods for handle plastic waste and decreasing environment problem from plastic include burial, incineration, de-polymerization and recycling which recycling is convenient way to manage waste problem. (Rapisa & Kasama, 2013) The interest in recycled materials has been growing rapidly during recent year cause of environment concern and wish to reduced energy consumption. (Chaitongrat, C. et al., 2013).

High density polyethylene (HDPE) is the most of thermoplastics used. HDPE is chosen to produce the composites since it is a major portion of used. In addition, HDPE outstanding properties such as high toughness, good impact resistance etc.

Melamine formaldehyde (MF) resin commonly known as melamine is one of famous thermosetting plastic which cannot be melted and re-shaped after it cured. Thermosetting plastic are generally excellent hardness, high thermal resistance (Phaiboon & Malika, 2008) low cost, relatively light weight and unbreakable characteristics (Chao-Yi Chien, et al., 2011) which suitable to use for Tableware products. Hence, waste melamine powder was generated in manufacturing process and it is cannot reformed or reused. Therefore, it needs to disposal by landfills or burning (S.J. Pickering, 2006) that leading to degradation of environment and cost for disposal. S.J. Pickering (2005) carried out studied on technologies for recycling thermoset composite materials by use of grinding techniques to comminute the scrap material for reuse as fillers or reinforcement in new composite. Hasan S. Dweil, Mohamed M. Ziara& Mohammed S. Hadidoun (2008) have studied to improve structural concrete properties with ground melamine. The waste was used as a sand replacement. The results, waste melamine that replacing sand can improve the mechanical and thermal properties of light weight concrete. In the same way Phaiboon and Mallika (2008) studied the utilization of waste melamine by filled waste melamine in mix proportion of lightweight concrete. The results, waste melamine can reduce light concrete density due to low specific gravity of melamine. So, waste melamine powder was chosen as filler.

In this study, consider the effect of waste melamine powder on mechanical properties by various particle size and content of waste melamine powder. The study results will be discussed by mean of statistical design of experimental (DOE) approach.

2. EXPERIMENT PROCESDURE

2.1 Materials

High density polyethylene (HDPE, EL-Lene H6007JU, SCG) was used as matrix composite.

Waste melamine powder (PWMF) generated by grinding process in Tableware manufacturer was used as filler with two difference particle sizes consist 23 and 36 μm, Code P1 and P2 respectively (ready mixed with cellulose and formaldehyde).

2.2 Design of experiment (DOE)

2^k factorials Design of experiment (DOE) was used to analyze the significant effect of 2 Factors summarized in Table 1. Therefore, total of 4 runs are shown in Table 3. Influence of 2 factors on mechanical properties of HDPE/PWMF composite was examined by using the multi variance analysis (ANOVA) with the level of significant 0.05 or 95% confidential. The significant effect was calculated by Minitab16 software.

Table 1 Factor in this study

Factor	Name	Low level (-)	High level (+)
A	Content of PWMF (%wt)	5	20
B	Particle size (μm)	23	36

2.3 Preparation of Test Specimens

The specimens were mixed by internal mixer (HAAKE PolyLab OS, RheoDrive7). Formed by Co-injection molding machine (TEDERIG, TRX-60C). Conditions are shown in Table2.

Table 2 Condition for Preparation of Test Specimens

Method	Conditions
Mixing	
- mixing temp (^oC)	170
- mixing time (min)	15
- rotor speed (rpm)	70
Injection	
- melting temp (^oC)	180
- molding temp (^oC)	30
- cooling time (min)	30
- holding pressure (bar)	100
- injection pressure (bar)	80

2.4 Mechanical Properties

Tensile tests according to ASTM D638 using a universal testing machine (Instron, 5565) with 5 kN load cell and crosshead speed of 50 mm/min. Ten samples were tested.

Izod Impact strength of HDPE/PWMF composites was performed according to ASTM D256 – 10 were using an impact testing machine (Instron, CEAST9050). Notched impact strength was tested using the impact pendulum with impact energy of 2.7 J.

Hardness according to ASTM D2240 test with Durometer hardness scale shore D. Five samples were tested.

3. RESULTS AND DISCUSSION

3.1 Mechanical Properties

The mechanical properties of HDPE/PWMF composites by mean of tensile strength, tensile modulus, impact strength and hardness are shown in Table 4. Effect of PWMF in this study found that Young's modulus and hardness increase with adding PWMF all case in the other hand impact strength are decreased.

Two factors DOE was analyzed by box plot, normal plot and ANOVA are illustrated in Fig. 1-6 respectively.

Table 3 the design of 2^k factorials for 2 factor (k=2)

RUN	Design Code		PWMF (wt%)	Particle size (μm)	Compatibilizer (phr)	Name
	A	B				
1	-	-	5	23	0	HDPE/5PWMF/P1
2	-	+	5	36	0	HDPE/5PWMF/P2
3	+	-	20	23	0	HDPE/20PWMF/P1
4	+	+	20	36	0	HDPE/20PWMF/P2

Table 4 Summarize of mechanical properties of HDPE/PWMF composites

Name	Tensile strength (MPa)	Young's modulus (MPa)	Impact strength (kJ/m^2)	Hardness
HDPE	24.53 ± 0.63	376.60 ± 10.94	3.30 ± 0.19	58.92 ± 1.12
HDPE/5PWMF/P1	24.84 ± 0.52	407.40 ± 20.19	2.36 ± 0.22	60.40 ± 0.87
HDPE/5PWMF/P2	23.67 ± 0.46	382.30 ± 13.84	2.54 ± 0.14	60.12 ± 0.83
HDPE/20PWMF/P1	25.73 ± 0.72	459.80 ± 13.50	1.90 ± 0.11	64.60 ± 1.12
HDPE/20PWMF/P2	23.15 ± 0.34	444.90 ± 11.53	2.16 ± 0.08	63.80 ± 0.58

3.2 Tensile properties

Fig. 1(a) shown box plot of tensile strength of HDPE/PWMF composites. It was found that tensile strength increased with adding PWMF small particle size but content of PWMF no effect to tensile strength. In addition, between statistical analyzed results and box plot (Fig.1 – Fig.2) are the same trends, particle size have significantly (consider from p-value less than the critical value,0.05) of tensile strength which is negative (-) effect it mean if large size of particle heading to tensile strength decreased and content of PWMF no significantly.

Young's modulus are increased with adding PWMF all case cause of PWMF high stiffness than HDPE which matrix (S-Y Fu, et al., 2008) more over filler prevent capable rotational movement and change shape of matrix (R. D. K. Misra et al., 2004).

3.3 Impact test

Box plot and normal plot of impact strength of HDPE/PWMF composites are shown in Fig.3. It was found that impact strength are increased which increasing particle size in the other hand impact strength deceased which decreasing content of PWMF. The ANOVA results, content of PWMF significantly negative (-) effect and particle size significantly positive (+) affect to impact strength. In addition content of PWMF is more effect than particle size.

Cause of impact strength decreased with increasing content of PWMF due to poor compatibility between PWMF and HDPE, the poor interfacial adhesion resulted in voids between the interface of filler and HDPE. Under the impact test, these voids acted as stress concentration at which the impact stress was magnified and made the composites fractured at lower stress (P. Pakdeechote, et al.,2009)

3.4 Hardness

The hardness results were plot by box plot and normal plot are shown in Fig.5. From Fig. 5(a) was found that increasing content of PWMF heading to harness increased. The ANOVA results (Fig.6) can expand that content of PWMF is significantly positive (+) affect to hardness on other way particle size has negative (-) effect. Moreover, content of filler have a too large effect which compared with particle size. Hardness increased which adding filler due to PWMF is high stiffness than HDPE that heading to improve the matrix surface resistance (S. C. Nwanonenyi, et al., 2013)

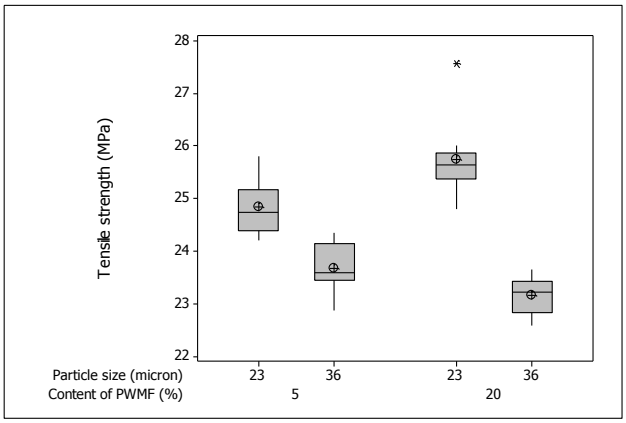

(a)

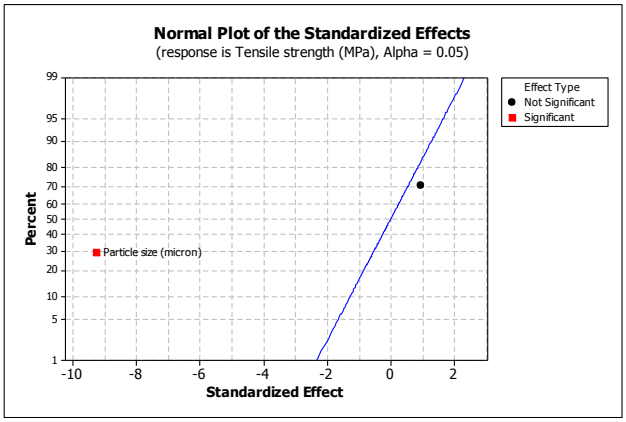

(b)

Fig. 1 Box plots of tensile strength (a) and normal plot of tensile strength (b)

Source	DF	SS	MS	F	P
PWMF (%)	1	0.369	0.369	0.90	0.349
Particle size	1	34.931	34.931	85.27	0.000
Error	37	15.158	0.409		
Total	39	50.459			

Fig. 2 ANOVA test results of Tensile strength

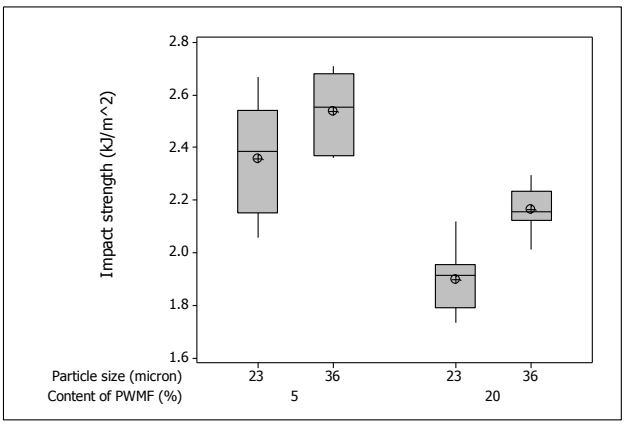

(a)

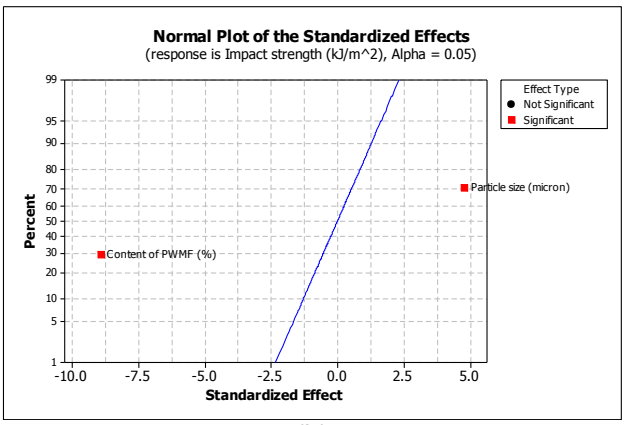

(b)

Fig. 3 Box plots of impact strength (a) and normal plot of impact strength (b)

Source	DF	SS	MS	F	P
PWMF (%)	1	2.231	1.734	79.41	0.000
Particle size	1	1.733	0.498	22.83	0.000
Error	37	0.808	0.022		
Total	39	3.039			

Fig. 4 ANOVA test results of Impact strength

(a)

(b)

Fig.5 Box plots of hardness (a) and normal plot of hardness (b)

Source	DF	SS	MS	F	P
PWMF (%)	1	388.090	388.090	493.18	0.000
Particle size	1	7.290	7.290	9.26	0.003
Error	97	76.330	0.787		
Total	99	471.710			

Fig. 4 ANOVA test results of Hardness

4. CONCLUSION

Young's modulus and hardness of HDPE/PWMF were higher than HDPE all whereas impact strength was lower. With increasing content of PWMF hardness increased, impact decreased and content of PWMF no effect to tensile properties. With decreasing particle size of PWMF tensile strength and hardness increased but impact strength decreased.

ACKNOWLEDGEMENT

The author wish to acknowledge Suranaree University of Technology for financial and facility support. Chemical Innovation Co., Ltd. for maleic anhydride grafted polyethylene Fusabond® M603, Siam Cement Group co., Ltd. for High density polyethylene, EL-Lene H6007JU. Srithai Superware PLC for Waste melamine formaldehyde powder.

REFERENCES

Chaitongrat, C. et al.,(2013). Thermal properties of recycled materials from waste melamine formed by hot molding process, South East Asian Technical University Consortium (SEATUC 2013). 4-6 March. ITB. Bandung Indonesia.

Chao-Yi Chien, Chia-Fang Wu, Chia-Chu Liu, Bai-Hsiun Chen, Shu-Pin Huang, Yii-Her Chou, Ai-Wen Chang, Hei-Hwa Lee, Chih-Hong Pan, Wen-Jeng Wu, Jung-Tsung Shen, Mei-Yu Chang, Chun-Hsiung Huang, Jentaie Shiea, Tusty-Jiuan Hsiehi, Ming-Tsang Wu., High melamine migration in daily-use melamine-made tableware, Journal of Hazardous Materials 188 (2011), pp. 350–356

Hasan S. Dweil, Mohamed M. Ziara& Mohammed S. Hadidoun., Enchancing concrete strength and thermal insulation using thermoset plastic waste, International Journal of Polymeric Materials, 57:635-656,2008

Phaiboon Panyakapo, Mallika Panyakapo., Reuse of thermosetting plastic waste for lightweight concrete, Waste Management 28 (2008), pp.1581–1588.

P. Pakdeechote, Y. Ruksakulpiwat, N. Suppakarn, and W. Sutapun, Preparation and Characterization of Heat Treated Eggshell for HDPE composites: A preliminary Study, Pure and Applied Chemistry International Conference (PACCON 2009), Phitsanulok, Thailand P325.

Rapisa, J., and Kasama, J. (2013). Mechanical properties and flammability of sawdust/recycled high density polyethylene composites. Pure and Applied Chemistry International Conference (PACCON2013)

R. D. K. Misra, P. Nerikar, K. Bertrand, and D. Murphy (2004). Some aspects of surface deformation and fracture of 5 – 20% calcium carbonate-reinforced polyethylene composites. Material Science Engineering. A384: 284-298

S. C. Nwanonenyi, M.U Obidiegwu, G.C Onuegbu., Effect of particle sizes, Filler content and compatibilization on the properties of linear low density polyethylene filled periwinklie shell powder, The International Jornal of Engineering and Science (IJES),volume2, 2013, pp1-8.

S.J. Pickering., Recycling technologies for thermoset composite materials—current status, Composites: Part A 37 (2006), pp.1206–1215.

S-Y Fu, X-Q Feng, B. Lauke, and Y-W. Mai (2008). Effect of particle size, particle/matrix interface adhesion and particle loading on mechanical properties of particulate-polymer composites. Composites Part B. 39: 933-961.

Somsak Siwadamrongpong received the B.Eng. (2004) degree in Mechanical Engineering from Chulalonglorn University, M.Eng. (2001) degree in Environmental System from Nagaoka University of Technology, and D.Eng. (2004) degree in Energy and Environment from Nagaoka University of Technology.

He is a Professor, Department of Manufacturing Engineering, Suranaree University of Technology. His current interests include material characteristics, recycle of industrial waste and manufacturing productivity improvement.

Janjira Aphirakmethawong received the B.Eng. (2011) degree in Manufacturing Engineering from Suranaree University of Technology. She is a 2st years of master degree student in Manufacturing Engineering.

Effect of gas sulfur-nitriding processes and gas soft-nitriding on the alloy and plain carbon steel

Somsak Siwadamrongpong*, Sirijit Champee
School of Manufacturing Engineering.
Institute of Engineering. Suranaree University of Technology.
111 University Avernue, Muang District, Nakhonratchasima 30000, Thailand.
* E-mail: somsaksi@sut.ac.th. Tel: 0-4422-4236, Fax: 0-4422-4566

Abstract

The metallurgy associated with improvement in mechanical properties tends to perform with the procedure of heat treatment. One kind of well-known heat treatment is a gas surface hardening method. For instance of gas soft-nitriding and gas sulfur-nitriding the process that mention above improving the surface hardness, wear, and resistance of friction in carbon steel and alloy steel. The aim of this study was thus investigated in influence of gas soft-nitriding and gas sulfur-nitriding on AISI 1045, AISI 4140 and AISI 4340 the specimens were reduced the residual stresses by normalizing and shot blasting. Then the specimens were treated by gas soft-nitriding, gas sulfur-nitriding. After that micro hardness and the optical microscopy were performed to characterize structure. In this work the process of gas soft-nitriding has greater surface hardness than gas sulfur-nitriding in both of steel.

Keyword: Gas soft-nitriding, Gas sulfur-nitriding, Shot Blast

1. INTRODUCTION

In the present plain carbon steel and alloy carbon steel widely used in many industries such as equipment manufacturers in agriculture, construction, machinery, and military are required to have superior fatigue and wear resistance qualities in order to satisfy such requirements, there are known methods that was gas surface hardening such gas soft-ntriding method in which iron parts are nitempered under relatively safe conditions using a gaseous medium containing nitrogen gas to improve the fatigue strength and wear resistance of the parts. And gas sulfur-nitriding is the techniques that suitable for steel, gas sulfur-nitriding of steel in an atmosphere of NH_3 and H_2S in endothermically derived propane carrier gas, has been investigated. (Osamu momose and Sosuke uchida, 1986)

In literature review, OSAMU MOMOSE and SOSUKE UCHIDA (1986) studied on technologies of gas sulphonitriding steels in a CS_2 and NH_3.The result, the surface composition of the gas sulphonitriding comprised $Fe_{1-x}S$ and Fe_3N

Wang Lijie, Xing Yazhe, Wang Hongbo, and Hao Jianmin (2009) have studied of effecf of nitriding sulfurizing composite treatment on Ti alloy and the result by nitriding sulfurizing composite treatment was covered by numerous spherical bulges while the modified layer for nitriding surface was composed of larger irregular particles. According to the results of friction and wear tests, the friction coefficient of alloy after nitriding-sulfurizing composite treatment was smaller than that of the alloy after nitriding treatment at different loads.

Although previous study has focused on gas sulphonitriding but no one study on and effect of gas soft-nitriding and gas sulfur-nitriding process on alloy and carbon steel

The aims of this study to investigate the influence of gas soft-nitriding and gas sulfur-nitriding to the plain carbon steel and alloy steel

2. EXPERIMENT

The steel graded AISI 1045, AISI 4140, and AISI 4340 were investigated. The major chemical compositions are shown in Table 1 (ASM v.1, 2005). The raw material were machining in shape of specimen with 12.5 mm. width and 12.5 mm. long and 0.5 mm. thick. The specimens were treated by normalizing process with 870 °C for 1 hour to eliminate residual stress. After that the specimen were shot blasting by 0.3 balls for cleaning the surface for 45 minute (ASM v.5, 1987). The process of gas surface hardening that were treated the specimen, soft-nitriding (SN), sulfur-nitriding (SUL) was shown in Fig1- 2. The 6 samples of each process condition were investigated. The surface hardness was observed by Future Tech FM-700

hardness tester, micro structure and compound layer were observed by Nikon MM-400 optical microscope and surface topologies were observed by Jeol-JSM6010LV scanning electron microscope (SEM).

Table 1 Compositions of raw materials (wt %)

AISI	C	Si	Mn	P	S	Cu	Ni	Cr	Mo	V	AL	Fe
1045	0.426	0.261	0.666	0.019	0.011	0.359	0.006	0.016	0.012	0.003	0.003	Bal.
4140	0.417	0.222	0.712	0.007	0.005	0.167	0.039	1.098	0.161	0.007	0.020	Bal.
4340	0.406	0.232	0.661	0.008	0.006	0.025	0.021	1.053	0.171	0.002	0.036	Bal.

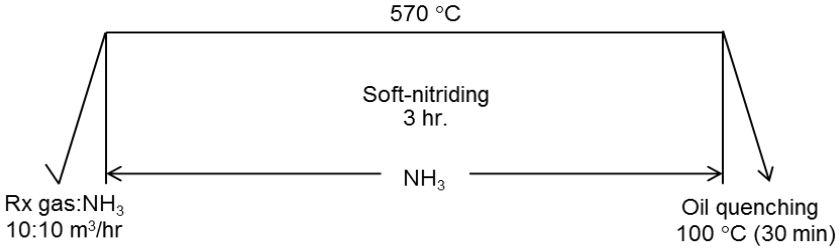

Fig. 1 Treatment conditions of soft-nitriding method

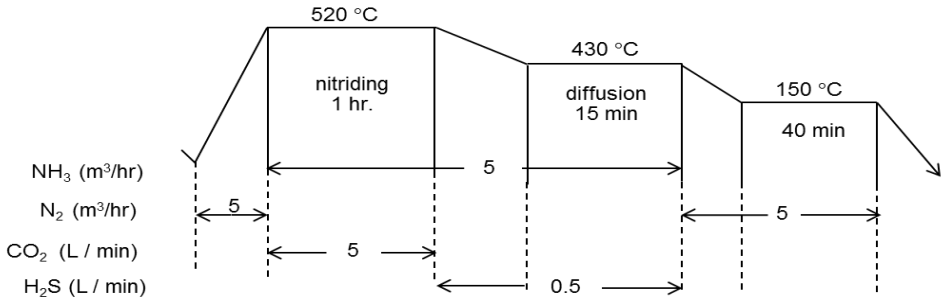

Fig. 2 Treatment conditions of sulfur-nitriding method

3. RESULT AND DISCUSSSIONS

Figure 3, it was shown the surface hardness of specimens which treated by soft-nitriding and sulfur-nitriding in two process the trend of alloy steel (AISI 4140, AISI 4340) have higher surface hardness than plain carbon steel (AISI1045). It is assumed that the chromium and molybdenum contained in the steels increased their hardness (Osamu, M., 1986) and from this result may suggest sulfur-nitriding have lower hardness than soft-nitriding.

Cross-sectional microstructure of specimen were observed with magnification was 400X as shown in Figure 4, It was found the compound layer thickness in case soft-nitriding of AISI 4340 was found about 24 μm, AISI 4140 21 μm, AISI 1045 15 μm, Considering the compound layer indicated the alloy steel were have thickness more than carbon steel cause effect of chromium and molybdenum (ASM Vol.4, 1987) and the same in case of gas sulfur-nitriding process the compound layer of AISI 4140 was found 6 μm, AISI 4340 9 μm and AISI 1045

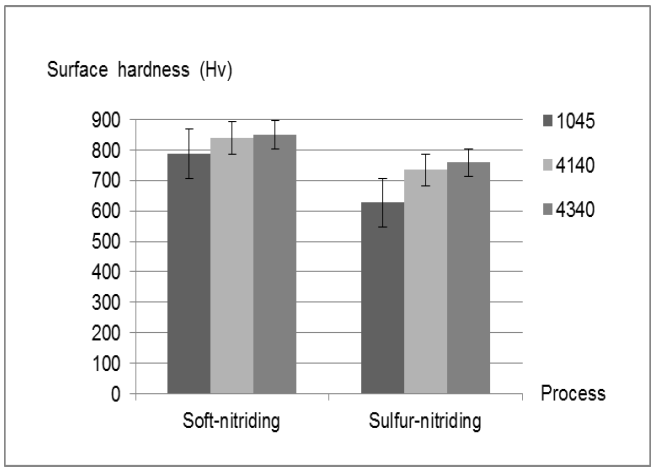

Fig. 3 Surface hardness of specimens

only 4-5 μm. And from this result of figure 4 conclude that the compound layer of sulfur-nitriding process was less than soft-nitriding. And the compound layer in soft-nitriding be composed of $Fe_{2-3}N$ while the compound layer in sulfur-nitriding was FeS.

Fig. 5 show surface topologies of gas soft-nitriding and gas sulfur-nitriding were observed by SEM. The average grain sizes of soft-nitriding larger than sulfur-nitriding the shape of grain quite spherical and crowded while the porous layer or irregular shape was form on surface of gas sulfur-nitriding process, several researches has been porous layer forming (Y.K. Ko., 2008) of the speculated that porous layer on gas sulfur-nitriding might be related to FeS on compound layer.

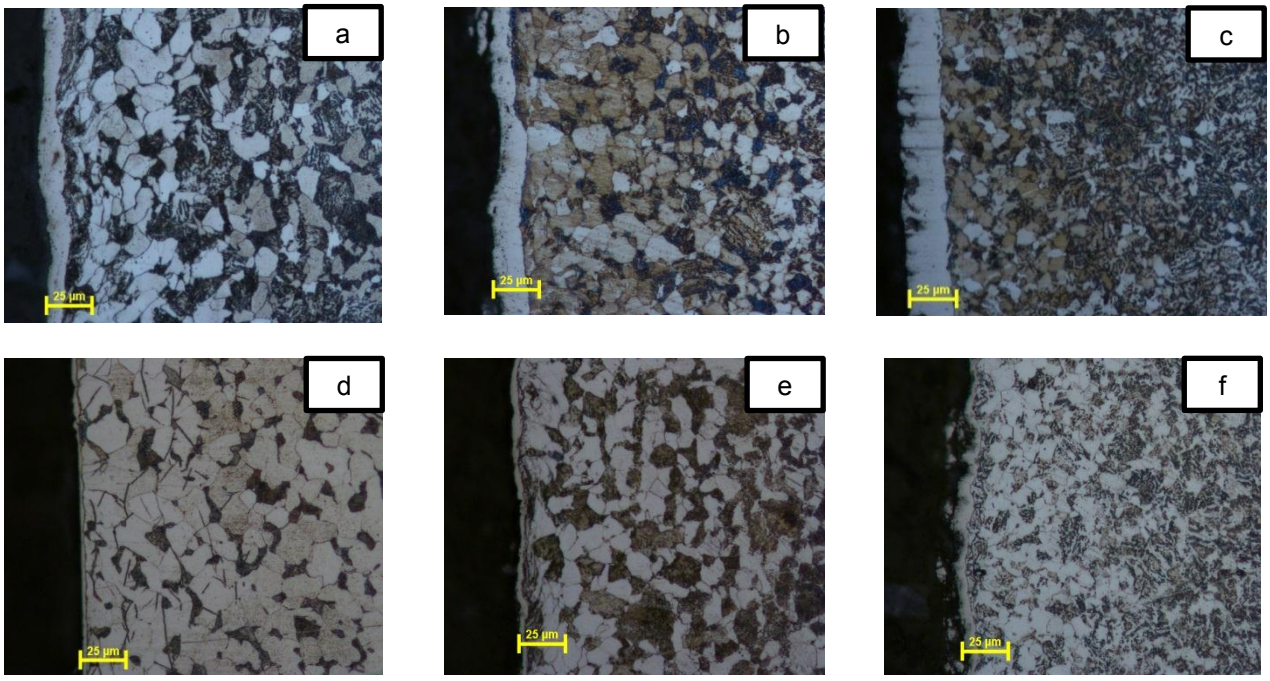

Fig. 4 Cross-sectional microstructure of soft-nitriding and sulfur-nitriding
(a) Soft-nitriding process on AISI 1045 (b) Soft-nitriding process on AISI 4140
(c) Soft-nitriding process on AISI 4340 (d) Sulfur-nitriding process on AISI 1045
(e) Sulfur-nitriding process on AISI 4140 (f) Sulfur-nitriding process on AISI 4340

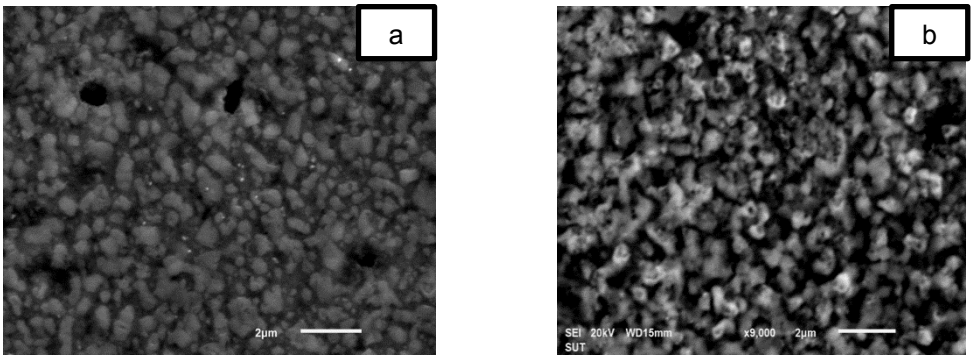

Fig. 5 SEM micrographs of specimens
(a) soft-nitriding AISI 4140 (b) sulfur-nitriding AISI 4140

4. CONCLUSION

The specimens AISI 1045, AISI 4140 and AISI 4340 were chosen in this study and the aimed to investigated influence of two process gas soft-nitriding and gas sulfur-nitriding. The specimens were normalized by normalizing and shot blasting. Then they were treated by gas soft-nitriding and gas sulfur-nitriding in surface hardness results found that

in two processes had the same trend by alloy steel have higher hardness than carbon steel. And all of surface hardness in gas sulfur-nitriding process less than gas soft-nitriding process. SEM report found that the porous layer with irregularly shape particles was formed on surface of gas sulfur-nitriding process this cause supported surface hardness of gas sulfur-nitriding less than gas soft-nitriding. And there were suggested that the friction of treated surface should be examined in the further study.

ACKNOWLEDGEMENTS

The authors would like to thank Suranaree University of Technology for financial support and Thai Tohken Thermo Co., Ltd

REFERENCES

Y.K. Ko, et al.,(2008). Plasma nitrosulfurizing techniques for low friction coefficient with H_2S and C_3H_8 gas addition, Journal of surface Coatings Technology 202 (2008) 5501-5504

Osamu Momose and Sosuke Uchida (1986). Gas sulphonitriding steels in a CS_2 and NH_3 atmosphere. Tokai University, Wear 116 (1987) pp.19-24

Wang lijie, Xing Yazhe, Wang hongbo, and Hao Jianmin (2009). Effect of nitriding-sulfurizing Composite treatment on tribological behavior of titanium alloys. Rare materials Vol.129 (2010) p.604

B. Selcuk, R.Ipek, M.B. Karamis, V.Kuzucu (1999). An investigation on surface properties of treated low carbon and alloyed steels (boriding and carburizing), Journal of Materials Processing Technology 103 (2000) 310-317

ASM Handbook., Heat Treating., Material Park Ohio.ASM International., Vol. 4, (1987)

ASM Handbook., Surface engineering., Meterial Park Ohio. ASM International, Vol. 5, (1987)

ASM Handbook., Properties and Selection: Irons, Steels, and High Performance Alloys., Meterial Park Ohio.ASM International, Vol. 5, (1987)

B. Selcuk. R. Ipek, M.B. Karamis: A study on Friction and wear behavior of carburized, carbonitrided and borided AISI 1020 and 5115, Journal of Materials Processing Technology 141 (2003) 189-196

Somsak Siwadamrongpong received the B.E. (1995) degree in Mechanical Engineering from Chulalongkorn University, M.E. (2001) degree in Environmental System from Nagaoka University of Technology, and D.E. (2004) degree in Energy and Environment from Nagaoka University of Technology.

He is a Professor, Department of Manufacturing Engineering, Suranaree University of Technology.

Sirijit Champee received the B.E. (2012) degree in Manufacturing Engineering for Suranaree University of Technology. She is a 2st years of master degree in Manufacturing Engineering.

ANTIMICROBIAL EFFECTS OF COTTON FABRIC TREATED WITH CHITOSAN AND LAURIC ACID AGAINST GRAM-POSITIVE AND GRAM-NEGATIVE BACTERIA

Siti Nur Hana Mamat, Eraricar Salleh and Basirah Fauzi
Department of Bioprocess Engineering, Faculty of Chemical Engineering, Universiti Teknologi Malaysia, 81310 Skudai, Johor

ABSTRACT

The growth of microbes on fabrics during use will negatively affect both wearer and fabric itself. The growth of microbes can be controlled by durable antimicrobial finishing on fabric by incorporating the natural antimicrobe into fabric's fiber during extrusion. Different concentration of lauric acid was added into chitosan solution to enhance their antimicrobial activity. Agar diffusion method was used in this study to measure the inhibition zone. FTIR analysis and SEM spectroscopy images shown that treated cotton fabrics are suitable to be used by the wearer. From this study, it revealed that at 15% concentration of lauric acid is the most optimum inhibition for the cotton treatment. This natural antibacterial fabric will provide better protection from the infection of microorganism and safe for consumer.

1.INTRODUCTION

Antimicrobial (AM) textile products keep increasing in demand due to it great properties such as have fresh odor, friendly towards skin, and high performance fabric. Many specialist applications required the AM properties of textile which have the AM property in order to minimize spread of infection. It need to exhibit high degree of performance in term of longevity and durability. The improvement of the textile properties can be done by imparting AM properties to the textile as well as increasing the comfort and hygiene factor making them more pleasant to wear.

Chitosan, a β-(1,4)-linked polysaccharide of D-glucosamine, is a deacetylated form of chitin, the second most abundant natural polymer in the world . It can be obtained from the shells of crustaceans like crabs, shrimps and others. Due to it properties which is non-toxic, biodegradable and biocompatible natural polymer, chitosan has long been used as a biopolymer and natural material in the pharmaceutical, medical, papermaking and food processing industries (Sashiwa & Aiba, 2004; Sandford PA, 1989). In textile industry processing, chitosan has got wide application in textile dyeing and finishing as a substitute for the various chemical used (Lim & Hudson, 2003). It has been used as a pretreatment agent in dyeing of cotton, in textile printing, wool dyeing and shrink proofing and in durable press finish.

Lauric acid, or its IUPAC name dodecanoic acid, is the main acid in coconut oil and in palm kernel oil. There are different techniques was used in order to extract the lauric acid from palm kernel. One of it by supercritical fluid extraction. Lauric acid is a crystalline fatty acid which has been shown to have antimicrobial effects towards Gram-positive bacteria and yeast (Beuchat and Golden, 1989; Kabara, 1993). Combination of chitosan with lauric acid together can inhibit wide spectrum bacterial hence increase the antibacterial properties of the fabric. In this paper having the goal to design an antimicrobial cotton fabric by incorporating chitosan with lauric acid to make an even more hygienic and give positive affect to both wearer and fabric itself.

2.EXPERIMENT

2.1 Pre-treatment of cotton fabric

The samples of cotton fabric were undergoing pre-treatman to remove all the foreign molecules, dust, and odor on the fabric. The fabric which is 100% cotton were cut onto small size (1cm x 1cm), scoured and bleech using sodium hydroxide. The fabric then immersed in solution of sodium hydroxide in deionized water (400 ml) at concentrations of 1.0 mg/ml and stirred for 1 hr at 60^{o}C. Treated cotton fabric then washed with deionized water for several times to remove the oxidant and soak in deionized water (400 ml) at ambient temperature. This oxidize material were used for the next reaction without drying.

2.2 Treatment with chitosan and Lauric Acid

Chitosan solution was prepared by stirring a dispersion of chitosan (2.0g) in 2.0% (v/v) aqueous acetic acid solution (100ml). Lauric acid was added at different concentration (5.0%, 10.0%, 15.0% and 20.0%) into the chitosan solution for 1h at 60^{o}C. The above mentioned oxidized cotton thread was immersed in the solution with constant stirring for 2h at 60^{o}C. the treated cotton then washed with deionized water several times and dried at 60^{o}C for 25 minutes to produce the drug carrier cotton thread.

2.3 UV curing

The dried fabric was cured under UV using CL-1000 Ultraviolet Crosslinker, UVP, Germany for 60 seconds with light intensity about 20mW/cm^2 and the oxygen content is under 20 ppm.

2.4 Antimicrobial Test

The comparison of antimicrobial activity of the four different concentrations of chitosan incorporated with lauric acid sample was carried out by disk diffusion method on an agar plate. Diameter of the zone of

inhibition was measured. To prepare an agar plate, solid culture was prepared according to method by Gupta and Haile (2006) by mixing 5 g agar-agar and 1.5g agar powder in 250 ml distilled water. The microbial used are *S.aureus* and *E. coli*. The agar plate was prepared by pouring the solid culture onto sterile circulate plate and let it solidified in Laminar Flow Chamber. One hundred microliters of microbial culture was uniformly distributed on each plate. Five millimeter disks of filter paper impregnated with chitosan -lauric acid (5.0%) solutions were placed on the plate. Same method was used for each different concentration of chitosan and lauric acid. All concentrations were prepared in triplicate. The plates then placed in an incubator for 24 hr at temperature 37^{o}C. Then , the zone of inhibition are measured.

2.5 Scanning Electron Microscope (SEM)

Scanning electron microscopy (SEM), Hitachi S570 was used to observe the morphological changes of the surface structure of the fabric fiber before and after treatment. Sample of the fabric before and after treatment was cut into small pieces and fixed on the standard SEM sample holders with a double-coated carbon conductive tab. All samples were sputter coated with a thin layer of gold in a vacuum. The morphology and structure of coated fabric is to be study from scan image. The scanning electron will be set to 25-35 kV acceleration voltage.

2.6Fourier Transform Infrared Spectroscopy (FTIR)

The characterization and analyzing of the treated fabric was determined using fourier transform infrared spectroscopy (FTIR) analysis. The oxidized material and chitosan coated cotton were dried by freeze dryer before analysis. KBr pellet was used for preparing the sample for FTIR analysis. The spectra then recorded using Nicolet MAGNA-IR 860 spectrometer. The IR spectra were collected using 32 scans with 4cm^{-1} spectral resolution between 650 and 4000 cm^{-1}.

3. ANALYSIS

3.1Antimicrobial Activity

The antimicrobial activity of cotton fabrics treated with different concentrations of lauric acid in the presence of chitosan clearly shows that lauric acid treated fabrics has higher antimicrobial activity against gram positive and gram negative bacteria. This study has used *Esterichia Coli* as a gram negative bacteria and *Staphylococcus Aureus* as the gram positive bacteria in order to obtain the result of the antimicrobial activity. There are crosslinking between the chitosan and lauric acid to the cotton fabric. As the amount of the lauric acid increase, there will be more attachment of the lauric acid itself and the chitosan to the fabric. However, as the lauric acid concentration reach at 15% it shows that the activity has reached the optimum condition and there will be no more significant different to the antimicrobial activity when the concentration of the lauric acid being increased.

Table 1: Inhibiton Zone of *E.coli* and *S.aureus*

Concentration of Lauric Acid (%)	Inhibition Zone of *E.coli* (mm)	Inhibition Zone of *S.aureus* (mm)
5	15	12
10	18	14
15	25	23
20	25	23

The results show that as the concentration of lauric acid increase, the zone of inhibition of *E.coli* and *S.aureus* will also gradually increase. This happen due to the fact that the lauric acid may crosslink to the cotton fabric and form stronger antimicrobial to the cotton fabric. The standard table of inhibition zone that can be refer to table 1 shows that a very strong antimicrobial activity is achieved by this experiment. However, as the concentration exceed the optimum concentration which is at 15%, the inhibition will not give any significant different to the cotton fabrics. Therefore, it is clearly reveals that 15% is the most optimum concentration to be used for treating cotton fabric to have the antimicrobial property.

3.2 Scanning Electron Microscope (SEM)

The scanning electron microscope (SEM) test is done in order to observe the morphology structure of the cotton fabric. The untreated cotton fabric is used as the control to compare with the treated fabrics. This test shows that as the concentration of lauric acid increase, the crosslinking of the lauric acid towards the chitosan will also increase. The crosslinking will gradually increase due to the attachment of the amine group of the chitosan to the carboxylic acid. There are significant crosslinking can be seen in the figure that reveal the presence of chitosan in different concentration of the lauric acid. The results can be seen in the figure below:

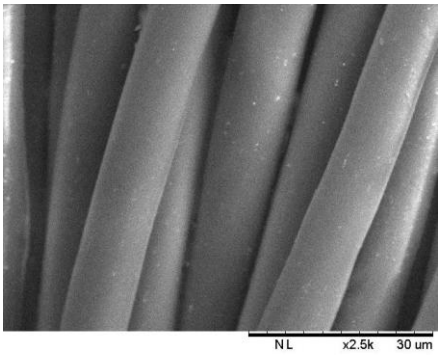

Fig 1(a) Fabric Structure with No Treatment

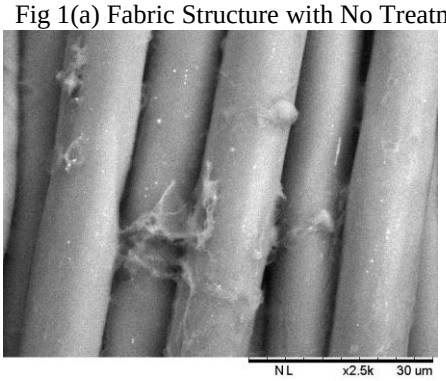

Fig 1(b) Fabric Structure at 5% Lauric Acid

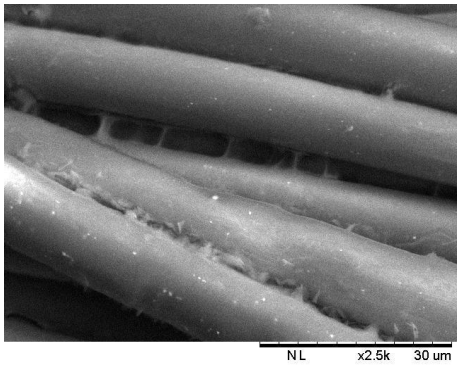

Fig 1(c) Fabric Structure at 10% Lauric Acid

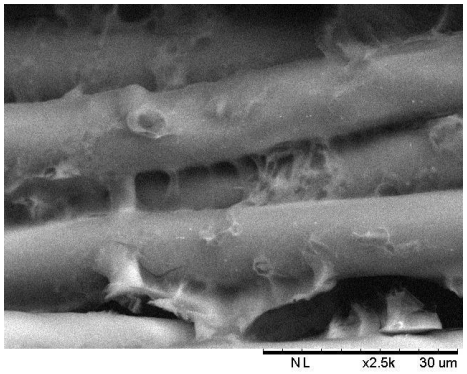

Fig 1(d) Fabric Structure at 15% Lauric Acid

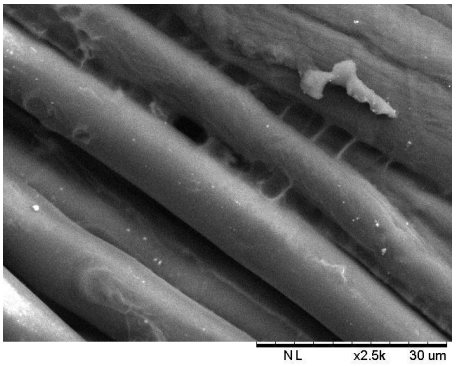

Fig 1(e) Fabric Structure at 20% Lauric Acid

The study is mainly wants to reveal that there are crosslinking between chitosan and lauric acid to the cotton fabric. In fact, it really shows that as the lauric acid concentration being increased, the crosslinking will also increase. SEM analysis only shows that the physical characteristics of the treated cotton fabric. Other factors such as physical colour and antimicrobial activity will support the results that 15% of lauric acid concentration will be the most optimum condition for the cotton fabric.

3.3 Fourier Transform Infrared Spectroscopy (FTIR)

FTIR is the analysis that reveals the existence of the functional group in a certain product. For this study, there are several absorbance has to be existed in the cotton fabric in order to support the result of the antimicrobial property. Therefore, by comparing FTIR spectra of treated and untreated cotton fabrics, the existed lauric acid in the presence of chitosan is revealed by its typical peak that is the N-H bending is between 1640- 1550 cm-1, OH group is in the range of 3550 – 3250 cm-1 and the carboxylic group is in between 1760 – 1690 cm-1 . Thus, these results have explained that the lauric acid and chitosan is absolutely contained in the treated cotton fabric. The FTIR peaks can be referred to figure below:

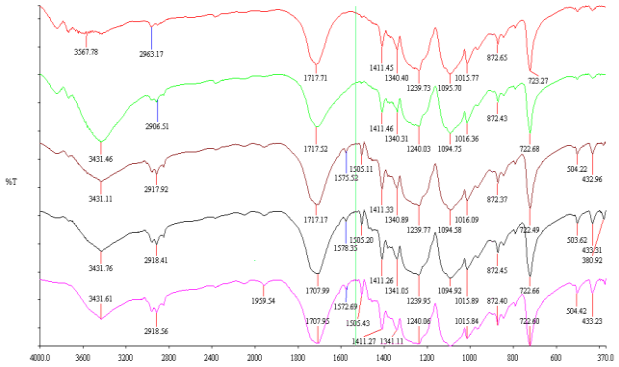

(a) Fig 2(a) Comparisons of All Peaks

CONCLUSION

The use of optimum concentration of lauric acid in the presence of chitosan will help the antimicrobial property to retain longer in the cotton fabrics. It can be seen from the antimicrobial test that shows 15% of lauric acid concentration gives a good result in accordance to inhibit the bacteria. Thus, it reveals that the optimum concentration that is suitable for the cotton fabric is at 15% after all the considerations of the cotton fabrics' property being analyzed. In addition, the SEM and FTIR analysis proposed the qualitative result of obtaining 15% of lauric acid concentration as the most suitable condition for the cotton fabric. Thus, as a conclusion, the use of lauric acid in the presence of chitosan will give the best result for treated cotton fabrics besides having the UV curing to help in retaining the antimicrobial property to the cotton fabrics.

ACKNOWLEDGEMENT

The authors would like to thank Ministry of Higher Education (MOHE) and Research Management Centre (RMC) Universiti Teknologi Malaysia, through the financial support of this work through the project number Q.J130000.2544.09H23.

REFERENCES

Berger, J., Reist, M., Mayer, J., Felt, O., Peppas, N. A. and Gurny R., (2004). Structure and interactions in covalently and ionically crosslinked chitosan hydrogels for biomedical applications. *European Journal of Pharmaceutics and Biopharmaceutics*, 57 (1), 19-34

Deepti Gupta and Adane Haile (2006). Multifunctional properties of cotton fabric treated with chitosan and carboxymethyl chitosan. *Carbohydrate Polymers*, 69, 164-171.

Gao, Y. and Cranston, R. (2008). Recent advances in antimicrobial treatments of textiles. *Textile Research Journal, 78*, 60-72. doi:10.1177/0040517507082332

Lim, S., H. and Hudson, M. (2003). Review of chitosan and its derivatives as antimicrobial agents and their uses as textile chemicals. *Journal of Macromolecular Science, C43*(2), 223- 269.

Lim, S. H. and Hudson, M, (2004a). Application of a fiber-reactive chitosan derivative to cotton fabric as an antimicrobial textile finish. *Carbohydrate Polymer*, 56, 227-234.

Sandford PA (1989). Chitin and chitosan. *London and NY: Elsevier Science Publisher*, 51-69.

Sang-Hoon Lim and Samuel M. Hudson (2004). Application of a fiber-reactive chitosan derivative to cotton fabric as an antimicrobial textile finish. *Carbohydrate Polymers*, 56, 227-234.

Siti Nur Hana Mamat, Currently doing Master in Bioprocess Engineering at Faculty of Chemical Engineering, Universiti Teknologi Malaysia, Skudai, Johor, Malaysia.

Dr. Eraricar Salleh. Senior lecturer in Department of Bioprocess Engineering, Faculty of Chemical Engineering, Universiti Teknologi Malaysia, Skudai, Johor, Malaysia

Antimicrobial Bio-plastic Incorporated with Chitosan and Extracted Chlorella sp.

Eraricar Salleh, Wan Rasna Syah Norsalehah and Siti Nur Hana Mamat
Bioprocess Engineering Department, Faculty of Chemical Engineering, Universiti Teknologi Malaysia, 81310 Skudai, Johor, Malaysia

ABSTRACT

Recently, bio-plastic has been developed as an alternative material to replace thermoplastic that had causes serious environmental pollution problem. The aims of this study are to formulate bio-plastics with different ratios of wheat starch, chitosan and Chlorella sp and characterize the bio-plastic in term of mechanical and antimicrobial properties. Incorporation of chitosan and extracted *Chlorella* sp can increase the film's antimicrobial activity and mechanical properties. The films had been formulated by blending the wheat starch, chitosan, extracted *Chlorella* sp, distilled water, glycerol and acetic acid together at 85ºC on hot plate and stirred with magnetic stirrer with 1.5 motion. The blending process was stopped when the mixture become viscous. The formulated film's ratios were 9:1:0.2, 8:2:0.64, 7:3:0.56, 6:4:0.48 and 5:5:0.40. The addition of chitosan and *Chlorella* sp had affected the film's thickness. The tensile strength increased from 2.435MPa to 7.5776MPa. It was found that the film's elongation had drop from 23.75% to 8.77%. The films showed good antimicrobial test towards *E.coli*. As a conclusion, incorporation of chitosan and extracted *Chlorella sp* can improve the film's mechanical strength to 7.5776 MPa, produced 23.75% of highest elongation at break and possess good antimicrobial properties with 1.0 cm inhibition zone diameter.

1. INTRODUCTION

The uses of plastic in Malaysia are high especially in food packaging industries. This is because plastics are needed to pack the food in order to maintain the quality and safety of food products during storage and transportation. Besides, food packaging like plastics are used to extend the shelf-life of food products by preventing them from undesired factors such as spoilage, chemical contamination, oxygen moisture, bacteria, light and also other external forces (Jong-Whan Rhim *et al*., 2013). However, the increasing of using these plastics material as food packaging can cause environmental problem not only in Malaysia but also all around the world. The problem is plastic difficult to break down. In fact, plastics take thousand years or more than that to break down. Hence, other alternative had been proposed to reduce this problem by fabricating bio-plastic as new food packaging material. The development and commercialization of bio-based plastics for a variety of uses in products and also in packaging is the great interest as manufacturers are looking for safer and healthier materials (Clara, 2011).

Before this, petroleum-based plastic materials have been widely used because they are cheap and convenient to use with good processing property, good aesthetic quality and excellent physic-chemical properties (Jong-Whan Rhim *et al*., 2013). This research is focus on the fabrication of starch-based bio-plastic incorporated with chitosan and extracted *Chlorella sp*. in order to enhance the antimicrobial properties of bio-plastic and also to improve the mechanical properties of bio-plastic. This research will use chitosan as the addition in production of bio-plastics because it is easy to manufacture and has little environmental impact (Michael Roppolo, 2014).

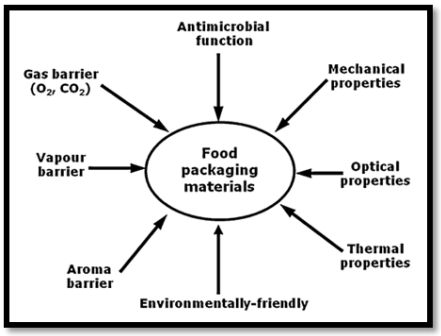

Figure 1.1: General properties for food packaging materials

Bio-plastics are plastics derived from renewable biomass sources such as vegetable fats and oils, corn starch, pea starch or microbe. The definition of bio-plastics given by European Bioplastics organization is as plastics based on renewable resources (biobased) or as plastics which are biodegradable and/or compostable. Figure 1.1 had shown the general properties that are required to create a food packaging material. As mention in the figure, a food packaging material should have antimicrobial function, good mechanical properties, good thermal properties and other important properties in order to ensure that food packaging material can extent the shelf life of product and for safety purpose.Bio-plastics are designed to biodegrade. Biodegradable bio-plastics can break down in either anaerobic or aerobic environments, depending on how they are manufactured. Biodegradable polymers are polymers that are able to undergo decomposition into CO_2, CH_4, H_2O, inorganic compounds or biomass through predominantly the enzymatic action of microorganisms. Bio-plastics products can be composed of starches, cellulose or other biopolymers. These bio-plastics products commonly apply on food packaging materials, dining utensils and insulation.

2. EXPERIMENT

The extracted *Chlorella* sp was bought from TST Bioceutical Sdn. Bhd, Ipoh, Perak, Malaysia.

2.1 Preparation and Formulation of Bio-plastic

A control starch-based film was formulated by blending wheat starch powder (5.0g), glycerol (2.5ml) and distilled water (92.5ml) together until the film's mixture become viscous. Next, second film controller namely chitosan-based film also had been formulated by blending chitosan (5.0g), distilled water (95ml) and acetic acid (5ml). Both of these control films were dried in oven with 50ºC for 24 hours.

Table 2.1: The composition of raw materials and chemical formulated in film's preparation

Film's ratio	Wheat starch (g)	Chitosan (g)	Extracted *Chlorella* sp (g)	Glycerol (ml)	Acetic acid (ml)	Distilled water (ml)
9:1:0.72	9.0	1.0	0.72	4.5	4.5	80.28
8:2:0.64	8.0	2.0	0.64	4.0	4.0	81.36
7:3:0.56	7.0	3.0	0.56	3.5	3.5	82.44
6:4:0.48	6.0	4.0	0.48	3.0	3.0	83.52
5:5:0.40	5.0	5.0	0.40	2.5	2.5	84.60

In this study, there were five different film's ratio that had been formulated with different amount of wheat starch, chitosan and extracted *Chlorella* sp. The film's ratios were 9:1:0.72, 8:2:0.64, 7:3:0.56, 6:4:0.48, and 5:5:0.40 (starch: chitosan: extracted *Chlorella* sp). The film's mixture was blended by using magnetic stirrer to ensure the mixture well-mixed. The temperature used for hot plate and motion of hot plate were 85^0C and 1.5 respectively. Stirring and heating were ended when the solution looked viscous.Then, 20ml of the viscous solution was poured into glass petri dish by using measuring cylinder for casting method. Each film's ratios had been casted for three samples. After all the films had fully dried, the films had cut into circular shape with 0.6 cm of their diameter for antimicrobial test. Besides, another cutting of films had been done but in rectangular shape with 4cm length and 1.2 cm width of the dimension. This rectangular shape of films was for mechanical test.

2.2 Film Characterization

2.2.1 Mechanical Properties of Film

Under mechanical test, there were two test involved namely tensile strength test and film's elongation at break test. Both of these tests had been used Lloyd LRX material testing machine to measure film's tensile strength and film's elongation at break. There were few parameters needed to measure for testing mechanical properties. There had been given manual guideline for using tensile tester machine. The crosshead speed, gauge length and width of films in this study were 10mm/min, 40mm and 12mm respectively.

All the film's samples need to tape at both tips with masking tape. This is to avoid fix length of film's samples from breaking during tensile test. Each film's ratios had been replicated for three times. The result for film's elongation at break was in mm unit. So, the unit of millimeter was needed to convert into percentage (%) in order to measure the percentage of elongation. The formula used to find the percentage of film's elongation at break was as below.

$$\% \text{ Elongation} = \frac{\text{Film elongation at break (mm)}}{\text{Initial gauge length of film}} \times 100\%$$

2.3 Film's Antimicrobial Activity

2.3.1 Agar Diffusion Method

Antimicrobial activity test was carried out by using agar diffusion method. Indicator cultures were *Bacillus* sp and *E.coli* that representing Gram-positive and Gram-negative bacteria. 0.1 ml of the inoculum solution was poured and spread on agar plate for both bacteria by using Hockey stick. Three film's samples for each film's ratio had been placed on the agar plate

with circular shape (0.6cm diameter). Then, all the agar plates were incubated in oven at 37ºC for 24 hours. The next day after 24 hours incubation, the inhibition zone diameter that had been produced by both bacteria had been measured by using ruler. Then, the result of film's inhibition zone diameter was average after three times replication.

3. ANALYSIS

3.1 Bio-plastic Appearance

The starch-based film obtained from this study which is one of the control films was transparent looked same as common plastic color. While the color for chitosan-based film (second control film) was yellow and the surface was a little bit rough. Next, the color of bio-plastics mixed between wheat starch, chitosan and extracted *Chlorella* sp were green. This green color came from the color of extracted *Chlorella* sp. However, the darkness of green color for the films was depending on the amount of extracted *Chlorella* sp added into the mixture. Moreover, the higher the amount of extracted *Chlorella* sp added into the mixture of film, resulted in darker the film would be. The figure of bio-plastics formulated in this study can be seen in Figure 3.1 to 3.7.The components that had been blended together in order to prepare the bio-plastic were wheat starch, chitosan, extracted *Chlorella sp*, glycerol, acetic acid and distilled water. All the components were prepared in five different ratios and had been produced by using casting method. The volume of film's mixture used for casting method was 20ml for each film's ratio. This 20ml was selected as the suitable volume due to it had produced enough thickness of films that will be used for other tests. The thickness of the films had been measured by using digital micrometer. The thickness of each film was measured at five different points. The measurement of the thickness had been averaged in millimeter unit (mm). The thickness of the films had shown in the table below.

Table 3.1: The thickness of controlled film and five different ratios of films

Film's Ratio	Average Thickness (mm)
Starch only	0.110
Chitosan only	0.133
9:1:0.72	0.106
8:2:0.64	0.101
7:3:0.56	0.114
6:4:0.48	0.125
5:5:0.40	0.107

The highest thickness of film was at film's ratio 6:4:0.48 with 0.125mm.This resulted due to there was unwell-mixed of the film's mixture during blending process. The lowest thickness was at film's ratio 8:2:0.64 with 0.101mm. This thin thickness is due to there was less than 20ml of film's mixture poured into the glass petri dish during casting method.Figure 3.1 to 3.7 shows the appearance of each film obtained from this study.

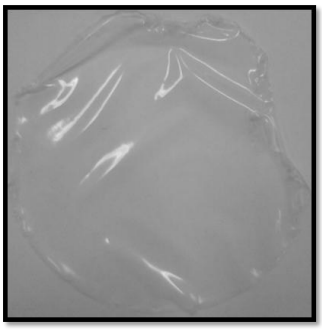

Figure 3.1: Starch-based film (controlled film)

Figure 3.2: Chitosan-based film (controlled film)

Figure 3.3: Film with ratio 9:1:0.72

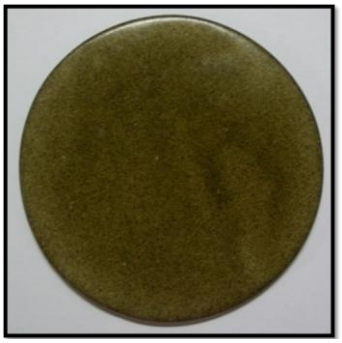

Figure 3.4: Film with ratio 8:2:0.64

Figure 3.5: Film with ratio 7:3:0.56

Figure 3.6: Film with ratio 6:4:0.48

Figure 3.7: Film with ratio 5:5:0.40

3.2 Tensile Test of Bio-plastic

Tensile test was done to identify the tensile strength of the films that had been formulated in this study. Tensile strength is one of the important tests under mechanical properties. Mechanical properties is refers to the measurement of tensile strength of the certain material, but in this study, we only focusing in the strength of the films. Mechanical properties are very important for packaging material in order to avoid any leakage, contamination from outside and also to know at what load the plastic can defend. As mention by Pitak *et al*., (2007), mechanical properties of packaging material can reflect the ability of it to maintain good integrity of certain product. Figure 3.8 below shows the effect of formulated different ratio of films toward the tensile strength of films. Chitosan-based film (control film) showed the highest tensile strength with 24.044MPa. This result is due to chitosan-based film produced higher stiffness of film's surface compared to the others formulated films.

S:C:CH as written on the Figure 3.8 was actually refer to the ratio of S-starch, C-chitosan and CH-extracted *Chlorella* sp. Other than that, based on the five formulated ratios, 5:5:0.40 film's ratio had produced highest tensile strength with 7.5776MPa. While, 9:1:0.72 film's ratio had gained lowest tensile strength with 2.435MPa. From the ratio itself, the lower amount of starch, higher amount of chitosan and lower amount of extracted *Chlorella* sp, resulted in the highest tensile strength of film.

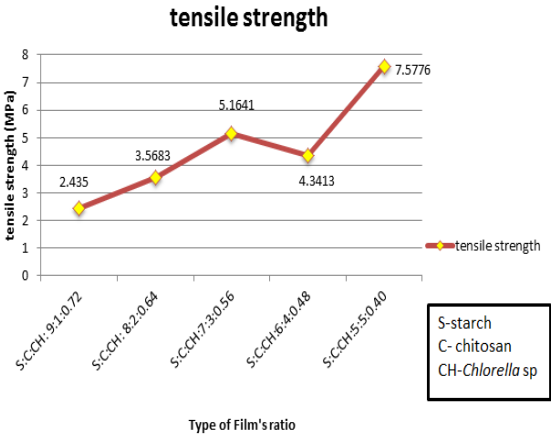

Figure 3.8: Effect of formulated different ratio of starch, chitosan and Chlorella sp. toward film's tensile strength

Besides, starch-based film that also as a control film in this study showed the lowest tensile strength if compared with the others films. The appearances of starch-based film were very soft and elastic. That is the reason for starch-based film produced very weak tensile strength with only 1.1884MPa. If high amount of starch added into film's mixture, the film will become more elastic but not strong or less tensile strength.However, the tensile strength of new formulation films by blending different ratio of starch, chitosan and extracted *Chlorella sp* did not high as chitosan-based film's tensile strength. The highest tensile strength is 7.5776MPa that had been produced by film at ratio 5:5:0.40. Furthermore, the amount of chitosan added into film's mixture should be higher in order to increase the film's tensile strength. But too highest amount of chitosan added was not efficient due to chitosan will affect the film appearance by producing lack elasticity film. So, film ratio 5:5:0.40 was the maximum ratio that yield good and highest film's tensile strength.

In order to apply these formulated films as food packaging material, the films should be strong enough

to resist heavy load or to avoid any leakage occur. Thus, the main reason on why the formulated films produced lower tensile strength if compared with the control film is because most of the films are flexible and brittle. The brittle of films also causes by the existing of bubbles of the film surface during preparation of films.The existing of bubbles on the film's surface causes the films easy to break. The resulted of poor tensile strength due to the present of air bubbles can be reduce by adjusting suitable temperature and motion (speed) of rotation during blending the film's mixture.

3.3 Film's Elongation at Break

Elongation at break is for analyze the elasticity of formulated films. More elasticity the films, means more time taken for the films to break at 10mm/min of crosshead speed. Figure 3.9 shows the effect of formulated different film's ratio toward film's elongation at break. From the figure, it shows decreasing in elongation at break of the films. Based on Figure 3.9, film with ratio 8:2:0.64 had produced longest elongation at break.

The reason was due to this type of film have highest elasticity among the other type of film's ratio. The elongation of film was shown in percentage measurement. Film's ratio 8:2:0.64 gives 23.75% of elongation at break which means it taken longest time to break at 10mm/min crosshead speed.

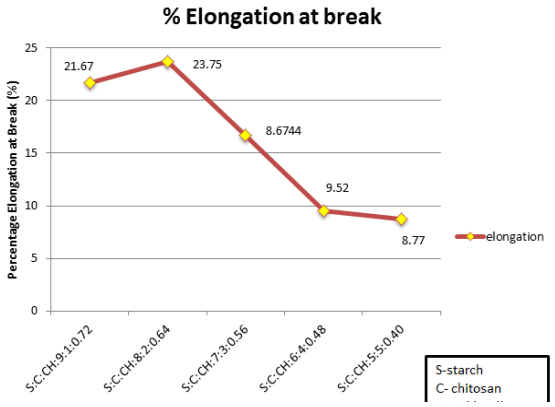

Figure 3.9: Effects of formulated different ratio of starch, chitosan and *Chlorella sp*. toward film's elongation at break

The percentage of two control films namely starch-based film and chitosan-based film shows 5.54% and 17.82% respectively in elongation at break. From the result, new formulated film with different ratio of them had produced better percentage of elongation at break than the control's elongation at break.

The higher amount of starch, lower amount of chitosan and higher amount of extracted *Chlorella* sp incorporated into film's mixture, resulted in higher percentage of elongation at break. More elastic the film, more time taken for it to elongate at 10mm/min crosshead speed during mechanical test. High content of amylose in starch had provided strong, flexible films which were thermally stable up to 180ºC. Starch itself was very brittle and has poor mechanical properties for plastic applications. However, by blending starch with glycerol, it can improve in elongation at break especially.

3.4 Antimicrobial Property of Bio-plastic

One of the purposes of this study is to analyze the antimicrobial activity of two different bacteria namely *E.coli* and *Bacillus* sp toward different film's ratios. The main factor in applying this bio-plastic as food packaging is to ensure it can prevent microbial contamination (Jong-Whan Rahim *et al*.,2013). In this study, agar plate had been used to test the antimicrobial activity of bacteria toward the films. This agar diffusion method was done as the mimic of food surface that will be inhibited by the bacteria. *E.coli* and *Bacillus* sp that had been spread on the agar plate had been incubated at 35ºC for 24 hours in incubator. Both of these bacteria had represented the Gram-negative and Gram-positive bacteria. The Table 3.2 below shows the result of antimicrobial activity test. The result of average inhibition zone diameter as tabulated in Table 3.2 had been charted into bar chart as shown in Figure 3.10.

Table 3.2: Average Inhibition Zone Diameter for *E.coli* and *Bacillus sp* toward different film's ratios

Film's ratios	Average Inhibition Zone Diameter (cm)	
	E.coli	*Bacillus sp*
Starch only	0.70	0.65
Chitosan only	0.93	0.70
9:1:0.72	0.77	0.70
8:2:0.64	0.73	0.83
7:3::0.56	0.80	0.0
6:4:0.48	0.90	0.0
5:5:0.40	1.00	0.0

As mention in the legend above, the blue bar chart is for *E.coli* inhibition zone diameter and the red bar chart is for *Bacillus* sp inhibition zone diameter. Based on Figure 3.10 above, antimicrobial activity of *E.coli* had shown positive test and good inhibition zone diameter toward the formulated films. *E.coli* had shown inhibition zone diameter for all the control films and five different film's ratio, but not for *Bacillus sp*. The highest inhibition zone diameter was 1.00 cm produced by 5:5:0.40 film's ratio and the initial diameter of cutting films (sample) that put on the agar plate was 0.6 cm. At film ratio 7:3:0.56,

6:4:0.48 and 5:5:0.40, *Bacillus* sp did not produce any inhibition zone area toward the films. *Bacillus* sp had growth on the film's sample but it shown negative test antimicrobial activity toward the film's samples.

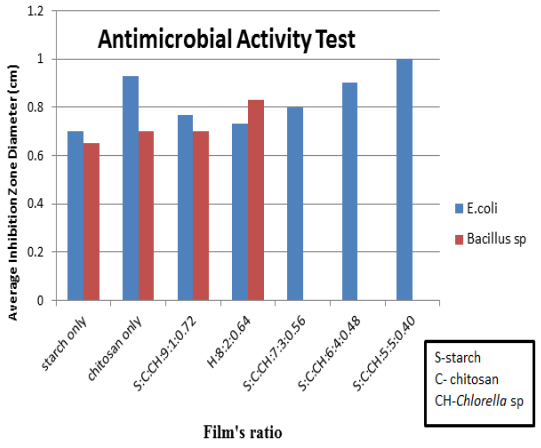

Figure 3.10: The result of inhibition zone inhibit by *E.coli* and *Bacillus sp* toward different film's ratios

Film ratio at 5:5:0.40 was contained higher amount of chitosan in this study and *E.coli* had shown good inhibition zone toward it. This means the higher amount of chitosan added into the film's mixture, the higher inhibition zone diameter produced. Chitosan is non-toxic (Kean and Thanou, 2010) and biodegradable polymer (Bagheri-Khoulenjani *et al.*, 2009) with antimicrobial activity whereby these qualities are important for food packaging purpose (Cruz-Romero *et al.*, 2013).Besides, the incorporation of extracted *Chlorella sp* into film's mixture also had affected the antimicrobial activity of films. *Chlorella sp* contains methanolic and hexanolic that can enhance the antimicrobial property of the bio-plastic (Ghasemi *et al.*, 2007).

CONCLUSION

In conclusion, bio-plastics were successful formulated at five different ratios namely 9:1:0.72, 8:2:0.64, 7:3:0.56, 6:4:0.48 and 5:5:0.40. The bio-plastics were in green color due to the color of extracted Chlorella sp added into the film's mixture. Based on the result of tensile test, the strongest tensile strength had been produced by film ratio 5:5:0.40 with 7.5776MPa. Film's tensile strength was increased due to the increasing of film's roughness. While the highest percentage of film's elongation at break was produced by film's ratio 8:2:0.64 with 23.75%. Elongation at break had decreased due to the decreasing of film's elasticity. E.coli had performed positive test toward antimicrobial test and it had produced highest inhibition zone diameter at film's ratio 5:5:0.40 with 1.0 cm. Overall, incorporation of chitosan and Chlorella sp into bio-plastic had improve film's mechanical and antimicrobial properties.

NOMENCLATURES

S:C:CH : Starch: chitosan: Chlorella sp

REFERENCES

Bagheri-Khoulenjani, S., Taghizadeh, S.M., & Mirzadeh, H. (2009). An investigation on short-term biodegradability of chitosan with various molecular weights and degrees of deacetylation. Carbohydrate Polymers, 78(4), 773-778.

Clara Rosalia Alvarez-Chavez. (2011). Sustainability of bio-based plastics: gereneral comparative analysis and recommendations for improvement. Journal of Cleaner Production. 23(2): 47-56.

Cruz-Romero, M.C., Murphy, T., Morris, M., Cummins, E., & Kerry, J.P. (2013). Antimicrobial activity of chitosan, organic acids and nano-sized solubilisates for potential use in smart antimicrobially-active packaging for potential food applications. Food Control, 34(2), 393-397.

Ghasemi Pirbalouti, A., Roshan Chaleshtori, A., Tajbakhsh, E., Momtaz, H., Rahimi, E., and F. Shahin (2009). Bioactivity of medicinal plants extracts against Listeria monocytogenes isolated from food. J. Food. Agric. Environ. 7, 132-135.

Jong-Whan Rhim, Hwan-Man Park, Chang-Sik Ha. (2013). Bio-nanocomposites for food packaging applications.

Kean, T., & Thanou, M. (2010). Biodegradation, biodistribution and toxicity of chitosan. Advanced Drug Delivery Reviews, 62(1), 3-11.

Michael Roppolo. (2014). Environmentally-friendly bioplastic created from shrimp shells. CBS News. (2014, May 8).

Pitak N., Rakshit S.K. (2007). Physical and antimicrobial properties of banana flour/chitosan biodegradable and self- sealing films used for preserving Fresh-cut vegetables. LWT-Food Science and Technology. 44,2310-2315.

Dr. Eraricar Salleh. Senior lecturer in Department of Bioprocess Engineering, Faculty of Chemical Engineering, Universiti Teknologi Malaysia, Skudai, Johor, Malaysia.

Siti Nur Hana Mamat, Currently doing Master in Bioprocess Engineering at Faculty of Chemical Engineering, Universiti Teknologi Malaysia, Skudai, Johor, Malaysia.

A PRACTICAL APPLICATION OF TEMPERATURE CYCLE ENHANCED-DERACEMIZATION: A NOVEL METHOD COMBINED WITH A RACEMIZATION REACTION AND A PREFERENTIAL CRYSTALLIZATION

Kittisak Suwannasang[a], Gérard Coquerel[b], Céline Rougeot[b], and Adrian E. Flood[a,*]
[a]School of Chemical Engineering, Suranaree University of Technology, Thailand
[b]Normandie Université, Crytal Genesis Unit SMS EA3233, Univerité de Rouen, France
***Corresponding author: E-mail adrianfl@sut.ac.th**

ABSTRACT

An effective route to achieve a pure enantiomer from a racemic mixture has been developed. This current work shows that an ordinary deracemization process is able to be made more efficient by using a series of temperature cycles and a simultaneous in-situ racemization in solution combined with a preferential crystallization. The implementation of this process is very easy. Seeding of a small amount of the pure enantiomorph at the beginning of the process is able to initiate the symmetry breaking, where the system can move away from the racemic state, leading to a swift occurrence of an autocatalytic phenomenon. That makes the combined process require a short time for operation to achieve an enantiopure solid state. It also guarantees that the desired enantiomorph will be the product. This combined process can also be made more efficient by monitoring the temperature profile during the operating period. As a result, the crystalline outcome of the combined process, which has a purity > 99% *e.e.*, can be obtained within a few hours. Moreover, the novel process can achieve 100% yield of the desired enantiomer based on the total amount of the solute existing in the crystal phase of the suspension.

INTRODUCTION

Many molecules of biological significance, for instance amino acids and sugars, potentially exist as a pair of enantiomers. Chiral molecules are very important in pharmaceutical products and production, since in biological systems the two enantiomers will have very different properties due to the presence of the other chiral materials in the body. In many cases one of the two enantiomers may have very good therapeutic or pharmaceutical effect, whereas the second enantiomer may be inert, or even toxic. This makes it necessary to produce many products in enantiomerically pure form – the active enantiomer must be separated essentially completely from the other form. Unfortunately, the physical and chemical properties of both enantiomers are identical in the absence of any chiral materials, excepting the value of the optical rotation. This makes it very difficult to separate enantiomers via traditional separations used in the chemical process industries.

Among the variety of methods of enantioseparation, a special crystallization process named preferential crystallization (here-after PC) is an important one to obtain a pure enantiomer (Levilain & Coquerel, 2010). PC is a direct crystallization for resolution of a racemic solution if the compound crystallizes as a conglomerate – a mixture of pure enantiomeric crystals. This method is an effective and also a cost productive technology for enantioseparation, but its production yield is limited at 50%.

In 2005 a counterintuitive method for breaking the symmetry of racemic mixtures of enantiomeric crystals, called Viedma ripening, was shown by Cristobal Viedma (Viedma, 2005). He demonstrated the effect of grinding on breaking the symmetry of sodium chlorate crystals – an achiral substance in solution but which forms optically active crystals. This method allows the process breakthroughs regarding the limitation of the production yield. This process also obtains single crystals of only one enantiomer. The extension of Viedma ripening to organic compounds is possible if the compound crystallizes as a conglomerate, and if the compound can be racemized in the liquid phase. Several studies have successfully deracemized organic materials using the grinding method after the demonstration of Viedma ripening (Noorduin, et al., 2008 a; Noorduin, et al., 2008 b; van der Meijden, et al., 2009; Noorduin, et al., 2009; Levilain et al., 2009).

Recently, a novel method of deracemization of an organic compound was proposed by our group (Suwannasang, et al., 2013). This new method is the use of a series of temperature cycles to create the phenomena of dissolution and re-crystallization

resulting in the conversion of one of the enanatiomorphs to the other enantiomorph in the crystal phase assuming that there is racemization in the solution phase. In a previous article we demonstrated that this is not due to grinding. The temperature cycling technique is one of the effective options for the deracemization process due to its easy implementation which provides ease of process scaling up. The product obtained from this method has an enantiomeric excess (*e.e.*) of more than 99% (starting from 0% *e.e.*) at high production yield. However, the time required for the system to reach the single-handedness solid state is quite long. As a consequently, the technique of temperature cycles was then combined with the ordinary PC with, in addition, a swift racemization reaction in the solution phase. This combination method is expected to be a productive process for enantioseparation, having an operating time shorter than the time required for the conventional deracemization process. Moreover, the product obtained from this process would have high purity and its production yield would be more than 50%.

METHODS

Material

A racemic mixture of 4,4-dimethyl-1-(p-toluyl)-2-(1H-1,2,4-triazol-1-yl)pentan-3-one (**1**) was synthesized in the SMS laboratory at the University of Rouen, according to Rougeot (Rougeot, 2012). The chemical structure of **1** is shown in Fig.1. Distilled water was used for all experiments. HPLC-grade n-heptane and ethanol, and reagent-grade methanol were purchased from Fisher Scientific.

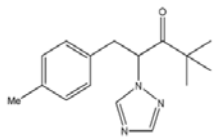

Figure 1. Chemical structure of 1.

Experimental Procedure

1.8 g of **1**, 25 g of methanol/water mixture (65/35 %wt), and 0.2 g of NaOH (racemizing agent) were chosen as a standard mixture. The excess amount of **1** crystal was stirred in the mixed solvent under racemization at the saturation temperature overnight. The suspension was filtered using a preheated glass-filter. The solution was held at a temperature higher than the saturated temperature for 5 min in order to prevent nucleation. The solution was cooled down to 20°C with a cooling rate of 10°C/45min. After the solution had reached the saturation temperature, 10 mg of pure crystals (seed) was introduced into the solution. The application of temperature cycles was begun after the suspension reached 20°C. A loop of temperature cycles consisted of four steps; holding at 20°C for 5 min, heating to the top temperature with a heating rate 2 °C/min, holding at the top temperature for 5 min, and cooling to 20°C with a cooling rate 10°C/45min. A profile of the temperature cycles is depicted in Fig.2.

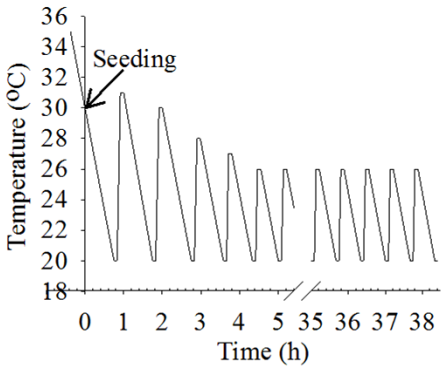

Figure 2. A series of temperature cycles versus time.

Analysis

The *e.e.* was monitored by chiral HPLC. Samples were taken at the end of cycles (at 20°C) using a plastic pipet. The solid was then filtered under a vacuum and washed with a sufficient amount of water to remove the rest of the sodium hydroxide (the solubility of **1** in water at 20°C is lower than 0.1%wt). A small amount of solid (ca 5 mg) was then dissolved into 1 mL of ethanol. A 20 µL sample of this solution was injected into a Chiracel OD column (250 × 4.6 mm) using a solution of 5 %vol ethanol in n-heptane as eluent at a flow rate of 1.5 mL/min. The two enantiomers were detected at retention times of ca 8 and ca 10 min using UV detection at a wavelength of 227 nm.

Enantiomeric Excess in the Crystal Phase

Enantiomeric excess *(e.e.)* in the crystal phase is defined in terms of the predominant enantiomer at the end of the experiment, depending on the form of the seed crystals used.

$$e.e. = \left[\frac{m_R - m_S}{m_R + m_S}\right] \times 100\%$$

where m_i represents the mass of component *i*. In the above definition the pure *R*-form is considered as +100% *e.e.*

RESULTS

Three preliminary experiments were conducted to investigate the ability of each process in producing single enantiomer crystals of the desired enantiomer. The first experiment was carried out using an ordinary preferential crystallization (PC mode) with no racemization in solution and no temperature cycles. The second experiment was carried out similarly to Exp.1, excepting the presence of racemization in the solution phase (PCR mode). The third experiment is the combination of PC and temperature cycling while racemization occurs in the solution phase. A series of temperature cycles was applied to the system after the PC period (PCRT mode). Experimental results of these three operating modes are depicted in Fig.3.

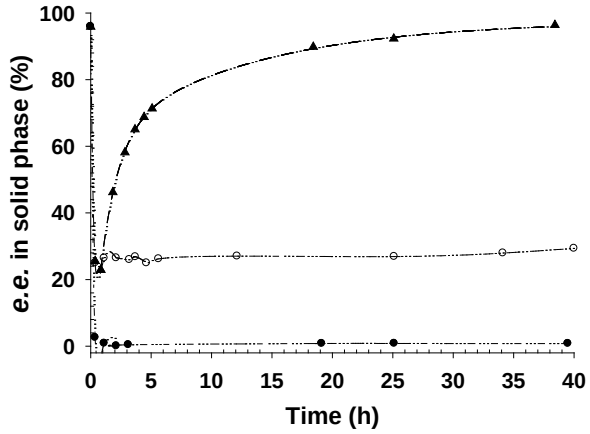

Figure 3. Evolution of *e.e.* versus time. ● Exp. 1 – PC mode, ○ Exp. 2 – PCR mode, ▲ Exp. 3 – PCRT mode (PC combined with temperature cycles and racemization).

The experimental results of Exp.1 show that after seeding the pure crystals of the designed enantiomer to the solution both enantiomers reached their saturation state - the nucleation is apparently dominant in the system rather than the entrainment effect via the preferential crystallization, decreasing the enantiomeric excess in the solid phase. The product obtained from this prototype is an equal amount of the two enantiomorphs. After operating with PC mode, the evolution of *e.e.* in solid phase does not change away from 0%. However, we can use the ordinary PC to separate two enantiomers via a kinetic resolution as in the traditional implementation of PC where pure enantiomorph product was collected before reaching the induction time of the undesired enantiomorph. It is also significant that the production yield of the ordinary PC mode is limited at 50% in theory.

A racemization reaction was then introduced into the system in order to allow the conversion of the unwanted enantiomer to the desired form as experimentally demonstrated in Exp.2 (PCR mode). The result of PCR mode indicates that racemization reaction in the solution phase affects the evolution of *e.e.* in the solid phase. During the cooling period, the enantio-pure seeded crystals had grown by consuming its supersaturation in solution. Thanks to racemization in the solution, the un-desired enantiomer was converted to the desired form. This conversion of the two enantiomers decreases the supersaturation of the unwanted form while operating the PC mode, decreasing the amount of primary nuclei of the undesired enantiomer. Unfortunately, there was no increase of the *e.e.* after the preferential crystallization period even through the stirrer still operated. Hence, it would be concluded that the grinding from the stirrer is not responsible for raising the *e.e* in solid phase even if a swift racemization is still present in the isothermal solution phase.

To improve the enantio-resolution process, PCRT mode was then designed. Using of a series of temperature cycles in order to create the phenomena of dissolution and re-crystallization was expected to be an effective technique for raising the *e.e*. in the solid phase after operating the ordinary PC. Experiment 3 was then carried out. The result of PCRT mode is depicted in Fig.3. The *e.e.* was obviously increased after using a series of temperature cycles in comparison with the result of Exp.2. It can be concluded that a single-enantiomorph crystalline state can be achieved via the application of temperature cycles to the system. A series of temperature cycles is effective to convert the undesired enantiomorph to the desired enantiomorph through the process of dissolution, re-growth and the entrainment effect as we described in our previous article (Suwannasang, et al., 2014). Thanks to a swift racemization in solution, the system can move over the limitation of yield and the primary nucleation of the un-desired enantiomer would also be suppressed. Furthermore, the PCRT mode is a simple process which is easy to implement, and it is still more effective to produce enantiopure crystals with high production yield.

CONCLUSION

The combination of temperature cycles with preferential crystallization in the presence of a swift racemization in solution is effective to produce enantiomerically pure crystals. The main phenomena which are responsible for this PCRT process are dissolution, crystallization, and the entrainment effect. Thanks to the initial seeding of enantiopure crystals, the PCRT process has a time required to reach a single handedness state that is significantly shorter than the conventional deracemization process. This combined process is possible to scale up due to the fact it is easy to implement and has high productivity.

ACKNOWLEDGMENT

This work was supported by the Thailand Research Fund (TRF) in collaboration with Suranaree University of Technology (SUT) through the Royal Golden Jubilee Ph.D. Program (PHD/0219/2551).

REFERENCES

Levilain, G., Coquerel, G., Pitfalls and rewards of preferential crystallization, *CrystEngComm*, vol. 12 (7), pp. 1983-1992, 2010.

Viedma, C., Chiral Symmetry Breaking During Crystallization: Complete Chiral Purity Induced by Nonlinear Autocatalysis and Recycling, *Phys. Rev. Lett.*, vol. 94 (6), pp. 065504-1, 2005.

(a) Noorduin, W. L., Izumi, T., Millemaggi, A., Leeman, M., Meekes, H., Van Enckevort, W. J. P., Kellogg, R. M.; Kaptein, B., Vlieg, E., Blackmond, D. G., Emergence of a Single Solid Chiral State from a

Nearly Racemic Amino Acid Derivative, *J. Am. Chem. Soc.* vol. 130, pp. 1158-1159, 2008.

(b) Noorduin, W. L., Meekes, H., van Enckevort, W. J. P., Millemaggi, A., Leeman, M., Kaptein, B.; Kellogg, R. M., Vlieg, E., Complete Deracemization by Attrition-Enhanced Ostwald Ripening Elucidated, *Angew. Chem., Int. Ed.*, vol. 47, pp. 6445-6447, 2008.

van der Meijden, M. W., Leeman, M., Gelens, E., Noorduin, W. L., Meekes, H., van Enckevort, W. J. P., Kaptein, B., Vlieg, E., Kellogg, R. M., Attrition-Enhanced Deracemization in the Synthesis of Clopidogrel - A Practical Application of a New Discovery, *Org. Process Res. Dev.*, vol. 13, pp. 1195-1198, 2009.

Noorduin, W. L., Kaptein, B., Meekes, H., van Enckevort, W. J. P., Kellogg, R. M., Vlieg, E., Fast Attrition-Enhanced Deracemization of Naproxen by a Gradual In Situ Feed, *Angew. Chem., Int. Ed.*, vol. 48 (25), pp. 4581-4583, 2009.

Levilain, G., Rougeot, C., Guillen, F., Plaquevent, J.-C., Coquerel, G., Attrition-enhanced preferential crystallization combined with racemization leading to redissolution of the antipode nuclei, *Tetrahedron: Asymmetry*, vol. 20 (24), pp. 2769-2771, 2009.

Suwannasang, K.; Flood, A. E.; Rougeot, C.; Coquerel, G., Using Programmed Heating–Cooling Cycles with Racemization in Solution for Complete Symmetry Breaking of a Conglomerate Forming System, *Crystal Growth & Design,* vol. 13 (8), pp. 3498-3504, 2013.

Rougeot, C., Deracemisation of active compound precursors by physical treatments, Ph.D. Thesis, *University Paul Sabatier of Toulouse III, Toulouse, France,* 2012.

Suwannasang, K.; Coquerel, G.; Rougeot, C.; Flood, A. E., Mathematical Modeling of Chiral Symmetry Breaking due to Differences in Crystal Growth Kinetics, *Chemical Engineering & Technology*, vol. 37 (8), pp. 1329-1339, 2014.

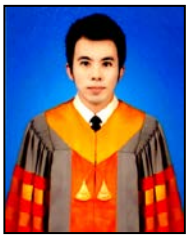

Kittisak Suwannasang received the B. Eng. (2009, First Class Honors), degrees in Chemical Engineering from Suranaree University of Technology (SUT), Thailand.

He is a Ph.D. student, School of Chemical Engineering, SUT. His current interests include enantiopurification, deracemization, and industrial crystallization.

Adrian E. Flood received the B.E. (1990), degrees in Chemical Engineering from the University of Sydney and Ph.D. (1996) from the University of Queensland, Australia.

He is a Professor, School of Chemical Engineering, SUT. His Current interests include separation of molecules of pharmaceutical interest and industrial crystallization.

Gérard Coquerel has made his whole academic career at the University of Rouen. He started first to specialize in inorganic chemistry and then in solid state chemistry of organic components.

He is a Professor at the University of Rouen, France and a corresponding member of the French National Academy of Pharmacy. His main research activities are focused on chirality, resolution of chiral molecules and deracemization, phase diagram determinations, molecular recognition, polymorphism, solvates and desolvation mechanisms, nucleation and crystal growth of molecular compounds.

Céline Rougeot received the Ph.D. (2012), degree in Chemistry from the University Paul Sabatier, Toulouse-France.

She is a postdoctoral researcher, Chez University of California, Marced

Adsorption and Isosteric heat studies for adsorption of fluid on porous silica glass using GCMC simulation

N. Ketprasoet, C. Nimjaroen, C. Tangsathitkulchai and A. Wongkoblap
School of Chemical Engineering, Suranaree University of Technology
Nakhon Ratchasima 30000, Thailand

ABSTRACT

In this study, the simulation for the adsorption of carbon dioxide (CO_2), nitrogen (N_2) and argon (Ar) on porous silica glass are presented. Porous glass represents an important adsorbents because of its high thermal stability and chemical resistance. The Grand Canonical Monte Carlo (GCMC) simulation method is used to investigate the adsorption behavior of different fluid on porous glass model. The molecular model of glass is assumed to be composed of SiO_4 crystal and the atoms in it are laid in different planes. The adsorption isotherm and isosteric heat obtained by GCMC are presented and compared against the experimental data for CO_2 and N_2 adsorptions. An early onset in adsorption isotherm can be observed in the case of small pore width. The adsorption capacity depends on temperature, it increases by decreasing temperature. The adsorption of argon in larger pore is different from those of nitrogen and carbon dioxide, where the capillary condensation cannot be observed. The adsorption isotherms and heat of adsorption for polar and non-polar fluids are qualitatively different, due to its quadruple moment.

1. INTRODUCTION

The development of new advanced adsorbents for gas separation processes using adsorption technology has been of significant interest to scientists and engineer. However, these materials need to be characterized for a wide variety of gases. The interesting in porous glass was investigated, because these materials have a high thermal, mechanical, and chemical stability.

Molecular simulation method have been used to investigate the microscopic properties of confined fluid in nanopores of different geometries for a long time. For the purpose of modelling, silica pores can be assumed to be either parallel-walled of slits or simple cylinder pores with smooth or structureless walls. Nevertheless, in reality, porous silica glass are amorphous. However it is found in the literature that the simple pore model can be used to describe the adsorption behavior on porous glass quite well (Xiaoning and Xiaopeng, 2006).

Characterization of porous solids using adsorption has traditionally been conducted by comparing isotherms from experiment and theory. This can provide valuable information about adsorbents and their interactions with the adsorbates used. However, isotherms can be insensitive to some of the features of the adsorbents properties, meaning that they can be hard to elucidate using isotherms alone. Therefore an additional property such as heat of adsorption should be taken into account (Birkett & Do, 2008). In this paper we investigate the adsorption isotherm and heat of adsorption behavior for a simple model of porous silica glass, the finite-length slit pore with SiO_4 crystal. The common adsorbates used for characterization are CO_2 N_2 and argon which were used in this study too.

In this work, we construct a highly mimetic model of porous silica glass to show the adsorption behavior of single component, CO_2, N_2 and Argon in different pore widths. In section 2, the mimetic model of porous glass and the fluid model are described, followed by simulation methodology for adsorption. In section 3, the experimental results for CO_2 and N_2 adsorptions are presented first and then the effect of pore width and that of different fluid on adsorption behavior will be discussed. Concluding remark are summarized in section 4.

2 Model and method

2.1 Preparation of porous glass and Experimental measurement

In this study, porous glass was prepared from coal fly ash. The heat treatment conditions of prepared porous glass were operated at temperature of 650°C and treatment time of 20 hours, the detail procedure was found in the literature (Nimjaroen et al., 2009). While experimental measurement of adsorption CO_2 was performed by using Intelligent Gravimetric Analyzer (IGA). The number of pressure points were specified and the measurement of the adsorbed amount at equilibrium for a given temperature. And adsorption N_2 was carried out by BET analyzer where represent adsorption isotherm, BET area and pore volume of porous glass.

2.2 Fluid model

In this study, CO_2 is modeled as a 3-center-Lennerd-Jones (LJ) molecule having LJ interaction site on the atom and point charge to account for the quadrupole moment proposed by Harris and Yung (1995). The C-O bond length and O-C-O bond angle are fixed at the experimental value of 1.16Å and 180°, respectivety. The parameter set for the CO_2 force field is listed in Table 1.

The N_2 force field consists of three site. Each nitrogen atom is modeled as Lennard-Jones site separated by the bond length of 1.10Å. The Lennard-Jones parameters for these sites are listed in Table 1. The gas-phase quadrupole moment of N_2 (Jeffrey and Siepmann, 2001) was produced by point charges of -0.482 *e* on each Lennard-Jones site. To maintain charge neutrality, a point charge of +0.964 *e* was placed at the center of mass (COM) of N_2 molecule.

Argon is modelled as a spherical Lennard-Jones particle (Maddox et al., 1995).

Table 1 Lennard-Jones Parameters and Partial Charge

Site	ε/k_b [K]	σ [Å]	q [e]
C (in CO_2)	28.129	2.757	+0.6512
O (in CO_2)	80.507	3.033	-0.3256
N (in N_2)	36.0	3.31	-0.482
COM (in N_2)	0.0	0.0	+0.964
Argon	119.8	3.410	0.0
O (in silica)	2.708	185	-0.36
Si (in silica)	0.0	0.0	+0.18

Where ε and σ are the energy well depth and the collision diameter, respectively. k_b is the Boltzman's constant, q is the point charge on each site. A cut-off radius of five time the collision diameter of fluid is used in this study. The interaction energy between fluids is calculated using the Lennard-Jones 12-6 equation (Do et al., 2003).

$$U_{ij}(r) = 4\cdot\varepsilon_{ij}\cdot\left[\left(\frac{\sigma_{ij}}{r}\right)^{12} - \left(\frac{\sigma_{ij}}{r}\right)^{6}\right] \qquad (1)$$

Where *r* is the separation distance. Beside the interaction between two LJ sites, the interaction between two charges should be taken into account for polar molecules of CO_2 and N_2. The interaction between two charges, each of which is on different molecule, takes the form of a Coulomb law of electrostatic interaction.

$$\varphi_{ij}(r) = \frac{1}{4\cdot\pi\cdot\varepsilon_0}\cdot\frac{q^i\cdot q^j}{r^{ij}} \qquad (2)$$

Where ε_0 is the permittivity of free space, r^{ij} is the distance between two charges *i* and *j*.

2.3 Solid model

The solid model used in this study is the SiO_4 crystal which formed tetrahedral structure, a silicon atom is at the center of a tetrahedron and the four oxygen atom are positioned at the vertices of the tetrahedron. These four sites represent the dispersive sites and have negative charge -0.36 *e* while the positive charge of +0.18 *e* is that of silicon atom (Burchart et al., 1992). The molecular parameter of SiO_4 used in this study are ε_{ss}/k_b of 185.0K, σ_{ss} of 2.708Å (He and Seaton, 2003) and the angle of O-Si-O about 147° (Calero et al., 2004). Two layers of crystal are stacked on each other with the pore width (H). The configuration of the solid model is represented in Figure 1. The length of porous silica has linear dimension of 40Å in x and y directions.

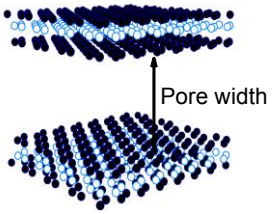

Figure 1 The porous silica model with SiO_4 crystal structure

2.3 Monte Carlo simulation

In this study, the Grand Canonical Monte Carlo (GCMC) simulation was used to investigate the adsorption isotherm and isosteric heat of adsorption on porous silica. The volume of the simulation box (i.e. pore volume), the chemical potential and the temperature of the system are specified to obtain the adsorption equilibrium. One GCMC cycle consists of one thousand displacement move and attempts of either insertion or deletion with equal probability. For an adsorption branch of the isotherm 30000 cycles are typically needed for the system to reach equilibrium, and additional 30000 cycles are used to obtain ensemble average, we use an empty box as the initial configuration, and the simulation is carried out until the number of particle in the simulation box does not change (in statistical sense). The pressure of the bulk gas corresponding to a given chemical potential are calculated form the equation of state proposed by Johnson et al. (1993). Isosteric heat of adsorption and pore density (adsorption capacity) were evaluated by equation 3 and 4, respectively.

$$q_{st} = \frac{\langle U\rangle\cdot\langle N\rangle - \langle U\cdot N\rangle}{\langle N^2\rangle - \langle N\rangle\cdot\langle N\rangle} + k\cdot T \qquad (3)$$

$$\rho = \frac{N_{inside}}{V_{pore}} \qquad (4)$$

Where *U* is energy of configuration, *N* is number of particle and < > is defined as an average.

3. Results and Discussion

3.1 Experimental results

The adsorbed amount versus relative pressure (P/P_0) for N_2 adsorption in porous silica glass derived from coal fly ash at 77K are present in Figure 2. The adsorption isotherm show type IV isotherm (type II with hysteresis loop) indicting that the adsorbent is dominantly mesoporous.

It is seen that the porous glass mostly composed of mesopores (87.6%), average pore size is 38 Å and its total pore volume is 0.293 cm^3/g. In the chemical composition of prepared porous glass in our laboratory consist of SiO_2 of 70% and AlO_2 of 10%. Therefore, we choose the structure of SiO_2 as the solid model in our simulation.

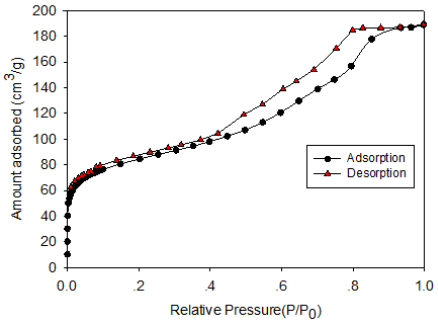

Figure 2 N_2 adsorption isotherm at 77K of prepared porous glass.

Furthermore, the adsorption isotherm of CO_2 obtained for porous glass at 283, 293 and 303K are shown in Figure 3. The same behavior can be observed, the experimental data show a gradual increase in that of isotherm at low pressure. The adsorption capacity decreases when the temperature increases. Indicating that the adsorption of CO_2 in porous silica is physical adsorption.

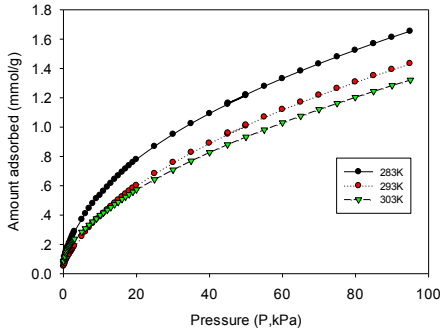

Figure 3 CO_2 adsorption isotherm at 283, 293 and 303K of prepared porous glass.

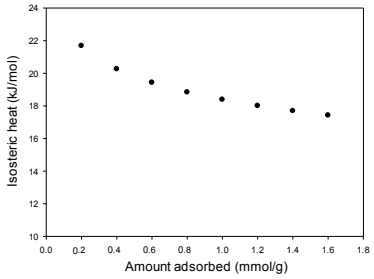

Figure 4 Isosteric heat of CO_2 adsorption of porous glass

The effect of CO_2 adsorption loading on the isosteric heat of adsorption is numerically obtained from Van't Hoff equation and its plot is shown in Figure 4. It is observed that the heat of adsorption decrease continuously with increasing CO_2 loading, and there is a tendency to approach a constant value at high loading. The heat adsorption is high initially owing to be strong interaction between the adsorbate molecule and the surface adsorption sites. At higher surface coverage, however, weak dispersive forces among adsorbate molecules start to play an important role, thus releasing less amount of heat of adsorption. The slow decrease of heat of adsorption with increased surface loading could result from the large value of permanent quadruple moment of CO_2 that could promote additional interaction with the polar surface of porous glass by electrostatic contribution.

3.2 GCMC simulation results

The simulation isotherm versus pressure for CO_2 at 283K, N_2 at 77K and Argon at 87.3K in porous silica of various pore width (from 10-60 Å) up to saturation pressure obtained by GCMC method, are shown in Figures 5, 6 and 7, respectively. While the isosteric heat of adsorption with loading for CO_2, N_2 and Ar are also shown in Figures 8, 9 and 10, respectively.

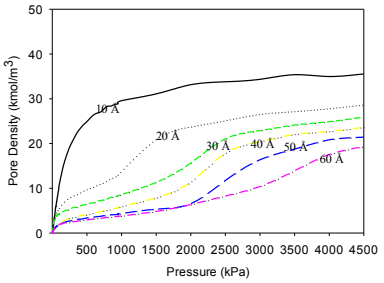

Figure 5 Simulation results of CO_2 in porous silica at 283K

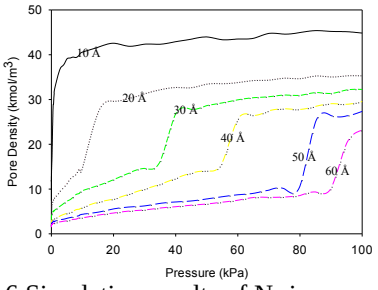

Figure 6 Simulation results of N_2 in porous silica at 77K

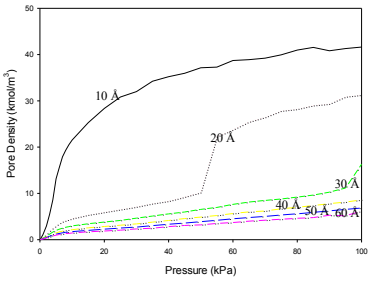

Figure 7 Simulation results of Argon in porous silica at 87.3K

The simulation isotherms of CO_2, N_2 and argon in the porous silica model show the single layer of particles in the pore width of 10Å. The maximum capacity at saturation condition decreases with increasing in pore widths. This may be due to the packing effect that leads to the difference in maximum density in each pore. For CO_2 adsorption in pore larger than 10 Å, CO_2 can form a monolayer along the pore wall and then the additional layer next to the monolayer, however the capillary condensation cannot be observed which differs from that observed for nitrogen and argon. In contrast for argon adsorption at pore larger than 30Å (see Figure 7), the surface affinity is very low the pore is not filled, even when the pressure approaches saturation vapour pressure. This phenomenon has been observed previously in the literature where weak adsorption occurs, for example, Thommes et al. (2002) found the argon adsorption in controlled pore glass (CPG) and Zukal (2006)

found the adsorption of krypton in silica. The effects of the surface affinity are also reflected in the plots of isosteric heat versus loading, where higher heat is observed for the stronger interaction between fluid and surface, especially in the sub-monolayer coverage region. At higher loadings, the heats are about the same, and this is due to that fluid–fluid interaction is dominant at high loadings.

The isosteric heat for CO_2 and N_2 is initially high and then decreases with loading which is the contribution of the fluid-solid interaction including the electrostatic force between charges. The isosteric heat obtained from simulation agrees well with the experimental result. However in the case of argon, the isosteric heat is less than those for CO_2 and N_2 and it increases with loadings until reaches the maximum and then decreases. At high loadings for all fluids, the isosteric heat becomes constant and close to the heat of liquefaction.

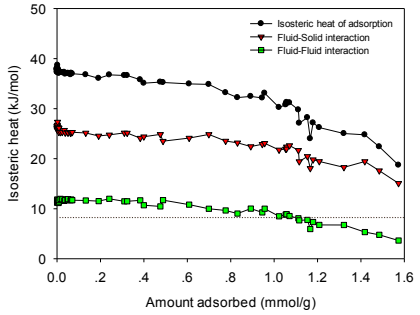

Figure 8 Isosteric heat of CO_2 adsorption using GCMC simulation

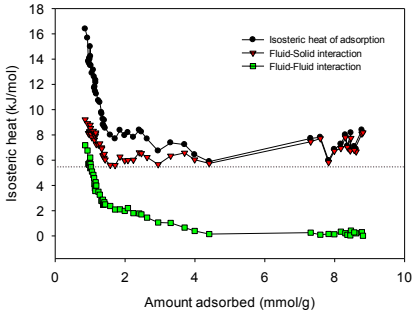

Figure 9 Isosteric heat of N_2 adsorption using GCMC simulation

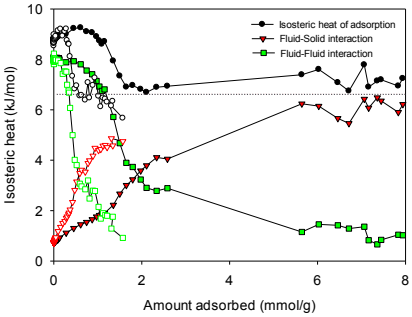

Figure 10 Isosteric heat of Argon adsorption using GCMC simulation at pore width 20 (filled symbols) and 50Å (unfilled symbols)

The CO_2 and N_2 adsorption from GCMC simulations were used to determine the pore size distribution (PSD). The total pore volume of 0.3064 cm^3/g obtained for CO_2 adsorption at 273K is quite closed to that of 0.2787 cm^3/g obtained for N_2 adsorption at 77K. The combined isotherm obtained from PSD of both CO_2 and N_2 are plotted against the experimental data and they are satisfied as shown in Figure 11 for CO_2 adsorption.

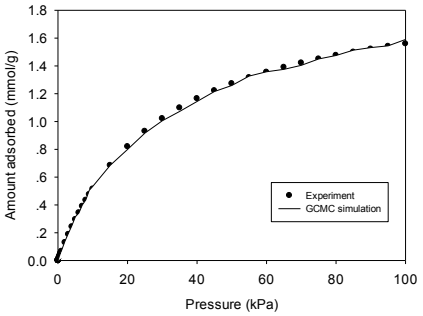

Figure 11 PSD for CO_2 adsorption

Conclusion

We have studied adsorption isotherm and heats of adsorption of CO_2, N_2 and argon in porous silica model. The adsorption behavior depend on the pore width. The quadruple moment of fluid affects the adsorption in porous silica glass.

Acknowledgement

We acknowledge School of Chemical Engineering and Institute of Research and Development, Suranaree University of Technology for financial support.

Reference

Birkett, G.R., and Do, D.D., Langmuir, 24, 4853-4856, 2008.

Burchart, E. D., Vandegraaf, B., Vogt, E. T. C., J. Chem. Soc., Faraday Trans., 88, 2761, 1992.

Calero, S., Dubbeldam, D., Krishna, R., Smit, B., Vlugt, T.J.H., Denayer, J.F.M., Martens, J.A., Maesen, T.L.M., Journal of the American Chemical Society. 126(36), 11377-11386, 2004.

Do, D.D. and Do, H.D., Adsorption Science & Technology, 21(5): 389-423, 2003.

Harris, J.G., Yung, K.H., Journal of Physical Chemistry. 99(31), 12021-12024, 1995.

He, Y. and Seaton, N.A., Langmuir, 19, 10132-10138, 2003.

Jeffrey, J,P. and Siepmann J.I., AIChE Journal, , Vol. 47, No. 7, July 2001.

Johnson, JK. Zollweg, JA. Gubbins, KE, Molecular Physics, 78(3), 591-618, 1993.

Maddox M., Ulberg D. and Gubbins K.E., Fluid Phase Equilibria, 104145-158 , 1995.

Nimjaroen C., Morimoto S., Tangsathitkulchai C., Journal of Non-Crystalline Solids, 355 (34-36, 1737-1741), 2009.

Thommes, M., Kohn Froba, R.M., Appl. Surf. Sci., 196 ,(1–4), 239–249, 2002.

Xiaoning Yang, Xiaopeng Yue, Colloids and Surfaces A: Physicochem. Eng. Aspects 301, 166–173, 2007.

Zukal, A., Microporous Mesoporous Mater., 92 , (1-3), 220–226, 2006.

An effect of part height, cross-sectional area and building time to part orientation base on 3D printing technology

Paphakorn Pitayachaval*Payungsak Junyusen and Aphichet Konkham

School of Industrial Engineering, Institute of Engineering, Suranaree University of Technology,

AmphurMuang, NakhornRatchasima 30000

Tel : 0-4422-4264 E-mail: paphakorn@g.sut.ac.th

Abstract

Rapid prototyping technology (RP) is a technology to construct prototype layer by layer directly from a computer file (CAD model). To minimize construction time and volume of material, a part orientation is determined before constructing model. However, the prefer orientation has be related to a number of layers, a volume of support material and a construction time. This paper presents the experiments that provide those relationships. The results shown that the relationship between constructing time, part height and cross-sectional area were a linear function. Furthermore, the part orientation directly affected to the part height, the number of layers and the volume of support material.

Key words: Rapid Prototyping technology (RP), Part orientation, Cross-sectional area, Support material

1. Introduction

Rapid prototyping process is a manufacturing process that manufactures products directly from CAD model without mold and die. It was introduced to shorten prototype construction time. This process converts a 3D CAD model to be a stack of 2D contours which are used to generate machine commands to build an object layer by layer. In this process, material is added to produce a part layer by layer. Several techniques have been developed for rapid prototyping process and they can be classified into 3 categories based on the initial state of materials [1] liquid-based, solid-based and powder-based. Stereolithography apparatus (SLA), a popular technique in a liquid-based system, is the first commercial rapid prototyping system. In this technique, UV laser is used to solidify photo-curable liquid polymer to form layers. Selective Laser Sintering (SLS) is a famous technique in a powder-based rapid prototyping system. This technique is similar to SLA but instead of curing liquid polymer with UV laser, CO_2 laser is used in SLS to sinter powder to form a layer. Similarly, 3D printing is also a popular technique in a powder-based rapid prototyping system. Besides using UV laser, glue had been applied. Last group of rapid prototyping system is solid-based. In this group, there are several types of solid material used including wire, roll of laminated sheet and pellets. Popular techniques of this group are Laminate Object Manufacturing (LOM) and Fused Deposition Modelling (FDM) [2]. For RP technique development, there are four issues base on process step such that the STL File modeling, a model slicing analysis, a tool path planning of RP process and an part orientation analysis.

STL file has been introduced as a neutral format to converse 3D CAD models to be ready for use in rapid prototyping. The STL file presents 3D solid model as the surfaced model patched by triangular facets. Although the STL file has been used in RP process, it has some disadvantages such as data redundancy and several defects [3]. So, the direct slicing from 3D CAD model and engineering drawing had been introduced [4], [5]. (Jamieson and Hacker, 1995).

Staircase effect, actually, is an inherent error of layer manufacturing that can be reduced by using smallest thickness. However, if this solution is applied to all layers, fabrication time is increased significant. To improve model accuracy while minimizing prototype construction time, an adaptive slicing concept and an adaptive direct slicing concept have been proposed to slice a model with non-uniform thickness in which the first concept is for slicing STL model while the second concept is for slicing CAD model directly. (Sabourin *et al.*, 1996; Hope *et al.*, 1997a, b; Zhao and Laperriére, 2000).[6]

A tool path planning is also an research issue to minimize RP processing time in which TSP had be applied to identify the optimize tool path [7].

Additionally, a part orientation has been investigated in order to identify a support structure and a creating time [8]. An appropriate part orientation can be presented the optimum cost according to a consuming raw material for support structure, use to create RP model.

In order to explore an effect of part height, cross-sectional area and building time to part orientation, this paper presents experiments in which part height and cross-sectional area are fix variables while a building time is dependent variable by using 3D printing technology. A model has been oriented into six direction base on Cartesian axes.

2. Literature Review

Part deposition orientation is very important factor of layered manufacturing as it effects build time, support structure, dimensional accuracy, surface finish and cost of the prototype[9-11] Figure 1 shows determination of build-up orientation. Minimise stairstepping effect. Minimise support structure. Minimise number oflayers by variable thickness. The amount of the base material and high quality.

Defect	Build-up orientation	
	Optimised	Non-optimised
Minimise stairstepping effect		
Minimise support structure		
Minimise number of layers		

Figure 1Determination of build-up orientation. Minimise stairstepping effect. Minimise support structure. Minimise number oflayers by variable thickness [9]

An analysis of the orientation part in the optimum direction has been studied by various researchers.[10-16]This research describes a method for determining the minimum oriented bounding box for arbitrary solid. The method simplifies a complex-dimensional problem by projecting the solid onto three principal planes and makes use of the projected contour for analysis.[10] Subsequent research describes a method of Artificial Neural Network (ANN) is used to determine the optimum solution. Predictions of the present methodology are in agreement with the results published earlier. The methodology proposed in this work is used to obtain the optimum part deposition orientation automatically and can be implemented in FDM technology.[11] The determine the optimal part orientation that improves the average weighted surface roughness (AWSR) generated from the stair stepping effect [12]In addition to an algorithm to determine the build orientation is described. It considers the deposition process attributes and the machining process attributes simultaneously.[13]

3. Experiment

To identify the effect of part height, cross-sectional area and building time to part orientation, experiments have been separated into two groups by using 3D printing technology. The first group is to establish the relationship between constructing time, part height and cross-sectional area. The second experiment is to present the relationship between a volume of support material and the part constructing time in any direction base on an assumption that a raw material created RP model is constant in any building direction. These experiments have been conducted base on 3D Printing Machine can build part maximum sized 8x8x12 inch.

3.1 The relationship between constructing time, part height and cross-sectional

The first experiment group, the relationship between constructing time, part height and cross-sectional area has been classified base on variables such that the part height and cross-sectional area are fix variables while the constructing time is dependent variable. Thus, the experiments have been conducted into two sets: 1) the part height is varied while cross-sectional area is constant and 2) the cross-sectional area is change while part height is constant, as follow a table 1. A simple box has been used to present this experiment due to its constant cross-sectional area, as shown in figure 2.

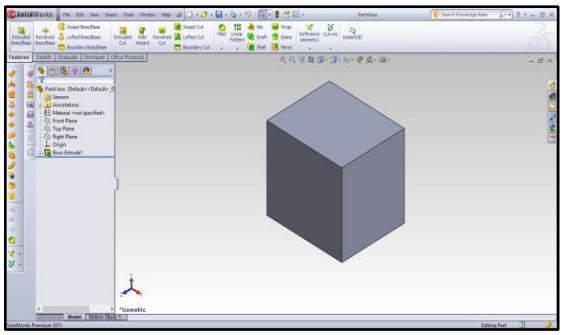

Figure 2: A simple box

Table 1: Two sets of the first experiment group

Experiment Set	Part Height	Cross-sectional area
1	Vary	Constant
2	Constant	Vary

3.2 The relationship between a volume of support material and the part constructing time

The second experiment group, the relationship between a volume of support material and the part constructing time in any direction has been investigated. Base on an assumption that a raw material created RP model is constant in any building direction, a model, as shown in figure 3, has been orientated into six postures following six directions of Cartesian axes.

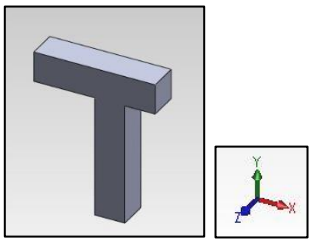

Figure 3: A 3D model for the section experiment

4. Results

4.1 The relationship between constructing time, part height and cross-sectional

There were two sets of experiment results: 1) the part height was varied while cross-sectional area was constant and 2) the cross-sectional area was change while part height was constant.

When the part height was increase, a number of layers and a volume of model were also enlarge, as shown in table 2. On the other hand, when the cross-sectional area was expanded, a number of layers and a volume of model were also enlarged, as shown in table 3. Therefore, the constructing time (T) has the linear relationship with the function of the part height (h) and cross-sectional area (a), as following equation 1.

$$T \ \alpha \ f(h,a) \qquad (1)$$

Table 2: The result of constructing time when the part height was varied while cross-sectional area was constant

Part Height ($x10^{-3}$m)	Cross-sectional area ($x10^{-6}m^2$)	Number of layers	Part volume (m^3)	Support volume (m^3)	Time (s)
5	10x10	200	$4.92x10^{-4}$	$1.64x10^{-4}$	240
10	10x10	400	$9.83x10^{-4}$	$1.64x10^{-4}$	420
15	10x10	600	$1.31x10^{-3}$	$1.64x10^{-4}$	600
20	10x10	790	$1.80x10^{-3}$	$1.64x10^{-4}$	780

Table 3: The result of constructing time when the cross-sectional area was expanded while part height was constant

Part Height ($x10^{-3}$m)	Cross-sectional area ($x10^{-6}m^2$)	Number of layers	Part volume (m^3)	Support volume (m^3)	Time (s)
5x5	10	400	$3.28x10^{-4}$	0	240
10x10	10	400	$9.83x10^{-4}$	$1.64x10^{-4}$	420
15x15	10	400	$1.97x10^{-3}$	$3.28x10^{-4}$	600
20x20	10	400	$3.44x10^{-3}$	$4.91x10^{-4}$	840

4.2 The relationship between a volume of support material and the part constructing time

The results of volume of support material and the part constructing time in any direction were presented as table 4. There results shown that the part orientation directly affected to the part height, the number of layers and the volume of support material. Moreover, the volumes of support material seem to relate the part constructing time even thought there was not a linear relationship.

Table 4: The results of volume of support material and the part constructing time in any direction

Orientation	Number of layer	Part volume(m^3)	Support volume(m^3)	Time(s)
	990	$9.83x10^{-4}$	$1.64x10^{-3}$	1980
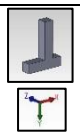	990	$9.83x10^{-4}$	$1.64x10^{-4}$	600
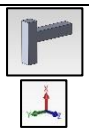	790	$9.83x10^{-4}$	$8.19x10^{-4}$	1080
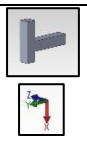	790	$9.83x10^{-4}$	$6.56x10^{-4}$	840
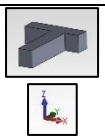	200	$9.83x10^{-4}$	$3.28x10^{-4}$	420
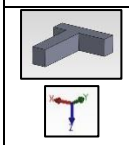	200	$9.83x10^{-4}$	$3.28x10^{-4}$	420

5. Conclusion

The relationship between constructing time, part height and cross-sectional area were linear function. When the part height was increase, a number of layers and a volume of model were also enlarge. Additionally, when the cross-sectional area

was expanded, a number of layers and a volume of model were also enlarged. Further, the volume of support material relate to the part constructing time, in which the part orientation directly affected to the part height, the number of layers and the volume of support material.

6. Acknowledge

This research has been supported by the research and development supporting fund, Suranaree University of Technology.

7. Reference

[1.] Bullinger, H.-J., J. Warschat, and D. Fischer, *Rapid product development—an overview.* Computers in industry, 2000. **42**(2): p. 99-108.

[2.] Pham, D. and R. Gault, *A comparison of rapid prototyping technologies.* International Journal of Machine Tools and Manufacture, 1998. **38**(10-11): p. 1257-1287.

[3.] Kai, C.C., G.G.K. Jacob, and T. Mei, *Interface between CAD and Rapid Prototyping System. Part1: A study of existing interfaces* International Journal of Advance Manufacturing Technology, 1997. **13**: p. 566-570.

[4.] Kumar, V. and D. Dutta, *An assessment of data formats for layered manufacturing.* Advances in Engineering Software, 1997. **28**(3): p. 151-164.

[5.] Soonanon, P. and P. Koomsap, *Towards direct transformation of orthographic-view drawings into a prototype.* Virtual and Physical Prototyping, 2009. **4**(2): p. 75-90.

[6.] Cao, W. and Y. Miyamoto, *Direct slicing from AutoCAD solid models for rapid prototyping.* The International Journal of Advanced Manufacturing Technology, 2003. **21**(10-11): p. 739-742.

[7.] Paphakorn Pitayachaval and Thanakarn Baothong, A tool path planning of rapid prototype technology base on a contour relationship. Journal of engineering Ubon ratchathani university No. 1 Vol. 6 January-June 2556, 2556: page 61-69.(in Thai)

[8.] Guo, K.B., et al., *Boolean operations of STL models based on loop detection.* The International Journal of Advanced Manufacturing Technology, 2006. **33**(5-6): p. 627-633.

[9.] Hur, J. and K. Lee, *The development of a CAD environment to determine the preferred build-up direction for layered manufacturing.* The International Journal of Advanced Manufacturing Technology, 1998. **14**(4): p. 247-254.

[10.] Chan, C. and S. Tan, *Determination of the minimum bounding box of an arbitrary solid: an iterative approach.* Computers & Structures, 2001. **79**(15): p. 1433-1449.

[11.] Karim, K.F., et al., *FEATURE-BASED SUPPORT GENERATION FOR OPTIMUM PART DEPOSITION ORIENTATION IN FDM.* ARPN Journal of Engineering and Applied Sciences, 2006. **9**.

[12.] Byun, H.-S. and K.H. Lee*, *Determination of the optimal part orientation in layered manufacturing using a genetic algorithm.* International journal of production research, 2005. **43**(13): p. 2709-2724.

[13.] Hua, Z., K. Leea, and J. Hurb, *Determination of optimal build orientation for hybrid rapid-prototyping.* Journal of Materials Processing Technology 130–131 (2002) 378–383, 2002.

[14.] Ziemian, C. and P. Crawn III, *Computer aided decision support for fused deposition modeling.* Rapid Prototyping Journal, 2001. **7**(3): p. 138-147.

[15.] Kumar Chalasani, S.I., Minneapolis,USA., S. Larry Jones, Cincinnati,USA., and S.I. Larry Roscoe, Minneapolis,USA, *Support Generation for Fused Deposition Modeling.* 1995: p. 229-241.

[16.] Huang, X., et al., *Sloping wall structure support generation for fused deposition modeling.* The International Journal of Advanced Manufacturing Technology, 2008. **42**(11-12): p. 1074-1081.

Basic Science

Beeswax harvested from the abandoned nests of the Asian cavity bees, *Apis cerana*

Ratchakon Chankhai[1],Pimpisa Jansamut[2],Preecha Rod-im[3]Sasitorn Suwannathep[4],Nongnat Phoka[5],Kanteera Soontharapirakkul[6], Orawan Duangphakdee[7]

[1,2,3]*Department of Natural Resource Management, School of Bioresources and Technology, King Mongkut's University of Technology Thonburi 126 PrachaUthit Rd, ThungKhru, Bangkok 10140, Thailand*

[4]*School of Liberal Arts, King Mongkut's University of Technology Thonburi, 126 PrachaUthit Rd, ThungKhru, Bangkok 10140, Thailand*

[5,6,7]*King Mongkut's University of Technology Thonburi, Ratchaburi Campus,Rang Bua, ChomBueng, Ratchaburi 70150, Thailand*

[1]rj_ko@hotmail.com, [2]pimpisa.jan@gmail.com, [3]preecha.rod@hotmail.com, [4]sasitorn.suw@kmutt.ac.th, [5]nongnat.pho@kmutt.ac.th, [6]kanteera.soo@kmutt.ac.th, [7]orawan.dua@kmutt.ac.th

ABSTRACT

Nest desertion by absconding or migrating colonies is a common adaptive feature of tropical honeybees relative to the non-suitable environments. Absconding behaviour of honey bees *Apis cerana* occurs when the movement of an entire colony away from its parental nest site. Generally, before the colonies take off to the new nest sites, foragers will load up honey into their crop for the sources of energy and have left the empty comb with some death brood in the old frames. In this study, beeswax was harvested from 30 absconded colonies of Asian cavity honeybees, *Apis cerana* from 4 apiaries in Chumphon and Ratchaburi Province, Thailand. Age of colony was 4.03±1.19 months (range, 1-6 months) and each colony consisted of 5.57±0.01 frames (range, 3-8 frames).Abandoned frames were molten in double boiler and filtrated through the filtration fabric. Yields of beeswax was 25.24±11.74% (range, 1.66-46.90%). The standard chemical and physical properties of beeswax were then analyzed based on Kenya, Ethiopian and European standards. All beeswax qualified to 6 standard characteristics which are melting point: 64.03±0.50^{o}C (range, 63.3-64.7^{o}C), specific gravity: 0.97±0.02 (range, 0.94-0.98), acid value: 15.97±4.72 mg (range, 10.60-21.62mg), saponification value: 92.06±4.90 (range, 85.83-95.62), ester value: 76.09±6.24 mg (range, 67.76-82.73mg) and passed the test off at and fatty acid. However, 1 of 6 samples shown peroxide value beyond standard. And 4 of 6 samples shown acid value lower than standard. This study demonstrated that beeswax harvested from natural abandoned nests is high quality and qualified to beeswax standards. This will help farmer to benefit from bees despite severe losses of bee colonies and can further be used for value added.

Keywords: Absconding, Honeybees, Abandoned nest, *Apis cerana*, Beeswax

1.INTRODUCTION

The cavity-nesting honeybee *Apis cerana* is found throughout in Asia. It occurs from India, through Southeast Asia, to Indonesia and Philippines and from China to Japan(P de La Rúa, et al., 2000).In Thailand, usually keep in Chiang Mai, Khon Kaen, Chanthaburi, Nakhon Si Thammarat, Chumphon and Surat Thani Thailand (Bureau Agricultural Commodities Promotion and Management, 2006),beekeeping with *Apis cerana* is increasing among beekeepers because local honey bees are more resistant to many pathogens than are European bees. Currently, there are about 600 beekeepers and more than 500 colonies in Thailand. However, the Asian cavity bees *Apis cerana* have high absconding rate 65-80% (Radloff. et al., 2011) in rainy season. The defection of bee hive in Asian cavity bees *Apis cerana* is an ordinary behaviour which is the movement of a whole colony of honeybees. There are two types of absconding, seasonal absconding which is escapade due to resource reduction and declining nest site quality, and disturbance absconding caused by natural disturbance, for example, fires, floods and *earthquakes.* Other *disturbances,* caused by anthropogenic and intervention by beekeepers (Hepburn and Radloff, 2011). After the colonies take off to the new areas, the empty combs were abandoned. The abandoned combs consist of beeswax which is the secretion of wax by the honeybees worker that related to the wax gland complexes (Cassier and Lensky, 1995).The comb colour turn from white to yellow, dark brown and black finally. The dark colour of old combs is the result from the larvae excrements and pupae skins. The old combs become lower the wax about 46-49% (Bogdanov, 2009).We use quality standard of beeswax to determine the characteristic of beeswax. Generally, beeswax have been use for candles, arts, cosmetics, food processing and medical. Therefore, beeswax from Asian cavity bees *Apis cerana* will help beekeepers to usefulness from abandoned combs although losses of bee colonies and used for value added. The objective of the present work was to determine the characteristics of beeswax in the term of yield in different ages of comb and analyze the quality standard of beeswax according to European, Ethiopian and Kenya standard.

2.EXPERIMENT

2.1 Samples and beeswax extraction

Abandoned combs of *Apis cerana* colonies were collected from 30 colonies from 4 apiaries in Chumphon and Ratchaburi provinces during February to August 2014. Beeswax were melted in a boiling water (beeswax: water ratio, 1:1), then melted beeswax were filtered through wire mess and filtration

fabric respectively (Whatman TM Cat No.1001-125) to eliminated all debris and dust.

2.2 Determination the chemical and physical properties of beeswax.

Thirty samples of abandoned combs were grouped into 6 groups according to coloration of the wax. Six beeswax samples were randomly selected for physical and chemical analysis. Beeswax were determined according to European Food Safety Authority, 2007, Ethiopian Standard 2005 and Kenya Standard, 2013 (Annex 2011). Total 6 Characteristics were analyzed; melting point, specific gravity at 20 ºC, acid value (mg KOH/g beeswax, saponification (mg KOH/g beeswax), ester value (mg KOH/g beeswax), peroxide value (mg H_2O_2/1000 g beeswax) and fats and fatty acids. The commercial beeswax (Suksapanpanit store) was used as control.

3. ANALYSIS

3.1 The physical properties of beeswax from abandoned frames.

The 30 samples abandoned combs were collected during February to August 2014by *Apis cerana*'s beekeepers in Chumphon and Ratchaburi Provincse. Total of 30 colonies consisted of 5.57±0.01frames (range, 3-8 frames). The combs colour range from white, yellow to brown and some were infested with wax moths. This coloration varies from the position of frame in the colony (N=6) of which number 1 was a newly built comb of white-yellow wax colour to number 6 has dark brown (Fig.1). The dark colour of old combs caused by bees 's larvae excrements and residues of wax moth (Bogdanov, 2009).

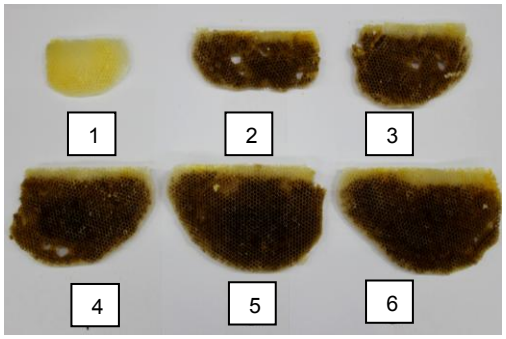

Fig.1 Abandoned frames of *Apis cerana*. Frame arranged most recent built frame located near the nest entrance (no.1) to the oldest frame located at most inside of the hive (no. 6).

Total weight of comb was 222.72±140.37 g (range, 68.82-711.03 g) which was 25.24% (48.17±27.07 g) of beeswax extracted (range, 1.66-46.90%). Yields increased regarding to the developmental stage of colony. Yield was approximately 86-100% for the newly build comb (comb no. 0-1) and decreased to 60% in comb no. 2 to 10 combs and then yield has decreased to 49% of 6-10 combs (Krivtsov and Lebedev, 1995). The average weight of residues was 166.58±119.42g (range, 36.55-596.63g) which was 3 times more than beeswax yield (48.17±11.74g). In addition, the yield of beeswax was significant lower in the wax moth infested comb. The reduction of beeswax yields affected by wax moth pervasive peats of honeybee colonies, that eat and destroy beeswax. After the female wax moth entering the hive and laid eggs in the abandoned combs. The eggs hatch in 3 days and developed to larvae. They begin to eat the wax, make a tunnel through and destroy the comb cells, spins and grow progressively in attacking neighbourhood combs until adult they will leave the hive (Tsegaye et al., 2014). Wax moth eat and destroy beeswax was effected to yields and quality of beeswax, while the residues fiber and dust was left. Moreover, old combs contained less wax and more protein (Bogdanov, 2009).

The 6 types of coloration of beeswax was shown in Fig. 2. Sample 1 was extracted from 1 month old comb with 5 frames. Sample 2 was extracted from 3 months old comb with 6 frames. Sample 3 was extracted from 4 month old comb with 5 frames. Sample 4 and 5 were extracted from 4 month old comb with 6 frames. Sample 6 was extracted from 6 month old comb with 6 frames. The dark colour of combs was caused by larvae excrements and pupae skins. Colour of beeswax depends on the age of comb. However, white commercial beeswax from Suksapanpanit store (control) were bleached for removed protein, residues and dark colour.

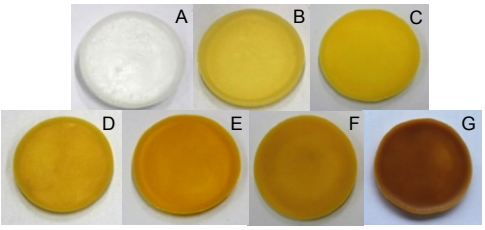

Fig. 2 Colour of beeswax (A= commercial beeswax (control), B= sample 1, C= sample 2, D= sample 3, E= sample 4, F= sample 5, G= sample 6)

3.2 The chemical properties of beeswax from abandoned frames.

Table 1 Properties of beeswax

characteristic	sample								standard		
	control	1	2	3	4	5	6	*A. mellifera**	European	Kenya	Ethiopia
Melting point (°C)	69.7^{b}	63.3^{a}	64.5^{a}	64.0^{a}	64.7^{a}	64.0^{a}	63.7^{a}	52-66	62-65	62-66	61-66
Specific gravity	0.89^{a}	0.97^{b}	0.98^{b}	0.96^{b}	0.97^{b}	0.94^{b}	0.98^{b}	-	0.96	095-0.96	0.95-0.98
Acid value[1]	3.54^{a}	21.75^{d}	13.25^{bc}	10.6^{b}	15.78^{bc}	12.84^{bc}	21.62^{d}	4.1-7.5	17-24	17-24	17-24
Peroxide value[2]	1.15^{a}	1.15^{a}	1.39^{a}	1.62^{a}	2.46^{a}	0.8^{a}	11.82^{b}	-	<5	-	-
Saponification value[3]	70.95^{a}	97.62^{a}	95.90^{a}	88.05^{a}	85.83^{a}	95.57^{a}	89.38^{a}	44.6-83.3	87-104	88-102	85-105
Ester value[4]	82.99^{a}	75.87^{a}	82.65^{a}	77.45^{a}	70.05^{a}	82.73^{a}	67.76^{a}	46.6-76.6	-	70-79	63-84
Fat and Fatty acid	pass	pass	pass	pass	pass	pass	pass	-	-	pass	pass
Ages of comb	-	1	3	4	5	5	6				
Number of frame	-	5	6	5	5	4	6				

Note:^{abcd}significant at the 95% confidence level,[1]unit of acid value was mg KOH/g beeswax,[2]Peroxide value was mg H_2O_2/ kg beeswax,[3]Saponification value was mg KOH/g beeswax, [4]Ester value was mg KOH/g beeswax and *Jyothi, 2006

3.2.1 Melting point

Melting point of beeswax sample was 64.03±0.50°C (range, 63.3-64.7°C) which was qualified to the standard. The melting point of commercial beeswax (control) was 69.7°C and significant higher than beeswax samples ($P \leq 0.05$) (Table 1). The melting points are usually expressed as a range between when the material begins to melt and when it has completely melted (Fessenden and

Feist, 2000) and were used to determine the type, purity and identification of solids in the material. Beeswax comprises hundreds of chemicals in at least nine principal compound families (Aichholz and Lorbeer, 1999) i.e. fatty acids and wax esters. Normally, pure compounds characteristically have a stable or sharp melting range for changed solid to liquid compound onset of melting occurring to end point 0.5-1^{o}C, while impure compounds have a broader melting range onset of melting occurring to end point more than 0.5-1^{o}C.Our beeswax samples had melting range approximately 0.5^{o}C revealed that it was a relative pure in composition. However, beeswax with higher melting points possibly contained relatively higher amounts of saturated compounds, polar compounds and higher molecular weight compounds or all threes (Buchwald et al., 2008).

3.2.2 Specific gravity

The specific gravity of beeswax sample was 0.97±0.02 (range,0.94-0.98). Specific gravity of all 6 beeswax samples were qualified to the standard. The specific gravity of commercial beeswax was 0.89 which was significant lower than our beeswax samples (Table 1). Generally, specific gravity is the ratio of a substance's density to the density of water. Substance is lighter than water it will have a specific gravity less than 1.0. While substances with a specific gravity greater than 1.0 will be heavier than water. In the case of beeswax with high residue and dust, will have the specific gravity more than 1.0 and could possibly drown to water. However, our specific gravity of beeswax sample was range 0.94-0.98 which lighter than water. The commercial beeswax was purified with bleaching by acid (citric acid or oxalic acid), hydrogen peroxide solution, potassium permanganate and sun bleaching (Bogdanov, 2009). The purification processes could be effect to destroy components(saturated compounds, polar compounds higher molecular weight compounds) of beeswax. While the components of beeswax was destroyed that effect to the mass of beeswax which was factor of density in a commercial beeswax.

3.2.3 Acid value

The acid value of beeswax was 15.97±4.72 mg (range, 10.60-21.62 mg). The result shown the significant difference ($P \leq 0.05$) between commercial beeswax and studied samples. Beeswax sample 1 and 6 qualified to the standard. Acid value indicate of free fatty acid content in fat and oil. The lower the acid value of oil is the better the quality than the higher one (Zhang et al. 2015). Acid value defined as the number of mg of potassium hydroxide required to neutralize the free acid in 1g of fat, fatty oil or other related substances to assess the rancidity. Beeswax sample which had acid value lower than standard (no 2-5) were probably have the higher content of saturated fatty acid such as palmitic acid and tetra-cosanoic acid (Buchwald et al., 2009). Normally, beeswax consists of long chain fatty acids 85% which most of saturated fatty acid (Kuznesof, 2005) that difficult to decomposed by hydrolysis reaction. However, acid value of beeswax samples were not significantly to standard.

3.2.4 Peroxide value

The peroxide value of beeswax was 3.21±4.26 mg (range, 0.08-11.82 mg). The result shown the peroxide value were not significant between commercial beeswax and studied samples (Table 1). Peroxide value of 5 beeswax samples were qualified to the standard but sample 6 was higher than standard (Fig. 2). The peroxide value in wax determine the amount of fats and oils that are oxidized, and lead to rancidity. The higher peroxide value referred to low quality of beeswax (Wannahari and Nordin, 2012). The larvae excrements and residues as an additional sources of free fatty acids has impregnated in the comb wax though colony generation. This induced oxidation and caused darker colour in beeswax (Wannahari and Nordin, 2012). Accordingly, sample 6 was old comb (6 months of age, 6 frames) show higher peroxide value than other.

3.2.5 Saponification and ester value

The saponification value of beeswax sample was 92.06±4.90 (range, 85.83-95.62) which qualified to the standard. The saponification value generally indicates the content of ester groups in a compound represented the number of milligrams of potassium hydroxide required to saponify 1g of fat under the conditions specified. Saponification value refer to the molecular weight of fatty acid contained in beeswax. High value of saponification value refer to small molecule of fatty acid contained in fat and oil. Low saponification value refer to large molecule of fatty acid contained in fat and oil (Wakita et al., 2014). Saponification value of beeswax samples were 92.06±4.90 (range, 85.83-95.62). Generally, beeswax consists of different long chain molecules of fatty acid (Masae and Pitsuwan, 2014) which large molecule. Beeswax samples had low saponification value when compared the other liquid oils (i.e. sunflower, palm and soybean oil have saponification value 193, 205, 194.61 respectively) (Gopinath et al.,2009).

The ester value of beeswax was 76.09±6.24 (range, 67.76-82.73) which was qualified to the standard. Ester value referred to characteristic compound of beeswax. Beeswax consists of complex wax esters 15-27% (Kuznesof, 2005). Low ester value refer to the decomposition of oils which high acid value.

3.2.6 Fat and Fatty acid

Fat and fatty acid test was qualified to the standard (standard of European, Kenya and Ethiopian standard). The beeswax samples from our study and commercial beeswax (control) passed the test since the liquid remains clear or shows not more than a slight amount of turbidity or precipitate. Fat and Fatty acid tested for determination of beeswax's impurity or examine the contaminated of fatty acid from other oils. This result demonstrated studied beeswax samples was purity.

CONCLUSION

In summary, beeswax sample which harvested from the abandoned nests of the Asian cavity bees, *Apis cerana* was qualified to the standard. Nevertheless, in order to higher quality, beeswax should be harvested immediately after colony

absconded to avoid the invasion of wax moth. The best quality of beeswax should be harvested at the age less than 6 months. Beekeepers could harvest to benefit from losses of bee colonies and the quality by the double boiled melting method can produced a high quality beeswax for value added, homemade products or sell.

REFERENCES

1. Aichholz, R. and Lorbeer, E., 1999, "Investigation of comb wax of honeybees with high temperature gas chromatography and high-temperature gas chromatography-chemical ionisation mass spectrometry. I. High-temperature gas chromatography",**Journal of Chromatography**, Vol. 855, pp. 601-615.
2. Buchwald, R., Breed, M. D. and Greenberg, A. R.,2008, "The thermal properties of beeswaxes: unexpected findings", **The Journal of Experimental Biology**, Vol. 211, pp.121-127.
3. Buchwald, R., Breed, M.D., Bjostad, L., Hibbard, B.E. and Greenberg,A.R., 2009, "The role of fatty acids in the mechanical properties of beeswax", **Apidologie**, Vol.40, pp.585-594.
4. De La Rúa, P., Simon, U.E. , Tilde, A.C., Moritz, R.F.A and Fuchs, S., 2000 "MtDNA variation in *Apiscerana* populations from the Philippines", **Heredity** , Vol. 84, pp. 124-130.
5. Ethiopian Standard,2005, **Bees wax-Specifcation**, 1st ed., ES1203: 2005.
6. European Food Safety Authority, 2007, "Beeswax (E 901) as a glazing agent and as carrier for flavours Scientific Opinion of the Panel on Food additives, Flavourings, Processing aids and Materials in Contact with Food (AFC)", **The EFSA Journal**, Vol. 615, pp. 1-28.
7. Fats and Fixed Oils, 2012, Omega-3 Fatty Acid Determination and Profile, The United States Pharmacopeial Convention, pp. 163-172.
8. Fessenden R.J., Fessenden J.S. and Feist, P., 2000, Organic Laboratory Techniques, 3rd Ed, Brooks Cole: California
9. Gopinath, A., Puhan, S. and Nagarajan, G., 2009 "Theoretical modeling of iodine value and saponification value of biodiesel fuels from their fatty acid composition", **Renewable Energy**, Vol. 34, pp. 1806-1811.
10. Hepburn, H.R. and Radloff, S.E., 2011, **Honeybees of Asia**, Springer Veerlag Berlin Hidelberg, New York.
11. Jyothi, J.V.A., 2006, "Physicochemical properties of Beeswax of Apis species"**, Journal of Entomological Research,** Vol.30, pp. 347-349.
12. Kenya Standard, 2013, **Specification for natural beeswax**, CD 05- 1279: 2013.
13. Krivtsov, N. and Lebedev, V., 1995 The bee products (In Russian). Editing House, Niwa Niwa, Russia
14. Kuznesof, P.M., 2005, "Beeswax Chemical and Technical Assessment (CTA)", **Chemical and Technical Assessment 65th JECFA**, pp.1-6.
15. Masae M. and Pitsuwan, P., 2014, " Thermo-physical characterization of paraffin and beeswax on cotton fabric", **Thammasat International Journal of Science and Technology**, Vol.19, pp.69-77.
16. Wakita, K., Kuwabara, H., Furusho, Noriko., Tatebe, C., Sato K. and Akiyama, H., 2014, " Comparative Study of the Hydroxyl and Saponification Values of Polysorbate 60 in International Food Additive Specifications", **American Journal of Analytical Chemistry**, Vol. 5, pp. 199-204.
17. Wannahari, R. and Nordin, M.F.N., 2012, "Reduction of Peroxide Value in Used Palm Cooking Oil Using Bagasse Adsorbent", **American International Journal of Contemporary Research**, Vol. 2, pp. 185-191.
18. Tsegaye, A., Wubie, A.J., Eshetu, A.B. and Lemma, M., 2014, " Evaluation of different non-chemical wax moth prevention methods in the backyards of rural beekeepers in the North West dry land areas of Ethiopia", **Journal of Agriculture and Veterinary Science**, Vol. 7, No. 3, pp. 29-36.
19. Zhang, W., Li, N., Feng, Y., Su, S., Li, T. and Liang, B., 2015, "A unique quantitative method of acid value of edible oils and studying the impact of heating on edible oils by UV-Vis spectrometry", **Food Chemistry**, Vol. 185, pp.326-332.

Miss Ratchakon Chankhai

have received the B.Sc. (2012) degrees in Microbiology, King Mongkut's University of Technology Thonburi. She is a student (Master degree), Department of Natural resource management, School of Bioresources and Technology, King Mongkut's University of Technology.

Asst. Prof. Orawan Duangphakdee

have received the B.Sc. (2002) degrees in Biology, Ph.D. (Biological Sciences, Entomology) Chulalongkorn University (2007). She experts in Entomology, Bee Biology, Behavior Biology and Chemical Ecology, Population Ecology and Honeybee Diversity.

Asst. Prof. Sasitorn Suwannathep

have received the B.Econ. inInternational Economics (1984), MSc.in Development Economics (1988), and Ph.D. (2003) in Development Administration. She is an expert in community economy. At present, she is anAssistant Professor, School of Liberal Arts, King Mongkut's University of Technology Thonburi.

Electrical Engineering

SIMULATING THE TRANSIENT STABILITY IN MULTI-MACHINE POWER SYSTEM CONSIDERING THE NEGATIVE-SEQUENCE BRAKING TORQUES AND THE ASYNCHRONOUS TORQUES

Luu Huu Vinh Quang

HoChiMinh City, Vietnam - lhv2uang@hotmail.com

ABSTRACT

A new algorithm simulating the impacts of the negative sequence braking torques and the asynchronous torques affecting to the transient stability of multi-machine power system is mentioned and some typical numerical examples are presented in this article. The unsymmetrical transient voltages of the VAR supporting devices such as the static var compensators and the synchronous machines are simulated under condition of the action of automatic voltage regulation system. The transient frequencies relating to the actions of the torque components such as the asynchronous and the negative-sequence braking torques are also calculated for the simulation of the transient stability in multi-machine power system. Based on the proposed algorithm this PC program uses the elements of the eigen-image matrix to bring the specific advantages for the simulation of the transient features of state variables.

INTRODUCTION

In recent years, the transient stability problems have been reported in power systems which originated broad studies in many literatures concerning [1],[2]. The power system is affected by high electromechanical oscillations while a disturbance occurs that may lead to loss of synchronism of generators. The unsymmetrical faults on a power system may be analyzed by appropriately the sequence networks of the system. Referring to [2], the negative-sequence resistance involving the active power losses in the machines can calculated as $R_2=(R_{stator}+0.5R_{rotor})$. The positive-sequence power outputs computed represent the actual power suplied by the machines including negative- and zero-sequence resistance losses. The generator negative-sequence current ($I_{stator2}$) can be determined from negative sequence network, and the negative-sequence braking torque (T_{b2}) begets the deceleration of the machine rotor, may be caculated as follow

$$T_{b2} = (R_2 - R_{stator})\, I^2_{stator2}; \qquad (1)$$

The asynchronous speed of the synchronous machines may be engendered in a power system during swings caused by symmetrical or unsymmetrical faults, its effect may be taken into account to the analyzing of the transient stability. The asynchronous regime is tested and allowable with small slip of speed of the synchronous machines operating in the power system. Excepting the test of behavior of the synchronous generators assuming the asynchronous operation, the most important is the problem of assessment of the transient stability in power system including the reclosing with asynchronism.

The main features of the synchronous operation are as follows: the current circulating through the synchronous machines and power network has components of two frequencies ω and ω_o. The synchronous machines assume the properties of an asynchronous machine, since the rotor current appears with a slip, the emf E_ω varies with the slip, the reactances of power network assume new value $X_\omega=X(\omega/\omega_o)$. There are three methods to assess the asynchronous parameters [1] such as the currents, powers, torques and emf. The first method is supperposition method applicating to a machine model consisting of two machine components. The second method is finding the asynchronous emf. The third method is using the Park-Gorev' equations to calculate all variations associating to the change in the emf and torque of synchronous machine. Using the first method, the the average value of the asynchronous torques can be determined as follow

$$T_{as} = \frac{-V^2}{2}\left(T_{asf} + T_{asD} + T_{asQ}\right); \qquad (2)$$

where T_{asf} is the asynchronous torque component relating to the rotor winding ; T_{asD} is the asynchronous torque components relating to the d-axis damper windings; T_{asQ} is the asynchronous torque components relating to the q-axis damper windings; V is the voltage of observing busbar relating to the receiving system. The torque components T_{asf}, T_{asD} and T_{asQ} have been written in [4].

In case of occurring of the unsymmetrical fault at a distance of one transformer level from the generator locations in power system, the e.m.f components calculating for the synchronous machines are only positive-sequence, taking into account of the action of automatic excitation regulation, the three phase voltages at the terminal of the synchronous machines are almost equals. During short time of the fault, the frequency variation is very small, neglecting the high harmonics, only the fundamental frequency is taking into account, the asynchronous torque may be approximately determined as how we calculated for the symmetrical fault mentioned above. The phase voltages may be determined by application of the symmetrical sequence components.

MATHEMATICAL MODELLING

The power system consists of the generators, exciters, governors, loads and other equipments such as the power transformers, the transmission lines, the synchronous condensers, the static var compensators. The equivalent models of the important components for the power system are illustrated below.

Referring to [1], [2], [3], [4], the mathematical model for analyzing of the transient stability in a multi-machine power system involving the negative-sequence and the asynchronous torque is developed from [4] as follow

$$\begin{cases} \dfrac{d^2\delta_i^t}{dt^2} = \dfrac{\omega_o}{2H_i}\left(\begin{array}{l} T_{tur\,i}^t(x_i, \Delta\delta_i^t) - \dfrac{p_i(E_i^t, \delta_i^t)}{1 + \dfrac{d\delta_i^t}{dt}\dfrac{1}{\omega_o}} \\ -T_{coi}^t - T_{b2i}^t - T_{asi}^t - \dfrac{p_{di}^t}{\omega_o}\dfrac{d\delta_i^t}{dt} \end{array} \right); \\ i = 1,2..M\_generator\ number; \end{cases} \quad (3)$$

where T_{coi}^t is an equivalent torque simulating the effect of an infinite bus at the t-th time interval in multi-machine power system; T_{b2i}^t, T_{asi}^t is the asynchronous torque and negative-sequence braking torque calculated for i-th synchronous machine at the t-th time interval; p_{di}^t is i-th variable damping factor depending on a set of different parameters such as the i-th elements of the eigen-image matrix, the phase angles δ_i^t at the t-th time interval, the voltages V_i^t at the i-th observing bus in power network at the t-th tim interval, the subtransient time constants T''_d, T''_q, the transient and subtransient reactances X'_d, X'_q, X''_d, X''_q and the rated frequency of the power system.

Synchronous Machine Model

The synchronous machines will be taken into account with the transient and subtransient effects. It is assumed that the d-axis and q-axis all have damping coils. The parameters of the synchronous machine will be taken as the input data concerning a set of numbers such as the inertia constant M_J, the d-axis and q-axis synchronous, transient, subtransient, negative-sequence resistances and reactances, stator resistance X_d,X_q, X'_d,X'_q,X''_d, X''_q, R_2, X_2 R_{stator} and the time constant of machine windings under no-load condition T_{fo}.

The synchronous electrical powers at the terminal of i-th synchronous machine are the functions of the transient e.m.f. and the bus admittances, determined in the t-th time as follow

$$\begin{cases} p_i^t = f_{pi}(E'^t_i, \delta_i^t, Y_{ij}^t, \Phi_{ij}^t) \\ q_i^t = f_{qi}(E'^t_i, \delta_i^t, Y_{ij}^t, \Phi_{ij}^t) \end{cases} \quad (4)$$

where $Y^t_{ij} \angle\Phi^t_{ij}$ is the driving-point (if j=i) or the transfer (if j≠i) elements of the equivalent augmented bus admittance matrix Y_{bus} at t-th time interval; $E'^t_i\angle\delta^t_i$ is the transient e.m.f. of i-th synchronous machine taking into account of AVR at t-th time interval.

Exciter Model

According to [1][4], the mathematical model simulating the action during the fault of automatic excitation system including the electromagnetic transient effects of i-th synchronous machine should be written as follow

$$E_i^t + T_{doi}\frac{dE'^t_i}{dt} = e_i(t, T_{Ei}, K_{Ei}^t, V_i^+, V_i^-, V_{Gi}^t); \quad (5)$$

where $e_i(t, T_{Ei}, K_{Ei}^t, V_i^+, V_i^-, V_{Gi}^t)$ is i-th function simulating the proportional action of automatic excitation system of i-th synchronous machine at t-th time interval; T_{Ei} is the equivalent time constant of the automatic excitation system; K_{Ei}^t is the equivalent gain of excitation; V_i^+ and V_i^- are the upper and under bounds of stator voltage allowing to decide a suitable action of automatic excitation regulation of i-th synchronous machine; V_{Gi}^t is the actual voltage at the terminal of synchronous machine under condition of excitation control at t-th time interval; E^t_i and E'^t_i are the synchronous and transient e.m.f taking into account of excitation control at t-th time interval; T_{doi} is the d-axis time constant of machine windings under no-load condition.

Speed Governor Model

In general, the impact of speed governor affects only slightly to the transient process. If the speed varies more than (1.5-2)% and the transient process is longer than (2-3)sec., then the turbine power variation caused by the speed governor should be taken into account as some turbine torque changement. Referring to [1], the transfer function of the governor can be written as

$$W_{ASG} = \frac{K_{ASG}}{(\rho + p\tau_{ASR})(1 + p\tau_{AE})}; \quad (6)$$

where ρ is the efficiency of the feedback; τ_{AE} is the time constant of the amplifying element, τ_{ASG} is the time constant of the servo-piston;

According to (6), the torque of i-th turbine at the t-th time interval should be found as a function as follow

$$T_{tur\,i}^t(x_i, \Delta\delta_i^t) = T_{tur\,i}^o + \Delta T_{ASG+AFR\,i}^t(x_i, t); \quad (7)$$

where $T_{tur\,i}^o$ is the initial torque of i-th turbine; $\Delta T_{ASG+AFR\,i}^t(x_i, t)$ is the change of torque of the i-th turbine depending on a set of i-th parameters $x_i = \{R_{ASG\,i}, \tau_{ASG\,i}, R_{AFR\,i}, \tau_{AFR\,i}\}$; $R_{ASG\,i}, \tau_{ASG\,i}$ are the speed drop and time constant of the i-th automatic speed governor (ASG) system; $R_{AFR\,i}, \tau_{AFR\,i}$ are the frequency drop and time constant of the i-th automatic frequency regulation (AFR) system;

Static VAR System Model

A static VAR system is an aggregation of Static VAR Compensator and mechanically switched capacitors or reactors whose outputs are coordinated. The SVC can

enhance the transient stability and the damping of system oscillations.

Referring to [2], the performance of the SVC is instantaneously provide unlimited Q_power to hold the voltage at a specific bus in power network with its V/I characteristic showing in figure 1 as follow

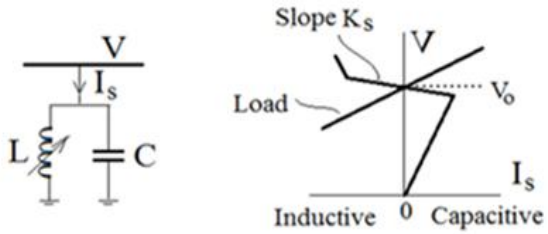

Figure 1. Equivalent circuit and V/I characteristic of SVC

The composite characteristic of SVC - Power System, within the control range defined by the slope K_S with reactance X_{SL} may be expressed as

$$V_o + X_{SL} I_S = E_{The} - X_{The} I_S; \qquad (8)$$

where E_{The} and X_{The} are the thevenin e.m.f and thevenin reactance at the bus of SVC location in multi-machine power system.

The main process of calculation of multi-machine transient stability by our PC program is developed [4].

NUMERICAL EXAMPLE

Let's survey the electro-mechanical transient process of a 38-bus power system consisting of 5 thermal stations, 1 synchronous condensers, 4 SVC stations and 28 composite loads. Total MW load power demand is 2682.5MW. Basic power is 100 MVA. The positive-sequence linedata is given in table 1 as follow

Table 1. Linedata

Bus		R	X	0.5B	t
m	n	(pu)	(pu)	(pu)	
10	13	0.0062	0.0353	0.1090	1
10	12	0.0146	0.0831	0.0642	1
10	11	0.0104	0.0591	0.0456	1
11	12	0.0103	0.0582	0.0449	1
12	28	0.0073	0.0415	0.1283	1
8	6	0.0124	0.0706	0.0545	1
8	7	0.0127	0.0720	0.0556	1
6	7	0.0090	0.0509	0.0393	1
19	21	0.0045	0.0313	0.0996	1
21	22	0.0064	0.0361	0.1115	1
19	20	0.0079	0.0449	0.1388	1
14	17	0.0046	0.0318	0.1013	1
14	15	0.0038	0.0267	0.0851	1
15	16	0.0036	0.0205	0.0634	1
8	9	0.0049	0.0276	0.0852	1
17	18	0.0039	0.0223	0.0689	1
18	19	0.0079	0.0446	0.1379	1
23	26	0.0039	0.0223	0.0689	1
26	27	0.0051	0.0291	0.0899	1
23	24	0.0051	0.0356	0.1136	1
24	25	0.0063	0.0360	0.1112	1
2	3	0.0076	0.0659	0.4284	1
4	5	0.0091	0.0791	0.5146	1
1	2	0.0025	0.0217	0.5635	1
12	27	0.0091	0.0635	0.2026	1
3	4	0.0101	0.0875	0.5692	1
2	8	0.0004	0.0098	0.0000	1
3	10	0.0004	0.0098	0.0000	1
4	19	0.0004	0.0098	0.0000	1
1	14	0.0006	0.0131	0.0000	1
5	23	0.0004	0.0098	0.0000	1
29	2	0.0013	0.0482	0.0000	1
32	16	0.0020	0.0651	0.0000	1
33	22	0.0020	0.0651	0.0000	1
30	5	0.0013	0.0482	0.0000	1
31	28	0.0020	0.0651	0.0000	1
37	8	0.0006	0.0262	0.0000	1
34	23	0.0004	0.0150	0.0000	1
35	27	0.0014	0.0376	0.0000	1
36	19	0.0005	0.0200	0.0000	1
38	10	0.0004	0.0150	0.0000	1

The busdata of composite loads is given in the table 2 and the initial generation data is given in the table 3 as follows

Table 2. Data of the bus loads

	Load			Load	
Bus	MW	MVAr	Bus	MW	MVAr
1	0.69	3.375	15	121.2	48.901
2	0.46	2.25	16	89.23	35.997
3	0.92	4.5	17	129.2	52.121
4	0.92	4.5	18	118.8	47.923
5	0.92	4.5	19	185.8	74.955
6	104.82	42.29	20	113.2	45.668
7	97.889	39.49	21	119.2	48.086
8	0.375	2.524	22	82.57	33.321
9	81.241	32.78	23	182.7	73.719
10	194.04	78.28	24	121.7	49.064
11	99.887	40.3	25	103.6	41.811
12	121.19	48.9	26	111.1	44.813
13	114.94	46.38	27	123.2	49.703
14	169.55	68.41	28	93.23	37.45

Table 3. Initial generation busdata

Bus	Device	Generation	
		MW	MVAR
29	Static VAR Compensator	0	5
30	Static VAR Compensator	0	5
31	Static VAR Compensator	0	28
32	Static VAR Compensator	0	55
33	Synchronous Condenser	0	31
34	Thermal Plant Generator	685	197.04
35	Thermal Plant Generator	345	91.92
36	Thermal Plant Generator	505	202.14
37	Thermal Plant Generator	535	195.11
38	Thermal Plant Generator	660.62	174.46

The input-data for the synchronous machines are given in the tables 4 and 5 as follows

Table 4. Synchronous Machine Reactances

	Xd	Xq	X'd	X"d	X"q	X2
Bus	p.u.					
33	0.635	0.351	0.137	0.06	0.92	0.14
34	0.225	0.214	0.04	0.028	0.045	0.04
35	0.757	0.727	0.119	0.079	0.102	0.06
36	0.304	0.292	0.054	0.037	0.06	0.05
37	0.308	0.295	0.035	0.024	0.043	0.03
38	0.225	0.214	0.04	0.028	0.045	0.04

Table 5. Resistances.
Time and Inertia Constants.

Bus	R2	Rrotor	T"d	T"q	Tdo	Te	H
	p.u.		Second				
33	0.0459	0.0079	0.161	0.171	8.3	0.52	6.56
34	0.0119	0.0028	0.15	0.161	5.4	0.15	23.64
35	0.0184	0.0095	0.16	0.172	6.2	0.19	13.1
36	0.0156	0.0038	0.15	0.161	5.4	0.15	17.73
37	0.011	0.0039	0.163	0.176	13	0.23	35.475
38	0.0119	0.0028	0.15	0.161	5.4	0.15	23.64

Let's assume that the V/I characteristics of the SVCs in p.u. at the buses 29, 30, 31 and 32 are given for input-data of this example and shown in the figures 2, 3 and 4 as follows

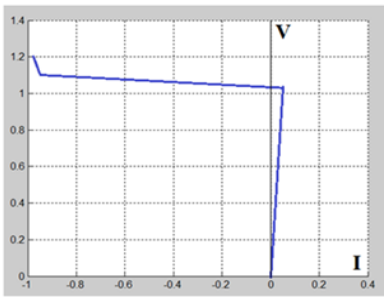

Figure 2. V/I characteristic of SVC at the bus 29 and bus 30

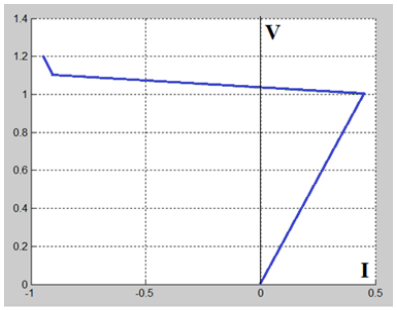

Figure 3. V/I characteristic of SVC at the bus 31

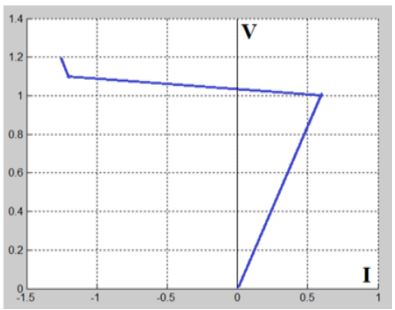

Figure 4. V/I characteristc of SVC at the bus 32

The typical surveying and obtained results

A single high voltage transmission line (3-4) connecting two power plants 36 and 38 is chosen simulating the fault of phase-to-phase-to-ground short circuit type to test the transient stability of the power system. Let's suppose that the fault occurs at the line (3-4) near the bus 3. Let's suppose that the fault will be cleared at 0.1sec by the circuit breakers, the typical results of surveying of the transient bus voltages of the network during in 4sec. are shown in the figures 5 - 7 as follows

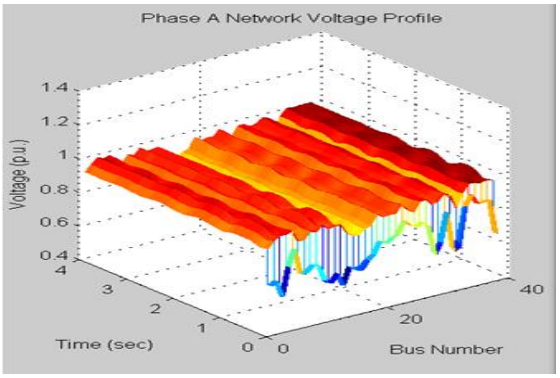

Figure 5. Phase A - Network Voltage Profile

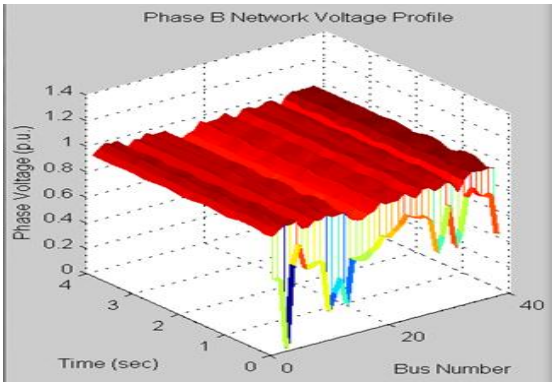

Figure 6. Phase B - Network Voltage Profile

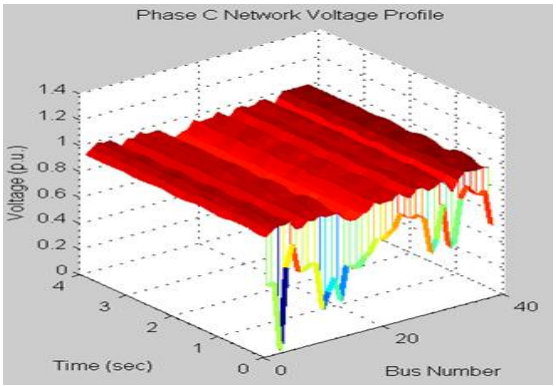

Figure 7. Phase C - Network Voltage Profile

For this fault, the critical clearing time is 0.41sec. Let's suppose that the line breakers lately clear this fault at the time of 0.42sec., the power system is unstable, the torques components strongly increase their oscillation amplitudes after 5sec. as shown in the figures 8 - 10 as follow

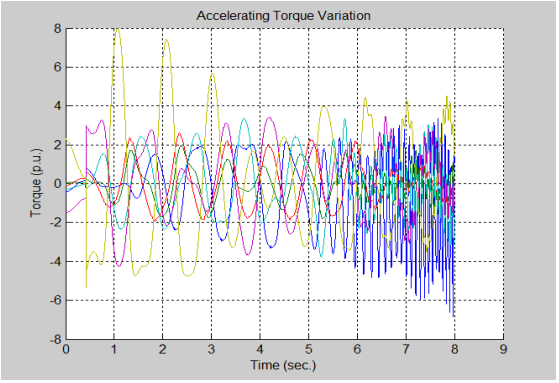

Figure 8. Generator Accelerating Torques

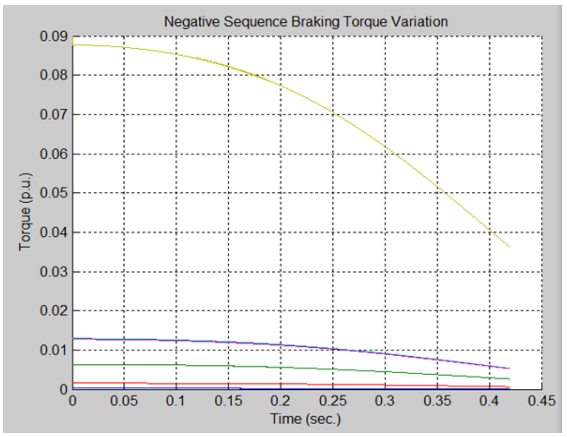

Figure 9. Generator Negative-Sequence Braking Torques

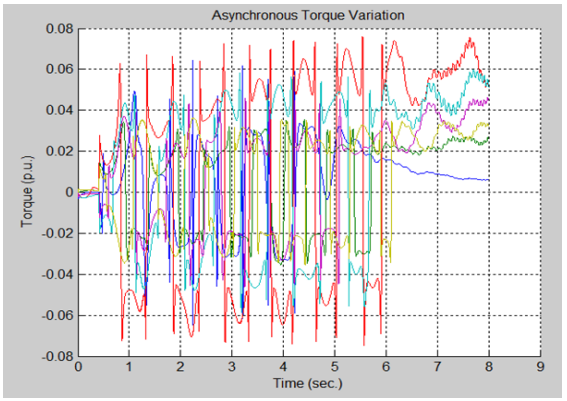

Figure 10. Generator Asynchronous Torques

The transient phase voltages unsymmetrically change and the voltage profiles during in 8sec. are shown in the figures 11 -13 as follow

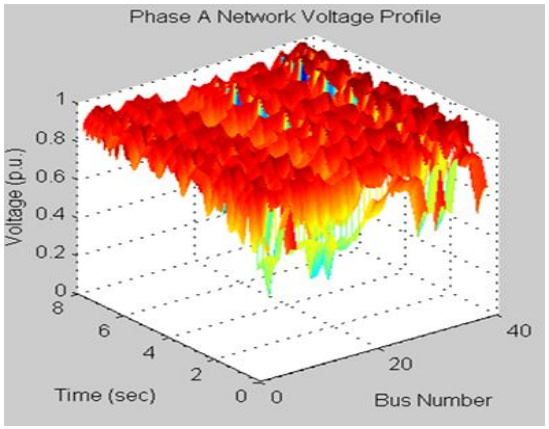

Figure 11. Phase A - Network Voltage Profile

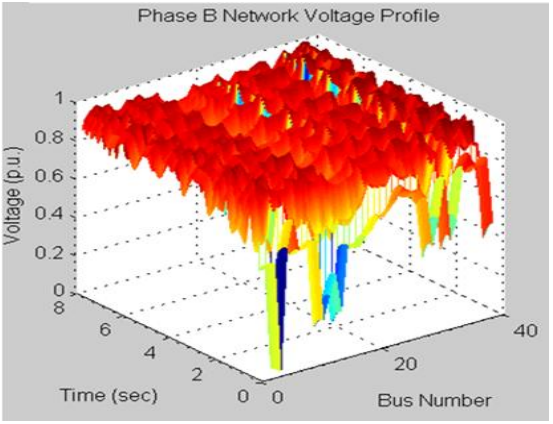

Figure 12. Phase B - Network Voltage Profile

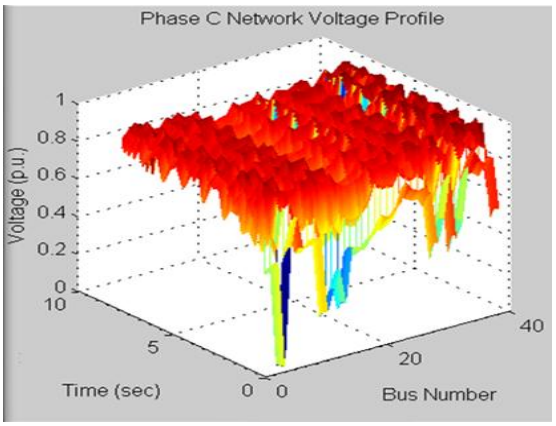

Figure 13. Phase C - Network Voltage Profile

The fault transient frequencies of the generators during in 8sec. are shown in the figure 14 as follow

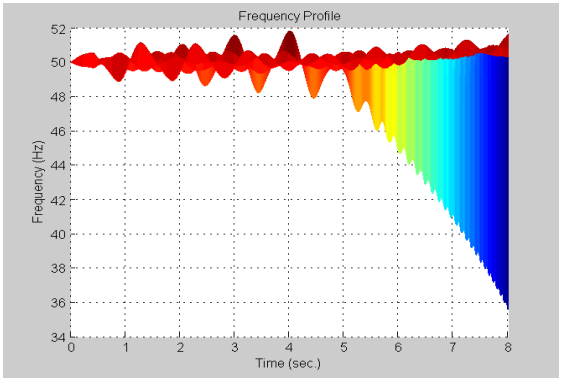

Figure 14. Frequency Variation of the Generators

The rotor of the synchronous condenser at the bus 33 oscillates during in 5 sec. and then hardly decelerate leading to stop the rotation. The time reponse of frequency and the phase voltages of the synchronous condenser are shown in the figures 15 - 16 as follow

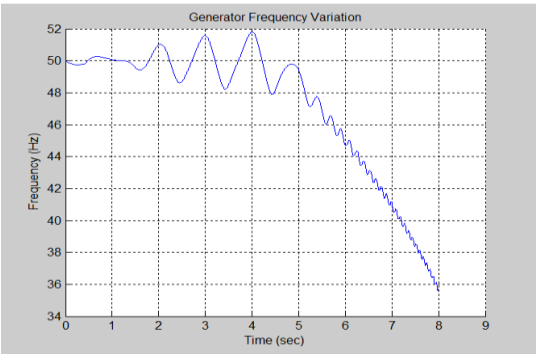

Figure 15. Condenser Frequency Variation at the bus 33

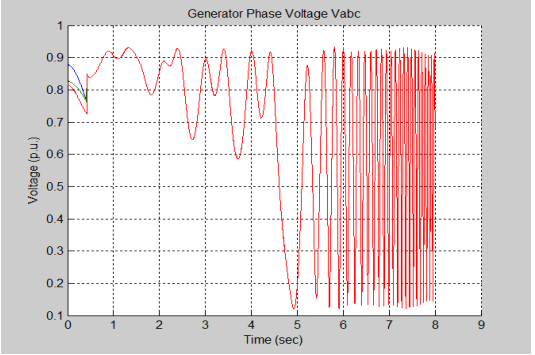

Figure 16. Condenser Voltage Variation at the bus 33

In the meantime, the generator rotors at the plant 34 accelerate their speed and the phase voltages at the generator terminals hardly oscillate, equivalently showing for the bus 34 in the figures 17 -18 as follow

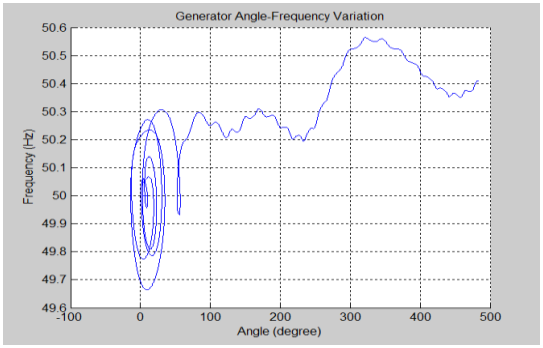

Figure 17. Generator Frequency-Angle at the bus 34

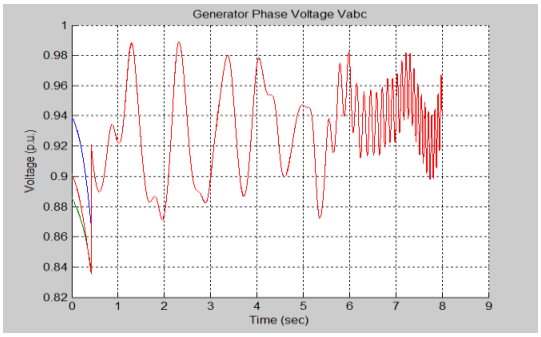

Figure 18. Generator Voltage Variation at the bus 34

If the line breakers clear the fault at the critical time moment of t=0.41sec. then the power system transient stability can be performed after 20 sec. The transient state variables of the power system decay their fluctuations as shown in the figures 19 - 25 as follow

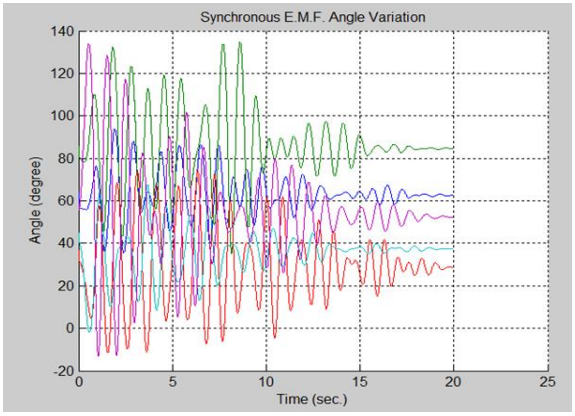

Figure 19. Generator E.M.F. Angles.

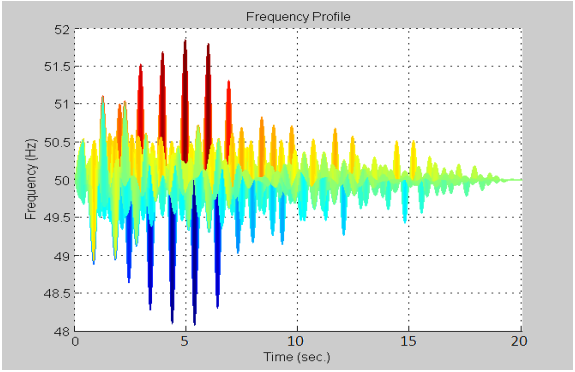

Figure 20. Generator Frequency Profile.

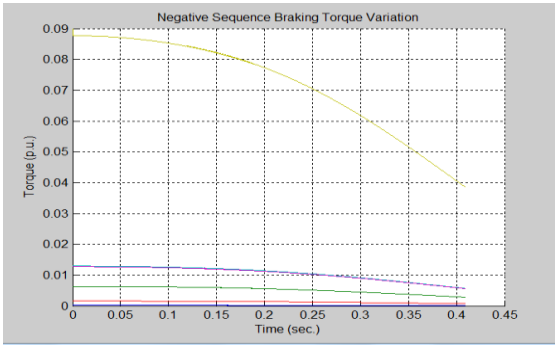

Figure 21. Generator Negative-Sequence Braking Torques

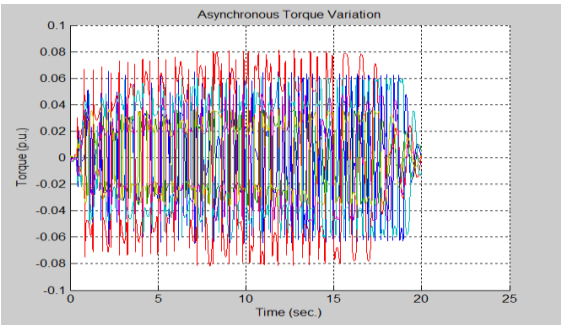

Figure 22. Generator Asynchronous Torques

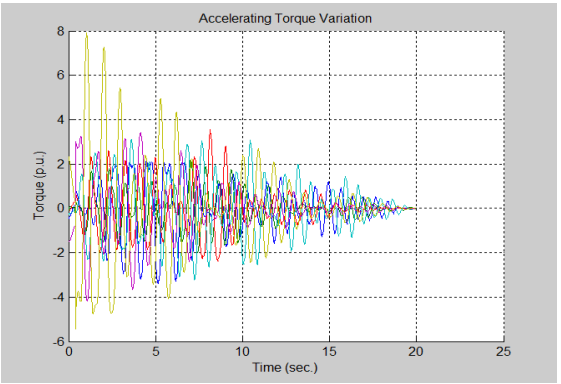

Figure 23. Generator Accelerating Torques

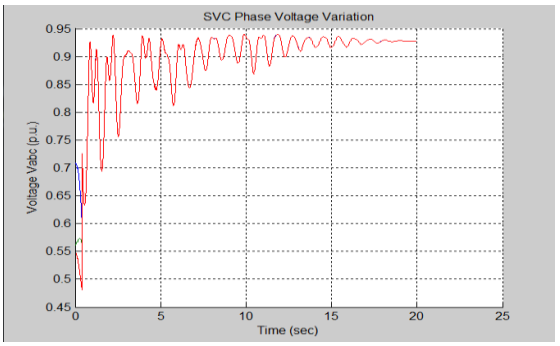

Figure 24. SVC Voltage Variation at the bus 30

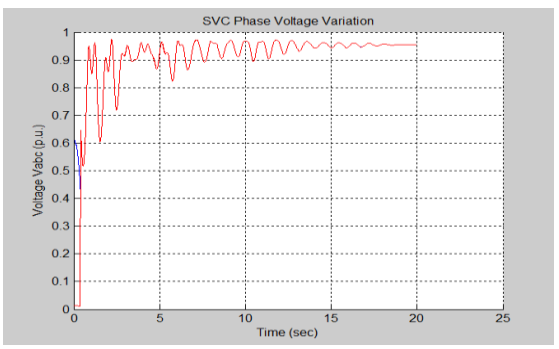

Figure 25. SVC Voltage Variation at the bus 31

In case of neglecting both the asynchronous torques and the negative-sequence braking torques in the simulation of transient process, the state variables such as the network voltage and the frequency oscillate with more large amplitudes, this have been investigated in [4].

CONCLUSION

The results of the surveys showed that the negative-sequence braking and the asynchronous torque effects are to damp the electromechanical transient process, to slightly increase the critical clearing time for the different type of fault occurring in the power system, to strengthen the transient stability of the multi-machine power system.

New algorithm calculating the transient stability of power system is formed to test a number of simulations which consist the participation of the eigen-image matrix elements into the calculation of the asynchronous torque and is proven having good effective by the results of the calculations surveying a number of the numerical examples for the different structures of power system.

REFERENCES

[1]. V.Venikov. *Transient processes in electrical power systems*. Mir Publishers, second edition 1980.

[2]. Prabha Kundur. *Power system stability and control*. Mc Graw Hill, Inc. 1993, ISBN 0-07-035958-X.

[3]. Luu Huu Vinh Quang. *Modeling the initial condition of P_power deficiency for multi-machine transient stability simulation*. Pages 74-79 [OS10], Proceedings of the 8th Seatuc Symposium 2014, ISBN 978-967-12214-1-9, Malaysia.

[4]. Luu Huu Vinh Quang. *Investigating the impacts of asynchronous torque affecting to the transient stability in multi-machine power system.* Pages 27-38, Vol.17-N^{o}K3, 2014, Science & Technology Development Journal, ISSN 1859-0128.

ELECTRIC VEHICLE IN-MOTION CHARGING -EMF EXPOSURE SAFETY REGULATION-

A. Z. Omar, N. A. Jalalludin, T. Takeuchi, Y. Honda, G. Fujita

Graduate School of Engineering and Science

Shibaura Institute of Technology

ABSTRACT

Environmental friendly vehicles such as electric vehicles (EV) and fuel cell vehicles (FCV) are forecasted to be the main transportation solution in future. However, due to infrastructure limitations for hydrogen refueling stations for the FCV case, electric vehicles are expected to have better advantage and dominance. Nonetheless, current energy storage modules such as battery packs for hybrid and pure EVs do have individual capacity limitations. As a result, users need to frequently stop and plug-in their vehicle and this consequently lead to inconveniences and also time-consuming. Plus, plug-in charging is easily affected by weather and risky as users need to hold high voltage conductors. In this paper, we study on the concept of track charging during vehicle cruising, using wireless power transfer concept, which charges the vehicle while in motion and mentioned about the safety standard regulations regarding the electromagnetic field exposures in establishing a safe system.

1. INTRODUCTION

The declination of global fossil fuel reserves and pollution issues has shifted automotive manufacturers' attention to clean technology vehicles such as electric vehicles and fuel cell vehicles. However, limitations in energy storage, particularly battery capacity for EVs require users to stop and plug-in the charger gun. Meanwhile, inconveniences during charging process, such as slow charging and the need for frequent charging sessions still remain as among issues that limit its further commercialization. Therefore, a more user-friendly and convenient charging mechanism known as wireless charging is being developed worldwide.

Korea Advanced Institute of Science and Technology (KAIST) developed a wireless charging system known as On-line Electric Vehicle (OLEV), as stated in [1]. In their results, they were able to obtain 52 [kW] of output power with 74% efficiency at 20 [cm] air gap for the OLEV bus. Additional studies had successfully developed a system that manages to store and supply energy back to the grid, called vehicle-to-grid (V2G) system as mentioned in [2]. This makes the circuit configuration more complex but on contrary, reduces the amount of power loss and increases the efficiency of total power usage.

In this study, the authors discuss about infrastructures required in realizing the dynamic charging concept and focus on developing a safe, high efficiency charging system that utilizes magnetic resonant coupling theory, a method which magnetically charges the vehicle while in motion. Consequently, this will limit the need for EV users to frequently stop at the charging station in future. The proposed WPT system uses the Industrial, Scientific and Medical (ISM) frequency of 13.56 [MHz] as an operation frequency, inverters of 10 [kW] output, transmitting coils with diameter set up at 50 [cm] and the targeted track length for this system is set at 1 [km], in which the charger being embedded into the road.

2. IN-MOTION CHARGING

Electric vehicle in-motion charging refers to charging process which takes place during the vehicle not only during the driving state, but fully utilizing all of the vehicle mobility dynamics. For instance, charging at intersections (short stops at traffic light), during highway cruising, etc. In other words, it is a charging process where the battery is being charged while the vehicle is during both moving and stationary state. One of the advantages of this system is it will eliminate users need to stop and plug-in charging cables every time the battery level falls.

At present, one of the implemented technologies that are in operation is the OLEV bus, an abbreviation of On-line Electric Vehicle, developed by KAIST. Currently, they are operating these electric buses between Gumi train station and the In-Dong district, approximately 24 [km] round trip with power supplied via technology called Shaped Magnetic Field in Resonance (SMFIR). A receiving coil (receiver) below the bus body tuned to the resonance frequency converts magnetic field to electricity, which then stored in a small battery pack that about one-third the size of normal battery. By reducing battery-size, this will lead to cost-reduction and ultimately reducing vehicle's price.

Figure 1 shows the embedded transmitter coils in construction and Fig. 2 shows the OLEV bus in operation.

Fig. 1 KAIST OLEV Project
(Underground coil segmentation embedded in road)

Fig. 2 KAIST OLEV Electric Bus in operation
(Installation at bus stops)

3. Safety Regulations

3.1 Radiation Limitations

In order to limit the magnetic field leakage created by the transmitter coils to a certain level which will not affect surrounding vehicles as well as human body, scientific bodies such as the International Commission on Non-Ionizing Radiation Protection (ICNIRP) standardized certain values that limit the amount of electric fields, magnetic fields and electromagnetic field (EMF) in regards with operational frequency [3]. Thus, in order to fulfill these standards, shielding methods such as active shielding and passive shielding for the leakage field needs to be taken into account.

3.2 International Commission on Non-Ionizing Radiation Protection (ICNIRP)

"The main objective of this publication is to establish guidelines for limiting EMF (electromagnetic field) exposure that will provide protection against known adverse health effects. An adverse health effect causes a detectable impairment of the health of the exposed individual or of his or her offspring; a biological effect on the other hand, may or may not result in an adverse health effect". [ICNIRP][3][4]

The organization regulates two limitation values in their guidelines based on operational frequency.

i. Basic restrictions (Exposure limits)

Restrictions on radio frequency (RF) exposure that are based directly on established health effects. ICNIRP provides basic restrictions: a) on induced current density (ICNIRP 1998) or induced electric field (ICNIRP 2010) to prevent nerve stimulation for frequencies below 10 MHz, b) on specific absorption rate (SAR) to prevent tissue heating for frequencies between 100 kHz and 10 GHz and c) on power density to prevent heating in tissue at or near body surface for above 10 GHz.

ii. Reference level (Action, Orientation values)

ICNIRP provides this reference levels in terms of Incident electric and magnetic fields for practical exposure assessment in order to determine whether the basic restrictions are likely to be exceeded. These values were derived from the basic restrictions under the worst case coupling condition of a homogenous human body exposed to uniform incident fields.

According to the guideline, if the reference level values are exceeded, it is necessary to check whether the basic restrictions values for public exposure are satisfied or not. For the final analysis, if the basic restrictions values are not exceeded, the system is regarded safe to be operated.

In the frequency range from 10 [MHz] to 10 [GHz], the basic restrictions are expressed as Specific Absorption Rate (SAR) limits. As our dynamic charging project will be implementing 13.56 [MHz] as the operational frequency, this complies with the SAR limits of the ICNIRP guideline. Basically, there are three different SAR limits; whole-body averaged SAR, localized SAR in the head and trunk and localized SAR in limbs (hand, wrist, ankle, and feet). As for the two latter cases, the averaging mass is 10 [g] of tissue and are primarily applied for partial-body and near-field exposures. The ICNIRP SAR limits for public exposure for frequencies ranging from 10 [MHz] to 10 [GHz] are shown in Table 3.

Table 3 Specific Absorption Rate (SAR) limits for general public exposure (10 [MHz] – 10 [GHz])

Body parts	SAR limit [W/kg]
Whole-body	0.08
Head and trunk	2
Limbs	4

Here, it needs to be known that limitation levels for general public exposure (with additional safety factor) and workers exposure are different. The present standard also includes a distinction between controlled and uncontrolled environments and guidelines for partial-body and near-field exposures. Exposure limits in the uncontrolled environment are lower than in the controlled environment under certain conditions, such as resonance, or when exposure is complicated by associated hazards like RF shock or burns.

3.3 Institute of Electrical and Electronic Engineers (IEEE)

"The purpose of this standard is to provide guideline on exposure limits to protect against established adverse health effects to human health induced by exposure to RF (radio frequency) electric, magnetic, and electromagnetic fields over the frequency range of 3 kHz to 300 GHz."[IEEE][5]

Similar to the ICNIRP reference levels, IEEE prescribes Maximum Permissible Exposure (MPE) levels in terms of external electric and magnetic fields, contact currents and power density, for convenience in exposure assessment to ensure that basic restrictions (Specific absorption rate) are met. In IEEE guideline, at frequencies between 100 [kHz] to 6 [GHz], the average SAR limit for whole-body is 0.08 [W/kg] and spatial peak values not exceeding 1.6 [W/kg] as averaged over any 1 [g] of tissue.

In their most recent reviews of the accumulated scientific literature, both the IEEE and ICNIRP groups have concluded that there is no established evidence showing that human exposure RF electromagnetic fields causes cancer, but on the other hand, there is established evidence showing that RF electromagnetic fields may increase a person's body temperature or may heat body tissues and likely to stimulate nerve and muscle tissues. The ICNIRP group also concludes that the induction of retinal phosphenes may be considered in determining human exposure limits. Both ICNIRP and IEEE safety guidelines are revised from time to time to take into account the significant expansion of the database, improvements in dosimetry, and increasing number of people in the general population exposed to RF fields. The changes in the standard included a wider frequency range, frequency dependence resulting from the recognition of whole-body resonance and incorporation of dosimetry.

In this paper, we will be focusing on implementing the ICNIRP regulations as the KAIST OLEV system which is already in operation applies their limitation values. Plus, for the SAR limit case, few regional and national standards and regulations are same as those in the ICNIRP guidelines. [6]

Table 4 Specific Absorption Rate standard by regions

Region	Localized SAR limits (head and trunk)
Europe (EU)	2.0 [W/kg]
Japan	2.0 [W/kg]
USA	1.6 [W/kg]
Australia	1.6 [W/kg]
Canada	1.6 [W/kg]
Korea	2.0 [W/kg]

4. Safety Improvement Mechanism

4.1 Electromagnetic Field (EMF) Shielding

Primarily, there are two methods of reducing radiation leakage and electromagnetic field; active shielding and passive shielding [7]. In active shielding, a conductor that carries the same frequency with current but opposite phase is installed at maximum leakage boundary. By applying this method, it will produce magnetic field with the opposite direction with the main leakage field and thus, cancelling out the excess magnetic field. On the other hand, passive shielding is a method by installing shielding elements which will directly block the excess magnetic field. For example, embedding vertical ground plate in the road surface and additionally, connecting the vehicle with the ground using metallic brush.

4.2 Autonomous Foreign Object Detection

Qualcomm HALO, a product of Qualcomm Company, developed the foreign object detection for metal objects at the transmitter (base pad) side. If the base pad detects any metallic objects, it will automatically turn OFF the power transmission process. When a metal object is located on the base pad other than the receiver pad, the magnetic field projected tends to concentrate at it and this will eventually raise its temperature which consequently may lead to fire hazards.

Fig. 4 Qualcomm HALO foreign object detection

5. Communication

Communication mechanism between vehicles and charging system during charging process is indeed necessary for operation supervision and increase system efficiency. Plus, for example, by continuously sending up-to-date information to the system, this will also lead to better management of the system, such as ability to gather vehicle data, statistics of traffic flow and supplying only necessary amount of power from inverter.

For these mechanisms, we proposed a system that uses sensors (photoreflectors) to detect presence of a vehicle, then identify and authenticate cars that can use the wireless charging system, using Radio Frequency Identification (RFID) technology. This technology is currently used in electronic money card, namely Suica in Japan. The system is basically made up of two components, which are RFID reader and RFID tag. The

tag will be attached to the vehicle and as it goes through the reader, which is place on the road, the reader will send signals to turn on the coil. Here, only vehicles that possess the ID for charging can use the system. At present, it has been proved that for the single tag scenario, the existing reader can identify tags with a maximum speed of 167.7 [km/h] as stated in [8]. Considering most the world's highway speed limit is mainly below that value, it is expected that this RFID technology is generally feasible for our system.

Fig. 5 Radio Frequency (RF) reader for fast moving RFID Tags in high-speed railway application

Additionally, this system can be operated with multiple-tags multiple-readers, as shown in Fig. 6 below is the multiple tag case. Multiple reader and tag capability is necessary assuming few EVs will simultaneously use the system at the same time.

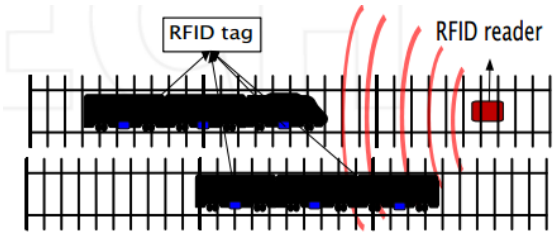

Fig. 6 Multiple tag RFID capability

6. CONCLUSION

Conclusively, it is a known fact that smart recharging solutions are required in order to encourage the general public on electric vehicles usage. Wireless power transfer for electric vehicle charging application does possess a great future prospect in changing general acceptance and attitudes towards electric vehicle. By eliminating charging process inconveniences and expanding charging infrastructure, this concept are expected to contribute to further popularization of electric vehicle.

In-motion wireless charging for electric vehicle will be developed and realized as a part of our effort in contribution to environmental solutions and society in future. It is ultimately expected that diminishing inconveniences during charging process will shift the general public attitudes and viewpoints towards electric vehicles in future. Plus, it is also anticipated that renewable energy source can be implemented to this system. Hence, we are also able to contribute in protecting our mother nature while maintaining our energy sustainability for future generations.

Nevertheless, it is clear that there many technological improvements as well as future issues related to this research still remains mainly related to power transfer efficiency as well as initial infrastructure costs. It is our confidence that this proposal will trigger more detailed researches regarding electric vehicle wireless charging.

REFERENCES

[1] S. Ahn, N. P. Suh, D. H. Chol, "Charging up the road", in Spectrum IEEE, Vol. 50, Issue 4, pp. 48-54

[2] Udaya K. Madawala, Duleepa J. Thrimawithana, "A bidirectional inductive power interface for electric vehicles in V2G systems," IEEE Transactions On Industrial Electronics, Vol. 58, No. 10, pp. 4789-4796, October 2011

[3] "Guidelines for limiting exposure to time-varying electric, magnetic and electromagnetic fields (Up to 300 GHz)", International Commission on Non-ionizing Radiation Protection (ICNIRP), Health Physics Society, 1998

[4] ICNIRP 2010, "Guidelines for limiting exposure to time-varying electric, magnetic and electromagnetic fields (1Hz to 100 kHz)", Health Physics, 99(6):818-836, 2010

[5] IEEE Standard for Safety Levels with Respect to Human Exposure to Radio Frequency Electromagnetic Fields, 3kHz to 300 GHz, IEEE Std C95.1, 1999 Edition

[6] 3rd Generation Partnership Project ; Technical Specification Group Terminals (TSG-IT), "Specific Absorption Rate(SAR) requirements and regulations in different regions (3G TR 34.925 version 3.0.0)", ARIB Technical Report, 1999-07

[7] S. Ahn, J. Y. Lee *et. al*, "Magnetic field design for low EMF and high efficiency wireless power transfer system in on-line electric vehicles", in Proceedings of the 21st CIRP Design Conference, 2011, pp 233-239

[8] Xiaoqiang Zhang, Manos Tentzeris, "Applications of fast-moving RFID tags in high-speed railway systems", International Journal of Engineering Business Management, vol. 3, No. 1 (2011), pp 27-31

Azreezal Zairee Bin Omar obtained his Graduate Diploma in Electrical Engineering (2012) from Industrial University of Selangor (UNISEL), Malaysia and B.E. (2014) degree in Electric, Electronic and Information Engineering from Tokyo University of Science, Japan. He is a member of IEEE and currently pursuing his M.E studies at Shibaura Institute of Technology, Japan. His interests include electric vehicle charging system and fuel cell system.

Prof. Goro Fujita received the B.E., M.E., and Ph.D. degrees in electrical engineering from Hosei University, Japan in 1992, 1994 and 1997 respectively. In 1997, he was a research student at Tokyo Metropolitan University, Japan. He is currently a Professor in Shibaura Institute of Technology, Japan. He is a member of IEEE and also a First Class Licensed Engineer of Electric Facility in Japan. His research interests include power system control including dispersed power systems.

INVESTIGATION OF CORE PARAMETERS ON ANALYTICAL INDUCTANCES IN A DISTRIBUTED CIRCUIT FOR FREQUENCY RESPONSE ANALYSIS OF POWER TRANSFORMERS

Ngoc Thach Tran[1], Thanh Phuong Nguyen[1], and Dinh Anh Khoi Pham[2]
[1] University of Technology (HUTECH), Vietnam
[2] Ho-Chi-Minh City University of Technology (HCMUT), Vietnam

ABSTRACT

There has been recently interest in applying the technique of Frequency Response Analysis (FRA) on diagnosis of mechanical failures in power transformer's active part, i.e., windings and the core. Mechanical failures in transformer windings reflect changes on measured terminal frequency responses normally in mid frequency range, from tens to hundreds of kHz, which is in fact not easy to interpret for diagnosis.

For the purpose of simulation based frequency response interpretation for power transformers at mid and high frequencies, the so-called distributed equivalent transformer circuit (DETC) consisting of per-segment self and mutual inductances and capacitances is recommended to use since it represents well interactions between winding segments at these frequencies. However, there has been no 'effective' way to determine inductive components of the circuit, i.e., self and mutual inductances, for in-service transformers, even when geometrical parameters of the core and windings are available, since there are two unknown prerequisite electrical and magnetic parameters of the core, namely effective resistivity (ρ_{eff}) and relative permeability of the solid treated core in axial direction (μ_{rel}), which cannot be identified practically.

The paper introduces an investigation on identifying frequency dependent μ_{rel} based on analysis of a distribution transformer (Yy6, 200 kVA, 10.4/0.46 kV) and influence of μ_{rel} and ρ_{eff} on analytical inductances for determination of DETC's inductive components to improve effectiveness of the simulation based frequency response interpretation for power transformers in practice.

1. INTRODUCTION

To understand what happens in transformer's active part after a suspected mechanical fault for diagnostic purpose, measurement of terminal frequency responses of voltage ratios (mainly end-to-end type) in broad frequency range, e.g., from 20 Hz to 2 MHz, are often made and then compared with those performed when transformers were in good condition. However, there is unfortunately no clear procedure from current relevant standards [CIGRE Brochure (2008), IEC Std 60076-18 (2012)] to identify which and level of fault based on the comparison since there are so many factors influencing measured frequency responses such as transformer type (normal/auto), winding type (disc/layer/interleaved/helical), winding number (two/three), winding connection (vector group), winding's terminal condition (open-circuited/short-circuited/floating), measurement set-up etc.

Mechanical failures in transformer windings show discrepancies on the frequency responses at mid frequencies. In order to understand such discrepancies between two measured frequency responses at these frequencies, simulation technique based on the DETC has been exploited [Rahimpour (2003), Abeywickrama (2008), Wang (2009) etc.]. Fig. 1 shows a per-phase distributed equivalent transformer circuit with a multi-segment high- and low-voltage winding, from which the complete DETC of three-phase two-winding transformers is derived by combination of three of them, adding their mutual effect and internal terminal connection.

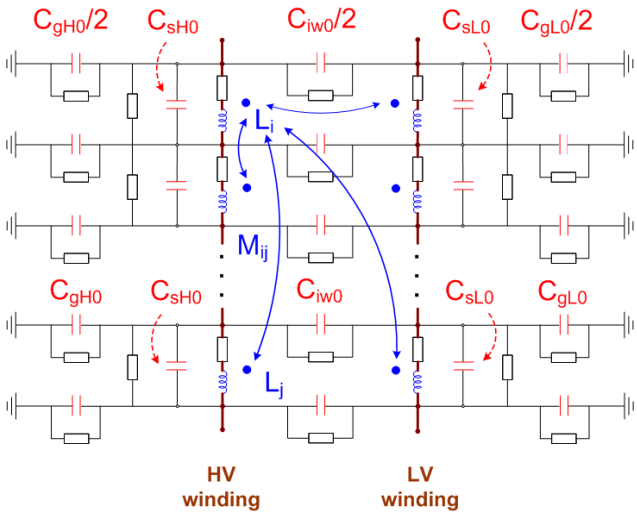

Fig. 1 Per-phase distributed transformer equivalent circuit

In Fig. 1, the HV and LV phase winding are divided into a number of segments each of which has equivalent electrical components: self/mutual inductances (L_i, L_j/M_{ij}), ground, series, inter-winding capacitances (C_{g0}, C_{s0}, C_{iw0} respectively) and corresponding resistances/conductances representing losses in core laminations, windings' conductors and insulations. The number of segments is selected depending on the desired accuracy and the circuit complexity.

There was an effective method proposed to determine electrical parameters in the so-called lumped equivalent transformer circuit (LETC) for FRA interpretation and

failure diagnosis at low frequencies [Pham (2013), Pham (2014)]. Since the capacitances between the two circuits, LETC and DETC, can be referred, the only problem now is how to find the inductances (and resistances) in the DETC.

Wilcox (1988, 1989) proposed an accurate analytical solution based on Maxwell's equations in determination of self and mutual inductances of transformer windings when dimensions of the core and windings are known. He used measured inductances of a single multi-turn coil as a winding segment to identify the electrical and magnetic property of the solid core, i.e., effective resistivity (ρ_{eff}) and constant relative permeability in axial direction (μ_{rel}). Since there is however no such direct measurement of winding segment inductances in practice, the ρ_{eff} and μ_{rel} could only be determined based on indirect measurements, e.g., driving-point impedances. For such cases it is very helpful to know how μ_{rel} and ρ_{eff} influence resultant inductances for their value determination based on a balance of impedance between measurement and simulation. In addition, Abeywickrama (2008) studied *frequency dependent* μ_{rel} in calculating winding segment inductances in the DETC for FRA purpose. As a result, subjects of frequency dependent μ_{rel} and influence of μ_{rel} and ρ_{eff} on analytical inductances will be investigated in this paper.

2. CONSTANT EFFECTIVE RELATIVE PERMEABILITY AND RESISTIVITY OF THE CORE

To determine constant μ_{rel} and ρ_{eff} of a solid treated core of a 25 kVA transformer, Wilcox (1989) compared measured and calculated inductances and resistances of two identical coils with dimensions illustrated in Fig. 2.

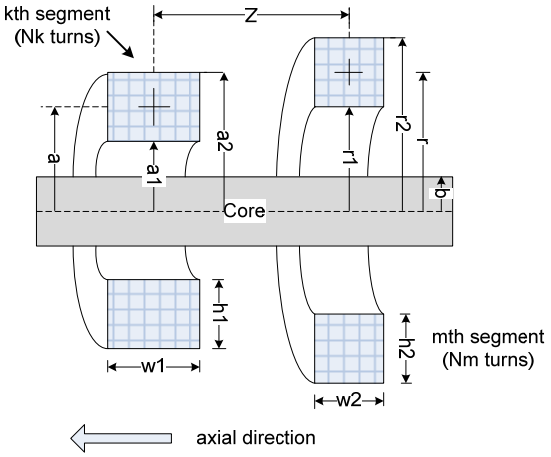

Fig. 2 Illustration of geometrical parameter of two winding segments with a core

Self or mutual inductances and resistances of the segments were calculated as:

$$Z_{km} = j\omega L_{km0} + Z_{1(km)} + Z_{2(km)} \equiv R_{km} + j\omega L_{km} \quad (1)$$

where

- L_{km0} mutual inductance between k^{th} and m^{th} segment without the core (air core)
- $Z_{1(km)}$ mutual impedance between k^{th} and m^{th} segment owing to flux confined in core
- $Z_{2(km)}$ mutual impedance between k^{th} and m^{th} segment owing to leakage field with core presence

The resistive component of Z_{km}, i.e., R_{km}, represents eddy current loss of the core whereas the inductive one, L_{km}, is the total mutual inductance between two sections. Self inductance is a special case of mutual inductance between a section with itself.

Following are formulas indicating relation between input electrical and magnetic properties (μ_{rel} and ρ_{eff}) and resultant inductances when geometrical parameters of winding segments and the core are available.

2.1. Air-core inductance L_{km0}

$$L_{km0} = \mu_0 N_k N_m r a \frac{\pi}{\lambda}\left\{\frac{r}{a} + 4\sum_{k=1}^{N} I_1(\beta_k r) K_1(\beta_k a)\cos(\beta_k z)\right\} \quad (2)$$

where

- N constant affecting accuracy degree
- λ apparent length of the magnetic circuit
- $\beta_k = \dfrac{2\pi \cdot k}{\lambda}$ summation parameter
- I_1, K_1 modified Bessel functions
- z distance between the two segments

2.2. Iron-core impedance (flux in the core) $Z_{1(km)}$

$$Z_{1(km)} = j\omega N_k N_m \frac{\pi b^2}{\lambda}\left\{\frac{2\mu_{rel} I_1(mb)}{mbI_0(mb)} - \mu_1\right\} \quad (3)$$

where

- $\mu_1 \approx \mu_0$ magnetic permeability of medium outside the core
- $m = \sqrt{j\omega\mu_{rel}/\rho_{eff}}$ skin effect parameter
- I_0, I_1 modified Bessel functions

2.3. Iron-core impedance (leakage flux) $Z_{2(km)}$

$$Z_{2(km)} = N_k N_m \frac{\pi}{\lambda}\frac{4}{h_1 h_2 w_1 w_2}\sum_{k=1}^{N} P_1(\beta_k a_2, \beta_k a_1) P_1(\beta_k r_2, \beta_k r_1) \times Q_1(\beta_k w_1, \beta_k w_2)\frac{I_1(\beta_k b)}{K_1(\beta_k b)} F_1(\beta_k, b)\cos(\beta_k z) \quad (4)$$

where

- $P_1(\beta_k x, \beta_k y) = \dfrac{1}{\beta_k^2}\left[p(\beta_k x) - p(\beta_k y)\right]$
- $p(\alpha) = \dfrac{\pi\alpha}{2}\left[K_1(\alpha)L_0(\alpha) - K_0(\alpha)L_1(\alpha)\right]$
- $L_n(\alpha) = \sum_{k=0}^{\infty}\dfrac{(\alpha/2)^{n+2k+1}}{[k+0.5]![n+k+0.5]!}$
- $Q_1(\beta_k x, \beta_k y) = \dfrac{2}{\beta_k^2}\left[\cos\left(\dfrac{\beta_k x - \beta_k y}{2}\right) - \cos\left(\dfrac{\beta_k x + \beta_k y}{2}\right)\right]$
- $F_1(\beta_k) = j\omega\mu_1\left[\dfrac{f(\beta_k) - \dfrac{\mu_1}{\mu_z} f(\Gamma_k)}{g(\beta_k) + \dfrac{\mu_1}{\mu_z} f(\Gamma_k)}\right]$
- $\Gamma_k = \sqrt{\dfrac{\mu_{rel}}{\mu_{rel\_radial}}\beta_k^2 + j\omega\mu_{rel}/\rho_{eff}}$
- $f(x) = x\dfrac{I_0(xb)}{I_1(xb)}$

- $g(x) = x\dfrac{K_0(xb)}{K_1(xb)}$

3. FREQUENCY DEPENDENT RELATIVE PERMEABILITY

Although inductances calculated by means of (1) with constant μ_{rel} and ρ_{eff} are found to have good agreement with ones measured on two tested winding coils wound around a 'Unisil' 27M4 25kVA core in Wilcox (1989), is it true that a frequency dependent μ_{rel} is still applicable, as confirmed from Abeywickrama (2008)?

Answer for the above mentioned hypothesis can be based on the fact that, due to eddy current effect in the core, μ_{rel} has common characteristic for all power transformers, i.e., it decreases much as frequency increases. Fig. 3 shows an example of a normalized effective frequency dependent μ_{rel} of the core of a 200 kVA transformer, calculated from (5):

$$\mu_{rel} = \Re e\left\{ k_{fe}\mu_{rel\_const}\frac{\tanh\{(1+j)b_o/\delta\}}{(1+j)b_o/\delta}\right\} \qquad (5)$$

where k_{fe} is stacking factor representing fraction of core steel in total cross-area section, μ_{rel_const} is the constant value of μ_{rel} at low frequencies, b_0 is half of lamination thickness, and δ is skin depth of eddy current [Lammeraner (1966), Abeywickrama (2008)]. In Fig. 3, the approximated curve is developed for convenience in application.

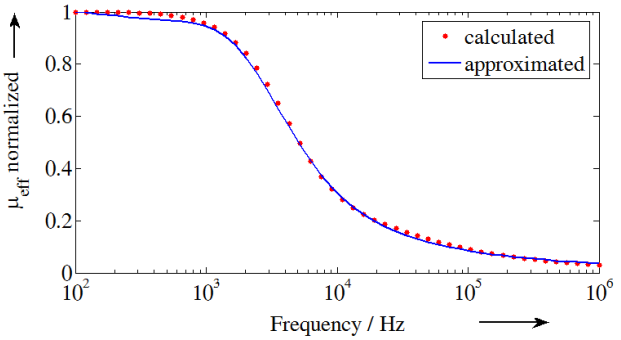

Fig. 3 Normalized frequency dependent relative permeability in axial direction of a 200 kVA transformer core

The point now is to check whether the frequency dependent curve of μ_{rel} in Fig. 3 is applicable for the core of the 25 kVA transformer in Wilcox (1989). From his analysis, μ_{rel} = 843 and ρ_{eff} = 0.0103 Sm^{-1} are identified after iteration algorithm based comparison between calculated and measured self impedance of a test coil. In our investigation, a new frequency dependent μ_{rel} is applied to (1) by multiplying the curve in Fig. 3 with factor of 843 to keep the low frequency values identical (ρ_{eff} hold unchanged). Fig. 4 compares self inductance of the test coil from measurement and calculation with constant and frequency dependent μ_{rel}. Result shows that there is a slight decrease of calculated inductance at high frequencies, when frequency dependent curve is taken into account. This proves that, better agreement between measurement and calculation could be achieved at high frequencies.

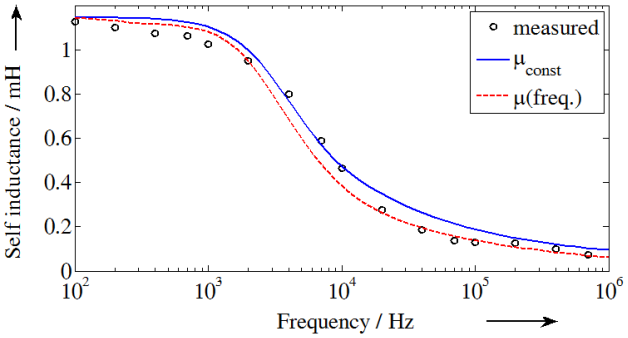

Fig. 4 Comparison of self inductances of a test coil in Wilcox (1989)

4. INLUENCE OF CORE'S RELATIVE PERMEABILITY AND RESISTIVITY

In reality, there is little chance to know exactly value of effective permeability and resistivity of the solid treated core for analytical calculation. On the other hand, it is still impossible to have measurements of winding segment inductance/resistance to check whether calculated values are acceptable when windings are inside transformer. The only chance is to base on indirect measurements, e.g., terminal driving-point impedance or voltage ratios for verification of internal parameters, i.e., μ_{rel} and ρ_{eff}. Therefore, it is necessary to know in advance how effective core permeability and resistivity influence calculated inductances.

Fig. 5 and 6 illustrate per-unit analytical inductances of a winding segment in the 200 kVA transformer calculated from (1) where (frequency dependent) μ_{rel} and ρ_{eff} changes respectively to observe the tendency. It is seen that μ_{rel} causes significant change of inductance at low frequencies whereas ρ_{eff} influences mostly at mid frequencies. This is helpful to find μ_{rel} and ρ_{eff} based on indirect measurements at low and mid frequencies respectively.

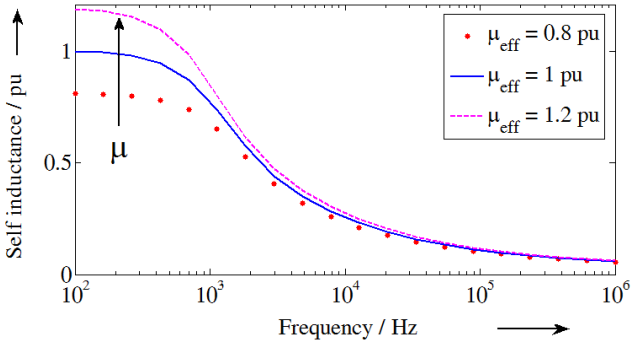

Fig. 5 Influence of μ_{rel} on a calculated normalized inductance (ρ_{eff} unchanged)

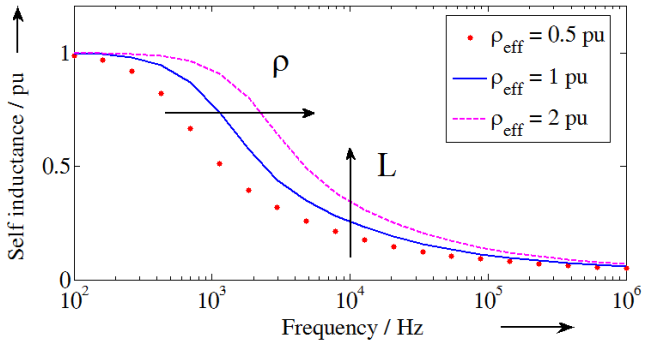

Fig. 6 Influence of ρ_{eff} on a calculated normalized inductance (μ_{eff} unchanged)

5. CONCLUSION

The paper solves two first problems in analyzing self and mutual impedances of transformer windings in the distributed equivalent transformer circuit with regard to electrical and magnetic property of the core, namely effective relative permeability and resistivity. Results show that, the frequency dependent relative permeability derived from analysis of a transformer can be used for calculating inductances of another transformer winding with better accuracy at high frequencies, compared with using constant relative permeability.

Moreover, changes of analytical inductances of winding segments in a transformer in terms of effective relative permeability and resistivity are also investigated, which helps to find out these parameters based on indirect measurements, e.g., driving-point impedances, for any transformer with available geometrical parameters of the core and windings. This enables the determination of DETC's inductive components for simulation based interpretation of frequency responses to diagnose mechanical failures in transformer core and windings.

REFERENCES

CIGRE Report 342 W.G. A2.26, Mechanical-condition assessment of transformer windings using FRA, Apr. 2008.

IEC 60076-18, Power transformers - Part 18: Measurement of frequency response, Jul. 2012.

Rahimpour E., Christian J., Feser K., and Mohseni H., Transfer function method to diagnose axial displacement and radial deformation of transformer windings, IEEE Transactions on Power Delivery, vol. 18, no. 2, pp. 493-505, Apr. 2003.

Abeywickrama N., Serdyuk Y. V., and Gubanski S. M., High-Frequency Modeling of Power Transformers for Use in Frequency Response Analysis, IEEE Transactions on Power Delivery, vol. 23, no. 4, pp. 2042-2049, Oct. 2008.

Wang Z., Li J., and Sofian D. M., Interpretation of transformer FRA responses—Part I: Influence of winding structure, IEEE Transactions on Power Delivery, vol. 24, no. 2, pp. 703-710, Apr. 2009.

Pham D. A. K., Pham T. M. T., Borsi H., and Gockenbach E., A new method for purposes of failure diagnostics and FRA interpretation applicable to power transformers, IEEE Transactions on Dielectrics and Electrical Insulation, vol. 20, no. 6, pp. 2026-2034, Dec. 2013.

Pham D. A. K., Pham T. M. T., Borsi H. and Gockenbach E., A New Diagnostic Method to Support Standard FRA Assessments for Diagnostics of Transformer Winding Mechanical Failures, IEEE Electrical Insulation Magazine, vol. 30, no. 2, pp. 34-41, Mar. 2014.

Wilcox D. J., Conlon M., and Hurley W. G., Calculation of self and mutual impedances for coils on ferromagnetic cores, IEE Proceedings, vol. 135, no. 7, Sept. 1988.

Wilcox D. J., Hurley W. G., and Conlon M., Calculation of self and mutual impedances between sections of transformer windings, IEE Proceedings, vol. 1365, no. 5, Sept. 1989.

Lammeraner J., and Stafl M., Eddy currents, Iliffe Book, 1966.

Ngoc Thach Tran received the B.E. (1997) and M.E. (2004), degrees in Electrical Engineering from Ho-Chi-Minh City University of Technology (HCMUT).

He is now a PhD student, Department of Electrical- Electronics - Mechanical Engineering, Ho Chi Minh University of Technology (HUTECH). His current interests include simulation and diagnostics of power transformers.

Thanh Phuong Nguyen received the B.E. (1998), M.E. (2003), and D.E. (2008) degrees in mechatronics engineering from Pukyong National University.

He is a Lecturer, Department of Electrical - Electronics -Mechanical Engineering, Ho Chi Minh University of Technology (HUTECH). His current interests include Robotics, Electric drives and Fault diagnostic.

Dinh Anh Khoi Pham received the B.E. (2002), M.E . (2004), and D.E. (2013) degrees in Electrical Engineering from Ho-Chi-Minh City University of Technology (HCMUT) and Leibniz University Hannover, respectively.

He is a Lecturer, Department of Power Systems, HCMUT. His current interests include High-voltage technology and simulation, testing and diagnostics of power transformers.

USING THE LINEAR PROGRAMMING TO SOLVE THE PROBLEM OF OPTIMAL UNIT COMMITMENT IN HYDRO-THERMAL ELECTRIC POWER SYSTEM

Luu Huu Vinh Quang
HoChiMinh City, Vietnam - lhv2uang@hotmail.com

ABSTRACT

The equivalent economic functions of fuel cost of the power plants is proposed to build the new algorithm for solving the optimal unit commitment problem in short-term period of the power system operation. The new algorithm of optimal unit commitment solution allows to handle large multi-machine power system consisting of both thermal and hydro generating units.

The problem of daily optimization of the active and reactive powers in a hydro-thermal power system is considered with equivalent economic fuel cost of the power plants. The water limit constraints of hydro power generation under condition of dry or rains seasons are considered and the back-pressure effect of thermal turbine regulation is simulated for the problem of optimization of the active and reactive powers in multi-machine hydro-thermal power system. A new loss factor formula containing a diagonal matrix called eigen-image matrix and representing the network transmission power losses. This loss factor formula is proposed for solution of optimization of active and reactive power generation in multi-machine power system. Some typical numerical examples with detail results are shown in this article.

INTRODUCTION

A problem that must be solved frequently by a power utility is to determine economically a schedule of what units will be used to meet the forecasted demand and operating constraints, such as spinning reserve requirements, over a short time horizon. This problem is commonly referred to as the unit commitment (UC) problem. The unit commitment problem determines the combination of available generating units and scheduling their respective outputs to satisfy the forecasted demand with the minimum total production cost under the operating constraints enforced by the system for a specified period that usually varies from 24 hours to one week. Attempts to develop rigid unit operating schedules more than one week in advance are extremely curtailed due to uncertainty in hourly load forecasts at lead times greater than one week.

Short-term hydro-thermal coordination is important problem to be solved in the management of a power utility when the hydro-electric plants are a part of the power system. Especially, the water deficiency for agricultural irrigation use in time period of dry season (of South Vietnam) causes some constraints of target function of problem optimizing the active and reactive powers, because of output powers of hydro-stations are limited. In the problem of hydro-thermal active and reactive power optimization for short-term period the water inflows is fully known and is constrained by amount of water available for draw down in the calculated time interval.

Optimal power generation contains the economic active power generation and optimum reactive power generation. The objective of the problem of optimization of the active and reactive powers is to determine the optimal combination of the active power and reactive power outputs of all of the generator units so as to meet the required load demand at minimum operating cost while satisfying system technical constraints.

The main objective of an economic power dispatch strategy is to determine the optimal operating state of a power system by optimizing a particular objective while satisfying certain specified physical and operating constraints.

The main objective of hydro-thermal operation is to minimize the total fuel cost for the system thermal generation subject to the operating hydro-thermal constraints of the electric power system.

The turbine fuel cost characteristics can be obtained in form of some fractures of line, this is notably arised from the back-pressure turbine characteristic, in addition, the turbine regulation method also raises some effect to the appearance of turbine fuel cost characteristics [1][2], and it may be briefly called the turbine back-pressure effect, for example, the fuel cost of a 62MVA thermal generator may be taken in form of some discrete line as follow:

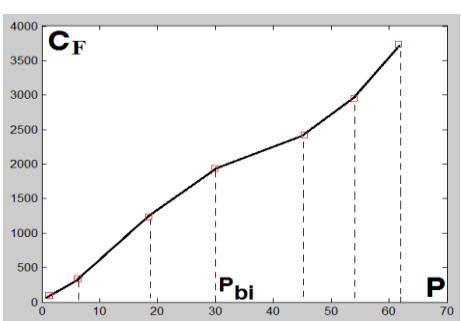

Figure 1. Rating Fuel Cost Function $C_F(P)$

According to the figure 1, the fuel cost characteristics of the units on the thermal electric plant may be approximately simulated as

$$C_F(P_g)=\begin{cases} a_1P_{g1}+b_1; & P_{b1}\le P_{g1}\le P_{b2}; \\ a_2P_{g2}+b_2; & P_{b2}\le P_{g2}\le P_{b3}; \\ \ldots\ldots \quad \ldots. \quad \ldots. \quad \ldots. \quad \ldots. \\ a_kP_{gk}+b_k; & P_{bk}\le P_{gk}\le P_{bk+1}; \end{cases} \qquad (1)$$

The water consumption amount per hour W(m^3/h) of a hydro unit for the active power generation depends on the water head H_W of reservoir of the hydro plant [2], this characteristic W(m^3/h) may be taken in form of some discrete lines, for example, the function of water consumption W(P,H_W) depending on active power generation of a 75 MW (rated) hydro unit may be represented as shown in figure 2

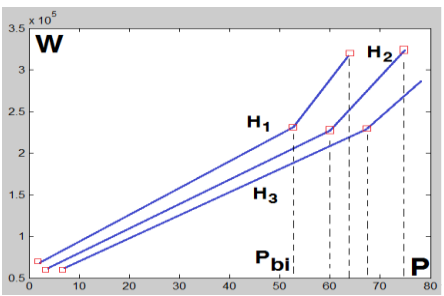

Figure 2. Rating Water Consumption W(P)

According to the figure 2, the characteristic of water consumption W(P,H_W) may be simulated as follow:

$$W(P_{gh},H_W)=\begin{cases} a_1P_{g1}+b_1; P_{b1}\le P_{g1}\le P_{b2}; \\ a_2P_{g2}+b_2; P_{b2}\le P_{g2}\le P_{b3}; \end{cases} \qquad (2)$$

In the rain seasons, the water can be plenty; the hydro units may generate the active power as much as possible, leading to minimize the total fuel cost of the thermal units. In the dry seasons, water may be deficiency, the hydro active power generation is limited because of many reasons, the main of which is agricultural irrigation. In reality, the water inflows and the water storage amounts are known for a daily period in 24h. Let's suppose the weather and hydrographic forecasts in short time are reliable, so that the average water availability per hour can be known. The average amount of water storage per hour $W^{1h}_{avr.stor.}$ and the average amount of water inflow per hour $W^{1h}_{avr.inf\ low}$ of the water reservoir of the hydro plants can be known in short-term forecast, leading to the solution of short-term problem optimization of hydro thermal active power can be satisfied the water availability constraint per hour as follow

$$W^{1h}_{avr.stor.}-W^{1h}_{avr.inf\ low}+W(P_g,H^{1h}_W)=0; \qquad (3)$$

This paper is organized following: Equivalent economic function of fuel cost of thermal plant; Economic generation of active power in hydro-thermal power system; Problem of optimization of reactive power generation; Numerical examples; Conclusion; References.

EQUIVALENT ECONOMIC FUNCTION OF FUEL COST OF THERMAL PLANT

In reality, the operation of power system is organized with a hierarchic structure and as is evident, it is not economical to run all the units available all the time, therefore, the economic generation problem can be solve with applying the unit commitment (UC) technique to determine the unit of a plant that should operate for a particular total system load in combination of different thermal plants unit so that to minimize the operating fuel cost of each individual power plant and also to minimize the operating cost of all thermal power plants in the whole of power system.

A hybrid-dynamic program is used to solve the unit commitment problem for each thermal plant, the object of unit commitment is to decide which of the available generators should start-up and shut-down over a given time horizon so that the overall operating cost $C_{Ther.Plant}$ is minimized and subject to the constraint as follows:

Objective function :

$$C_{Ther.Plant}=\sum_{i=1}^{Nu}C_i(P_{gi})+SU_i; \qquad (4)$$

Subject to

$$\sum_{i=1}^{Nu}P_{gi}=P_D; \qquad (5)$$

$$P_{gi\,min}\le P_{gi}\le P_{gi\,max}; \qquad (6)$$

$$P_D\le\sum_{i=1}^{Nu}P_{gi\,max}; \qquad (7)$$

where $C_{Ther.Plant}$ is thermal plant fuel cost; SU_i is i^{th} start-up fuel cost; P_D is MW demand of the thermal plant; $P_{gi\ max}$ is maximum MW output; Nu is number of running unit; i=(1..Nu);

If the thermal plant consists of different power rating units, then the unit commitment problem can be solved with a priority list technique.

The solution of unit commitment problem involves the UC table allowing to decide which of the available generators should start-up and shut-down over a given time horizon.

The equivalent economic function of fuel cost of every thermal plant can be created by the results of solving of the optimal unit commitment problem and will be employed for economic power dispatching to minimize the total fuel cost in the whole of the power system.

Let's denote the $C_i(P_{gi})$ representing the i^{th} unit fuel cost considering the thermal turbine back-pressure effect [1] as follow

$$C_F(P_{gi})=\sum_{m=0}^{n}a_{i,n-m}P_{gi}^{n-m}+b_i\sin(c_i(P_{gi}-d_i)); \qquad (8)$$

We can obtain the equivalent economic function of fuel cost considering the turbine back-pressure effect in form of some fractures of line and simulate corresponding to (1) which is graphically shown in figure 3a as follows:

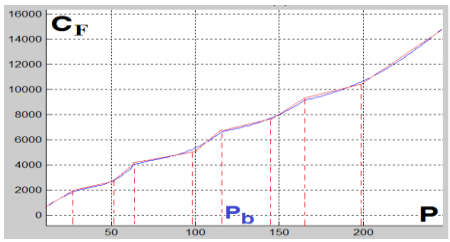

Figure 3a. Equivalent economic plant fuel cost with turbine back-pressure effect

We can also obtain the equivalent economic function of fuel cost in form of some ladder graphically shown in figure 3b as follows:

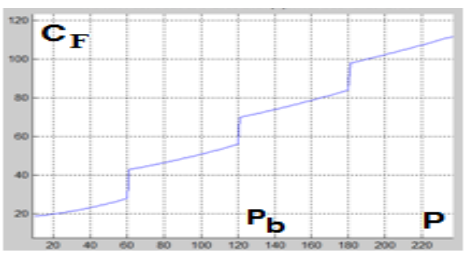

Figure 3b. Equivalent economic plant fuel cost without turbine back-pressure effect

Usually, a hydro power plants consists of some generating units which are similar in rated power, then, the equivalent function of water consumption of the hydro plant can be simulated corresponding to (2), typical graphically shown in figure 4 as follows:

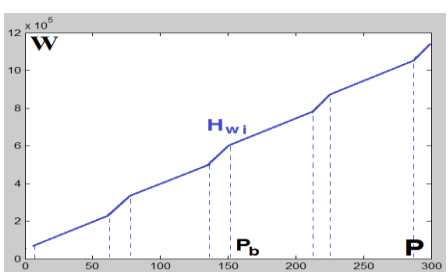

Figure 4. Equivalent plant water consumption

ECONOMIC GENERATION OF ACTIVE POWER IN HYDRO-THERMAL POWER SYSTEM

Using the fuel costs function (1) to solve the hydro-thermal economic p_power generation problem by minimizing the total fuel cost (C_F) considering the minimization of the cost of p_power transmission losses ($C_{\Delta P}$) in the whole of electrical power system which consists of N_{gh} hydro plants and N_{gt} thermal plants. Let's denote the active power losses in the transmission network by ΔP, the main objective function for the problem of short-term hydro-thermal optimization can be written as follow

$$C_F(P_{i\,gt}) + C_{\Delta P}(P_{igt}, P_{igh}) \rightarrow min; \qquad (9)$$

Where

$$\begin{cases} C_F(P_{i\,gt}) = \sum_{i=1}^{N_{gt}} \sum_{j=1}^{k} (a_{it\,j} P_{igt\,j} + b_{it\,j}) \rightarrow min; \\ P_{ibt\,j} \le P_{igt\,j} \le P_{ibt(\,j+1)}; \end{cases} \qquad (10)$$

$$C_{\Delta P}(P_{igt}, P_{igh}) = \left(\Delta P_o - \sum_{i=1}^{N_{gt}} H_{ipt} P_{igto} - \sum_{i=1}^{N_{gh}} H_{iph} P_{igho} \right) + \left(\sum_{i=1}^{N_{gt}} H_{ipt} P_{igt} + \sum_{i=1}^{N_{gh}} H_{iph} P_{igh} \right) \rightarrow min; \qquad (11)$$

Subject to the technical hydro-thermal constraints for the active power outputs in t-time interval

$$\begin{cases} (P^-_{i\,gt} \le P_{i\,gt} \le P^+_{i\,gt}); \\ (P^-_{i\,gh} \le P_{i\,gh} \le P^+_{i\,gh}); \\ i = (1 \ldots N_{gt}); \end{cases} \qquad (12)$$

Subject to the hydro generations in t-time interval

$$\begin{cases} W_{\Sigma}(P_{igh}) = \sum_{i=1}^{N_{gh}} \sum_{j=1}^{k} (a_{ih\,j} P_{igh\,j} + b_{ih\,j}); \\ P_{ibh\,j} \le P_{igh\,j} \le P_{ibh(\,j+1)}; \end{cases} \qquad (13a)$$

Subject to the seasonal water availability constraints in t-time interval according to the i[th] water head $H^{1h}{}_{i\,W}$ as follows:

$$\Delta W^{1h}_{i\,avr.min} \le W_{i\,gh}(P_{i\,gh}, H^{1h}_{iW}) \le \Delta W^{1h}_{i\,avr.max}; \qquad (13b)$$
$$i = (1 \ldots N_{gh});$$

Subject to the operating condition of active power balancing in hydro-thermal system

$$\sum_{i=1}^{N_{gt}} P_{i\,gt} + \sum_{i=N_{gt}+1}^{N_{gt}+N_{gh}} P_{i\,gh} = \sum_{i=1}^{N} P_{i\,load} + \Delta P(P_{i\,gt}, P_{i\,gh}); \qquad (14)$$

This problem of optimization of the short-term hydro-thermal economic active power generation is performed by applying the linear programming method.

All of the quantities such as the P_{igto}, P_{igho} and ΔP_o are determined in the previous step of the process of iterative calculation.

PROBLEM OF OPTIMIZATION OF REACTIVE POWER GENERATION

The problem of optimization of reactive power generation is to minimize the transmission active power losses. Let's write the target function in linear form as follow

$$\sum_{i=1}^{N_g} H_{ip} Q_{ig} + \left(\Delta P_o - \sum_{i=1}^{N_g} H_{iq} Q_{igo} \right) \rightarrow min; \qquad (15)$$

Subject to

$$Q^-_{ig}(S_{ig}) \le Q_{ig} \le Q^+_{ig}(S_{ig}); \qquad (16)$$

$$V_i^- \le V(Q_{ig})_i \le V_i^+; \qquad (17)$$

$$\sum_{i=1}^{N_g} (1 - H_{iq}) Q_{ig} = Q_o - \sum_{i=1}^{N_g} H_{iq} Q_{igo}; \qquad (18)$$

Where Q_{ig} is the MVAR output from i^{th} generator; S_{ig} is the MVA output from i^{th} generator; $Q_o=(Q_D+Q_L-Q_C)$; Q_D is the total MVAR load demand in power system; Q_L is the total MVAR losses in the inductive elements of network ; Q_C is the total capacitive reactive power charging by the transmission lines.

The expressions (15),(16),(17),(18) form a system of linear equations which can be solving by successive linear programming algorithm.

The coefficients of the system of equation can be determined in form of the functions of structure of current steady-state of the power system : $H_{ip}=2\alpha_i Q_{igo}$ and $H_{iq}=2\alpha_{iq}Q_{igo}$; where α_i and α_{iq} are the p_power and q_power loss-factors, the quantities of which are depending on the linedata, on the busdata and on the steady-state voltages, representing the participation of the i^{th} bus for the whole power losses in the electrical transmission network.

All of the quantities such as the Q_{igo}, Q_o, ΔP_o, α_i, and α_{iq} are determined in the previous step of the process of iterative calculation.

NUMERICAL EXAMPLE

Let's survey the optimum condition operation of a 45-bus power system consisting of 2 thermal plants with 8 generator units and of 2 hydro plants with 7 generator units. Basic power is 100 MVA. The linedata is given in p.u. in the table 1 as follows:

Table 1. Linedata

Bus (i)	Bus (j)	R (p.u.)	X (p.u.)	0.5B (p.u.)
3	1	0.00040	0.03926	0.00000
3	4	0.02455	0.08909	0.01937
3	11	0.04294	0.13144	0.00684
3	12	0.07532	0.23056	0.01200
3	15	0.00269	0.07149	0.00000
3	30	0.02504	0.09087	0.01975
45	1	0.00620	0.04664	0.27298
45	31	0.00040	0.03926	0.00000
45	32	0.00431	0.03240	0.18961
1	42	0.00477	0.03586	0.20987
1	43	0.00396	0.02977	0.17425
4	12	0.03207	0.09816	0.02043
4	18	0.00360	0.09091	0.00000
4	29	0.01553	0.05637	0.01225
5	6	0.02149	0.06578	0.01369
5	19	0.00595	0.14380	0.00000
5	30	0.03205	0.09810	0.02042
5	42	0.00040	0.03926	0.00000
6	7	0.03367	0.10307	0.02145
6	20	0.00595	0.14380	0.00000
6	35	0.03207	0.09816	0.02043
7	8	0.05327	0.16305	0.00848
7	10	0.04915	0.15046	0.00783
7	21	0.00595	0.14380	0.00000
7	32	0.00040	0.03926	0.00000
8	9	0.02458	0.07523	0.01566
8	10	0.06414	0.19632	0.01021
8	22	0.00595	0.14380	0.00000
8	31	0.02977	0.09114	0.01897
9	23	0.00595	0.14380	0.00000
10	24	0.00595	0.14380	0.00000
11	12	0.04915	0.15046	0.00783
11	13	0.04210	0.12888	0.02682
11	14	0.03037	0.09296	0.01935
11	25	0.00360	0.09091	0.00000
12	26	0.00360	0.09091	0.00000
13	14	0.02382	0.07291	0.01517
13	27	0.00595	0.14380	0.00000
13	39	0.04294	0.13144	0.00684
14	28	0.00595	0.14380	0.00000
14	43	0.00040	0.03926	0.00000
16	30	0.00360	0.09091	0.00000
17	29	0.00360	0.09091	0.00000
29	30	0.02455	0.07515	0.01564
33	34	0.00595	0.14380	0.00000
33	37	0.02526	0.07733	0.01609
33	39	0.06413	0.19631	0.01021
35	36	0.00595	0.14380	0.00000
37	38	0.00595	0.14380	0.00000
37	40	0.02382	0.07291	0.01517
39	44	0.00595	0.14380	0.00000
40	41	0.00595	0.14380	0.00000
40	2	0.00040	0.03926	0.00000
43	2	0.00203	0.01530	0.08952

The load busdata of the hydro-thermal power system are given in the tables 2 as follow:

Table 2. Load busdata

Bus	Load Level 1		Load Level 2		Load Level 3	
(i)	MW	MVAR	MW	MVAR	MW	MVAR
4	0.118	0.840	0.118	0.840	0.118	0.840
5	0.084	0.560	0.084	0.560	0.084	0.560
6	0.084	0.560	0.084	0.560	0.084	0.560
7	0.084	0.560	0.084	0.560	0.084	0.560
8	0.084	0.560	0.084	0.560	0.084	0.560
9	0.084	0.560	0.084	0.560	0.084	0.560
10	0.084	0.560	0.084	0.560	0.084	0.560
11	0.118	0.840	0.118	0.840	0.118	0.840
12	0.118	0.840	0.118	0.840	0.118	0.840
13	0.084	0.560	0.084	0.560	0.084	0.560
14	0.084	0.560	0.084	0.560	0.084	0.560
15	83.904	17.215	72.960	14.970	71.318	14.633
16	42.688	8.669	37.120	7.538	36.285	7.368
17	36.064	4.914	31.360	4.273	30.654	4.177
18	45.632	5.749	39.680	4.999	38.787	4.887
19	30.176	9.910	26.240	8.617	25.650	8.423
20	25.760	7.688	22.400	6.685	21.896	6.535
21	27.232	8.943	23.680	7.777	23.147	7.602
22	30.912	9.330	26.880	8.113	26.275	7.931
23	33.856	7.380	29.440	6.417	28.778	6.273
24	27.968	6.489	24.320	5.643	23.773	5.516
25	40.480	7.069	35.200	6.147	34.408	6.008
26	35.328	5.214	30.720	4.534	30.029	4.432
27	25.024	3.978	21.760	3.459	21.270	3.381
28	27.232	6.023	23.680	5.238	23.147	5.120
29	0.680	4.000	0.680	4.000	0.680	4.000
30	0.600	3.600	0.600	3.600	0.600	3.600
40	0.084	0.560	0.084	0.560	0.084	0.560
41	24.288	2.713	21.120	2.359	20.645	2.306
2	0.680	2.560	0.680	2.560	0.680	2.560
43	0.200	1.600	0.200	1.600	0.200	1.600
42	0.200	1.600	0.200	1.600	0.200	1.600
32	0.200	1.600	0.200	1.600	0.200	1.600
33	0.084	0.560	0.084	0.560	0.084	0.560

34	30.360	1.429	26.400	1.242	25.806	1.214
35	0.084	0.560	0.084	0.560	0.084	0.560
36	40.250	6.232	35.000	5.419	34.213	5.297
37	0.084	0.560	0.084	0.560	0.084	0.560
38	32.200	3.236	28.000	2.814	27.370	2.751
39	0.084	0.560	0.084	0.560	0.084	0.560
44	22.816	2.039	19.840	1.773	19.394	1.733

Let's suppose that the solutions of UC problem for each separate thermal plant are established in the UC tables of the thermal plants which are shown in the table 3 as follows:

Table 3. UC Table of Thermal Plant

Plant	Posibility of Load Demand Level	Operating Generator			
		G1	G2	G3	G4
Bus 3	P < 72MW	0	0	1	0
	(73 < P < 125)MW	1	0	1	0
	(126 < P < 185)MW	1	1	1	0
	P > 186MW	1	1	1	1
Bus 45	P < 73MW	0	0	0	1
	(74 < P < 114)MW	0	1	0	1
	(115 < P < 177)MW	1	1	0	0
	P > 178MW	1	1	1	1

According to the solutions of UC problem that shown in the table 3 above, the equivalent economic functions of fuel cost of the thermal plants and the equivalent function of water consumption of the hydro plants are given in the table 4 with the suitable coefficients as follows:

Table 4. Coefficients of the equivalent economic function of fuel costs of the power plants

Plant Bus	a_i	b_i	Lower Bounds	Upper Bounds
Hydro Plant Bus 1	29.29	510.71	1	60
	64.8	-1620	60	75
	29.29	1042.5	75	135
	64.8	-3732	135	150
	29.29	1594.71	150	210
	64.8	-1620	210	225
	29.29	2127.71	225	285
	64.8	-8000	285	300
Hydro Plant Bus 2	29.29	510.71	1	60
	64.8	-1620	60	75
	29.29	1042.5	75	135
	64.8	-3732	135	150
	29.29	1594.71	150	210
	64.8	-1620	210	225
Thermal Plant Bus 3	63.618	-48.4	11	33
	64	-61	33	64
	30.6538	2073.2	64	90
	67.889	-1278	90	117
	36.538	2390	117	143
	66.2083	-1852.79	143	167
	49.667	909.667	167	209
	93.684	-8290	209	247
Thermal Plant Bus 45	64.9954	5.1545	12	34
	69	-131	34	64
	34.5	2077	64	90
	70.2857	-1143.7	90	118
	41.4615	2257.54	118	144
	72.227	-2172.73	144	166
	52.9286	1030.857	166	208
	96.8421	-8103.16	208	246

Hydro-seasonal and technical limit data of the active powers of the plants are given in the table 5 as follows

Table 5. Active Power Limits of the Plants

Bus(i)	Plant	P_{min}(MW)	P_{max}(MW)	$S_{nominal}$(MVA)
1	Hydro	50	235	300
2	Hydro	30	189	225
3	Thermal	60	245	247
45	Thermal	59	240	246

Let's suppose that the total load forecast in 24 hours for the 45-buses power system is given in a graphic form containing different load levels representing in the figure 5 as follow

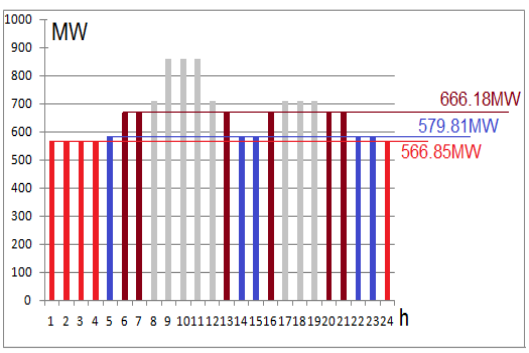

Figure 5. Total load graphic of the power system

The unit commitment problem is to find the optimal solutions deciding which of the available generators should start-up and shut-down over a given time period for the 3 load levels of 666.18MW, of 579.81MW and of 566.85MW according to the given data of the daily load, to minimize the fuel cost in the whole of power system.

The bus 45 is pilot-slack, voltage of which is 1 (pu). The optimal unit commitment solutions for the whole of power system are shown in the table 6, 7 and 8 as follows:

Table 6. Optimal Solution for the Load Level 1

Bus (i)	Optimum Generation		**Optimal UC Solution for the whole of power system**
	MW	MVAR	**Operating Generators**
1	225	-47.359	**H1, H2, H3**
2	150	6.7585	**H1, H2, H3**
3	238.382	45.595	**G1, G2, G3, G4**
45	63.809	-35.067	**G4**
MW_Losses ΔP = 11.015 MW Total Economic Fuel-Cost C = 18314.371 $/h			

Table 7. Optimal Solution for the Load Level 2

Bus (i)	Optimum Generation		**Optimal UC Solution for the whole of power system**
	MW	MVAR	**Operating Generators**
1	150	-39.246	**H1, H2, H3**
2	165.257	-6.574	**H1, H2, H3**
3	209	33.599	**G1, G2, G3, G4**
45	63.7116	-56.667	**G4**
MW_Losses ΔP = 8.163 MW Total Economic Fuel-Cost C = 15555.17 $/h			

Table 8. Optimal Solutions for the Load Level 3

Bus (i)	Optimum Generation		**Optimal UC Solution for the whole of power system**
	MW	MVAR	**Operating Generators**
1	150	-44.709	**H1, H2, H3**
2	150	-6.067	**H1, H2**
3	213.746	30.941	**G1, G2, G3, G4**
45	60.914	-54.086	**G4**
MW_Losses ΔP = 7.81 MW Total Economic Fuel-Cost C = 15806.708 $/h			

CONCLUSION

The new algorithm using the linear programming to calculate the optimal active and reactive powers to solve the hydro-thermal unit commitment problem in short-term period of power system operation is proved with good convergence.

The application of the specific type of the fuel cost functions for the problem of optimal active and reactive power generation allows simulating the back-pressure effect of turbine regulation. The eigen-image matrix allows to simply determining the bus sensitivities of network transmission losses to active and reactive power changes, then, the process of calculation obtains a good results of voltage optimum levels according to the solution of problem of optimization of the active and reactive power flow.

REFERENCES

[1]. Luu Huu Vinh Quang. *Considering the turbine back-pressure effect of thermal units for solving of generator pq_power optimization in power system.* Science&Technology Development Journal N°K3 Vol.16 - 2013, VNU HCMC, ISSN 1859-0128.

[2]. Luu Huu Vinh Quang. *Hydro-thermal pq_power optimization with the thermal turbine back-pressure effect.* Proceedings of 8th SEATUC Symposium, [OS10] 57, ISBN 978-967-12214-1-9, 4–5 March 2014, Malaysia.

[3]. Luu Huu Vinh Quang. *PQ_power optimization in hydro-thermal electrical power system with the network eigen-image matrix*. Authorship testimonial N°922/2015/QTG - Copyright Office of Vietnam.

[4]. Luu Huu Vinh Quang. *Using equivalent fuel cost characteristics of the thermal stations to optimize the p_power flows for economic power system operation*. Proceedings of the International Symposium on Electrical and Electronics Engineering 2011, HCMUT, Authorship testimonial N°2282/2013 /QTG - Copyright Office of Vietnam.

[5]. Luu Huu Vinh Quang. *Optimal Solution of Unit Commitment Problem in Hydro-Thermal Electrical Power System.* Proceedings of the International Symposium on Electrical and Electronics Engineering 2013, p.264-272, ISBN 978-604-73-2039-4, HCMUT, Authorship testimonial N°921/2015/QTG - Copyright Office of Vietnam.

AVERAGING MODEL OF BUCK CONVERTER FED BY SOLAR PHOTOVOLTAIC SOURCE

Patumporn Wongyai, Kongpan Areerak*, and Kongpol Areerak
Power electronics, Energy, Machines, and Control Research Group,
School of Electrical Engineering, Suranaree University of Technology,
Nakhon Ratchasima, Thailand *kongpan@sut.ac.th

ABSTRACT

Recently, the solar photovoltaic sources have become a useful renewable energy for a power generation. Normally, the solar cell is operated with the power electronic devices. For analysis and design of such system, the mathematical model is required. Unfortunately, dynamic models of power converter are time-varying in nature because of their switching actions. As a result, the system analysis and design via the time-varying model is very complicated. Therefore, this paper presents the mathematical model of buck converter fed by the PV array. The proposed model is derived from the generalized state-space averaging method. This method is used to eliminate the switching behavior to achieve the time-invariant model suitable for a system analysis and design via the conventional control theory. The intensive time-domain simulations show that the resulting model can provide high accuracies in both transient and steady-state responses with fast simulation time compared with the exact topology model. The results show that the reported models provide high accuracies in both transient and steady-state responses. Moreover, the fast simulation time can be obtained. Hence, the reported model in the paper can then be applied as the objective function for the optimal controller design using the artificial intelligence techniques in the future works. However, the aim of this paper is focus on only how to derive the time-invariant model of the considered power system.

The paper is structured as follows. In Section 2, the considered system is illustrated. In Section 3, deriving the dynamic model of the considered system using the GSSA methods is explained. In Section 4, the model validation using the small-signal simulation is illustrated. Finally, Section 5 concludes and discusses the advantages of proposed model derived from the GSSA method.

1. INTRODUCTION

Generally, dynamic models are very important for system analysis and design. Unfortunately, the models of power electronic based systems are time-varying in nature in which the system analysis and designs via these time-varying models are very complicated. Therefore, several approaches are commonly used for eliminating the switching actions to achieve the time-invariant model. Then, the classical linear control theory can be easily applied. This paper presents how to derive the dynamic model of the example system, a solar photovoltaic feeding a buck converter with a resistive load, by using the generalized state-space averaging (GSSA) method [1]-[4]. The derived model is validated by the intensive time-domain simulation via the exact topology model from SimPowerSystems^{TM} (SPS^{TM}) of MATLAB.

2. STUDIED SYSTEM

The considered system is depicted in Fig. 1. It consists of a PV array, buck converter, and resistive load. It is assumed that the buck converter is operated under a continuous conduction mode (CCM). In Section 3, the model derivation using a GSSA method to achieve the time-invariant model due to eliminating switching actions of switch S_1 will be explained.

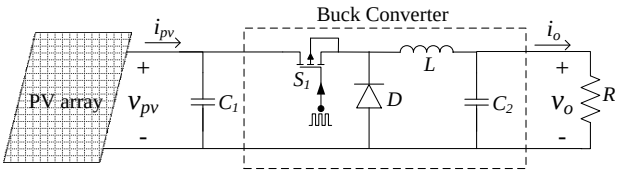

Fig. 1 The studied system

3. DYNAMIC MODEL

In this paper, the GSSA method is used to derive the dynamic model of buck converter in which the switching function under the CCM condition is firstly defined in (1).

$$u(t)=\begin{cases}1, & 0<t<dT_s\\ 0, & dT_s<t<T_s\end{cases} \tag{1}$$

where d is the duty cycle of the switch S_1 as shown in Fig. 1.

Applying the KVL and KCL to Fig. 1, the time-varying model of the studied system is given by (2).

$$\left.\begin{aligned}\dot{v}_{pv}&=\frac{1}{C_1}i_{pv}-\frac{1}{C_1}i_L u(t)\\ \dot{i}_L&=\frac{1}{L}v_{pv}u(t)-\frac{1}{L}v_o\\ \dot{v}_o&=\frac{1}{C_2}i_L-\frac{1}{RC_2}v_o\end{aligned}\right\} \tag{2}$$

By using the GSSA method, the zero and the first order components of the function $u(t)$ can be expressed as

$$\langle u\rangle_0=\frac{1}{T_s}\int_0^{dT_s}1e^0dt=\frac{1}{T_s}[t]_{t=0}^{t=dT_s}=d \tag{3}$$

$$\langle u\rangle_1=\frac{1}{T_s}\int_0^{dT_s}1e^{-j\omega_s t}dt=\frac{\sin(2\pi d)}{2\pi}-j\frac{\sin^2(\pi d)}{\pi} \tag{4}$$

Based on the complex Fourier series, the first-order approximations of the actual states are denoted as

$$\left.\begin{aligned}v_{pv}&=\langle v_{pv}\rangle_{-1}e^{-jk\omega_s t}+\langle v_{pv}\rangle_0+\langle v_{pv}\rangle_1 e^{jk\omega_s t}\\ i_L&=\langle i_L\rangle_{-1}e^{-jk\omega_s t}+\langle i_L\rangle_0+\langle i_L\rangle_1 e^{jk\omega_s t}\\ v_o&=\langle v_o\rangle_{-1}e^{-jk\omega_s t}+\langle v_o\rangle_0+\langle v_o\rangle_1 e^{jk\omega_s t}\end{aligned}\right\} \tag{5}$$

The Fourier expansion leads to 9 state variables denoted by x_k as follows:

$$\langle v_{pv}\rangle_1=x_1+jx_2 \qquad \langle i_L\rangle_1=x_3+jx_4 \qquad \langle v_o\rangle_1=x_5+jx_6$$
$$\langle v_{pv}\rangle_0=x_7 \qquad \langle i_L\rangle_0=x_8 \qquad \langle v_o\rangle_0=x_9$$

For k=1, one can obtain $\frac{d}{dt}\langle v_{pv}\rangle_1$ and $\langle i_L u(t)\rangle_1$ as follows:

$$\frac{d}{dt}\langle v_{pv}\rangle_1=\frac{1}{C_1}\langle i_{pv}\rangle_1-\frac{1}{C_1}\langle i_L u(t)\rangle_1-j\omega_s\langle v_{pv}\rangle_1$$
$$\langle i_L u(t)\rangle_1=\langle i_L\rangle_1\langle u(t)\rangle_0+\langle i_L\rangle_0\langle u(t)\rangle_1$$

Therefore,

$$\frac{d}{dt}\langle v_{pv}\rangle_1=\frac{1}{C_1}\langle i_{pv}\rangle_1-\frac{1}{C_1}\left(\langle i_L\rangle_1\langle u(t)\rangle_0\right)-\frac{1}{C_1}\left(\langle i_L\rangle_0\langle u(t)\rangle_1\right)-j\omega_s\langle v_{pv}\rangle_1 \tag{6}$$

By substitution, the following relations for $\dot{x}_1$ and $\dot{x}_2$ can be obtained

$$\dot{x}_1=\omega_s x_2-\frac{d}{C_1}x_3-\frac{\sin(2\pi d)}{2\pi C_1}x_8 \tag{7}$$

$$\dot{x}_2=-\omega_s x_1-\frac{d}{C_1}x_4+\frac{\sin^2(\pi d)}{\pi C_1}x_8 \tag{8}$$

Considering the terms $\frac{d}{dt}\langle i_L\rangle_1$ and $\frac{d}{dt}\langle v_o\rangle_1$, in a similar manner one can obtain $\dot{x}_3$, $\dot{x}_4$, $\dot{x}_5$ and $\dot{x}_6$ expressed as

$$\dot{x}_3=\frac{d}{L}x_1+\omega_s x_4-\frac{1}{L}x_5+\frac{\sin(2\pi d)}{2\pi L}x_7 \tag{9}$$

$$\dot{x}_4=\frac{d}{L}x_2-\omega_s x_3-\frac{1}{L}x_6-\frac{\sin^2(\pi d)}{\pi L}x_7 \tag{10}$$

$$\dot{x}_5=\frac{1}{C_2}x_3-\frac{1}{RC_2}x_5+\omega_s x_6 \tag{11}$$

$$\dot{x}_6=\frac{1}{C_2}x_4-\omega_s x_5-\frac{1}{RC_2}x_6 \tag{12}$$

For k=0, $\frac{d}{dt}\langle v_{pv}\rangle_0$ and $\langle i_L u(t)\rangle_0$ can be derived and expressed by

$$\frac{d}{dt}\langle v_{pv}\rangle_0=\frac{1}{C_1}\langle i_{pv}\rangle_0-\frac{1}{C_1}\langle i_L u(t)\rangle_0$$
$$\langle i_L u(t)\rangle_0=\langle i_L\rangle_0\langle u(t)\rangle_0$$

Therefore,

$$\frac{d}{dt}\langle v_{pv}\rangle_0=\frac{1}{C_1}\langle i_{pv}\rangle_0-\frac{1}{C_1}\left(\langle i_L\rangle_0\langle u(t)\rangle_0\right) \tag{13}$$

Hence, $\dot{x}_7$ can be obtained by substitution as

$$\dot{x}_7=\frac{1}{C_1}i_{pv}-\frac{d}{C_1}x_8 \tag{14}$$

In a similar manner, considering $\frac{d}{dt}\langle i_L\rangle_0$ and $\frac{d}{dt}\langle v_o\rangle_0$, the terms $\dot{x}_8$ and $\dot{x}_9$ can be derived and expressed by

$$\dot{x}_8=\frac{d}{L}x_7-\frac{1}{L}x_9 \tag{15}$$

$$\dot{x}_9=\frac{1}{C_2}x_8-\frac{1}{RC_2}x_9 \tag{16}$$

Let $x=[x_1 \;\; x_2 \;\; \ldots \;\; x_9]^T$ be the state vector, $u=[i_{pv}]$ and $y=[x_1 \;\; x_2 \;\; \ldots \;\; x_9]$ be the input and the output, respectively. Hence, the obtained linear time-invariant model in the form of

$$\left.\begin{aligned}\dot{\mathbf{x}}&=\mathbf{A}x+\mathbf{B}u\\ \mathbf{y}&=\mathbf{C}x+\mathbf{D}u\end{aligned}\right\} \tag{17}$$

The details of **A, B, C** and **D** are show as follow:

$$\mathbf{A}=\begin{bmatrix} 0 & \omega_s & -\frac{d}{C_1} & 0 & 0 & 0 & 0 & -\frac{\sin(2\pi d)}{2\pi C_1} & 0 \\ -\omega_s & 0 & 0 & -\frac{d}{C_1} & 0 & 0 & 0 & \frac{\sin^2(\pi d)}{\pi C_1} & 0 \\ \frac{d}{L} & 0 & 0 & \omega_s & -\frac{1}{L} & 0 & \frac{\sin(2\pi d)}{2\pi L} & 0 & 0 \\ 0 & \frac{d}{L} & -\omega_s & 0 & 0 & -\frac{1}{L} & -\frac{\sin^2(\pi d)}{\pi L} & 0 & 0 \\ 0 & 0 & \frac{1}{C_2} & 0 & -\frac{1}{RC_2} & \omega_s & 0 & 0 & 0 \\ 0 & 0 & 0 & \frac{1}{C_2} & -\omega_s & -\frac{1}{RC_2} & 0 & 0 & 0 \\ 0 & 0 & 0 & 0 & 0 & 0 & 0 & -\frac{d}{C_1} & 0 \\ 0 & 0 & 0 & 0 & 0 & 0 & \frac{d}{L} & 0 & -\frac{1}{L} \\ 0 & 0 & 0 & 0 & 0 & 0 & 0 & \frac{1}{C_2} & -\frac{1}{RC_2} \end{bmatrix}$$

$$\mathbf{B}=\begin{bmatrix} 0 & 0 & 0 & 0 & 0 & 0 & \frac{1}{C_1} & 0 & 0 \end{bmatrix}^T \quad \mathbf{C}=\mathbf{I}_{9x9} \quad \mathbf{D}=\mathbf{0}_{9x1}$$

Based on the first-order approximation (k=1), the output waveforms can then be calculated by the resulting state variables as follow:

$$v_{pv} = x_7 + 2x_1\cos(\omega t) - 2x_2\sin(\omega t)$$

$$i_L = x_8 + 2x_3\cos(\omega t) - 2x_4\sin(\omega t)$$

$$v_o = x_9 + 2x_5\cos(\omega t) - 2x_6\sin(\omega t)$$

where i_{pv} is the output current from the PV array. This current depends on irradiance (Irr) and temperature (T) [5] in which it can be calculated by

$$\frac{1}{C_1}\left[\left(i_{sc}+K_i\left(T-T_{ref}\right)\right)\frac{Irr}{Irr_o}-\left(\frac{i_{sc}}{e^{\frac{qV_{oc}}{CkTn}}-1}\left(e^{\frac{qV_{pv}}{CkTn}}-1\right)\right)\right] \qquad (18)$$

where

i_{sc} = short circuit current
V_{oc} = open circuit voltage
K_i = current proportionality constant ($2.2\text{x}10^{-3}$)
T = panel temperature(Kelvin)
Irr = irradiance (W/m^2)
q = electronic charge($1.6\text{x}10^{-19}$ coulombs)
C = number of cells in 1 module
k = Boltzmann's constant ($1.3805\text{x}10^{-23}$ j/K)
n = diode factor (Silicon diode=1.2)

Standard Test Conditions (STC) : Irr_o=1000W/m^2, T_{ref} =25^{o}C, AM=1.5

The dynamic model in (17) is called the first-order approximation of GSSA model. If the considered waveforms can be assumed that they do not have the ripple, the zero-order approximation can be applied. As a result, only $\dot{x}_7$ $\dot{x}_8$ and $\dot{x}_9$ are remained in the dynamic model as shown in (19).

$$\begin{bmatrix}\dot{x}_7\\ \dot{x}_8\\ \dot{x}_9\end{bmatrix}=\begin{bmatrix} 0 & -\frac{d}{C_1} & 0 \\ \frac{d}{L} & 0 & -\frac{1}{L} \\ 0 & \frac{1}{C_2} & -\frac{1}{RC_2}\end{bmatrix}\begin{bmatrix}x_7\\ x_8\\ x_9\end{bmatrix}+\begin{bmatrix}\frac{1}{C_1}i_{pv}\\ 0\\ 0\end{bmatrix} \qquad (19)$$

It can be seen in (19) that when k is equal to 0 for the zero-order approximation, $\dot{x}_7$ $\dot{x}_8$ and $\dot{x}_9$ are equal to v_{pv}, i_L and v_o, respectively.

4. MODEL VALIDATION

The obtained models are coded in MATLAB for simulation comparisons with SPS^{TM} software. The simulated circuit as shown in Fig. 2 has the following components:

Photovoltaic:T_{ref} =273.15+25 Kelvin, Irr_o=1000W/m^2, T =273.15+25 Kelvin, Irr=1000 W/m^2, i_{sc}=2.35 A, V_{oc}=21.3 V, K_i=$2.2\text{x}10^{-3}$, C=36, k=$1.3806504\text{x}10^{23}$ j/K, n=1.2

Buck Converter : $C_1 = 470\mu F$, $C_2 = 1000\mu F$, $L = 15mH$, $R = 5\Omega$

Simulation results in Fig. 3 to Fig. 5 are the output voltage waveforms of the PV array, the inductor current of buck converter, and the output voltage of buck converter from the zero-order and first-order approximations compared with the results from topology model of SPS^{TM} when the d equal to 0.3.

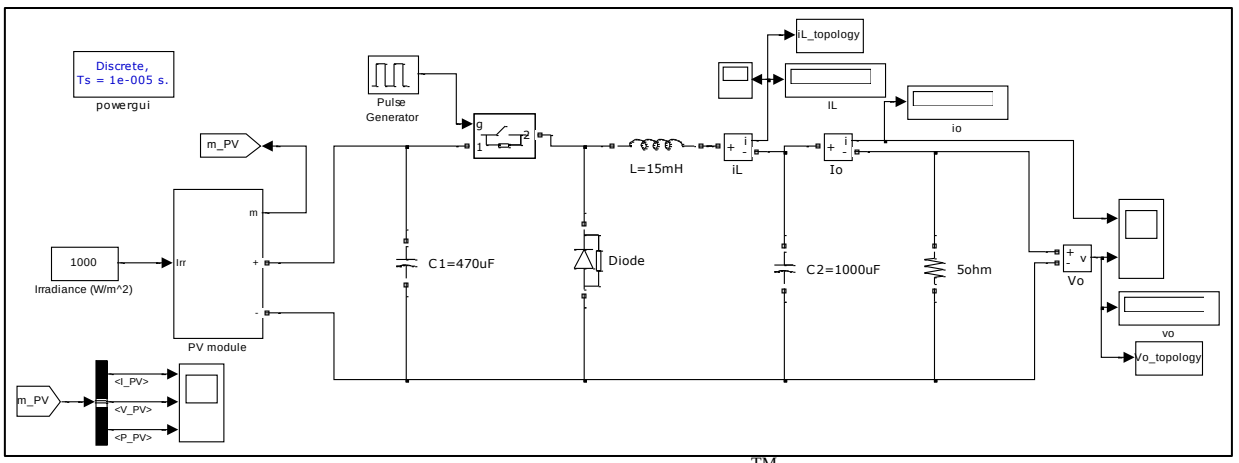

Fig. 2 Topology model simulated in SPS^{TM} of MATLAB

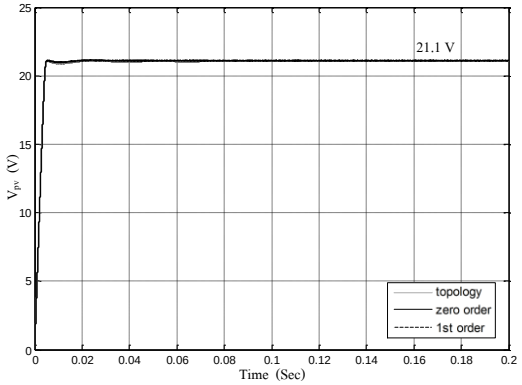

Fig. 3 The output voltage of PV array when d=0.3

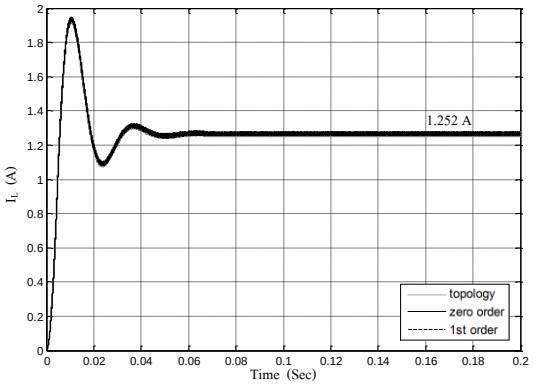

Fig. 4 The inductor current of buck converter when d= 0.3

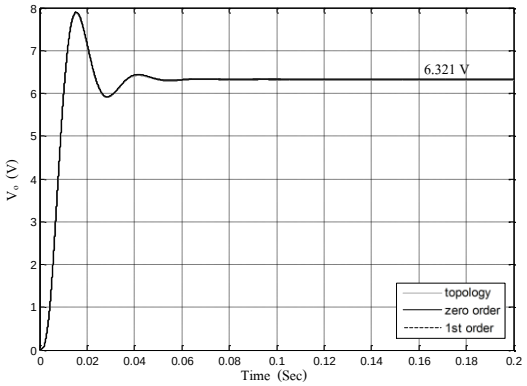

Fig. 5 The output voltage of buck converter when d=0.3

The computing times taken by MATLAB coding for the zero- and first-order models are 0.56 s. and 2.54 s., respectively, while SPS™ consumes 11.87 s. for full topology simulation. The comparison of simulation time can be illustrated in terms of computational time saving defined by:

$$\%t_{saving} = \frac{t_{fs} - t_{av}}{t_{fs}} \times 100\% \qquad (20)$$

where t_{fs} and t_{av} are the simulation times of full topology and the averaged GSSA models, respectively. According to (20), the zero- and first-order GSSA models can provide $\%t_{saving}$ of 95.28% and 78.60%, respectively. These values indicate that the simulation using the averaged models requires short computational time compared with SPS™. Note that, more accurate models can be obtained by increasing k in the GSSA derivation in an exchange of more tedious derivation, and computational time increase.

5. CONCLUSION

This paper presents how to derive the dynamic model of the PV array feeding a buck converter. The GSSA method is used to eliminate the switching behaviour of the buck converter. The simulation results show that the proposed averaging model provide a good accuracy in both transient and steady-state responses. Moreover, the proposed model consumes the fast simulation time compared with those of the exact topology model. According to the advantages of the resulting model, the classical control theory can be easily used for the system analysis and design. In addition, the dynamic model derived from the paper is suitable for the optimal controller design using the artificial intelligence techniques because the fast simulation time can be achieved from the proposed model.

ACKNOWLEDGEMENT

This work was supported by Suranaree University of Technology (SUT) and by the office of the Higher Education Commission under NRU project of Thailand.

REFERENCES

[1] J. Mahdavi, A. Emadi, M.D. Bellar, M. Ehsani, Analysis of Power Electronic Converter Using the Generalized State-Space Averaging Approach, *IEEE Trans. On Circuit and System*., vol. 44, August 1997, pp.767-770

[2] A. Emadi, Modeling and Analysis of Multiconverter DC Power Electronic System Using the Generalized State-Space Averaging Method, *IEEE Trans. On Indus. Elect*., vol. 51, n. 3, June 2004, pp. 661-668.

[3] S.F. Glover, Modeling and stability analysis of power electronics based systems, Ph.D. dissertation, Purdue Univ., 2003.

[4] S.D. Sudhoff, Analysis and Average-Value Modeling of Dual Line-Commutate Converter-6-Phase Synchronous Machine Systems, *IEEE Trans. on Energy Convention.*, vol. 8, n. 3, September 1993, pp. 411-417.

[5] Afshin Izadian, Arash Pourtaherian, and Sarasadat Motahari, Basic model and governing equation of solar cells used in power and control applications, *Energy Conversion Congress and Exposition (ECCE), 2012 IEEE.*, 15-20 September 2012, Raleigh, NC, pp. 1483-1488

OPTIMIZATION OF PQ_POWER GENERATION IN HYDRO-THERMAL POWER SYSTEM BY GRADIENT SEARCH METHOD

Luu Huu Vinh Quang
HoChiMinh City, Vietnam - lhv2uang@hotmail.com

ABSTRACT

A new algorithm of optimum coordination of power of the generator units in hydro-thermal power system is proposed and some typical numerical examples are presented in this article. The water consumption characteristic of the hydro-unit is approximately simulated in form considering the water limit constraints of hydro power generation under condition of dry or rains seasons. The fuel cost characteristics of the thermal generator is simulated in form of superposition of some high order polynomial and sinusoidal functions considering the turbine back-pressure effect of the thermal generator units. A new loss factor formula expressing the network transmission power losses is proposed to build the new algorithm using the gradient search technique for optimization of the active and reactive powers of the generator units in hydro-thermal multi-machine power system.

INTRODUCTION

The main objective of an economic power dispatch strategy is to determine the optimal operating state of a power system by optimizing a particular objective while satisfying certain specified physical and operating constraints. In its most general formulation, the economic power dispatch is a nonlinear, nonconvex, large-scale, static optimization problem.

In reality, the water consumption amount per hour W(m^3/h) of a hydro unit for the active power generation depends on the water head H_w of reservoir of the hydro plant. The characteristic W(m^3/h) may be taken in form of some curve, for example, the function of water consumption W(P,H_W) depending on the active power generation of a hydro unit may be represented as shown in the figure 1

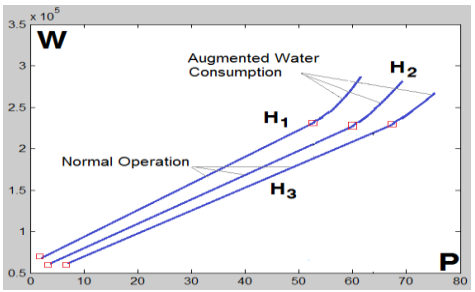

Figure 1. Rating Water Consumption W(P)

The most of the curve W(P_{gh}, H_w) is almost linear, simulating the state of normal operation. An end of the characteristic is a supplementary small fragment simulating the state of augmented water consumption for a large load operation. According to the figure 1, we propose to simulate the characteristic of water consumption W(P,H_W) as follow:

$$W(P_{gh},H_W)=a_h P_{gh}^2+b_h P_{gh}+c_h; \qquad (1a)$$

The coefficient a_h is small under condition of normal operation and may be neglected, i.e. setting a_h=0, so that the characteristic of water consumption W(P,H_W) may be simulating in form of a linear equation

$$W(P_{gh},H_W)=b_h P_{gh}+c_h; \qquad (1b)$$

In the rain seasons, the water is plenty, the hydro units can generate the active power as much as possible, leading to minimize the total fuel cost of the thermal units. In the dry seasons, water may be deficiency, the hydro active power generation is limited because of many reasons, the main of which is agricultural irrigation. In reality, the water inflows and the water storage amounts are known for a daily period in 24h. Let's suppose the weather and hydrographic forecasts in short time are reliable, it is possible so that the average water availability per hour can be known. The average amount of water storage per hour and the average amount of water inflow per hour for the water reservoir of hydro plants can be known in short-term forecast, leading to the solution of the short-term problem of optimization of the hydro thermal active power generation can be satisfied the water availability constraint per hour as follow

$$W_{avr.stor.}^{1h}-W_{avr.inf\ low}^{1h}+W(P_{gh},H_W^{1h})=0; \qquad (2)$$

where $W_{avr.stor.}^{1h}$ is the average amount of water storage per hour;
$W_{avr.inf\ low}^{1h}$ is the average amount of water inflow per hour ;

The turbine fuel cost characteristics can be obtained in form of some convex fracture, this is notably arised by the back-pressure characteristic of turbine, in addition, the method of turbine regulation also raises some effect to the appearance of the fuel cost characteristics of turbine, and it may be briefly called the turbine back-pressure effect.

In most cases, the fuel cost characteristics of the thermal units rating under 25 MW may be determined experimentally and fit for the 2nd order polynomial function. The fuel cost characteristics of thermal unit rating upper 25MW may be fit for nth order polynomial superposing some sinusoidal function to simulate the turbine back-pressure effect of generator on the thermal electrical stations, approximately

$$C(P_{gt}) = \sum_{m=0}^{n} a_{n-m} P_{gt}^{n-m} + b\sin(c(P_{gt} - d)); \quad (3)$$

A typical fuel-cost characteristic is approximately rated for the simulation of the turbine back-pressure effect as follows

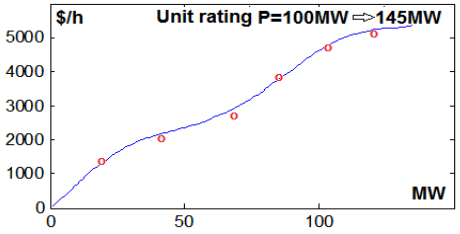

Figure 2. Typical rating fuel cost functions.

This paper is organized following: Problem of optimization of active power generation; Problem of optimization of reactive power generation; Numerical examples; Conclusion; References.

PROBLEM OF OPTIMIZATION OF ACTIVE POWER GENERATION

The optimization of hydro-thermal active power generation is an important problem to be solved in the operation and planning of a power system. The objective of the problem of optimal active power generation of all generator units so as to meet the required load demand at minimum operating cost while satisfying system technical constraints.

Using the fuel costs (3) of thermal power generation considering the condition of water consumption (1) with the constraint (2) of hydro power generation to solve the problem of economic active power generation, minimizing the total fuel cost $C_t(P_{gti})$ and the active power transmission losses $\Delta P(P_{gti},P_{ghi})$ in the whole of hydro-thermal electric power system. Let's denote the target function by C which can be written as follow

$$C = C_t(P_{gti}) + \Delta P(P_{gti}, P_{ghi}) \to min; \quad (4)$$

where

$$C_t(P_{gti}) = \sum_{i=1}^{N_{gt}} \left(\sum_{k=0}^{n} a_{i,n-k} P_{gti}^{n-k} + b_i \sin(c_i(P_{gti} - d_i)) \right) \to min; \quad (5)$$

$$\Delta P(P_g) = \sum_{m=1}^{N_g} \sum_{n=1}^{N_g} P_{gm} B_{mn} P_{gn} \to min; \quad (6)$$

subject to (1), (2) and satisfying to

$$(P_{gti}^{-} \le P_{gti} \le P_{gti}^{+}); \quad (7)$$

$$(P_{ghi}^{-} \le P_{ghi} \le P_{ghi}^{+}); \quad (8)$$

$$P_D + \Delta P(P_{gt}, P_{gh}) - \sum_{i=1}^{N_{gt}} P_{gti} - \sum_{i=1}^{N_{gh}} P_{ghi} = 0; \quad (9)$$

where P_{gti}, is active powers of the ith thermal generator; P_{ghi} is active powers of the ith hydro generator; P_{gi} is active power of a generator which may be a hydro or a thermal; N_{gt} is number of thermal generator unit; N_{gh} is number of hydro generator unit; $N_g=(N_{gt}+N_{gh})$ is number of all hydro and thermal generators; P_D is total active power load demand in the elctric network.

The MW-loss factor B_{mn} can be found under condition of the tth solution of load power flow problem [1] as follow

$$B_{mn} = \frac{\cos(\alpha_m - \alpha_n)}{V_m V_n \cos\varphi_m \cos\varphi_n} + \sum_{r=1}^{N_b} \frac{\left|\sum_{h=1}^{N} C_{rh} J_h - C_{rm} J_\Sigma\right| \times \left|\sum_{h=1}^{N} C_{rh} J_h - C_{rn} J_\Sigma\right|}{|J_\Sigma|^2}; \quad (10)$$

where V_m, V_n are bus voltage modules of the mth and nth generators; α_m, α_n are arguments of the current output from the mth and nth generators; $\cos\varphi_m$, $\cos\varphi_n$ are power factors of the mth and nth generators; J_h is bus current at the hth bus ; J_Σ is sum of all of bus currents; C_{rh}, C_{rm} and C_{rn} are current distribution factors relating to the first rule of Kirchhoff; N is number of bus (h=1..N) and N_b is number of branch (r=1..N_b) of electric network.

The problem (1), (2), (3), (4), (5), (6), (7), (8), (9) can be solved by using the iteration of alternative calculation of the gradients of the function (4) to adjust the control variables which are active powers of the generators. For the sth step of iteration with a positive scalar γ_C, the active power of ith thermal unit can be controlled as follows

$$P_{gti(S+1)} = P_{gti(S)} - \gamma_C \nabla_i C_{ti}(P_{gti})_{(S)}; \quad (11)$$

where

$$\nabla_i C_{ti}(P_{gti})_{(S)} = D_i + (H_i - 1) \sum_{m=1}^{N_g} \frac{D_m}{N_g(1 - H_m)};$$

$$i = 1...N_{gt};$$

$H_m = \sum_{r=1}^{N_g} 2B_{m,r} P_{gr}$, H_m is a coefficient for mth generator unit;

D_m is a coefficient; $D_m = a_{hm}$ for a hydro unit; and $D_m = b_m c_m \cos(c_m(P_{gtm} - d_m)) + \sum_{k=0}^{n-1} (n-k) a_{m,n-k} P_{gtm}^{n-1-k}$; for a thermal unit;

$H_i = \sum_{r=1}^{N_g} 2B_{i,r} P_{gr}$, H_i is a coefficient for ith thermal unit;

$D_i = b_i c_i \cos(c_i(P_{gti} - d_i)) + \sum_{k=0}^{n-1} (n-k) a_{i,n-k} P_{gti}^{n-1-k}$; D_i is a coefficient for ith thermal unit,

And for the sth step of iteration with a positive scalar $\gamma_{\Delta P}$, the kth hydro or thermal active powers can be adjusted as follows

$$P_{gk(S+1)} = P_{gk(S)} - \gamma_{\Delta P} \nabla_k \Delta P(P_{gk})_{(S)}; \quad (12)$$

where

$$\nabla_k \Delta P(P_{gk}) = H_k + (H_k - 1)\sum_{n=1}^{N_g} \frac{H_n}{N_g(1-H_n)};$$

$$k = 1...N_g;$$

H_k and H_n are the coefficients for the k^{th} and m^{th} generator unit; $H_k = \sum_{r=1}^{N_g} 2B_{k,r}P_{gr};$ $H_n = \sum_{r=1}^{N_g} 2B_{n,r}P_{gr};$

PROBLEM OF OPTIMIZATION OF REACTIVE POWER GENERATION

The problem of optimization of reactive power generation is to minimize the transmission active power losses, taking into account the steady-state stability margin of every generator in electric power system. The target function is

$$\Delta P_q(Q_g) = \sum_{m=1}^{N_g}\sum_{n=1}^{N_g} Q_{gm}B_{mn}Q_{gn} \to min; \quad (13)$$

subject to

$$Q_{gi}^{-}(S_i) \le Q_{gi} \le Q_{gi}^{+}(S_i); \quad (14)$$

$$V_i^{-} \le V(Q_g)_i \le V_i^{+}; \quad (15)$$

$$Q_D + \Delta Q_L - Q_C - \sum_{i=1}^{N_g} Q_{gi} = 0; \quad (16)$$

where $Q_{g\,i}$ and S_i are MVAR and MVA output of the i^{th} generator; Q_D is total MVAR load in power system; ΔQ_L is total transmission MVAR loss in the inductive elements of network; Q_C is total capacitive reactive power charging by transmission lines.

The solution of the problem (13), (14), (15), (16) is obtained by iterative calculation adjusting the reactive power as follow

$$Q_{gi}^{(s+1)} = Q_{gi}^{(s)} - \gamma_q \nabla \Delta P_q^{(s)}(Q_{gi}); \quad (17)$$

where γ_q is positive gradient step;

The gradient of target function for the s^{th} iteration step can be determined as follow

$$\nabla \Delta P_q^{(s)}(Q_{gi}) = 2\sum_{j=1}^{N_g} B_{ij}Q_{gi}^{(s)} + 2\mu_q Q_{gi}^{(s)} - \frac{1}{N_g}\sum_{i=1}^{N_g}\left(2\sum_{j=1}^{N_g} B_{ij}Q_{gi}^{(s)} + 2\mu_q Q_{gi}^{(s)}\right); \quad (18)$$

μ_q is a penalty factor;

NUMERICAL EXAMPLE

Let's survey the optimum condition operation of a 75-bus power system consisting of 3 thermal plants with 11 generator units and 2 hydro plants with 7 generator units. Basic power is 100 MVA. The linedata is given in p.u. in table 1 as follows

Table 1. Linedata

Bus (i)	Bus (j)	R (pu)	X (pu)	B/2 (pu)
1	45	0.0083	0.2066	0
2	45	0.0083	0.2066	0
3	45	0.0083	0.2066	0
4	45	0.0083	0.2066	0
5	47	0.0055	0.1504	0
6	47	0.0055	0.1504	0
7	47	0.0055	0.1504	0
8	48	0.0083	0.2066	0
9	48	0.0083	0.2066	0
10	48	0.0083	0.2066	0
11	48	0.0083	0.2066	0
12	50	0.0083	0.2066	0
13	50	0.0083	0.2066	0
14	44	0.0021	0.2066	0
15	44	0.0083	0.2066	0
16	44	0.0083	0.2066	0
17	44	0.0083	0.2066	0
18	19	0.0353	0.0856	0.021192
18	39	0.0102	0.2087	0
18	74	0.0563	0.0886	0.020215
19	20	0.0219	0.0531	0.013146
19	40	0.0102	0.2087	0
19	48	0.0009	0.0393	0
19	53	0.0007	0.0702	0
20	21	0.0456	0.0717	0.016359
20	41	0.0058	0.1299	0
21	42	0.0102	0.2087	0
21	60	0.0547	0.1328	0.032865
22	58	0.0026	0.0646	0
23	59	0.0102	0.2087	0
24	60	0.0102	0.2087	0
25	61	0.0102	0.2087	0
26	62	0.0075	0.1624	0
27	63	0.0102	0.2087	0
28	64	0.0102	0.2087	0
29	65	0.0102	0.2087	0
30	66	0.0102	0.2087	0
31	67	0.0058	0.1299	0
32	68	0.0177	0.3236	0
33	69	0.0177	0.3236	0
34	70	0.0177	0.3236	0
35	71	0.0177	0.3236	0
36	72	0.0177	0.3236	0
37	73	0.0177	0.3236	0
38	74	0.0102	0.2087	0
43	44	0.0015	0.0628	0
43	54	0.0013	0.1033	0
43	62	0.0288	0.0823	0.020998
43	63	0.0706	0.1713	0.010596
43	68	0.0728	0.0703	0.015034
44	45	0.0090	0.0471	0.266829
44	46	0.0071	0.0313	0.172652
45	47	0.0108	0.0566	0.320553
45	58	0.0009	0.0393	0
46	71	0.0015	0.0628	0
47	48	0.0144	0.0633	0.349357
47	67	0.0009	0.0393	0
49	50	0.0090	0.0471	0.266829
49	60	0.0009	0.0393	0
50	51	0.0015	0.0628	0
50	75	0.0083	0.2066	0

51	52	0.0026	0.0646	0
55	58	0.0007	0.0702	0
56	67	0.0007	0.0702	0
57	71	0.0013	0.1033	0
58	59	0.0552	0.0868	0.019819
58	60	0.0340	0.0970	0.024739
58	61	0.0242	0.0690	0.017600
60	61	0.0476	0.1359	0.008666
62	63	0.0797	0.1254	0.007153
64	65	0.0354	0.0859	0.021268
65	67	0.0258	0.0736	0.018783
66	67	0.0441	0.1070	0.026481
67	73	0.1397	0.2198	0.012540
69	70	0.0405	0.0512	0.011359
70	71	0.0422	0.0663	0.015134
71	72	0.0502	0.0789	0.018017
72	73	0.0695	0.1093	0.006234

Let's investigate the case of large load. The busdata of initial operation condition of power system is given in table 2 as follow

Table 2. Load-Data

Bus (i)	Load		Fixed MVAR Compensation
	MW	MVAR	
18	0.058	0.4	0
19	0.058	0.4	0
20	0.084	0.56	0
21	0.058	0.4	0
22	87.5	59	20
23	29.5	21.12	7
24	35	29.47	12
25	35	26.63	10
26	37	26.54	11
27	29	21.68	8
28	27	19.17	7
29	31	20.26	7
30	33	22.96	8
31	59	37.8	15
32	19	13.61	3
33	21	15.2	4
34	18	15.31	6
35	20	15.5	5
36	21	19.47	7
37	27	21.85	9
38	29	27.92	12
39	24	22.36	8
40	42	33	15
41	21	19.32	7
42	21	15.38	6
43	0.15	1	0
44	0.2	1.6	0
45	0.2	1.6	0
46	0.15	1	0
47	0.2	1.6	0
48	0.2	1.6	0
49	0.2	1.6	0
50	0.2	1.6	0
51	0.14	0.96	0
52	78.5	58	20
53	0	0	20
54	0	0	13.854
55	0	0	30
56	0	0	24.028
57	0	0	19.306
58	0.14	0.96	0
59	0.058	0.4	0
60	0.058	0.4	0
61	0.058	0.4	0
62	0.07	0.48	0
63	0.058	0.4	0
64	0.058	0.4	0
65	0.058	0.4	0
66	0.058	0.4	0
67	0.084	0.56	0
68	0.042	0.272	0
69	0.042	0.272	0
70	0.042	0.272	0
71	0.042	0.272	0
72	0.042	0.272	0
73	0.042	0.272	0
74	0.058	0.4	0

The technical and seasonal limits of generation are given in table 3 as follow

Bus (i)	Unit Type	P_{min} (MW)	P_{max} (MW)	$S_{nominal}$ (MVA)
1	Hydro	1	51	62
2	Hydro	1	51	62
3	Hydro	1	51	62
4	Hydro	1	51	62
5	Hydro	1	47	72
6	Hydro	1	47	72
7	Hydro	1	47	72
8	Thermal	1	67	75
9	Thermal	1	67	75
10	Thermal	1	67	75
11	Thermal	1	67	75
12	Thermal	1	55	63
13	Thermal	1	55	63
14	Thermal	1	55	63
15	Thermal	1	55	63
16	Thermal	1	52	60
17	Thermal	1	52	60
75	Thermal	1	52	60

The fuel cost characteristics of the thermal units are given in form of a third order polynomial adding a sinusoidal function of active power generation

$$C(P_{gt}) = a_3 P_g^3 + a_2 P_g^2 + a_1 P_g + a_o + b\sin(c(P_g - d));$$

The characteristics of water consumption of the hydro units are given in form of a second order polynomial

$$W(P_{gh}) = a_2 P_g^2 + a_1 P_g + a_o;$$

and the specific datum of which are given in the tables 4a and 4b with suitable coefficients as follows

Table 4a. Characteristic Coefficients

Thermal Unit							
Bus	a_3	a_2	a_1	a_o	b	c	d
8	0.00022	0.3039	40.5	323	270	0.126	14
9	0.000168	0.3017	39.19	304	267	0.126	14

10	0.000167	0.3021	39.2	305	267	0.126	14
11	0.000167	0.3019	39.18	304	267	0.126	14
12	0.000199	0.3037	41.51	321	270	0.126	14
13	0.0002	0.304	41.49	322	270	0.126	14
14	0.0002	0.3038	41.49	323	270	0.126	14
15	0.000198	0.304	41.48	322	270	0.126	14
16	0.000145	0.3007	38.17	301	270	0.126	14
17	0.000147	0.3009	38.2	302	270	0.126	14
75	0.00019	0.304	40.5	322	270	0.126	14

Table 4b. Characteristic Coefficients

Hydro Unit			
Bus	a_2	a_1	a_o
1	0.015	42.349	252.65
2	0.016	41.292	253.95
3	0.015	43.146	251.25
4	0.014	42.451	253.32
5	0.023	47.945	283.83
6	0.021	48.121	282.97
7	0.022	47.915	285.18

The 75th bus is pilot-slack, the voltage of which is 1.05p.u. Typical results are shown in table 5 by comparing the initial powers with the optimum powers as follows

Table 5. Comparison of generation

	Initial Generation		Optimum Generation	
Bus	MW	MVAR	MW	MVAR
1	42	10.3959	42.6576	3.0234
2	42	10.3959	42.6377	3.0171
3	42	10.3959	42.6182	3.0108
4	42	10.3959	42.5991	3.0044
5	42	15.3233	47.0000	4.4711
6	42	15.3233	47.0000	4.4622
7	42	15.3233	47.0000	4.4535
8	42	11.1967	38.3904	3.6657
9	42	11.1967	40.2780	3.7146
10	42	11.1967	41.3711	3.7443
11	42	11.1967	42.2282	3.7685
12	42	14.4848	46.9609	7.6043
13	42	14.4848	46.3337	7.6644
14	42	14.4003	47.9190	6.1385
15	42	13.1097	43.8007	4.0387
16	42	13.1097	43.9749	4.0345
17	42	13.1097	43.9859	4.0250
75	51.7912	14.9684	17.1187	8.8859
Optimum Fuel Cost 26249.5 $/h				
Economic Power losses 16.468 MW				

The comparison of the voltage levels may be graphically shown in the figure 3

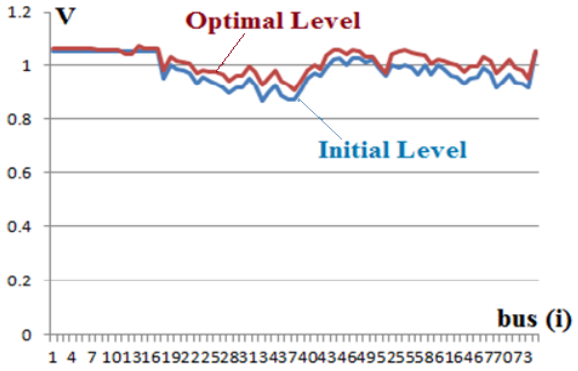

Figure 3. Voltage levels in case of large load

CONCLUSION

The new algorithm of optimization of the hydro thermal power generation has a good convergence, using the gradient search technique to solve the problem controlling the power outputs of thermal unit coordinating with the power outputs of hydro unit satisfying to the specific technical and the seasonal constraints to minimize the thermal fuel cost and the active power losses in a hydro-thermal multi-machine power system.

The application of the specific type of fuel cost function for the problem of optimal active and reactive power generation allows simulating the back-pressure effect of thermal turbine regulation.

The process of calculation obtains a good result of optimum voltage level.

REFERENCES

[1]. Luu Huu Vinh Quang. *Considering the turbine back-pressure effect of thermal units for solving of generator pq_power optimization in power system*. Science & Technology Development Journal N^{0}K3, Vol.16, 2013, VNU HCMC, ISSN 1859-0128.

[2]. Luu Huu Vinh Quang. *Hydro-thermal pq_power optimization with the thermal turbine back-pressure effect.* Proceedings of 8th SEATUC Symposium, [OS10] 57, 4–5 March 2014, Malaysia, ISBN 978-967-12214-1-9.

[3]. I.J. Nagrath D.P.Kothari. *Power System Engineering*. 1994, Tata McGraw-Hill Publishing Companie Limited, ISBN 0-07-460274-8.

[4]. Allen J.Wood Bruce F.Wollenberg. *Power generation operation and control*.1996, John Wiley & Sons, Inc, ISBN 0-471-58699-4.

[5]. James A.Momoh. *Electric Power System Applications of Optimization.* 2001, Marcel Dekker, Inc. ISBN 0-8247-9105-3.

MODELING OF TWO-STAGE CASCADED BOOST CONVERTER USING GENERALIZED STATE-SPACE AVERAGING APPROACH

Sauwalak Wongsrisai, Sudarat Khwan-on* and Kongpan Areerak
School of Electrical Engineering, Suranaree University of Technology
Nakhon Ratchasima, Thailand, 30000
*corresponding author: sudarat_kh@sut.ac.th

ABSTRACT

This paper presents the dynamic model of the two-stage cascaded boost converter under the continuous conduction mode (CCM) operation. Generally, the mathematical model of the power converters is naturally time-varying due to the switching behavior, resulting in the extremely complicated model for the system analysis and control. Therefore, in this paper the Generalized State-Space Averaging (GSSA) technique is employed to generate the time-invariant model of the two-stage cascaded boost converter. In addition, the principle of operation of the two-stage cascaded boost converter under the steady-state operating condition is analytically described. The developed mathematical model is verified by time-domain simulations in MATLAB software. The simulation results show that the proposed dynamic model for the two-stage cascaded boost converter can provide the accurate responses in both transient and steady-state operations.

1. INTRODUCTION

Power converters have been widely applied in many applications such as renewable energy systems, electric vehicles and motor drive systems. Due to the switching actions of the power converters the time-varying mathematical model is extremely complicated for the system analysis and control design [1]-[2]. In order to eliminate the switching action behavior in time-varying model, the time-invariant mathematical model is introduced to the power converters. Thus, the simplification of the system analysis and control design based on time-invariant model can be achieved. The generalized state-space averaging (GSSA) approach is a useful tool for time-invariant dynamic modeling of the power converters [3]-[5]

The conventional boost converter is an interesting topology of the dc-dc power converters in order to boost the low input voltage up to the higher level of the output voltage. Unfortunately, the conventional boost converter cannot provide higher voltage gains without an extreme duty cycle, resulting in deteriorated converter efficiency [6]. The cascaded boost converter has receive some attention in the applications where the high step-up voltage conversion ratios are required [7].

This paper presents the mathematically dynamic model of the two-stage cascaded boost converter, using the generalized state-space averaging method. In order to derive the time-invariant model correctly, the steady-state characteristic operations of the two-stage cascaded boost converter are analytically described under continuous conduction mode. In addition, the derivation of the model using the generalized state-space averaging technique is developed for the two-stage cascaded boost converter in the form of Fourier series expansion. The simulation results are shown to validate the accuracy of the developed dynamic model compared with results obtained from the exact topology. The comparison results show that the developed mathematical model can provide the satisfactory accuracy in both transient and steady-state responses of the two-stage cascaded boost converter.

2. PRINCIPLE OF OPERATION

The two-stage cascaded boost converter topology is shown in Fig. 1. Where V_{in} is the input voltage, S_1 and S_2 are the active switches, D_1 and D_2 are the power diodes, R is the load resistor. L_1, L_2 and C_1, C_2 are the inductances and the capacitances of the converter, respectively. The output voltage is given by $V_{out} = v_{C2}$. As can be seen in Fig.1, the two-stage boost converter consists of two conventional boost converters connected in cascade. The converter components in the first and second stages are usually identical.

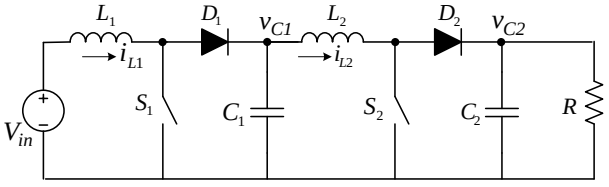

Fig. 1 The two-stage cascaded boost converter topology

Since there are two active switches located in two-stage cascaded boost converter, four stages of operation are analyzed in the continuous conduction mode. The circuit operation in each stage is shown in Fig. 2.

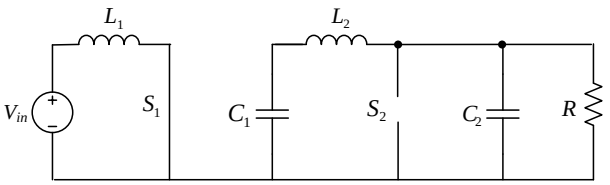

(a) Stage 1: S_1 is turned on and S_2 is turned off

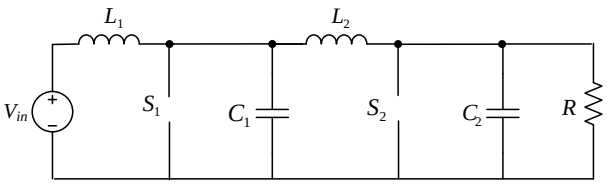

(b) Stage 2: S_1 is turned off and S_2 is turned off

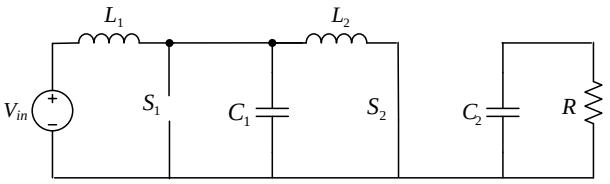

(c) Stage 3: S_1 is turned off and S_2 is turned on

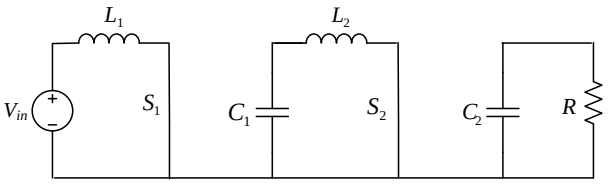

(d) Stage 4: S_1 is turned on and S_2 is turned on

Fig. 2 Circuit operations of two-stage boost converter

In order to simplify the analysis of converter operations, some assumptions have been taken into consideration. All the active elements of the converter are ideal. The inductors and capacitors are large enough to eliminate the current and voltage ripples of the converter. As can be seen in Fig. 2, the operation stages are explained as follows:

Stage 1: The switch S_1 is turned on and S_2 is turned off. The diodes D_1 and D_2 are reverse bias and forward bias, respectively. The input voltage delivers energy to the inductor L_1. Thus, this inductor will store energy.

Stage 2: The switch S_1 continues turning off and S_2 will remain off. The diodes D_1 and D_2 are forward bias, connecting the first stage to the second stage of the converter. The capacitor C_1 receives energy from the inductor L_1. Thus, the step-up output voltage can be achieved. The output filter capacitor C_2 is assumed to be very large to guarantee constant output voltage V_{out} .

Stage 3: The switch S_1 is turned off and S_2 starts turning on. The diode D_1 is forward bias and D_2 is reverse bias, isolating the output of the second stage. The capacitor C_1 supplies energy to the inductor L_2. Thus, this inductor will store energy.

Stage 4: The switches S_1 and S_2 are turned on. The diodes D_1 and D_2 are reverse bias, isolating the first stage from the second stage. The inductors L_1 and L_2 store energy supplied by the input source and the capacitor C_1, respectively. The capacitor C_2 supplies energy to the load resistor R.

The equivalent circuit of the two-stage cascaded boost converter operating in the continuous conduction mode is shown in Fig. 3. Where $u(t)$ is the switching function of the active power switch.

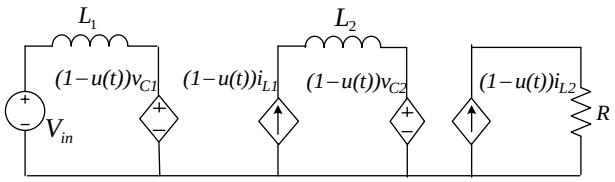

Fig. 3 Equivalent circuit of two-stage boost converter

3. TWO-STAGE CASCADED BOOST MODELING

The dynamic model of the two-stage cascaded boost converter is developed by using the generalized state-space averaging technique. The GSSA is an approximation technique that approximates the switching power converter in time-invariant model. The switching function under the continuous conduction mode operation is defined as

$$u(t)=\begin{cases}1, 0<t<dT_s\\ 0, dT_s<t<T\end{cases} \tag{1}$$

where d and T_s are the duty cycle of the active switch and the switching period of the converter, respectively.

Applying Kirchhoff's Laws in Fig.1, the dynamic equations can be expressed as

$$\dot{i}_{L1}=\frac{V_{in}-(1-u(t))v_{C1}}{L_1} \tag{2}$$

$$\dot{i}_{L2}=\frac{v_{C1}-(1-u(t))v_{C2}}{L_2} \tag{3}$$

$$\dot{v}_{C1}=\frac{(1-u(t))i_{L1}-i_{L2}}{C_1} \tag{4}$$

$$\dot{v}_{C2}=\frac{(1-u(t))i_{L2}-v_{C2}}{C_2} \tag{5}$$

where i_{L1} and i_{L2} are the inductor currents and v_{C1} and v_{C2} are the capacitor voltages, considering as the state variables of the system. V_{in} is determined as an input signal of the system.

Based on the GSSA approach, the complex Fourier series expansion under the first-order approximation of state variables can be given by

$$i_{L1}=\langle i_{L1}\rangle_{-1}e^{-j\omega t}+\langle i_{L1}\rangle_0+\langle i_{L1}\rangle_1 e^{-j\omega t} \tag{6}$$

$$i_{L2}=\langle i_{L2}\rangle_{-1}e^{-j\omega t}+\langle i_{L2}\rangle_0+\langle i_{L2}\rangle_1 e^{-j\omega t} \tag{7}$$

$$v_{C1}=\langle v_{C1}\rangle_{-1}e^{-j\omega t}+\langle v_{C1}\rangle_0+\langle v_{C1}\rangle_1 e^{-j\omega t} \tag{8}$$

$$v_{C2}=\langle v_{C2}\rangle_{-1}e^{-j\omega t}+\langle v_{C2}\rangle_0+\langle v_{C2}\rangle_1 e^{-j\omega t} \tag{9}$$

where ω is the angular frequency of the modulating signal. The state variables can be represented by complex Fourier series as follows

$$\langle i_{L1}\rangle_1 = x_1 + jx_2, \quad \langle i_{L1}\rangle_0 = x_9 \tag{10}$$

$$\langle i_{L2}\rangle_1 = x_3 + jx_4, \quad \langle i_{L2}\rangle_0 = x_{10} \tag{11}$$

$$\langle v_{C1}\rangle_1 = x_5 + jx_6, \quad \langle v_{C1}\rangle_0 = x_{11} \tag{12}$$

$$\langle v_{C2}\rangle_1 = x_7 + jx_8, \quad \langle v_{C2}\rangle_0 = x_{12} \tag{13}$$

By applying the conjugate property for real signal, the state variables are given by

$$\langle i_{L1}\rangle_{-1} = \langle i_{L1}\rangle_1^*, \qquad \langle v_{C1}\rangle_{-1} = \langle v_{C1}\rangle_1^* \tag{14}$$

$$\langle i_{L2}\rangle_{-1} = \langle i_{L2}\rangle_1^*, \qquad \langle v_{C2}\rangle_{-1} = \langle v_{C2}\rangle_1^* \tag{15}$$

The zero- and first-order approximations for the switching function can be expresses as

$$\langle u\rangle_0 = d, \tag{16}$$

$$\langle u\rangle_1 = \frac{\sin(2\pi d) + j(\cos 2\pi d - 1)}{2\pi} \tag{17}$$

By employing the first-order approximation the state variables can be derived as

$$i_{L1} = x_9 + 2x_1\cos(\omega t) - 2x_2\sin(\omega t) \tag{18}$$

$$i_{L2} = x_{10} + 2x_3\cos(\omega t) - 2x_4\sin(\omega t) \tag{19}$$

$$v_{C1} = x_{11} + 2x_5\cos(\omega t) - 2x_6\sin(\omega t) \tag{20}$$

$$v_{C2} = x_{12} + 2x_7\cos(\omega t) - 2x_8\sin(\omega t) \tag{21}$$

Let $x = [x_1 \;\; x_2 \;\; \ldots \;\; x_{12}]^{\mathrm{T}}$ be the state vector and $u = [V_{in}]$ be the input signal. Thus, the linear time-invariant state-space model can be written in the form

$$x^{\bullet} = \mathbf{A}x + \mathbf{B}u \tag{22}$$

By considering the generalized state-space averaging method described previously, the dynamic model of the two-stage cascaded boost converter can be achieved. The system matrix **A** and the input matrix **B** are represented in (23) and (24), respectively. where d_1 and d_2 are the independent duty cycle for the switches S_1 and S_2, respectively.

$$\mathbf{B} = [0 \;\; 0 \;\; 0 \;\; 0 \;\; 0 \;\; 0 \;\; 0 \;\; 0 \;\; V_{in}/L_1 \;\; 0 \;\; 0 \;\; 0] \tag{24}$$

The terms $x_9^{\bullet}$ to $x_{12}^{\bullet}$ can be expressed as follows

$$\dot{x}_9 = \frac{(d_1 - 1)}{L_1}x_{11} + \frac{V_{in}}{L_1} \tag{25}$$

$$\dot{x}_{10} = \frac{1}{L_2}x_{11} + \frac{(d_2 - 1)}{L_1}x_{12} \tag{26}$$

$$\dot{x}_{11} = \frac{(1 - d_1)}{C_1}x_9 - \frac{1}{C_1}x_{10} \tag{27}$$

$$\dot{x}_{12} = \frac{(1 - d_2)}{C_2}x_{10} - \frac{1}{RC_2}x_{12} \tag{28}$$

4. MODEL VALIDATIONS

In order to validate the accuracy of mathematical modeling of the two-stage cascaded boost converter based on the generalized state-space averaging approach, the simulation was carried out using MATLAB software. The results of converter based on the exact topology circuit shown in Fig.1 were simulated using MATLAB/SIMULINK software in order to compare with the results obtained from the developed model. The switching frequency of the converter is 20 kHz. The input voltage supplied to the two-stage cascaded boost converter is defined as 20 V. The converter parameters shown in Fig. 1 are chosen as: L_1 = 200 μH, L_2 = 360 μH, $C_1 = C_2$ = 200 μF, R = 5 Ω.

Fig. 4 shows the comparison results obtained from the exact topological model and the developed model based on the GSSA method with both zero- and first-order approximations. The two-stage cascaded boost converter operates under the duty cycles d_1 = 0.5 and d_2 = 0.6. The simulation results considering the inductor currents i_{L1} and i_{L2} and the capacitor voltages v_{C1} and v_{C2} are shown in Fig. 4 (a)-(d), respectively.

$$\mathbf{A} = \begin{bmatrix}
0 & \omega & 0 & 0 & \frac{(d_1-1)}{L_1} & 0 & 0 & 0 & 0 & 0 & \frac{\sin(2\pi\pi_1)}{2\pi\pi_1} & 0 \\
-\omega & 0 & 0 & 0 & 0 & \frac{(d_1-1)}{L_1} & 0 & 0 & 0 & 0 & -\frac{\sin^2(\pi d_1)}{\pi L_1} & 0 \\
0 & 0 & 0 & \omega & \frac{1}{L_2} & 0 & \frac{(d_2-1)}{L_2} & 0 & 0 & 0 & 0 & \frac{\sin(2\pi\pi_2)}{2\pi\pi_2} \\
0 & 0 & -\omega & 0 & 0 & \frac{1}{L_2} & 0 & \frac{(d_2-1)}{L_2} & 0 & 0 & 0 & -\frac{\sin^2(\pi d_2)}{\pi L_2} \\
\frac{(1-d_1)}{C_1} & 0 & -\frac{1}{C_1} & 0 & 0 & \omega & 0 & 0 & -\frac{\sin(2\pi\pi_1)}{2\pi\pi_1} & 0 & 0 & 0 \\
0 & \frac{(1-d_1)}{C_1} & 0 & -\frac{1}{C_1} & -\omega & 0 & 0 & 0 & \frac{\sin^2(\pi d_1)}{\pi C_1} & 0 & 0 & 0 \\
0 & 0 & \frac{(1-d_2)}{C_2} & 0 & 0 & 0 & -\frac{1}{RC_2} & \omega & 0 & -\frac{\sin(2\pi\pi_2)}{2\pi\pi_2} & 0 & 0 \\
0 & 0 & 0 & \frac{(1-d_2)}{C_2} & 0 & 0 & -\omega & -\frac{1}{RC_2} & 0 & \frac{\sin^2(\pi d_2)}{\pi C_2} & 0 & 0 \\
0 & 0 & 0 & 0 & \frac{\sin(2\pi\pi_1)}{\pi L_1} & -\frac{2\sin^2(\pi d_1)}{\pi L_1} & 0 & 0 & 0 & 0 & \frac{(d_1-1)}{L_1} & 0 \\
0 & 0 & 0 & 0 & 0 & 0 & \frac{\sin(2\pi\pi_2)}{\pi L_2} & -\frac{2\sin^2(\pi d_2)}{\pi L_2} & 0 & 0 & \frac{1}{L_2} & \frac{(d_2-1)}{L_2} \\
-\frac{\sin(2\pi\pi_1)}{\pi C_1} & \frac{2\sin^2(\pi d_1)}{\pi C_1} & 0 & 0 & 0 & 0 & 0 & 0 & \frac{(1-d_1)}{C_1} & -\frac{1}{C_1} & 0 & 0 \\
0 & 0 & -\frac{\sin(2\pi\pi_2)}{\pi C_2} & \frac{2\sin^2(\pi d_2)}{\pi C_2} & 0 & 0 & 0 & 0 & 0 & \frac{(1-d_2)}{C_2} & 0 & -\frac{1}{RC_2}
\end{bmatrix} \tag{23}$$

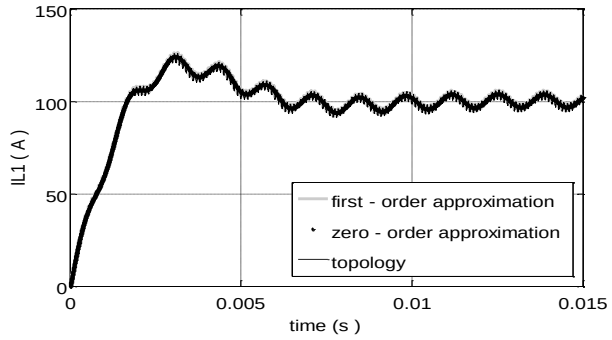

(a) The inductor current i_{L1}

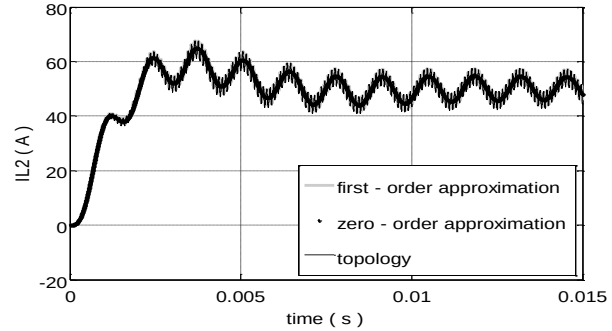

(b) The inductor current i_{L2}

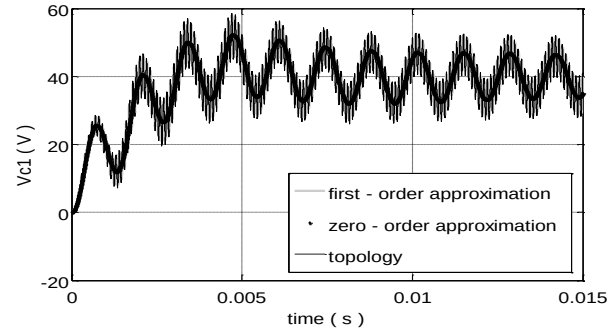

(c) The capacitor voltage v_{C1}

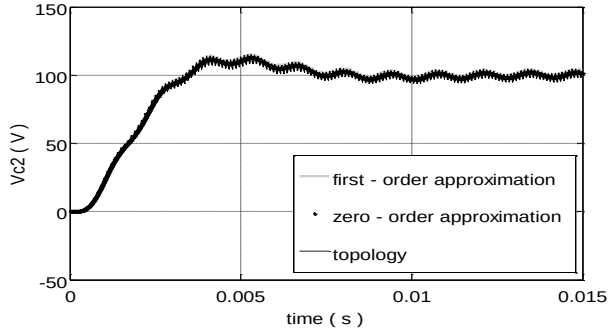

(d) The capacitor voltage v_{C2}

Fig. 4 Comparison results of two-stage boost converter

As can be seen in Fig. 4 (a)-(d), it is clear that the results obtained from the developed model match dynamically to the exact topological model in both transient and steady-state responses. According to the theoretical analysis of the steady-state converter gain at $d_1 = 0.5$ and $d_2 = 0.6$, the approximated output voltage would be 100V. It can be seen in Fig. 4 (d) that the output voltage is about 100 V, including the small ripples.

5. CONCLUSION

In this paper the mathematical model for the two-stage cascaded boost converter operating in CCM has been presented using the generalized state-space averaging method (GSSA). The principle of operating of the two-stage cascaded boost converter is analytically described. Simulation results show that the results of the developed dynamic model with zero- and first-order approximations are very close to the corresponding ones of the exact topological model. In addition, the comparison results indicate that the developed mathematical model can provide the satisfactory accuracy in both transient and steady-state responses of the two-stage cascaded boost converter.

ACKNOWLEDGEMENT

This work was supported by Suranaree University of Technology (SUT).

REFERENCES

[1] J. Mahdavi, A. Emadi, M.D. Bellar, and M. Ehsani, "Analysis of Power Electronic Converters Using the Generalized State-Space Averaging Approach", *IEEE Trans. Circuit and Systems.*, Vol. 44, August 1997, pp.767-770.

[2] A. Emadi, "Modeling and Analysis of Multiconverter DC Power Electronic System Using the Generalized State-Space Averaging Method", *IEEE Trans. Industrial Electronics*, Vol. 51, No.3, June 2004, pp. 661-668.

[3] F.S. Garcia, J.A. Pomilio and G. Spiazzi, "Modeling and Control Design of the Interleaved Double Dual Boost Converter", *IEEE Trans. Industrial Electronics*, Vol. 30, No. 8, August 2013, pp.3283-3290.

[4] A. Yazdani and R. Iravani, "A Generalized State-Space Averaged Model of the Three-Level NPC Converter for Systematic DC-Voltage-Balanced and Current-Controller Design", *IEEE Trans. on Power Delivery*, Vol. 20, No. 3, April 2005, pp. 1105-1114.

[5] Z. Lin and H. Ma, "Modeling and Analysis of Three-Phase Inverter Based on Generalized State Space Averaging Method", *IECON 2013*, pp. 1007-1012.

[6] E.H. Ismail, M.A. Al-Saffar, A.J. Sabzali and A.A. Fardoun, "A Family of Single-Switch PWM Converters with High Step-Up Conversion Ratio", *IEEE Trans. Circuits and Systems*, Vol. 55, No. 4, May 2008, pp.1159-1171.

[7] M. Aamir and M.Y. Shinwari, "Design, Implementation and Experimental Analysis of Two-Stage Boost Converter for Grid Connected Photovoltaic System", *ICCSIT 2013*, pp.194-199.

ANALYSIS OF TEMPERATURE DISTRIBUTION IN FINNED HEAT SINK OF LED STREET LAMP USING 3-D FINITE ELEMENT METHOD

Supaluk Rachso, Padej Pao-la-or
School of Electrical Engineering, Institute of Engineering
Suranaree University of Technology, Nakhon Ratchasima, THAILAND

ABSTRACT

This paper proposes a set of mathematical model of LED Street Lighting luminaire which performs in second-order partial differential equation. The paper simulate the distribution of temperature in finned heat sink of LED street lamp. The computer simulation is applied using 3-D finite element method that is developed by MATLAB program with the graphical performance of the temperature within LED Street Light Luminaire.

Keywords : LED Street Light Luminaire, temperature, 3-D finite element method (3-D FEM), Computer Simulation

1. INTRODUCTION

Light Emitting Diodes (LEDs) applied to street lighting are gaining much interest in the last years, they can provide energy saving, reliability and long lifetime (50-100khrs) resulting in low upkeep costs . The main portion of input energy into LED is turned into heat (around of 70-85%) (Chen, Tao and Hui, 2012). The device heating increases the junction temperature, which can lead to reliability problems such as low quantum efficiency, wavelength shifts, short lifetime, and even catastrophic failure (Tsai, Chen and Kang ,2008).

To analyze temperature of LED Street Lighting luminaire, temperature calculation: numerical approximation methods (e.g. finite difference: FD or finite element methods: FEM). With lack of accuracy, the first approach is not often used for this purpose, especially when nonlinearity of temperature is involved. The FEM is applicable to a broad range of solving temperature problems due to its flexibility, and accuracy. Application of the FEM to LED Street Lighting luminaire is inclusive. In addition, this method is more efficient than the FD method due to flexibility and accuracy, and it can gain several advantages when it is applied to LED Street Lighting luminaire.

In this paper, a steady-state condition in an LED Street Lighting luminaire is used for test. This results in a set of partial differential equations (PDE). Section II presents the mathematical model of temperature in LED street lamp based on a set of Heat transfer equations, while Section III describes the 3-D FEM by using Galerkin approach applied to LED street lamp for the purpose of obtaining temperature distribution. The domain of study with the 3-D FEM can be discretized by using linear tetrahedron elements. The simulation conducted herein is based on the 3-D FEM method given in Section III. All the programming instructions are coded in MATLAB program environment. Information of the test example and simulation results are shown in Section IV. Finally, the last section provides the conclusion.

2. MODELING OF TEMPERATURE FOR THE SIMULATION

The following steady-state heat transfer equation with heat source show in Eq. (1), is used to obtain the temperature distribution in LED Street Light Luminaire (Lewis, Nithiarasu & Seetharamu, 2004).

$$\lambda \frac{\partial}{\partial x}\frac{\partial T}{\partial x} + \lambda \frac{\partial}{\partial y}\frac{\partial T}{\partial y} + \lambda \frac{\partial}{\partial z}\frac{\partial T}{\partial z} + Q = 0 \qquad (1)$$

where λ is thermal conductivity. The convective heat transfer coefficient (h) of heat sink is 10 $W.m^{-2}.^{\circ}c$. The thermal conductivity of packaging material is show in Table 1 (Wang, Lei & Zhu, 2009)

Table 1 Thermal conductivity of the LED packaging

	Thermal conductivity (W/m.˚c)
LED chip	130
Soaking block	40
Substrate	200
Heat sink	240

Assuming that ambient temperature (T_{∞}) is constant at 37 ˚c and heat source (Q) of LED chip is 200,000 $W.m^{-3}$

3. 3D-FEM FOR LED STREET LIGHT LUMINAIRE

3.1 Discretization

This paper conducts the simulation study by considering the LED Street Lighting luminaire. as shown in Fig. 1. Also

Fig. 1 LED Street Lamp (LEDs mounted on the heat sink)

The domain of study with the 3D-FEM can be discretized by using linear tetrahedron elements. This can be accomplished by using Solid Work for 3D grid generation. Fig. 2-3 displays detail and grid representation of LED street lamp. The region domain consists of 38,280 nodes and 146,826 elements.

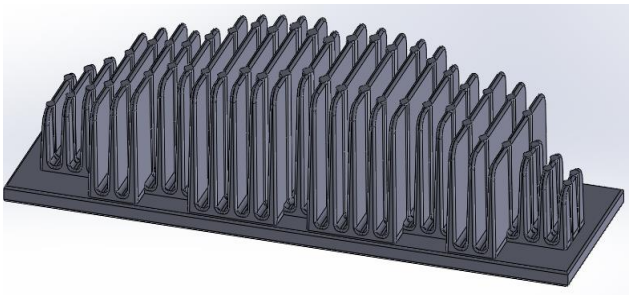

Fig. 2 Detail of LED street lamp

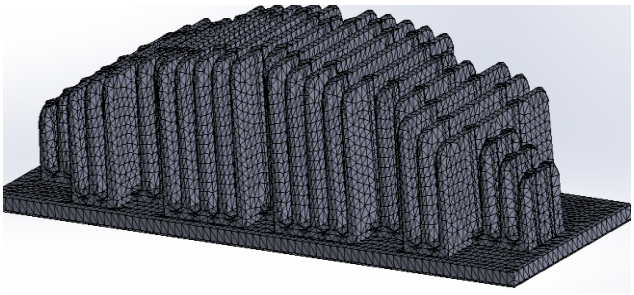

Fig. 3 Discretization of LED street lamp

3.2 Finite element formulation

An equation governing each element is derived from heat transfer equations directly by using Galerkin approach, which is the particular weighted residual method for which the weighting functions are the same as the shape function. The shape function for 3D-FEM used in this research is the application of 4-node tetrahedron element (three-dimensional linear element) (Bhatti, 2006) and (Kattan, 2007) .According to the method, the temperature is expressed as follows

$$T(x, y, z) = T_1N_1 + T_2N_2 + T_3N_3 + T_4N_4 \qquad (2)$$

where N_i , i = 1, 2, 3, 4 is the element shape function and the T_i , i = 1, 2, 3, 4 is the approximation of the temperature at each node (1, 2, 3, 4) of the elements, which is

$$N_i = \frac{1}{6V}(a_i + b_i x + c_i y + d_i z)$$

where V is the volume of the tetrahedron element, which is expressed as

$$V = \frac{1}{6}\begin{vmatrix} 1 & x_1 & y_1 & z_1 \\ 1 & x_2 & y_2 & z_2 \\ 1 & x_3 & y_3 & z_3 \\ 1 & x_4 & y_4 & z_4 \end{vmatrix}$$

and

$$a_1 = x_4(y_2z_3 - y_3z_2) + x_3(y_4z_2 - y_2z_4) + x_2(y_3z_4 - y_4z_3)$$
$$a_2 = x_4(y_3z_1 - y_1z_3) + x_3(y_1z_4 - y_4z_1) + x_1(y_4z_3 - y_3z_4)$$
$$a_3 = x_4(y_1z_2 - y_2z_1) + x_2(y_4z_1 - y_1z_4) + x_1(y_2z_4 - y_4z_2)$$
$$a_4 = x_3(y_2z_1 - y_1z_2) + x_2(y_1z_3 - y_3z_1) + x_1(y_3z_2 - y_2z_3)$$

$$b_1 = y_4(z_3 - z_2) + y_3(z_2 - z_4) + y_2(z_4 - z_3)$$
$$b_2 = y_4(z_1 - z_3) + y_1(z_3 - z_4) + y_3(z_4 - z_1)$$
$$b_3 = y_4(z_2 - z_1) + y_2(z_1 - z_4) + y_1(z_4 - z_2)$$
$$b_4 = y_3(z_1 - z_2) + y_1(z_2 - z_3) + y_2(z_3 - z_1)$$

$$c_1 = x_4(z_2 - z_3) + x_2(z_3 - z_4) + x_3(z_4 - z_2)$$
$$c_2 = x_4(z_3 - z_1) + x_3(z_1 - z_4) + x_1(z_4 - z_3)$$
$$c_3 = x_4(z_1 - z_2) + x_1(z_2 - z_4) + x_2(z_4 - z_1)$$
$$c_4 = x_3(z_2 - z_1) + x_2(z_1 - z_3) + x_1(z_3 - z_2)$$

$$d_1 = x_4(y_3 - y_2) + x_3(y_2 - y_4) + x_2(y_4 - y_3)$$
$$d_2 = x_4(y_1 - y_3) + x_1(y_3 - y_4) + x_3(y_4 - y_1)$$
$$d_3 = x_4(y_2 - y_1) + x_2(y_1 - y_4) + x_1(y_4 - y_2)$$
$$d_4 = x_3(y_1 - y_2) + x_1(y_2 - y_3) + x_2(y_3 - y_1)$$

The method of the weighted residual with Galerkin approach is then applied to the differential equation, refer to (1), where the integrations are performed over the element domain V .

$$\int_V \left(\lambda\frac{\partial}{\partial x}\frac{\partial T}{\partial x} + \lambda\frac{\partial}{\partial y}\frac{\partial T}{\partial y} + \lambda\frac{\partial}{\partial z}\frac{\partial T}{\partial z}\right)dV + \int_\Gamma N_n(hT)d\Gamma$$

$$= \int_V N_n Q dV + \int_\Gamma N_n\left(h(T_\infty)\right)d\Gamma$$

, or in the compact matrix form

$$\left[[K_c] + [K_h]\right]\{T\} = \{Q_h\} + \{Q_Q\} \qquad (3)$$

$$[K_c] =$$

$$\int_V \left(\lambda\left[\frac{\partial N}{\partial x}\right]_{4\times1}\left[\frac{\partial N}{\partial x}\right]_{1\times4} + \lambda\left[\frac{\partial N}{\partial y}\right]_{4\times1}\left[\frac{\partial N}{\partial y}\right]_{1\times4} + \lambda\left[\frac{\partial N}{\partial z}\right]_{4\times1}\left[\frac{\partial N}{\partial z}\right]_{1\times4}\right)dV$$

$$= \frac{\lambda}{36V}\begin{bmatrix} b_1b_1+c_1c_1+d_1d_1 & b_1b_2+c_1c_2+d_1d_2 & b_1b_3+c_1c_3+d_1d_3 & b_1b_4+c_1c_4+d_1d_4 \\ & b_2b_2+c_2c_2+d_2d_2 & b_2b_3+c_2c_3+d_2d_3 & b_2b_4+c_2c_4+d_2d_4 \\ & & b_3b_3+c_3c_3+d_3d_3 & b_3b_4+c_3c_4+d_3d_4 \\ \text{Sym} & & & b_4b_4+c_4c_4+d_4d_4 \end{bmatrix} \qquad (4)$$

$$[K_h] = h\int N_n N_m\, dxdydz = \frac{hV}{20}\begin{bmatrix} 2 & 1 & 1 & 1 \\ 1 & 2 & 1 & 1 \\ 1 & 1 & 2 & 1 \\ 1 & 1 & 1 & 2 \end{bmatrix} \qquad (5)$$

$$[Q_h] = hT_\infty \int N_n dxdydz = \frac{hT_\infty V}{4}\begin{bmatrix} 1 \\ 1 \\ 1 \\ 1 \end{bmatrix} \qquad (6)$$

$$[Q_Q] = Q\int N_n\, dxdydz = \frac{QV}{4}\begin{bmatrix} 1 \\ 1 \\ 1 \\ 1 \end{bmatrix} \qquad (7)$$

For one element containing 4 nodes, the expression of the FEM approximation is a 4×4 matrix. With the account of all elements in the system of n nodes, the system equation is sizable as an n×n matrix.

4. 3D – FEM Simulation Result

The FEM-based simulation conducted in this paper is coded with MATLAB programming for calculation of temperature dispersion. To utilize a graphical feature of MATLAB, the graphical representation for temperature, contour of temperature distribution are presented in Fig. 4

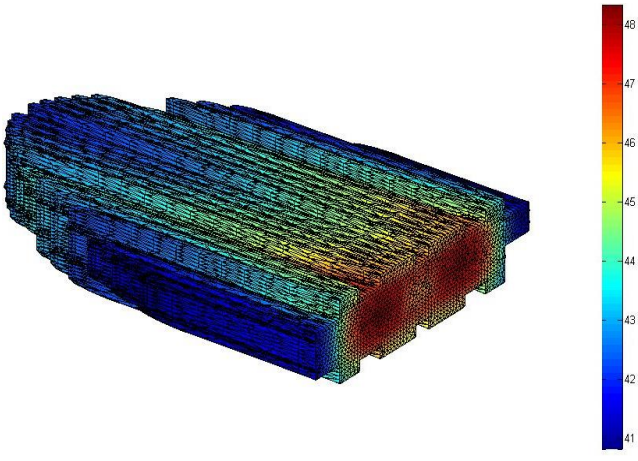

Fig.4 Simulates Temperature distribution in heat sink (˚c)

From Fig.4 shows the temperature distribution of LED street light by using 3D FEM program which is developed. It can be noticed that the temperature distribution will happen from the LED junction at the

highest level of temperature to the LED street light heat sink. Based on the article, LED junction temperature (T_j) is 47.95 ˚c.

5. CONCLUSION

This article investigated the temperature that took place in LED street light. The sample model from computer applied the 3D FEM which developed by MATLAB. The result showed that the temperature will distribute itself from the LED Chip junction which is the highest temperature part to heat sink, including the average, standard deviation in heat sink and LED junction temperature which it will be able to use in temperature distribution analysis.

REFERENCES

Bhatti , M.A., Advanced Topics in Finite Element Analysis of Structures, John Wiley & Sons, USA, 2006.

Chen, H.T., Tao, X.H. and Hui, S.Y.R., Estimation of Optical Power and Heat-Dissipation Coefficient for the Photo-Electro-Thermal Theory for LED Systems, IEEE Transactions on Power Electronics, vol. 27, pp. 2176-2183, 2012.

Kattan , P.I., MATLAB Guide to Finite Elements (2nd edition), Springer Berlin Heidelberg, USA, 2007.

Lewis, R.W., Nithiarasu, P. and Seetharamu, K.N. Fundamentals of the Finite Element Method for Heat and Fluid Flow, John Wiley & Sons, USA, 2004.

Tsai, M.Y., Chen, C.H. and Kang, C.S., Thermal analyses and measurements of low-Cost COP package for high-power LED," in 58th Elect. Comp. and Technology Conference, 2008, pp. 1812-1818.

Wang, N., Wang, C.H., Lei, J.X. and Zhu, D.S. (2009). Numerical study on thermal management of LED packaging by using thermoelectric cooling. 09th International Conference on Electronic Packaging Technology & High Density Packaging. : 433-437

Supaluk Rachso is a pursuing master degree of the School of Electrical Engineering, Institute of Engineering, Suranaree University of Technology, Nakhon Ratchasima, THAILAND. She received B.Eng. (2012) in Electrical Engineering from Suranaree University of Technology, Thailand.

Padej Pao-la-or is a lecturer of the School of Electrical Engineering, Institute of Engineering, Suranaree University of Technology, Nakhon Ratchasima, THAILAND. He received B.Eng. (1998), M.Eng. (2002) and D.Eng. (2006) in Electrical Engineering from Suranaree University of Technology, Thailand. His fields of research interest include a broad range of power systems, electrical drives, FEM simulation and artificial intelligent techniques.

FREQUENCY RESPONSE ANALYSIS OF PROTOTYPE HIGH-FREQUENCY AND HIGH-VOLTAGE TESTING TRANSFORMER

Satoshi Matsumoto, Haruki Yamaguchi, Toshitsugu Maeda
Takahiro Ogiya and Satoshi Ogihara
Department of Electrical Engineering, Shibaura Institute of Technology

ABSTRACT

Insulation reliability of an inverter-fed motor is very important from the safety point of view, because it is used in many fields such as electric vehicle, consumer electrical appliance, industrial equipment etc. This paper deals with the frequency response analysis of prototype high-voltage and high-frequency testing transformer to conduct the high voltage testing of motor coil winding. High voltage transformer has high winding ratio between primary and secondary windings to generate the high voltage. And frequency range to be covered in the test is so wide. Then three kind of prototype testing transformers were fabricated to clarify the frequency characteristics and electromagnetic performance. Frequency response analysis shows that the resonances caused by leakage flux and stray capacitance of the winding appear. This phenomena was validated by its equivalent circuit based on the measurement data. Experimental data obtained by three different prototype transformers are useful for the design and reasonable agreement with each other.

INTRODUCTION

An inverter-fed motor is commonly used in many fields such as consumer electrical appliances, many industrial areas and so on. Recently, electric vehicle uses many inverter-fed motors having high voltage operation to get high power. The principle of inverter is pulse width modulation (PWM) control system. The PWM waves contain overshoots or higher frequency components up to several 100 kHz by the FFT analysis [1]. To maintain the high reliability of the inverter-fed motor system, it is important to establish the test method for inverter surge insulation.

In the high voltage engineering field, AC partial discharge test and impulse withstand test have been conducted to assess the insulation performance of the equipment [2].The paper deals with the frequency response analysis and electromagnetic properties of high voltage high frequency testing transformer for motor coil tests.

DESIGN CONCEPT AND SPECIFICATION

We have designed three transformers covering the different frequency ranges. Table 1 shows the general specifications of the testing transformer. The transformer has high winding ratio, therefore we have to pay attention to the coil winding structure to prevent electrical breakdown caused by high voltage, and magnetic core selection for high frequency operation. Note that magnetic steel sheet has high iron core loss compared with the ferrite core in high frequency region, however saturated magnetic flux density of the ferrite core is half or one-third, then the cross section is larger than that of magnetic steel core.

Table 2 summarizes the design specifications for three different kind of transformers covering different frequency range.

Table 1 General specifications of the testing transformer

Items	Specifications	Remarks
Input voltage	$50\sqrt{2}$ V_p (Maximum)	50 V_{rms}
Output voltage	$5\sqrt{2}$ kV_p (Maximum)	5 kV_{rms}
Power	200 VA	
Target frequency	50Hz ～ 50kHz	
Dimensions	H100×W100×D100	mm

PROTOTYPE TRANSFORMER

Figs.1-3 shows the photos of prototype transformers for lower frequency range (I), (II) and higher frequency range (III), respectively. Magnet wire UEW made by polyurethane is used for the primary and secondary windings.

The secondary winding shown in Fig.1 has five-layer winding coils to strengthen the electrical insulation performance. The turns for each layer shown in Fig.1 (b) are 2300, 2500, 2300, 1900 and 1000, respectively. The turns for each layer shown in Fig.2 (b) are 2300, 2300, 2300, 2000

and 1100, respectively. The secondary winding for higher frequency shown in Fig. 3 (b) consists of eight layers having 320 turns for each layer.

Table 2 Design specifications of the testing transformer

Items	Lower frequency range (I)	Lower frequency range (II)	Higher frequency range (III)
Frequenc y range	50 Hz ～ 5 kHz	50 Hz ～ 5 kHz	5 kHz～ 50 kHz
Magnetic core	Magnetic steel sheet (JFE:CS-100)	Amorphous steel sheet (ACS100)	Ferrite Core (TDK:EC90 ×90×30)
Primary turns N_1	100	100	16
Secondary turns N_2	10000	10000	2560
Turn ratio	1：100	1：100	1:160
Primary winding	UEW ϕ0.7 mm × 1	UEW ϕ0.7 mm × 1	UEW ϕ0.35 mm × 19
Secondary winding	UEW ϕ0.16 mm	UEW ϕ0.16 mm	UEW ϕ0.16 mm

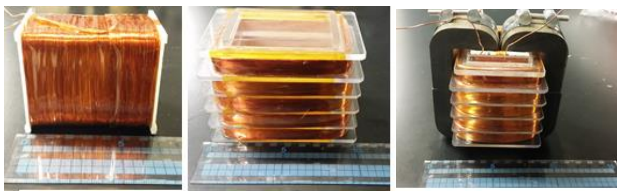

(a) Primary winding (b) Secondary winding (c) Main body

Fig.1 Prototype for LF and HV transformer (I)

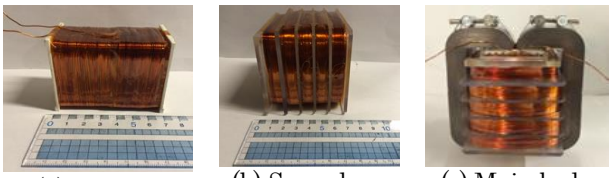

(a)Primary winding (b) Secondary winding (c) Main body

Fig.2 Prototype for LF and HV transformer (II)

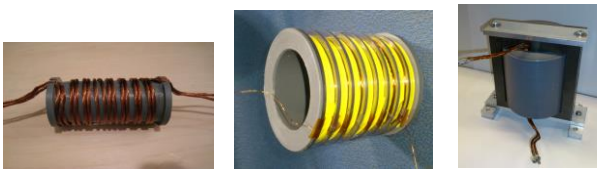

(a)Primary winding (b)Secondary winding (c)Main body

Fig.3 Prototype (III) for HF and HV transformer

EXPERIMENTAL APPARATUS

Fig. 4 shows the equivalent circuit for frequency characteristics of the prototype transformer. The primary voltage is applied from the power amplifier varying the frequency with the function generator. The voltage waveform was measured by the oscilloscope connecting with 1:100 high voltage probe.

Frequency response analysis (FRA) was also conducted to obtain the transfer function of the transformer using FRA analyzer (NF FRA5022) in the frequency range between 1 Hz and 100 kHz. Frequency-response analysis (FRA) has been accepted as one of the most sensitive tools to detect mechanical faults of power transformers [2-5].

Additional capacitor was inserted with parallel in primary circuit to confirm the dominant resonance frequency.

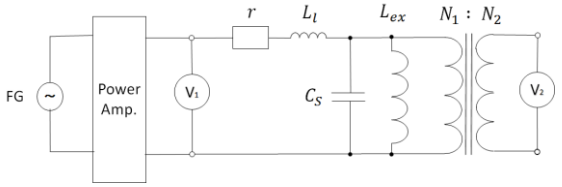

Fig.4 Equivalent circuit of test circuit

FREQUENCY CHARACTERISTICS

Fig. 5 show the frequency characteristics of voltage ratio of secondary voltage to primary voltage. The winding ratio of prototype I and II is 100, and 160 of prototype III respectively. The figure shows that the ratio increases in higher frequency regions. This means the circuit resonance appears for all of prototypes. Unfortunately we could not measure the higher frequency characteristics because of shortage of power amplifier at this moment.

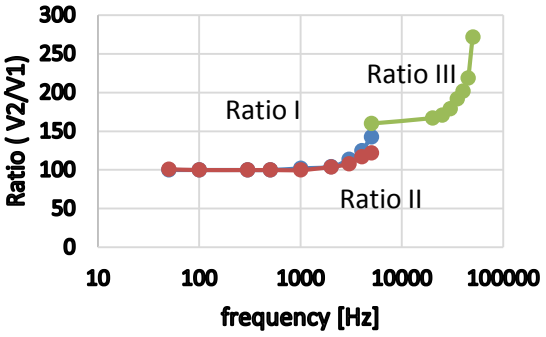

Fig. 5 Frequency characteristics of voltage ratio of secondary voltage to primary voltage

FREQUENCY RESPONSE ANALYSIS (FRA)

The higher frequency characteristics are obtained by the frequency response analysis (FRA) as shown in Figs. 6 and 7 in the frequency ranges between 1 Hz to 100 kHz. From the figures, we can see that the gain is stable for lower frequency, however there are several resonance frequencies in higher frequency region together with the attenuation.

Fig. 8 shows the FRA for prototype (III). Resonance frequency is high compared with previous ones (I) and (II).

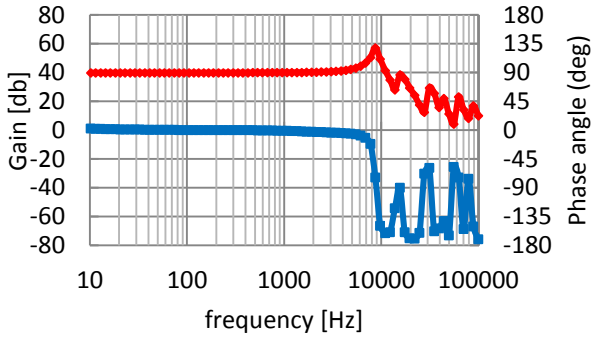

Fig. 6 Frequency Response Analysis (FRA) for prototype transformer I (N_1: N_2 =100:10000=1:100)

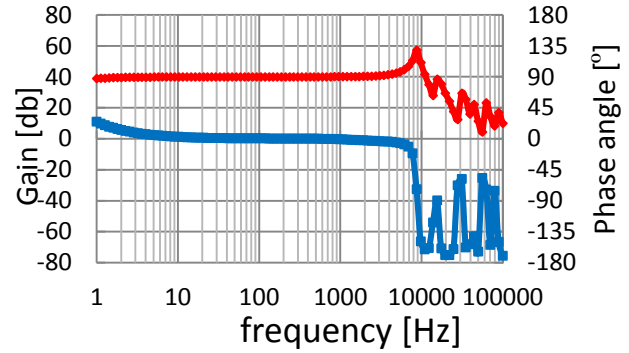

Fig. 7 Frequency Response Analysis (FRA) for prototype transformer II (N_1: N_2 =100:10000=1:100)

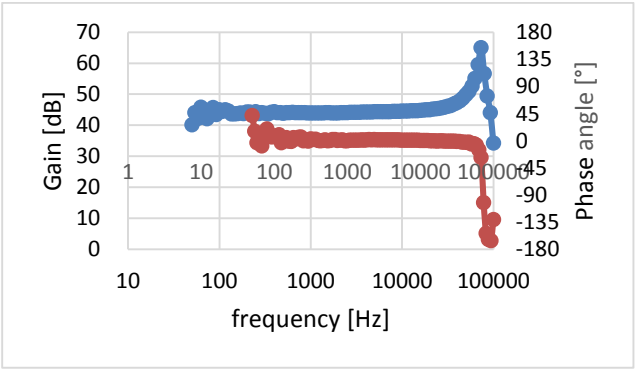

Fig. 8 Frequency Response Analysis (FRA) for prototype transformer III (N_1: N_2 =16:2560=1:160)

DISCUSSION

It seems that resonances in higher frequency region are caused by stray capacitance and leakage inductance between primary winding and secondary winding.

Fig. 9 shows the two dimensional model for leakage flux and magnetic flux density. We can estimate the leakage flux ϕ_2 caused by primary current I_1as follows;

$$\phi_2 = \int_{d_1}^{d_2} \mu_0 H dx \ [\mathrm{W_b/m}] \qquad (1)$$

Then leakage inductance L_l can be calculated by

$$L_l = \frac{N_1 \phi_2}{I_1} \ [\mathrm{H}] \qquad (2)$$

Table 3 summaries the equivalent circuit parameters as illustrated in Fig. 4. The primary stray capacitance and leakage inductance are obtained by experimental data. The equivalent primary stray capacitance C_S has large value because of winding ratio is large for high voltage testing transformer.

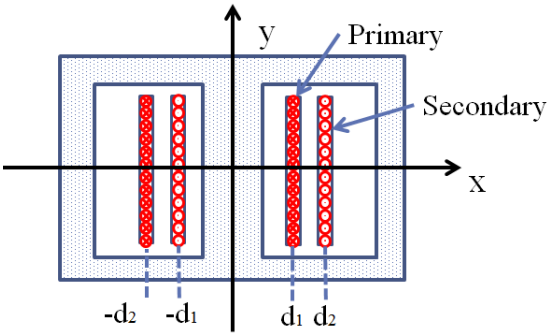

(a) Leakage flux calculation model

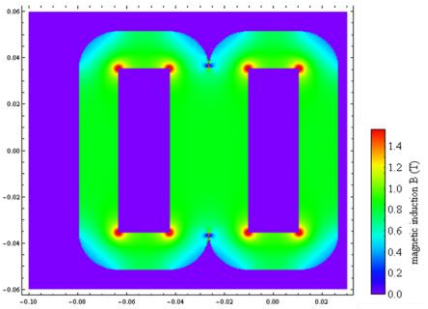

(b) Magnetic flux density

Fig. 9 Magnetic field analysis for Type II

Table 3 Equivalent circuit parameters

Prototype	I	II	III
Stray capacitance C_s	0.51 μF	0.36 μF	0.39 μF
Exciting inductance L_{ex}	394 mH	203 mH	1.58 mH
Leakage inductance L_l	477 μH	475 μH	4.7 μH
Reduced primary resistance r	1.13 Ω	1.74 Ω	0.021 Ω
Primary resistance	0.892 Ω	1.49 Ω	0.025 Ω
Secondary resistance	2.35 kΩ	2.5 kΩ	131 Ω

From the equivalent circuit as shown in Fig. 4, we can derive the transfer function as follows.

$$\frac{V_2}{V_1} = \frac{z}{r + sL_1 + z}\frac{N_2}{N_1} \qquad (3)$$

where,

$$z = \frac{sL_{ex}}{1 + s^2 L_{ex} C_p} \qquad (4)$$

Fig. 10 shows the calculated frequency characteristics for the prototype I. Both of calculation result of lowest resonance frequency and experimental result are in

reasonable agreement with each other. Generally speaking, the stray capacitance between the coils increases in higher frequency range. It is considered that multi resonances shown in Figs.6 and 7 were caused by this reason.

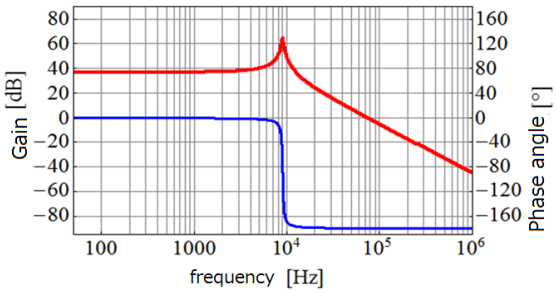

Fig. 10 Calculated frequency characteristics

CONCLUSIONS

The prototype high frequency and high voltage transformers were designed and fabricated to clarify the frequency characteristics and to validate the insulation performance. The frequency range is so wide from 50 Hz to 50 kHz that prototypes were made under the three different design concept.

Frequency response analysis and experimental data show that prototypes have resonance frequencies in higher frequency regions because of large winding turns. Numerical analysis based on the leakage flux and stray capacitance supported the resonance frequency characteristics.

To improve the higher frequency characteristics up to 200 kHz, followings are important points.

(1) Reduction of the winding ratio to decrease the stray capacitance

(2) Usage of high primary voltage

(3) Enlargement of the core size

(4) Less leakage flux

(5) Reduction of skin effect for the windings

(6) Usage of high power and high frequency power amplifier

ACKNOWLEDGMENT

The authors would like to thank Dr. Kazuo Kobayashi and Professor Emeritus Yoshikazu Shibuya for valuable discussions and contributions throughout the course of our study.

References

[1] Nguyen Nhat Nam, Satoshi Matsumoto, “Electrical and Thermal Computation of Stress Grading System in Inverter-Driven Medium Voltage Motors”, IEEJ Transactions on Fundamentals and Materials, Vol.133, No.11, pp.591-597 (2013)

[2] Satoshi Matsumoto, Nguyen Nhat Nam, Daichi Nagaba, Takahiro Ogiya, “Partial Discharge Characteristics of Twisted Magnet Wire under High Frequency AC Voltage”, Proceedings of 2014 International Symposium on Electrical Insulating Materials, No.B5, pp.57-60 (2014)

[3] J.A.S.B.Jayasinghe, Z.D.Wang, A.W.Darwin, P.N.Jarman, “Practical Issues in Making FRA Measurements on Power Transformers”, Proceedings of 14th ISH, G-013 (2005)

[4] T.Sano, K.Miyagi, “Experimental Investigations on FRA Diagnosis of Transformer Faults”, IEEJ Transaction on Power and Energy, Vol.127, No.7, pp.791-796 (2007)

[5] Zhongdong Wang, Jie Li, Dahlina M.Sofian, “Interpretation of Transformer FRA Responses, Part I: Influence of Winding Structure”, IEEE Transactions on Power Delivery, Vol.24, No.2, pp.703-710 (2009)

[6] International Electrotechnical Commission, “Power Transformers- Part 18: Measurement of frequency response”, IEC60076-18 (2012)

[7] Kazuhiro Urata, Akihisa Kameari : ” Static Magnetic Field Analyses by Integral Method using Magnetization with Normal Continuity in Shell Structure ” ,IEEE Transactions on magnetics, Vol.31,No.3, pp.1440-1443 (1995)

[8] D. J. Wilcox, W. G. Hurley, M.Conlon, ”Calculation of self and mutual impedances between sections of transformer windings”, IEE Proceedings C, Vol. 136, No. 5, pp308-314 (1989.9)

[9] Casimiro Alvarez-Marino, Francisco de Leon, Xose M. Lopez-Fernandez, “Equivalent Circuit for the Leakage Inductance of Multiwinding Transformers: Unification of Terminal and Duality Models”, IEEE Transactions on Power Delivery, Vol.27, No.1, pp.353 – 361 (2012.1)

Satoshi Matsumoto received the M. Eng. and Dr. degrees in electrical engineering from the University of Tokyo in 1981 and 1984, respectively. In 1984, he joined Toshiba Corporation. He has been a Professor in the Department of Electrical Engineering of Shibaura Institute of Technology since 2007. He is a Senior Member of IEEE and IEEJ, vice president of IEEDJ.

Haruki Yamaguchi received the B. Eng. in the Department of Electrical Engineering from Shibaura Institute of Technology.

Toshitsugu Maeda received the B. Eng. in the Department of Electrical Engineering from Shibaura Institute of Technology.

Takahiro Ogiya received the B. Eng. in the Department of Electrical Engineering from Shibaura Institute of Technology. He is currently pursuing his M. Eng. degree in the same institute. He is a student member of IEEJ and IEEDJ.

Satoshi Ogihara received the B. Eng. in the Department of Electrical Engineering from Shibaura Institute of Technology. He is currently pursuing his M. Eng. degree in the same institute. He is a student member of IEEJ and IEEDJ.

Electronics and Telecommunications

DUAL BAND INVERTED-F ANTENNA FOR DISASTER PREVENTION HELMET

Nur Fatin Fatina Bt Mohd Ramli and Hisao IWASAKI
Department of System Engineering and Science, Shibaura Institute of Technology

ABSTRACT

We proposed the dual band inverted-F antenna which is can operated at 150MHz for communication between workers and disaster prevention base station and also operated at 2.45GHz for communication between workers. Return loss less than 6dB was obtained at both bands. Omni-directional radiation pattern was realized at horizontal plane and also good durability in actual deployment.

1. INTRODUCTION

In recent years, fire fighter and Self-Defense Forces are dispatched to rescue when natural disaster occurred is increasing. Fig.1 shows the communication image. They are working in state that one hand is blocked due to radio used while rescuing and work efficiency not being effective. To solve the problem, by attaching the radio at a helmet in order for them to rescue victims with ease and easy have been developed [1].

150MHz band (148MHz~152MHz) for communication with base station and 2.45GHz band (2.4GHz~2.5GHz) for communication between workers is used. Therefore, dual band antenna mounted on the helmet have been studied [2].

When antenna is mounted on human head, gain decreases because the helmet consists of the dielectric material. To overcome the gain reduction, the inverted F antenna on the hemispherical metal ground plane has been studied [3]. However, the bandwidth at 150MHz band was narrow, 0.4% respectively at return loss≦6dB.

In this paper, inverted-F antenna with unite ground element is proposed to overcome the narrow bandwidth at 150MH band.

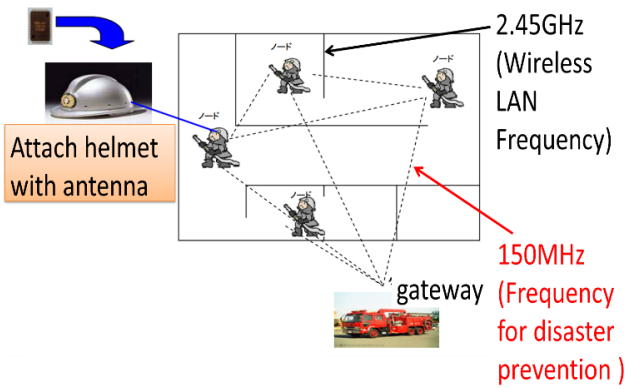

Fig.1 Communication image.

2. PROPOSED ANTENNA MODEL A

Inverted-F antenna, can be operated at length λ/4 and antenna height can be low profile, is suitable to be mounted on the helmet. Fig.2 shows the proposed antenna Model A. The antenna element is arranged parallel with the ground element. Two long antenna element is for 150MHz and short antenna element is for 2.4GHz. Diameter of helmet is used for antenna diameter as the antenna model will be attached at the helmet. Both antenna and ground element thickness is 1.5mm.

To improve return loss value for 150MHz band, distance between short and feed is studied. 150MHz and 2.45GHz antenna element height is changed to achieve low profile antenna. Both antenna heights are 20mm for 150MHz and 2.45GHz is 18mm, respectively.

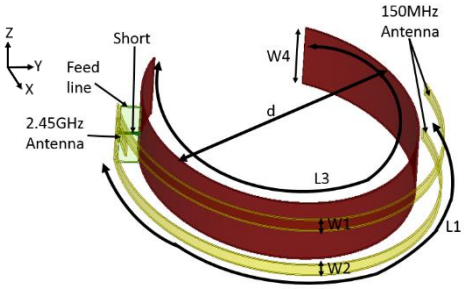

(a) Model A (Not unite ground)

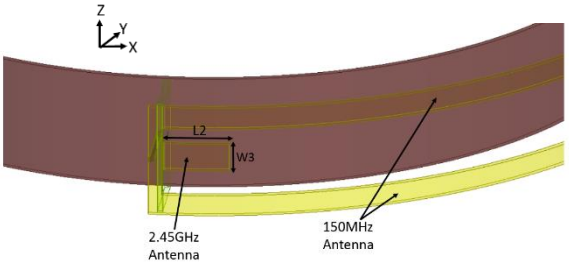

(b) 2.45GHz antenna element

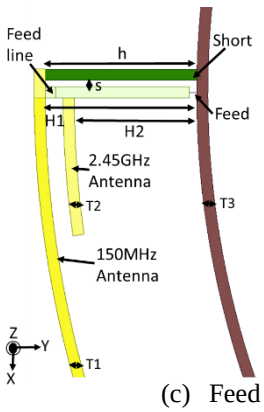

L1=500mm, L2=31mm,
L3=600mm
W1=W2=6.5mm, W3=8mm,
W4=33mm,
T1=T2=T3=1.5mm
H1=20mm, H2=18mm
d=242mm,
Short: h=20mm, w=1mm,
t=1.5mm, s=1.6mm

(c) Feed and short positions

L1=150MHz length, L2=2.45GHz length,
L3=Ground length
W1=W2=150MHz width, W3=2.45GHz width,
W4=Ground width
T1=T2=Antenna thickness, T3=Ground thickness
H1(150MHz)=H2(2.45GHz)=distance between antenna element and ground
d=Diameter of helmet,
Short: h=Short height, w=Short width, t=Short thickness,
s= distance between feed line and short

Fig. 2 Simulation antenna Model A.

3. ANTENNA CHARACTERISTICS OF MODEL A

The proposed antenna was simulated using HFSS (High Frequency Structural Simulator) software.

3.1. 150MHz Band

3.1.1 Return Loss

Fig.3 shows the simulated return loss for Model A as a parameter of distance between short and feed position. As shown in the Fig.3, when the distance between short and feed is small, return loss was improved. The resonance frequency of 150MHz band was 149.5MHz and return loss ≦ 6dB was obtained. Fig.4 shows simulated return loss graph for distance (H1) between antenna element and ground. Return loss≦6dB was achieved at all distance. For the antenna mounted on helmet, H1=20mm was chosen as the suitable value. However bandwidth was narrow.

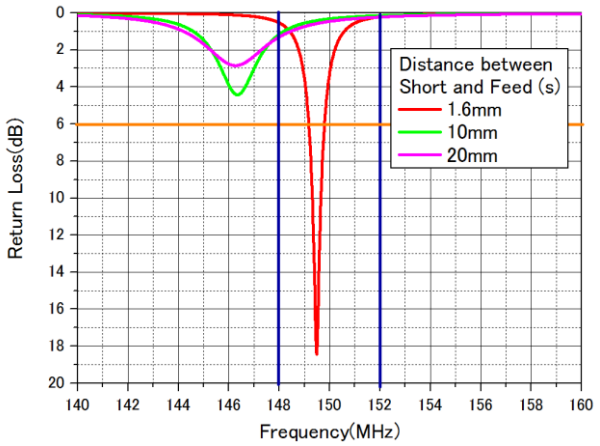

Fig. 3 Simulated return loss of Model A as a parameter of distance between feed and short position.

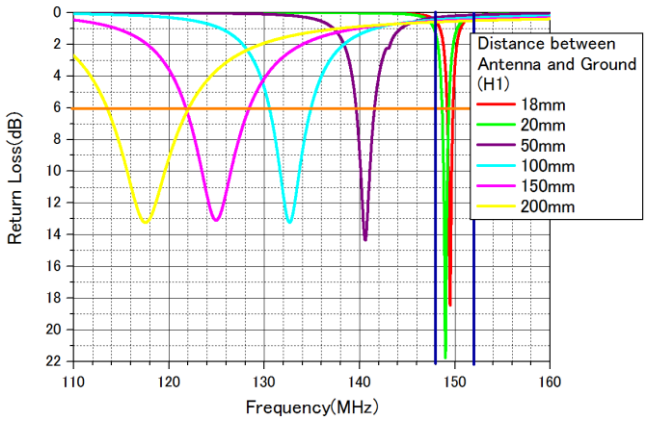

Fig. 4 Simulated return loss of Model A as a parameter of H1.

3.2. 2.45GHz

Fig.5 shows the simulated return loss. Return loss≦6dB was obtained at 2GHz~2.6GHz.

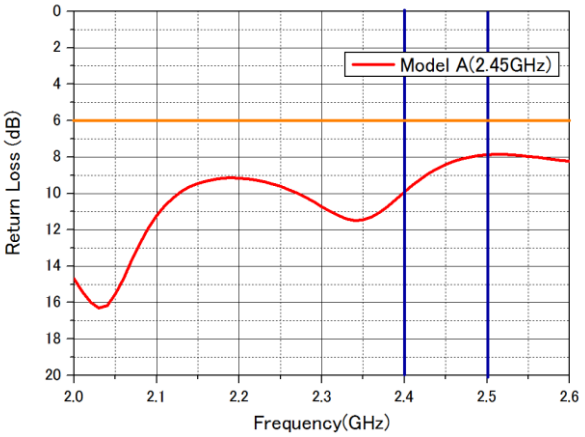

Fig. 5 Simulated return loss of Model A at H2=18mm.

4. PROPOSED ANTENNA MODEL B

To overcome narrow bandwidth at Model A, Model B is proposed. Fig. 6 shows the proposed antenna Model B. Model B is designed with ground element is united. Ground length of Model B is L3=760mm. Other parameters are same as Model A.

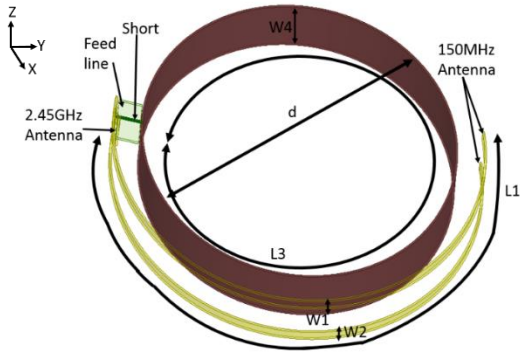

Fig. 6 Simulation antenna Model B (Unite Ground).

5. ANTENNA CHARACTERISTICS OF MODEL B

5.1. 150MHz Band

5.1.1 Return Loss

Fig.7 shows the simulated return loss of Model A and B. When the ground is united, the bandwidth becomes wider. Bandwidth of Model A was 0.7MHz and Model B was 0.98MHz at return loss≦6dB. Bandwidth of Model B was 0.28MHz wider than Model A.

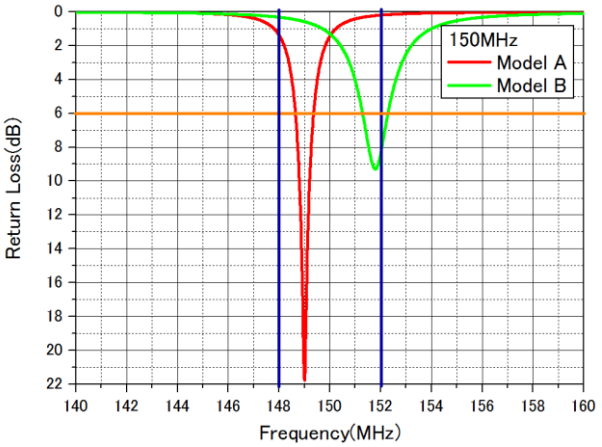

Fig. 7 Simulated return loss of Model A and Model B.

5.1.2 Current Distributions

Fig. 8 shows the simulated current distributions for Model A and Model B at 150MHz band. Red colour shows the current is strongly flowing and blue colour shows the current is slightly flowing. Direction of the arrows show the direction of current is flowing.

As shown in Fig.7, current at short part is flowing strongly for both model. The current length becomes shorter when the ground is united and the resonance frequency was shifted to high frequency.

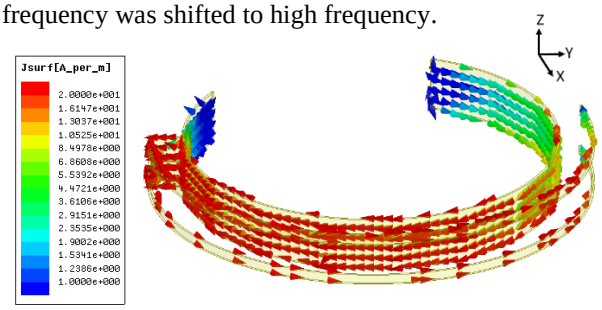

(a) Model A at 149.5MHz

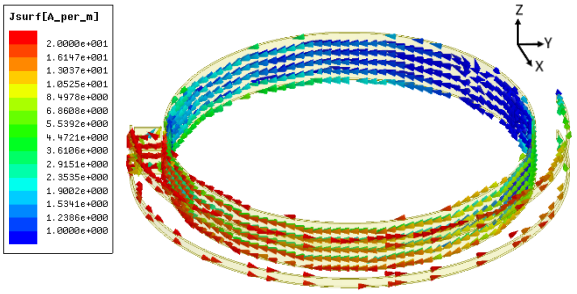

(b) Model B at 151.8MHz

Fig. 8 Simulated current distributions.

5.1.3 Radiation Patterns

Fig.9 shows simulated radiation patterns for Model B at 150MHz. As shows in Fig. 9, at X-Y plane the radiation pattern was nearly omni-directional pattern with gain was -1.31dBi.The gain of X-Z plane and Y-Z plane were -4.23dBi and -7.50dBi, respectively.

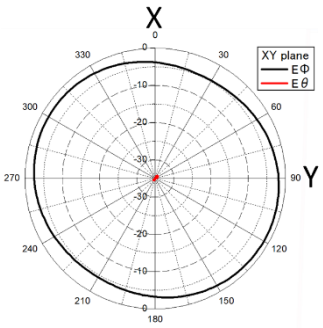

(a) X-Y plane

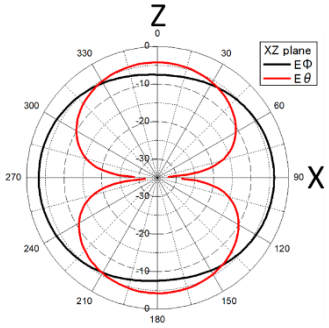

(b) X-Z plane

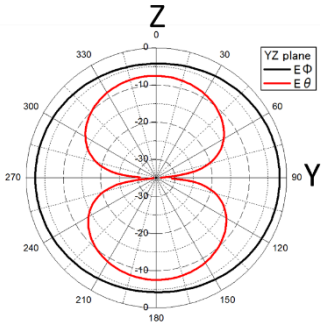

(c) Y-Z plane

Fig. 9 Simulated radiation patterns of Model B.

5.2 2.45GHz

5.2.1 Return Loss

Fig.10 shows the simulated return loss of Model B. Return loss≦6dB is obtained at 2GHz~2.6GHz.

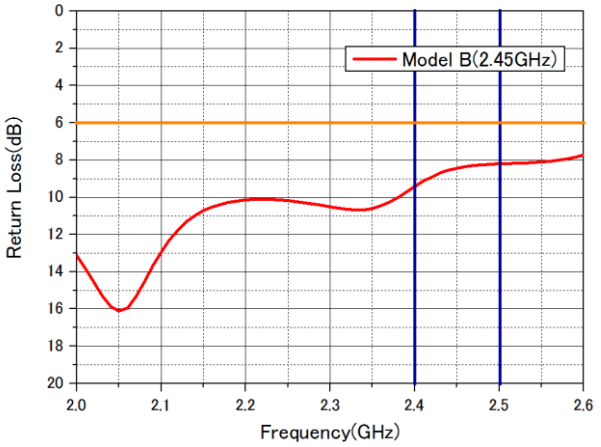

Fig. 10 Simulated return loss of Model B at 2.45GHz band

5.2.2 Current Distributions

Fig.11 shows the simulated current distributions for Model B at 2.45GHz. As shown in Fig.11, current is flowing strongly at short part and 2.45GHz antenna element.

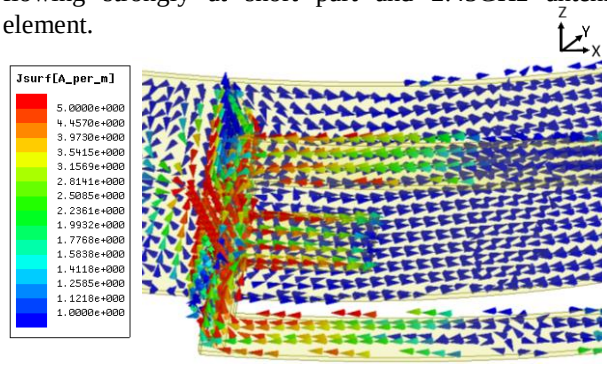

Fig. 11 Simulated current distributions for Model B at 2.45GHz.

5.2.3 Radiation Patterns

Fig.12 shows the simulated radiation patterns of Model B at 2.45GHz. X-Y plane, X-Z plane and Y-Z plane, the radiation pattern was nearly omni-directional pattern. The gain of X-Y plane at EΦ was 0.11dBi. The gain of Eθ at X-Z plane and X-Y plane were 0.01dBi. It shows that the antenna was radiated at all direction.

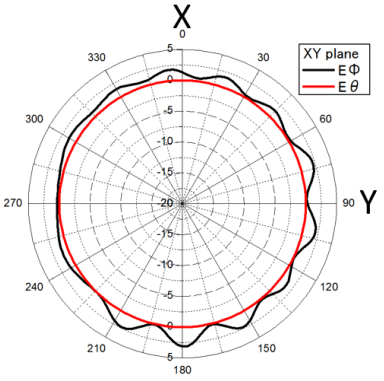

(a) X-Y plane

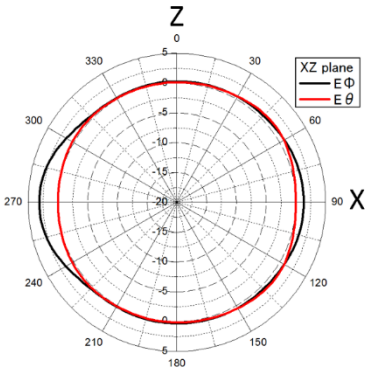

(b) X-Z plane

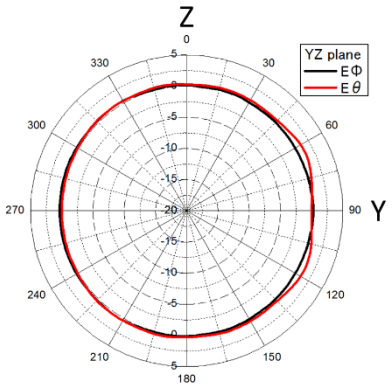

(c) Y-Z plane

Fig. 12 Simulated radiation patterns of Model B at 2.45GHz.

6. CONCLUSION

This paper presents two models A and B of antenna with different ground and simulated return loss, current distribution and radiation pattern characteristic at 150MHz band and 2.45GHz band, respectively.

For 150MHz band, the bandwidth becomes wider at return loss≦6dB with bandwidth of 0.6% for Model B. For radiation pattern, gain was -1.31dBi at X-Y plane and nearly omni-radiation radiation pattern was obtained.

For 2.45GHz antenna element, return loss≦6dB was obtained at desired band for Model B. For radiation pattern, at X-Y plane, gain of 0.11dBi was obtained.

7. REFERENCES

[1] Kagiyama Noriyuki, Ito Atsushi, Hisashi Morishita, "Basic Study of Dual Band Helmet Antenna at 150MHz/2.45GHz for Disaster prevention", IEICE, B-1-105.

[2] Suzuki Tomohiro, Iwasaki Hisao, "A Study of the Helmet Wearing Type Dual Band Antenna for Disaster Prevention", Final Presentation, Shibaura Institute of Technology.

[3] Yusuke Saita, Tsutomu Ito, Naobumi Michishita, and Hisashi Morishita, "Low-frequency Inverted F Antenna on Hemispherical Ground Plane", ASAP 2014, WE3C_16.

Nur Fatin Fatina bt Mohd Ramli received B.E from Shibaura Institute of Technology in 2012. She admitted to Graduate School of Shibaura Institute of Technology in 2014.

Hisao Iwasaki received B.E and Ph.D from Tohoku University in 1975 and 1996, respectively. From 1975 to 2001, he was with Toshiba Research and Development Center. He has been professor of Shibaura Institute of Technology since 2001. He has been engaged in the development of the wide band and multiband antenna for mobile equipment and BAN use. He is a member of IEICE and IEEE.

TRAFFIC PLANNING FOR ENERGY EFFICIENCY IN IP OVER WDM NETWORKS WITH LOAD BALANCING UNDER TRAFFIC UNCERTAINTY

Patidja Sangdanuch and Chutima Prommak
School of Telecommunication Engineering
Institute of Engineering, Suranaree University of Technology

ABSTRACT
Traffic internet volume tends to increase every year. This will result in increasing the energy used on the core network. Nowadays the core networks that have been deployed most is the Internet Protocol (IP) over Wavelength-Division Multiplexing (WDM). The uncertainty of traffic volume caused by variations of traffic demand could affect the reliability of the logical connectivity in IP over WDM network. In this research, the Multi-Objective Optimization using weighted sum approach is applied to achieve traffic load balancing and energy consumption efficiency in IP over WDM networks. Specifically, the integer linear programming is used to solve this problem. In particular, we studied the tradeoff between two objective functions, including maximizing traffic balance across the network and minimizing energy consumption of the core network equipments. The results show that as the traffic balancing increases, the traffic tends to distributed widely across the network links. This results in high network energy consumption.

1. INTRODUCTION

The usage of electrical power in the related field of Information and Communication Technology (ICT) tend to increase every year. It is predicted that the electrical power consumption in ICT will increase up to 14% of global electricity consumption. From the situation that greatly increased in power consumption of the network, we should consider to plan the uses of electric power in the network for effectively used. The reason for increasing of this power consumption is the increase of internet traffic. This will have direct impacts on the usability of network devices. Especially, in the core networks that have high energy consumption. Therefore, it is necessary to plan the use of network resources appropriately in order to optimize the power consumption of the network's devices.

Several works have paid attention to investigate the network planning problems to improve the efficiency of the network energy consumption. (F. Musumeci, et al., 2012) analyzed the energy consumption of IP over WDM networks with different network architectures. This analysis examines the energy used to operate the network by evaluating the energy consumption of devices in the transport layer with the objective to minimize the energy consumption. The aim to analyze the energy consumption of different network architecture is to be able to choose the most appropriate network architecture. While the above research studies are important and show interesting results, but the main issue of traffic uncertainty did not considered. However, some researchers that have been focused on planning the uncertainty of traffic network. (K. Meesublak, 2009) discussed about the uncertainty caused by the dynamic nature of the IP-based traffic. The main aims of this research is to determine the transit traffic in the network with the objective to minimize the cost within the network by considering the capacity that used to support traffic transportation within the network. They considered the uncertainty of traffic in two layers of the network. (P. Keeratichairitnara and C. Prommak, 2012) considers traffic balancing in the IP over WDM networks. They measured the traffic balancing by using the *Mean Absolute Deviation* of IP traffic that transported onto optical link of WDM. Small value of this indicator means that traffic tends to distribute evenly across the network. Whereas high value of this indicator means that traffic transportation in the network is unbalance.

In this study, we present an analysis of the impact of the values of weights used in the proposed multi-objective optimization model. In particular, we consider two objective functions. The first objective function is to minimize the mean absolute deviation of IP traffic volume transported onto optical links of the WDM layer (P. Keeratichairitnara and C. Prommak, 2012) and another objective function is to minimize energy consumption to transport traffic in IP over WDM networks.

The rest of this paper is organized as followed. Section 2 presents the definition and describes the problem formulation. Section 3 presents experiment setup and shows results. Finally, section 4 concludes this paper.

2. PROBLEM DEFINITION AND FORMULATION

2.1 TRAFFIC UNCERTAINTY

Chance-Constrained Programming (CCP) is usually applied in order to manage the variables to generate the

optimal answer (B. Liu, 2009). When considering traffic uncertainty, amount of traffic cannot be absolutely defined. We need to estimate probability that traffic volume will exceed a certain threshold as written in equation (1).

$$P(x \geq \xi) \geq \alpha \quad (1)$$

where ξ is a random variable (traffic volume)

x is a capacity reserved on a link to support traffic volume ξ

α is probability that x will be greater than ξ., $0 \leq \alpha \leq 1$

In equation (1), random variable ξ has a cumulative distribution function $\Phi(.)$ in which an inverse transform is $\Phi^{-1}(.)$. Define $\Phi^{-1}(\alpha) = K$. value of K will be defined from probability of random variable, so the equation can be written as $P(K \geq \xi) \geq \alpha$ where $x \geq K$. In this case, we assume that traffic demand ξ is a normal distribution with mean (μ), and the variance (σ^2). Standardizing the equation (1) using the unit normal random variable (z), then the equation can be written as $P(\frac{x-\mu}{\sigma} \geq z) \geq \alpha$. Obtaining $\frac{x-\mu}{\sigma} \geq \Phi^{-1}(\alpha)$, so the equation of x can be written in an equation (2).

$$x \geq \mu + \Phi^{-1}(\alpha)\sigma \quad (2)$$

Considering the chance constraint, it can be ensured that bandwidth allocation on the network will be more than or equal to the amount of traffic uncertainty ($\xi = \mu + \Phi^{-1}(\alpha)\sigma$). Therefore, it is guaranteed that the network can handle the uncertainty of traffic volume up to 100(α) %.

2.2 PROBLEM FORMULATION

To achieve traffic balancing in IP over WDM networks under the traffic uncertainty with efficient energy consumption, we propose a novel approach based on the Multi-Objective Optimization using weighted sum. Specifically, we apply an integer linear programming method. In particular, we studied the tradeoff between two objective functions, including maximizing traffic balance across the network and minimizing energy consumption of the core network equipments. Table 1 defines the notations used in the mathematical formulations.

Table 1: Notations used in the mathematical formulations

Notations	*Definitions*
Sets:	
A	A set of links in WDM layer
D	A set of traffic demands
P^k	A set of predetermined paths for demand k, $\forall k \in D$
N	A set of nodes
Decision variables:	
$f^{k,p}$	A binary {0, 1} variable that equals equals to 1 if the demand k selects path p from the predetermined path set P^k; 0 otherwise
ω_j	An integer indicating number of wavelength channels that are requested for traffic transport on physical link j, $\forall j \in A$
Nf_j	An integer indicating number of fibers that are used on physical link j, $\forall j \in A$
MD_j	An integer indicating number of multi/demultiplexers that are used at source – destination node of physical link j, $\forall j \in A$
Constant parameters:	
V_m	The number of line cards that used by each node m, $\forall m \in N$
Y_m	The number of route processor that used by each node m, $\forall m \in N$
β_k	The number of wavelength channels that were requested for use by traffic k that wants to transport through link, $\forall k \in D$
x_k	The number of traffic data k (traffic demand k), $\forall k \in D$
T_k^m	A binary {0, 1} parameter that equals to 1 if traffic demand k flowed from source node m; 0 otherwise, $\forall k \in D$, $\forall m \in N$
$\delta_j^{k,p}$	A binary {0, 1} parameter that equals to 1 if path $p \in P^k$ for demand k using link j; 0 otherwise, $\forall j \in A$
N	The number of physical links in set A
r_j	The capacity requested for link j, $\forall j \in A$
L_j	The length of the physical link j
EA_j	The number of EDFAs on physical link j, which can be obtained from $EA_j = \lfloor L_j/S - 1 \rfloor + 2$ (G. Shen and R. S. Tucker, 2009), where S is the distance between two neighboring EDFAs
EG_j	The number of regenerators on physical network link j, which can be obtained $EG_j = \lfloor L_j/5S - 1 \rfloor$ (M. Yagi, et al., 2005)
B_ω	Bandwidth of wavelength channel
B_{LC}	Bandwidth of line card
N_{LC}	The number of slot (line card) that can be used by each route processor
W_f	The number of wavelength per fiber
W_{MD}	The number of wavelength per multi/demultiplexers
P_{LC}	The power consumption of line card
P_{RP}	The power consumption of route processor
P_{tr}	The power consumption of transponder
P_E	The power consumption of amplifier (EDFA)
P_G	The power consumption of regenerator
P_O	The power consumption of optical switch
P_{MD}	The power consumption of multiplexer/demultiplexer
f_1	The unbalance index of traffic load in the network
f_2	The sum of power consumption of all devices for transport traffic demands in the network
F_1	The value of the first objective function is normalize
F_2	The value of the second objective function is normalize
f_1^{min}	Minimum of the first objective function
f_1^{max}	Maximum of the first objective function
f_2^{min}	Minimum of the second objective function
f_2^{max}	Maximum of the second objective function
w_1	Weight values for first objective function
w_2	Weight values for second objective function

Objective functions:

The First objective: Minimize the mean absolute deviation of IP traffic volume transported onto optical links of the WDM layer (P. Keeratichairitnara and C. Prommak, 2012).

$$f_1 = \frac{1}{n}\sum_{j \in A}\left| r_j - \frac{\sum_{j \in A} r_j}{n} \right| \quad (4)$$

The Second objective: Minimize energy consumption to transport traffic in IP over WDM network which can be written in the mathematical equations as following.

$$f_2 = \sum_{m \in N} P_{\mathrm{LC}} \cdot V_m + \sum_{m \in N} P_{\mathrm{RP}} \cdot Y_m + 2 \cdot \sum_{k \in D} P_{\mathrm{tr}} \cdot \beta_k + \sum_{j \in A} P_{\mathrm{O}} \cdot \omega_j + \sum_{j \in A} P_{\mathrm{MD}} \cdot MD_j + \sum_{j \in A} \left(P_{\mathrm{E}} \cdot EA_j + P_{\mathrm{G}} \cdot EG_j \right) \cdot Nf_j \quad (5)$$

Both objective functions in equation (4) and (5) are normalized by using an equation (6) as follows.

$$F_1 = \frac{f_1 - f_1^{\min}}{f_1^{\max} - f_1^{\min}} \quad \text{and} \quad F_2 = \frac{f_2 - f_2^{\min}}{f_2^{\max} - f_2^{\min}} \quad (6)$$

multiplying the objective function by weights

$$Minimize \;\; z = w_1F_1+w_2F_2 \qquad (7)$$

The proposed problem consists of constraints (8) – (14) which specify the optical capacity limitation and the network specification.

$$\sum_{p\in P^k} f^{k,p} = 1 \qquad \forall k \in D \qquad (8)$$

$$\sum_{k\in D}\sum_{p\in P^k} \delta_j^{k,p} \cdot f^{k,p} \cdot x_k \le B_\omega \cdot \omega_j \qquad \forall j \in A \qquad (9)$$

$$\omega_j \le W_{MD} \cdot MD_j \qquad \forall j \in A \qquad (10)$$

$$\omega_j \le W_f \cdot Nf_j \qquad \forall j \in A \qquad (11)$$

$$\omega_j \ge 0 \qquad \forall j \in A \qquad (12)$$

$$Nf_j \ge 0 \qquad \forall j \in A \qquad (13)$$

$$MD_j \ge 0 \qquad \forall j \in A \qquad (14)$$

Constraint (8) prevents duplication of a route selection in the network by indicating that traffic k can select only one path from the paths defined in set P^k. Constraint (9) ensures that the sufficient number of wavelengths is provided for an optical link j, so that link j can accommodate the fluctuation of traffic volume transported through a link j. Parameter x_k incorporates the variation of traffic demand in order to guarantee that the network can support the traffic uncertainty. Constraint (10) ensures that the fiber optic is sufficient for the number of wavelength that used on link j. Constraint (11) ensures that the multi/demultiplexers have sufficient number for wavelengths on link j. Constraint (12) – (14) specify that ω_j, Nf_j, and MD_j are non-negative number.

The following equations are used to calculate essential parameters which are applied in the constraints.

Equation (15) calculates the amount of traffic that flow on link j. It is the sum of all traffic k that flow on link j in the selected route p.

$$r_j = \sum_{k\in D}\sum_{p\in P^k} \delta_j^{k,p} \cdot f^{k,p} \cdot x_k \qquad \forall j \in A \qquad (15)$$

Equation (16) calculates the number of line card that used on node m. It is the sum of all traffic demand k that flows from source node m divided by the bandwidth of line card.

$$V_m = \left\lceil \frac{\sum_{k\in D} x_k \mathrm{T}_k^m}{B_{LC}} \right\rceil \qquad \forall m \in N \qquad (16)$$

Equation (17) calculates the number of wavelengths for traffic demand k. It is the amount of traffic demand k divided by bandwidth of wavelength.

$$\beta_k = \left\lceil \frac{x_k}{B_\omega} \right\rceil \qquad \forall k \in D \qquad (17)$$

Lastly, equation (18) calculates the number of route processors that needed on node m. It is the number of line cards that used in node m divided by the number of line cards that each route processor can support.

$$Y_m = \left\lceil \frac{V_m}{N_{LC}} \right\rceil \qquad \forall m \in N \qquad (18)$$

3. NUMERICAL EXPERIMENTS AND ANALYSIS

3.1 EXPERIMENTS SETUP

In this section we present numerical evaluations of the proposed Multi-Objective Optimization model. In our experiment, we adopted the IP over WDM network of the NSFNET which consist of 14 nodes and 44 physical links (Y. Miyao and H. Saito, 1998).

The constant parameters used in our experiments are given in table 2 and table 3. We considered 100, 140 and 180 IP traffic demands between 100, 140 and 180 source-destination node-pairs, respectively (randomly selected). We consider the traffic uncertainty based on the normal distribution with a value of mean and standard deviation of 2 Gbps and 0.19 Gbps, respectively (P. Nualmuenwai and C. Prommak, 2011). Specifically, we consider 90% traffic uncertainty guarantee. So, we obtained the traffic volume ξ equals to 2.24 Gbps.

The weight coefficient w_1 and w_2 were applied in the experiments. The relationship between the weight coefficients is that, given w_1, $w_2 = 1 - w_1$. Solving the multi-objective problem, the maximum point found is a particular point on the Pareto front corresponding to the weight coefficients used. An approximated Pareto front can be generated by solving the multi-objective model many times using different weight sets. In particular, our experiments vary w_1 from 0 to 1, with a step size of 0.02.

The traffic planning for energy efficient in NSFNET IP over WDM network was solved by implementing the mathematical formulations with the ILOG-OPL development studio and inputting a set of predetermined paths for each traffic demand (P^k) to the model. Then it was solved with IBM ILOG CPLEX Optimization Studio version 12.4. Computations were performed on Intel® Core™ 2 Duo CPU speed 2.1 GHz RAM 3 GB DDR2.

Table 2: Input data for model and simulation

Input	Value
The distance between two neighboring EDFAs (S)	80 km
The distance between two neighboring regenerators	400 km
Bandwidth of wavelength channel	2.5 Gbps
The number of wavelength per fiber	40 wavelengths
The number of wavelength per multiplexers and demultiplexers	80 wavelengths
Bandwidth of line card	40 Gbps
The number of slot (line card) per route processor	16 slot card
Uncertainty guarantee levels	90%
Amount of Traffic demand between node-pair	100, 140, 180

Table 3: The power consumption of devices

Devices	Power (W)
Line card	415
Route processor	166
Transponder	34.5
EDFA	25
Regenerator	100
Optical switch (OXC)	1.5
Multiplexer/demultiplexer	811

3.2 NUMERICAL RESULT AND DISCUSSION

Figure 1 plots the results of traffic planning for 100, 140 and 180 traffic demands over the NFSNET network. The graph compares the network performances in term of the unbalance index representing how evenly traffic is distributed across the network and the amount of total energy consumption to transport all traffic demands of each case.

The points in figure 1 are the minimum points found with different weight sets. It can be observed that as the w_2 increases from 0 to 1 (from left to right of the X axes), for the case of 100 traffic demands, the amount of total energy consumption increases about 2.1 times (from 38,000 WAh to 78,000 WAh) whereas the unbalance index decreases about 3.5 times, i.e. the load balancing increases about 3.5 times. For the case of 140 and 180 demands, the amount of total energy consumption increases about 1.6 and 1.4 times whereas the load balancing increases about 3.5 and 3.0 times, respectively. We can see that as the number of traffic demands increases, the proposed model can achieve about the same ratio of load balancing at lower ratio of the energy consumption.

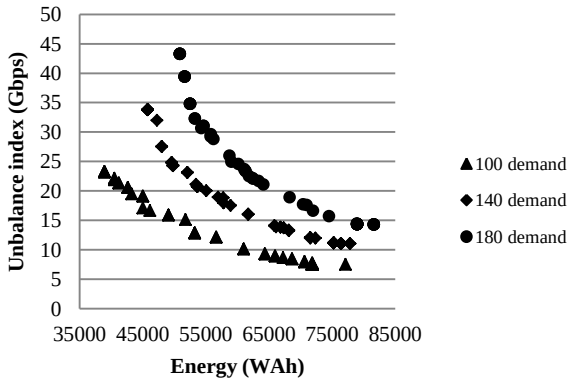

Fig. 1. Compare the energy consumption and the unbalance index using weighted sum approach at traffic uncertainty guarantee 90%.

4 CONCLUSION

This study presents the Multi-Objective Optimization using weights sum approach. We formulate the problem as an integer linear programming problem aiming to select the optimal path and the sufficient capacity for traffic demands, based on its uncertainty with consideration of two opposite objectives which are to minimize unbalance index of traffic on links in IP over WDM networks and to minimize energy consumption to transport traffic. In particular, we use weighted sum approach to transform two objectives to single objective and compare effect of weighting value in each one. The numerical results show that when compared the case of low traffic demands with the case of high traffic demands, the proposed multi-objective model can achieve about the same ratio of load balancing while the case of high traffic demands has lower ratio of the total energy consumption. This means that the proposed model can improve the energy efficiency of the networks that carry high traffic volume.

REFERENCES

Y. Zhanga, M. Tornatore, P. Chowdhurya and B. Mukherjee, Energy optimization in IP-over-WDM networks, Journal of Optical Switching and Networking, vol. 8, July 2011, pp. 171–180.

F. Musumeci, M. Tornatore and A. Pattavina, A power consumption analysis for IP-over-WDM core network architectures, IEEE/OSA Journal of Optical Communications and Networking, vol. 4, February 2012, pp. 108–117.

K. Meesublak, A two-layer network design problem under traffic uncertainty, in Conf. ECTI-CON, vol. 2, May 2009, pp. 914–917.

P. Keeratichairitnara and C. Prommak, "Logical Topology Design in IP over WDM Networks with Load Balancing under Traffic Uncertainty", in *IEEE Int. Conf. Communication Systems* (*ICCS*), Singapore, 2012, pp. 55–59.

B. Liu, Theory and Practice of Uncertain Programming, 3rd ed., UTLAB: Beijing, 2009, pp. 37–42.

G. Shen and R. S. Tucker, "Energy-Minimized Design for IP Over WDM Networks," *Optical Communication and Networking*, vol.1, 2009, pp. 176–186.

M. Yagi, et al., "Field trial of optical 3R regenerator over installed cable" *31st European Conference on Optical Communication*., ECOC 2005, vol. 4, 2005, pp. 975–976.

Y. Miyao and H. Saito, "Optimal design and evaluation of survivable WDM transport networks," *IEEE J. Sel. Areas Commun.*, vol. 16, pp. 1190–1198, 1998.

P. Nualmuenwai and C. Prommak, "On the analysis of IP traffic distribution in the network of Suranaree University of Technology," in Conf. WASET, Thailand, 2011, pp. 362–365

Patidja Sangdanuch received B.Eng (2013) in Telecommunication Engineering from Suranaree University of Technology. Currently he is pursuing Master's degree in Telecommunication Engineering at Suranaree University of Technology, Nakhon Ratchasima, Thailand.

Chutima Prommak received B.Eng (Hons) in Electrical Engineering from Khon Kaen University, Thailand in 1992. She received M.Sc. and Ph.D. in Telecommunications from University of Colorado at Boulder, CO, USA in 1998 and University of Pittsburgh, PA, USA in 2004, respectively. Currently she is an assistant professor in Suranaree University of Technology, Thailand. Her research interests are in the areas of wireless network design and planning, network optimization, WiMAX, wireless sensor networks and heuristic optimization for telecommunication networks.

IMPACT OF USER VELOCITY CONSIDERATION IN SINR BASED VERTICAL HANDOFF DECISION ON THE HETEROGENEOUS WIRELESS NETWORK PERFORMANCE

DAMAR WIDJAJA AND PEERAPONG UTHANSAKUL
SCHOOL OF TELECOMMUNICATION ENGINEERING
SURANAREE UNIVERSITY OF TECHNOLOGY

ABSTRACT

A heterogeneous network that consists of various wireless networks is being developed to achieve high speed transmission. The seamless and efficient handoff between different access technologies known as vertical handoff (VHO) is essential and remains a challenging problem. Several criteria for VHO decision have been proposed in the literature. In this paper, we propose velocity consideration, as a part of user mobility, as an additional criterion for SINR based VHO decision. Simulation results show that there is a tradeoff between average throughput and the number of handoff and unnecessary handoff. Although the average throughput is slightly dropped, the velocity consideration gives better performance on the number of handoff and unnecessary handoff, especially in the high noise power environment.

Keywords: Vertical handoff, SINR, user velocity, heterogeneous networks.

INTRODUCTION

A heterogeneous network that consists of various wireless networks, including Worldwide Interoperability for Microwave Access (WiMAX), Wireless Fidelity (Wi-Fi), and mobile communications, such as Wideband Code Division Multiple Access (WCDMA), and High Speed Download Packet Access/High Speed Upload Packet Access (HSDPA/HSUPA), is being developed to achieve high speed transmission (Chang & Chen, 2008). These heterogeneous wireless networks have differences in data rates, transmission range, traffic classes, and access costs.

For seamless communication, the integration of the networks, such as WLAN and 3G WCDMA systems should be error free to achieve the next generation multimedia wireless networks (Yang, et al., 2007). The seamless and efficient handoff between different access technologies known as vertical handoff (VHO) is essential and remains a challenging problem. Cooperation-based handover schemes provide not only service continuity in the entire network area, but also an effective solution for enhancing cell edge throughput, which is a major issue in fourth generations (4G) standardization (Choi, 2010).

Several criteria for VHO decision have been proposed in the literature and the main criteria used are Received Signal Strength (RSS), Signal to Interference plus Noise Ratio (SINR), and available bandwidth (Mardini, et al., 2012). From the throughput performance, the combining receiving SINR based VHO gives superior value compare to RSS based VHO (Yang, et al., 2007). However, in the literature, user mobility has never been considered during SINR based VHO is performed.

In this paper, we propose velocity consideration, as a part of user mobility, as an additional criterion for SINR based VHO decision. The heterogeneous network consists of WLAN and WCDMA system. Simulation results show that there is a tradeoff between average throughput and the number of handoff and unnecessary handoff. Although the average throughput is slightly dropped, the velocity consideration gives better performance on the number of handoff and unnecessary handoff, especially in the high noise power environment.

The paper is organized as follows; section 2 describes the SINR based handover legacy, proposed algorithm, the calculation of performance parameters, and the simulation scenario. Section 3 provides simulation results and discussion. Section 4 provides some conclusions.

PROPOSED VHO DECISION ALGORITHM

Legacy Handover Decision

Handover decision algorithms have been designed mainly to guarantee continuity of service (Choi, 2010). A basic principle of the algorithms is to use the difference between the quality of the signal received from the serving base station (BS) and from the neighboring BS. The *SINR* based handover decision algorithm then can be simply expressed as

$$SINR_o - SINR_i < \delta \quad (1)$$

where $SINR_o$ is received SINR from the serving BS and $SINR_i$ is received SINR from the neighboring BS, and δ is the handoff additional threshold determined by the system.

Neighboring cells that satisfy (1) will be designated by mobile station (MS) as candidate cells for handover (Choi, 2010). If the MS reports the identity and SINR information of candidate cells to its serving BS, then the serving BS finally determines a target cell among the reported candidate cells. In this paper, the handoff additional threshold, δ, will be used to force the MS with the certain velocity value to stay longer in the certain cell according their velocity. This mechanism will be further described in the next section.

Handover Decision Algorithm

The basic principle of this algorithm is that slow speed MS should stay longer in WLAN and high speed MS should stay longer in WCDMA. There are some advantages that can be achieved by this basic principle. This approach assigns MS to appropriate cells so that frequent call handoff from fast-speed users in small cells can be avoided (Huang, et al., 2011) and signaling overheads and processing load reduced (Kim, et al., 2010) and (Shafiee, et al., 2011). VHO blocking probability can be reduced while maintaining reasonable throughput in the WLAN (Kim, et al., 2010). It will also reduce ping-pong effect (Rizvi, et al., 2010) and (Cha, et al., 2008) and dropping probability (Dan, et al., 2012) . The proposed VHO decision algorithm is depicted as a flow chart in Figure 1.

When MS is low speed (lower than velocity threshold) and in WLAN coverage, then system will force MS to stay longer in WLAN until the SINR of neighboring WCDMA cell has a higher value than the preset threshold and the handoff is triggered. The low speed MS will stay in WCDMA cell until the SINR of neighboring WLAN cell has higher value than the SINR of serving WCDMA cell. The next handoff will be directly triggered without any preset threshold.

The same way will works on high speed (higher than velocity threshold) MS that is initially served by WCDMA cell. System will force MS to stay longer in WCDMA until the SINR of neighboring WLAN cell has a higher value than the preset threshold and the handoff is triggered. The high speed MS will stay in WLAN cell until the SINR of neighboring WCDMA cell has higher value than the SINR of serving WLAN cell. The handoff will be directly triggered without any preset threshold.

Performance Parameters

In this paper, 3 performance parameters will be used; average throughput, average number of handoff, and average number of unnecessary handoff. Average throughput calculation is based on the maximum achievable data rate for a given carrier bandwidth and SINR can be determined with the help of Shannon capacity formula (Yang, et al., 2007) and (Ayyappan, et al., 2009).

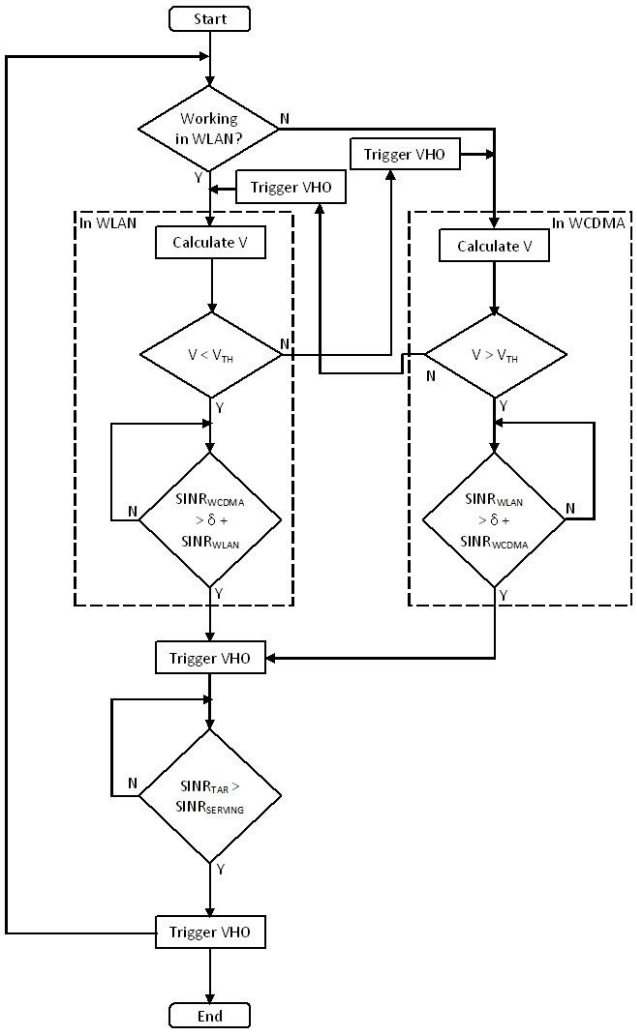

Fig. 1. The proposed VHO decision.

The maximum achievable data rate R is given by:

$$R = W \log_2\left(1 + \frac{\gamma}{\Gamma}\right) \quad (2)$$

where W is the carrier bandwidth, γ is SINR received at user end when associated with WLAN or WCDMA, and Γ is the dB gap between uncoded Quadrature Amplitude Modulation (QAM) and channel capacity, minus the coding gain. The SINR, γ, received by user from its associated WLAN Access Point (AP) i or WCDMA Base Station (BS) i is

$$\gamma_i = \frac{G_i P_i}{N + I_i} = \frac{G_i P_i}{N + \sum_{\substack{k \neq i \\ k \in AP/BS}} G_k P_k} \quad (3)$$

where G_i is the channel gain between user and its associated AP or BS, P_i is the transmitting power of AP or BS, N is the background noise power at user receiving end, and I_i is the interference from other neighboring APs or BSs.

The average throughput calculation in the combined SINR based VHO decision algorithm (Yang, et al., 2007) and (Ayyappan, et al., 2009), will be used as the reference calculation and will be compared to the averaged

throughput result of the proposed algorithm. In the combined SINR based VHO decision algorithm, the VHO is triggered while the user is getting higher equivalent SINR from another access network. The higher equivalent SINR is calculated by letting received data rate from AP is equal to received data rate from AP and vice versa, $R_{AP} = R_{BS}$, then the relationship between γ_{AP} and γ_{BS} is determined as

$$\gamma_{AP} = \Gamma_{AP}\left(\left(1+\frac{\gamma_{BS}}{\Gamma_{BS}}\right)^{\frac{W_{BS}}{W_{AP}}}-1\right) \quad (4)$$

The VHO is taken place at handoff point X_h in Figure 2 and the total downlink throughput, θ, can be represented as in equation (5)

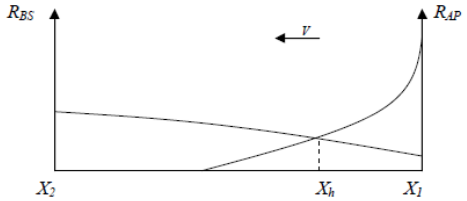

Fig. 2. Point to point model (Yang, et al., 2007).

$$\theta = \int_{X_1}^{X_h} R_{AP}(x) \times CRT_{AP} + \int_{X_h}^{X_2} R_{BS}(x) \times CRT_{BS} \quad (5)$$

where CRTAP and CRTBS is the cell residence time inside WLAN and WCDMA.

Average number of handoff is determined by averaging the entire handoff occurrence in every user. This value includes VHO and horizontal handoff (HHO). Average number of unnecessary handoff is determined by averaging the entire unnecessary handoff occurrence in every user. Unnecessary handoff occurs when MS stays in the cell not more than 1/15 time of the previous handover period. This calculation is adopted from ping pong handoff calculation in (Ghanem, et al., 2012).

Simulation Scenario

The performance of proposed algorithm has been evaluated with the same scenario in (Yang, et al., 2007), and is shown in Figure 3. There are 7 BS (indicated as triangle) and 12 AP (indicated as rectangular) at fix place and 200 MS randomly generated inside the simulation area. The MS position changes every time interval, depending on their random moving speed and direction. Simulation parameters for WCDMA are as follows; maximum BS transmitting power is 40dBm, average downlink load factor is 75%, background noise power equals to $7.66*10^{-14}$ W (around –131dBm), carrier frequency is 2GHz, and channel bandwidth is 5MHz. Simulation parameters for WLAN are as follows; maximum AP transmitting power is 20dBm, background noise power equals to –96dBm, carrier frequency is 2.4GHz, and channel bandwidth is 1MHz.

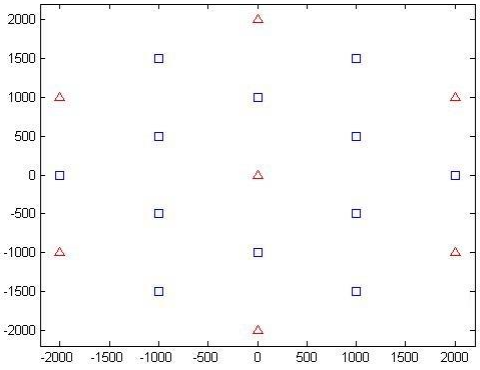

Fig. 3. Simulation Area

SIMULATION RESULT AND DISCUSSION

The user's average throughput under different noise power of WLAN with velocity threshold V_{th} = 5m/s. is shown in Figure 4. The average throughput becomes lower with higher noise power. The average throughput of velocity considered-SINR based VHO is always lower than the average throughput of combined-SINR based VHO. It happen because of the proposed algorithm will force low velocity users to stay connected in WLAN longer and high velocity users to stay connected in WCDMA longer than it should be. The higher the δ value, the longer the users stay in their velocity associated cells. For the combined-SINR based VHO, the users will directly handoff to neighbor cells that have SINR equivalently higher than current cell and have same throughput. For velocity considered-SINR based VHO, users will be force to stay in the cells associated with their velocity, even the throughput is lower than neighbor candidate cell.

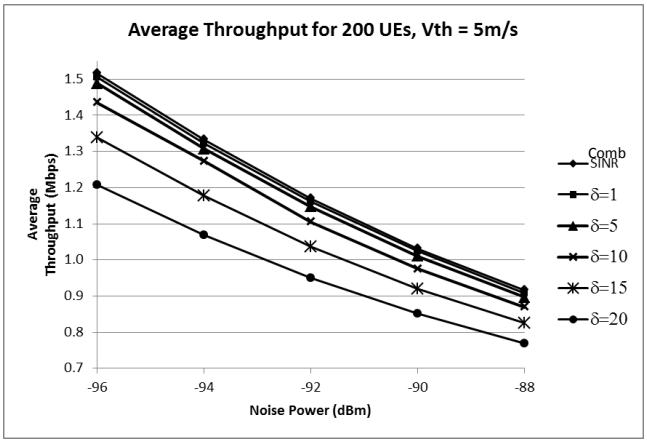

Fig. 4. Average Throughput for V_{th} = 5m/s

Figure 5 shows the different impact of velocity threshold on the average throughput at δ = 15dB. The average throughput becomes lower with higher velocity threshold. The velocity threshold divides all users into two groups, low speed users and high speed users. From the simulation, at V_{th} = 11m/s, 45.8% of users are categorized

as slow speed users and forced to stay in WLAN longer. At V_{th} = 5m/s, 18.9% of users are categorized as slow speed users and forced to stay in WLAN longer. As WLAN has lower bandwidth compare to WCDMA, so that fewer users will be served by lower bandwidth, more users will be served by higher bandwidth, and it will results high average throughput. The slow speed users will be fewer at low velocity threshold and more users will be served in WCDMA longer resulting higher average throughput.

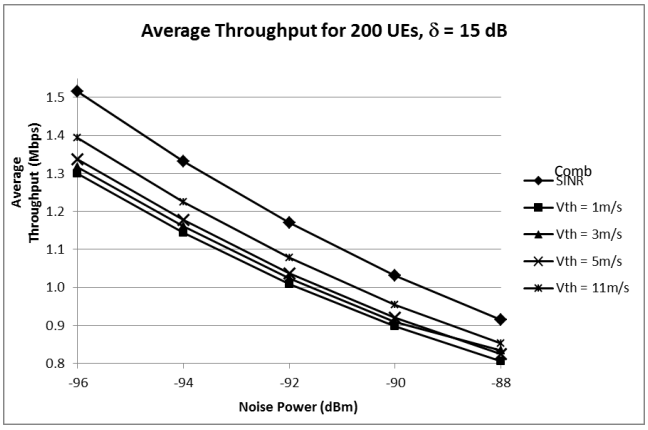

Fig. 5. Average Throughput for δ = 15dB

Figure 6 shows the average throughput comparison of basic SINR based VHO according to equation (1), velocity considered-SINR based VHO and combined-SINR based VHO. The velocity considered-SINR based VHO improves the average throughput from the basic SINR based VHO as the algorithm only apply the threshold δ when user stay in the velocity associated cell. Basic SINR based VHO always apply δ during handoff process, so that user will always receive lower throughput before it can performs handoff.

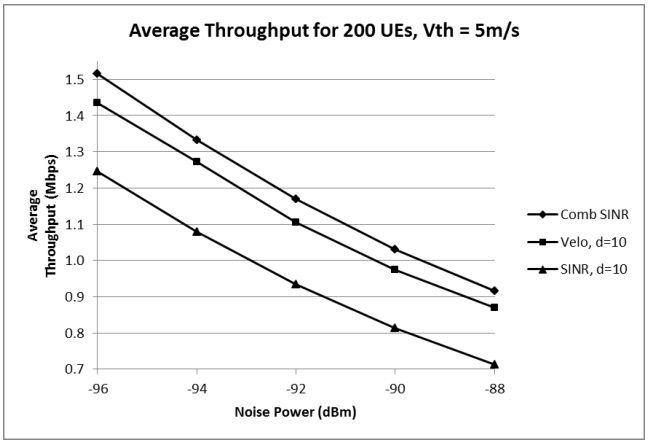

Fig. 6. Average Throughput for V_{th} = 5m/s compare to basic SINR based VHO

The average number of handoff and unnecessary handoff are shown in Figure 7 and Figure 8 respectively. Velocity considered-SINR based VHO has better performance (lower value) than combined-SINR based VHO in the high noise power environment. The threshold δ will force the user to stay longer in the velocity associated cell until the condition is satisfied. Handoff will not be initiated, even when SINR and throughput of neighbor cell is higher, as long as δ is not reached yet. In the combined-SINR based VHO, user will initiate handoff process whenever equivalent neighbor SINR is higher than current serving cell or in other words, whenever the neighbor cell reaches the same throughput. This handoff will be repeated as long as the condition is satisfied, even the last handoff just performed in a short period.

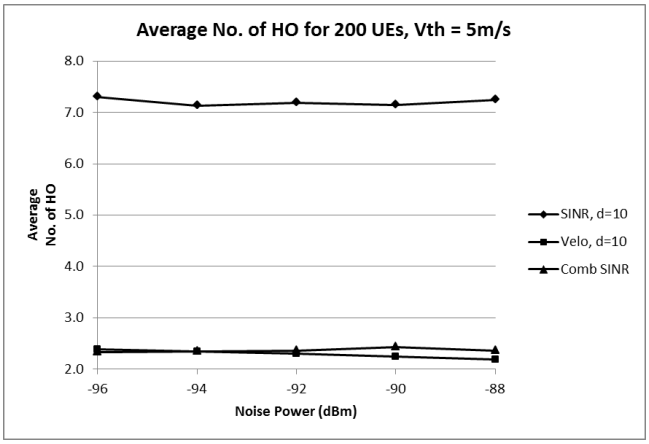

Fig. 7. Average Number of Handoff for V_{th} = 5m/s

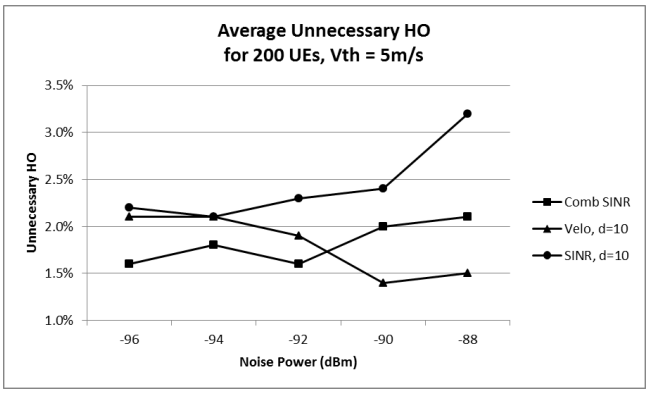

Fig. 8. Average Number of Unnecessary Handoff for V_{th} = 5m/s

CONCLUSION

The velocity considered–SINR based VHO algorithm is proposed to elaborate the user mobility as an additional criterion for VHO decision making. The simulation results shows that the velocity consideration makes the average throughput is slightly dropped, but gives better performance on the number of handoff and unnecessary handoff, especially in the high noise power environment. If the velocity threshold and additional SINR threshold is set lower, then the average throughput becomes higher.

REFERENCES

Ayyappan, K., Narasiman, K., and Dananjayan, P.,

SINR Based Vertical Handoff Scheme for QoS in Heterogeneous Wireless Networks, Proc. International Conference on Future Computer and Communication, pp. 117–121, 2009.

Cha, B., Seo, SH., Choi, YM., and Song, JS., Mobile-Velocity Adaptive Vertical Handoff in Integrated WLAN and WiBro Netmorks, Proc. 4th International Conference on Information and Automation for Sustainability, pp. 384-389, 2008.

Chang, B-J., and Chen, J-F, Cross-Layer-Based Adaptive Vertical Handoff With Predictive RSS in Heterogeneous Networks, IEEE Transactions on Vehicular Technology, vol. 57, no. 6, pp. 3679-3692, 2008.

Choi, H-H., An Optimal Handover Decision for Throughput Enhancement, IEEE Communication Letters, vol. 14, no. 9, pp. 851-853, 2010.

Dan, F., Huang, C., Zhu, J., Wang, X., and Xu, L., Trusted Vertical Handoff Algorithm in Multihop-enabled Heterogeneous Wireless Networks, Proc. 8th International Conference on Wireless Communications, Networking and Mobile Computing, pp. 1 – 4, 2012.

Ghanem, K., Alradwan, H., Motermawy, A., and Ahmad, A., Reducing Ping-Pong Handover Effects In Intra EUTRA Networks, Proc. 8th IEEE, IET International Symposium on Communication Systems, Networks and Digital Signal Processing, pp. , 2012.

Huang, Q., Huang, Y-C., Ko, K-T., and Iversen, V.B., Loss Performance Modeling for Hierarchical Heterogeneous Wireless Networks With Speed-Sensitive Call Admission Control, IEEE Transactions On Vehicular Technology, vol. 60, no. 5, pp. 2209-2223, 2011.

Kim, D.K., Griffith, D., and Golmie, N., A New Call Admission Control Scheme for Heterogeneous Wireless Networks, IEEE Transactions On Wireless Communications, vol. 9, no. 10, pp. 3000-3005, 2010.

Mardini, W., Al-Ghadi, M.Q., and Ababneh, I.M., Distance Based Scheme for Vertical Handoff in Heterogeneous Wireless Networks, Journal of Emerging Technologies in Web Intelligence, vol. 4, no. 1, pp. 67-75, 2012.

Rizvi, S., Aziz, A., and Saad, N.M., An Overview of Vertical Handoff Decision Policies for Next Generation Wireless Networks, Proc. IEEE Asia Pacific Conference on Circuits and Systems, pp. 88-91, 2010.

Shafiee, K., Attar, A., and Leung, V.C.M., Optimal Distributed Vertical Handoff Strategies in Vehicular Heterogeneous Networks, IEEE Journal On Selected Areas In Communications, vol. 29, no. 3, pp. 534-544, 2011.

Yang, K., Gondal, I., Qiu, B., and Dooley, L.S., Combined SINR Based Vertical Handoff Algorithm for Next Generation Heterogeneous Wireless Networks, Proc. IEEE Global Telecommunications Conference, pp. 4483-4487, 2007.

Damar Widjaja received B.E. (1994) degrees in electrical engineering from Gadjah Mada University, Yogyakarta, Indonesia and M.E. (2005) in electrical engineering from University of Indonesia, Jakarta, Indonesia.
He is currently a Ph.D. student in School of Telecommunication Engineering, Suranaree University of Technology, Thailand and working as a faculty member in Electrical Engineering Department, Sanata Dharma University, Yogyakarta, Indonesia.

Peerapong Uthansakul received B.S. (1996) and M.E (1998) degrees in electrical engineering from Chulalongkorn University, Thailand and Ph.D (2002) in Communications Technologies from The Univeristy of Queensland, Australia.
He is an Associate Professor in School of Telecommunication Engineering, Suranaree University of Technology, Thailand.

PERFORMANCE ANALYSIS OF GPS-AIDED OSDMA SYSTEMS

Phimchan Chaichana, Peerapong Uthansakul and Monthippa Uthansakul
School of Telecommunication Engineering
Suranaree University of Technology,
Nakhon Ratchasima, Thailand
Email: M5640300@g.sut.ac.th, uthansakul@sut.ac.th, mtp@sut.ac.th

ABSTRACT

The recent communication technology has evolved dramatically due to its convenience and flexibility. This means that the demand for data access increases rapidly. However, since the frequency resources in LTE systems are limited, lots of researchers have developed techniques to maximize the benefits of existing frequency resources. Among those, Opportunistic Space-Division Multiple Access (OSDMA) is one of the most promising techniques that can be implemented in practice. This technique provides a higher data rate for multiple User Equipments (UEs) and requires a less feedback information than conventional SDMA. However, the feedback requirement is still a big drawback for this technique. Although some works in literatures try to reduce the feedback information, unfortunately the high throughput relies on the feedback bit of Channel State Information (CSI) for each UE at the transmitter. Such a system has limited a full CSI by large feedback overhead and it causes performance degradation due to channel estimation errors. In this paper, a novel OSDMA technique based on the use of location update information has been proposed. In fact, the knowledge of location for each UE is always updated at Base Station (BS). Hence, the proposed method does not require any extra procedures for achieving the location information. The simulation results confirm the success of using the proposed technique for LTE systems in which it is also simple to implement in practice.

Keywords—Location Update Information; Opportunistic Space Division Multiple Access (OSDMA); LTE systems.

1. INTRODUCTION

It is the fact that the wireless communication technology allows everyday life with ease and flexibility. Mobile devices such as laptop, personal radio, cell phone, tablet and digital camera become one part of daily complementary. Customers can check in a personal account to use various mobile services such as check on the service, abreast of news, entertainment news, travel information and others. In addition, the growth of new applications that run on the network is developing very fast [1]. Therefore, the mobile communication market drives the new technology to serve its demand. This is the reason why the first generation (1G) is driven into the fifth generation (5G).

Currently, the LTE system is popularly employed for 4G operators and it is the ground base of 5G development. The advancement of LTE technology has been recently presented through lots of publications. However, no matter which techniques were proposed for LTE systems, they have to face the problem of limited frequency resources. Hence, the trend of future improvement is to further maximize the utilization of frequency as described in [2], [3], and [4]. Among techniques in the area of efficient allocation, Beam Division Multiple Access (BDMA) [2] becomes an interesting technique to increase the system capacity without any cost of frequency resources. The mechanism of BDMA is just like the other multiple accesses except that each UE is distinguished from each other by allocating the orthogonal beam. Hence, each UE will not get the inference effect from the other UEs which is able to receive data at full capacity for each user.

In the past decade, there has been enormous research and developments regarding BDMA technique. The most common technique is called as Multiple-Input Multiple-Output (MIMO) technique or Space Division Multiple Access (SDMA) which provide a high system throughput. However, to achieve the hopeful high throughput, BS requires CSI [5]. In practice, for full CSI systems, it has a limitation if large feedback affects both performance degradation and channel estimation errors. An alternative method is Opportunistic Space Division Multiple Access (OSDMA) technique [6] which is able to reduce a feedback bit. The mechanism of this technique is that BS sends a random beam with training sequence to each UE. Then each UE feedback evaluates the best Signal-to-Interference-plus-Noise Ratio (SINR) according with index beam. The BS will schedule beam according to the information from UE with the highest SINR for transmission. In addition, Angle-of-Departure-Aided OSDMA (AOD-OSDMA) technique [7] has been proposed to use the knowledge of angle-of-departure (AODs) at BS for finding the strongest signal received at each UE to form beams. However, OSDMA techniques in literatures can partially reduce the feedback information but they still require the knowledge feedback CSI.

This paper proposes novel transmission technique that can realize the knowledge of UE locations indirectly by using UE's location update. For LTE systems and future mobile network generation, every UE has GPS technology along with other hardware platform [2]. Therefore, based on the knowledge of updated location information of UE at BS serving cell [8], the feedback information from UE is not

necessary anymore. When UE requests the data transmission, the serving BS is able to calculate angle of UE to form beams and data transmission instantly set up without any known feedback CSI from UE.

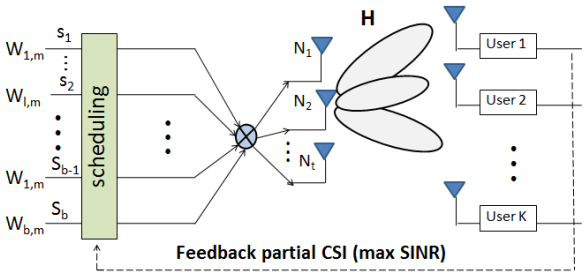

Fig.1. Block diagram of OSDMA systems.

The remainder of paper is organized as follows. Section II presents the overview of OSDMA technique. In Section III, the proposed technique is described. The simulation results and discussions are given in Section IV. Finally, the conclusion of this paper is presented in Section V.

2. OVERVIEW OF OPPORTUNISTIC SPACE-DIVISION MULTIPLE ACCESS (OSDMA)

2.1 OSDMA System Model

The OSDMA system is modeled by considering MIMO broadcast channel with Nt transmitting antennas and K users with one receiving antenna [6]. Fig.1 shows the block diagram of a typical OSDMA systems. The transmitter having B (≥ Nt) randoms orthonormal beams and sends B pilot symbols forward each user. Each user will feedback the best pilot symbol indexing to the transmitter. Then the transmitter provides subset users selected for data transmission according with scheduling criterion SNR feedback information. In practice, it is assumed that every time-slot has a length L with training period of M mini-slot having length of each τ. The maximum value of M is [L/ τ] in which τM is used for training sequence and L-τM is used for data transmission in every time-slot. In this case, we define M = 1, in every mini-slot, B random orthonormal vector {wb,m ∈ CNt x1, m=1, …, M}. The signal receiver at each user in mth mini-slot is given by

$$y_{k,m} = h_k^T w_{b,m} s_b + n_k \qquad \text{for k=1, ..., K} \qquad (1)$$

where hk ∈ CNt x1 is channel vector for kth user, wb,m ∈ CNtx1 is bth random beamforming vector at mth mini-slot, sb is bth transmission pilot symbol and nk is Gaussian noise vector at kth user.

In every time-slot, the kth user calculates value of signal interference plus noise (SINR) following B as given by

$$SINR_{k,b,m} = \frac{\left|h_k^T w_{b,m}\right|^2}{1/\rho + \sum_{l\neq b}\left|h_k^T w_{l,m}\right|^2} \qquad (2)$$

where ρ =P/N0 is input SNR received by $SINR_{k,b,m}$ at each k = 1,…,K , b = 1,…,B and m = 1,...,M. Each user feeds back maximum SINR according with index b and compute throughput R_m of mth given by

$$R_m = \sum_{b=1}^{B} \log_2\left(1 + \max_{1\le k\le K} SNIR_{k,b,m}\right) \text{ for } m = 1, \ldots, M \qquad (3)$$

When transmitter received feedback information, it provides data transmission forward to B at each selected beam. Finally, value of current time-slot with B selected beam can be utilized to compute throughput as given by

$$R = (L - \tau M)\max_{1\le k\le K} R_m \qquad (4)$$

where τM is total overhead due to training sequence.

2.2 Typical OSDMA technique

As mentioned earlier, there are many techniques in literatures developed for OSDMA. There is one technique that requires the least feedback information and still provides the best performance, so called Angle-of-Departure-Aided OSDMA (AOD-OSDMA) [7]. In this paper, this technique is considered in order to be our benchmark for the proposed systems. The concept of AOD-OSDMA is that it is one of typical OSDMA systems utilizing the knowledge of angles-of-departure (AODs) and angles-of arrival (AOAs) at the BS for the strongest signal received by each user to opportunistic beamforming. Fig.2 shows the block diagram of AOD-OSDMA systems comprising U user equipments and a BS equipped with an N-element. Each UE's terminal is equipped with M antennas. A MIMO block-fading channel $\mathbf{H_u^{MxN}}$ between the BS and each UE (u) is considered. The AOD estimation and the joint Tx-Rx beamforming is done as follows:

AOD estimation is started if each Tx antenna at the BS sends a pilot symbol, then the signal received by the u-th UE is given by

$$\mathbf{y_u^{MxN}} = \mathbf{H_u^{MxN}}\left[s_1 s_2 \cdots s_N\right]^T + n_u^{Mx1} \qquad (5)$$

where $[\ldots]^T$ is the transpose, n_u^{MxN} is the AWGN and si is the pilot signal transmitted from the nth Tx antenna at the BS. The $\mathbf{H}_u^{MxN}$ is the matrix representing of the radio channel between the BS and the uth UE and it can be written as:

$$\mathbf{H_u^{MxN}} = \sum_{l=1}^{L_u} \alpha_{l,u} e^{j\phi_{l,u}} SV_{AOA_{l,u}}^T SV_{AOD_{l,u}} \qquad (6)$$

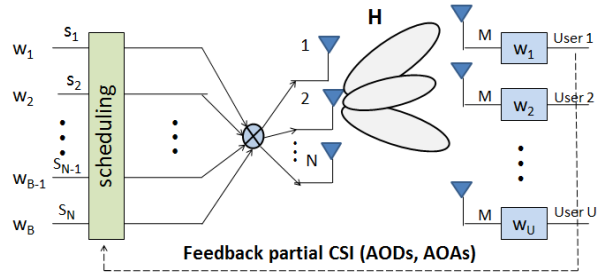

Fig.2. Block diagram of AOD-OSDMA systems [7].

where $SV_{AOD_{l,u}}$ is the BS element-space steering vector in the $AOD_{l,u}$ direction, $SV_{AOA_{l,u}}$ is the element space steering vector at the u^{th} UE station in the $AOA_{l,u}$ direction, φ_n, BS is the angular position of the n^{th} element in the BS array. The Lu is the total number of MPCs associated with the channel between the BS and u^{th} user; and $\alpha_{l,u}$, $\phi_{l,u}$, $AOD_{l,u}$ and $AOA_{l,u}$ are the amplitude, phase, AOD, and AOA of the l-th such MPC. The AOD of strongest beam to the u^{th} user ($AODst$) can be found by a simple beam scan as:

$$AOD_{st,u} = \arg \max_{0 \le AOD \le 2\pi} \sum_{m=1}^{M} \left| \hat{h}_{m,u} SV_{AOD}^{H} \right| \quad (7)$$

where $|..|$ denotes the absolute value, $(..)^{H}$ is the Hermitian transpose, and $\hat{h}_{m,u}$ is the m^{th} row of $\hat{\mathbf{H}}_{\mathbf{u}}^{\mathbf{MxN}}$.

If M >1, each user estimates the AOA of the strongest beam, in addition to its AOD, and performs a joint Tx-Rx beamforming towards the strongest cluster at both BS and user terminals simultaneously. The AOA of the strongest beam received by the u^{th} user can be found as:

$$AOA_{st,u} = \arg \max_{0 \le AOA \le 2\pi} \left| SV_{AOA_{st,u}}^{*} \hat{H}_{u}^{MxN} SV_{AOD_{st,u}}^{H} \right| \quad (8)$$

where $(...)^{*}$ is the complex conjugate, and $SV_{AOD_{st,u}}$ is the BS element-space steering vector of the strongest beam associated with the u^{th} UE. The SNR from the joint Tx-Rx beamforming can be written as:

$$SNR\left(AOD_{st,u}, AOA_{st,u}\right) = \frac{\left| SV_{AOA_{st,u}}^{*} \hat{H}_{u}^{MxN} SV_{AOD_{st,u}}^{H} \right|^{2}}{1/\rho} \quad (9)$$

where ρ is input SNR at each UE's terminal and the achieved sum capacity is calculated by:

$$C = \left(T - \tau\right) \sum_{n=1}^{N} \log_2\left(1 + SINR_n\right) \quad (10)$$

where T is length of every time slot, τ is length of training minislots, n^{th} Tx at BS, 1 is Identity matrix has dimension equal MxM, and SINRn is the total signal-to-interference-plus-noise ratio of the nth selected UE.

3. PROPOSED OSDMA BASED LOCATION UPDATE INFPRMATION

3.1. Location update in LTE system

Location services (LCS) [8] is a technology that determines the geographic location and velocity of UE by measuring radio signal.

Table 1. Mapping between positioning methods and positioning modes.

Positioning Method	UE-based	UE-assisted
E-CID	No	Yes
OTDOA	No	Yes
A-GPS	Yes	Yes

Table 2. Horizontal positioning accuracy ranges of each positioning method (unit : m).

Positioning Method	67%	95%
E-CID	90 to 300	180 to 1000
OTDOA	50 to 100	140 to 280
A-GPS	15 to 60	40 to 200

Table 3. Response time.

Positioning Method	Response Time (Unit: s)
E-CID	0.1 to 0.5
OTDOA	0.5 to 2
A-GPS	5 to 16

The LTE systems support three positioning methods including Enhanced Cell ID (E-CID), Observed Time Difference of Arrival (OTDOA), and Assisted GPS (A-GPS). All three methods have different levels of accuracy and been applied to a different place. The LCS have two positioning modes which are UE-based and UE-assisted as shown in Table I. Both modes utilize different network elements (NEs) to calculate the UE location. If the NE is a UE, the mode is UE-based. If the NE is an E-SMLC, the mode is UE-assisted. The UE-assisted mode is also call network-based mode. As seen in Table I, E-CID and OTDOA positioning methods work only for UE-assisted mode while A-GPS works in both modes.

In the same environment, each positioning method has different levels of positioning accuracy. Generally, A-GPS-based positioning has the highest positioning accuracy, followed by OTDOA-based and then E-CID-based positioning. However, there are exceptions such as A-GPS, which may fail or provide low positioning accuracy in an environment where many obstacles prevent the UE from searching for satellite signals. In such an environment, E-CID may provide relatively high positioning accuracy. Table II lists the horizontal positioning accuracy ranges of each positioning method. The 67% or 95% column lists the statistical horizontal positioning accuracy range that can achieve by higher

than 67% or 95% of all the positioning results of each method. The results in Table III are the response time for calculating location of each method. Although E-CID method uses minimal time following by OTDOA method and then A-GPS method, but A-GPS method provides the highest positioning accuracy.

Fig. 3 shows the principles of E-CID method which can determine UE location from timing advance (T_{ADV}) and angle of arrive (AoA) information. Fig.4 illustrates the principles of OTDOA method, which measures difference in the arrival time between signals transmitted from multiple eNodeBs. The UE tracks multiple eNodeBs by measuring the time that it takes for positioning reference signals (PRSs) to travel from the eNodeBs to the UE, and calculates the OTDOA between the competitor cells and reference cells.

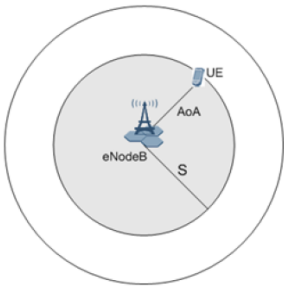

Fig.3. Principles of E-CID-based positioning.

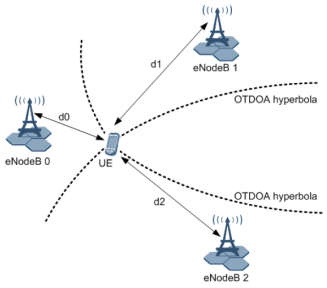

Fig.4. Network architecture for LCS. Principles of OTDOA-based.

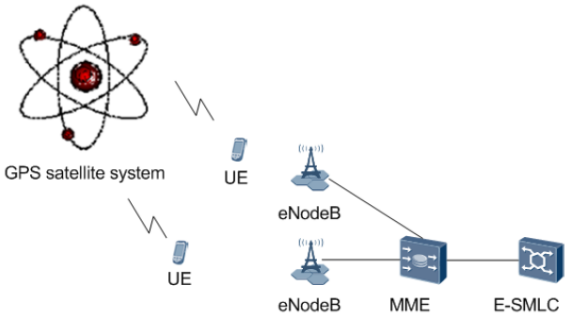

Fig.5. Principles of the A-GPS-based positioning.

The two hyperbola branches formed a difference of distances from the UE to eNodeB 0 and eNodeB 1 is a constant (d1 – d0) and from the UE to eNodeB 1 and eNodeB 2 is a constant (d2 – d1). The UE location is determined as the cross point of the two hyperbola branches.

Fig. 5 presents the principles of A-GPS based positioning which is a network-assisted positioning method. The A-GPS positioning have provided positioning assistance information from satellite navigation systems in the world conducted by the U.S. Department of Defense. Also, it can calculate the precise location of objects around the world. There will be a total of 24 satellites orbiting the earth which is divided into six planes, each of 4angles of 55 degrees. UEs will find GPS satellites and measure the extent to calculate the UE position.

3.2 Proposed OSDMA model

When the location information is organized in the UE's server if requested by a UE into the system, BS calculates all directions to form beams to each UE, without random beam to the received feedback CSI. The direction to form beams is given by

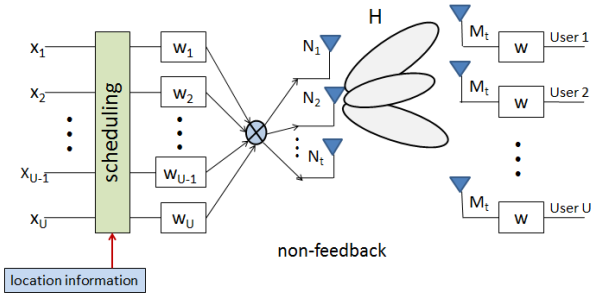

Fig.6. Block diagram of OSDMA(proposed) systems.

$$\theta_u = \tan^{-1}\left(\frac{y_u}{x_u}\right) \tag{11}$$

The proposed OSDMA system model is described in Fig. 6. It consists of 1 BS with the element Nt antennas to u = 1,..,U users for each element Mt antennas. The received signal at user is given by

$$Y = HWX + n_u \qquad \text{for} \quad u = 1,\ldots,U \tag{12}$$

where H is the channel matrix at BS forward each user with dimension MtxNt , W=[w1,w2,..wU] is matrix set weight data transmission to each user, X=[x1,x2,…,xU] is set data forward each user and how to find the set weight is given by

$$w_u = \ell^{-j(Nt-1)kd\sin\theta_u} \tag{13}$$

where k is the wave number and d is distance space between element antenna and nu is Gaussian noise vector at u[th] user, the sum of capacity is given by

$$C = B\log_2\left(\det\left(I + \frac{\rho}{N_t}\left(WH*(WH)^H\right)\right)\right) \tag{17}$$

447

where B is the bandwidth, I is the identity matrix, ρ is power at BS and ^H means Hermitian matrix.

4. SIMULATION RESULTS

This section presents the comparison between the proposed OSDMA system and typical OSDMA [7] technique. MATLAB programming is used for simulation, considering a case in 4x4 multiple-antennas, $d = 2/\lambda$, the noise is neglected and the direction of wave travelling is in Line of Sight (LOS) only.

Fig.7 shows the performance comparison when using OSDMA (proposed), OSDMA [7] and SDMA (full) techniques, where SDMA (full) is an ideal technique that the transmitter has the full knowledge of channel.

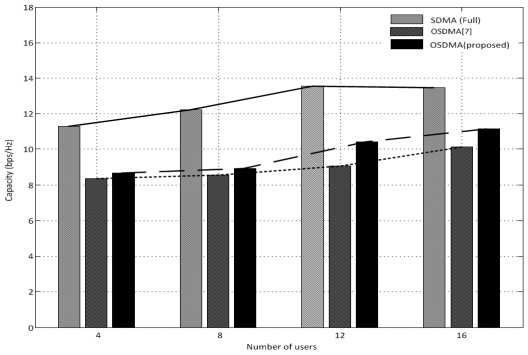

Fig.7. Peformance comparison of SDMA(full) , OSDMA[7] and OSDMA(proposed) schemes, the number of users=4, 8, 12 and 16 with SNR=10dB.

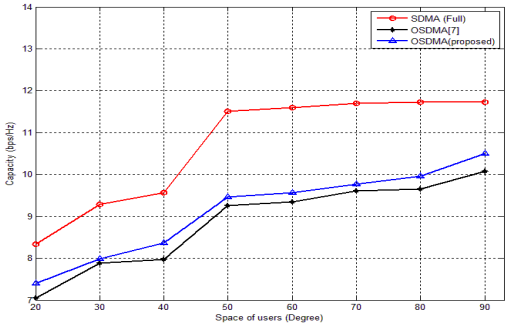

Fig.8. Peformance comparison of SDMA(full) , OSDMA[7] and OSDMA(proposed) schemes, the space of users = 20,30, 40 ,50, 60, 70, 80 and 90 degrees, around BS 360 degree.

We focus on the first 2 techniques and the third technique SDMA (full) is given as reference. The number of users is increased by 4, 8, 12, and 16 respectively. It can be seen that when the number of users increases the sum capacity also increases. The SDMA (full) technique has maximum sum capacity because it is ideal. For OSDMA techniques, the OSDMA (proposed) has higher capacity than OSDMA[7].

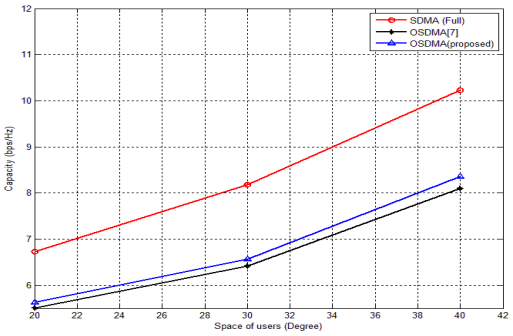

Fig.9. Peformance comparison of SDMA(full) , OSDMA[7] and OSDMA(proposed) schemes, the space of users = 20,30 and 40 degree, around BS 180 degrees.

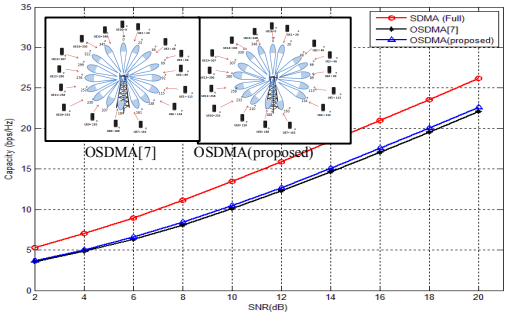

Fig.10. Peformance comparison of SDMA(full) , OSDMA[7] and OSDMA(proposed) schemes, the number of users = 16, for case 1.

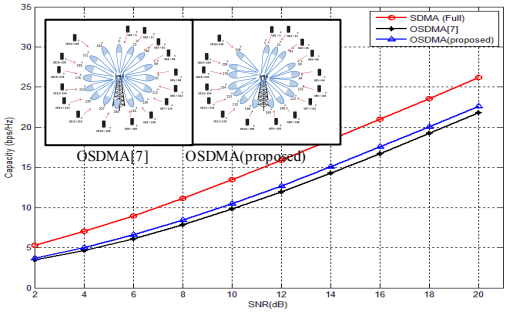

Fig.11. Peformance comparison of SDMA(full) , OSDMA[7] and OSDMA(proposed) schemes, the number of users = 16, for case 2.

Fig. 8 shows the performance comparison when using OSDMA (proposed), OSDMA[7] and SDMA (full) techniques, which compares the space of 4 users locating around BS, 360 degrees. Each user has a space from 20, 30, 40, 50, 60, 70, 80, and 90 degrees. It can be seen that when the number of users increases the sum capacity increases for all techniques. This simulation is repeated by reducing the range of user spread from 360 to 180 degrees as seen in Fig. 9. Similarly, the results shown in Fig. 9 reveal the same conclusion as Fig. 8.

Figs.10 and 11 show the performance comparison when using OSDMA (proposed), OSDMA[7] and SDMA (full) techniques when the number of users is 16. Two random cases are simulated, named as case 1 and case 2. The small images on the top-left illustrate the experimental scenarios, in which the locations of users are taken into account. Each UE requests access to BS and is able to form beam to the direction of each available angle. In contrast, the OSDMA [7] technique has to be selected by a random beam delivered to the user feedback on the maximum SNR beam. It will send data to that beam in which the direction of the beam is not the same for all users. When considering sum capacity, OSDMA (proposed) technique outperforms OSDMA [7] technique.

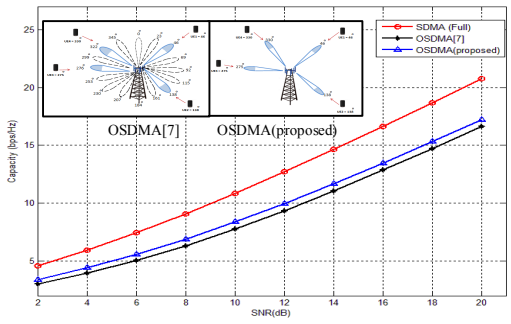

Fig.12. Peformance comparison of SDMA(full) , OSDMA[7] and OSDMA(proposed) schemes, the number of users = 4 for case 1.

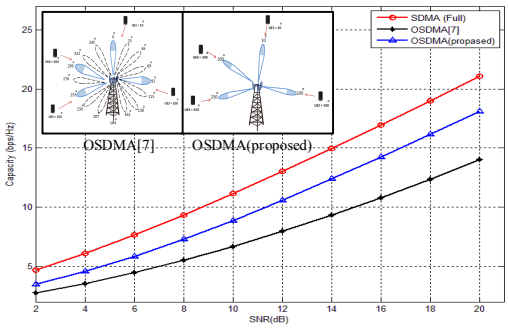

Fig.13. Peformance comparison of SDMA(full) , OSDMA[7] and OSDMA(proposed) schemes, the number of users = 4, for case 2.

Figs.12 and 13 show the performance comparison when using OSDMA (proposed), OSDMA [7] and SDMA (full) techniques with the number of users of 4. Two random cases are simulated, named as case 1 and case 2. In similar to the results shown in Figs. 10 and 11, they confirm the benefit of using the proposed OSDMA systems.

CONCLUSION

This paper has proposed a new technique transmission for mobile communication networks such as LTE systems. The advantage of this technique is to perform OSDMA without the feedback knowledge from all UEs. The proposed concept uses the knowledge of location update information for forming beams to the direction of UE position. This technique can eliminate the feedback information and does not require a random beam to each user for channel estimation. The simulation results show that the proposed technique overcomes the typical OSDMA systems for all scenarios.

REFERENCES

P. Lertareepong, “5G Technology,” unpublished.

S. Patil, V. Patil, and P. Bhat, “A review on 5G technology,” vol. 1, no.e 1, ISSN: 2277-3754, January 2012.

C. Felita and M. Suryanegara, “5G key technologies: identifying innovation opportunity," QiR (Quality in Research), 2013 International Conference on , pp.235-238, 25-28 June 2013.

A. Gohil, H. Modi and S. K. Patel, “5G technology of mobile communication: A survey,” 2013 International Conference on Intelligent Systems and Signal Processing (ISSP), pp.288-292, 1-2 March 2013.

I. Telatar, “Capacity of multi-antenna gaussian channels,” European Trans. Telecommun., vol. 10, pp. 585–595, Nov. 1999.

W. Choi, A. Forenza, J. G. Andrews and R. W. Heath, “Opportunistic space-division multiple access with beam selection," Communications, IEEE Transactions on, vol. 55, no. 12, pp.2371-2380, Dec. 2007.

G. S. Dahman, R. Hafez, R. Bultitude, “Angle-of-departure-aided opportunistic space-division multiple access for MIMO applications,” Wireless Communications, IEEE Transactions on , vol.9, no.4, pp.1303,1307, April 2010.

“LCS feature parameter description,” Copyright © Huawei Technologies Co., Ltd., Issue 01, April 2014.

GPS-Aided V2V Collision Warning Systems

Terut Boonphoka, Peerapong Uthansakul, Monthippa Uthansakul

School of Telecommunication Engineering, Suranaree University of Technology
Muang, Nakhon Ratchasima, Thailand 30000
Email: M5640263@g.sut.ac.th,uthansakul@sut.ac.th and mtp@sut.ac.th

***Abstract*—Safety** Applications are currently on focus for Vehicle-to-Vehicle (V2V) communications. Many researchers have studied this topic in order to reduce the road accidents. In the previous work, the authors have theoretically proposed the technique for vehicle direction detection based on GPS information. It has been demonstrated that the proposed technique can improve the performance of V2V warning systems. However, only simulation results have been presented in the previous work. In this paper, the extended work is carried out in the area of implementation. The experimental study of the proposed method is presented to confirm that the GPS direction detection can enhance the performance of V2V collision warning systems. The results validate the success of proposed technique in practice.

Keywords—Vehicle-to Vehicle Communication; Direction Detection; V2V Communication; ITS

1. INTRODUCTION

An Intelligent Transportation System (ITS) provides the innovative services relating to enable various users to be better informed and to make the drivers safer than the normal transportation systems. A vehicular communication systems are a kind of networks in which the vehicle units and the roadside units can communicate and share the useful information to each other [1], such as automatic road enforcement, variable speed limit, dynamic traffic light sequence and cooperative systems on the road [2]-[4].The ITS technology becomes intelligent by embedding them with microchips as well as sensors and empowering them to communicate with each other through wireless communication technologies. The ITS technology brings a significant improvement in transportation system performance, including to reduce congestion and to increase a safety of drivers. This technology can be classified into two major groups including Vehicle-to-Vehicle (V2V) and Vehicle-to-Infrastructure (V2I) communications. Both groups are functioned by Dedicated Short-Range Communications (DSRC) devices.

Many researchers have studied in the topic of safety applications for V2V communication systems such as, real-time vehicle safety systems, optical vehicle-to-vehicle communication systems using LED transmitter and camera receiver, etc. In fact, in some cases, the accident is still unnecessarily happened. For example, the drivers receive the warning message without any clues where it is occurred. Sometimes the warning message comes from vehicle behind in which the drivers have passed and will not get into the dangerous area. However, the drivers cannot get any information to realize which direction the warning message comes from. Hence, without any choices, the drivers have to drive slowly or immediately break the vehicle. This can cause the unnecessary traffic jam and it increases the chances of accidents. So far in literatures, there has not been any work that concerns this issue. Therefore, the authors have firstly proposed the concept of using GPS information to predict the direction of moving vehicles. This information can help the warning systems to decide whether this vehicle will move into the dangerous area or not. If the direction of vehicles is out of critical scope, then it will be safe for the drivers to drive normally. This work can directly improve the safety on the road. The theoretical work was presented in [15] by the authors. The simulation results show the benefit of using GPS information to detect the direction of moving vehicle for the V2V collision warning systems. However, the work in [6] presented only the simulation results. It cannot claim the success of using the proposed system in practice. Hence, in this paper, the extended work is carried out in the area of implementation. The experimental study of the proposed method is presented to confirm that the GPS direction detection can enhance the performance of V2V collision warning systems. The results validate the success of proposed technique in practice.

The remainder of this paper is presented as follows. Section II presents the problem of the

roadside accident and then the proposed systems are detailed in Section III. In this section, the direction detection and the calculation of remaining time are described. The experimental results and discussion are given in Section IV. Finally, the conclusion of this paper is addressed in Section V.

2. PROBLEM FORMULATION

The illustration of situation when vehicles do not know where the warning message comes from is presented in Fig. 1.The accidental vehicle sends the warning message to all vehicles around it via V2V communication systems, to warn the other vehicles about the accident. As seen in this figure, the vehicle number 1 to 4 got the warning message from the accidental vehicle. If the drivers don't know the position of the accidental vehicle, then the drivers of vehicle number 1 to 4 have to stop or slow down the vehicle. In fact, only the vehicle number 3 and 4 need to be warned because they are moving to the accidental area. In turn, the vehicle number 1 and 2 are moving out of the accidental area so they should drive normally. In order to help the drivers have more accurate decision, the direction of moving vehicle should be concerned. As a result, the authors have proposed the concept that the drivers can make a decision based on the direction of vehicles. If the direction of vehicle is out of accidental scope, then the drivers can ignore the warning message and drive normally.

So far in literatures, the research works regarding safety application are not related to our problem and there is no clue on how the vehicle can realize the direction of moving vehicle. The authors have introduced the use of GPS information to estimate the moving direction which will be detailed in the next section. After that, the performance of proposed system has been investigated by implementing the proposed concept to traditional V2V collision warning systems.

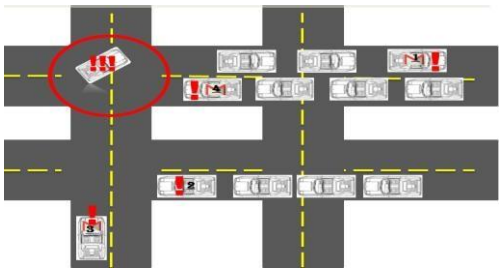

Fig. 1 Illustration of situation when vehicles do not know where the warning message comes from.

3. PROPOSED SYSTEM

3.1 Direction detection

When the accident is happened, the moving vehicle receives the warning messages from accidental vehicle via vehicle-to-vehicle communications for either one or multiple hops as shown in Fig.2. The vehicle is always moving while receiving the warning message. Then, the position when receiving message is not the same position when processing the data. Thus, we have to collect more than one point to use in our method. By using GPS benefits, the vehicle realizes the location of the accidental vehicle as well as itself ($positions\ of\ the\ moving\ vehicle\ is\ P_v = (x_i, y_i)$). This paper utilizes these GPS locations to find the moving direction of the moving vehicle related to the accidental point. ($positions\ of\ the\ accidental\ point\ is\ P_a = (x, y)$)

At first, the GPS position from the moving vehicle is averaged by

$$P_{va} = \left(\frac{\sum x_i}{i}, \frac{\sum y_i}{i}\right) = (x_{va}, y_{va}) \quad (1)$$

Then, the distances between the moving vehicle and accidental point are calculated in (2) and (3).

$$d_f = \sqrt{(x_1 - x)^2 + (y_1 - y)^2} \quad (2)$$

$$d_a = \sqrt{(x_{va} - x)^2 + (y_{va} - y)^2} \quad (3)$$

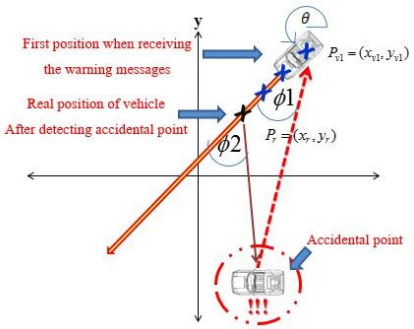

Fig. 2 Model of detection.

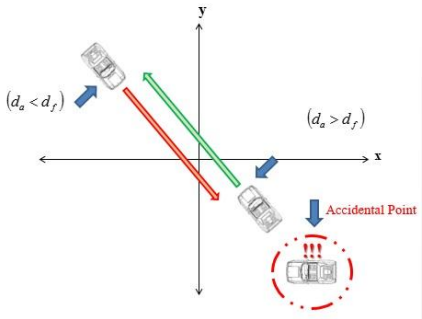

Fig.3 The direction of moving vehicle.

From (2) and (3), d_a is the distance between accidental point and the average positions of the moving vehicle, d_f is the distance between accidental

point and first position receiving warning message. If $d_f < d_a$, the vehicle moves backward to the accidental area. In turn, if $d_f > d_a$, the vehicle moves forward from the accidental area. The calculation of distance can be seen in (2) and (3). Then, the authors show the sample situation of toward and backward direction in Fig.3.

3.2 Estimation of the moving direction

By relocating P_{v1} to the origin point, all positions are related to the accidental point. The new coordinates are as:

$$P_{vn\_ag} = (x_{v1} - x_{v1}, y_{v1} - y_{v1}) = (0,0) \quad (4)$$

$$P_{an\_ag} = (x - x_{v1}, - y_{v1}) \quad (5)$$

After that, the moving direction θ can be obtained by

$$\theta = \left|\tan^{-1}\left(\frac{\Delta y}{\Delta x}\right)\right| = \left|\tan^{-1}\left[\frac{(y_{va} - y_{v1})}{(x_{va} - x_{v1})}\right]\right| \quad (6)$$

Then, check θ and change it to θ_r. The rotation equation of axis is shown in Fig.4.

The rotating axis to move the position of the accidental point to the new coordinates is given in (7) and (8).

$$x' = x_0 \cos\theta + {}_0 \sin\theta \quad (7)$$

$$y' = -x_0 \sin\theta + y_0 \cos\theta \quad (8)$$

Thus, we can find P_{an}in a new coordinate and change its name to be $P_{ar\_ag} = (x_{ar\_ag}, y_{ar\_ag})$ (position of accident after rotating the axis). But the GPS position in degrees coordinate system is achieved. As a result, the change of rectangular coordinate system is necessary as shown in (9) and (10).

$$x_{ar\_ag} = x_{an\_ag} \cos\theta_r + y_{an\_ag} \sin\theta_r \quad (9)$$

$$y_{ar\_ag} = -x_{an\_ag} \sin\theta_r + y_{an\_ag} \cos\theta_r \quad (10)$$

Finally, all positions after relocating the axis are shown in Fig.5.Next the real distance and real angle between the moving vehicle and accidental point can be estimated by taking into account of time, velocity (v)(GPS can generate positions in every 50 millisecond and v= velocity (km/hr.)). The estimated real distance (d_2) and the estimated real angle can be expressed in (11) and (12) and the illustration of dangerous area and real position of moving vehicle is shown in Fig. 5.

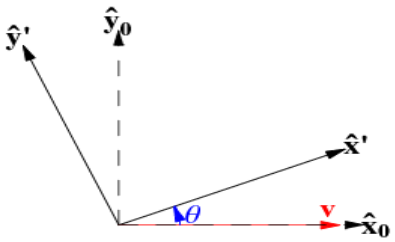

Fig.4 The rotation of axis to find the moving direction.

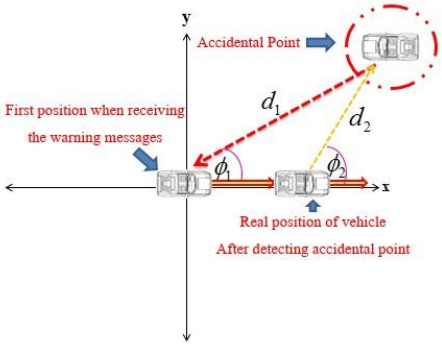

Fig.5 Vehicle positions after relocating the axis.

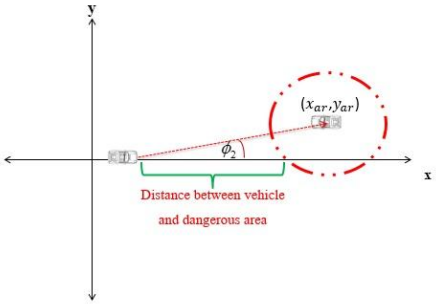

Fig.6 Illustration of dangerous area and real position of moving vehicle.

$$d_2 = \sqrt{\left(x_{ar} - \left(\frac{5v}{18}\right)\right)^2 + (y_{ar})^2} \quad (11)$$

$$\emptyset_2 = \left|\tan^{-1}\left(\frac{y_{ar}}{x_{ar} - \left(\frac{5v}{18}\right)}\right)\right| \quad (12)$$

Equations (13) and (14) is the estimation of distance and angle in the directions of moving vehicle with the accidental point at the first time receiving warning message. In this paper, it is assumed that GPS can generate the locations in every 50milliseconds and the processing time is about 50 milliseconds. If one uses a higher band frequency and a larger number of positions, then the error of different distance and angle between estimated and real value will be decreased [6].

3.3 Calculation of remaining time

Using the proposed method, the remaining time (t_r) can be estimated from the moving direction of the vehicle related to the incident area. Then, we can calculate t_r from the locations of them in (13) – (20)

From circle equation at dangerous area

$$(x - x_{ar})^2 + (y - y_{ar})^2 = r_d^2 \quad (13)$$

And direction of the moving vehicle is

$$y = mx + c \quad (14)$$

From the Fig. 7, the direction of the vehicle is moving on x-axis; $m = 0$ and $c = 0$. Using $y = 0$ in (15) yields

$$(x - x_{ar})^2 + y_{ar}^2 = r_d^2 \quad (15)$$

$$x^2 - 2x_{ar}x + x_{ar}^2 + y_{ar}^2 = r_d^2 \quad (16)$$

$$x^2 - 2x_{ar}x + [x_{ar}^2 + y_{ar}^2 - r_d^2] = 0 \quad (17)$$

$$\text{Hence } x = \frac{2x_{ar} \pm \sqrt{2x_{ar}^2 - 4(1)(x_{ar}^2 + y_{ar}^2 - r_d^2)}}{2(1)} \quad (18)$$

If $x_1 > x_2$

$x_c = x_2$

Else $x_1 \leq x_2$

$x_c = x_1$

$$d_3 = x_c - \frac{5v}{18} \quad (19)$$

$$t_r = \frac{d_3}{v} \quad (20)$$

4. EXPERIMENTAL RESULTS AND DISCUSSION

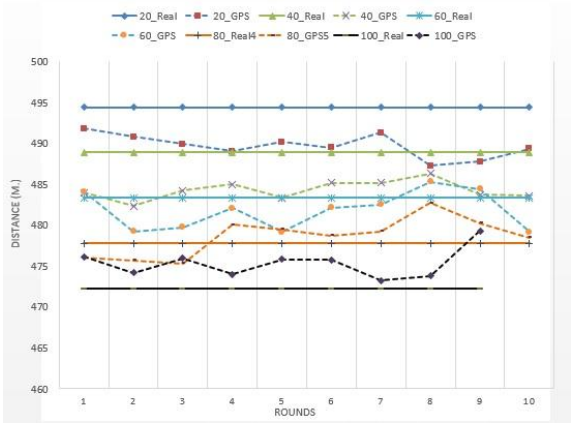

Fig.7 Estimated distance from GPS information for various speeds

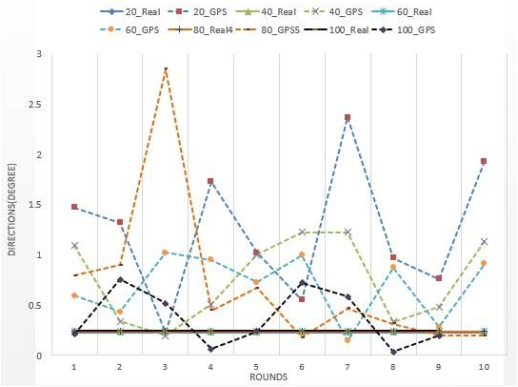

Fig.8 Estimated direction from GPS information for various speeds.

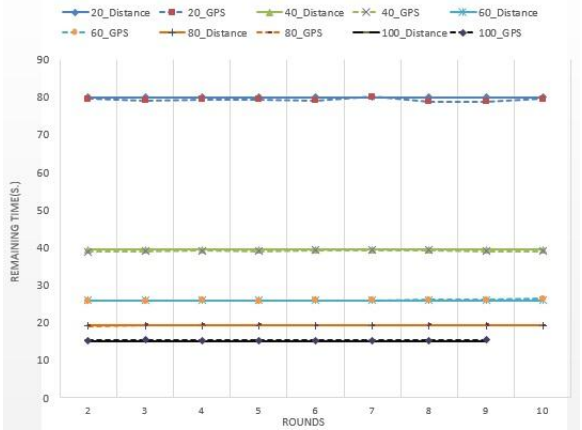

Fig.9 Remaining time to the dangerous area for various speeds.

In dynamic scenario, it is assumed that one vehicle is the accidental vehicle and sends the warning message to the moving vehicle in 500 m which is moving with different speeds as illustrated in Fig. 8. The 10 packets of warning message are transmitted and the measurement is repeated for 10 rounds per speed. The radius of dangerous area is 50 m which is used to calculate the remaining time. The results of dynamic scenario in terms of estimated distance, estimated direction and remaining time are presented in Figs. 8, 9 and 10, respectively.

The results show that the estimated distance has error within 5 the estimated direction has error within 3 degrees and the remaining time to dangerous area has error within 0.5 second. These results show the success of using the proposed method in practice.

5. CONCLUSION

This paper has proposed the method to estimate the moving direction of the vehicle related to the accidental point. The aim is to increase the safety for drivers to make the right decision after receiving the warning message. The main contribution of this paper is on the verification of the proposed concept by implementing the GPS aided direction detection on V2V communication. The experimental results show that the proposed method has a very low error on estimating the directions. This implies the success of using the proposed method in practice.

REFERENCES

[1] http://en.wikipedia.org/wiki/Vehicular_communication_systems

[2] http://www.ertico.com/cooperative-intelligent-transportsystems-on-the-road-to-deployment

[3] K. Sung, J. J. Yoo and D. Kim, “Collision warning system on a curved road using wireless sensor networks,” IEEE 66thVehicular Technology Conference, pp.1942-1946, Sept. 30 -Oct. 3 2007.

[4] R. Azimi, G. Bhatia, R. Rajkumar, and P. Mudalige, “Vehicular networks for collision avoidance at intersections," SAE Int. J. Passeng. Cars – Mech. Syst. 4(1):406-416, 2011.

[5] http://www.kapsch.net.

[6] Y. Shimonaka, S. Tasaka, Y. Hatta, T. Wada andH. Okada, “Accuracy improvement of vehicular collision avoidance support system (VCASS) for the next generation ITS," IEEE Wireless Communications and Networking Conference, pp.2517-2522, 11-15 March 2007.

IMPEDANCE ANALYSIS ON MINIATURIZED RECEIVER IN MAGNETIC RESONANCE COUPLING WIRELESS POWER TRANSFER SYSTEM

Fatin Najihah Ab Aziz, Masahiro Sasaki
Division of Electrical Engineering and Computer Science,
Graduate School of Engineering and Science,
Shibaura Institute of Technology

ABSTRACT

Recently, wireless power transfer has become the focus of discussions, particularly the one that uses magnetic resonance coupling method. In this method, the need to maintain the resonant condition emerges because the transmitter and the receiver circuits have to be tuned to the same frequency. Here, we use an impedance matching circuit called Automatic Tuning Assist Circuit (ATAC) that can adjust the frequency of the transmitter to maintain the resonant condition automatically.

In order to achieve maximum power transfer efficiency, we focus on how to optimize the receiver's design specifications. However, due to the variation of the load impedance, a few problems such as frequency splitting and shifting have occurred.

Therefore, in this paper, we did some impedance analysis on the effect for the resonance frequency. The results have provided us with a fundamental requirement for our future design.

1. INTRODUCTION

Researches and developments about the wireless power transfer technology continue to heat up and its related applications continue to broaden more (Tan, 2007).

The idea of transferring power through the air has been around for over a century. With Nikola Tesla's pioneering ideas and experiments are the most well-known early attempts (A. Kurs, 2007).

This idea was later pursued by a team from Massachusetts Institute of Technology (MIT) in 2007 where they have successfully demonstrated the system. Since then, it has been receiving a lot of attentions due to its practical range and efficiency. In the near future, this wireless power transfer is expected to be feasible all around the world.

In this paper, we did some early analysis for designing the receiver. We also analyze the impedance characteristic through circuit simulator. This is because impedance plays a key role in obtaining the maximum power transfer. The results were studied and a few conclusions are drawn.

2. THEORY

2.1. Magnetic Resonance Coupling

Magnetic resonance coupling wireless power transfer is defined as the energy transfer between two magnetically coupled coils that are tuned to resonate at the same resonance frequency. These resonant objects of the same resonance frequency tend to exchange energy at maximum.

Figure 1 and 2 show the magnetic resonance coupling circuit and the equivalent circuit respectively.

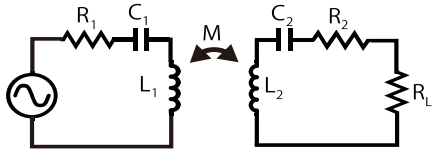

Fig. 1 Magnetic resonance coupling circuit.

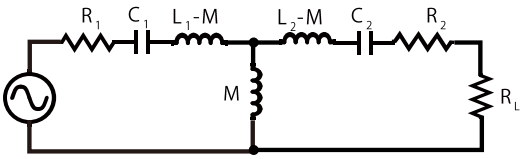

Fig. 2 Magnetic resonance coupling equivalent circuit.

2.2. Wireless Power Transfer System

Figure 3 shows the wireless power transfer system which consists of resonating two components (transmitter and receiver) at the same frequency. The power is transmitted through the magnetic field from the transmitter to the receiver at the resonance frequency.

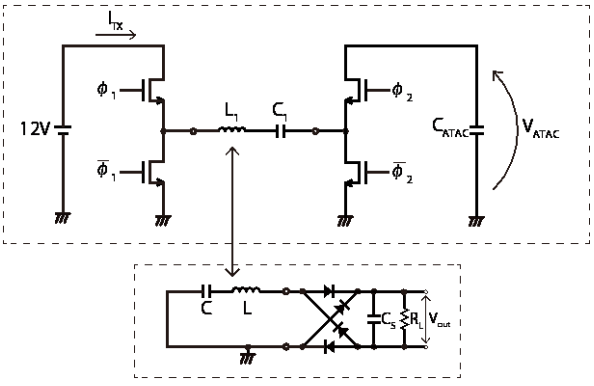

Fig. 3 Wireless power transfer system circuits.

2.3. Transmitter

Transmitter circuit is shown in Fig. 4 where it is divided into three parts; Inverter, Resonance circuit, ATAC.

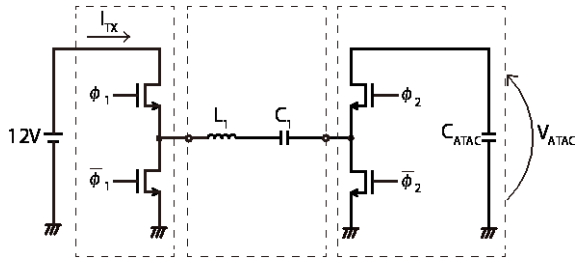

Fig. 4 Transmitter circuit.

2.3.1. Inverter

We use a class-D amplifier which is also known as the switching amplifier. To avoid through current from power supply to reach the ground, ϕ_1 and $\overline{\phi_1}$ are controlled so as not to be overlapped.

2.3.2. LC Resonance Circuit

LC resonance circuit uses a capacitor and an inductor. The inductor is represented by the solenoid coil as shown in Fig. 5.

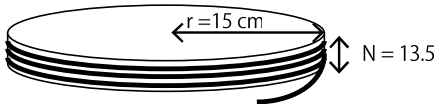

Fig. 5 Transmitter coil.

2.3.3. Automatic Tuning Assist Circuit (ATAC)

In power transmission using a resonance circuit with a Quality factor (Q) of 500, resonance frequencies of transmitter and receiver need to be adjusted within 0.1% difference (Y. Endo, 2012). There is a need to appropriately adjust the transmitter-side and receiver-side resonance frequencies. A variable capacitance diode cannot be used in this high-power application (Y. Endo, 2012). Here, we implement a new technology from Advantest Corporation that has been patented as Automatic Tuning Assist Circuit (ATAC). Figure 6 shows it's circuit.

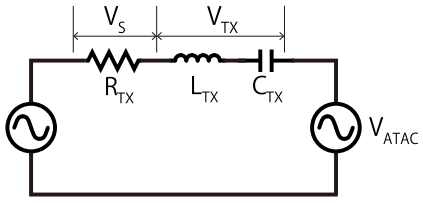

Fig. 6 Automatic Tuning Assist Circuit (ATAC)

The impedance of the transmitter side can be calculated through,

$$Z_{TX} = R_{TX} + jX_{TX} = R_{TX} + j\omega L_{TX} - \frac{1}{j\omega C_{TX}} \quad (1)$$

When the system is in resonant state, the phase of both voltage $\dot{V_S}$ and the transmitting current $\dot{I_{TX}}$ are the same thus reactance X_{TX} becomes zero. In this state, the optimum power transfer is achieved as the only impedance of this circuit becomes R_{TX} by making $\dot{E} = \dot{V_S}$.

Figure 7 (a) shows the circuit's voltage when it is not in resonant state. In contrast, Fig. 7 (b) shows the circuit's voltage when ATAC is inserted where the circuit achieved its maximum power transfer. We can see that there is an addition of auxiliary voltage $\dot{V_A}$ as shown in Eq. (2).

$$\dot{E} = \dot{V_S} + \dot{V_{TX}} + \dot{V_A} \quad (2)$$
$$= \dot{V_S} + \dot{V_{TX}} - \dot{V_{TX}} \quad (3)$$
$$= \dot{V_S} \ (\therefore \dot{V_A} = -\dot{V_{TX}}) \quad (4)$$

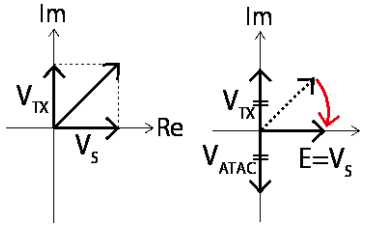

(a) Without ATAC (b) With ATAC

Fig. 7 Circuit's voltage characteristic.

2.4. Receiver

Figure 8 shows the detailed receiver circuit.

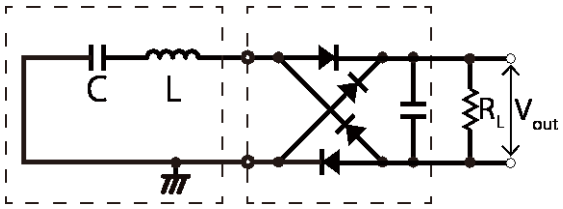

Fig. 8 Receiver

LC resonance circuit in this receiver uses one capacitor and an inductor to form a resonance circuit that has to be tuned to resonate at 500 kHz.

Since the received power from the inductor would have an alternating current (AC), a full-wave bridge rectifier is needed to rectify the AC voltage to output a clean stable direct current (DC) voltage. In addition, the smoothing capacitor is added to smooth the output of the rectified signal.

3. IMPEDANCE ANALYSIS ON THE RECEIVER

The use of small components increases the variation of the load impedance and eventually disturbing the resonance frequency.

Here, early impedance analysis on how the circuit components affect the load impedance, is essential. This basic analysis is also very important in order to understand the fundamental receiver performance. This is because, a slight change in the receiver's load impedance will change the resonance frequency and eventually, affect the power

transfer efficiency.

Therefore, in this paper, we did some impedance analysis on the effect for the resonance frequency due to the change in the load impedance.

4. RESULTS

4.1. Characteristics of Impedance Variance

4.1.1 Coupling coefficient

Figure 9 shows that as the coupling coefficient increases, the impedance peak increases. This is until to a certain value, where frequency splitting phenomenon occurs.

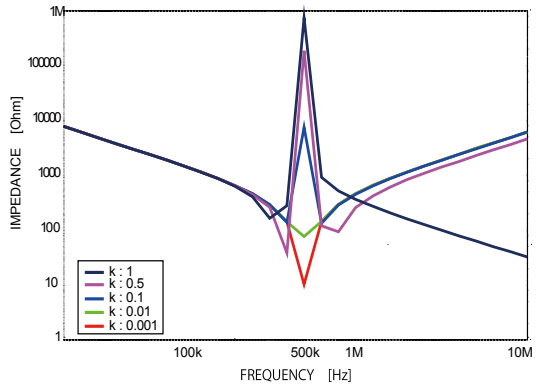

Fig. 9 Impedance characteristic by the coupling coefficient.

4.1.2 Choke inductor

Figure 10 and 11 show the receiver circuit with the insertion of choke inductor and the impedance characteristic respectively. Fig. 11 shows that choke inductor values do not affect the resonance frequency.

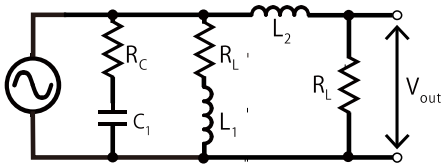

Fig. 10 Receiver circuit with a choke inductor

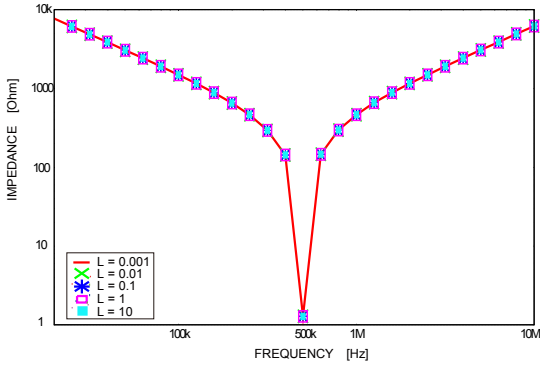

Fig. 11 Impedance characteristic by the choke inductor.

4.1.3 LC filter

Figure 12 shows the receiver circuit with the addition of an LC filter.

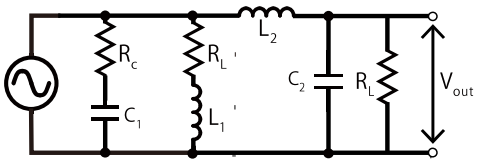

Fig. 12 Receiver circuit with an LC filter

Figure 13 and 14 show that the impedance characteristic varies due to the combination values of LC filter and also the maximum power received respectively.

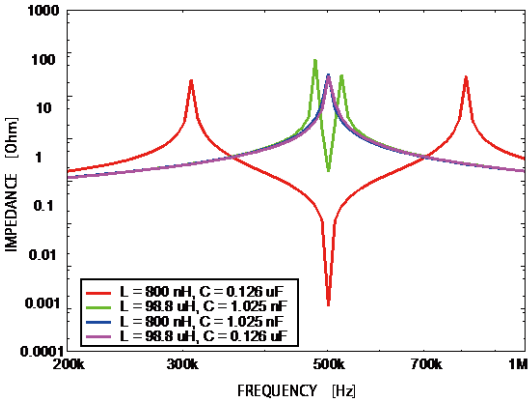

Fig. 13 Impedance characteristic by the LC filter.

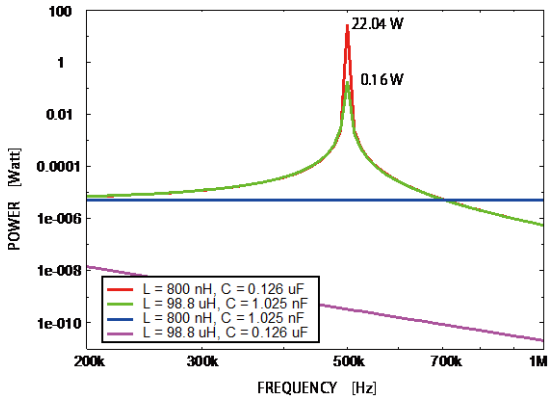

Fig. 14 Power received by the LC filter.

5 CONCLUSION

The overall results have provided us with a guideline, or in another words, a fundamental requirement for our future design.

Based on the results, a few conclusions are drawn. Firstly, the relationship between the coupling coefficient and the impedance. When the coils are closely coupled($k > 0.5$), frequency will be split and this leads to the decrease of power transfer efficiency.

The results also prove that the impedance characteristic does not change with the addition of a choke inductor. This however, changes when a capacitor is inserted forming an LC filter at the end of the receiver circuit. The frequency

will split at some points, but it is observed that the circuit achieves its maximum power when the LC filter values are the same as the LC resonance circuit.

ON the future work, we will design the system's receiver with optimum performance utilizing the analysis data that we've obtained in this paper. Finally, we do hope that we can successfully demonstrate this wireless power transfer system with the optimum performance in water.

REFERENCES

Tan, L., X.Huang, W. Wang, et al., "Application of Magnetic Coupled Resonance Wireless Power Transfer Technology in Electric Vehicle", Lecture notes in Information Technology, Vol. 9, 70-75, 2011.

A. Kurs, A. Karalis, R. Moffatt, P. Fisher, & M. Soljacic, "Wireless Power Transfer Via Strongly Coupled Magnetic Resonances", Science Express, (n.d.), 2007.

Y. Endo, Y. Furukawa, "Proposal for a New Resonance Adjustment Method in Magnetically Coupled Resonance Type Wireless Power Transmission", IMWS-IWPT2012 Proceedings, 2012.

Fatin Najihah received her bachelor degree in Electronics Engineering (2012) from Shibaura Institute of Technology.
She is currently in graduate school of Masters 1st year, in Electronics Engineering at Shibaura Institute of Technology.

Masahiro Sasaki received B.Eng., M.Eng. and Dr.Eng. degrees in Electrical Engineering from Waseda University in 1994, 1996 and 2003, respectively. He joined NISSAN motor Corp. Tokyo, Japan in 1996, where he was engaged in the research and development related to electronic control units and electrical vehicle. He belonged to VLSI Design and Education Center (VDEC), the University of Tokyo as an assistant professor. Since 2011, he has been an associate professor with Dept. of Electronic Engineering, College of Engineering at Shibaura Institute of Technology.
His research interests include high-speed high-resolution analog circuits, nonlinearity analysis and improvement in analog circuits, digital integrated circuits design and signal processing algorithms. He is a Member of IEEE Solid-State Circuits Society as well as a member of Institute of Electronics, Information, and Communication Engineers (IEICE) Electronics Society.

PERFORMANCE OF FIXED WEIGHT COORDINATED BEAMFORMING FOR HETNET SCENARIO

Wista Songserm, Peerapong Uthansakul and Monthippa Uthansakul
School of Telecommunication Engineering
Suranaree University of Technology, SUT
Nakhon Ratchasima, Thailand
Email: M5640287@g.sut.ac.th, uthansakul@sut.ac.th, mtp@sut.ac.th

ABSTRACT—The age of traffic overload has been recently arisen so that the help of sharing traffic between the different networks become more necessary and important. This sharing between different networks is introduced by the concept of Heterogeneous Network (HetNet). In this scheme, there are a lot of picocells operating within a coverage area of one microcell. The dense base stations cause the problem of stronger Inter-Cell Interfeences (ICI). The coordinated beamforming has been introduced to solve this ICI problem. By knowing the complete channels of all users, all base stations can calculate the weights to beam the desired signals to each user with the minimum ICI from other users. However, this technique required a lot of overhead on sharing the knowledge of user channels among all base stations. Also in some cases the calculated weights cannot be implemented in practice due to the limits of RF hardware. In this paper, the concept of fixed weight has been proposed for coordinated beamforming which can guarantee that all weights can be implemented and the overhead information can be enormously reduced. Also in this paper, the optimal number of fixed weights and the optimal angle space between beams have been investigated.

1. INTRODUCTION

In the past, the concept of picocell was only to fulfill some small areas of macrocell that the signal strength is too weak. The benefit of picocell is that it consumes a low energy and the installation is very easy. Hence, the mobile operators always use the picocell just for a backup plan of overall mobile networks. With the growth of internet demands, all mobile users require a lot of more data rate transmission. Morever, the population of mobile users increases rapidly. Therefore, the new topology of old fashioned network has to be introduced. The new concept is to support a huge demand of data traffic throughout the coverage area. The merging operation between macrocells and picocells has been developed [1], [2].

Recently, the inter cooperation between different networks has been introduced as Heterogeneous Networks (HetNet). The transition between two networks is the main core of HetNet as well as the changeable configuration for both physical and logical process is a necessary part. To simplify the use of frequency resources for HetNet, there has been a proposal to use the same frequency for all picocells and microcells. This is to reduce the cost of RF hardware to reconfigure the device according to serving cells. However, the expense of this concept is the problem of strong Inter-Cell Interfeences (ICI). All base stations of picocells and microcells are the interferers to all users in HetNet. Hence, the development of efficient technique to eliminate ICI is significantly required.

The beamforming technique becomes the promising technique to handle with ICI problem as evidences in many publications. The original idea is to form beams to each user and to form nulls to the directions of interference signals. To do such an idea, all base stations need to know full knowledge of user locations not only in serving cells but also in the other cells. The full coordination of user locations help each base station to find the suitable weight that will make all users in either picocells and macrocells obtain the best signal quality at once. This technique is so called as Inter-Cell Interference Coordiation (ICIC) [3] or coordinated beamforming [4]. Another benefit of coordinated beamforming is that the user in picocells is always served by a good quality of service even the transmitted power of macrocell base station is 10 times of transmitted power of picocell base station.

The success of coordinated beamforming depends on the finding of weights to form beams to each user. There are many techniques proposed in literatures to apply for coordinated beamforming [5]-[7]. Most of them require the full knowledge of user channels to spread among base stations in order to calculate the suitable weights. If the user channels are correctly obtained, the ICI problem can be eliminate successfully. However, the deficiency of this approach is that there are so many errors from many acquiring processes including channel estimation, information feedback and multi-hop spreading. Moreover, the calculated weights sometimes cannot be implemented because its values are beyond the limit of RF hardware. These errors make the coordinated beamforming system inefficient as expected in practice. To overcome this

problem, the concept of fixed beams for coordinated beamforming has been proposed. The multiple weights have been fixed on each base station. The suitable weight for each user is selected by finding the best weight among all that can offer the best performance after changing weights one by one. This method can reduce a lot of overhead in comparing with the full knowledge of channels and also it can guarantee the possible implementation of RF hardware in practice. It is the fact that the more number of fixed weights can increase the system performance but the more processing time and higher hardware cost are also happened.

In this paper, the optimal number of fixed weights has been studied. The authors point out the sufficient number of beams which is suitable for HetNet downlink scheme. Moreover, the optimal angle spread between beams has also examined. This can help the researchers when fully implement this concept in practice. The remainder of this paper is organized as follows. The system model is described in Section II. Section III, the concept of beamforming and coordinated beamforming is presented and then the simulation results and discussion are given in Section IV. Finally, the conclusion of this paper is presented in Section V.

2. SYSTEM MODEL

The system model is illustrated in Fig. 1 which is used as the graphical information for simulating the results. As seen in this figure, four picocell base stations are located inside the coverage area of macrocell. This paper focuses on a downlink transmission of HetNet. Then, the interference of picocell users (PUE) is different from macrocell users (MUE). Note that the symbol *M* is the short term of macrocell and the symbol *p* is the short term of picocell which is in the set of *B*. The number of antennas at base station of macrocell and picocell are N_p and N_M, respectively. Each user uses the single antenna. This paper focuses on the downlink scenario by using the frequcney reuse. It means that all base stations become the interferers to each other. The received signal of MUE can be expressed as

$$Y_{K_M} = \sqrt{P_M}\,\mathbf{H}^{M}_{K_M}\mathbf{w}_{K_M}x_{K_M} + \sum_{p\in B}\sqrt{P_p}\,\mathbf{H}^{p}_{K_M}\mathbf{w}_{K_p}x_{K_p} + n_{K_M} \qquad (1)$$

where $\mathbf{H}^{s}_{K_M}$, $s \in \{M\} \cup B$ represents the vector of channel from transmission node s to K_M which consists of two components as $\mathbf{H}^{s}_{K_M} = L^{s}_{K_M}\,\bar{h}^{s}_{K_M}$. Note that $L^{s}_{K_M} = \left(d^{s}_{K_M}\right)^{-\alpha}$, where $d^{s}_{K_M}$ is the distance between user and macrocell base station and $\propto$ is a path loss exponent. The member entry of $\bar{h}^{s}_{K_M}$ is an independent and identically distributed (i.i.d.) complex Gaussian distribution. w_{K_M} is the beamforming vector and n_{K_M} is the additive complex white Gaussian noise. Considering that BSs are generally organized by the operator, we assume the distances from the MBS and PBSs to KM are exactly known. i.e. the value of $d^{s}_{K_M}$ is deterministic. The transmission signal to noise ratio (SNR) can be represented as $\boldsymbol{\rho}_M = P_M / \sigma_n^2$, $\boldsymbol{\rho}_p = Pp / \sigma_n^2$, where σ_n^2 is the noise power. Similarly, the received signal of PUE K_p can be given by

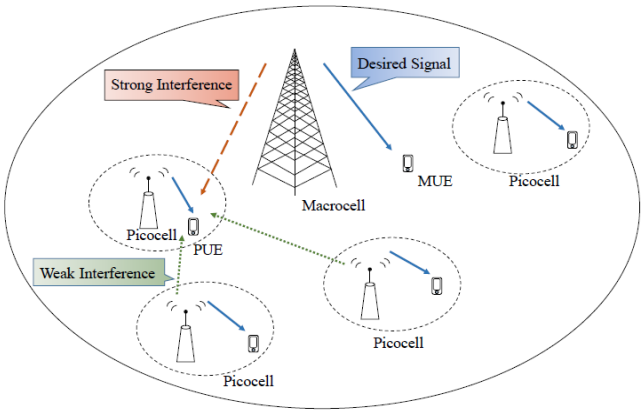

Fig.1. Macrocell base station and picocell base stations for downlink transmission of HetNet.

$$Y_{K_p} = \sqrt{P_p}\,\mathbf{H}^{p}_{K_p}\mathbf{w}_{K_p}x_{K_p} + \sqrt{P_M}\,\mathbf{H}^{M}_{K_p}\mathbf{w}_{K_M}x_{K_M} + \sum_{\substack{p'\in B\\ p'\neq p}}\sqrt{P_p}\,\mathbf{H}^{p'}_{K_{p'}}\mathbf{w}_{K_{p'}}x_{K_{p'}} + n_{K_{p'}} \qquad (2)$$

For picocell, PUE receives the inference signals from both macrocell and other picocell base stations. Hence, the Signal to Interference plus Noise Ratio (SINR) of K_p is given by

$$SINR_{K_p} = \frac{\lambda^{p}_{K_p}\left|\bar{h}^{p}_{K_p}w_{K_p}\right|^2}{\lambda^{M}_{K_p}\left|\bar{h}^{M}_{K_p}w_{K_M}\right|^2 + \sum_{\substack{p'\in B\\ p'\neq p}}\lambda^{p'}_{K_p}\left|\bar{h}^{p'}_{K_p}w_{K_{p'}}\right|^2 + 1} \qquad (3)$$

where $\lambda^{M}_{K_p} = \rho_M\ L^{M}_{K_p}$.

For macrocell, MUE receives the inference signals from all picocell base stations. Hence, SINR of K_M is expressed as

$$SINR_{K_M} = \frac{\lambda^{M}_{K_M}\left|\bar{h}^{M}_{K_M}w_{K_M}\right|^2}{\sum_{p'\in B}\lambda^{p}_{K_M}\left|\bar{h}^{p}_{K_M}w_{K_p}\right|^2 + 1} \qquad (4)$$

From (2) and (3), if we desire to obtain the best SINR, not only weighting of macrocell is considered but all weightings of macrocell and picocell need to be concerned. It is possible that each weighting must be orthogonal to all channel vectors except its own base station. Regarding this, the coordinated action of all users and base stations is required

3. COORDINATED BEAMFORMING

3.1 Zero-Forcing (ZF), without Coordinated Beamforming

One simple and popular method to find the optimal weight is Zero-Forcing (ZF) technique. This method requires the user channel to be available at base station according to the feedback of users. This is not a coordinated beamforming yet because it aims to maximize only SINR within each cell. The weighting matrix can be presented by

$$\mathbf{W} = \mathbf{H}^{-1} \tag{5}$$

where H represents the channel matrix which is a $\mathbf{H}_{\kappa_M}^{M}$.

3.2 Coordinated beamforming with Zero-Forcing

As mentioned earlier, the solution of coordinated beamforming is to find weightings that are orthogonal to the channel vectors. This method requires all information of user channels to be available at base stations according to the feedback of all users. There is a large overhead on transmission among macrocell and microcell base stations. The downlink access bias is generally adopted in HetNet to balance the uplink and downlink coverage. Hence, severe downlink co-channel interference from MBS is suffered by PUEs, especially those located at the edge of the picocell. To suppress this co-channel interference, we appliy the coordinated beamforming technique at the MBS, and Zero-Forcing beamforming is utilized in this paper. Assuming that the interference channel to PUEs could be obtained by MBS according to the feedback of PUEs or reciprocity, the coordinated Zero-Forcing matrix can be presented by

$$\mathbf{W} = \mathbf{H}^{\mathrm{H}}\left(\mathbf{H} * \mathbf{H}^{\mathrm{H}}\right)^{-1} \tag{6}$$

where **H** means the combination matrix containing $\mathbf{H}_{\kappa_M}^{M}$ at the first row and interference channel vector to PUEs. The beamforming w_{κ_M} is derived by normalizing the first column of **W,** which is in the null space of interference channel vector to coordinated PUEs.

3.3 Fixed Weight, without Coordinated Beamforming

The solution from ZF method cannot guarantee whether it can be real implemented under the limitation of hardware or not. Also, the effect of channel estimation error and a lot of channel feedback information degrade the overall system performances. As a result, the fixed weight method is proposed. This technique determines the specific weightings which can be implemented in practice. Then the base station transmit all beams at once to all users and each user estimate the quality of each beam and then report to base station that which beam is the best for transmission. Then, the base station will select the suitable beams for each user. The feedback process is still used but only small information on beam selection is required. The weighting of fixed weight can be found by

$$\mathbf{W} = \operatorname{argmax}\left|\mathbf{H} * \mathbf{w}\right|^2 \tag{7}$$

where **W** chooses a beamforming code word to maximize the channel gain. Where **H** means the combination matrix containing $\mathbf{H}_{\kappa_M}^{M}$.

3.4 Coordinated Beamforming with Fixed Weight

By extending the concept of fixed weight, the coordinated beamforming with fixed weight can be implemented. This method considers all base station at the same time. Hence, all beams from all base stations are transmitted at the same time. It is the user duty to measure and evaluate that which beam provide them the best SINR. This technique solve the co-channel interference for all users at the same time. Then, the weightings of coordinated fixed weight method can be given by

$$\mathbf{W} = \operatorname{argmax} \mid SINR_{Ki} \mid^2 \tag{8}$$

4. SIMULATION RESULTS

From the previous section, it can be expected that the performance of coordinated beamforming might be better than without coordinated beamforming. However, the more number of beams is fixed, the more processing time and delay are obtained. So far in literatures, there is no investigation into the optimal beams for coordinated beamforming. This paper initially investigates the finding of optimal beams in order to make all resources efficient.

Here we assume a HetNet scenario of a macrocell overlaid by |B| = 4 co-channel picocells which are randomly deployed. The macrocell radius is normalized to one for simplicity, and the radius of each picocell is considered to be 0.2. The path loss exponent is considered to be $\propto$ = 3.5. 200 drops are performed and the picocells are deployed randomly in each drop so that picocells observe different levels of co-channel interference. Round robin (RR) scheduling is applied to both macrocell and picocells to gurantee the fairness, and single user MISO transmission is applied for both macrocell and picocells. The transmission power gap between MBS and PBS is set as ρ_M / ρ_p = 20dB, and noise power is normalized to one so that the transmission power can be expressed as SNR.

4.1 Total Throughput Performance

Fig.2 shows the total throughput of macrocell and picocells for N = 4. The total throughput is the summation of throughputs from all macrocell and picocells. The results indicate the success of using coordinated beamforming because

it outperforms the other. As seen in this figure, ZF with coordinated beamforming is slightly better than coordinated fixed weight but it needs more feedback information as well as more accuracy on channel estimation. This cost sometimes is not worth for real implementation.

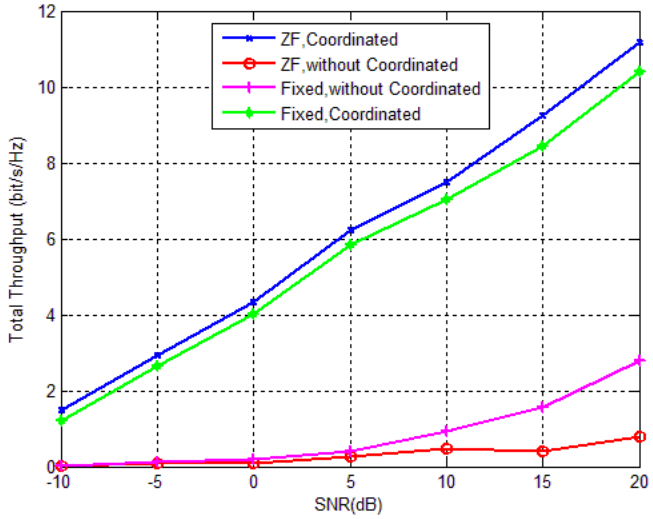

Fig.2. Total throughput of macrocell and picocells, N = 4.

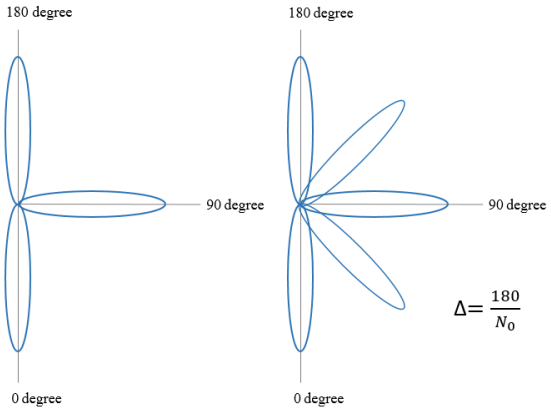

Fig.3. Illustration of beam separation over 180 degree sector.

4.2 Optimal Beams

This section aims to find the optimal beams for fixed weight coordinated beamforming. The number of beams which is optimal cannot be obtained by using closed form solution. As seen in Fig 3, the illustration of beam separation over 180 degree sector is presented. The equal beam spacing and equal spread covering 180 degree sector are assumed. When the number of beams increases, the beam separation is smaller. Hence, this paper investigates the performance of throughput by varying the number of beams as shown in Fig. 4.

The results in Fig. 4 shows that only fixed weight methods have the throughput varied by the number of beams. This is because the ZF methods do not use the number of beams when computing the weight scheme. Also in this figure, it is interesting that the throughput of fixed weight without coordinated beamforming decrease as a function of the number of beams. This is because the more number of beams increase the more chance of having interference signals. However, the coordinated beamforming can utilize the more choices of number of beams to get rid of the interference signals. In order to find the optimal number of beams, the results reveal that the throughput is changed slowly after 7 beams. It is noted that the more number of beams require more delays.

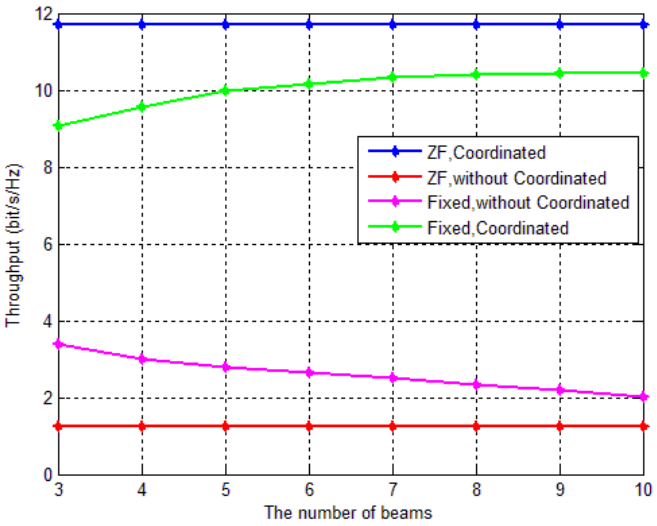

Fig.4. Average throughput of macrocell and picocells, SNR=20 dB, N = 4.

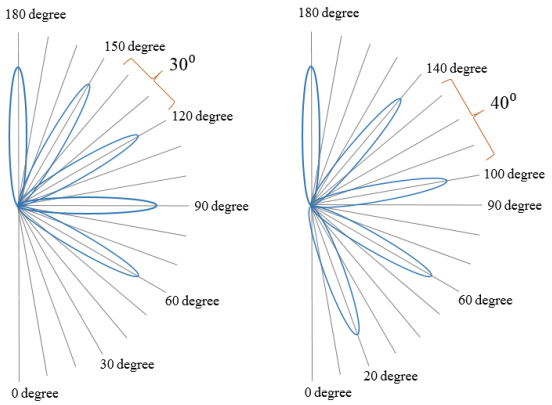

Fig.5. Illustration of angle separation over 180 degree sector.

4.3 Optimal Angle Spread

In the previous results, the optimal number of beams is already suggested. Next, the investigation of angle separation between beams is on focus. The purpose is to find the suitable weighting according to the optimal beams. The illustration of angle spread over 180 degree sector is presented in Fig. 5. As seen in this figure, both left and right pictures have the same number of beams at 5 beams but their beam separations are different. The direction of beams is important to specify the value of weighting. Hence, we vary the angle separation from 10 to 40 degrees to investigate the throughput.

Fig. 6 shows the throughput of fixed weight coordinated beamforming when changing the beam separation. The results

show that the 30 degree separation offers the best throughput for fixed weight type. This can make a good agreement with the number of optimal beams at 7 beams. Because the 7 beams with 30 degree spacing can cover all area of 180 degree sector.

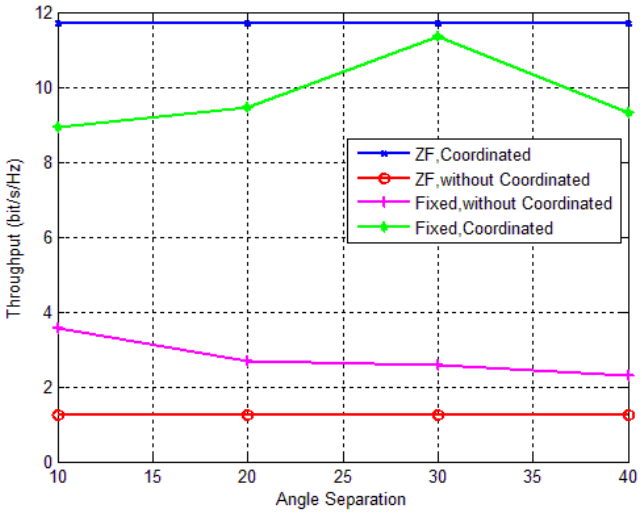

Fig.6. Average throughput of macrocell and picocells, SNR=20 dB, N = 4.

CONCLUSION

This paper presented the performance of coordinated beamforming in order to eliminate the co-channel interference. Also this paper investigates into the optimal number of beams that should be implemented. This study can be a good guidance for researcher to design the fixed weight coordinated beamforming in practice. Moreover, this paper presents the throughput of changing the angle separation between beams. The angle separation is also important to define the direction of beams and then get the weighting values.

REFERENCES

[1] Namyoon Lee; Morales-Jimenez, D.; Lozano, A.; Heath, R.W., "Spectral Efficiency of Dynamic Coordinated Beamforming: A Stochastic Geometry Approach," Wireless Communications, IEEE Transactions on , vol.14, no.1, pp.230,241, Jan. 2015

[2] Namyoon Lee; Heath, R.W.; Morales-Jimenez, D.; Lozano, A., "Coordinated beamforming with dynamic clustering: A stochastic geometry approach," Communications (ICC), 2014 IEEE International Conference on , vol., no., pp.2165,2170, 10-14 June 2014

[3] Lagen, Sandra; Agustin, Adrian; Vidal, Josep, "Decentralized Beamforming with Coordinated Sounding for Inter-Cell Interference Management," European Wireless 2014; 20th European Wireless Conference; Proceedings of , vol., no., pp.1,6, 14-16 May 2014

[4] Yuan Li; Jian Li; Li Zhang; Mugen Peng, "Adaptive heterogeneous coordinated beamforming algorithm in LTE-advanced systems," Wireless Communications and Networking Conference (WCNC), 2013 IEEE, vol., no., pp.1893,1897, 7-10 April 2013

[5] Tam, H.H.M.; Tuan, H.D.; Che, E., "Coordinated downlink beamforming in multicell wireless network," Communications and Electronics (ICCE), 2014 IEEE Fifth International Conference on , vol., no., pp.83,86, July 30 2014-Aug. 1 2014

[6] Jeongchan Kim; Youngnam Han; Seung-Hwan Lee, "An Efficient Downlink Coordinated Beamforming for Heterogeneous Networks," Vehicular Technology Conference (VTC Fall), 2013 IEEE 78th , vol., no., pp.1,5, 2-5 Sept. 2013

[7] Nagaraj, S.; Hsieh, F.; Pengoria, D.; Raghavendra, M.R.; Schamberger, M.; Honig, M., "Coordinated beamforming in clustered HetNets: System design and performance evaluation," Wireless Communications and Networking Conference Workshops (WCNCW), 2014 IEEE , vol., no., pp.70,75, 6-9 April 2014

[8] Yi Zheng; Blostein, S., "Downlink beamforming through relays: imperfect CSI and coordinated transmission," Electrical and Computer Engineering, Canadian Journal of , vol.36, no.2, pp.68,77, Spring 2013

WIMAX MULTI-HOP ACCESS NETWORK PLANNING USING MULTI-OBJECTIVE OPTIMIZATION

Chitapong Wechtaigsong[1], Teeraphan Suttithep[1] and Chutima Prommak[2]
[1]Faculty of Industrial Technology, Nakhon Ratchasima Rajabhat University
[2]Institute of Engineering, Suranaree University of Technology

ABSTRACT
Site placement is an important process for designing wireless access networks in order to optimize the investment cost and quality of services. This paper presents a novel multi-hop access network planning model for Wireless Interoperability for Microwave Access (WiMAX). The proposed model aims to assign optimal number and location of Base Stations and Relay Stations in the service areas. Integer Linear Programming is used for formulating an optimization problem which aims to minimize the installation cost and maximize the service coverage simultaneously. Numerical network planning results demonstrate that proposed model can achieve overall service area with economical implementation cost comparing with the existing works. In addition, it can efficient serve users in the target service area in under the specified budget limitation.

1. INTRODUCTION

Wireless Interoperability for Microwave Access (WiMAX) is a wireless access technology that serves broadband networks to reach target users in the remote areas. Both a high data rate and large coverage are attractive advantages of WiMAX. In country side areas where a wired broadband infrastructure cannot be provided, WiMAX is a good choice to offer broadband services. Moreover, it can be used for expanding wireless broadband services in the existing wireless networks. With the support of the IEEE 802.16j standard, the access network topology using multi-hop relay stations (RSes) can be deployed to enhance services of the base stations (BSes). The RSes can provide coverage extension to the cell boundary area, the coverage-hole area and the shadowing area (Upase and Hunukumbure, 2008). To provide low cost coverage with quality of services guarantee, network operators need an efficient technique for the wireless access network planning.

In WiMAX network planning, sites placement which include BSes and RSes installation is an important process to optimize investment cost and quality of services. If the objective of the planning is to increase the network coverage and the signal strength (Prommak and Wechtaison, 2011), many sites would be placed close to each other. This can improve the quality of services. However, it is not good in terms of investment cost. In contrast, economical objective can be attained by restricting distances between sites (Prommak and Wechtaison, 2010a; Prommak and Wechtaison, 2010b), but signal strength problem can occur. Hence, there is a tradeoff between investment cost and the quality of services in which many research groups are interested.

Our previous paper presents the multi-objective planning and the optimization problem for only BSes placement (Wechtaisong, et al., 2014). For more economical investment of the access network installation cost, the multi-hop relay station topology should be incorporated into the network structure. Therefore, the multi-objective planning and optimization model that includes both BSes and RSes placement is needed.

In this study, we examined the planning of WiMAX multi-hop access network in which the site placement for both BSes and RSes are considered. The proposed optimization model was formulated as an Integer linear programming (ILP) problem which is usually adopted by other existing research works when deal with the facility location problems. Specifially, the weighted sum method (WSM) was proposed here to solve the multi-objective optimization problem by combining two objectives and transforming them to one function to simplify the solution searching process.

The rest of paper is organized as follows. Section 2 presents the problem definition and mathematical formulation. We present the numerical experiment in Section 3 and conclude the paper in Section 4.

2. MULTI-OBJECTIVE OPTIMIZATION

2.1 PROBLEM DEFINITION

In this research presents the method for consider location for placement BSes and RSes from candidate sites along with effect of weighted value with optimization result from two opposite objectives. The first objective was minimize investment cost that considers from (Prommak and Wechtaison, 2010a; Prommak and Wechtaison, 2010b) and another one was enhance network service coverage from (Prommak and Wechtaison, 2011).

ILP was applied to formulate network planning problem. We used WSM to combine two opposite ILP objective function for easier calculation.

In the network design model, we considered that every BSes have same infrastructure and transmitting power. In addition, every RSes are considered same as each other too. Signal test points (STPs) were represented demand of users in study area. The STPs can connect with network through BS directly or via only one RS that mean maximum hop from STPs to BSes is not more than two. We guarantee quality of service in terms of receive signal strength by threshold (*Pt*).

2.2 PROBLEM FORMULATION

The WiMAX network planning problem in this research was formulated as an ILP model which consisted of three necessary parts. There were decision variables, objective functions and constraints. This model is popular to use as optimization tools for many research works. Table 1 describes the notation used in the proposed model.

Table 1 Definition of Notation Used in Proposed Model

Notations	*Definitions*
Sets:	
B	A set of candidate sites to install base stations (BSes); $(1,2,3,..,b) \subset B$
R	A set of candidate sites to install relay stations (BSes); $(1,2,3,..,r) \subset R$
T	A set of signal test points (STPs); $(1,2,3,..,t) \subset T$
Decision variables:	
β_j	A binary {0, 1} variable that equals 1 if the BS is installed at site j, $j \in B$; 0 otherwise
γ_i	A binary {0, 1} variable that equals 1 if the RS is installed at site i, $i \in R$; 0 otherwise
u_{hj}	A binary {0, 1} variable that equals 1 if the STP h is assigned to BS j, $h \in T$ and $j \in B$; 0 otherwise
v_{hi}	A binary {0, 1} variable that equals 1 if the STP h is assigned to RS i, $h \in T$ and $i \in R$; 0 otherwise
w_{ij}	A binary {0, 1} variable that equals 1 if the RS i is assigned to BS j, $i \in R$ and $j \in B$; 0 otherwise
Constant parameters:	
C_b	Cost to install base station
C_r	Cost to install relay station
P_{hj}	The signal strength that a STP h receives from BS j, $h \in T$ and $j \in B$
P_{hi}	The signal strength that a STP h receives from RS i, $h \in T$ and $i \in R$
P_{ij}	The signal strength that a RS i receives from BS j, $i \in R$ and $j \in B$
Pt	The received signal strength threshold for STPs

There were five binary decision variables in our study. Installation of BS and RS sites was represented by β_j and γ_i respectively. It equal 1 if BS or RS was installed at candidate position j or i. In contrast, it equal 0 if candidate position j or i was not chosen to install site. In addition, Connection of STPs to BSes, STPs to RSes and RSes to BSes were represented by u_{hj}, v_{hi} and w_{ij} respectively. They equal 1 if connections between their pairs were established and equal 0 if there were no connection.

We considered two different objective functions for effectively cover many side of network design problem. The first objective function aimed to minimize the network cost in terms of BS and RS installation cost which can be written as objective function (1). The second objective function aimed to maximize coverage in terms of number of STP as show in objective function (2). These objective functions would be collaborated with each other by WSM that would be explained in next topic.

We defined the network design requirement to a set of constraints. There were two groups of mathematical equations that represent purpose of radio network planning. The first group was constrains that guarantee network service coverage. Equation (3) and (4) are constraints that ensure STPs connect with only installed BSes and RSes. The guarantee of receive signal strength from installed BSes and RSes for each STPs defined in equation (5) and (6) respectively. The second group was constrains that enforce connection between BSes and RSes. Equation (7) ensures RSes connect with only one parent BS. Equation (8) is constraint that ensures RSes connect with only installed BSes. The guarantee of received signal strength for each RSes defined in equation (9).

Objective functions:

$$minimize \sum_{j=1}^{b} C_b \times \beta_j + \sum_{i=1}^{r} C_r \times \gamma_j \quad (1)$$

$$maximize \sum_{j=1}^{b} u_{hj} + \sum_{i=1}^{r} v_{hi} \quad ,\forall h \epsilon\, T \quad (2)$$

Subject to:

C1: Network service coverage

$$u_{hj} \leq \beta_j \quad ,\forall h \epsilon T, j \epsilon B \quad (3)$$

$$v_{hi} \leq R_i \quad ,\forall h \epsilon T, i \epsilon R \quad (4)$$

$$u_{hj}(P_{hj} - Pt) \geq 0 \quad ,\forall h \epsilon T, j \epsilon B \quad (5)$$

$$v_{hi}(P_{hi} - Pt) \geq 0 \quad ,\forall h \epsilon T, i\, \epsilon R \quad (6)$$

C2: BS-RS connections

$$\sum_{j=1}^{b} w_{ij} = \gamma_i \quad ,\forall i \epsilon R \quad (7)$$

$$w_{ij} \leq \beta_j \quad ,\forall i \epsilon R, j \epsilon B \quad (8)$$

$$v_{hi}(P_{hi} - Pt) \geq 0 \quad ,\forall i \epsilon R, j \epsilon B \quad (9)$$

2.3 COMBINATION OF OBJECTIVE FUNCTIONS

In this topic, we developed multi-objective optimization mathematical equation for ILP. The tradeoff between two opposite objective function is considered. There were objectives that minimize network implementation cost and increase network coverage. The WSM is necessary tool for study tradeoff between two difference objective function. We explained detail of combination two objective functions by WSM method in our existing paper (Wechtaisong, et al., 2014).

To divisibly combine two different objectives, the maximization objective of equation (2) was reversed to minimization objective in equation (10) which t was amount of total STPs in study area however it still was same as original meaning. The final equation of multi objective optimization by WSM is shown in (11).

Reverse form of equation (2):

$$minimize \ \ t - (\sum_{j=1}^{b} u_{hj} + \sum_{i=1}^{r} v_{hi}) \quad ,\forall h \epsilon T \quad (10)$$

Final WSM multi-objective function:

$$minimize \ W_1 \left[\frac{\left(\sum_{j=1}^{b} C_b \times \beta_j + \sum_{i=1}^{r} C_r \times \gamma_j\right) - {f_1}^{min}}{{f_1}^{max} - {f_1}^{min}} \right] + W_2 \left[\frac{\left(t - \left(\sum_{j=1}^{b} u_{hj} + \sum_{i=1}^{r} v_{hj}\right)\right) - {f_2}^{min}}{{f_2}^{max} - {f_2}^{min}} \right] \quad ,\forall h \epsilon T \quad (11)$$

3. NUMERICAL EXPERIMENTS

3.1 PARAMETER SETUP

In numerical experiments, we designed 10km x 10km as study area. There are 45 candidate positions for BS and RS sites installation. The number of STPs was 100. We used the Stanford University Interim (SUI) model which was recommended by the IEEE 802.16 to obtain the path loss in WiMAX networks (Erceg, et al., 2001). Received signal threshold at RSes and STPs were set at -91.4 dBm and -93.9 dBm respectively (WiMAX Forum, 2010). Implement cost of each BS was $120,000 (Prommak and Wechtaison, 2011) and cost of RS was 40% of BS (Upase and Hunukumbure, 2008). Table 2 shows the parameters used in numerical experiments (WiMAX Forum, 2010). Positions of candidate sites and STPs were simulated which spread over study area with uniform random as shows in (Wechtaisong, et al., 2014).

Table 2 Parameters Used in Numerical Experiments

Parameters	Value
Height of BSes	40 m
Height of RSes	12 m
Height of TPs	1.5 m
Transmitted Power (BS)	43 dBm
Transmitted Power (RS)	39dBm
Transceived antenna gain (BS)	15dBi
Transceived antenna gain (RS)	7 dBi
Transceived antenna gain (STP)	0 dBi
Frequency	3.5 GHz
Terrain type	A
Bandwidth	10 MHz
Cost of each base station	120,000 $
Cost of each relay station	48,000 $

3.2 NUMERICAL RESULTS

The numerical experiments were implemented with the ILOG-OPL development studio same as in (Prommak and Wechtaison, 2010a; Prommak and Wechtaison, 2010b; Prommak and Wechtaison, 2011; Wechtaisong, et al., 2014). The ILP problems were solved with CPLEX 5.2 optimization solver. The computation was run on an Intel Centrino Core2 Duo Processor 2.0 GHz and 2.0 GB of RAM. The network performance was evaluated in term of the physical receive signal strength guarantee at the specified parameters.

Weighted values were set to change 0.25 for each step, W_1 decrease from 1.0 to 0.0 and W_2 increase from 0.0 to 1.0, to consider the tradeoff results between conflict objectives. From position of candidate site as decision variable in table 1 with muti-objective function in equation (14) and constraint equations (3)-(9), this numerical information were inserted to calculation method. We compare experiment of WiMAX multi-hop network planning in this study with WiMAX single hop network planning in our existing study (Wechtaisong, et al., 2014). The numerical results of WiMAX network planning in terms of site placement by ILP and WSM are shown in table 3.

Table 3 Results of Network Planning Experiment

W_1	W_2	Multi-hop network				Single hop network		
		BS	RS	STP	Cost (M$)	BS	STP	Cost (M$)
1.00	0.00	0	0	0	0.000	0	0	0.000
0.75	0.25	6	1	82	0.768	6	79	0.720
0.50	0.50	10	2	99	1.296	10	96	1.200
0.25	**0.75**	**10**	**4**	**100**	**1.392**	**13**	**100**	**1.560**
0.00	1.00	45	29	100	6.792	45	100	5.400

3.3 ANALYSIS AND DISCUSSION

In table 3, W_1 and W_2 represent weighted values of objective function 1 and objective function 2 respectively. In case of W_1 equal 0.25 and W_2 equal 0.75, both the multi-hop network planning scenario and the single hop network planning scenario can efficient optimize installation cost and serve signal coverage for every STPs in study area. From 45 candidate site for installing BSes and RSes, our purposed scheme use only 10 BSes and 4 RSes to serve WiMAX signal for overall experimental area. In addition, investment cost of our purpose scheme is cheaper than our existing scheme that has to deploy 13 BSes for overall coverage. For another scenario of weighted values, installation cost and percent coverage of STPs are related with W_2. In the other hand, they are inversely related with W_1.

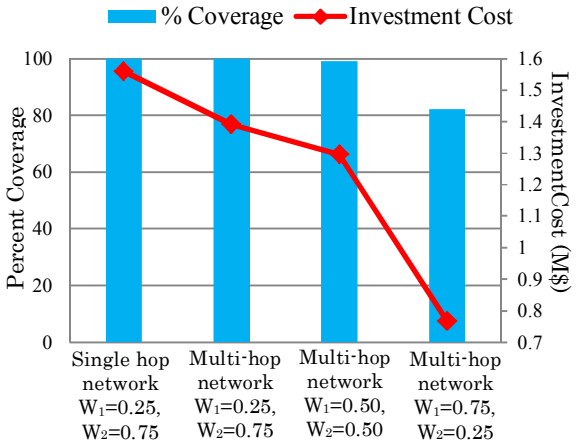

Fig. 1. Coverage and investment cost of existing scheme and proposed scheme in various weighted values.

Figure 1 shows coverage and investment cost comparing between single hop network planning in our existing work and multi-hop network planning in this research. Both of them can achieve 100% of STPs with weighted value W_1 and W_2 equal 0.25 and 0.75

respectively. However, when consider site installation cost of these schemes, our multi-hop network planning scheme can reduce 10% of investment cost. For the scenario that weighted values W_1 and W_2 equal 0.75 and 0.25 respectively, our purposed scheme still efficient save 45% investment cost by reduce only 18% of serviced coverage.

From these results, our purposed scheme can efficient optimize network planning in term of BSes and RSes placement. In case of signal coverage guarantee, it can provide service to every STPs in designing area. Moreover, it can effectively optimize installation cost and coverage area in case of budget limitation.

4 CONCLUSION

This study presents a novel mathematical model for an efficient optimization planning of WiMAX multi-hop access network which RSes can extend services of BSes for economize network installation cost. We formulate the problem as integer linear programming problem with consideration of two opposite objectives which are minimize the installation cost and maximize service coverage. In particular, we use weighted sum method to transform two objectives to single objective and compare effect of weighting value in each one. In addition, the proposed model can determine optimal numbers and locations for BSes and RSes installation. The numerical results illustrate that our WiMAX multi-hop access network planning model can achieve overall coverage in study area. In case of limited budget, our model can produce optimized configuration which still achieve almost coverage. Simulation result is the limitation of this study. However, we will conduct experiment in realistic study area and consider another optional constrains in our future work.

REFERENCES

Erceg V., Hari K.V.S., Smith M.S., Baum D.S., Sheikh K.P., Tappenden C., Costa J.M., Bushue C., Sarajedini A., Schwartz R., Branlund D., Kaitz T., Trinkwon D., Channel Models for Fixed Wireless Applications, *IEEE 802.16 Broadband Wireless Access Working Group*, 2001

Prommak C. and Wechtaison C., WiMAX Network Design and Optimization Using Multi-hop Relay Stations, *the 10th International Conference on Applied Informatics and Communications (AIC)*, pp. 75-80, 2010a.

Prommak C. and Wechtaison C., WiMAX Network Design for Cost Minimization and Access Data Rate Guarantee Using Multi-hop Relay Stations. *International Journal of Communications, vol*4: pp.36-46, 2010b.

Prommak C. and Wechtaison C., On the quality of service optimization for WiMAX networks using multi-hop relay stations. *Communication in Computer and Information Science, Springer-Verlag Berlin Heidelberg,* pp.93-106, 2011.

Upase B., Hunukumbure M., Dimensioning and cost analysis of multihop-relay-enabled WiMAX networks. *Fujitsu Science Technology Journal,* vol.43, pp.303-307, 2008.

Wechtaisong C., Sutthitep T., Prommak C. Multi-objective planning and optimization for base station placement in WiMAX network, *the 11th International Conference on Electrical Engineering/Electronics, Computer, Telecommunications and Information Technology (ECTI-CON2014),* pp. 1-4, 2014.

WiMAX Forum., Requirement and Recommendations for Multi-hop Relay profile of WiMAX networks, pp. 1-35, 2010.

ACKNOWLEDGEMENT

The authors would like to thanks Assoc. Prof. Hiroaki Morino and Prof. Atsuko K. Yamazaki at Shibaura Institute of Technology for their useful advice. We also would like to extend our gratitude to the Wireless Communication Laboratory, Suranaree University of Technology for their support throughout this study.

Chitapong Wechtaisong received B.Eng (2006) and M.Eng (2011) in Telecommunication Engineering from Suranaree University of Technology, Thailand. Currently he is teaching staff of Faculty of Industrial Technology, Nakhon Ratchasima Rajabhat University. His research interest includes wireless access network optimization and P2P traffic localization.

Teeraphan Suttitep received B.Eng (1997) in Telecommunication Engineering and M.Eng. (2004) in Electrical Engineering from Suranaree University of Technology, Thailand. Currently he is teaching staff of Faculty of Industrial Technology, Nakhon Ratchasima Rajabhat University.

Chutima Prommak received B.Eng (Hons) in Electrical Engineering from Khon Kaen University, Thailand in 1992. She received M.Sc. and Ph.D. in Telecommunications from University of Colorado at Boulder, CO, USA in 1998 and University of Pittsburgh, PA, USA in 2004, respectively. Currently she is an assistant professor in Suranaree University of Technology, Thailand. Her research interests are in the areas of wireless network design and planning, network optimization, WiMAX, wireless sensor networks and heuristic optimization for telecommunication network

South East Asian Technical University Consortium (SEATUC)
Suranaree University of Technology
111 University Avenue, Sub District Suranaree,
Muang District, Nakhon Ratchasima 30000, Thailand

ISSN 1882-5796